Geologic, Hydrothermal, and Biologic Studies at Escanaba Trough, Gorda Ridge, Offshore Northern California

U.S. GEOLOGICAL SURVEY BULLETIN 2022

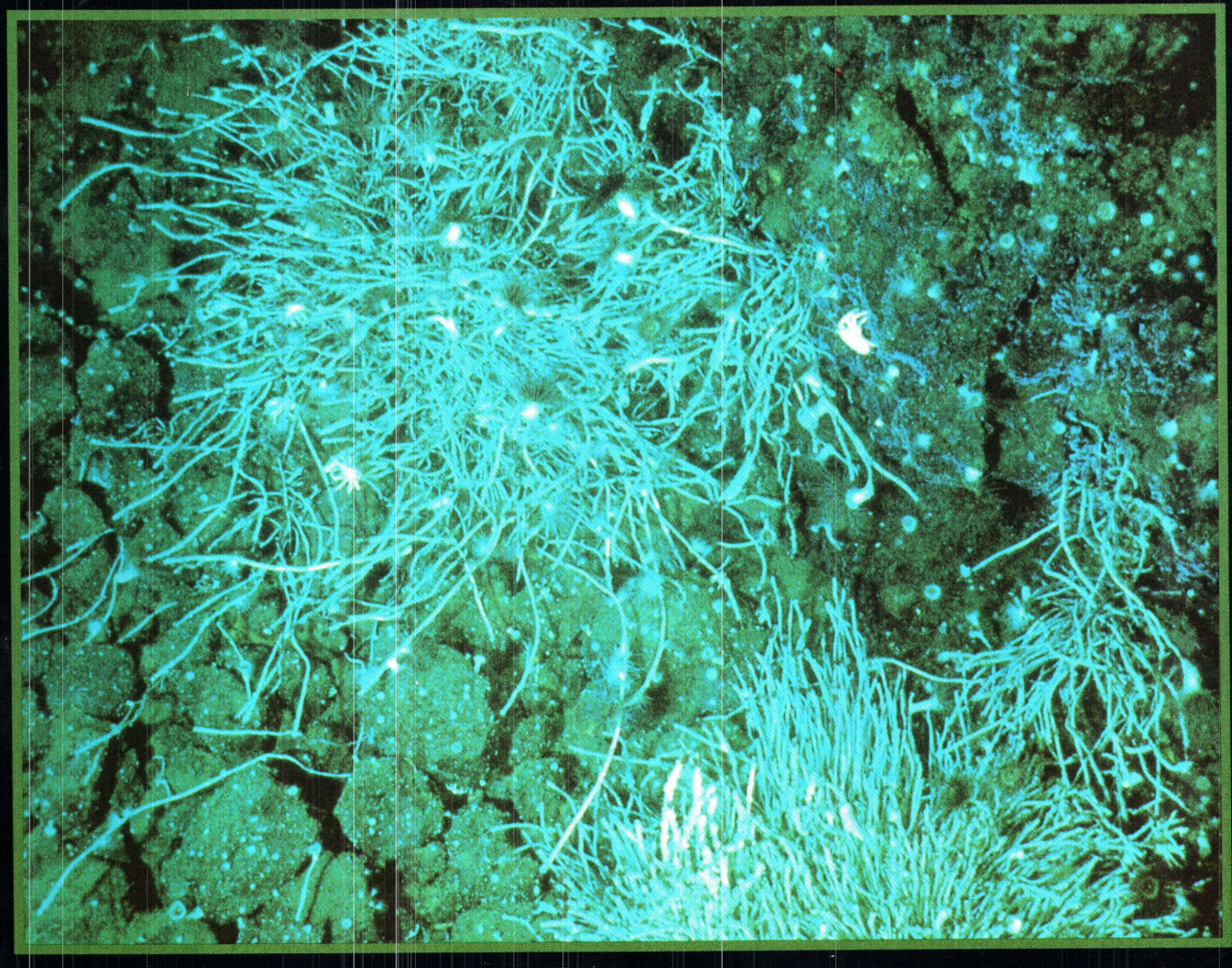

Cover—Photograph of massive sulfide mound in the NESCA area in the Escanaba Trough, offshore of northern California, depth 3232 m. Diffuse venting of hydrothermal fluid through pyrrhotite-rich massive sulfide rubble supports a hydrothermal vent community dominated by tube worms. The tubeworms are colonized by vent-specific anemones with red tentacles, white galatheid crabs and clumps of white filamentous bacteria. The white spots on the massive sulfide are gastropods and limpets; bluish filaments on massive sulfide may be colonies of the protozoan *Girvanella*. Photograph taken from the bow camera of the *Alvin* submersible; field of view is approximately 2 m across.

Geologic, Hydrothermal, and Biologic Studies at Escanaba Trough, Gorda Ridge, Offshore Northern California

JANET L. MORTON, ROBERT A. ZIERENBERG, and CAROL A. REISS, Editors

U.S. GEOLOGICAL SURVEY BULLETIN 2022

U.S. DEPARTMENT OF THE INTERIOR

BRUCE BABBITT, *Secretary*

U.S. GEOLOGICAL SURVEY

Gordon P. Eaton, *Director*

For sale by
U.S. Geological Survey, Map Distribution
Box 25286, MS 306, Federal Center
Denver, CO 80225

Library of Congress Cataloging-in-Publication Data

Geologic, hydrothermal, and biologic studies at Escanaba Trough, Gorda Ridge, offshore northern California / Janet L. Morton, Robert A. Zierenberg, and Carol A. Reiss, editors.
p. cm. — (U.S. Geological Survey bulletin ; 2022)
Includes bibliographical references.
1. Geology—Escanaba Trough. 2. Hydrothermal vents—Escanaba Trough. 3. Hydrothermal vent fauna—Escanaba Trough. 4. Escanaba Trough. I. Morton, Janet L. II. Zierenberg, Robert A. III. Reiss, Carol A. IV. Series.
QE75.B9 no. 2022
[QE350.42.N65]
557.3 s—dc20
[551.46'08'09432]
94-13924

CIP

CONTENTS

FIGURES

TABLES

Chapter 1. Geologic, Hydrothermal, and Biologic Studies at Escanaba Trough: An Introduction

By Janet L. Morton, Robert A. Zierenberg, *and* Carol A. Reiss[1]

CONTENTS

INTRODUCTION

The discovery of sea-floor hot springs at Galápagos Rise in 1977 (Corliss and others, 1979) confirmed the predictions of hydrothermal venting at oceanic spreading centers, which had been inferred from several lines of evidence, including low heat flow near mid-oceanic ridges (Elder, 1965; Talwani and others, 1971; Lister, 1972; Sclater and Klitgord, 1973; Williams and others, 1974), metalliferous deep-sea sediments (Boström and Peterson, 1966; Boström, 1973), chemical tracers in the water column (Weiss and others, 1977; Lupton and others, 1977; Klinkhammer and others, 1977; Bolger and others, 1978), near bottom temperature anomalies (Detrick and others, 1974; Rona and others, 1975), and hydrothermal alteration and mineralization in ophiolites (Sillitoe, 1972; Spooner and Fyfe, 1973; Duke and Hutchinson, 1974; Spooner and Bray, 1977). The hydrothermal vents at Galápagos Rise were low temperature (less than about 20°C) and were surrounded by exotic biologic communities. In the following two years, massive sulfide deposits (Francheteau and others, 1979) and high-temperature vents (about 350°C) (RISE, 1980) were discovered on the East Pacific Rise near latitude 21° N., and in subsequent years, additional vents and deposits were located at many locations in the Pacific and Atlantic Oceans. These hydrothermal systems have been the focus of intense interdisciplinary studies of fundamental problems such as the formation of mineral deposits, the chemical and thermal effects of vents on the ocean, alteration of oceanic crust, and interaction of vent animals and hydrothermal fluids.

In 1979, the U.S. Geological Survey (USGS) began a project to study volcanic, tectonic, and hydrothermal processes at oceanic spreading centers. Much of the work has been conducted in the northeast Pacific Ocean, in conjunction with research programs conducted by the National Oceanic and Atmospheric Administration (NOAA), various academic institutions, and foreign government agencies. With the declaration of the U.S. Exclusive Economic Zone (EEZ) in 1983, much of the USGS effort became focused on Gorda Ridge (fig. 1.1), the only mid-oceanic ridge spreading center located within the U.S. EEZ. Two sites at Gorda Ridge became the focus of multi-institutional studies: northern Gorda Ridge at a locale where water column chemical anomalies indicated regional hydrothermal venting (Baker and others, 1987) and at Escanaba Trough, southern Gorda Ridge, where the spreading axis is buried by several hundred meters of sediment.

Mid-oceanic ridges can be classified as sediment starved or sediment dominated. Owing to their setting far from continental sediment sources, most mid-oceanic ridges, including the northern Gorda Ridge, fall into the sediment-starved category. Hydrothermal systems at these ridges reflect the interactions of the two-component system basalt-seawater, and the resulting hydrothermal deposits are fairly similar in form and composition at various locations (Bischoff and others, 1983; Kappel and Franklin, 1989). A blanket of sediment covering the ridge crest changes the thermal, hydrologic, and chemical regime, and can have major effects on the composition of the hydrothermal fluids and on the process of venting hydrothermal fluid to the sea floor. These effects are reflected in the form and composition of the resulting hydrothermal deposits. Sediment-dominated ridges are relatively uncommon, and hydrothermal systems at sediment-dominated ridges have been studied at only a few locations. At Guaymas Basin in the Gulf of California, hydrothermal products reflect the organic-rich composition of the sediment (Lonsdale and others, 1980; Simoneit and Lonsdale, 1982; Koski and others, 1985). At both Middle Valley (northern Juan de Fuca

[1] U.S. Geological Survey, Menlo Park, California.

Ridge) and Escanaba Trough, turbiditic and hemipelagic sedimentary rocks host the hydrothermal deposits. The papers in this volume describe the results of studies made during 12 cruises to Escanaba Trough, mostly between 1985 and 1989. Collectively, they represent one of the most comprehensive studies to date of geologic, hydrothermal, and biologic processes at a sedimented spreading center.

ACKNOWLEDGMENTS

This work represents the efforts of many people located at several institutions and was possible only as a result of close cooperation and coordination. We thank all of the authors who contributed chapters to the volume. We are especially grateful to the captains and crews of the various vessels listed in table 1.1 that supported work in Escanaba Trough. We gratefully acknowledge the expert drafting assistance of Phyllis Swenson and Brigitta Fulop.

GEOLOGIC SETTING OF ESCANABA TROUGH

Gorda Ridge is located in the northeast Pacific Ocean, 200 to 300 km west of northern California and Oregon (fig. 1.1). It is bounded to the north by the Blanco Fracture Zone and to the south by the Mendocino Fracture Zone.

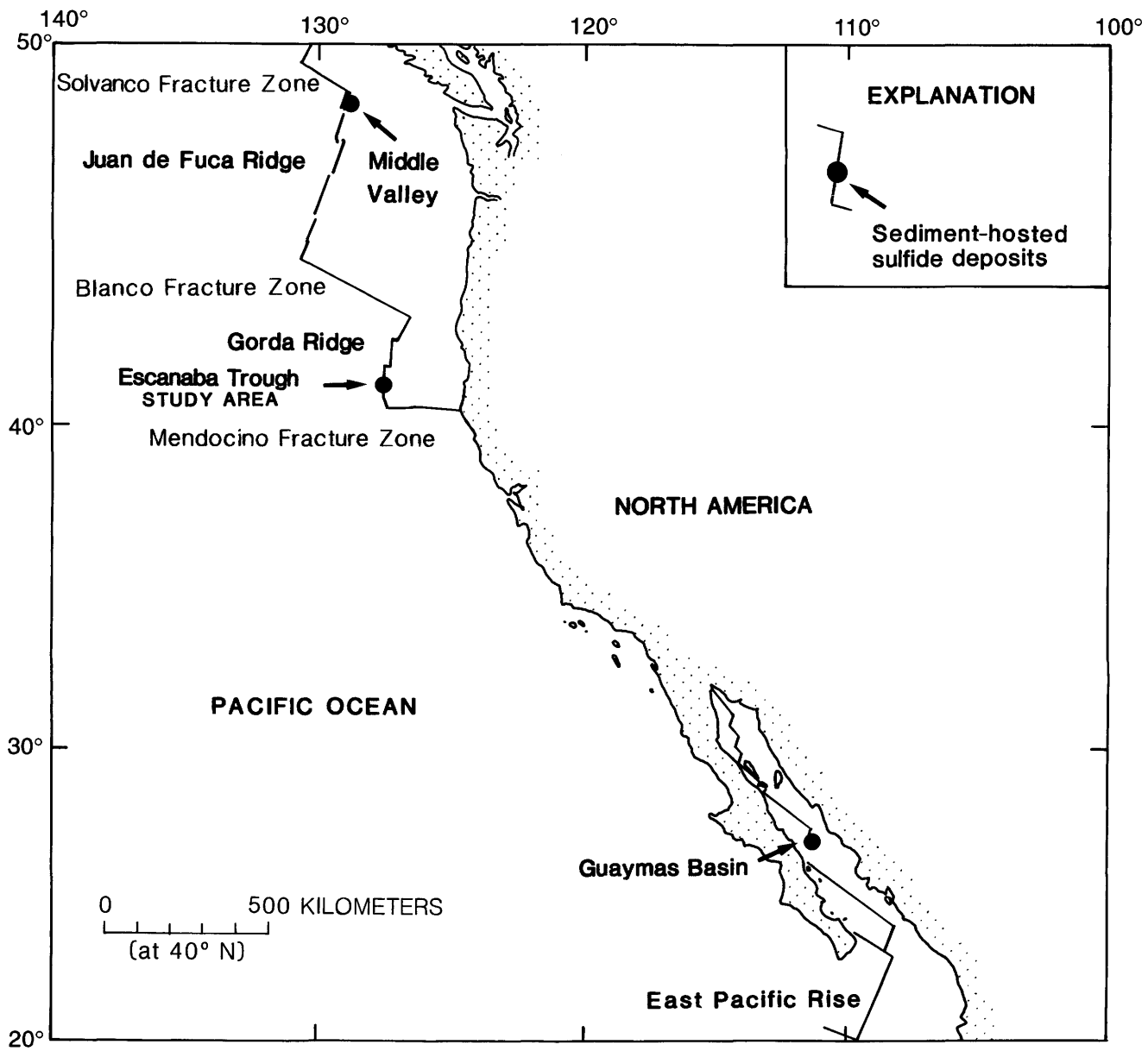

Figure 1.1. Location map showing Gorda Ridge and other mid-oceanic ridge spreading centers in northeast Pacific Ocean.

Table 1.1. Cruises to Escanaba Trough that contributed to this study.

Cruise ID	Year	Vessel	Type of studies reported in this volume
L12-81-NC	1981	R/V *S.P. Lee*	Multi-channel seismic reflection profiling
KK2-83-NP	1983	R/V *Kana Keoki*	Dredging
L6-85-NC	1985	R/V *S.P. Lee*	Single-channel seismic reflection profiling, magnetics profiling, sediment coring, dredging
MMS-86-1	1986	NOAA ship *Surveyor*	Sea Beam bathymetric mapping
N1-86-NC	1986	USNS *Narragansett*	Bathymetric profiling, camera tows
L1-86-NC	1986	R/V *S.P. Lee*	Bathymetric profiling, single-channel seismic reflection profiling, camera tows, dredging, sediment coring
L2-86-NC	1986	R/V *S.P. Lee*, DSV *Sea Cliff*	Bathymetric profiling, camera tows, dredging, sediment coring, submersible dives
L3-86-NC	1986	R/V *S.P. Lee*	Dredging, sediment coring
T1-86-NC	1986	R/V *Transquest*, DSV *Sea Cliff*	Submersible dives
A2-88-NC	1988	R/V *Atlantis II*, DSV *Alvin*	Submersible dives
C1-88-NC	1988	M/V *Laney Chouest*, DSV *Sea Cliff*	Submersible dives
TUL-89D	1989	R/V *Tully*	Sediment coring, heat flow measurements, single-channel seismic reflection profiling

Gorda Ridge and Juan de Fuca Ridge, located to its north, are remnants of the Pacific-Farallon spreading center and form the present-day accreting plate boundary between the Pacific and Juan de Fuca plates. The spreading rate at Gorda Ridge varies from medium (about 5.5 cm/yr) at the northern end to slow (about 2.4 cm/yr) at the southern end (Atwater and Mudie, 1973; Riddihough, 1980; Wilson, 1989). The ridge displays a Mid-Atlantic Ridge style morphology with a deep axial valley (2,500 to 3,300 m water depth) and flanking ridges that rise to as shallow as 1,500 m.

Right-lateral offsets near latitudes 42°26′ N. and 41°37′ N. divide Gorda Ridge into three segments (fig. 1.1; Clague and Holmes, 1987). The northern segment trends north-northeast, normal to the Blanco Fracture Zone, and the southern segment trends approximately north-south, normal to the Mendocino Fracture Zone. The trend of the middle segment is less well defined but is generally between that of the northern and southern segments.

Escanaba Trough occupies the southern, north-south-trending segment of Gorda Ridge. At the northern end of the trough, the axial valley is only a few kilometers wide, but it widens to about 18 km at the south. As the ridge approaches the Mendocino Fracture Zone, it curves to the east (Clague and Holmes, 1987; EEZ-SCAN 84 Scientific Staff, 1986). Immediately north of the Mendocino Fracture Zone, the topographic expression of the ridge disappears, and the zone of active extension is marked by a region of extensional faulting detectable on seismic-reflection profiles (Clague and Holmes, 1987; Morton and Fox, chap. 2, this volume).

The absence of a topographic ridge at the southern end of Escanaba Trough has allowed turbidity currents to enter and flow northward along the trough (Vallier and others, 1973). Consequently, south of about latitude 41°17′ N. most of the axial valley floor is sediment covered. At the southern end of the trough, sediment thickness may reach 900 m (Clague and Holmes, 1987). Hemipelagic sediment is interbedded with the turbidites (McManus and others, 1970; Karlin and Lyle, 1986; Normark and others, chap. 6, this volume). Volcanic bodies pierce the sediment fill at several localities along the trough (fig. 1.2; Moore and Sharman, 1970; Clague and Holmes, 1987; Morton and others, 1987a).

HISTORY OF WORK AT ESCANABA TROUGH

McManus (1964) named the median valley of southern Gorda Ridge Escanaba Trough. Wilde and others (1978) compiled the locations of early seismic profiles, underway geophysical lines, sediment samples, and heat-flow stations in the Gorda Ridge area. Early work in the area included topographic and sedimentologic studies, summarized by McManus (1967), and magnetic surveying by Raff and Mason (1961). Vine and Matthews (1963) interpreted the axis-parallel linear magnetic anomalies in this region to be the result of sea-floor spreading. McManus (1967) noted that the flat floor of southern Escanaba Trough results from a partial filling of the valley by sediment. Heat-flow measurements obtained near Gorda Ridge (Dehlinger, 1969) indicated that the region is characterized by high heat flow, and seismic-refraction work (Raitt, 1963) indicated low mantle velocities beneath the ridge.

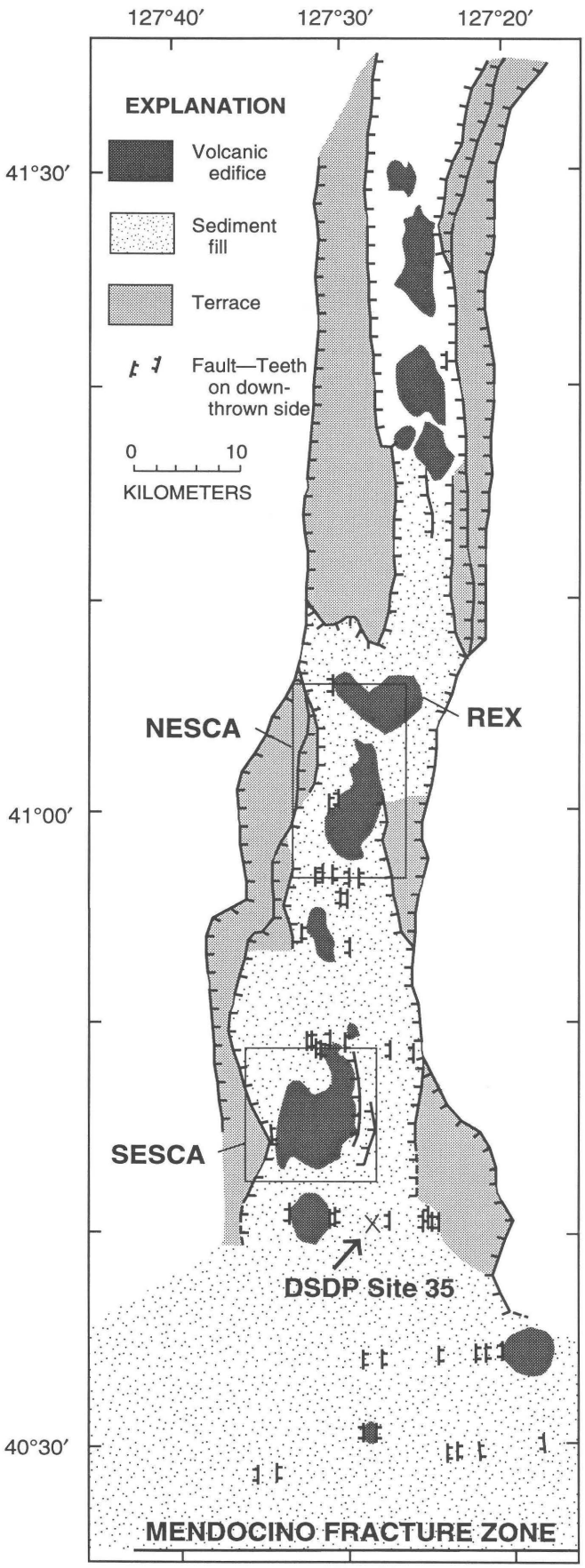

Atwater and Mudie (1973) used a deep-towed survey (side-scan sonar and subbottom profiling) to describe the details of block faulting within one area of the axial valley.

Escanaba Trough was chosen as Site 35 of the Deep Sea Drilling Program (DSDP) because the sediment cover permitted drilling at the axis of a mid-oceanic ridge. Site-survey seismic-reflection profiles indicated that the sediment cover averages about 500 m in thickness and is cut by several faults (Moore and Sharman, 1970; Moore, 1970). A low ridge visible on the seismic records was interpreted by Moore and Sharman (1970) as a volcanic ridge at the axis of the trough. Drilling at DSDP Site 35 (fig. 1.2) penetrated 395 m of predominantly Pleistocene turbidites without reaching basement rock (McManus and others, 1970). Vallier and others (1973) examined sand grains from turbidites in selected cores of Site 35 and concluded that much of the sediment is derived from the Klamath and Columbia River drainage basins.

In 1981, three 24-channel seismic-reflection profiles were collected over Escanaba Trough. Hyperbolic reflectors within the sediment fill at the center of the trough were interpreted as sills (Clague and others, 1984; Clague and Holmes, 1987).

The work reported in this volume was conducted primarily between 1985 and 1989. In 1985, cruise L6-85-NC, of the research vessel *S.P. Lee,* jointly sponsored by the USGS and the Gorda Ridge Technical Task Force, conducted a reconnaissance geophysical and sampling study at Escanaba Trough. Seismic-reflection profiles identified several discrete volcanic edifices, spaced at about 15 km intervals, that intrude the sediment fill (Morton and others, 1987a). High heat-flow values (up to 1,600 mW/m^2) measured at two of the volcanic edifices were interpreted to indicate flow of hydrothermal fluids through the sediment (Abbott and others, 1986). Pyrrhotite-rich massive sulfide samples and a sediment sample impregnated with petroleum and interlayered with massive sulfide were recovered from one of the edifices (Kvenvolden and others, 1986; Morton and others, 1987a; Koski and others, 1988).

Two volcanic edifices were selected for more detailed follow-up studies on several cruises from 1986 to 1989. The northern Escanaba Trough study area (NESCA) (fig. 1.3) is located near latitude 41°00′ N., longitude 127°30′ W. (fig. 1.2), and the southern Escanaba Trough study area (SESCA) (fig. 1.4) is located near latitude 40°45′ N., longitude 127°30′ W. (fig. 1.2). The purpose of these cruises was to determine the location, form, and composition of hydrothermal deposits, the geologic setting and structural controls of the deposits, the nature of active venting, and

Figure 1.2. Generalized geologic map of Escanaba Trough showing location of volcanic edifices, approximate extent of sediment fill, location of terraces, NESCA and SESCA study areas (rectangles), location of edifice REX, and location of DSDP Site 35.

the type of biological communities associated with hydrothermal vents and deposits. Studies conducted during these cruises included bathymetric surveying, seismic-reflection profiling, sea-floor photography, dredging, sediment coring, and submersible dives. A total of 26 dredge hauls, 22 camera stations (figs. 1.5, 1.6) and 22 submersible dives were conducted in the NESCA and SESCA areas (figs. 1.7, 1.8). In addition, 33 sediment cores (see Normark and others, chap. 6, this volume) and approximately 1,350 km of seismic-reflection data (see Morton and Fox, chap. 2, this volume; Davis and Becker, chap. 3, this volume) have been collected at Escanaba Trough.

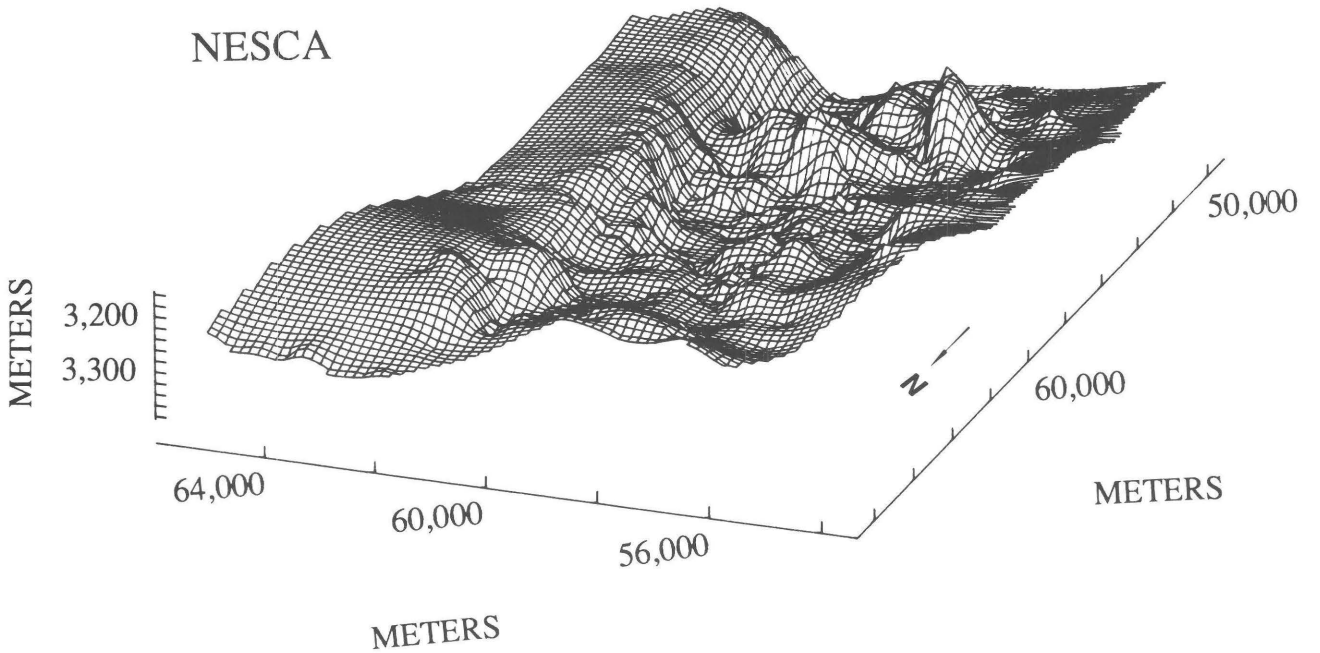

Figure 1.3. Bathymetric relief map of axial valley floor of Escanaba Trough at NESCA area, viewed from northwest. Notations along horizontal axes are coordinates of local transponder net, in meters. Axial valley floor is bounded to east and west by low terraces, most prominent here on the east (left). Valley floor at NESCA area is characterized by two major hills with relief of about 100 m and several smaller features.

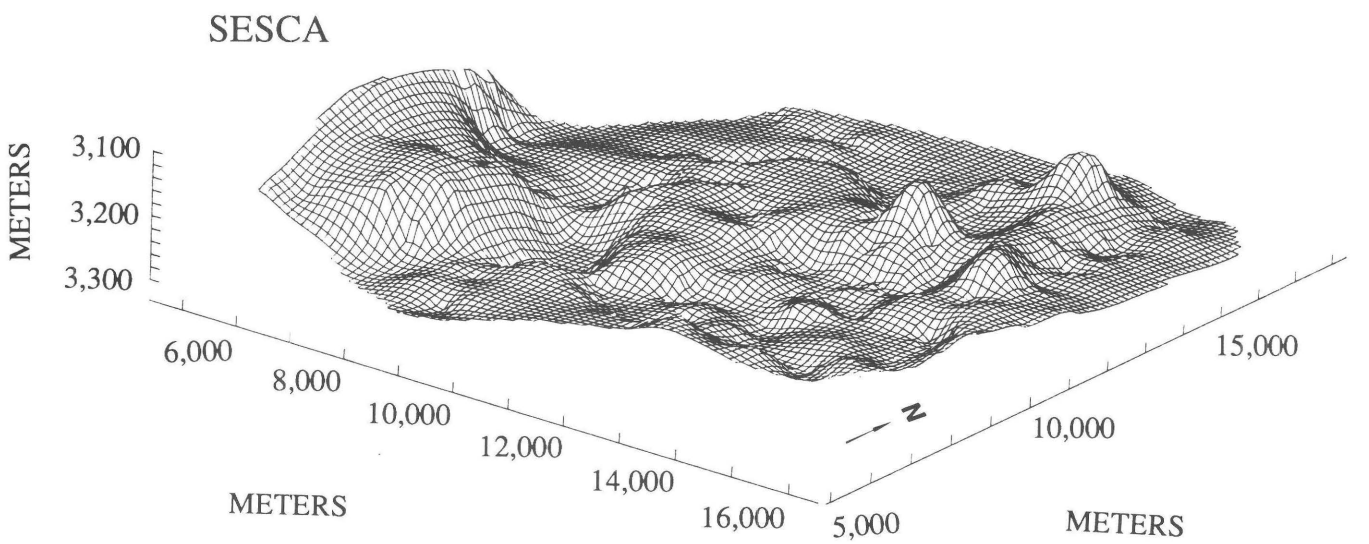

Figure 1.4. Bathymetric relief map of axial valley floor of Escanaba Trough at SESCA area, viewed from southeast. Notations along horizontal axes are coordinates of local transponder net, in meters. Three prominent hills are located near east (right) side of area. High region on left is part of west wall that bounds axial valley floor.

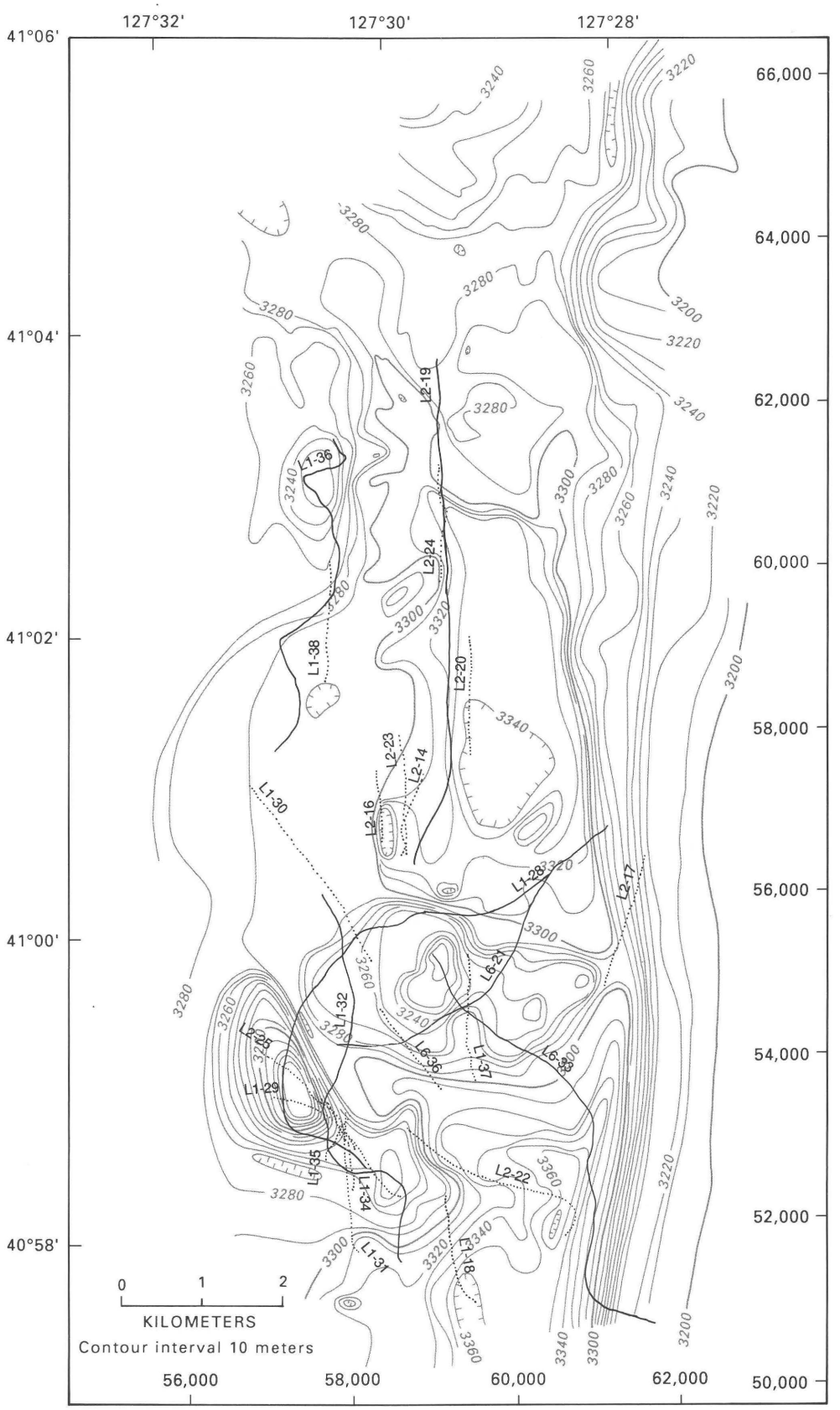

Figure 1.5. Bathymetric map of NESCA area showing location of 6 camera tows (solid lines) and 17 dredge hauls (dotted lines). Numbers along right and bottom give coordinates of local transponder net (in meters). Hachures indicate area of closed low.

Sea Beam swath bathymetric surveying of most of Escanaba Trough was conducted in 1986, but was classified until 1989 (Morton and Fox, chap. 2, this volume). Conventional bathymetric surveys of the SESCA and NESCA areas with line spacings of approximately 300 m were also conducted in 1986 (Morton and others, 1987b). The bathymetric maps of the NESCA and SESCA areas used to show station locations in most chapters in this volume are based on the conventional bathymetric surveying, with minor modifications based on submersible dive profiles and Sea Beam mapping. Although the Sea Beam maps reveal considerable more detail of the sea-floor morphology, the relative positions of major bathymetric features in the SESCA and NESCA areas are distorted owing to inaccuracies in the Loran C navigation used during the survey. The conventional bathymetric surveys were navigated using the same acoustic transponder nets used for all sampling stations, camera tows, and submersible dives, and thus the relative positions of sampling stations and major bathymetric features are more accurately depicted using these conventional bathymetric maps.

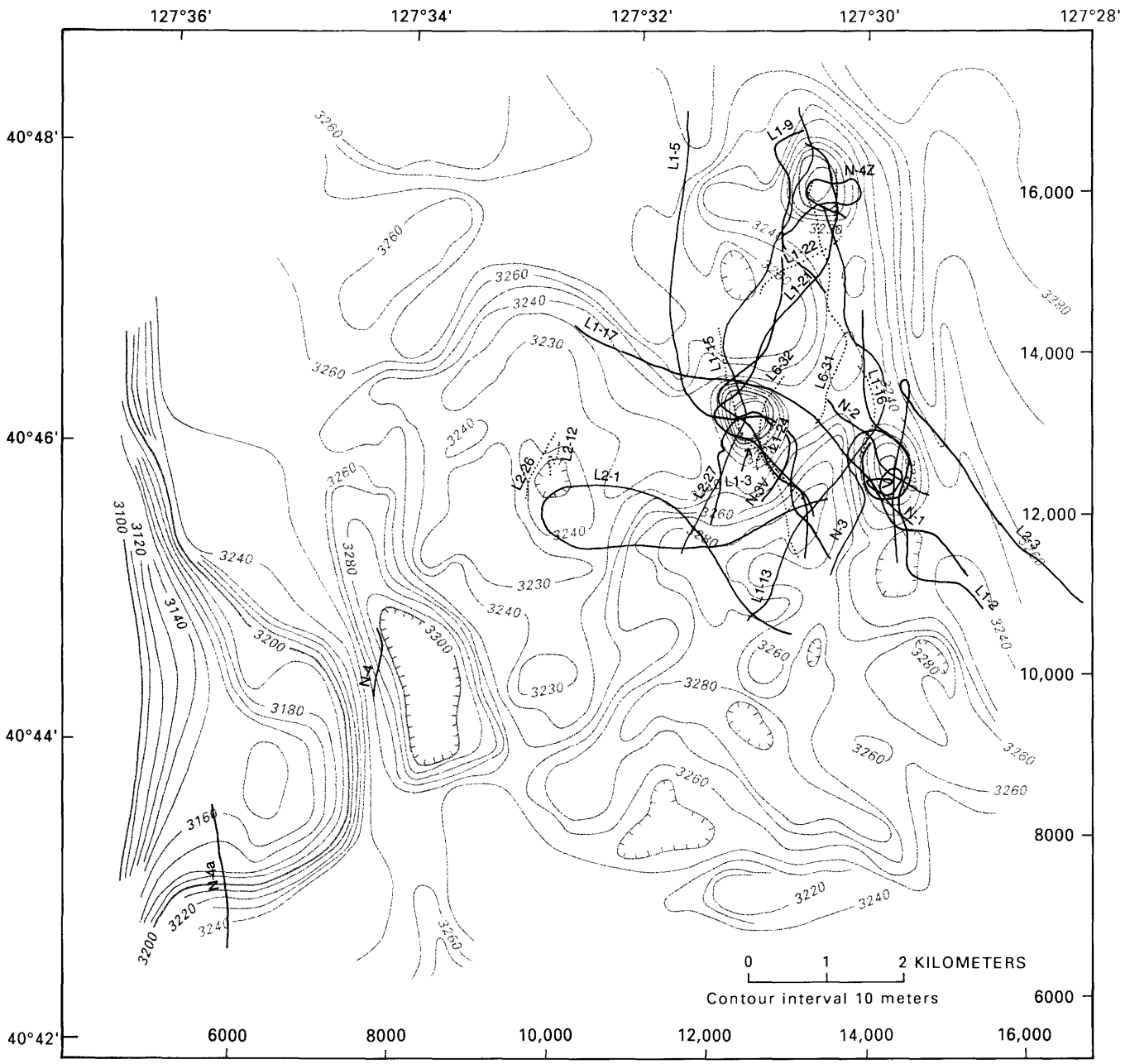

Figure 1.6. Bathymetric map of SESCA area showing location of 16 camera tows (solid lines) and 9 dredge hauls (dotted lines). Numbers along right and bottom give coordinates of local transponder net (in meters). Hachures indicate area of closed low.

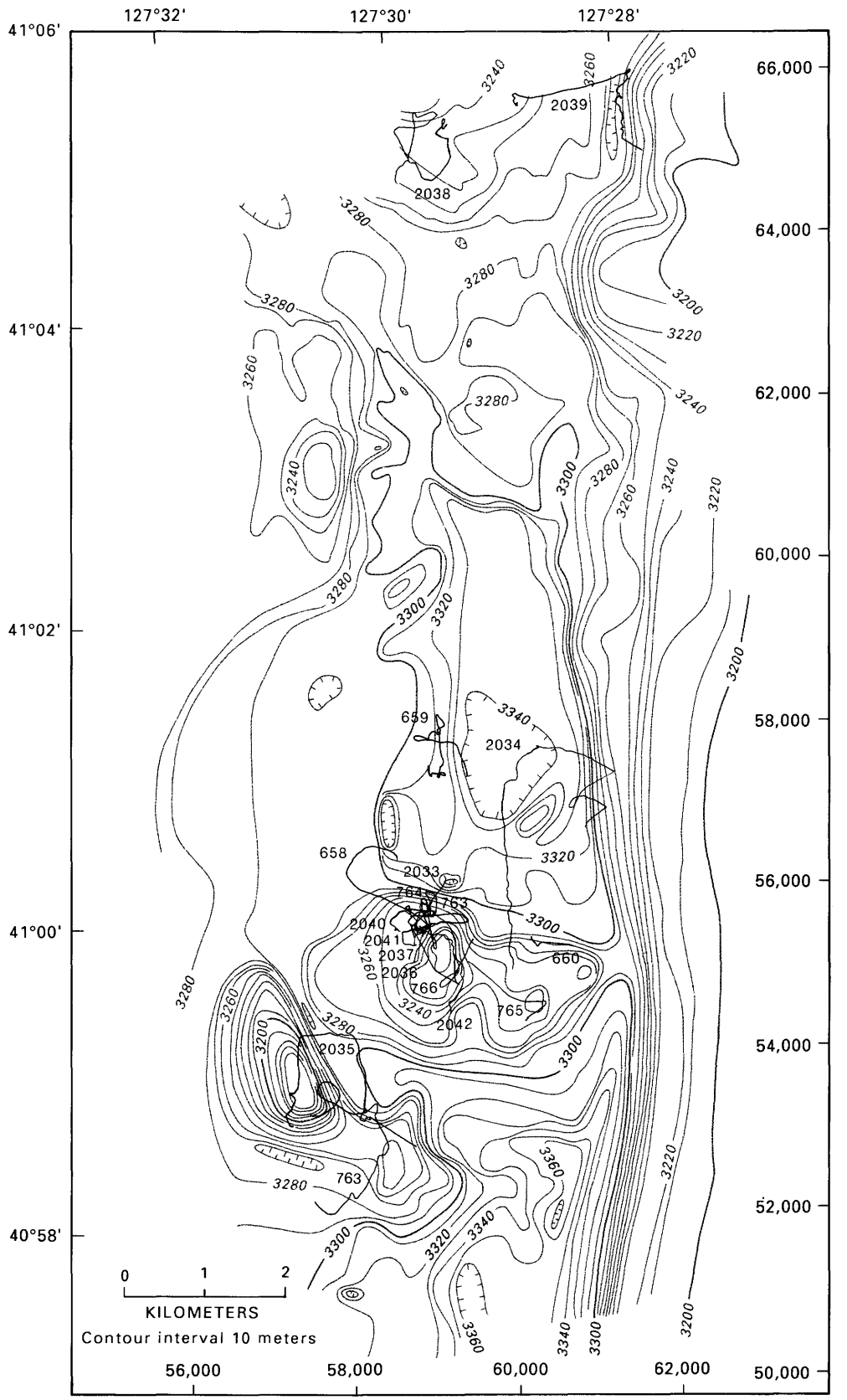

Figure 1.7. Bathymetric map of NESCA area showing location of 17 submersible dives. Numbers along right and bottom give coordinates of local transponder net (in meters). Hachures indicate area of closed low.

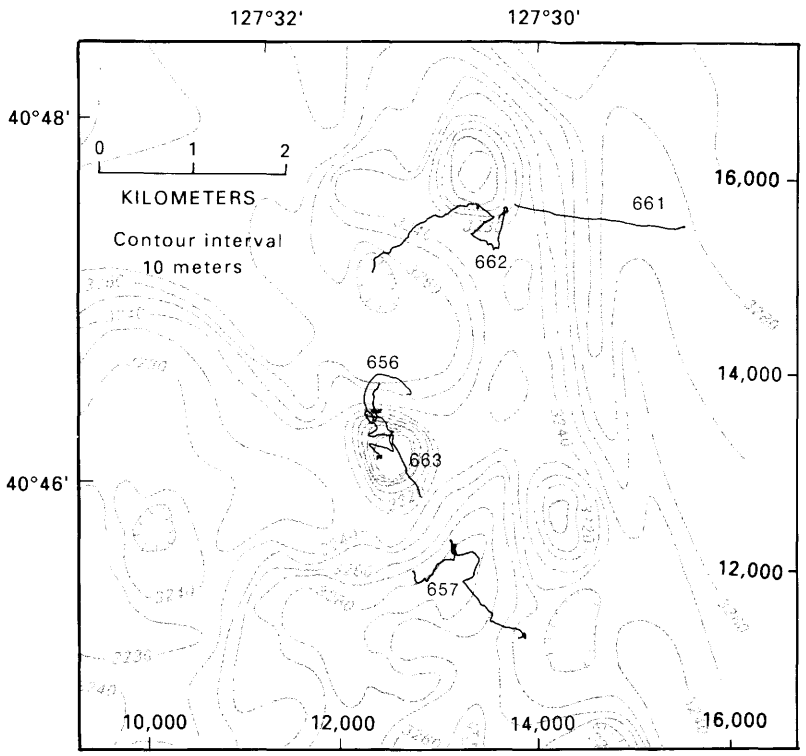

Figure 1.8. Bathymetric map of SESCA area showing location of 5 submersible dives. Numbers along right and bottom give coordinates of local transponder net (in meters). Hachures indicate area of closed low.

NAVIGATION METHODS

The positioning data for the NESCA and SESCA areas were obtained by sea-floor anchored acoustic transponder nets, continuously maintained since 1985 and 1986, respectively. This allows ongoing work to be directly correlated with previous data sets collected in the areas, ensuring internal consistency.

Each net consists of five to seven transponders, deployed in specific locations within a 100 to 160 km^2 area. An integrated satellite (NNSS)–Doppler sonar–Loran C navigation system and a satellite Global Positioning System (GPS) provided supplemental navigation during transponder deployment and provided greater accuracy for calibration of the net. GPS coverage was available in this area about 14 hours per day (Morton and others, 1987b).

Acoustical data received simultaneously from three or more sea-floor transponders provided position accuracy within ±5 meters relative to the net. This provides sufficient accuracy for future reoccupation of hydrothermal deposits and vent sites.

CONTENTS OF THIS VOLUME

This volume presents the findings of geological, geophysical, and biological investigations conducted on several cruises to Escanaba Trough between 1985 and 1989 (table 1.1). Preliminary findings of some of these studies have been reported in various internal reports (Benninger and Koski, 1987; Clague and others, 1984; Karlin and Lyle, 1986; Morton and others, 1987b; Bibee, 1986) and at the Gorda Ridge Symposium in May 1987 (McMurray, 1990; Holmes and Zierenberg, 1990; Morton and others, 1990; Carey and others, 1990; Van Dover and others, 1990). This volume contains the most complete synthesis to date of studies on sediment-hosted sulfide deposits at Escanaba Trough, and it includes much previously unpublished data.

The volume is divided into three sections: (1) Geologic Processes; (2) Hydrothermal and Geochemical Studies; and (3) Biologic Studies. In the first section, chapters 2 to 9 are topical studies, including geophysical, sedimentologic, petrologic, and theoretical, which address aspects of the geologic setting of Escanaba Trough and (or) the SESCA and NESCA study areas. Chapter 10 synthesizes the results of several studies to present our current understanding of the geologic processes at the SESCA and NESCA sites. The six chapters in the second section address sediment alteration, hydrothermal vent fluid chemistry, hydrothermal petroleum formation, and the mineralogy, chemistry, and isotope geochemistry of sulfide deposits at SESCA and NESCA. The two chapters in the third section present studies of soft-sediment hydrothermal

vent communities and benthic foraminifers of the SESCA and NESCA areas.

SIGNIFICANT FINDINGS

Sea Beam mapping indicates that Escanaba Trough consists of two segments with a small right-lateral offset near latitude 41°07′ N. In most places, the depth of the axial valley is greater than 3,300 m; however, between latitudes 41°17′ N. and 41°28′ N., the valley floor rises abruptly to less than 3,250 m. This shallow region appears to act as a topographic barrier to turbidity flows, which enter the valley at its southern end and flow northward (Morton and Fox, chap. 2, this volume). In contrast to sediment-free spreading centers, the sedimented axis of Escanaba Trough lacks a central magnetic anomaly high, perhaps indicating extensive alteration of the basaltic basement (Karlin and Morton, chap. 5, this volume). Normark and others (chap. 6, this volume) consider probable sediment accumulation rates and constraints on the age of the underlying crust at Escanaba Trough and conclude that the majority of the sediment fill probably accumulated during the last two (or at most three) sea-level low stands during the Pleistocene. The Columbia and Klamath river drainages are the probable sediment source regions. Magnetic susceptibility of the surface sediment in the SESCA area records a change in sedimentation correlated with the change from glacial to interglacial conditions at the Pleistocene-Holocene transition (Karlin and Zierenberg, chap. 7, this volume). Locally derived Holocene turbidites and erosion of Holocene sediment are indications of recent tectonism.

Bathymetric and seismic-reflection data (Morton and Fox, chap. 2, this volume; Davis and Becker, chap. 3, this volume) delineate six major volcanic centers along the sediment-covered part of the spreading axis. The volcanic edifices are characterized by an abrupt transition from undisturbed sediment layers to deformed, tilted, and commonly uplifted sediment layers. Sills intrude and disrupt the sediment layers, and basalt flows are locally extruded at the sea floor. These volcanic centers are areas of elevated heat flow (Abbott and others, 1986; Davis and Becker, chap. 3, this volume) and hydrothermal mineralization. Regionally, away from areas of venting, heat flow and predicted basement temperatures are relatively low. This result suggests that either the heat sources are localized and the upper crustal temperatures have not been significantly affected by volcanism, or that the basement temperatures are elevated but there has been insufficient time since heating for the thermal conditions to equilibrate in the thick sedimentary section (Davis and Becker, chap. 3, this volume).

Much of the work reported in this volume was conducted at two of these volcanic edifices, at the NESCA and SESCA sites; figures 1.9 to 1.12 illustrate some of the geologic and hydrothermal features of these two sites. Most of the sea floor at NESCA and SESCA is sediment covered (fig. 1.9*A*; Zierenberg and others, chap. 10, this volume); the sedimentary layer varies abruptly from a thin covering to several hundred meters thick (Morton and Fox, chap. 2, this volume). Several steep-sided hills, formed of uplifted and tilted sediment, are present at NESCA and SESCA (fig. 1.9*B*, *C*). Mechanical modeling suggests that the hills formed by the inflation of basaltic sills near the sediment-basement interface; permeable fault zones developed during uplift focus hydrothermal flow at the perimeters of the hills (Denlinger and Holmes, chap. 4, this volume). Volcanic rocks are exposed locally on the sea floor at both NESCA and SESCA sites (fig. 1.9*D,E,F*). The morphology of the exposed volcanic rocks in the NESCA area indicates a central source region for eruption; sea-floor relief provides the primary control on the distribution of pillow lavas and sheet flows (Ross and Zierenberg, chap. 8, this volume). Chemical analyses of several basalt samples, especially lead isotope measurements, suggest that locally the basalt assimilated small amounts of sediment prior to eruption (Davis and others, chap. 9, this volume).

Several large massive sulfide deposits, up to several tens of meters high and a few hundred meters across, occur at the base of several of the small hills at NESCA and SESCA (fig. 1.10; Zierenberg and others, chap. 10, this volume). Active hydrothermal venting has been observed at three locations at the NESCA site (fig. 1.11). The processes and products of hydrothermal activity in Escanaba Trough are discussed in a series of papers in the second section of this volume.

The effects of hydrothermal activity on near-surface sediment are described by Zierenberg and Shanks (chap. 14, this volume). Replacement of hemipelagic sediment by magnesium-rich chlorite results from intense Mg-metasomatism in a mixing zone where hydrothermal fluid interacts with seawater and sediment at temperatures above 200°C. Lower temperature reactions related to flow of hydrothermal fluid through sediment are recorded by changes in surface sediment chemistry and vertical changes in pore fluid composition (Magenheim and Gieskes, chap. 13, this volume).

Organic matter in near-surface sediments is derived predominantly from terrigenous sources (Kvenvolden and others, chap. 15, this volume). The organic geochemistry of near-surface sediment shows that organic matter in the Holocene sediment is more mature than the organic matter in underlying Pleistocene sediment. This inverted degree of maturation may reflect resedimentation of older sediment transported in locally derived Holocene turbidites. Sediment cores displaying mineralogical evidence of hydrothermal alteration (fig. 12*D*) also contain organic matter altered at elevated temperature.

The analyses of hydrothermal fluids collected at active vents over a temperature range from 15°C to 217°C are reported by Campbell and others (chap. 11, this volume). The vent fluids are slightly alkaline and have chlorinity elevated by approximately 19 percent relative to seawater. Concentrations of dissolved transition metals are low, and alkali and alkaline earth elements and ammonia are high relative to hydrothermal fluids issuing from

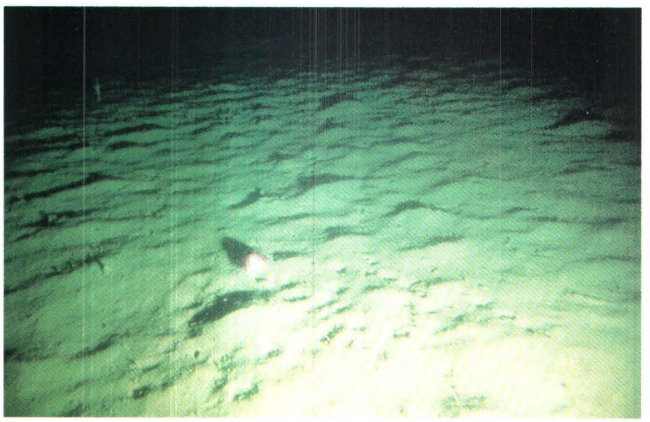

A

B

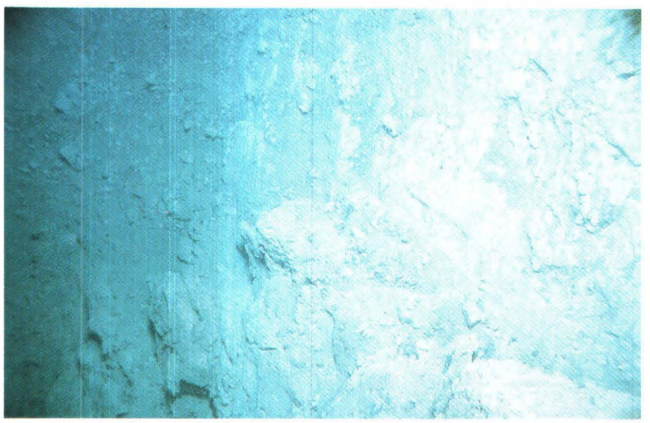

C

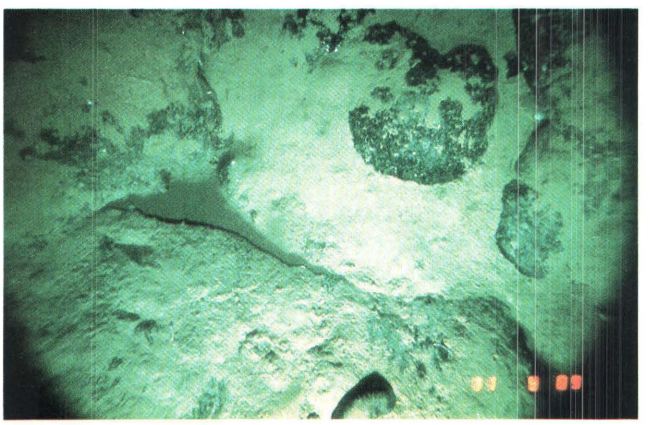

D

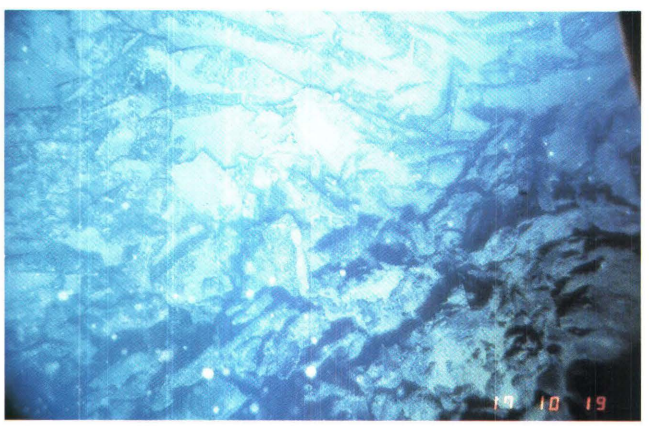

E

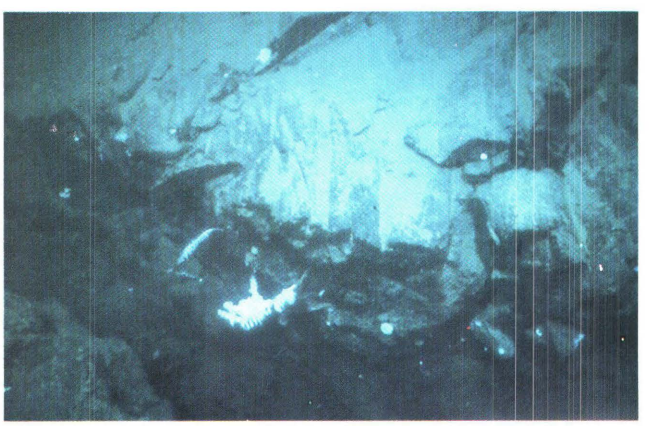

F

Figure 1.9. Sedimentary and volcanic features at NESCA and SESCA sites. Width of images is about 1.5 to 3 m. *A*, Typical sediment-covered sea floor at NESCA site showing pyramid urchin. Photograph taken from DSV *Alvin* by John Edmond. *B*, Lithified mudstone outcropping on steep face of small hill at NESCA site. *C*, Mudstone outcrops and talus at base of small hill at SESCA site showing effect of mass-wasting processes. *D*, Glassy, fresh pillow basalt flow at NESCA site. *E*, Glassy sheet flow from NESCA site. *F*, Older, fissured basalt flow exposed at SESCA site.

vents on sediment-free spreading centers. Chemical and isotopic compositions of the hydrothermal fluids require extensive interaction with sediment within the hydrothermal circulation system. Hydrogen and oxygen isotope compositions of vent fluids are close to those of starting seawater (Böhlke and Shanks, chap. 12, this volume).

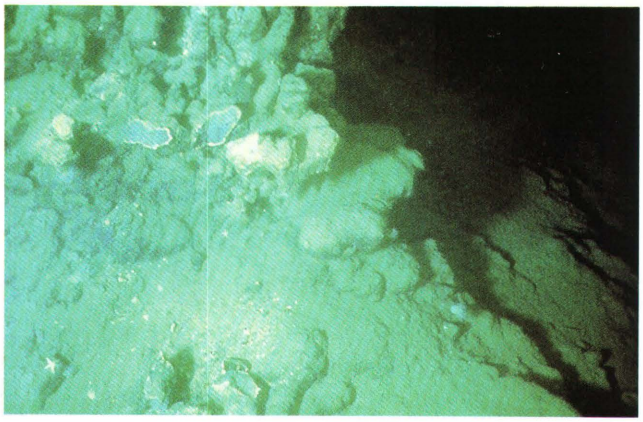

A

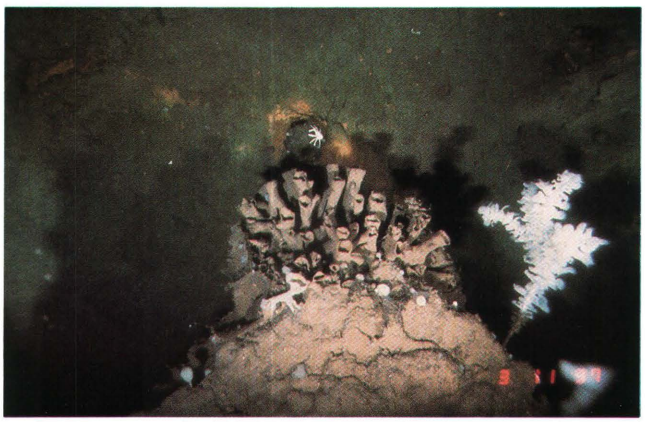

B

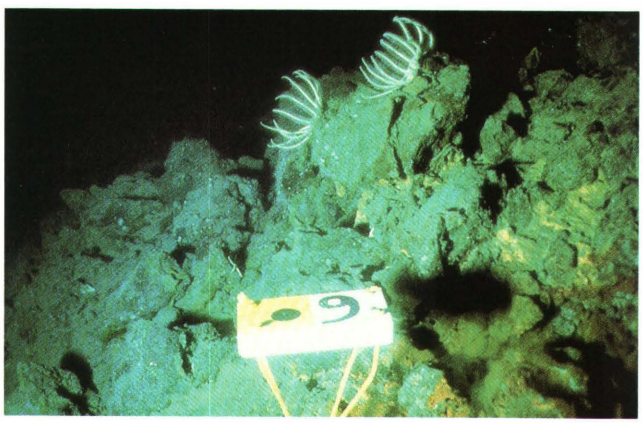

C

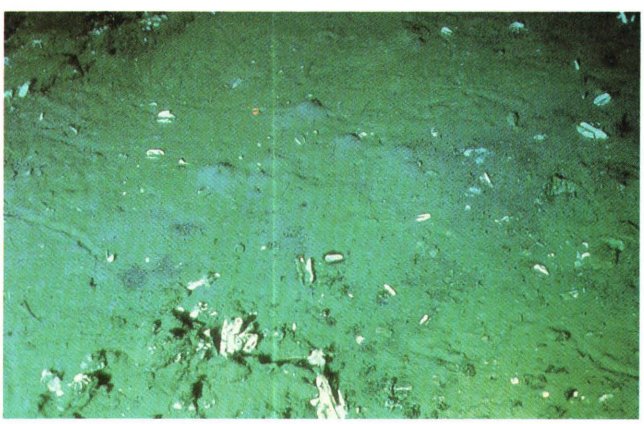

D

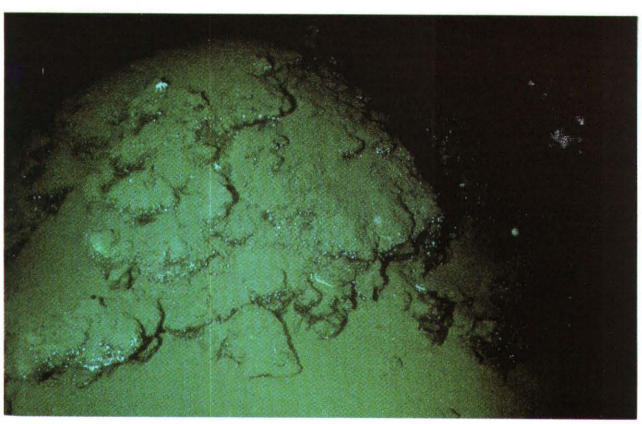

E

F

Figure 1.10. Massive sulfide deposits and hydrothermal features at NESCA and SESCA sites. Width of images is about 1.5 to 3 m. *A*, Coalesced sulfide and sulfate chimneys atop massive sulfide mound at NESCA site. In center of photograph, fresh surface has been exposed by removal of barite sample (fig. 1.12*B*). *B*, Older, oxidized sulfide deposit colonized by sponges at SESCA site. *C*, Sulfide mound and talus at NESCA site. Rectangular marker at center of photograph is 15 by 30 cm. *D*, Sulfide talus and sediment colonized by clams and bacterial mats adjacent to sulfide mound at NESCA site. *E*, Small dome of massive sulfide with crude layering parallel to the surface at NESCA site. *F*, Hydrothermally lithified sediment located about 1 m from sulfide deposit at NESCA site.

Sulfur isotope values of H_2S in the fluid and in hydrothermal sulfide minerals are elevated relative to values in samples from sediment-free ridge crests and require incorporation of seawater sulfate that has been reduced to sulfide by high-temperature interaction with organic matter in the sediment.

The composition of the hydrothermal deposits also requires extensive chemical input to the hydrothermal system from sediment (Koski and others, chap. 16, this volume). The sulfide deposits are pyrrhotite-rich (fig. 12*A*) and have significant contents of copper, generally in the mineral isocubanite. Many samples are highly enriched in gold. Relative to sulfide deposits on sediment-free ridge crests, Escanaba Trough samples are enriched in arsenic, antimony, bismuth, lead, and tin derived from altered sediment in the high-temperature reaction zone at depth. In polymetallic sulfide samples, the telescoped chemical zonation from high-temperature, copper-arsenic-rich assemblages to lower temperature silver-lead assemblages with barite is evidence of steep thermal gradients across fluid conduits at sites of sea-floor hydrothermal discharge.

The hydrothermal vent sites in the NESCA area are the southernmost known occurrence of chemautotrophic fauna on the Juan de Fuca-Gorda Ridge system, and as such provide important data on the distribution, propagation, and speciation of hydrothermal vent fauna. The Escanaba Trough vent fauna resemble those found to the north on the Juan de Fuca Ridge rather than the well-studied vent communities distributed along the East Pacific Rise and at hydrothermal sites in the sediment-covered Guaymas Basin (Van Dover and others, 1990; Grassle and Petrecca, chap. 17, this volume). Agglutinated foraminifers, abundant in dredge and core samples from Escanaba Trough, often display an unusual feature, the use of angular basaltic glass fragments in test construction (Quinterno, chap. 18, this volume). An agglutinated foraminifer recovered in dredge samples has not been previously described and may be a new genus.

A

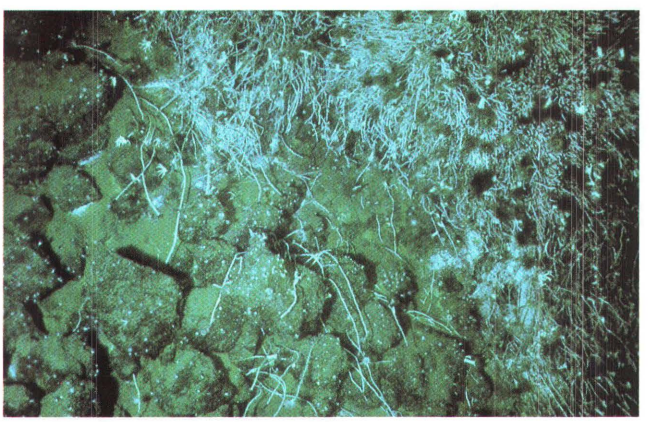

B

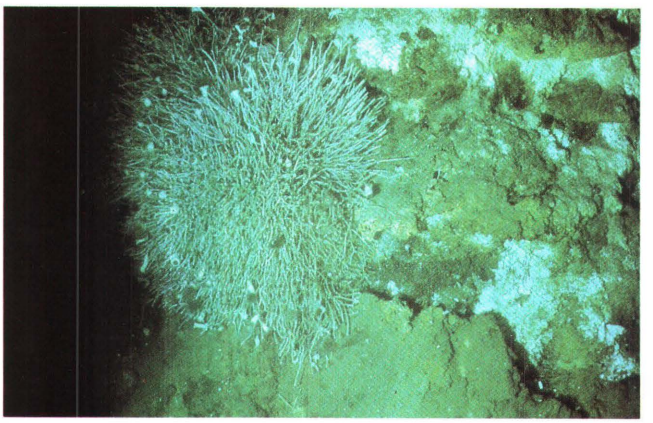

C

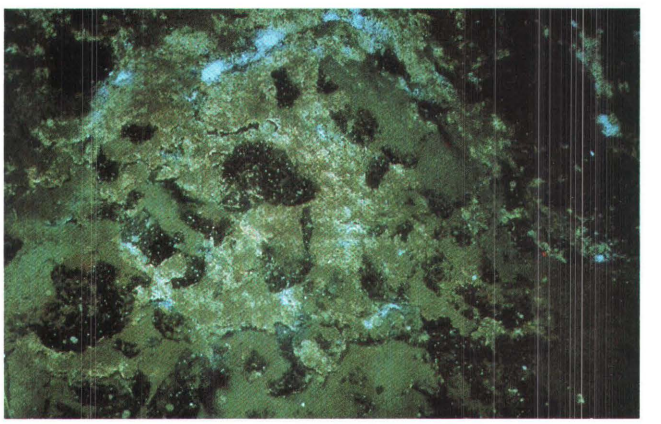

D

Figure 1.11. Massive sulfide deposits and active hydrothermal vents on sea floor at NESCA site. Width of images is about 1.5 to 3 m. *A*, Side of actively venting massive sulfide chimney colonized by tube worms and palm worms. *B*, Tube worms and anemones colonize massive sulfide talus where diffuse hydrothermal venting is occurring. *C*, Side of sulfide mound showing cluster of tube worms, anemones, and bacterial mats. *D*, Hydrothermal deposits (primarily barite) adjacent to site of active venting. Shiny black material is possibly pyrobitumen.

DIRECTIONS OF FUTURE WORK

Geophysical studies have identified at least six major volcanic centers within the sediment-covered part of Escanaba Trough. Reconnaissance geologic mapping has been carried out only in the SESCA and NESCA study areas. Both of these areas contain extensive areas of outcropping massive sulfide mineralization. Exploratory submersible dives on the volcanic center at the northern edge of the NESCA study area (edifice REX) also discovered extensive areas of sulfide mineralization (Zierenberg and others, chap. 10, this volume). Reconnaissance sediment coring at the volcanic center between the SESCA and NESCA areas recovered hydrothermally altered and mineralized sediment (Normark and others, chap. 6, this volume). Our present understanding of the processes leading to sulfide mineralization at the SESCA and NESCA sites suggests that the same processes should have operated at each of the volcanic centers, and it is reasonable to speculate that the Escanaba Trough represents a major mineral deposit district with multiple centers of hydrothermal activity. An obvious next step is to delineate the volcanic centers in Escanaba Trough and to carry out reconnaissance-scale geologic and geophysical mapping to identify other areas of mineralization. The most efficient means of doing this would be a medium-resolution side-scan sonar and seismic-reflection survey of the floor of the axial valley in Escanaba Trough, followed by camera mapping and sampling cruises in areas identified as targets by the geophysical studies.

Temporal evolution of the hydrothermal processes can be investigated in addition to the spatial distribution of deposits. The known sulfide mineralization at the volcanic center at the northern end of the NESCA area and the deposits in the SESCA area are inactive, mature deposits. Some of these deposits are being chemically degraded by oxidative dissolution on the sea floor or are being actively eroded by mass wasting (Holmes and Zierenberg, 1990; Zierenberg and others, chap. 10, this volume). Massive sulfide deposits in the NESCA area are large, mature deposits, but are still locally hydrothermally active. Seismic data from the volcanic center between the SESCA and

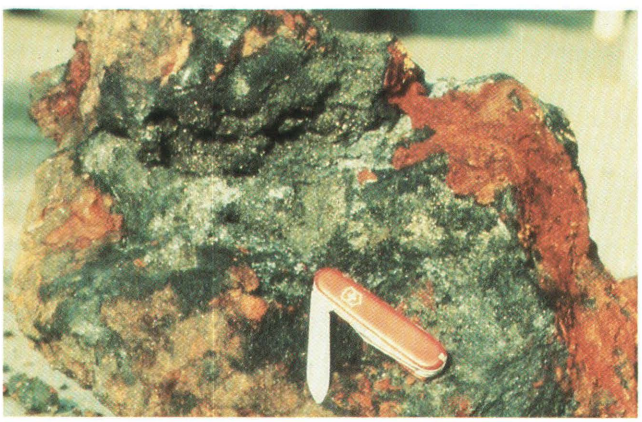

A

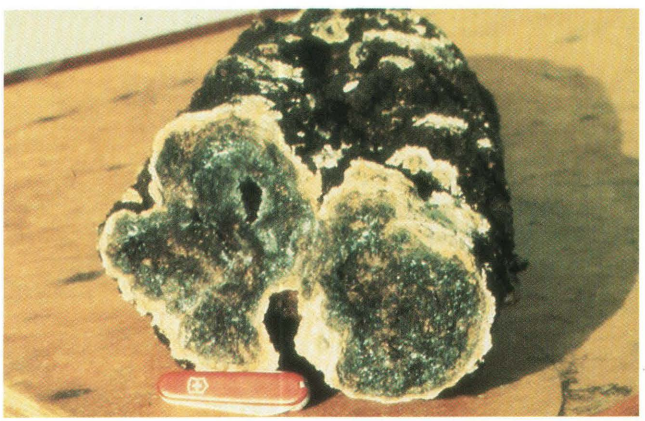

B

C

D

Figure 1.12. Mineralized samples collected from NESCA and SESCA sites. *A*, Typical pyrrhotite-rich massive sulfide sample. *B*, Chimney composed mostly of barite recovered from NESCA site (fig. 1.10*A*). *C*, Mudstone breccia cemented by sulfide. Sample is approximately 7.5 cm wide. *D*, Sediment core with sulfide mineralization at 70 to 80 cm interval.

NESCA areas suggest that the volcanic center is in the early stages of formation and has not affected the surface sediments to the same extent as at the NESCA and SESCA centers (Davis and Becker, chap. 3, this volume; Morton and Fox, chap. 2, this volume). Hydrothermal activity in this area may also be relatively immature. Comparative studies between the different volcanic centers could provide the opportunity to study the volcanic-sedimentary-hydrothermal interactions at various stages of evolution.

Although our knowledge of the SESCA and NESCA areas is extensive, even when compared to many well-studied areas of the sea floor, our actual data base is small. Less than 0.5 percent of the sea floor in the SESCA and NESCA areas has actually been observed by camera tows or submersible dives. The areal extent of outcropping sulfide mineralization has not been determined for any of the deposits; only minimum figures are known. Available time and scientific resources preclude complete photographic or submersible coverage of even a small part of the sea floor, so that we will always be forced to extrapolate our knowledge beyond the limits of our actual observations. However, there are tools available both to assist in extrapolating our data base and to guide future detailed investigations that have not been used in Escanaba Trough. One of the most useful techniques to aid in interpreting the geology in the areas of hydrothermal activity is high-resolution side-scan sonar, especially in combination with simultaneously collected swath bathymetry. A detailed side-scan survey, coupled with the local knowledge gained by camera and submersible mapping, would allow delineation of the extent of outcropping sulfide deposits, provide detailed information on the surface exposure of structures that localize sites of hydrothermal discharge, and provide a larger scale understanding of the processes of sedimentation and sediment remobilization.

A deeply towed side-scan-sonar package can also be equipped with a magnetometer and a bottom-penetrating sonar system. High-resolution magnetic data can provide important constraints on the locations of both exposed and sediment buried sulfide deposits. These data are also critical to constrain models of magma-sediment interaction including the size and depth of emplacement of igneous intrusions. Bottom-penetrating sonar would allow detailed mapping of structures by the tracing of turbidite seismic reflectors. In addition, the near-bottom high-resolution seismic data would provide our first opportunity to examine the distribution and extent of sulfide mineralization in the shallow subsurface. Nearly all of our data relate only to the superficial surface skin of the deposits, and a greater understanding of the subsurface processes critical to massive sulfide formation and sediment alteration cannot be achieved until we can address these problems in a three-dimensional manner.

The true frontier area that must be explored to expand our understanding of hydrothermal, geochemical, and geophysical processes operating at sediment-covered spreading centers is the region of the lowermost sediment and the uppermost oceanic crust. This unexplored territory holds the secrets to a larger scale understanding of genetic processes. The interface between the oceanic crust and overlying sedimentary section is a fundamental chemical, mechanical, and hydrodynamic boundary, and is the area of dynamic interplay between igneous and sedimentary processes. This is the region that controls the thermal and chemical fluxes from the lithosphere to the hydrosphere. These fluxes control the composition of the sulfide deposits, sustain the biological communities at vent sites, and alter the composition of the ocean, the sedimentary section, and the basaltic crust. Novel application of sonar imagery to steeply inclined fault surfaces may identify fortuitous exposures of this zone, amenable to study by submersible, on the normal faults that bound the axial valleys. A more systematic approach to the study of these fundamental problems clearly requires oceanic drilling. Proposals have been advanced for drilling in this area to study the sedimentary record of climatic, tectonic, volcanic, and hydrothermal events, to determine the physical properties of the sediment and upper oceanic crust that control the hydrologic circulation, and to investigate the energy and mass fluxes and the chemical reactions that affect the hydrosphere, the sedimentary section, and the upper oceanic crust. A reasonable understanding of the formation of oceanic crust at sedimented spreading centers and the processes that control the associated hydrothermal systems depends on extending our studies into the third dimension.

REFERENCES CITED

Abbott, D.H., Morton, J.L., and Holmes, M.L., 1986, Heat flow measurements on a hydrothermally-active, slow-spreading ridge: The Escanaba Trough: Geophysical Research Letters, v. 13, p. 678–680.

Atwater, Tanya, and Mudie, J.D., 1973, Detailed near-bottom geophysical study of the Gorda Ridge: Journal of Geophysical Research, v. 78, p. 8665–8686.

Baker, E.T., Massoth, G.J., Collier, R.W., Trefry, J.H., Kadko, D., Nelsen, T.A., Rona, P.A., and Lupton, J.E., 1987, Evidence for high-temperature hydrothermal venting on the Gorda Ridge, northeast Pacific Ocean: Deep-Sea Research, v. 34, p. 1461–1476.

Benninger, L.A., and Koski, R.A., 1987, Descriptions and chemical analyses of sulfide samples dredged in 1986 from Escanaba Trough, southern Gorda Ridge: U.S. Geological Survey Open-File Report 87-375-B, 26 p.

Bibee, L.D., 1986, Ocean bottom seismometer measurements on the Gorda Ridge: Oregon Department of Geology and Mineral Industries Open-File Report O-86-15, 25 p.

Bischoff, J.L., Rosenbauer, R.J., Aruscavage, P.J., Baedecker, P.A., and Crock, J.G., 1983, Sea-floor massive sulfide deposits from 21° N, East Pacific Rise; Juan de Fuca Ridge;

and Galápagos Rift: Bulk chemical composition and economic implications: Economic Geology, v. 78, p. 1711–1720.

Böhlke, J.K., and Shanks, W.C., III, Stable isotope study of hydrothermal vents at Escanaba Trough: Observed and calculated effects of sediment-seawater interaction, *in* Morton, J.L., Zierenberg, R.A., and Reiss, C.A., eds., Geologic, hydrothermal, and biologic studies at Escanaba Trough, Gorda Ridge, offshore northern California: U.S. Geological Survey Bulletin 2022, chapter 12 (this volume).

Bolger, G.W., Betzer, P.R., and Gordeev, V.V., 1978, Hydrothermally-derived manganese suspended over the Galápagos spreading center: Deep-Sea Research, v. 25, p. 721–733.

Boström, K., 1973, The origin and fate of ferromanganoan active ridge sediments: Stockholm Contributions in Geology, v. 27, p. 150–243.

Boström, K., and Peterson, M.N.A., 1966, Precipitates from hydrothermal exhalations on the East Pacific Rise: Economic Geology, v. 61, p. 1258–1265.

Campbell, A.C., German, C.R., Palmer, M.R., Gamo, T. and Edmond, J.M., Chemistry of hydrothermal fluids from the Escanaba Trough, Gorda Ridge, *in* Morton, J.L., Zierenberg, R.A., and Reiss, C.A., eds., Geologic, hydrothermal, and biologic studies at Escanaba Trough, Gorda Ridge, offshore northern California: U.S. Geological Survey Bulletin 2022, chapter 11 (this volume).

Carey, A.G., Jr., Taghon, G.L., Stein, D.L., and Rona, P.A., 1990, Distributional ecology of benthic megaepifauna and fishes in Gorda Ridge Axial Valley, *in* McMurray, G.R., ed., Gorda Ridge: A seafloor spreading center in the United States' Exclusive Economic Zone: New York, Springer-Verlag, p. 225–240.

Clague, D.A., Friesen, W., Quinterno, P., Holmes, M., Morton, J., Bouse, R., Morgenson, L., and Davis, A., 1984, Preliminary geological, geophysical, and biological data from the Gorda Ridge: U.S. Geological Survey Open-File Report 84-364, 46 p.

Clague, D.A., and Holmes, M.L., 1987, Geology, petrology, and mineral potential of the Gorda Ridge, *in* Scholl, D.W., Grantz, A., and Vedder, J.G., eds., Geology and resource potential of the continental margin of western North America and adjacent ocean basins—Beaufort Sea to Baja California: Houston, Circum-Pacific Council for Energy and Mineral Resources, Earth Science Series, v. 6, p. 563–580.

Corliss, J.B., Dymond, J., Gordon, L.I., Edmond, J.M., von Herzen, R.P., Ballard, R.D., Green, K., Williams, D., Bainbridge, A., Crane, K., and van Andel, T.H., 1979, Submarine thermal springs on the Galápagos Rift: Science, v. 203, p. 1073–1083.

Davis, A.S., Clague, D.A., and Friesen, W.B., Petrology and mineral chemistry of basalt from Escanaba Trough, *in* Morton, J.L., Zierenberg, R.A., and Reiss, C.A., eds., Geologic, hydrothermal, and biologic studies at Escanaba Trough, Gorda Ridge, offshore northern California: U.S. Geological Survey Bulletin 2022, chapter 9 (this volume).

Davis, Earl, and Becker, Keir, Thermal and tectonic structure of the Escanaba Trough: New heat-flow measurements and seismic-reflection profiles, *in* Morton, J.L., Zierenberg, R.A., and Reiss, C.A., eds., Geologic, hydrothermal, and biologic studies at Escanaba Trough, Gorda Ridge, offshore northern California: U.S. Geological Survey Bulletin 2022, chapter 3 (this volume).

Dehlinger, P., 1969, Evidence regarding the development of Juan de Fuca and Gorda Ridges in the northeast Pacific Ocean: New York Academy of Sciences Transactions, v. 31, p. 379–403.

Denlinger, R.P., and Holmes, M.L., A thermal and mechanical model for sediment hills and associated sulfide deposits along the Escanaba Trough, *in* Morton, J.L., Zierenberg, R.A., and Reiss, C.A., eds., Geologic, hydrothermal, and biologic studies at Escanaba Trough, Gorda Ridge, offshore northern California: U.S. Geological Survey Bulletin 2022, chapter 4 (this volume).

Detrick, R.S., Williams, D.L., Mudie, J.D., and Sclater, J.G., 1974, The Galápagos spreading centre: Bottom-water temperatures and the significance of geothermal heating: Geophysical Journal of the Royal Astronomical Society, v. 38, p. 627–637.

Duke, N.A., and Hutchinson, R.W., 1974, Geological relationships between massive sulfide bodies and ophiolitic volcanic rocks near York Harbour, Newfoundland: Canadian Journal of Earth Sciences, v. 11, p. 53–69.

EEZ-SCAN 84 Scientific Staff, 1986, Atlas of the Exclusive Economic Zone, Western Conterminous United States: U.S. Geological Survey Miscellaneous Investigations Series Map I-1792, 152 p., scale 1:500,000.

Elder, J.W., 1965, Physical processes in geothermal areas, *in* Lee, W.H.K., ed., Terrestrial heat flow: Washington, D.C., American Geophysical Union Monograph 8, p. 211–239.

Francheteau, J., Needham, H.D., Choukroune, P., Juteau, T., Séguret, M., Ballard, R.D., Fox, P.J., Normark, W., Carranza, A., Cordoba, D., Guerrero, J., Rangin, C., Bougault, H., Cambon, R., and Hekinian, R., 1979, Massive deep-sea sulphide ore deposits discovered on the East Pacific Rise: Nature, v. 277, p. 523–528.

Grassle, J.F., and Petrecca, Rosemarie, Soft-Sediment hydrothermal vent communities of Escanaba Trough, *in* Morton, J.L., Zierenberg, R.A., and Reiss, C.A., eds., Geologic, hydrothermal, and biologic studies at Escanaba Trough, Gorda Ridge, offshore northern California: U.S. Geological Survey Bulletin 2022, chapter 17 (this volume).

Holmes, M.L., and Zierenberg, R.A., 1990, Submersible operations in Escanaba Trough, southern Gorda Ridge, *in* McMurray, G.R., ed., Gorda Ridge: A seafloor spreading center in the United States' Exclusive Economic Zone: New York, Springer-Verlag, p. 93–115.

Kappel, E.S., and Franklin, J.M., 1989, Relationships between geologic development of ridge crests and sulfide deposits in the northeast Pacific Ocean: Economic Geology, v. 84, p. 485–505.

Karlin, Robert, and Lyle, Mitchell, 1986, Sediment studies on the Gorda Ridge: Oregon Department of Geology and Mineral Industries Open-File Report O-86-19, 76 p.

Karlin, R.E., and Morton, J.L., Crustal magnetization and basement structure of the Escanaba Trough, *in* Morton, J.L., Zierenberg, R.A., and Reiss, C.A., eds., Geologic, hydrothermal, and biologic studies at Escanaba Trough, Gorda Ridge, offshore northern California: U.S. Geological Survey Bulletin 2022, chapter 5 (this volume).

Karlin, R.E., and Zierenberg, R.A., Sedimentation and

neotectonism in the SESCA area, Escanaba Trough, southern Gorda Ridge, *in* Morton, J.L., Zierenberg, R.A., and Reiss, C.A., eds., Geologic, hydrothermal, and biologic studies at Escanaba Trough, Gorda Ridge, offshore northern California: U.S. Geological Survey Bulletin 2022, chapter 7 (this volume).

Klinkhammer, G.P., Bender, M., and Weiss, R.F., 1977, Hydrothermal manganese in the Galápagos Rift: Nature, v. 269, p. 319–320.

Koski, R.A., Lonsdale, P.F., Shanks, W.C., III, Berndt, M.E., and Howe, S.S., 1985, Mineralogy and geochemistry of a sediment-hosted hydrothermal deposit from the Southern Trough of Guaymas Basin, Gulf of California: Journal of Geophysical Research, v. 90, p. 6695–6707.

Koski, R.A., Shanks, W.C., III, Bohrson, W.A., and Oscarson, R.L., 1988, The composition of massive sulfide deposits from the sediment-covered floor of Escanaba Trough, Gorda Ridge: Implications for depositional processes: Canadian Mineralogist, v. 26, p. 655–673.

Koski, R.A., Benninger, L.M., Zierenberg, R.A., and Jonasson, I.R., Composition and growth history of hydrothermal deposits in Escanaba Trough, southern Gorda Ridge, *in* Morton, J.L., Zierenberg, R.A., and Reiss, C.A., eds., Geologic, hydrothermal, and biologic studies at Escanaba Trough, Gorda Ridge, offshore northern California: U.S. Geological Survey Bulletin 2022, chapter 16 (this volume).

Kvenvolden, K.A., Rapp, J.B., and Hostettler, F.D., Hydrocarbons in sediment from Escanaba Trough, *in* Morton, J.L., Zierenberg, R.A., and Reiss, C.A., eds., Geologic, hydrothermal, and biologic studies at Escanaba Trough, Gorda Ridge, offshore northern California: U.S. Geological Survey Bulletin 2022, chapter 15, (this volume).

Kvenvolden, K.A., Rapp, J.B., Hostettler, F.D., Morton, J.L., King, J.D., and Claypool, G.F., 1986, Petroleum associated with polymetallic sulfide in sediment from Gorda Ridge: Science, v. 234, p. 1231–1234.

Lister, C.R.B., 1972, On the thermal balance of a mid-ocean ridge: Geophysical Journal of the Royal Astronomical Society, v. 26, p. 515–535.

Lonsdale, P.F., Bischoff, J.L., Burns, V.M., Kastner, M., and Sweeney, R.E., 1980, A high-temperature hydrothermal deposit on the seabed at a Gulf of California spreading center: Earth and Planetary Science Letters, v. 49, p. 8–20.

Lupton, J.E., Weiss, R.F., and Craig, H., 1977, Mantle helium in hydrothermal plumes in the Galápagos Rift: Nature, v. 267, p. 603–604.

Magenheim, A.J., and Gieskes, J.M., Evidence for hydrothermal flow through surficial sediments, Escanaba Trough, *in* Morton, J.L., Zierenberg, R.A., and Reiss, C.A., eds., Geologic, hydrothermal, and biologic studies at Escanaba Trough, Gorda Ridge, offshore northern California: U.S. Geological Survey Bulletin 2022, chapter 13, (this volume).

McManus, D.A., 1964, Major bathymetric features near the coast of Oregon, Washington, and Vancouver Island: Northwest Science, v. 38, p. 65–82.

———1967, Physiography of Cobb and Gorda Rises, Northeast Pacific Ocean: Geological Society of America Bulletin, v. 78, p. 527–546.

McManus, D.A., and others, 1970, Site 35, *in* McManus, D.A., and others, eds., Initial reports of the Deep Sea Drilling Project: Washington, U.S. Government Printing Office, v. 5, p. 165–172.

McMurray, G.R., ed., 1990, Gorda Ridge: A seafloor spreading center in the United States' Exclusive Economic Zone: New York, Springer-Verlag, 311 p.

Moore, G.W., 1970, Sea-floor spreading at the junction between Gorda Rise and Mendocino Ridge: Geological Society of America Bulletin, v. 81, p. 2817–2824.

Moore, G.W., and Sharman, G.F., 1970, Summary of scan Site 4, *in* McManus, D.A., and others, eds., Initial reports of the Deep Sea Drilling Project: Washington, U.S. Government Printing Office, v. 5, p. 761–773.

Morton, J.L., Holmes, M.L., and Koski, R.A., 1987a, Volcanism and massive sulfide formation at a sedimented spreading center, Escanaba Trough, Gorda Ridge, northeast Pacific Ocean: Geophysical Research Letters, v. 14, p. 769–772.

Morton, J.L., Normark, W.R., Ross, S.L., Koski, R.A., Holmes, M.L., Shanks, W.C., III, Zierenberg, R.A., Lyle, Mitchell, and Benninger, L.M., 1987b, Preliminary report, cruises L1-86-NC and L2-86-NC, Escanaba Trough, Gorda Ridge: U.S. Geological Survey Open-File Report 87-375-A, 20 p.

Morton, J.L., Koski, R.A., Normark, W.R., and Ross, S.L., 1990, Distribution and composition of massive sulfide deposits at Escanaba Trough, southern Gorda Ridge, *in* McMurray, G.R., ed., Gorda Ridge: A seafloor spreading center in the United States' Exclusive Economic Zone: New York, Springer-Verlag, p. 77–92.

Morton, J.L., and Fox, C.G., Structural setting and interaction of volcanism and sedimentation at Escanaba Trough: Geophysical results, *in* Morton, J.L., Zierenberg, R.A., and Reiss, C.A., eds., Geologic, hydrothermal, and biologic studies at Escanaba Trough, Gorda Ridge, offshore northern California: U.S. Geological Survey Bulletin 2022, chapter 2 (this volume).

Normark, W.R., Gutmacher, C.E., Zierenberg, R.A., Wong, F.L., and Rosenbauer, R.J., Sediment fill of Escanaba Trough, *in* Morton, J.L., Zierenberg, R.A., and Reiss, C.A., eds., Geologic, hydrothermal, and biologic studies at Escanaba Trough, Gorda Ridge, offshore northern California: U.S. Geological Survey Bulletin 2022, chapter 6 (this volume).

Quinterno, P.J., Quaternary foraminifers from Escanaba Trough, northeast Pacific Ocean, *in* Morton, J.L., Zierenberg, R.A., and Reiss, C.A., eds., Geologic, hydrothermal, and biologic studies at Escanaba Trough, Gorda Ridge, offshore northern California: U.S. Geological Survey Bulletin 2022, chapter 18, (this volume).

Raff, A.D., and Mason, R.G., 1961, Magnetic survey off the west coast of North America, 40° N. latitude to 52° N. latitude: Geological Society of America Bulletin, v. 72, p. 1267–1270.

Raitt, R.W., 1963, Seismic refraction studies of the Mendocino Fracture Zone: International Union of Geodesy and Geophysics, XIII General Assembly, Abstract of Papers, v. 5, p. 71.

Riddihough, R.P., 1980, Gorda plate motions from magnetic anomaly analysis: Earth and Planetary Science Letters, v. 51, p. 163–170.

RISE Project Group (Spiess, F.N., Macdonald, K.C., Atwater, T., Ballard, R., Carranza, A., Cordoba, D., Cox, C., Diaz Garcia, V.M., Francheteau, J., Guerrero, J., Hawkins, J., Haymon,

R., Hessler, R., Juteau, T., Kastner, M., Larson, R., Luyendyk, B., Macdougall, J.D., Miller, S., Normark, W., Orcutt, J., and Rangin, C.), 1980, East Pacific Rise: Hot springs and geophysical experiments: Science, v. 207, p. 1421–1432.

Rona, P.A., McGregor, B.A., Betzer, P.R., Bolger, G.W., and Krause, D.C., 1975, Anomalous water temperatures over Mid-Atlantic Ridge crest at 26° North latitude: Deep-Sea Research, v. 22, p. 611–618.

Ross, S.L., and Zierenberg, R.A., Volcanic geomorphology of the SESCA and NESCA sites, Escanaba Trough, *in* Morton, J.L., Zierenberg, R.A., and Reiss, C.A., eds., Geologic, hydrothermal, and biologic studies at Escanaba Trough, Gorda Ridge, offshore northern California: U.S. Geological Survey Bulletin 2022, chapter 8 (this volume).

Sclater, J.G., and Klitgord, K.D., 1973, A detailed heat flow, topographic, and magnetic survey across the Galápagos spreading center at 86° W: Journal of Geophysical Research, v. 78, p. 6951–6975.

Sillitoe, R.H., 1972, Formation of certain massive sulphide deposits at sites of sea-floor spreading: Institute of Mining and Metallurgy Transactions, v. 81, p. 141B–148B.

Simoneit, B.R.T., and Lonsdale, P.G., 1982, Hydrothermal petroleum in mineral mounds at the seabed of Guaymas Basin: Nature, v. 295, p. 198–202.

Spooner, E.T.C., and Bray, C.J., 1977, Hydrothermal fluids of seawater salinity in ophiolitic sulphide ore deposits in Cyprus: Nature, v. 266, p. 808–812.

Spooner, E.T.C., and Fyfe, W.S., 1973, Sub-sea-floor metamorphism, heat and mass transfer: Contributions to Mineralogy and Petrology, v. 42, p. 287–304.

Talwani, M., Windisch, C.C., and Langseth, M.G., 1971, Reykjanes ridge crest: A detailed geophysical study: Journal of Geophysical Research, v. 76, p. 473–517.

Vallier, T.L., Harold, P.J., and Girdley, W.A., 1973, Provenances and dispersal patterns of turbidite sand in Escanaba Trough, northeastern Pacific Ocean: Marine Geology, v. 15, p. 67–87.

Van Dover, C.L., Grassle, J.F., and Boudrias, Michel, 1990, Hydrothermal vent fauna of Escanaba Trough (Gorda Ridge), *in* McMurray, G.R., ed., Gorda Ridge: A seafloor spreading center in the United States' Exclusive Economic Zone: New York, Springer-Verlag, p. 285–287.

Vine, F.J., and Matthews, D.H., 1963, Magnetic anomalies over oceanic ridges: Nature, v. 199, p. 947–949.

Weiss, R.F., Lonsdale, P., Lupton, J.E., Bainbridge, A.E., and Craig, H., 1977, Hydrothermal plumes in the Galápagos Rift: Nature, v. 267, p. 600–603.

Wilde, P., Chase, T.E., Holmes, M.L., Normark, W.R., Thomas, J.A., McCulloch, D.S., and Kulm, L.D., 1978, Oceanographic data off northern California—southern Oregon, 40°–43° N including the Gorda deep-sea fan: Berkeley, Lawrence Berkeley Laboratories Publication 251, scale 1:815,482.

Williams, D.L., Von Herzen, R.P., Sclater, J.G., and Anderson, R.N., 1974, The Galápagos spreading centre: Lithospheric cooling and hydrothermal circulation: Geophysical Journal of the Royal Astronomical Society, v. 38, p. 587–608.

Wilson, D.S., 1989, Deformation of the so-called Gorda plate: Journal of Geophysical Research, v. 94, p. 3065–3075.

Zierenberg, R.A., Morton, J.L., Koski, R.A., and Ross, S.L., Geologic setting of massive sulfide mineralization in the Escanaba Trough, *in* Morton, J.L., Zierenberg, R.A., and Reiss, C.A., eds., Geologic, hydrothermal, and biologic studies at Escanaba Trough, Gorda Ridge, offshore northern California: U.S. Geological Survey Bulletin 2022, chapter 10 (this volume).

Zierenberg, R.A., and Shanks, W.C., III, Sediment alteration associated with massive sulfide formation in the Escanaba Trough, Gorda Ridge: The importance of seawater mixing and magnesium metasomatism, *in* Morton, J.L., Zierenberg, R.A., and Reiss, C.A., eds., Geologic, hydrothermal, and biologic studies at Escanaba Trough, Gorda Ridge, offshore northern California: U.S. Geological Survey Bulletin 2022, chapter 14 (this volume).

Section I:

Geologic Processes

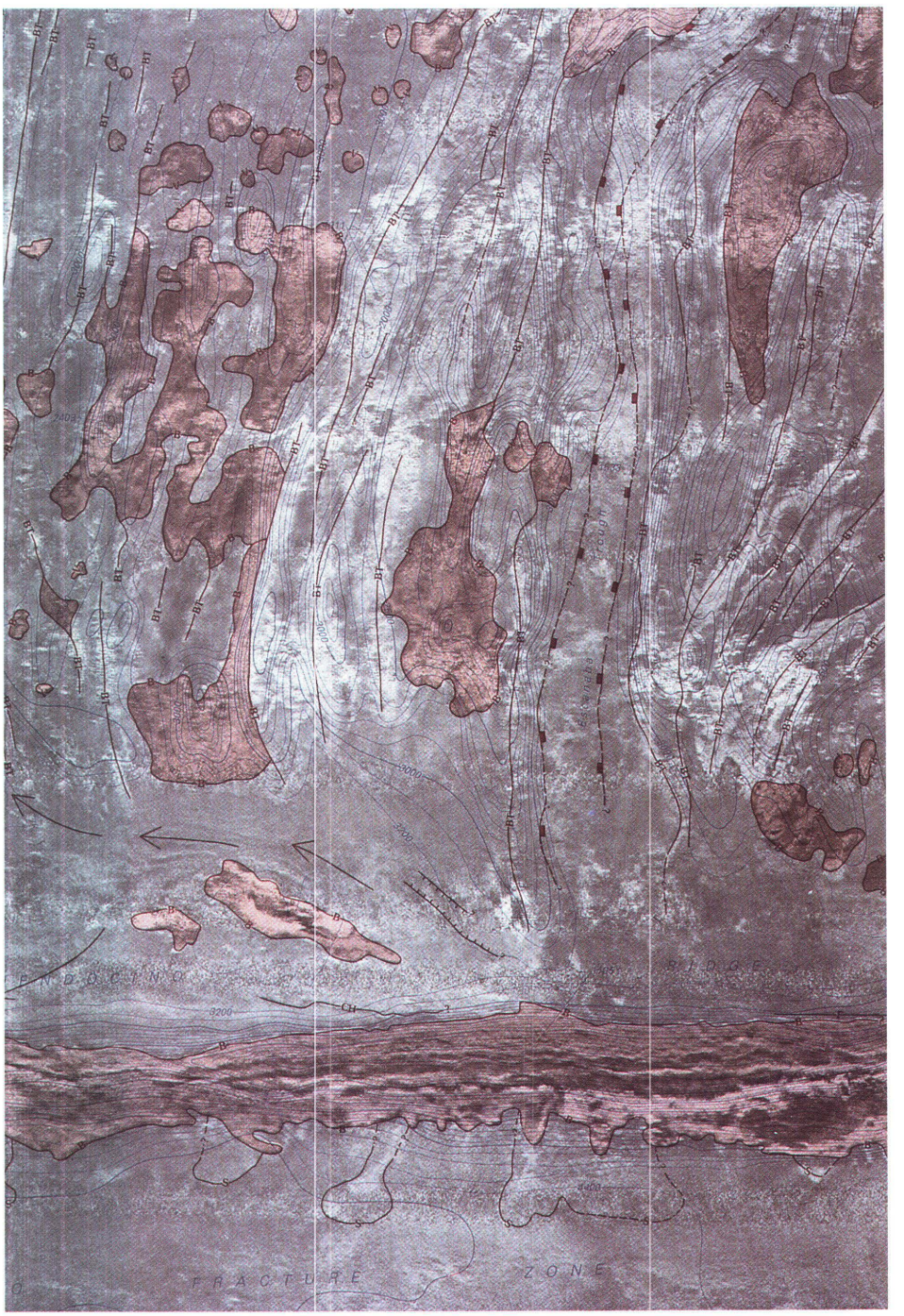

Acoustic sidescan mosaic of the Escanaba Trough area superimposed on the bathymetric map (contour interval 200 m). Areas of reversed magnetic polarity are shown in red. Steep slopes and rough-textured volcanic rocks have strong acoustic backscatter and are shown as light areas on this image. Smooth sediment-covered sea floor is dark. The main trough of the Gorda Ridge spreading center is outlined by the red hachured lines running north-south to the right of center of the image. The northern one-third of the spreading center is bright in this image due to the presence of young volcanic rocks. The southern two-thirds of the spreading center is the Escanaba Trough where the spreading center is covered by turbiditic sediment. Local bright patches within the Escanaba Trough are volcanic edifices that have stronger acoustic backscatter due to locally exposed basalts flows and intrusion of sills that disrupt the sediment. These volcanic edifices are the sites of hydrothermal activity and massive sulfide formation.

Chapter 2. Structural Setting and Interaction of Volcanism and Sedimentation at Escanaba Trough: Geophysical Results

By Janet L. Morton[1] *and* Christopher G. Fox[2]

CONTENTS

ABSTRACT

Escanaba Trough forms the axial valley of the slow-spreading southern Gorda Ridge and is characterized by a relatively flat 5- to 15-km-wide valley floor at a depth of 3,300 m, flanked by steep ridges rising 900 to 1,500 m above the valley floor. Turbidites and hemipelagic sediment cover the southern two-thirds of the trough to an average depth of 300 to 700 m. Subbottom profiler records of the sedimentary fill show thin, often continuous reflective zones 2 to 10 m apart in the upper several tens of meters of sediment, indicative of predominantly mud-rich sediment with a low percentage of thin, coarse-grained beds. A widespread acoustically transparent zone from approximately 85 to 130 m below the sea floor was imaged on seismic-reflection records. This interval is interpreted from drilling as a homogeneous, probably rapidly deposited, coarse-grained interval. Recent igneous activity along the trough is confined to discrete locations, termed volcanic edifices, where sills intrude and disrupt the sediment layers; basalt flows are locally extruded at the sea floor. Steep-sided hills of uplifted sediment about 1 km in diameter, probably formed by intrusion of basaltic sills near the sediment-basement interface, rise 50 to 100 m above the volcanic edifices. Massive sulfide deposits with lateral dimensions up to 200 m and thicknesses of several tens of meters occur near the base of these sediment hills. Smaller sulfide mounds and chimneys occur on the sediment-covered sea floor away from the hills; disseminated sulfide in a sand-rich layer was cored at one location. Two main factors control the location of sulfide mineralization: (1) faults that formed as the hills were uplifted provide the primary conduits for ascending hydrothermal fluids, localizing the sea-floor sulfide deposition along the perimeters of the hills, and (2) sand layers allow horizontal migration of hydrothermal fluids away from the fault zones and may feed the smaller deposits. Subsurface mineral deposition is probably occurring in these coarser sediment layers.

INTRODUCTION

Most mid-oceanic ridges lack a significant sediment cover, owing to the slow accumulation of sediment and the relatively fast creation of new crust. When sediment accumulation rates greatly exceed crustal accretion rates, the ridge axis becomes sediment dominated. The axis of Escanaba Trough, on the southern Gorda Ridge, is sediment dominated owing to its proximity to continental sediment sources, the lack of a topographic barrier between the continental margin and the ridge axis (see also Normark and others, chap. 6, this volume, fig. 6.1), and the relatively slow spreading rate of 2.4 cm/yr (Atwater and Mudie, 1973; Riddihough, 1980; Wilson, 1989). The sedimentary fill consists of turbidite flows and hemipelagic mud (McManus and others, 1970; Karlin and Lyle, 1986; Normark and others, chap. 6, this volume) and locally exceeds 900 m in thickness (Clague and Holmes, 1987). Recent igneous activity at the ridge axis appears to have been confined to discrete volcanic edifices where sills intrude and uplift the sediment and basalt flows may be extruded onto the sea floor (Morton and others, 1987a). Hydrothermal mineral deposits are spatially associated with these volcanic edifices (Koski and others, 1988; Morton and others, 1990; Zierenberg and others, chap. 10, this volume).

The sedimentary fill at Escanaba Trough provides a record of recent deformation at the ridge axis. In this chapter we use geophysical records, including Sea Beam

[1] U.S. Geological Survey, Menlo Park, California.
[2] National Oceanic and Atmospheric Administration, Newport, Oregon.

bathymetry, single- and multi-channel seismic-reflection records, and 3.5 kHz subbottom profiles, to describe the morphology, structure, and sedimentation of the trough and the surface and subsurface expression of igneous activity. These geophysical results, combined with sea-floor observations and subsurface sampling, are used to construct a model of the structural and stratigraphic controls on the localization of hydrothermal mineral deposition.

ACKNOWLEDGMENTS

We thank Jon Childs and Eric Geist for assistance with the seismic data processing, and Carol Reiss, Maria Restrepo, and Gini Curl for assistance with the data reduction and figure preparation. Valuable discussions with Robert Zierenberg, William Normark, Stephanie Ross, Roger Denlinger, Mark Holmes, and Robert Karlin and reviews by Earl Davis and Tom Brocher helped clarify the interpretations presented in this paper.

METHODS

The data presented in this paper were collected during five different cruises between 1981 and 1986. Cruise L12-81-NP, in 1981, collected approximately 400 km of 24-channel seismic- reflection data along three profiles using a 34.9 L (2,130 in^3) air-gun array discharged at 13.8 MPa (2,000 psi). Two of the profiles are oriented perpendicular to the axis of Escanaba Trough, near latitudes 41°00′ N. and 40°30′ N., respectively (fig. 2.1). A third profile runs approximately north-south along the axis of the trough. The processing of each line included velocity analysis, normal moveout correction, common midpoint stacking, predictive deconvolution, bandpass filtering, and automatic gain control. Sections of the data were affected by severe streamer noise that was greater in the higher frequency band. To reduce this noise problem, the bandpass filtering step used an upper frequency limit of 30 Hz.

Cruise L6-85-NC, in 1985, conducted a regional single-channel seismic-reflection survey of Escanaba Trough (900 km of trackline) using a 3.9 L (237 in^3) air-gun array (fig. 2.1). The data were originally recorded in analog format. Subsequent processing included digitization, predictive deconvolution, bandpass filtering, and automatic gain control. We applied a constant-velocity finite-difference migration to selected profiles from cruises L12-81-NP and L6-85-NC to reduce diffraction hyperbolas. Gravity data and total field magnetic data were also collected on cruise L12-81-NP and magnetic data on cruise L6-85-NC. These geopotential data are discussed by Karlin and Morton (chap. 5, this volume).

Cruise L1-86-NC, in 1986, collected 160 km of single-channel seismic-reflection profiles at the northern (NESCA) and southern (SESCA) Escanaba Trough study areas utilizing a 1.3 L (80 in^3) water gun source. These data were not digitally recorded; processing for these data included bandpass filtering and automatic gain control.

Higher resolution images of the shallow subsurface were obtained with a hull-mounted 3.5 kHz subbottom profiling system using a short ping (< 1 ms). The 3.5 kHz system on the R/V *S.P. Lee* was used during all seismic-reflection profiling as well as during many sampling stations on the above-mentioned cruises and cruise L2-86-NC in 1986. On selected camera and heat-flow stations, a 3.5 kHz pinger was mounted on the wire and towed 100 to 300 m above the sea floor.

Sea Beam bathymetric data were collected in 1986 aboard the NOAA ship *Surveyor* (cruise MMS-86-1). Approximately 1,300 km of tracks were run, including cross lines for navigation control. The Sea Beam data were processed at the National Oceanic and Atmospheric Administration in Newport, Oregon.

Navigation for all geophysical profiles was provided by an integrated satellite–Loran C–Doppler sonar system, or a Loran C system. Since there is a consistent offset between Loran C coordinates and true geodetic, the Loran C navigation has been adjusted to match transit satellite fixes. Additional navigation for profiles and stations in the NESCA and SESCA work areas (cruises L1-86-NC and L2-86-NC) was provided by an acoustic navigation system and the satellite Global Positioning System (GPS) (see Morton and others, chap. 1, this volume). Sea Beam data were collected under Loran C control only, and shifted to match the geophysical data controlled by transit satellite or GPS positioning.

RESULTS

MORPHOLOGY AND STRUCTURE OF ESCANABA TROUGH

Gorda Ridge exhibits a "Mid-Atlantic Ridge" morphology with a deep axial valley. A right lateral offset of the ridge near latitude 41°40′ N. separates Escanaba Trough, the southern part of Gorda Ridge, from the middle segment of Gorda Ridge. The east-west-striking Mendocino Fracture Zone marks the southern boundary of Escanaba Trough at latitude 40°25′ N. The floor of Escanaba Trough is at a depth of 3,200 to 3,400 m, and the flanking ridges rise 900 to 1,500 m above the valley floor (fig. 2.2). The axis of Escanaba Trough is divided into two segments by a 5-km right-lateral offset near latitude 41°08′ N. (fig. 2.2). This offset may represent an overlap zone between discrete ridge segments; however, this structure cannot be conclusively inferred from the bathymetry alone owing to the thick sediment cover. The lengths of the two individual segments (80 to 100 km) are consistent with segment lengths on the northern Gorda Ridge.

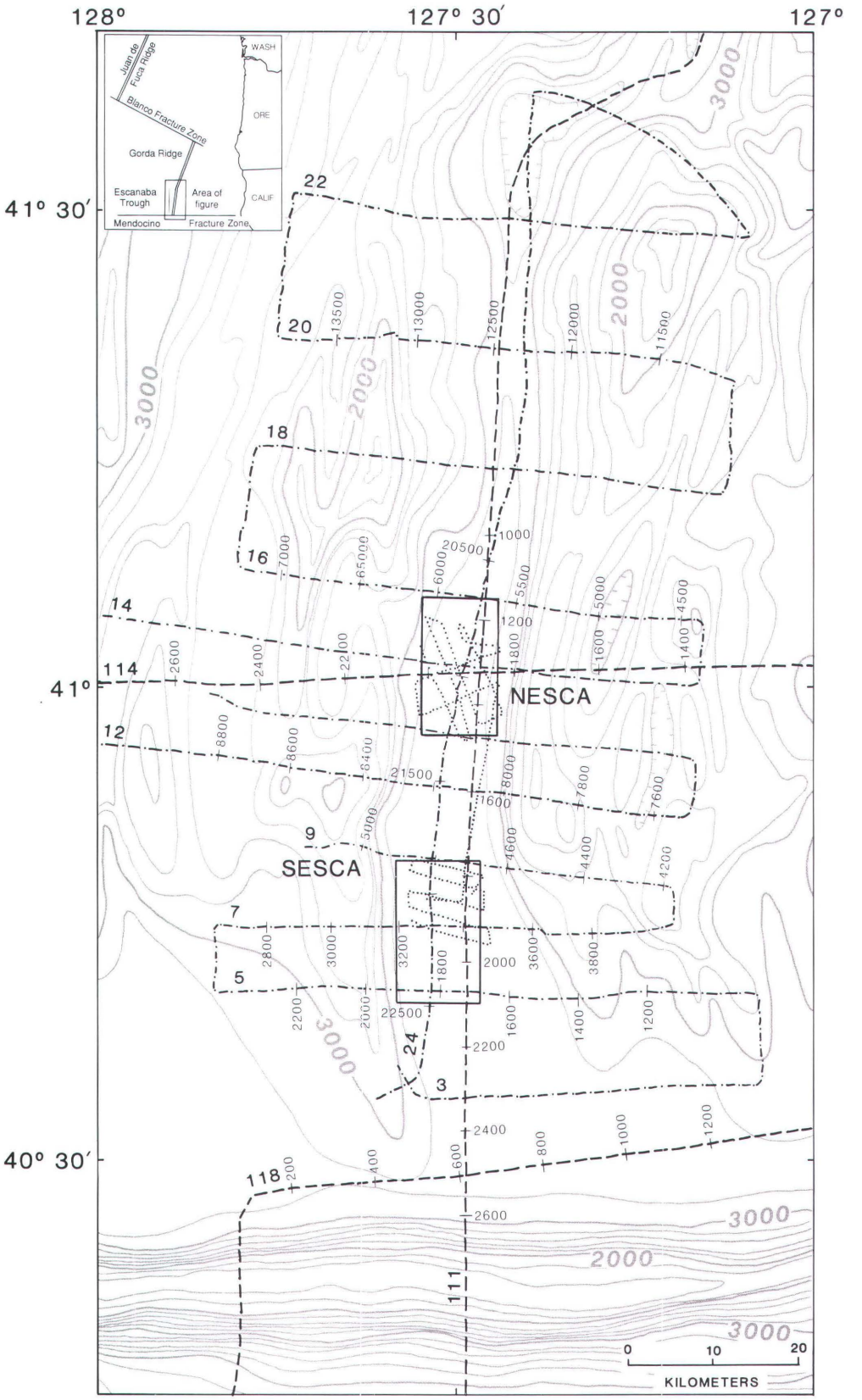

Figure 2.1. Regional bathymetry of Escanaba Trough modified from Wilde and others (1978); contour interval 200 m. Locations of seismic reflection profiles used in this study are shown: 24-channel seismic-reflection lines from cruise L12-81-NP (dashed); single-channel air-gun lines from cruise L6-85-NC (dot-dash); single-channel water-gun lines from cruise L1-86-NC (dotted). Numbers along selected multi- and single-channel air-gun lines indicate shot number. Selected profiles are shown in figures 2.3 to 2.7.

From north to south, the axis of the northern segment of Escanaba Trough is characterized by a deep basin (> 3,500 m deep) with thin sediment cover; a narrow axial high (about 3,200 to 3,250 m deep) that extends from about latitude 41°28′ N. to 41°17′ N. (figs. 2.2, 2.3 top); and a flat, sediment-covered floor about 5 km wide and 3,300 m deep (fig. 2.3 bottom). The axial high block appears to have been a topographic barrier for continentally derived sediment that entered the trough at the southern end and flowed northward (Normark and others, chap. 6, this volume). Sea Beam mapping reveals numerous small volcanoes at the ridge axis on the axial high block and along the wide terrace bounding the western side of the valley (fig. 2.2).

The axis of the segment south of latitude 41°08′ N. is characterized by a flat floor 12 to 20 km wide and covered by as much as 900 m of sediment (figs. 2.4, 2.5, 2.6; see also Karlin and Morton, chap. 5, this volume, fig. 5.2). The walls that bound the axial valley decrease in elevation southward; and south of about latitude 40°35′ N. the bathymetric expression of these ridges ends and they are apparent only as buried basement highs on the seismic-reflection records (fig. 2.6 bottom).

In most places, the sediment fill of the southern part of the trough is characterized by subhorizontal, reflective layers (figs. 2.4, 2.5, 2.7). High-angle extensional faults cross-cut the sediment fill near the axis of the trough (figs. 2.4, 2.6). In places, the floor of the trough is bounded by

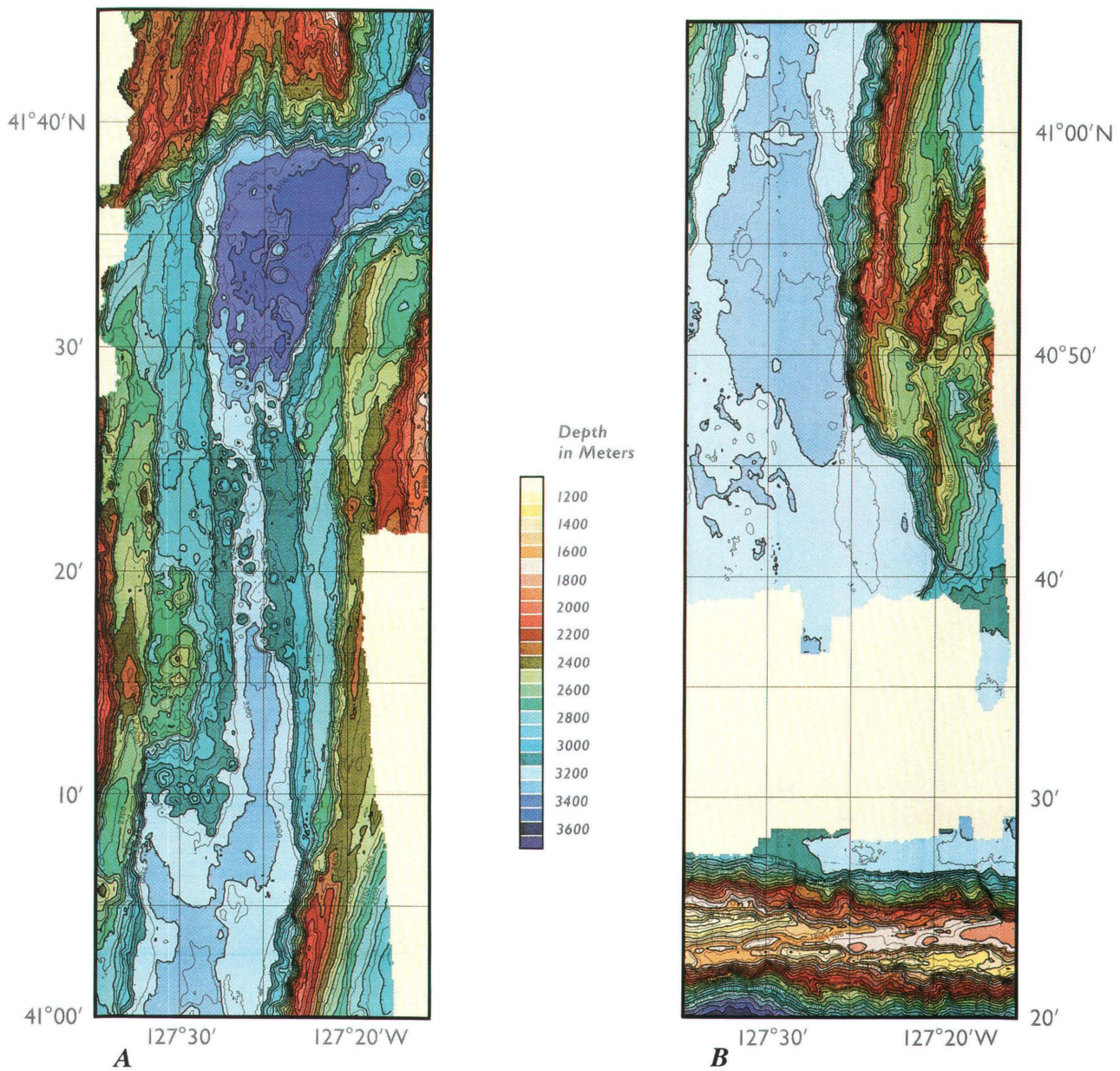

Figure 2.2. Sea Beam bathymetric map of Escanaba Trough. *A*, Northern half. *B*, Southern half. Contour interval is 50 m; each color change represents 100 m. Yellow indicates areas of no data.

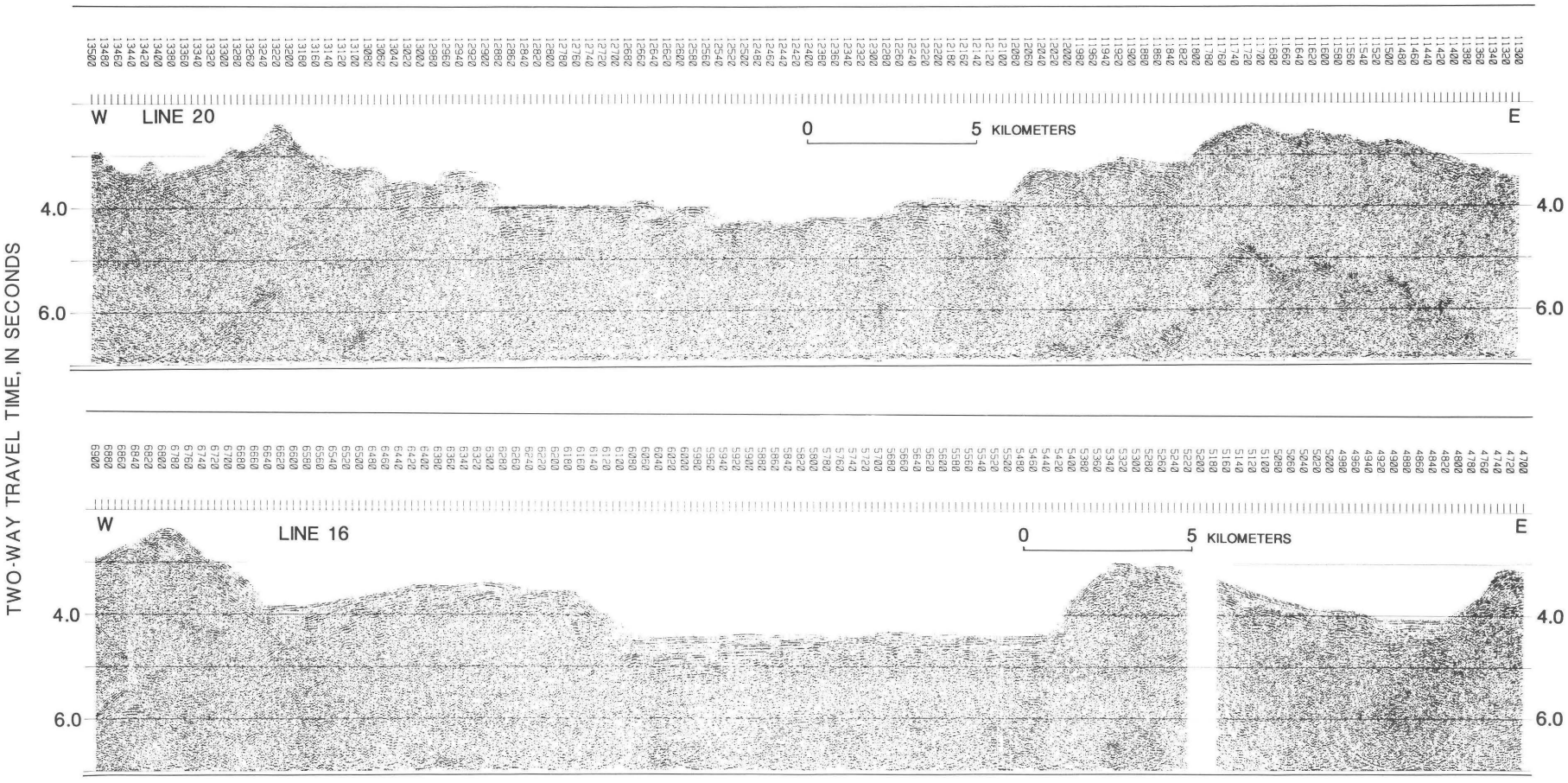

Figure 2.3. Migrated single-channel air-gun seismic-reflection profiles across Escanaba Trough from cruise L6-85-NC: line 20 (top) and line 16 (bottom). Vertical exaggeration is about 2:1. There is little or no sediment cover in axial valley on line 20. Numbers above profile indicate shot points along that line. See figure 2.1 for location of profiles.

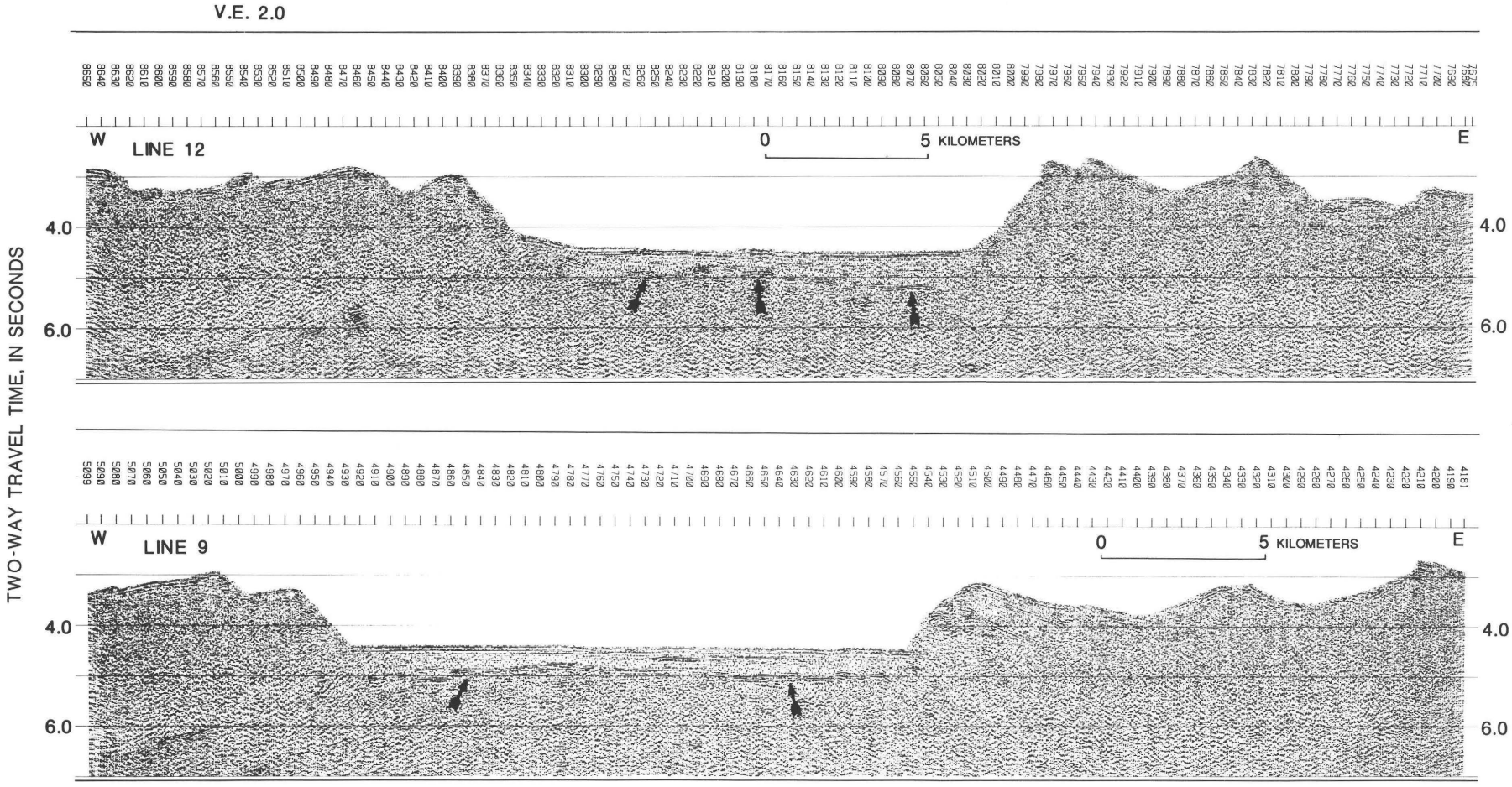

Figure 2.4. Migrated single-channel air-gun seismic-reflection profiles across Escanaba Trough from cruise L6-85-NC: line 12 (top) and line 9 (bottom). Vertical exaggeration is about 2:1. Arrows mark reflection characterized by coalescing hyperbolas that is interpreted as top of igneous basement. High-amplitude, horizontal reflection near shot points 4,690 to 4,720 on line 9 is probably a basaltic sill. Region of uplifted and disturbed sediment near shot points 8,170 to 8,200 on line 12 is an edifice where mineralized sand bed was cored (Morton and others, 1987b; Normark and others, chap. 6, this volume). Numbers above profile indicate shot points along that line. See figure 2.1 for location of profiles.

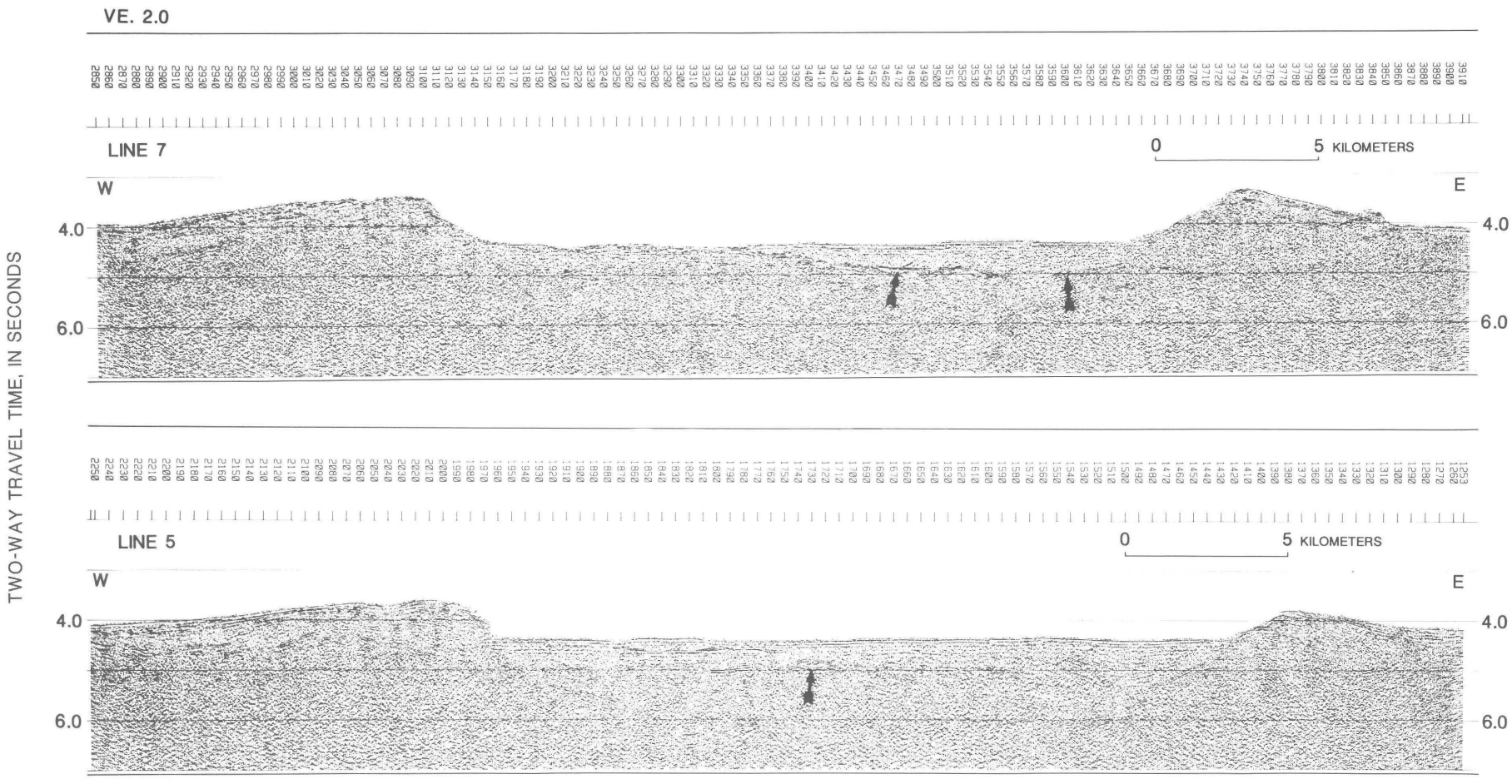

Figure 2.5. Migrated single-channel air-gun seismic-reflection profiles across Escanaba Trough from cruise L6-85-NC: line 7 (top) and line 5 (bottom). Vertical exaggeration is about 2:1. Upper part of sedimentary section within trough is characterized by flat-lying reflectors that in most places appear relatively undisturbed except for occasional high-angle faults. Remainder of sedimentary section is less reflective and well layered, more deformed, and characterized by discontinuous and dipping reflections. Near eastern side of axial valley along line 5, sedimentary section thickens to more than 1.5 s two-way travel time. Arrows mark top of igneous basement. Flat-lying, higher amplitude sections of this reflection, such as between shot points 3,450 to 3,490 along line 7, could represent igneous sills emplaced near sediment-basement interface. Numbers above profile indicate shot points along that line. See figure 2.1 for location of profiles.

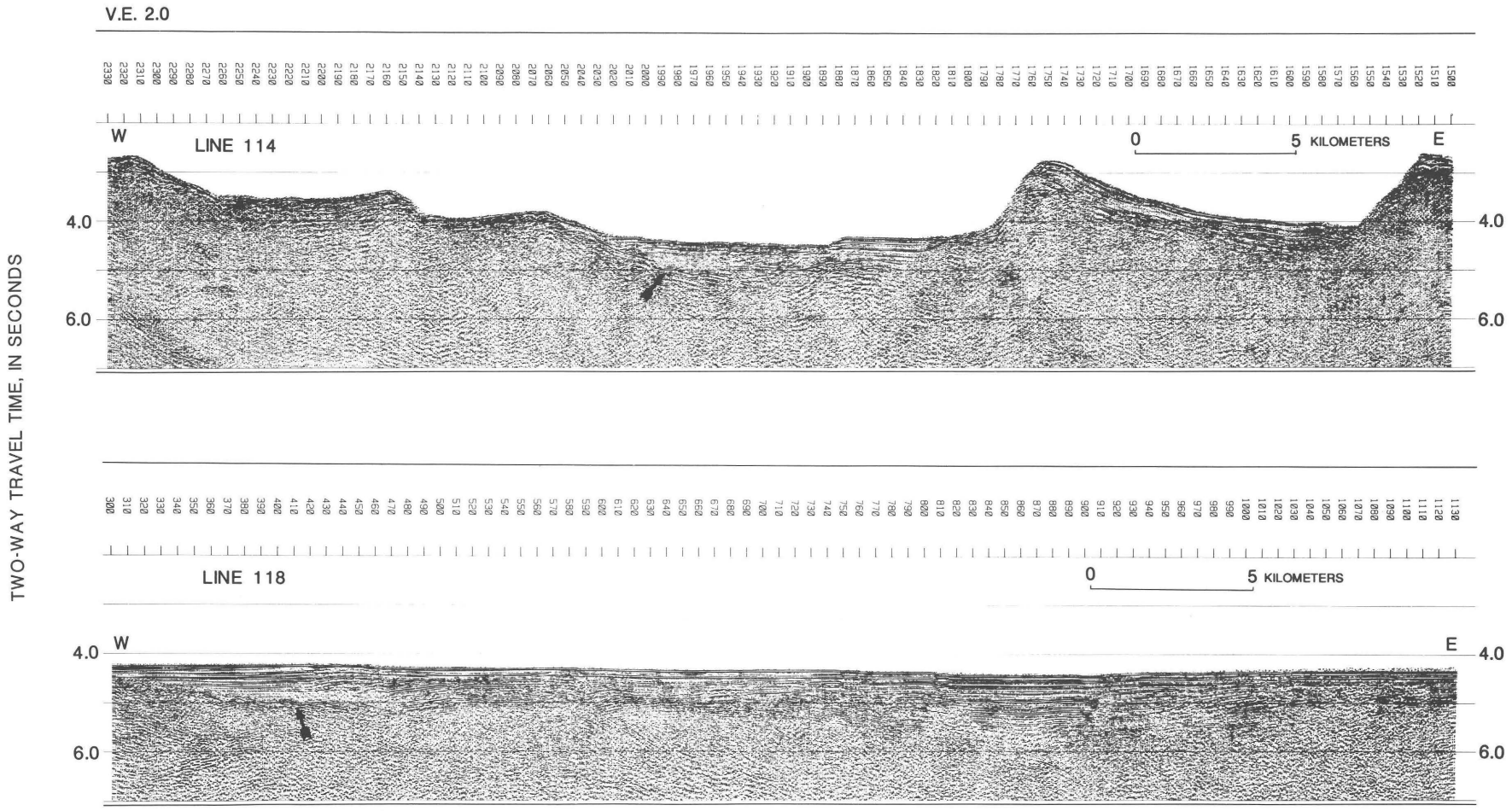

Figure 2.6. Migrated multi-channel seismic-reflection profiles across Escanaba Trough from cruise L12-81-NP: line 114 (top) and line 118 (bottom). Vertical exaggeration is about 2:1. Arrows mark top of igneous basement. Line 114 crosses axis of trough near volcanic edifice at latitude 41° N. (NESCA site), and line 118 crosses axis immediately north of Mendocino Fracture Zone. Shot points 1,800 to 1,880 on line 114 show example of terrace of relatively undisturbed sediment bounding axial valley floor. On line 118, sedimentary section consists of two primary intervals: deeper interval that has been faulted, tilted, and folded, and less disturbed upper interval that is cut by high-angle faults. Region of down-dropped and thickened sediment layers near shot points 820 to 910 marks region of recent extension. Numbers above profile indicate shot points along that line. See figure 2.1 for location of profiles.

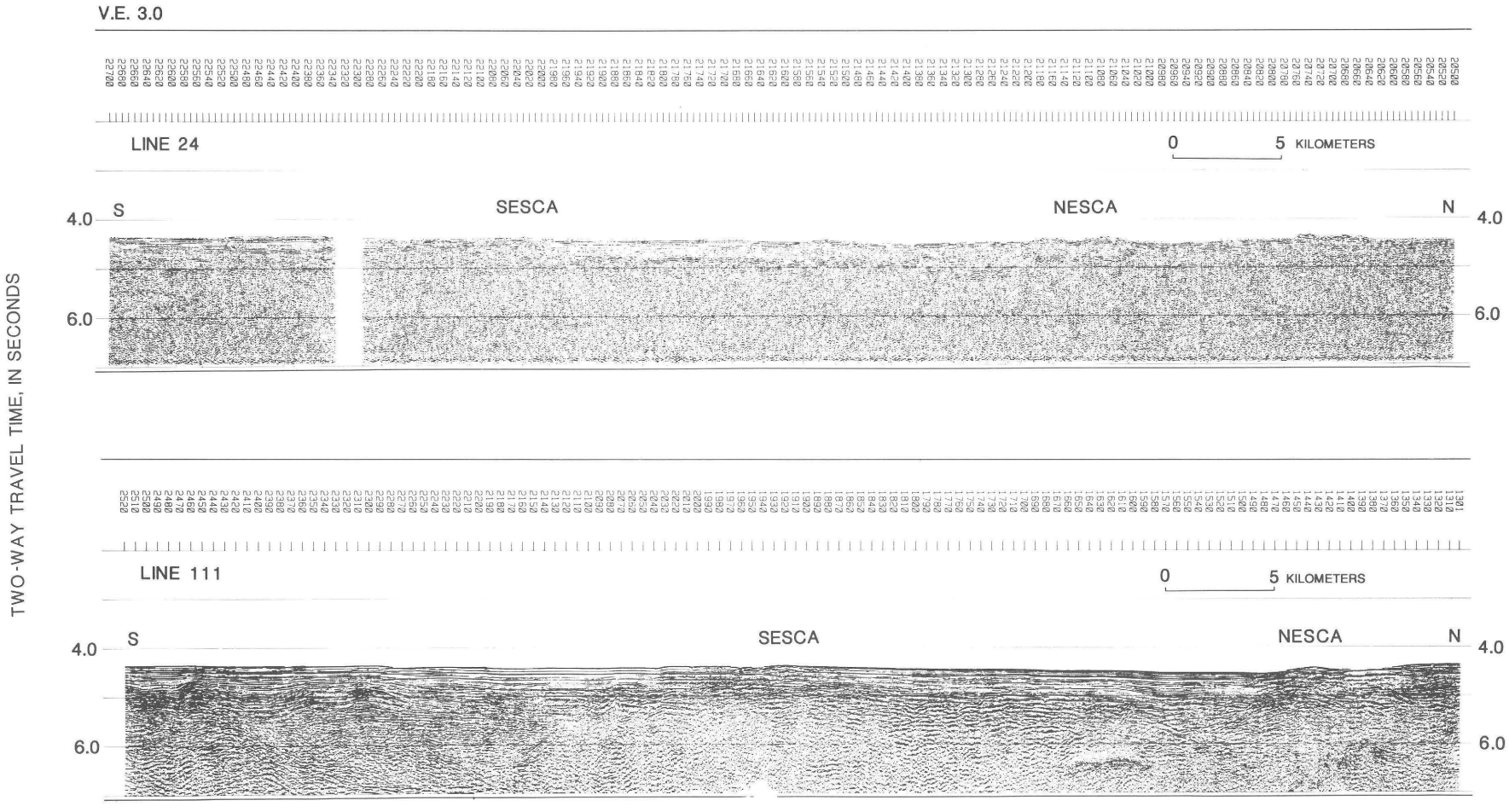

Figure 2.7. Migrated single-channel seismic-reflection line 24 from cruise L6-85-NC (top) and multi-channel seismic-reflection line 111 from cruise L12-81-NP (bottom) along axis of sediment-covered part of Escanaba Trough. Vertical exaggeration is about 3:1. Location of SESCA and NESCA sites is marked on each profile. Numbers above profile indicate shot points along that line. See figure 2.1 for location of profiles.

terraces where sediment has been uplifted a few tens of meters to about 100 m (figs. 2.6 top, 2.8). The outer flanks of the ridges that bound the trough are commonly covered by several hundred meters of outward-dipping sediment layers (figs. 2.5, 2.6).

The sediment fill of Escanaba Trough reaches its maximum thickness at the southern end of the trough. Multichannel seismic-reflection profile 118 crossed the axis of Escanaba Trough just north of the Mendocino Fracture Zone (fig. 2.1). Although the basement reflector cannot be identified along all of line 118, in places the thickness of the sediment fill exceeds 900 to 1,000 m (fig. 2.6 bottom). Here the sediment fill is characterized by an upper unit of subhorizontal reflectors, cut by normal faults, which overlies an interval of tilted, more highly deformed layers.

At the south end of Gorda Ridge, near the Mendocino Fracture Zone, the axis of spreading, as defined by the occurrence of extensional faults, and the ridge bounding the eastern side of the axis curve markedly to the east (figs. 2.2, 2.8). This eastward curvature is also apparent in structural trends outside of the ridge axis, as imaged by GLORIA side-scan images of the area where Gorda Ridge intersects the Mendocino Fracture Zone (EEZ-SCAN 84, 1986).

Igneous rocks intrude the sediment cover at several locations along Escanaba Trough. These igneous complexes are here referred to as volcanic edifices, as they are composed of both intrusive and extrusive components. On bathymetric records, the edifices are typically characterized by a broad uplift of a few tens of meters or less and greater topographic roughness than the surrounding less disturbed sediment fill (figs. 2.2, 2.9, 2.10). Igneous basement appears to shallow beneath these edifices (fig. 2.7). Single-channel reflection line 7 (fig. 2.5 top), which images a volcanic edifice at the SESCA area, shows a broad basement high that appears to reach the sea floor. Volcanic rocks have been observed at the sea floor (Morton and others, 1990; Zierenberg and others, chap. 10, this volume) and recovered by dredging from the SESCA edifice (Davis and others, chap. 9, this volume). Other edifices (fig. 2.4, 2.5 bottom) are characterized by disrupted sediment layers and high-amplitude subhorizontal reflectors within the sediment section. These reflectors probably represent sills emplaced within the sediment section.

SESCA AND NESCA AREAS

The sediment fill surrounding the volcanic edifices is generally well layered and flat lying. In these regions,

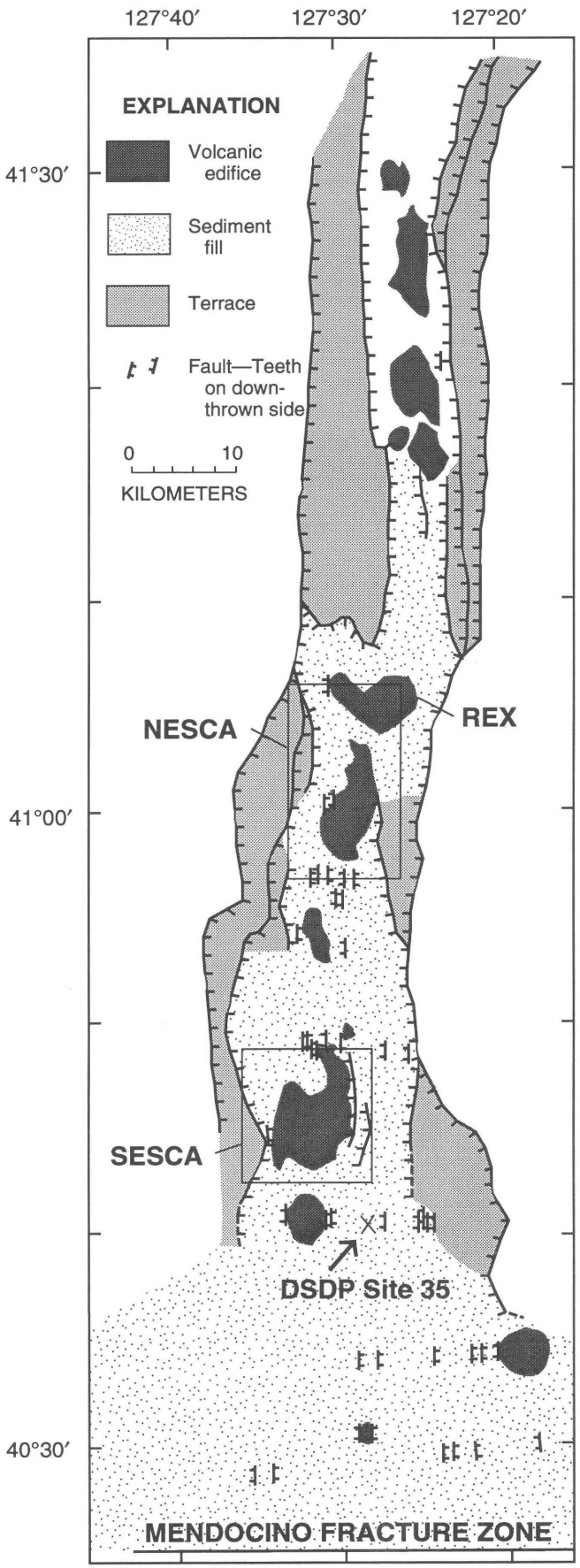

Figure 2.8. Generalized geologic map of Escanaba Trough showing location of volcanic edifices, approximate extent of sediment fill, location of terraces, NESCA and SESCA study areas (rectangles), location of edifice REX, and location of DSDP Site 35.

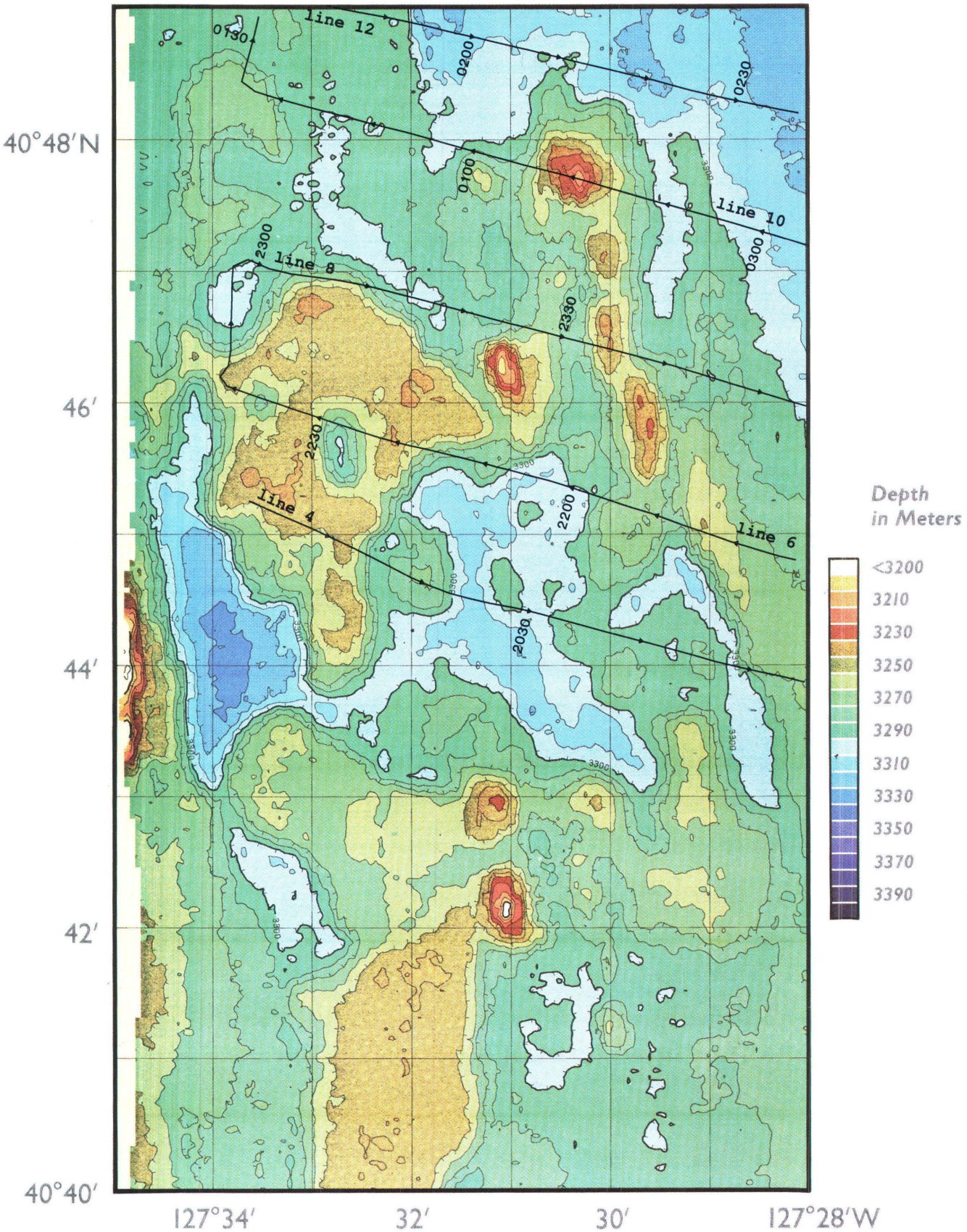

Figure 2.9. Sea Beam bathymetric map of SESCA study area. Contour interval is 10 m and is noted by color change. Locations of single-channel water-gun reflection profiles 4 to 12, cruise L1-86-NC, are shown. Numbers along tracklines represent time of day corresponding to annotations at top of seismic reflection profiles in figure 2.12. Hachures indicate area of closed low. Map area is approximately 10 km wide.

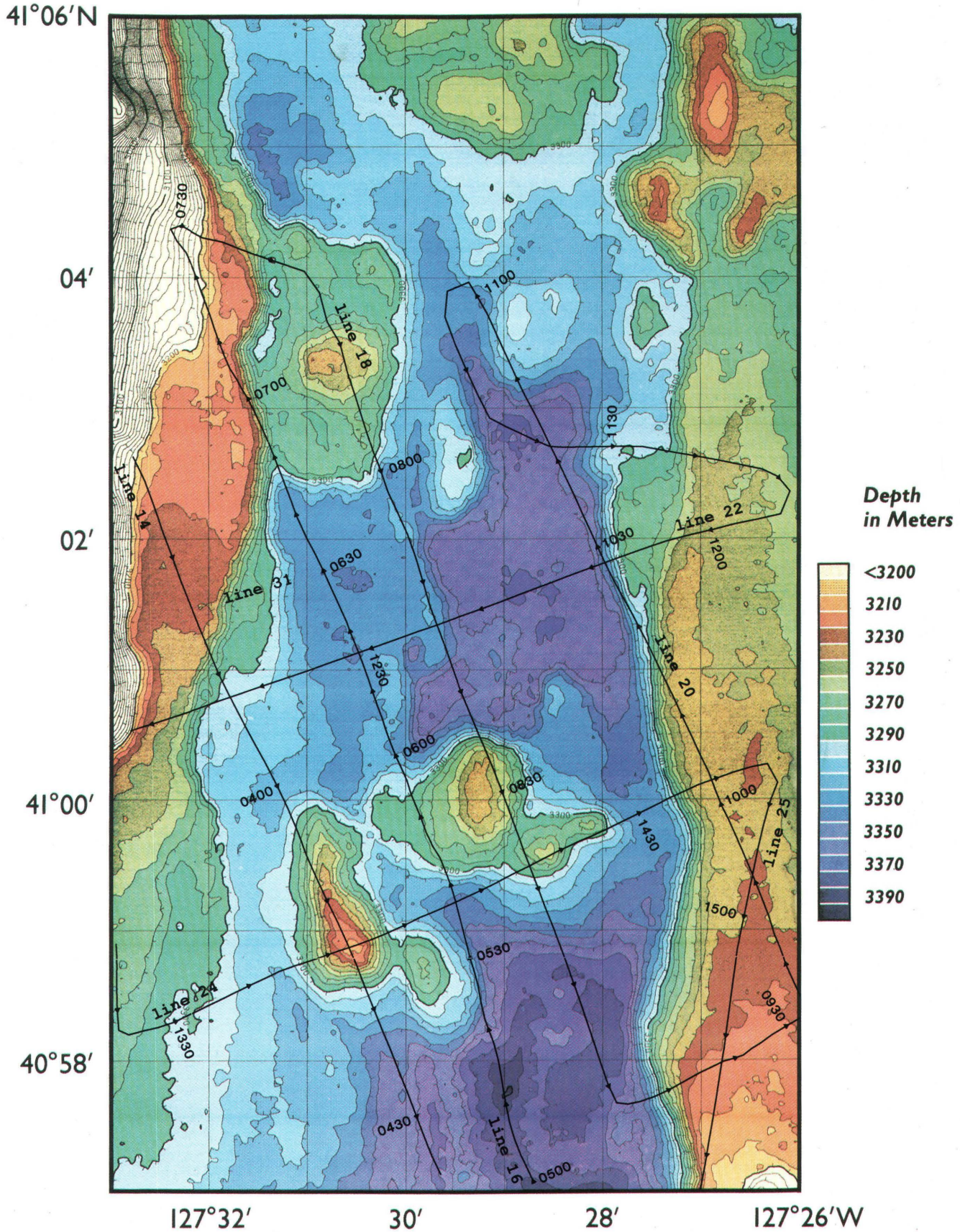

Figure 2.10. Sea Beam bathymetric map of NESCA study area. Contour interval is 10 m and is noted by color change. Locations of single-channel water-gun reflection profiles 14 to 25 and 3.5 kHz profile 31, cruise L1-86-NC, are shown. Numbers along tracklines represent time of day corresponding to annotations at top of seismic-reflection profiles in figures 2.13 and 2.14. Hachures indicate area of closed low. Map area is approximately 10 km wide.

subbottom penetration on 3.5 kHz records ranged from about 25 to 50 m. Within the upper 50 m of sediment, as many as eight thin, well-defined subbottom reflectors are identified (fig. 2.11). The spacing of these reflectors is often consistent over distances of several kilometers. In places, the distinct layering grades into regions of thicker, less continuous reflections. These echo characteristics are considered indicative of fine-grained sediments with small to moderate amounts of thin coarser grained beds (sand and silt) (Damuth, 1975; Damuth and Hayes, 1977). Surficial cores and DSDP sections from Escanaba Trough confirm that the sediment section imaged by the 3.5 kHz profiles consists predominantly of mud with thin silt-and-sand turbidites (Normark and others, chap. 6, this volume). The thickness of many of these turbidite beds is less than the resolution of the 3.5 kHz recording system; however, the layers on the 3.5 kHz records could represent reflections from sandy turbidites a few tens of centimeters thick or groups of several thinner beds. O'Connell and Normark (1986) carefully correlated acoustic units with lithologies of cores recovered by DSDP drilling on the Mississippi fan and suggested in several instances a causal relationship between coarse-grained beds or groups of beds and reflections of a character similar to those observed at Escanaba Trough.

Single-channel water-gun reflection records reveal the same well-layered character of the entire sediment section adjacent to the SESCA and NESCA sites (figs. 2.12, 2.13, 2.14). Steeply dipping normal faults displace the sediment layers in a few locations. An acoustically transparent zone from approximately 85 to 130 m below the sea floor is imaged on nearly all of the profiles near SESCA and NESCA. Single-channel air-gun reflection profiles from the region between SESCA and NESCA also imaged this transparent zone (Davis and Becker, chap. 3, this volume), suggesting that the horizon is continuous, at least from SESCA through the NESCA area. Low-amplitude or nonreflective intervals on seismic records of sedimentary rocks generally indicate a homogeneous zone of predominantly one lithologic type, which can be either coarse grained or fine grained (Sangree and Widmier, 1977). DSDP Site 35 cores 3, 4, and 5 were sampled within the interval corresponding to this acoustically transparent zone. These three cores consist predominantly of sand, as opposed to the rest of the section which is predominantly mud with thin sand or silt layers (McManus and others, 1970; Normark and others, chap. 6, this volume). This acoustically transparent zone thus probably corresponds to a coarser grained unit deposited during a period of rapid sedimentation in the trough.

At the margins of the volcanic edifices, there is an abrupt transition from well-layered, undisturbed sediment to highly disturbed (faulted and tilted) layers. This transition is apparent on both 3.5 kHz subbottom profiles (fig. 2.11) and water-gun reflection profiles (figs. 2.12, 2.13, 2.14) and corresponds approximately with the topographic expression of the edifices (figs. 2.15, 2.16). A volcanic edifice located between SESCA and NESCA sites has little sea-floor topographic expression but is readily identified by this abrupt transition from undisturbed to disturbed sediment layers. At both the SESCA and NESCA edifices, 3.5 kHz profiles indicate that this disturbance of the sediment layering affects the youngest beds at the sea floor, indicating recent movement at the edifices (fig. 2.11).

Although the single- and multi-channel seismic-reflection profiles suggest that acoustic basement is present at or near the sea floor at volcanic edifices such as SESCA and NESCA (fig. 2.5), higher resolution profiling and visual observations indicate that much of the sea floor at the SESCA and NESCA sites is sediment covered. A hard sea-floor return on 3.5 kHz records, and camera and submersible observations indicate that basalt is locally present at or near the sea floor. At the SESCA site, the two primary areas of basalt exposure are west of "3170 Hill" and at the base of "North Hill" on the south side (fig. 2.15). The extent of the first area is inferred primarily from

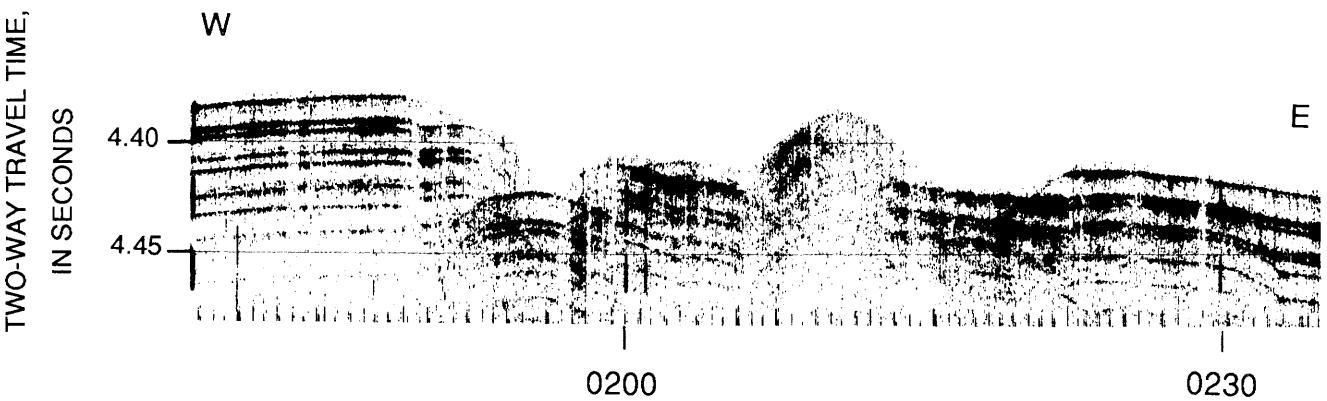

Figure 2.11. 3.5 kHz record along L1-86-NC line 12 at north end of SESCA area. See figure 2.9 for location of profile. Well-layered sediment at west side of profile illustrates typical reflectivity of sediment in trough away from volcanic edifices. Central part of profile shows faulted and tilted sediment typical of volcanic edifices. Numbers along bottom indicate shot points along line 12.

geophysical profiles; several visual observations confirm the presence of basalt at the sea floor in the second area (Ross and Zierenberg, chap. 8, this volume). In the NESCA area, basalt is exposed on the eastern part of "Central Hill" and in the flat-floored basins north and south of Central Hill (fig. 2.16). Over most of the basin north of Central Hill, 3.5 kHz subbottom profiles reveal a hard sea-floor return characteristic of basalt; on two profiles, however, layering appears to be present beneath this hard return (fig. 2.17). It is unlikely that the 3.5 kHz system could "see through" thick basalt flows to image underlying structure. Three possible explanations are suggested for this observation: (1) Parts of the basin floor are covered not by basalt but rather by sand-rich sediment that gives rise to

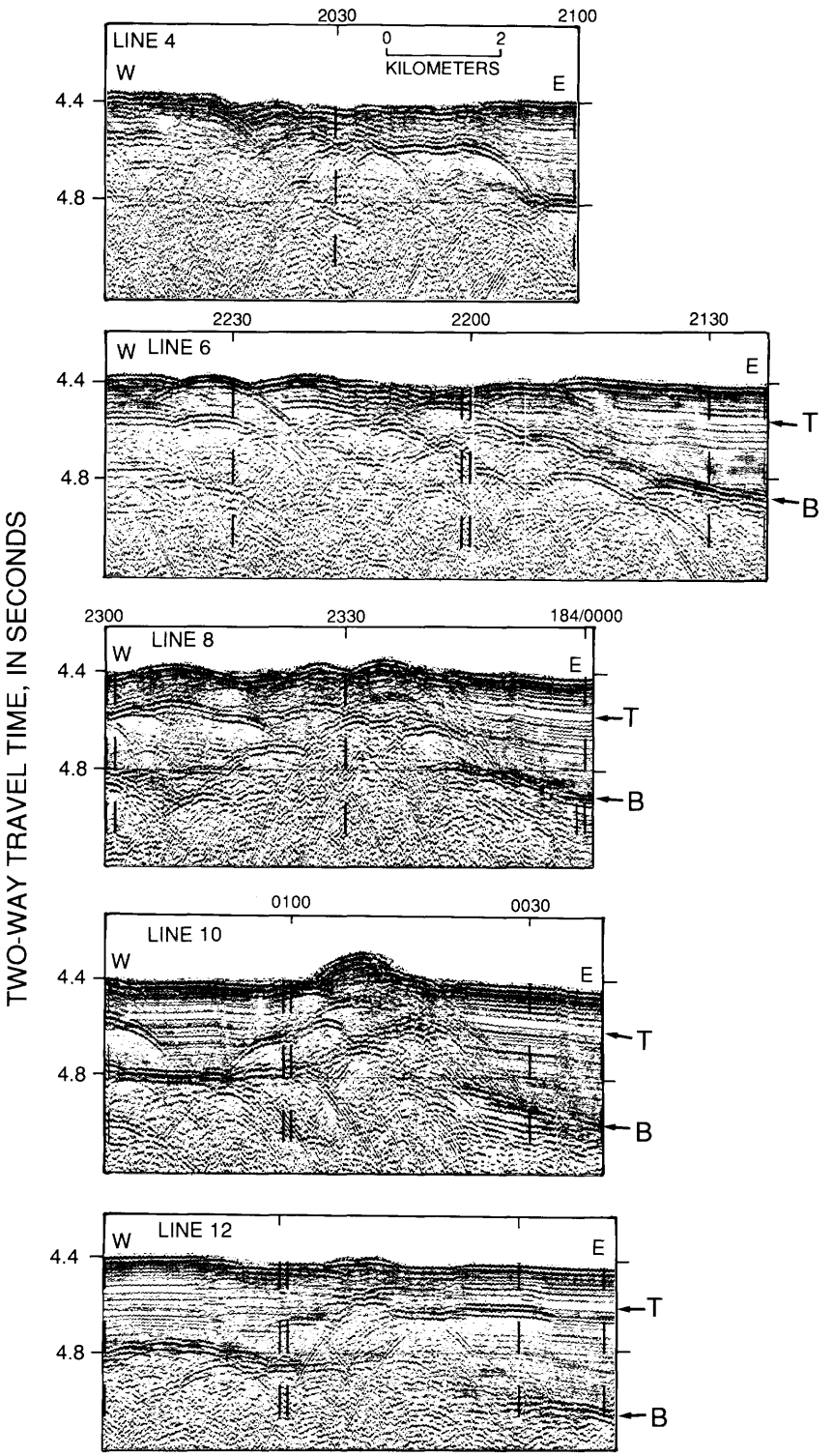

Figure 2.12. Single-channel water-gun profiles 4, 6, 8, 10, and 12 from cruise L1-86-NC in SESCA area. See figure 2.9 for location of profiles. Vertical exaggeration is about 5.7. "T" marks acoustically transparent zone about 85 to 130 m below sea floor. Reflector "B" is interpreted as top of igneous basement. Numbers above profile indicate shot points along lines.

the high-amplitude return and allows some penetration of 3.5 kHz energy; (2) most of the basin floor is covered by sheet flow basalt, but isolated sediment kipukas exist, thus the wide beam pattern of the 3.5 kHz echo sounder could result in imaging both a sedimentary section and a nearby hard basalt sea floor; and (3) the basin floor consists of sediment overlain by basalt sheet flow(s) thin enough that the 3.5 kHz energy is able to partially image the underlying sedimentary section. The flat character of the basin floor (fig. 2.10) and the limited visual observations (Ross

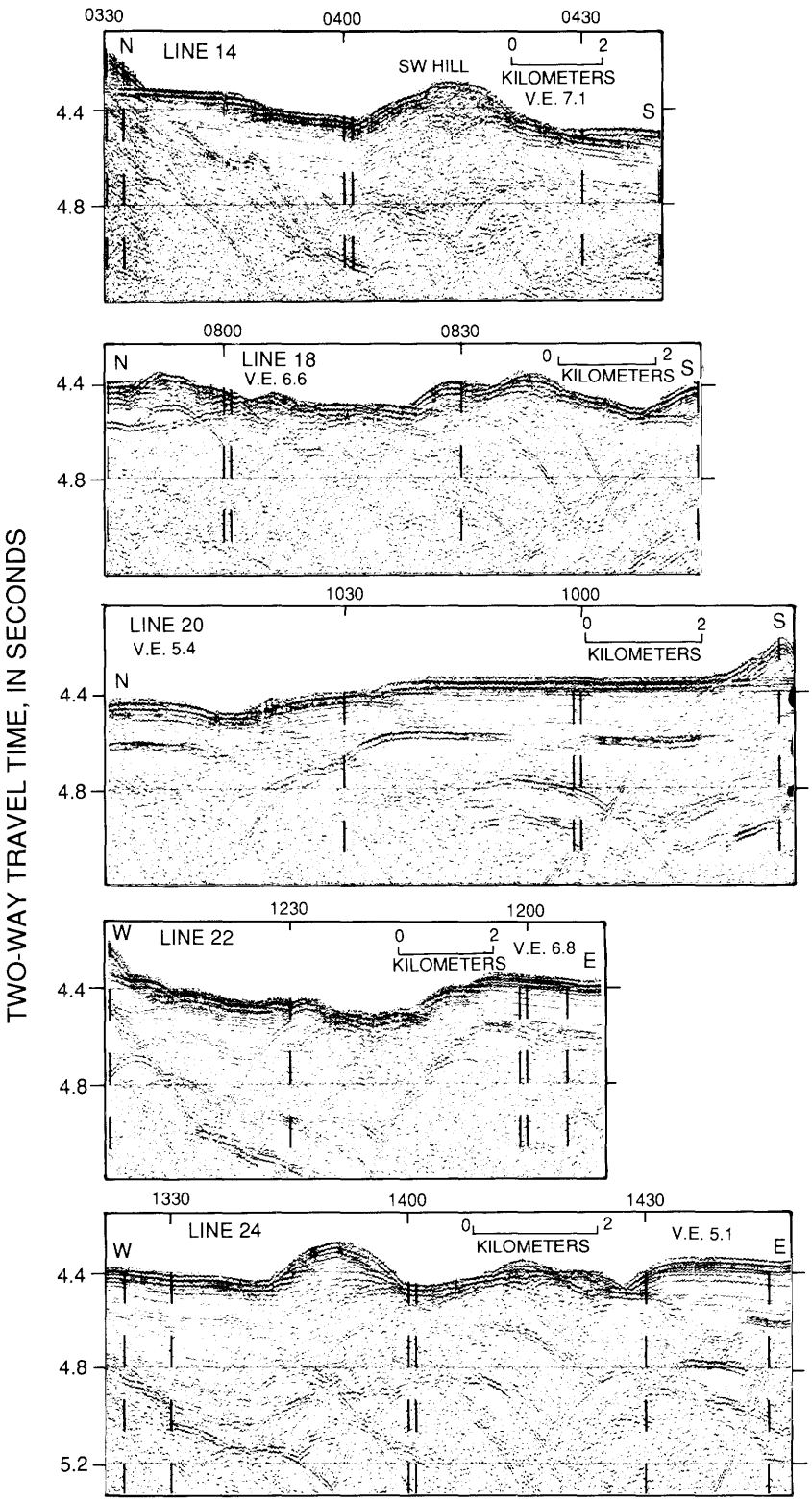

Figure 2.13. Single-channel water-gun profiles 14, 18, 20, 22, and 24 from cruise L1-86-NC in NESCA area. See figure 2.10 for location of profiles. Vertical exaggeration (V.E.) varies and is noted on each profile. Top of igneous basement is marked by discontinuous reflection frequently consisting of coalesced hyperbolas. Thickness of sedimentary section varies considerably in NESCA area from 0 to more than 0.6 s two-way travel time (about 550 m). Transparent zone noted on SESCA profiles is also present in undisturbed parts of NESCA area. High-amplitude reflections within sedimentary section and parallel to sediment layering are observed along parts of lines 20 and 24 and on lines 16 and 25 (fig. 2.14). These horizontal reflections probably represent buried basalt flows or sills. Alternatively, they could represent coarse-grained, more reflective sediment layers, or mineralized zones within sedimentary section. Numbers above profile indicate shot points along lines.

and Zierenberg, chap. 8, this volume; Zierenberg and others, chap. 10, this volume) favor the basin floor being formed by basalt sheet flow(s); however, the extent of our visual observations is not sufficient to distinguish among these possible scenarios. High-amplitude reflections on water-gun profiles (figs. 2.13, 2.14) within the sedimentary section suggest the presence of shallowly buried flows or shallow sills at several locations in the NESCA area. Original glass surfaces on basalt samples dredged from both the SESCA and NESCA sites have no measurable palagonite, indicating very recent volcanic activity at both sites (Morton and others, 1987a).

Detailed topographic mapping from Sea Beam (figs. 2.9, 2.10) reveals several small hills less than 1 km in diameter and up to 100 m high at several of the volcanic edifices, including the SESCA and NESCA sites. Massive sulfide deposits up to 200 m in length occur near the base of these hills (Morton and others, 1990; Zierenberg and others, chap. 10, this volume). The hills are relatively flat topped and exhibit the same well-layered sedimentary character on 3.5 kHz profiles as the surrounding sea floor (fig. 2.18; see also Morton and others, 1990, fig. 5.5). Water-gun line 10 (fig. 2.12) over North Hill at SESCA as well as 3.5 kHz profiles over other hills indicate that the layers at the top of the hills commonly dip to the west. Faulting is apparent at or near the base of the hills on several profiles. Visual observations from submersibles indicate that the slopes of the hills are steep, frequently veneered by debris resulting from mass wasting, and in places expose bedded sediment (Zierenberg and others, chapter 10, this volume). A well-defined reflection interpreted as igneous basement is seen on line 10 immediately east and west of North Hill at a depth of 0.5 s and 0.4 s, respectively. The reflector appears to shallow slightly near the hill, then terminates in a series of discontinuous strong hyperbolic reflections beneath the hill that probably represent sills.

To obtain better resolution in the shallow subsurface, and in particular to attempt to resolve areas of near-surface mineralization we mounted a 3.5 kHz pinger on the camera sled during selected stations. In most cases we obtained poor results with the 3.5 kHz pinger in the SESCA and NESCA sites, with little or no penetration of the subsurface. Penetration ranged from 0 to about 50 ms (about 38 m) on the best records, and subsurface layering, where observed, resembles a fainter version of that imaged with the hull-mounted system. The pinger was rigidly attached to the camera sled, and it is likely that considerable energy was transmitted to the sled rather than downward. On one station in the NESCA area, a strong horizontal reflection was recorded about 30 ms (about 23 m) below the sea floor (fig. 2.19). Along the camera track before and after this reflector, the sea floor is characterized by the typical flat-lying sediment cover with no hydrothermal deposits. Directly above the bright subsurface reflection, the camera system revealed outcrops of probable hydrothermal deposits on the sea floor (Zierenberg and others, chap. 10, this

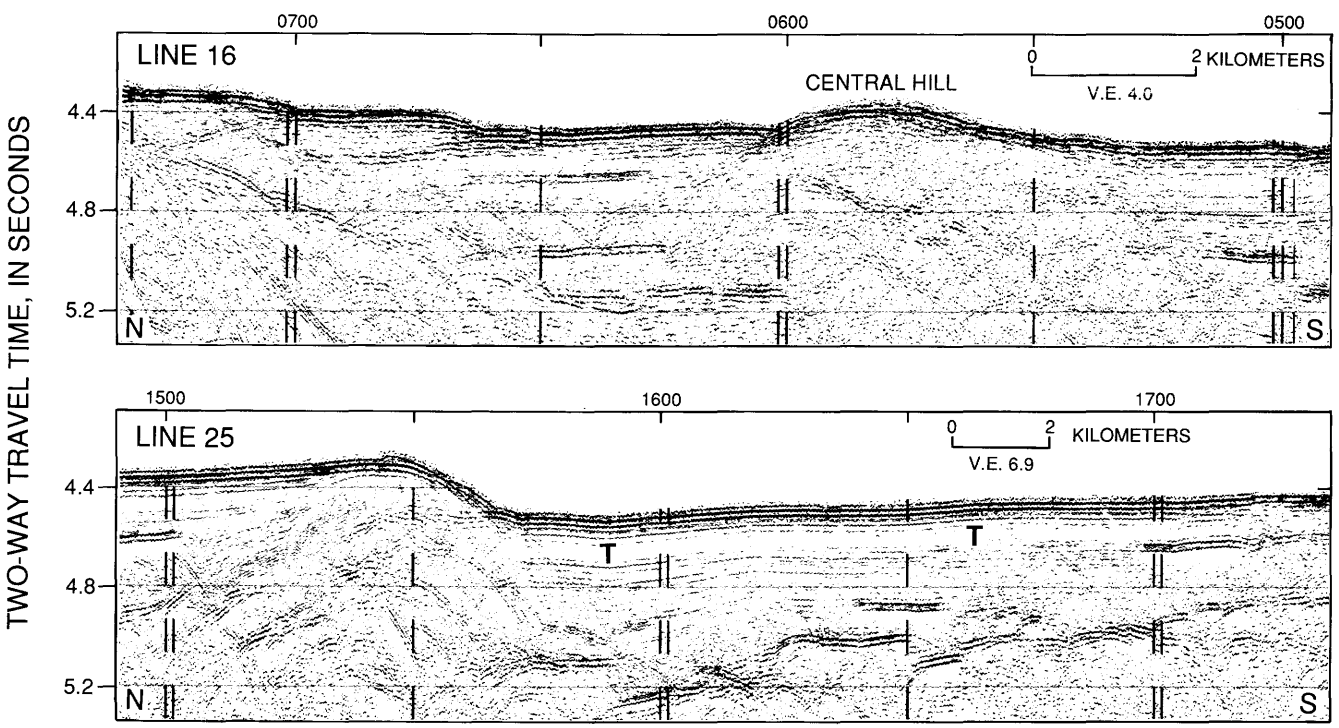

Figure 2.14. Single-channel water-gun profiles 16 and 25 from cruise L1-86-NC in NESCA area. See figure 2.10 for location of profiles. Vertical exaggeration (V.E.) is noted on each profile. "T" marks acoustically transparent zone. Numbers above profile indicate shot points along lines.

volume). The concordance of this bright reflection with the local layering and the camera observations suggest one possible interpretation of this reflector: that it represents a mineralized bed underlying the sea-floor deposit, such as that cored at station L1-86-27G south of NESCA (Normark and others, chap. 6, this volume). Other possible causes of the higher reflectivity cannot be ruled out, such as an along-strike change in composition or compaction of the sediments, increased amounts of volcanic detritus or a buried flow, or a change in the overlying sedimentary section allowing more energy to penetrate to this reflector. Explanations calling on volcanic detritus or flows are not, however, supported by observation of nearby volcanic exposures.

DISCUSSION AND CONCLUSIONS

Results from DSDP Site 35 indicate a Pleistocene age for most of the sediment fill of Escanaba Trough (Bukry and Bramlette, 1970; Gartner, 1970) and rapid sedimentation rates are suggested (Normark and others, chap. 6, this

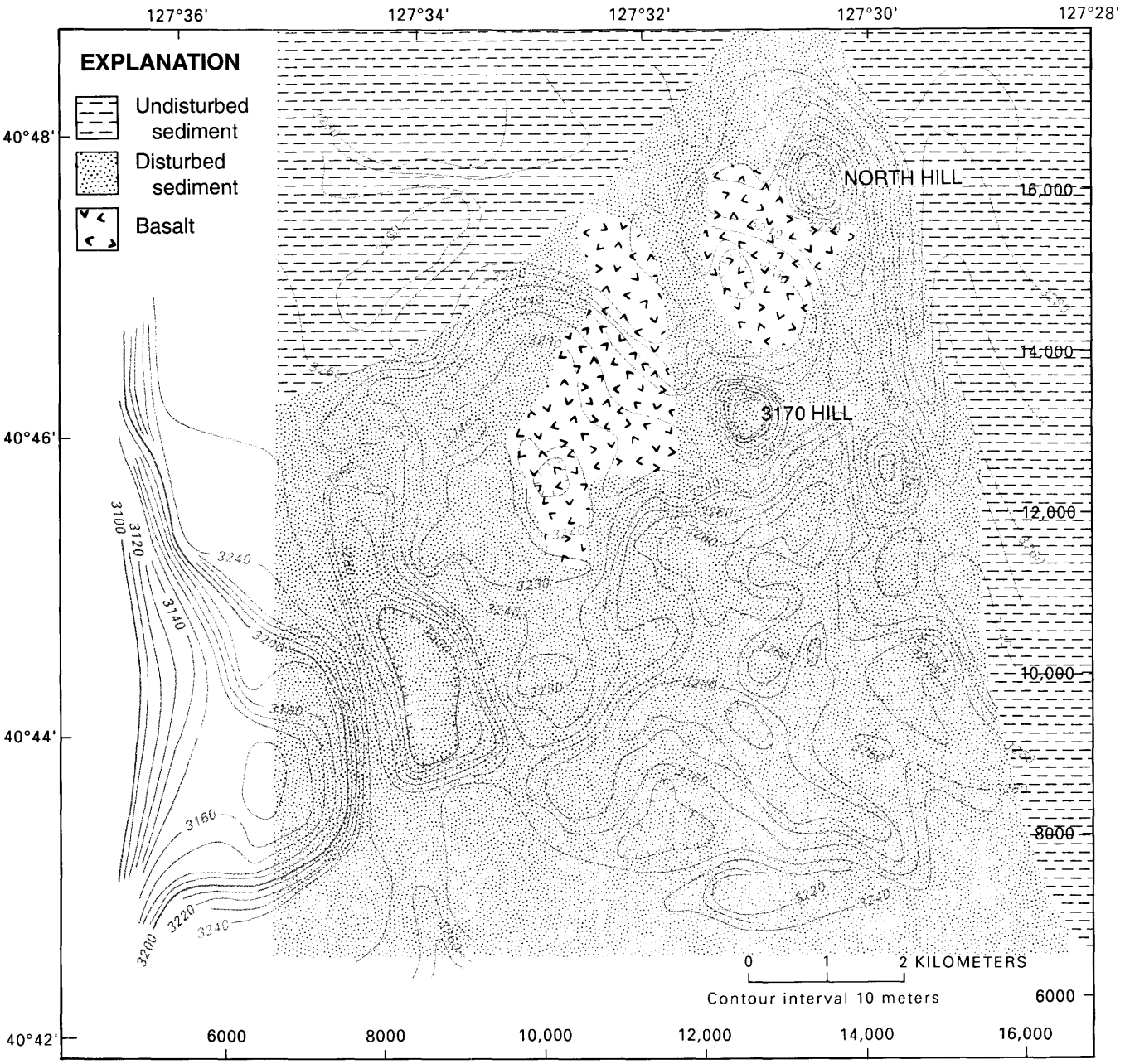

Figure 2.15. Map of SESCA area showing regions of disturbed and undisturbed sediment and inferred extent of volcanic flows at or near sea floor based on geophysical records and visual observations. Numbers along right and bottom give coordinates of local transponder net (in meters). Hachures indicate area of closed low.

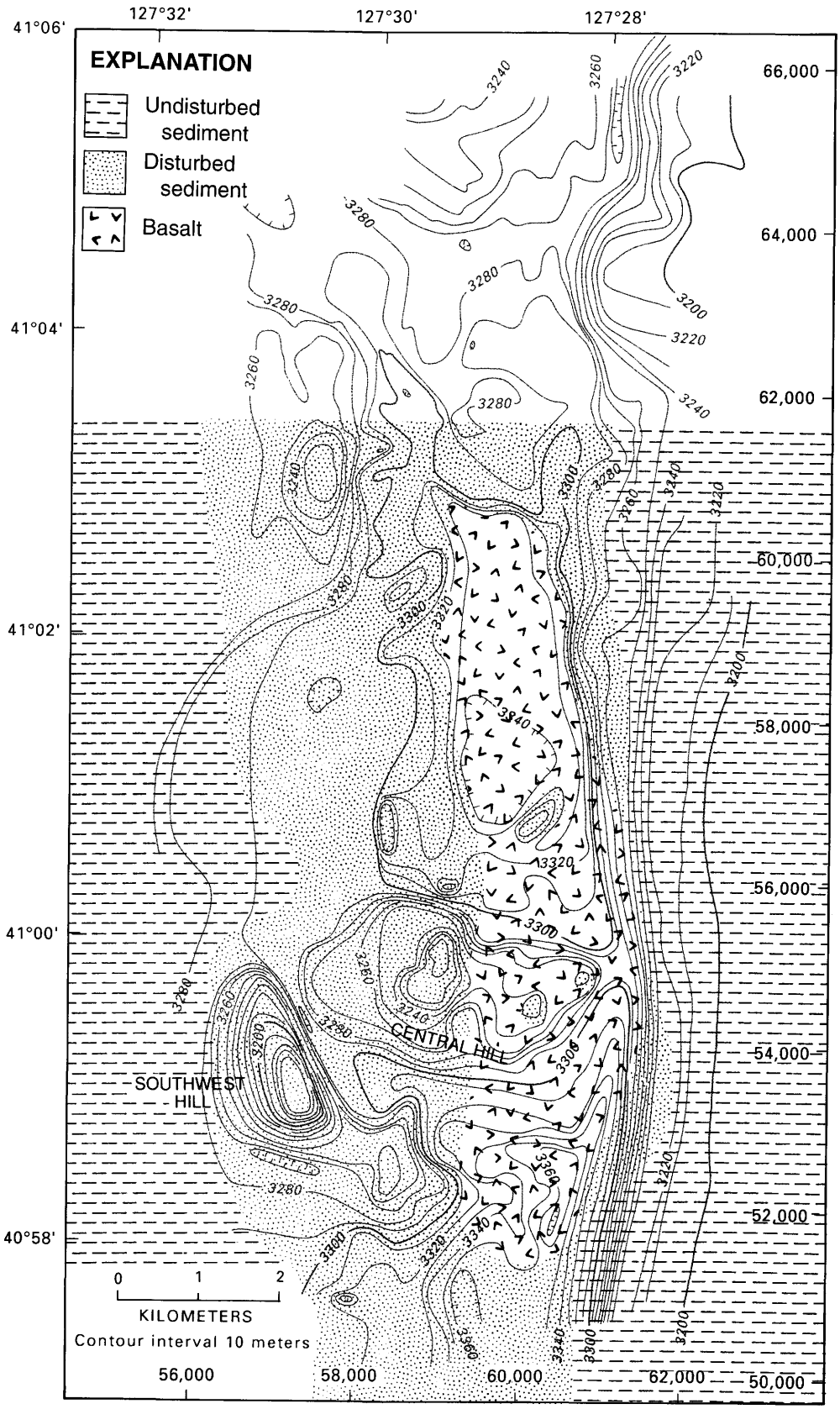

Figure 2.16. Map of NESCA area showing regions of disturbed and undisturbed sediment and inferred extent of volcanic flows at or near sea floor based on geophysical records and visual observations. Numbers along right and bottom give coordinates of local transponder net (in meters). Hachures indicate area of closed low.

volume). Seismic profiles indicate two distinct episodes of sedimentation and deformation in the southern part of the trough. At the eastern side of the trough, along L6-85-NC profiles 3 (not shown) and 5 (fig. 2.5 bottom) and L12-81-NP profile 118 (fig. 2.6), depth to basement and the thickness of the sedimentary section increase significantly. The lower sedimentary interval has been tilted to dips of at least 10° and is unconformably overlain by flat-lying sediment layers. This older episode of deformation appears to be associated with the eastward deflection and gradual disappearance of the eastern bounding ridge approaching the Mendocino Fracture Zone. We postulate an episode of rapid extension resulting in down-dropping of the basement, tilting of the overlying sediment section, and rapid sediment infilling of the resulting graben. Deformation of the upper sedimentary interval consists of normal faulting associated with extension, and localized uplift and disruption associated with emplacement of the volcanic edifices.

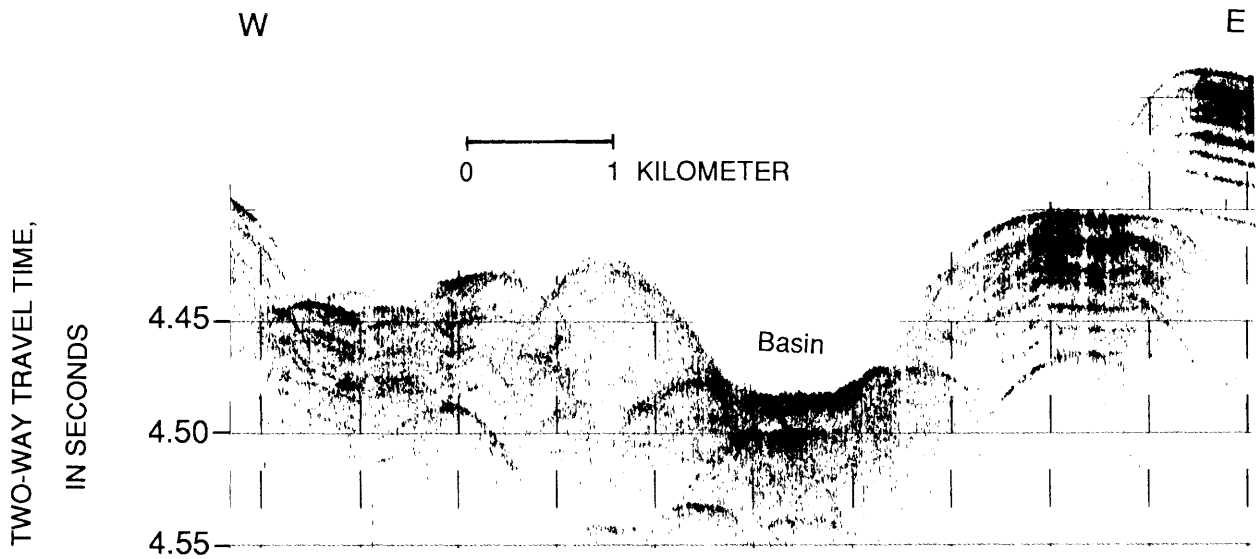

Figure 2.17. 3.5 kHz subbottom profile (L1-86-NC line 31) across basin north of Central Hill at NESCA site (see fig. 2.10 for location of profile). High-amplitude sea-floor return within basin, as well as bathymetric expression of basin, suggest presence of basalt flows at or near surface. Some layering is imaged beneath sea-floor return, possibly indicating that basin is floored by thin basalt sheet flow(s) overlying sediment. Other possible interpretations are discussed in text.

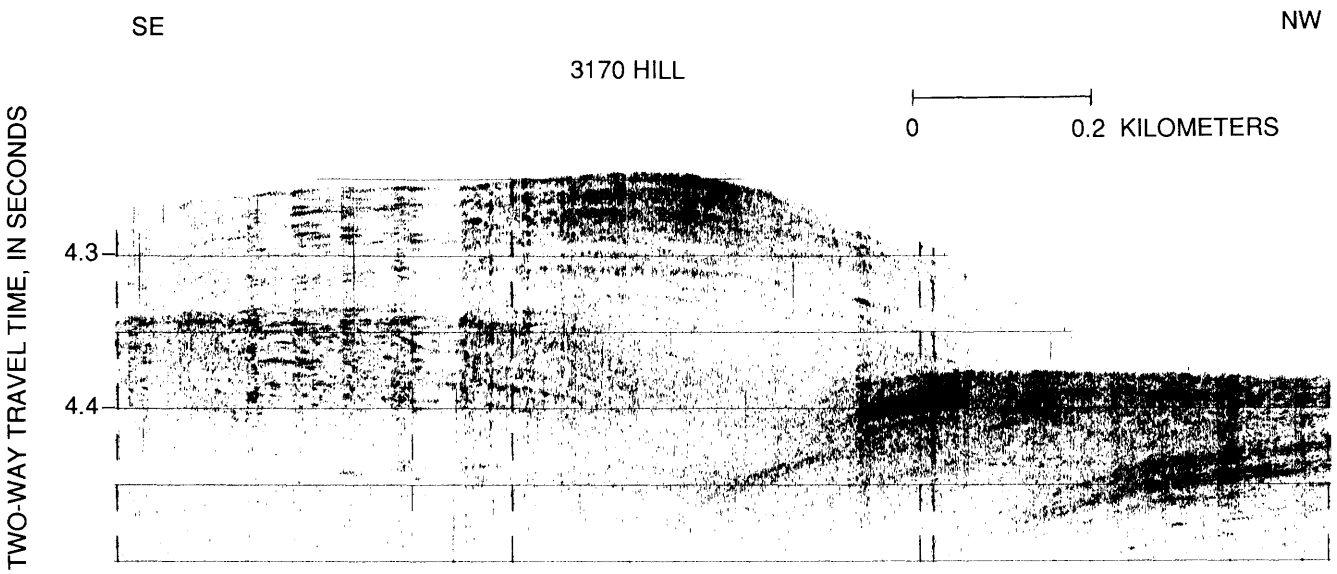

Figure 2.18. 3.5 kHz profile over 3170 Hill (fig. 2.15) at SESCA site obtained during dredging station. Horizontal scale bar is approximate as ship speed was varying. Sediment layers of hill have seismic-reflection character similar to that of shallow sediment of surrounding sea floor.

Recent igneous activity is not evenly distributed along the length of the trough, but rather is confined to discrete centers. Models of ridge system dynamics (Francheteau and Ballard, 1983; Crane, 1985; Macdonald and Fox, 1988) would predict magma sources beneath the intrasegment topographic highs; however, no clear correlation is evident in this case. The trough does appear to be undergoing extension along its entire length, as indicated by the presence of normal faults at the axis that cut the youngest sediment on all seismic crossings. The restriction of volcanism to a few discrete centers could reflect the geometry of magma supply, the relatively short time interval represented by the volcanic edifices, and (or) possibly control by the thick sediment cover. The few multi-channel seismic-reflection profiles did not reveal the presence of an axial magma chamber along Escanaba Trough. However, the data do not preclude the presence of a narrow chamber or one with a small velocity contrast. As has been suggested for other slow-spreading ridges (see Macdonald, 1986 and references therein), it is possible that the surface flows are fed from small isolated magma bodies rather than a laterally continuous crustal magma chamber. If each edifice derives from a separate source, we might expect chemical differences in the eruptive products. Chemical analyses of basalt samples from several edifices do show variation among the edifices (Davis and others, chap. 9, this volume) that could be compatible with a separate source model; however, the results are also compatible with a single, poorly mixed magma chamber. The sediment fill may also exert some localizing influence on the sea-floor volcanic distribution. An ascending magma loses buoyancy when it reaches the sediment-basement interface and tends to form a sill there. Some magma might follow faults through the sediment to form flows at the sea floor and once a pathway has been established, future eruptions will likely utilize it.

Sea Beam mapping indicates that the small hills that have been studied at SESCA and NESCA site are also common at other locations along the valley (see, for example, the southern end of fig. 2.9). Smaller hills may well occur in the area but have dimensions below the resolution of the Sea Beam system acoustic footprint, which is about 2×10^4 m^2 in these water depths. Seismic profiling and visual observations (Zierenberg and others, chap. 10, this volume) indicate that the hills are composed of sediment. Basalt flows are present at the perimeter of some hills (figs. 2.15, 2.16). The hills probably form as igneous intrusions uplift and possibly tilt the overlying sediment. Evidence for sills beneath one hill is seen on L1-86-NC line 10 (fig. 2.12). High-angle faults in the sediment were also imaged near the base of the hills. The location of these faults appears to be consistent with the predicted location of faulting from mechanical and theoretical modeling of uplift above a sill (Denlinger and Holmes, chap. 4, this volume). There is considerable evidence for mass wasting at the sides of the hills (Holmes and Zierenberg, 1990; Morton and others, 1990), and their present form is that of buttes. The prevalence of mass wasting suggests one other possible mechanism of formation of the hills: that they are erosional remnants of much more widespread uplift. This explanation would suggest, for example, that the several hills aligned in the northeast quadrant of SESCA (fig. 2.9) are the eroded remnants of a north-northeast-trending horst block. The amount of geophysical data needed to distinguish between these two models, especially high-resolution seismic-reflection and magnetic data directly over the hills, is limited. We conclude, however, that the direct observation of faulting near the base of the hills and the indirect

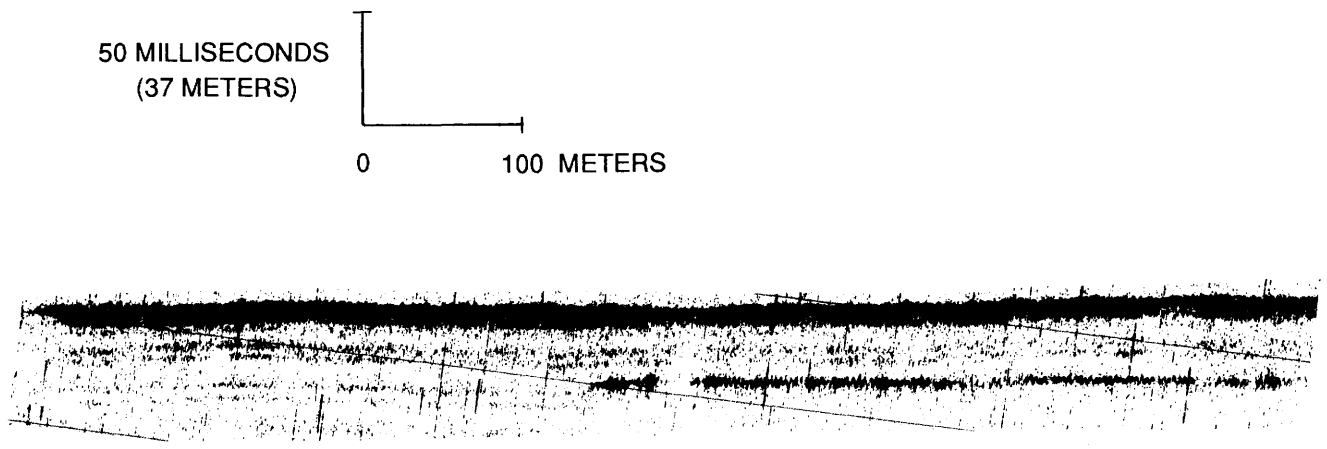

Figure 2.19. 3.5 kHz record from NESCA site obtained with pinger mounted in camera sled and receiver mounted in the ship's hull. Camera sled was towed only a few meters above sea floor. Heavy black return at top of record is a combination of direct return and sea-floor reflection. Weak subsurface layering seen on left side of figure is typical of records obtained with sled-mounted pinger and, although penetration is much poorer than with ship's 3.5 kHz system, is not unlike layering imaged with ship's system. High-amplitude return at about 30 ms below sea floor on right side of figure is unusual. Camera system photographed small hydrothermal deposits on sea floor at this location; thus, we speculate that high-amplitude return could represent bed with subsurface mineralization.

evidence of faulting based on the distribution of large sulfide deposits (Zierenberg and others, chap. 10, this volume), as well as the presence of sills identified on seismic profiles strongly favor the former interpretation, that the hills are the result of localized uplift caused by the intrusion of basaltic sills. Basalt flows located adjacent to some of the hills probably erupted along the faults associated with this uplift.

Numerous hydrothermal sulfide and sulfate deposits have been mapped at the SESCA and NESCA sites (Morton and others, 1990; Zierenberg and others, chap. 10, this volume). Several large sulfide mounds (100 to 200 m in length and tens of meters thick) occur at or near the base of the small hills. Smaller isolated chimneys and mounds are widely distributed on the sediment- covered sea floor. A sand layer with disseminated pyrrhotite was cored at one location (Morton and others, 1987b; Normark and other, chap. 6, this volume), indicating that subsurface sulfide deposition is also occurring. The geophysical results combined with the geologic mapping and sampling suggest two primary controls on the localization of hydrothermal flow and sulfide deposition (fig. 2.20). The predominantly mud-rich sediment should have a low permeability, which restricts hydrothermal flow. Faults created during the uplift of the small hills provide the primary conduits for upwelling hydrothermal fluids, resulting in the deposition of large mineral deposits at the base of the hills. Sand-rich sediment layers provide horizontal pathways for hydrothermal fluids to migrate away from these fault zones. Such flow might feed the smaller, isolated sulfide deposits. We also predict that considerable mineralization is occurring in the subsurface in these sand-rich beds.

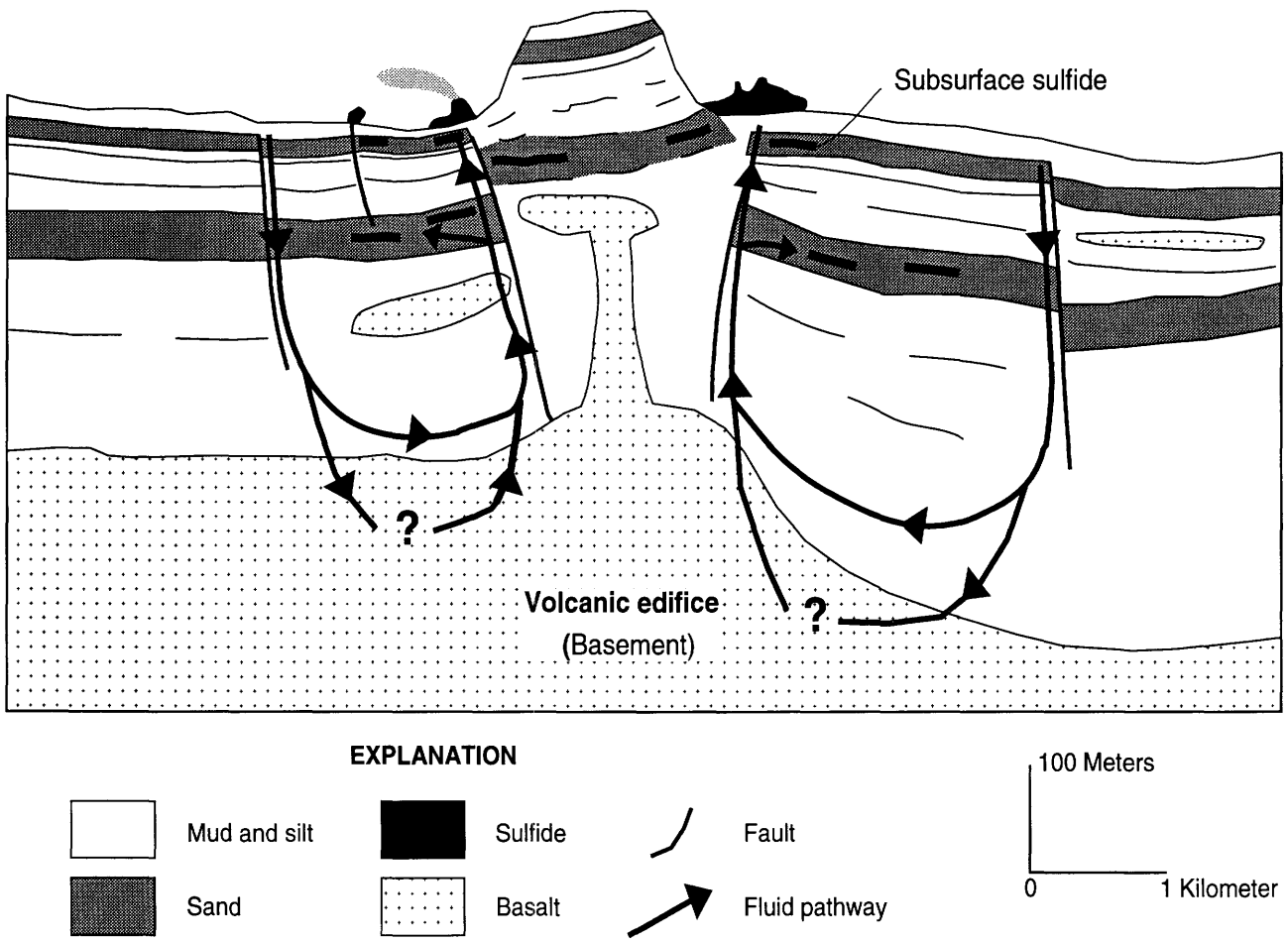

Figure 2.20. Schematic cross section summarizing basic features controlling formation of sulfide deposits at Escanaba Trough in SESCA and NESCA areas. Basaltic sills inflate near sediment-basement interface, assimilating sediment into magma (Davis and others, chap. 9, this volume) and uplifting overlying sedimentary section to form small hills. Fault zones created by uplift are likely to be considerably more permeable than mud-rich sedimentary layers, providing primary pathways for hydrothermal fluids, which cool sills, to ascend to sea floor. Large massive sulfide deposits are formed at sea floor near base of small hills above these fault zones. Sand-rich layers allow horizontal migration of hydrothermal fluids away from fault zones, resulting in subsurface mineral deposition along these beds and feeding smaller sea-floor deposits.

REFERENCES CITED

Atwater, Tanya, and Mudie, J.D., 1973, Detailed near-bottom geophysical study of the Gorda Ridge: Journal of Geophysical Research, v. 78, p. 8665–8686.

Bukry, David, and Bramlette, M.N., 1970, Coccolith age determinations Leg 5, Deep Sea Drilling Project, *in* McManus, D.A., and others, eds., Initial reports of the Deep Sea Drilling Project: Washington, U.S. Government Printing Office, v. 5, p. 487–494.

Clague, D.A., and Holmes, M.L., 1987, Geology, petrology, and mineral potential of the Gorda Ridge, *in* Scholl, D.W., Grantz, A., and Vedder, J.G., eds., Geology and resource potential of the continental margin of western North America and adjacent ocean basins–Beaufort Sea to Baja California: Houston, Circum-Pacific Council for Energy and Mineral Resources, Earth Science Series, v. 6, p. 563–580.

Crane, Kathleen, 1985, The spacing of rift axis highs: Dependence upon diapiric processes in the underlying asthenosphere?: Earth and Planetary Science Letters, v. 72, p. 405–414.

Damuth, J.E., 1975, Echo character of the western equatorial Atlantic floor and its relationship to the dispersal and distribution of terrigenous sediments: Marine Geology, v. 18, p. 17–45.

Damuth, J.E., and Hayes, D.E., 1977, Echo character of the east Brazilian continental margin and its relationship to sedimentary processes: Marine Geology, v. 24, p. 73–95.

Davis, A.S., Clague, D.A., and Friesen, W.B., Petrology and mineral chemistry of basalt from Escanaba Trough, *in* Morton, J.L., Zierenberg, R.A., and Reiss, C.A., eds., Geologic, Hydrothermal, and Biologic Studies at Escanaba Trough, Gorda Ridge, Offshore Northern California: U.S. Geological Survey Bulletin 2022, chapter 9 (this volume).

Davis, E.E., and Becker, Keir, Thermal and tectonic structure of the Escanaba Trough: New heat-flow measurements and seismic-reflection profiles, *in* Morton, J.L., Zierenberg, R.A., and Reiss, C.A., eds., Geologic, Hydrothermal, and Biologic Studies at Escanaba Trough, Gorda Ridge, Offshore Northern California: U.S. Geological Survey Bulletin 2022, chapter 3 (this volume).

Denlinger, R.P., and Holmes, M.L., A thermal and mechanical model for sediment hills and associated sulfide deposits along the Escanaba Trough, *in* Morton, J.L., Zierenberg, R.A., and Reiss, C.A., eds., Geologic, Hydrothermal, and Biologic Studies at Escanaba Trough, Gorda Ridge, Offshore Northern California: U.S. Geological Survey Bulletin 2022, chapter 4 (this volume).

EEZ-SCAN 84 Scientific Staff, 1986, Atlas of the Exclusive Economic Zone, Western Conterminous United States: U.S. Geological Survey Miscellaneous Investigations Series Map I-1792, 152 p., scale 1:500,000.

Francheteau, Jean, and Ballard, R.D., 1983, The East Pacific Rise near 21° N, 13° N and 20° S: inferences for along-strike variability of axial processes of the mid-ocean ridge: Earth and Planetary Science Letters, v. 64, p. 93–116.

Gartner, Stefan, Jr., 1970, Coccolith age determinations Leg 5, Deep Sea Drilling Project, *in* McManus, D. A., and others, eds., Initial reports of the Deep Sea Drilling Project: Washington, U.S. Government Printing Office, v. 5, p. 495–500.

Holmes, M.L., and Zierenberg, R.A., 1990, Submersible observations in Escanaba Trough, southern Gorda Ridge, *in* McMurray, G.R., ed., Gorda Ridge: A seafloor spreading center in the United States' Exclusive Economic Zone: New York, Springer-Verlag, p. 93–115.

Karlin, R., and Lyle, M., 1986, Sediment studies on the Gorda Ridge: Oregon Department of Geology and Mineral Industries Open-File Report O-86-19, 76 p.

Karlin, R.E., and Morton, J.L., Crustal magnetization and basement structure of the Escanaba Trough, *in* Morton, J.L., Zierenberg, R.A., and Reiss, C.A., eds., Geologic, Hydrothermal, and Biologic Studies at Escanaba Trough, Gorda Ridge, Offshore Northern California: U.S. Geological Survey Bulletin 2022, chapter 5 (this volume).

Koski, R.A., Shanks, W.C., III, Bohrson, W.A., and Oscarson, R.L., 1988, The composition of massive sulfide deposits from the sediment-covered floor of Escanaba Trough, Gorda Ridge: Implications for depositional processes: Canadian Mineralogist, v. 26, p. 655–673.

Macdonald, K.C., 1986, The crest of the Mid-Atlantic Ridge: Models for crustal generation processes and tectonics, *in* Vogt, P.R., and Tucholke, B.E., eds., The geology of North America, Volume M, The Western North Atlantic region: Boulder, Colorado, Geological Society of America, p. 51–68.

Macdonald, K.C., and Fox, P.J., 1988, The axial summit graben and cross-sectional shape of the East Pacific Rise as indicators of axial magma chambers and recent volcanic eruptions: Earth and Planetary Science Letters, v. 88, p. 119–131.

McManus, D.A., and others, 1970, Site 35, *in* McManus, D.A., and others, eds., Initial reports of the Deep Sea Drilling Project: Washington, U.S. Government Printing Office, v. 5, p. 165–172.

Morton, J.L., Holmes, M.L., and Koski, R.A., 1987a, Volcanism and massive sulfide formation at a sedimented spreading center, Escanaba Trough, Gorda Ridge, northeast Pacific Ocean: Geophysical Research Letters, v. 14, p. 769–772.

Morton, J.L., Normark, W.R., Ross, S.L., Koski, R.A., Holmes, M.L., Shanks, W.C., III, Zierenberg, R.A., Lyle, M., and Benninger, L.M., 1987b, Preliminary report, cruises L1-86-NC and L2-86-NC, Escanaba Trough, Gorda Ridge: U.S. Geological Survey Open-File Report 87-375-A, 20 p.

Morton, J.L., Koski, R.A., Normark, W.R., and Ross, S.L., 1990, Distribution and composition of massive sulfide deposits at Escanaba Trough, southern Gorda Ridge, *in* McMurray, G.R., ed., Gorda Ridge: A seafloor spreading center in the United States' Exclusive Economic Zone: New York, Springer-Verlag, p. 77–92.

Morton, J.L., Zierenberg, R.A., and Reiss, C.A., Geologic, hydrothermal, and biologic studies at Escanaba Trough: An introduction, *in* Morton, J.L., Zierenberg, R.A., and Reiss, C.A., eds., Geologic, Hydrothermal, and Biologic Studies at Escanaba Trough, Gorda Ridge, Offshore Northern California: U.S. Geological Survey Bulletin 2022, chapter 1 (this volume).

Normark, W.R., Gutmacher, C.E., Zierenberg, R.A., Wong, F.L., and Rosenbauer, R.J., Sediment fill of Escanaba Trough, *in* Morton, J.L., Zierenberg, R.A., and Reiss, C.A., eds., Geologic, Hydrothermal, and Biologic Studies at Escanaba

Trough, Gorda Ridge, Offshore Northern California: U.S. Geological Survey Bulletin 2022, chapter 6 (this volume).

O'Connell, S., and Normark, W.R., 1986, Acoustic facies and sediment composition of the Mississippi fan drill sites, Deep Sea Drilling Project leg 96, *in* Bouma, A.H., Coleman, J.M., Meyer, A.W., and others, eds., Initial reports of the Deep Sea Drilling Project: Washington, U.S. Government Printing Office, v. 96, p. 457–473.

Riddihough, R.P., 1980, Gorda plate motions from magnetic anomaly analysis: Earth and Planetary Science Letters, v. 51, p. 163–170.

Ross, S.L., and Zierenberg, R.A., Volcanic geomorphology of the SESCA and NESCA sites, Escanaba Trough, *in* Morton, J.L., Zierenberg, R.A., and Reiss, C.A., eds., Geologic, Hydrothermal, and Biologic Studies at Escanaba Trough, Gorda Ridge, Offshore Northern California: U.S. Geological Survey Bulletin 2022, chapter 8 (this volume).

Sangree, J.B., and Widmier, J.M., 1977, Seismic stratigraphy and global changes of sea level, part 9: Seismic interpretation of clastic depositional facies, *in* Payton, C.E., ed., Seismic stratigraphy–Applications to hydrocarbon exploration: Tulsa, American Association of Petroleum Geologists, p. 165–184.

Wilde, P., Chase, T.E., Holmes, M.L., Normark, W.R., Thomas, J.A., McCulloch, D.S., and Kulm, L.D., 1978, Oceanographic data off northern California–southern Oregon, 40°–43° N including the Gorda deep-sea fan: Berkeley, Lawrence Berkeley Laboratories Publication 251, scale 1:815,482.

Wilson, D.S., 1989, Deformation of the so-called Gorda plate: Journal of Geophysical Research, v. 94, p. 3065–3075.

Zierenberg, R.A., Morton, J.L., Koski, R.A., and Ross, S.L., Geologic setting of massive sulfide mineralization in the Escanaba Trough, *in* Morton, J.L., Zierenberg, R.A., and Reiss, C.A., eds., Geologic, Hydrothermal, and Biologic Studies at Escanaba Trough, Gorda Ridge, Offshore Northern California: U.S. Geological Survey Bulletin 2022, chapter 10 (this volume).

Chapter 3. Thermal and Tectonic Structure of Escanaba Trough: New Heat-Flow Measurements and Seismic-Reflection Profiles

By Earl E. Davis[1] *and* Keir Becker[2]

CONTENTS

ABSTRACT

Twelve closely spaced single-channel seismic profiles and 75 heat-flow measurements along four multi-penetration transects crossing the Escanaba Trough provide new information about this setting in which large sediment-hosted sulfide deposits have formed. A layer of turbidites roughly 600 m thick buries basement across the full width of the rift valley in the study area. The sediment section is disrupted by numerous normal faults and volcanic intrusions, although seismic reflectors remain coherent in most areas, which allows stratigraphic displacements to be quantified. A well-defined transparent acoustic layer is seen within the upper 200 m of the section on all profiles; the top and bottom of this layer, and the valley floor itself, provide excellent stratigraphic and tectonic marker horizons. We conclude that displacements on individual faults have been accumulating at rates of up to 15 mm/yr. The valley floor appears to be subsiding in most areas, at rates of up to 20 mm/yr. The sedimentation rate during the late Pleistocene is calculated to be in excess of 25 mm/yr. Depths to the marker horizons at the centers of volcanic activity are not well resolved, but little syn-sedimentary deformation is apparent, implying that most of the volcanic activity has taken place during the Holocene.

Heat flow in the valley is regionally low and relatively constant, averaging about 0.2 W/m^2, as are temperatures predicted for the sediment-basement interface, which average approximately 80°C. Some variability is associated with disrupted zones in the inner rift. The highest heat-flow values are near the centers of intrusive volcanism. The pattern of heat flow suggests that volcanism and associated hydrothermal activity are both highly focused, that little or no intrusive volcanism has occurred in the rift between the observed volcanic centers, and that thermal conditions within the upper crust regionally beneath the sediment have not have been affected by the recent intrusive volcanism. A simple mass- and thermal-balance hydrothermal model that is consistent with the geophysical observations demonstrates that sufficient heat and material would be available locally to produce the large hydrothermal deposits at the volcanic centers.

INTRODUCTION

BACKGROUND

Sediment-covered spreading centers, although relatively rare, provide unusual opportunities for quantitative studies of sea-floor spreading and associated submarine hydrothermal systems. The sediment may preserve a relatively continuous stratigraphic record of magmatic, tectonic, and thermal events associated with sea-floor spreading and provide clues to the spatial and temporal variability of these processes. A regionally continuous, relatively impermeable sediment cover conductively insulates the underlying young crust and limits the possible pathways for recharge and discharge of hydrothermal fluids. Where discharge does occur, it can be strongly focused, and very large sulfide deposits can be produced. A sediment layer also provides a benign sea-floor environment that allows the use of certain observational techniques that cannot be used easily at unsedimented ridge crests, such as sea-floor heat-flow measurements, coring, and

[1] Geological Survey of Canada, Sidney, British Columbia, Canada.
[2] University of Miami, Miami, Florida.

deep-sea drilling. In particular, a sediment cover allows detailed heat-flow surveys to constrain axial geothermal processes, although these processes are considerably modified by the sediment cover and cannot be taken to represent those at unsedimented ridge crests.

There are three well-studied sediment-covered spreading centers in the eastern Pacific Ocean: Middle Valley on the Juan de Fuca Ridge, Escanaba Trough on the Gorda Ridge, and Guaymas Basin in the Gulf of California. The first two of these are the axial rift valleys of mid-ocean spreading centers that have migrated close enough to the continental margin of western North America to have received large quantities of turbidite sediment during the Pleistocene. The last, a youthful spreading center that has developed in the wake of continental rifting between Baja California and mainland Mexico, is covered by a mixture of terrigenous and pelagic sediments. High-temperature hydrothermal venting and sulfide deposits have been observed and sampled at all three locations (see, for example, Lonsdale and Becker, 1985; Davis and others, 1987; Koski and others, 1988; Davis and Villinger, 1992).

Middle Valley and Guaymas Basin are medium-rate (about 60 mm/yr) spreading centers, with virtually no basement exposures within the axial rifts. This has allowed the surface heat flow to be well mapped over these "zero-age" valleys. Over the last 20 years, numerous heat-flow surveys have been conducted at both locations, providing dense distributions of several hundred well-located measurements (see, for example, Lawver and others, 1975; Lawver and Williams, 1979; Williams and others, 1979; Lonsdale and Becker, 1985; Becker and Fisher, 1991; and Fisher and Becker, 1992 for Guaymas Basin and Davis and Lister, 1977; Davis and others, 1980; Villinger and Davis, 1984, and Davis and Villinger, 1992 for Middle Valley). The results have shown that reconnaissance surveys can easily detect the large variability and the isolated highs in heat flow caused by hydrothermal activity, but that much more detailed surveys, with spacings between measurements of hundreds of meters or less, are required to characterize properly the nature of heat-flow variability so that clear inferences can be drawn about the associated geothermal processes.

At Escanaba Trough only one reconnaissance heat-flow survey had been conducted prior to 1989 (Abbott and others, 1986); this comprised 34 measurements made in three transects. The heat flow was observed to be highly variable, and locally high (up to 1.8 W/m^2) near two volcanic edifices that penetrate the sediment within the axial rift. These results indicated clearly that volcanic and related hydrothermal processes are active within the axial rift, but did not allow the nature of the heat flow variability to be resolved further.

The general structure of the rift and its sediment fill had been documented at the time of our study with a number of single- and multi-channel seismic-reflection profiles (Clague and Holmes, 1987; Morton and others, 1987; Morton and Fox, chap. 2, this volume), although the low trackline density and limited resolution of the profiles limited the interpretation of the detailed tectonic and volcanic structure of the rift.

To further elucidate the structural, volcanic, and hydrothermal history and processes currently active in this rift, we returned to Escanaba Trough on CSS *John P. Tully* for 10 days in May 1989 and conducted detailed single-channel seismic and heat-flow surveys in the central part of the trough (figs. 3.1 and 3.2). We report here the analyses of 12 selected seismic lines, and 75 heat-flow measurements acquired in four transects along representative seismic lines crossing the trough.

TECTONIC AND GEOTHERMAL SETTING

Escanaba Trough is the most southerly of three spreading segments that form the Gorda Ridge between the Mendocino and Blanco fracture zones (fig. 3.1). This segment is also the slowest spreading of the three, opening at a total rate of about 23 mm/yr, whereas the two segments to the north open at about 60 mm/yr (Atwater and Mudie, 1973; Riddihough, 1980). Escanaba Trough is structurally and morphologically typical of a slow-spreading ridge; the deep rift valley is bordered by steep rift mountains with up to 1,500 m of normal-faulted relief. The valley floor widens from 3–5 km at the northern end of Escanaba Trough to roughly 18 km near the southern junction with the Mendocino fracture zone.

Terrigenous sediments enter the valley from their source along the North American continental margin at the trough's junction with the Mendocino Fracture Zone. Several hundred meters of sediment cover the rift valley south of about latitude 41°17′ N. (Moore, 1970; Vallier and others, 1973); a 390-m section of Pleistocene turbidites was drilled at Deep Sea Drilling Project (DSDP) Site 35 in the southern Escanaba Trough (McManus and others, 1970). A U.S. Geological Survey single-channel seismic survey in 1985 identified six major volcanic centers that penetrate or disrupt the sediment of the trough (Morton and others, 1987). These are spaced roughly at 12 km intervals along the trough axis. Two of these centers, at about latitude 40°45′ N. and latitude 41° N. (see figs. 3.2 and 3.3), referred to as the Southern Escanaba and Northern Escanaba (SESCA and NESCA) sites, have been studied extensively. Exposed volcanic rocks, sulfide deposits, high heat flow, and hydrothermal venting were observed at the northern site (Abbott and others, 1986; Koski and others, 1988; Morton and others, 1990; Holmes and Zierenberg, 1990).

Given the limitations of ship time and the need to conduct relatively detailed measurements, our seismic and heat-flow survey was concentrated on the axial rift from

the NESCA site at about latitude 41° N. southward to another center of volcanic activity at about latitude 40°53′ N., roughly midway between the NESCA and SESCA sites. North of this part of the valley, the sediment cover is not continuous enough for a systematic distribution of heat-flow measurements to be established.

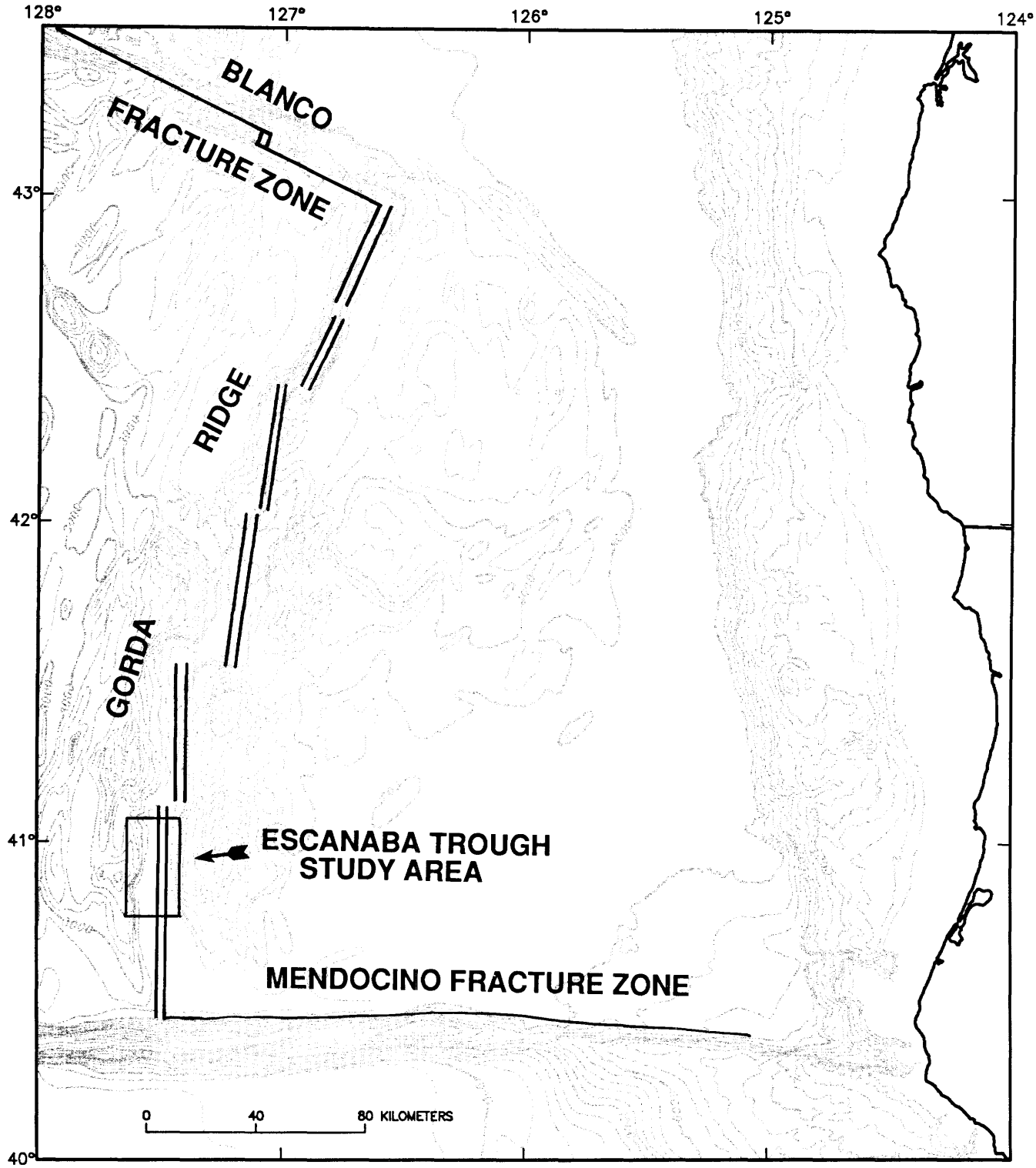

Figure 3.1. Bathymetric map of Gorda Ridge region, showing Escanaba Trough study area and approximate area included in figure 3.2. Bold lines indicate approximate locations of extensional and transform plate boundaries, and the coastline. Contours define edge of continental shelf and base of continental slope. Contour interval is 200 m.

ACKNOWLEDGMENTS

We thank Wanda Bentkowski, who helped reduce the heat-flow data during and after the field program, Ivan Frydecky and Gerald Horel, who provided assistance with heat-flow, seismic-reflection, and navigation operations, Henny Groschel-Becker, Joann Bessler, and Stephanie Ross, who provided watchkeeping leadership, and the captain, officers, and crew of the CSS *John P. Tully* for capable assistance with equipment and for excellent stationkeeping. Chris Fox of NOAA provided the Sea Beam data from which figure 3.2 was derived. Figures were prepared by Brian Sawyer, Linda Bedard, and Gina L'Esperance. Financial support to Keir Becker was provided by JOI-USSSP Site Survey Augmentation contract JSC7-89. W. Normark and J. Morton provided critical reviews of the manuscript. This document is Geological Survey of Canada Contribution No. 51190.

NEW DATA

Twelve new seismic-reflection profiles and four heat-flow transects across the rift valley were completed during the *Tully* cruise (fig. 3.2). All lines were navigated with a shipboard system that integrates Loran-C with Global Positioning System (GPS) coordinate determinations; resulting ship's positions are believed to be accurate to within about 100 m. During heat-flow operations, the position of the probe was determined by correlating structures recognized on both the ship's 3.5 kHz echo-sounding system and the record of the probe's 3.5 kHz pinger. During heat-flow station 15, the probe was navigated by acoustic relay transponder. Owing to the heavy weight of the probe, the separation of the probe and ship was modest, and usually ranged from 100 to 500 m. The azimuth was well determined as a result of the consistent orientation of the ship's tracks, and the resultant determinations of probe penetration locations along heat flow stations 3, 7, and 11 are probably accurate to about ±200 m along the direction of the tracks and ±100 m across tracks; along station 15, the errors of penetration positions are probably less than 100 m.

The seismic lines and the 75 successful heat-flow measurements (shown superimposed on a Sea Beam-derived bathymetric map in figure 3.2) are distributed throughout the central and northern part of the rift valley where sediments are present; seismic line spacing varies according to the local features of interest, with the closest spacing (about 1 km) being over an area of very recent centralized disruption of the sediment section. The four heat-flow transects are situated across parts of the valley (1) where the sea floor and underlying sediment section are generally undisrupted (line 6, station 7), (2) where substantial recent extension has occurred in the central rift (line 5, station 3), (3) where the central rift sediments are highly disrupted by small-scale faulting, minor volcanic intrusion, or fluid flow and associated sediment alteration (line 10, station 11), and (4) where a mature sulfide deposit has formed over a volcanic intrusion (Central Hill, NESCA site) and where moderately high-temperature fluids vent at the sea floor (line 3, station 15).

The seismic-reflection profiles, shown in figure 3.3, extend the full width of the valley to the major rift-bounding normal fault scarps, and in some cases, across the innermost rotated fault blocks that have been lifted above the valley floor. The seismic source used was a single 650-cm^3 air gun fired every 10 seconds. Lines were completed at a speed of roughly 3.5 knots, yielding a shot spacing of roughly 20 m. Signals were received on a Teledyne array having a single active section 50 m in length. Analog records (shown in fig. 3.3) were made in real time; data were also recorded digitally for later processing and playback. The profiles generally show clearly the seismic stratigraphy and tectonic structure of the sediment section that fills the valley. Basement arrivals from beneath the typically 500- to 700-ms-thick sediment section are everywhere strong, except for the areas of steep topography or areas that have been disrupted by volcanic intrusions, hydrothermal induration, or small-scale deformation.

Heat-flow data were obtained with a Lister-type probe 4 m long that has 11 thermistors and a heating wire housed within an 8-mm-diameter tube held in tension beside a 65-mm-diameter strength member (see Davis, 1988, for general description). The thermistors are spaced 30 cm apart along the sensor string. A low-resolution acoustic link allows the state of the instrument to be monitored at all times. Full resolution (16 bit) data are recorded internally in solid state memory. This digital resolution and the nonlinear response characteristics of the thermistors allow relative temperatures of each of the 11 probe sensors, a water-temperature probe, and an internal water-temperature sensor to be determined to roughly 0.5 mK at low temperatures, while maintaining a useful range of over 50 K. Tilt and absolute pressure are also determined; tilt is used to assess the quality of questionable penetrations, and pressure is used to assist in the hindsight navigation of the probe as well as for automatic detection of penetrations by a heat-pulse firing circuit. All channels, including low temperature-coefficient reference resistors and an internal temperature sensor, are sampled and logged every 10 seconds.

⇒

Figure 3.2. Sea Beam-derived bathymetry of central part of Escanaba Trough, with locations of heat-flow measurements (dots) and seismic-reflection profiles with times along tracklines (lines 1–12) superimposed. Contours are shown at 10-m intervals except in areas of high topographic gradient. Water depths are computed with assumed sound velocity of 1,500 m/s. Coordinates have been adjusted from those of original NOAA Sea Beam data (Loran-C control) according to GPS-controlled bathymetric constraints provided by data presented in figure 3.3. Map area is approximately 20 km wide. Hachures indicate area of closed low.

Typical penetrations include (1) a brief period during which a "zero-gradient" reference is obtained with the instrument held in the near-bottom water, (2) an undisturbed period of 7 minutes in the bottom while the sensor string equilibrates, and (3) a period of roughly 7 minutes while the decay of a calibrated heat pulse is monitored. From

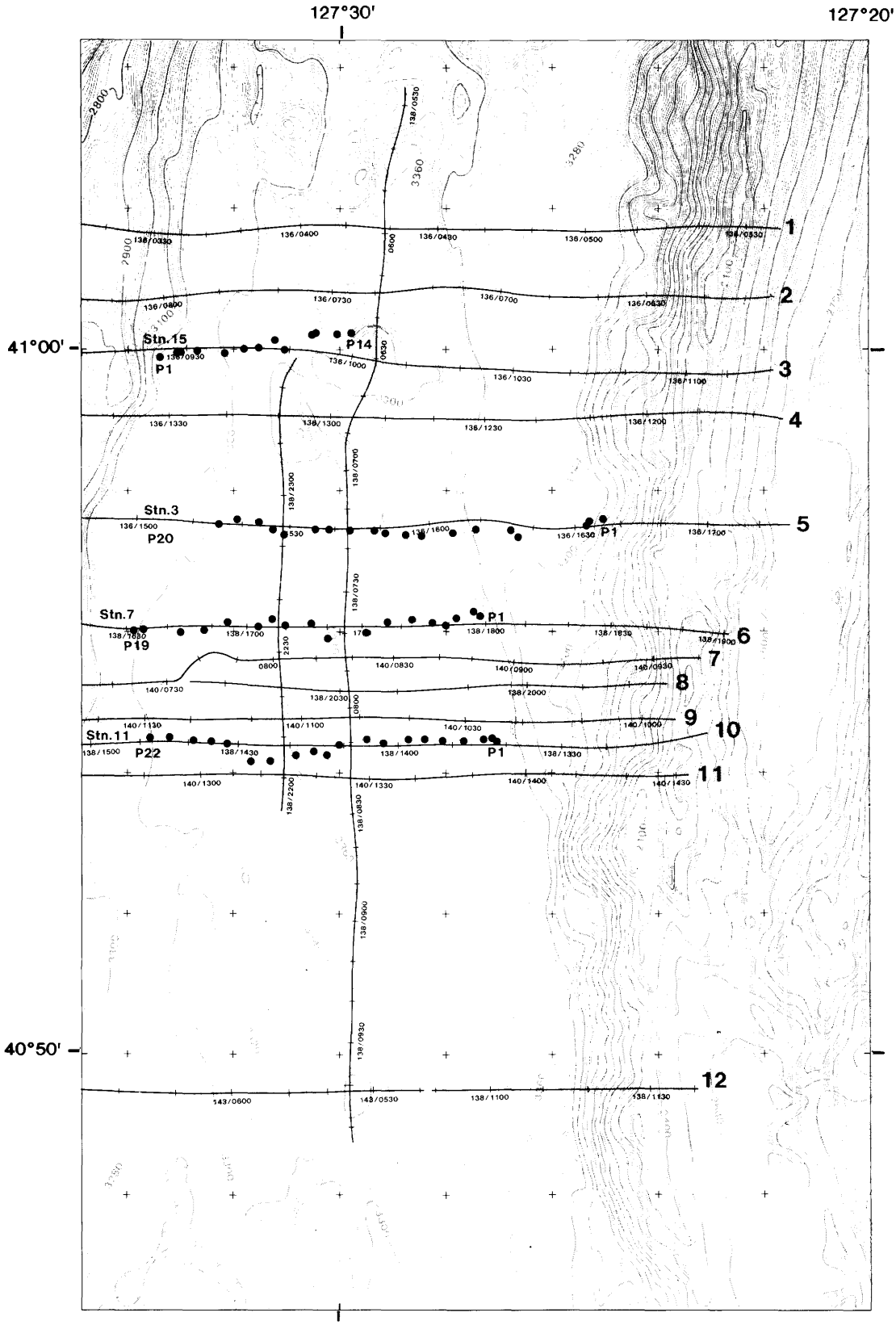

these data the thermal gradient and thermal conductivity are determined in the manner described in detail by Villinger and Davis (1987). Two typical measurements from the Escanaba Trough are shown in figure 3.4; the final heat-flow values are computed as the slopes of temperature versus vertically integrated thermal resistance. Thermal conductivity measurements were not made during many of the penetrations (see table 3.1), either inadvertently because of premature probe disturbances or deliberately as a trade-off between fewer complete measurements and more gradient measurements. For penetrations without conductivity measurements, an assumed conductivity structure, derived from the average measured conductivity-depth structure determined from all measurements, was used to estimate the heat flow. As can be seen in figure 3.4, there is a substantial variation in the conductivity with

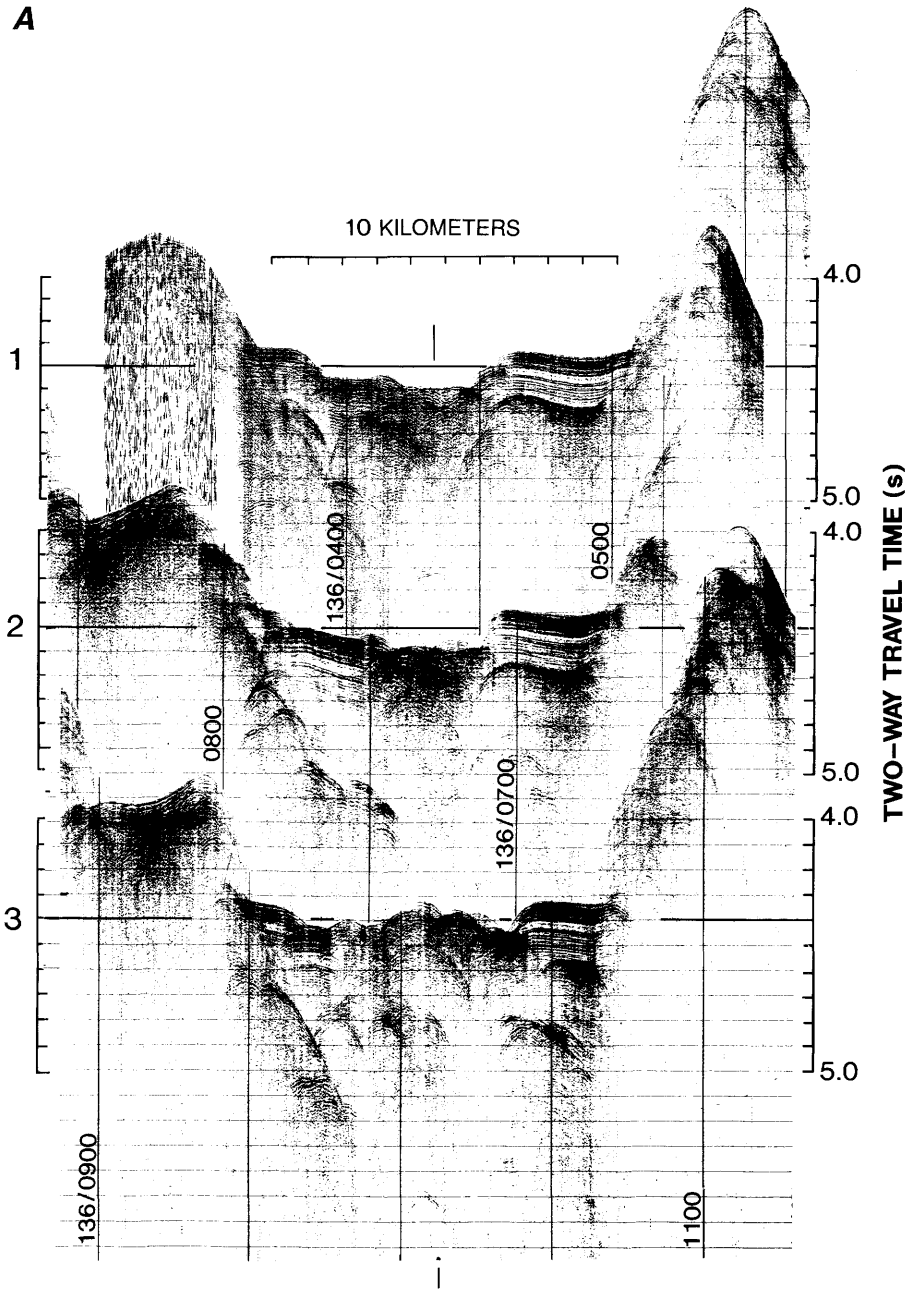

Figure 3.3. Single-channel seismic-reflection profiles stacked along mid-valley north-south common reference line (shown by tick marks above and below each set of three profiles, labeled *A–D*). Horizontal scales of all profiles are equal; vertical scales vary. Horizontal reference line at 4.4 seconds is shown for each profile. Vertical exaggeration is roughly 10:1. Profile locations and times along tracklines are shown in figure 3.2.

depth; this is the largest source of uncertainty in those heat-flow determinations where in situ conductivity measurements were not made. Values from all penetrations are given in table 3.1, along with penetration locations, water depths, and estimated errors.

DISCUSSION

IMPLICATIONS FROM SEISMIC-REFLECTION DATA

The structure of the rift and its sediment fill is simple. Regionally, the valley floor possesses modest relief; over the 12-km width and 22-km length of the valley surveyed, water depths generally vary by less than 150 m (figs. 3.2 and 3.3). This relief is associated with displacements on normal faults in the central part of the rift and with local uplift of the sediment section and the sea floor over volcanic intrusions. Where well imaged, the basement surface is relatively flat. Sediment thicknesses vary between about 500 and 700 ms. Depth to basement cannot be resolved in the vicinity of the volcanic centers because of the acoustic disruption of the sediment stratigraphy by local deformation and by the presence of volcanic rocks within the sediment and at the sea floor.

Numerous observations can be used to constrain the structural and volcanic history of the rift. A crude constraint

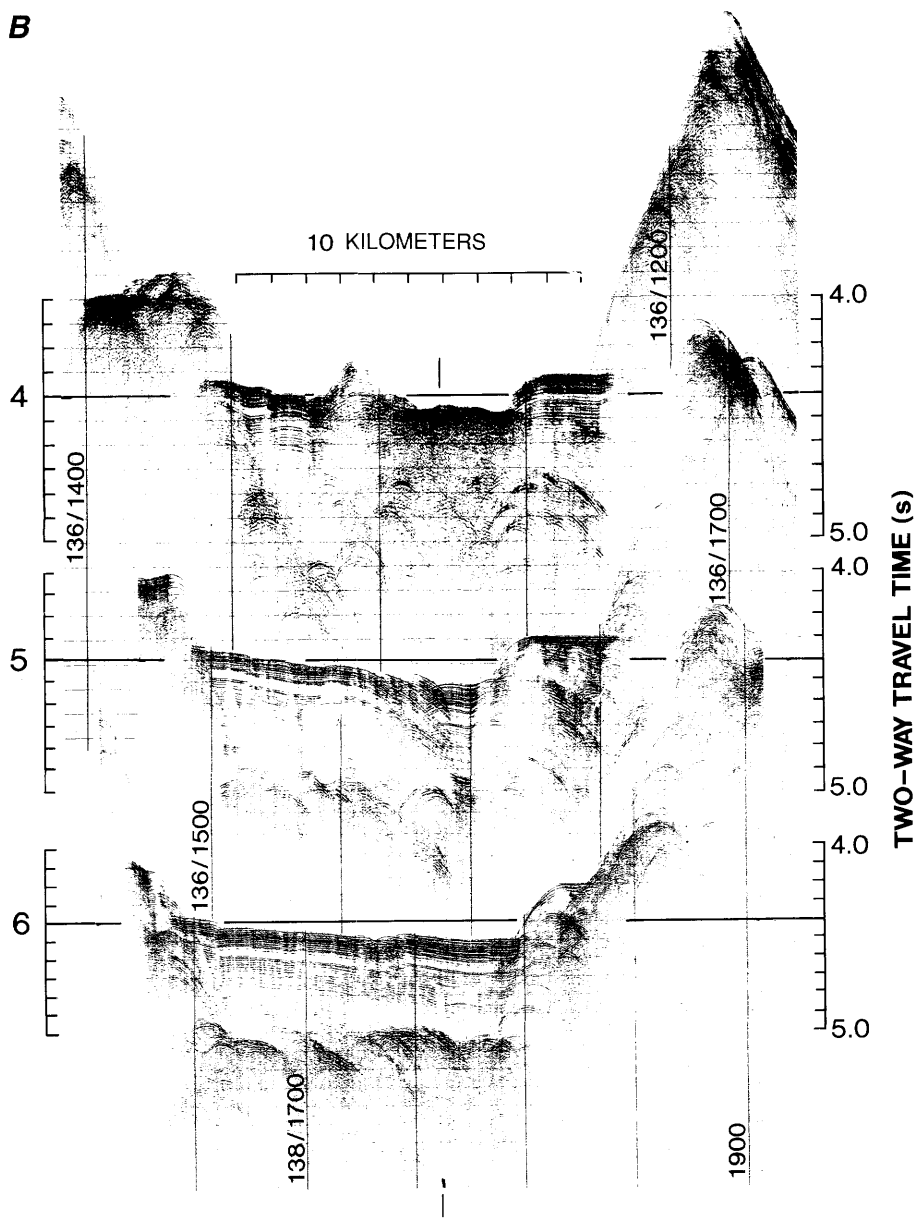

Figure 3.3. Continued.

on the maximum age of the crust within the rift is provided by the width of the valley (12 km at the valley floor) and the spreading rate (24 mm/yr), or equivalently the fraction of the width of the Brunhes normal-polarity Chron occupied by the valley. A 500,000-year history is implied as an upper limit, and this in turn provides a lower limit for a sedimentation rate of about 1 mm/yr. Unfortunately, no more precise constraints were obtained from the cores obtained from DSDP Site 35 (McManus and others, 1970; Vallier and others, 1973); much of the section was barren of microfossils, and all those observed were simply Pleistocene in age, with no further resolution possible. That observation has been substantiated through the re-examination of DSDP Site 35 cores by Normark and others (chap. 6, this volume).

Ages of the uppermost part of the sediment section have been determined from piston cores collected in the valley by McManus and others (1970), Karlin and Lyle

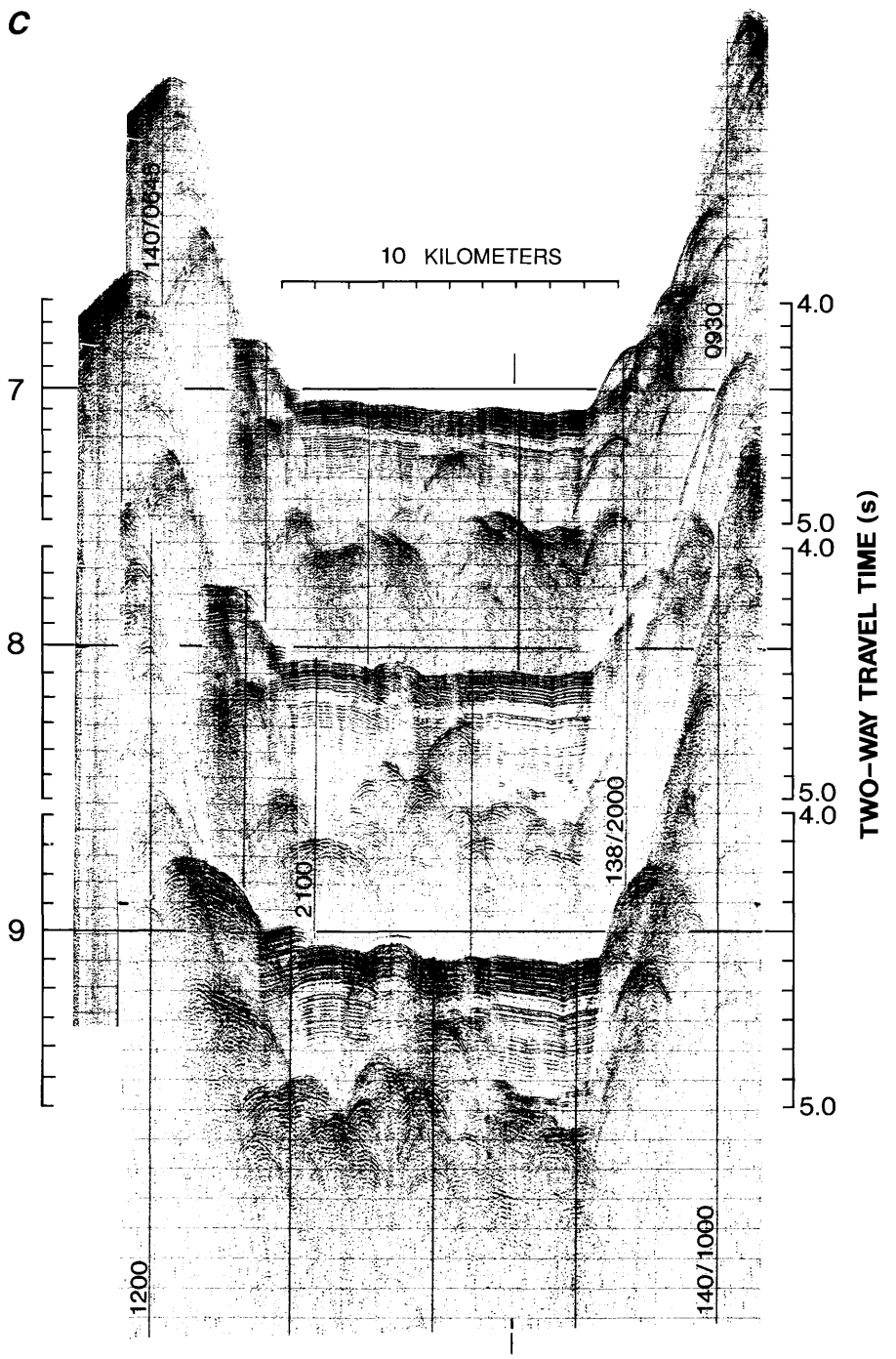

Figure 3.3. Continued.

(1986), and Karlin and Zierenberg (chap. 7, this volume). These authors conclude that sediment accumulation during the Holocene has been generally less than 2 m. This, and the high rates of supply inferred for the Pleistocene that would have kept developing structures buried (see discussion below), imply that the tectonic and volcanic disruptions observed to disrupt the valley floor at present are probably of post-Pleistocene age. This allows a lower limit on the rates of deformation in the valley to be established. Assuming that the vigorous sediment supply virtually ended 8,000 to 10,000 years ago (Mix, 1987), the rate inferred for the accumulation of the 150 m of throw on the fault bounding the eastern block in the valley at profiles 1 to 5 is roughly 15 mm/yr.

The rate of subsidence of the valley floor can be estimated in the same way as the rate of relative motion across faults. The same argument is used that during the Pleistocene period of copious sediment supply, the valley floor was maintained flat (at least to the degree that the turbidite plain outside the trough is flat, with a slope of less than 0.001). A reference depth of 4.27 s = 3,200 m has been selected from the region immediately southeast of the

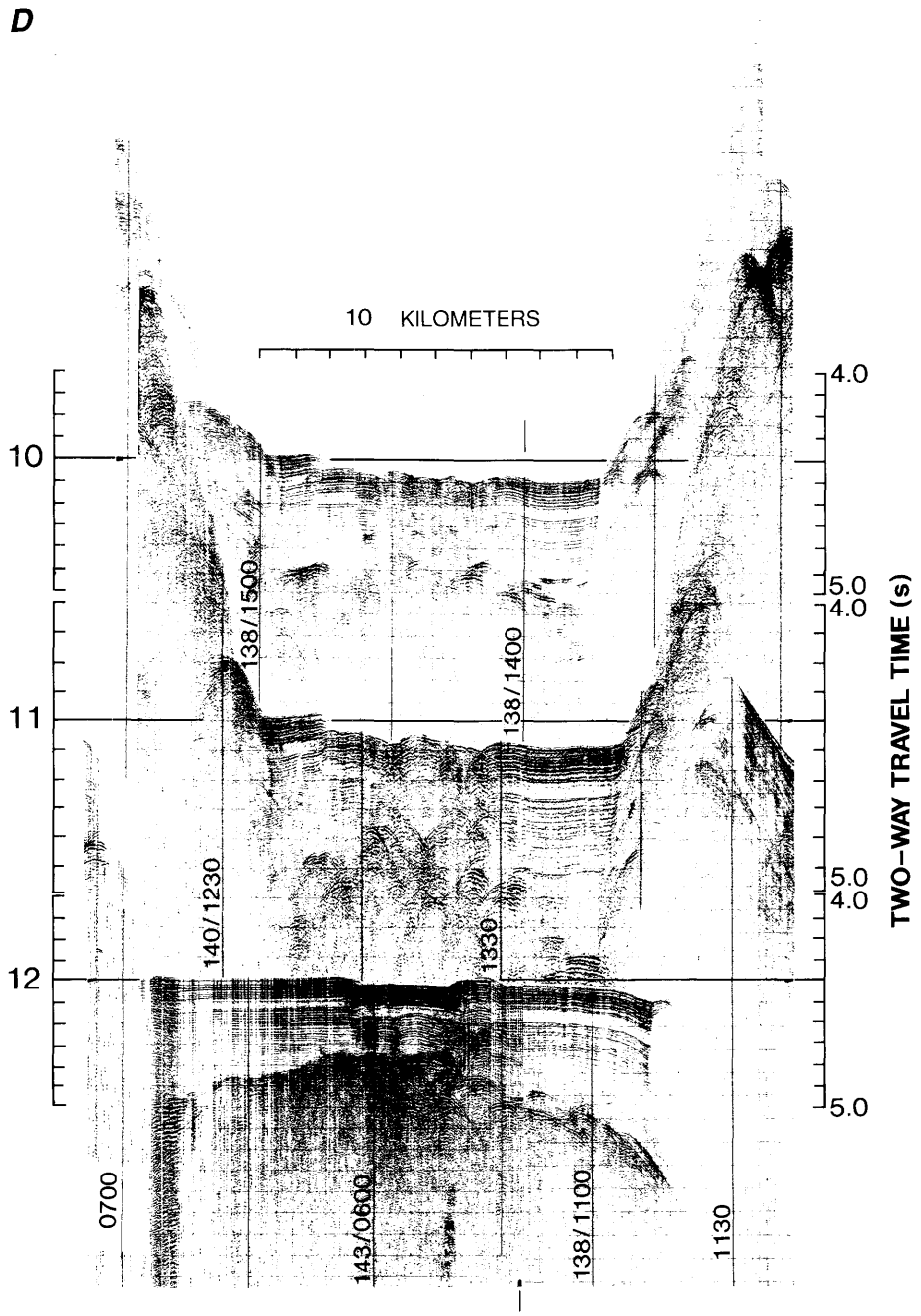

Figure 3.3. Continued.

trough that is presumably outside the influence of the rift tectonics. The fault block along the eastern side of the valley (fig. 3.3, lines 1–5) lies only slightly deeper than this level; post-Pleistocene motion of this block is arguable. The remainder of the valley floor lies well below the reference depth (up to 200 m; figs. 3.2 and 3.3), however, and it can be concluded that most of the central part of the trough has subsided substantially. The subsidence, which averages 100 to 150 m across the 10-km width of the valley floor, is commensurate with the amount—135 m—that would be produced by nonisostatic stretching of a 6-km-thick crust at the full 23 mm/yr spreading rate.

Constraints on earlier subsidence and on the sedimentation rate during the Pleistocene are provided by one of

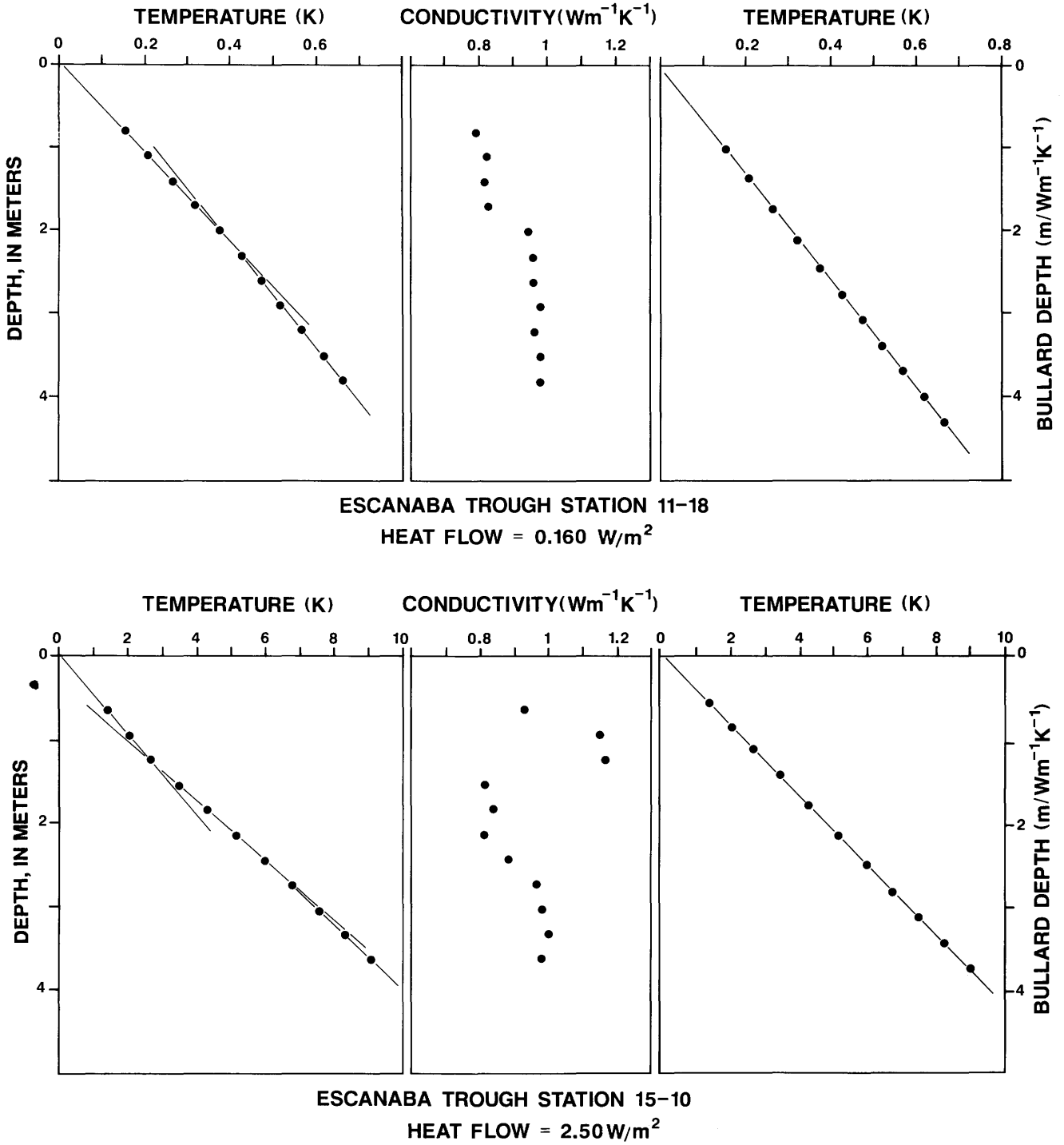

Figure 3.4. Temperature versus depth, conductivity (W/m K) versus depth, and temperature versus integrated thermal resistance (Bullard depth), representative of measurements of high (2.50 W/m) and low (0.160 W/m) heat flow.

the most striking features of the acoustic stratigraphy of the sediment section. A relatively transparent layer roughly 50 ms thick is visible throughout the valley at about 100 ms depth below the sea floor. This horizon can be traced through many areas where local disruptions have obscured the finer-scale acoustic layering (for example, profiles 3, 6, and 8–12); it provides an easily identifiable marker horizon for the Escanaba Trough fill. The horizon was observed in the site-survey data collected before DSDP Site 35 drilling (McManus and others, 1970), and a massive unit, grading from sand at the base to sandy silty mud at the top, was sampled in cores 3 to 5 (between 79 and 107 m below the sea floor) at that site. No internal bedding contacts were observed, although this could reflect drilling disturbances (Normark and others, chap. 6, this volume). For the massive lithologic unit to be coincident with the transparent acoustic unit, very reasonable velocities of roughly 1,600 m/s are required for both the overlying section and the massive unit itself. Several characteristics of the unit suggest a unique origin. First, the unit is unusually coarse grained, with a mean grain size that generally decreases upwards. Second, fossils in the finer-grained part of the unit include neritic and freshwater forms (McManus and others, 1970). And third, although not unusual for the turbidites of Escanaba Trough, the mineralogy of the unit indicates source rocks for the material in the Cascade Range and the Columbia River Plateau. A reasonable speculation is that the layer contains debris produced by the Bretz floods, which were caused by the catastrophic draining of the ice-dammed Lake Missoula (Bretz, 1923, 1925; Pardee, 1942; Bretz and others, 1956). Gravel from the Bretz floods has been sampled in Cascadia Channel as far as 750 km from the continental margin (Griggs and others, 1970), and it is likely that a considerable amount of finer grained material was delivered to Escanaba Trough via Astoria Channel. The most recent flooding events are believed to have occurred between about 18,000 and 13,000 years B.P. (Baker, 1983). The more recent time, the assumed 10,000-year age of the present sediment surface, and the approximately 75 m thickness of the overlying section provide an estimate for the late-Pleistocene turbidite sedimentation rate of 25 mm/yr. This rate is high, but comparable to rates estimated for other rapidly subsiding basins to which Pleistocene turbidites have had access, such as the Winona Basin off northern Vancouver Island (4 mm/yr; Davis and Riddihough, 1982), and Middle Valley of the northern Juan de Fuca Ridge (10 mm/yr; Davis and Lister, 1977). If this rate were characteristic for "average" Pleistocene conditions, the entire 500 to 600 m of valley fill could have been deposited in as little as 30,000 years (this estimate includes the effect of consolidation at depth). As an average for the full section, the rate is probably high because it represents the period following the last glacial maximum and including the sea-level transgression across the continental shelf (which could also be the source of the material in the transparent horizon). Thus the estimate of age of the sediment fill derived using 25 mm/yr as an average sedimentation rate is probably an extreme and somewhat unreasonable lower limit. The sedimentation rate is greater than the displacement rates across faults and the subsidence rates estimated above (up to 15–20 mm/yr), and thus the assumptions that sedimentation maintained low relief of the valley floor and kept fault offsets buried during the late Pleistocene are supported.

That the sedimentation rate and rates of vertical tectonism are similar is also supported by the correlation of stratigraphy across normal faults beneath the floor of the valley. If rates of syntectonic sedimentation were much lower than the growth of the faults, then acoustic stratigraphy would be uncorrelatable across the faults. If sedimentation rates were extremely high, then the hanging-wall and footwall sections would be identical, and the displacement of the Pleistocene stratigraphy would mirror precisely the post-Pleistocene displacement of the sea floor. The case in Escanaba Trough lies between these extremes. This is illustrated graphically in figure 3.5, where the local stratigraphic depths of the top and bottom of the transparent marker horizon discussed above are plotted against the local depth of the sea floor. Clear trends with slightly divergent slopes are defined. Sea-floor depths are shown relative to the 3,200-m reference depth discussed above. The difference between the local depth of sea floor in the trough and the regional reference depth (abscissa in fig. 3.5) must reflect the local rate of subsidence averaged over the post-Pleistocene period of low sediment supply (assumed again to be 10,000 years). Stratigraphic depths can be taken as the product of the horizon age (relative to the 10,000-year sea floor) and the sum of the regional sedimentation rate and the local syn-sedimentary subsidence rate. The latter is assumed to be constant at any given point and equal to that estimated for the post-Pleistocene. Using the least-squares-regression fits shown on figure 3.5 yields times for the top and bottom of the horizon of 3,250 and 4,650 years (pre-seafloor ages), or ages of 13,250 and 14,650 years B.P. respectively. Late-Pleistocene sedimentation rates for the intervals from the sea floor to the top of the marker horizon and for the horizon interval itself (in the central part of the rift, where the sea floor depth is 3,350 m) are 27 and 31 mm/yr respectively. These estimates are in remarkably close agreement with one another and with the independently derived estimate given above.

In addition to extensional faulting and subsidence, recent volcanic activity has disrupted the Escanaba Trough sediment fill. Volcanism and related sediment deformation are focused at several centers along the axis of the trough (see Morton and Fox, chap. 2, this volume). Two of these volcanic centers, at latitudes 41° N. (NESCA) and 40°53′ N., and the northern edge of a third (SESCA site centered at latitude 40°45′ N.) are included in this study. Volcanism has penetrated to the surface at the northernmost

Table 3.1. Heat-flow data collected during *Tully* cruise 89-04, Escanaba Trough.

[Errors defined by goodness of fit of linear regression through temperature versus Bullard depth. Positions of measurement locations along seismic profiles (last two columns) were determined by projecting heat-flow measurement locations due north or south onto nearly co-located seismic lines]

Station number	Penetration number	Latitude N.	Longitude W.	Depth (m)	Penetration (m)	k[1]	Heat flow (mW/m^2)	Error (mW/m^2)	Profile	Time
3	1	40°57.51′	127°25.07′	3220	4.29	1	2521	2	5	1636
3	2	40°57.49′	127°25.3′	3220	4.11	1	693	0.2	5	1630.5
3	3	40°57.44′	127°25.36′	3220	4.08	2	444	0.2	5	1630.5
3	4	40°57.26′	127°26.66′	3220	4.01	1	341	0.2	5	1617
3	5	40°57.36′	127°26.8′	3220	3.88	2	301	0.2	5	1616
3	6	40°57.33′	127°27.13′	3220						
3	7	40°57.36′	127°27.46′	3220	3.85	2	233	0.2	5	1609
3	8	40°57.32′	127°27.89′	3365	3.67	2	356	0.2	5	1604.5
3	9	40°57.28′	127°28.48′	3385	3.71	1	433	0.2	5	1558
3	10	40°57.3′	127°28.78′	3385	3.63	1	416	0.3	5	1555.5
3	11	40°57.31′	127°29.15′	3385	3.65	2	395	0.3	5	1551.5
3	12	40°57.35′	127°29.36′	3410	3.89	1	396	0.3	5	1548.5
3	13	40°57.35′	127°29.83′	3365	3.86	2	212	0.2	5	1544
3	14	40°57.37′	127°30.22′	3360	3.68	1	207	0.2	5	1538
3	15	40°57.37′	127°30.48′	3325	3.79	2	148	0.2	5	1535
3	16	40°57.3′	127°31.05′	3315	3.78	2	180	0.3	5	1529
3	17	40°57.38′	127°31.26′	3320	3.83	2	160	0.3	5	1526.5
3	18	40°57.47′	127°31.52′	3310	3.84	2	191	0.2	5	1523
3	19	40°57.52′	127°31.93′	3305	3.87	2	219	0.2	5	1518.5
3	20	40°57.45′	127°32.28′	3295	3.81	2	236	0.3	5	1515.5
7	1	40°56.14′	127°27.38′	3375	3.61	2	612	0.2	6	1758
7	2	40°56.21′	127°27.5′	3380	3.72	1	211	0.2	6	1756
7	3	40°56.11′	127°27.83′	3380	3.73	2	174	0.2	6	1752
7	4	40°56.02′	127°28.03′	3380	3.75	1	157	0.2	6	1749
7	5	40°56.05′	127°28.28′	3380	3.76	1	152	0.2	6	1746.5
7	6	40°56.08′	127°28.66′	3375	3.73	2	148	0.2	6	1742
7	7	40°56.05′	127°29.13′	3365	3.94	1	151	0.2	6	1736
7	8	40°55.91′	127°29.53′	3355	3.84	2	160	0.2	6	1729
7	9	40°55.87′	127°29.97′	3365						
7	10	40°55.83′	127°30.25′	3370	3.62	1	192	0.2	6	1720
7	11	40°56.03′	127°30.55′	3350	3.91	2	153	0.3	6	1716
7	12	40°56.02′	127°31.04′	3340	3.89	1	149	0.2	6	1709.5
7	13	40°56.1′	127°31.28′	3335	3.85	1	133	0.2	6	1706
7	14	40°55.99′	127°31.55′	3335	3.94	2	153	0.4	6	1702
7	15	40°56.06′	127°32.13′	3332	4.07	1	169	0.2	6	1654
7	16	40°55.95′	127°32.57′	3322	3.94	1	179	0.2	6	1648.5
7	17	40°55.92′	127°33.02′	3320	3.79	2	204	0.3	6	1642
7	18	40°55.95′	127°33.71′	3320	3.86	2	247	0.3	6	1633.5
7	19	40°55.93′	127°33.88′	3320	3.81	2	284	0.2	6	1631.5
11	1	40°54.36′	127°27.07′	3360	4.23	1	217	0.2	10	1342
11	2	40°54.41′	127°27.16′	3370	3.71	2	201	0.2	10	1343
11	3	40°54.4′	127°27.31′	3375	3.66	1	194	0.2	10	1344
11	4	40°54.37′	127°27.69′	3380	3.69	2	176	0.3	10	1348.5
11	5	40°54.38′	127°28.09′	3380	3.84	1	164	0.2	10	1352
11	6	40°54.4′	127°28.43′	3380	3.81	1	155	0.2	10	1355.5
11	7	40°54.4′	127°28.72′	3352	3.65	2	167	0.3	10	1358
11	8	40°54.35′	127°29.2′	3362	3.69	2	131	0.3	10	1403.5
11	9	40°54.39′	127°29.52′	3380	3.85	1	229	0.3	10	1408
11	10	40°54.33′	127°30.03′	3373	3.52	2	219	0.2	10	1411
11	11	40°54.19′	127°30.26′	3363	3.68	1	83	0.2	10	1414
11	12	40°54.22′	127°30.51′	3365	3.52	2	254	0.2	10	1416
11	13	40°54.19′	127°30.85′	3350	3.75	1	317	0.2	10	1419
11	14	40°54.1′	127°31.32′	3350	3.75	1	707	0.2	10	1424
11	15	40°54.1′	127°31.69′	3354	3.68	2	298	0.2	10	1428
11	16	40°54.04′	127°32.1′	3350						
11	17	40°54.35′	127°32.13′	3350	3.79	2	561	0.2	10	1432.5
11	18	40°54.38′	127°32.42′	3333	3.99	1	160	0.2	10	1446

Table 3.1. Heat-flow data collected during *Tully* cruise 89-04, Escanaba Trough—Continued.

Station number	Penetration number	Latitude N.	Longitude W.	Depth (m)	Penetration (m)	k[1]	Heat flow (mW/m^2)	Error (mW/m^2)	Profile	Time
11	19	40°54.39′	127°32.76′	3335	3.78	2	212	0.3	10	1439.5
11	20	40°54.43′	127°33.22′	3290	3.87	2	137	0.2	10	1443.5
11	21	40°54.43′	127°33.58′	3295	3.78	1	409	0.2	10	1448
11	22	40°54.44′	127°33.96′	3290						
15	1	40°59.81′	127°33.35′	3240	3.71	1	949	0.2	3	925.5
15	2	40°59.87′	127°33.01′	3254	3.73	2	851	0.2	3	928.5
15	3	40°59.87′	127°32.97′	3260	3.68	1	670	0.2	3	929
15	4	40°59.89′	127°32.65′	3285	3.72	2	482	0.2	3	932
15	5	40°59.87′	127°32.13′	3320	3.68	1	384	0.2	3	937
15	6	40°59.93′	127°31.75′	3325	3.64	2	320	0.2	3	940.5
15	7	40°59.95′	127°31.48′	3320	3.76	1	415	0.2	3	944
15	8	41°0.02′	127°31.37′	3315	3.84	2	410	0.2	3	945
15	9	41°0.05′	127°31.18′	3325	3.64	1	726	0.2	3	948
15	10	41°0.07′	127°30.85′	3310	3.55	1	2495	0.2	3	950.5
15	11	41°0.14′	127°30.62′	3300	3.66	1	1117	0.2	3	954.5
15	12	41°0.16′	127°30.46′	3295	3.71	1	1331	0.2	3	955
15	13	41°0.15′	127°30.06′	3270	3.75	1	3176	0.2	3	958
15	14	41°0.15′	127°29.9′	3270	3.58	1	1675	0.3	3	1000

[1]Conductivity code: 1, Conductivity measured in situ; 2, Assumed (survey average) conductivity, as listed below.

Nominal depth (m)	k (W/mK)	Nominal depth (m)	k (W/mK)	Nominal depth (m)	k (W/mK)
1.0	0.84	2.2	0.94	3.4	1.00
1.3	0.83	2.5	0.96	3.7	1.01
1.6	0.87	2.8	0.98	4.0	1.04
1.9	0.90	3.1	0.99		

location, where a ponded flow buries the sediment surface over several square kilometers (fig. 3.3, profiles 1–3; see also Ross and Zierenberg, chap. 8, this volume; Morton and Fox, chap. 2, this volume). The thickness of the flow is not well constrained. Much of the relief of the flow near its source (near profile 3) relative to the floor of the graben in which it is contained may be due to local uplift at the volcanic center. The flow appears to be thin or discontinuous enough in its distal parts to allow some acoustic penetration by the small acoustic source, as some faint layering is visible beneath the flow along profiles 1 and 4. Volcanism at the more southerly locations is observed to be limited to intrusions within and beneath the sediment section (profiles 7–12), although south of profile 12, extrusive rocks are present at the SESCA site (Morton and Fox, chap. 2, this volume; Ross and Zierenberg, chap. 8, this volume).

Localized uplift of the sediment section is common at the centers of volcanic activity. Clear examples occur along profiles 3, 4, 8, 9, 11, and 12 (fig. 3.3). The uplifted structures are circular in plan (fig. 3.2), and commonly about 1 to 1.5 km in diameter. The structures appear to be domed in cross-section, although some of this appearance results from acoustic diffraction at their perimeters. It can be seen in the profiles and it has been observed directly that the uplift is fault bounded (Zierenberg and others, chap. 10, this volume; Denlinger and Holmes, chap. 4, this volume).

Constraints on the timing of the uplift of the sediments at the volcanic centers are provided by considering the stratigraphic depth and thickness of the transparent marker horizon with respect to the local sea-floor depth, in the same way that subsidence and sedimentation histories were estimated (see discussion above). Unfortunately, where the uplift is large (for example, line 4, fig. 3.3), the coherence of the stratigraphy is nearly completely destroyed and a quantitative assessment cannot be made. The stratigraphy is well preserved at profiles 8 and 9, however, and the horizon depths can be determined there with confidence. These are plotted with respect to the local sea-floor depth in figure 3.5. Although the points fall within the range of scatter of the points derived from the "normal" sediment fill, they are offset systematically from the regression lines through the "normal"-section points in a direction (shallow) and by an amount (20 m) that is consistent with the local uplift of the sea floor at these volcanic centers (20–40 m). Thus it is reasonable to conclude that unlike the normal faulting and subsidence of the valley floor, much

of the volcanic activity and the associated uplift of sediment occurred during the post-Pleistocene period of low sediment supply (roughly the last 10,000 yr).

The exact relationship of the pluglike uplift and underlying intrusive volcanism is not clear. In some cases (such as profiles 7, 8, and 9), bright reflectors are seen within the sediment section where there is virtually no relief at the sea floor. In other cases (profiles 8, 9, 11, and 12) there is a correspondence between uplift and underlying bright reflectors, although the geometry is poorly defined. In general, the bright reflections within the sediment section are far more chaotic than the overlying deformation of the sediments. From these observations, we infer that if the local bright reflections are from intrusive sills within the sediments, they are relatively thin, and that the sediment uplift is not caused by these intrusions. We suggest instead that the uplift is caused by a deeper, more centralized intrusive process, possibly the construction of a volcanic edifice at the base of the sediment pile. Unfortunately, the deeper structure is obscured by the small but numerous higher level sills (see also Denlinger and Holmes, chap. 4, this volume).

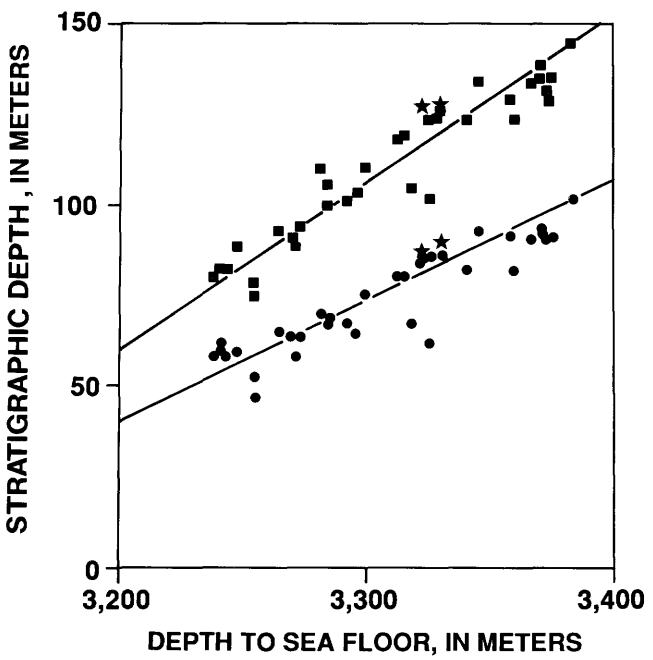

Figure 3.5. Depths below sea floor of top (circles) and bottom (squares) of widespread, clearly defined, acoustically "transparent" horizon in Escanaba Trough, plotted as a function of local sea floor depth. Origin for depth axis chosen to equal depth of turbidite plain outside rift valley at its southern end. Depths are inferred to represent amount of local subsidence in rift since the end of rapid late Pleistocene sedimentation. Trends of least-squares regression lines fitted through points, combined with subsidence yield estimates for rates of syn-tectonic sedimentation. Stratigraphic depths at volcanic center at seismic-reflection lines 8 and 9 are shown with stars.

INFERRED THERMAL STRUCTURE

In most cases, the probe penetrations were spaced closely enough to define the nature of heat-flow variability well (fig. 3.6). Along line 6, the heat flow is remarkably uniform. All values fall very close to 0.2 W/m^2 across the full width of the valley, with the exception of the measurements made near the bounding normal-fault scarps. Toward the west end of the line, the heat flow increases slightly, and one value at the east end exceeds the rest by a factor of 3. More extreme examples of this pattern are seen at the west end of line 3 and the east end of line 5. This pattern appears to occur in measurements wherever the basement shoals in proximity to the bounding normal fault scarps.

"Background" values elsewhere in the valley are virtually identical to those measured along line 6, suggesting either that hydrothermal circulation in the valley is currently weak and the heat flow is dominantly conductive and uniform, or that circulation within the crust beneath the sediment section is sufficiently vigorous to maintain roughly isothermal conditions near the sediment-basement (low permeability-high permeability) boundary. The sense of the variability near the bounding faults is consistent with either conductive or hydrothermal effects; high values near the valley walls could be caused either by conductive focusing of heat or by the thinning of the sediment cover over a hydrothermally warmed basement aquifer. However, the magnitude of the anomalies observed at the east end of line 5 and the west end of line 3 is far too large to be accounted for by conductive effects, and the effect of hydrothermal heat transport in basement is very likely to be the cause. Some fluid leakage from beneath the sediments of the valley may occur along the valley-bounding normal faults, although there is no direct evidence for this in our observations.

Three scattered high values occur along line 10 where the sediment is disturbed on a small scale by tectonic or underlying intrusive activity near the center of the valley. The anomalies are small and very localized (on a scale smaller than the measurement spacing), and probably result from very recent mechanical disturbances of the sediments at the sea floor. A piston core from this location (TUL 89D-7P, Normark and others, chap. 6, this volume), containing irregular bedding, suspended mud clasts, and a nearly vertical vein of sandy silt, supports this conclusion. Along line 5, values over the rifted central part of the valley are systematically high. These values may reflect the higher degree of extension in this part of the valley; they also may be part of the anomaly at the NESCA volcanic center that lies only 3 km to the north. Measurements along line 3 extend into the NESCA volcanic center itself; they show the heat flow to increase fairly systematically from a minimum of about 0.3 to well over 1 W/m^2 toward the center of the valley and the center of the area disrupted

by volcanic activity. This pattern undoubtedly results from the local volcanism and hydrothermal activity at this location along the rift. The two extreme values along the eastern part of the profile are probably associated with nearby localized hydrothermal fluid discharge. A 108°C and a 220°C vent are known to exist a few hundred meters from the easternmost two penetrations (Zierenberg and others, chap. 10, this volume). The systematic increase in heat flow at the western end of the line is discussed above.

If the sediment permeability is low enough to prohibit thermally significant vertical fluid flux through the sediment, then a reasonable estimate of the regional hydrothermal fluid temperatures within basement can be derived by simply extrapolating the measured surface gradients to the base of the sediment section. This is probably the case, as the more permeable sandy interbeds in the turbidite section are probably not well interconnected, and as a result, the vertical component of permeability is controlled by the

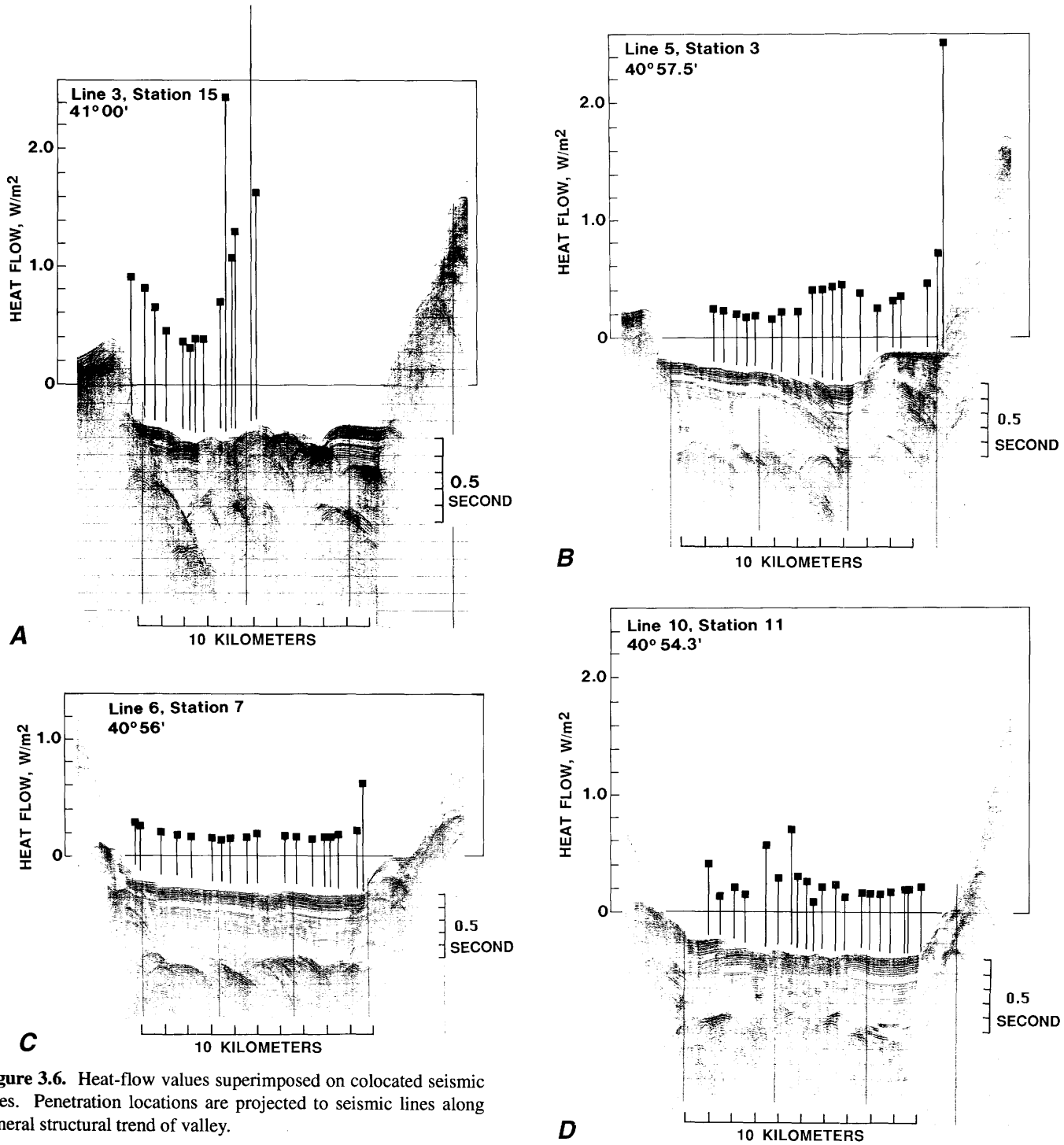

Figure 3.6. Heat-flow values superimposed on colocated seismic lines. Penetration locations are projected to seismic lines along general structural trend of valley.

fine-grained layers. Horizontal fluid transport will not disturb the thermal field significantly. Using a reasonable function for the porosity of the sediments at depth and an appropriate relationship between porosity and conductivity (see Nobes and others, 1986), an average conductivity of 1.46 W/m K is estimated for the roughly 600-m-thick sediment section. The resulting extrapolated temperatures calculated for the sediment-basement interface in the areas away from the NESCA volcanic site are roughly 80°C. This temperature is much lower than either temperatures measured in hydrothermal fluids that currently discharge through the sea floor at the NESCA site (up to 220°C; Zierenberg and others, chap. 10, this volume) or the even higher temperatures (300°C–350°C) that must have existed when the major sulfide mineral deposits were formed in this part of the valley (Morton and others, 1990).

Two hypotheses can be developed to explain this apparent local contrast in crustal thermal conditions. One is that the sediment fill of the valley is in a transient thermal state, and that high temperatures (around 350°C) do occur in the crust beneath the valley. The estimated regional basement temperatures are based on the assumption of steady-state conditions, and they could be erroneously low. Two effects must be considered, one being that of the rapid sedimentation and the other the possible youth of the volcanic and hydrothermal activity.

The sedimentation rate estimated above is very high, but because of the brief history of sedimentation and the modest total accumulation, the effect is not large. Using the simple correction derived from Carslaw and Jaeger (1959) by Von Herzen and Uyeda (1963) as a limiting case, we find that the surface heat flow would have been reduced by about 35 percent at the end of the Pleistocene; after 9,000 to 10,000 years of post-Pleistocene nondeposition, the effect of sedimentation on the present heat flow would have diminished and would be less than this. The correction for the case of sedimentation on a basement that is maintained at a constant temperature by hydrothermal circulation is even less (Wang and Davis, 1992). Thus the effect of rapid sedimentation is probably not the cause of the low regional heat flow in the valley. The other possibility is that the high temperatures and hydrothermal activity associated with recent volcanism are widespread but very recent. This possibility cannot be eliminated with the existing data. The time for a significant thermal signal to penetrate the 600-m-thick sediment section that buries basement would be roughly 6,000 years, and as concluded above, the volcanism that disrupts the sediment fill could be younger than this. Any associated thermal events that may have affected regional basement temperatures recently would not be reflected in the present surface heat flow. The anomalous heat flow seen along line 5 near the NESCA volcanic center is probably a result of conductive heat transfer through most of the sediment section, however, and this suggests that volcanism and hydrothermal activity in the crust is at least a few thousand years old.

An alternate and preferred explanation is that all of the heat associated with the volcanism that has produced the sediment uplift and hydrothermal products has been lost by very efficiently focused hydrothermal discharge, with no regional heating having taken place. In fact, the crust surrounding the volcanic centers may have functioned as a fluid supply zone for the hydrothermal systems, and the crust and overlying sediment section may have been slightly cooled by distributed slow recharge during the activity. The cause for highly focused hydrothermal discharge may be twofold: (1) The source of heat is probably highly focused and limited to the intrusions and magma supply zones immediately beneath the volcanic centers. (2) The permeability of the sediments may be highly enhanced by the intrusion process: rapid heating of the sediments causes local hydrofracturing; hydrothermal induration increases the strength of the sediment and allows open fractures to be supported; and the continuing deformation induced by the emplacement of sub- and intra-sedimentary intrusions creates more new fracture-permeability as the volcanism continues (see discussion in Denlinger and Holmes, chap. 4, this volume). The resulting hydrologic configuration acts as a chimney, the base of which is underpressured with respect to the regional conductive thermal-profile hydrostat and overpressured with respect to the isothermally hot hydrostat directly overhead.

With respect to the generation of metalliferous hydrothermal fluids, these two hypotheses concerning the nature of circulation beneath and within the sediment of Escanaba Trough differ in a fundamental way. In the first case, high-temperature fluids could be "trapped" regionally beneath the sediment of the valley. This would permit widespread high-temperature water-rock interaction within the crust and deeper sediment of the valley. In the second case, fluids would be in contact with sediment and crust at high temperatures only in the immediate vicinity of the volcanic centers. Neither case is prohibited by the data presented here. Both allow ample interaction between high-temperature fluids and sediment, as implied by the composition of hydrothermal minerals sampled at the sea floor (Koski and others, 1988). Both provide sufficient heat, although in the focused case a relatively large reservoir of heat must be tapped at depth to produce the volume of minerals that may be present.

To support these conclusions, we have estimated mass and heat budgets with a very simple model that is shown schematically in figure 3.7. The geometry chosen is simple: a uniformly thick sediment fill buries a permeable igneous upper crust of the rift valley. A localized volcanic heat source lies beneath the center of the valley, underlying a zone of enhanced permeability in the sediment section created by the volcanism and the related tectonic and hydrothermal effects. Fluids are supplied via distributed recharge

through the sediment section and basement outcrops in the region surrounding the volcanic center. Local porous-medium convection, which occurs wherever the permeability, thermal gradients, and permeable-layer thicknesses are sufficient to yield supercritical conditions, undoubtedly occurs in the upper crust but is not shown in the diagram. The large-scale fluid flow that is shown is driven by the difference between the pressure within an ascending hot column of fluid (taken to be 380°C) and the regional pressure beneath the impermeable sediment section, which probably lies close to the hydrostat defined by the density of a fluid column having a conductive thermal gradient. This is assumed to be 0.16 K/m. Using the thermal expansivity of seawater defined by Bischoff and Rosenbauer (1985), a maximum pressure difference of nearly 2 MPa at the level of the base of the sediment section (500 m below sea floor) results. Depending on the permeability structure, much of this pressure differential may be available to drive hot fluids through the sediment section above the volcanic centers. A small pressure differential may also exist to drive fluids from beneath the sediment "seal" through warm, fault-controlled conduits along the edges of the valley; applied over the same 500 m depth interval, the density difference between warm (80°C) and cold (conductive) fluid columns would produce a pressure difference of about 0.1 MPa.

If known, the quantity and composition of hydrothermal products present in the mineral deposits associated with the volcanic centers would set limits on the volumes of fluid and rock that must be involved in the system at depth. The quantities of hydrothermal minerals produced are poorly constrained; observations of hydrothermal mineralization in outcrop are numerous (see Zierenberg and others, chap. 10, this volume) but provide little quantitative information about mineralization at depth. We used a deposit size of 10 million tonnes (10^{10} kg) for the purposes of the model calculation. It is reasonable to assume that roughly half of this mass would be iron (Koski and others, 1988; Morton and others, 1990); if this had precipitated at 100 percent efficiency from high-temperature hydrothermal fluid saturated with iron at a concentration of 500 ppm, then 10^{13} kg, or 10^{10} m^3 of water would be required. To heat this mass of water by 350 to 400 K requires roughly 10^{19} J of heat. To supply this heat requires the solidification and cooling from 1,200°C to 400°C of roughly 4 km^3 of rock, which is commensurate with the size that one might expect for an intrusion beneath a volcanic center like those in Escanaba Trough. Lesser volumes of rock (for example, a volume equivalent to a series of sills emplaced within and beneath the sediment section) could not provide enough heat to produce the deposit of the size assumed. Deposits of greater size would require commensurately larger heat sources or a series of intrusions sharing the same discharge zone.

A simple estimate for the time required to dissipate the quantity of heat calculated above can be had by assuming an average rate of hydrothermal discharge for the system. At a rate of 500 MW, a value that falls at the low end of the range for vent fields summarized by Schultz and others (1990), 10^{19} J of heat would be fully dissipated in about 600 years. If this were the case, then the rate of flow through the system would be roughly 0.5 m^3/s.

To maintain this rate of fluid flux would require more than distributed recharge through the sediment section in the vicinity of the volcanic centers. Much of the buoyancy-derived pressure differential in the hydrothermal system is probably lost in the discharge path above the volcanic centers; the differential available to drive distributed recharge

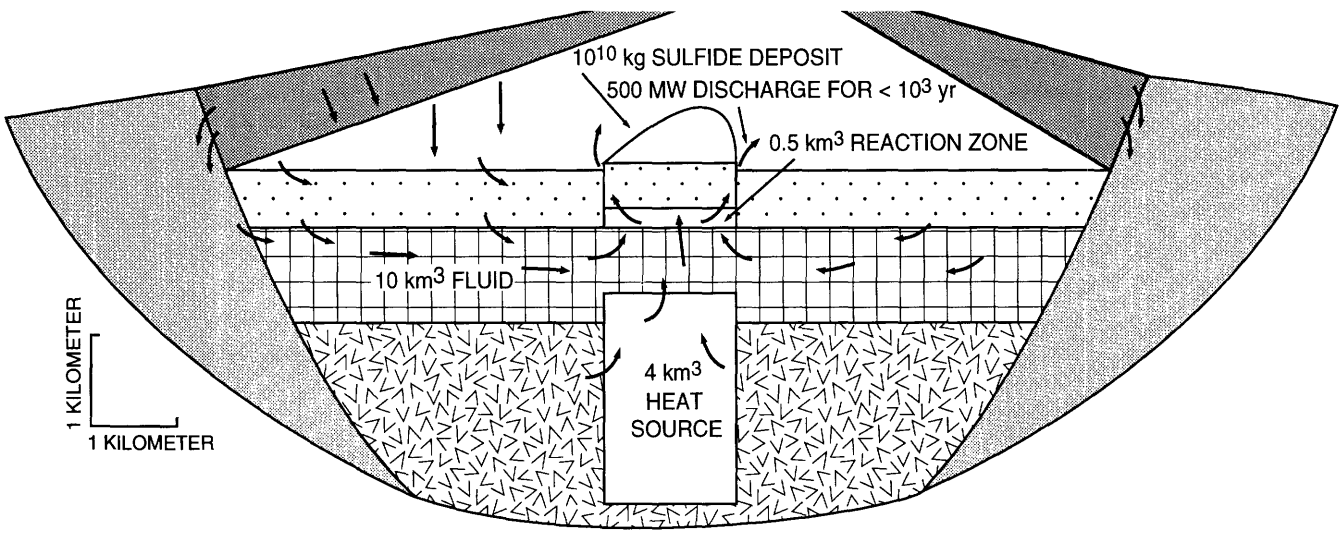

Figure 3.7. Schematic illustration of heat- and mass-balance model for regional hydrothermal circulation, fluid discharge, and mineralization associated with volcanic centers in Escanaba Trough. Arrows show fluid flow. See text for discussion of model.

is probably less than a few tenths of a megapascal. This driving force, and the low vertical permeability of the sediment section, set a limit on the rate of distributed recharge. A value for the permeability of the sediment section of 10^{-16} m^2, and a pressure differential over the 600 m thickness of sediment of 0.1 MPa would result in a limiting velocity of roughly 1.5×10^{-11} m/s (0.5 mm/yr). To maintain a flux of 0.5 m^3/s would require recharge to be distributed over an area of roughly 30,000 km^2, which is clearly unreasonable given the dimensions of the valley and the distances between volcanic centers. This implies that most of the recharge is probably supplied along the normal-fault scarps that bound the valley, where the sediment cover is thin or basement rocks are exposed, and thus where the hydraulic impedance to flow is low.

Although a large volume of rock is required to supply the necessary heat for the construction of a 10-million-tonne mineral deposit, a relatively small volume of rock is required to supply the necessary mass. This can be shown by considering the balance of the quantities of lead and sulfur (elements that are particularly mobile and likely to be fully stripped from the rock in the alteration zone) in the deposit and in the source. For this simple calculation, 10 ppm lead and 0.2 percent sulfur have been used for concentrations (by weight) in the source rocks, and 0.06 percent lead and 35 percent sulfur have been used for concentrations in the sulfide deposit. Assuming the source to be in the sediment section, where the porosity could be as high as 50 percent, a source volume of between 0.4 and 0.7 km^3 is implied. This volume is nearly 10 times smaller than the volume of rock required to supply the heat; it is small enough that it could be contained entirely within the sediment section in the immediate vicinity of an individual volcanic center. For this to be the case, the water-rock interaction would have to be very efficient, but this is not unreasonable. Intimate contact between sediments and high-temperature fluids may be permitted by the high porosity of the sediments, intergranular flow in high-permeability coarse-grained layers, and fine-scale fracturing produced through the deformation of the sediment caused by the volcanism, and by hydrofracturing due to rapid heating events or overpressuring in the hydrothermal system. Within the igneous section, less chemical interaction may take place, as the permeability there is probably dominated by relatively widely spaced, large-aperture fractures.

CONCLUSIONS

New single-channel seismic and heat-flow data across the central Escanaba Trough provide new insight into the tectonic, volcanic, and hydrothermal structure and history of this sediment-filled rift valley. The history of the valley contained within the sediment section may be very brief. The depth and inferred age of a ubiquitous, thick, transparent acoustic layer that may be related to the most recent catastrophic draining events of the Pleistocene Lake Missoula, and a simple stratigraphic analysis provide independent estimates of the sedimentation rate for the upper part of the sediment section. The rates agree and are high, on the order of 25 to 30 mm/yr. At this rate, the entire section of sediment could have been deposited in only 30,000 years; the sediment at the base of the section would be only 40,000 years old. The rates estimated are derived from only the upper third of the section, however, and are representative only for the period of rapid deposition following the last glacial maximum. This age for the section is thus an extreme lower limit.

The sediment fill is disrupted by normal faulting and by localized volcanic intrusions. Syn-sedimentary deformation across the normal faults is modest but resolvable. The timing of the deformation associated with the igneous intrusions is less well defined, but it appears that the intrusions have deformed the entire sediment section uniformly. Thus the igneous and associated hydrothermal activity at the volcanic centers may postdate the period of rapid Pleistocene sedimentation, which is assumed to have ended roughly 8,000 to 10,000 years ago.

The heat flow in the valley regionally is relatively low, averaging roughly 0.2 W/m. Temperatures at the sediment-basement interface estimated by extrapolating the surface gradients through the thickness of the underlying sediment section are low also, averaging about 80°C, despite the recent volcanism and indications of high-temperature hydrothermal activity at several locations along the valley axis. High heat-flow values occur where basement shoals near the valley-bounding faults, but this can be attributed to the thinning of the sediment section above a crustal aquifer, the temperature of which is maintained at a roughly constant level by efficient fluid circulation. The highest heat flow occurs in the vicinity of the NESCA volcanic center, which is known to be hydrothermally active.

Two explanations are suggested for the localized nature of the thermal anomaly associated with the volcanic center and the low heat flow elsewhere. One possibility is that high-temperature crustal hydrothermal circulation associated with the volcanism in the valley is widespread, but too recent (less than a few thousand years) for the thermal effects to have reached the sea floor by conduction. Temperatures at depth estimated by simple extrapolation from sea-floor measurements are correct only for steady-state thermal conditions, and would be erroneously low if a transient state were present. The other, more likely, possibility is that the hydrothermal systems driven by the volcanic heat sources are highly focused by the localized nature of the intrusive volcanism, by the enhanced permeability of the sediment as it is modified by the induration, hydrofracturing, and deformation in the vicinity of the volcanic centers, and by the consequent geometry and

thermal structure of the chimney-like hydrologic system. If temperatures within the sediment are low regionally, then the interaction between high-temperature fluids and sediment that is known to occur must be limited to the region directly above the volcanic intrusions. A simple model of heat, fluid, and chemical balance demonstrates that this is reasonable, and provides constraints on the nature and rates of fluid flow through the crust and sediments of the valley.

REFERENCES CITED

Abbott, D.H., Morton, J.L., and Holmes, M.L., 1986, Heat flow measurements on a hydrothermally active, slow-spreading ridge: The Escanaba Trough: Geophysical Research Letters, v. 13, p. 678–680.

Atwater, T., and Mudie, J.D., 1973, Detailed near-bottom geophysical study of the Gorda Rise: Journal of Geophysical Research, v. 78, p. 8665–8686.

Baker, V.R., 1983, Late Pleistocene fluvial systems, *in* Porter, S.C. ed., Late Quaternary environments of the United States: Minneapolis, University of Minnesota Press, v. 1, p. 115–129.

Becker, K., and Fisher, A.T., 1991, A brief review of heat flow studies in the Guaymas Basin, Gulf of California, *in* Dauphin, J.P., and Simonet, B.R.T., eds., The Gulf and Peninsular Province of the Californias: Tulsa, Oklahoma, American Association of Petroleum Geologists Memoir 47.

Bischoff, J.L., and Rosenbauer, R.J., 1985, An empirical equation of state for hydrothermal seawater (3.2 percent NaCl): American Journal of Science, v. 285, p. 725–763.

Bretz, J H., 1923, The channeled scabland of the Columbia Plateau: Journal of Geology, v. 31, p. 617–649.

———1925, The Spokane flood beyond the Channeled Scabland: Journal of Geology, v. 33, p. 236–259.

Bretz, J H., Smith, H.T.U., and Neff, G.E., 1956, Channeled scabland of eastern Washington: New data and interpretations: Geological Society of America Bulletin, v. 67, p. 957–1049.

Carslaw, H.S., and Jaeger, J.C., 1959, Conduction of heat in solids: London, Oxford University Press, 510 p.

Clague, D.A., and Holmes, M.L., 1987, Geology, petrology, and mineral potential of the Gorda Ridge, *in* Scholl, D.W., Grantz, A., and Vedder, J.G., eds., Geology and resource potential of the continental margin of western North America and adjacent ocean basins—Beaufort Sea to Baja California: Houston, Circum-Pacific Council for Energy and Mineral Resources, Earth Science Series, v. 6, p. 563–580.

Davis, E.E., 1988, Oceanic heat flow density, *in* Haenel, R., Rybach, L., and Stegena, L., eds., Handbook of terrestrial heat-flow density determination: Dordrecht, Kluwer Academic Publishers, p. 223–246.

Davis, E.E., Goodfellow, W.D., Bornhold, B.D., Adshead, J., Blaise, B., Villinger, H., and Le Cheminant, G.M., 1987, Massive sulfides in a sedimented rift valley, northern Juan de Fuca Ridge: Earth and Planetary Science Letters, v. 82, p. 49–61.

Davis, E.E., and Lister, C.R.B., 1977, Heat flow measured over the Juan de Fuca Ridge: Evidence for widespread hydrothermal circulation in a highly heat transportive crust: Journal of Geophysical Research, v. 82, p. 4845–4860.

Davis, E.E., Lister, C.R.B., Wade, U.S., and Hyndman, R.D., 1980, Detailed heat flow measurements over the Juan de Fuca Ridge system: Journal of Geophysical Research, v. 85, p. 299–310.

Davis, E.E, and Riddihough, R.P., 1982, The Winona Basin: Structure and tectonics: Canadian Journal of Earth Sciences, v. 19, p. 767–788.

Davis, E.E., and Villinger, H., 1992, Thermal and tectonic structure of the Middle Valley sedimented rift, northern Juan de Fuca Ridge, *in* Davis, E.E., Mottl, M.J., Fisher, A.T., and others, eds., Proceedings of the Ocean Drilling Program, initial results: Ocean Drilling Program, v. 139, p. 9–41.

Denlinger, R.P., and Holmes, M.L., A thermal and mechanical model for sediment hills and associated sulfide deposits along the Escanaba Trough, *in* Morton, J.L., Zierenberg, R.A., and Reiss, C.A., eds., Geologic, hydrothermal, and biologic studies at Escanaba Trough, Gorda Ridge, offshore northern California: U.S. Geological Survey Bulletin 2022, chapter 4 (this volume).

Fisher, A.T., and Becker, K., 1992, Heat flow, hydrothermal circulation, and basalt intrusions in the Guaymas Basin, Gulf of California: Earth and Planetary Science Letters, v. 103, p. 84–99.

Griggs, G.B., Kulm, L.D., Waters, A.C., and Fowler, G.A., 1970, Deep-sea gravel from Cascadia Channel: Journal of Geology, v. 78, p. 611–619.

Holmes, M.L., and Zierenberg, R.A., 1990, Submersible operations in Escanaba Trough, southern Gorda Ridge, *in* McMurray, G.R., ed., Gorda Ridge: A seafloor spreading center in the United States' Exclusive Economic Zone: New York, Springer-Verlag, p. 93–116.

Karlin, R., and Lyle, M., 1986, Sediment studies on the Gorda Ridge: Oregon Department of Geology and Mineral Industries Open-File Report O-86-19, 76 p.

Karlin, R.E., and Zierenberg, R.A., Sedimentation and neotectonism in the SESCA area, Escanaba Trough, southern Gorda Ridge, *in* Morton, J.L., Zierenberg, R.A., and Reiss, C.A., eds., Geologic, hydrothermal, and biologic studies at Escanaba Trough, Gorda Ridge, offshore northern California: U.S. Geological Survey Bulletin 2022, chapter 7 (this volume).

Koski, R.A., Shanks, W.C., III, Bohrson, W.A., and Oscarson, R.L., 1988, The composition of massive sulfide deposits from the sediment-covered floor of Escanaba Trough, Gorda Ridge: Implications for depositional processes: Canadian Mineralogist, v. 26, p. 655–673.

Lawver, L.A., and Williams, D., 1979, Heat flow in the central Gulf of California, Journal of Geophysical Research, v. 84, p. 3465–3478.

Lawver, L.A., Williams, D., and Von Herzen, R.P., 1975, A major geothermal anomaly in the Gulf of California: Nature, v. 257, p. 23–28.

Lonsdale, P., and Becker, K., 1985, Hydrothermal plumes, hot springs, and conductive heat flow in the southern trough of Guaymas Basin: Earth and Planetary Science Letters, v. 73, p. 211–225.

McManus, D.A., and others, 1970, Site 35, *in* McManus, D.A., and others, eds., Initial reports of the Deep Sea Drilling

Project: Washington, U.S. Government Printing Office, v. 5, p. 165–172.

Mix, A.C., 1987, The oxygen-isotope record of glaciation, *in* Ruddiman, W.F., and Wright, H.E., Jr., eds., The geology of North America, volume K-3, North America and adjacent oceans during the last deglaciation: Boulder, Colorado, Geological Society of America, p. 111–135.

Moore, G.W., 1970, Sea-floor spreading at the junction between Gorda Rise and Mendocino Ridge: Geological Society of America Bulletin, v. 81, p. 2817–2824.

Morton, J.L., Holmes, M.L., and Koski, R.A., 1987, Volcanism and massive sulfide formation at a sedimented spreading center, Escanaba Trough, Gorda Ridge, northeast Pacific Ocean: Geophysical Research Letters, v. 14, p. 769–772.

Morton, J.L., Koski, R.A., Normark, W.R., and Ross, S.L., 1990, Distribution and composition of massive sulfide deposits at Escanaba Trough, southern Gorda Ridge, *in* McMurray, G.R., ed., Gorda Ridge: A seafloor spreading center in the United States' Exclusive Economic Zone: New York, Springer-Verlag, p. 77–92.

Morton, J.L., and Fox, C.G., Structural setting and interaction of volcanism and sedimentation at Escanaba Trough: Geophysical results, *in* Morton, J.L., Zierenberg, R.A., and Reiss, C.A., eds., Geologic, hydrothermal, and biologic studies at Escanaba Trough, Gorda Ridge, offshore northern California: U.S. Geological Survey Bulletin 2022, chapter 2 (this volume).

Nobes, D.C., Villinger, H., Davis, E.E., and Law, L.K., 1986, Estimation of marine sediment bulk physical properties at depth from seafloor geophysical measurements: Journal of Geophysical Research, v. 91, p. 14,033–14,043.

Normark, W.R., Gutmacher, C.E., Zierenberg, R.A., Wong, F.L., and Rosenbauer, R.J., Sediment fill of Escanaba Trough, *in* Morton, J.L., Zierenberg, R.A., and Reiss, C.A., eds., Geologic, hydrothermal, and biologic studies at Escanaba Trough, Gorda Ridge, offshore northern California: U.S. Geological Survey Bulletin 2022, chapter 6 (this volume).

Pardee, J.T., 1942, Unusual currents in Glacial Lake Missoula, Montana: Geological Society of America Bulletin, v. 53, p. 1569–1600.

Riddihough, R.P., 1980, Gorda plate motions from magnetic anomaly analysis: Earth and Planetary Science Letters, v. 51, p. 163–170.

Schultz, A., Delaney, J.R., and McDuff, R.E., 1990, Extended observations of ridge crest hydrothermal systems: Heat flux and related quantities [abs.]: Eos, Transactions American Geophysical Union, v. 71, p. 1619.

Vallier, T.L., Harold, P.J., and Girdley, W.A., 1973, Provenances and dispersal patterns of turbidite sand in Escanaba Trough, northeastern Pacific Ocean: Marine Geology, v. 15, p. 67–87.

Villinger, H., and Davis, E.E., 1984, Heat flow and bottom water temperature measurements from the rift valley of the northern Juan de Fuca Ridge [abs.]: Eos, Transactions American Geophysical Union, v. 65, p. 1111.

———1987, A new reduction algorithm for marine heat flow measurements: Journal of Geophysical Research, v. 92, p. 12,846–12,856.

Von Herzen, R.P., and Uyeda, S., 1963, Heat flow through the eastern Pacific Ocean floor: Journal of Geophysical Research, v. 68, p. 4219–4250.

Wang, K., and Davis, E.E., 1992, Thermal effects of marine sedimentation in hydrothermally active areas: Geophysical Journal International, v. 110, p. 70–78.

Williams, D., Becker, K., Lawver, L., and Von Herzen, R., 1979, Heat flow at the spreading centers of the Guaymas Basin, Gulf of California: Journal of Geophysical Research, v. 84, p. 6757–6769.

Zierenberg, R.A., Morton, J.L., Koski, R.A., and Ross, S.L., Geologic setting of massive sulfide mineralization in the Escanaba Trough, *in* Morton, J.L., Zierenberg, R.A., and Reiss, C.A., eds., Geologic, hydrothermal, and biologic studies at Escanaba Trough, Gorda Ridge, offshore northern California: U.S. Geological Survey Bulletin 2022, chapter 10 (this volume).

Chapter 4. A Thermal and Mechanical Model for Sediment Hills and Associated Sulfide Deposits along Escanaba Trough

By Roger P. Denlinger *and* Mark L. Holmes[1]

CONTENTS

ABSTRACT

The flat valley floor of Escanaba Trough contains a series of mesalike sediment hills that are flanked in places by basalt flows. Geologic and geophysical observations show that massive sulfide deposits are common near the base of these sediment hills, but they have not been found on the gently rounded tops. Submersible observations indicate that the hydrothermal deposits consist of elongate mounds that occur around the flanks of the sediment hills. The geochemistry of hydrothermal fluids and sulfide deposits requires extensive circulation of the hydrothermal fluids through sediments.

We combine these data with the physical properties of basalt and sediment to develop a quantitative model for localized hydrothermal circulation along faults associated with sediment hill growth. Uplifted sediment hills are modeled as the surface expression of a thin basalt laccolith intruded along the basalt-sediment interface about 400 to 600 m below the sea floor.

Laboratory experiments and theoretical analyses suggest that inflation of each laccolith uplifted and bent the overlying sediments, generating thrust faults that curve outward as they approach the surface. In this way each laccolith lifts and dilates the surface material, leading to the development of normal faults that break initially at the surface and propagate downward. With continued uplift these normal faults eventually supersede the thrust faults and form a horst structure.

Cooling of each laccolith occurs both through conduction and through fluid convection along these fault zones. Using simple assumptions about the interaction of basalt and seawater, we calculate the rate of heat loss with time for the life of the hydrothermal system. If the fault zones described above are more permeable than the surrounding sediment, then convection of fluid up these fault zones controls the rate of heat loss from each laccolith for 90 percent of its cooling history.

For a fault zone 2 meters wide with a permeability of 10^{-13} m^2, a laccolith forming a typical sediment hill in the Escanaba Trough (70 m high, 1,200 m in diameter) will cool completely in less than 500 years. If mineral precipitation reduces this permeability to 10^{-14} m^2 and the effective fault zone thickness to 1 m, then the cooling time is extended to 23,200 years, and more heat is lost to the subsurface sediments than is delivered to the sea floor. A more accurate estimate of cooling will require detailed information on the permeability and thickness of each fault zone.

INTRODUCTION

Gorda Ridge is an actively spreading mid-ocean rift system that is close to the western margin of North America. The southern 100-km segment of this rift system, Escanaba Trough, receives turbidites from the continental shelf and slope (Vallier and others, 1973; Normark and others, chap. 6, this volume). Regional geologic and geophysical studies of the trough have been studied to assess the geologic setting (Zierenberg and others, chap. 10, this volume), petrology (Clague and Holmes, 1987; Davis and others, chap. 9, this volume), heat flow (Abbott and others, 1986; Davis and Becker, chap. 3, this volume), association of massive sulfides with centers of volcanic intrusion along axis (Morton and others, 1987), hydrothermal mineralogy (Koski and others, 1988; chap. 16, this volume), and sediment stratigraphy to estimate age relationships (Karlin and Lyle, 1986; Karlin and Zierenberg, chap. 7, this volume; Normark and others, chap. 6, this volume).

[1] U.S. Geological Survey, Seattle, Washington.

These studies show that the volcanic products of rifting are confined to discrete centers (Morton and Fox, chap. 2, this volume). Mesalike sediment hills that are flanked by basalt flows are common along axis, and have been studied in both the northern part of the trough (NESCA area) and the southern part of the trough (SESCA area). A cross section of a typical sediment hill, from detailed Sea Beam bathymetry (Morton and Fox, chap. 2, this volume), is shown in figure 4.1 along with an interpretive cross section based on the study described below.

The detailed Sea Beam data show that the sediment hills in Escanaba Trough typically have about 70 m of relief, and seismic profiles show that they rest on a sedimentary layer 400 to 600 m thick (Morton and others, 1987; Morton and Fox, chap. 2, this volume). Vents that fed basalt flows surrounding the sediment hills penetrated this sediment thickness in NESCA and SESCA, and these lava flows locally lap up against the sediment hills to form a complicated surface topography (Holmes and Zierenberg, 1990; Ross and Zierenberg, chap. 8, this volume). Submersible observations (Holmes and Zierenberg, 1990) and camera tows (Morton and others, 1990; Zierenberg and others, chap. 10, this volume) show that steep fault scarps on the flanks of the sediment hills typically expose layered sediments and that massive sulfide deposits occur near the base of these escarpments.

Preliminary models for these sediment hills proposed that the hills were underlain at shallow depth by volcanic rock (Morton and others, 1990) in order to explain a lack of layering in seismic records and an association of sediment hills with sulfide deposits. Subsequent submersible observations of the sediment hills showed that they were formed by uplift, and that no basalt is exposed along the steep flanks (Holmes and Zierenberg, 1990). Massive sulfide deposits were observed near the base of the hills, but do not occur on the tops of the sediment hills. This information, along with in situ measurements of permeability of basalt and sediment (Touloukian and others, 1981) and the results of chemical studies of the sulfide minerals (Koski and others, 1988), is used to constrain geophysical models of sill emplacement and cooling by hydrothermal circulation.

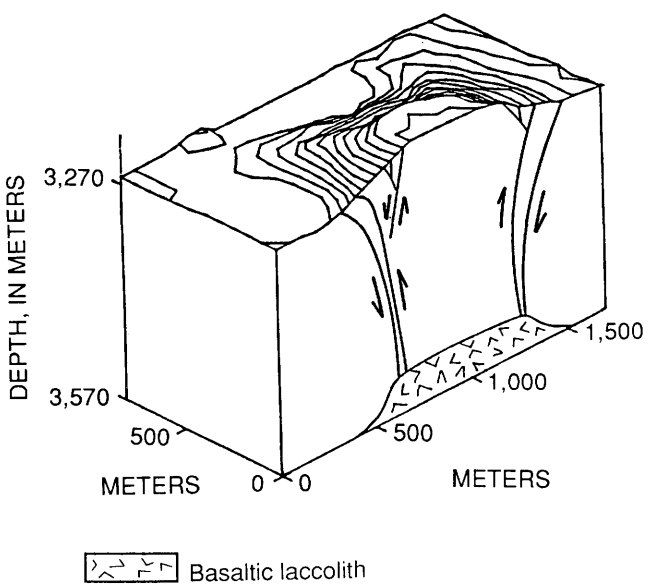

Figure 4.1. Perspective view of typical sediment hill in SESCA, illustrating geometry and scale of these hills as well as location of hydrothermal deposits to the inferred structure. Arrows indicate relative direction of movement along fault.

This chapter develops and evaluates models for the structure and geothermal circulation associated with sediment hills in Escanaba Trough. Using geologic and geophysical information on this area as a guide, we employ the results of theoretical and experimental studies of fluid convection in porous media to eliminate several possible models for the sediment hills. Then we develop a simple mechanical and thermal model of an idealized sediment hill. Our mechanical model is a model for the growth of each hill and identifies permeable pathways for fluid flow, whereas our thermal model provides an estimate of the basic time scales in the hydrothermal flow producing the sulfide deposits on the flanks of each sediment hill. These results may be compared to cooling estimates for sills in the Guaymas Basin (Einsele and others, 1980; Lonsdale and Lawver, 1980; Becker and Fisher, 1991) for a similar boundary-value problem. More refined studies are possible with numerical methods (for example, Norton and Knight, 1977) but are not warranted until more information is available on the physical properties of the sediment and the heat sources. The structure we predict may be tested by drilling, and estimates of the lifetime of each geothermal system may be refined using measurements of the permeability of the sediment.

ACKNOWLEDGMENTS

Reviews by George Bergantz, John Sass, Jan Morton, and Rob Zierenberg tightened and helped focus our arguments.

GEOLOGIC AND GEOPHYSICAL CONSTRAINTS

The surface morphology observed in Sea Beam studies (Morton and Fox, chap. 2, this volume) combined with the submersible observations (Holmes and Zierenberg, 1990; Zierenberg and others, chap. 10, this volume) show that the sediment hills are uplifted sections of the sediment fill that predate the surface volcanic activity (Morton and Fox, chap. 2, this volume). Sulfides are absent from the gently rounded tops of these hills (Zierenberg and others, chap. 10, this volume) but are common on the flanks and in a few places on the flat valley floor. These observations

motivated the development of a model for uplift of the sediment section that produces structural conduits for upward flow of hydrothermal fluids during the uplift process. These structural channels may intersect stratigraphic zones of higher permeability (Morton and Fox, chap. 2, this volume), further complicating the subsurface distribution of sulfides.

Submersible observations also provide temperature measurements from active hydrothermal vents in NESCA and qualitative assessments of deposit age in both NESCA and SESCA. The most eroded and apparently oldest deposits are in SESCA and are confined to the flanks of the sediment hills (Holmes and Zierenberg, 1990; Zierenberg and others, chap. 10, this volume). The deposits at NESCA appear fresher and are also confined to the sediment hill flanks; active venting was found on the northwest and southeast flank of the Central Hill. Temperatures of vent fluid at this location range up to 220°C (Campbell and others, chap. 11, this volume). Assuming a fluid velocity of 8×10^{-6} m/s (appropriate for our fault zone model), diffuse flow produces a surface heat flow of 7,000 W/m^2. This is much larger than the conductive heat flow of 2 to 3 W/m^2 measured near this location by Abbott and others (1986) and Davis and Becker (chap. 3, this volume).

In situ measurements of the intrinsic permeability of fractured subaerial basalt and of various sediments (table 4.1) show that the permeability of basalt is typically greater by three to five orders of magnitude. If comparable differences are realized in Escanaba Trough, then basalt is the preferred conduit for circulation where it is surrounded by sediment, particularly if it is the heat source driving the circulation.

Two important constraints on our models are that hydrothermal fluid must circulate through a large volume of sediments to produce the hydrothermal fluid chemistry (Campbell and others, chap. 11, this volume) and the sulfide deposit chemistry (Koski and others, 1988; Koski and others, chap. 16, this volume), and that sulfide deposits only occur on the flanks of the hills. Extensive circulation of hydrothermal fluids through sediments is possible above an intrusion through the development of Bernard convection cells (Hsu and others, 1978), but this type of convection would concentrate surface sulfide deposits near the top of each hill. For these reasons we constructed a model in which there is strong structural control of permeability. In this model fluid circulates through a thick section of sediments along the same fault structure that formed with the uplift of each sediment hill (fig. 4.2). A likely cause for the uplift is the inflation of a basaltic sill intruded along the basalt-sediment interface several hundred meters or more below the sea floor.

The possible mechanisms for the creation of the sediment hills can be examined with laboratory and theoretical studies of sediment deformation as well as hydrothermal circulation. These studies are used here to define a basic geologic and hydrologic model for the sediment hills in Escanaba Trough. We assume that the deformation and structure is the governing influence on permeability and flow, and so structure is discussed first.

Table 4.1. Physical properties of sediment and basalt and parameters of hydrothermal model.

Property	Value
Permeability[a] (m^2)	
Oahu basalt	10^{-10}
Snake River Plain basalt	10^{-10}
Altered pyroclastics, Wairakei, NZ	10^{-16}
Fractured graywacke	4.5×10^{-14}
Fractured shale	3.5×10^{-13}
Density (kg/m^3)	
Basalt	3,000
Escanaba Trough sediment[b]	1,600
Thermal conductivity (W/m°C)	
Basalt	1.25
Escanaba Trough sediment[c]	0.88
Thermal diffusivity (m^2/s)	
Basalt	0.5×10^{-6}
Escanaba Trough sediment	0.5×10^{-6}
Specific heat at constant pressure (J/g·°C)	
Basalt	1.1
Escanaba Trough sediment[d]	1.2
Seawater	4.5
Initial temperature of laccolith (°C)	1,200
Latent heat of basalt[e] (J/kg)	4.18×10^5
Dynamic viscosity of seawater[f] (g/m·s)	8.7×10^{-2}

[a]Field tests; average values.
[b]Assumed saturated bulk density.
[c]Abbott and others, 1986.
[d]Estimated from siltstone.
[e]Approximate combined heat of solidification.
[f]Estimated from pure water at 315°C and 137 bars.

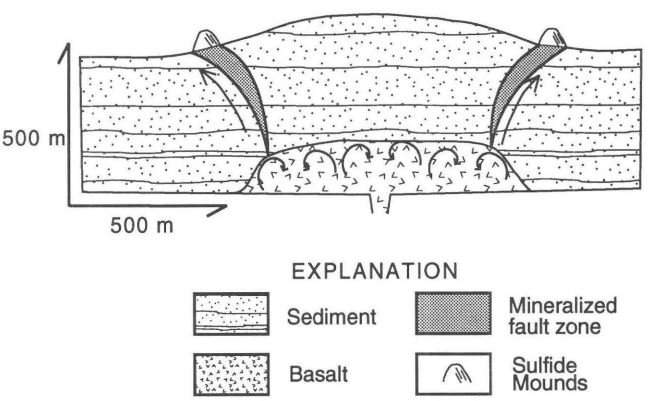

Figure 4.2. Simplified geologic model for sediment hills in NESCA and SESCA, showing circulation patterns (arrows).

A MECHANICAL MODEL FOR GROWTH OF THE SEDIMENT HILLS

The data and analyses described above require that near-surface upflow occurs along the steep flanks of the sediment hills. The simplest model that explains this pattern isolates fluid flow along faults that result from the deformation creating the sediment hill. Such a model is supported by laboratory and theoretical studies.

Laboratory sandbox experiments of vertical uplift of a block into a thick layer of sediments (fig. 4.3*A*; Mandl, 1988) show that curved thrust faults form as precursors to

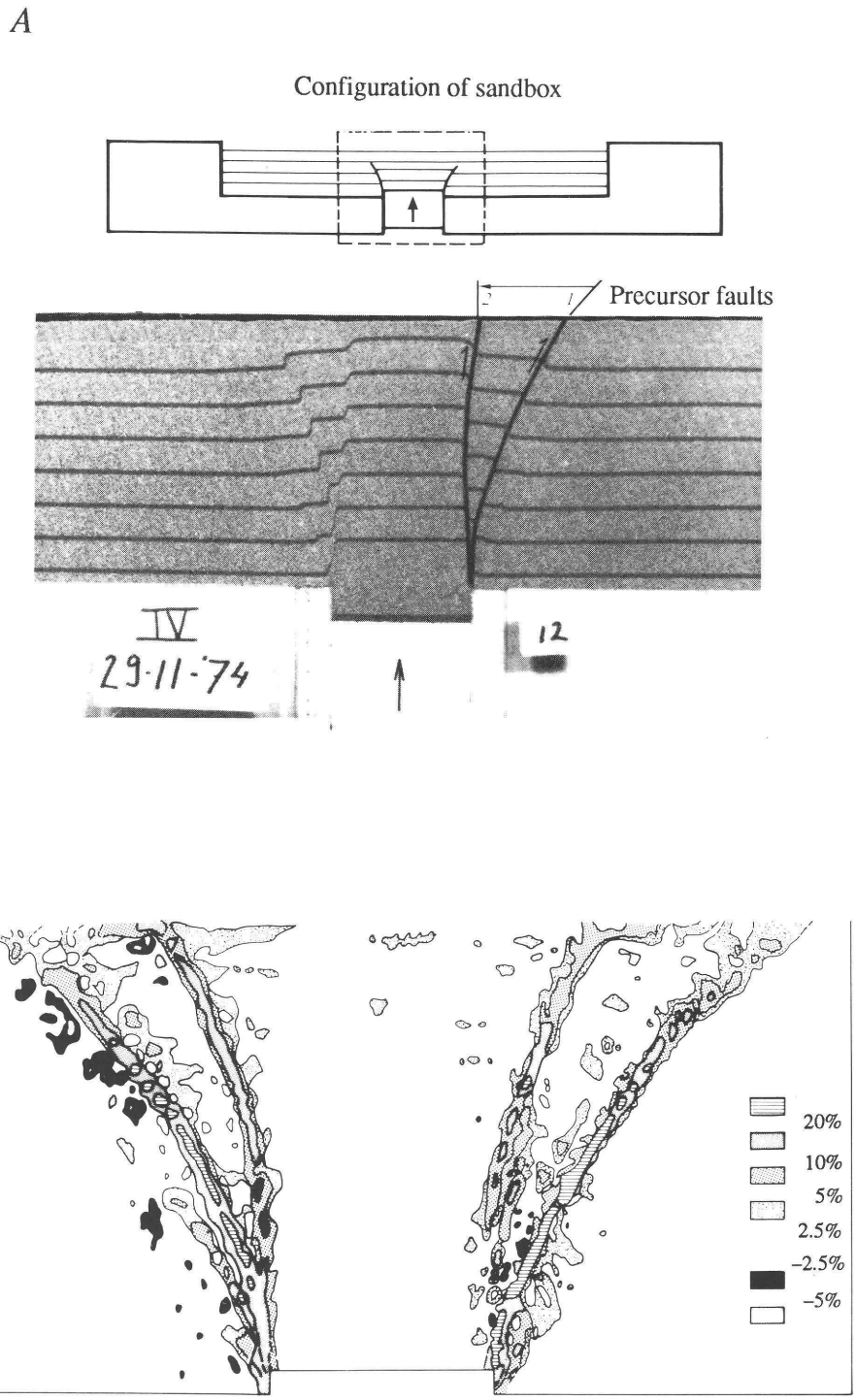

Figure 4.3. *A,* Sandbox model (Walters and Thomas, 1982) for sediment hills in NESCA and SESCA where uplift is presumed to be due to inflation of a sill. *B,* Stereophotogrammetric determination of change in porosity along faults formed during uplift of model in *A* (Mandl, 1988, p. 74).

the final, nearly vertical fault that accommodates uplift. These thrust faults start from the base and grow in imbricate fashion, each successive fault steeper than its predecessor until the final vertical fault is formed. Shear-induced dilation of the sediment produces high-porosity (and presumably high-permeability) channels along the fault zones, as shown in figure 4.3*B* (Mandl, 1988).

Theoretical studies of this problem for plane strain conditions require incremental solutions of the highly nonlinear equations governing sediment behavior during inelastic deformation. This was first done by Walters and Thomas (1982) for an idealized conical yield surface and plane strain conditions. Extensions of this work to the Coulomb surface governing the behavior and stress-strain laws for sand have been made by Denlinger (unpublished work). These studies show that dilatancy of the sediment under shear is required for structural high-porosity channels to develop during uplift and that the pattern of deformation in figure 4.3 (Mandl, 1988) also applies to axisymmetric uplifts. Furthermore, the first channels to develop, those likely to carry the hottest effluent, curve away from the uplifting block of sediment and end partway into the adjacent sedimentary section. These precursor faults are the most likely candidates to pipe hydrothermal fluids into stratigraphic layers with high permeability.

As the thrust faults approach the surface, the upward doming and spreading of the surface material is accommodated by internal dilation of the sediment hill. The subsequent development of normal faults along the flanks modifies the shape of the sediment uplifted above the sea floor.

A MODEL FOR HYDROTHERMAL CIRCULATION

The faults that give shape to the uplifted sediment hill may be more permeable pathways for hydrothermal fluids than the surrounding sediments, thereby providing a simple mechanism for the production of sediment hills with sulfide deposits on their flanks.

Without such a permeable channel, the theoretical circulation pattern in homogeneous sediment should consist of convection cells within the sediment and centered over the heat source. This conclusion is inferred from theoretical studies of the cooling of intrusions (Norton and Knight, 1977) and from theoretical and experimental studies of the convection in porous media over a heated plate (Hsu and others, 1978). These studies support the interpretation that upflow of the highest temperature fluid in an unfaulted, uniform layer of sediment would be centered over the cooling intrusion. Presumably such a circulation pattern would produce sulfide deposits near the top of the sediment hills.

We assume here that the creation of fault zones flanking the uplift creates permeable pathways for convection that inhibits the development of a high-temperature plume centered over the intrusion. Instead, high-temperature flow is preferentially channeled along these flanking fault zones to produce sulfide deposits on the flanks of the uplifted sediment hills (fig. 4.4).

After initial intrusion, the sill inflates to form a laccolith that is 75 to 100 m thick. This is the magnitude of uplift required at the base of a 500-m-thick layer of sediment in order to produce a 75-m-high sediment hill on the sea floor, depending upon cohesion in the sediment. Dewatering of the sediment is not considered here. The water depth is only relevant to the amount of work done in inflating the sill and does not affect the mechanics of sediment deformation.

We infer from the lack of continuity of the surface basalt flows that a similar distribution of basalt flows is interlayered in the sediment cover and prevents these flows from serving as primary pathways for hydrothermal cooling. Instead, we postulate that fluids circulate through a fault system created by bending and uplift of the sediment cover, and that these fluids convectively cool the basalt laccolith that caused the uplift.

The magnitude of fluid circulation depends upon the mechanisms controlling the cooling of the basalt. Based on theoretical studies of magma-water interaction (Delaney, 1982; Hardee, 1980), experimental studies of seawater (Bischoff and Rosenbauer, 1985), and field studies of magma intrusion into soft, water-saturated sediment (Kokelaar, 1982), we assume that there are three stages of cooling. These are (fig. 4.5): (1) an initial stage of porewater pressurization due to rapid heating; (2) a secondary stage during which (a) high-temperature phase separation of the seawater occurs at the boundaries of the basalt intrusion, (b) thermal cracking allows penetration of two-phase fluid (steam and water) until solidification is

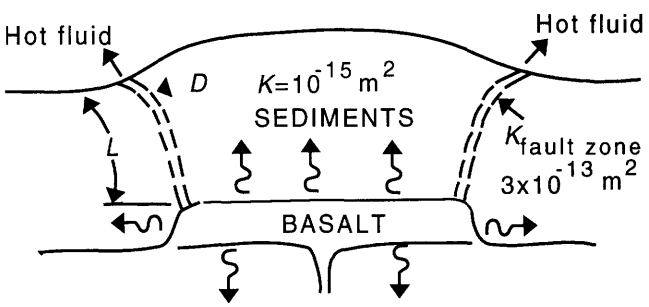

Figure 4.4. Idealized cooling model used to obtain rate of cooling of sediment-covered basalt laccolith: conductive cooling occurs from all sides, and seawater heated by laccolith flows up fault zone that is one to two orders of magnitude more permeable than surrounding sediments. Abbreviations: *L*, length of fault zone; *D*, width of fault zone; *K*, permeability.

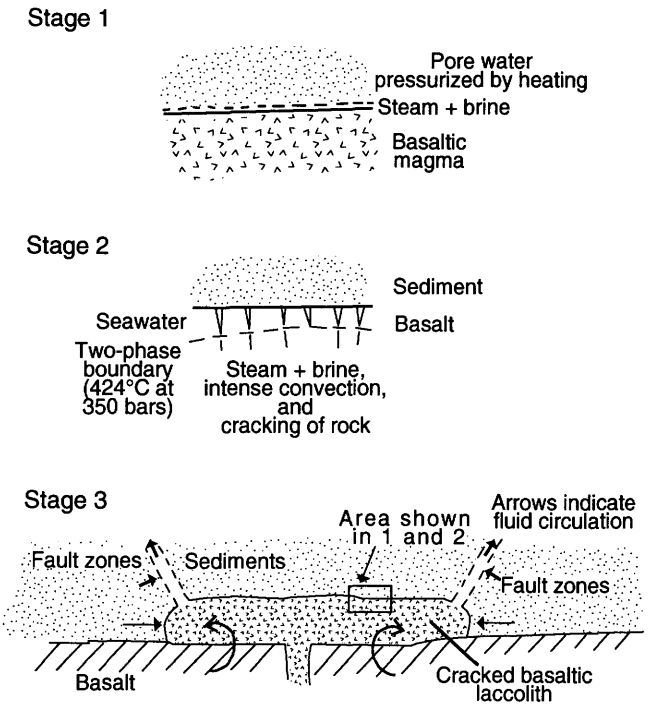

Figure 4.5. Three stages of cooling for a sediment-covered basaltic laccolith (discussed in text). Most cooling occurs as a two-phase mixture of seawater invades cracks in cooling laccolith. Heat loss is controlled by mechanisms of heat transport away from intrusion.

complete, and (c) fluid convection decreases the average rock temperature to the temperature at the two-phase boundary of seawater; and (3) a tertiary stage during which seawater convection through the hot, fractured basalt cools it to ambient temperatures. The heat loss from the basalt is ignored for the first stage, which is short lived (Delaney, 1982), and is estimated for the next two stages.

THE SECOND STAGE OF COOLING

The actual mechanisms of cracking and water penetration during the second stage of cooling are complicated by the thermodynamic properties of seawater at 350 bars, the pressure at the assumed depth of the base of the sediment section at 3,500 m water depth. An equation of state for seawater is presented by Bischoff and Rosenbauer (1985), but a quantitative model for hot basalt-seawater interaction does not exist due to its thermodynamic and mechanical complexity.

For the purposes of this report, we simply assume that a surface separating single-phase and two-phase fluid encases the basalt and is held at 424°C, the temperature of two-phase separation at 350 bars (Bischoff and Rosenbauer, 1985). We assume here that the heat flux across this interface is controlled by the conductive and radiative processes that transport heat from within the basalt to this surface, with convection as the primary process outside the surface. This assumption is supported by studies of heat loss from basaltic lava lakes (Hardee, 1980) and active lava domes (Dzurisin and others, 1990). The position and movement of this surface depends upon the balance of this flux with that due to processes on the hot basalt side, as shown in figure 4.5, and a detailed analysis of these processes is beyond the scope of this paper.

The heat-loss calculations assume that the basalt is wrapped in an envelope defined by a surface at constant temperature, the two-phase boundary of seawater. Hydrothermal circulation may develop above the platelike intrusion as well as along the faults flanking the uplift. Eventually enough heat is lost from the basalt to lower its temperature to the point where seawater can circulate through the basalt without phase separation.

The presence of the two-phase boundary layer prevents convective cooling of the sill during stage 2, so that all of the heat loss is by conduction and radiation. Radiative losses are neglected below a basalt temperature of 900°C. Conductive heat losses during the second stage of cooling are calculated assuming a constant temperature boundary at the two-phase separation temperature of 424°C. The conductive component of the basalt surface heat flux decreases as the square root of time (Carslaw and Jaeger, 1959) according to

$$q = \frac{kT_s}{\sqrt{\pi \alpha t}} \qquad (1)$$

where

q is the heat flux per unit area,
T_s is the surface temperature,
k is the sediment thermal conductivity,
α is the sediment thermal diffusivity, and
t is time.

The initial heat flux is calculated assuming that the basalt laccolith is emplaced instantaneously, and a 2-mm-thick layer of steam plus brine develops in 1 second over the outer surface as it contacts sediment saturated with seawater. This assumed envelope thickness and timing for development is comparable to the envelope observed to develop on cooling pillow basalts (Moore, 1975). The enthalpy change for high-pressure boiling of a synthetic 3 percent NaCl water solution (Dave Butterfield, written commun., 1989) was used to estimate the enthalpy change for seawater as it forms a high-density brine film. The variation in depth over a 70-m-thick sill would produce a temperature difference for the phase transition of 4°C and is neglected here. The volume of seawater, timing, surface area of the sill, and the enthalpy change give the initial estimate for heat flux shown in table 4.2 for a constant temperature interface. The conductive heat flux then decreases according to equation 1 as shown in table 4.2 and figure 4.6, becoming less than the convective flux in about 5 years with the assumptions of fault-zone thickness and permeability used in the model.

Table 4.2. Dimensions, energy loss, and rates of energy loss for model laccolith.

Dimensions of typical disc-shaped laccolith[1]:
radius = 600 m, thickness = 75 m
Model fault zone controlling cooling:
2 m thick; permeability 3×10^{-13} m^2
Stages of cooling:
First stage, groundwater pressurization; energy loss, 0 J; duration, seconds to minutes.
Second stage, two-phase separation of seawater with enhanced convection and thermal cracking of basalt; energy loss, 0.8×10^{17}J; duration, 44 years; 34 million cubic meters of seawater circulated.
Third stage, single-phase convection within fractured laccolith; energy loss, 0.3×10^{17}J; duration, 200 years; 15 million cubic meters of seawater circulated.

Cooling history:

Time since intrusion	Conductive heat flux (10^6W)	Convective fault heat flux (10^6W)
1 second	380,000	0
5 days	578	<33
1 month	236	<33
6 months	96	33
1 year	68	33
2 years	48	33
5 years	30	33
8 years	24	33
50 years	10	33
60 years	9	19
70 years	8	12.5
90 years	7	7.3
110 years	6.5	5.0
130 years	5.9	3.6
150 years	5.5	2.8
250 years	4.2	1.3
300 years	4	—

[1]Determined from mechanical modeling of sediment hill structures in Escanaba Trough.

The convective heat flux due to fluid circulation has two components, as shown in figure 4.4. One component is due to fluid flow developed as hot fluid rises over the hot upper surface of the intrusion and draws cooler fluid in behind it. This problem has been analyzed by Hsu and others (1978). Using Hsu's model, the maximum thickness of the thermal boundary layer that develops due to penetrating flow is about 270 m with the parameters given in table 4.1. If these are representative of the conditions in Escanaba Trough, then a convection cell of hydrothermal fluid developed over a sill along the basalt-sediment interface will not penetrate the 400 to 600 m of sediment cover to reach the sea floor.

Development of such a convection cell of hot water would be subdued or prevented by fluid circulation up more permeable fault zones flanking the intrusion as shown in figure 4.4. In such a case, the rise of hydrothermal fluids along the fault zones would occur more easily than through undisturbed sediments, and would rob any centrally located hot plume of the fluid it needs to rise to the surface.

Fluid flow up the fault zones is driven by a pressure gradient that is a result of the average density difference between fluid in the fault zone and cold seawater. This density difference can be calculated from the temperature difference between hot and cold seawater and the equation of state of seawater (Bischoff and Rosenbauer, 1985). Flow is calculated assuming Darcy's law,

$$v = \frac{K}{\mu}\,\Delta\rho_w g \qquad \Delta\rho_w = \rho_{0°C} - \rho_T \qquad (2)$$

where

v is velocity,
K is permeability,
μ is the dynamic viscosity, and
$\Delta\rho_w g$ is the pressure gradient driving the flow.

The viscosity is expected to vary exponentially with temperature, but this effect is neglected here. Qualitatively, the inclusion of the viscosity change would enhance the driving force for convection up the faults. If the permeability is at least an order of magnitude greater than the surrounding sediments, then fluid flow up the fault zone is a very efficient means of heat loss (table 4.2). Coupling of the flow and temperature fields occurs since heat losses from the fault zone during flow affect the temperature differences, and hence the density differences driving flow.

We attacked this problem by first assuming an average temperature for the conduit fluid, using its density at this temperature to calculate a velocity (v) from equation

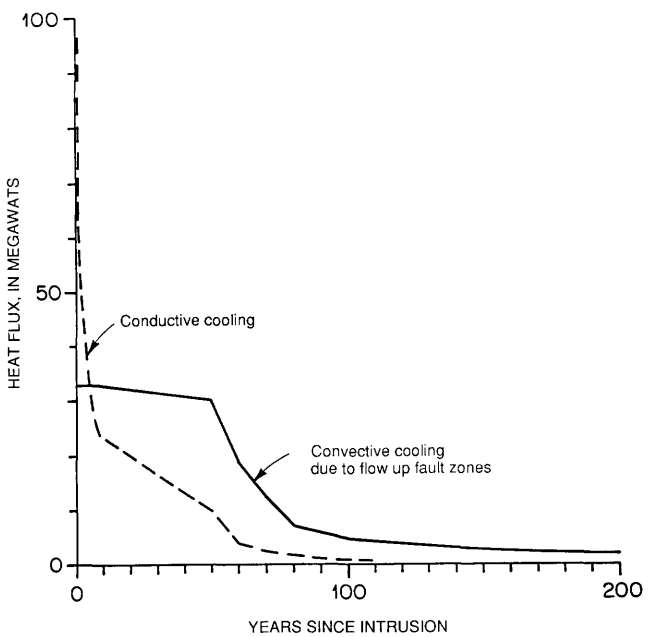

Figure 4.6. Estimated conductive heat flux from intrusion and convective flux due to flow along fault zone. Curves derived from idealized geometry in figure 4.4 as described in text. Model has one-fourth the volume of a typical intrusion, so flux expected from typical Escanaba Trough intrusion is about twice these values, and total heat loss about four times greater.

2. From the velocity we calculated the transit time (t_D) for a 300-m-long fault zone and the duration of flow using the heat-balance equation

$$t_D = \frac{\Delta E}{\rho_w C_w v(2\pi RD)T_w} \quad (3)$$

where

ΔE is the total stored energy that must be removed to drop the temperature of the laccolith to 424°C

C_w is specific heat of fluid,

T_w is average temperature of fluid, and

$v(2\pi RD)$ is the flux from the side of the intrusion with flank area in parentheses (R is the radius and D is the height).

Here duration of flow for stage two is assumed equal to the time required to decrease the temperature of this body from 1,200°C to 424°C (when two-phase separation ceases). The energy loss required to do this is given by

$$\Delta E = \rho_r V_r [L + C_r(1{,}200° - 424°)] \quad (4)$$

where

L is the latent heat of solidification estimated for basalt,

C_r is the specific heat of basalt at constant pressure,

ρ_r is the basalt density, and

V_r is the volume of basalt (see table 4.1).

The average temperature ($\overline{T}$) of the fluid in the conduit may be written, assuming a conductive heat loss from the sides, as

$$\overline{T} = \frac{T_i - qt_r}{\rho_w C_w D} \quad (5)$$

where the heat flux q is

$$\frac{k\overline{T}}{\sqrt{\pi\alpha t_D}} \quad (6)$$

The parameters are defined in table 4.1. Equation 5 gives a relationship between the transit time t_r, the duration of flow t_D (through q in equation 6), and the average fluid temperature $\overline{T}$ in terms of the initial fluid temperature. From the duration of flow and transit time, an average temperature was determined and the procedure above redone until the process converged on a solution.

The solution we obtain for a 2-m-wide fault zone that is 260 m long (estimated from the mechanical models in figure 4.3; Mandl, 1988) and has a permeability of 3×10^{-13} m^2, with an initial temperature of 424°C, is an average temperature of 330°C and a surface temperature of 239°C. This compares well with measured vent temperatures at NESCA of 220°C and temperatures estimated for the copper-rich sulfide assemblages in excess of 300°C to 330°C. The model gives an average flow velocity of 7.5×10^{-6} m/s. For these conditions, fluid convection up the fault zone takes a few days to develop (table 4.2), and it takes about 400 days for a given parcel of fluid to travel from the laccolith to the sea floor. The total convective heat loss from the sill is expected to be approximately constant because of two-phase separation of seawater within the basalt, and with these conditions our second stage lasts about 45 years.

The amount of water circulated during stage two may be calculated either from the duration of flow or from an energy balance for the intrusion. Correcting for the conductive heat loss, the energy balance gives 34 million cubic meters of seawater. The duration of flow approach overestimates this volume because steady flow was assumed to start immediately, and gives 39 million cubic meters of seawater. The energy balance is more accurate and closer to the true value.

THE THIRD STAGE OF COOLING

We define the third stage of cooling as the stage when sill solidification is complete and seawater can circulate through the basalt without a phase separation. Stage three heat loss is calculated assuming that the basalt is much more permeable than the surrounding sediment or sediment fault zones. The three- to four-order-of-magnitude contrast in permeability between basalt and relatively impermeable sediment simplifies the calculation of heat loss. The entire laccolith is assumed to be at a temperature below 424°C and is cooled by circulation of seawater through cracks in the sill developed in stage two.

To calculate the rate and amount of cooling, we assume that heat is distributed much more efficiently by flow within fractures in the laccolith than it can be carried away by flow up the fault zone. This assumption is supported by measurements that show that (in situ) basalt is typically orders of magnitude more permeable than sediments (Touloukian and others, 1981; see table 4.1). With this condition,

$$\rho_r C_r V_r \frac{\partial T}{\partial t} = \rho_w C_w v_w (2\pi RD)T \quad (7)$$

where the left-hand side is the change in the internal energy of the basalt and the right-hand side is the heat flux up the fault zone. Since by Darcy's law

$$v_w = \frac{K}{\mu} g(\rho_{0°C} - \rho_T) = \frac{K}{\mu} \Delta\rho_w g \quad (8)$$

then the change in temperature of the basalt may be written

$$\frac{1}{\rho\Delta\rho}\frac{dT}{T} = \frac{C_w}{C_r}\frac{1}{\rho_r}\frac{2\pi RD}{V_r}\frac{Kg}{\mu}\,dt \quad (9)$$

where $\rho_w\Delta\rho_w$ is written as $\rho\Delta\rho$.

An expression is needed for $\rho\Delta\rho T$ as a function of temperature. Values for density as a function of temperature at a mean pressure of 330 bars were obtained from Bischoff and Rosenbauer (1985), and $\rho\Delta\rho T$ was calculated and

plotted versus temperature. A function was fit to the resulting curve to obtain

$$\rho\Delta\rho T = (1.05 \times 10^4) \times T^{3.6} \quad (10)$$

Using this expression in equation 9 and integrating,

$$T = \frac{693\text{K}}{(t/\tau+1)^{0.38}} \quad (11)$$

where

$$\tau = 39 \text{ years} \times \frac{K}{10^{-13}\text{m}^2} \quad \frac{D}{1 \text{ meter}} \quad (12)$$

The rate of heat loss is

$$\frac{dQ}{dt} = C_w (2\pi RD)\frac{Kg}{\mu} = \frac{16.5 \ \frac{D}{1 \text{ meter}}}{\left(\frac{t}{\tau}+1\right)^{1.38}} \text{ megawatts} \quad (13)$$

per meter of fault zone width.

The parameters in table 4.1 were used in equations 11 and 12 above to give the asymptotically decaying portion of the convection curve in figure 4.6 for a fault zone 2 m wide. The uncertainty in both the width of the fault zone and the permeability of the fault zone is large, and both have a direct effect on these lifetime estimates. For example, a fault zone 1 m wide with a permeability of 10^{-14} m^2 would sustain a hydrothermal system 20 times longer than is estimated here, extending the lifetime from 290 years to 5,800 years.

The conductive heat loss continues to decline with the inverse square root of time since intrusion, and after a few decades convection of hot fluid up the fault zones is the primary source of heat loss and controls the rate of cooling.

The flow of hot fluids up the fault zones could produce sulfide deposits around the steep flanks of the sediment hills, with some leakage also probable along the stepped normal faults that form the break in slope. Each parcel of fluid would be in contact with the sediment for at least a year in transit, at an average temperature of 330°C, whereas the same fluid would be in contact with basalt less than one-fourth this time.

The total amount of fluid required to cool our model laccolith (600 m across and 75 m thick) from 1,200°C to 424°C may be calculated from either the flow/duration or an energy balance. The energy-balance method is more accurate and gives 1.1×10^8 m^3 as the volume of seawater circulated during our second stage cooling.

The mechanical models show that the surface expressions of sediment hills are a rough indicator of intrusion diameter. Therefore many intrusions in NESCA and SESCA are as much as 1,200 m across and 75 m thick, and would produce four times the volume of hydrothermal fluids during the second stage of cooling.

The actual distribution of sub-seafloor sulfides would depend upon a precipitation mechanism such as cooling, mixing with seawater, or pH titration by wall rock alteration. It is expected that much of the deposition would be associated with the higher permeability fault structure produced by uplift.

CONCLUSIONS

A combination of geologic and geophysical observations constrain models for the genesis and structure of the sediment hills in Escanaba Trough, an active oceanic rift covered by 400 to 600 m of sediment. Mechanical, chemical, and fluid circulation analyses support the interpretation that the sediment hills are the surface expression of basalt laccoliths with about the same dimensions (diameters of 1 km and thicknesses of 70–100 m). The bending of the sediment overburden as uplift occurs initially generates a set of imbricate thrust faults that curve outward and end in the sedimentary section. These faults carry the hottest effluent and may carry these hydrothermal fluids to permeable stratigraphic horizons within the sedimentary section. With continued uplift these thrust faults are superseded by younger, more steeply dipping faults until a final, vertical fault forms that accommodates all later deformation. The shape of the sediment lifted above the seafloor is modified by normal faulting.

According to our model, both normal and thrust fault structures not only localize the sediment deformation but also guide the upward flow of hot seawater through the sediment to the sea floor. This upward flow, combined with fracturing of the laccoliths during cooling, accelerates the rate of heat loss for most of the cooling history of the laccoliths; for the permeable fault zone in our model, hot fluid flow drains half of the heat energy in the system. The typical lifetime of hydrothermal systems surrounding the sediment hills in Escanaba Trough varies with the permeability within the fault zones created by sediment uplift. For a 2-m-wide fault zone with a permeability of 10^{-13} m^2, the lifetime of hydrothermal circulation associated with a typical sediment hill is expected to be about 1,000 years (four times the 250-year estimate for our model, which is one-fourth the size of a typical intrusion in Escanaba Trough).

The uncertainty in both the width and the permeability of the fault zones is large, and both have a direct effect on these time estimates. For example, if mineral precipitation reduced the effective fault zone width to 1 m, and reduced its permeability to 10^{-14} m^2, then the rate of heat flow to the sea floor would be reduced and spread out over a period that is 20 times longer than is estimated here. This would extend the time required to cool an average laccolith from 1,000 years to 23,200 years.

For fault permeability values in the neighborhood of 10^{-13} m^2 and fault-zone thicknesses of 2 m, about half of the heat loss occurs due to conductive heat flow from the

surface of the intrusion and about half occurs due to convective fluid flow up the fault zones flanking the intrusion. With these parameters, about 34 million cubic meters of seawater is circulated to cool our 24-million-cubic-meter intrusion during the second stage of cooling, and about 15 million cubic meters is circulated during the final stage of cooling. Since our model is one-fourth the size of a typical intrusion in Escanaba Trough, these numbers should be multiplied by 4 for comparison with field studies. If the permeability-thickness product of the fault zones is much less than this, more energy is lost by conduction, more time is required to cool the intrusion, and less water is circulated during the cooling process.

REFERENCES CITED

Abbott, D.H., Morton, J.L., and Holmes, M.L., 1986, Heat flow measurements on a hydrothermally-active, slow spreading ridge: The Escanaba Trough: Geophysical Research Letters, v. 13, p. 678–680.

Becker, K., and Fisher, A.T., 1991, A brief review of heat flow studies in the Guaymas Basin, Gulf of California, *in* Dauphin, J.P., and Simonet, B.R.T., eds., The Gulf and Peninsular Province of the Californias: Tulsa, Oklahoma, American Association of Petroleum Geologists Memoir 47, p. 709–720.

Bischoff, J.L., and Rosenbauer, R.J., 1985, An empirical equation of state for hydrothermal seawater (3.2 percent NaCl): American Journal of Science, v. 285, p. 725–763.

Campbell, A.C., German, C.R., Palmer, M.R., Gamo, T., and Edmond, J.M., Chemistry of hydrothermal fluids from the Escanaba Trough, Gorda Ridge, *in* Morton, J.L., Zierenberg, R.A., and Reiss, C.A., eds., Geologic, hydrothermal, and biologic studies at Escanaba Trough, Gorda Ridge, offshore northern California: U.S. Geological Survey Bulletin 2022, chapter 11 (this volume).

Carslaw, H.S., and Jaeger, J.C., 1959, Conduction of heat in solids (2d ed.): Oxford, Clarendon Press, 510 p.

Clague, D.A., and Holmes, M.L., 1987, Geology, petrology, and mineral potential of the Gorda Ridge, *in* Scholl, D.W., Grantz, A., and Vedder, J.G., eds., Geology and resource potential of the continental margin of western North America and adjacent ocean basin—Beaufort Sea to Baja California: Houston, Circum-Pacific Council of Energy and Mineral Resources, Earth Science Series, v. 6, p. 563–580.

Davis, A.S., Clague, D.A., and Friesen, W.B., Petrology and mineral chemistry of basalt from Escanaba Trough, *in* Morton, J.L., Zierenberg, R.A., and Reiss, C.A., eds., Geologic, hydrothermal, and biologic studies at Escanaba Trough, Gorda Ridge, offshore northern California: U.S. Geological Survey Bulletin 2022, chapter 9 (this volume).

Davis, E.E., and Becker, Keir, Thermal and tectonic structure of the Escanaba Trough: New heat-flow measurements and seismic-reflection profiles, *in* Morton, J.L., Zierenberg, R.A., and Reiss, C.A., eds., Geologic, hydrothermal, and biologic studies at Escanaba Trough, Gorda Ridge, offshore northern California: U.S. Geological Survey Bulletin 2022, chapter 3 (this volume).

Delaney, P.T., 1982, Rapid intrusion of magma into wet rock: Groundwater flow due to pore pressure increases: Journal of Geophysical Research, v. 87, p. 7739–7756.

Dzurisin, Daniel, Denlinger, R.P., and Rosenbaum, J.G., 1990, Cooling rate and thermal structure determined from progressive magnetization of the dacite dome at Mount St. Helens, Washington: Journal of Geophysical Research, v. 95, p. 2763–2780.

Einsele, Gerhardt, Gieskes, J.M., Curray, J., Moore, D.M., Aguayo, Eduardo, Aubry, M.-P., Fornari, Daniel, Guerro, Jose, Kastner, Miriam, Kelts, Kerry, Lyle, Mitchell, Matoba, Yasumochi, Molina-Cruz, Adolfo, Niemitz, Jeffrey, Rueda, Jaime, Saunders, Andrew, Schrader, Hans, Simoneit, Bernd, and Vacquier, Victor, 1980, Intrusion of basaltic sills into highly porous sediments, and resulting hydrothermal activity: Nature, v. 283, p. 441–445.

Hardee, H.C., 1980, Solidification in Kiluaea Iki lava lake: Journal of Volcanology and Geothermal Research, v. 7, p. 211–223.

Holmes, M.L., and Zierenberg, R.A., 1990, Submersible observations in Escanaba Trough, Southern Gorda Ridge, *in* McMurray, G.R., ed., Gorda Ridge: A seafloor spreading center in the United States' Exclusive Economic Zone: New York, Springer-Verlag, p. 92–115.

Hsu, C.T., Cheng, P., and Homsy, G.M., 1978, Instability of free convection flow over a horizontal impermeable surface in a porous medium: International Journal of Heat Transfer, v. 21, p. 1221–1228.

Jaeger, J.C., and Cook, N.G.W., 1979, Fundamentals of rock mechanics (3d ed.): London, Chapman and Hall, 593 p.

Karlin, R., and Lyle, M., 1986, Sediment studies on the Gorda Ridge: Oregon Department of Geology and Mineral Industries Open File Report O-86-19, 76 p.

Karlin, R.E., and Zierenberg, R.A., Sedimentation and neotectonism in the SESCA area, Escanaba Trough, southern Gorda Ridge, *in* Morton, J.L., Zierenberg, R.A., and Reiss, C.A., eds., Geologic, hydrothermal, and biologic studies at Escanaba Trough, Gorda Ridge, offshore northern California: U.S. Geological Survey Bulletin 2022, chapter 7 (this volume).

Kokelaar, B.P., 1982, Fluidization of wet sediments during the emplacement and cooling of various igneous bodies: Journal of the Geological Society of London, v. 139, p. 21–33.

Koski, R.A., Shanks, W.C., III, Bohrson, W.A., and Oscarson, R.L., 1988, The composition of massive sulfide deposits from the sediment-covered floor of Escanaba Trough, Gorda Ridge: Implications for depositional processes: Canadian Mineralogist, v. 26, p. 655–673.

Koski, R.A., Benninger, L.M., Zierenberg, R.A., and Jonasson, I.R., Composition and growth history of hydrothermal deposits in Escanaba Trough, southern Gorda Ridge, *in* Morton, J.L., Zierenberg, R.A., and Reiss, C.A., eds., Geologic, hydrothermal, and biologic studies at Escanaba Trough, Gorda Ridge, offshore northern California: U.S. Geological Survey Bulletin 2022, chapter 16 (this volume).

Lonsdale, P., and Lawver, L.A., 1980, Immature plate boundary zones studied with a submersible in the Gulf of California: Geological Society of America Bulletin, v. 91, p. 555–569.

Mandl, G., 1988, Mechanics of tectonic faulting: Amsterdam, Elsevier, 407 p.

Moore, J.G., 1975, Mechanism of formation of pillow lava: American Scientist, v. 63, p. 269–277.

Morton, J.L., Holmes, M.L., and Koski, R.A., 1987, Volcanism and massive sulfide formation at a sedimented spreading center, Escanaba Trough, Gorda Ridge, northeast Pacific ocean: Geophysical Research Letters, v. 14, p. 769–772.

Morton, J.L., Koski, R.A., Normark, W.R., and Ross, S.L., 1990, Distribution and composition of massive sulfide deposits at Escanaba Trough, southern Gorda Ridge, *in* McMurray, G.R., ed., Gorda Ridge: A seafloor spreading center in the United States' Exclusive Economic Zone: New York, Springer-Verlag, p. 77–92.

Morton, J.L., and Fox, C.G., Structural setting and interaction of volcanism and sedimentation at Escanaba Trough: Geophysical results, *in* Morton, J.L., Zierenberg, R.A., and Reiss, C.A., eds., Geologic, hydrothermal, and biologic studies at Escanaba Trough, Gorda Ridge, offshore northern California: U.S. Geological Survey Bulletin 2022, chapter 2 (this volume).

Normark, W.R., Gutmacher, C.E., Zierenberg, R.A., Wong, F.L., and Rosenbauer, R.J., Sediment fill of Escanaba Trough, *in* Morton, J.L., Zierenberg, R.A., and Reiss, C.A., eds., Geologic, hydrothermal, and biologic studies at Escanaba Trough, Gorda Ridge, offshore northern California: U.S. Geological Survey Bulletin 2022, chapter 6 (this volume).

Norton, D., and Knight, J., 1977, Transport phenomena in hydrothermal systems: Cooling plutons: American Journal of Science, v. 277, p. 937–981.

Ross, S.L., and Zierenberg, R.A., Volcanic geomorphology of the SESCA and NESCA sites, Escanaba Trough, *in* Morton, J.L., Zierenberg, R.A., and Reiss, C.A., eds., Geologic, hydrothermal, and biologic studies at Escanaba Trough, Gorda Ridge, offshore northern California: U.S. Geological Survey Bulletin 2022, chapter 8 (this volume).

Touloukian, Y.S., Judd, W.R., and Roy, R.F., 1981, Physical properties of rocks and minerals: New York, McGraw-Hill/CINDAS Data Series on Material Properties, v. II-2, 548 p.

Vallier, T.L., Harold, P.J., and Girdley, W.A., 1973, Provenances and dispersal patterns of turbidite sand in Escanaba Trough, northeastern Pacific Ocean: Marine Geology, v. 15, p. 67–87.

Walters, J.V., and Thomas, J.N., 1982, Shear zone development in granular materials, *in* Proceedings of the 4th International Conference on Numerical Methods in Geomechanics, Edmonton, p. 263–274.

Zierenberg, R.A., Morton, J.L., Koski, R.A., and Ross, S.L., Geologic setting of massive sulfide mineralization in the Escanaba Trough, *in* Morton, J.L., Zierenberg, R.A., and Reiss, C.A., eds., Geologic, hydrothermal, and biologic studies at Escanaba Trough, Gorda Ridge, offshore northern California: U.S. Geological Survey Bulletin 2022, chapter 10 (this volume).

Chapter 5. Crustal Magnetization and Basement Structure of Escanaba Trough

By Robert E. Karlin[1] *and* Janet L. Morton[2]

CONTENTS

ABSTRACT

Sediment isopach and basement topography maps are derived from single-channel seismic-reflection lines run in 1985 during the R/V *S.P. Lee* cruise L6-85-NC. Crustal magnetization and the geometry of magnetized crustal bodies are estimated using inverse three-dimensional and forward two-dimensional modeling of magnetic data taken on the cruise. Our results indicate that tectonic extension has dominated over volcanic construction in Escanaba Trough during the Brunhes Normal-Polarity Chron (that is, since 730 ka). In the southernmost part of Escanaba Trough, very little volcanism has occurred. Mantle diapirs, as evidenced by igneous intrusions and uplifted sediments, have arisen along the rift valley at discrete locations. In general, magnetic anomaly amplitudes are suppressed where sediment cover is present, probably because of crustal alteration induced by closed-system hydrothermal activity. However, the volcanic edifices do show a magnetic signature, suggesting that alteration is not pervasive. The southern Escanaba Trough contains deep basins in the rift valley, suggesting the absence of recent volcanism. Areal changes in magnetic anomaly and basement topography patterns suggest that northwest-southeast-striking transform faults create discrete tilted blocks. The faulting is at a 30° angle to the active spreading direction, perhaps indicating that the deformation is caused by readjustment of the ridge to be perpendicular to the Mendocino Fracture Zone.

INTRODUCTION

Gorda Ridge is a slow-spreading mid-oceanic ridge located within the U.S. Exclusive Economic Zone off northern California and Oregon. The ridge is unusual in the world's rifting system, because the southern part, called Escanaba Trough, is covered by a thick sequence of sediments derived from glacial weathering of the American continent during the Pleistocene. The thermal regime and crustal formation processes at such a sediment-covered spreading center are significantly different from those found on normal open, unsedimented ridges. The sediments form a semipermeable, wet thermal blanket that traps heat associated with the creation of new oceanic crust along the rift zone. The sediment cover restricts hydrothermal circulation, leading to high upper crustal temperatures, and possibly pervasive crustal alteration and sediment-hosted mineralization.

Hydrothermal activity associated with ridge-crest volcanism can result in baking and alteration of the host sediments and precipitation of metals leached from basaltic intrusions (Zierenberg and others, chap. 10, this volume). These processes may give rise to massive stratiform polymetallic ore deposits in the axial rift zone. Today, sedimented spreading centers are relatively uncommon except in such areas as Middle Valley (Juan de Fuca Ridge; Davis and others, 1987), Dellwood Knolls and Winona Basin (Explorer Ridge), Guaymas Basin (Gulf of California; Lonsdale and others, 1980), and the Eastern Chile Ridge as well as certain back-arc basins in the western

[1] Mackay School of Mines, University of Nevada-Reno, Reno, Nevada.

[2] U.S. Geological Survey, Menlo Park, California.

Pacific Ocean. However, heavily sedimented ridges may have been much more prevalent in the past, such as in the early rifting of the Atlantic Ocean during the Jurassic. An understanding of the relations between sedimentation, volcanism, neotectonic, and hydrothermal activity in areas such as the Escanaba Trough could provide valuable insights into hydrothermal ore formation processes that could be applied to ancient massive ore deposits.

In this chapter, we examine the magnetic and basement structure of the Escanaba Trough region. The main goals of this work are to evaluate the possible causes of the suppressed magnetic anomalies observed in the heavily sedimented parts of Escanaba Trough and to better delineate the tectonic and volcanic framework and history of the area during the Brunhes Normal-Polarity Chron. Three-dimensional inversions and two-dimensional forward modeling are used to evaluate the character of crustal magnetization and the geometry of sea-floor spreading and volcanism throughout the area. We also attempt to assess what thickness of sediment is required to suppress the magnetic anomaly amplitude and how the volcanic edifices are influenced by this effect.

SEDIMENTATION AND SUPPRESSION OF MAGNETIC ANOMALIES

Most of the world's spreading centers exhibit a high-amplitude central magnetic anomaly that is centered in the middle of normally magnetized Brunhes-age crust (Klitgord, 1976; Tivey and Johnson, 1987, for review). The amplitude of the anomaly decreases with age due to progressive oxidation of titanomagnetites within the basaltic lavas (Irving, 1970; Marshall and Cox, 1972; Bleil and Petersen, 1983).

In a deep-tow study of the Gorda Ridge axial valley from latitude 41°15′ to 41°30′ N., Atwater and Mudie (1973) found magnetic lows over sedimented areas. They attributed these features to slow cooling and consequently coarser grain size of magnetic minerals in the basaltic rocks intruded into the sediments. A second possible mechanism is that the rocks are thermally demagnetized under a sediment cap and that magnetization blocking would be delayed until the intrusions cooled. Levi and Riddihough (1986) argued that such thermal demagnetization is unlikely because the delay in remanence lock-in would result in displaced magnetic anomalies, which are not observed. Instead, they suggested that the upper oceanic crust was chemically altered by pervasive hydrothermal alteration, and thus the rocks are made permanently nonmagnetic. Another hypothesis is that the anomalies are suppressed simply because of the presence of an axial valley depression filled with a thick sediment cover.

PLATE TECTONIC SETTING

Although the Gorda/Juan de Fuca Ridge spreading system was the first to be used to develop the plate tectonics paradigm (Vine, 1966; Atwater and Mudie, 1968), the tectonic history of Gorda Ridge is complex and not fully understood. Gorda Ridge is divided into three sections, each with a different spreading history (Atwater and Mudie, 1973; Riddihough, 1980; Wilson, 1986; Stoddard, 1987). The northern section presently has a relatively fast total opening rate of 5.8 cm/yr, whereas the southern and central ridge segments have total opening rates of 2.0 to 2.4 cm/yr (Riddihough, 1980). From offsets in Pacific plate anomalies, Wilson (1986) and Stoddard (1987) suggested that since 5.3 Ma the northern segment has been propagating southward and the southern segment has been propagating northward, both at the expense of the central segment. Spreading rates apparently decreased at about 3 Ma and possibly 2 Ma (Riddihough, 1980; Stoddard, 1987). The ridge may be spreading asymmetrically at present (Solano-Borrego, 1982); however, Masson and others (1988) argued that asymmetrical spreading cannot be differentiated from ridge jumps, based on then available magnetic and GLORIA side-scan sonar data.

After 20 years of study, the mechanisms of deformation of the Gorda plate and the nature of its interaction with the Mendocino Fracture Zone remain controversial. The magnetic anomaly patterns on the Gorda plate are fan-shaped, and the 3.8 to 4.8 Ma isochrons appear to have been shortened by almost 20 percent (Silver, 1971). Moreover, seismicity is broadly distributed throughout the region. Several models have been suggested to explain these features. Riddihough (1980) proposed simple rigid block rotation of the southern and central subplates. Silver (1971) favored left-lateral shear with strike-slip reactivation of isochron-parallel normal faults formed at the spreading center. In a modification of Knapp's (1982) model of left-lateral shear and rotation of the central Gorda Ridge segment, Stoddard (1987) suggested that the deformation occurred as elastic flexural-slip with distributed shear along major left-lateral faults.

All of these models account for the fanned anomalies, but require oblique subduction of the Gorda plate under the Mendocino Fracture Zone to account for anomaly shortening. Wilson (1986, 1989) argued that strike-slip focal mechanisms along the Mendocino Fracture Zone and simple gravity modeling do not support oblique subduction. From magnetic anomaly analysis and lineation mapping of side-scan imagery, he suggested that the Gorda plate deformation was accommodated by distributed northwest-southeast right-lateral shear near the spreading centers that changed to northeast-southwest left-lateral faulting at about the 2 to 3 Ma isochron. The style of deformation

in the zone of active rifting and its relations to the regional stress field have not been addressed to date, mainly because of the lack of closely spaced profiles along the spreading axis.

AXIAL VOLCANISM AND HYDROTHERMAL ACTIVITY

Several discrete volcanic centers in the sedimented part of the axial valley were identified during the seismic-reflection profiling of R/V *S.P. Lee* cruise L6-85-NC in 1985 (fig. 5.1; Morton and Fox, chap. 2, this volume). A number of these features had been crossed previously on a site survey for DSDP Site 35 (Moore, 1970; Moore and Sharman, 1970), but they were interpreted as one long continuous basement ridge due to the lack of adequately spaced seismic-reflection lines. The centers are commonly offset to the west of the axis of the valley. Although the exact nature of the volcanic-sedimentary contacts at the centers is difficult to decipher owing to numerous hyperbolic diffractions from sills, the volcanic edifices appear to consist of a combination of deep-seated plugs and thin, high-level sills (Davis and Becker, chap. 3, this volume; Morton and Fox, chap. 2, this volume). On GLORIA sidescan records, the volcanic edifices appear as almost circular, highly reflective zones within the less reflective axial valley sediments (EEZ-SCAN 84 Scientific Staff, 1986). Near some of the intrusions, the sediments have been uplifted by 50 to 100 m, forming elevated terraces and hills.

Two of the five volcanic centers have been studied in more detail (Morton and others, chap. 1, this volume). Reconnaissance bottom camera and dredging work in 1985 in the northern Escanaba Trough (NESCA) and southern Escanaba Trough (SESCA) sites (edifices D and B in fig. 5.1) suggest that the volcanic centers are sites of recent and possibly active volcanic and hydrothermal activity (Morton and others, 1987a). Fresh pillow basalt outcrops are exposed on parts of the NESCA area, and fresh basaltic glass was dredged from both edifices. Unweathered hydrothermal sulfide samples associated with altered mudstone were dredged at the SESCA site. Heat-flow surveys also in 1985 near the two centers show values in excess of 1,200 mW/m^2 (Abbott and others, 1986), suggesting that both of these centers are still hydrothermally active.

A detailed transponder-navigated bathymetric, camera, and seismic-reflection survey of the two sites in 1986 showed the centers to be characterized by several small, uplifted sediment hills (Morton and others, 1987b; Morton and Fox, chap. 2, this volume). DSV *Sea Cliff* submersible observations (Holmes and Zierenberg, 1990) as well as bottom camera, dredging, and coring (Morton and others, 1990) reveal that most of the SESCA site is sediment covered, with only limited basaltic exposures. At the NESCA site, fresh basaltic flows were observed on the flanks of one hill, and large flat basins were observed that may be thinly sedimented lava lakes (Ross and Zierenberg, chap. 8, this volume). At both sites, large sediment-hosted sulfide deposits were found (Koski and others, 1988). The areal distribution of these deposits is not known, but constructional ledges, mounds, and chimneys of massive sulfide extend up to 200 m along steep scarps at the base of the sediment hills (Morton and others, 1990; Zierenberg

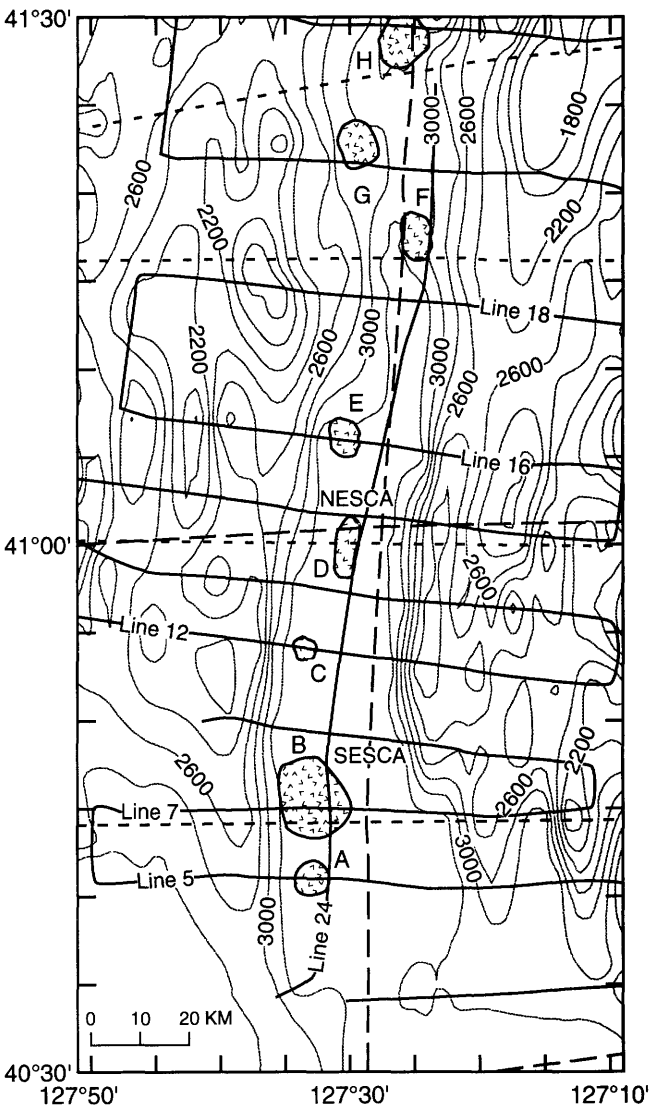

Figure 5.1. Bathymetric map of Escanaba Trough study area, compiled from available 12 kHz records with additional data from Wilde and others (1978). Volcanic edifices in axial valley marked by patterns and labeled from A to H. Cruise tracks shown for L6-85-NC (solid line), L12-81-NP (long dashed line), and F3-84-NC (short dashed line). Contours are at 200-m intervals and a sound velocity of 1500 m/s was assumed.

and others, chap. 10, this volume). DSV *Alvin* submersible observations conducted in 1988 confirmed that active hydrothermal venting is occurring at the NESCA site (Zierenberg and others, 1988).

ACKNOWLEDGMENTS

We thank Jane Yu and Roger Burnley for help with data processing and reduction, Maurice Tivey for his assistance in the initial magnetic modeling, and Mark Holmes for his valiant efforts to obtain high-quality geophysical data during the L6-85-NC cruise.

METHODS

Bathymetric maps presented here were generated from 12-kHz records obtained during U.S. Geological Survey cruises L12-81-NP, L6-85-NC, and F3-84-NC, as well as data filed at the NOAA National Geophysical Data Center. Reflection travel times to basement were digitized at 5-minute (about 1 km) intervals from analog recordings of 1,050 km of single-channel seismic-reflection lines run during cruise L6-85-NC using a 3.9 L (237 $in.^3$) air-gun array. The velocity function for the deep-sea sediment column of Carlson and others (1986) was used to convert reflection travel times to sediment thickness in meters. These sediment velocity values are in good agreement with those derived from stacking velocities for multichannel seismic-reflection records at Escanaba Trough (Morton and Fox, chap. 2, this volume; J.L. Morton, unpub. data, 1991). The minimum detection limit for sediment cover was about 25 m in smooth terrain. However, the initial pulse envelope and diffraction hyperbolas made it difficult to differentiate sediment-covered ridges from basaltic ridges; thus, sediment thicknesses should be considered a minimum estimate, especially in rough topography. Basement topography was estimated by subtracting the sediment cover from the bathymetry.

Magnetic data on the three cruises were collected with a Geometrics 801 proton precession magnetometer at 1-minute intervals from a "fish" towed 350 m behind the ship. The observed values, corrected for towing distance, were merged with navigation obtained using an integrated satellite–Loran C–doppler sonar system. Magnetic anomalies were calculated by removing the appropriate International Geomagnetic Reference Field (IGRF) field, but diurnal variation corrections were not made. Crossings of different lines at the same location agreed to within 25 nT.

To estimate crustal magnetization in the presence of topography, the magnetic anomaly data were inverted using the techniques of Macdonald and others (1980, 1983) and Miller (1977). To perform the inversion, grids of basement topography and magnetic anomalies were established at approximately 1 km spacing. Mirror images of the 50 by 50 grids were added at the borders of the data set to minimize edge effects. A bandpass filter with 3.5- and 100-km wavelengths was used to suppress high-frequency noise and long-wavelength trends. The inversion scheme, which is based on the methods developed by Parker and Huestis (1974), assumes that the crustal magnetization resides in a layer of constant thickness that follows the basement topography. The magnetization in each layer can vary areally and reverse in sign, but has a uniform direction. A best-fitting areal distribution of magnetization is calculated in an iterative manner to minimize the mean-square residual differences between the model and observed field data. Because of the inherent lack of uniqueness of potential field data, the solution is not unique. However, Parker and Huestis (1974) showed that the magnetizations are confined to a class of solutions that can be thought of as a basis solution combined with an annihilator function. The annihilator is the magnetization distribution that gives no net external magnetic field. The amount of annihilator added to the basis solution must be constrained by geologic intuition and, if possible, by magnetic intensity measurements on individual samples.

DATA PRESENTATION

BASEMENT TOPOGRAPHY AND STRUCTURE

Escanaba Trough, forming the southern part of Gorda Ridge, is bounded by the Mendocino Fracture Zone to the south and is separated from the central segment of Gorda Ridge by a small fracture zone at latitude 41°40′ N. The L6-85-NC single-channel seismic-reflection lines broadly define the structure of Escanaba Trough (Morton and others, 1987a; Morton and Fox, chap. 2, this volume).

Seismic profiling (Morton and Fox, chap. 2, this volume) shows that sediment covers the axial valley south of about latitude 41°17′ N. and blankets the southernmost 80 km of the rise axis. At 3,200 to 3,300 m depth, the axial valley is relatively flat and is flanked by a series of subparallel ridges 1,100 to 1,200 m high (fig 5.1). The valley is filled with several hundred meters of sediment in the south, but the sediment thins to the north where the axial valley shoals. Much of this sediment flowed off the continents as turbidites during Pleistocene low sea-level stands (Vallier and others, 1973), although the Holocene veneer is mainly hemipelagic (Karlin and Lyle, 1986).

The reflection profiles show that the flanks of the axial valley are composed of uplifted and back-tilted crustal blocks, with the intervening valleys containing perched sediment ponds (Morton and Fox, chap. 2, this volume). At least some of the ridges appear to have a sediment cap, although the fine-scale lithology and structural relations cannot be readily deciphered.

The sediment fill in the axial valley is mainly composed of strongly reflecting, horizontally bedded strata (see Morton and Fox, chap. 2, this volume and Davis and Becker, chap. 3, this volume, for seismic-reflection profiles), presumably Pleistocene turbidites such as those found at DSDP Site 35 (McManus and others, 1970; Normark and others, chap. 6, this volume). High-angle faults cut through the strata, forming raised terraces and small horst and graben structures.

As seen in the sediment isopach map in figure 5.2, the sediment is thickest on the eastern side of the axial valley where it fills a long, narrow trough. This feature may have been formed by a combination of uplift of the flanking ridges and constructional volcanism on the western side of the valley. In the southeastern part of the axial valley, the sediment is more than 1,700 m thick, while in the central region, thickness averages about 500 m and thins to the north. The deep graben in the southeast contains large coherent sediment blocks that appear to have been downdropped and tilted with subsequent channel infill by turbidites (Morton and others, chap. 2, this volume). The eastern edges of the block show evidence of major drag folding whereas the contacts on the western edges are sharp. This block appears to be a downwarped extension of the steep sediment-capped ridge immediately to the north.

In the basement topography map of figure 5.3, where the sediment cover has been removed where identifiable using the reflection profiles, a deep, sediment-filled axial valley in the south is clearly evident. The flanking ridges

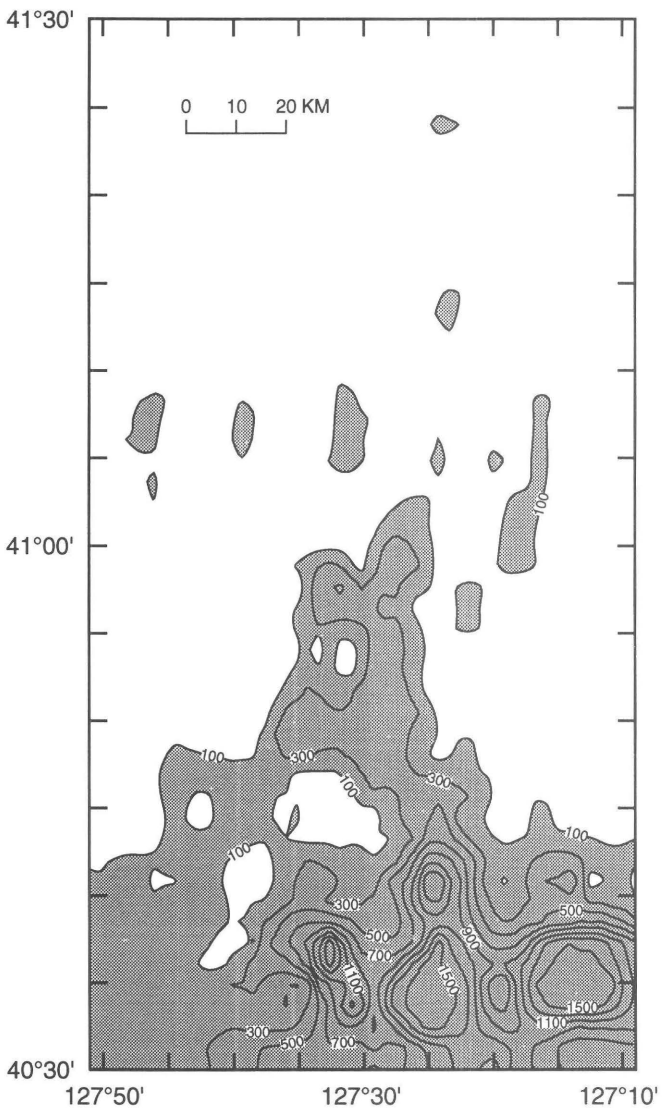

Figure 5.2. Sediment isopach map of study area, contoured at 200-m intervals, as estimated from L6-85-NC seismic-reflection lines. Areas of sediment thicknesses greater than 100 m are shaded.

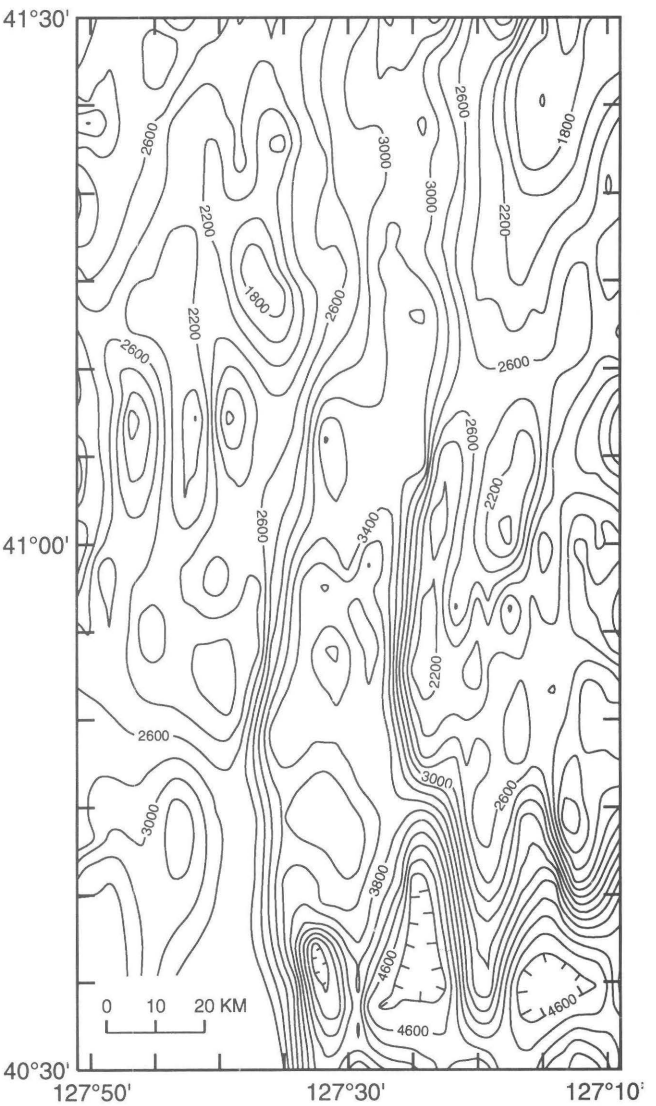

Figure 5.3. Basement topography map of study area, obtained by removing sediment cover, using sediment thicknesses estimated from L6-85-NC seismic-reflection profiles. Note large hole in southeast part of valley, arched ridges in central area, and regularly spaced domal structures along axis. Contour interval is 200 m.

are highest in a central area from around latitude 40°54′ N. to 41°20′ N. and decrease in elevation to the north and south. This broad regional arching is also seen in the basement of the axial valley; however, several domal structures occur in a regular pattern along the axis about 15 to 20 km apart. The arching must postdate the major Pleistocene turbidite deposition, since the flanking walls are sediment capped and perched sediment ponds occur on at least three of the tilted blocks on either side of the axial valley.

MAGNETIC ANOMALIES

A magnetic anomaly map of the area shows a strong, well-developed central anomaly in the north, which decays in amplitude to the south (fig. 5.4). The boundaries between the Brunhes Normal-Polarity Chron and Matuyama Reversed-Polarity Chron (0.73 Ma) and between the Matuyama and the Olduvai Normal-Polarity Chron (1.66 Ma) are clearly defined north of latitude 40°54′ N. and yield a full spreading rate of 2.0 to 2.1 cm/yr. Most of the volcanic edifices appear to have a magnetic signature, although the anomalies over the large volcanic intrusions at latitude 40°42′ N. and 40°45′ N. (edifices A and B) appear to be attenuated.

Cross-axis transects of magnetic anomalies and basement structure were prepared for the lines from cruise L6-85-NC. Line 18 (fig. 5.5), the most northerly profile shown here, has a well-developed anomaly pattern. Normally magnetized crust of Olduvai age (1.66 to 1.88 Ma) flanks reversely magnetized Matuyama-age (0.73 to 1.66 Ma) crust, which in turn surrounds normally magnetized

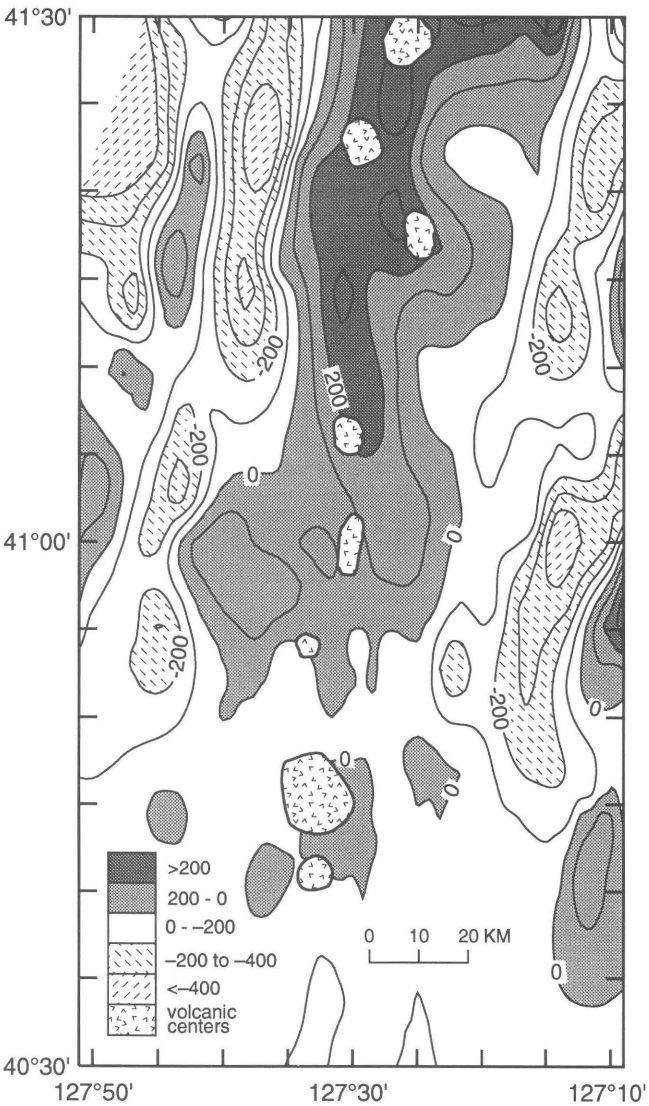

Figure 5.4. Magnetic anomaly map for Escanaba Trough study area from L6-85-NC cruise, contoured at 100-nT intervals. Positive anomalies are shaded. Note low anomaly amplitudes in heavily sedimented southern part of Escanaba Trough.

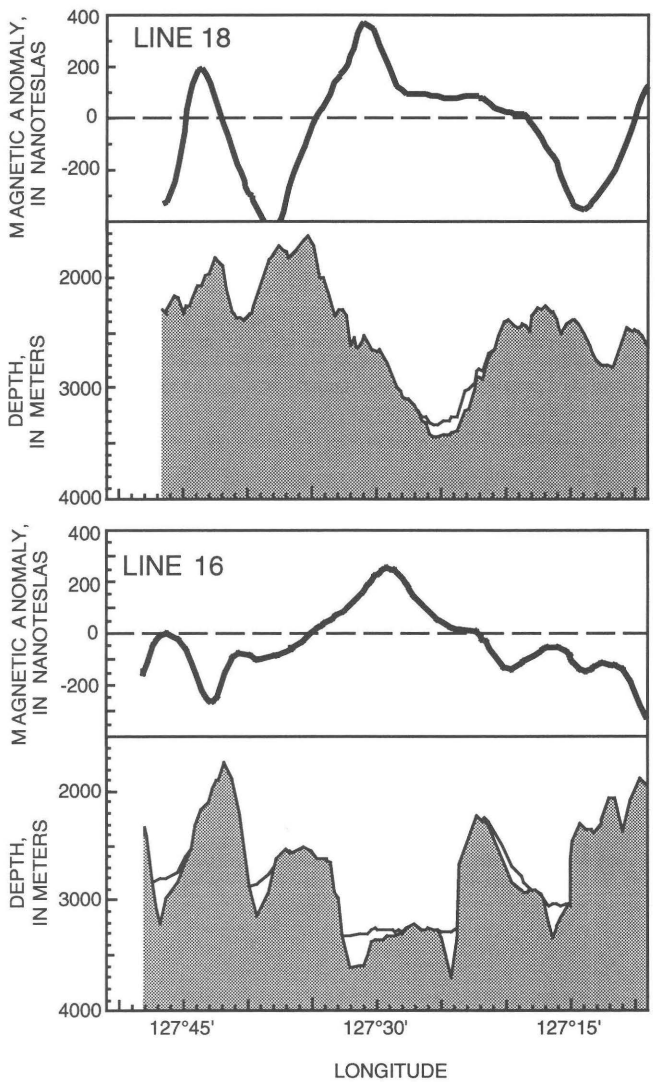

Figure 5.5. Magnetic anomaly (top), sediment cover (solid line), and basement bathymetry (shaded) profiles of lines 18 and 16 from cruise L6-85-NC (see fig. 5.1 for location).

Brunhes-age material (post 0.73 Ma). The structure of the basement and the location of the central anomaly suggest that the zone of neovolcanism is displaced to the west side of the axial rift. The amplitude of the magnetic anomaly over the sedimented trough is less than that over the nearby unsedimented intrusion.

Line 16 (fig. 5.5), the next line to the south, shows relatively low amplitude negative anomalies on the sediment-capped ridge flanks. The central anomaly is more symmetrical than on line 18 but is still displaced slightly to the west. On line 12 (fig. 5.6), the central anomaly is almost absent in the sediment-covered valley, and the axial intrusion shows very little magnetic expression. Line 7 (fig. 5.6), the southernmost of the lines shown, shows very low amplitude anomalies over ridges with a thick sediment cover. A small positive anomaly is centered over the volcanic edifice on the western side of the axial valley. It is curious that the center of the axial rift shows a negative value of about −100 nT.

Line 24 was run along the axis of the rift valley; figure 5.7 shows the basement structure, sediment cover, and magnetic anomaly patterns. Broad regional arching of the basement is evident, suggesting enhanced crustal generation in the north. Magma supply appears to decrease to the south, leading to diapiric intrusions. The sediment fill covers the valley floor and shows a gentle northward gradient to about latitude 41° N. but appears to be ponded and uplifted north of the NESCA edifice. The magnetic anomaly profile shows a clear trend toward decreasing amplitudes in the south. In areas with any appreciable sediment cover, magnetic anomaly amplitudes are suppressed. However, both edifices B (SESCA) and C (fig. 5.1) show small positive anomalies. These areas may have been subjected to domal uplift and associated intrusion of sills into thick sedimentary sequences. Volcanism has reached the sea floor at only a few locations in the SESCA area (Ross and Zierenberg, chap. 8, this volume), and edifice C may not contain a near-surface volcanic intrusion. The NESCA area shows transitional behavior. Near latitude 41° N., the magnetic anomaly amplitude is low, but slightly further to the north, the uplifted blocks show little sediment cover and a strong magnetic anomaly signature of up to 200 nT.

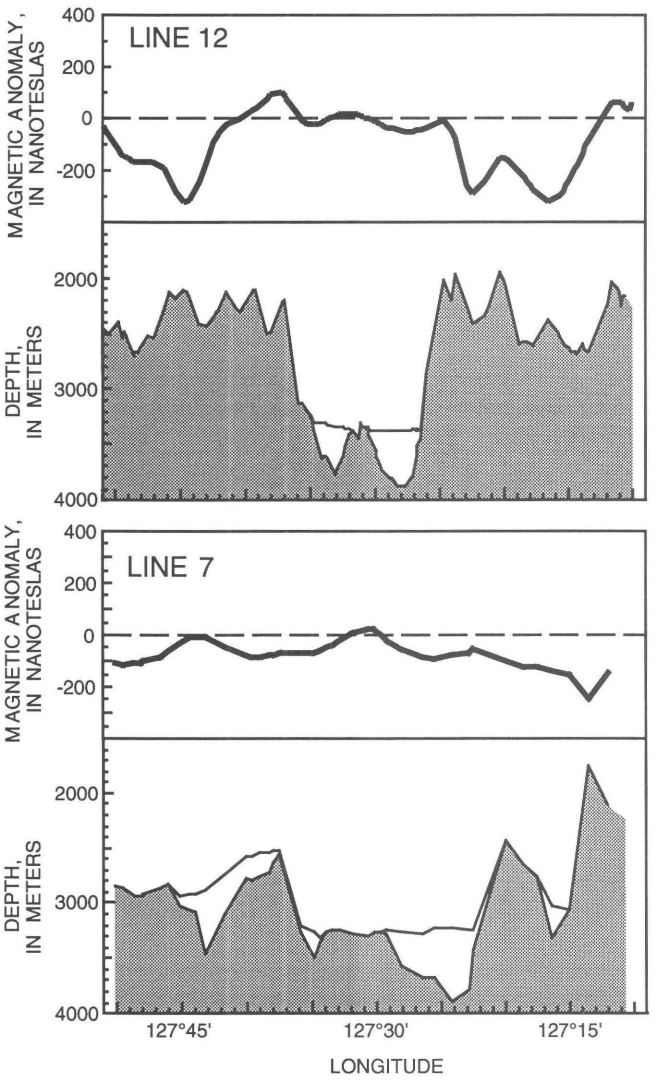

Figure 5.6. Magnetic anomaly (top), sediment cover (solid line), and basement bathymetry (shaded) profiles of lines 12 and 7 from cruise L6-85-NC (see fig. 5.1 for location).

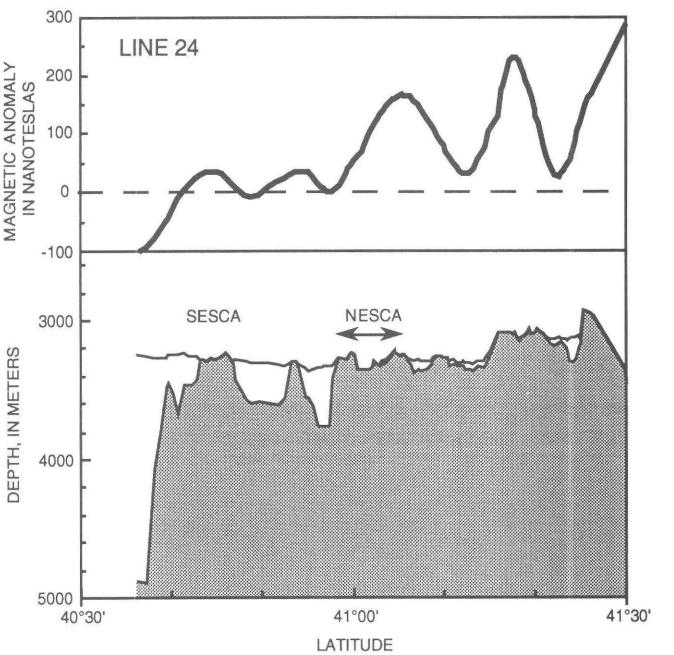

Figure 5.7. Magnetic anomaly (top), sediment cover (solid line), and basement bathymetry (shaded) profiles of line 24 from cruise L6-85-NC along rift valley axis (see fig. 5.1 for location). Magnetic anomalies appear to be attenuated in areas with sediment cover; however, anomalies are observed over volcanic edifices.

MAGNETIC MODELING RESULTS

INVERSE MAGNETIC MODELING

Levi and Riddihough (1986) proposed that in the southern area, high heat flow combined with an impermeable sediment cap caused permanent chemical alteration of the underlying crust. While this interpretation is plausible, the effects of the basement topography on the anomalies must be considered before it can be evaluated (Parker and Huestis, 1974).

The magnetic data were inverted into magnetization distributions for source layer thicknesses of 0.1, 1.0, and 3.0 km. All three cases give essentially similar magnetization patterns except that the thinner the source layer, the stronger its magnetization. Difference maps (observed minus modeled) for the three cases are very similar, suggesting that the models are not good predictors of the thickness of the magnetized layer. The model fit generally agrees with the observed data within 50 nT (fig. 5.8*A*), except in the northwest sector where data coverage is more sparse and the amplitude variations are greater. The annihilator function (fig. 5.8*B*) is generally ridge parallel, and adding various amounts of the annihilator to the model results in similar patterns, but a DC shift in magnetization values and stronger magnetization contrasts.

We reproduce here an inversion of the gridded magnetic field data into magnetization using a 1.0-km source layer (fig. 5.9). The choice of this thickness is arbitrary, but drilling results at DSDP Site 504B (Smith, 1985) suggest this thickness to be reasonable. The magnitudes of the positive and negative off-axis crustal magnetizations are comparable, so no additional annihilators are added to the solution. After inversion, the crustal magnetizations show

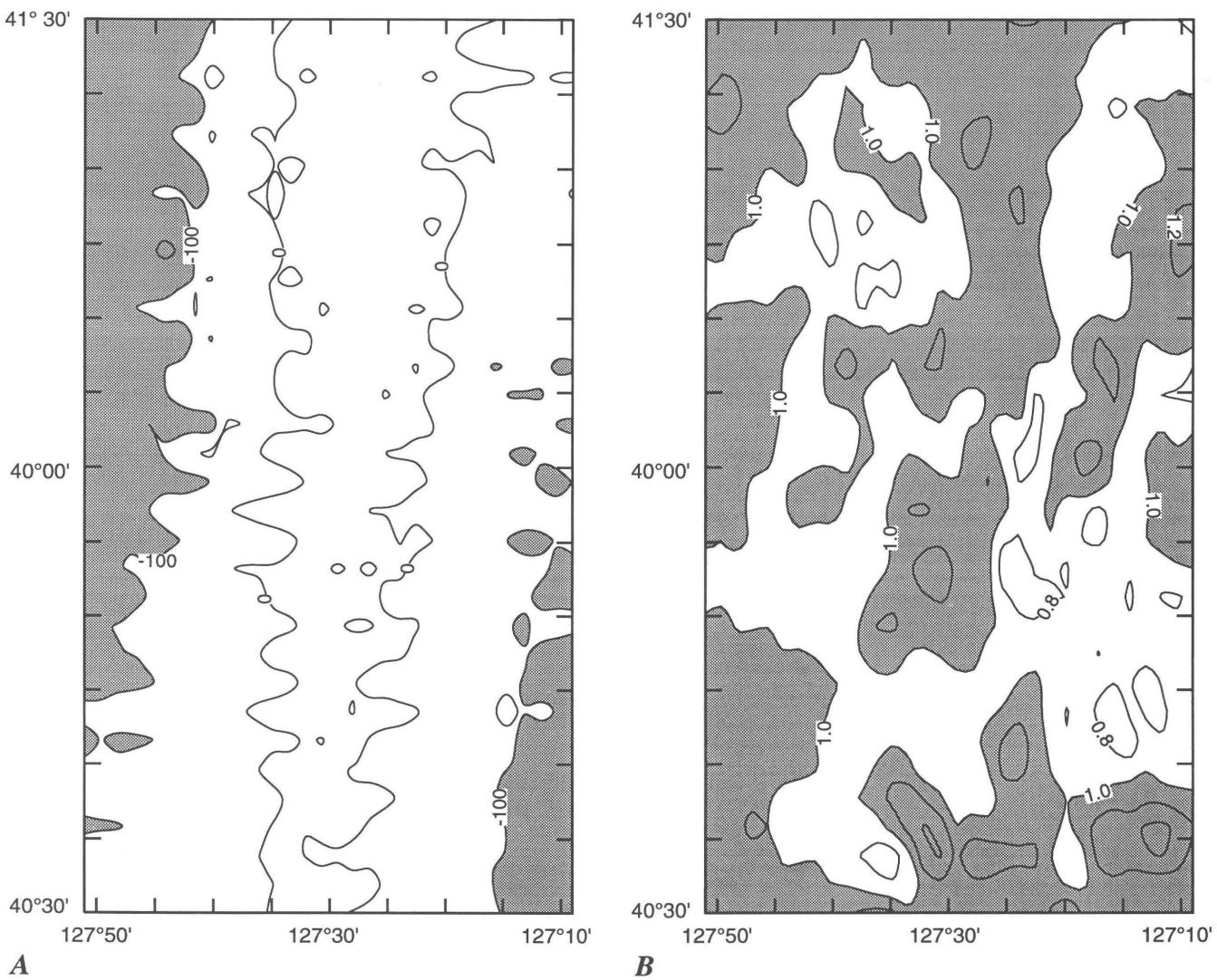

Figure 5.8. *A,* Map of misfit between observed and modeled values for 1-km source layer trial. Values are contoured at 100-nT intervals. Areas less than −100 nT are shaded. *B,* Magnetic annihilator distribution for 1-km source layer model. Contour interval is 0.2 Am^{-1}. Areas greater than 1.0 Am^{-1} are shaded.

low values in the heavily sedimented southern end of Escanaba Trough, consistent with Levi and Riddihough's (1986) earlier interpretation from the magnetic anomaly data. Thus, the sediment does indeed appear to suppress the magnetic crustal signatures. However, the various volcanic edifices show evidence of positive crustal magnetizations.

An interesting aspect of the anomaly and crustal magnetization map is that the axial valley south of latitude 40°42′ N. shows negative values. Anomalies vary from −50 to −100 nT and magnetizations range from −1 to −2 A/m. The anomaly values do not appear to be due to instrumentation miscalibration or drift, because the same behavior is observed in all three cruises. Adding sufficient annihilator to give zero net magnetization in the area causes severe distortion of the symmetrical patterns to the north; thus, the calculated magnetizations are robust in the inversion. The negative magnetic anomalies could reflect (1) incomplete removal of a regional field not accounted for by the IGRF, (2) negatively magnetized post-0.73 Ma crust in the valley axis, or (3) edge effects from the nearby 1,500-m-high Mendocino Escarpment.

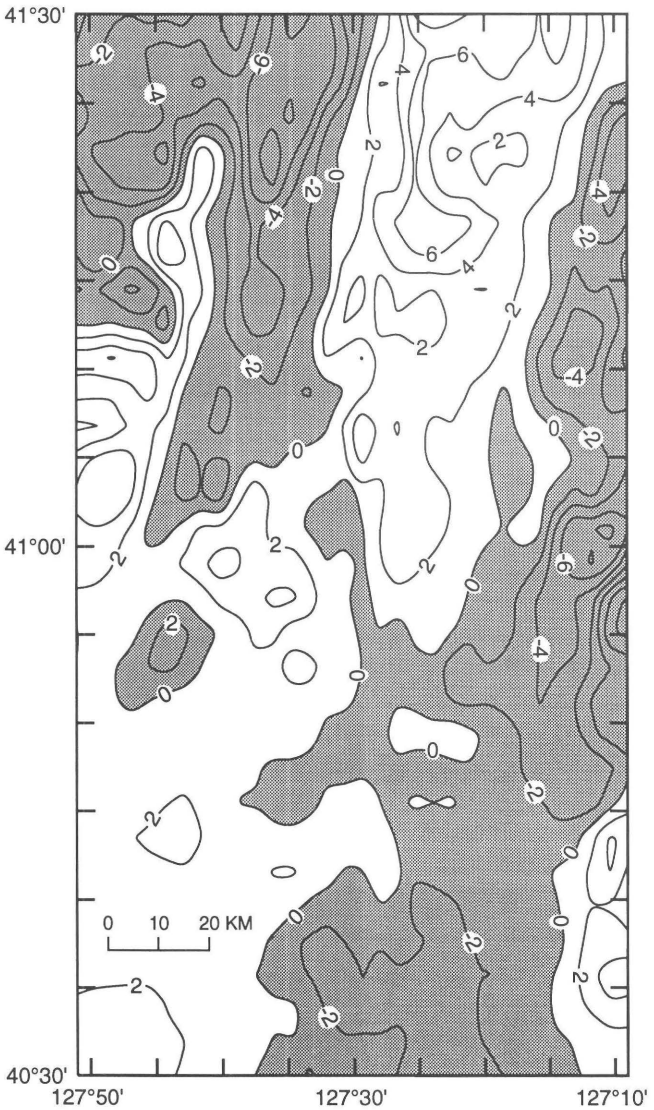

Figure 5.9. Distribution of crustal magnetizations computed for 1-km magnetic source layer. Areas with negative magnetizations are shaded. Contour interval is 2 Am^{-1}.

FORWARD MAGNETIC MODELING

To gain further insight into the nature and distribution of the magnetized layer, we did two-dimensional forward modeling of line 24 using techniques developed by Talwani and others (1959) and Talwani and Heirtzler (1964). The forward method differs from the inverse method in that the geometry and magnetic intensities are allowed to vary, and the assumption that the magnetic layer follows the topography is not required. The criterion for the modeling was that a satisfactory fit be achieved with the simplest possible model. The model is not designed to replicate the actual magnetization distribution, but represents an equivalent magnetization combination that illustrates several salient features that are required to explain the observed magnetic anomaly patterns. In all trials, a site Cenozoic field direction of I=60°, D=0° (or I=−60°, D=180°) was used; distances were calculated from latitude 40°30′ N.; the modeled magnetic anomalies were calculated for sea level; and basement topography was estimated from the seismic reflection profiles.

The best result of a large number of trials is shown in figure 5.10. The modeling revealed several interesting points:

1. A minimum of three magnetic polygons are needed to adequately fit the data: a strongly magnetic block in the north, an irregularly distributed central block, and a positively magnetized block representing the Mendocino Escarpment. The Mendocino block is needed to produce the observed negative values in the southern part of the profile. This block also induces a long-wavelength positive trend extending the length of the section. Thus, it appears that the negative anomaly values observed in the southern Escanaba Trough are due to an edge effect caused by the topography associated with the Mendocino Fracture Zone. The three-dimensional inversion gives misleading negative magnetizations, because regional effects are not considered.

2. The magnetic layer is relatively thin (less than 0.5 km) and close to the surface. This result arises because of the relatively short wavelengths of the anomalies.

3. Although the magnetization distribution follows the topography between 70 and 90 km distance, this is not true in general, regardless of whether sediment-capped ridges or altered zones are added to the model. This is because the observed anomalies are relatively smooth and are not always centered over the topographic highs and lows.

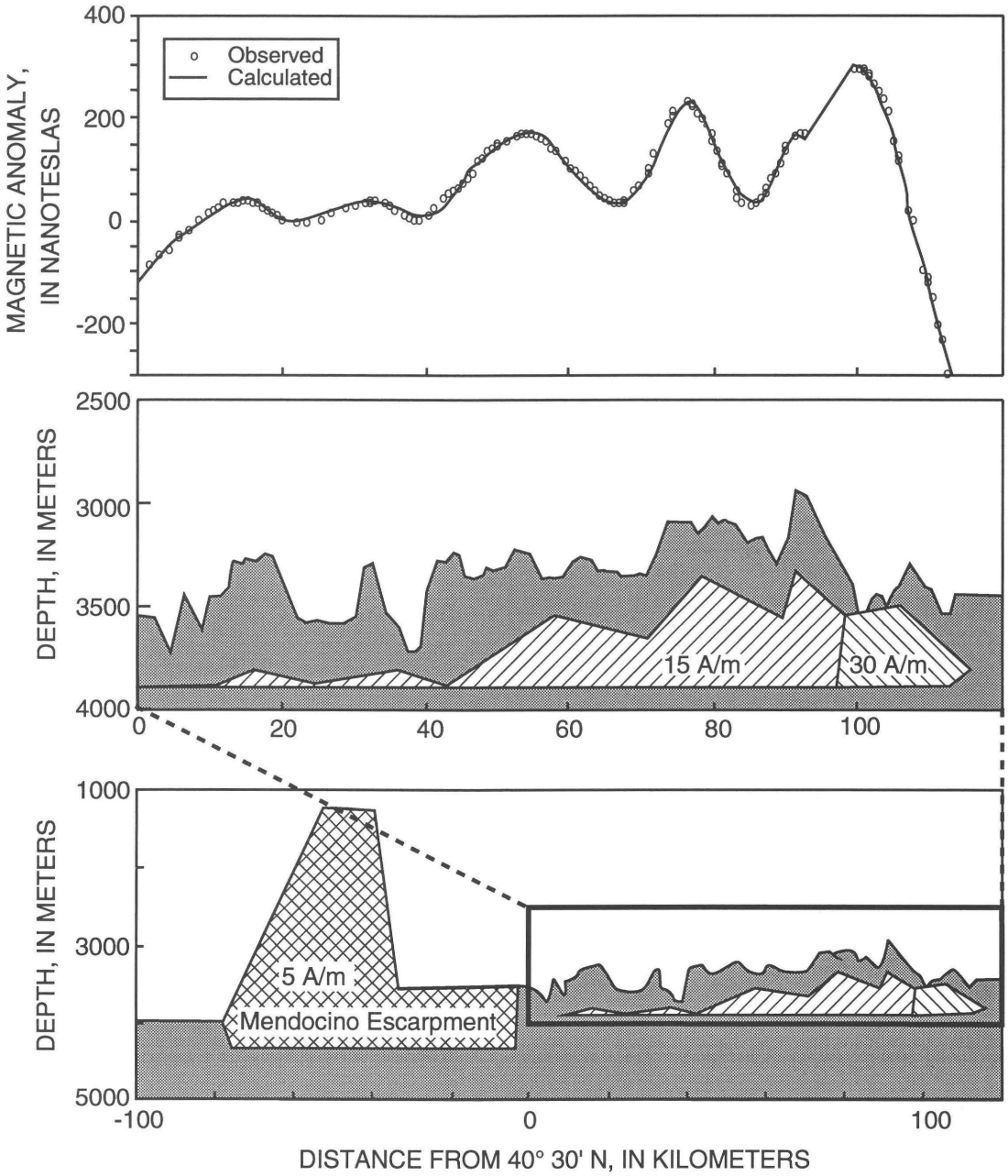

Figure 5.10. Two-dimensional magnetic modeling of line 24. Observed (open circles) and modeled (solid lines) magnetic anomaly values at top; basement topography and magnetic polygons at bottom. Distances are given north of latitude 40°30′ N. Three polygons were required to produce observed fit: Mendocino polygon with D=0°, I =60°, M=5 Am^{-1}; central block with D=0°, I=60°, M=15 Am^{-1}; and smaller northern block with D=0°, I =60°, M=30 Am^{-1}. D, declination; I, inclination; M, magnetization.

4. In the southern part of the profile, only a small amount of magnetic material is needed to simulate the anomaly patterns. These polygons could represent shallow sills, infrequent small, narrow intrusions, or alternatively, larger intrusions that have been partially altered.

CRUSTAL MAGNETIZATION AND SEDIMENTATION

In figure 5.11, magnetic anomaly values lie within an envelope that decreases in intensity with increasing sediment thickness. Over the entire area, magnetic anomalies

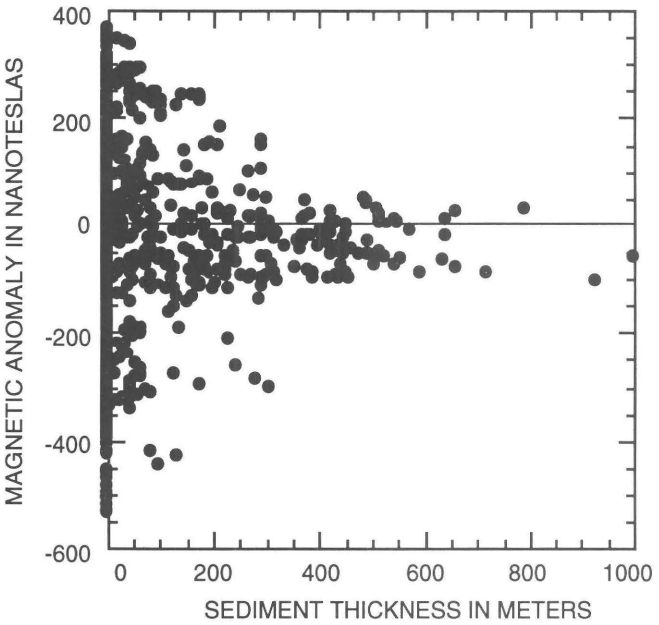

Figure 5.11. Scatter plot of magnetic anomaly values (in nT) and sediment thicknesses (in m). Magnetic anomaly values lie within an envelope that decreases with increasing sediment thickness.

range from 400 nT to about –500 nT; however, at sediment thicknesses greater than 300 m, values seldom exceed 100 nT, suggesting that magnetic anomalies are indeed suppressed in areas of thick sediment cover. The trend toward slightly negative magnetic anomaly values at sediment thicknesses greater than 300 m is probably due to the influence of the Mendocino Escarpment on the thick sediment section in the southernmost Escanaba Trough.

TECTONICS IN ESCANABA TROUGH

Several factors probably combine to create the present basement topography of Escanaba Trough: axial valley volcanism, sea-floor spreading, off-axis isostatic readjustment, and subsequent tectonic deformation. Joint consideration of the basement topography and magnetic data (fig. 5.12) suggests that the area is presently subject to asymmetrical spreading and volcanism offset to the western side of the axial valley. The flanks of the ridge appear to be cut by several transform faults. These are evidenced by a shift in orientation of the ridge flanks and curvature of the magnetic anomaly patterns. The absence of matching features on the opposite side of the spreading axis suggests that the changes in topography and magnetic signatures are not due to primary volcanism or initial spreading.

The eastern wall of the axial valley appears to be part of a single, coherent tilted block extending from about latitude 40°48′ N. to 41°10′ N. Its counterpart on the western side of the trough has a somewhat more limited extent (about latitude 40°42′ N. to 41°0′ N.) and appears to be broken up in the north. Without better imaging, it is not possible to determine if these features are due to the initial distribution of volcanism or later faulting.

The basement deep at the southern end of the trough suggests an absence of volcanism near the intersection with the Mendocino Fracture Zone. This feature is similar to a large nodal basin at the juncture of the Kane Fracture Zone and the Mid-Atlantic Ridge (Macdonald, 1986). The hole may reflect depression of mantle isotherms because of cooling effects from the cold Pacific plate nearby. However, the lack of volcanism cannot be maintained indefinitely.

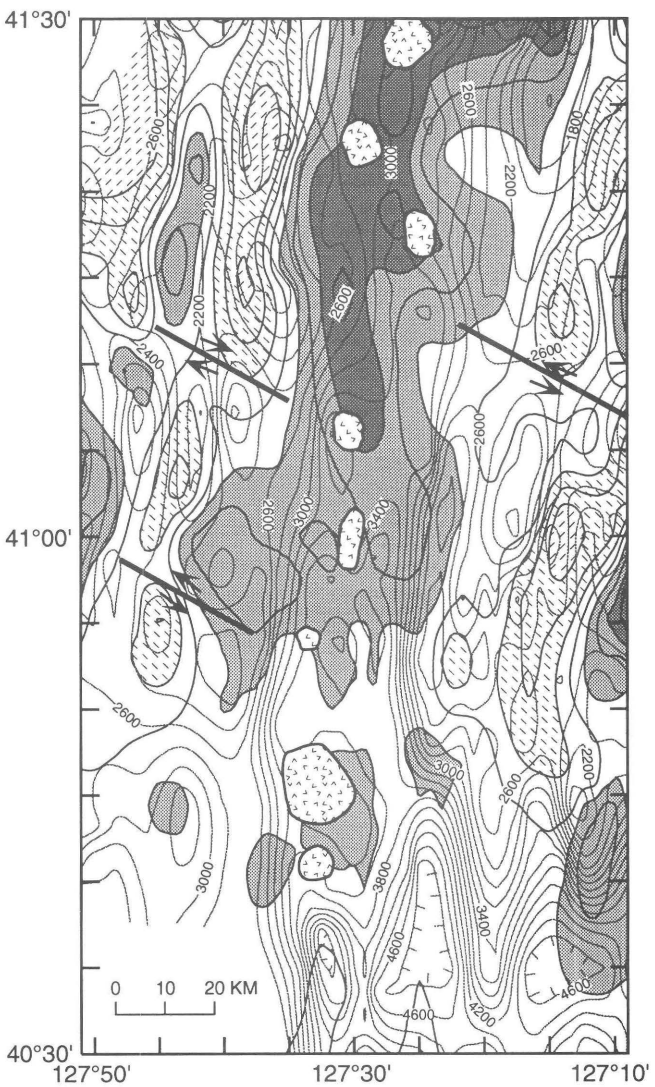

Figure 5.12. Magnetic anomaly patterns superimposed on basement topography. Note offsets of magnetic anomaly trends and basement structures to west and east of axial valley. Heavy lines on figure mark approximate location of inferred shear zones that have created discrete tilted blocks on flanks of ridge; arrows indicate relative direction of movement. Shading of magnetic anomaly intervals as in figure 5.4. Hachures indicate area of closed low. Contour interval is 200 m.

Either the spreading axis has shifted under the sediment blanket (probably to the west) or no spreading is occurring, requiring a transform fault extending to the Mendocino Fracture Zone. More reflection and magnetic data are required to distinguish between these possibilities.

There are at least two possible interpretations for the north-northeast trend of the magnetic anomalies outside of the axial valley: either they formed initially north-south and have been deformed into their current orientation, or the axis trended slightly east of north at the time of formation and has shifted to a more north-south orientation (normal to the Mendocino Fracture Zone) only since about the start of the Brunhes. We favor the latter explanation for the crust west of the axis; however, crust east of the axis has been affected by additional deformation, especially further east. To the west of the axis, north-northeast trends are quite striking on GLORIA imagery. Older lineations trend north-south only right near the Mendocino Fracture Zone. Gorda Ridge appears to be adjusting its spreading to become perpendicular to the fracture zone. The possible westward shift of the northern part of the Escanaba Trough axis (as indicated by the peak magnetic anomaly on line 18) could be part of this continuing adjustment.

Magnetic profiles over the northern part of Escanaba Trough, where there is little or no sediment cover at the axis, exhibit a well-developed axial magnetic high within the normally magnetized Brunhes-age crust. However, on some profiles, the axial high is not at the center of the Brunhes anomaly and the axial valley, but is displaced westward. The central high is, however, located above a broad terrace at the west side of the axial valley that is characterized on Sea Beam bathymetric maps by circular features resembling volcanic cones (Morton and Fox, chap. 2, this volume). Further south, the volcanic edifices that penetrate the sediment cover of the trough are similarly displaced toward the west side of the axial valley. These features suggest a recent westward shift of the spreading axis.

The ridge flanks of Escanaba Trough are being deformed along northwest-southeast-striking faults, as evidenced by offsets in magnetic anomaly and basement topographic trends. The axis of Escanaba Trough and the Brunhes magnetic anomaly trend approximately north-south; older magnetic anomalies trend slightly east of north. These observations indicate that the trend of the southern Gorda Ridge axis is shifting slightly to become perpendicular to the strike of the Mendocino Fracture Zone.

CONCLUSIONS

Magnetic anomaly data, combined with seismic-reflection profiling, provide a record of tectonic and volcanic activity at the sediment-covered Escanaba Trough. Within Brunhes time, represented approximately by the crust within the axial valley, tectonic extension has dominated over volcanism. Recent volcanic activity is primarily confined to several volcanic edifices, discrete complexes of sills and surface flows. The basement topography and the size and distribution of the volcanic edifices suggest that the amount of volcanism is greater in the northern part of the trough. An absence of volcanism near the Mendocino Fracture Zone has resulted in the formation of a basement hole more than 1,000 m deep in the southeast part of the trough. This apparent lack of crustal generation coupled with continued horizontal extension is not a stable situation, and it suggests either that the site of crustal generation is shifting or that a transform fault must eventually form.

Crustal magnetization values, obtained by three-dimensional inversion of the anomaly data, are low in the sediment-covered part of the trough, probably owing to crustal alteration beneath the sediment blanket. Small-amplitude positive anomalies are observed over the volcanic edifices, indicating incomplete alteration of shallow intrusions. Observed negative anomaly values over the center of the axis at the southern end probably are a result of edge effects of the magnetic signature of the Mendocino escarpment.

REFERENCES CITED

Abbott, D.H., Morton, J.L., and Holmes, M.L., 1986, Heat flow measurements on a hydrothermally-active, slow-spreading ridge: The Escanaba Trough: Geophysical Research Letters, v. 13, p. 678–680.

Atwater, T.M., and Mudie, J.D., 1968, Block faulting on the Gorda Rise: Science, v. 159, p. 729–731.

———1973, Detailed near-bottom geophysical study of the Gorda Ridge: Journal of Geophysical Research, v. 78, p. 8665–8686.

Bleil, Ulrich, and Petersen, Nikolai, 1983, Variations in magnetization intensity and low temperature titanomagnetite oxidation of ocean floor basalts: Nature, v. 301, p. 384–388.

Carlson, R.L., Gangi, A.F., and Snow, K.R., 1986, Empirical reflection travel time versus depth and velocity versus depth functions for the deep-sea sediment column: Journal of Geophysical Research, v. 91, p. 8249–8266.

Davis, E.E., Goodfellow, W.D., Bornhold, B.D., Adshead, J., Blaise, B., Villinger, H., and Le Cheminant, G.M., 1987, Massive sulfides in a sedimented rift valley, northern Juan de Fuca Ridge: Earth and Planetary Science Letters, v. 82, p. 49–61.

Davis, E.E., and Becker, Keir, Thermal and tectonic structure of the Escanaba Trough: New heat-flow measurements and seismic-reflection profiles, *in* Morton, J.L., Zierenberg, R.A., and Reiss, C.A., eds., Geologic, hydrothermal, and biologic studies at Escanaba Trough, Gorda Ridge, offshore northern California: U.S. Geological Survey Bulletin 2022, chapter 3 (this volume).

EEZ-SCAN 84 Scientific Staff, 1986, Atlas of the Exclusive Economic Zone, Western Conterminous United States: U.S. Geological Survey Miscellaneous Investigations Series Map I-1792, 152 p., scale 1:500,000.

Holmes, M.L., and Zierenberg, R.A., 1990, Submersible operations in Escanaba Trough, southern Gorda Ridge, *in* McMurray, G.R., ed., Gorda Ridge: A seafloor spreading center in the United States' Exclusive Economic Zone: New York, Springer-Verlag, p. 93–115.

Irving, E., 1970, The Mid-Atlantic Ridge at 45°N, Oxidation and magnetic properties of basalt; Review and discussion: Canadian Journal of Earth Science, v. 7, p. 1528–1538.

Karlin, Robert, and Lyle, Mitchell, 1986, Sediment studies on the Gorda Ridge: Oregon Department of Geology and Mineral Industries Open-File Report O-86-19, 76 p.

Klitgord, K.D., 1976, Sea-floor spreading: The central anomaly magnetization high: Earth Planetary Science Letters, v. 29, p. 201–209.

Knapp, J.S., 1982, Seismicity, crustal structure, and tectonics near the northern termination of the San Andreas fault: Seattle, University of Washington, Ph.D. thesis, 343 p.

Koski, R.A., Shanks, W.C., III, Bohrson, W.A., and Oscarson, R.L., 1988, The composition of massive sulfide deposits from the sediment-covered floor of Escanaba Trough, Gorda Ridge: Implications for depositional processes: Canadian Mineralogist, v. 26, p. 655–673.

Levi, Shaul, and Riddihough, Robin, 1986, Why are marine magnetic anomalies suppressed over sedimented spreading centers?: Geology, v. 14, p. 651–654.

Lonsdale, P.F., Bischoff, J.L., Burns, V.M., Kastner, M., and Sweeney, R.E., 1980, A high-temperature hydrothermal deposit on the seabed at a Gulf of California spreading center: Earth and Planetary Science Letters, v. 49, p. 8–20.

Macdonald, K.C., 1986, The crest of the Mid-Atlantic Ridge: Models for crustal generation processes and tectonics, *in* Vogt, P.R., and Tucholke, B.E., eds., The geology of North America, Volume M: The Western North Atlantic Region: Boulder, Colorado, Geological Society of America, p. 51–68.

Macdonald, K.C., Miller, S.P., Huestis, S.P., and Spiess, F.N., 1980, Three dimensional modeling of a magnetic reversal boundary from inversion of Deep-Tow magnetics: Journal of Geophysical Research, v. 85, p. 3670–3680.

Macdonald, K.C, Miller, S.P., Luyendyk, B.P., Atwater, T.M., and Shure, Loren, 1983, Investigation of a Vine-Matthews magnetic lineation from a submersible: The source and character of marine magnetic anomalies: Journal of Geophysical Research, v. 88, p. 3403–3418.

Marshall, Monte, and Cox, Allan, 1972, Magnetic changes in pillow basalt due to sea floor weathering: Journal of Geophysical Research, v. 77, p. 6469–6469.

Masson, D.G., Wilson, D.S., Cacchione, D.A., and Drake, D.E., 1988, Tectonic evolution of Gorda Ridge inferred from sidescan sonar images: Marine Geophysical Researches, v. 10, p. 191–204.

McManus, D.A., and others, eds., 1970, Initial reports of the Deep Sea Drilling Project: Washington, U.S. Government Printing Office, v. 5, 827 p.

Miller, S.P., 1977, The validity of the geological interpretation of marine magnetic anomalies: Geophysical Journal of the Royal Astronomical Society, v. 50, p 1–21.

Moore, G.W., 1970, Sea-floor spreading at the junction between Gorda Rise and Mendocino Ridge: Geological Society of America Bulletin, v. 81, p. 2817–2824.

Moore, G.W., and Sharman, G.F., 1970, Summary of scan Site 4, *in* McManus, D.A., and others, eds., Initial reports of the Deep Sea Drilling Project: Washington, U.S. Government Printing Office, v. 5, p. 761–773.

Morton, J.L., and Fox, C.G., Structural setting and interaction of volcanism and sedimentation at Escanaba Trough: Geophysical results, *in* Morton, J.L., Zierenberg, R.A., and Reiss, C.A., eds., Geologic, hydrothermal, and biologic studies at Escanaba Trough, Gorda Ridge, offshore northern California: U.S. Geological Survey Bulletin 2022, chapter 2 (this volume).

Morton, J.L., Holmes, M.L., and Koski, R.A., 1987a, Volcanism and massive sulfide formation at a sedimented spreading center, Escanaba Trough, Gorda Ridge, northeast Pacific Ocean: Geophysical Research Letters, v. 14, p. 769–772.

Morton, J.L., Koski, R.A., Normark, W.R., and Ross, S.L., 1990, Distribution and composition of massive sulfide deposits at Escanaba Trough, southern Gorda Ridge, *in* McMurray, G.R., ed., Gorda Ridge: A seafloor spreading center in the United States' Exclusive Economic Zone: New York, Springer-Verlag, p. 77–92.

Morton, J.L., Normark, W.R., Ross, S.L., Koski, R.A., Holmes, M.L., Shanks, W.C., III, Zierenberg, R.A., Lyle, M., and Benninger, L.M., 1987b, Preliminary report, cruises L1-86-NC and L2-86-NC, Escanaba Trough, Gorda Ridge: U.S. Geological Survey Open-File Report 87-375-A, 20 p.

Morton, J.L., Zierenberg, R.A., and Reiss, C.A., Geologic, hydrothermal, and biologic studies at Escanaba Trough: An introduction, *in* Morton, J.L., Zierenberg, R.A., and Reiss, C.A., eds., Geologic, hydrothermal, and biologic studies at Escanaba Trough, Gorda Ridge, offshore northern California: U.S. Geological Survey Bulletin 2022, chapter 1 (this volume).

Normark, W.R., Gutmacher, C.E., Zierenberg, R.A., Wong, F.L., and Rosenbauer, R.J., Sediment fill of Escanaba Trough, *in* Morton, J.L., Zierenberg, R.A., and Reiss, C.A., eds., Geologic, hydrothermal, and biologic studies at Escanaba Trough, Gorda Ridge, offshore northern California: U.S. Geological Survey Bulletin 2022, chapter 6 (this volume).

Parker, R.L., and Huestis, S.P., 1974, The inversion of magnetic anomalies in the presence of topography: Journal of Geophysical Research, v. 79, p. 1587–1593.

Riddihough, R.P., 1980, Gorda plate motions from magnetic anomaly analysis: Earth Planetary Science Letters, v. 51, p. 163–170.

Ross, S.L., and Zierenberg, R.A., Volcanic geomorphology of the SESCA and NESCA sites, Escanaba Trough, *in* Morton, J.L., Zierenberg, R.A., and Reiss, C.A., eds., Geologic, hydrothermal, and biologic studies at Escanaba Trough, Gorda Ridge, offshore northern California: U.S. Geological Survey Bulletin 2022, chapter 8 (this volume).

Silver, E.A., 1971, Tectonics of the Mendocino triple junction: Geological Society of America Bulletin, v. 82, p. 2965–2978.

Smith, G.M., 1985, Source of marine magnetic anomalies: Some results from DSDP Leg 83: Geology, v. 13, p. 162–165.

Solano-Borrego, A.E., 1982, Microseismicity on the Gorda Ridge: Corvallis, Oregon State University, M.S. thesis.

Stoddard, P.R., 1987, A kinematic model for the evolution of the Gorda plate: Journal of Geophysical Research, v. 92, p. 11,524–11,532.

Talwani, Manik, and Heirtzler, J.R., 1964, Computation of magnetic anomalies caused by two dimensional bodies of arbitrary shape, *in* Parks, G.A., ed., Computers in the mineral industries, Part 1: Stanford, California, Stanford University Publications Geological Sciences, v. 9, p. 464–480.

Talwani, Manik, Worzel, J.L., and Landisman, M., 1959, Rapid gravity computations for two-dimensional bodies with application to the Mendocino submarine fracture zone: Journal of Geophysical Research, v. 64, p. 49–59.

Tivey, M.A., and Johnson, H.P., 1987, The central anomaly high: Implications for ocean crust construction and evolution: Journal of Geophysical Research, v. 92, p. 12,685–12,694.

Vallier, T.L., Harold, P.J., and Girdley, W.A., 1973, Provenances and dispersal patterns of turbidite sand in Escanaba Trough, northeastern Pacific Ocean: Marine Geology, v. 15, p. 67–87.

Vine, F.J., 1966, Spreading of the ocean floor: New evidence: Science, v. 154, p. 1,405–1,415.

Wilde, P., Chase, T.E., Holmes, M.L., Normark, W.R., Thomas, J.A., McCulloch, D.S., and Kulm, L.D., 1978, Oceanographic data off northern California-southern Oregon, 40°–43°N including the Gorda deep-sea fan: Berkeley, Lawrence Berkeley Laboratories Publication 251, scale 1:815,482.

Wilson, D.S., 1986, A kinematic model for the Gorda deformation zone as a diffuse southern boundary of the Juan de Fuca Plate: Journal of Geophysical Research, v. 91, p. 10,259–10,270.

———1989, Deformation of the so-called Gorda plate: Journal of Geophysical Research, v. 94, p. 3065–3075.

Zierenberg, R.A., Koski, R.A., and Shanks, W.C., 1988, Preliminary results of ALVIN dives on active sediment-hosted massive sulfide deposits in the Escanaba Trough [abs.]: Eos, Transactions American Geophysical Union, v. 69, p. 1488.

Zierenberg, R.A., Morton, J.L., Koski, R.A., and Ross, S.L., Geologic setting of massive sulfide mineralization in the Escanaba Trough, *in* Morton, J.L., Zierenberg, R.A., and Reiss, C.A., eds., Geologic, hydrothermal, and biologic studies at Escanaba Trough, Gorda Ridge, offshore northern California: U.S. Geological Survey Bulletin 2022, chapter 10 (this volume).

Chapter 6. Sediment Fill of Escanaba Trough

By William R. Normark, Christina E. Gutmacher, Robert A. Zierenberg, Florence L. Wong, *and* Robert J. Rosenbauer[1]

CONTENTS

ABSTRACT

The turbidite-sediment fill of Escanaba Trough distinguishes this segment from the rest of the Gorda Ridge axial valley and shows clear evidence for interaction with hydrothermal fluids that form the observed massive sulfide deposits at the sea floor. This conclusion is supported by reexamination of the sediment and chemical data from Deep Sea Drilling Project Site 35 and description of 41 (of a total of 69) core sections not examined by the shipboard party. In addition, descriptions and subsample data from 34 short gravity and piston cores taken mostly in or near areas of known sea-floor mineral deposits document (1) hydrothermal alteration of turbidite mud (locally to chlorite), (2) hydrothermal mineralization within porous sandy turbidite units, and (3) the presence of massive-sulfide talus debris. The source of the turbidite-sediment fill includes the Columbia River drainage basin and the Klamath Mountains of southern Oregon and northern California. Conservative estimates of the age of the ocean crust underlying the floor of Escanaba Trough give sediment accumulation rates for the Pleistocene that are more than an order of magnitude greater than for the Holocene.

INTRODUCTION

The youngest or "zero-age" (meaning that under assumptions of continuous active spreading the axial zone includes very recent new volcanic material) crust along the axis of the Gorda Ridge spreading center in Escanaba Trough is overlain by a thick cover of dominantly terrigenous sediment, which locally exceeds a thickness of 500 m (Moore, 1970; Moore and Sharmin, 1970; Vallier and others, 1973; Clague and Holmes, 1987; Morton and others, 1987a; Morton and Fox, chap. 2, this volume). Reflection-profiling and deep-tow geophysical studies conducted in the late 1960's provided a general knowledge of the structure and geometry of the sediment fill of the trough (Atwater and Mudie, 1968, 1973; Moore, 1970). Drilling at Deep Sea Drilling Project (DSDP) Site 35 in Escanaba Trough was the first attempt to study the environment of sediment-covered, zero-age oceanic crust, but coring stopped short of the basement (McManus and others, 1970).

Until Site 35 was drilled, little was known about the nature of the sediment fill itself, except for the inference (based on the flat-lying sea floor and subparallel reflecting horizons) that a significant part of the fill was composed of turbidite deposits (Atwater and Mudie, 1968, 1973; Moore, 1970). The sediment in Escanaba Trough could have come from source areas ranging from northern

[1] U.S. Geological Survey, Menlo Park, California.

California (Eel and Klamath rivers) to as far away as the Columbia River basin (fig. 6.1). Several studies have observed that there is a clear pathway, at least at present, for sediment to reach Escanaba Trough from Astoria fan, which has received material from the Columbia River drainage area (Nelson and others, 1968; Moore, 1970;

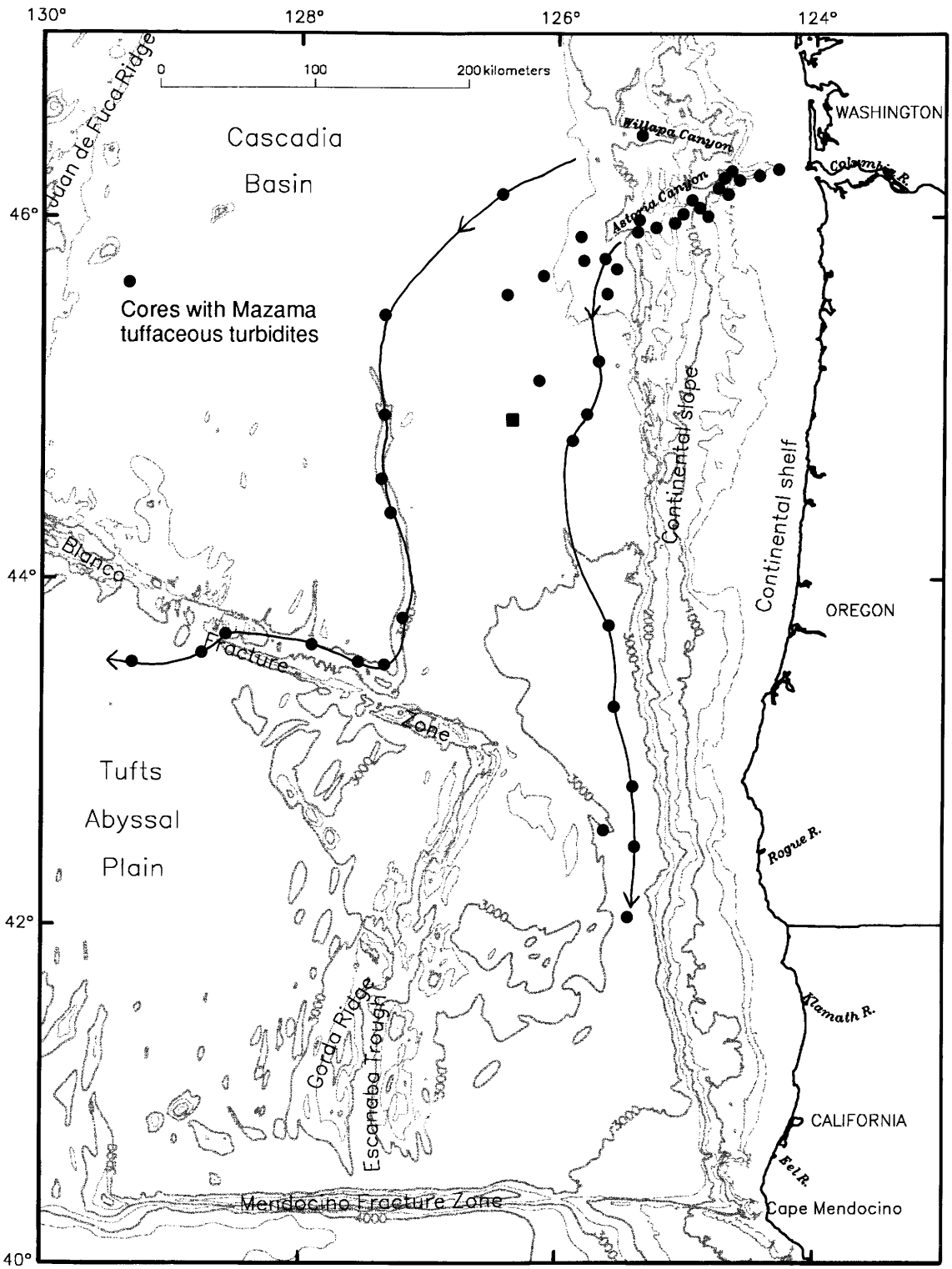

Figure 6.1. Location map showing possible sources and pathways for terrigenous sediment to move into Escanaba Trough (modified from Nelson and others, 1988). Dots denote sites where cores contain tuffaceous turbidites derived from Mount Mazama. Contour interval is 500 m.

Atwater and Mudie, 1973; Kulm and others, 1973; Nelson, 1976; Clague and Holmes, 1987). Vallier and others (1973) concluded that there may be a substantial component of Columbia River sediment in Escanaba Trough based on petrographic analysis of a limited number of sand samples from the cored intervals in DSDP Site 35. Recent long-range side-looking sonar coverage of the Exclusive Economic Zone (EEZ) off the Western United States includes the entire Gorda Ridge and provides additional support for the concept that source areas could include any drainage basin between the Columbia River and Cape Mendocino (EEZ-SCAN 84 Scientific Staff, 1986; Masson and others, 1988).

Beginning in 1983, the sediment fill of Escanaba Trough was sampled as part of a program to study the hydrothermal mineralization along the Gorda Ridge spreading axis. Short (0.5 to 5.5 m long) gravity cores and a very limited number of piston cores are available from cruises in 1985, 1986, and 1989 (fig. 6.2). These samples are herein referred to as "surficial" cores to emphasize that nearly all of the gravity and piston cores are restricted to the upper 1 percent or less of the average thickness of sediment fill in Escanaba Trough and, therefore, are only representative of the most recent depositional processes in the area.

ACKNOWLEDGMENTS

The Gorda Ridge shipboard activities over the years have involved many participants, without whose help we would not have the comparative wealth of core material to present here. We thank the ships' crews and scientific staff for their support, commonly under less than ideal weather conditions, during cruises L6-85-NC; L1-, L2-, and L3-86-NC; and TUL-89D. J.L. Morton and S.L. Ross assisted with the descriptions of cores from L1- and L2-86-NC operations. T. Nelson kindly provided core descriptions for the L3-86-NC cruise. G.G. Zuffa and P. Okita assisted in the description of the DSDP cores in August 1988. P. Swenson provided invaluable training to allow us to utilize Macintosh applications for core log compilations. The manuscript was reviewed by R. Karlin and D. E. Drake.

PURPOSE

This chapter presents a compilation of much of the available data on the composition, age, sources, and depositional processes of the sediment within Escanaba Trough. This compilation is done to provide a better understanding of the sediment that hosts the mineral deposits (and provides the pathways for fluids forming these deposits) described elsewhere in this volume. Much of the data included has not been presented elsewhere. Some of the surficial cores have been described in varying detail by different groups of investigators only in internal reports (Karlin and Lyle, 1986; Morton and others, 1987b; Karlin, 1989). The chapter for Site 35 of the Initial Reports for DSDP Leg 5, as well as all investigations of the sediment fill based on the described drilling results, include data from only 28 of the 69 core sections that were recovered (McManus and others, 1970). We include summary logs in appendix A of the remaining core sections that were opened more than a decade after the cruise report was published. Summary logs (appendix B) as well as sediment and pore-water analyses are also provided for the surficial core samples collected during the studies of the hydrothermal-vent areas.

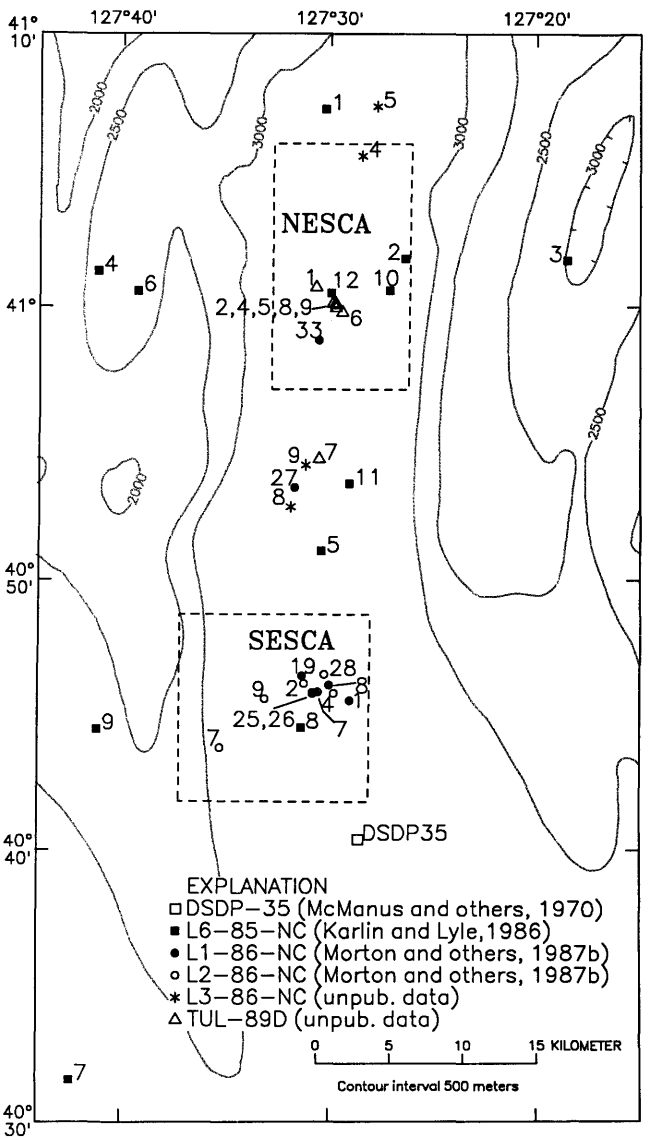

Figure 6.2. Location of cores taken in Escanaba Trough. Study areas: NESCA, northern Escanaba Trough (see fig. 6.9); SESCA, southern Escanaba Trough (see fig. 6.10). Bathymetry from Wilde and others (1978). Hachures indicate area of closed low.

The data, including review of the methods used, are presented in two sections; the first deals with DSDP Site 35 and the second with all the surficial cores.

SITE 35

METHODS

When Site 35 was drilled in late April and early May 1969, the limited size of the shipboard scientific party precluded the normal operation of splitting and describing all core sections immediately after recovery (T.L. Vallier, oral commun., 1988). As a result, the Initial Reports volume for Leg 5 contains core descriptions, photographs, and subsample data for only 28 of the 69 sections recovered in the 17 cores. The remaining 41 sections eventually were split when the entire set of samples from DSDP Leg 5 were rephotographed more than 10 years after they were taken. These recently split sections, however, were not described until August 1988, after our inquiries to the Ocean Drilling Program (ODP) could find no record of any earlier logs of these newly opened intervals.

We publish here as table 6.1 a revised summary of the cored intervals and extent of recovery for Site 35, modified from table 1 of McManus and others (1970). This revision is necessary because the core sections found in the DSDP collection did not always match the site-chapter tabulations. In addition, table 6.1 shows which sections were described by the shipboard scientific party; it should be emphasized that existing reports of the deeper section at Site 35 data are based on physical descriptions and subsamples from only 7 of the 29 core sections recovered from the bottom 100 m of the hole.

The source of the core descriptions used for this report is summarized in a chart (fig 6.3). Direct comparison of the original shipboard descriptions with those we did in 1988 is difficult because of marked changes in the condition of the sediment during the nearly 20 years that had passed. We reexamined nine of the core sections described by the shipboard scientific party (fig. 6.3) in an attempt to calibrate the differences in appearance and condition of the sediment between 1969 and 1988. This attempt generally was not successful because (1) the color change was extreme and not consistent in trend because the mud sequences exhibited a wide variation in degree of desiccation, (2) the sand-rich sequences were completely dried and handling of the cores had resulted in mixing the sandy intervals throughout the length of the liner section, and (3) the technique for description of the cores used in 1988 follows the current guide for sedimentologists involved in the ODP (Mazzullo and Graham, 1987) and is not always consistent with the original descriptions. There was insufficient time for redescribing all of the core sections in 1988, but we did attempt to confirm the presence of sand beds in all sections so reported by the shipboard scientific party.

Table 6.1. Summary of Site 35, Deep Sea Drilling Program.

[Modified from table 1 of McManus and others (1970) to correct errors in original (changes are shown in **bold** type). Sections described by shipboard scientific party also are shown in **bold** type, and sections described in 1988 are given in plain type (maximum of six sections for any given core excluding core-catcher sample). See figure 6.3]

Date (1969)	Core	Depth below sea floor (m)	Core cut (m)	Recovery (percent)	Sections
29 April	1	0-9	9.1	100	**1 2 3 4 5** 6
	2	39-48	9.1	100	**1 2 3 4 5 6**
30 April	3	79-88	9.1	100	1 2 3 4 5 6
	4	88-97	9.1	33	1 2
	5	97-**106**	9.1	**100**	1 2 3 4 5 6
	6	157-166	9.1	100	1 **2 3 4 5 6**
	7	233-**242**	**9.1**	**69**	1 2 **3 4**
	8	256-261	4.6	27	**1**
1 May	9	280-289	9.1	43	**1 2 3**
	10	289-298	9.1	13	1
	11	298-307	9.1	90	1 2 3 4 5 **6**
	12	323-**332**	**9.1**	**87**	1 2 3 4 5 **6**
2 May	13	345-353	**7.5**	**95**	1 2 3 **4** 5
	14	354-362	7.6	60	1 2 3 **4**
	15	362-371	9.1	70	1 2 3 **4**
	16	372-382	9.1	33	1 **2**
	17	382-390	7.6	8	**1**

We compiled a summary section for the entire Site 35 sequence (fig. 6.4), presented here together with the accompanying electric logs presented in the Initial Reports (McManus and others, 1970). A rough estimate of the relative proportion of the sediment section in the cored intervals that is characterized by (1) the presence of sand even in minor amounts, (2) the presence of silty mud, or (3) generally clayey mud is represented graphically in figure 6.4. This estimate cannot be interpreted as a typical sand/silt/clay ratio, but is given to indicate the general presence of coarser grained intervals; recovery of unconsolidated sandy sequences was generally very poor for all DSDP sites. Our newly compiled and updated lithologic summary of the sediment sequence (app. A) provides the basis for reexamining the observations reported by McManus and others (1970) and later scientific reports based on Site 35 studies.

CORE DATA

Only about 100 m of the 390-m-deep hole was sampled by coring (fig. 6.4; table 6.1). Samples are especially sparse in the interval from 106 to 280 m below the sea floor. On the basis of the cores recovered, only one interval with sand-size sediment commonly present is documented: cores 3 to 6, from 80 to 160 m depth (fig.

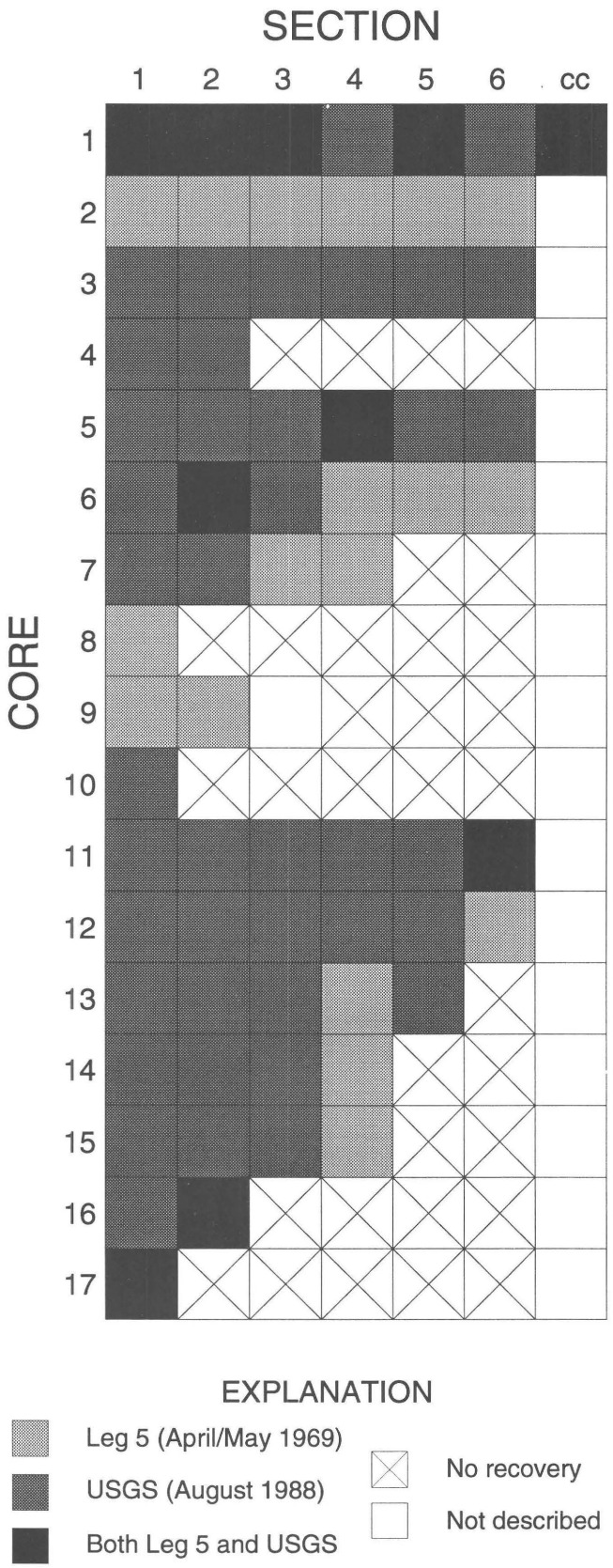

Figure 6.3. Summary of core sections recovered and source of descriptions used for Site 35, Deep Sea Drilling Project; CC, core catcher.

6.4; app. A). Because only 2 of 17 sections from these four cores were described by the shipboard party, the extent of this interval with some interbedded sand was poorly documented, although Vallier and others (1973) interpreted the electric logs to suggest that both cores 4 and 5 are generally sandy (see their fig. 3). This interval with more common sand-sized material, like most of the other coarser grained units cored at Site 35, shows a fair degree of core disturbance; as a result, few distinct bedding contacts are preserved, and the presence of sand and silt beds commonly is based on the recognition of blebs and streaks of coarser sediment within a generally muddy section. Much sand is probably lost during the coring disturbance, so it is not possible to construct a true sand to mud ratio for this site.

With the exception of a sequence of thin-bedded turbidite units in core 10 (with a drilled interval of 9 m but only 1 m of recovery) and the lowest one-third meter of

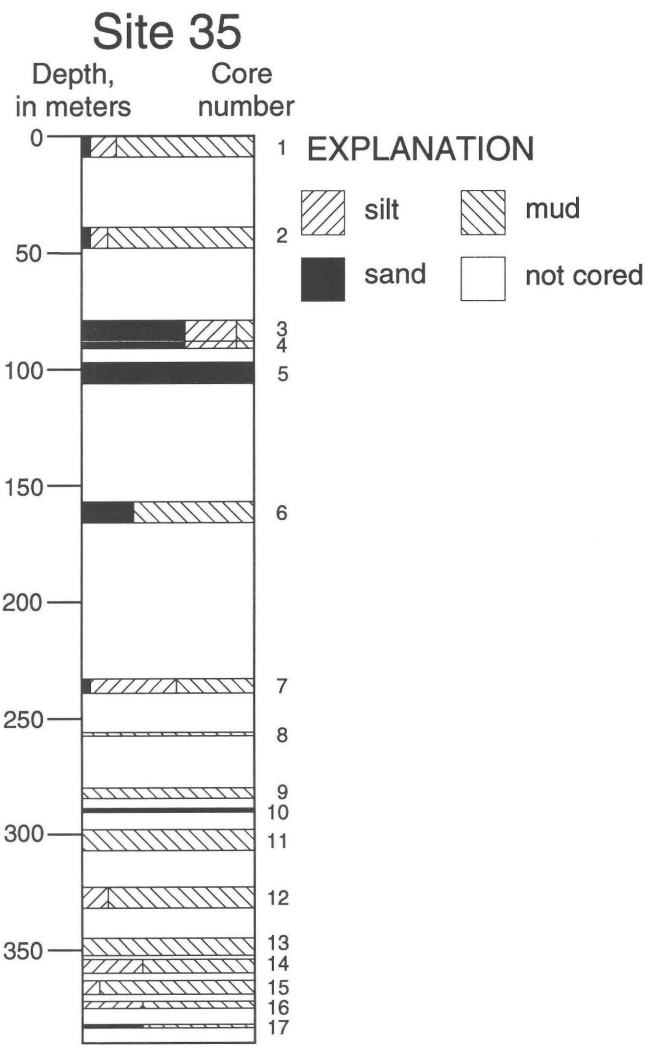

Figure 6.4. Summary core log for Site 35, Deep Sea Drilling Project. Interval between core recovery shown in white. Extent of patterning within cored intervals is proportionally to length of core with sand present, silt present, or mud only.

core 17, sand recovery is rare in the lower 200 m of the hole (app. A). Silty clay intervals are slightly more common (app. A), but the bulk of the cores we described in 1988 that were not examined onboard during the drilling on station contain little sand. Thus, we do not see evidence for a generally coarser sequence in the bottom 100 m of the hole as suggested by Vallier and others (1973; compare their fig. 3 with our fig. 6.4 and app. A).

One of the more impressive coarse-grained units, however, is just below 350 m depth. The upper section of core 14 was almost entirely a thick bed of very well sorted fine sand and coarse silt that probably represents the distal deposit of a large-volume turbidity current. A sample from 40 to 43 cm depth in section 1 of core 14 consists mostly of quartz, feldspar, and minor pyrite with the proportion of light grains similar to that of other samples higher in the hole (see later section on the mineralogic study of surficial cores). The pyrite occurs as free crystals or partially coating the quartz, feldspar, or occasional carbonate grains. Besides the pyrite, the heavy fraction consists of minor or trace amounts of biotite, epidote, etched garnet, sphene, augite, and tourmaline. There are too few nonopaque grains to determine this sample's relationship to the other heavy mineral samples.

Examination of the previously unopened core sections confirmed the shipboard observation that below 260 m subbottom depth, the muds are generally more calcareous than in the upper part of the hole.

PORE-WATER CHEMISTRY

Manheim and others (1970) provided data on pore-fluid chemistry from Escanaba Trough sediment samples recovered at DSDP Site 35 (table 6.2). The strong vertical gradients observed in the pore-fluid chemistry were generally attributed by them to diagenetic interaction in the sediment, but were not further explained.

The pore-fluid gradients are interpreted herein as an indication of high-temperature seawater-sediment interaction. Major-element chemistry (figs. 6.5–6.7) and minor-element chemistry of pore water (fig. 6.8) are plotted here as a function of depth within the sediment section. For comparison, the values for seawater are plotted at zero depth (sea floor), and the end-member values for hydrothermal-vent fluid measured at the Northern Escanaba Trough (NESCA) site (Campbell and others, chap. 11, this volume) are plotted at 500 m, the approximate depth of the sediment-basalt interface. The trend of increasing sodium and chloride of pore fluid with depth is consistent with mixing of seawater with a fluid of salinity similar to Escanaba Trough vent fluid (fig. 6.5). The lowermost pore-fluid sample also shows increased potassium and calcium, consistent with mixing of vent fluid with a pore fluid derived from seawater (fig 6.6). Pore fluid from the upper part of the hole generally shows an inverse correlation of potassium and calcium. The decrease in potassium between 237 m and 350 m could result from the

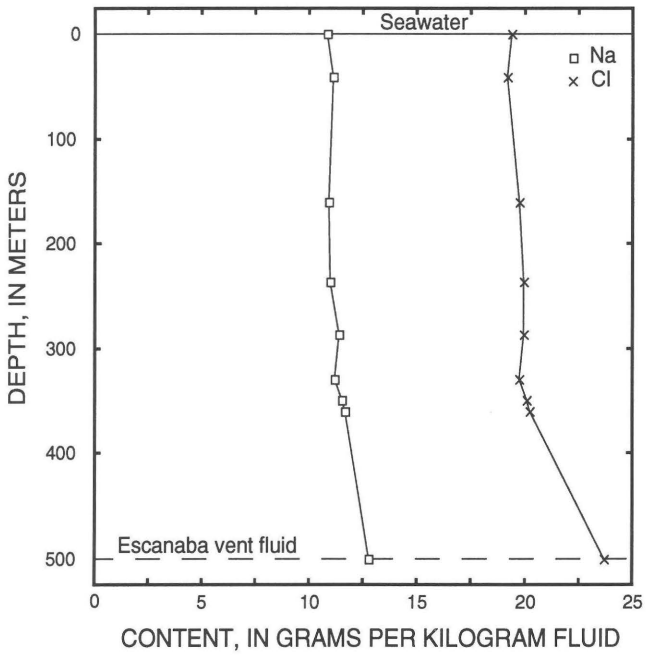

Figure 6.5. Pore-water salinity as a function of depth from Deep Sea Drilling Project Site 35 (adapted from Manheim and others, 1970). Escanaba Trough vent-fluid composition (Campbell and others, chap. 11, this volume) is plotted at 500 m depth, the approximate sediment-basalt interface, for comparison.

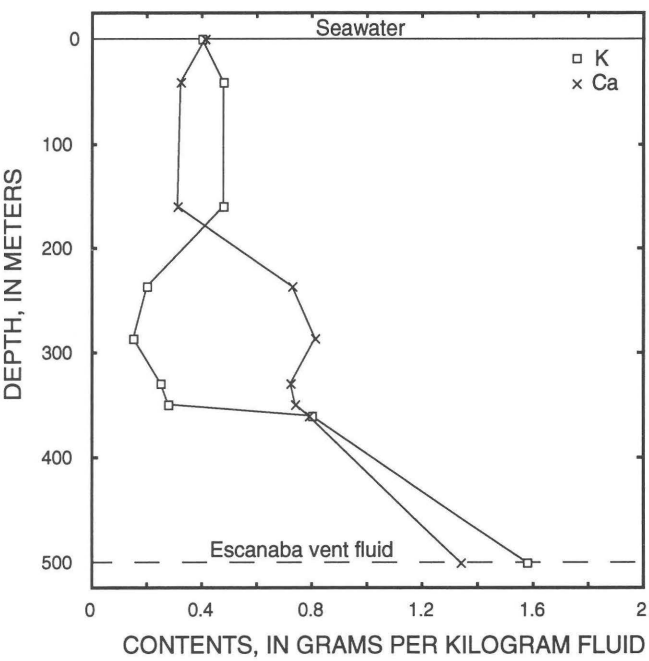

Figure 6.6. K and Ca composition of pore-water as a function of depth for samples from Deep Sea Drilling Project Site 35 (adapted from Manheim and others, 1970).

Table 6.2. Deep Sea Drilling Project Site 35 pore-water chemistry.

[Values in ppm, alkalinity (Alk) in meq/kg, adapted from Manheim and others (1970)]

Depth (m)	Na	K	Ca	Mg	Cl	SO_4	Alk	Li	B	Sr	Ba	Si
41	11,100	480	320	1,230	19,200	1,640	17.6	0.07	5	6.9	0.09	—
160	10,900	480	310	950	19,700	340	7.1	.13	3	9.2	4.6	12.0
237	11,000	200	730	600	19,900	210	4.7	.72	3	13	5.4	5.9
287	11,400	150	810	460	19,900	200	2.9	.44	3	17	6.2	3.4
330	11,200	250	720	370	19,700	200	2.8	.71	7	14	6.2	5.5
350	11,500	280	740	310	20,100	110	3.9	.79	10	19	7.7	5.6
360	11,700	800	790	220	20,200	210	4.2	.92	9	20	8.1	9.9

diagenetic conversion of smectite to illite in response to increasing temperature with depth (Perry and Hower, 1972). Magnesium and sulfate contents of the pore fluid decrease with depth (fig. 6.7), consistent with high-temperature interaction of saline fluid with the sediment. Magnesium and sulfate depletion is caused by formation of magnesium-rich silicate alteration phases and precipitation of anhydrite (Rosenbauer and others, 1983; Thornton and Seyfried, 1985; Zierenberg and Shanks, chap. 14, this volume). Magnesium metasomatism and accompanying production of hydrogen ions causes hydrolitic alteration of silicate minerals that releases cations to the fluid phase. Minor-element concentrations are also elevated in the pore fluid due to hydrothermal alteration of the sediment (fig. 6.8).

The composition of Escanaba Trough hydrothermal fluid is strongly influenced by sediment alteration (Campbell and others, chap. 11, this volume). Detrital minerals from the lower section of DSDP Site 35 show evidence of hydrothermal dissolution (T.L. Vallier, oral commun., 1988). The pore-fluid chemistry from Site 35 appears to reflect both diagenetic reactions in the sediment occurring at elevated temperature and influx of higher salinity hydrothermal fluid derived by high-temperature alteration of sediment and (or) basalt. Site 35 was drilled approximately 8 km southeast of the SESCA hydrothermal deposits and 35 km south of the NESCA site where active venting of hydrothermal fluid was subsequently discovered.

A covering of sediment with relatively low cross-stratal permeability reduces the cooling rate of the oceanic

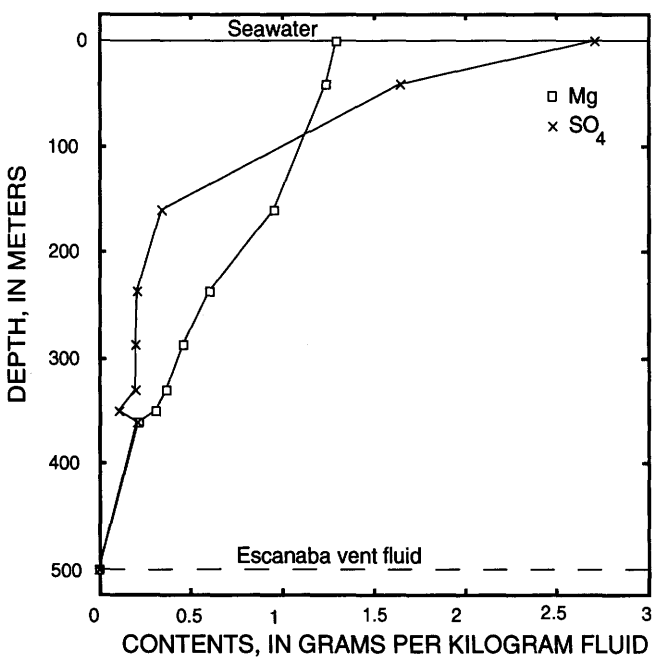

Figure 6.7. Mg and SO_4 composition of pore-water as a function of depth for samples from Deep Sea Drilling Project Site 35 (adapted from Manheim and others, 1970).

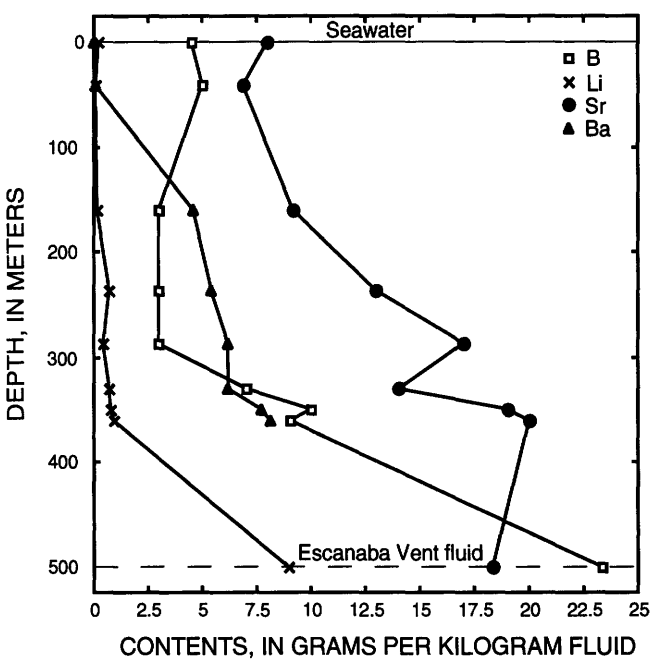

Figure 6.8. Minor-element composition as a function of depth for pore-water samples from Deep Sea Drilling Project Site 35 (adapted from Manheim and others, 1970).

crust by hydrothermal circulation. The low thermal conductivity of sediment relative to basalt and the intrusion of basalt into the sediment column results in increased temperature in the upper part of the basalt relative to sediment-free ridges. High-temperature alteration of sediment may be occurring throughout the sediment-covered areas within Escanaba Trough, rather than being limited to known sites of hydrothermal discharge. The lower part of the sediment section represents a large potential reservoir for hydrothermal fluids. The volcanic centers, which are the known sites of hydrothermal deposits, provide both thermal and topographic foci for hydrothermal discharge. The large volume of the hydrothermal alteration zone and of the potential reservoir for hydrothermal fluids, coupled with efficient focusing of hydrothermal discharge, results in long-lived, high-volume hydrothermal systems capable of forming the large sulfide deposits observed in Escanaba Trough.

SURFICIAL CORES

METHODS

The gravity and piston cores available for this study were collected during a series of cruises by the U.S. Geological Survey and the Geological Survey of Canada from 1985 to 1989 (figs. 6.2, 6.9, and 6.10). Table 6.3 lists the cruises, dates, core length, source of description used in this report, and certain ancillary observations that are available. Specific subsample intervals are given in the data sections that follow. The lithologic logs for cruises L1- and L2-86-NC (app. B) show that whole-round samples were taken for pore-water analysis (see below) and for heavy and light hydrocarbon analyses (HHC and LHC, respectively; see Kvenvolden and others, chap. 15, this volume). Different sets of cores were described at various times after the cores were collected by different personnel, thus there is a lack of consistency among the sets of descriptions, and the data are presented in separate figures (app. B).

Data obtained from subsamples of the surficial cores reported herein are generally restricted to three subjects: (1) coarse-fraction composition, including both light and heavy mineral components, (2) fine-fraction (mud) composition based on X-ray diffraction measurements, and (3) pore-water composition for a limited number of samples. The techniques employed are described below. Other data obtained from the cores, including hydrocarbon composition and magnetic susceptibility logs, are reported in other chapters in this volume.

LIGHT AND HEAVY MINERAL SEPARATION

Twenty-four subsamples (volume 1 to 2 cm^3) were taken from sediment layers initially described as either "sandy" or "silty." By decantation and sieving, three grain-size fractions were retained, 30 to 63 μm, 63 to 250 μm, and greater than 250 μm (table 6.4).

Heavy and light mineral components separated from the 63- to 250-μm fraction in tetrabromoethane (specific gravity 2.96) were permanently mounted in piccolyte (refractive index 1.52) to determine mineral abundance by point count. Counts of more than 350 points were made for the heavy minerals and about 300 points for the light minerals.

Not all samples yielded enough material in this fraction for heavy mineral separation, and a few samples had insufficient nonopaque grains to justify point counting. Compositions of the uncounted samples were estimated through low-power (about 30×) binocular microscopy. The >250-μm fraction was also examined by binocular microscopy to determine qualitative mineral abundances. Both the 63- to 250-μm and greater than 250-μm fractions were examined for foraminifers (Quinterno, chap. 18, this volume). The 30- to 63-μm fraction was not examined further. Other material obtained as by-products of subsampling for foraminifers or separated for magnetic susceptibility were also examined for mineral occurrences.

FINE SEDIMENT FRACTION

Sediment samples of the dominantly muddy intervals were examined by X-ray diffraction to determine the bulk and clay-fraction mineralogy. Samples for clay mineralogy were repeatedly dispersed in deionized water by ultrasonic probe and settled by centrifugation. Smear mounts on glass slides were prepared from the finest grain-size fraction (top layer of centrifuged samples) and were examined by X-ray diffraction three times: once dry, once after treatment with ethylene glycol, and again after heating to 400°C.

PORE-WATER CHEMISTRY

Pore-water samples were extracted by hydraulically squeezing the sediment in the whole round core sections in a refrigerated laboratory environment; the samples are limited to cores from cruise L2-86-NC (app. B). The fluid extracted was filtered sequentially through 0.45-μm and 0.2-μm membrane filters. Major and minor cations were determined by atomic absorption spectroscopy, except for sodium, which was calculated by charge balance. The pH was determined by a Ross-type combination electrode. Sulfate was determined by ion-liquid chromatography. Silica was determined colorimetrically by the molybdate blue complex. Total inorganic carbon (C_T=CO_2+$H_2CO_3^-$ +CO_3^{2-}) was determined using an IR analyzer. Chloride was determined potentiometrically by titration.

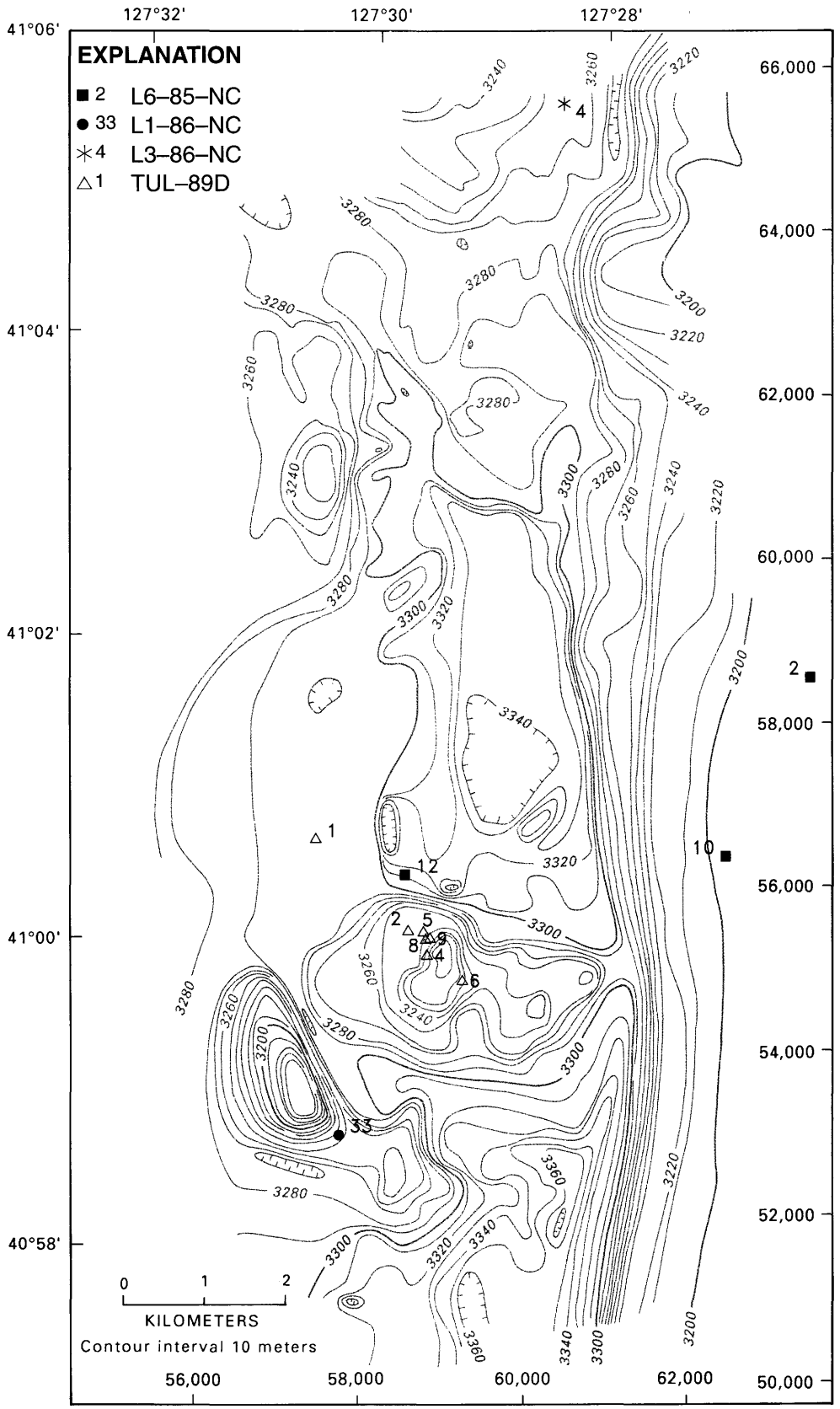

Figure 6.9. Bathymetry of NESCA area (Morton and others, 1987b; Morton and others, chap. 1, this volume), showing core locations. Numbers along right and bottom give coordinates of local transponder net (in meters). Hachures indicate area of closed low.

CORE DESCRIPTIONS AND ANALYSES

The cores taken during cruise L6-85-NC are from the main floor of Escanaba Trough and from the ridge areas both east and west of the trough (fig. 6.2). The core logs (app. B) are based on the core descriptions (without graphic logs) given in Karlin and Lyle (1986) and color photographs of the archive half taken later. These cores are dominantly mud with few silt and sand interbeds. The upper 27 cm of core L6-85-5G repeats the interval below, possibly as a result of local slumping.

The Karlin and Lyle (1986) report provides much useful data including detailed chemical profiles, whole-core magnetic-susceptibility profiles, and radiocarbon dating. The resulting age control allowed Karlin and Lyle (1986) to recognize the Pleistocene-Holocene boundary, which is generally correlated to color and compositional changes in the cores, and to date several turbidity-current units that might be relatively local events in the Northern (NESCA) and Southern Escanaba Trough (SESCA) study areas. In addition, they recognized several discrete intervals of hydrothermal activity that provide a mineral or chemical signal in

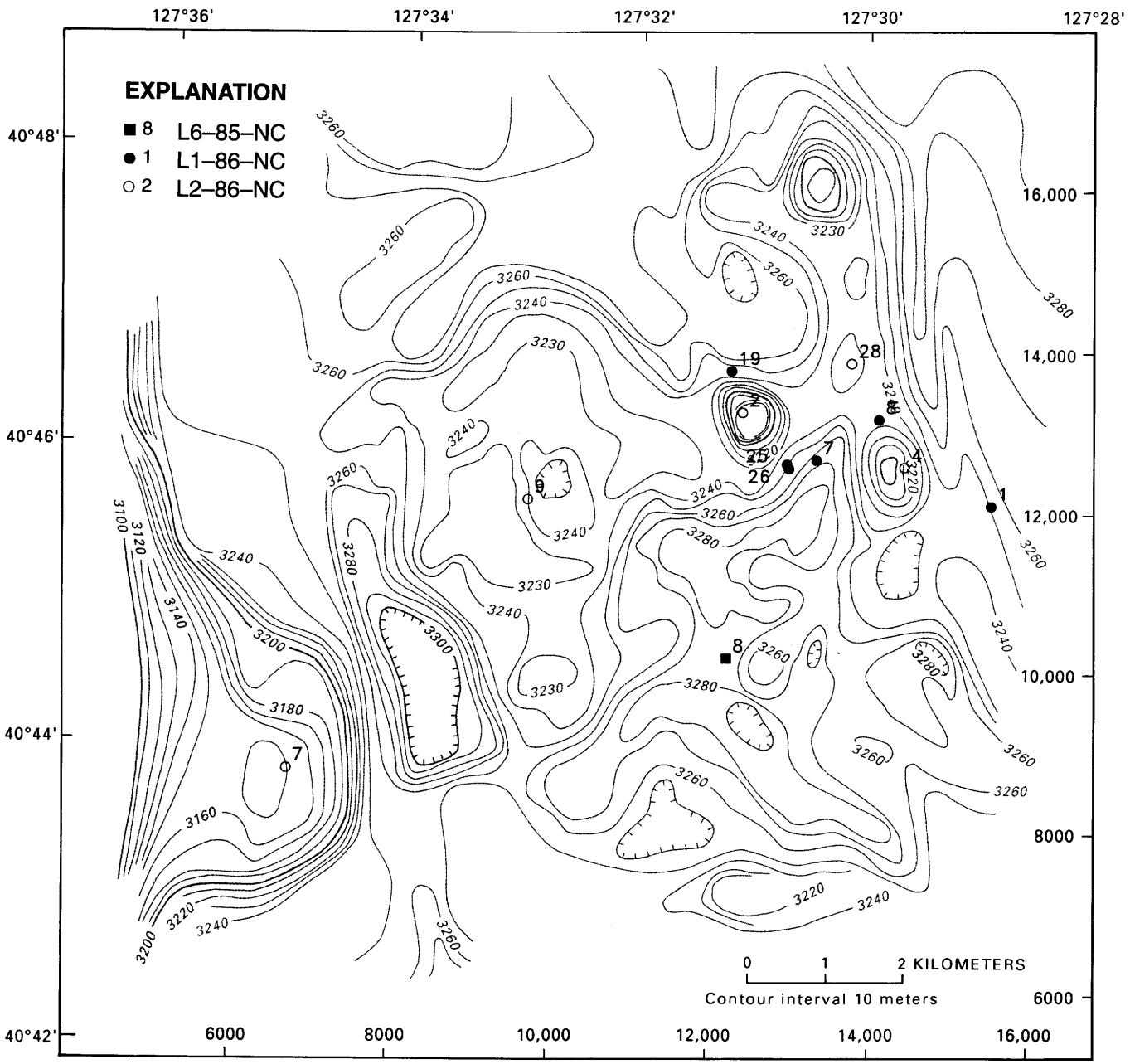

Figure 6.10. Bathymetry of SESCA area (Morton and others, 1987b; Morton and others, chap. 1, this volume), showing core locations. Numbers along right and bottom give coordinates of local transponder net (in meters). Hachures indicate area of closed low.

Table 6.3. Surficial cores from Escanaba Trough and adjacent ridge flanks.

[Cruise ID: L6-85-NC, L1-86-NC, L2-86-NC, and L3-86-NC refer to separate cruise legs of U.S. Geological Survey R/V *S. P. Lee* in 1985 and 1986; TUL-89D, 1989 cruise leg of R/V *Tully* used by Geological Survey of Canada. See figures 6.2, 6.9, and 6.10 for location of cores. Symbols as follows: GS1 and GS2, described by different groups of U.S. Geological Survey personnel; OSU, description adapted from Karlin and Lyle (1986); TN, description adapted from T. Nelson (written commun., 1989); na, not available. Checklists of three right-hand columns indicate that the following data exist for cores (but will not be presented in detail in this report): continuous flow-camera color photographs, X-radiographs, and profiles of magnetic susceptibility (see Karlin and Lyle, 1986; Karlin, 1989; Karlin and Zierenberg, chap. 7, this volume)]

Cruise ID	Core number	Length (cm)	Description by	Color photograph	X-radiograph	Magnetic susceptibility
L6-85-NC	1G	202	OSU			x
	2G	241	OSU			x
	3G	241	OSU			
	4G	3	na			
	5G	232.5	OSU			x
	6G	257	OSU			x
	7G	242	OSU			x
	8G	234	OSU			x
	9G	211	OSU			x
	10G	249	OSU			
	11K	31	na			
	12G	154	OSU			x
L1-86-NC	1G	273	GS1	x	x	x
	7G	233	GS1	x	x	x
	8G	197	GS1	x	x	x
	19G	255	GS1	x	x	x
	25G	227	GS1	x	x	x
	26G	239	GS1	x	x	x
	27G	105	GS1	x	x	x
	33G	124	GS1	x	x	x
L2-86-NC	2G	101	GS1	x	x	x
	4G	263	GS1	x	x	x
	7G	241	GS1	x	x	x
	9G	200	GS1	x	x	x
	28G	244	GS1	x	x	x
L3-86-NC	4G	143	TN		x	
	5G	62	TN		x	
	8G	92	TN		x	
	9G	101	TN		x	
TUL-89D	1P	63	GS2		x	
	2G	267	GS2		x	
	4G	277	GS2		x	
	5G	41	na			
	6G	187	GS2		x	
	7P	537	GS2		x	
	8G	10	GS2			
	9TR	50	GS2		x	

adjacent cores. The core logs (app. B) are synthesized to provide the closest possible match to core logs for samples taken on succeeding cruises and thus do not incorporate all these compositional details from Karlin and Lyle (1986).

Cores taken during the first two legs (L1- and L2-86-NC) of the 1986 cruise are represented by the most detailed lithologic logs (app. B). This detail is possible because (1) the cores were described immediately after being split, thus giving the best range of sediment color and contrast before oxidation and desiccation began; (2) both color photographs and X-radiographs were taken at the same time (see examples in figs. 6.11 and 6.12). The wide variety in sediment units recognized, however, also reflects the effects of local tectonic and hydrothermal activity.

Many of the cores from L1- and L2-86-NC record mass-wasting and turbidity-current depositional processes

Table 6.4. Grain-size and heavy mineral data of mineralogical samples.

[Silt content includes only 30- to 63-μm grains. Samples rich in clay minerals were not processed further. After heavy mineral separation, samples rich in opaque components were not counted]

Sample[a]	100 × sand/ sand+silt	Weight percent heavies (63–250 μm)	Comments
DSDP 35-14-1 40–43 cm	56	4.8	Pyrite-rich
L1-86 7G 124–126 cm	69	—	Clayey
L1-86 7G 211–212 cm	16	—	
L1-86 8G 52–53 cm	63	1.9	
L1-86 8G 150–151 cm	91	1.7	
L1-86 8G 175–176 cm	94	1.1	
L1-86 25G 48–49 cm	74	3.6	
L1-86 25G 119–120 cm	46	1.9	
L1-86 26G 33.5–35 cm	60	1.4	
L1-86 26G 40–41 cm	49	2.2	
L1-86 27G 29–30 cm	60	—	
L1-86 27G 64–65 cm	58	50.0	Metallic
L1-86 27G 72 cm	95	8.3	Metallic
L1-86 33G 47–49 cm	41	—	Clayey
L2-86 2G 72–74 cm	66	3.1	
L2-86 7G 235–237 cm	1	—	
L2-86 9G 106–107 cm	93	—	Clayey
TUL-89D 2G 94–95 cm	40	2.9	
TUL-89D 6G 25–26 cm	86	1.5	
TUL-89D 7P 8–9 cm	82	3.1	
TUL-89D 7P 24–25 cm	92	3.1	
TUL-89D 7P 42–43 cm	90	3.8	
TUL-89D 7P 240–242 cm	71	1.4	
TUL-89D 9T 12–14 cm	28	—	Micaceous

[a]Except for standard DSDP designation, sample identification includes cruise number (L1-86, L2-86, TUL-89D), core number and type (G, gravity; P, piston; T, trigger for piston), and sampling interval.

(app. B). Coarser (silty and sandy) turbidites commonly have erosive bases and irregular bed thicknesses. In a few cores, sand units are associated with mud-clast units of rounded mud balls in a mud or sandy-mud matrix (core L2-86-2G, app. B and fig. 6.12). We recognize turbidite-mud units on the basis of a distinctive mud color that is the same found where turbidite mud overlies graded sand and silt beds that generally have sharp, erosive bases. In X-radiographs, muddy turbidites commonly appear as well-laminated units that are overlain by more bioturbated pelagic(?) mud. Comparison of subtle differences in the texture of the nonturbidite mud units (porous versus nonporous) with the magnetic-susceptibility profiles from Karlin (1989) and Karlin and Zierenberg (chap. 7, this volume) suggests that the textural change commonly corresponds to the 11 ka boundary based on the Karlin and Lyle (1986) stratigraphy. Using this age assignment, it is clear that turbidity currents have entered or were generated within Escanaba Trough several times during the Holocene. Samples from the thicker, coarser sand beds were examined to determine the possible sources for these turbidity currents (see following section).

The cores obtained during the 1986 surveys provide information about both hydrothermal and tectonic activity. Core L2-86-9G (app. B) penetrated metalliferous sediment overlying talus (sand to pebble size) of massive-sulfide deposits; this, in turn, overlies a completely altered mud interval more than 1 meter thick. In the X-radiograph (fig. 6.12), the sulfide talus is observed to occur in two layers 8 and 12 cm thick separated by a more sandy interval of several centimeters. Core L1-86-27G terminates in bedded sand units containing hydrothermal mineralization products. In figure 6.11, the mineralized sand layers of core L1-86-27G show as reddish-brown intervals on the oxidized core surface, but in X-radiographs the mineralization is clearly observed to be confined to several thin intervals in this sandy section (compare core log of app. B with fig. 6.12; see below and Zierenberg and Shanks, chap. 14, this volume, for discussion).

Core L1-86-8G is a lighter gray color and has a more porous texture than normal mud. This core may contain mineralized and altered sediment that has been redeposited by a local mass flow. Pyrrhotite is common in the magnetic fraction of sediment samples from this core (Karlin and Zierenberg, chap. 7, this volume).

Local relative uplift is documented in core L1-86-33G, where an older clay unit has been exposed, probably through mass wasting from the edge of a sediment section from the trough floor uplifted during volcanic intrusion (Morton and Fox, chap. 2, this volume). This clay is markedly stiffer than in the other cores, and the oxidized zone at the top is thinner and of a different hue; both characteristics suggest different physical properties of this clay relative to the "normal."

The L3-86-NC core logs are based on unpublished descriptions provided by T. Nelson (app. B). Two of the cores (L3-86-4G and L3-86-5G), from the northern edge of the NESCA area, are dominantly mud with little internal structure or lithologic variation. The other two cores (L3-86-8G and L3-86-9G) are from the area between NESCA and SESCA (fig. 6.2) near core L1-86-27G, which terminated in turbidite sand beds with postdepositional sulfide-mineral precipitation; both of these cores have substantial sections of turbidite units but without signs of mineralization.

The cores taken in 1989 from the Canadian research vessel *Tully* were split onboard during the cruise. Several months later, the cores were shipped to Menlo Park where we attempted to describe them using the same criteria used for the L1- and L2-86-NC cores; X-radiographs were taken at this time. The core logs in appendix B show that we were unable to recognize the range of mud colors and textural differences documented in the detailed logs for the L1- and L2-86-NC cores, but the X-radiographs generally confirmed the details observed when the cores were first split and described (unpublished cruise logbook).

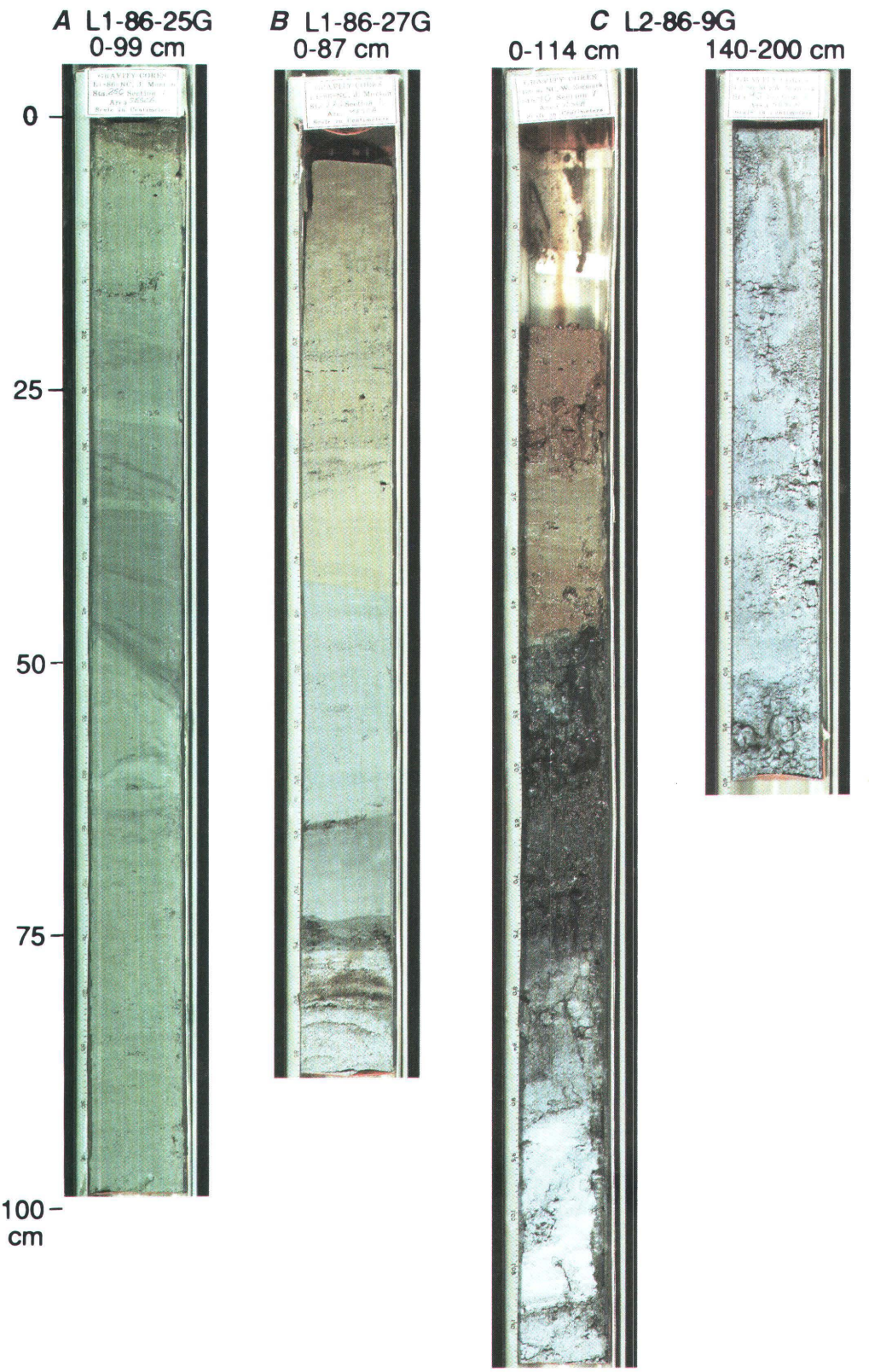

Figure 6.11. Photographs of selected core intervals: *A*, Core L1-86-25G depicting silty mud turbidites (darker color) overlying bioturbated mud. *B*, Core L1-86-27G showing interbedded silty turbidite units overlying a 12-cm-thick, bedded sand sequence that shows reddish stained horizons indicative of mineralization. *C*, Core L2-86-9G showing metalliferous reddish and chocolate brown mud overlying black sulfide talus (see fig. 6.12); lower part of core is bluish chloritized unit. See figures 6.2 and 6.9 for locations.

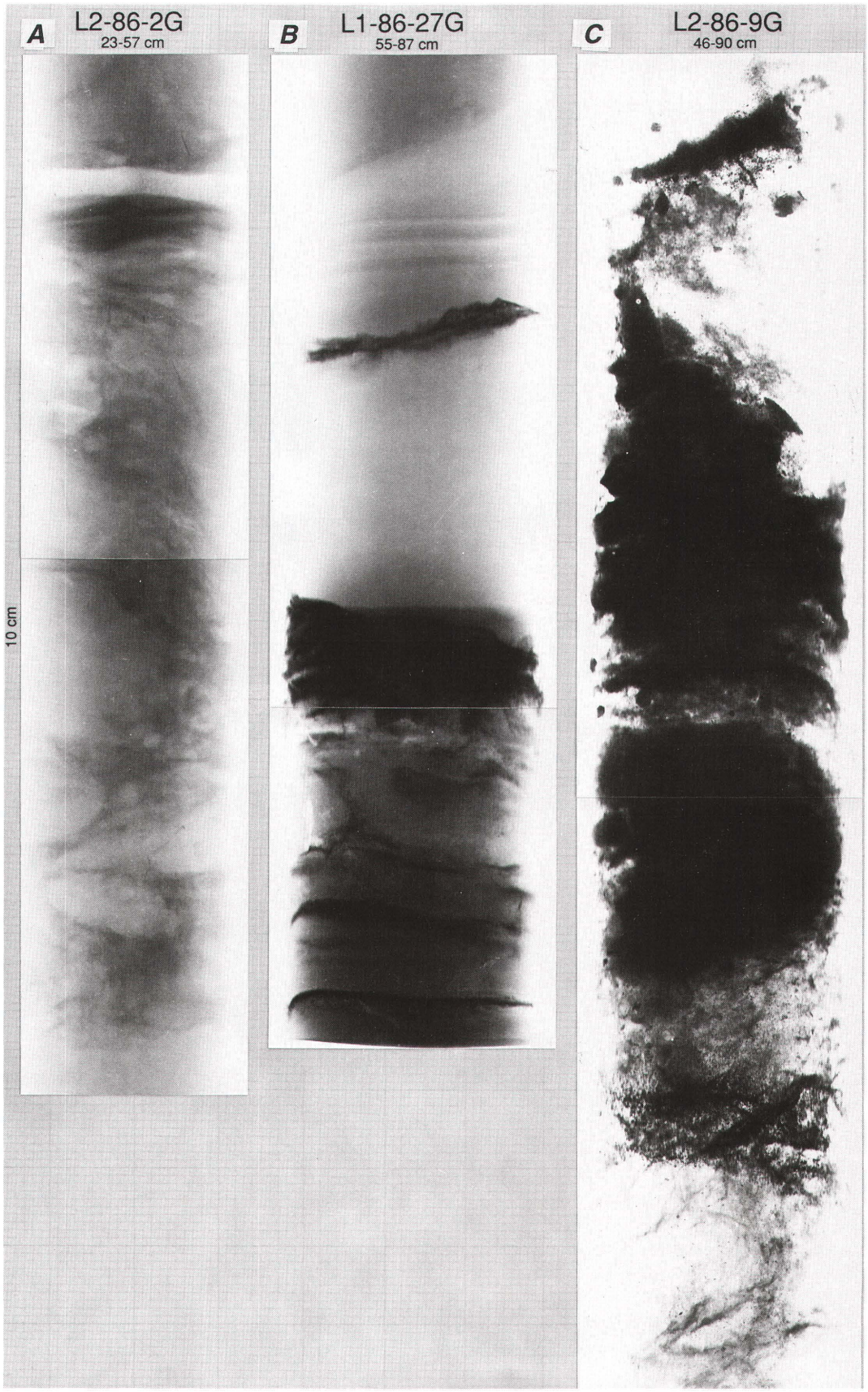

Figure 6.12. X-radiographs of selected core intervals. *A*, Mud-clast unit in core L2-86-2G. *B*, Mineralization within turbidite sand beds at base of core L1-86-27G. *C*, Sulfide talus in core L2-86-9G. See text and Zierenberg and Shanks (chap. 14, this volume) for details.

Table 6.5. Summary of light-mineral grain counts.

Area	NESCA	Other			SESCA								
Cruise	TUL89D	L2-86	TUL89D	TUL89D	L1-86	L1-86	L1-86	L1-86	L1-86	L2-86			DSDP35
Sample[a]	6G-25	27G-29	7P-24	7P-240	7G-211	8G-52	8G-175	25G-48	26G-40	2G-72	Mean	StD	14–40
Grains counted	297	393	300	298	295	403	322	356	396	349			399
Summary percent:													
Quartz, chert, etc.	13	6	22	37	11	10	7	22	25	29	18	10	33
Feldspar	28	12	31	34	9	35	36	30	24	28	27	9	52
Rock fragments	42	65	26	18	23	34	42	29	23	29	33	13	6
Mica	15	13	15	7	44	14	7	11	21	8	16	10	7
Opaques	2	3	5	3	7	6	7	6	6	5	5	2	<.5
Others		1	1	2	6	<.5	<.5	1	1	2	1	2	3
Ternary ratio:													
Quartz	15	7	28	42	27	13	8	27	35	35	24	11	36
Feldspar	34	14	39	39	23	45	42	37	33	33	34	9	57
Lithics	51	78	33	20	50	42	49	36	32	33	42	15	6

[a]Sample identification is abbreviated to core number and upper limit of sample interval.

The R/V *Tully* cores appear to consist predominantly of laminated turbidite mud units with silty interbeds (found in all cores except TUL-89-1P) and of mass-wasted sediment exhibiting steeply inclined bedding and mud-clast intervals (cores TUL-89-2G, 4G, and 7P).

COARSE-FRACTION MINERALOGY

A summary of the mineralogy of the surficial cores, presented in tables 6.5 and 6.6, is excerpted from a more detailed analysis in Wong (1989). The subsample nomenclature follows the scheme YY-CC-DD, where YY is L1 for cruise L1-86-NC, L2 for L2-86-NC, and TD for TUL-89D; CC is the core number; and DD is the core depth (cm). For example, L2-2G-72 is from 72 cm depth in core 2G from cruise L2-86-NC.

A qualitative grain-size relation was determined for the 30- to 63-μm and greater than 63-μm fraction without considering the clay fraction. The resultant dominant "grain size" ranged from silt to medium sand (table 6.4).

The heavy-mineral yield of the 63- to 250-μm fraction ranges from 1.9 to 3.8 percent by weight for those samples that do not have an abundance of oxide or sulfide particles. In the few samples that are enriched in opaque minerals, the heavy-mineral content is slightly greater. In contrast, the sulfide-mineralized sand unit (L1-27G-64) contains 50 percent heavy mineral grains.

Mica minerals, opaque grains, and volcanic rock fragments occur in both light and heavy mineral fractions. Chlorite is the primary mica in both fractions with lesser amounts of muscovite and biotite; phlogopite is a trace component. Except for the finer grained samples (such as TD-9T-12, L1-7G-211) and the greater than 250-μm fraction, micas make up no more than 10 percent of the heavy fraction and 20 percent of the light fraction.

Opaque grains (undifferentiated) make up as much as 7 percent of the light fraction and, except for L2-7G-211, 10 to 26 percent of the heavy fraction (tables 6.5 and 6.6). Opaque grains in the light fraction consist of thick books of mica, extremely fine-grained clay or oxide, or sulfide particles apparently buoyed by attachment to lighter grains. In the heavy fraction, the opaque grains include mica, oxide, and sulfide particles.

Volcanic rock fragments consisting of plagioclase, clinopyroxene, and (or) opaque groundmass (oxide grains or opaque alteration product) occur in both the light and heavy fraction depending on the mineral composition; more plagioclase lifts the grain into the light fraction, more oxide components drop it to the heavy fraction.

Light Fraction

In addition to the grain types noted above, the light fraction includes feldspar minerals, quartz, other lithic fragments, and some nonmineralic material. Quartz generally occurs as angular to subangular monocrystalline and polycrystalline grains. Inclusion-bearing, undulose, and unstrained quartz grains are present but not separately tabulated.

Plagioclase is the primary feldspar; rare microcline grains are present in several samples. The feldspar grains include both pristine fragments and altered fragments; some grains bear opaque inclusions and others are chloritized.

Besides volcanic rock fragments, several types of lithic components were distinguished in the light fraction; their abundances are detailed elsewhere (Wong, 1989). Many samples contain homogeneous clay fragments that are

Table 6.6. Summary and selected ratios of heavy-mineral grain counts.

Area	NESCA			Other					SESCA							
Cruise	TUL89D	TUL89D	TUL89D	L1-86	TUL89D	TUL89D	TUL89D	TUL89D	L1-86	L1-86	L1-86	L1-86	L1-86	L2-86		
Sample[a]	2G-94	6G-25	9T-12	27G-29	7P-8	7P-24	7P-42	7P-240	7G-211	8G-52	8G-175	25G-48	26G-40	2G-72	Mean	StD
Wt. pct. heavy (63–250μm)	2.9	1.5	—	—	3.1	3.1	3.8	1.4	—	1.9	1.1	3.6	2.2	4.7		
Grains counted	401	388	329	416	391	355	362	344	377	356	424	411	414	416		
Summary percent:																
Amph, nonmetamorphic	18	17	5	14	16	17	16	16	5	15	19	12	13	11	14	4
Amph, metamorphic	15	17	3	14	18	12	12	16	8	18	13	15	12	9	13	4
Orthopyroxene	4	5	1	7	6	6	4	8	3	5	6	6	4	4	5	2
Clinopyroxene	18	23	3	20	24	25	22	19	22	26	13	26	22	21	20	6
Epidote	7	6	3	7	4	5	5	6	2	5	7	3	7	3	5	2
Mica	14	11	70	7	7	4	3	4	2	3	3	3	9	4	10	17
Rock fragments	7	8	5	12	8	11	10	12	18	13	9	10	11	19	11	4
Opaques	12	10	10	16	15	18	24	17	38	13	26	23	19	26	19	8
Others	4	2	1	4	1	2	3	2	1	3	4	2	3	2	2	1
Ternary ratios:																
Nonopaques	76	80	51	71	75	70	65	69	42	73	64	66	67	53	66	10
Opaques	14	11	33	17	17	19	25	18	39	13	27	24	21	27	22	8
Rock fragments	10	9	16	13	9	12	10	13	18	14	9	10	12	20	13	3
Amphibole	53	50	56	44	51	45	47	49	33	48	56	43	43	42	47	6
Epidote	12	9	19	12	5	8	9	9	6	7	12	5	12	7	9	4
Pyroxene	35	41	25	44	44	47	45	42	61	45	33	51	45	51	43	8
Binary ratios:																
pyroxene/amphibole	0.66	0.83	0.44	0.98	0.87	1.06	0.96	0.87	1.88	0.94	0.58	1.19	1.04	1.20	1.0	0.3
meta-amphibole/amphibole	.46	.50	.41	.49	.53	.42	.43	.50	.58	.54	.40	.54	.50	.45	.5	.1
orthopyroxene/pyroxene	.16	.18	.17	.26	.19	.20	.17	.29	.11	.16	.30	.20	.15	.16	.2	.1

[a]Sample identification abbreviated to core number and upper limit of sample interval.

subrounded (fecal?) pellets or ragged crusts (for example, L1-27G-29 or TD-6G-25). Quartzofeldspathic sedimentary, metamorphic, and plutonic grains are scattered throughout. A few samples (such as L1-25G-48) host rare manganese(?)-coated clay nodules.

Volcanic-glass fragments range from colorless or brown isotropic grains to partly devitrified or altered to clay minerals. In none of the samples examined (63- to 250-μm size fraction) is the glass as abundant as in the samples examined by Karlin and Lyle (1986, p. 38), who reported as much as 35 percent glass in one sample. Glass globules and fragments of glass crust were noted in several greater than 250-μm samples, some with bluish opaline coating (for example, TD-7P-8).

Nonmineralogic items in the light fraction include hydrocarbon blebs, sponge parts, plant and wood fragments, and tests of foraminifers, radiolarians, and diatoms. A few carbonate fragments include biogenic clasts and replaced feldspar(?) grains.

A ternary plot of the quartz, feldspar, and lithic grains demonstrates that most of the Escanaba Trough samples would qualify as lithic arenites or feldspathic litharenites (fig. 6.13). The most quartz-rich sample is TD-7P-240, from a disturbed sandy lens near the bottom of this core, which was collected adjacent to a volcanic edifice near latitude 40°53′ N. Sample L1-27G-29 is lithic rich, probably reflecting the higher content of clay particles. Except for the deepest sample (V381, fig. 6.13), the sands from various depths of hole DSDP 35 are much richer in feldspar than the surficial Escanaba Trough sediment samples (Vallier, 1970).

Heavy Fraction

Nonopaque grains make up the bulk of the heavy fraction of the sand samples; except for L1-7G-211, opaque grains constitute less than 26 percent of the total, and rock fragments make up less than 20 percent (table 6.4). Clinopyroxene (mean 20 percent), ordinary green and brown hornblende, and metamorphic amphibole (mean 13 percent; mainly blue-green) are the main nonopaque heavy minerals (table 6.6). Epidote and hypersthene each comprise about 5 percent of the grain population. Actinolite-tremolite, zircon, apatite, garnet, and sphene amount to less than 5 percent of the grains in most samples. Trace amounts of basaltic hornblende, serpentinite, glaucophane, tourmaline, and barite are present.

A ternary plot of the major components amphibole, epidote, and pyroxene confirms that these samples are epidote-poor with roughly equal amounts of total amphibole and total pyroxene. The pyroxene-to-amphibole ratio, which is a diagnostic value of different sedimentary prov-

enances along the Oregon-California coast (Kulm and others, 1968; Whetten and others, 1969; Scheidegger and others, 1973; Wong and Klise, 1986), ranges between 0.4 and 1.2, with most about 1.0 (fig. 6.14). Orthopyroxene minerals, mostly hypersthene, make up less than 30 percent of the pyroxene population (fig. 6.15).

Altered and volcanic rock fragments are similar to those in the light fraction. The rare metamorphic grains include amphibolite and albite-epidote greenschist.

There is rare evidence of dissolution in the heavy minerals of the surficial cores, in contrast to reports of some samples from DSDP Site 35 (Vallier and others, 1973). A few of the pyroxene and amphibole grains exhibit coxcomb morphology, but none of the garnets are etched to cubic outlines.

Sulfide minerals dominate the heavy fraction in sample L1-27G-64, a sand layer in a generally hydrothermally altered core (Morton and others, 1987b). X-ray diffraction and scanning electron microscope investigation identify the sulfide component to include pyrrhotite, sphalerite, and pyrite. Barite is common in this sample and was noted in several other cores (Wong, 1989). Sample L1-27G-72 consists of yellowish to reddish-yellow oxidized grains in both light and heavy fractions. Tests filled with opaque minerals were noted in sample L2-2G-72.

Pleistocene(?) Samples

The characteristics of known Pleistocene turbidite sequences in Escanaba Trough might bear on the problem of provenance, but unfortunately only one surficial core (L2-86-2G) is firmly interpreted to contain a Pleistocene section (Karlin, 1989). Three other turbidite units from cores in which the Pleistocene-Holocene boundary cannot be

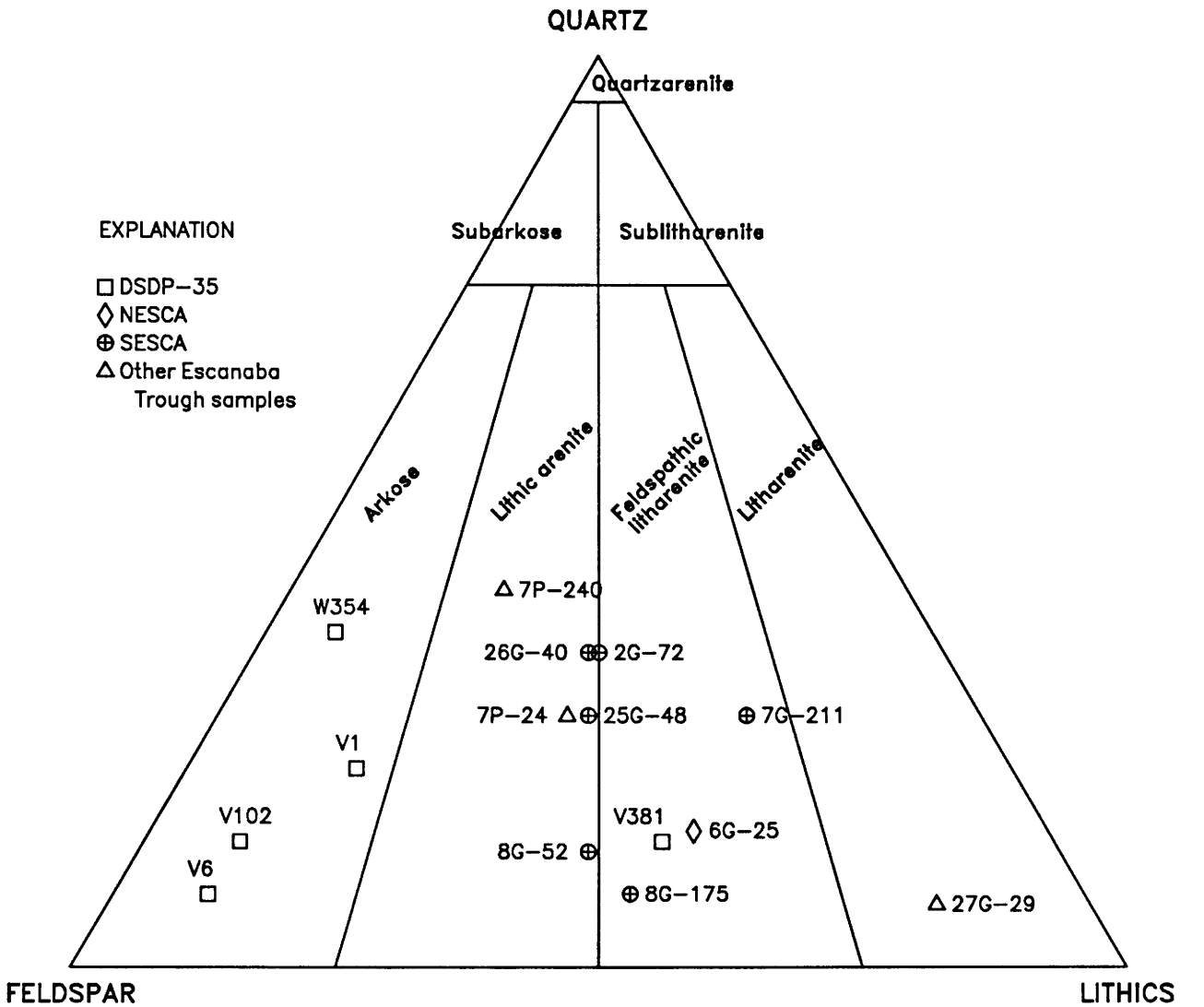

Figure 6.13. Ternary plot of quartz, feldspar, and lithic data (Folk, 1980) from this study and DSDP Site 35 samples (Wxxx, this study; Vxxx Vallier, 1970; where xxx is depth in meters below sea floor). Surficial core samples annotated by core number and core depth (cm); see table 6.5.

determined are of probable Pleistocene age (all are from greater than 150 cm core depth). Sample TD-7P-240 is enriched in quartz and hypersthene. Sample L1-7G-211 from SESCA is enriched in light lithic fragments (mostly clay pellets), has the fewest nonopaque heavy mineral grains, and is richest in pyroxenes. Sample L1-8G-175 from SESCA is also enriched in light lithic fragments but has little quartz and the least amount of pyroxenes. Sample L2-2G-72 is unremarkable except for a slightly high pyroxene abundance. If L1-8G-175 is excluded, the increased pyroxene abundance seems to be the only common thread.

FINE-FRACTION MINERALOGY

Bulk mineralogy was determined by X-ray diffraction for 67 samples of mud and sandy mud from both the sediment cores and additional material recovered during rock dredging. Sediment that has not been hydrothermally altered has very consistent bulk mineralogy regardless of grain size. Quartz is the dominant mineral in all samples and is followed in abundance by feldspar, predominantly plagioclase. Mica is more abundant than chlorite in most samples, and many samples contain trace amounts of amphibole. No carbonate or zeolite minerals were detected.

Clay-fraction smear slides were prepared for 33 samples. The finest clay fraction, which is taken from the uppermost layer of centrifuged unaltered sediment, is green-brown to red-brown smectite. The smectite is poorly crystallized and gave broad diffraction peaks at approximately 1.25 nm that expanded to 1.7 to 1.8 nm after glycolation and collapsed to approximately 1 nm after heating to 400°C. This smectite is easily distinguished from hydrothermal smectite, which was generally dark green and had much higher X-ray diffraction peak-to-background ratios and narrower diffraction peaks.

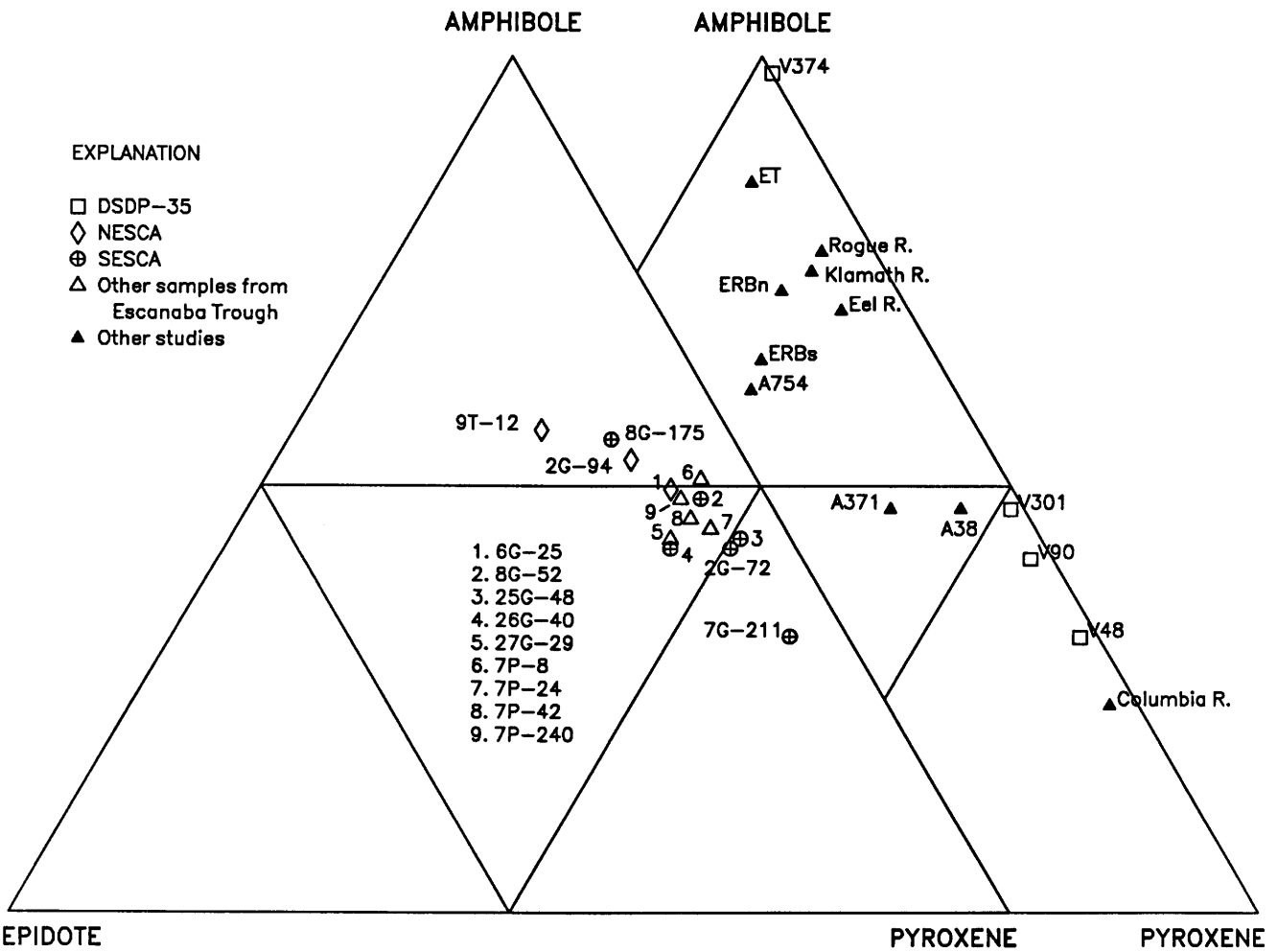

Figure 6.14. Ternary plot of total amphibole, epidote, and pyroxene grains in heavy mineral suites from this and previous studies. Annotation of samples: ET, flanks of Escanaba Trough (Fowler and Kulm, 1970); V48, V90, V301, V374 from DSDP Site 35 (Vallier and others, 1973); A38, A371, A754 from DSDP Site 174A on Astoria fan (Scheidegger and others, 1973); Rogue River (Kulm and others, 1968); Columbia River (Whetten and others, 1969); Eel and Klamath Rivers (Wong and Klise, 1986); ERBn, ERBs, northern and southern offshore Eel River basin (unpub. data).

The coarser clay fraction is generally brown to gray and contains variable amounts of chlorite, illite, and smectite and varying but minor amounts of quartz. Kaolinite probably occurs as a minor phase in the coarser clay fraction, but the presence of kaolinite is generally masked by chlorite, which occurs in greater abundance. Chlorite, illite, and quartz in the coarsest clay fraction are detrital grains that also occur in the coarser fractions of the sediment. The observed mineralogy is consistent with the findings of Karlin (1980), who demonstrated that fine-grained sediment off the southern Oregon coast is dominantly chlorite and illite derived from the California Coast Range with less abundant smectite derived in part from the Columbia River drainage. The minor amount of smectite that forms the finest grain size fraction of the Escanaba Trough samples is interpreted to include low-temperature diagenetic alteration products of basaltic glass and unstable minerals (Zierenberg and Shanks, chap. 14, this volume).

PORE WATER

Pore fluid was extracted from four samples to look for evidence of hydrothermal fluid flow through the shallow sediment section. Pore-fluid samples from L2-86-NC cores 2G, 4G, and 28G come from sediment intervals that show no evidence of hydrothermal alteration, and the pore fluids are nearly identical to seawater in composition (table 6.7). The sediment interval sampled in core L2-86-9G is highly altered by high-temperature magnesium metasomatism (Zierenberg and Shanks, chap. 14, this volume). Magnesium-rich chlorite has replaced the normal sediment. Minor amounts of talc, gypsum, and pyrite accompany the chlorite. Pore fluid from this interval has a lower pH, is depleted in magnesium, and is enriched in calcium and sulfate relative to seawater or pore fluids from the other samples (table 6.7; fig. 6.16).

High-temperature interaction of seawater with basalt or sediment results in the depletion of magnesium in the fluid phase by formation of secondary magnesium silicates (Bischoff and Dickson, 1975). Replacement of hemipelagic sediment in core L2-86-9G by magnesium-rich smectite is evidence of the transfer of magnesium from seawater to the alteration products during high-temperature interaction with hydrothermal fluids. The pore waters from this core retain a signature of this process as recorded by reduced magnesium concentrations.

Heating of seawater also leads to precipitation of anhydrite because of the retrograde solubility of this mineral at high temperature (Bischoff and Seyfried, 1978). Anhydrite hydrates to gypsum and redissolves in seawater at ambient sea-floor temperature. Minor amounts of gypsum,

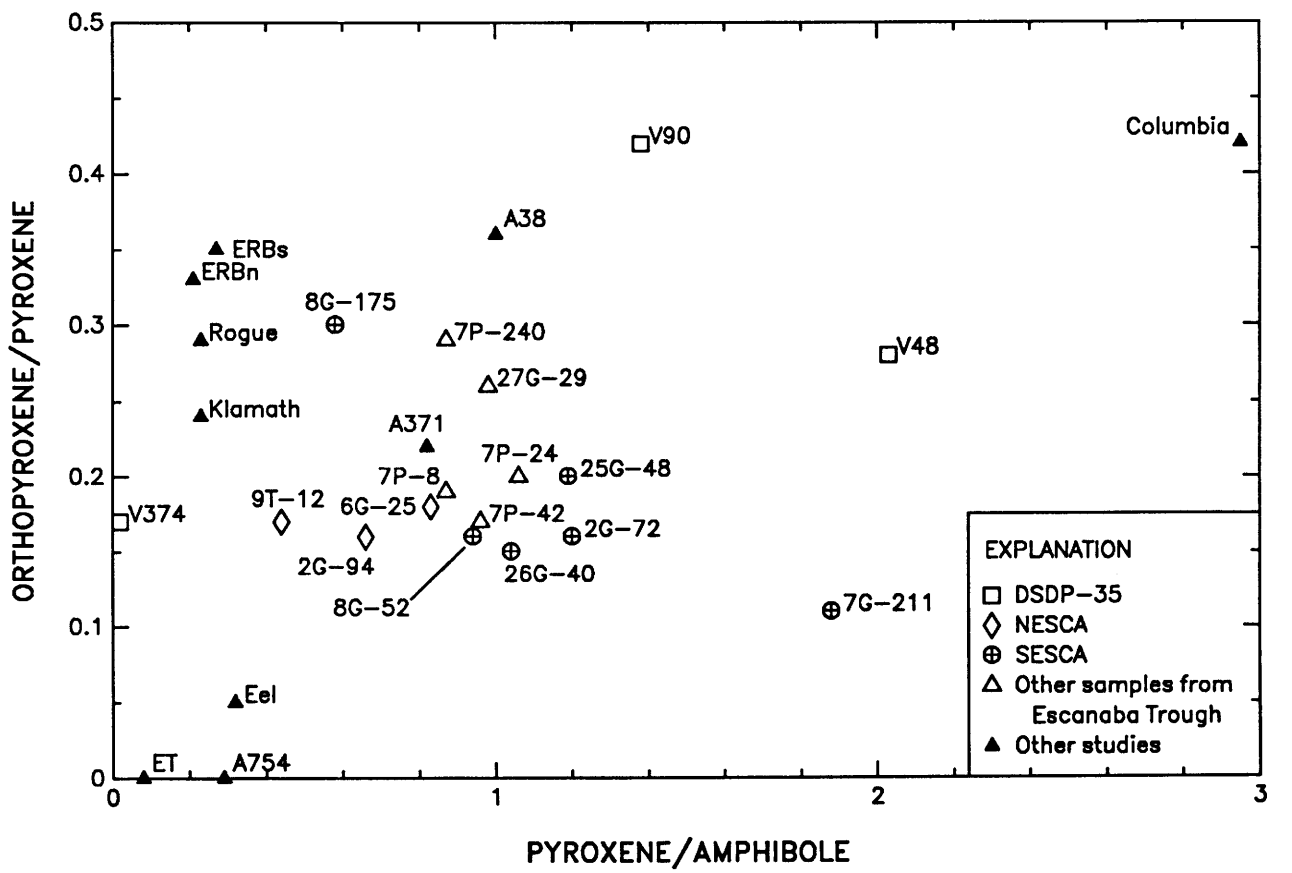

Figure 6.15. Plot of ratios orthopyroxene/pyroxene versus pyroxene/amphibole. Annotation and data sources as for fig. 6.14.

Table 6.7. Pore-water chemistry of surficial core samples from cruise L2-86-NC.

[Values in ppm; C_T=H_2CO_3+HCO_3^-+CO_3^{2-} in mmole/kg; na, not analyzed]

	2G 96–101 cm	4G 138–145 cm	9G 115–122 cm	28G 119–126 cm	Seawater
Cl	19,300	19,300	19,300	19,200	19,350
Na	10,800	10,700	10,500	10,600	10,760
K	542	435	423	426	399
Mg	1,220	1,260	1,150	1,270	1,290
Ca	362	394	1,320	385	411
SO_4	2,562	2,560	3,860	2,375	2,710
SiO_2	9.6	7.7	8.9	15.2	_
Fe	<1	<1	<1	<1	<1
Mn	1.0	1.6	3.0	4.5	<1
C_T	na	3.8	1.6	6.3	2.3
pH	8.2	7.8	6.9	7.9	8.2

which are interpreted to have formed by hydration of anhydrite, are observed in the altered sediment (Zierenberg and Shanks, chap. 14, this volume). Calcium and sulfate enrichments are not, however, stoichiometrically equivalent as would be predicted from the dissolution of anhydrite alone. Some of the excess calcium beyond that available by dissolution of anhydrite can be attributed to cation exchange during magnesium metasomatism of the sediment. The remaining excess calcium in the pore water could signal the presence of residual hydrothermal fluid, but this hypothesis is not supported by the observed concentrations of magnesium and potassium. Alternatively, sulfate could have been depleted by sulfate reduction. The altered sediment contains minor amounts of pyrite that apparently includes some sulfur formed by sulfate reduction (Zierenberg and Shanks, chap. 14, this volume). However, not only is the amount of pyrite in the core very small, but it is interpreted to have formed at high temperature during alteration of the sediment by inorganic sulfate reduction. Low-temperature biogenic sulfate reduction is rejected as a means of sulfate depletion because of the low content of organic matter in the altered sediment (Kvenvolden and others, chap. 15, this volume) and the absence of biogenic pyrite in the core. The source of the elevated calcium in the pore fluid, therefore, remains to be explained.

The lower pH in the core L2-86-9G pore fluid could reflect the presence of residual low-pH hydrothermal fluid, hydrogen ions released during formation of magnesian chlorite, hydrogen ions released during minor oxidation of accessory pyrite, or a combination of these processes.

DISCUSSION

The composition of the core samples presented in this study provides good documentation of the interaction between hydrothermal fluids, volcanism, and the sediments filling Escanaba Trough. Major questions that we hoped to address from examination of these samples were (1) how long the sediment fill has been "available" to interact with hydrothermal fluids associated with the volcanic intrusions in the zones of sea-floor mineralization and (2) what are the products of this interaction; that is, do the mineral

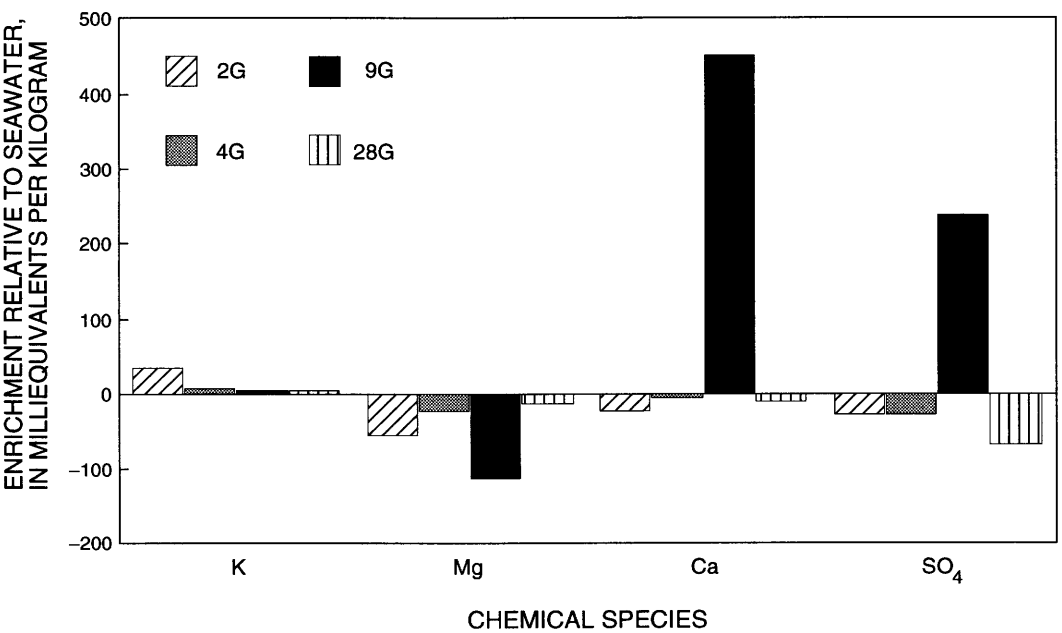

Figure 6.16. Pore-water chemistry for selected surficial cores from cruise L2-86-NC in Escanaba Trough; see table 6.7 and figure 6.10 for location.

deposits reflect the composition of the sediments, and are there sedimentary products from the mineralization zones that are now part of the sediment fill? The data presented in the preceding section answer the second question fairly clearly, but the timing aspect has not been addressed. As reported by McManus and others (1970) and Vallier and others (1973), the lower part of the sequence cored at Site 35 is barren of microfossils or other components that could give a direct age determination. Therefore, we will first discuss the nature of the sedimentologic and tectonic constraints on the timing and rate of sedimentation in Escanaba Trough and relate these to probable changes in source areas of the sediment.

SEDIMENTATION RATES

To better understand the time frame for deposition of the sediment fill of Escanaba Trough, we can consider the amount of extension and possible rates of accumulation that might be reasonable for the late Pleistocene. It is unlikely that the trough would fill during the last lowstand of sea level in the Pleistocene because 500 m of sediment accumulation would correspond to a rate of about 25 m/1,000 yr. This rate is more than double that found by DSDP drilling on the Mississippi fan, which is fed by a very large, nearby river (Kohl and others, 1985). On the other extreme, it would take only about 300,000 years to form the entire width of Escanaba Trough at a spreading rate of 2.4 cm/yr and assuming that only 80 percent of the total separation occurs between the innermost major faults forming the bounding ridges of the trough. Even if the trough existed in its present form for the entire 300,000 years (an impossibility), the sedimentation rate implied is nearly an order of magnitude higher than the Holocene rate. The Holocene sedimentation rates derived from Karlin and Lyle (1986) and Karlin and Zierenberg (chap. 7, this volume) are generally less than 20 cm/1,000 yr; figure 6.17 shows the sediment accumulation since 11,000 years ago for the cores based on their magnetic-susceptibility profiles. At the Holocene accumulation rate, it would take more than 2,500,000 years to fill Escanaba Trough, another unacceptable proposal following the arguments above.

The arguments above suggest that it is reasonable to consider that the sediment fill of Escanaba Trough was deposited over an interval greater than 30,000 years but certainly less than 300,000 years. The character of many of the seismic-reflection profiles from Escanaba Trough show two intervals with strong parallel reflectors (Moore, 1970; Clague and Holmes, 1987; Morton and others, 1987a). These intervals might correspond to periods of very rapid input of turbidite fill during the lower sea-level stands. The interval with interbedded sand within the DSDP Site 35 cores (fig. 6.4) roughly corresponds to the shallower of the two intervals with laterally persistent reflecting horizons. The sandy turbidite beds sampled at Site 35 are relatively fine grained with common mud interbeds. This lithology is consistent with the seismic-reflection character observed for overbank and distal depositional elements on submarine fans (not the channel-fill and lobe elements that are the general sites of coarse-sediment turbidite deposition; see Mutti and Normark, 1991; Normark and others, 1993).

Assuming that both intervals of prominent reflectors represent periods of increased accumulation of coarser (nonmud) material, several possible causes can be suggested: (1) lowered sea level, (2) uplift of source area (relative sea-level change), (3) new sediment sources as a result of tectonic activity either onshore or along the

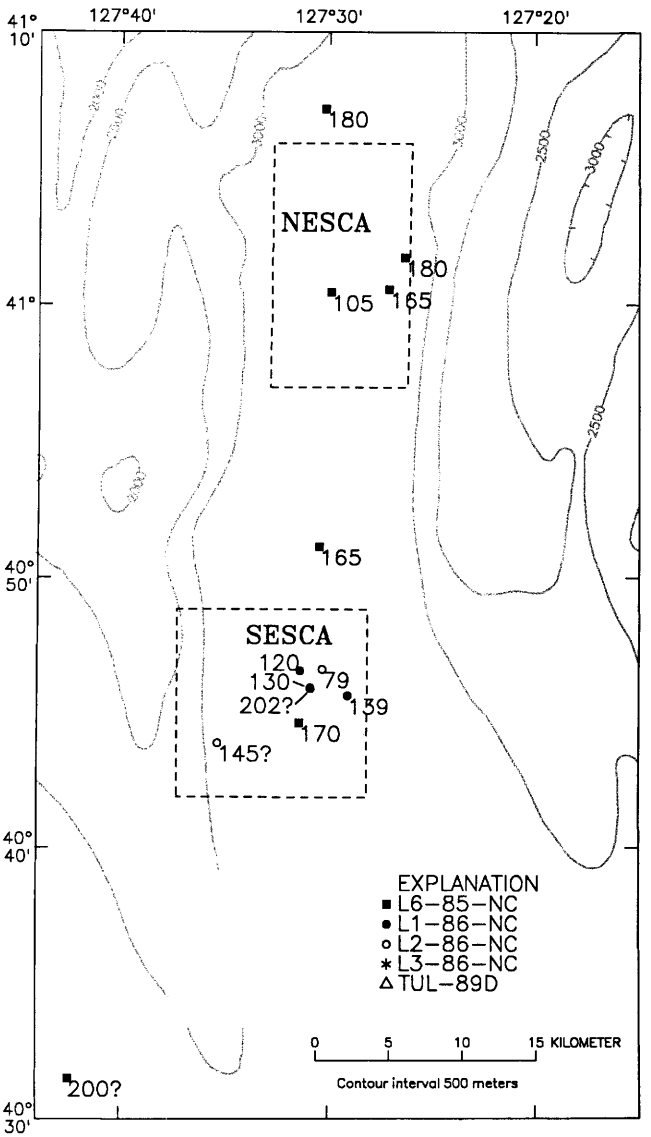

Figure 6.17. Compilation of depth (cm) to 11 ka boundary for surficial cores from Escanaba Trough. L1-86-NC and L2-86-NC values determined by Karlin (1989). L6-85-NC extracted by Karlin's 1989 criteria from data in Karlin and Lyle (1986). Bathymetry from Wilde and others (1978). Hachures indicate area of closed low.

continental rise and lower slope, and (4) major change in the depth or configuration of Escanaba Trough itself. The coarse fraction compositions as reported by McManus and others (1970), Vallier (1970), and Vallier and others (1973) for Site 35 and in this paper for the youngest sediment, appear to rule out any major change in sources. Given the short period under discussion (less than 300,000 years), tectonic changes in source rates appear to be insufficient to explain an abrupt change in sediment input. A non-steady-state model for spreading-ridge morphology (Kappel, 1985, Kappel and Ryan, 1986) could explain either or both of the intervals of stronger reflectors. In such a model, periods of ridge volcanism and crustal accretion alternating with periods of extension lead to a relatively rapid collapse of the ridge axis, forming a major graben. There are no data to constrain the timing of any such non-steady-state episodes in the Escanaba Trough area, so this process (if operative) provides no control on the history of filling of the trough.

The simplest hypothesis of the four is to relate low eustatic sea-level intervals with the intervals of coarser sediment in the Escanaba Trough fill. In this scenario, the upper seismic-reflection interval would correspond to the last sea-level lowstand, with most of the section from approximately 150 m to the sea floor being deposited in approximately 20,000 years (from 30 to 11 ka; the timing for sea-level history used in this section follows Chappell and Shackleton (1986), who compare oxygen-isotope data in deep-marine sediment with dating from a sequence of uplifted marine terraces). The coarsest sediment might correspond to the period of rapid sea-level fall using the arguments of Mutti (1985), Mitchum (1985), and Vail (1987) about lowstand turbidite fans. The rate of sedimentation for the last lowstand would be approximately 7 to 8 m/1,000 yr, and the entire Escanaba Trough fill would require only 60,000 to 70,000 years at this rate. The previous lowstand of comparable magnitude to the last was from 170 to 130 ka; however, because a section of acoustically transparent (nonturbidite) sediment lies below the lower interval, the implication is that the Escanaba Trough fill is about 200 ka old at the base. This should be considered the upper age limit for the axial zone. Sea-level history based on uplifted reef sequences suggests that the lower interval of stronger reflectors might relate to a 75- to 80-m lowstand at about 70 ka (see discussion in Chappell and Shackleton, 1986). This would give an age of no earlier than 100 ka for Escanaba Trough itself and an average sedimentation rate of 5 m/1,000 yr; both values are quite reasonable within the limits discussed earlier. Also, the much lower sea level during the last lowering would be expected to give the higher accumulation rate of 7 to 8 m/1,000 yr.

In any of the above scenarios, the deduced Pleistocene accumulation rate far exceeds that observed for the Holocene (fig. 6.17; Karlin and Zierenberg, chap. 7, this volume). An order-of-magnitude change in turbidite sedimentation rates between the Pleistocene and Holocene has been observed elsewhere in the northeast Pacific Ocean. The proximal overbank (levee) area on Monterey fan about 400 km south of Escanaba Trough aggraded at a rate of about 3 m/1,000 yr during the late Pleistocene (Normark, unpublished data); during the Holocene, the rate determined for several core locations on the same levee area ranges from 25 to 35 cm/1,000 yr (Brunner and Normark, 1985). The differences in rates for both the Holocene and late Pleistocene between Escanaba Trough and Monterey fan are consistent with the size of the probable source areas for turbidity-current transport. Davis and Becker (1989) suggested that regional sedimentation in Escanaba Trough occurred during a tectonically and volcanically quiet period. This conclusion must be regarded with caution considering that sedimentation rates might have been extremely high for short periods of time during the latest Pleistocene.

SEDIMENT SOURCES

The composition of the sediment from the surficial cores in Escanaba Trough differs little in major light and heavy mineral components (in the 63- to 250-μm size range) among the sampling sites (figs. 6.13 to 6.15). Some minor differences appear in the minor and trace minerals, such as opaque grains, indeterminate rock fragments, and the greater than 250-μm fraction. Except for the highly altered sediment recovered in core L1-86-27G, barite is a trace component in samples obtained near areas with active hydrothermal venting.

The nearest source of terrigenous debris to Escanaba Trough is the northern California continental margin, where the Eel and Klamath rivers provide substantial coarse debris (fig. 6.1). However, the present morphology of the continental rise along the eastern margin of the Juan de Fuca plate would permit gravity-flow deposits from as far north as the Oregon-Washington shelf to reach Escanaba Trough. The heavy-mineral contributions of the major rivers (Columbia: Whetten and others, 1969; Rogue: Kulm and others, 1968; Klamath, Eel: Wong and Klise, 1986) and of the continental shelf (Scheidegger and others, 1973; F.L. Wong, unpub. data) along this margin are relatively well known. Previous studies of sediment from Escanaba Trough identified sources in the Columbia River and (or) Klamath Mountains regions (Vallier, 1970). Fowler and Kulm (1970) sampled uplifted terraces on either side of Escanaba Trough and, based on the abundant blue-green amphibole and low pyroxene-to-amphibole ratios, determined that the sediments were probably from the Klamath Mountains region (fig. 6.14).

Vallier (1970) and Vallier and others (1973) in their examination of the Site 35 core attributed an earlier source of Escanaba Trough sediment (more than 301 m below the

sea floor) to the Klamath region alone and the younger sediment to a mixed Columbia and Klamath source based on the depletion of pyroxene downcore. Vallier subsequently expressed some concern regarding diagenetic processes for the mineral depletion in an environment where a great thickness of sediment is being "cooked" (T.L. Vallier, oral commun., 1989). Scheidegger and others (1973) examined a similar mineralogic change in DSDP core 174A from Astoria fan, at a site well away from a ridge-crest heat source. About 370 m below the sea floor at this drill site, an amphibole-rich assemblage lower in the hole gives way upward to a mineralogy diagnostic of the modern upper Columbia River basin. On the basis of altered hypersthene grains, they concluded that dissolution, though present, has not persisted long enough to remove any substantial amount of pyroxenes in the lower part of the cored sequence. For Astoria fan, Scheidegger and others (1973) included the Vancouver Island and British Columbia region as an alternate source of amphibole-rich sediment, although this potential source is sensitive to the configuration of the Juan de Fuca plate at 2 Ma.

The abundance of clinopyroxene readily identifies a Columbia River factor in the Escanaba Trough samples available for this study, but pyroxenes, specifically orthopyroxene, are less abundant than is typical for the Columbia River assemblage. The metamorphic amphibole minerals in the surficial cores require contributions from rivers draining the Klamath Mountains of southern Oregon and northern California: the Rogue, Klamath, and Eel. This mixed sediment source is evident in the AEP ternary diagram and the pyroxene ratios (figs. 6.14 and 6.15) because the Escanaba Trough samples plot between those of the Columbia River and of the Rogue, Klamath, and Eel rivers. DSDP samples similar to Escanaba Trough surficial sediment were recovered from the Astoria fan Site 174A at 38 m and 371 m depth and from the Escanaba Trough Site 35 at 301 m (note: all these samples lie above the mineralogic change mentioned above).

If the turbidite beds sampled for this study are Holocene in age, the Columbia and Klamath regions may be less likely primary sources because it is generally assumed that submarine-canyon gradients are smaller and sediment supply is less than during the last low sea-level stand. Ash derived from the eruption of Mount Mazama (6,900 yr ago) has been traced in turbidite deposits south of the Blanco Fracture Zone along the base of the continental slope via Astoria Channel (fig. 6.1) and onto the Tufts Abyssal Plain farther west (Nelson and others, 1968, 1988). This suggests that the Columbia River, and by inference the more adjacent Klamath region, could provide Holocene sediment to Escanaba Trough. Glass from Escanaba Trough samples, however, has been attributed to local volcanic activity (Karlin and Lyle, 1986).

Without an external source, the Holocene turbidite beds in Escanaba Trough sampled in the surficial cores might be reworked from Pleistocene deposits by slumping or other mass-wasting processes (Karlin and Lyle, 1986). The one sample from the Pleistocene(?) terrace on the flank of Gorda Ridge has a strong affinity with the Klamath sources but none with the Columbia (fig. 6.14; Fowler and Kulm, 1970). More samples are needed from the flanks of southern Gorda Ridge to identify the possible Pleistocene deposits of Columbia or mixed Columbia-Klamath sources that might be supplying terrigenous material to Escanaba Trough during the Holocene.

CONCLUSIONS

Under any assumptions involving steady and continuing spreading along the southern Gorda Ridge during the Brunhes Normal-Polarity Chron (the only time control on the plate motions), the sediment fill of Escanaba Trough accumulated in less than 200,000 years. This limit is consistent with available biostratigraphic data from Site 35 (J. Barron, oral commun., 1989). Sediment components linked to the Columbia River and Klamath Mountain rivers indicate that a large area of the northeast Pacific margin is available as a sediment source. The turbidite fill is dominantly fine grained as observed in both Site 35 and surficial cores. The parallel-reflector, flat-lying internal structure of the fill observed in seismic-reflection profiles (Clague and Holmes, 1987; Morton and others, 1987a; Morton and Fox, chap. 2, this volume) is consistent with fine-grained distal-turbidite accumulation. Channel-fill and mounded-lobe reflector geometries with high-amplitude, discontinuous reflectors characteristic of coarse-grained facies are not observed.

Accumulation rates as high as 8 m/1,000 yr of dominantly muddy sediment seals off hydrothermal circulation that normally cools oceanic crust. Ridge crest extension and localized basaltic intrusions and associated fault systems provide the only conduits to the sea floor and therefore control hydrothermal discharge. The muddy fill of Escanaba Trough provides relatively few bedding intervals for lateral migration of the fluids (compared to turbidite sequences with more coarse-grained facies) so that fluid discharge is concentrated at the site where cross-stratal permeability intersects coarse-grained sediment aquifers or the more permeable upper oceanic crust.

The probable high sediment accumulation rate during the latest Pleistocene, as much as 40 times the Holocene rate, should have filled most of the topographic lows in the southern Escanaba Trough. The irregular, fine-scale morphology of the sea floor in the study areas (figs. 6.9 and 6.10) might well be Holocene in age. The hydrothermal deposits and the fluid conduits are associated with these Holocene structures. Fluids contributing to the deposits, however, could be substantially older if they were generally prevented from reaching the sea floor during the

intervals of most rapid sediment accumulation. The effective sealing of the system by the rapidly deposited, fine-grained sediment allows for long periods of interaction between interstitial fluid and sediment that overlies hot oceanic crust. When the system is sealed from hydrothermal circulation, the oceanic crust cools by conductive heat transfer through the sediment cover. Volcanic intrusion into the sediment provides both a thermal and topographic focus for hydrothermal fluid flow. Faulting associated with uplift of the sediment over the intrusions provides a pathway for the hydrothermal fluids derived from a large volume of sediment. We envision that this interplay between sedimentation and tectonic-volcanic activity is responsible for the large-volume, focused discharge of hydrothermal fluid required to form the extensive sulfide deposits observed in Escanaba Trough.

REFERENCES CITED

Atwater, T., and Mudie, J.D., 1968, Block faulting on the Gorda Rise: Science, v. 159, p. 729–731.

———1973, Detailed near-bottom geophysical study of the Gorda Rise: Journal of Geophysical Research, v. 78, p. 8665–8686.

Bischoff, J.L., and Dickson, F.W., 1975, Seawater-basalt interaction at 200°C and 500 bars: Implications for origin of sea-floor heavy-metal deposits and the regulation of seawater chemistry: Earth and Planetary Science Letters, v. 25, p. 385–397.

Bischoff, J.L., and Seyfried, W.E., 1978, Hydrothermal chemistry of seawater from 25° to 350°C: American Journal of Science, v. 278, p. 838–860.

Brunner, C.A., and Normark, W.R., 1985, Biostratigraphic implications for turbidite depositional processes on the Monterey deep-sea fan, central California: Journal of Sedimentary Petrology, v. 55, p. 495–505.

Campbell, A.C., German, C.R., Palmer, M.R., Gamo, T., and Edmond, J.M., Chemistry of hydrothermal fluids from the Escanaba Trough, Gorda Ridge, *in* Morton, J.L., Zierenberg, R.A., and Reiss, C.A., eds., Geologic, hydrothermal, and biologic studies at Escanaba Trough, Gorda Ridge, offshore northern California: U.S. Geological Survey Bulletin 2022, chapter 11 (this volume).

Chappell, J., and Shackleton, N.J., 1986, Oxygen isotopes and sea level: Nature, v. 324, p. 137–140.

Clague, D.A., and Holmes, M.L., 1987, Geology, petrology, and mineral potential of the Gorda Ridge, *in* Scholl, D.W., Grantz, A., and Vedder, J.G., eds., Geology and resource potential of the continental margin of western North America and adjacent ocean basins—Beaufort Sea to Baja California: Houston, Circum-Pacific Council for Energy and Mineral Resources, Earth Science Series, v. 6, p. 563–580.

Davis, E., and Becker, K., 1989, Thermal and tectonic structure of the northern Escanaba Rift valley: New seismic reflection and heat flow data [abs.]: Eos, Transactions American Geophysical Union, v. 70, p. 1328.

EEZ-SCAN 84 Scientific Staff, 1986, Atlas of the Exclusive Economic Zone, Western Conterminous United States: U.S. Geological Survey Miscellaneous Investigations Series Map I-1792, 152 p., scale 1:500,000.

Folk, R.L., 1980, Petrology of sedimentary rocks: Austin, Hemphill, 185 p.

Fowler, G.A., and Kulm, L.D., 1970, Foraminiferal and sedimentological evidence for uplift of the deep-sea floor, Gorda Rise, northeastern Pacific: Journal of Marine Research, v. 28, p. 321–329.

Kappel, E.S., 1985, Volcanic episodicity and a non-steady state rift valley: New York, Columbia University, Ph.D. thesis, 123 p.

Kappel, E.S., and Ryan, W.B.F., 1986, Volcanic episodicity and non-steady state rift valley along northeast Pacific spreading centers: Evidence from Sea MARC I: Journal of Geophysical Research, v. 91, p. 13,925–13,940.

Karlin, R., 1980, Sediment sources and clay mineral distributions off the Oregon coast: Journal of Sedimentary Petrology, v. 50, p. 543–560.

———1989, SEA CLIFF diving and sediment studies on the Gorda Ridge: Final report on Oregon Department of Geology and Mineral Industries contract 63-630-8806, 17 p.

Karlin, R., and Lyle, M., 1986, Sediment studies on the Gorda Ridge: Oregon Department of Geology and Mineral Industries Open-File Report O-86-19, 76 p.

Karlin, R.E., and Zierenberg, R.A., Sedimentation and neotectonism in the SESCA area, Escanaba Trough, southern Gorda Ridge, *in* Morton, J.L., Zierenberg, R.A., and Reiss, C.A., eds., Geologic, hydrothermal, and biologic studies at Escanaba Trough, Gorda Ridge, offshore northern California: U.S. Geological Survey Bulletin 2022, chapter 7 (this volume).

Kohl, B., and DSDP Leg 96 Shipboard Scientists, 1985, Biostratigraphy and sedimentation rates of the Mississippi fan, *in* Bouma, A.H., Normark, W.R., and Barnes, N.E., eds., Submarine fans and related turbidite systems: New York, Springer-Verlag, p. 267–273.

Kulm, L.D., Scheidegger, K.F., Byrne, J.V., and Spigai, J.J., 1968, A preliminary investigation of the heavy mineral suites of the coastal rivers and beaches of Oregon and northern California: The Ore Bin, v. 30, no. 9, p. 165–180.

Kulm, L.D., von Huene, R., and others, 1973, Site 174, *in* Kulm, L.D., and von Huene, R., eds., Initial reports of the Deep Sea Drilling Project: Washington, U.S. Government Printing Office, v. 18, p. 97–167.

Kvenvolden, K.A., Rapp, J.B., and Hostettler, F.D., Hydrocarbons in sediment from Escanaba Trough, *in* Morton, J.L., Zierenberg, R.A., and Reiss, C.A., eds., Geologic, hydrothermal, and biologic studies at Escanaba Trough, Gorda Ridge, offshore northern California: U.S. Geological Survey Bulletin 2022, chapter 15 (this volume).

Manheim, F.T., Chan, K.M., and Sayles, F.L., 1970, Interstitial water studies on small core samples, Deep Sea Drilling Project, Leg 5, *in* McManus, D.A., and others, eds., Initial reports of the Deep Sea Drilling Project: Washington, U.S. Government Printing Office, v. 5, p. 501–511.

Masson, D.G., Cacchione, D.A., and Drake, D.E., 1988, Tectonic evolution of Gorda Ridge inferred from sidescan sonar images: Marine Geophysical Researches, v. 10, p. 191–204.

Mazzullo, J., and Graham, A.G., 1987, Handbook for shipboard sedimentologists: Ocean Drilling Program Technical Note 8, 67 p.

McManus, D.A., and others, 1970, Site 35, *in* McManus, D.A.,

and others, eds., Initial reports of the Deep Sea Drilling Project: Washington, U.S. Government Printing Office, v. 5, p. 165–202.

Mitchum, R.M., Jr., 1985, Seismic stratigraphic expression of submarine fans, *in* Berg, O.R., and Woolverton, D.G., eds., Seismic stratigraphy II: American Association of Petroleum Geologists Memoir 39, p. 117–136.

Moore, G.W., 1970, Sea-floor spreading at the junction between Gorda Rise and Mendocino Ridge: Geological Society America Bulletin, v. 81, p. 2817–2823.

Moore, G.W., and Sharmin, G.F., 1970, Summary of SCAN site 4, *in* McManus, D.A., and others, eds., Initial reports of the Deep Sea Drilling Project: Washington, U.S. Government Printing Office, v. 5, p. 761–773.

Morton, J.L., and Fox, C.G., Structural setting and interaction of volcanism and sedimentation at Escanaba Trough: Geophysical results, *in* Morton, J.L., Zierenberg, R.A., and Reiss, C.A., eds., Geologic, hydrothermal, and biologic studies at Escanaba Trough, Gorda Ridge, offshore northern California: U.S. Geological Survey Bulletin 2022, chapter 2 (this volume).

Morton, J.L., Holmes, M.L., and Koski, R.A., 1987a, Volcanism and massive sulfide formation at a sedimented spreading center, Escanaba Trough, Gorda Ridge, northeast Pacific Ocean: Geophysical Research Letters, v. 14, p. 769–772.

Morton, J.L., Normark, W.R., Ross, S.L., Koski, R.A., Holmes, M.L., Shanks, W.C., III, Zierenberg, R.A., Lyle, M., and Benninger, L.M., 1987b, Preliminary report, cruises L1-86-NC and L2-86-NC, Escanaba Trough, Gorda Ridge: U.S. Geological Survey Open-File Report 87-375-A, 20 p.

Morton, J.L., Zierenberg, R.A., and Reiss, C.A., Geologic, hydrothermal, and biologic studies at Escanaba Trough: An introduction, *in* Morton, J.L., Zierenberg, R.A., and Reiss, C.A., eds., Geologic, hydrothermal, and biologic studies at Escanaba Trough, Gorda Ridge, offshore northern California: U.S. Geological Survey Bulletin 2022, chapter 1 (this volume).

Mutti, E., 1985, Turbidite systems and their relations to depositional sequences, *in* Zuffa, G.G., ed., Provenance of arenites: Dordrechts, Reidel Publishing Company, NATO-ASI Seriesp. 65–93.

Mutti, E., and Normark, W.R., 1991, An integrated approach to the study of turbidite systems, *in* Weimer, P., and Link, M. H., eds., Seismic facies and sedimentary processes of submarine fans and turbidite systems: New York, Springer-Verlag, p. 75–106.

Nelson, C.H., 1976, Late Pleistocene and Holocene depositional trends, processes and history of Astoria deep-sea fan, northeast Pacific: Marine Geology, v. 20, p. 129–173.

Nelson, C.H., Carlson, P.R., and Bacon, C.R., 1988, The Mount Mazama climactic eruption (~6900 yr B.P.) and resulting convulsive sedimentation on the Crater Lake caldera floor, continent, and ocean basin: Geological Society of America Special Paper 229, p. 37–57.

Nelson, C.H., Kulm, L.D., Carlson, P.R., and Duncan, J.R., 1968, Mazama ash in the northeastern Pacific: Science, v. 161, p. 46–49.

Normark, W.R., Posamentier, H., and Mutti, E., 1993, Turbidite systems: state of the art and future directions: Reviews of Geophysics, v. 31, p. 91–116.

Perry, E.A., and Hower, J., 1972, Late-stage dehydration in deeply buried pelitic sediments: American Association of Petroleum Geologists Bulletin, v. 56, p. 2013–2021.

Quinterno, P.J., Quaternary foraminifers from Escanaba Trough, northeast Pacific Ocean, *in* Morton, J.L., Zierenberg, R.A., and Reiss, C.A., eds., Geologic, hydrothermal, and biologic studies at Escanaba Trough, Gorda Ridge, offshore northern California: U.S. Geological Survey Bulletin 2022, chapter 18 (this volume).

Rosenbauer, R.J., Bischoff, J.L., and Radtke, A.S., 1983, Hydrothermal alteration of graywacke and basalt by 4M NaCl: Economic Geology, v. 78, p. 1701–1710.

Scheidegger, K.F., Kulm, L.D., and Piper, D.J.W., 1973, Heavy mineralogy of unconsolidated sands in northeastern Pacific sediments: Leg 18, Deep Sea Drilling Project, *in* Kulm, L.D., and von Huene, R., eds., Initial reports of the Deep Sea Drilling Project: Washington, U.S. Government Printing Office, v. 18, p. 877–887.

Thornton, E.C., and Seyfried, W.E., Jr., 1985, Sediment-seawater interaction at 200 and 300°C, 500 bars pressure: The role of sediment composition in diagenesis and low grade metamorphism of marine clay: Geological Society America Bulletin, v. 96, p. 1287–1295.

Vail, P.R., 1987, Seismic stratigraphic interpretation using sequence stratigraphy—Part 1: Seismic stratigraphy interpretation procedure, *in* Bally, A.W., ed., Atlas of seismic stratigraphy, v. 1: American Association of Petroleum Geologists Studies in Geology 27, p. 1–10.

Vallier, T.L., 1970, The mineralogy of some turbidite sands from Sites 32 and 35, *in* McManus, D.A., and others, eds., Initial reports of the Deep Sea Drilling Project: Washington, U.S. Government Printing Office, v. 5, p. 535–539.

Vallier, T.L., Harold, P.J., and Girdley, W.A., 1973, Provenances and dispersal patterns of turbidite sand in Escanaba Trough, northeastern Pacific Ocean: Marine Geology, v. 15, p. 67–87.

Whetten, J.T., Kelley, J.C., and Hanson, L.G., 1969, Characteristics of Columbia River sediment and sediment transport: Journal of Sedimentary Petrology, v. 39, p. 1149–1166.

Wilde, P., Chase, T.E., Holmes, M.L., Normark, W.R., Thomas, J.A., McCulloch, D.S., and Kulm, L.D., 1978, Oceanographic data off northern California-southern Oregon, 40–43° North including the Gorda deep-sea fan: Berkeley, Lawrence Berkeley Laboratory Publication 251, 1 mapsheet, scale 1:815,482.

Wong, F.L., 1989, Mineralogy of sand in turbidites from Escanaba Trough, northeast Pacific Ocean: U. S. Geological Survey Open-File Report 89-661, 10 p.

Wong, F.L., and Klise, D.H., 1986, Heavy mineral, clay mineral, and geochemical data of surface sediments from coastal northern California rivers: U.S. Geological Survey Open-File Report 86-574, 13 p.

Zierenberg, R.A., and Shanks, W.C., III, Sediment alteration associated with massive sulfide formation in the Escanaba Trough, Gorda Ridge: The importance of seawater mixing and magnesium metasomatism, *in* Morton, J.L., Zierenberg, R.A., and Reiss, C.A., eds., Geologic, hydrothermal, and biologic studies at Escanaba Trough, Gorda Ridge, offshore northern California: U.S. Geological Survey Bulletin 2022, chapter 14 (this volume).

Appendix A: Lithologic summary logs for 17 cores recovered from Escanaba Trough at DSDP Site 35

This section presents lithologic summary logs for 17 cores recovered from Escanaba Trough at Site 35 of the Deep Sea Drilling Program. The lithologic characters selected have been simplified to allow combination of the original shipboard descriptions for 28 sections with those done in 1988 (see text). A solid vertical line to the right of the core means the description used is by the U.S. Geological Survey; a dashed vertical line indicates the description is from McManus and others, 1970 (see fig. 6.3).

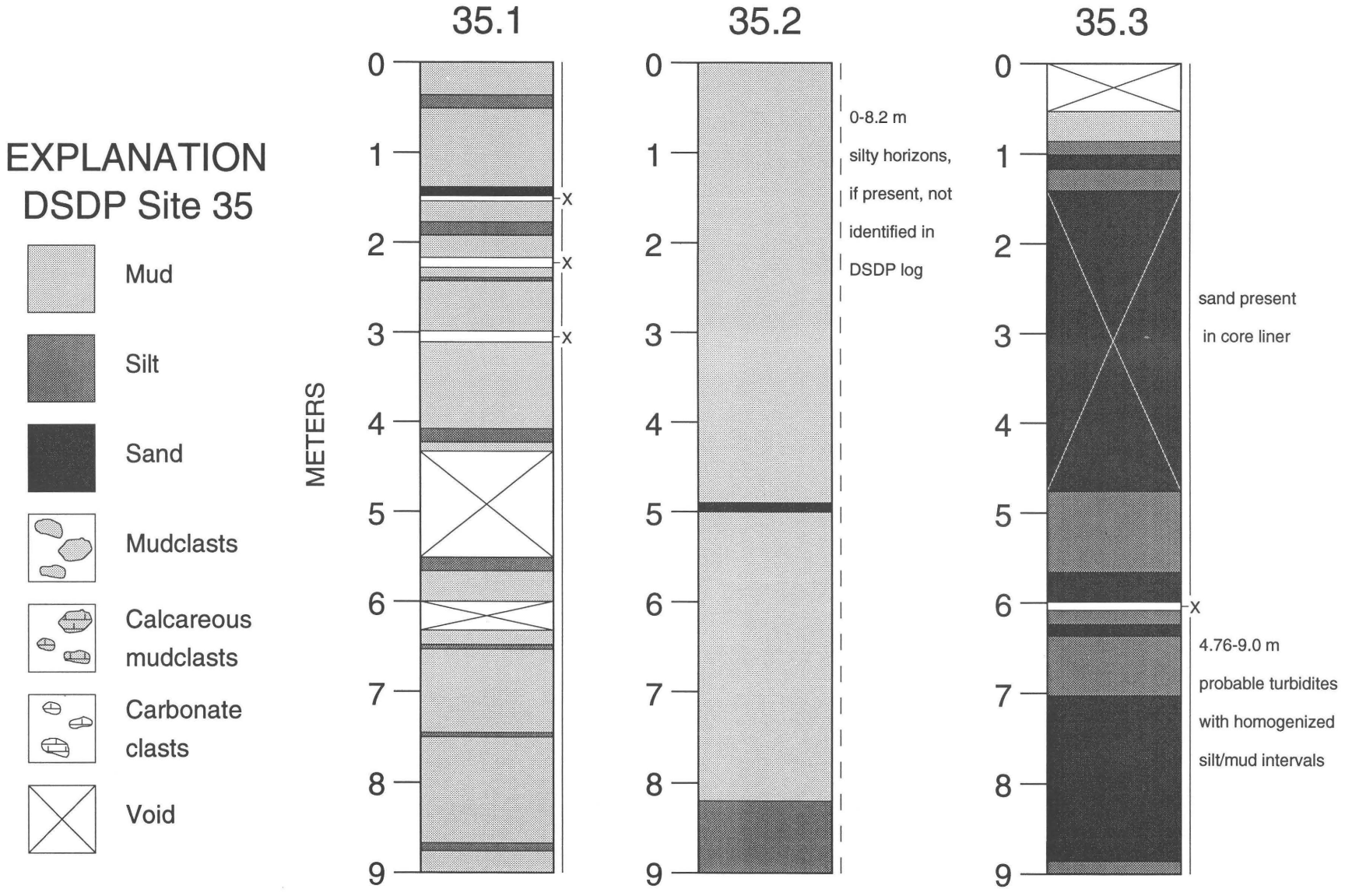

Appendix A: Lithologic summary logs for 17 cores recovered from Escanaba Trough at DSDP Site 35—Continued

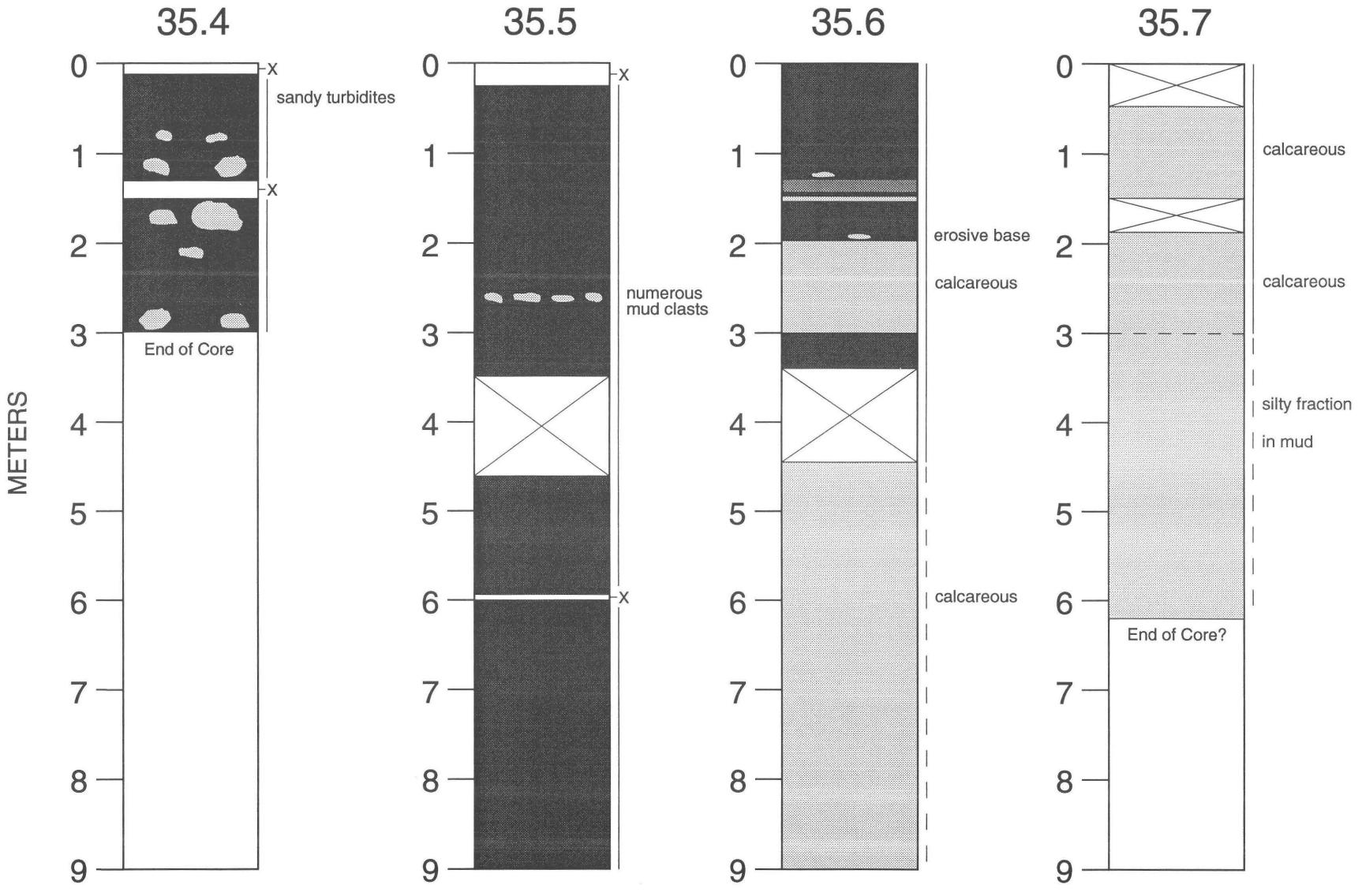

Appendix A: Lithologic summary logs for 17 cores recovered from Escanaba Trough at DSDP Site 35—Continued

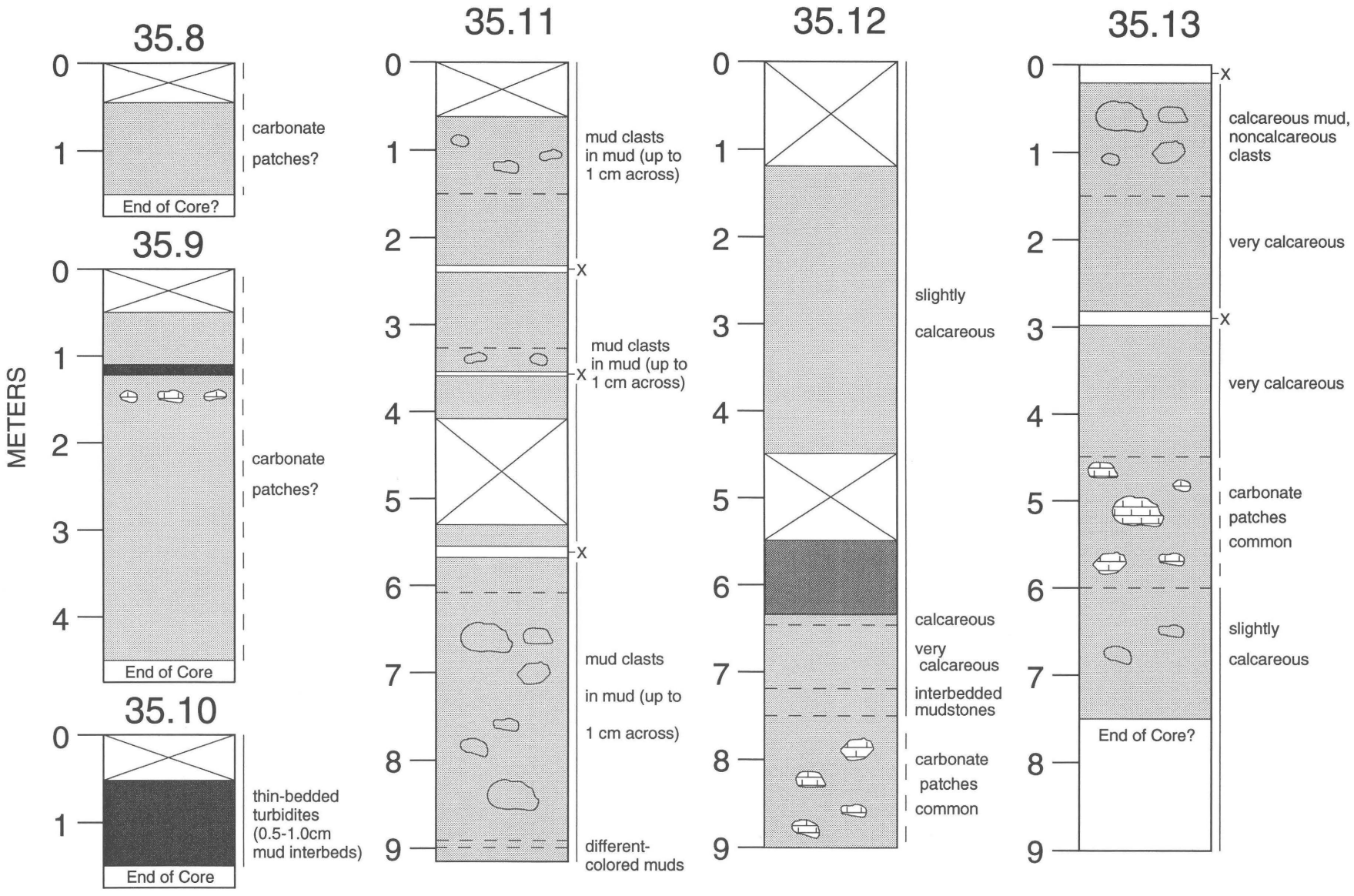

Appendix A: Lithologic summary logs for 17 cores recovered from Escanaba Trough at DSDP Site 35—Continued

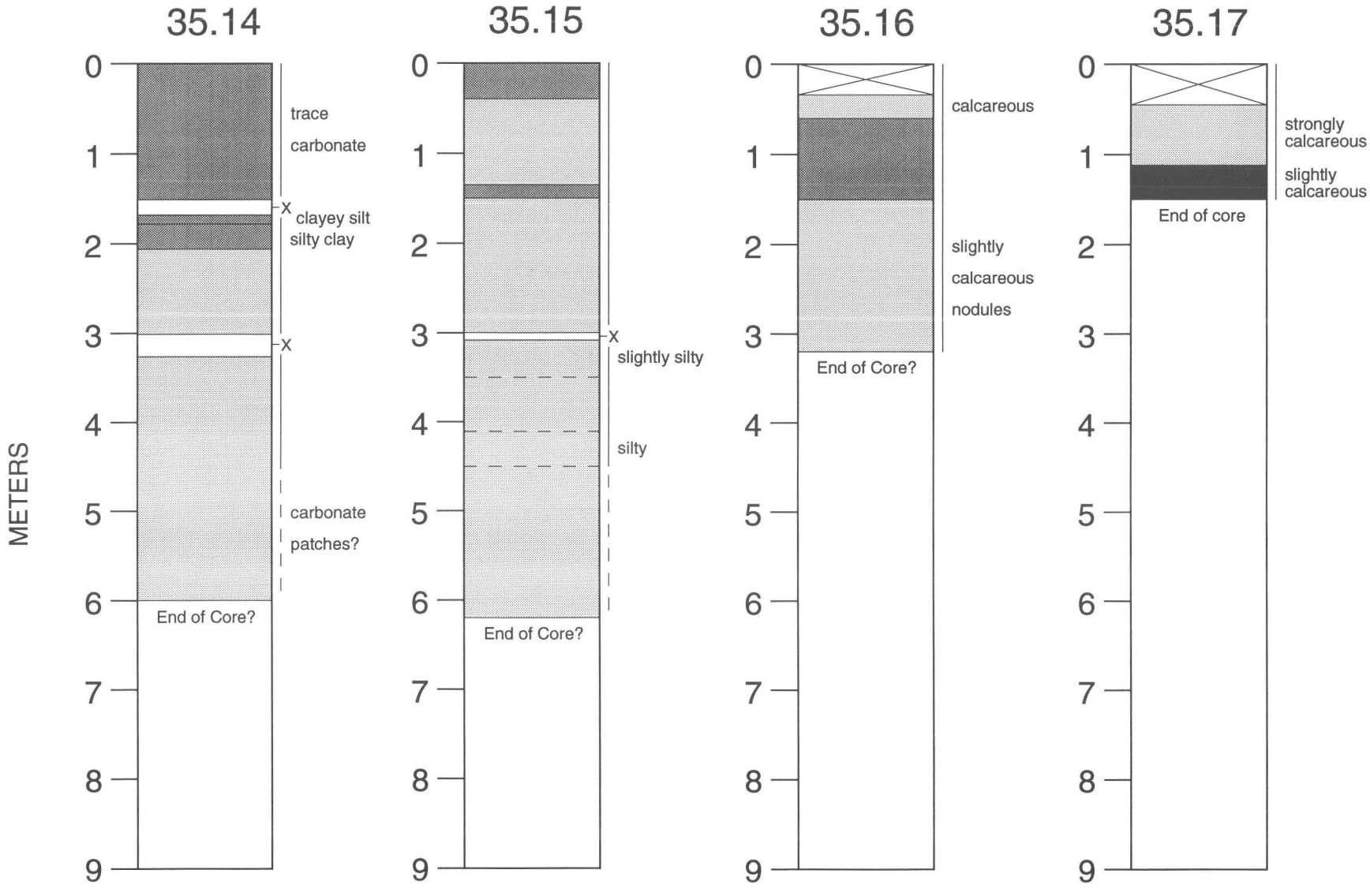

Appendix B: Lithologic summary logs for surficial cores from Escanaba Trough

This section presents lithologic summary logs for surficial cores from *A*, U.S. Geological Survey cruise L6-85-NC constructed from data in Karlin and Lyle (1986; no description available for cores 4G and 11G); *B, C, D*, USGS cruises L1-, L2-, and L3-86-NC; and *E*, Geological Survey of Canada cruise TUL-89D (no description available for cores 5G and 9P). Core locations are shown in figures 6.2, 6.9, and 6.10; see table 6.3. Where applicable, the lithologic patterns used in the logs—for example, the symbols for void spaces, oxidized zone, turbidite mud, silt, and sand—are common to all core sets. The shading patterns, however, are unique within each set of cores, as shown by the accompanying explanations. HHC, interval sampled for heavy hydrocarbon analyses; LHC, interval sampled for light hydrocarbon analyses; PW, interval sampled for pore-fluid analyses.

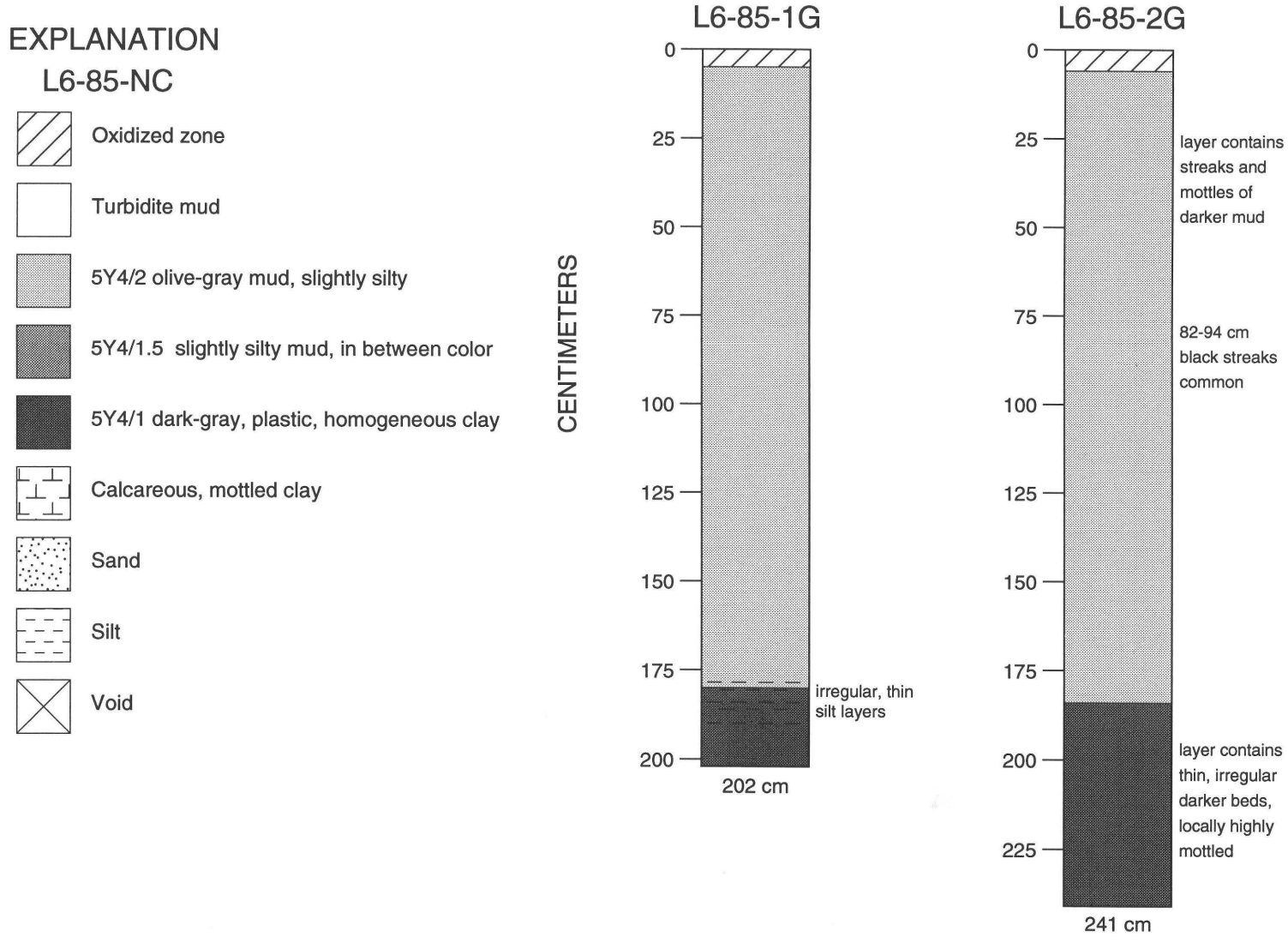

Appendix B: Lithologic summary logs for surficial cores from Escanaba Trough—Continued

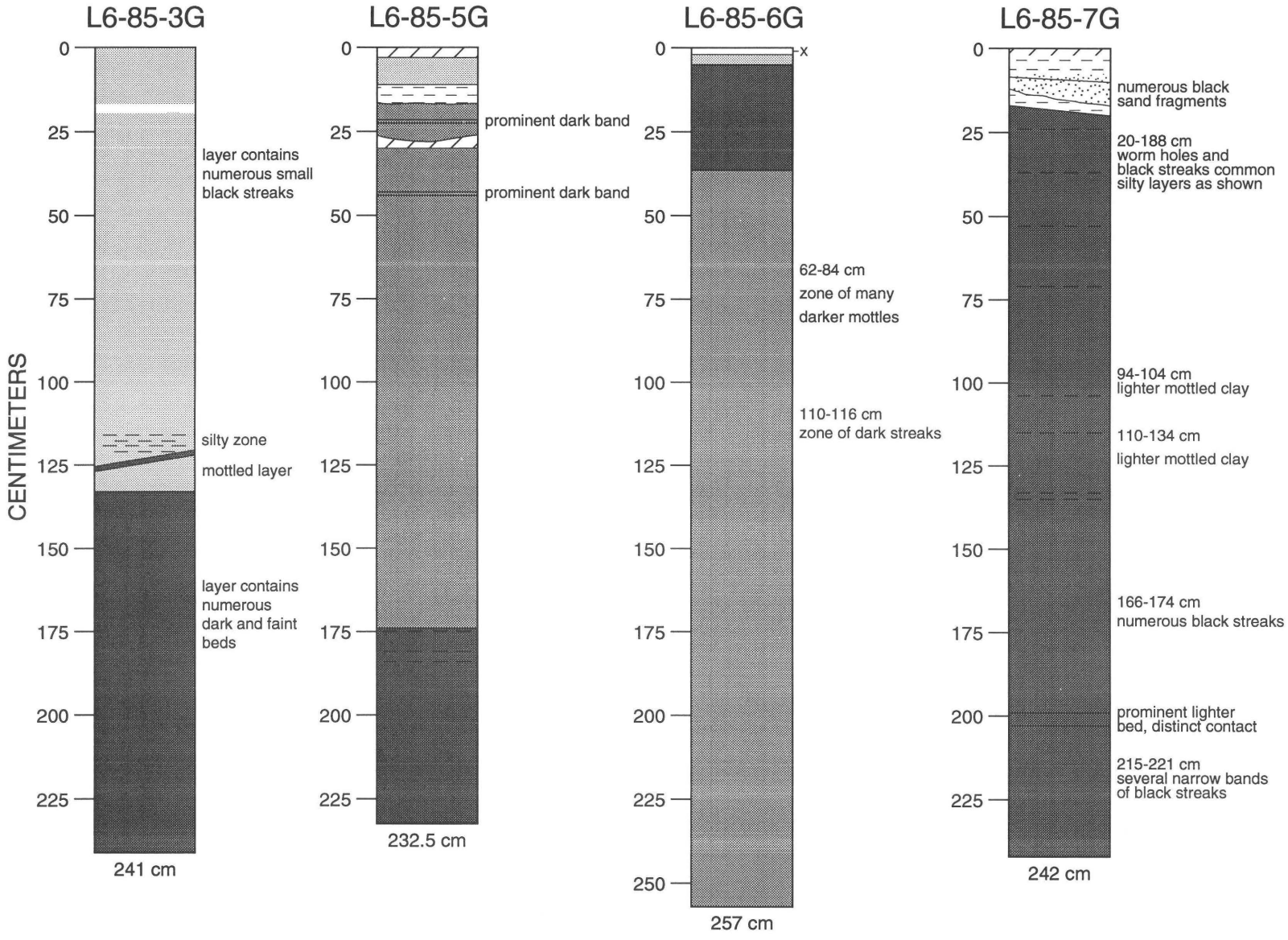

Appendix B: Lithologic summary logs for surficial cores from Escanaba Trough—Continued

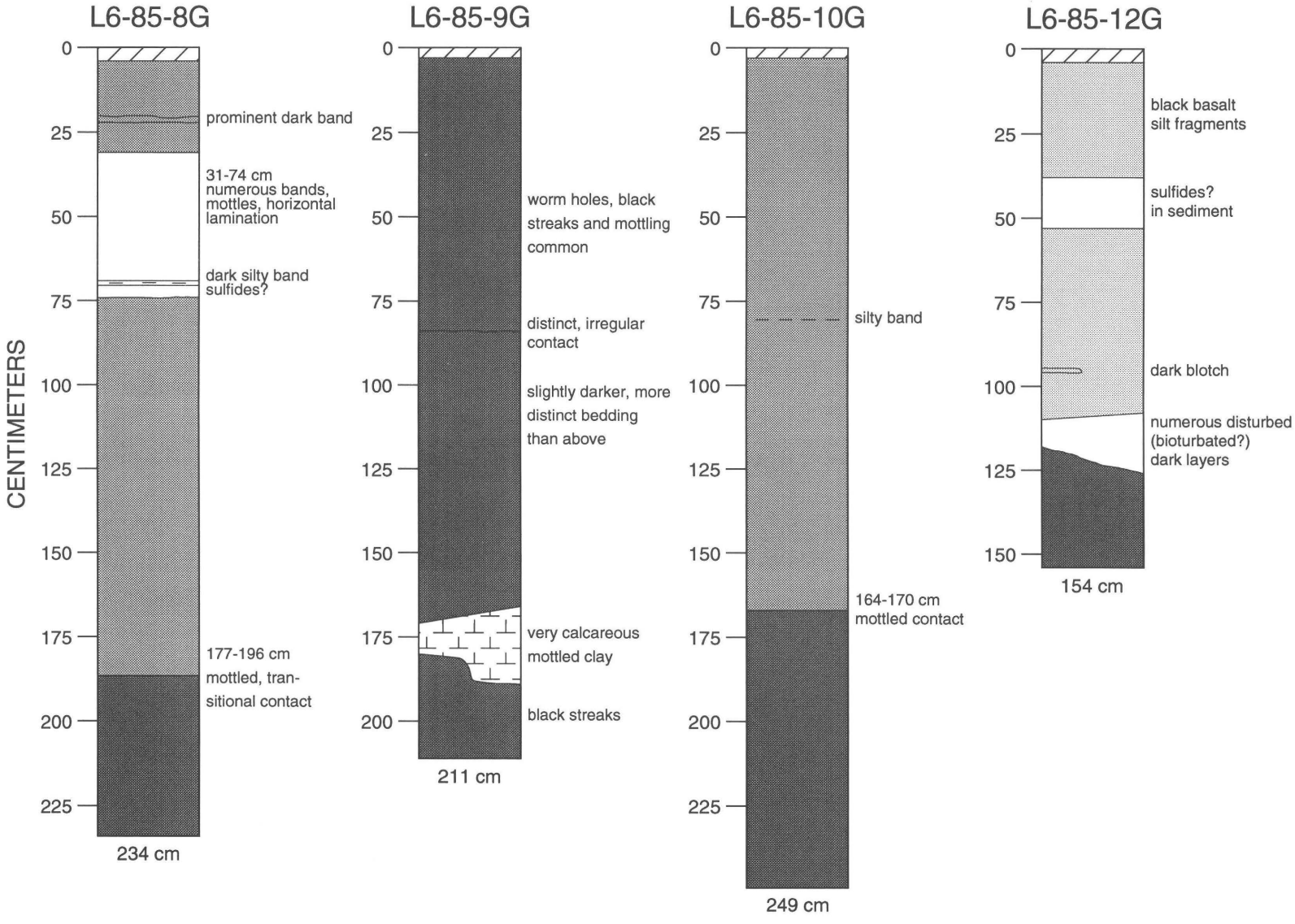

Appendix B: Lithologic summary logs for surficial cores from Escanaba Trough—Continued

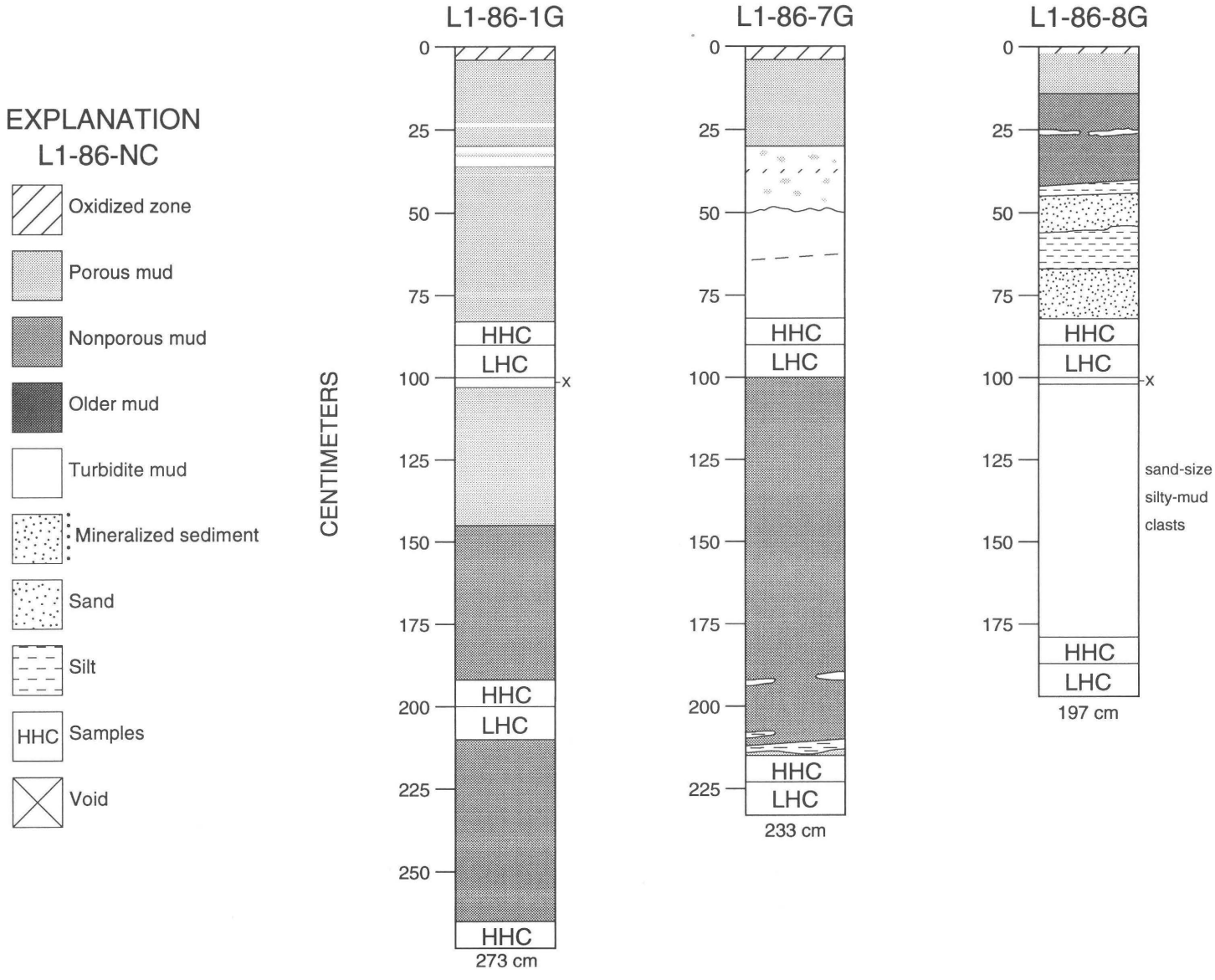

Appendix B: Lithologic summary logs for surficial cores from Escanaba Trough—Continued

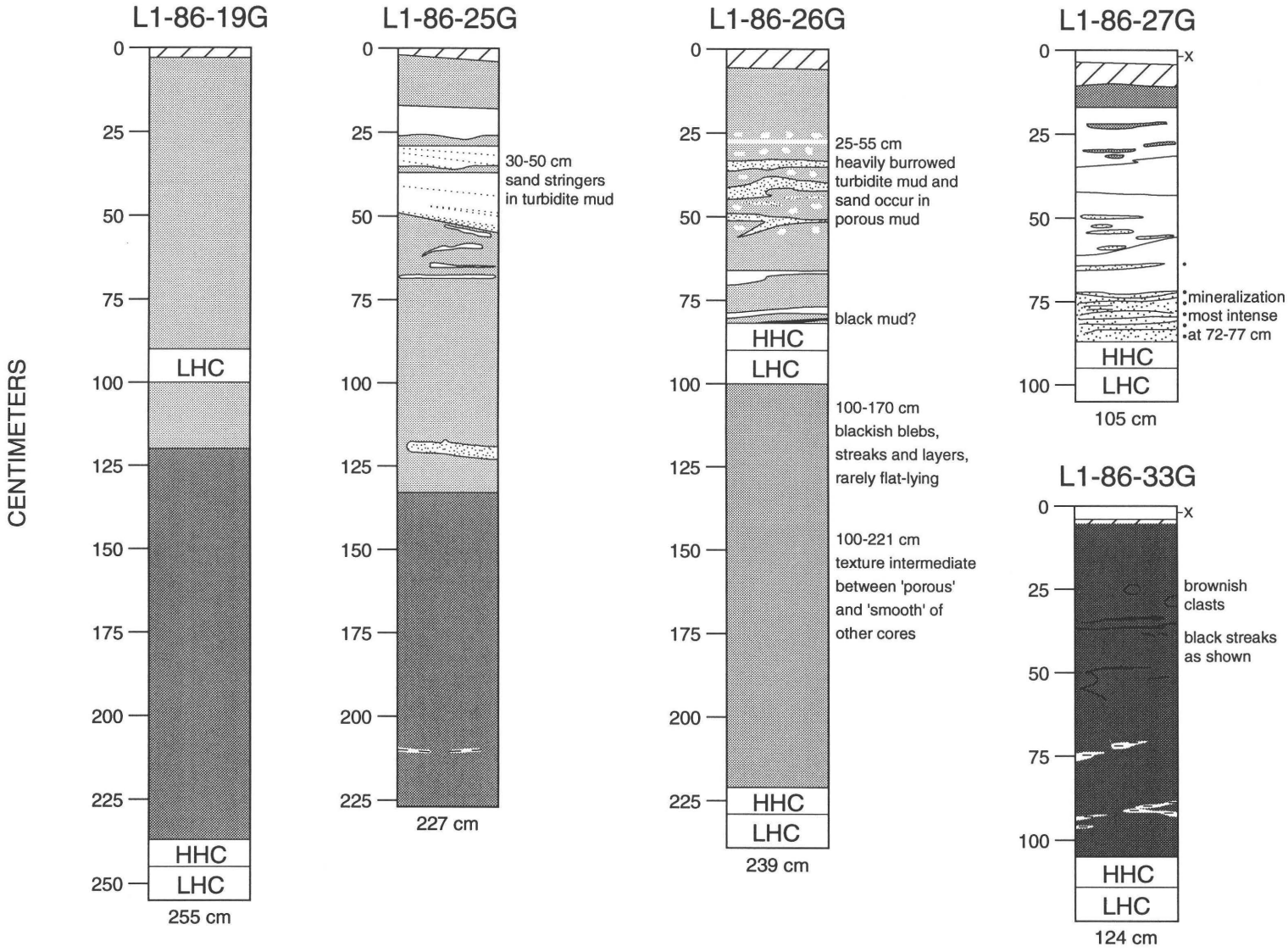

Appendix B: Lithologic summary logs for surficial cores from Escanaba Trough—Continued

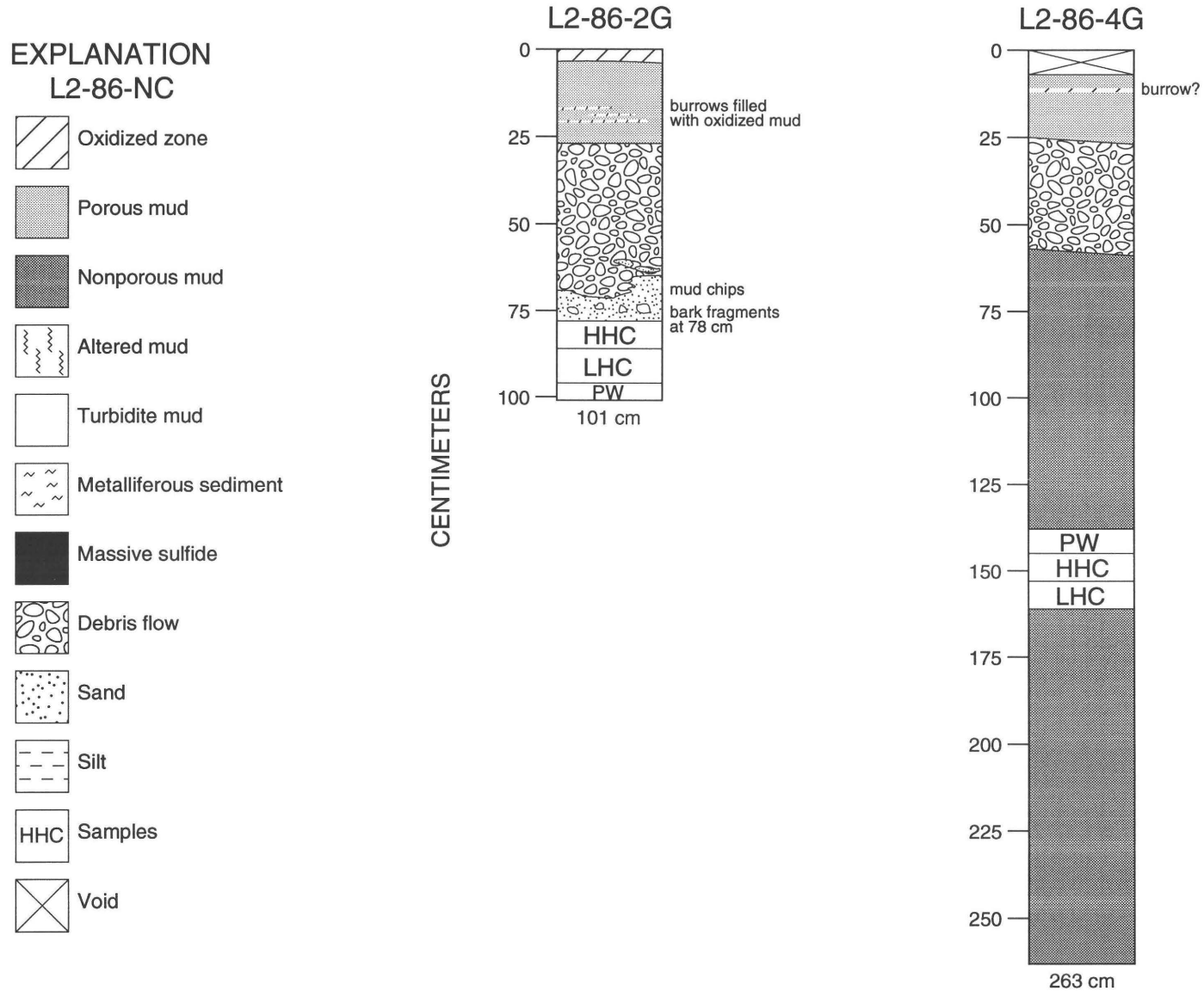

Appendix B: Lithologic summary logs for surficial cores from Escanaba Trough—Continued

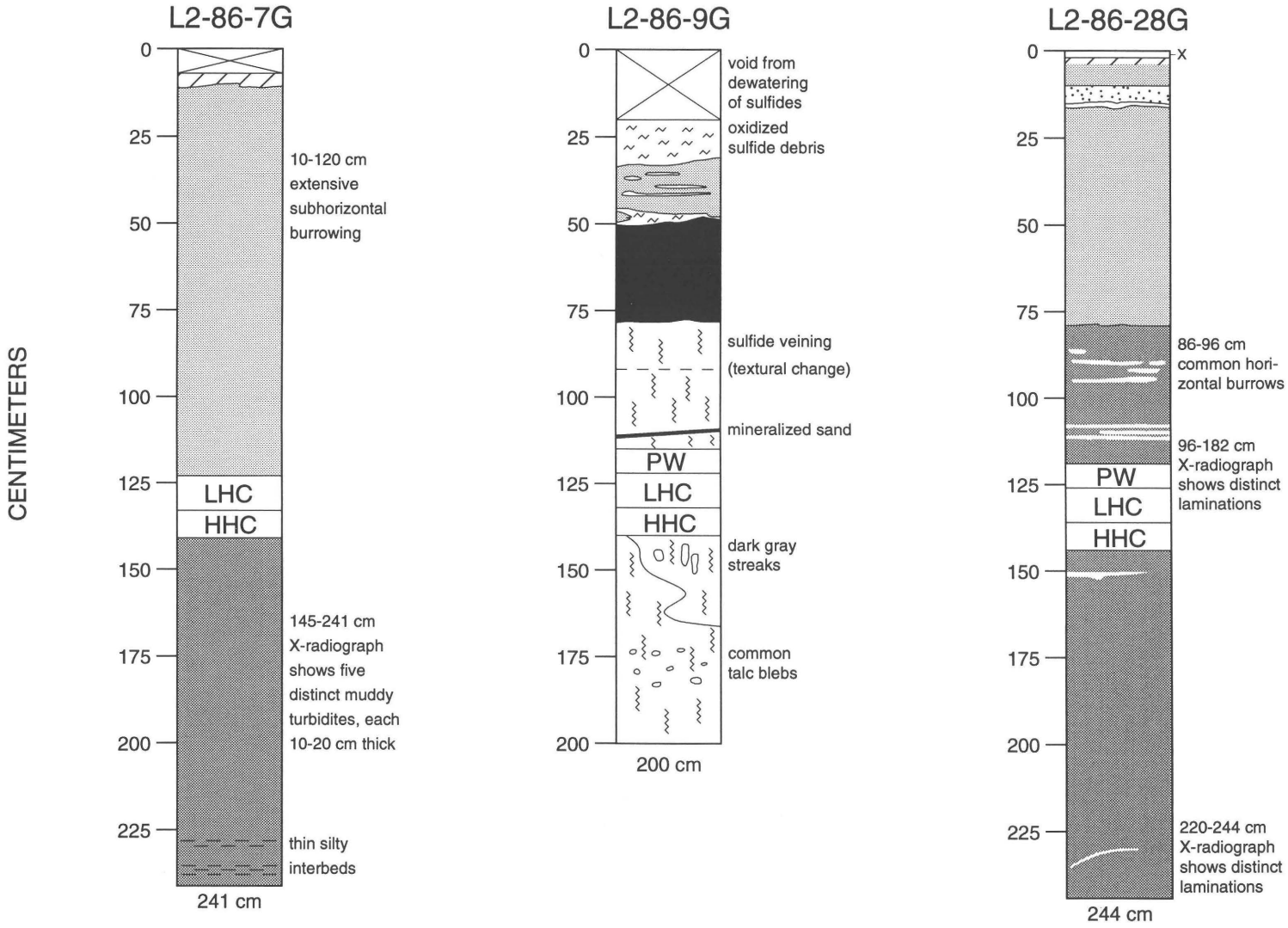

Appendix B: Lithologic summary logs for surficial cores from Escanaba Trough—Continued

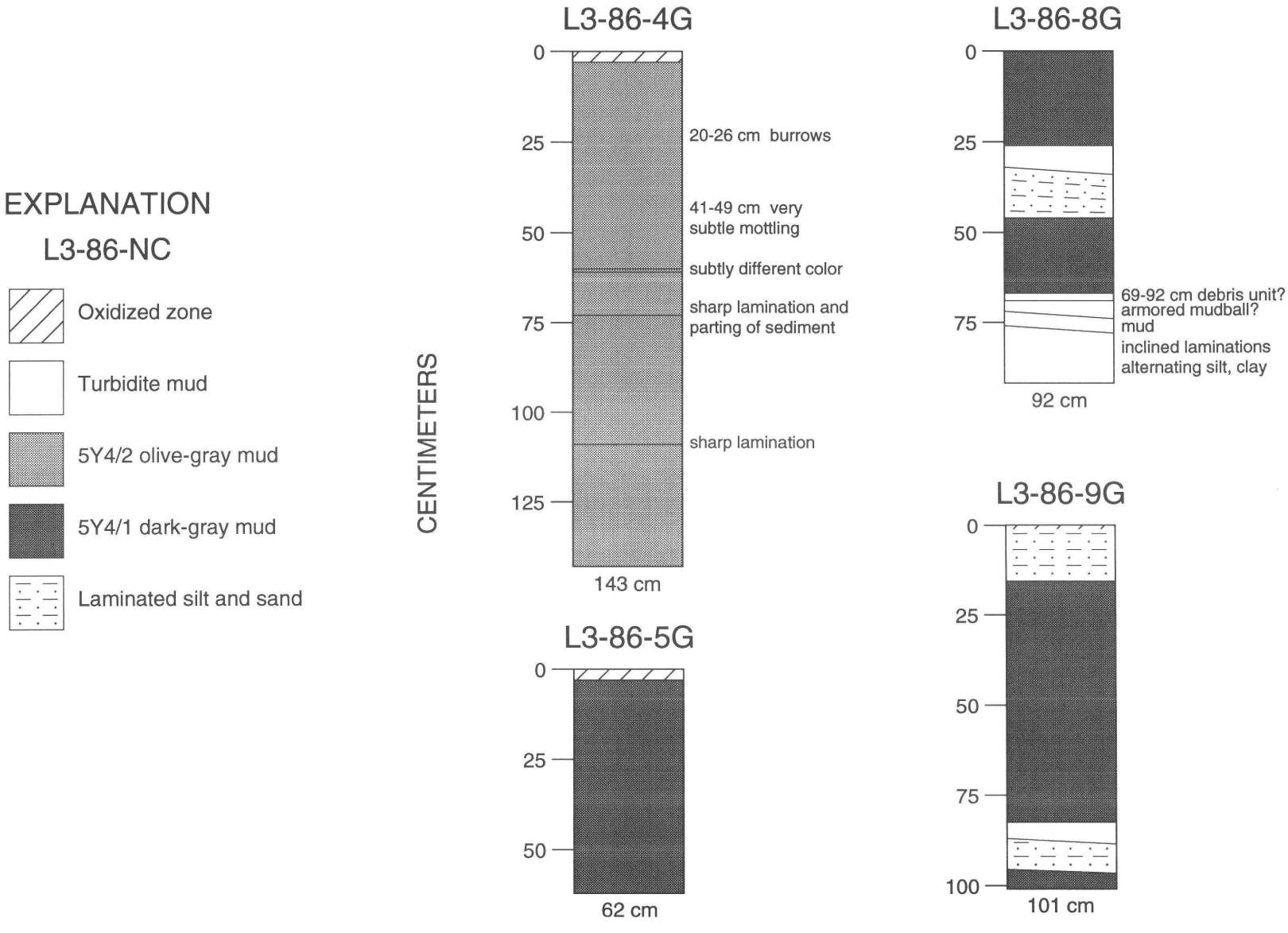

Appendix B: Lithologic summary logs for surficial cores from Escanaba Trough—Continued

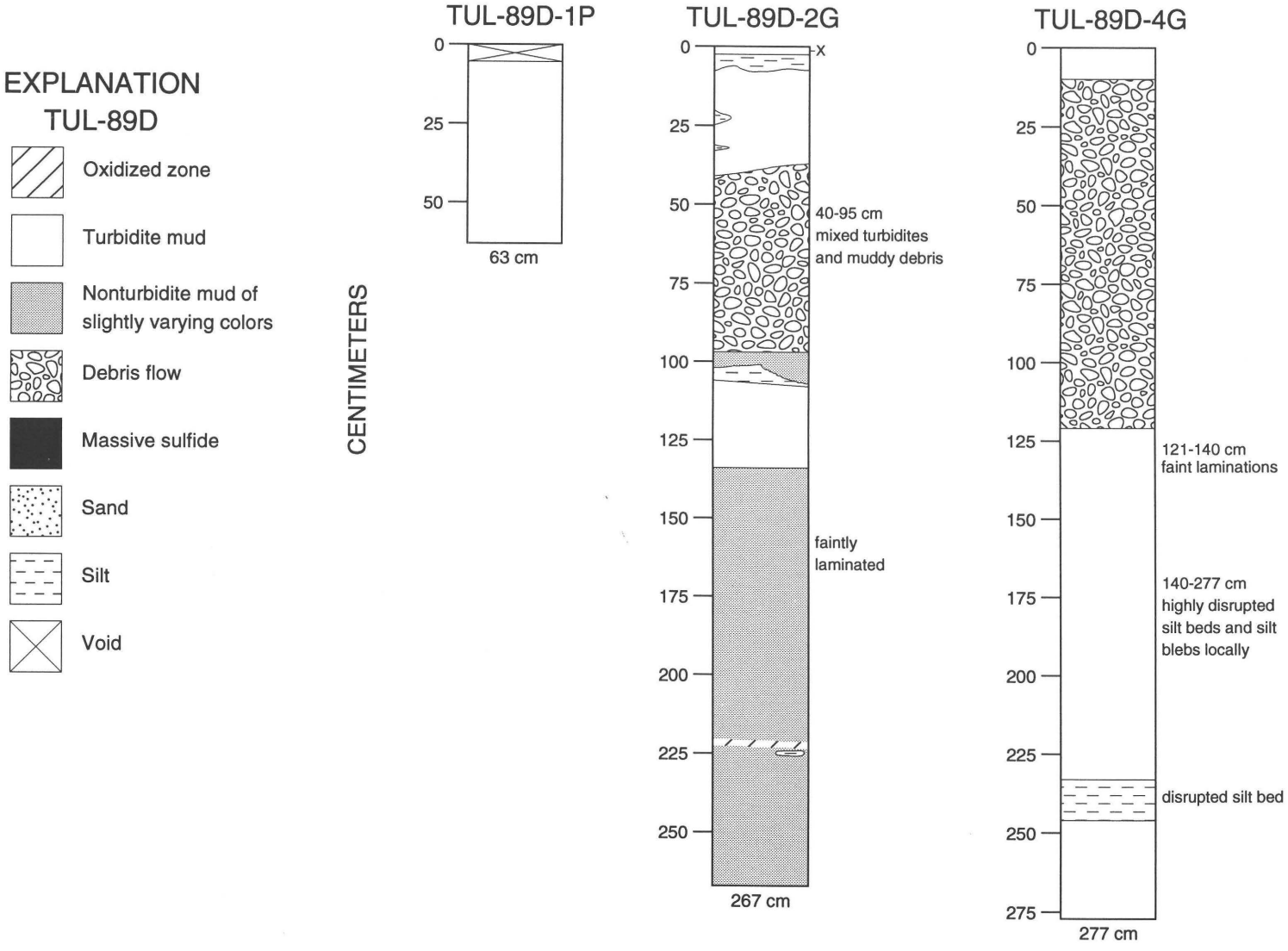

Appendix B: Lithologic summary logs for surficial cores from Escanaba Trough—Continued

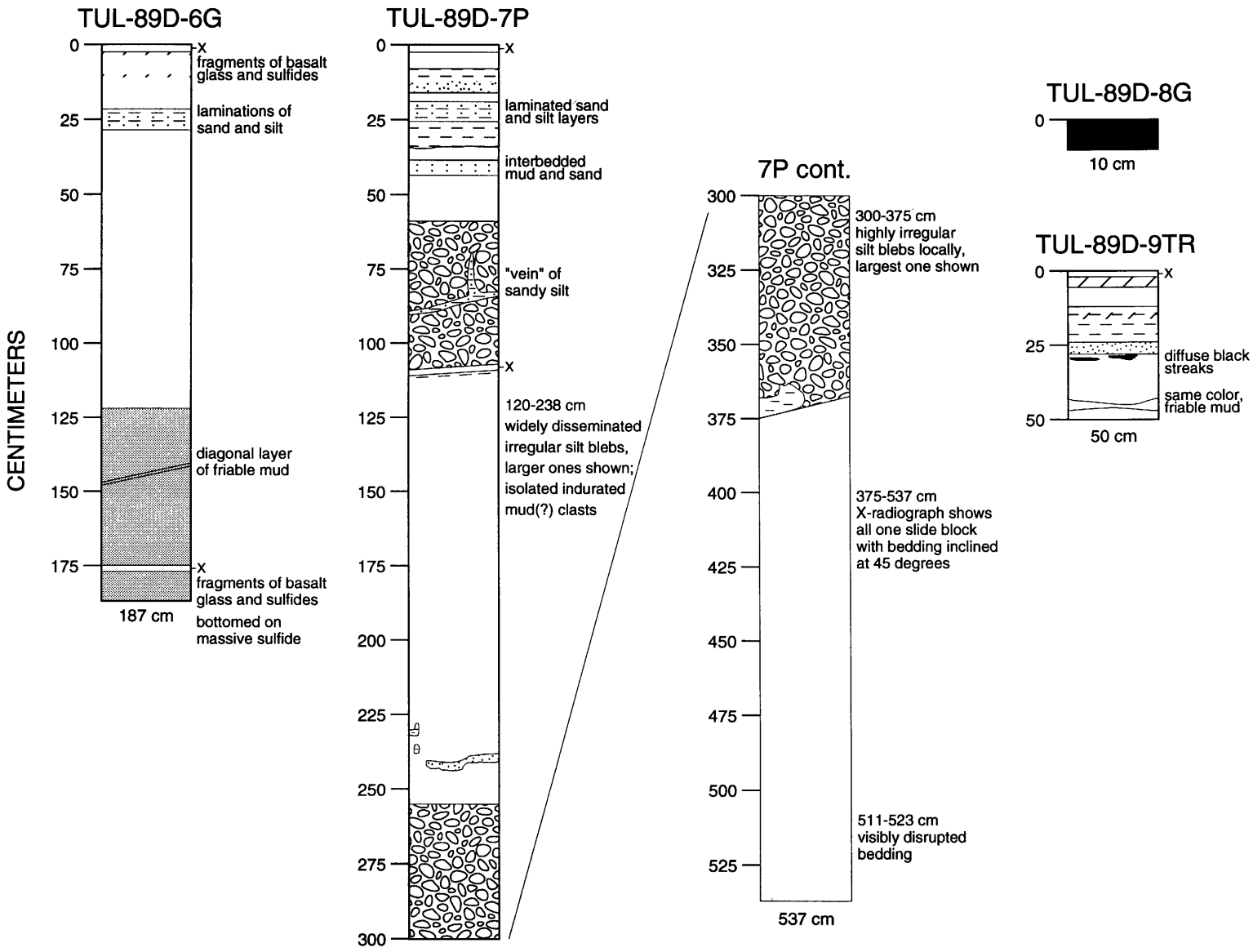

Chapter 7. Sedimentation and Neotectonism in the SESCA Area, Escanaba Trough, Southern Gorda Ridge

By Robert E. Karlin[1] *and* Robert A. Zierenberg[2]

CONTENTS

ABSTRACT

The lithology and stratigraphy of gravity cores recovered from the SESCA area in Escanaba Trough were evaluated by combining magnetic susceptibility profiles with visual observations. Hemipelagic sedimentation rates during the Holocene are variable and range up to 14 cm/kyr. Sediment hills are actively eroding, and mass wasting is common on the flanks. Erosional channels funnel sediment to the deeper parts of the axial valley. Holocene turbidites on the valley floor appear to be locally derived and indicate local seismotectonic activity in the last 2.5 kyr. Hydrothermal deposits are irregularly distributed around the base of the hills. The hills appear to be the source of mass flow deposits, and some turbidites contain hydrothermally precipitated pyrrhotite. Intensely altered sediment and massive sulfide mineralization also occur in relatively unexplored basins in the axial valley away from the sediment hills.

[1] Mackay School of Mines, University of Nevada-Reno, Reno, Nevada.

[2] U.S. Geological Survey, Menlo Park, California.

INTRODUCTION

Escanaba Trough forms the southernmost segment of the Gorda–Juan de Fuca spreading system and is about 200 km west of the California-Oregon coast. Slow sea-floor spreading combined with high terrigenous sedimentation has resulted in a wedge of over 500 m of Pleistocene sediment fill in the southern part of the axial valley that thins to the north (Atwater and Mudie, 1973; Riddihough, 1980; Morton and Fox, chap. 2, this volume). Volcanism along the rift resulted in penetration of the sediment cover by several volcanic complexes (Morton and Fox, chap. 2, this volume). Camera tows and sampling have revealed massive sulfide deposits associated with the volcanic centers (Morton and others, 1987a,b, 1990), and these deposits have subsequently been investigated by submersible (Holmes and Zierenberg, 1990). Such deposits may be the modern analogs of ancient sediment-hosted polymetallic sulfide ore bodies. Active hydrothermal vents have been explored and sampled at the NESCA site near latitude 41°00′ N., longitude 127°30′ W. (Zierenberg and others, 1988). Thus, Escanaba Trough is a natural laboratory to study ore generation processes and the timing of volcanism, tectonism, and hydrothermal activity at an active spreading center.

During two 1986 cruises of the R/V *S.P. Lee*, a series of gravity cores was collected at the Southern Escanaba site (SESCA) in the vicinity of the volcanic complex near latitude 40°46′ N., longitude 127°31′ W. (fig. 7.1). The purposes of the sampling were to determine the late Quaternary history of neotectonism and hydrothermal activity of the complex and assess, if possible, the areal extent of sediment alteration associated with volcanism. In earlier studies of sediments from the volcanic edifice in the Northern Escanaba (NESCA) area, Karlin and Lyle (1986) found that magnetic susceptibility measurements were very helpful in characterizing lithologic changes in the sediment column and in dating the sediments. Magnetic susceptibility is the response of a material to an applied field and is a sensitive measure of the concentration and grain size of magnetic mineral assemblages. Here we report magnetic susceptibility results for gravity cores taken in the SESCA area as well as scanning electron microscopy of

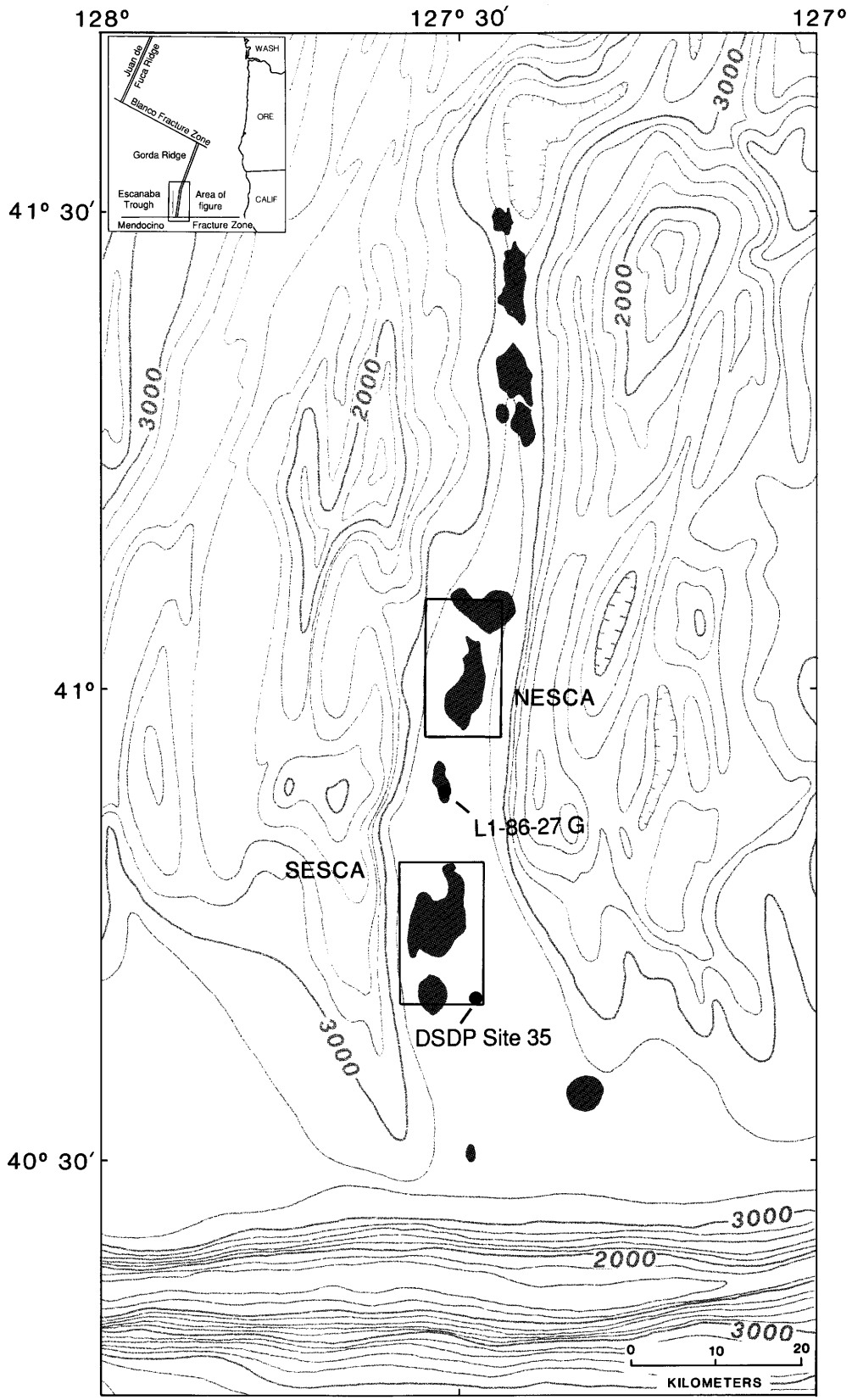

Figure 7.1. Bathymetric map of Escanaba Trough, showing location of volcanic edifices (dark gray), SESCA and NESCA sites, DSDP Site 35, and core L1-86-27G in axial valley of Escanaba Trough outside of SESCA area. Contour interval is 200 m. Hachures indicate area of closed low.

magnetic separates extracted from selected intervals. In this preliminary work, our objectives are to define the sedimentary regime and establish a stratigraphic framework in order to address the timing of neotectonic activity. Our results provide constraints on the rates and mechanisms of sedimentation in the area and suggest that local seismotectonic activity and resulting mass-wasting processes have been prevalent in the last few thousand years.

ACKNOWLEDGMENTS

We thank the officers and crew of the R/V *S.P. Lee* for their excellent support during the 1986 cruise.

METHODS

Thirteen sediment cores were taken in the Escanaba Trough during the R/V *S.P. Lee* cruises L1-86-NC and L2-86-NC. They were recovered using a conventional Benthos gravity corer (8.6 cm diameter) with a 3-m-long barrel. Locations were established by transponder navigation (see Morton and others, chap. 1, this volume). All of the cores were cut onboard into 1.5-m lengths and selected subsections of some of the cores were removed for pore water and hydrocarbon analyses. The cores were kept in refrigerated storage during and after transport to the USGS Core Repository in Palo Alto, California, where they were opened and described (Normark and others, chap. 6, this volume).

Whole-core magnetic susceptibility measurements were made on the split core sections at 1-cm intervals using a Bartington MS-2 susceptibility meter equipped with a 125-mm ring sensor. Susceptibility values are reported here in 10^{-6} cgs units (4π cgs units = 1 SI unit). Depths were determined relative to the top of the sediment rather than from the top of the core liner, because of compaction during transport and storage. Because of the sensor geometry, each value represents a center-weighted average over an interval of about 5 cm. The stability of the instrument was about $\pm$ 1 $\times$ 10^{-6} cgs. The split-core susceptibility values reported here can be doubled to obtain whole-core values for a core liner 8.6 cm in diameter, or multiplied by 3.36 for comparison with 11.4-cm (4.5 inch) diameter cores.

Magnetic separates were extracted in selected cores from sandy turbiditic intervals using a Franz isodynamic separator. The extracts were analyzed by X-ray diffraction as well as optical and by scanning electron microscopy to establish their mineralogy.

GEOLOGIC SETTING

The SESCA area contains one of several volcanic complexes that locally pierce the thick sediment cover along the axis of Escanaba Trough. The physiography of the area is described by Morton and others (1987b, 1990) and Morton and Fox (chap. 2, this volume). The most prominent features in the area are three roughly circular sediment-covered hills that rise 60 to 100 m above the surrounding valley floor (fig. 7.2). Submersible observations indicate that the hills are flat-topped and resemble buttes. The sides of the hills are retreating by mass wasting, and sedimentary strata are locally exposed (Holmes and Zierenberg, 1990; Zierenberg and others, chap. 10, this volume). The steep slopes are deeply incised by a complex network of erosional channels, and the lower slopes are covered by mudstone talus. Pillows and sheet flows of basalt, partially covered by sediment, are exposed to the southwest of North Hill (fig. 7.2) (Ross and Zierenberg, chap. 8, this volume). Locally, the basalt flows are cut by fissures and normal faults that strike parallel to the spreading axis. Sediment-hosted sulfide deposits were discovered near the base of each of the hills and may discontinuously rim the perimeter of all of the uplifted sediment hills (Morton and others, 1990; Holmes and Zierenberg, 1990; Zierenberg and others, chap. 10, this volume). Many of the deposits are old and apparently inactive, because they show signs of extensive sea-floor weathering and erosion. We believe that morphologic differences between deposits suggest multiple episodes of sulfide precipitation, sea-floor weathering, and erosion. Active hydrothermal venting has not been observed in the SESCA area.

With two exceptions, the coring during the L1-86-NC and L2-86-NC cruises was concentrated in the vicinity of the 3170 Hill and the East Hill at approximately latitude 40°46′ N. (fig. 7.2). Cores L2-86-2G and L2-86-4G were taken near the summit of each hill, whereas cores L1-86-19G, L1-86-25G, L1-86-26G, and L1-86-7G were collected along the flanks of the 3170 Hill. The relatively flat areas on the surrounding sediment plain were sampled by cores L1-86-1G, L2-86-9G, and L2-86-28G. Core L2-86-7G came from the top of a terrace approximately 100 m shallower than the valley floor at the western edge of the SESCA map area. Core L1-86-27G was taken outside of the SESCA map area (fig. 7.1), in a poorly studied area of disturbed sediment between NESCA and SESCA where the volcanic basement rises near the sea floor (edifice C of Abbott and others, 1986; Davis and Becker, chap. 3, this volume).

STRATIGRAPHY

The sediment in the study area is dominantly hemipelagic and typically consist of olive green to olive gray mottled silty clay. The cores are described in Normark and others (chap. 6, this volume). In an earlier study of Escanaba Trough sediments, Karlin and Lyle (1986) found

that a region-wide lithologic change occurred at approximately 11 ka and was associated with a transition from glacial to interglacial conditions. This boundary was initially dated by radiocarbon analyses on cores from the NESCA area and the northern Gorda Ridge. More recently, oxygen isotope analyses on cores from either side of Gorda Ridge confirm this age assignment (Karlin and others, 1992).

In the NESCA sediments studied by Karlin and Lyle (1986), the 11-ka lithologic change was recognizable as a subtle down core color transition from olive gray to gray and a fining of the sediment from a mottled silty clay to a slightly calcareous homogeneous stiff clay with a texture similar to a gley-type soil. Water contents abruptly decreased down core at the boundary from about 60 percent to less than 50 percent. The boundary is readily identifiable in whole-core susceptibility profiles as a doubling in susceptibility in the lower sediment. Holocene sediment has higher levels of Si, Mg, Zn, Cu, and Ba and lower levels of $CaCO_3$, Al, Na, K, and Ti relative to Pleistocene sediment. These abundances suggest that Pleistocene sediment consists primarily of terrigenous clay mixed with calcare-

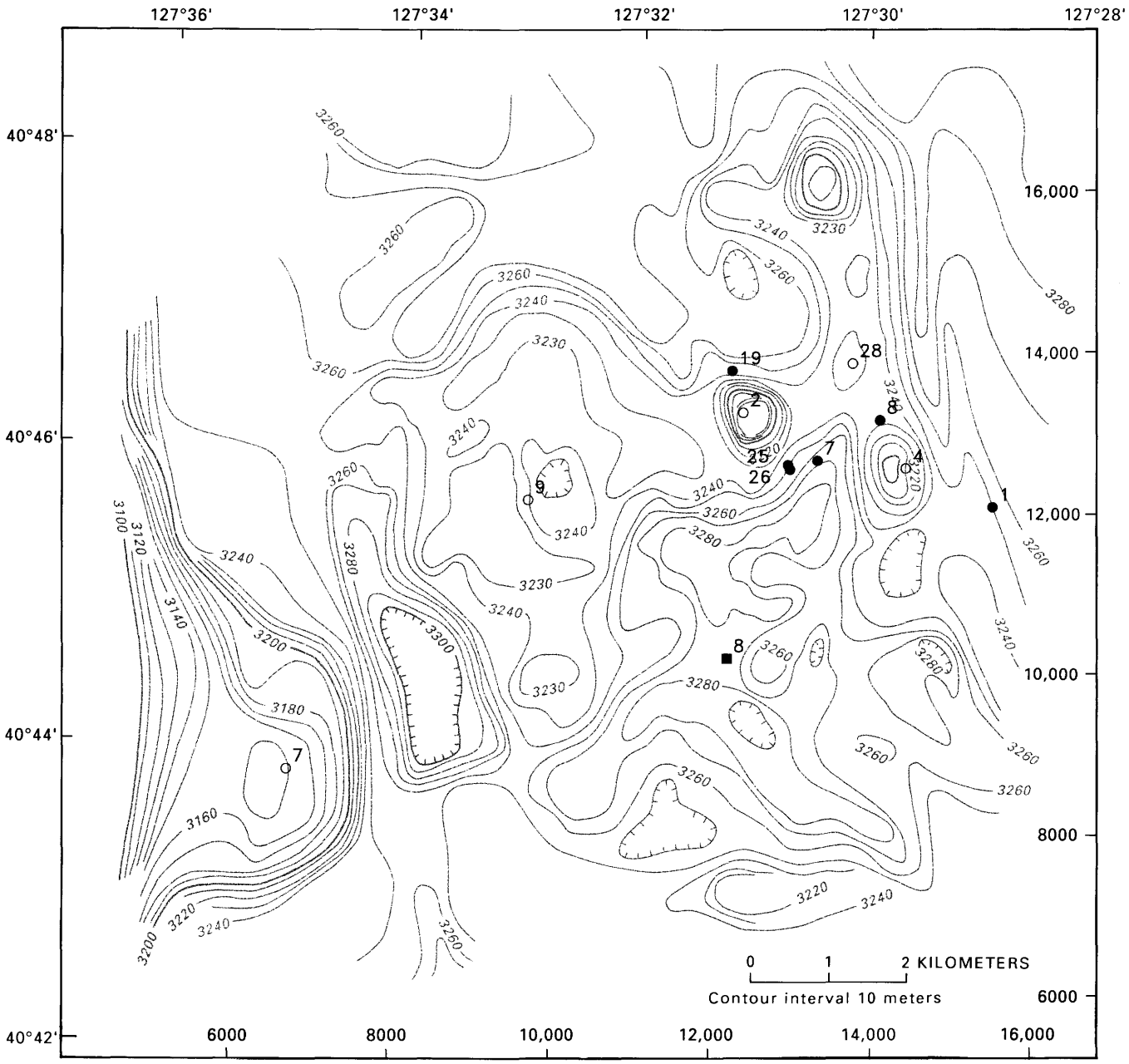

Figure 7.2. Bathymetry and core locations in SESCA area. Cores from L1-86 and L2-86 cruises denoted by filled and open circles, respectively; core L6-85-8G is marked as filled square. Numbers along right and bottom give coordinates of local transponder net (in meters). Hachures indicate area of closed low.

ous nannofossil ooze. The clay has a composition similar to illite or a mixture of illite and chlorite. In contrast, Holocene sediment contains a coarser grained, more felsic terrigenous assemblage combined with biogenic opal. These observations are consistent with decreased terrigenous input and relatively increased siliceous biogenic flux resulting from decreased continental weathering and enhanced coastal upwelling in the Holocene. The higher susceptibility values in the Pleistocene samples are probably due to the relatively greater proportion of fine-grained detrital minerals. Organic geochemical markers also distinguish Pleistocene sediment from Holocene sediment (Kvenvolden and others, chap. 15, this volume).

The ages of the SESCA cores were established using the criteria developed by Karlin and Lyle (1986) to identify the lithologic change at 11 ka. The best indicator of this boundary is an increase in half-core susceptibility from about 10 in the nonturbiditic Holocene intervals to 20 to 30 in the finer grained Pleistocene sediment intervals. The increase generally coincides with a down-core change in color and texture (Normark and others, chap. 6, this volume). The location of the boundary is further constrained by X-radiography, because the nonturbiditic Holocene sediments are less opaque and typically more heavily bioturbated than the Pleistocene sediments. Although visually the Pleistocene sediment appears to be homogeneous dark-gray mud, the X-radiographs show that the Pleistocene intervals often contain very fine clay laminations typical of distal turbidites. In some of the cores, the lithologic change is disturbed by bioturbation.

RESULTS FROM THE SESCA AREA

HOLOCENE SEDIMENTATION

Interpreted susceptibility profiles for the cores in the vicinity of the SESCA area (shown in figs. 7.3, 7.4, and 7.5) are grouped roughly by sedimentary regime, based on their locations and common characteristics in the profiles. Intervals denoted as gaps in the profiles are places where sections are missing due to earlier porewater and hydrocarbon sampling.

It is evident that the susceptibility profiles share several common features. From the susceptibilities and lithologic characteristics, the 11-ka lithologic boundary can be identified in many of the cores. In addition, several of the cores (L1-86-1G, L1-86-8G, L1-86-25G, L1-86-26G, and L2-86-28G) contain large susceptibility peaks in the upper parts of the Holocene section (figs. 7.3–7.5). These susceptibility highs correspond closely to sand and silt layers, which, in some cases, show graded bedding and sharp irregular contacts. These intervals almost certainly represent turbidites. The zones of elevated susceptibility are broader than the discrete coarse sediment layers seen in the cores and define both the coarse-grained, high-energy part of the flow and the fine-grained tail, which is not visually apparent. Magnetic separates of turbidite intervals in cores L1-86-25G and L1-86-26G contain mainly detrital terrigenous minerals such as magnetite and ilmenite.

In certain cores (L1-86-8G, L1-86-25G, and L1-86-26G), the interval immediately underlying the turbidite zones contains relatively homogeneous, stiff gray clay. On visual inspection, the differences between these sediments and typical Holocene lutites are subtle; however, as seen in figure 7.3, the susceptibilities in these intervals are elevated. Because the texture, color, and magnetic properties are similar to those of the Pleistocene sediments and as these intervals overlie typical Holocene mud with low susceptibilities, these zones may contain Pleistocene sediment that was displaced from another locality and transported to the sites, possibly as a mud flow.

The lithologic transition from Holocene to Pleistocene is either missing or lies at an anomalously shallow depth in three of the sediment cores (fig. 7.4). The high values of susceptibility as well as organic geochemical markers (Kvenvolden and others, chap. 15, this volume) in each core suggest that the sections are mostly Pleistocene in age. Cores L2-86-2G and L2-86-4G were recovered near the tops of two hills in SESCA. The upper parts of the core section contain mud clasts in a mud matrix, which we interpret as a debris flow or slump deposit. This is consistent with submersible observations that indicate that the edges of the hills were subject to erosion and mass wasting (Holmes and Zierenberg, 1990; Zierenberg and others, chap. 10, this volume). Core L1-86-7G was collected near the base of one of the uplifted hills. In this area, steep-sided channels from 1 to 20 m deep were frequently observed during submersible dives (Holmes and Zierenberg, 1990). The channels appear to be erosional and serve to funnel material that has been mobilized by mass wasting from the adjacent hill slopes to the floor of the axial valley. It is possible that this core was recovered from one of these channels, in which active scouring inhibited deposition of Holocene sediment.

PLEISTOCENE SEDIMENTATION

The record of Pleistocene sedimentation is limited by the shallow penetration of the gravity cores. Visual examination reveals little or no down-core variation. The magnetic susceptibility profiles are also generally smooth for most of the Pleistocene intervals (figs. 7.3, 7.4), but certain cores show peaks consistent with the presence of turbidites (for example, L1-86-1G, L1-86-7G, L2-86-2G). The X-radiographs of the cores from the valley floor show well-defined millimeter-scale laminations, suggesting deposition in the distal parts of turbidite flows. The preservation of finely laminated structures indicates that bioturbation was

precluded, either because of the high sedimentation rates or disoxic conditions that discourage burrowing.

The Pleistocene section of core L2-86-7G also has distinctive peaks in the susceptibility profiles (fig. 7.4) that suggest the presence of turbidites. Although this section was described as homogeneous gray mud (Normark and others, chap. 6, this volume), the X-radiographs show that this interval is composed of a sequence of at least four turbidite units, with sharp basal contacts for the upper three at 174 cm, 188 cm, and 204 cm. The thick turbidite units contrast with the finely laminated distal turbidites in the cores taken from the valley floor. The presence of turbidites in this core is somewhat unusual in that the core was recovered from a terrace about 100 m above the floor of Escanaba Trough. The terrace appears to have been uplifted by normal faulting prior to deposition of the turbidites. Because turbidity currents flowing along the valley floor would not have enough volume or energy to

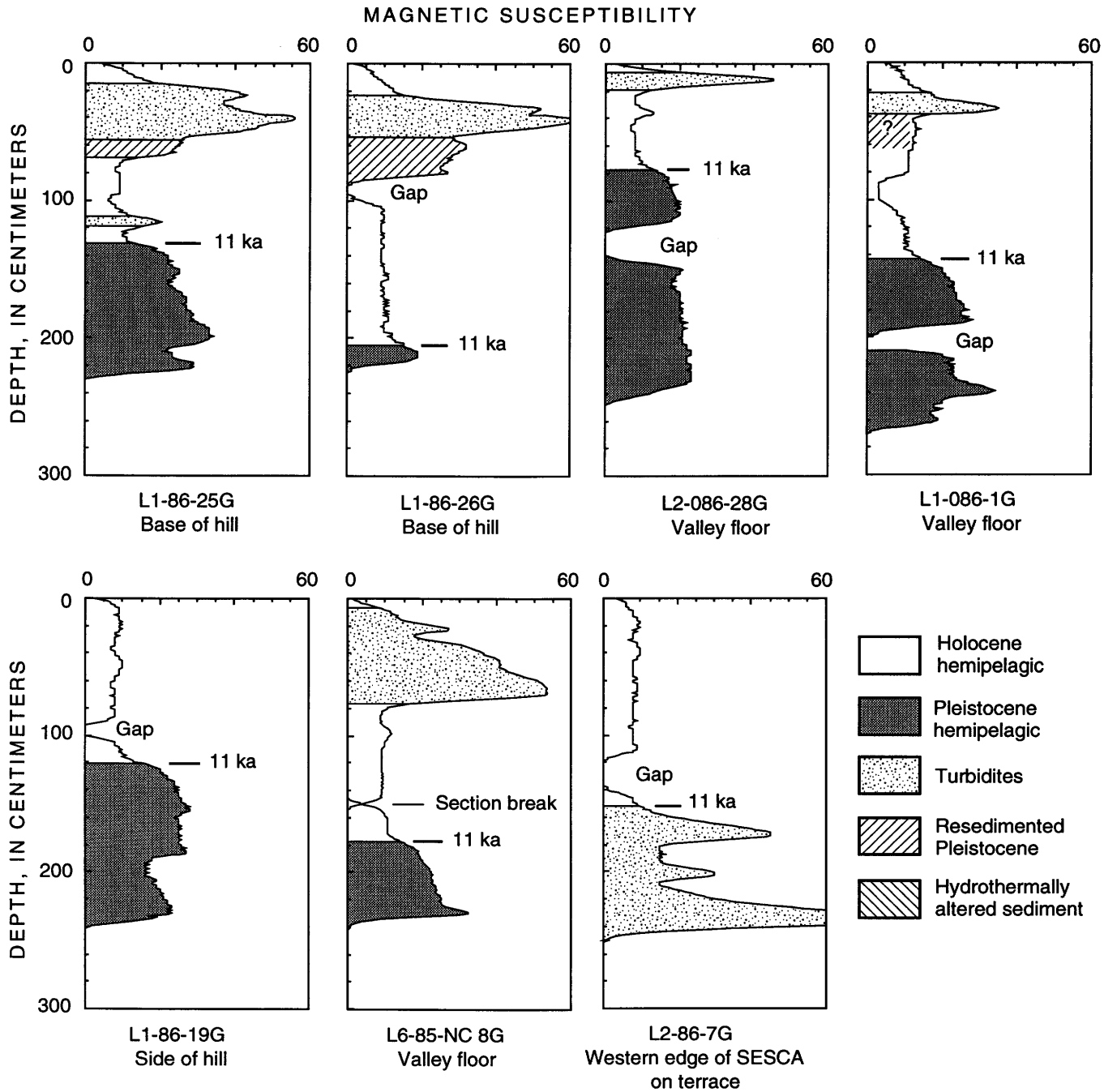

Figure 7.3. Split-core magnetic susceptibility profiles of sediments on valley floor at SESCA. These cores contain turbidite intervals in the Holocene, as evidenced by elevated susceptibility values.

reach this elevation, it is likely that the turbidites originated from the walls flanking the axial valley. Thus, Pleistocene sedimentation patterns may have been complex. Proximal turbidites were deposited on the terraces as a result of mass wasting of the sedimented axial valley walls. In contrast, sedimentation on the axial valley floor consisted mainly of hemipelagic input and distal turbidity flows.

HYDROTHERMALLY ALTERED SEDIMENTS

Three cores contain evidence of sulfide mineralization and hydrothermal alteration (fig. 7.5). The alteration processes are described by Zierenberg and Shanks (chap. 14, this volume). Core L1-86-8G is located near the base of East Hill at SESCA. The upper part of the core contains a thin veneer about 15 cm thick of typical Holocene hemipelagic sediment overlying a series of silty turbidites. The interval from 55 to 85 cm may contain redeposited Pleistocene material. The section below 85 cm appears bleached gray and contains mud clasts. The susceptibility profile and gross stratigraphy (fig. 7.5) show a close resemblance to other valley cores, especially L1-86-25G, L1-86-26G, L1-86-1G, and L2-86-28G. However, unlike these cores, the sediment in L1-86-8G is bleached gray and the turbidite layers contain trace amounts of sand-sized sulfide grains. Scanning electron micrographs of magnetic separates show abundant aggregates of thin-bladed or stubby hexagonal pyrrhotite with the morphology of "black smoke" particles (fig. 7.6). In some cases, the pyrrhotite is intergrown with hydrothermal talc. These associations suggest that the core is in close proximity to a hydrothermal vent area, possibly the same sites that rim the base of the hill that were identified by submersible and camera observations (Zierenberg and others, chap. 10, this volume). The lower bleached part of the core may contain resedimented material that includes hydrothermally altered clay (Zierenberg and Shanks, chap. 14, this volume). Organic geochemical analyses on this core suggest maturation at elevated temperatures (Kvenvolden and others, chap. 15, this volume). This core does not record the 11-ka boundary, thus the age of the section is unknown. However, if the turbidites represent the same set of events as in the other valley cores, then the hydrothermal activity may be contemporaneous with the turbidity flows.

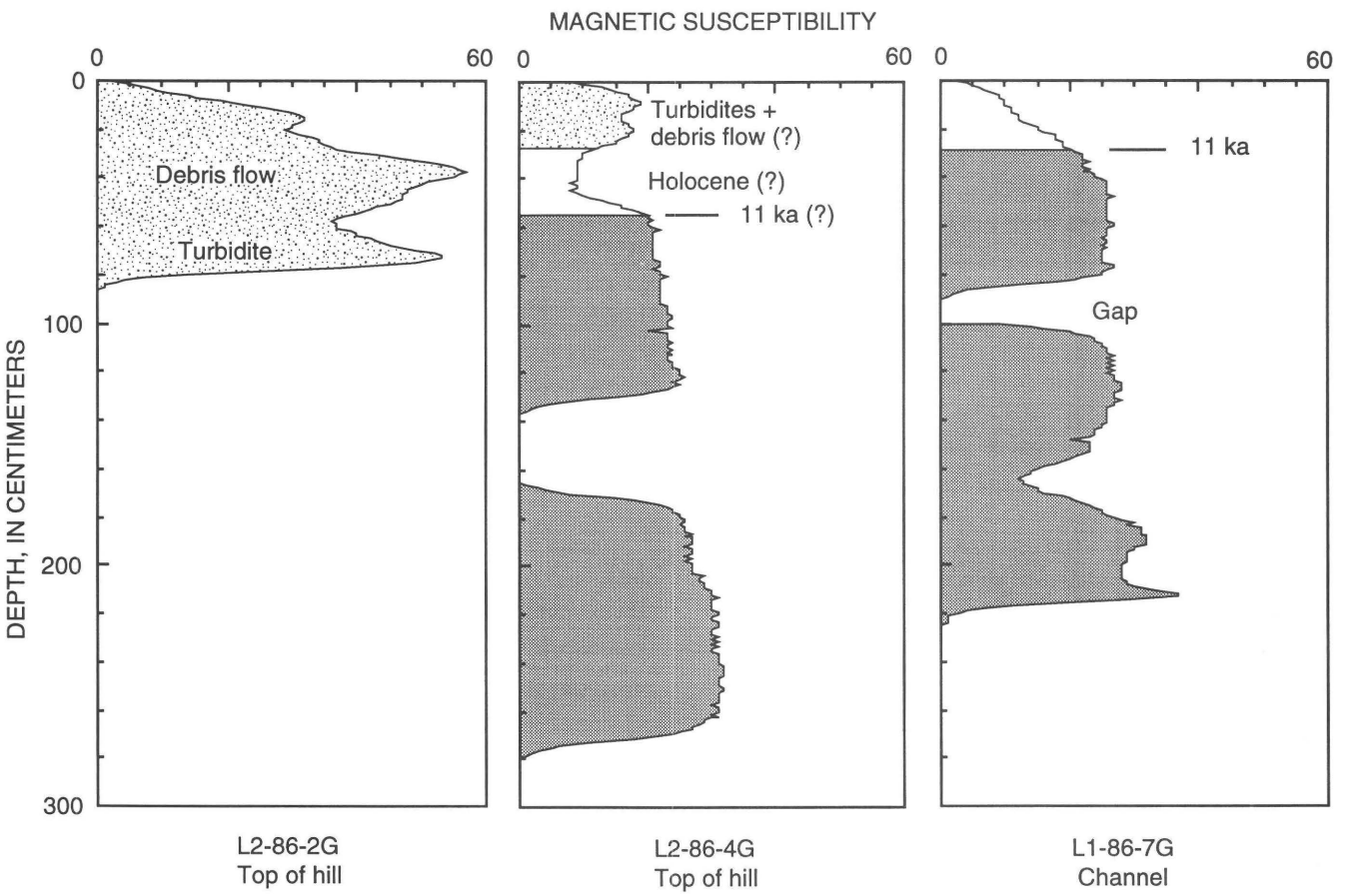

Figure 7.4. Split-core susceptibility profiles of cores taken in SESCA area. These sediments appear to be relict Pleistocene muds exposed near hill tops (L2-86-2G and L2-86-4G) and in an erosion channel(?) (L1-86-7G). Units same as in figure 7.3.

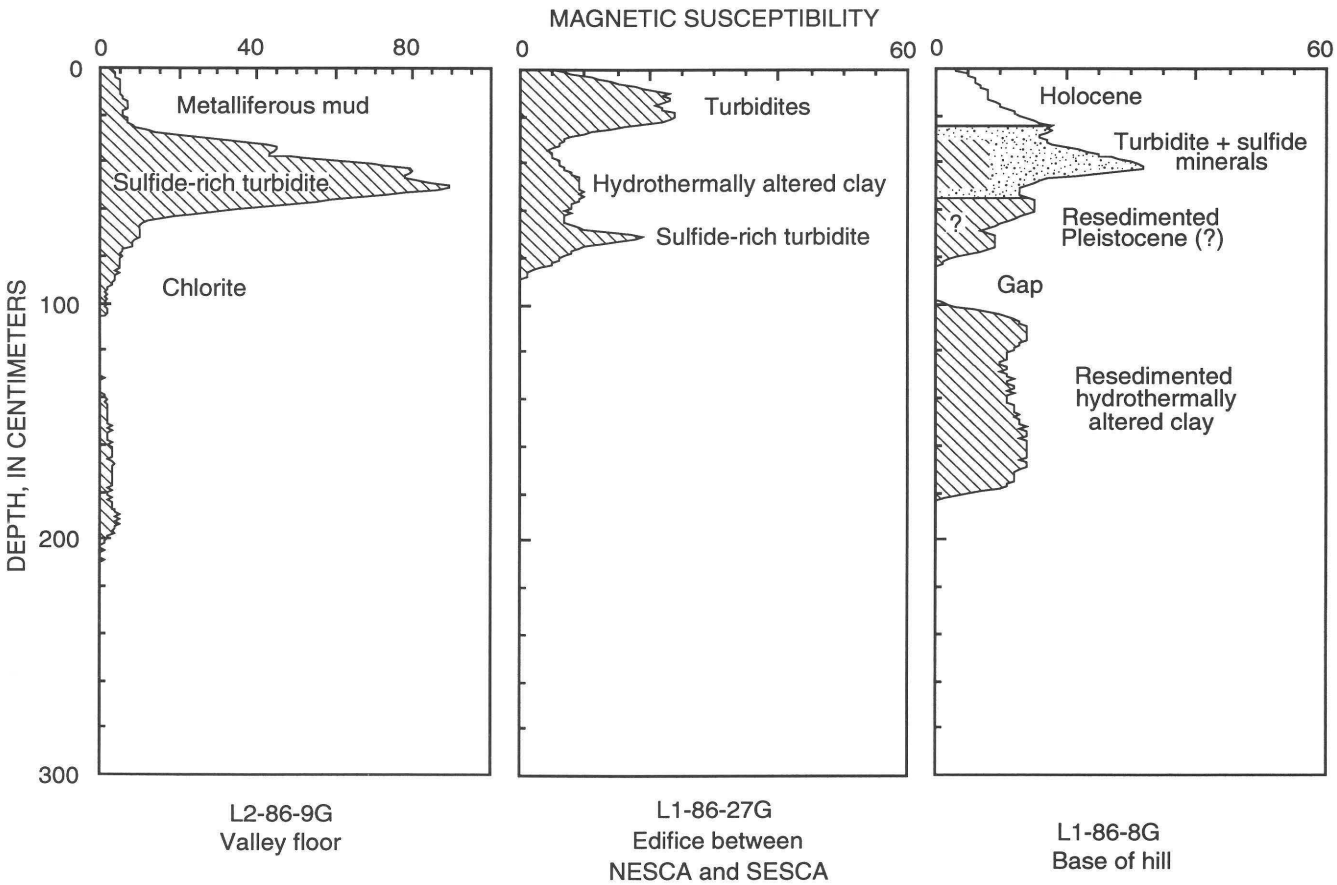

Figure 7.5. Split-core susceptibility profiles of hydrothermally altered sediments (shown by diagonal pattern) at SESCA. Units same as in figure 7.3.

Core L2-86-9G, recovered from a basin in the western part of the SESCA area, contains highly altered sediment underlying an interval of massive sulfide. The core is unusual in that metalliferous red-brown mud overlies a 30-cm-thick clastic zone of sand and nodules composed of hexagonal pyrrhotite, with less abundant isocubanite, sphalerite, and barite (Zierenberg and Shanks, chap. 14, this volume). The lower part of the section is extensively altered to monominerallic chlorite, which Zierenberg and Shanks (chap. 14, this volume) attribute to intensive magnesium metasomatism. The susceptibility profile for this core (fig. 7.5) shows a strong peak in the metalliferous mud and sulfide-rich zones, but almost no signal in the lower chlorite-rich layer. The low magnetic susceptibility of the lower chloritized zone probably results from the dissolution of detrital minerals during hydrothermal alteration. The intense alteration precludes any age identification by magnetic means.

Core L1-86-27G was taken in a relatively unexplored area between the SESCA and NESCA sites where volcanic basement or sills are only shallowly covered by sediment (edifice C of Abbott and others, 1986). The sediment lacks the continuous layering observed in seismic-reflection profiles from surrounding areas (Davis and Becker,

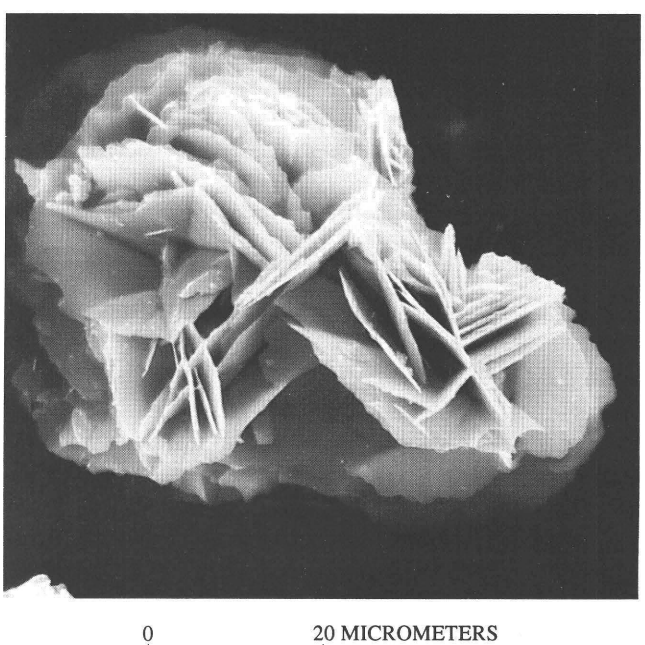

Figure 7.6. Scanning electron micrograph of aggregate containing thin-bladed pyrrhotite grains from magnetic separates of turbidite in core L1-86-8G at 53 to 55 cm.

chap. 3, this volume). The base of the core has a sand layer that contains massive sulfide veins, particularly pyrrhotite, with lesser amounts of copper, zinc, and lead sulfide minerals and barite (Zierenberg and Shanks, chap. 14, this volume). The mineralized turbidite sand may have acted as a conduit for hot sulfide- and metal-rich water. Hydrothermal smectite is the dominant alteration mineral in the sediment outside of the sulfide veins. The susceptibility profile (fig. 7.5) shows a high associated with the red-brown oxidized surface layer. A peak also occurs in the turbidite-sulfide zone near the base of the core. X-ray diffraction indicates that the mineralized zone contains dominantly hexagonal pyrrhotite, which has a relatively low specific mass susceptibility compared to magnetite. However, considering its abundance, the magnetic susceptibility peak for this interval is not strong. If this property is representative of such hydrothermally altered sediments, then magnetic surveying may not be a useful tool in exploring for such deposits. Given the short length of this core, it is not possible to estimate its age.

DISCUSSION

HOLOCENE SEDIMENTATION RATES

The 11-ka lithologic boundary provides a convenient stratigraphic marker that is useful in establishing sedimentation rates and in making a rough estimate of the timing of the episodes of turbidity current activity. A necessary assumption that the top of the core has been preserved is reasonable for those cores where the surficial brown oxidized layer was recovered (Normark and others, chap. 6, this volume).

Holocene hemipelagic sedimentation rates for the various cores (table 7.1), with the turbidite intervals removed, range from 5 to 14 cm/kyr. The lower rates may reflect some degree of erosion and scour of underlying strata during turbidity flows; however, more detailed dating is required to assess this possibility. The Holocene sedimentation rates are comparable to those found in hemipelagic sediments south of the Mendocino Escarpment (Karlin, 1990). However, they are considerably lower than average Pleistocene rates of over 50 cm/ky reported at DSDP Site 35 (McManus and others, 1970) and probably reflect lesser continental erosion during interglacial intervals.

Table 7.1. Holocene sedimentation rates of SESCA cores.

Core	Location	Length (cm)	Holocene total rate (cm/kyr)	Holocene hemipelagic rate (cm/kyr)
L1-86-1G	Valley floor	273	13	11
L1-86-7G	Erosional channel ?	233	2.7	2.7
L1-86-8G	Base of East Hill	197	2.4?	?
L1-86-19G	NW side of 3170 Hill	255	11	11
L1-86-25G	Base of 3170 Hill	227	12	6.5
L1-86-26G	Base of 3170 Hill	239	19	11
L2-86-2G	Top of 3170 Hill	101	0	0
L2-86-4G	Top of East Hill	263	5.3	0?
L2-86-7G	Terrace	241	14	14
L2-86-9G	West valley floor	200	?	?
L2-86-28G	Valley floor	244	7	5
L6-85-8G	Valley floor, south	244	16	11

ORIGIN OF THE TURBIDITES

The presence of a series of turbidites in similar stratigraphic positions in several cores suggests that the cores are recording the same set of turbidite events. As seen in figures 7.3*A* and 7.5, the valley cores, especially cores L1-86-8G, L1-86-25G, L1-86-26G, L1-86-1G, and maybe L2-86-28G, contain a series of four well-defined events that have a similar magnetic character. Only one valley core (L1-86-7G) does not record these events, but this core appears to contain only Pleistocene material, suggesting that the core may have been recovered from one of the many erosional channels observed from the submersible. In addition, core L6-85-8G (fig. 7.3*B*), located about 1.5 km south of the hills, also contains a similar series of turbidites. For this core, Karlin and Lyle (1986) dated the layer immediately underneath the basal turbidite by ^{14}C at 2.4 ka.

If the turbidites do indeed record the same set of events, then the turbidites would appear to be proximal and from the nearby 3170 Hill, because the highest susceptibility values and the coarsest sand (Wong, 1989) are from cores L1-86-8G, L1-86-25G, and L1-86-26G from the side of the 3170 Hill. The lowest values are from core L1-86-1G, in the basin to the east. The turbidites in cores L1-86-25G and L1-86-26G also may be underlain by relict Pleistocene sediment redeposited by a nearby mud flow associated with slumping of the sides of the hill. Core L1-86-19G from the western flank of the hill does not show these events, suggesting that mass wasting may have occurred only on the eastern side. These episodes are also not seen in core L2-86-7G located on the terrace at the western edge of the SESCA area; thus, the turbidites do not appear to have originated from the western valley walls.

There are two problems in relating the turbidites in the different cores to a series of events from a common source. The turbidites in cores L1-86-25G and L1-86-26G both contain detrital magnetic phases with no appreciable volcanic glass or sulfide constituents. Initial petrographic scans of the silt layers suggest erosion and reworking of relict terrigenous material, such as might occur as a result of slumping and mass wasting of the uplifted sediment-capped hills. In contrast, core L1-86-8G and the L6-85-8G core described by Karlin and Lyle (1986) contain fresh volcanic glass and high temperature hexagonal pyrrhotite.

Thus it appears that the turbidites may have come from different sources.

Although the timing of the events is not well constrained, it is evident that the cores contain somewhat different thicknesses of Holocene hemipelagic sediment between the 11-ka boundary and the basal Holocene turbidite contact. Assuming the sedimentation rates discussed above, the age of the basal contact varies between about 1.45 ka and 2.4 ka. A major source of uncertainty is how much sediment was eroded as a result of flow associated with the turbidite. Without more accurate radiometric age control, it is impossible to establish whether the flows occurred simultaneously. For the present, the most that we can conclude is that the turbidites seem to have occurred at about the same time and may have been derived from different sources. The susceptibility profiles, as well as the physiographic setting of the cores, suggest that the source areas were local.

Regardless of the exact ages of the turbidite events, it is clear that the late Holocene (since about 2.5 ka) was a period of intensified seismotectonic activity, possibly related to renewed uplift of the sediment hills. The presence of high temperature sulfide minerals such as pyrrhotite in some of the turbidites suggests that the tectonism was accompanied by hydrothermal activity. It is interesting that the turbidites found here appear to be similar in timing and gross structure to those found at NESCA by Karlin and Lyle (1986). The NESCA cores also contain significant amounts of volcanic glass and sulfide minerals. Further work is necessary to determine whether these similarities are a coincidence or due to coseismic disturbances associated with simultaneous uplift or volcanism at both sites.

CONCLUSIONS

The results from the cores collected to date show that the sedimentary regime in the vicinity of the volcanic edifices is active and complex. Neotectonic activity appears to have occurred episodically in the last 2.5 kyr following an indeterminate period of quiescence. The seismotectonic activity caused mass wasting of the sides of uplifted sediment hills. The relations between mass-wasting events, volcanism, and hydrothermal activity are unclear, although several of the turbidites contain fresh volcanic glass and sulfide minerals.

The available core coverage is not adequate to resolve the distribution of hydrothermal deposits or the extent of sediment alteration due to baking and fluid migration. However, the recovery of intensely altered and sulfidized sediments in isolated cores from relatively unexplored areas around the base of the hills and on the valley floor underscores how much we have to learn about the dynamics of hydrothermal activity and the distribution and nature of sediment-hosted sulfide deposits.

REFERENCES CITED

Abbott, D.H., Morton, J.L., and Holmes, M.L., 1986, Heat flow measurements on a hydrothermally-active, slow-spreading ridge: The Escanaba Trough: Geophysical Research Letters, v. 13, p. 678–680.

Atwater, T.M., and Mudie, J.D., 1973, Detailed near bottom geophysical study of the Gorda rise: Journal of Geophysical Research, v. 78, p. 8665–8686.

Davis, E.E., and Becker, Keir, Thermal and tectonic structure of the Escanaba Trough: New heat-flow measurements and seismic-reflection profiles, *in* Morton, J.L., Zierenberg, R.A., and Reiss, C.A., eds., Geologic, hydrothermal, and biologic studies at Escanaba Trough, Gorda Ridge, offshore northern California: U.S. Geological Survey Bulletin 2022, chapter 3 (this volume).

Holmes, M.L., and Zierenberg, R.A., 1990, Submersible observations in Escanaba Trough, southern Gorda Ridge, *in* McMurray, G.R., ed., Gorda Ridge: A seafloor spreading center in the United States' Exclusive Economic Zone: New York, Springer-Verlag, p. 93–115.

Karlin, Robert, 1990, Biogenic magnetite formation and destruction process in suboxic sediments at Bettis Site W-N, NE Pacific Ocean: Journal of Geophysical Research, v. 95, p. 4421–4436.

Karlin, Robert, and Lyle, Mitchell, 1986, Sediment studies on the Gorda Ridge: Oregon Department of Geological and Mineral Industries Open-File Report O-86-19, 76 p.

Karlin, Robert, Lyle, Mitchell, and Zahn, Rainer, 1992, Late Quaternary variations in the calcite compensation depth in the North East Pacific Ocean: Paleoceanography, v. 7, p.43-61.

Kvenvolden, K.A., Rapp, J.B., and Hostettler, F.D., Hydrocarbons in sediment from Escanaba Trough, *in* Morton, J.L., Zierenberg, R.A., and Reiss, C.A., eds., Geologic, hydrothermal, and biologic studies at Escanaba Trough, Gorda Ridge, offshore northern California: U.S. Geological Survey Bulletin 2022, chapter 15 (this volume).

McManus, D.A., and others, 1970, Site 35, *in* McManus, D.A., and others, eds., Initial reports of the Deep Sea Drilling Project: Washington, U.S. Government Printing Office, v. 5, p. 165–172.

Morton, J.L., Holmes, M.L., and Koski, R.A., 1987a, Volcanism and massive sulfide formation at a sedimented spreading center, Escanaba Trough, Gorda Ridge, northeast Pacific Ocean: Geophysical Research Letters, v. 14, p. 769–772.

Morton, J.L., Normark, W.R., Ross, S.L., Koski, R.A., Holmes, M.L., Shanks, W.C., III, Zierenberg, R.A., Lyle, M., and Benninger, L.M., 1987b, Preliminary report, cruises L1-86-NC and L2-86-NC, Escanaba Trough, Gorda Ridge: U.S. Geological Survey Open-File Report 87-375-A, 20 p.

Morton, J.L., Koski, R.A., Normark, W.R., and Ross, S.L., 1990, Distribution and composition of massive sulfide deposits at Escanaba Trough, southern Gorda Ridge, *in* McMurray, G.R., ed., Gorda Ridge: A seafloor spreading center in the United States' Exclusive Economic Zone: New York, Springer-Verlag, p. 77–92.

Morton, J.L., and Fox, C.G., Structural setting and interaction of volcanism and sedimentation at Escanaba Trough: Geophysical results, *in* Morton, J.L., Zierenberg, R.A., and Reiss, C.A., eds., Geologic, hydrothermal, and biologic stud-

ies at Escanaba Trough, Gorda Ridge, offshore northern California: U.S. Geological Survey Bulletin 2022, chapter 2 (this volume).

Morton, J.L., Zierenberg, R.A., and Reiss, C.A., Geologic, hydrothermal, and biologic studies at Escanaba Trough: An introduction, *in* Morton, J.L., Zierenberg, R.A., and Reiss, C.A., eds., Geologic, hydrothermal, and biologic studies at Escanaba Trough, Gorda Ridge, offshore northern California: U.S. Geological Survey Bulletin 2022, chapter 1 (this volume).

Normark, W.R., Gutmacher, C.E., Zierenberg, R.A., Wong, F.L., and Rosenbauer, R.J., Sediment fill of Escanaba Trough, *in* Morton, J.L., Zierenberg, R.A., and Reiss, C.A., eds., Geologic, hydrothermal, and biologic studies at Escanaba Trough, Gorda Ridge, offshore northern California: U.S. Geological Survey Bulletin 2022, chapter 6 (this volume).

Riddihough, R.P., 1980, Gorda plate motions from magnetic anomaly analysis: Earth and Planetary Science Letters, v. 51, p. 163–170.

Ross, S.L., and Zierenberg, R.A., Volcanic geomorphology of the SESCA and NESCA sites, Escanaba Trough, *in* Morton, J.L., Zierenberg, R.A., and Reiss, C.A., eds., Geologic, hydrothermal, and biologic studies at Escanaba Trough, Gorda Ridge, offshore northern California: U.S. Geological Survey Bulletin 2022, chapter 8 (this volume).

Wong, F.L., 1989, Mineralogy of sand in turbidites from the Escanaba Trough, Northeast Pacific Ocean: U.S. Geological Survey Open-File Report 89-661, 10 p.

Zierenberg, R.A., Koski, R.A., Ross, S.L., Shanks, W.C. III, and Slack, J.F, 1988, Preliminary results of ALVIN dives on active sediment-hosted massive sulfide deposits in the Escanaba Trough, Southern Gorda Ridge [abs.]: Eos, Transactions American Geophysical Union, v. 44, p. 1488.

Zierenberg, R.A., Morton, J.L., Koski, R.A., and Ross, S.L., Geologic setting of massive sulfide mineralization in the Escanaba Trough, *in* Morton, J.L., Zierenberg, R.A., and Reiss, C.A., eds., Geologic, hydrothermal, and biologic studies at Escanaba Trough, Gorda Ridge, offshore northern California: U.S. Geological Survey Bulletin 2022, chapter 10 (this volume).

Zierenberg, R.A., and Shanks, W.C., III, Sediment alteration associated with massive sulfide formation in the Escanaba Trough, Gorda Ridge: The importance of seawater mixing and magnesium metasomatism, *in* Morton, J.L., Zierenberg, R.A., and Reiss, C.A., eds., Geologic, hydrothermal, and biologic studies at Escanaba Trough, Gorda Ridge, offshore northern California: U.S. Geological Survey Bulletin 2022, chapter 14 (this volume).

Chapter 8. Volcanic Geomorphology of the SESCA and NESCA Sites, Escanaba Trough

By Stephanie L. Ross *and* Robert A. Zierenberg[1]

CONTENTS

ABSTRACT

Volcanic outcrops have been observed on several camera tows and submersible dives at the southern Escanaba Trough (SESCA) and northern Escanaba Trough (NESCA) sites. Pillow flows dominate the outcrops at both sites; sheet flows are also common but are often poorly exposed due to sediment cover. Basalt flows at SESCA appear older than at NESCA. Volcanic flow morphology correlates with bathymetric slope at the NESCA site, as sheet flow basalt is restricted to relatively flat areas. Relationships between volcanic flows, faults, and the base of the SESCA North Hill, combined with available seismic-reflection data, support the hypothesis that uplift of the sediment hills results from deep emplacement of volcanic sills. The faults that uplifted the hills provided a conduit for hydrothermal fluids and may also have been the path for erupted basalt.

INTRODUCTION

The sediment-covered Escanaba Trough comprises the axial valley of the southern Gorda Ridge, a slow-spreading mid-ocean ridge (full rate 2.4 cm/yr). Seismic-reflection records reveal a discontinuous chain of volcanic edifices along the axial zone of Escanaba Trough (Morton and others, 1987), similar to observations at other slow spreading centers (Macdonald, 1982). Geochemical analyses of basalt suggest that magma chambers along Escanaba Trough are not continuous between volcanic centers (Davis and others, chap. 9, this volume).

Sediment-hosted massive sulfide deposits have been mapped at two sites in Escanaba Trough in areas where ridge volcanism forms volcanic centers that rise through the sediment cover: the southern Escanaba Trough (SESCA) site at latitude 40°45′ N., longitude 127°30′ W., and the northern Escanaba Trough (NESCA) site at latitude 41° N., longitude 127°30′ W. At these sites, several steep-sided circular hills, from 500 to 1,000 m in diameter, rise 40 to 100 m above the surrounding sea floor. These include the North Hill, East Hill, and 3170 Hill at SESCA (fig. 8.1) and the Southwest Sediment Hill at NESCA (fig. 8.2). These hills are probably the result of localized uplift of sediment above small basaltic sills (Morton and Fox, chap. 2, this volume).

Fifteen transponder-navigated camera stations and 22 submersible dives (10 with DSV *Alvin* and 12 with DSV *Sea Cliff*) were conducted at SESCA and NESCA on several cruises between 1985 and 1988. The volcanic geomorphology observed on these surveys provides constraints on models proposed to explain the evolution of these areas.

ACKNOWLEDGMENTS

This work is based on several seasons of cruises. We greatly appreciate the efforts of the ship crews and cruise participants involved, especially Hank Chezar, designer of the U.S.G.S. camera sled. We thank Alicé Davis, Robin Holcomb, and Janet Morton for thorough reviews and Roger Denlinger for stimulating scientific discussions.

DATA COLLECTION

Two camera tows in 1985 and six in 1986 revealed volcanic rocks exposed through the sediment cover at

[1] U.S. Geological Survey, Menlo Park, California.

Escanaba Trough. All stations used the U.S. Geological Survey's deep-towed camera sled (Chezar and Lee, 1985), which records 4½ hours of color videotape and shoots color 35-mm still photographs at a preset interval, generally 14 seconds. Four of these camera tows collected fairly complete sets of both video and still images. Three of the other stations (L6-85-33C, L1-86-5C, and L1-86-9C) have full video coverage, but few or no photographs. The remaining station, L6-85-21C, obtained nearly 4 hours of still pictures, but no video record.

The camera tows were navigated using a sea-floor net of acoustic transponders; the tracklines shown in figures 8.1 and 8.2 reflect the position of the relay transponder, which was located on the tow cable usually 100 m above the camera sled. Most of the camera stations were successfully transponder navigated and the position errors are

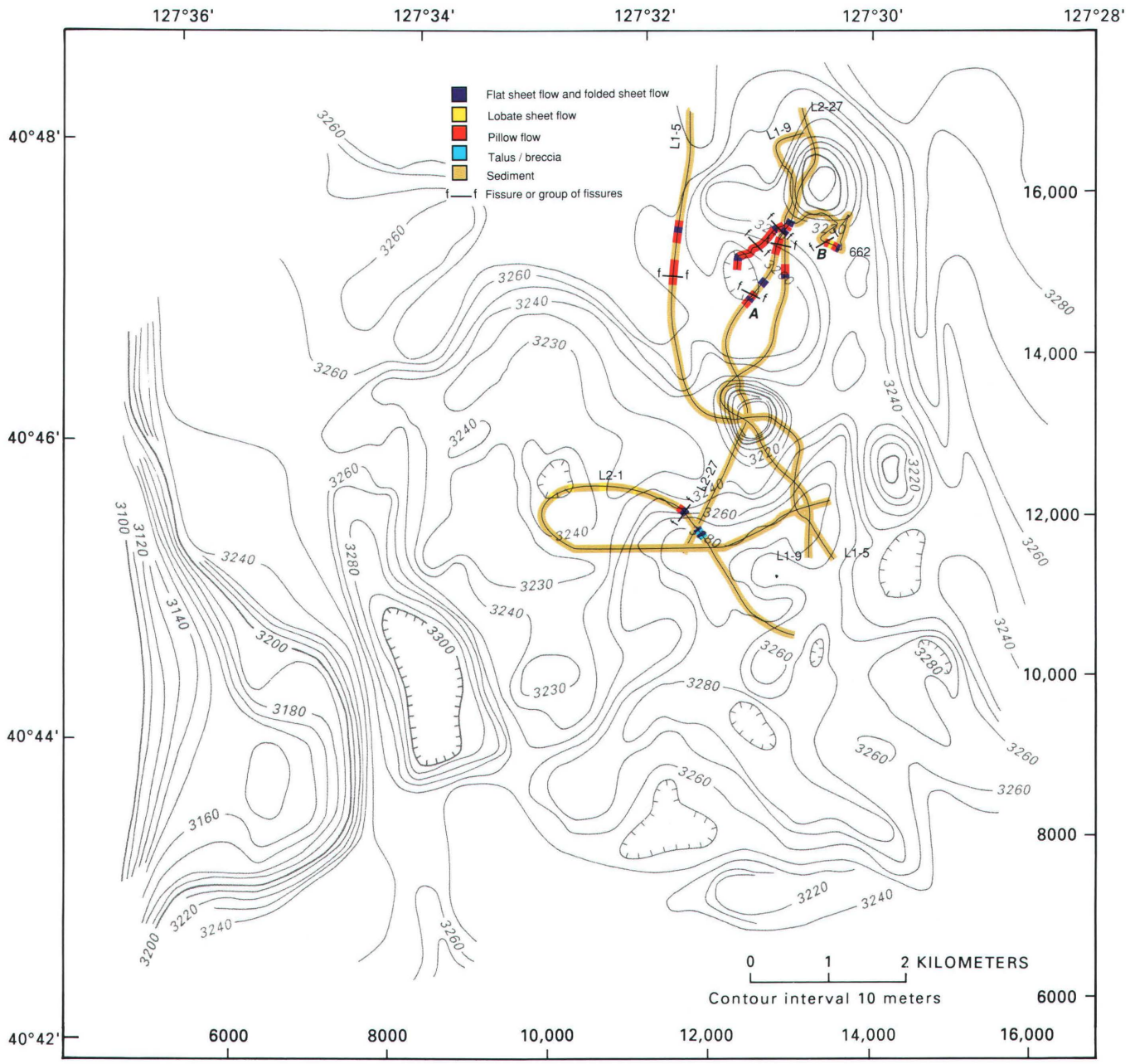

Figure 8.1. Bathymetric map showing volcanic geology along camera and submersible tracklines at SESCA site. *A* and *B* indicate locations of photographs shown in figure 8.3. Numbers along right and bottom give coordinates of local transponder net (in meters). Hachures indicate area of closed low. Only stations and dives with observed volcanic rocks are illustrated; see Morton and others (chap. 1, this volume), figures 1.6 and 1.8 for tracklines of all SESCA dives and camera tows. Bathymetry is based on surface soundings and shows slopes as less steep than they are; for example, divers' observations from dive 662 place volcanic rocks at base of North Hill, not on its side.

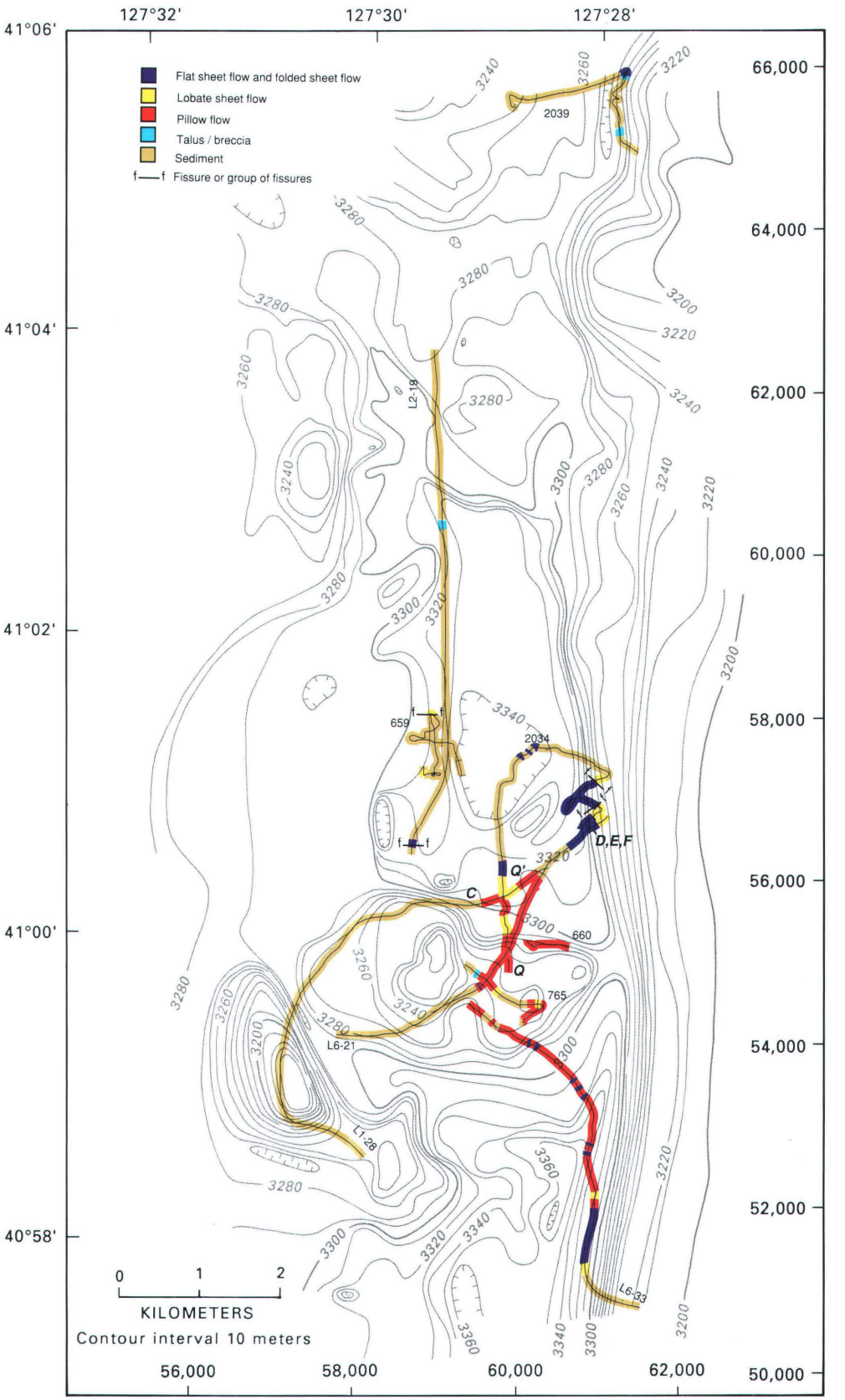

Figure 8.2. Bathymetric map showing volcanic geology along camera and submersible tracklines at NESCA site. Letters *C*, *D*, *E*, and *F* indicate locations of photographs shown in figure 8.3. *Q* and *Q'* indicate start and end of segment diagrammed in figure 8.4. Numbers along right and bottom give coordinates of local transponder net (in meters). Hachures indicate area of closed low. Only stations and dives with observed volcanic rocks are illustrated; see Morton and others (chap. 1, this volume), figures 1.5 and 1.7 for tracklines of all NESCA dives and camera tows. Bathymetry is based on surface soundings and shows slopes as less steep than they are; for example, divers' observations place 2039 trackline in graben, not on valley wall, and easternmost basalts on dive 2034 at foot of wall, not up on it.

less than 5 m relative to the net, sufficiently accurate for site reoccupation. The agreement of surficial geology at trackline intersections confirms this accuracy. Relay navigation did not function during two of the stations. The tracklines for stations L6-85-21C and L2-86-19C were estimated from transponder-navigated shiptracks, except for the first hour of L2-86-19C, which lacked any transponder navigation; that section of trackline is extrapolated from the ship's integrated satellite (NNSS)-Doppler sonar-Loran C navigation system.

Volcanic rocks were observed and photographed during six submersible dives (*Sea Cliff* dives 659, 660, 662, and 765, and *Alvin* dives 2034 and 2039). Both submersibles are equipped with video and externally mounted 35-mm still cameras. In cases where the photography is incomplete, geologic interpretation relies heavily on the divers' observations (Zierenberg and others, 1991). The dives were navigated using the same transponder net as the camera stations and had position errors of generally less than 20 m. Dives 2039 and 765 had significantly greater errors; the 765 navigation has gaps of up to 1 hour in duration (500 m in projected trackline length).

OBSERVATIONS

SESCA AREA

In the SESCA area, volcanic outcrops were observed in four of the nine camera stations and on one of the five submersible dives. Most of the volcanic exposures occur south to southwest of the North Hill; a few are southwest of the 3170 Hill (fig. 8.1). These observations agree well with the distribution of near-surface volcanic rocks inferred from seismic-reflection data (Morton and Fox, chap. 2, this volume).

Most of the observed volcanic outcrops are pillow lava (fig. 8.3*A*), but flat, folded, and lobate sheet flows were also observed in the SESCA area intermixed with the pillow lavas. The pillow lobes are generally 1 to 2 m wide, display inflationary "bread-crust" type fractures, and often have "trap doors" attached to their tops; these occur when one pillow sprouts through a crack in older crust and tears off a remnant of that crust to form a cap (Moore, 1975). Submersible observations at SESCA show that the trap-door pillows commonly extruded upward from sheet flow, indicating that the sheet flow and pillow formed during the same eruptive event. This is consistent with the uniform chemistry of the two samples recovered from this area (Davis and others, chap. 9, this volume). Since the pillow forms have more relief than sheet flows, the pillow flows protrude higher above the sediment cover and are more readily observed; the ratio of pillow to sheet flows observed at the sea floor may thus be very different from what lies beneath the sediment.

Although fresh volcanic glass was sampled in two SESCA dredges (Davis and others, chap. 9, this volume), glassy reflections from the surface of exposed basalt were not observed in the photographs. Also, no small projections or buds, indicative of youth, were observed, and the sediment generally obscures all but the largest pillows.

The basalt flows are cut in some places by fissures up to 2 m wide and as deep as 3 m or more (fig. 8.3*B*; also Morton and others, chap. 1, this volume, fig. 1.9*F*). The observed fissures generally trend subperpendicular to the camera or dive track; however, fissures that are subparallel to the track may escape observation. Fissures observed on dive 662 apparently parallel the ridge crest (Zierenberg and others, 1991). The four fissures observed by camera tows are oblique to the ridge trend. Volcanic outcrops exposed in the fissures and in fault scarps confirm that sheet flows are more common than suggested by outcrops protruding through the sediment. No hydrothermal discharge or alteration was observed associated with any of the fissures.

At SESCA, volcanic rocks were observed only at the base of the uplifted sediment hills and in the low-lying areas between them; outcrops exposed on the steep to near-vertical sides of the hills reveal only sediment. As the submersible approached the North Hill from the west on dive 662, the observers noticed many normal faults, first small ones, with offsets up to 1 m, and then, starting near the base of the hill, larger ones (Zierenberg and others, 1991). The last basalt exposure was observed near the base of the first large fault. Most of the small faults cut the basalt flows. However, one fault offsets some basalt flows and is overrun by another basalt flow; the basalt flows are all of similar apparent ages. This observation suggests that faulting and the extrusion of basalt were penecontemporaneous.

NESCA AREA

The largest exposed area of volcanic outcrops in the NESCA area occurs near the eastern peak of the Central Hill (fig. 8.2), extending north and south to the area inferred by seismic-reflection techniques to be underlain by near-surface volcanic rocks (Morton and Fox, chap. 2, this volume). Many flow morphologies were observed in this area (fig. 8.2), with no clear differences in age between the different flow types. Pillow basalt (fig. 8.3*C*; Morton and others, chap. 1, this volume, fig. 1.9*D*) accounts for approximately two-thirds of the observed basalt, while sheet flows, including minor amounts of lobate type, account for the remainder. The pillows are typically large, from 1 m to more than 4 m in diameter, and hemispheric in shape. Bread-crust fracturing formed by inflation is characteristic of the pillows observed, but evidence of local subsidence, in the form of hollow pillows and collapsed lobate sheet flows (fig. 8.3*D*) was also observed, although infre-

quently. The pillows are young enough and so little altered that glassy reflections and glass buds are common. Sediment cover on the observed pillows is moderate, generally ranging from 30 to 70 percent, but even pillows covered by 70 percent sediment have glassy reflections on exposed surfaces.

A

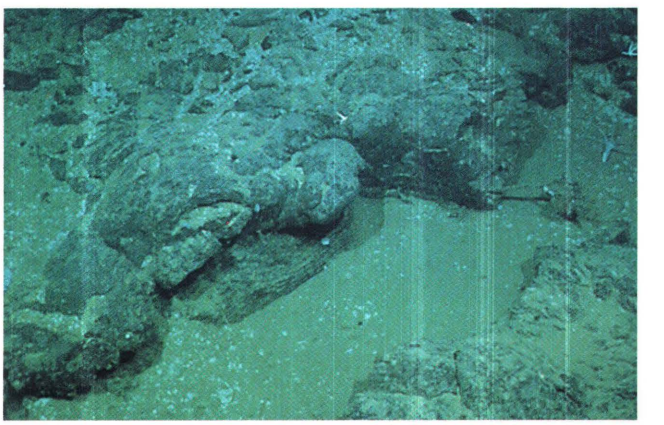

B

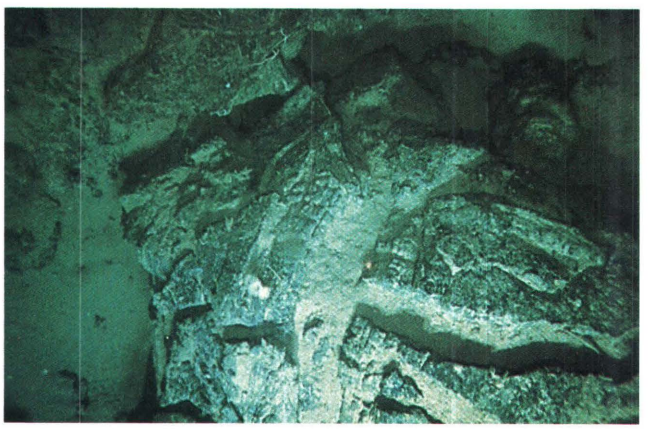

C

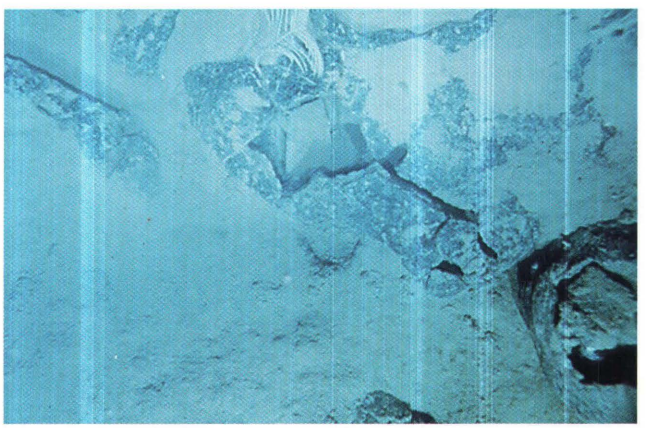

D

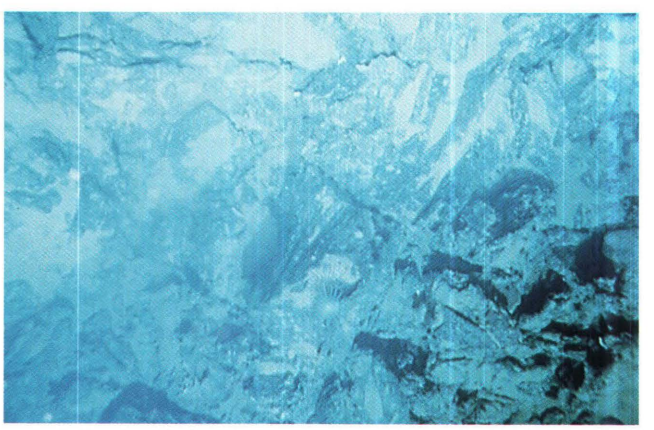

E

F

Figure 8.3. Representative sea-floor photographs of volcanic features. *A*, Inflationary pillow protruding through heavy sediment cover at SESCA site. *B*, Fissured basalt flow at SESCA site. *C*, Pillow basalt at NESCA site. *D*, Collapsed lobes of sheet flow at NESCA site. *E*, Jumbled sheet flow at NESCA site. *F*, Longer, well-formed folds on sheet flow at NESCA site. Field of view of each photograph is approximately 2 to 3 m. All but *B* were taken by USGS camera sled with downward-looking camera; *B* is external still photograph from submersible *Sea Cliff*.

Observed sheet flows at NESCA occur mostly as jumbled broken short folds (fig. 8.3*E*; Morton and others, chap. 1, this volume, fig. 1.9*E*) with longer, more intact folds (fig. 8.3*F*) scattered throughout the jumbled sections and along their margins. Much of the sheet flow seemed to be ponded within a troughlike depression along the base of the eastern valley-bounding scarp. The sheet flows are cut in some places by 0.5-m-wide fissures that are generally parallel to the ridge. Minor amounts of jumbled, folded, and lobate sheet flows also occur among the pillow flows. While glassy reflections were commonly observed on the jumbled and folded sheet flows, as well as on the pillow flows, they were most readily discerned on the lobate sheet flows, probably because lobate sheet flows generally are smoother and better reflect the camera lights. At one site on dive 765 near the top of the eastern peak of the Central Hill, extremely glassy folds and very glassy lobate sheet flows were simultaneously observed out different portholes.

The seismic-reflection records from the NESCA area suggest that sediment layers underlie thin basalt flows in the flat basins north of the Central Hill (Morton and Fox, chap. 2, this volume). The lava flows northeast of the Central Hill are interpreted to onlap a sediment hill that rises above the basalt-covered plain (Zierenberg and others, chap. 10, this volume). Brecciated basalt in sediment observed at the northernmost point of dive 2034 may have formed near the margin of a basalt flow where advancing lava might intermix with sediment.

On a north-to-south traverse of dive 2034, across the lava-covered plain and up the slope of the eastern side of the Central Hill, observers noted an apparent correlation between slope and volcanic morphology. Pillow flows were observed on the steep sections whereas sheet flows were seen on the flatter parts of the traverse. No differences in sediment cover or glass surfaces were observed, nor were distinct flow contacts noted. Lava drapes and elongate lava pillows and tubes on the eastern part of the Central Hill provide evidence for northward flow of lava down toward the lava plain, indicating that the source region for at least the last eruption lay upslope to the south.

The contact between the western sediment-covered part of the Central Hill and the eastern part covered by pillow lava was best observed on dive 765. The contact is a sharp transition from flat-lying basalt (pillows and lobate sheet flows) to a steep sediment-covered slope. No lava or basaltic talus was observed on the sediment slope; this is consistent with the ponding of basalt against a preeruptive sediment slope. The original contact may have been partly obscured by downslope movement of sediment. Sediment-covered areas on the flanks of a localized topographic high on the eastern side of the Central Hill were also observed on dive 765 (fig. 8.2). This hill and a smaller companion hill further to the east have been interpreted as the exposed remnants of sediment hills surrounded by later basalt flows (Zierenberg and others, chap. 10, this volume).

Camera tows and submersible dives west of the lava outcrop examined on dive 2034 rarely imaged basalt. The few observed exposures (fig. 8.2, station L2-86-19 and dive 659) occur near the break in slope that marks the western edge of the innermost basin (Zierenberg and others, chap. 10, this volume; also Morton and Fox, chap. 2, this volume, fig. 2.17); all are on steep scarps covered by blocky basalt talus. Isolated occurrences of sediment-hosted sulfide mineralization were observed near the tops of some of the talus-covered scarps.

Two dives but no camera stations were made onto edifice REX, the topographic high within the axial trough at the northern end of the NESCA site (latitude 41°05.5′ N., edifice E of Abbott and others, 1986). This hill may be the surface manifestation of a volcanic edifice in the sediment fill of the trough (Morton and Fox, chap. 2, this volume). Volcanic rocks were observed on one of those dives, dive 2039; most occur as isolated sediment-dusted talus blocks of sheet flow approximately 0.5 m wide, perched on top of sediment and heavily colonized by attached filter-feeding organisms. The talus blocks occur on the floor of a small graben imaged during bathymetric profiling using a 12 kHz echosounder. The lone volcanic outcrop was found on the east scarp of the graben-bounding fault on a bench 8 to 9 m above the graben floor. Flat to folded sheet flow crops out for approximately 250 m along the north-south-trending scarp. This flow overlies sediment and is overlain by at least 10 cm of additional sediment; crinoids, anemones, tunicates, starfish, and crabs colonize the volcanic outcrops. The talus blocks on the graben floor were likely derived from the observed flow following the formation of the graben by normal faulting. The lack of glassy reflections, the sediment cover, and the displacement of the basalt flow by faulting suggest that it is older than basalt observed to the south at the NESCA site.

DISCUSSION AND CONCLUSIONS

RELATIVE AGE OF VOLCANIC FLOWS

Pillow flows dominate the volcanic outcrops at Escanaba Trough, but exposures in fissures suggest that sheet flows exist below the sediment cover in greater abundance than is apparent from visual observations. Heavy sediment cover on very glassy pillows indicates high sedimentation rates that could quickly bury sheet flows, especially in the flatter regions where sheet flows are generally expected.

Based on observed sediment cover and preservation of glass, the NESCA volcanic flows exposed on and adjacent to the east part of the Central Hill appear to be approximately the same age. This agrees with the homogeneous

geochemistry of basalt samples collected from this area (Davis and others, chap. 9, this volume), which indicates that most of the NESCA flows may be from one eruptive episode. The analyzed glasses have a small range of compositions and could suggest either many short discontinuous flows or one flow large enough to produce minor geochemical variation.

The single volcanic outcrop at edifice REX at the northern edge of the NESCA area appears older than the other NESCA basalt flows. The analyzed glass sample from this site not only is distinct from the other NESCA samples, but it exhibits the most distinctive composition of all the Gorda Ridge glasses (Davis and Clague, 1987; Davis and others, chap. 9, this volume).

The volcanic outcrops at SESCA all appear to be of one general age, and the trap-door remnants of the parent sheet flows on pillows indicate that the pillows and sheets formed during one eruptive event. While the volcanic flows at SESCA appear older than those near the eastern part of the Central Hill at NESCA, they may still be relatively young. Palagonite measurements on original glass surfaces of dredged samples indicate recent volcanism at both SESCA and NESCA (Morton and others, 1987). Also, a high sedimentation rate (Karlin and Lyle, 1986; Karlin and Zierenberg, chap. 7, this volume; Normark and others, chap. 6, this volume) could account for the heavy sediment cover, which generally obscures all but the largest pillows.

RELATIONSHIP OF FLOW MORPHOLOGY TO TOPOGRAPHIC SLOPE

Volcanic flow morphology on the north flank of the Central Hill in the NESCA area was observed to correlate with topographic slope. Projection of flow morphology observed on dive 2034 onto a straight-line path (fig. 8.4) illustrates the change from pillow basalt where the slope is steep to sheets where it is not. Observations of lava draping and elongate lava pillows and tubes on the hillside evince northward flow of lava from a vent area near the crest of the hill downhill toward the lava plain. There were no obvious changes in sediment cover or preservation of volcanic glass, and no sharp boundaries between flow types to suggest an age difference between the different flow morphologies. The composition of all the rocks analyzed from this area agrees with derivation from a single eruptive event (Davis and others, chap. 9, this volume). The simplest explanation is that lava flowing downslope from an eruptive vent near the top of the hill created pillows on the steep sections and sheets on the flat areas. Alternatively, rapid initial eruption of basalt could have flooded the inner rift floor, forming a ponded sheet flow, followed by growth of a pillow volcano over the vent area on the east side of the Central Hill as effusion rates subsided. This scenario seems unlikely as it requires construction of a large volcanic edifice in a single eruptive episode. The presence of sediment hills above the pillow lavas

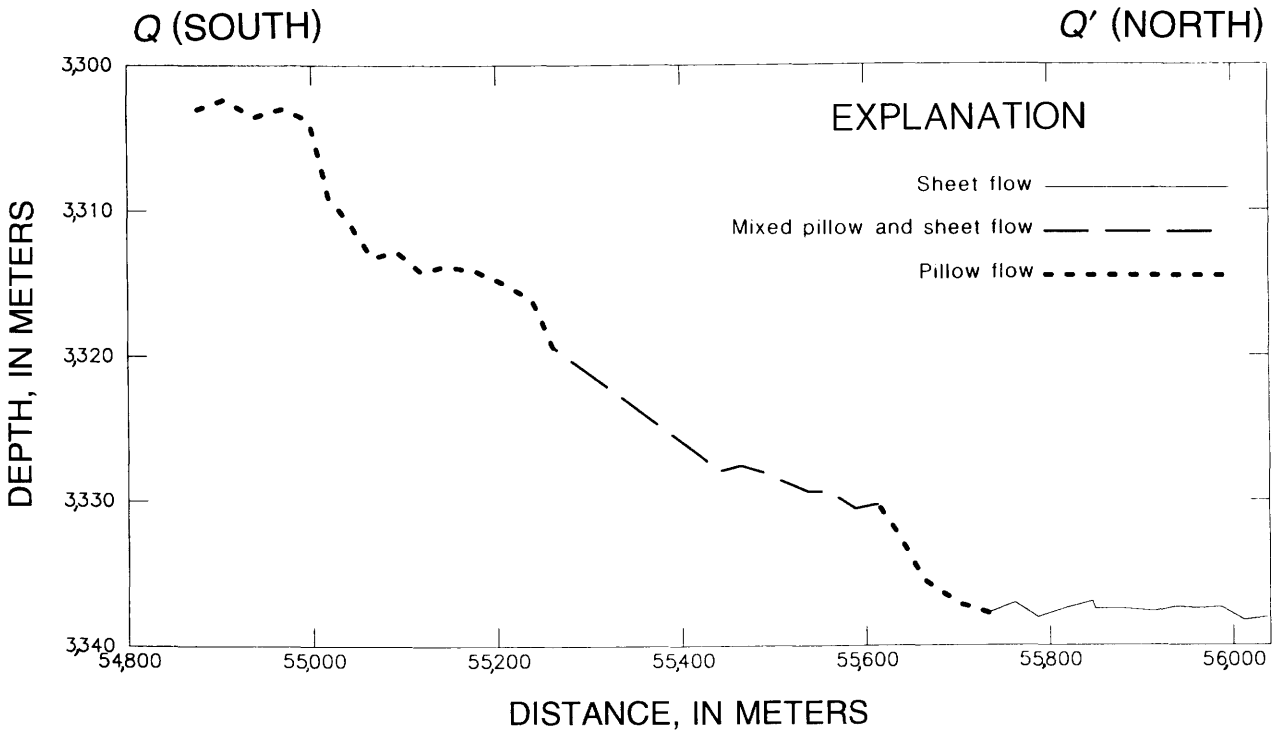

Figure 8.4. Profile of basalt geomorphology on NESCA Central Hill made by projecting a section of dive 2034 trackline onto north-south line and plotting it against bottom depth. Trackline segment marked on figure 8.2; distance marked along bottom of figure corresponds to local grid marked on right side of figure 8.2. Vertical exaggeration is 20 times.

and the contacts between basalt flows and sediment indicate that the sediment hill topography predates the last volcanic eruption. The uplift of sediment hills in Escanaba Trough has been interpreted as a manifestation of the intrusion of basaltic sills into the sediment covering the spreading center (Morton and Fox, chap. 2, this volume; Denlinger and Holmes, chap. 4, this volume; Zierenberg and others, chap. 10, this volume). These relationships lead us to speculate that the surface eruption of basalt near the Central Hill was preceded by intrusion of basaltic sills. If these interpretations are correct, than the preexisting slope of the sediment hill may have influenced the morphology of the overlying basalt flow.

Many theories have been proffered to explain the relation between the two basic types of sea-floor volcanic morphologies: pillow and sheet flows. Studies generalize that pillow flows dominate at slow spreading centers while sheet flows tend to be more prevalent at intermediate and fast ridges (Macdonald, 1982). As most of the observed volcanics at Escanaba Trough are indeed pillow lavas, this study concurs with that broad assertion.

Many studies indicate a relationship between slope and flow morphology (Duffield, 1969; Moore and others, 1971; Moore and others, 1973; Lonsdale, 1977; Ballard and others, 1979); pillow lavas dominate on steep slopes and sheet flows cover the flattest plains. Normark (1976) and MacDonald (1982) suggested that pillows create relief as they build edifices on previously formed sheet flows. Ballard and others (1979) suggested that sheet flows form at the beginning of an eruptive cycle and pillow basalts form later as the flows become channelized and effusion rate decreases. This may have occurred at the NESCA site; however, the presence of a preexisting slope near the vent area atop the east side of the Central Hill precluded the formation of sheet flow until lava reached the flat inner rift floor where it could pond and spread into a laterally extensive sheet flow. Deep-towed camera observations show that the plain south of the pillow-lava-covered crest of the Central Hill is covered by young glassy sheet flow(s), which may also have been fed by eruption(s) from a vent area near the top of the hill.

RELATIONSHIP OF VOLCANIC FLOWS TO FORMATION OF SEDIMENT HILLS

The penecontemporaneous faulting and volcanism at the base of the SESCA North Hill, combined with the observation of volcanic outcrops only at the base and downslope of the hill, suggest a causal relationship between volcanism and the uplift of the hill. Uplift of sediment hills along circular normal faults may be driven by the same intrusions that fed volcanic flows near their bases. This is further support of a connection between formation of the sediment hills and ridge-crest volcanism.

Lonsdale and Lawver (1980) presented a model for the uplift of similar sediment hills in the Guaymas Basin by intrusion of shallow basaltic sills, or bysmaliths, into unconsolidated sediment. The density of the basaltic melt initially prevents it from rising to the sediment surface; the magma flows laterally into the weak, low-density unconsolidated sediment, lifting the sediment cap. The area and height of uplift is controlled by the relative magnitude of the lateral and vertical confining pressures of the sediment and the volume of the intrusion. The uplifted hills at both Escanaba Trough and Guaymas Basin are typically 1 km in diameter with uplifts of approximately 100 m.

Solidification of magma at the margins of an intrusion, or the presence of a preexisting intrusion, could provide lateral support allowing magma to build upward and feed surface flows provided there is a sufficient supply of magma. The observation of volcanic rocks up to the base of the North Hill at SESCA suggests surface eruption of basalt from the flanks of a sediment hill uplifted by bysmalithic intrusion; however, the seismic-reflection data (Morton and Fox, chap. 2, this volume) do not indicate the presence of a shallow solid plug of basalt underlying the North Hill. Denlinger and Holmes (chap. 4, this volume, fig. 4.4*B*) propose a model for uplift of sediment hills above sills emplaced near the sediment-basalt interface. The hills are uplifted along curved faults that grow outward from the top of the volcanic body to the base of the hill. In Denlinger and Holmes' model, the faults are the conduits for the hydrothermal fluids. The available visual and seismic observations of the SESCA and NESCA sediment hills support that model and suggest that the faults also provide a path for the basaltic magma that fed surface eruptions.

REFERENCES CITED

Abbott, D.H., Morton, J.L., and Holmes, M.L., 1986, Heat flow measurements on a hydrothermally-active, slow-spreading ridge: The Escanaba Trough: Geophysical Research Letters, v. 13, p. 678–680.

Ballard, R.D., Holcomb, R.T., and van Andel, T.H., 1979, The Galapagos Rift at 86°W: 3. Sheet flows, collapse pits, and lava lakes of the rift valley: Journal of Geophysical Research, v. 84, p. 5407–5422.

Chezar, H., and Lee, J., 1985, A new look at deep-sea video: Deep-Sea Research, v. 32, p. 1429–1436.

Davis, A.S., and Clague, D.A., 1987 Geochemistry, mineralogy, and petrogenesis of basalt from Gorda Ridge: Journal of Geophysical Research, v. 92, p. 10,467–10,483.

Davis, A.S., Clague, D.A., and Friesen, W.B., Petrology and mineral chemistry of basalt from Escanaba Trough, *in* Morton, J.L., Zierenberg, R.A., and Reiss, C.A., eds., Geologic, hydrothermal, and biologic studies at Escanaba Trough, Gorda Ridge, offshore northern California: U.S. Geological Survey Bulletin 2022, chapter 9 (this volume).

Denlinger, R.P., and Holmes, M.L., A thermal and mechanical model for sediment hills and associated sulfide deposits along the Escanaba Trough, *in* Morton, J.L., Zierenberg, R.A., and Reiss, C.A., eds., Geologic, hydrothermal, and biologic studies at Escanaba Trough, Gorda Ridge, offshore northern California: U.S. Geological Survey Bulletin 2022, chapter 4 (this volume).

Duffield, W.A., 1969, Concentric structure in elongate pillows, Amador County, California: U.S. Geological Survey Professional Paper 650-D, p. D19–25.

Karlin, R., and Lyle, M., 1986, Sediment studies on the Gorda Ridge: Oregon Department of Geology and Mineral Industries Open-File Report O-86-19, 76 p.

Karlin, R.E., and Zierenberg, R.A., Sedimentation and neotectonism in the SESCA area, Escanaba Trough, southern Gorda Ridge, *in* Morton, J.L., Zierenberg, R.A., and Reiss, C.A., eds., Geologic, hydrothermal, and biologic studies at Escanaba Trough, Gorda Ridge, offshore northern California: U.S. Geological Survey Bulletin 2022, chapter 7, (this volume).

Lonsdale, P., 1977, Abyssal pahoehoe with lava coils at the Galapagos rift: Geology, v. 5, p. 147–152.

Lonsdale, P., and Lawver, L.A., 1980, Immature plate boundary zones studied with a submersible in the Gulf of California: Geological Society of America Bulletin, v. 91, p. 555–569.

Macdonald, K.C., 1982, Mid-ocean ridges: Fine scale tectonic, volcanic, and hydrothermal processes within the plate boundary zone: Annual Review of Earth and Planetary Science, v. 10, p. 155–190.

Moore, J.G., 1975, Mechanism of formation of pillow lava: American Scientist, v. 63, p. 269–277.

Moore, J.G., Phillips, R.L., Grigg, R.W., and Swanson, D.A., 1973, Flow of lava into the sea, 1969-1971: Geological Society of America Bulletin, v. 84, p. 537–546.

Moore, J.G., Cristofolini, R., and Lo Guidice, A., 1971, Development of pillows on the submarine extension of recent lava flows, Mount Etna, Sicily: U.S. Geological Survey Professional Paper 750-C, p. C89–C97.

Morton, J.L., Holmes, M.L., and Koski, R.A., 1987, Volcanism and massive sulfide formation at a sedimented spreading center, Escanaba Trough, Gorda Ridge, northeast Pacific Ocean: Geophysical Research Letters, v. 14, p. 769–772.

Morton, J.L., and Fox, C.G., Structural setting and interaction of volcanism and sedimentation at Escanaba Trough: Geophysical results, *in* Morton, J.L., Zierenberg, R.A., and Reiss, C.A., eds., Geologic, hydrothermal, and biologic studies at Escanaba Trough, Gorda Ridge, offshore northern California: U.S. Geological Survey Bulletin 2022, chapter 2 (this volume).

Morton, J.L., Zierenberg, R.A., and Reiss, C.A., 1991, Geologic, hydrothermal, and biologic studies at Escanaba Trough: An introduction, *in* Morton, J.L., Zierenberg, R.A., and Reiss, C.A., eds., Geologic, hydrothermal, and biologic studies at Escanaba Trough, Gorda Ridge, offshore northern California: U.S. Geological Survey Bulletin 2022, chapter 1 (this volume).

Normark, W.R., 1976, Delineation of the main extrusion zone of the East Pacific Rise at lat 21°N: Geology, v. 4, p. 681–685.

Normark, W.R., Gutmacher, C.E., Zierenberg, R.A., Wong, F.L., and Rosenbauer, R.J., Sediment fill of Escanaba Trough, *in* Morton, J.L., Zierenberg, R.A., and Reiss, C.A., eds., Geologic, hydrothermal, and biologic studies at Escanaba Trough, Gorda Ridge, offshore northern California: U.S. Geological Survey Bulletin 2022, chapter 6 (this volume).

Zierenberg, R.A., Morton, J.L., Koski, R.A., Ross, S.L., and Holmes, M.L., 1991, Geologic setting of massive sulfide mineralization in the Escanaba Trough, *in* Morton, J.L., Zierenberg, R.A., and Reiss, C.A., eds., Geologic, hydrothermal, and biologic studies at Escanaba Trough, Gorda Ridge, offshore northern California: U.S. Geological Survey Bulletin 2022, chapter 10 (this volume).

Zierenberg, R.A., Morton, J.L., Reiss, C.A., and Holmes, M.L., 1991, Preliminary results of the 1986 *Sea Cliff* dive program, Escanaba Trough: U.S. Geological Survey Open-File Report 91-137, 176 p.

Chapter 9. Petrology and Mineral Chemistry of Basalt from Escanaba Trough

By Alicé S. Davis, David A. Clague, *and* Walter B. Friesen[1]

CONTENTS

ABSTRACT

Basalt pillow and sheet flow fragments with glassy rinds were recovered by dredging, coring, and diving from six sites in Escanaba Trough. Of 48 glasses analyzed, all except one are normal, low-K_2O mid-ocean ridge basalt (MORB). One sample from about latitude 41°00′ N. has a high K_2O content similar to enriched (E-type) MORB. The basaltic glasses from Escanaba Trough range from relatively primitive (Mg# = 67) to moderately fractionated (Mg# = 56), where Mg# is $100\times Mg/(Mg+Fe^{2+})$. Compositional trends are similar to those observed for other MORB suites, with incompatible elements like potassium, phosphorus, and titanium generally increasing with differentiation, but a large amount of scatter indicates that the observed variations are not simply caused by crystal fractionation. Textural features and compositions of mineral phases suggest that magma mixing may have been an important process at some sites. Variations in incompatible-element ratios along the strike of Escanaba Trough indicate complex petrogenetic processes, involving heterogeneous source compositions, different degrees of partial melting, and magma mixing. Mixing with material more enriched in large-ion-lithophile (LIL) elements is indicated for the high-K_2O sample. Normal MORB glasses from this location are also higher in K_2O than comparably fractionated samples from the other sites. Spinel compositions in these lavas are higher in titanium and ferric iron than is normally observed for MORB, suggesting higher oxygen fugacity of the melt. Lead isotopic compositions of samples from this area are more radiogenic than other Gorda Ridge basalt and appear to lie on a mixing line with sediment from this area. Similar high K_2O compositions have been reported from the Explorer Deep segment of Explorer Ridge and Guaymas Basin, which have similar tectonic settings as Escanaba Trough, suggesting that incipient rifting into a sediment-filled basin may produce magmas that are contaminated by small amounts of sediment.

INTRODUCTION

Fresh basaltic glass from the chilled margins of submarine-erupted lavas provides an indirect means to assess the chemical characteristics of magmatic liquids erupted along oceanic spreading centers. Mineral chemistry in conjunction with host glass chemical compositions provide information on fractionation and magma mixing that may help to evaluate chemical and physical processes in magma chambers. The quantity of data on oceanic ridge basalt has increased steadily over the last 10 years, and major chemical features of spreading centers in the North Pacific have become better known (Eaby and others, 1984; Cousens and others, 1984; Dixon and others, 1986; Davis and Clague, 1987; 1990; White and others, 1987).

Prior to this study, the only published glass compositions from Escanaba Trough were five glass analyses from three sites (Davis and Clague, 1987). In this report we present the compositions of 48 glasses from six sites in

[1] U.S. Geological Survey, Menlo Park, California.

Escanaba Trough, the estimated eruption temperatures, densities, and viscosities of the melts, and the compositions of crystalline phases. The data are used to assess petrogenetic processes beneath Escanaba Trough and to compare basalt from Escanaba Trough with those from the northern Gorda Ridge and other spreading centers.

ACKNOWLEDGMENTS

We thank J. Morton, W. Normark, M. Holmes, P. Rona, R. Zierenberg, and J. Edmond for providing samples from their cruises.

GEOLOGIC SETTING

Escanaba Trough comprises the sediment-filled, southernmost segment of Gorda Ridge (fig. 9.1), extending 130 km northward from the Mendocino Fracture Zone at about latitude 40°25′ N. to a right-lateral offset near latitude 41°35′ N. A series of discrete volcanic edifices in Escanaba Trough uplift and locally pierce the sediment cover (Morton and others, 1987 a,b). DSDP Site 35, drilled slightly off axis in the southern end of Escanaba Trough (fig. 9.1), penetrated 390 m of Pleistocene sediment but recovered no volcanic rocks (McManus, 1970). Two of the larger volcanic edifices were studied in detail (Morton and others, chap. 1, this volume) in sites SESCA and NESCA. Volcanic rocks were dredged from four additional sites north of NESCA.

The volcanic edifices at NESCA and SESCA are broad uplifts that are largely sediment covered. At SESCA, exposed basaltic rocks are primarily pillow basalt, whereas sheet flows and pillow basalt occur at the NESCA site (Ross and Zierenberg, chap. 8, this volume).

SAMPLING AND ANALYTICAL METHODS

The 48 samples analyzed in this study are glassy rims of pillow or sheet flow fragments. Locations at start and end of dredge were averaged, and the resulting averaged sample locations are included in table 9.1 and shown in figure 9.1. Most of these samples were recovered by dredging on three U.S. Geological Survey cruises of the R/V *S.P. Lee* in 1985 (L6-85-NC) and 1986 (L2-86-NC and L3-86-NC). One sample (L1-86-33G) is glass sand recovered in a gravity core on a third cruise in 1986 (L1-86-NC), and samples labeled Alv2034, Alv2039, and SC660 were recovered by the submersibles *Alvin* and *Sea Cliff*, respectively. Three samples dredged on a 1983 U.S. Geological Survey cruise of the R/V *Kana Keoki*, for which analyses were previously published (Davis and Clague, 1987), have been included. For brevity, dredge sample designation is limited to the year and dredge number (for example, 85-xx); for years with multiple cruises the number of the leg is shown before the year (2-86-xx).

Several glass fragments were typically chosen from each dredge; more were selected if the dredge haul was large or if variation in crystal and (or) vesicle content suggested different lithologies. The polished glass mounts were analyzed with a nine-channel ARL-SEMQ electron microprobe at the U.S. Geological Survey in Menlo Park. The entire Escanaba Trough glass set, including previously analyzed samples, were reanalyzed in a single microprobe session to improve analytical precision. Analytical precision is 1 to 2 percent for major elements except sodium, and 3 to 5 percent for sodium and minor elements. Glass was analyzed with an accelerating voltage of 15 kV, a sample current of 10 nA, and a defocused beam (~ 50 μm).

Eleven samples were selected for microprobe analyses of mineral phases. The mineral phases were analyzed with the same accelerating voltage as the glass but with a narrowly focused beam (< 2 μm) and with sample currents ranging from 15 nA for plagioclase to 20 and 30 nA for olivine and spinel, respectively. The data were reduced using a modified version of the Bence and Albee method (1968). Details of analytical methods, the standards used, and precision and accuracy of microprobe analyses are given in Davis and Clague (1987). Analyses of glasses and mineral phases from the entire Gorda Ridge (Davis and Clague, 1987) were performed under the same conditions and hence represent an internally consistent data set in which small variations in glass and mineral compositions can be considered significant.

COMPOSITIONAL VARIATION OF GLASSES

The major- and minor-element concentrations of 48 glasses are presented in table 9.1 and shown in figures 9.2 to 9.6. The glasses from a single dredge haul have been grouped into flow units, if all elements are within analytical precision. Most frequently, samples from the same dredge represent the same flow unit (for example, 85-36). However, several dredges apparently sampled several flow units (for example, 3-86-10, 2-86-17, 83-16). At intensively sampled sites, such as NESCA, different dredges also apparently sampled the same flow unit. It is important to note that assignment to flow units is somewhat uncertain as lavas with nearly identical compositions have been reported from different stratigraphic horizons in DSDP sites (Rhodes and others, 1979; Natland and others, 1983). Conversely, changes in glass chemistry with fractionation in large single flows are not well documented, and it is possible that compositions treated as different flow units may be variations caused by crystal fractionation within larger flows.

The basaltic glasses from Escanaba Trough range from relatively primitive (Mg# = 67) to moderately fractionated (Mg# = 56), where Mg# =100×Mg/(Mg + Fe^{2+}). Except for one *Alvin* dive sample (2039-2) from the northernmost part of the NESCA site, all glasses are low-K_2O normal mid-ocean ridge basalt (MORB). Sample Alv2039-2 has

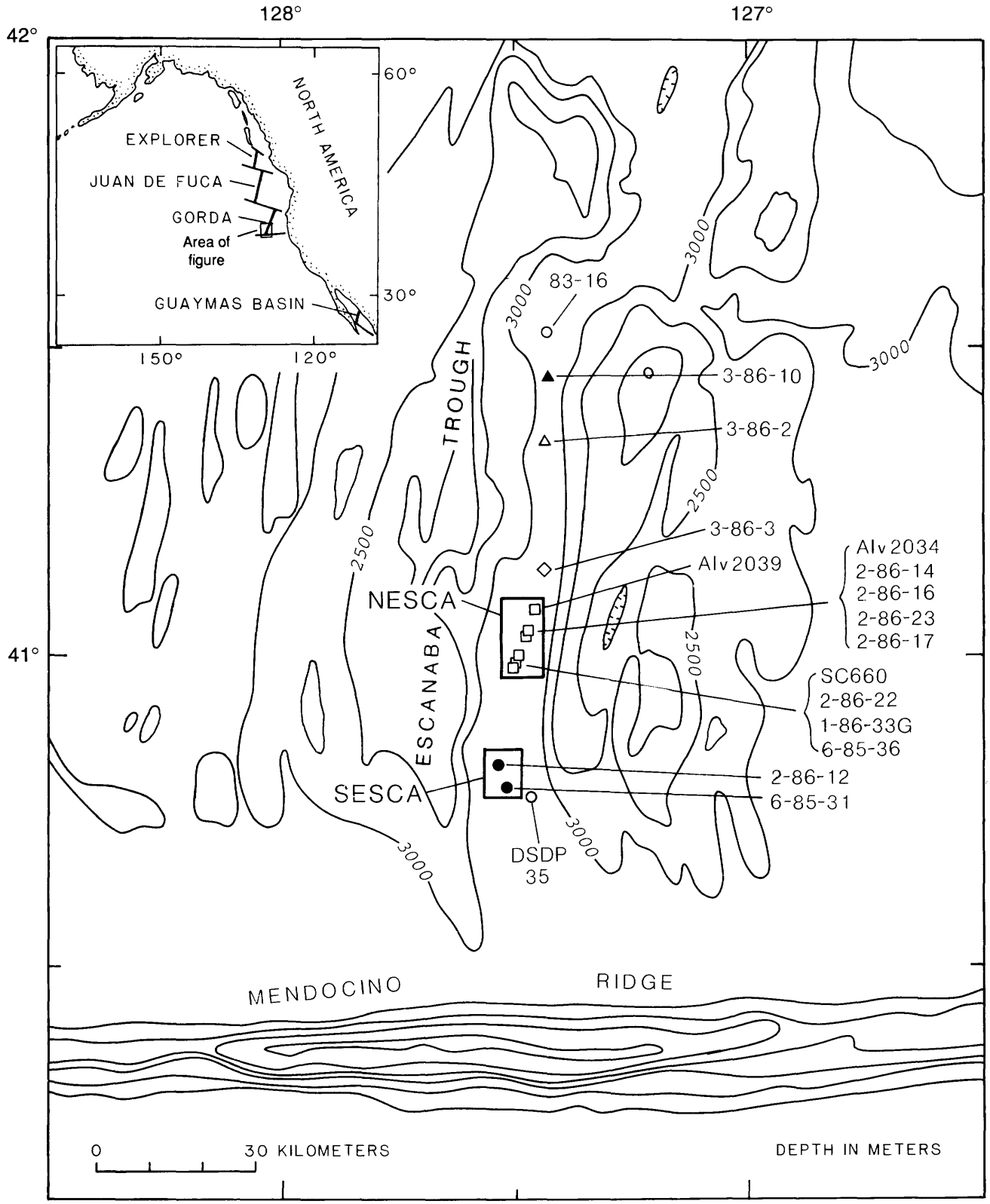

Figure 9.1. Bathymetric map of Escanaba Trough showing sample locations and DSDP Site 35. NESCA and SESCA sites are indicated. Inset map shows location of oceanic ridge segments in northern Pacific Ocean. Hachures indicate area of closed low.

Table 9.1. Locations and compositions of basaltic glasses from Escanaba Trough.

[FeO^T is total Fe calculated as FeO. Mg# is 100×Mg/(Mg+Fe^{2+}); where Fe^{2+}=0.9 Fe^T]

Sample	Latitude N.	Longitude W.	Flow unit	SiO_2	Al_2O_3	FeO^T	MnO	MgO	CaO	Na_2O	K_2O	P_2O_5	TiO_2	S	Total	Mg#
Northern sites																
83-16-1	41°31.3′	127°27.4′	1	50.0	14.8	10.8	0.21	7.08	11.2	2.76	0.24	0.21	1.89	0.12	99.3	56.5
83-16-2			1	50.5	14.3	11.0	.20	7.12	11.2	2.35	.27	.20	1.95	.13	99.2	56.2
83-16-3			2	50.0	15.3	9.69	.18	7.80	11.6	2.80	.13	.11	1.58	.11	99.3	61.5
3-86-10-1a	41°26.9′	127°25.4′	1	50.9	15.5	9.44	.17	8.22	11.8	2.53	.06	.11	1.31	.10	100.1	63.3
3-86-10-1b			1	50.9	15.7	9.33	.17	8.18	11.6	2.52	.06	.12	1.26	.09	99.9	63.5
3-86-10-2a			2	50.6	15.1	10.6	.20	7.40	11.3	2.77	.09	.16	1.71	.12	100.1	58.1
3-86-10-2b			3	50.7	15.9	9.73	.20	7.30	11.7	2.83	.09	.12	1.51	.11	100.4	59.8
3-86-10-3a			4	50.4	15.4	10.1	.20	7.55	11.5	2.74	.09	.13	1.64	.11	99.8	59.7
3-86-10-3b			1	51.1	15.2	9.37	.18	8.12	11.9	2.48	.06	.11	1.32	.10	99.8	63.2
3-86-10-4a			1	51.1	15.4	9.40	.18	8.05	11.8	2.50	.06	.12	1.30	.10	100.0	63.0
3-86-10-4b			1	50.8	15.6	9.45	.17	8.16	11.7	2.56	.07	.10	1.30	.09	100.0	63.1
3-86-10-5a			1	51.1	15.2	9.37	.17	8.10	11.8	2.49	.05	.13	1.31	.11	99.8	63.2
3-86-10-5b			4	50.8	14.8	10.2	.18	7.58	11.6	2.66	.09	.14	1.60	.12	99.8	59.6
3-86-2-1	41°20.1′	127°26.5′	1	50.0	16.4	8.81	.16	8.96	12.0	2.48	.05	.08	1.07	.09	100.1	66.9
3-86-2-2			1	50.4	16.3	8.84	.16	8.88	12.0	2.44	.05	.10	1.07	.09	99.9	66.6
3-86-3-1	41°07.6′	127°27.6′	1	50.2	15.7	9.30	.17	8.11	11.6	2.62	.13	.14	1.45	.10	99.5	63.4
3-86-3-2			1	50.3	15.8	9.31	.17	8.16	11.6	2.73	.13	.17	1.43	.10	99.8	63.5
NESCA																
Alv2039-2	41°05.3′	127°28.5′	1	50.4	15.5	10.4	0.19	7.52	11.3	2.19	0.43	0.27	1.74	0.12	100.1	59.0
Alv2034-1	41°01.0′	127°29.5′	1	50.8	15.3	9.98	.19	7.35	11.4	2.77	.25	.25	1.63	.11	100.0	59.4
Alv2034-2			1	50.7	14.9	10.1	.20	7.21	11.4	2.79	.28	.21	1.65	.11	99.6	58.6
2-86-14-1	41°00.7′	127°29.7′	1	51.0	15.0	10.2	.18	7.20	11.3	2.76	.26	.21	1.75	.11	100.0	58.3
2-86-14-2			1	50.4	14.6	10.3	.20	7.30	11.2	2.82	.25	.22	1.71	.12	99.1	58.4
2-86-16-1	41°00.7′	127°29.8′	1	50.8	14.7	10.4	.20	7.41	11.2	2.81	.25	.19	1.75	.12	99.8	58.6
2-86-16-2			1	50.8	14.8	10.3	.19	7.29	11.2	2.82	.25	.22	1.70	.12	99.7	58.4
2-86-23-1-1	41°00.5′	127°29.8′	1	50.7	14.8	10.4	.19	7.27	11.2	2.83	.25	.22	1.74	.12	99.7	58.1
2-86-23-1-2			1	50.8	14.6	10.3	.20	7.28	11.2	2.83	.25	.21	1.72	.12	99.5	58.4
2-86-23-4-1			1	51.0	14.7	10.0	.19	6.96	11.4	2.82	.25	.21	1.71	.12	99.4	58.0
2-86-23-4-2			1	50.7	14.9	10.5	.20	7.10	11.3	2.87	.26	.18	1.77	.12	99.9	57.3
2-86-17-1-1	40°59.7′	127°28.1′	1	50.8	15.0	9.99	.18	7.27	11.4	2.68	.27	.23	1.67	.11	99.6	59.1
2-86-17-1-2			1	50.8	15.2	10.0	.18	7.36	11.2	2.76	.27	.18	1.68	.10	99.7	59.4
2-86-17-2-1			2	51.1	15.2	10.6	.20	7.36	11.2	2.28	.28	.22	1.80	.12	100.4	57.9
SC-660	40°59.5′	127°29.4′	1	51.0	15.3	9.87	.18	7.87	11.3	2.77	.26	.21	1.61	.11	100.5	61.3
6-85-36-10	40°59.0′	127°30.2′	1	50.4	15.4	9.77	.19	7.58	11.3	2.72	.25	.19	1.55	.10	99.5	60.6
6-85-36-11			1	50.4	15.5	9.60	.19	7.57	11.4	2.73	.24	.18	1.53	.11	99.5	61.0
6-85-36-12			1	50.3	15.5	9.71	.18	7.65	11.4	2.71	.24	.17	1.53	.10	99.5	61.0
6-85-36-13			1	50.3	15.3	9.76	.19	7.63	11.4	2.69	.24	.17	1.56	.11	99.4	60.8
6-85-36-14			1	50.4	15.5	9.60	.18	7.50	11.4	2.74	.25	.18	1.52	.11	99.4	60.8
6-85-36-15			1	50.3	15.4	9.73	.20	7.53	11.3	2.70	.25	.19	1.53	.11	99.2	60.6
6-85-36-16			1	50.4	15.3	9.69	.19	7.57	11.4	2.72	.24	.20	1.57	.11	99.4	60.8
6-85-36-17			1	50.1	15.4	9.73	.20	7.67	11.3	2.68	.25	.18	1.52	.11	99.1	61.0
6-85-36-18			1	50.1	15.1	9.82	.19	7.56	11.3	2.72	.24	.19	1.55	.11	98.9	60.4
1-86-33G	40°58.8′	127°30.5′	1	50.5	15.4	9.93	.18	7.57	11.1	2.76	.25	.19	1.67	.11	99.7	60.2
2-86-22-1	40°58.5′	127°27.9′	1	50.8	15.4	10.1	.18	7.47	11.2	2.79	.27	.20	1.66	.11	100.2	59.5
2-86-22-2			2	51.0	15.1	10.2	.19	7.68	11.1	2.82	.28	.21	1.73	.11	100.4	59.9
SESCA																
6-85-31-10	40°46.4′	127°30.8′	1	51.7	14.8	8.66	0.18	8.32	12.6	2.44	0.11	0.10	1.05	0.10	100.1	65.6
6-85-31-11			1	51.6	14.8	8.70	.17	8.35	12.5	2.45	.12	.10	1.07	.09	100.0	65.6
2-86-12-1	40°45.9′	127°32.7′	1	51.3	15.6	8.43	.16	8.33	12.7	2.38	.14	.12	1.03	.09	100.2	66.2
2-86-12-2			1	51.1	15.3	8.50	.17	8.40	12.6	2.37	.14	.11	1.03	.10	99.8	66.2

a K_2O content of 0.43 percent, much higher than is typical for normal MORB. Besides a slightly elevated P_2O_5 content and lower Na_2O abundance, this sample appears ordinary with respect to the other elements analyzed. Although the other glasses have K_2O contents within the range typically encompassed by normal MORBs, two groups with distinct K_2O contents are apparent (fig. 9.2*A*). All samples at the NESCA site have higher K_2O contents than samples from the other sites, except for the two fractionated compositions from 83-16 (Mg# = 56), from the northernmost site in Escanaba Trough. Unlike K_2O, TiO_2 contents show a narrower, better defined trend, increasing with Mg# (fig. 9.2*B*). Al_2O_3 and CaO in general decrease with fractionation, whereas Na_2O and P_2O_5 increase with decreasing Mg#, but all show considerable scatter (figures not shown). SiO_2 ranges from 50 to 52 percent and shows no correlation with Mg#.

Sulfur apparently behaved like an incompatible element, showing a general increase with differentiation (fig. 9.3*A*), but variation in sulfur content at a given Mg# is greater than analytical precision. As expected, sulfur shows a positive correlation with FeO* (total iron as FeO, fig. 9.3*B*), and the trend lies below or close to the sulfur saturation line determined for MORB (Mathez, 1976). On a TiO_2 versus FeO* plot (fig. 9.4*A*) the glass compositions show two trends, with samples of NESCA and 3-86-3 and 83-16 higher in TiO_2 at a given FeO* content, suggesting

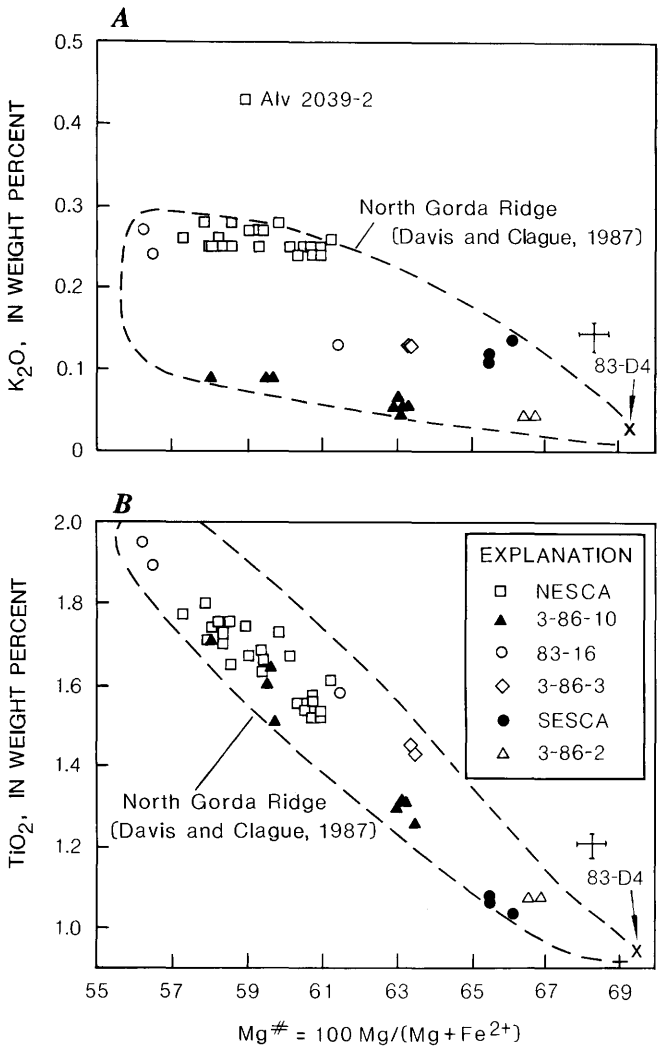

Figure 9.2. Variation diagrams of (*A*) K_2O and (*B*) TiO_2 versus Mg#, or 100×Mg/(Mg+Fe^{2+}), shows large amount of scatter in K_2O at a given Mg#. Samples from NESCA and two samples (83-16) from near offset at latitude 41°35′ N. have higher K_2O contents than comparably fractionated samples from other sites. TiO_2 versus Mg# shows better defined increasing trend with decreasing Mg# but also shows some scatter. Basalts from northern Gorda Ridge, shown for comparison (Davis and Clague, 1987), have a similar compositional range (outlines), but high-K_2O compositions like that of Alv 2039-2 are absent. Crosses show analytical precision.

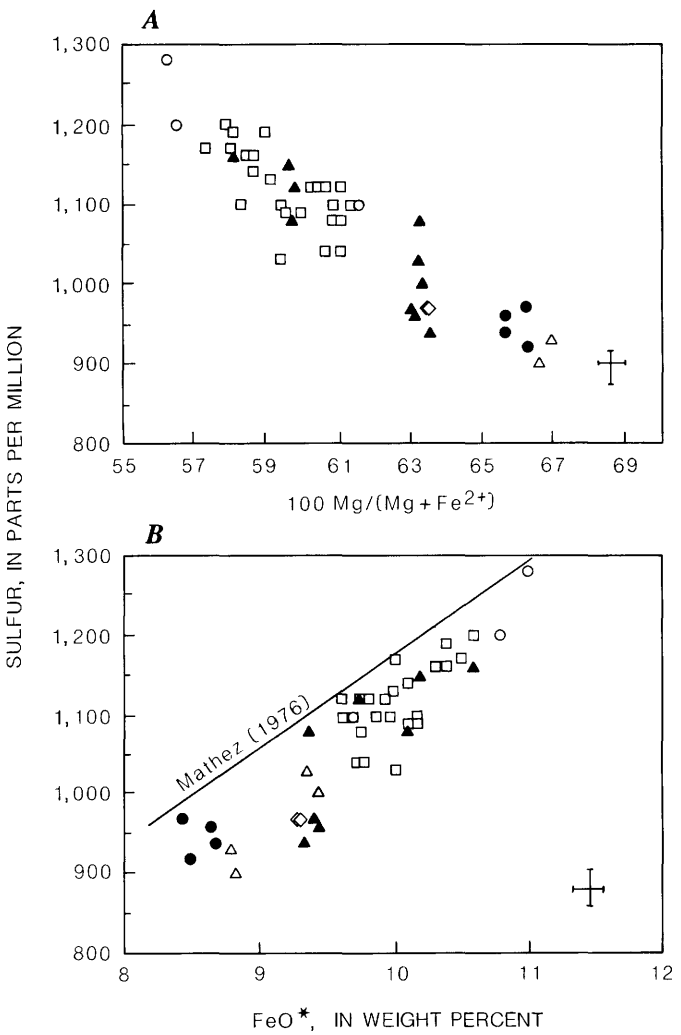

Figure 9.3. Sulfur versus (*A*) fractionation index of Mg (Mg#) and (*B*) total iron (FeO*) show generalized increasing trends with differentiation, but scatter at a given Mg# is larger than analytical precision (crosses). Compositions lie close to, or below, the sulfur saturation line determined for MORB (Mathez, 1976). Symbols as in figure 9.2.

that they fractionated from parental melts with higher TiO_2 contents than the other samples.

The effects of crystallization may be qualitatively evaluated on a CaO/Al_2O_3 versus Mg# plot (fig. 9.4*B*). Olivine fractionation lowers the Mg# without affecting the CaO/Al_2O_3 ratio, whereas plagioclase fractionation increases the CaO/Al_2O_3 ratio without changing the Mg#. Clinopyroxene fractionation lowers both numbers. The Escanaba Trough glasses show different fractionation paths involving different proportions of olivine and plagioclase,

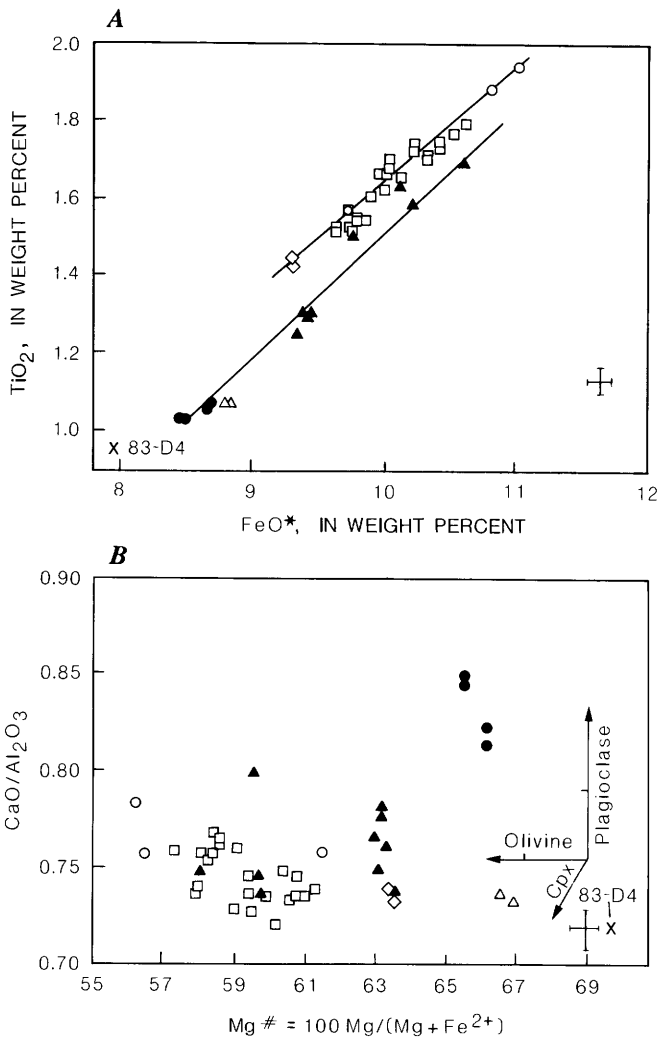

Figure 9.4. *A*, TiO_2 versus total iron (FeO*) shows two trends suggesting that samples from NESCA and some northern sites are fractionated from parental magmas higher in TiO_2. *B*, CaO/Al_2O_3 versus fractionation index of Mg (Mg#) shows different fractionation trends. Samples from SESCA have high CaO/Al_2O_3 ratios, suggesting that fractionation was controlled mostly by plagioclase, whereas samples from the other sites show trends compatible with mostly olivine and minor plagioclase fractionation. Arrows indicate compositional changes with plagioclase, olivine, and clinopyroxene fractionation; ticks on arrows show effects of 5 percent fractionation of olivine and plagioclase. Symbols as in figure 9.2.

Table 9.2. Modal analyses of Escanaba Trough basalt samples.

[Data based on 1,000 point counts. Mg#, 100xMg/(Mg+Fe^{2+}). A, in glass; B, in or attached to olivine; C, in or attached to plagioclase; _, absent; <, less than]

Sample	Mg#	Volume percent				Spinel
		Ground-mass	Plagio-clase	Olivine	Vesicles	
Northern sites						
83-16-1	56.5	70	21	4	5	B,C
83-16-3	61.5	71	26	<1	2	B
3-86-10-2a	58.1	78	19	2	1	C
3-86-10-3b	63.2	94	4	<1	<1	—
3-86-10-5b	59.6	87	10	1	2	C
3-86-2-2	66.6	97	<1	1	<1	C
3-86-3-1	63.4	98	0	1	1	A,C
NESCA						
Alv2039-2	59.0	97	<1	<1	<1	A
2-86-23-1-1	58.1	93	2	<1	4	B
2-86-17-1-1	59.1	95	3	<1	<1	B,C
6-85-36-11	61.0	96	1	2	1	A,C
2-86-22-1	59.5	98	0	<1	1	C
SESCA						
6-85-31-10	65.6	90	7	1	2	_
2-86-12-2	66.2	92	5	2	<1	_

assuming a parental composition similar to the most primitive composition from Escanaba Trough (3-86-2). The large increase in CaO/Al_2O_3 ratio, without a significant change in Mg#, shown by SESCA glasses suggests primarily plagioclase fractionation with only minor olivine. Modal abundance of plagioclase in these samples is somewhat greater than for NESCA samples (table 9.2), but crystal fractionation calculations (Stormer and Nicholls, 1978) suggest more than 10 percent plagioclase would have to fractionate to increase the CaO/Al_2O_3 ratio to that observed. The small variation in CaO/Al_2O_3 over a large range of Mg#s observed for the NESCA samples is compatible with primarily olivine and minor plagioclase fractionation. Since isolated magma chambers and different source compositions generated by different degrees of partial melting are indicated for the northern segments of the Gorda Ridge (Davis and Clague, 1987), different fractionation paths are probably to be expected from geographically separated areas. However, samples from the same dredge haul (for example, 3-86-10) also show different trends, suggesting that variations are not the result of closed system fractionation. The range in CaO/Al_2O_3 at a constant Mg# for samples from 3-86-10 (fig. 9.4*B*) suggests different amounts of plagioclase fractionation.

K_2O/P_2O_5 ratios versus Mg# (fig. 9.5*A*) show a low ratio of about 0.5 for most samples from the northern sites, high ratios of about 1.3 or more for NESCA and samples of 83-16, and ratios that are between these for samples from SESCA and 3-86-3. K_2O/TiO_2 ratios show a similar

pattern (fig. 9.5*B*). Ratios of incompatible elements like potassium, phosphorus, and titanium should not be significantly changed by fractionation over the differentiation range shown by these samples. Hence, variations in these ratios suggest complex petrogenetic processes involving different percentages of partial melting and (or) different source compositions.

Compositional variation along the strike of Escanaba Trough (fig. 9.6) shows relatively unfractionated compositions at SESCA and 3-86-2 and 3-86-3. At NESCA, all lavas are relatively fractionated (Mg# = 59 ± 2.0). Sites 83-16 and 3-86-10 have relatively primitive and evolved compositions at the same location (fig. 9.6*A*). K_2O/P_2O_5 ratios along the strike of Escanaba Trough show more enriched compositions at NESCA, with the highest ratio shown by the high-K_2O sample Alv2039-2 (fig. 9.6*B*). Samples from SESCA and from the northernmost site close to the offset (83-16) also have relatively high K_2O/P_2O_5 ratios (>1), whereas samples from the other sites have lower ratios. Variations in K_2O/P_2O_5 beyond analytical uncertainties at a given location may indicate small-scale heterogeneities.

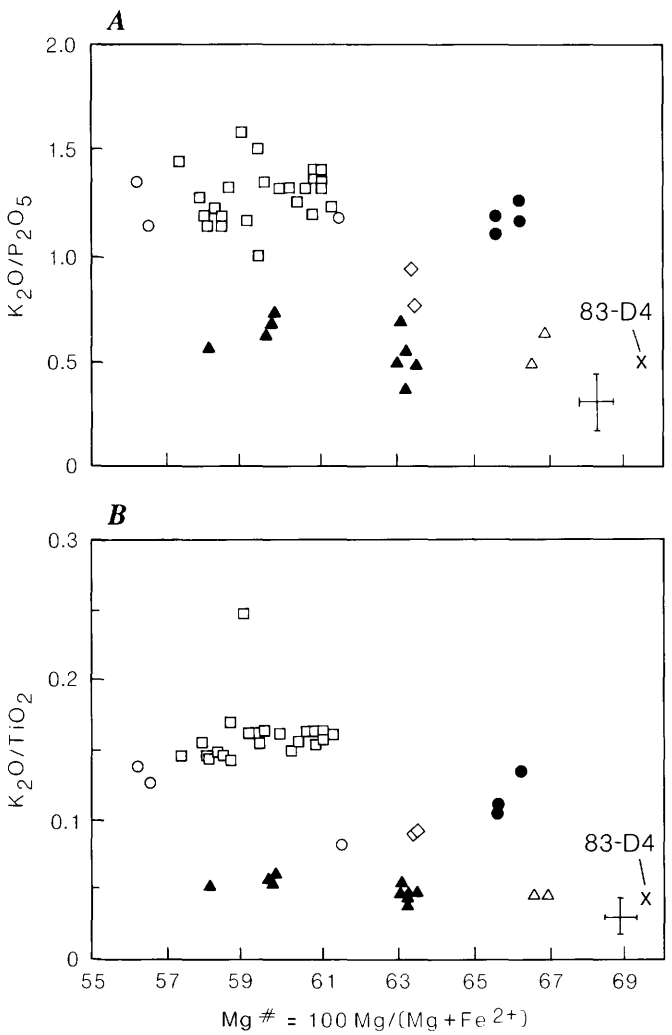

Figure 9.5. K_2O/P_2O_5 (*A*) and K_2O/TiO_2 (*B*) versus fractionation index of Mg (Mg#) show ratios for samples from NESCA and 83-16, the northernmost site close to the offset, that are twice as high as samples from other sites. Symbols as in figure 9.2.

PETROGRAPHY

Most of the analyzed samples from the NESCA site are sheet flow fragments, whereas samples from the other sites are predominantly pillow basalt. All samples are fresh with glass rinds a millimeter to a centimeter thick. Palagonite is thin or absent. Modal compositions of samples selected for analyses of mineral phases are given in table 9.2. Typically the glassy rind grades into a variolitic zone and then into a pilotaxitic zone toward the pillow interior. Except for samples from dredges 83-16 and 3-86-10, the samples are sparsely porphyritic, with plagioclase and olivine phenocrysts. In the sparsely porphyritic samples, phenocrysts are most commonly small, euhedral single crystals or small glomerocrysts. The NESCA

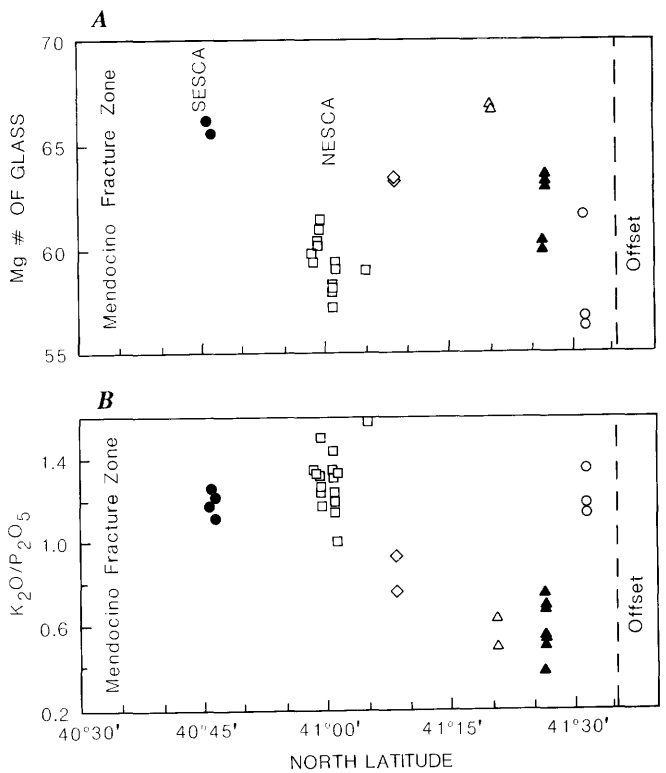

Figure 9.6. Compositional variation along ridge axis of Escanaba Trough. *A*, Mg# versus latitude shows only relatively fractionated compositions at NESCA, only unfractionated compositions at SESCA, and larger range in compositions at 83-16 and 3-86-10. *B*, K_2O/P_2O_5 ratios along ridge axis are variable with high and low ratios in close proximity, indicating complex petrogenetic processes. Symbols as in figure 9.2.

samples have a greater abundance of minute crystallites, which show a pronounced flow alignment. Some samples from dredges 83-16 and 3-86-10 are highly porphyritic (>30 percent), containing plagioclase phenocrysts up to a centimeter across with disequilibrium textures. The plagioclase phenocrysts are usually anhedral, with fritted or embayed margins, and show strong optical zoning. Some plagioclase crystals enclose other plagioclase crystals and (or) devitrified glass inclusions. A few larger olivine phenocrysts in the highly plagioclase-phyric samples also contain glass inclusions and have embayed margins. Some olivine crystals in samples from 3-86-10 subophitically enclose plagioclase or occur as rare coronate overgrowths on plagioclase.

Minute euhedral to subhedral spinel crystals occur in many samples and may be included or attached to olivine, plagioclase, or in the groundmass. No clinopyroxene, either as phenocryst or as groundmass phase, was observed.

MINERAL CHEMISTRY

OLIVINE

Representative olivine compositions are given in table 9.3. Previously published analyses of olivine in samples from 83-16 (Davis and Clague, 1987) are not included in the table but are shown in figure 9.7. Olivine compositions for the Escanaba Trough set collectively range from Fo_{83} to Fo_{89}, but Fo_{84} and Fo_{86} are the most common compositions (fig. 9.7*A*). Most samples show a narrow range of Fo contents spanning only 1 molar percent in a given section, but the highly plagioclase-phyric samples of 83-16 and 3-86-10 show more variability, with the largest range of Fo contents in 83-16-1 (Fo_{83-89}). However, individual crystals in these samples are typically unzoned or only very slightly zoned (<1 molar percent). Maximum zoning of about 2 molar percent is observed in rare crystals of samples 3-86-2, 3-86-10-5b and 3-86-10-2a. Zoning, when present, is normal with cores more magnesian than the rims.

The NiO contents of olivine range from 0.14 percent in an embayed phenocryst of sample 83-16-1 to 0.31 percent in a euhedral microphenocryst in sample 3-86-2-2. NiO decreases with decreasing Fo contents but shows broad scatter in excess of analytical uncertainty (fig. 9.7*B*). Samples from the SESCA site are generally lower in NiO at comparable Fo contents than the other samples. The magnesian-rich core of one olivine crystal in sample 3-86-2-2 is lower in NiO than the less magnesian rim. The highest NiO contents of 0.31 percent occurs in this sample in a euhedral microlite (Fo_{87}). Fo contents versus Mg# of the host glasses shows that the aphyric and sparsely porphyritic glasses have some olivine compositions close to the calculated equilibrium Fo contents (fig. 9.7*C*), assuming a

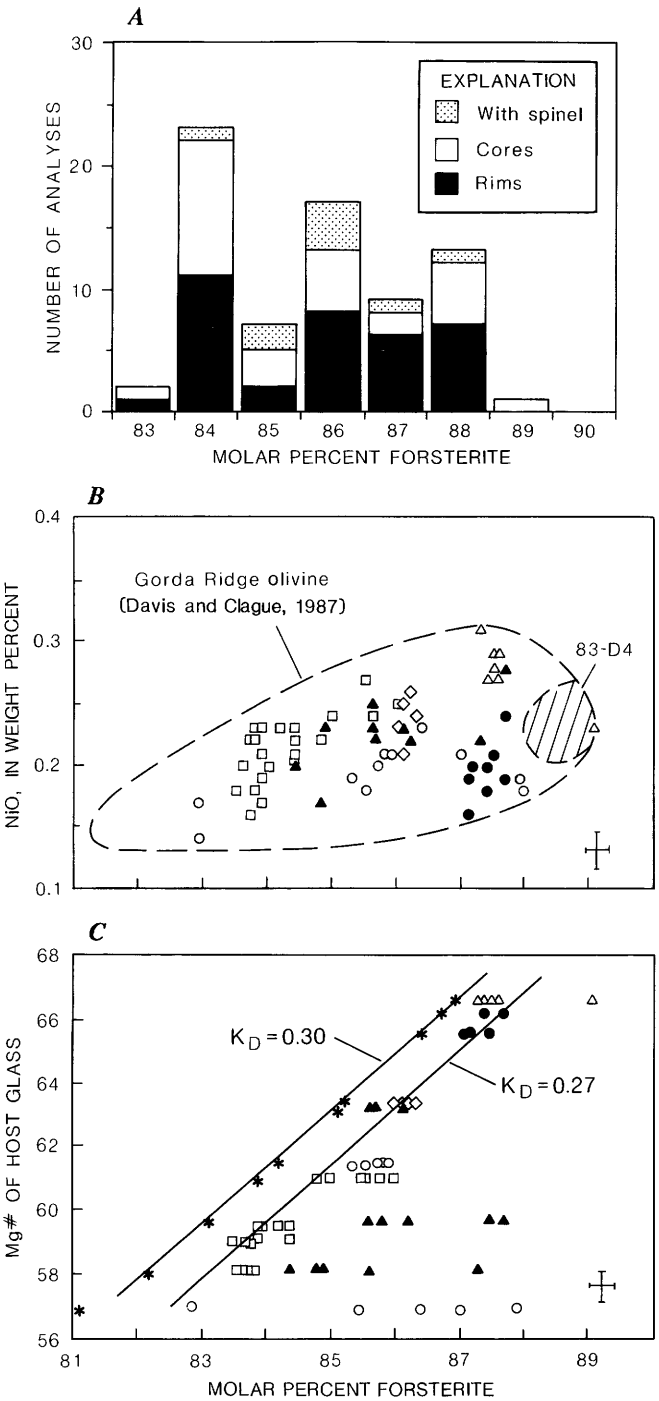

Figure 9.7. *A*, Olivine compositions of Escanaba Trough lavas show narrow range in Fo contents, ranging from 83 to 89. *B*, NiO decreases with decreasing Fo content but shows large amount of scatter. Field of northern Gorda Ridge olivine is shown for comparison. Striped field shows compositional range of olivine in most primitive glass from northern Gorda Ridge (83-D4). *C*, Fo of olivine versus Mg# of host glass shows most evolved olivine compositions close to being in equilibrium with their host glass. Equilibrium Fo content, shown for reference (stars), was calculated assuming distribution coefficient (K_D) = 0.30. Many olivine crystals are too magnesian to be in equilibrium with their host glass. Symbols as in figure 9.2.

Table 9.3. Representative olivine analyses from Escanaba Trough.

[C, core; R, rim of phenocryst; mc, center of microphenocryst; ^{s}, spinel included or attached]

	Northern sites										
Sample no.	16-1	10-2a	10-2a	10-3b	10-3b	10-5b	10-5b	2-2	2-2	3-1	3-1
Position	C	R	C	R	C	R^{s}	C^{s}	R	C	R^{s}	C^{s}
SiO_2	40.3	39.5	39.9	39.1	39.7	39.6	39.4	39.4	39.9	39.8	39.4
FeO	11.4	14.6	12.2	13.7	13.7	13.8	13.3	12.0	10.4	13.4	13.4
MgO	47.6	45.8	47.3	45.6	45.8	46.1	46.4	47.0	47.9	46.3	46.4
CaO	.31	.28	.29	.25	.26	.29	.29	.30	.31	.28	.28
MnO	.18	.25	.20	.24	.21	.26	.25	.20	.18	.21	.23
NiO	.22	.23	.22	.25	.25	.23	.22	.27	.23	.23	.25
Total	100.0	100.7	100.2	99.1	100.0	100.3	99.8	99.0	98.9	100.1	99.9
Fo mol pct.	88.1	84.9	87.3	85.6	85.6	85.6	86.2	87.6	89.1	86.0	86.1

	NESCA							SESCA			
Sample no.	2039-2	2-23-1	2-22-1	17-1	36-11	36-11	36-11	31-10	31-10	12-2	12-2
Position	mc	C	C	mc^{s}	R	C	mc	R	C	mc	mc
SiO_2	39.0	39.3	38.9	39.1	39.4	39.3	38.8	40.0	39.8	39.8	39.7
FeO	15.6	15.3	14.8	14.7	13.7	13.5	14.2	12.3	12.1	11.9	12.0
MgO	44.3	44.7	44.8	44.6	45.8	45.8	46.0	46.4	47.3	47.2	46.6
CaO	.29	.29	.28	.30	.26	.26	.32	.31	.30	.32	.34
MnO	.25	.29	.20	.26	.23	.21	.24	.22	.20	.24	.23
NiO	.18	.19	.22	.23	.24	.24	.20	.16	.21	.24	.20
Total	99.7	100.1	99.2	99.1	99.7	99.3	99.7	99.3	99.9	99.7	99.0
Fo mol pct.	83.5	83.9	84.4	84.4	85.6	85.8	85.0	87.1	87.5	87.7	87.4

distribution coefficient (K_D) of 0.30. The distribution of iron and magnesium between olivine and liquid can vary between K_D = 0.25 and 0.35, depending on the oxygen fugacity, temperature, and pressure (Walker and others, 1979; Bender and others, 1978). More crystal-rich samples have a wider range of olivine compositions, containing magnesian-rich crystals that are not in equilibrium with their host glass.

PLAGIOCLASE

Compositions of plagioclase in Escanaba Trough glasses (table 9.4, fig. 9.8) range from An_{65} for a phenocryst core in sample 3-86-10-2a to An_{87} in the core of a phenocryst in 83-16-3. Except for anorthite-rich phenocrysts in the highly plagioclase-phyric samples from the northernmost site in Escanaba Trough (83-16), phenocrysts with An contents above 80 are rare, and An contents between 72 to 75 are most common (fig. 9.8). Plagioclase phenocrysts from the SESCA site show small amounts of normal zoning. By contrast, all the plagioclase from the NESCA site show only reverse zoning with rims higher in An contents than cores by 1 to 10 molar percent. Samples from both flow units of 83-16 show mostly normal zoning by 2 to 4 molar percent but can show up to 12 molar percent difference between core and rim. Unfractionated samples of 3-86-2 and 3-86-3 are almost devoid of plagioclase phenocrysts but contain rare microlites with An contents of 72 or less. K_2O contents are close to or below detection limit for most samples, but the higher K_2O host glasses from NESCA contain plagioclase with measurable K_2O contents, and the high-K_2O sample Alv2039-2 has 0.06 percent K_2O in plagioclase (table 9.4).

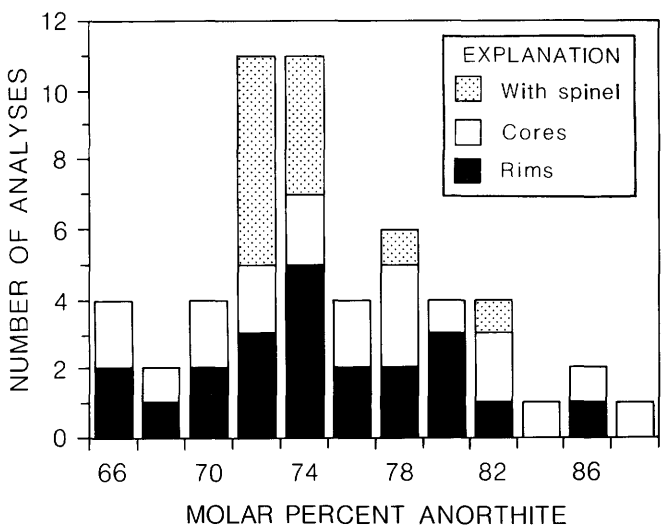

Figure 9.8. Histogram of plagioclase anorthite content in Escanaba Trough lavas shows compositions ranging from An_{87} to An_{65}, with An_{72} and An_{74} most frequently occurring compositions.

Table 9.4. Representative plagioclase analyses from Escanaba Trough.

[C, core; R, rim of phenocryst; mc, center of microphenocryst; ^{s}, spinel included or attached]

	Northern sites												
Sample no.	16-1	16-1	16-3	10-2a	10-2a	10-2a	10-2a	10-3b	10-3b	10-5b	10-5b	2-2	3-1
Position	C	R	C^s	C	R	C	R	R	C	R	C	mc	mc
SiO_2	47.1	50.8	45.9	52.1	49.9	52.3	52.1	48.3	48.9	51.5	50.8	48.6	51.3
Al_2O_3	33.2	30.3	34.2	30.2	32.1	30.5	30.4	33.1	32.2	30.5	30.6	32.4	30.7
FeO	.29	.47	.23	.41	.42	.44	.39	.39	.41	.50	.48	.45	.83
CaO	16.6	14.3	17.9	13.3	15.0	13.4	13.6	16.4	15.9	13.7	13.8	15.8	14.3
Na_2O	1.97	3.32	1.49	3.95	3.07	4.04	3.84	2.21	2.54	3.83	3.73	2.51	3.34
K_2O	0	.05	0	.02	.02	.03	.03	.01	.01	.02	.01	.01	.03
MgO	.26	.29	.21	.31	.28	.24	.27	.26	.28	.25	.22	.29	.44
Total	99.4	99.6	99.1	100.4	100.8	99.5	100.6	100.6	100.3	100.3	99.6	100.1	100.7
An mol pct.	82.3	70.2	87.0	65.0	72.8	64.5	66.1	80.3	77.6	66.3	67.1	77.6	70.1

	NESCA							SESCA					
Sample no.	2039-2	17-1	17-1	17-1	36-11	36-11	36-11	31-10	31-10	31-10	12-2	12-2	12-2
Position	mc	R	C	mc^s	R^s	C^s	mc	C	R	mc	R	C	mc
SiO_2	50.5	48.6	51.0	50.3	49.8	50.1	50.0	50.0	50.8	50.5	47.7	47.3	50.1
Al_2O_3	30.8	33.1	31.1	30.7	31.2	30.8	31.7	31.2	31.1	31.7	32.4	32.8	31.1
FeO	.56	.49	.45	.49	.45	.41	.58	.42	.42	.53	.43	.35	.56
CaO	14.2	16.3	14.4	14.5	15.0	14.9	15.3	15.4	15.0	15.1	16.6	17.0	15.0
Na_2O	3.35	2.20	3.25	3.30	3.02	3.22	2.99	2.79	3.03	2.94	2.11	1.85	2.96
K_2O	.06	.02	.04	.05	.04	.04	.04	.02	.03	.03	.02	.02	.03
MgO	.28	.28	.29	.26	.25	.26	.27	.33	.31	.32	.26	.28	.39
Total	99.9	101.1	100.6	99.7	99.8	99.6	100.9	100.1	100.1	101.0	99.6	99.6	100.1
An mol pct.	69.8	80.4	70.9	70.7	73.2	71.6	73.8	75.2	73.1	73.8	81.3	83.5	73.6

SPINEL

The majority of spinel crystals are included in or attached to olivine or plagioclase, but a few occur in the groundmass. Spinel crystals in most of the glasses are magnesiochromites (table 9.5). Mg numbers of spinel range from 0.70 to 0.56 and are negatively correlated with Cr/(Cr+Al) or Cr#, which ranges from 0.42 to 0.56 (fig. 9.9*A*). Like Cr#, TiO_2 generally increases with decreasing Mg#, ranging from 0.4 to 1.6 percent, but shows two different trends with high- and low-TiO_2 spinel at comparable Mg#s. In samples from 3-86-10, high- and low-TiO_2 spinel occur in the same sample. The most magnesian spinels occur in olivines in the unfractionated glasses from the locations north of NESCA. Spinels in NESCA glasses are all higher in TiO_2 and ferric iron than is commonly observed for MORB spinel (Sigurdsson and Schilling, 1976; Davis and Clague, 1987; 1990). Spinel compositions in the NESCA samples show a narrow range, regardless of host phase. No spinel was observed in the SESCA glasses, although they are much less fractionated than NESCA glasses. Mg# of the host glass versus Mg# of spinel (fig. 9.9*C*) shows a positive correlation, but two distinct trends exist. The crystal-rich, relatively fractionated glasses from 83-16 and 3-86-10 contain some spinel crystals that are too magnesian to be in equilibrium with their host glass.

TEMPERATURE, DENSITY, AND VISCOSITY OF LAVA

Estimated eruption temperatures, densities, and viscosities for Escanaba Trough glasses are given in table 9.6. Eruption temperatures have been calculated using the olivine-glass geothermometers of Roeder (1974) and Bender and others (1978) for samples with coexisting olivine data. For other samples, temperatures were determined from a graphic geothermometer using only the MgO of the glass (Davis and Clague, 1990). Density and viscosity were calculated using the method of Bottinga and others (1982) and Shaw (1972), respectively, using temperatures determined with the graphic geothermometer (fig. 9.10*A*). Eruption temperatures range from 1,170°C to 1,220°C (fig. 9.10*A*). Densities also show a limited range from 2.654 g/cm^3 for one of the least fractionated samples of 3-86-2, to about 2.687 g/cm^3 for the most fractionated composition of 83-16-1. As observed for other MORB suites (Sparks and others, 1980), density increases with differentiation over the compositional range present, but shows considerable scatter at a given MgO content (fig. 9.10*B*). Viscosity is low in the unfractionated compositions and increases with differentiation but is not directly correlated with density (table 9.6).

Table 9.5. Representative analyses of chromian spinel from Escanaba Trough.

[C, core; R, rim of larger crystals; mc, center of microphenocryst. Fe^{3+} calculated from total Fe and structural formula. Spinel occurrence: O, in olivine; P, in plagioclase; G, in groundmass]

	Northern sites										
Sample no.	16-1	16-1	16-1	16-3	10-2a	10-2a	10-5b	2-2	3-1	3-1	3-1
Occurrence	O	O	O	O	O	P	O	O	G	G	O
Position	mc	R	C	mc	mc	mc	mc	mc	R	C	mc
Al_2O_3	31.0	26.9	26.5	28.8	27.2	22.2	29.0	28.1	26.2	25.2	26.1
Fe_2O_3	6.47	7.71	6.68	6.25	6.86	8.26	5.92	6.61	6.90	6.91	7.12
FeO	13.9	14.9	14.0	12.2	14.9	17.3	13.3	12.7	14.6	14.5	14.5
MgO	15.0	14.1	14.5	15.9	14.5	12.6	15.7	15.8	14.6	14.4	14.8
MnO	.29	.30	.29	.26	.25	.29	.22	.25	.25	.25	.26
TiO_2	.40	.64	.53	.49	.69	1.37	.68	.63	.98	1.06	1.01
Cr_2O_3	32.9	35.6	37.2	35.7	37.1	38.5	36.3	36.3	37.1	37.3	37.5
Total	99.9	100.6	99.7	99.6	101.5	100.5	101.1	100.3	100.6	99.6	101.2
Cationic proportions											
$Mg/Mg+Fe^{2+}$	.658	.628	.649	.699	.634	.565	.678	.690	.641	.640	.646
Cr/Cr+Al	.416	.470	.485	.454	.478	.538	.457	.464	.487	.498	.491

	NESCA										
Sample no.	2039-2	2039-2	23-1-1	22-1	22-1	17-1-1	17-1-1	17-1-1	36-11	36-11	36-11
Occurrence	G	G	P	O	O	P	P	O	O	O	G
Position	mc	mc	mc	C	R	mc	mc	mc	mc	mc	mc
Al_2O_3	22.3	22.0	20.7	21.9	21.4	20.5	21.1	21.5	22.2	22.2	22.5
Fe_2O_3	9.37	9.68	9.28	8.60	9.63	9.26	8.77	8.70	8.91	8.37	8.30
FeO	16.9	16.6	17.1	17.3	16.6	16.8	16.8	17.0	15.7	16.1	15.6
MgO	12.8	13.0	12.6	12.7	12.9	12.6	12.8	12.8	13.4	13.2	13.4
MnO	.29	.29	.30	.29	.29	.29	.20	.28	.27	.28	.28
TiO_2	1.48	1.53	1.51	1.55	1.50	1.48	1.46	1.56	1.32	1.34	1.20
Cr_2O_3	36.8	36.9	38.8	38.3	37.7	38.6	39.1	38.5	37.7	38.2	38.2
Total	99.9	99.9	100.2	100.6	100.1	99.5	100.3	100.3	99.5	99.7	99.5
Cationic proportions											
$Mg/Mg+Fe^{2+}$	.575	.583	.569	.567	.580	.573	.576	.573	.604	.594	.604
Cr/Cr+Al	.525	.529	.557	.540	.542	.558	.554	.546	.533	.536	.533

COMPARISON WITH NORTHERN GORDA RIDGE

Escanaba Trough glasses have a compositional range similar to those from the two northern segments of the Gorda Ridge (Davis and Clague, 1987). However, at the northernmost segment of the Gorda Ridge there is one sample with a composition more primitive (Mg# = 69) than the least fractionated Escanaba Trough glass (Mg# = 67), and at the middle section of Gorda Ridge there is one more fractionated (Mg# = 55.5) than the most fractionated Escanaba Trough glass (Mg# = 56.6). K_2O in northern Gorda Ridge glasses also shows considerable scatter at a given Mg# (Davis and Clague, 1987). However, none of the higher K_2O samples has a K_2O content as high as Alv2039-2 from the northern end of the NESCA site. Other elements in northern Gorda Ridge glasses show trends similar to those from Escanaba Trough. K_2O/P_2O_5 and K_2O/TiO_2 ratios also show two groups, one with low ratios (~0.5) and one about twice as high, erupted in close proximity, indicating heterogeneity at a ridge segment and even within the area sampled by a single dredge.

Mineralogically, Escanaba Trough samples are also similar to those from the northern Gorda Ridge, with highly plagioclase-phyric glasses and nearly aphyric samples in close proximity. Fo contents in olivine from northern Gorda Ridge also show a slightly larger range (Fo_{89-82}), in accord with a slightly larger range of glass compositions. Unlike Escanaba Trough samples, some of the northern Gorda Ridge glasses contain olivine with significant normal or reverse zoning (> 2 molar percent; Davis and Clague, 1987).

Plagioclase from northern Gorda Ridge also has a larger compositional range, ranging from An_{92} to An_{64}. Most Escanaba Trough plagioclase compositions cluster around An contents of 72 to 74 and appear to be in equilibrium with their host glass. A similar range of An contents is also observed for microlites in northern Gorda Ridge glasses, but An contents of 82 to 86 are most frequent for phenocrysts. A higher frequency of more calcic plagioclase at northern Gorda Ridge most likely reflects an analytical bias of preferentially analyzing larger phenocrysts, which are more abundant than in Escanaba Trough lavas. Unusually calcic plagioclase (An_{92}) occurs at one

place on the northern Gorda Ridge that has no counterpart in Escanaba Trough glasses. These unusually calcic compositions are limited to large megacrysts (> 1 cm) with pronounced disequilibrium textures (Davis and Clague, 1987).

Spinel compositions from northern Gorda Ridge are similar to those from Escanaba Trough with respect to Cr#

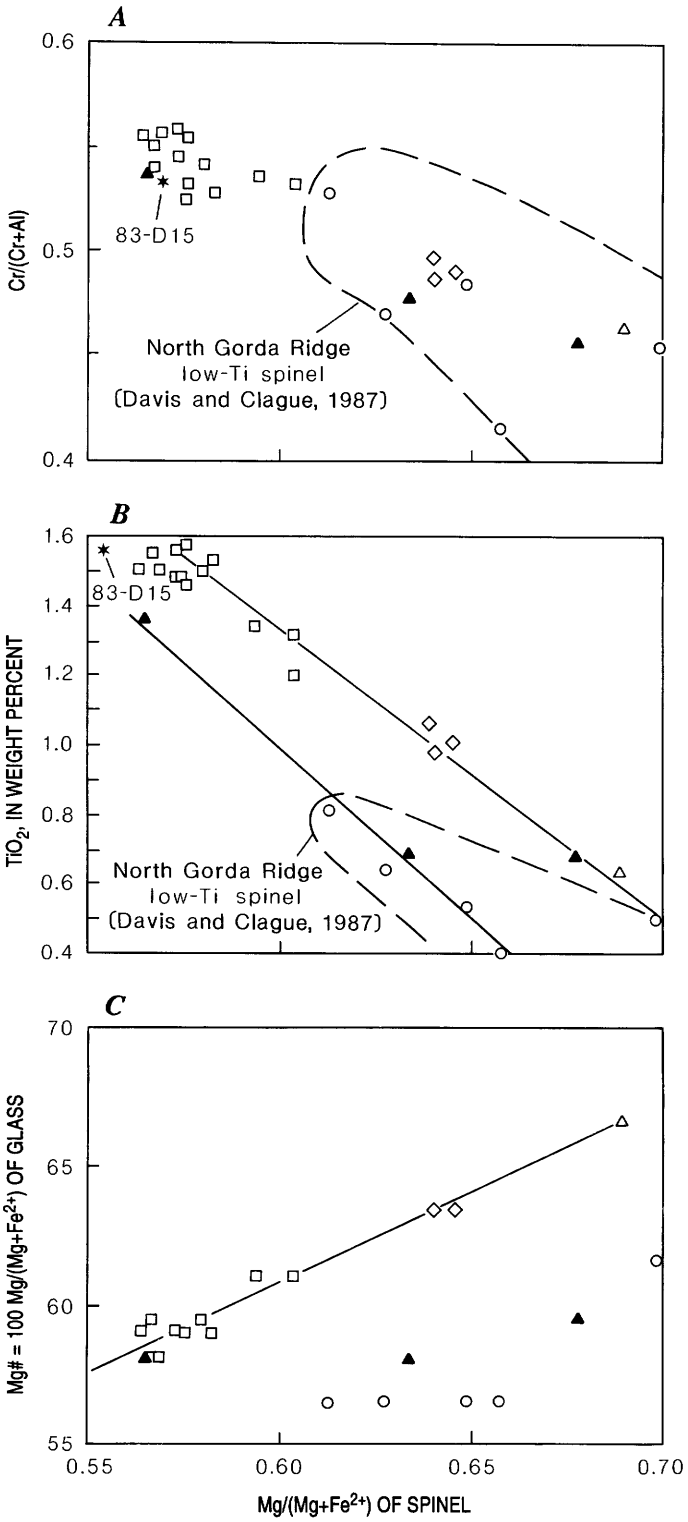

Table 9.6. Temperature, density, and viscosity of selected Escanaba Trough glasses.

[Mg-Gls1, olivine-glass geothermometer of Roeder (1974); Mg-Gls2, olivine-glass geothermometer of Bender and others (1978); MgO-Gls, graphic geothermometer (fig. 9.10A); —, not determined. Density and viscosity calculated crystal-free at 1 kbar, following methods of Bottinga and others (1982) and Shaw (1972), respectively, using temperatures determined with graphic geothermometer]

Sample number	Temperature Mg-Gls1 (°C)	Mg-Gls2 (°C)	MgO-Gls (°C)	Density (g/cm^3)	Viscosity (poise)
Northern sites					
83-16-1	1,182	1,168	1,176	2.687	131
83-16-3	1,199	1,187	1,193	2.671	108
3-86-10-2a	—	—	1,184	2.683	133
3-86-10-1b	—	—	1,200	2.663	122
3-86-10-5b	—	—	1,187	2.677	132
3-86-2-2	—	—	1,217	2.661	86
3-86-3-2	—	—	1,200	2.666	109
NESCA					
Alv2039-2	1,194	1,181	1,186	2.683	135
2-86-23-4-1	—	—	1,173	2.671	190
2-86-17-1-1	1,184	1,181	1,212	2.672	160
6-85-36-11	1,193	1,180	1,185	2.668	144
2-86-22-1	1,189	1,175	1,184	2.672	145
SESCA					
6-85-31-10	1,207	1,196	1,204	2.653	126
2-86-12-2	1,209	1,198	1,206	2.654	117

⇐

Figure 9.9. Compositions of chromian spinel in Escanaba Trough lavas. *A*, Cr/(Cr+Al) versus Mg/(Mg+Fe^{2+}) shows Cr/(Cr+Al) increasing with decreasing Mg/(Mg+Fe^{2+}). *B*, TiO_2 versus Mg/(Mg+Fe^{2+}) shows two distinct trends with NESCA samples containing only high-Ti spinel, whereas some other samples contain high- and low-Ti spinel in the same section. Field of northern Gorda Ridge spinel shows compositions more magnesian and lower in Ti than most Escanaba Trough spinel. Only one resorbed spinel (83-D15) from northern Gorda Ridge resembles high-Ti spinel found in NESCA lavas. *C*, Mg/(Mg+Fe^{2+}) of spinel versus Mg# of host glass also shows two trends, with some spinel in equilibrium with their host glass and some containing spinel that is too magnesian. All NESCA samples appear to be in equilibrium with their host glass. Symbols as in figure 9.2.

⇒

Figure 9.10. *A*, MgO versus experimentally determined temperatures of olivine-glass pairs in MORB (Walker and others, 1979; Bender and others, 1978) and calculated temperatures of Gorda Ridge lavas form well-defined trend, indicating that this plot can be used as a crude graphical geothermometer. Temperatures of Escanaba Trough lavas without coexisting olivine data were estimated from this plot. *B*, Densities of Escanaba Trough lavas (filled circles) calculated after the method of Bottinga and others (1982) show general increase with differentiation, as commonly observed for other MORB suites, but diffuse pattern is similar to that of type B basalt from Mid-Atlantic Ridge (Sparks and others, 1980). EPR, East Pacific Rise; MAR, Mid-Atlantic Ridge. Solid line shows calculated change in density with differentiation for an aphyric lava.

and Mg# but include many more magnesian crystals. However, except for one resorbed spinel crystal in glass from one sample from the middle segment of the ridge, all northern Gorda Ridge spinel is low in TiO_2 as is typical for MORBs. All spinels from NESCA have more than 1 percent TiO_2 and higher Fe_2O_3 contents than is commonly

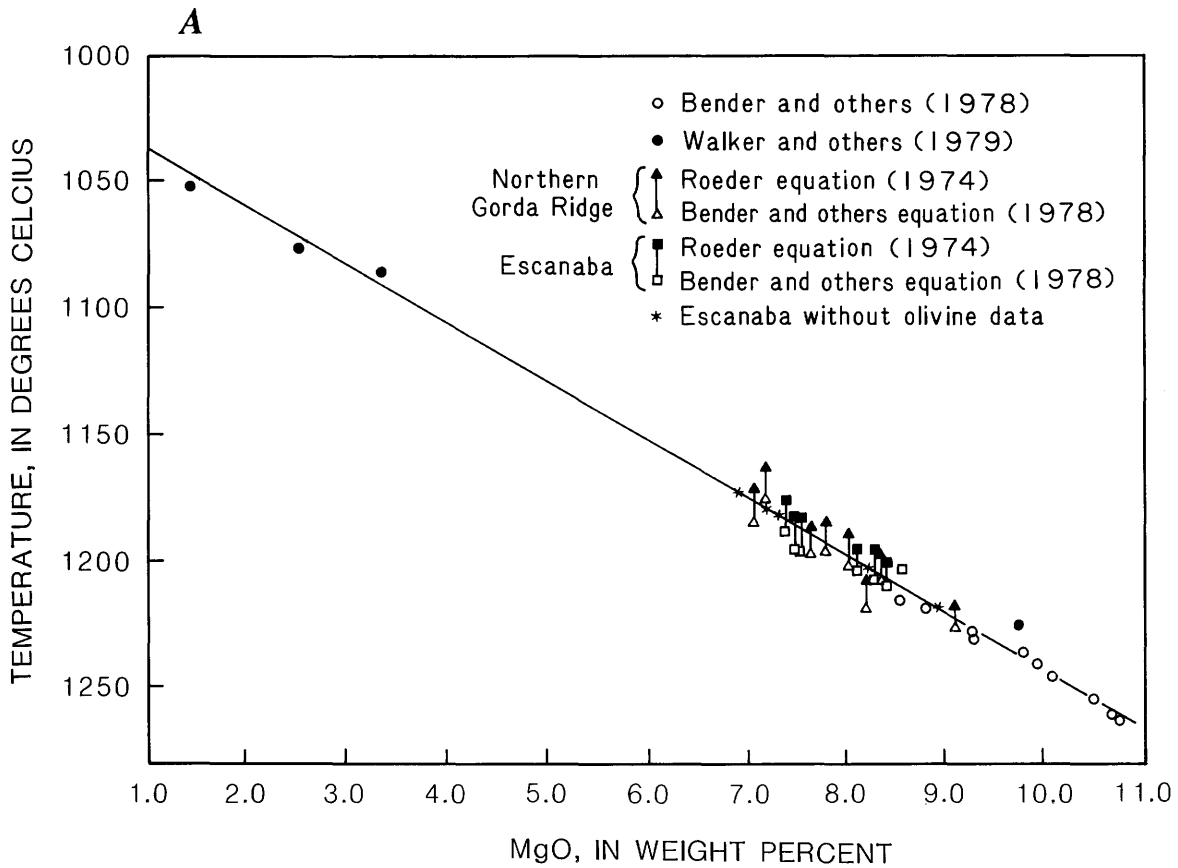

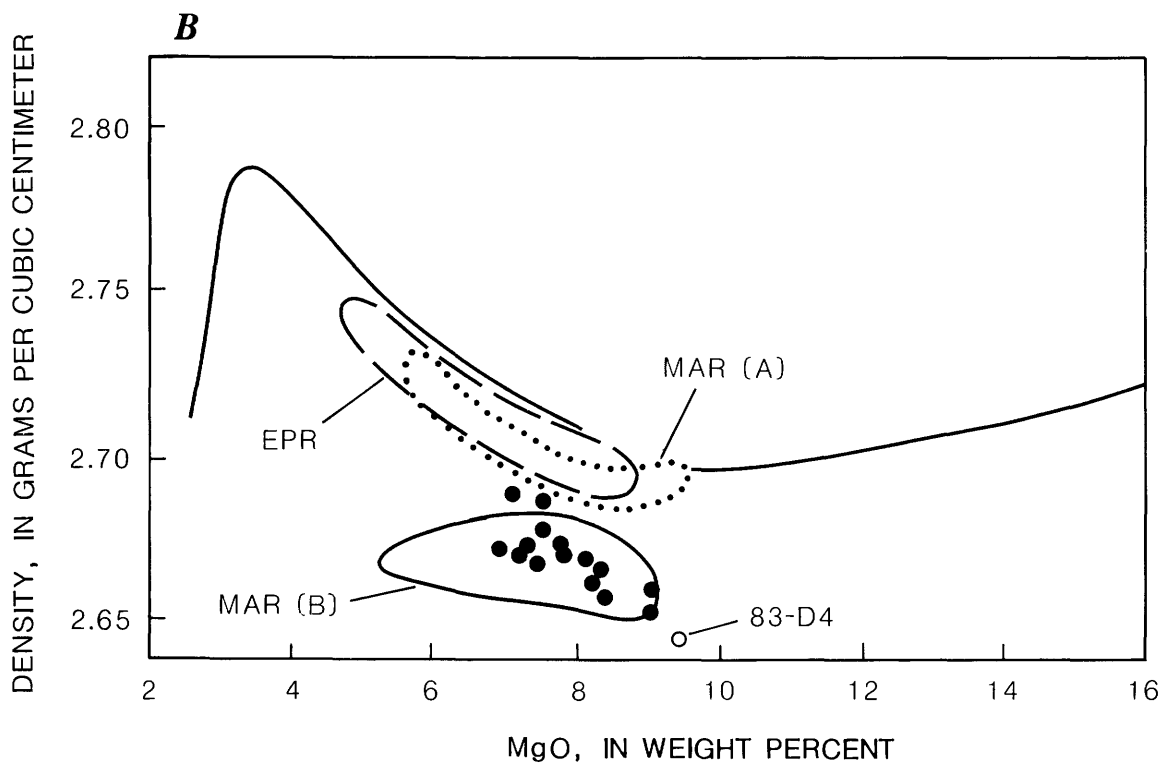

observed for MORB (Sigurdsson and Schilling, 1976; Davis and Clague, 1987; 1990).

Consistent with their low degree of crystallinity and high calculated eruption temperatures, Escanaba Trough glasses have no clinopyroxene, although the imprint of clinopyroxene fractionation is suggested by low CaO/Al_2O_3 ratios and displacement into the diopside field on the diopside-olivine-silica projection (fig. 9.11; Walker and others, 1979). Glasses from northern Gorda Ridge are also typically without clinopyroxene except for one xenolith-bearing glass (Davis and Clague, 1990). The presence of large clinopyroxene oikocrysts in these xenoliths, which appear to be crystalline mush of the margins of a magma chamber, indicate that clinopyroxene fractionation is an important process in the magma chambers, although clinopyroxene phenocrysts are rarely observed in the lavas.

DISCUSSION

CRYSTAL FRACTIONATION

Crystal fractionation clearly was an important process in the evolution of Escanaba Trough glasses, since Mg#s of 60 or less are quite common. Compositions converge toward a potential parental composition similar to the most primitive glass recovered from the Gorda Ridge (83-D4 from the northern segment; Davis and Clague, 1987), but

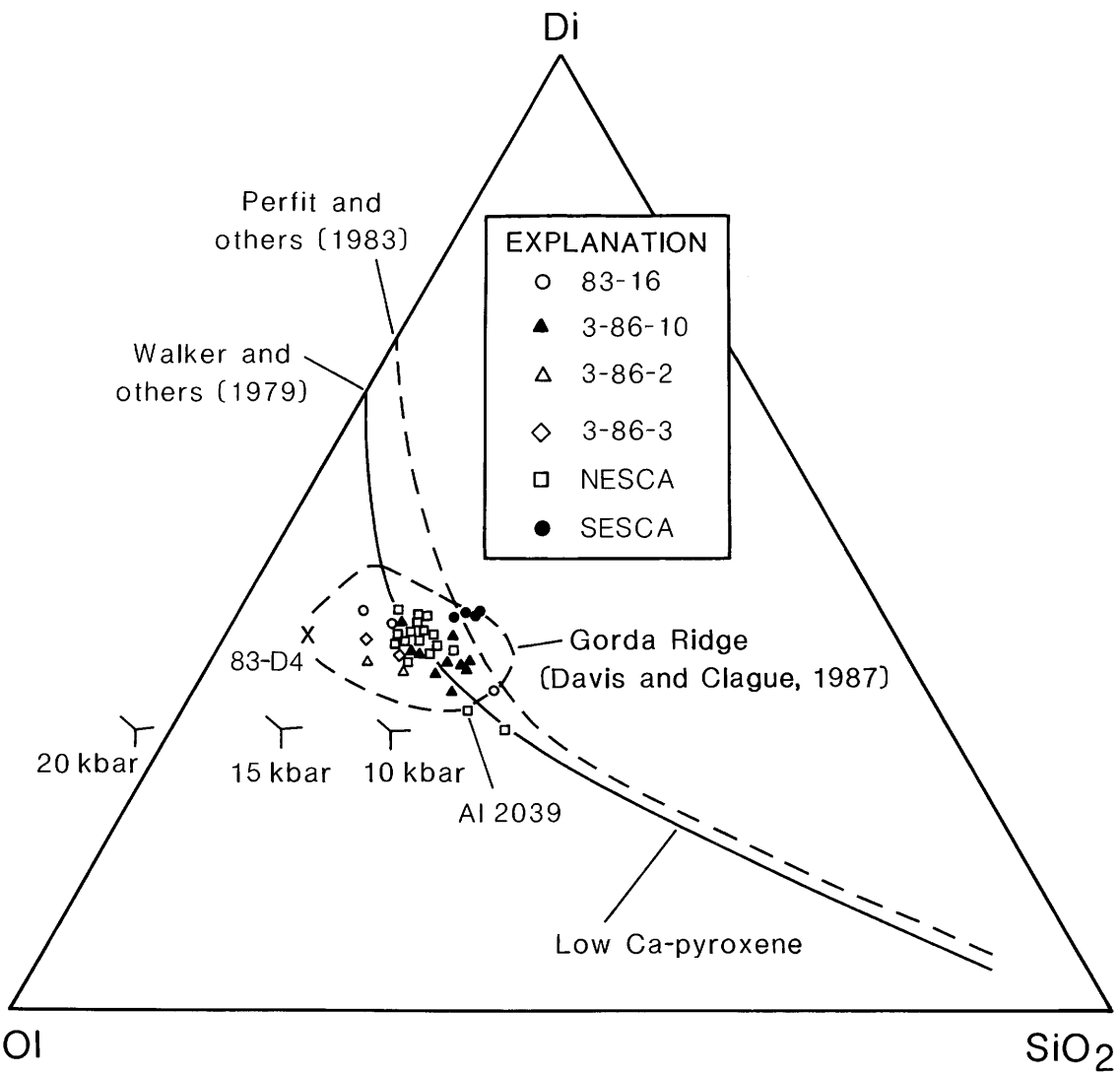

Figure 9.11. Compositions of Escanaba Trough glasses shown on plagioclase-saturated diopside-olivine-silica projection of Walker and others (1979). Solid curve is experimentally determined liquidus at 1 atm. Dashed line represents natural phase boundary for lavas from Galápagos Rift, Inca transform, and Ecuador Rift (Perfit and others, 1983). Cotectics for 10, 15, and 20 kbar of Stolper (1980) are shown for reference. Many Escanaba Trough glasses plot in diopside field, although modal clinopyroxene is not present. Displacement toward concave side of the liquidus may be result of mixing differentiated residue with a more primitive magma.

a large amount of scatter indicates complex petrogenetic processes. Fractionation at the SESCA site apparently involved mostly plagioclase, whereas predominantly olivine with lesser plagioclase fractionation is indicated by the flat trend on the CaO/Al_2O_3 versus Mg# plot for the NESCA site. Different trends shown by fractionated samples at 3-86-10 are not compatible with a single liquid line of descent (fig. 9.4*B*). Compared with experimental studies of MORB by Walker and others (1979), the Escanaba Trough glasses form a cluster across the plagioclase-saturated olivine-diopside boundary (fig. 9.11), with many compositions in the diopside field. In accord with their low degree of crystallinity and high calculated eruption temperatures, clinopyroxene should not be a liquidus phase in the sparsely porphyritic samples, and no modal clinopyroxene is observed. Highly porphyritic samples also lack clinopyroxene, but the abundance of plagioclase suggests plagioclase accumulation. Walker and others (1979) suggested that displacement to the right of the curved liquidus could result from mixing a primitive melt with differentiated residue. If the experimentally determined liquidus of MORB from the Mid-Atlantic Ridge (Walker and others, 1979) is appropriate for Escanaba Trough magmas, many of these lavas represent hybrids. Alternatively, the liquidus may not be appropriate, and a liquidus shifted toward the diopside-silica join, as proposed for lavas from the Galápagos Rift spreading center (Perfit and others, 1983), may be more appropriate (fig. 9.11).

MAGMA MIXING

Different fractionation paths at geographically widely separated regions is probably to be expected. Variations in compositions that are not compatible with simple crystal fractionation may have resulted from magma mixing. Magma mixing in continuously replenished magma chambers appears to be a common process at oceanic spreading centers (O'Hara, 1977; O'Hara and Mathews, 1981; Dungan and Rhodes, 1978; Rhodes and others, 1979; Dixon and others, 1986; Davis and Clague, 1987). Mineral phases that are texturally and compositionally not in equilibrium with their host glass and glass inclusion data provide evidence of magma mixing. Phenocrysts in samples from 83-16 and 3-86-10 show textural disequilibrium features such as embayed and resorbed margins of olivine and plagioclase crystals with fritted zones, overgrown by a layer that is compositionally different from the core of the crystal. A phenocryst core with An as low as 65, observed for plagioclase in 3-86-10 (table 9.4), could have crystallized in a highly differentiated melt. Higher NiO contents in rims and skeletal olivine than in phenocryst cores and prevalent reverse zoning of plagioclase suggest mixing with a more mafic, hotter magma. No such phenocrysts were observed in NESCA samples. All of the NESCA glasses contain small euhedral microphenocrysts that are compositionally in equilibrium with their host glass (fig. 9.7*C*), but all plagioclase shows a small amount of reverse zoning. However, lack of textural evidence does not preclude magma mixing. Mixing of a fractionated magma with a more primitive one can result in superheated magma that is aphyric and shows only the chemical imprint of magma mixing. This chemical imprint consists mostly of enrichment in incompatible elements beyond what would be expected by simple crystal fractionation. At the same time, compatible elements are buffered and do not show the depletion expected from closed system fractionation. Higher K_2O, P_2O_5, and TiO_2 content, as observed in the NESCA samples, and higher NiO and Cr_2O_3 contents, as indicated by olivine and spinel compositions, is just what would be expected from mixing evolved with more primitive melt.

PARTIAL MELTING AND MANTLE HETEROGENEITY

Potassium, phosphorus, and titanium are incompatible elements, and ratios of these elements should not be significantly changed by fractionation over the compositional range shown by Escanaba Trough glasses, hence they may provide some evidence for source compositions. However, different degrees of partial melting can cause significant variations in incompatible-element ratios, especially when very small percentages of melt are involved. Complex melting processes such as dynamic melting (Langmuir and others, 1977) and complex magma chamber processes involving multiple mixing cycles (O'Hara, 1980; Elthon, 1984) may also change incompatible-element ratios of melts. Variation in incompatible-element ratios, as observed for Escanaba Trough glasses, is also observed for the other segments of the mid-oceanic ridge system in the northern Pacific Ocean. Values of La/Sm from the northern segments of Gorda Ridge are low but variable (0.34 to 0.76; Davis and Clague, 1987), whereas La/Sm ratios for the Juan de Fuca-Explorer Ridge segments show a larger range and include some higher ratios (0.6 to 1.9; Schilling and others, 1983; Cousens and others, 1984). Yet Sr isotopic compositions suggest a relatively uniform, depleted mantle source, 0.70232 to 0.70267 for northern Gorda Ridge (Davis and Clague, 1987; White and others, 1987) and 0.70232 to 0.70254 for the Juan de Fuca-Explorer Ridge (Eaby and others, 1984; Cousens and others, 1984).

It is commonly accepted that radiogenic isotopic ratios are not fractionated by partial melting processes (for example, Hoffmann and Hart, 1978). Incompatible-element ratios at northern Gorda Ridge show no correlation with Sr isotopic ratios, as would be expected if variations were caused by source heterogeneities (Davis and Clague, 1987). Existing isotopic data for Escanaba Trough glasses

show $^{87}Sr/^{86}Sr$ ratios of 0.70261 for 83-16-1 (Davis and Clague, 1987) and 0.70284 for a NESCA sample (White and others, 1987) at comparably high K_2O/P_2O_5 values. These Sr isotopic values are well within the range typical for normal MORB, but the isotopic ratio of the NESCA sample is the highest $^{87}Sr/^{86}Sr$ ratio reported for the entire spreading center in the northern Pacific Ocean. Decoupling between incompatible-element ratios and Sr isotopic compositions suggests that incompatible-element variation resulted from melting processes or that source heterogeneities are of recent origin.

CONTAMINATION

Trace-element abundances and isotopic ratios can be significantly altered if hydrothermally altered crust and (or) sediment are assimilated in oceanic crustal magma chambers and conduits (O'Hara, 1980). Lead isotopic ratios, which are particularly sensitive indicators of sediment contamination, show Escanaba Trough basalt from NESCA more enriched in radiogenic lead than other Gorda Ridge basalt (fig. 9.12). Ratios of $^{207}Pb/^{204}Pb$ (fig. 9.12*A*) and $^{208}Pb/^{204}Pb$ (fig. 9.12*B*) versus $^{206}Pb/^{204}Pb$ show NESCA basalt displaced from the trend shown by other Gorda Ridge basalt toward lead compositions of sediments. However, the lead isotopic composition of a sample from northern Escanaba Trough (near 83-16) plots within the depleted end of Gorda Ridge basalt (White and others, 1987; fig. 9.12).

The samples with enriched lead isotopic composition from NESCA are low-K_2O normal MORB. The high-K_2O sample from NESCA resembles enriched (E-type) MORB. E-type MORB is enriched in LIL elements, such as K, Ba, Rb, and Cs, but with major-element concentrations that are largely indistinguishable from normal MORB. Enriched MORB from some other spreading centers, such as Iceland, Galápagos, and the Azores, have been attributed to mixing with a mantle plume or hotspot component (Schilling and others, 1983). These MORB also have light-rare-earth-element (REE) and isotopic signatures more enriched than normal MORB. Samples with high-K_2O compositions, similar to Alv2039-2, have also been reported from Explorer Ridge (Cousens and others, 1984) and from basaltic dikes and sills in Guaymas Basin (Saunders and others, 1982; Fornari and others, 1982). However, a strontium isotopic ratio of 0.70252 determined for one of the high-K_2O samples from the Explorer Ridge is well within the range of normal MORB (Cousens and others, 1984) and shows no plume influence. The high-K_2O samples from Guaymas Basin are light-REE depleted, like normal MORB (Saunders and others, 1982). Saunders and others (1982) suggested that the enrichment in LIL elements without a corresponding enrichment in REE and isotopic composition is due to contamination by a small component of "continental" material in the source region. No lead isotopic data are available for these samples. If the high-K_2O content of Alv2039-2 resulted from contamination with a small amount of sediment, the lead isotopic composition should be even more enriched and plot closer to that of the sediment.

MAGMA CHAMBERS

The presence of genetically unrelated lavas suggests that magma chambers along Escanaba Trough are isolated.

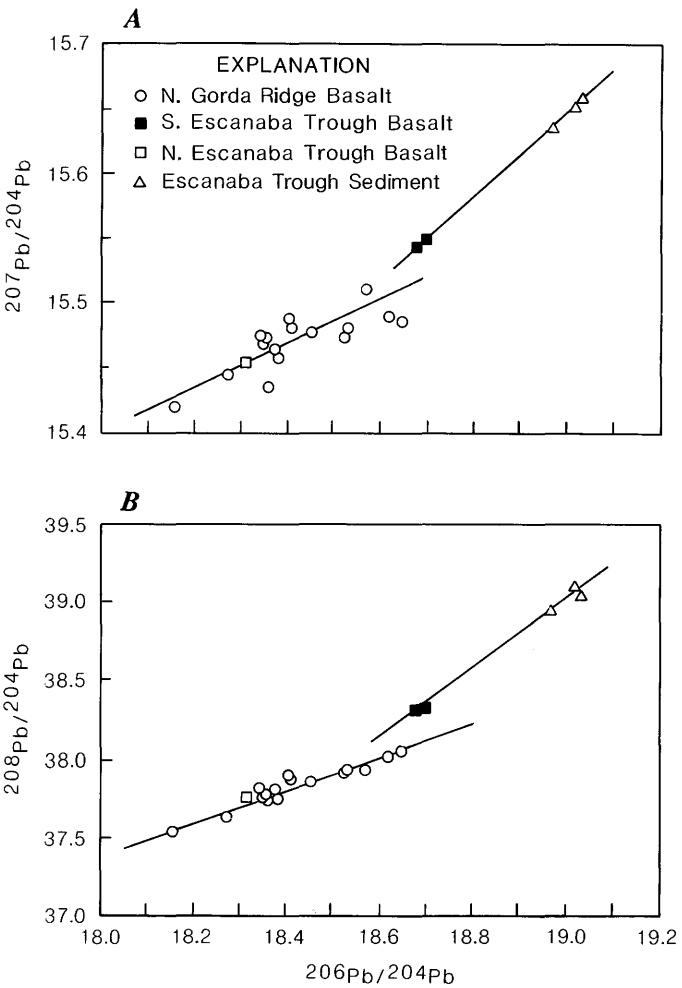

Figure 9.12. Lead isotope compositions of (*A*) $^{207}Pb/^{204}Pb$ and (*B*) $^{208}Pb/^{204}Pb$ versus $^{206}Pb/^{204}Pb$ for southern Escanaba Trough glasses show more enriched compositions than other Gorda Ridge lavas. One sample from northern end of Escanaba Trough (near 83-16) plots within depleted compositions shown by northern Gorda Ridge basalts. Southern Escanaba Trough basalts are displaced from trend shown by northern Gorda Ridge basalts toward the compositions of sediments, suggesting contamination with small amount of sediment. Data for northern Gorda Ridge basalt from Church and Tatsumoto (1975) and White and others (1987); data for northern Escanaba Trough basalt and for Escanaba Trough sediments from LeHuray and others (1987).

The magma chambers are probably small, because flow units appear to be small and pillow lavas predominate, but the magma chamber at the NESCA site may be larger since flow units appear more extensive and sheet flows are common. The abundance of sheet flows indicates a rapid extrusion rate and probably a larger magma supply, whereas pillow basalts have generally been linked to narrow conduits and small magma supply (Ballard and others, 1979).

The gradational nature of the compositional range shown by NESCA glasses makes it difficult to assign them to specific flow units. Most of the sheet flows may stem from the same eruption, which may have fractionated small amounts of primarily olivine and minor plagioclase as they were rising through isolated fissures from a common magma chamber. Similar compositional variations and nearly aphyric lavas have been observed in sheeted dikes associated with some ophiolites (Smewing, 1981; Pallister and Hopson, 1981).

CONCLUSIONS

Basaltic glasses from Escanaba Trough consist predominantly of normal MORB. One glass composition is high in K_2O, resembling E-type MORB. Compositions range from relatively primitive to moderately fractionated. Chemical trends shown by glass and mineral phases suggest complex petrogenetic processes, involving fractionation, magma mixing, and different degrees of partial melting and (or) different source compositions. Mixing with LIL-element-enriched material is indicated for the high-K_2O sample from the NESCA site. Other glasses from this site also have somewhat higher K_2O contents than comparably fractionated samples from the other Escanaba Trough sites. Spinel in these lavas is higher in titanium and ferric iron than is typical for normal MORB, suggesting higher oxygen fugacity of the melt. Lead isotopic compositions of samples from Escanaba Trough (NESCA) are displaced from the trend shown by other Gorda Ridge basalt toward the isotopic compositions of sediment in this region, suggesting contamination by a small sediment-derived component. Normal MORB from Escanaba Trough is similar to that from the northern part of the Gorda Ridge, and to normal MORB from many other spreading centers. The unusual LIL-element-enriched composition from the northernmost part of the NESCA site has no counterpart on the northern Gorda Ridge, but similar compositions have been reported from the Explorer Deep segment of Explorer Ridge and Guaymas Basin, where they show no trace-element or isotopic enrichment compatible with a plume or hotspot influence. The similar tectonic setting of incipient spreading into a sediment-filled basin may suggest selective enrichment of some LIL elements, which may have resulted from contamination by a small amount of sediment.

REFERENCES CITED

Ballard, R.D., Holcomb, R.T., and van Andel, T.H., 1979, The Galapagos Rift at 86°W, 3, sheet flows, collapse pits, and lava lakes of the rift valley: Journal of Geophysical Research, v. 84, p. 5407–5422.

Bence, A.E., and Albee, A.L., 1968, Empirical correction factors for the electron microanalysis of silicates and oxides: Journal of Geology, v. 76, p. 382–403.

Bender, J.F., Hodges, F.N., and Bence, A.E., 1978, Petrogenesis of basalts from the project FAMOUS area: Experimental study from 0 to 15 kbars: Earth and Planetary Science Letters, v. 41, p. 277–302.

Bottinga, Y., Weill, D., and Richet, P., 1982, Density calculations for silicate liquids: Geochimica et Cosmochimica Acta, v. 46, p. 909–919.

Church, S.E., and Tatsumoto, M., 1975, Lead isotope relations in oceanic ridge basalts from the Juan de Fuca-Gorda Ridge area, N.E. Pacific Ocean: Contributions to Mineralogy and Petrology, v. 53, p. 253–279.

Cousens, B.L., Chase, R.L., and Schilling, J.G., 1984, Basalt geochemistry of the Explorer Ridge area, northeast Pacific Ocean: Canadian Journal of Earth Sciences, v. 157, p. 157–170.

Davis, A.S., and Clague, D.A., 1987, Geochemistry, mineralogy, and petrogenesis of basalt from the Gorda Ridge: Journal of Geophysical Research, v. 92, p. 10,467–10,483.

———1990, Gabbroic xenoliths from the northern Gorda Ridge: Implications for magma chamber processes under slow spreading centers: Journal of Geophysical Research, v. 95, p. 10,885–10,905.

Dixon, J.E., Clague, D.A., and Eissen, J.P., 1986, Gabbroic xenoliths and host ferrobasalt from the southern Juan de Fuca Ridge: Journal of Geophysical Research, v. 91, p. 3795–3820.

Dungan, M.A., and Rhodes, J.M., 1978, Residual glasses and melt inclusions in basalts from DSDP legs 45 and 46: Evidence for magma mixing: Contributions to Mineralogy and Petrology, v. 67, p. 417–433.

Eaby, J., Clague, D.A., and Delaney, J.R., 1984, Sr isotopic variations along the Juan de Fuca Ridge: Journal of Geophysical Research, v. 89, p. 7883–7890.

Elthon, D., 1984, Plagioclase buoyancy in oceanic basalts: Chemical effects: Geochimica et Cosmochimica Acta, v. 48, p.753–768.

Fornari, D.J., Saunders, A.D., and Perfit, M.R., 1982, Major-element chemistry of basaltic glasses recovered during Deep Sea Drilling Project leg 64, *in* Curray, J.R., Moore, D.G., and others, eds., Initial reports of the Deep Sea Drilling Project: Washington, U.S. Government Printing Office, v. 64, p. 643–647.

Hoffmann, A.W., and Hart, S.R., 1978, An assessment of local and regional isotopic equilibrium in the mantle: Earth and Planetary Science Letters, v. 38, p. 44–62.

Langmuir, C.H., Bender, J.F., Bence, A.E., Hanson, G.N., and Taylor, S.R., 1977, Petrogenesis of basalts from the FAMOUS area, Mid-Atlantic Ridge: Earth and Planetary Science Letters, v. 36, p. 133–156.

LeHuray, A.P., Church, S.E., Koski, R.A., and Bouse, R.M., 1987, Pb isotopes in sulfides from mid-ocean ridge hydrothermal sites: Geology, v. 16, p. 362–365.

Mathez, E.A., 1976, Sulfur solubility and magmatic sulfides in submarine basalt glass: Journal of Geophysical Research, v. 81, p. 4269–4276.

McManus, D.A., 1970, Site 35, *in* McManus, D.A., and others, eds., Initial reports of the Deep Sea Drilling Project: Washington, U.S. Government Printing Office, v. 5, p. 165–172.

Morton, J.L., Normark, W.R., Ross, S.L., Koski, R.A., Holmes, M.L., Shanks, W.C., III, Zierenberg, R.A., Lyle, M., and Benninger, L.M., 1987a, Preliminary report, cruises L1-86-NC and L2-86-NC, Escanaba Trough, Gorda Ridge: U.S. Geological Survey Open-File Report 87-375-A, 13 p.

Morton, J.L., Holmes, M.L., and Koski, R.A., 1987b, Volcanism and massive sulfide formation at a sedimented spreading center, Escanaba Trough, Gorda Ridge, northeast Pacific Ocean: Geophysical Research Letters, v. 14, p. 769–772.

Morton, J.L., Zierenberg, R.A., and Reiss, C.A., Geologic, hydrothermal, and biologic studies at Escanaba Trough: An introduction, *in* Morton, J.L., Zierenberg, R.A., and Reiss, C.A., eds., Geologic, hydrothermal, and biologic studies at Escanaba Trough, Gorda Ridge, offshore northern California: U.S. Geological Survey Bulletin 2022, chapter 1 (this volume).

Natland, J.H., Adamson, A.C., Laverne, C., Melson, W.G., and O'Hearn, T., 1983, A compositionally nearly steady-state magma chamber at the Costa Rica Rift: Evidence from basalt glass and mineral data, Deep Sea Drilling Project sites 501, 504, and 505, *in* Cann, J.R., Langseth, M.G., Honnorez, J., von Herzen, R.P., White, S.M., and others, eds., Initial reports of the Deep Sea Drilling Project: Washington, U.S. Government Printing Office, v. 69, p. 811–858.

O'Hara, M.J., 1977, Geochemical evolution during fractional crystallization of a periodically refilled magma chamber: Nature, v. 266, p. 503–508.

———1980, Nonlinear nature of the unavoidable long-lived isotopic, trace and major element contamination of a developing magma chamber: Philosophical Transactions of the Royal Society of London, Series A, v. 297, p. 215–277.

O'Hara, M.J., and Mathews, R.E., 1981, Geochemical evolution in an advancing, periodically replenished, periodically tapped, continuously fractionated magma chamber: Journal of the Geological Society of London, v. 138, p. 237–277.

Pallister, J.S., and Hopson, C.A., 1981, Samail ophiolite plutonic suite: Field relations, phase variation, cryptic layering, and a model of a spreading ridge magma chamber: Journal of Geophysical Research, v. 86, p.2593–2644.

Perfit, M.R., Fornari, D.J., Malahoff, A., and Embley, R.W., 1983, Geochemical studies of abyssal lavas recovered by DSRV *Alvin* from eastern Galapagos Rift, Inca Transform, and Ecuador Rift, 3, trace element abundances and petrogenesis: Journal of Geophysical Research, v. 88, p. 10,551–10,572.

Rhodes, J.M., Dungan, M.A., Blanchard, D.P., and Long, P.E., 1979, Magma mixing at mid-ocean ridges: Evidence from basalts drilled near 22° N on the Mid-Atlantic Ridge: Tectonophysics, v. 55, p. 35–62.

Roeder, P.L., 1974, Activity of iron and olivine solubility in basaltic liquids: Earth and Planetary Science Letters, v. 23, p. 397–410.

Ross, S.L., and Zierenberg, R.A., Volcanic geomorphology of the SESCA and NESCA sites, Escanaba Trough, *in* Morton, J.L., Zierenberg, R.A., and Reiss, C.A., eds., Geologic, hydrothermal, and biologic studies at Escanaba Trough, Gorda Ridge, offshore northern California: U.S. Geological Survey Bulletin 2022, chapter 8 (this volume).

Saunders, A.D., Fornari, J.D., Joron, J.L., Tarney, J., and Treuil, M., 1982, Geochemistry of basic igneous rocks, Gulf of California, Deep Sea Drilling Project leg 64, *in* Curray, J.R., Moore, D.G., and others, eds., Initial reports of the Deep Sea Drilling Project: Washington, U.S. Government Printing Office, v. 64, p. 595–642.

Schilling, J.-G., Zajac, M., Evans, R., Johnston, T., White, W., Devine, J.D., and Kingsley, R., 1983, Petrologic and geochemical variations along the Mid-Atlantic Ridge from 29° N to 73° N: American Journal of Science, v. 283, p. 510–586.

Shaw, H.R., 1972, Viscosities of magmatic silicate liquids: An empirical method of prediction: American Journal of Science, v. 272, p. 870–893.

Sigurdsson, H., and Schilling, J.G., 1976, Spinels in Mid-Atlantic Ridge basalts: Chemistry and occurrence: Earth and Planetary Science Letters, v. 29, p. 7–20.

Smewing, J.D., 1981, Mixing characteristics and compositional differences in mantle-derived melts beneath spreading axes: Evidence from cyclically layered rocks in the ophiolite of north Oman: Journal of Geophysical Research, v. 86, p. 2645–2660.

Sparks, R.S.J., Meyer, P., and Sigurdsson, H., 1980, Density variation amongst mid-ocean ridge basalts: Implications for magma mixing and the scarcity of primitive lavas: Earth and Planetary Science Letters, v. 46, p. 419–430.

Stolper, E.M., 1980, A phase diagram for mid-ocean ridge basalts: Preliminary results and implications for petrogenesis: Contributions to Mineralogy and Petrology, v. 74, p. 13–27.

Stormer, J.C., and Nicholls, J., 1978, XLFRAC: A program for the interactive testing of magmatic differentiation models: Computer Geoscience, v. 4, p. 143–159.

Walker, D., Shibata, T., and Long, S.E., 1979, Abyssal tholeiites from the Oceanographer Fracture Zone, II, Phase equilibria and mixing: Contributions to Mineralogy and Petrology, v. 70, p. 111–125.

White, W.M., Hofman, A.W., and Puchelt, H., 1987, Isotope geochemistry of Pacific mid-ocean ridge basalt: Journal of Geophysical Research, v. 92, p. 4881–4893.

Chapter 10. Geologic Setting of Massive Sulfide Mineralization in Escanaba Trough

By Robert A. Zierenberg, Janet L. Morton, Randolph A. Koski, *and* Stephanie L. Ross[1]

CONTENTS

[1] U.S. Geological Survey, Menlo Park, California.

ABSTRACT

Extensive massive sulfide deposits occur in the sediment-covered rift valley of Escanaba Trough. The deposits are sediment hosted, but are associated spatially and genetically with centers of recent volcanic activity along the spreading axis. This chapter focuses on geologic data obtained on 22 submersible dives in the area by the DSV *Alvin* and DSV *Sea Cliff*, supplemented by observations from towed camera traverses and geophysical profiles.

The sea floor in the area of the volcanic edifices is characterized by irregular topography formed by uplift of sediment hills above igneous intrusions. The uplifted sediment hills are eroding by mass wasting and are the source of locally derived debris flows and turbidites. Faults bounding the uplifted areas provide enhanced cross-stratal permeability and are the primary conduits for hydrothermal discharge. The largest massive sulfide deposits occur near the base of the uplifted sediment hills.

Two volcanic edifices have received the most detailed investigation: the southern Escanaba (SESCA) site near latitude 40°45′ N., longitude 127°30′ W. and the northern Escanaba (NESCA) site near latitude 41°00′ N., longitude 127°30′ W. Exposed volcanic rocks and massive sulfide deposits at the SESCA site are older than those at the NESCA site. At least three large massive sulfide deposits occur in the SESCA area. The deposits are not hydrothermally active and are being degraded by oxidative sea-floor weathering and mass wasting.

Relatively young, glassy pillow basalts are exposed on the east flank of the Central Hill in the NESCA area. These pillow basalts formed over an eruptive vent that also fed volcanic sheet flows, which overlie approximately 500 m of sediment fill north and south of the Central Hill. Large massive sulfide deposits on the sediment-covered west flank of the Central Hill locally vent hydrothermal fluid at temperatures up to 220°C. Large, but apparently inactive sulfide deposits also occur around the base of the SW Hill at the NESCA site and are associated with a sediment hill astride the spreading axis at Edifice REX at the northern edge of the NESCA area.

The enrichment of certain elements (such as As, Bi, Pb, Sb, and Sn) in massive sulfide indicates that sediment

alteration provides at least some of the metals to the hydrothermal systems in Escanaba Trough. The enrichment of the radiogenic isotopes of lead in sulfide minerals and strontium in hydrothermal fluid, and the presence of thermogenic hydrocarbon in sediment, provides additional evidence of contribution from the sediment. Some samples show impregnation and veining of sediment by sulfide. Sulfide crusts in sediment and the surfaces of sulfide mounds are buckled and cracked by growth of sulfide below the sediment interface. Deposition of sulfide in the shallow subsurface is interpreted to be an important process in the formation of massive sulfide mounds. Structural conduits underlying massive sulfide and high-permeability turbidite beds are presumed to localize hydrothermal fluid flow and are potential sites of extensive subsurface deposition of sulfide.

INTRODUCTION

Escanaba Trough is an important natural laboratory for investigating the processes that control the formation of massive sulfide deposits. In this chapter we describe the structure, sedimentology, volcanology, and hydrothermal deposits that occur at two detailed study areas within Escanaba Trough, the southern Escanaba (SESCA) and northern Escanaba (NESCA) areas, and at less well studied areas of sea-floor mineralization between the NESCA and SESCA areas and at the northern edge of the NESCA area (fig. 10.1). Our primary data sources are the observations and photographic records collected during 8 dives by DSV *Sea Cliff* in 1986, and 10 dives by DSV *Alvin* and 4 by *Sea Cliff* in 1988. Geophysical, photogeological, and geochemical data supplement the submersible observations and help to constrain our interpretations of the structural controls on massive sulfide distribution and the geochemical and physical controls on the deposition of massive sulfide on and below the sea floor.

REGIONAL SETTING

Escanaba Trough is the southernmost part of the Gorda Ridge spreading center, which extends northward from the Mendocino Fracture Zone to a right-stepping ridge offset at latitude 41°37′ N. (Clague and Holmes, 1987). This segment of the Gorda Ridge spreads at a slow rate of about 2.4 cm/yr and has a Mid-Atlantic Ridge style morphology (Riddihough, 1980; Wilson, 1989). The axial valley is generally deeper than 3,200 m and is bounded by steep

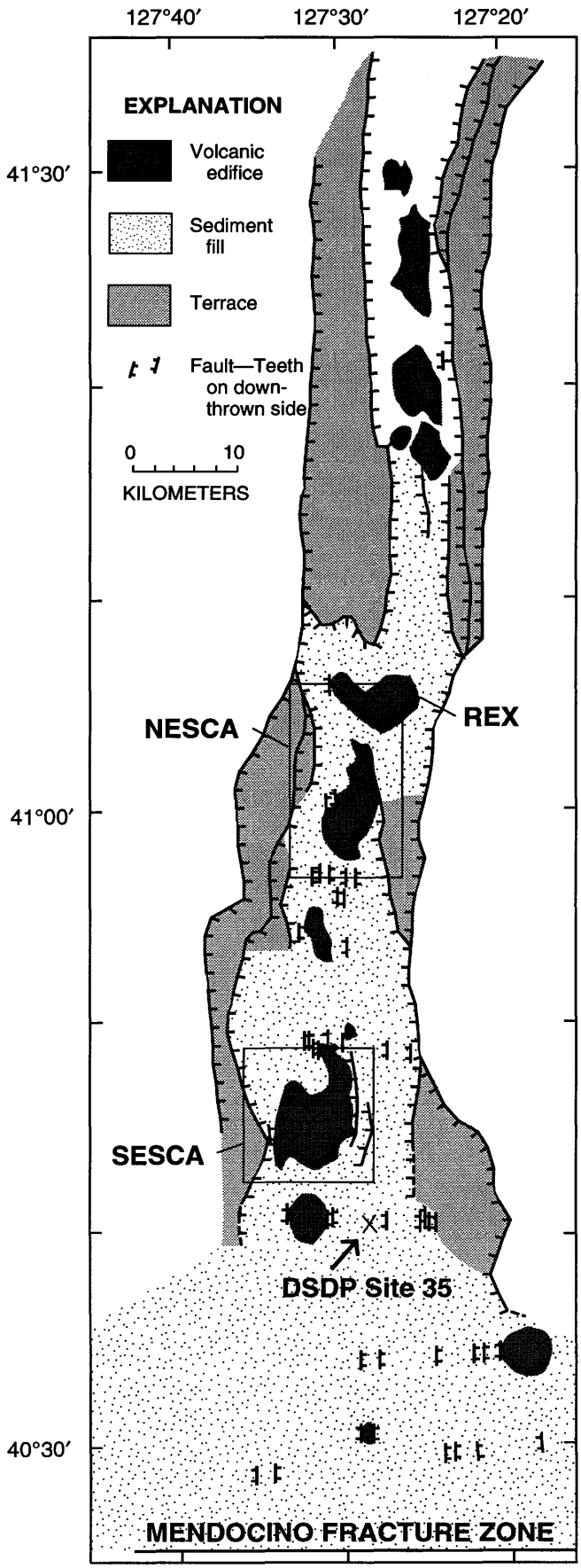

⇒

Figure 10.1. Generalized map of Escanaba Trough showing locations of NESCA and SESCA study areas (rectangles), volcanic edifices (including edifice Rex), and DSDP Site 35.

normal faults with back-tilted, sediment-covered blocks that rise to depths as shallow as 1,500 m (Atwater and Mudie, 1973; Riddihough, 1980). The axial valley is 20 km wide at the southern end and narrows to a few kilometers wide to the north (Morton and Fox, chap. 2, this volume). The floor of the axial valley south of about latitude 41°17′ N. is nearly flat due to burial by hemipelagic and turbiditic sediment that enters the valley at the southern end (McManus and others, 1970; Vallier and others, 1973). Basement topography below the sediment cover is irregular, and several volcanic complexes rise through the sediment cover (fig. 10.1; Morton and others, chap. 1, this volume), resulting in local exposures of basalt at the sea floor (Clague and Holmes, 1987; Morton and others, 1987). Two of these volcanic edifices, labeled B and D in Abbott and others (1986) have been investigated in more detail and are referred to as the SESCA and NESCA study areas, respectively. Both of these areas contain large massive sulfide deposits. Sulfide mineralization also occurs at volcanic edifices C and E.

The sedimentary fill of Escanaba Trough has an average thickness of 500 to 700 m over the spreading center; it is thickest at the south end near the Mendocino Fracture Zone, where it exceeds 900 m (Clague and Holmes, 1987). Sediment cover thins northward, and the spreading center is sediment-free north of approximately latitude 41°17′ N. (Morton and Fox, chap. 2, this volume). Seismic-reflection surveys of Escanaba Trough show continuous, subparallel sediment layering indicative of distal turbidite deposition (McManus and others, 1970; Clague and Holmes, 1987, Normark and others, chap. 6, this volume). Site 35 of the Deep Sea Drilling Project (DSDP) was drilled in the southern part of Escanaba Trough (fig. 10.1) and penetrated to a depth of 390 m without reaching the underlying basaltic basement (McManus and others, 1970). Terrigenous mud, silt, and sand turbidites interlayered with hemipelagic sediment were recovered (McManus and others, 1970; Vallier and others, 1973); the maximum age determined by microfossils contained in the sediment was Pleistocene. The bulk of the sediment fill in the Escanaba Trough was apparently deposited rapidly during the last two glacial lowstands of sea level within the last 100,000 yr (Normark and others, chap. 6, this volume).

Holocene sediment in Escanaba Trough is generally 0.5 to 2 m thick, reflecting lower terrigenous input during times of higher sea level (Karlin and Lyle, 1986; Karlin and Zierenberg, chap. 7, this volume). The Holocene sediment is predominantly hemipelagic with locally derived turbidites.

The sediment cover of Escanaba Trough precludes detailed mapping of the neovolcanic zone, structural domains, and along-strike variations in ridge volcanism. Ridge segmentation is recognized by the alignment of structural and volcanic features along the ridge axis (Morton and Fox, chap. 2, this volume). Several discrete volcanic centers are spaced approximately 12 to 15 km apart along the ridge axis, where a relative excess of magma supply formed volcanic edifices that rise above the base level of the ridge axis (fig. 10.1; Morton and Fox, chap. 2, this volume). These edifices are generally elongate along axis and are typically 5 to 7 km long and 3 to 5 km wide. Escanaba Trough basalts are mostly normal mid-ocean ridge basalts (MORB), but have lead isotope ratios more radiogenic than basalt from the northern Gorda Ridge, consistent with assimilation of sediment (Davis and others, chap. 9, this volume). Basalt compositional variations within each volcanic edifice are limited, but basalt compositional variations between centers indicate that different centers may have separate magma supplies (Davis and others, chap. 9, this volume).

ACKNOWLEDGMENTS

This work represents the efforts of many people located at several institutions and was possible only as a result of close cooperation and coordination. We gratefully acknowledge the support of the captains and crews of the various vessels listed in table 1.1 of Morton and others (chap. 1, this volume) that supported work in Escanaba Trough. The cooperation of the U.S. Navy and the dedicated efforts of the DSV *Sea Cliff* crew, often under difficult weather conditions, were critical to our investigations. We thank co-chief scientists John Edmond and J. Frederick Grassle for the opportunity to participate in the DSV *Alvin* dive program in 1988, and the DSV *Alvin* crew for executing an efficient and highly successful dive series in Escanaba Trough.

SESCA STUDY AREA

MORPHOLOGY AND STRUCTURE

The SESCA study area is a broad domal region characterized by a general elevation of the sea floor above 3,300 m and smaller scale variability of sea-floor morphology not typically developed on the sediment fill of the trough (fig. 10.2; Morton and Fox, chap. 2, this volume). The broad-scale shoaling occurs on the west side of the trough floor across an area approximately 10 by 15 km elongate along the direction of the ridge axis (fig. 2.2*B*, Morton and Fox, chap. 2, this volume). Seismic-reflection surveys over this area indicate that the volcanic basement occurs at shallower levels under thinner sediment cover compared to most areas of the trough floor (Clague and Holmes, 1987; Morton and Fox, chap. 2, this volume). The continuous seismic reflections from turbidite layers that characterize the fill of Escanaba Trough are disrupted by small-scale folding and faulting or are absent within much

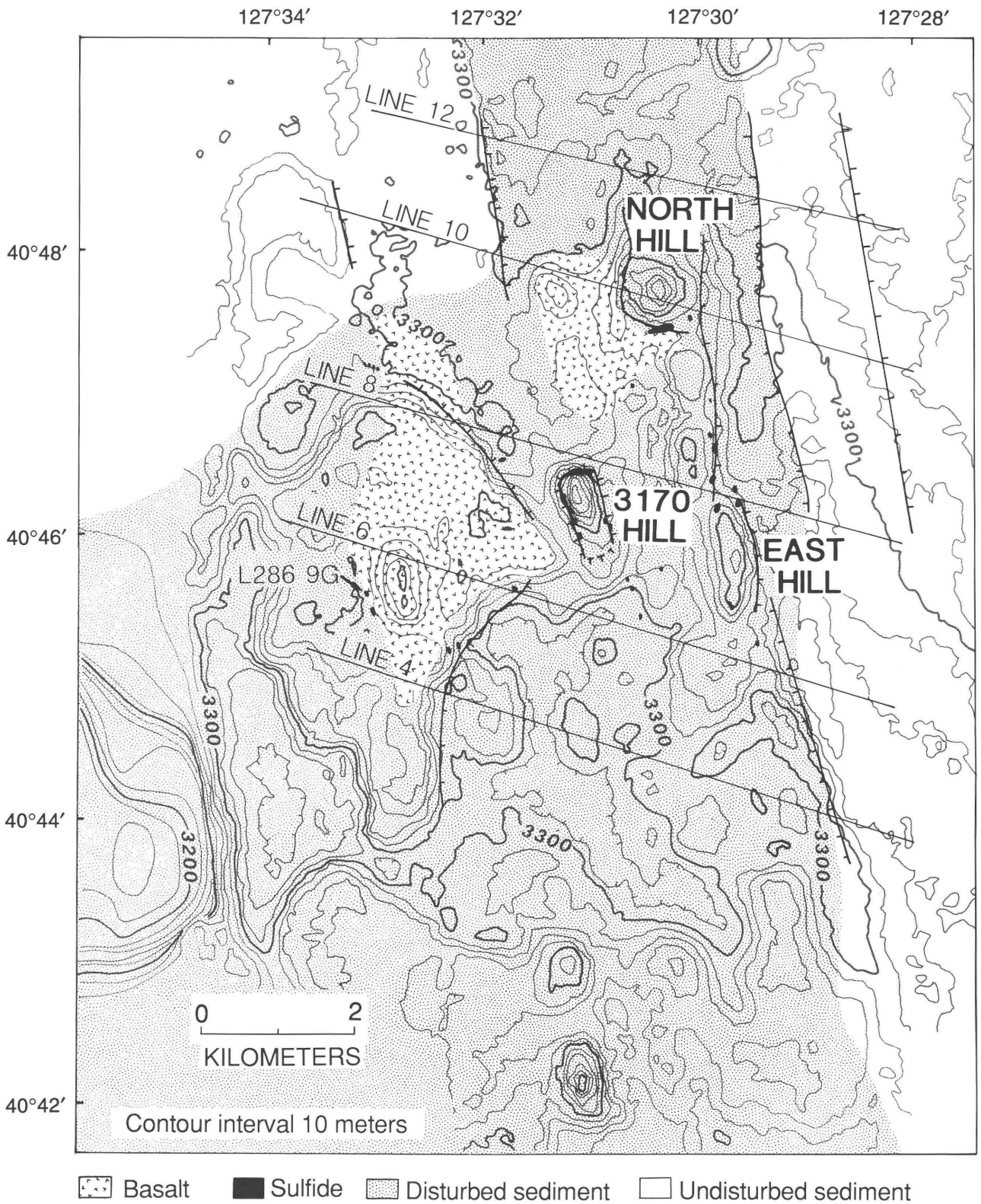

Figure 10.2. Geologic map of SESCA area. Sea Beam bathymetry and areas with outcropping and shallowly buried volcanic rock and disturbed sediment from Morton and Fox (chap. 2, this volume). Fault locations are extrapolated based on seismic-reflection profiles and Sea Beam bathymetric data; teeth are on downthrown side. Locations of cross-section lines presented in figure 10.9*A* are shown. Hachures indicate area of closed low.

of the SESCA area (fig. 10.2; Morton and Fox, chap. 2, this volume).

Superimposed on the larger bathymetric swell are numerous steep-sided, roughly circular hills from 500 to 1,000 m in diameter that rise 40 to 100 m above the surrounding sea floor. The cluster of hills between approximately latitude 40°45′ N. and latitude 40°48′ N. are spatially associated with large deposits of massive sulfide (fig. 10.2), and have been the focus of investigation in the SESCA area. Other morphologically similar hills between latitude 40°42′ N. and latitude 40°43′ N. in the southern part of the SESCA area and near latitude 40°49′ N. at the north edge of the SESCA map area (fig. 10.2) have not been investigated by geologic mapping techniques that would reveal the presence of sea-floor mineralization.

VOLCANOLOGY

Exposed basalt at the SESCA site is limited to the area southwest of the North Hill (fig. 10.2; Morton and Fox, chap. 2, this volume). The volcanic rocks are largely sediment covered with only bulbous pillows 1 to 2 m wide exposed. Where sheet flows are observed, they are often overlain by large trap-door pillows formed by vertical break-out of lava through the top of the sheet flow crust, indicating inflation of the flows. The flows are locally cut by fissures 0.5 to 1 m wide interpreted to be related to extension parallel to the spreading direction (Ross and Zierenberg, chap. 8, this volume). The walls of the fissures are predominantly sheet flows. The extent of surface outcrop of sheet flows is not representative of their volumetric proportion, because their low relief results in rapid burial by sediment. Hydrothermal activity was not observed in the fissures. The presence of filter-feeding organisms in the fissures may indicate downward flow of seawater into the fissures, and they may serve as high-permeability zones that enhance recharge to the hydrothermal systems. Basalt flows extend up to the base of the North Hill (fig. 10.2). Normal faults near the base of the North Hill with 1 to 2 m offsets cut basalt sheet flows and are draped by unfaulted flow lobes, indicating that eruption and uplift were contemporaneous. No basalt is exposed on the steep sides of the uplifted sediment hill.

SEDIMENTOLOGY

The sediment hills in the SESCA area are spatially associated with massive sulfide deposits and have therefore been the focus of detailed investigation. Numerous camera tracks cross the hills, but the flanks of the hills are poorly imaged due to steep slopes. DSV *Sea Cliff* dives in 1986 (Holmes and Zierenberg, 1990; Zierenberg and others, 1991) provided detailed observations of the geologic setting of the 3170 Hill (dives 656 and 663) and the North Hill (dives 661 and 662). A typical bathymetric profile across one of these hills has a shallow slope at the base that becomes increasingly steep upwards, resulting in an approximately parabolic slope. From the submersible, the tops of the hills appear to be subhorizontal and monotonously planar. There is a lower abundance of organisms and more large bioturbation mounds and burrows on the tops of the hills than on areas of comparable slope between the hills. Sediment ripples, with typical wavelengths of 10 cm and amplitudes generally less than 1 cm (fig. 10.3*A*), and lag deposits of coarser sediment were observed near the edges of the top of the 3170 Hill. Near-vertical cliffs exposing semiconsolidated mud interlayered with siltstone and sandstone beds, interpreted to be turbidites, are characteristic of the upper slopes of the hills (fig. 10.4*A*). The scarps that mark the edges of the hills can be extremely sharp. In the case of the North Hill at SESCA, as the submersible traversed along the scarp edge, the observer on one side could see a flat sediment plain a meter below stretching off into the distance while the observer on the other side could not see bottom below the vertical scarp. These scarps mark the headwalls of mass-wasting slumps. Locally, several smaller sets of slumps and flat-lying or back-tilted terraces are developed near the tops of the hills, suggesting that slumping along listric faults has occurred without catastrophic slope failure. However, the primary means of slope retreat and scarp formation is by slope failure producing mud-clast debris flows. The bases of the hills are surrounded by mud-clast talus aprons. Mudstone talus blocks in excess of 1 meter on a side are present, but the debris aprons are typically covered by mud with 0.5-to-2-cm mudstone clasts. The thickness and extent of the debris aprons are difficult to estimate from submersible traverses. However, the debris aprons appear to be relatively small compared to the amount of material removed from hill sides to maintain the near-vertical scarps, greater than 50 m high, that bound the hills. Locally derived mud-clast breccia debris flows and turbidites were recovered by piston and gravity cores collected on the sediment plain surrounding the hills (Normark and others, chap. 6, this volume; Karlin and Zierenberg, chap. 7, this volume).

Locally, canyons and channels scallop the hill slopes. Many areas of the hill slopes display vertical scour grooves cut by downslope sediment transport. An incised valley, estimated to be at least 10 m deep and 30 m across, on the side of the 3170 Hill at SESCA cut into a 5-m-thick layer of massive sulfide, providing a continuous outcrop of the sulfide body. Areas away from the steep-sided hills also have channels cut into sediment (fig. 10.3*B*), including areas that appear flat from submersible observation. Channels cutting the slopes south of the 3170 Hill were observed at several locations during *Sea Cliff* dive 657. Similar channels were observed on multiple dives in the NESCA area and are described in more detail in a later section.

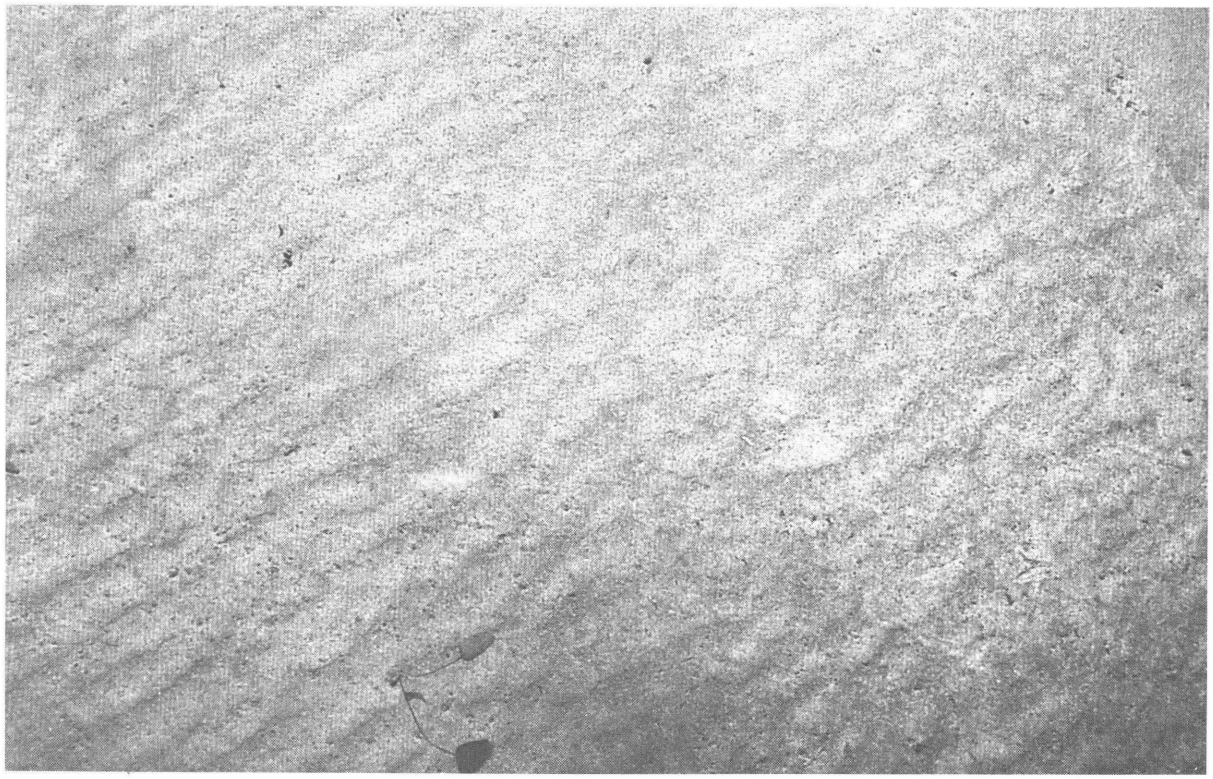

A

B

Figure 10.3. Down-looking bottom photographs taken from towed camera system deployed from USNS *Narragansett.* *A*, Sediment ripples near edge of top of 3170 Hill. Field of view is approximately 4 m across. *B*, Channel cut into surface sediment near base of 3170 Hill. Note curved bank of channel, consistent with down-cutting on a meander bend of an erosional channel. Field of view is approximately 4 m across.

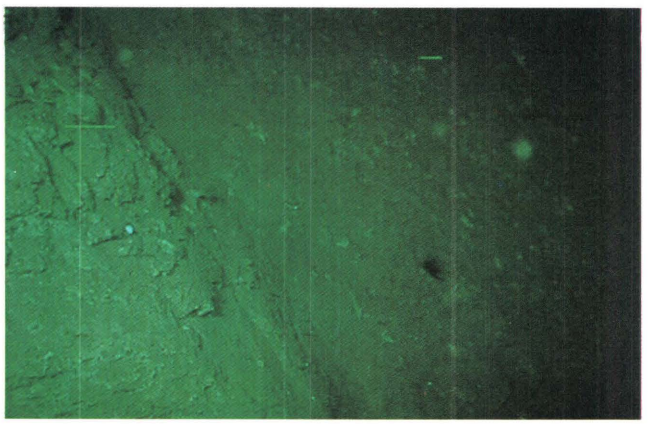

A

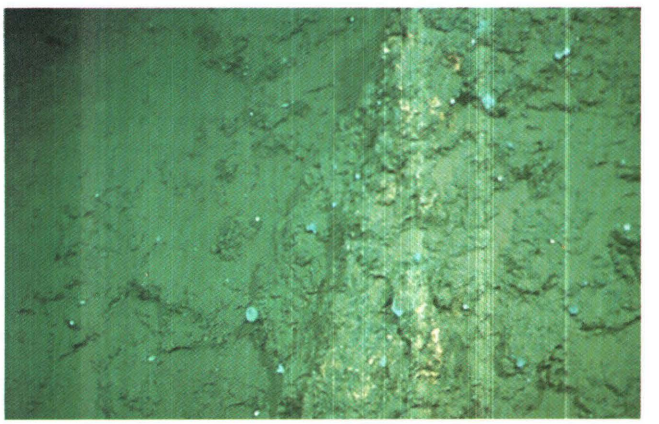

B

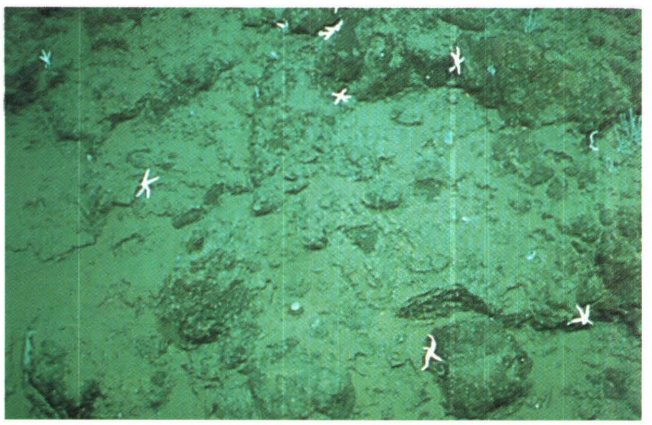

C

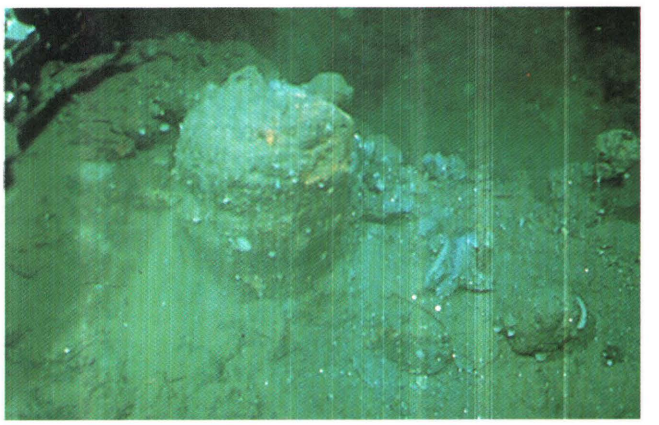

D

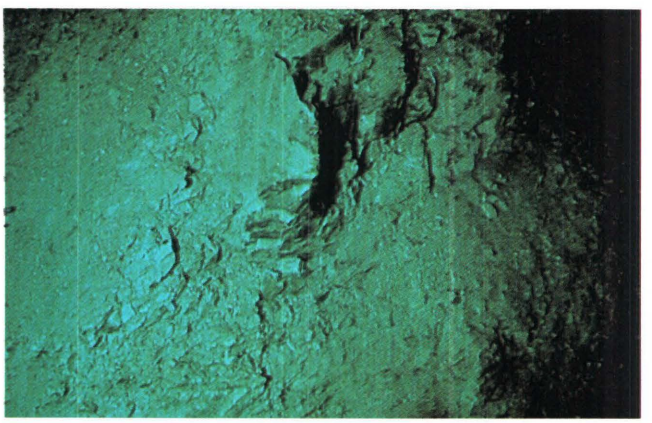

E

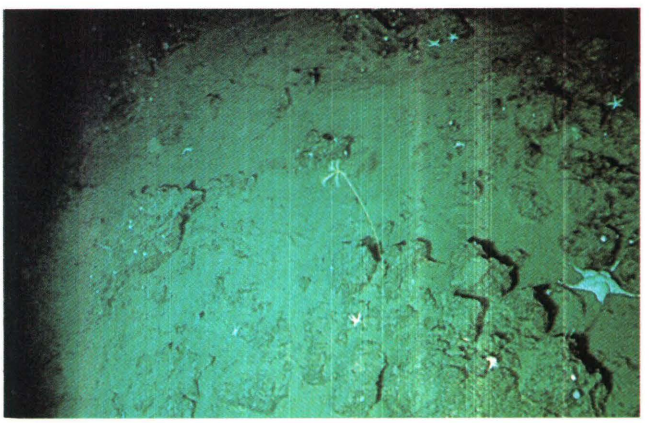

F

Figure 10.4. Color photographs from external 35-mm cameras of DSV *Alvin* and DSV *Sea Cliff*. *A*, Steep scarp forming side of 3170 Hill. Scarps are typically mud covered, but locally expose sedimentary layering, as seen in foreground. Field of view approximately 4 m across (*Sea Cliff* dive 663). *B*, Steep-sided outcrop of weathered massive sulfide exposed near base of 3170 Hill. Field of view approximately 3 m across (*Sea Cliff* dive 663). *C*, Massive sulfide mound from North Hill deposit showing crude layering. Outcrop is colonized by starfish, sponges, and branching corals(?). Field of view approximately 1.5 m across (*Sea Cliff* dive 662). *D*, Small inactive sulfide chimney from deposit on east side of North Hill. Field of view approximately 1 m across (*Sea Cliff* dive 661). *E*, Semiconsolidated layered sediment exposed by mass wasting on near-vertical side of SW Hill. Field of view approximately 3 m across (*Alvin* dive 2035). *F*, Brecciated massive sulfide and sulfide talus blocks from SW Hill colonized by yellow crinoid and large white starfish. Field of view approximately 3 m across (*Alvin* dive 2035).

HYDROTHERMAL DEPOSITS

The most extensive deposits of massive sulfide observed in the SESCA area are associated with the three circular hills referred to as the 3170, East, and North hills on figure 10.2. The deposits occur within a 3 by 4 km area, and would probably be considered separate lenses of a single ore deposit on land. None of the deposits were hydrothermally active, but all have formed recently enough to escape burial by sediment. The distribution, morphology, and apparent relative ages of the deposits suggest that each hill was a separate hydrothermal center, and they were not active contemporaneously . Numerous camera tracks cross the deposits, and the North Hill and 3170 Hill deposits have been investigated during DSV *Sea Cliff* dives; however, none of the deposits are well explored.

3170 HILL

The sulfide deposit investigated on *Sea Cliff* dive 663 on the north flank of the 3170 Hill occurs near the base of the slope at an average depth of 3,250 m, approximately 25 m above the surrounding sediment plain and 80 m below the flat top of the hill. The thickness of exposed massive sulfide, determined from the submersible depth recordings at the top and bottom of sulfide outcrop, ranges between 4 and 6 m. The outcrop of the deposit generally follows the contours of the slope, and neither the east nor west limits of the deposit are established. The available data indicate that the exposure of the sulfide body is in excess of 120 m parallel to the hill slope. Photographs from camera tows confirm that the massive sulfide is exposed to both the east and west of the area, on trend with the deposit observed by submersible. Camera tows also imaged sulfide deposits at four other sites near the base of the 3170 Hill, including the south side of the hill, suggesting that the hill may be surrounded with outcropping sulfide deposits.

The surface of the sulfide deposit on the north side of the 3170 Hill is rounded and smooth at the 1-to-10-m scale and lacks chimneylike projections (fig. 10.4*B*). At a finer scale, the surface is jagged and pitted due to selective dissolution of sulfide minerals during sea-floor oxidation. Samples collected from the exposed surface are predominantly porous crusts of residual amorphous silica, barite, and secondary iron oxyhydroxides formed by oxidation of pyrrhotite-rich massive sulfide (Holmes and Zierenberg, 1990; Zierenberg and others, 1991). The deposit surface is heavily colonized by stalked biota, including large and presumably mature sponge colonies. Areas of the deposit with relatively flat slopes are partially sediment covered, and the uphill contact of the sulfide deposit is buried by flat-lying sediment. The sulfide deposit appears to have formed a topographic dam retarding downslope movement of sediment until the moat behind the barrier was eventually filled, allowing sediment to overflow the deposit. In one area, the deposit is incised by a V-shaped erosional canyon. The morphology of the deposit reflects extensive sea-floor oxidation and erosion, indicating that this is one of the oldest deposits observed in Escanaba Trough.

NORTH HILL

A massive sulfide deposit at the base of the south side of the North Hill (fig. 10.2) was investigated during *Sea Cliff* dive 662. The deposit occurs between the depths of 3,228 and 3,242 m. Sonar imaging of the deposit from the submersible revealed a linear ridge of outcropping sulfide trending N. 75° E. Transponder navigation of the submersible indicates a minimum length of 175 m with a width of 75 m at one point. The western limit of the deposit was not observed. Eastward projection of the trend of the sulfide ridge intersects massive sulfide cropping out between 3,225 and 3,231 m that was observed, but not extensively investigated, at the end of *Sea Cliff* dive 661. However, the submersible track for dive 662 crossed over sediment-covered sea floor between the two areas of sulfide outcrop, indicating that sulfide does not crop out continuously between the two deposits.

Small isolated chimneys, less than 1 m high, occur in the flat sediment-covered area around the periphery of the deposit. The periphery of the deposit is marked by sediment-buried sulfide mounds and sulfide crusts in the sediment that coalesce into crudely layered sulfide ledges at the edges of the massive sulfide mounds. The bulk of the deposit is composed of large, steep-sided constructional mounds of massive sulfide that are several tens of meters long and up to 11 m high, as measured from the submersible depth recorder. In the process of exploring the deposits, the submersible encountered steep-walled cul-de-sacs formed by coalescence of adjacent mounds in which outcropping massive sulfide extended above the field of view of all three observers. The surfaces of the mounds are generally smooth and rounded, with less common areas of brecciated or crudely layered sulfide (fig. 10.4*C*). The mounds are heavily colonized by attached filter-feeding and grazing biota, especially asteroids (fig. 10.4*C*). A few rounded stubby remnants of degraded chimneys were observed on the tops of the sulfide mounds. Chimney forms were also observed at the deposit to the east investigated by *Sea Cliff* dive 661 (fig. 10.4*D*), which appears to be approximately the same age. Based on the morphology, degree of weathering, and amount of sediment cover observed, the deposits around the base of the North Hill are clearly younger than the deposits of the 3170 Hill, and are approximately the same age as the deposits of the East Hill.

EAST HILL

The deposits associated with the East Hill were not investigated by submersible, and the limited camera observations place few constraints on the extent or continuity of these deposits. Observations of sulfide deposits at the base of the hill on both the north and south flanks are consistent with the geological setting of sulfide mineralization at the 3170 and North Hills; by analogy, massive sulfide deposits may also occur around the base of the East Hill. In contrast to the known deposits at the 3170 and North Hills, outcropping massive sulfide appears to extend northward from the base of the East Hill, occurring near the break in slope of a narrow ridge that may mark the surface expression of an extensional fault (fig. 10.2).

The East Hill deposits are rugged, and constructional mounds with stubby projections are still preserved. They do not appear as degraded by weathering and erosion as the 3170 Hill deposits. The morphology of the East Hill deposits indicates that they are younger than those at the 3170 Hill; however, there are no observations that suggest they are still hydrothermally active.

CORE L2-86-9G LOCATION

Additional areas of sulfide outcrops are known only from camera crossings, dredge collections, and in one case from recovery of sulfide breccia in gravity core L2-86-9G (fig. 10.2). The area where L2-86-9G was collected has not been investigated by camera or submersible mapping, but small, isolated sulfide outcrops were imaged during a camera tow to the east. In contrast to the setting of the explored deposits, these sulfide occurrences are in a flat basin that produced a hard echo return on 3.5 kHz sonic records interpreted as thinly sedimented basalt (Morton and Fox, chap. 2, this volume). The sulfide recovered in core L2-86-9G is overlain by 50 cm of hemipelagic sediment mixed with abundant iron oxide. The sulfide unit is a 25-cm-thick mass-flow deposit of pyrrhotite-rich massive sulfide clasts in a matrix of sand- to silt-size pyrrhotite grains. The sulfide debris flow was deposited above magnesium-metasomatized sediment altered to chlorite (Zierenberg and Shanks, chap. 14, this volume). This occurrence is evidence for an earlier episode of sulfide mineralization at the SESCA area that is now at least partly sediment covered.

EDIFICE C NEAR 40°53′ N.

The volcanic (?) edifice near latitude 40°53′ N. (edifice C of Abbott and others, 1986) between the SESCA and NESCA areas (fig. 10.1) was not explored by either towed camera or submersible. Seismic-reflection profiles show that sediment in this area is disrupted, but the area does not show the topographic relief seen in the SESCA and NESCA areas (Davis and Becker, chap. 3, this volume). There is no indication that volcanic rocks are exposed at the sea floor. Of four sediment cores collected from the area of edifice C, one (L1-86-27G) contains turbiditic sands veined and mineralized by hydrothermal sulfides and barite (Normark and others, chap. 6, this volume; Zierenberg and Shanks, chap. 14, this volume). This core demonstrates that hydrothermal activity has occurred at this site, and that at least some sulfide mineralization is occurring within the accreted sediment, not just above the sediment-water interface.

NESCA STUDY AREA

MORPHOLOGY AND STRUCTURE

The NESCA study area has a sea-floor morphology similar to the SESCA area and is distinguishable from areas of Escanaba Trough away from volcanic centers by the presence of sediment hills up to 1,500 m in diameter and more than 120 m in height (fig. 10.5). Massive sulfide mineralization is extensive in the NESCA area, and the largest deposits are spatially associated with the prominent sediment hills.

The dominant morphologic features in the NESCA area are the SW Hill and the Central Hill, in the southern part of the area shown on figure 10.5, and the hill in the center of the axial trough near latitude 41°05.5′ N. at the northern edge of the NESCA area that corresponds with edifice E of Abbott and others (1986). The SW and Central hills have been explored by a series of bottom-towed camera traverses and several submersible dives, and are crossed by several geophysical lines (Morton and others, chap. 1, this volume; Morton and Fox, chap. 2, this volume; Davis and Becker, chap. 3, this volume). The hill near latitude 41°05.5′ N. was investigated on two Reconnaissance and EXploration submersible dives, and is referred to as Edifice REX. Sediment hills of similar and smaller size occurring both within and adjacent to the central graben (fig. 10.5) are generally unexplored. The central part of the trough is defined by throughgoing normal faults that separate an inner zone of disturbed and disrupted sediment from well-layered sediment typical of the turbidite fill of the trough away from volcanic centers.

VOLCANOLOGY

Volcanic rocks exposed at the sea floor and interpreted (from seismic data) to occur near the sea floor beneath a shallow sediment cover are more abundant at the NESCA site than at the SESCA site (fig. 10.5). The largest exposure of volcanic rock at the NESCA site occurs east of the

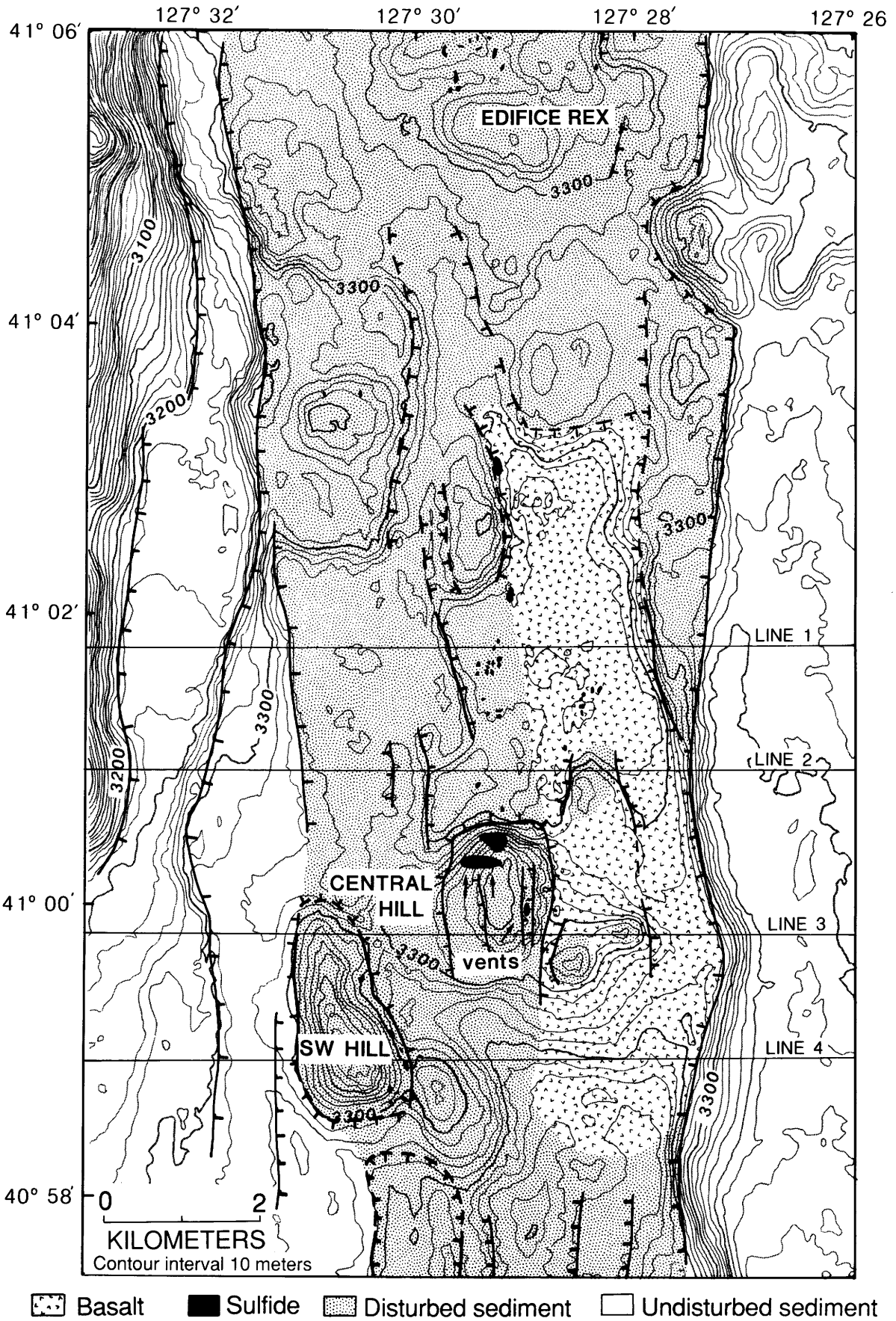
127° 32′
127° 30′
127° 28′
127° 26
41° 06′
41° 04′
41° 02′
41° 00′
40° 58′
EDIFICE REX
3300
3100
3200
LINE 1
LINE 2
LINE 3
LINE 4
CENTRAL HILL
vents
SW HILL
0
2
KILOMETERS
Contour interval 10 meters
Basalt
Sulfide
Disturbed sediment
Undisturbed sediment

crest of the Central Hill (fig. 10.6). The elevated area east of the Central Hill is covered by glassy basalt pillows 1 to 2 m in diameter. Lava tubes drape the north flank of the hill, indicating flow to the north, toward sheet-flow basalt ponded within the central depression of the spreading center (Ross and Zierenberg, chap. 8, this volume). The transition from pillow flow to sheet flow observed north of the hill coincides with the break in topographic slope (Ross and Zierenberg, chap. 8, this volume). Sediment cover and relative age determined from the appearance of glass are similar for the pillow basalts and the sheet flow; no distinct flow boundaries indicative of an age difference in lava emplacement were recognized. Basalts from the NESCA site have a limited range of major- and minor-element composition, and individual flow units are not distinguishable from the chemical data (Davis and others, chap. 9, this volume). Ross and Zierenberg (chap. 8, this volume) propose that the pillow basalt and sheet-flow lavas are of the same relative age and formed during a single eruptive episode from a vent area located somewhere on the pillow-covered hill top.

Two small sediment hills protrude above the pillow-basalt-covered hill top (fig. 10.6); a third circular topographic high further east is interpreted, by analogy, also to be a protruding sediment hill, but could be composed of basalt. The small hill at approximately latitude 41°00.8′ N., north of the pillow-basalt-covered hill top, is also composed of sediment and is surrounded by basaltic sheet flow. The east margin of this sheet-flow-covered area is a sediment-covered scarp of a graben-bounding normal fault that rises to a sediment-covered terrace 100 m above the eastern flank of the volcanic hill (fig. 10.5). A submersible traverse up the base of the scarp just north of the volcanic hill showed that this scarp was formed prior to the last basalt flow, and no basalt was exposed in the up-faulted sediment section.

The area of the Central Hill west of the outcropping pillow basalt is interpreted to have been uplifted by intrusion of basalt into the sediment, but the timing of uplift relative to eruption of pillow basalts to the east is uncertain. The basalt-sediment contact, observed on *Sea Cliff* dive 765, occurs between relatively flat lying pillow basalt flows and a steep sediment slope, consistent with ponding of basalt against an uplifted sediment hill. The central peak of the sediment hill is surrounded by a steep sediment-covered scarp, and the north slope of the hill is a series of normal faults downdropped to the north (fig. 10.6; Holmes and Zierenberg, 1990). Basalt flows have not been observed on any of the sediment scarps.

A small exposure of basaltic sheet flow was also observed near Edifice REX (Ross and Zierenberg, chap. 8, this volume). Sheet flow is exposed on a flat bench at the top of a 9-m-high sediment-covered fault scarp near the base of the eastern graben-bounding normal fault. Basalt does not crop out on the floor of the graben, but isolated talus blocks of basalt derived from the faulted basalt flow are scattered across the flat sediment surface near the base of the scarp. These blocks are dusted with sediment and extensively colonized by filter-feeding fauna. A minimum of 9 m of normal fault uplift has occurred after eruption of this flow, but the depth of sediment burial prior to faulting is not known. Rapid sedimentation has buried the assumed continuation of the flow on the graben floor, but talus blocks derived from the faulted part of the flow have not been buried by sediment. Basalt from this area has a high K_2O content and is chemically distinct from all other samples analyzed from the Gorda Ridge (Davis and others, chap. 9, this volume).

SEDIMENTOLOGY

Observations from submersible dives in the vicinity of the SW and Central Hills attest to the importance of sediment redistribution, similar to observations at the SESCA site. Traverses up the steep walls of the SW Hill reveal truncated sedimentary bedding exposed by mass wasting of the hillside. Blocks of mudstone and siltstone talus, some longer than 1 m, occur at the base of the hill and on flatter benches on the hill slope. Massive sulfide talus associated with mudstone talus was observed and sampled along the southeastern flank of the hill. The top of the SW Hill is flat and sparsely populated by bottom-dwelling organisms. Centimeter-scale sediment layering dipping at a very shallow angle into the hill top is exposed and accentuated by erosion near the fringe of the hill top.

The sediment-covered eastern side of the Central Hill is bounded on the north and east by a series of stepped scarps each a few meters high, which contrast with the large mass-wasting scarps that bound most of the sediment hills. Sediment redistribution is also apparent in this area. Piston cores collected from the Central Hill recovered mudstone breccias (Normark and others, chap. 6, this volume). The hill slopes are cut by numerous channels, some of which are tens of meters deep. Large channels occur at all levels of the hill slope, even near the highest point of the hill. The eastern flank of the Central Hill is an area of complex bottom morphology including grabenlike depressions that are locally floored by meter-size mudstone talus. Hummocky and channeled areas with relatively low levels of biologic colonization and bioturbation are indicative of reduced sedimentation or sediment erosion.

⇐

Figure 10.5. Geologic map of NESCA area. Sea Beam bathymetry and areas with outcropping and shallowly buried volcanic rock and disturbed sediment from Morton and Fox (chap. 2, this volume). Fault locations are extrapolated based on seismic-reflection profiles and Sea Beam bathymetric data; fault teeth are on downthrown side. Locations of cross-section lines presented in figure 10.9*B* are shown.

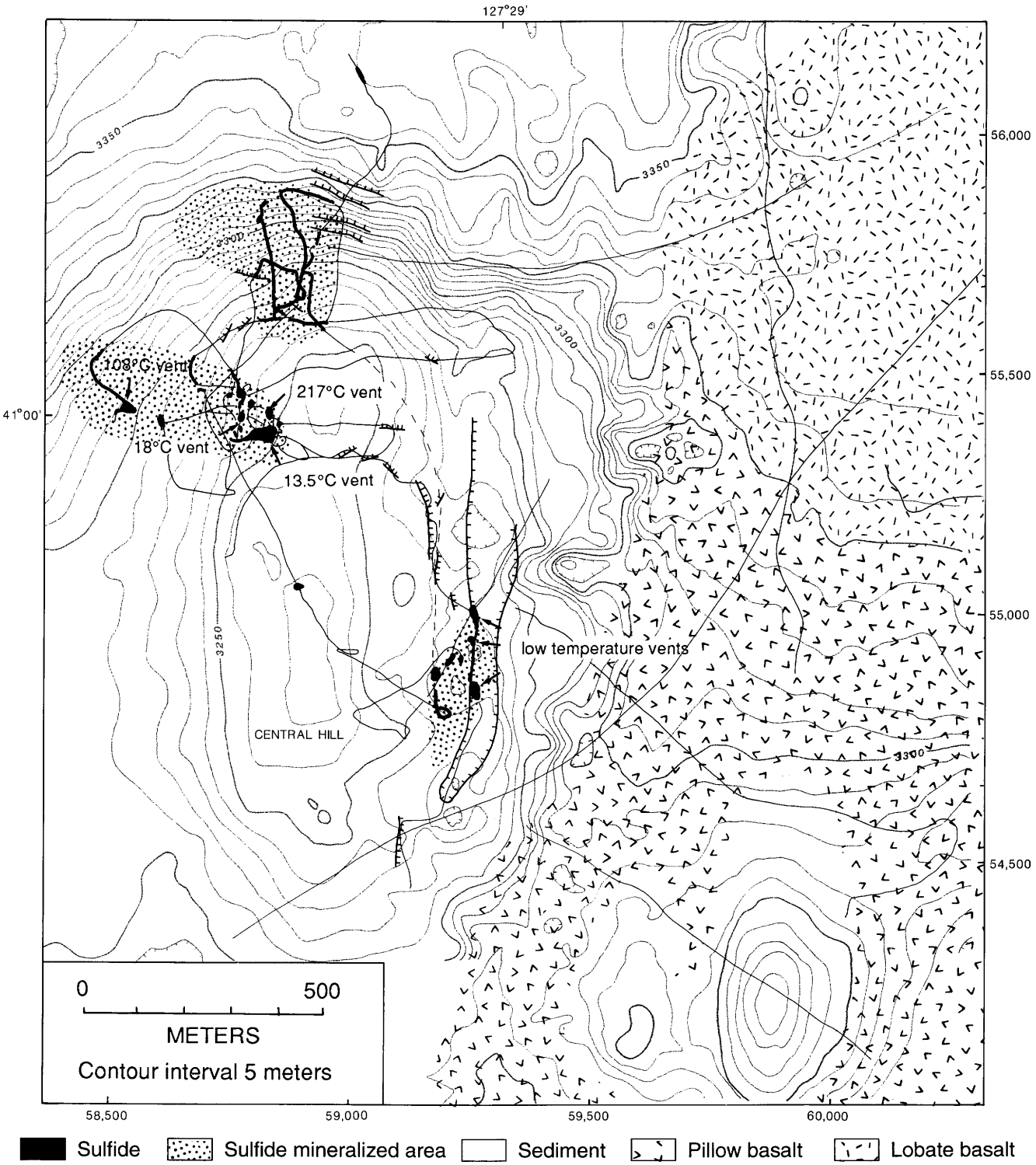

Figure 10.6. Geologic map of Central Hill area of NESCA site. Bathymetric map base is from full-resolution Sea Beam map with 5 m contours, adjusted in latitude and longitude so that major topographic features are aligned with transponder navigated map of NESCA area presented in Morton and others (chap. 1, this volume). Numbers along right and bottom give coordinates of local transponder net (in meters). Hachures indicate area of closed low. Thin solid lines show location of transponder navigated submersible tracks, dashed where submersible was too high above sea floor for visual observations during extensive traverses. Major structural features are shown where sufficient data exist. Teeth on faults are on the downthrown side.

Valleys with downslope scour grooves were also observed cutting into the planar surface of the normal fault that bounds the innermost graben (*Alvin* dive 2034, location shown on fig. 1.7, Morton and others, chap. 1, this volume). The scarp face generally dips 60° to 80° toward the spreading axis and is completely sediment covered. V-shaped channels up to 10 m across cut into the scarp face, locally exposing layered sediment. A small sediment slump, with a headwall scarp and a mudstone debris apron a few meters across, was observed on a flatter bench on the scarp face.

Despite the generally low relief, the flat sediment-covered plain north of the Central Hill investigated on *Sea Cliff* dive 659 is also cut by numerous channels that locally expose sediment layering in the channel walls. The channels range from 1–2 m wide to at least 40 m wide. Smaller channels are typically about half as deep as they are wide. The floors of large channels often dropped below the extent of view of the observers in the submersible; some channels are at least 20 m deep. The walls of the channels range from near vertical to about 45°. Many channels are asymmetric, with one wall steeper than the other. Submersible and camera observations show that the channels locally have curved banks with the convex outer bank steeper than the inner bank (fig. 3*B*). Sediment slumping and scour down the walls of the channels is common, but there is no evidence of recent transport of sediment along the axis of the channels. The one-dimensional nature of both camera-track and submersible mapping provides little data on the lateral continuity of the channels.

HYDROTHERMAL DEPOSITS

Areas of sulfide mineralization observed either by submersible or bottom camera are also shown on figure 10.5. Camera observations suggest that the extent of sulfide mineralization may be larger than shown. Areas of extensive sulfide mineralization associated with the SW Hill, the Central Hill (fig. 10.6), and Edifice REX have been examined by submersible. Additional areas of sulfide mineralization sampled by dredging are not included on figure 10.5; the tracks of dredge runs that recovered hydrothermal minerals are shown on figure 16.2 of Koski and others (chap. 16, this volume). The deposits associated with the Central Hill are the only ones in Escanaba Trough known to be actively venting hydrothermal fluid.

SW HILL

The sulfide deposits near the base of the SW Hill were investigated by two camera runs, *Alvin* dive 2035, and *Sea Cliff* dive 763, and were sampled by four dredge runs. The geologic setting of the SW Hill is analogous to the sediment hills at the SESCA site. The mesalike sediment hill has a planar top and steep sides retreating by mass wasting, which exposes semiconsolidated sediment (fig. 10.4*E*). However, the SW Hill is not circular, but is elongate parallel to a very steep eastern side bounded by a fault trending approximately N. 25° W. (fig. 10.5).

The occurrence of massive sulfide deposits at the SW Hill is also similar to the sediment hills in the SESCA area. Each camera and submersible crossing of the base of the slope of the SW Hill encountered sulfide mineralization, suggesting that sulfide mineralization may at least discontinuously surround the hill. In contrast to the SESCA area, two areas of massive sulfide mineralization occur at different depths on the slope of the SW Hill; one is developed near the base of the slope on the flat sediment-covered saddle that extends southeast from the hill, and the other is exposed at a higher elevation on the steep slope forming the base of the hill (fig. 10.5). The lower deposits consist of large unweathered sulfide mounds topped by narrow spires and inactive chimneys, a morphology that shows these deposits formed recently and are younger than any of the deposits investigated at the SESCA site. Water-column temperature anomalies were recorded by a temperature sensor mounted on the camera sled towed in the area of the sulfide deposits (Morton and others, 1990). The photo crossings also indicate that these deposits are laterally extensive in the direction of the camera track, but the limits of mineralization are not determined. The deposits further up the slope consist of large talus blocks of sulfide below a steep exposure of massive sulfide several meters thick. This deposit is not topped by chimney or sulfide spires. The presence of extensive sulfide talus and the lack of easily degraded sulfide spires indicates that the upper deposits are older than the lower deposits. The upper deposits may have been exposed by, and are clearly modified by, either normal faulting or mass wasting.

The youthful appearance of the lower deposit made it a prime target for submersible investigation in search of hydrothermal activity. Unfortunately, both dives in this area experienced problems with transponder navigation, and neither dive investigated the area photographed during the camera runs. *Alvin* dive 2035 encountered sulfide mineralization at a depth between 3,295 and 3,304 m in the area north of the deposits crossed by the camera runs. Much of the observed mineralization occurs as talus blocks of sulfide up to a few meters across (fig. 10.4*F*). Samples recovered from this site include a fragment of a concentrically zoned sulfide chimney. When the submersible crossed the base of the hill near its northeast side, divers observed massive sulfide between the depths of 3,300 and 3,304 m. In this area, the sulfide deposit is a massive body exposed on the steep sediment-covered hill slope surrounded by sulfide and mudstone talus blocks. The deposit has been disrupted by mass wasting, similar to the upper sulfide zone observed in the camera runs.

An area of massive sulfide mineralization estimated to be several tens of meters long was crossed on *Sea Cliff* dive 763 in the area north of the camera runs. The base of the deposit was at 3,272 m and the top was at approximately 3,255 m. The deposit is blocky and fractured, and large blocks of sulfide talus are common. Although no chimneylike projections were observed, the sulfide is not extensively weathered, and reflections off large crystal faces of sulfide minerals could be clearly seen. The slope below the deposit is cut by several normal fault scarps, 1 to 5 m high, that expose bedded mudstone. Blocks of mudstone talus 1 to 2 m wide occur at the base of the slope. The base of the sulfide deposit is exposed near the top of one of the normal faults, and it appears that the sulfide is disrupted by faulting. This deposit occurs near the sulfide deposit observed on *Alvin* dive 2035, but at a shallower depth. It is possible that the lower deposit is a displaced fragment of the upper deposit. However, massive sulfide occurs 1 km further north along the structural boundary of the hill at the same depth as the lower deposit, and camera observations of the upper and lower deposits to the south clearly show that the lower deposit in this area is a constructional deposit formed in situ. Further mapping will be required to establish the continuity of the two levels of mineralization and to determine the temporal and genetic relationship between them.

CENTRAL HILL

The western, sediment-covered part of the Central Hill (fig. 10.6) is the area of the most extensive sulfide deposit observed in Escanaba Trough. It is also the only area known to have active hydrothermal vents. Three areas of outcropping massive sulfide mineralization were discovered and partly explored during 10 submersible dives (fig. 10.6). The areas of outcropping massive sulfide are separated by sediment-covered sea floor, and the relationship between these areas is not known. The massive sulfide deposits on the west and southeast flanks of the Central Hill are actively venting hydrothermal fluid, and the area on the northern flank shows indications of very recent hydrothermal activity, suggesting that these deposits are all part of the same hydrothermal system.

The geologic setting of these deposits is somewhat different than the deposits at the SW Hill or the three sediment hills at the SESCA site. Similar to the SESCA site, the deposits are all developed on the sediment-covered western part of the Central Hill; no hydrothermal deposits have been observed on exposed volcanic rock to the east (fig. 10.6). However, the deposits are not confined to the structural boundary around the perimeter of the hill, but extend to near the top of the hill.

Uplift of the western part of the Central Hill was accommodated by a series of stepped normal faults, downdropped to the north (fig. 10.6). The western and eastern flank are also formed by sediment-covered scarps that may also represent normal faults. Uplift on the eastern flank of the sediment hill resulted in extensive disturbance of the sediment cover, including formation of small grabens in the overlying sediment, one of which apparently controls the location of the southernmost area of massive sulfide mineralization (fig. 10.6). The eastern flank of the sediment hill has irregular topography near the contact with the basalt. The topography is characterized by swales and sediment-covered scarps a few meters high. Mudstone talus formed from slumping along steep slopes is common.

The southernmost area of massive sulfide mineralization (fig. 10.6) was investigated on *Alvin* dives 2040 and 2042 and on *Sea Cliff* dive 766. The apparent eastern edge of sulfide mineralization was explored for 190 m along a north-south-trending scarp. Sonar images from *Alvin* suggest that this scarp is the west wall of a small graben. The floor of the graben is at a depth of 3,260 m and is sediment covered. In the area of the sulfide deposit, the graben floor near the west wall is colonized by clusters of the vent clam *Calyptogena* (fig. 10.7*A*; Van Dover and others, 1990) and is locally covered by bacterial mat. Black sulfidic sediment and hydrothermal crusts were observed at the base of the graben wall (fig. 10.7*B*) and where the surface layer of brown hemipelagic sediment was disturbed by the submersible. No flow of hydrothermal fluid through

⇒

Figure 10.7. Color photographs from hand-held and external 35-mm cameras of DSV *Alvin*. *A*, Abundant *Calyptogena* in sediment near base of outcropping massive sulfide on east wall of small graben on southwest flank of Central Hill. Some crusts of sulfide and indurated sediment are shown; nearby areas are colonized by bacterial mats. Field of view approximately 3 m across (*Alvin* dive 2042). *B*, Sulfide crust and indurated sediment at base of graben wall. Field of view approximately 3 m across (*Alvin* dive 2042). *C*, Indurated sediment on flank of massive sulfide mound discharging low-temperature hydrothermal fluid. Field of view approximately 2 m across (photo by D. Foster, *Alvin* dive 2041). *D*, Dense tube worm cluster obscuring low-temperature vent. Tube worms are locally coated by white bacterial mat and are colonized by anemones with red tentacles. Some galatheid crabs occur on brecciated massive sulfide of mound. Field of view approximately 3 m across (*Alvin* dive 2036). *E*, White, porous, sinterlike crust of anhydrite, with barite, minor sulfides, and magnesium-rich smectite, capping a mound of pyrrhotite-rich massive sulfide. Right side of photo is out of focus due to shimmering from discharge of 217°C clear vent fluid. Yellow palm worms colonize anhydrite crust near active vents. Field of view approximately 2 m across (*Alvin* dive 2036). *F*, Sulfide talus and breccia fragments of fresh coarse-grained pyrrhotite at base of inactive sulfide mound. Light spots are reflections from large pyrrhotite crystals. Although there are many fracture surfaces that expose unweathered sulfide, most sulfide fragments are dusted by sediment. Field of view approximately 2 m across (*Alvin* dive 2033).

the sediment was observed, even in areas of dense clam and bacterial colonies. The steep graben wall exposes a 7-m-thick section of massive sulfide that is locally colonized by bacterial mats and tube worms. Diffuse flow of warm hydrothermal fluid was observed from the graben wall, but no high-temperature vents were encountered. The area has not been explored in detail, and it is possible that high-temperature hydrothermal discharge may be occurring at this site. Massive sulfide mounds extend for at least 100 m west of the graben edge, and some mounds reach up to at least 3,240 m depth. Some of the mounds to the west are also colonized by tube worms and bacterial mats, indicating that hydrothermal fluid flow is at least weakly active throughout this area. Intact but inactive sulfide and barite chimneys on top of some mounds suggest recent higher temperature focused discharge.

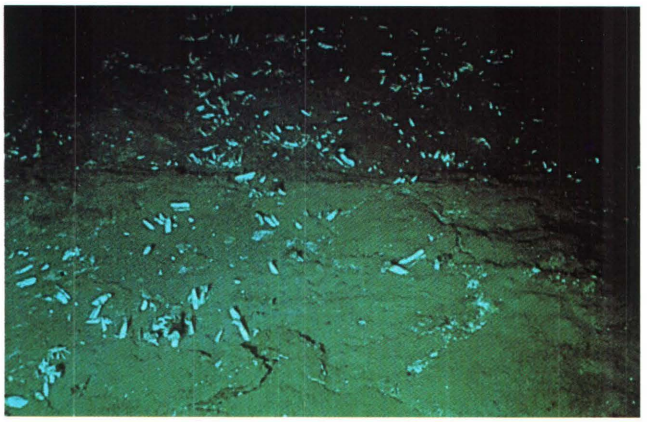

A

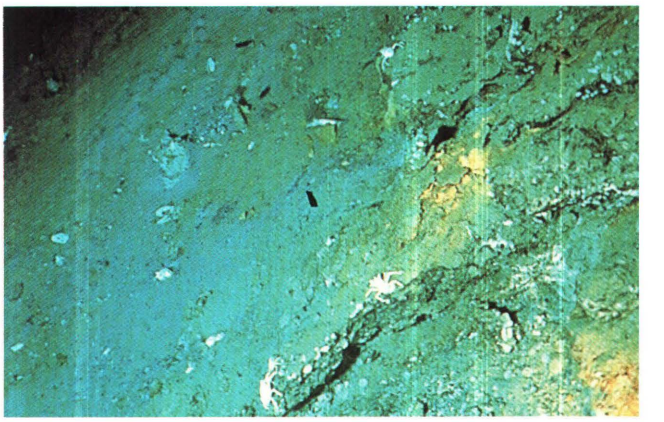

B

C

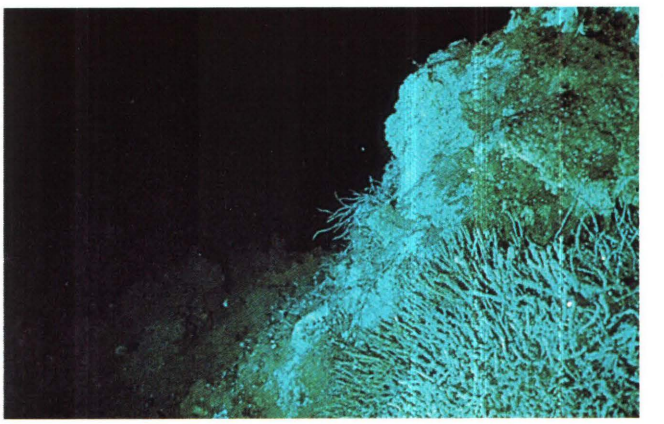

D

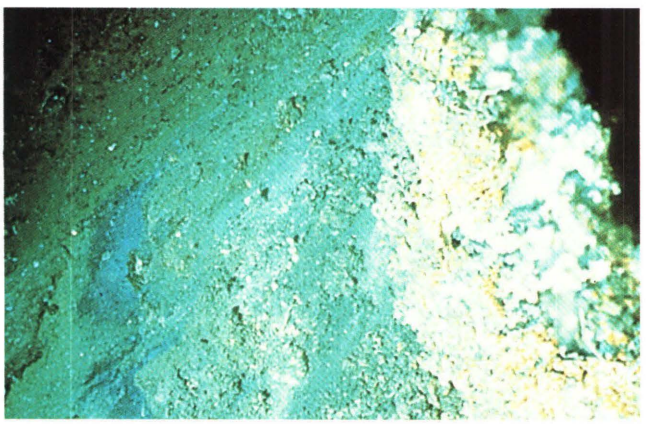

E

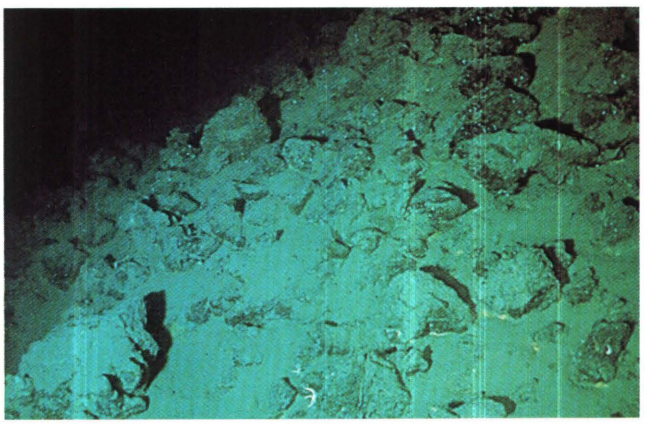

F

The best explored and most hydrothermally active area of sulfide mineralization on the Central Hill extends west from the northern end of the sediment-covered hill top (fig. 10.6). This is not an area of continuous sulfide outcrop, but rather a region of abundant, closely spaced sulfide mounds. The mounds are typically 20 to 60 m in diameter and 5 to 10 m high. One of the larger mounds investigated lies along the steep sediment-covered hill slope and had continuous outcrop of massive sulfide from 3,245 m to 3,225 m depth. The base of the westernmost known sulfide mound is at 3,275 m. Mineralization extends from 70 to 120 m in a north-south direction and for at least 300 m in an east-west direction, but the western edge of sulfide mineralization has not been determined. The distance between mounds is similar to their lateral dimensions such that often more than one sulfide structure was visible from the submersible. The mounds may be connected in the shallow subsurface, thus the sediment ponds between mounds may represent a surficial veneer over massive sulfide in the low areas. Sediment near some of the mounds is semilithified, presumably due to hydrothermal alteration (fig. 10.7*C*). About one-third of the mounds are colonized by live vent-specific biota and have diffuse discharge of low-temperature hydrothermal fluid. Vent fluids with temperatures of 13.5°C and 18°C were sampled from diffuse discharge at two mounds (fig. 10.6). Two mounds were observed to actively discharge high-temperature hydrothermal fluid; one near the eastern margin of the sulfide area was venting 217°C fluid, and one on the western edge of the explored area was venting 108°C fluid (fig. 10.6). Even though these mounds are 275 m apart, the major-element composition of the end-member fluid at each vent is identical (Campbell and others, chap. 11, this volume), a result that is consistent with the hypothesis that this large mineralized area is a single hydrothermal system hydrologically interconnected at depth.

The massive sulfide mounds generally have smooth, rounded surface profiles. Both sulfide and barite chimneys occur atop some mounds, but chimneys are not common, even on hydrothermally active mounds. The morphology of the low-temperature hydrothermal vents was generally obscured by dense clusters of tube worms (fig. 10.7*D*), which occur in patches estimated to be up to 8 m long and 2 m wide. High-temperature fluid flows diffusely from 1-to-2-m long areas of porous anhydrite-barite sinter capping massive pyrrhotite-rich sulfide mounds (fig. 10.7*E*; Koski and others, chap. 16, this volume). The bases of the mounds, including those still active, are onlapped by hemipelagic sediment and are fringed by sulfide talus. The range from nearly sediment-buried to sediment-free blocks (fig. 10.7*F*) indicates a long history of sulfide formation relative to the sedimentation rate. Angular, slab-shaped sulfide fragments a few centimeters thick and several tens of centimeters on a side are common around the base of the mounds. The surfaces of the mounds are also covered by sulfide breccia (fig. 10.8*A*) and are locally cut by fissures exposing fresh, coarse-grained sulfide crystals (fig. 10.8*B*). Some of the sulfide blocks surrounding the mounds are true talus, related to the breakup of unstable sulfide structures and gravitational transport down steep slopes. However, many areas of sulfide breccia on low-relief slopes lack chimneylike structures (fig. 10.8*B*). These breccias, and the fissures cutting the mounds, are forming in situ at the mound surface. Sulfide crusts forming in the sediment are also brecciated and locally buckled upward into "teepee" structures or "pressure ridges" (fig. 10.8*C*).

The vent fauna colonizing the active mounds have affinities to faunal assemblages of Juan de Fuca Ridge and have been described by Van Dover and others (1990) and Grassle and Petrecca (chap. 17, this volume). The most obvious biologic features are the clusters of tube worms (fig. 10.7*D*, 10.8*D*), which themselves are heavily colonized by greenish-orange palm worms, white-bodied anemones with reddish tentacles, white bacterial mats, and blue filamentous mats interpreted to be the protozoan *Girvanella* (fig. 10.8*D*). Close inspection reveals that rock surfaces near vents are very heavily colonized by small mollusks, mostly gastropods. Galatheid crabs are common, but not overly abundant around the vents. Scattered shells of dead *Calyptogena* occur in the area, but no live clams were seen in this vent field. Inactive mounds are generally heavily colonized by tunicates, anemones lacking the red-tinted tentacles, and asteroids (fig. 10.8*E*).

An extensive area of massive sulfide is exposed on the north slope of the Central Hill. Parts of this deposit were explored on *Sea Cliff* dive 658 and *Alvin* dives 2033, 2037, and 2040. The deposit formed on the steeply sloping, step-faulted flank of the hill and is exposed between the depths of 3,235 and 3,276 m. The deposit extends more than 270 m from north to south and more than 100 m from east to west, but the western edge has not been determined. Within this area there is nearly continuous outcrop of massive sulfide with few sediment-covered areas. Constructional sulfide mounds, some topped by barite chimneys (fig. 10.8*E*), occur throughout the deposit, including near the lowest depth. Much of the surface exposure is coarse breccia and talus of massive sulfide. Sulfide fragments exceeding 1 m in length are common, including slabs of sulfide 5 to 20 cm thick. These fragments often expose fresh, coarse-grained massive sulfide with pyrrhotite crystals large enough to be visible from the submersible (fig. 10.7*F*). No active venting has been observed in this area, but recent hydrothermal activity is indicated by the morphology of the deposits, the presence of fresh sulfide at the surface, and the limited occurrence of live bacterial mats, dead tube worms, and vent clam shells.

The three areas of massive sulfide outcrops on the Central Hill are contemporaneous and are interpreted to be part of the same hydrothermal system related to igneous

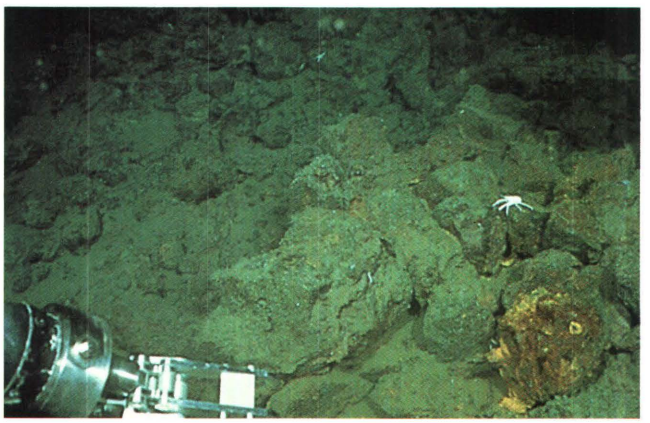

A

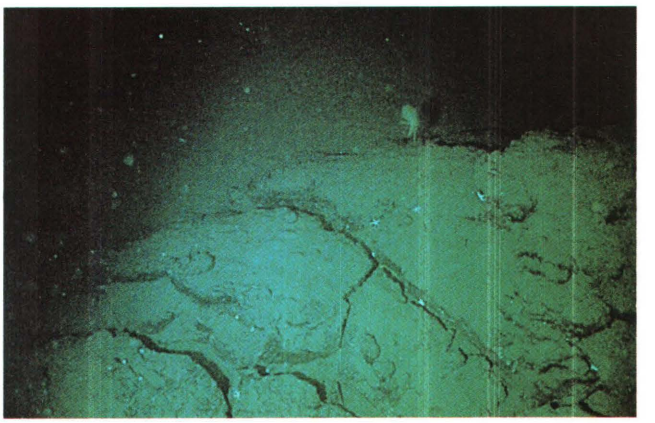

B

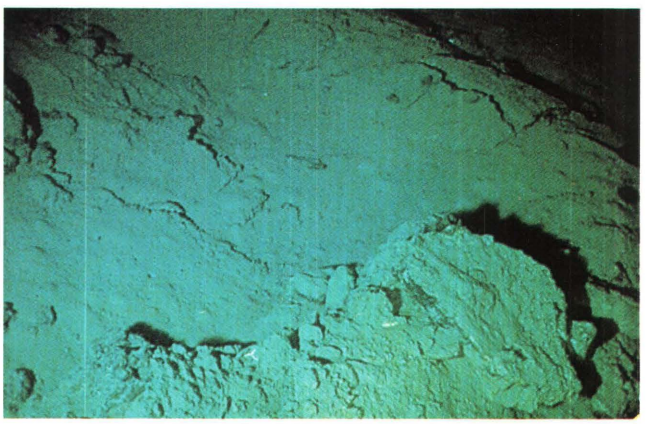

C

D

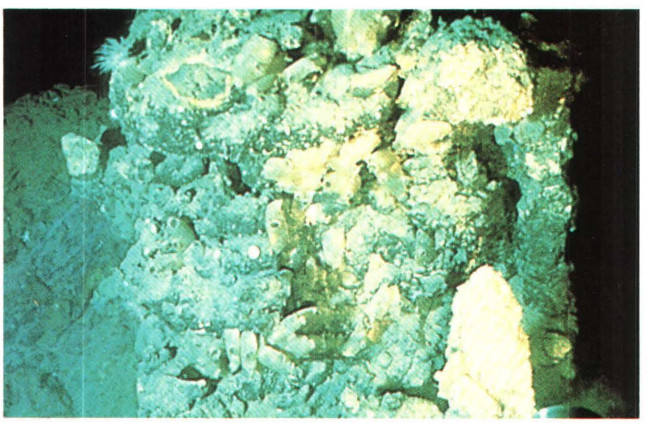

E

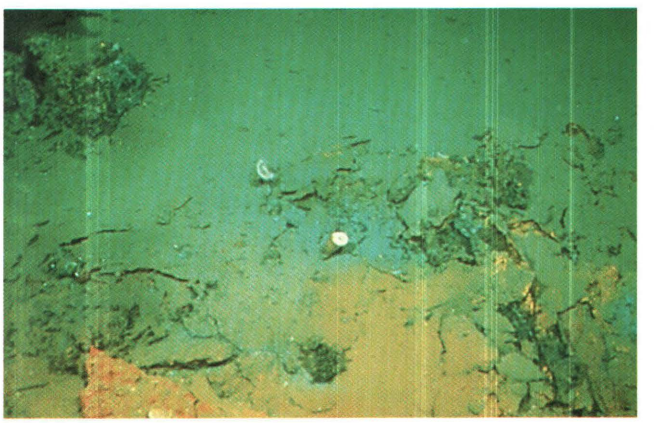

F

Figure 10.8. Color photographs from external 35-mm cameras of DSV *Alvin* and DSV *Sea Cliff*. *A*, Coarse breccia of massive sulfide, some showing extensive oxidation to yellow iron oxyhydroxides. Field of view approximately 1.5 m across (*Sea Cliff* dive 658). *B*, Fissures cutting flat-lying crust of massive sulfide. Field of view approximately 1.5 m across (*Alvin* dive 2040). *C*, Sulfide crust in sediment buckled upward by displacive subsurface growth. Field of view approximately 1.5 m across (*Alvin* dive 2033). *D*, Tube worms on mound of brecciated massive sulfide. Tube worms are colonized by anemones with red tentacles. White galatheid crabs and blue filamentous mats interpreted to be the protozoan *Girvanella* can be seen on massive sulfide. Field of view approximately 1 m across (*Alvin* dive 2041). *E*, Inactive barite chimneys on massive sulfide mound colonized by tunicates and anemones lacking red pigment of those associated with active vents. Field of view approximately 0.75 m across (*Alvin* dive 2033). *F*, Isolated sulfide chimneys and sulfide crust in sediment exposed at top of channel cut into sediment-covered bottom north of Central Hill. Field of view approximately 1.5 m across (*Sea Cliff* dive 659).

intrusion causing uplift of the Central Hill. The outcrops are contained within an area 600 by 1,200 m, but their extent is not constrained by present observation. Exposure of massive sulfide for 5 to 10 m above the surrounding sea floor is common, and the depth range between the deepest and shallowest deposits exceeds 50 m. We cannot reliably estimate the tonnage of massive sulfide, not knowing thickness of the sulfide deposits or the extent of both sediment-buried and subsurface mineralization. However, the scale of these deposits, both in terms of areal distribution and intensity and duration of hydrothermal activity, is comparable to massive sulfide deposits that are mined on land.

AREA NORTH OF THE CENTRAL HILL

Isolated areas of sulfide mineralization have been observed throughout the NESCA area from both submersible and camera runs (fig. 10.5). Numerous areas with isolated sulfide chimneys and crusts developed in hemipelagic sediment were seen on *Sea Cliff* dive 659. Many of these are exposed near the tops of the channels that commonly cut through this area (fig. 10.8*F*). The sulfide crusts, as well as the base of a small chimney recovered in this area (Holmes and Zierenberg, 1990), provide evidence that mineralization is occurring at and below the sediment-water interface.

Areas of older, weathered, and partly sediment-buried sulfide mineralization were observed during *Alvin* dive 2034 on the margins of a small sediment hill onlapped by sheet-flow basalt flowing northward from the Central Hill (fig. 10.5). Based on 3.5 kHz profiles, this area is interpreted to be underlain at shallow depth by basalt (Morton and Fox, chap. 2, this volume). However, all of the sulfide observed in this area occurs on sediment-covered bottom, and no outcrops of basalt were observed between exposures of sulfide.

Isolated sulfide occurrences were also observed from towed camera traverses along the topographic break that bounds the west side of the deepest part of the axial graben and the base of the small sediment hills on the west side of the axial graben near latitude 41°02′ N., longitude 127°30′ W. (fig. 10.5). The extent of outcropping sulfide observed in the camera runs suggests that some of these occurrences may be substantial sulfide deposits, but they have not been investigated in detail.

EDIFICE REX

The previously unexplored area of Edifice REX, approximately 10 km north of the Central Hill, was investigated on two reconnaissance and exploration dives during the 1988 *Alvin* dive series in hopes of finding additional high-temperature hydrothermal discharge. No camera mapping had been done at the site, and no bathymetric map was available. A bathymetric map was constructed following an overnight survey using the 12 kHz echo sounding system of the R/V *Atlantis II*. The resulting map and the knowledge of the sulfide occurrences at the SESCA and NESCA areas were used to target *Alvin* dive 2038 on the south slope of a large hill. This dive encountered massive sulfide mineralization at a depth of 3,260 m 15 minutes after reaching bottom. *Alvin* dive 2039 was targeted on the east flank of Edifice REX and encountered sulfide mineralization at a depth of 3,254 m. The area of these two dives was mostly beyond the range of the NESCA transponder grid (Morton and others, chap. 1, this volume); two additional transponders deployed in this area were used to navigate the bathymetric survey and the dives. Locations were justified to the NESCA net by transponder fixes at the southern part of the area and correlation of the global positioning system (GPS) locations.

The only volcanic rocks observed at Edifice REX are sheet-flow basalt exposed at the top of an upfaulted block east of the hill top and basaltic talus derived from this scarp. The entire area of the hill top investigated by submersible is sediment covered. Extensive areas of massive sulfide were encountered throughout *Alvin* dive 2038. The size of the outcrops observed suggest that these are large deposits. The deposits are weathered and often sediment covered. The best exposures are along steep to vertical faces several meters high that exposed continuous walls of massive sulfide. One steep exposure appeared to show a massive sulfide layer a few meters thick interbedded with sediment. Some of the steep exposures are probably fault scarps that expose the sediment-buried massive sulfide. These faults may form the walls of a graben that controlled the location of hydrothermal discharge. Locally, sonar scans from the submersible displayed parallel reflections trending in the direction of the sulfide walls, consistent with the interpretation that the sulfides are exposed along small grabens a few tens of meters wide and 5 to 10 m deep. Neither the structures nor the deposits were systematically mapped, but at least some of the sulfide scarps are not parallel to the spreading axis. The deposits discovered on *Alvin* dive 2038 appear to be distributed around the edges of the southwesternmost of the three hills that can be seen on the Sea Beam map of this area (fig. 10.5). The deposits occur near the top of this hill between depths of 3,250 and 3,265 m. Smaller deposits on the east flank of this hill, discovered on *Alvin* dive 2039, occur at a depth of 3,254 m.

DISCUSSION

VOLCANIC-SEDIMENT INTERACTION

Sediment cover thins over the volcanic edifices, and the parallel seismic reflectors that typify the Escanaba

Trough fill are often disrupted over the tops of the edifices (figs. 10.2, 10.5; Morton and Fox, chap. 2, this volume). The volcanic edifices are interpreted to have formed by a combination of intrusive and extrusive igneous activity (Morton and Fox, chap. 2, this volume). Igneous and sedimentary processes are contemporaneous and interrelated in this setting. Volcanic flows and sills are intercalated with the sedimentary fill of the trough (Morton and Fox, chap. 2, this volume; Davis and Becker, chap. 3, this volume). Uplift of sediment over basalt intrusions leads to redistribution of sediment by mass wasting (Holmes and Zierenberg, 1990; Karlin and Zierenberg, chap. 7, this volume). The distribution of volcanic centers also provides a first order control on the location of hydrothermal activity. Intrusive bodies in sediment are inferred to be responsible for localization of zones of hydrothermal discharge by the thermal focusing of fluid flow and enhancement of cross-stratal permeability caused by both thermal and mechanical disturbance in the intruded sediment (Denlinger and Holmes, chap. 4, this volume).

Schematic cross sections for the SESCA (fig. 10.9*A*) and NESCA (fig. 10.9*B*) study areas show the known and inferred relationships between sediment cover, igneous intrusive and extrusive rocks, faulting, and hydrothermal deposits (figs. 10.2, 10.5). The cross-section lines are drawn along seismic lines (lines 4, 6, 8, 10, and 12 for the SESCA area, shown on figure 2.9 of Morton and Fox (chap. 2, this volume) and lines 1 to 5 of Davis and Becker (chap. 3, this volume) for the NESCA area). These seismic profiles, and lines 14 to 25 of Morton and Fox (chap. 2, this volume) in the NESCA area were used to constrain subsurface geology where possible. However, these are schematic cross sections, not strict seismic interpretations, and as such contain information and speculative interpretations based on the Sea Beam bathymetry, 3.5 kHz seismic profiles, and sea-floor geology observed from submersible and bottom-towed camera. Fault traces shown on figures 10.9 are extrapolated between cross-section lines and (or) inferred from the Sea Beam bathymetry and submersible observations of scarps.

SESCA CROSS SECTIONS

The SESCA section lines (fig. 10.9*A*) run slightly oblique to the east-west spreading direction and are confined to the trough floor; they do not extend to the normal faults that bound the axial valley, which are located approximately 2 km west and 5 km east of the ends of the section lines. Sediment fill in the northern part of the SESCA area is interpreted to be approximately 400 m thick, but thins southward to approximately 300 m where volcanic basement is interpreted to rise closer to the sea floor. The northernmost sections show an inner set of graben-bounding faults of small displacement that mark the boundary between seismically disturbed and undisturbed sediment (figs. 10.2, 10.9*A*; Morton and Fox, chap. 2, this volume). The zone of disrupted sedimentary layering widens southward and extends west of the cross sections to the first large normal fault that bounds the west side of the axial valley. A seismically transparent layer that occurs throughout Escanaba Trough approximately 100 m below the sea floor (Morton and Fox, chap. 2, this volume; Davis and Becker, chap. 3, this volume) is generally not clearly imaged within the innermost graben, but can be traced discontinuously through the zone of disrupted sediment west of the inner graben. The eastern boundary of the inner graben is shown as a horst on the northern two cross sections, but the strike of the fault bounding the eastern side of this block is oblique to the ridge axis and extends beyond the eastern end of line 8 (fig. 10.2).

Basement is poorly imaged in much of the disturbed central area, but is interpreted to be generally shallower than outside the central graben, especially on the southernmost lines. Some deeper seismic reflectors shown as sills and flows on the cross sections may actually be the top of irregular basement highs. The inferred process of oceanic crust formation at sediment-covered spreading centers by injection of sills near the base of the sediment fill (Morton and Fox, chap. 2, this volume; Denlinger and Holmes, chap. 4, this volume) will result in a complex transition zone between oceanic basement and sediment, rather than the sharp interface formed by sediment burial of an inactive rift. High-amplitude subsurface reflectors are interpreted on these sections as either basaltic sills and flows or volcanic basement. However, subsurface sulfide mineralization or hydrothermal lithification of sediment could also produce similar localized high-amplitude seismic reflections within the sediment column, and the interpretation presented on these sections is not unique. Shallow seismic reflectors, interpreted as sills, are especially prevalent beneath the small sediment hills crossed on lines 8 and 10.

NESCA CROSS SECTIONS

The NESCA sections show that the trough at this latitude is filled to an average depth of approximately 600 m with sediment (fig. 10.9*B*). The shoaling of igneous basement characteristic of the Escanaba Trough volcanic centers is not apparent on the NESCA cross sections. However, acoustic reflections from volcanic basement are not well developed below the central zone of disturbed sediment, so the depth to basement is poorly constrained. Sediment layering is generally well developed, and the transparent seismic marker bed observed throughout Escanaba Trough (Davis and Becker, chap. 3, this volume) is easily traced outside a central zone of disturbed sediment. In the center of the trough, sediment layering shows the disruption typical of the Escanaba Trough volcanic

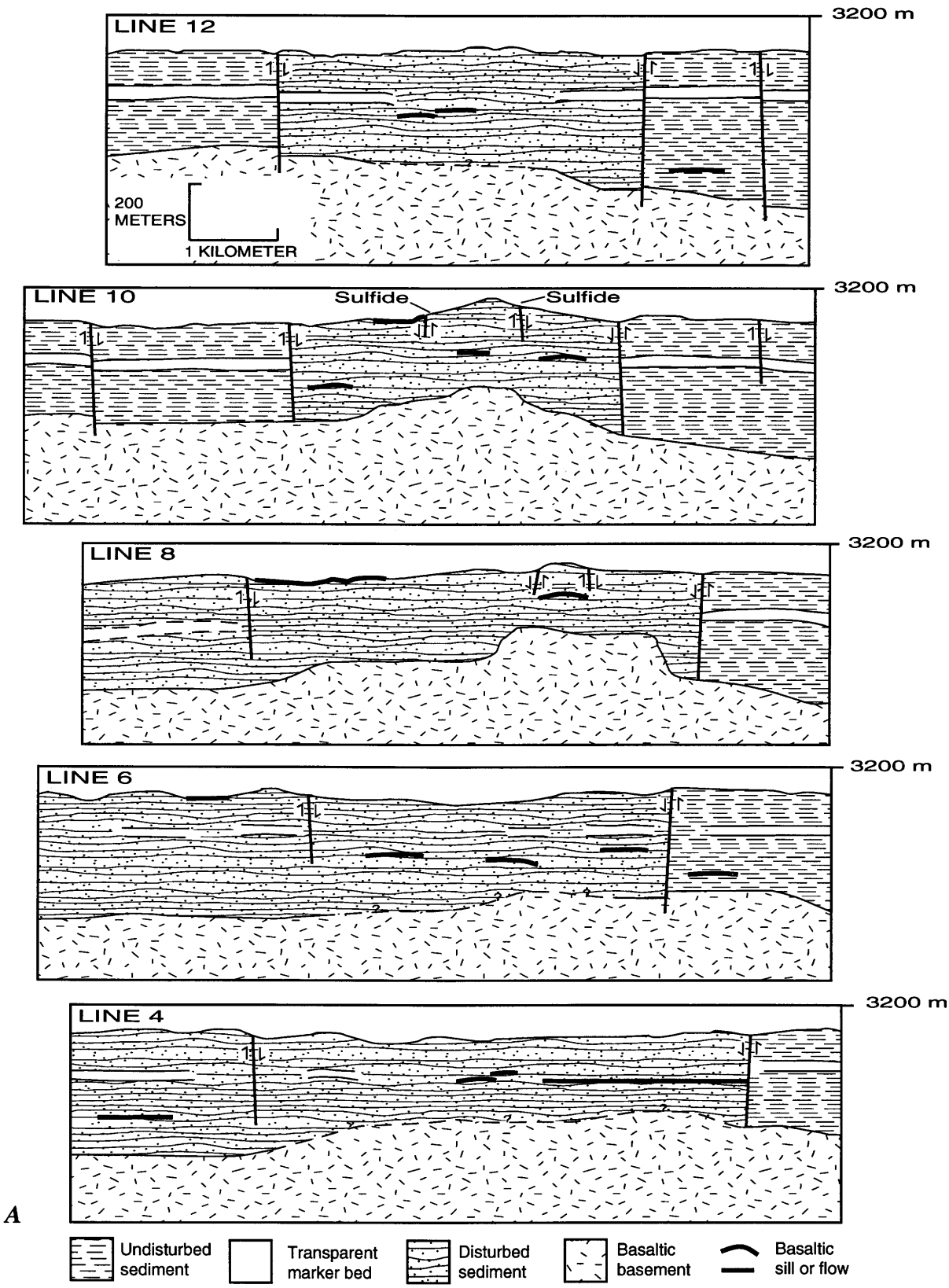

Figure 10.9. Schematic cross sections of SESCA and NESCA areas. *A*, Schematic cross sections of SESCA area drawn along seismic reflection profiles 4, 6, 8, 10, and 12 from Morton and Fox (chap. 2, this volume). Cross sections are constrained where possible by seismic-reflection data but also include data from surface-towed camera, submersible observations, and Sea Beam bathymetry. Vertical exaggeration 5.3×. *B*, Schematic cross sections of NESCA area drawn along seismic-reflection profiles 1 to 5 from Davis and

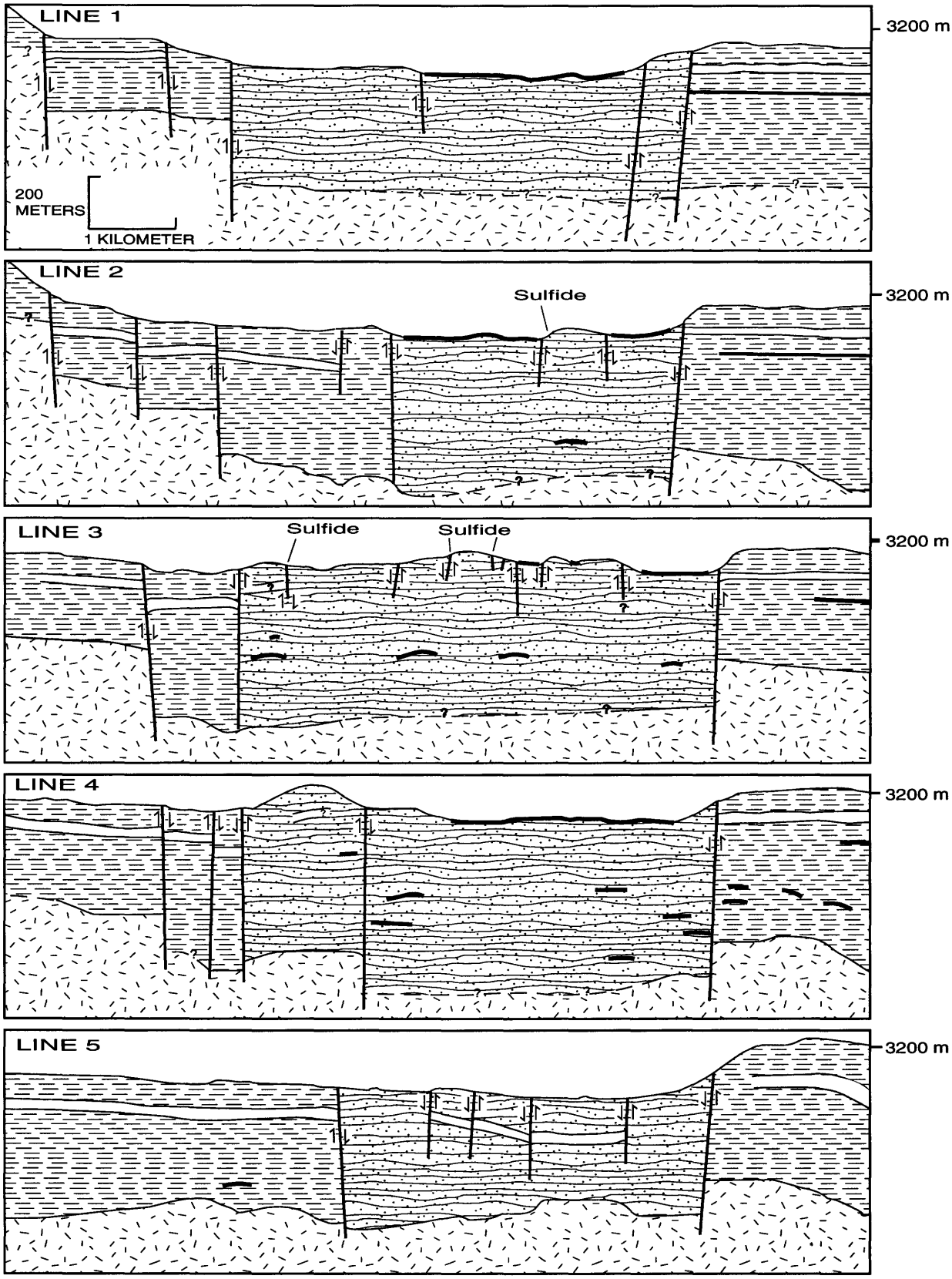

B

others (chap. 3, this volume). Cross sections are constrained where possible by seismic-reflection data from Davis and others (chap. 3, this volume) and Morton and Fox (chap. 2, this volume), but also include data from surface-towed camera, submersible observations, and Sea Beam bathymetry. Vertical exaggeration 3.8 ×. Arrows show relative direction of movement along the fault.

centers. Strong acoustic reflectors within the sediment section have been interpreted as both basaltic sills and flows (Morton and Fox, chap. 2, this volume; Davis and Becker, chap. 3, this volume). A continuous acoustic reflector at a depth of approximately 220 m visible at the eastern edge of lines 1 to 4 is interpreted to be a large basalt flow (Davis and Becker, chap. 3, this volume), indicating that intermittent volcanism is contemporaneous with sedimentation. Near-surface basalt flows shown on lines 1 to 4 are interpreted to overlie the sediment fill of the trough. Sediment hills protruding through the basalt flows east and northeast of the crest of the Central Hill (fig. 10.5, 10.6) are consistent with the interpretation that the basalt forms a thin veneer over the sediment-filled rift valley that had undergone previous uplift of sediment hills.

Numerous smaller acoustic reflectors within the sedimentary section are interpreted as basaltic sills, but as with the SESCA sections, this interpretation is not unique, and we cannot rule out zones of subsurface sulfide mineralization or hydrothermally induced lithification of sediment. Sills are especially abundant on lines 3 and 4, which cross the large sediment hills.

UPLIFT OF SEDIMENT HILLS

The circular sediment hills spatially associated with the largest massive sulfide deposits have been observed from submersibles and are interpreted as uplifted cylindrical blocks of sediment bounded by curvilinear normal faults. The 3.5 kHz seismic-reflection profiles over some of the hills show slight tilting of sediment layers over the uplifted areas that appear to be correlatable with untilted sediment layers adjacent to the hills (Morton and Fox, chap. 2, this volume). The mechanism proposed for these localized uplifts is intrusion of large basaltic sills near the basalt-sediment interface (Morton and Fox, chap. 2, this volume; Denlinger and Holmes, chap. 4, this volume), but seismic imaging below the disturbed sediment hills provides few constraints on the location of basaltic basement. The surface exposure of volcanic rock in Escanaba Trough is limited in areal extent (figs. 10.5, 10.6), but appears to be related to the uplifted sediment hills (Ross and Zierenberg, chap. 8, this volume). Seismic reflectors interpreted as shallow sills are also common beneath the uplifted hills. Shallow sills and volcanic flows that occur near the perimeter of the uplifted hills may be fed by dikes following the faulted margins of the uplifted sediment hills.

Surface eruption of basalt is inhibited in areas of thick sediment cover. Basaltic magma will rise through unconsolidated sediment until it is energetically more favorable to flow laterally under lower density sediment, thus forming sill complexes. Sedimentary cap rocks to the intrusions are uplifted in pistonlike cylindrical hills analogous to "punched laccoliths" (Correy, 1988). Uplifted sediment hills in the Guaymas Basin spreading center are also interpreted to have formed over "bysmalithic" intrusions (Lonsdale and Lawver, 1980). Thin sills that were intruded at shallow depth within the sediment cover of the Guaymas Basin were drilled at DSDP Sites 477 and 481. These thin shallow sills produce little uplift of the overlying sediment (Lonsdale and Becker, 1985); the volume for emplacement of these sills is apparently created by dewatering and compaction of the intruded sediment (Einsele and others, 1980). Magmatism at sediment-covered spreading centers can be anticipated to form sill complexes due to the large density contrast between basalt and unconsolidated sediment. More problematic is the occurrence of volcanic flows at the sediment surface. Magma can only reach the surface where the lateral confining pressure on an intrusion is sufficient to prevent intrusion into the sediment. Previous intrusives that have solidified could provide support for magma conduits to reach near the surface. Rapid effusion rates could result in surface lava flows capable of overriding the surface sediment, as observed at the SESCA and NESCA sites. Feeder dikes for these surface flows might preferentially intrude along preexisting structures, including the faults that bound the uplifted sediment hills (Ross and Zierenberg, chap. 8, this volume).

Petrologic investigations of basalt recovered from surface exposures also provide limited evidence for subsurface interaction of basalt with sediment covering the ridge axis. Basalt samples from the sediment-covered part of Escanaba Trough have lead isotopic ratios that appear to lie along a mixing line between Gorda Ridge basalt and Escanaba Trough sediment and may be evidence of chemical interaction of basalt with sediment (Davis and others, chap. 9, this volume).

SEDIMENT REDISTRIBUTION

Submersible observations and gravity core sampling have established that sediment redistribution is an important process in the volcanically and tectonically active parts of the central graben of the Escanaba Trough. The Holocene sections of piston and gravity cores collected from the floor of the axial trough commonly contain turbidite layers and mass-flow deposits (Karlin and Lyle, 1986; Karlin and Zierenberg, chap. 7, this volume; Normark and others, chap. 6, this volume). Cores collected from terraces uplifted a few tens of meters along normal faults that bound the innermost floor of the axial graben (for example, core L2-86-7G) do not have Holocene turbidites (Normark and others, chap. 6, this volume). The thickness of turbidite units decreases with distance from uplifted hills (Karlin and Zierenberg, chap. 7, this volume). The distribution and composition of the Holocene turbidite layers and debris flows indicate that the deposits were derived locally from the uplifted hills (Karlin and Lyle, 1986; Karlin and

Zierenberg, chap. 7, this volume). Incorporation of volcanic glass and hydrothermal sulfide in some of the Holocene turbidites indicates that volcanism and hydrothermal activity are penecontemporaneous with the local redistribution of sediment (Karlin and Lyle, 1986; Karlin and Zierenberg, chap. 7, this volume). The available evidence indicates that tectonic and volcanic processes that formed the uplifted hills occurred during the Holocene, and that contemporaneous hydrothermal activity is related to these events (Karlin and Lyle, 1986; Karlin and Zierenberg, chap. 7, this volume).

EROSIONAL CHANNELS

The erosive power of the mass flows generated by slope failure on the uplifted sediment hills is evident in the canyons cut into the hill slopes. Many areas of the hill slopes display vertical scour grooves cut by downslope sediment transport. Locally, channels and valleys scallop the hill slopes and fault scarps.

An unexpected observation over large areas at both the SESCA and NESCA sites is the abundance of channels cut into sediment in areas with very gentle slopes, including areas that appear flat from submersible observation. Some channels could also be small grabens related to ridge extension. This explanation is likely for some of the depressions observed on the east side of the Central Hill and on Edifice REX in the NESCA area. In both of these areas, the grabenlike features are the site of massive sulfide mineralization. However, the most likely origin for the majority of the channels is formation due to erosion of the surface sediment. Locally derived turbidites and debris flows apparently have sufficient energy to erode several meters into the surface sediment. Some channels were observed at the base of the steep mass-wasting scarps that form the sides of uplifted sediment hills. The channels appear to be sufficiently mature that some have developed meander patterns displayed by curved banks with asymmetric profiles (fig. 10.3*B*). The lack of evidence of downchannel sediment transport may be related to the high background sedimentation rate, relative to mass-flow events. If the channels are forming by active erosion, their widespread occurrence and extensive development show that redistribution of sediment in this setting is an important process.

CURRENT EROSION

Submersible observations suggest that sediment deposition and redistribution is also locally controlled by bottom currents. A current meter mounted on DSV *Sea Cliff* recorded bottom currents as strong as 2 knots. High current velocities appear to be associated with major topographic features, especially the edges of the uplifted sediment hills, where sediment ripples (fig. 10.3*A*) and lag deposits of coarser sediment were observed. High concentrations of near-bottom suspended flocculant matter often reduced visibility during parts of some dives. Local areas near the edges of hill tops displayed subhorizontal sedimentary layering enhanced by differential erosion and exposed by bottom currents. Areas of slow sediment accumulation and (or) subtle erosion are also recognizable by the effects on bottom fauna. Current-swept areas have lower abundance of organisms, many large bioturbation mounds and burrows, and were generally described as extensively bioturbated by divers. However, extensive bioturbation in areas of normal sedimentation homogenizes surface sediment, producing a smoother bottom microtopography where the larger burrows and mounds have been degraded by burrowing and grazing organisms. We therefore reinterpret these as areas with lower bioturbation due to reduced availability of organic matter in area of reduced sediment accumulation or erosion.

HYDROTHERMAL PROCESSES

LOCALIZATION AND TIMING OF HYDROTHERMAL DISCHARGE

The spatial distribution of sulfide deposits within Escanaba Trough is indeterminate because only a small percentage of the sea floor has been observed. The known distribution of sulfide deposits shows a close spatial relationship to the volcanic edifices, even though mineralization is not found in areas of outcropping volcanic rock. Each of the four volcanic complexes investigated has associated sulfide mineralization, but the other volcanic edifices identified on figure 10.1 have not been investigated by methods capable of detecting sulfide mineralization. At three of the volcanic edifices, submersible dives found large sulfide deposits (SESCA, NESCA, and Edifice REX). A fourth volcanic edifice (latitude 40°53′ N.) has been investigated only by sediment coring, so the extent of sulfide mineralization is unknown. The data base for the flat turbidite-covered plains between the volcanic edifices is limited, but sediment cores collected away from the volcanic centers show no signs of previous or active hydrothermal discharge (Karlin and Lyle, 1986; Normark and others, chap. 6, this volume).

The largest massive sulfide deposits are located on the flanks of uplifted sediment hills developed above the volcanic edifices. The hills are interpreted as the consequence of igneous intrusion into the base of the sediment column, and the structural boundaries that accommodated uplift of the hills are interpreted as high-permeability, dilatant fault zones (Denlinger and Holmes, chap. 4, this volume) that focus hydrothermal discharge at the sea floor. If

this interpretation is correct, fluid discharge and massive sulfide formation should immediately postdate uplift of the hills. Information on the timing of sulfide deposition is limited. Although their degree of oxidative weathering and surface degradation shows that the deposits at different uplifted hills formed at different times, the deposits around any given hill all appear to be of the same relative age, except that the SW Hill in the NESCA area appears to have had two episodes of mineralization. We infer that each significant episode of sill intrusion and sediment uplift is followed by a pulse of hydrothermal discharge and massive sulfide formation. The observations provide qualitative support for this model. The old, weathered sulfide deposits associated with the 3170 Hill in the SESCA area are cut by mass-wasting channels and are partly buried by sediment due to degradation of the uplifted hill by sediment slumping; the young and active deposits associated with the Central Hill in the NESCA area occur on a hill that has been modified less by mass wasting and still displays relatively unmodified normal fault scarps. A more detailed record of the relative timing of uplift and hydrothermal activity should be contained in the sediment aprons surrounding the hills. Holocene turbidites derived from the 3170 Hill in the SESCA area contain hydrothermal pyrrhotite (Karlin and Zierenberg, chap. 7, this volume), but higher resolution dating of these units is needed to document the onset and duration of hydrothermal activity.

The scale of exposed massive sulfide is similar to that of ore lenses mined at massive sulfide deposits on land. Extrapolation of the geologic observations at the four volcanic complexes investigated suggests that each of the volcanic centers in Escanaba Trough (fig. 10.1) may be associated with massive sulfide mineralization. Mineralization in Escanaba Trough appears to be developed on a scale similar to that observed in major mining districts of ancient massive sulfide deposits, with numerous large sulfide deposits forming within a geologically short period of time along the rift axis of Gorda Ridge.

FLUID-SEDIMENT INTERACTION

The presence of a relatively low-permeability sediment blanket on the spreading axis results in a hydrologic and thermal regime that is different from sediment-free spreading centers (Davis and Becker, chap. 3, this volume). A significant proportion of heat loss at sediment-free spreading centers occurs by hydrothermal convection (Wolery and Sleep, 1976; Morton and Sleep, 1985), but low cross-stratal permeability at sediment-covered spreading centers restricts hydrothermal circulation to higher permeability zones, such as turbiditic sand beds and zones of tectonic or igneous disturbance. Conductive transfer of heat by diffusion through the insulating sediment blanket results in a high geothermal gradient in the sediment pile, which affects sediment diagenesis, lithification, and alteration or metamorphism. Sediment-fluid interaction at elevated temperatures within the sediment of Escanaba Trough may be responsible for altered pore fluid composition in DSDP Site 35 (Manheim and others, 1970; Normark and others, chap. 6, this volume).

Sediment-fluid interaction provides a primary control on the chemistry of hydrothermal fluid and precipitates in the Escanaba Trough sulfide deposits. The major-element, trace-element, and isotopic composition of hydrothermal fluid sampled from vents at the NESCA site are explained in terms of major input from sedimentary source material altered at high temperature (Campbell and others, chap. 11, this volume; Böhlke and Shanks, chap. 12, this volume). Escanaba Trough hydrothermal fluids have elevated alkali metal and boron contents, similar to fluids from the Guaymas Basin hydrothermal system (Campbell and others, chap. 11, this volume). Low $\delta^{11}B$ and radiogenic $^{87/86}Sr$ ratios are further indications of sediment interaction (Campbell and others, chap. 11, this volume). Alteration of organic matter in the sediment results in elevated ammonium and iodide relative to vent fluid from sediment-free spreading centers (Campbell and others, chap. 11, this volume). Terrigenous organic matter present in the sediment is the source material for hydrothermal hydrocarbon associated with the sulfide deposits (Kvenvolden and others, 1986; chap. 15, this volume). The only components of the hydrothermal fluid that require significant input from basaltic source material are ^{3}He (T. Gamo, oral commun., 1989, referenced in Campbell and others, chap. 11, this volume) and ^{13}C in CO_2 (B. Taylor, oral commun., 1989), both of which could be transported by a vapor phase separating from basalt, and therefore do not require direct basalt-fluid interaction.

Fluid-sediment interaction provides controls on fundamental fluid properties such as oxygen and sulfur fugacities and pH (Böhlke and Shanks, chap. 12, this volume; Koski and others, chap. 16, this volume). Pyrrhotite is the dominant sulfide mineral in Escanaba Trough and is accompanied by minor to trace amounts of arsenopyrite, löllingite, alabandite, and native bismuth, minerals that indicate formation at relatively low sulfur fugacity. Elevated concentration of arsenic, antimony, bismuth, lead and tin in massive sulfide, relative to deposits on sediment-free spreading centers, are derived from sediment (Koski and others, chap. 16, this volume). The lead isotope composition of Escanaba Trough massive sulfide overlaps the composition of Escanaba Trough sediment (LeHuray and others, 1988).

The geochemical data require extensive fluid-sediment interaction, but the data at hand are also consistent with fluid-basalt interaction as a contributing factor in evolution of fluid composition of the hydrothermal vents. Davis

and Becker (chap. 3, this volume) calculate the volume of magma necessary to supply the heat to form a large sulfide deposit and estimate that the lead and sulfur contained in the Escanaba Trough deposits could be leached from the volume of sediment that immediately underlies the deposits. Alternatively, if the temperature at depth in the sediment is sufficiently high, hydrothermal fluid may circulate in regionally extensive high-permeability turbidite layers and never penetrate significantly into basement. If this is true, the volcanic centers could serve principally as thermal and structural foci of hydrothermal discharge. The relative contribution of energy and material from the basaltic and sedimentary sources remains a critical unknown.

SULFIDE DEPOSITION

The larger sulfide deposits in Escanaba Trough that have not been degraded by sea-floor weathering are characterized by steep-sided constructional mounds composed predominantly of massive pyrrhotite. Chimneys occur on the tops of some mounds but are not abundant. Sulfate is less abundant than pyrrhotite in the bulk of the deposits, but barite chimneys appear to be more common than sulfide chimneys. Many fragments of massive sulfide have a layer of barite as an outer rim between the sulfide and seawater, and active high-temperature venting occurs from sinterlike carapaces of anhydrite and barite on massive sulfide mounds.

Growth of sulfide mounds at sea-floor hydrothermal sites is preceded by growth and replacement of sulfate chimneys by sulfide, followed by collapse of gravitationally unstable chimneys and incorporation of the chimney talus into a massive structure by sulfide cementation due to diffusely circulating hydrothermal fluid (Goldfarb and others, 1983). However, the large sulfide mounds in Escanaba Trough do not appear to be growing primarily by incorporation of chimney fragments, because active or relict chimneys are uncommon on the mounds and recognizable chimney fragments do not occur in samples collected from the mounds.

A surprising feature of the massive sulfide deposits is the degree of brecciation developed on and around the mounds. Many of the deposits are developed on slopes, and the constructional sulfide mounds are typically steep-sided. Some brecciation is clearly related to formation of sulfide talus; however, large sulfide slabs are common and are often found on gentle slopes. The surfaces of several mounds are cut by open fissures exposing fresh sulfide (fig. 10.8*B*). There is no evidence to suggest these fissures are tectonic as they do not occur in coherently oriented sets and are not observed in the surrounding sediment-covered areas. The fissures have the appearance of expansion joints. In other areas, sulfide crusts near the sediment-water interface have buckled to form small ridges (fig. 10.8*C*). These observations suggest that subsurface mineral precipitation within the mounds and the sediment causes fracturing and formation of sulfide breccia.

Samples recovered from the mounds contain numerous anastomosing zones of coarser grained pyrrhotite interpreted to have formed in solution channelways (Koski and others, chap. 16, this volume). High thermal conductivity of the massive sulfide mounds could enhance cooling of hydrothermal fluids percolating through the mounds, causing mineral precipitation within the mounds. The abundance of diffuse, relatively low temperature, metal-depleted (Campbell and others, chap. 11, this volume) hydrothermal fluids leaking from the mound surfaces may result in part from efficient cooling and metal precipitation occurring within the large mound structures, in contrast to sulfide precipitation within the turbulent plumes of high-temperature black smoker vents. Reactions in this zone of high thermal gradients are important in concentrating metals such as gold, silver, antimony, mercury, and lead near and in the sulfate-rich crust that form on the outer surfaces of sulfide mounds where hydrothermal fluid can mix with seawater. There is limited textural evidence for replacement of sulfate by sulfide at the interface between massive sulfide and seawater (Koski and others, chap. 16, this volume), but this process does not appear to be a quantitatively important growth mechanism for formation of pyrrhotite-rich massive sulfide mounds.

SUBSURFACE MINERALIZATION

Bottom-towed camera and submersible observations of sea-floor sulfide deposits are limited to surface exposures with the rare exception of fault scarps. Three-dimensional exposures in ancient massive sulfide deposits indicate that sub-sea-floor processes can be a fundamental control on mineralization (Zierenberg and Schmidt, 1987; Zierenberg and others, 1988). Limited evidence exists for shallow sub-sea-floor mineralization in Escanaba Trough, such as the sulfide crusts formed near the sediment-water interface discussed above (fig. 10.8*C*). One example is a small chimney constructed on a sulfide crust that formed below the sediment-water interface. The sulfide substrate incorporated sediment during its growth (Holmes and Zierenberg, 1990). Dredged samples include sediment clast breccias cemented with sulfide (Koski and others, 1988; Koski and others, chap. 16, this volume). Sediment cores have recovered vein and disseminated sulfide and barite mineralization in turbiditic sands (Normark and others, chap. 6, this volume; Zierenberg and Shanks, chap. 14, this volume). However, all these observations relate to processes occurring within the top few centimeters to meters of the sediment.

The location of sulfide deposits along the structural boundaries of uplifted sediment hills suggests that the deposits are underlain by fracture-controlled mineralization, similar to some ancient sediment-hosted massive sulfide deposits (Turner, 1990). The highly permeable silty and sandy turbidite layers within the sediment fill of Escanaba Trough may act as conduits for both hydrothermal fluid and seawater entrained in secondary circulation cells above the upper portions of vigorous hydrothermal discharge sites. Fluid mixing and (or) cooling within the permeable turbidite units could result in subsurface precipitation of sulfide and other hydrothermal minerals. We infer that the extensive surface expression of the massive sulfide deposits represents only part of the total volume of precipitated sulfide. However, the vertical extent and zoning of subsurface mineralization will remain a matter of speculation until the deposits can be investigated by drilling.

REFERENCES CITED

Abbott, D.H., Morton, J.L., and Holmes, M.L., 1986, Heat flow measurements on a hydrothermally-active, slow-spreading ridge: The Escanaba Trough: Geophysical Research Letters, v. 13, p. 678–680.

Atwater, T., and Mudie, J.D., 1973, Detailed near-bottom geophysical study of the Gorda Ridge: Journal of Geophysical Research, v. 78, p. 8665–8686.

Böhlke, J.K., and Shanks, W.C., III, Stable isotope study of hydrothermal vents at Escanaba Trough: Observed and calculated effects of sediment-seawater interaction, *in* Morton, J.L., Zierenberg, R.A., and Reiss, C.A., eds., Geologic, hydrothermal, and biologic studies at Escanaba Trough, Gorda Ridge, offshore northern California: U.S. Geological Survey Bulletin 2022, chapter 12 (this volume).

Campbell, A.C., German, C.R., Palmer, M.R., Gamo, T., and Edmond, J.M., Chemistry of hydrothermal fluids from the Escanaba Trough, Gorda Ridge, *in* Morton, J.L., Zierenberg, R.A., and Reiss, C.A., eds., Geologic, hydrothermal, and biologic studies at Escanaba Trough, Gorda Ridge, offshore northern California: U.S. Geological Survey Bulletin 2022, chapter 11 (this volume).

Clague, D.A., and Holmes, M.L., 1987, Geology, petrology, and mineral potential of the Gorda Ridge, *in* Scholl, D.W., Grantz, A., and Vedder, J.G., eds., Geology and resource potential of the continental margin of western North America and adjacent ocean basins-Beaufort Sea to Baja California: Houston, Circum-Pacific Council for Energy and Mineral Resources, Earth Science Series, v. 6, p. 563–580.

Correy, C.E., 1988, Laccoliths; Mechanics of emplacement and growth: Geological Society of America Special Paper 220, 110 p.

Davis, A.S., Clague, D.A., and Friesen, W.B., Petrology and mineral chemistry of basalt from Escanaba Trough, *in* Morton, J.L., Zierenberg, R.A., and Reiss, C.A., eds., Geologic, hydrothermal, and biologic studies at Escanaba Trough, Gorda Ridge, offshore northern California: U.S. Geological Survey Bulletin 2022, chapter 9 (this volume).

Davis, E.E., and Becker, Keir, Thermal and tectonic structure of the Escanaba Trough: New heat-flow measurements and seismic-reflection profiles, *in* Morton, J.L., Zierenberg, R.A., and Reiss, C.A., eds., Geologic, hydrothermal, and biologic studies at Escanaba Trough, Gorda Ridge, offshore northern California: U.S. Geological Survey Bulletin 2022, chapter 3 (this volume).

Denlinger, R.P., and Holmes, M.L., A thermal and mechanical model for sediment hills and associated sulfide deposits along the Escanaba Trough, *in* Morton, J.L., Zierenberg, R.A., and Reiss, C.A., eds., Geologic, hydrothermal, and biologic studies at Escanaba Trough, Gorda Ridge, offshore northern California: U.S. Geological Survey Bulletin 2022, chapter 4 (this volume).

Einsele, G., Gieskes, J.M., Curray, J., Moore, D.J., Aguayo, E., Aubry, M., Fornari, D., Guerrero, J., Kastner, M., Ketts, K., Lyle, M., Matoba, Y., Molina-Cruz, A., Niemitz, J., Rueda, J., Saunders, A., Schrader, H., Simoneit, B., and Vacquier, V., 1980, Intrusion of basaltic sills into highly porous sediments and resulting hydrothermal activity: Nature, v. 283, p. 441–445.

Goldfarb, M.S., Converse, D.R., Holland, H.D., and Edmond, J.M., 1983, The genesis of hot spring deposits on the East Pacific Rise, 21° N: Economic Geology Monograph 5, p. 184–198.

Grassle, J.F., and Petrecca, Rosemarie, Soft-Sediment hydrothermal vent communities of Escanaba Trough, *in* Morton, J.L., Zierenberg, R.A., and Reiss, C.A., eds., Geologic, hydrothermal, and biologic studies at Escanaba Trough, Gorda Ridge, offshore northern California: U.S. Geological Survey Bulletin 2022, chapter 17 (this volume).

Holmes, M.L., and Zierenberg, R.A., 1990, Submersible operations in Escanaba Trough, southern Gorda Ridge, *in* McMurray, G.R., ed., Gorda Ridge: A seafloor spreading center in the United States' Exclusive Economic Zone: New York, Springer-Verlag, p. 93–116.

Karlin, R., and Lyle, M., 1986, Sediment studies on the Gorda Ridge: Oregon Department of Geology and Mineral Industries Open-File Report O-86-19, 76 p.

Karlin, R.E., and Zierenberg, R.A., Sedimentation and neotectonism in the SESCA area, Escanaba Trough, southern Gorda Ridge, *in* Morton, J.L., Zierenberg, R.A., and Reiss, C.A., eds., Geologic, hydrothermal, and biologic studies at Escanaba Trough, Gorda Ridge, offshore northern California: U.S. Geological Survey Bulletin 2022, chapter 7 (this volume).

Koski, R.A., Shanks, W.C., III, Bohrson, W.A., and Oscarson, R.L., 1988, The composition of massive sulfide deposits from the sediment-covered floor of Escanaba Trough, Gorda Ridge: Implications for depositional processes: Canadian Mineralogist, v. 26, p. 655–674.

Koski, R.A., Benninger, L.M., Zierenberg, R.A., and Jonasson, I.R., Composition and growth history of hydrothermal deposits in Escanaba Trough, southern Gorda Ridge, *in* Morton, J.L., Zierenberg, R.A., and Reiss, C.A., eds., Geologic, hydrothermal, and biologic studies at Escanaba Trough, Gorda Ridge, offshore northern California: U.S. Geological Survey Bulletin 2022, chapter 16 (this volume).

Kvenvolden, K.A., Rapp, J.B., Hostettler, F.D., Morton, J.L.,

King, J.D., and Claypool, G.F., 1986, Petroleum associated with polymetallic sulfide in sediment from Gorda Ridge: Science, v. 234, p. 1231–1234.

Kvenvolden, K.A., Rapp, J.B., and Hostettler, F.D., Hydrocarbons in sediment from Escanaba Trough, *in* Morton, J.L., Zierenberg, R.A., and Reiss, C.A., eds., Geologic, hydrothermal, and biologic studies at Escanaba Trough, Gorda Ridge, offshore northern California: U.S. Geological Survey Bulletin 2022, chapter 15 (this volume).

LeHuray, A.P., Church, S.E., Koski, R.A., and Bouse, R.M., 1988, Pb isotopes in sulfides from mid-ocean ridge hydrothermal sites: Geology, v. 16, p. 362–365.

Lonsdale, P., and Becker, K., 1985, Hydrothermal plumes, hot springs, and conductive heat flow in the southern trough of Guaymas Basin: Earth and Planetary Science Letters, v. 73, p. 211–225.

Lonsdale, P., and Lawver, L.A., 1980, Immature plate boundary zones studied with a submersible in the Gulf of California: Geological Society of America Bulletin, v. 91, p. 555–569.

Manheim, L.D., Chan, K.M., and Sayles, F.L., 1970, Interstitial water studies on small core samples, Deep Sea Drilling Project, Leg 5, *in* McManus, D.A., and others, eds., Initial reports of the Deep Sea Drilling Project: Washington, U.S. Government Printing Office, v. 5, p. 501–511.

McManus, D.A., and others, 1970, Site 35, *in* McManus, D.A., and others, eds., Initial reports of the Deep Sea Drilling Project: Washington, U.S. Government Printing Office, v. 5, p. 165–172.

Morton, J.L., and Sleep, N.L., 1985, Mid-ocean ridge thermal model: Constraints on the volume of axial hydrothermal heat flux: Journal of Geophysical Research, v. 90, p. 11,345–11,353.

Morton, J.L., Holmes, M.L., and Koski, R.A., 1987, Volcanism and massive sulfide formation at a sedimented spreading center, Escanaba Trough, Gorda Ridge, northeast Pacific Ocean: Geophysical Research Letters, v. 14, p. 769–772.

Morton, J.L., Koski, R.A., Normark, W.R., and Ross, S.L., 1990, Distribution and composition of massive sulfide deposits at Escanaba Trough, southern Gorda Ridge, *in* McMurray, G.R., ed., Gorda Ridge: A seafloor spreading center in the United States' Exclusive Economic Zone: New York, Springer-Verlag, p. 77–92.

Morton, J.L., and Fox, C.G., Structural setting and interaction of volcanism and sedimentation at Escanaba Trough: Geophysical results, *in* Morton, J.L., Zierenberg, R.A., and Reiss, C.A., eds., Geologic, hydrothermal, and biologic studies at Escanaba Trough, Gorda Ridge, offshore northern California: U.S. Geological Survey Bulletin 2022, chapter 2 (this volume).

Morton, J.L., Zierenberg, R.A., and Reiss, C.A., Geologic, Hydrothermal, and biologic studies at Escanaba Trough: An introduction, *in* Morton, J.L., Zierenberg, R.A., and Reiss, C.A., eds., Geologic, hydrothermal, and biologic studies at Escanaba Trough, Gorda Ridge, offshore northern California: U.S. Geological Survey Bulletin 2022, chapter 1 (this volume).

Normark, W.R., Gutmacher, C.E., Zierenberg, R.A., Wong, F.L., and Rosenbauer, R.J., Sediment fill of Escanaba Trough, *in* Morton, J.L., Zierenberg, R.A., and Reiss, C.A., eds., Geologic, hydrothermal, and biologic studies at Escanaba Trough, Gorda Ridge, offshore northern California: U.S. Geological Survey Bulletin 2022, chapter 6 (this volume).

Riddihough, R.P., 1980, Gorda plate motions from magnetic anomaly analysis: Earth and Planetary Science Letters, v. 51, p. 163–170.

Ross, S.L., and Zierenberg, R.A., Volcanic geomorphology of the SESCA and NESCA sites, Escanaba Trough, *in* Morton, J.L., Zierenberg, R.A., and Reiss, C.A., eds., Geologic, hydrothermal, and biologic studies at Escanaba Trough, Gorda Ridge, offshore northern California: U.S. Geological Survey Bulletin 2022, chapter 8 (this volume).

Turner, R.J.W., 1990, Jason stratiform Zn-Pb-barite deposit, Selwyn Basin, Canada (NTS 105–0–1): Geological setting, hydrothermal facies and genesis, *in* Abbott, J.G. and Turner, R.J.W., Mineral deposits of the northern Canadian Cordillera, Yukon-Northeastern British Columbia, 8th IAGOD Symposium Field Excursion Guide Book, Trip 14: Geological Survey of Canada Open-File 2169, p. 137–175.

Vallier, T.L., Harold, P.J., and Girdley, W.A., 1973, Provenances and dispersal patterns of turbidite sand in Escanaba Trough, northeastern Pacific Ocean: Marine Geology, v. 15, p. 67–87.

Van Dover, C.L., Grassle, J.F., and Boudrias, M., 1990, Hydrothermal vent fauna of Escanaba Trough (Gorda Ridge), *in* McMurray, G.R., ed., Gorda Ridge: A seafloor spreading center in the United States' Exclusive Economic Zone: New York, Springer-Verlag, p. 285–287.

Wilson, D.S., 1989, Deformation of the so-called Gorda plate: Journal of Geophysical Research, v. 94, p. 3065–3075.

Wolery, T.J., and Sleep, N.L., 1976, Hydrothermal circulation and geochemical flux at mid-ocean ridges: Journal of Geology, v. 84, p. 249–275.

Zierenberg, R.A., and Schmidt, J.M., 1987, Subsurface mineralization and sulfur isotope systematics at the Red Dog Zn-Pb-Ag deposit, Noatak District, Alaska [abs.]: Geological Society of America Abstracts with Programs, v. 19, p. 905.

Zierenberg, R.A., Shanks, W.C., III, Seyfried, W.E., Jr., Koski, R.A., and Strickler, M.D., 1988, Mineralization, alteration and sub-seafloor metamorphism of the ophiolite-hosted Turner-Albright sulfide deposit, southwestern Oregon: Journal of Geophysical Research, v. 93, p. 4657–4674.

Zierenberg, R.A., Morton, J.L., Reiss, C.A., and Holmes, M.L., 1991, Preliminary results of the 1986 Sea Cliff dive program, Escanaba Trough: U.S. Geological Survey Open-File Report 91–137, 176 p.

Zierenberg, R.A., and Shanks, W.C., III, Sediment alteration associated with massive sulfide formation in the Escanaba Trough, Gorda Ridge: The importance of seawater mixing and magnesium metasomatism, *in* Morton, J.L., Zierenberg, R.A., and Reiss, C.A., eds., Geologic, hydrothermal, and biologic studies at Escanaba Trough, Gorda Ridge, offshore northern California: U.S. Geological Survey Bulletin 2022, chapter 14 (this volume).

Section II:

Hydrothermal and Geochemical Studies

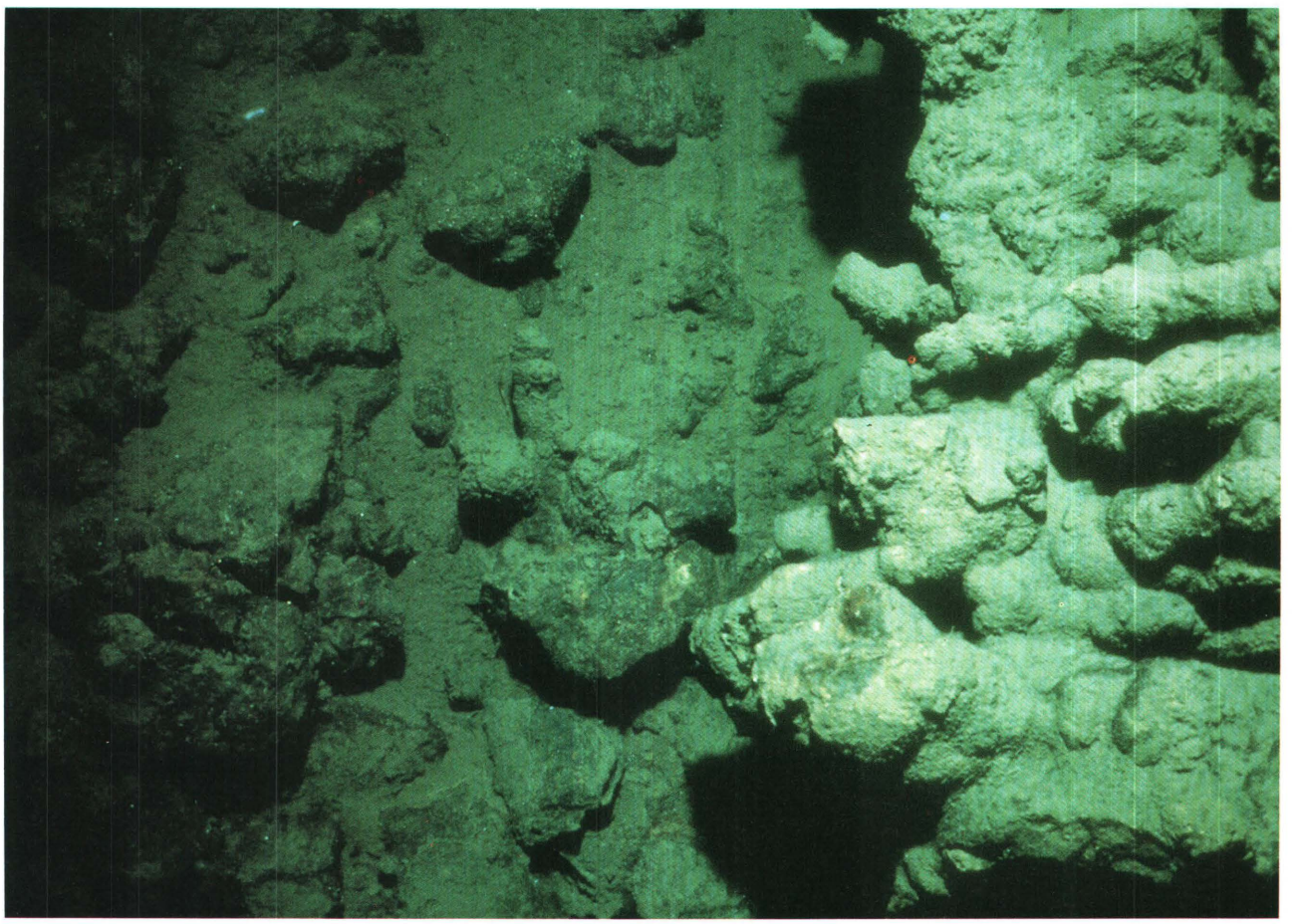

View looking down on dark massive sulfide capped by a ledge of lighter colored barite with inactive barite chimneys projecting upward. This photo was provided by C. Van Dover from a camera mounted on the *Alvin* submersible; field of view is approximately 2 m across.

Chapter 11. Chemistry of Hydrothermal Fluids from Escanaba Trough, Gorda Ridge

By Andrew C. Campbell,[1, 2] Chris R. German,[1, 3] Martin R. Palmer,[1, 4] Toshitaka Gamo,[5] *and* John M. Edmond[1]

CONTENTS

ABSTRACT

Hydrothermal fluids from the sediment-covered Escanaba Trough are substantially different from sediment-starved mid-ocean ridge (MOR) hot springs. They are enriched in K, Sr, Rb, Cs, B, and Tl, depleted in sulfide-forming metals, have lighter B isotope ratios, and more radiogenic $^{87}Sr/^{86}Sr$ ratios than MOR vent fluids. Similar trends are observed for the sediment-hosted Guaymas Basin vents; however, the Escanaba Trough fluids, which interact with a more felsic sediment, have higher Rb, Cs, and B concentrations, lower $\delta^{11}B$ values, and more radiogenic $^{87}Sr/^{86}Sr$ ratios. In general, sediment-hosted systems have higher pH, alkalinity, NH_4, I, and Br compared to sediment-starved MOR systems. The presence of less organic matter, sulfur, and carbonate in Escanaba Trough sediments relative to the Guaymas Basin produces lower pH, total alkalinity, NH_4, and H_2S in the fluids. However, I is significantly higher in the Escanaba Trough solutions due to the higher I/C ratio of the sediments compared to the Guaymas Basin. The Escanaba Trough hot-spring waters, perhaps because of their relatively alkaline composition and low end-member temperature of 217°C, have the lowest transition-metal content of any end-member vent fluid yet sampled. They likely reflect the waning phase of hydrothermal activity accompanying the cooling of a magmatic heat source.

INTRODUCTION

More than a decade has passed since the discovery of submarine hydrothermal vents at the Galápagos Rift spreading center (Corliss and others, 1979). Hot springs have now been sampled in a wide variety of tectonic settings, including sediment-starved systems along the slow rifting Mid-Atlantic Ridge (MAR) (Campbell and others, 1988a), at intermediate and fast spreading parts of the East Pacific Rise (EPR) (Michard and others, 1984; Von Damm and others, 1985a; Campbell and others, 1988b; Bowers and others, 1988), at the intermediate spreading Juan de Fuca Ridge (JdF) (Von Damm and Bischoff, 1987; Massoth and others, 1989), from the Marianas Trough and Okinawa Trough back-arc basins (Campbell and others, 1987; Sakai and others, 1990), and sediment-hosted systems in Guaymas Basin, Gulf of California (Von Damm and others, 1985b, Campbell and others, 1988b), as shown on figure 11.1. This wide variety of environments allows us to compare and contrast the effects of depth, spreading rate, and reaction substrate on the resulting solution chemistry.

Until the expedition to Escanaba Trough in June 1988, Guaymas Basin was the only sediment-hosted system sampled for hydrothermal fluids (Campbell and others, 1988c). Time series studies of the Guaymas Basin vents have shown that the inter-field variations in fluid chemistry, as in

[1] Massachusetts Institute of Technology, Cambridge, Massachusetts
[2] Present address: U.S. Nuclear Regulatory Commission, Washington, D.C.
[3] Present address: Institute of Oceanographic Sciences, Wormley, Godalming, Surrey GU8 5UB, England
[4] Present address: University of Bristol, Bristol B58 1RJ, England
[5] Ocean Research Institute, University of Tokyo, Tokyo, Japan

sediment-starved systems, have remained stable for many years (Campbell and others, 1988b). A number of characteristics of the Guaymas Basin fluids, such as enrichment in alkali metals and ammonium, high pH and total alkalinity, and depletion in sulfide-forming metals, were attributed to the interaction of the hydrothermal fluids with the sediment column (Von Damm and others, 1985b).

This paper presents the results of hydrothermal fluid chemistry studies of the Escanaba Trough vents. This work provides an important comparison to the Guaymas Basin and mid-ocean ridge (MOR) vents and allows us to draw some general conclusions about fluid chemistry in sediment-hosted hydrothermal systems in contrast to sediment-starved vent systems. One important question is whether differences in the sediment composition at the two sites result in significant differences in fluid chemistry. Another question is to determine which elements can be used as indicators of variations in reaction substrate. In particular, one goal is to ascertain if the extent of fluid-sediment reaction can be determined by the isotope systematics and (or) chemical variations in the vent fluids. The world's largest massive sulfide deposits are sediment hosted; this work allows us to better understand the formation of these deposits.

ACKNOWLEDGMENTS

We wish to acknowledge the expertise and professionalism of the DSV *Alvin* group, chief pilot Ralph Hollis, Captain Gary Chiljean, and the officers and crew of the R/V *Atlantis II*. The comments and suggestions of J. Gieskes, T. Bowers and reviewers R. Zierenberg, K. Von Damm, and J. Bischoff greatly improved the manuscript. Funding for this work was provided by the National Science Foundation through grant OCE-8721793.

GEOLOGIC SETTING

Escanaba Trough, located on the southern part of Gorda Ridge (fig. 11.1), is a slow spreading rate center (2.4 cm/yr) possessing a typical deep axial valley (Atwater and Mudie, 1973). South of about latitude 41°15′ N. it is filled with several hundred meters of sediment derived from both the Klamath and Columbia river drainages (Vallier and others, 1973). The present sedimentation rates are about 10 to 20 cm/kyr, although they have been much higher in the past (McManus and others, 1970). The sediment consists

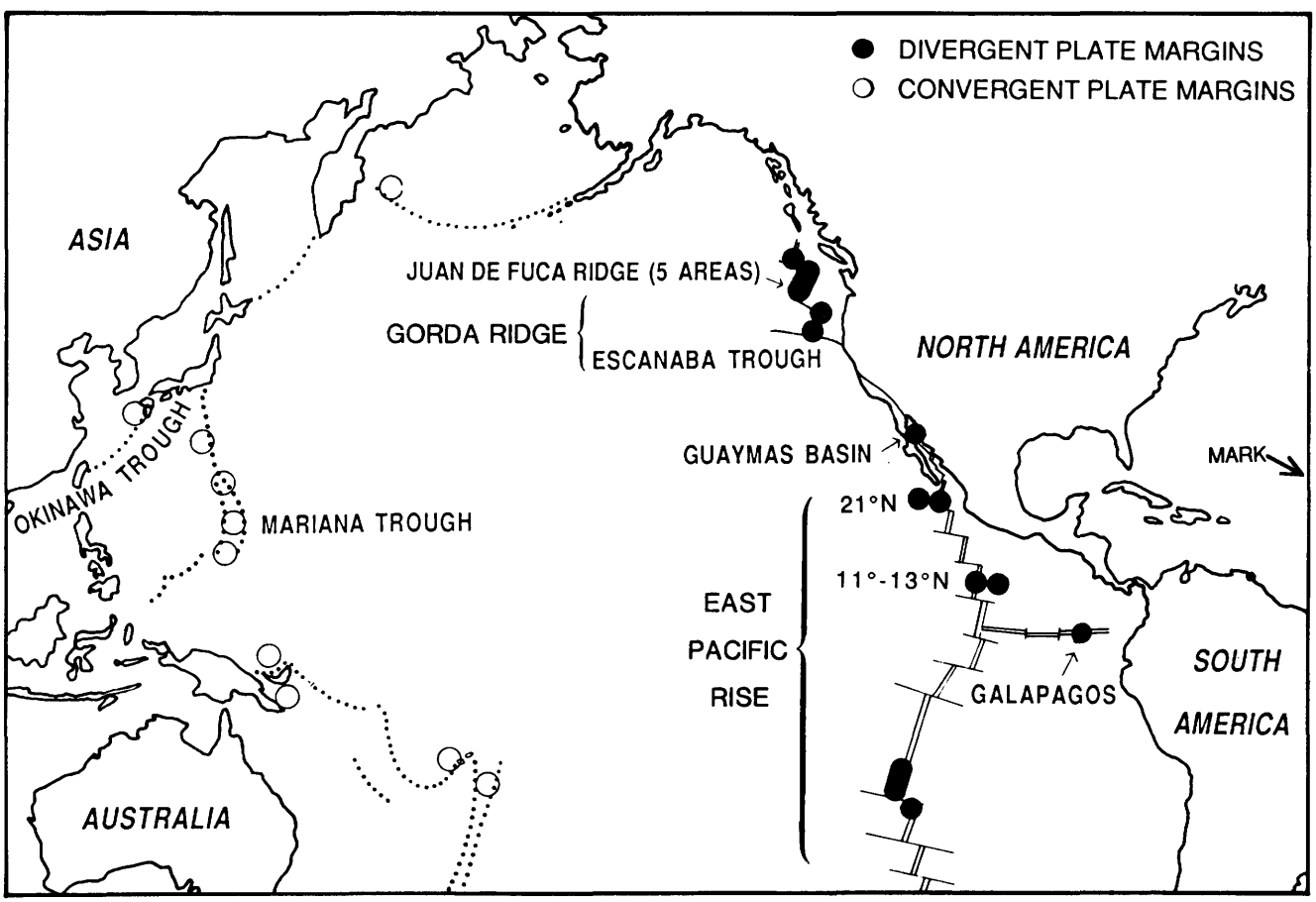

Figure 11.1. Locations of submarine hydrothermal vent sites discussed in text. Mid-Atlantic Ridge Kane (MARK) site is located off the figure (arrow).

mainly of hemipelagic and turbidite material, and smaller amounts of biological debris from the surface waters (Karlin and Lyle, 1986, McManus and others, 1970). Turbidite flows from Astoria Fan travel southward along the coast of Oregon through the Blanco Gap into Gorda Basin off northern California and make their way into Escanaba Trough from the south (Atwater and Mudie, 1973; Vallier and others, 1973). Thus felsic detritus from the upper Columbia and Snake rivers constitutes a significant fraction of the sedimentary fill in Escanaba Trough. The mineralogical composition of these sediments in comparison to those in Guaymas Basin is presented in table 11.1. Gravity cores taken in the area have about 1 to 2 percent carbonate, 0.1 to 0.3 percent sulfur, and 4 to 14 percent opaline silica (Karlin and Lyle, 1986). The carbonate content of the surface sediments is about 0.5 percent or less, and the organic carbon content is about 1 percent or less (Magenheim and Gieskes, chap. 13, this volume).

A series of volcanic structures, displaying both intrusive and extrusive magmatism, occur at intervals of about 15 km within this valley, and massive sulfide deposits are found at numerous locations associated with these features (Morton and others, 1990). In June 1988 a DSV *Alvin* diving program was conducted at the northern Escanaba (NESCA) site (Morton and others, 1990) between latitude 40°58′ and 41°04′ N. Massive sulfide deposits and hydrothermal venting activity were discovered at several places on an intra-rift hill at latitude 41°00′ N., longitude 127°29.3′ W. (fig. 11.2). The greatest amount of hydrothermal activity was found at a large mound structure where fluids averaging 217±2°C were debouching from distinct orifices and also flowing diffusely from sulfide rubble. Several low-temperature (13°C to 18°C) vents were also found in the immediate vicinity of this mound. About 275 meters west, a smaller active mound was found where 108±2°C fluids emanated from beneath a thicket of apparently dying tube worms (fig. 11.2). Fluid samples were obtained from both vent sites. A third area on the southeast side of Central Hill (fig. 10.2) has extensive sulfide mineralization, abundant clams, and bacterial mats and was found to have diffuse, presumably low-temperature fluid issuing from a small mound (no fluid samples were obtained).

Table 11.1. Escanaba Trough and Guaymas Basin sediments: selected chemical and mineral components.

[Escanaba data: Magenheim and Gieskes (chap. 13, this volume); Rex and Murray (1970); Karlin and Lyle(1986). Guaymas data: Kastner (1982); Niemitz (1982)]

Weight percent	Escanaba Trough	Guaymas Basin
Organic carbon	0.3 – 0.5	2 – 4
Sulfur	.08 – .2	1 – 2
$CaCO_3$	1 – 3	10 – 15
Opaline silica	5 – 14	30 – 50
Detrital clay	42 – 65	30 – 45
Feldspar	12 – 20	4 – 15
Quartz	20 – 25	3 – 10

METHODS

SAMPLING AND ANALYTICAL TECHNIQUES

The methods used for field collection and major-element analyses in this work have been reported previously (see Campbell and others, 1988a,b, and Von Damm and others, 1985a,b). High-temperature fluid samples were collected in titanium syringe bottles deployed from DSV *Alvin* (Von Damm and others, 1985a). Measurements of pH and alkalinity were made as soon as possible on board the support ship R/V *Atlantis II* to avoid oxidation and precipitation artifacts, which drastically change the proton balance of the solutions. Hydrogen sulfide samples were drawn anaerobically into stoppered glass vials back-filled with argon. A subsample (100 μL) from each vial was fixed with reagents for the methylene blue dissolved sulfide technique (Cline, 1969) and measured on a spectrophotometer the next day. Dissolved silica was measured spectrophotometrically by the molybdate blue technique (Strickland and Parsons, 1968). The major elements were analyzed in the shore laboratory by an array of routine techniques (see Campbell and others, 1988a,b, and Von Damm and others, 1985a,b). Some of the alkali and alkaline-earth elements (Rb, Cs, and Sr) were measured by isotope dilution–thermal ionization mass spectrometry (ID-TIMS), and $^{87}Sr/^{86}Sr$ was measured by isotope ratio TIMS (Palmer and Edmond, 1989a,b). Boron and $\delta^{11}B$ were measured by the method of Spivack and Edmond (1987). Thallium and other trace metals were analyzed by inductively coupled plasma–mass spectrometry (ICP-MS) multielement standard additions.

Total Br and I were analyzed by ICP-MS; details of the Br analyses are given in Campbell and Edmond (1989). A significant memory effect in the sample introduction system proved to be a problem with the iodide determinations, and the previous I data are about 10 to 12 percent low. To solve this problem, a flow injection technique was adopted to minimize the amount of sample introduced into the tubing and glassware and to allow memory blank correction of each sample injection. Samples were prepared by making 1:100 dilutions in 0.25 percent HCl (from triply distilled acid). Standards were made both in ambient seawater at 1:100 dilution and also in a pure 0.25 percent HCl matrix. No difference in response was observed for these two standards, hence suppression of the sample signal due to salinity variations is not a problem. An injection volume of 0.2 mL was used, and each sample and standard was run in duplicate. A mid-range standard was run every three samples, and all data were normalized to a constant

monitor signal to correct for drift in instrumental response (approximately 9 percent in 4 hours). The signal was monitored with respect to time at 127 atomic mass units (amu). The peak area was determined by integrating from the onset of the signal to where the remaining tail of the peak was less than 2 percent of the total peak area. Blanks were determined by integrating a similar time period just before onset of the sample signal. Standard additions on some samples gave the

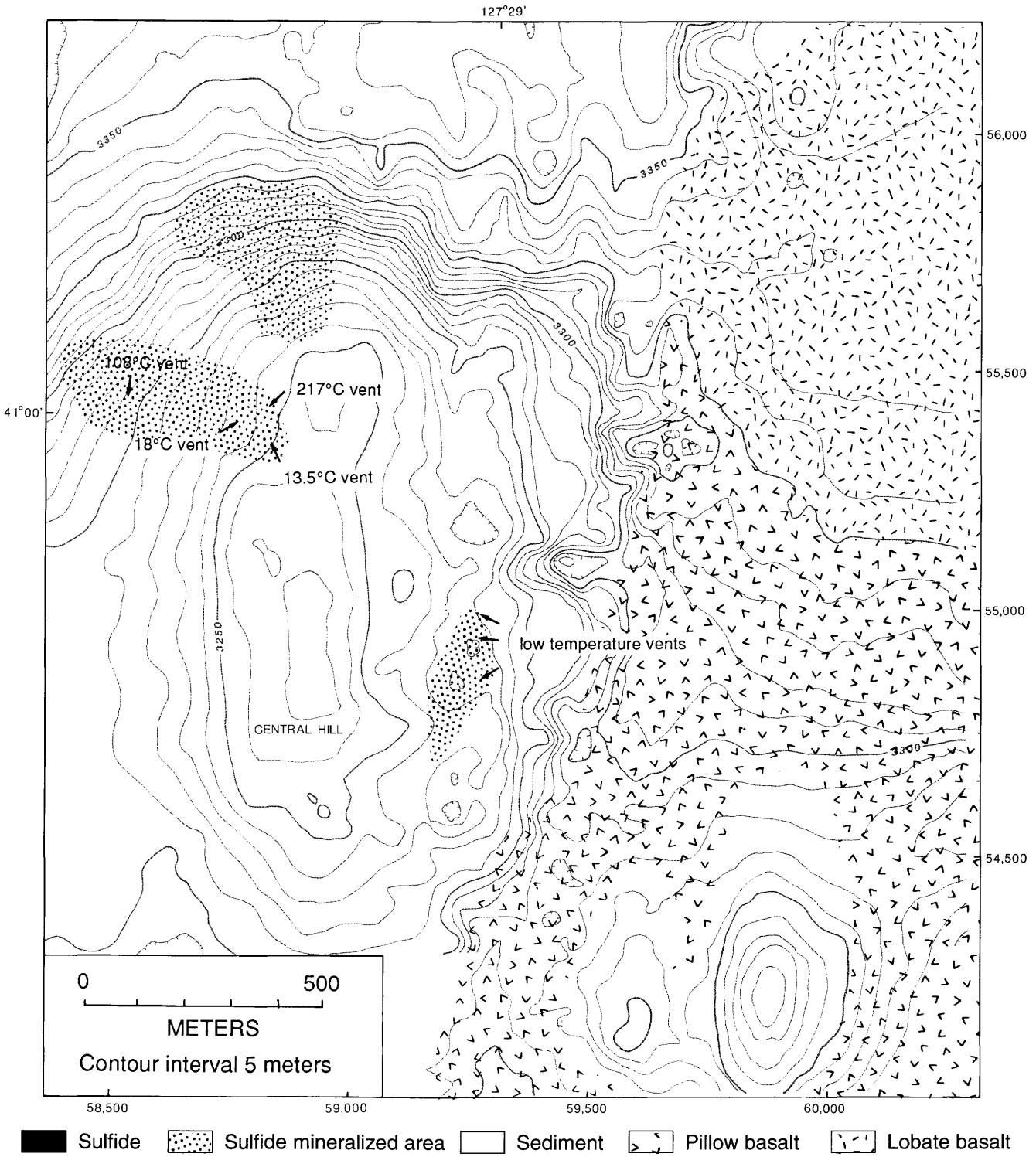

Figure 11.2. Bathymetric map of active hydrothermal vents and associated massive sulfide deposits at Central Hill in NESCA area (modified from Zierenberg and others, chap. 10, this volume). Fluid samples were obtained from the 217°C and 108°C vents. Numbers along right and bottom give coordinates of local transponder net (in meters). Hachures indicate area of closed low.

same values as those calculated from the calibration curve. Reproducibility was better than ±2 percent.

CALIBRATION OF DSV *ALVIN* HIGH-TEMPERATURE PROBES

Submarine vent fluid temperatures have been of great interest since the discovery of high-temperature venting activity at the 21° N. East Pacific Rise site (Spiess and others, 1980). Measured fluid temperatures there were remarkably close to the "end-member" temperature predicted from studies of the highly diluted, low-temperature Galápagos Rift vent fluids (Edmond and others, 1979). Campbell and others (1988a) showed that the vast majority of measured hot-spring temperatures tend to a maximum around 355°C and only a few values have been reported at higher temperatures. However, experimental studies of hydrothermal fluid-basalt reactions in the laboratory are unable to reproduce the compositions of vent fluids below about 380°C (Berndt and others, 1989). Furthermore, invoking phase separation to explain different vent salinities requires substantial cooling of the fluids (as much as 200°C for the Escanaba Trough fluids) (Bischoff and Rosenbauer, 1984). However, the high flow rates of "black smoker" vents precludes large-scale conductive cooling of the fluids (Converse and others, 1984; Macdonald and others, 1980; Sleep and Wolery, 1978).

Previous attempts to calibrate the DSV *Alvin* high-temperature (HT) probes using the melting points of metals have suggested they are systematically biased to low readings (Delaney and others, 1989; Bischoff and Rosenbauer, 1984). In the absence of any published details, it is difficult to assess these results. Therefore, an experiment was conducted during the expedition on June 2, 1988, to establish a simple, at-sea HT probe calibration and determine the accuracy of the devices. The details are published here to facilitate future calibrations by other researchers.

The calibration was done with a gas chromatograph oven (Hewlett Packard model 5710a; fig. 11.3), which can be quickly set to any temperature between 10°C above ambient and 400°C and is stable to ±0.5°C. A "melting-point" thermometer (−10°C to 360°C) and an air thermocouple probe (0°C to 816°C), both NBS traceable, were used as reference devices. The calibration of the mercury thermometer (Kessler model 2060-6M), which is accurate to ±0.5°C, was checked in an ice bath and a beaker of boiling water. The air thermocouple probe (Fluke model 80PK-4 Type K air probe) has a stated accuracy of ±1.1°C up to 275°C and ±0.4 percent above 275°C. It was connected to a Fluke model 80TK thermocouple module that converts the output of the thermocouple to a temperature readout on a digital voltmeter (1 millivolt/°C). The module has an electronic reference junction, which was calibrated at room temperature. Disagreement between the mercury thermometer and the air probe was less than ±1°C up to 360°C (upper limit of the thermometer; see table 11.2). An oven thermocouple graduated in 10°C increments agreed with the reference probes.

Two HT probes (SN 18HT and SN 25HT) were installed on DSV *Alvin* according to standard operating procedures and were subsequently used on this and other expeditions through the summer of 1988. Each probe consists of a "type K" Chromel-Alumel thermocouple that is mounted in a steel sheath attached to the pressure case containing the electronics package. The voltage signal is converted to a frequency, transmitted through the submarine pressure sphere via a 20-foot-long cable, and recorded on the data logger. The probes use an electronic reference junction and are electronically calibrated at Woods Hole Oceanographic Institute against voltages corresponding to temperatures of 0°C and 400°C (J. Aikens, DSV *Alvin* group, oral commun., 1988). The DSV *Alvin* probe, the air thermocouple probe, and the mercury thermometer were mounted so that all three were inserted about 3 inches into the oven cabinet (fig. 11.3). Glass wool insulation was packed around the holes. Probe SN 25HT was wrapped

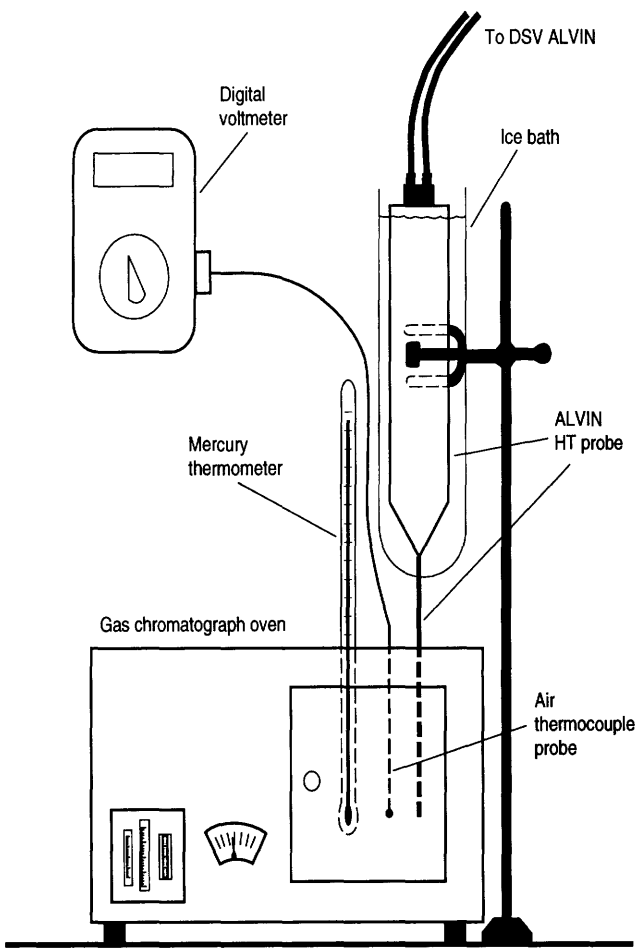

Figure 11.3. Schematic drawing of experimental set-up for at sea calibration of DSV *Alvin* high temperature (HT) probes.

Table 11.2. Calibration data for DSV *Alvin* high-temperature probes.

[—, not measured]

Mercury thermometer (°C)	Air thermocouple (°C)	*Alvin* probe (°C)	Ambient (°C)	Corrected *Alvin* (°C)
DSV *Alvin* probe SN 25HT in ambient air				
109	110	90	21	111
196	197	176	21	197
264	264	244	21	265
323	322	300	21	321
352	353	334	21	355
—	393	373	21	394
DSV *Alvin* probe SN 18HT in ice bath				
—	128	125	0	125
—	196	196	0	196
—	274	276	0	276
—	333	335	0	335
—	353	357	0	357
—	396	398	0	398

in a thick rubber sheet that acted as an insulation blanket protecting it from air currents. The reading displayed in the sub was corrected for ambient temperature (table 11.2). Probe SN 18HT was mounted in a fresh water and ice bath at 0°C, and no correction of the readout value was necessary (fig. 11.3). Six calibration points were measured for each probe; three below 300°C and three between 300°C and 400°C.

RESULTS

FLUID TEMPERATURES

The results of the HT probe calibrations in table 11.2 and figure 11.4 demonstrate that their accuracy is better than ±1 percent up to at least 400°C, which is within the stated National Bureau of Standards (NBS) specifications for this type of thermocouple. The precision of the probes, as determined by replicate measurements, is generally about ±2 to 3°C. Differences in temperature of less than about 4°C to 5°C are within the 2-standard-deviation error margin. This calibration demonstrates that the DSV *Alvin* HT probes are not biased to low temperature readings and no intrinsic flaw exists in their design. Recent at-sea calibration of three other DSV *Alvin* HT probes (Mid-Atlantic Ridge Vent Program, January 1990) have confirmed these results. Temperature measurements of vent fluids using this system are true to about ±1 percent when corrected for bottom water values, but only if the electronic calibration is done properly and no electronic or other technical problems occur. One such problem is accidental heating of the pressure case during measurement. Although gentle heating simply reduces the reading by the difference between 0°C and the true case temperature (see table 11.2), more intense heating causes the electronics to behave improperly, and seemingly stable high temperatures have been observed (Campbell and others, 1988b).

The temperatures measured at the main active hydrothermal mound (fig. 11.2) varied from 217°C near the top to 215°C closer to the base. On a subsequent dive, fluids were measured at 216°C. This variability is typical of measurements of the same vent at other hot springs and, although these differences may be real, they are within the error margin of the HT probes. Two months after the expedition, the same mound was visited by DSV *Sea Cliff*, which measured a temperature of 220°C with a probe constructed and calibrated by the DSV *Alvin* group at Woods Hole (Reiss and others, 1992). The mean fluid temperature and standard deviation of the measurements at this mound is thus 217±2°C. Some fluid samples collected from this mound had magnesium concentrations less than 2 mmol/kg. Therefore, this is an end-member temperature and is not due to subsurface dilution by seawater. In contrast, fluid samples obtained from an active mound 275 meters away (see fig. 11.2), which had a measured temperature of 108±2°C, contain 50 percent or more seawater Mg. Mixing of seawater and hydrothermal fluids apparently occurs within the mound or subsurface region at this site, as discussed later.

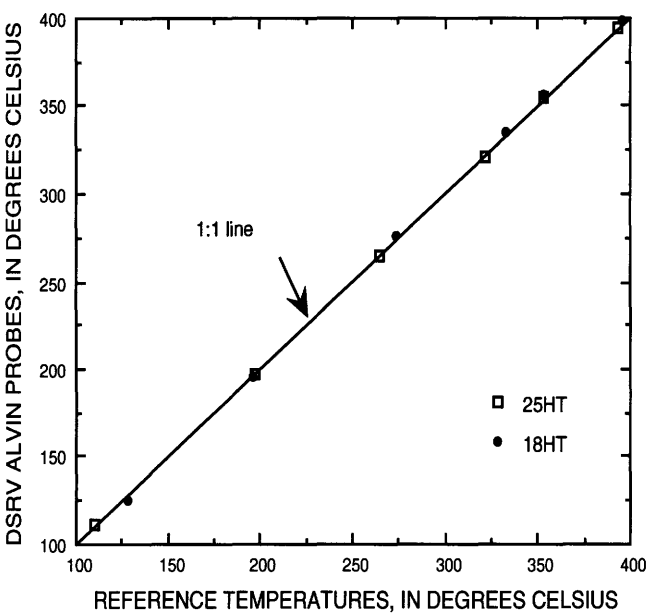

Figure 11.4. DSV *Alvin* high temperature (HT) probe readings versus reference thermocouple and mercury thermometer readings. Measured HT probe readings plot along 1:1 line. Hence, HT probes have no intrinsic bias with respect to true temperature and are completely linear over temperature ranges of all submarine hydrothermal vents sampled to date.

FLUID CHEMISTRY

The major-element concentrations of individual samples are plotted against magnesium in figures 11.5 and 11.6. The zero-Mg intercept of the regression line (drawn on the figures) for each element is the end-member concentration. We assume that any significant amount of Mg in the sample is due to seawater entrainment during sampling or subsurface mixing prior to venting of the fluids (Von Damm and others, 1985a). It is important to note that small, non-zero Mg concentrations in the end-member fluid (on the order of 1–3 mmol/kg) will not generate a significant error in the calculated end-member values of other elements. Within the scatter of the data, the samples from the 108°C vent plot along the same regression lines as the 217°C vent, except for silica (fig. 11.6*A*) and the alkali elements. This suggests a common fluid source at depth for these two mounds with some subsurface mixing and precipitation of alkali-containing silicates at the second mound before the fluids are vented. The end-member data for Escanaba Trough are compared in table 11.3 with the Guaymas Basin vent fields (Campbell and others, 1988b) and sediment-starved MOR vents at the Mid-Atlantic Ridge Kane (MARK) site (Campbell and others, 1988a) and the latitude 11° to 13° N. East Pacific Rise (EPR) sites (Bowers and others, 1988).

The pH and total alkalinity of hydrothermal vent fluids do not form linear mixing lines with respect to seawater because the process is essentially a weak acid–weak base titration. To estimate end-member values, we fit the pH and total alkalinity data with third-order and second-order polynomials, respectively (fig. 11.5*A,B*). The end-member pH obtained by the fit is 5.3, and the total alkalinity is 3.2 meq/kg. These are lower values than the Guaymas Basin vents, which are buffered at a pH of 5.9 and have a total alkalinity of about 9 meq/kg. Both systems have a higher total alkalinity than seawater (2.3 meq/kg). Sediment-starved hydrothermal vents have pH values that range from 3 to 4 and possess negative total alkalinities, indicating an excess of protons over proton acceptors in solution.

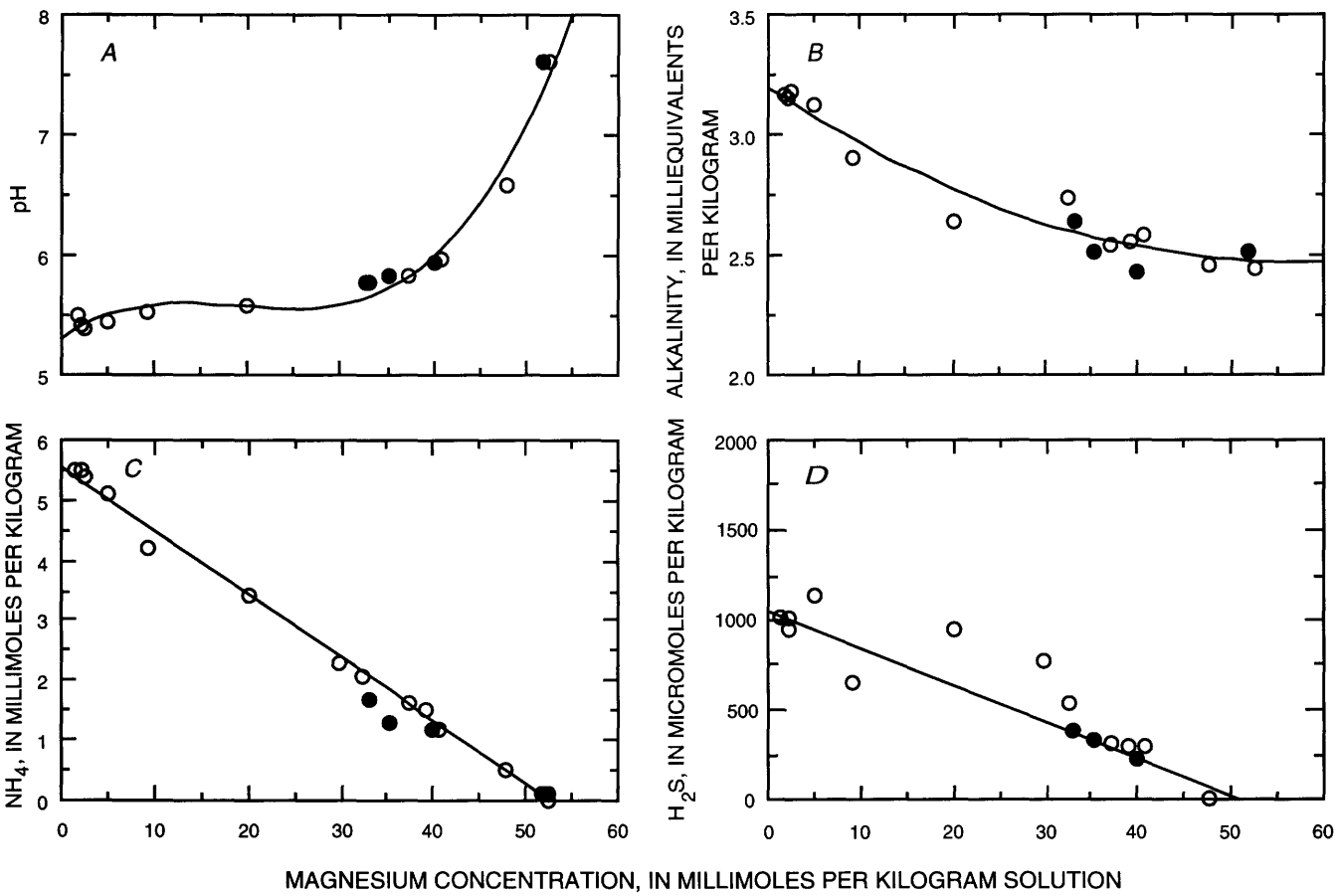

Figure 11.5. Magnesium content versus (*A*) pH, (*B*) total alkalinity, (*C*) ammonium, and (*D*) hydrogen sulfide in Escanaba Trough vent fluids. Open circles are data from 217±2°C vent, closed circles are data from 108±2°C vent. The pH data are fit with a third-order polynomial (r^2=0.979) and the alkalinity data are fit with a second-order polynomial (r^2=0.947). All other data are fit with linear regressions (NH_4: r^2=0.997; H_2S: r^2=0.99).

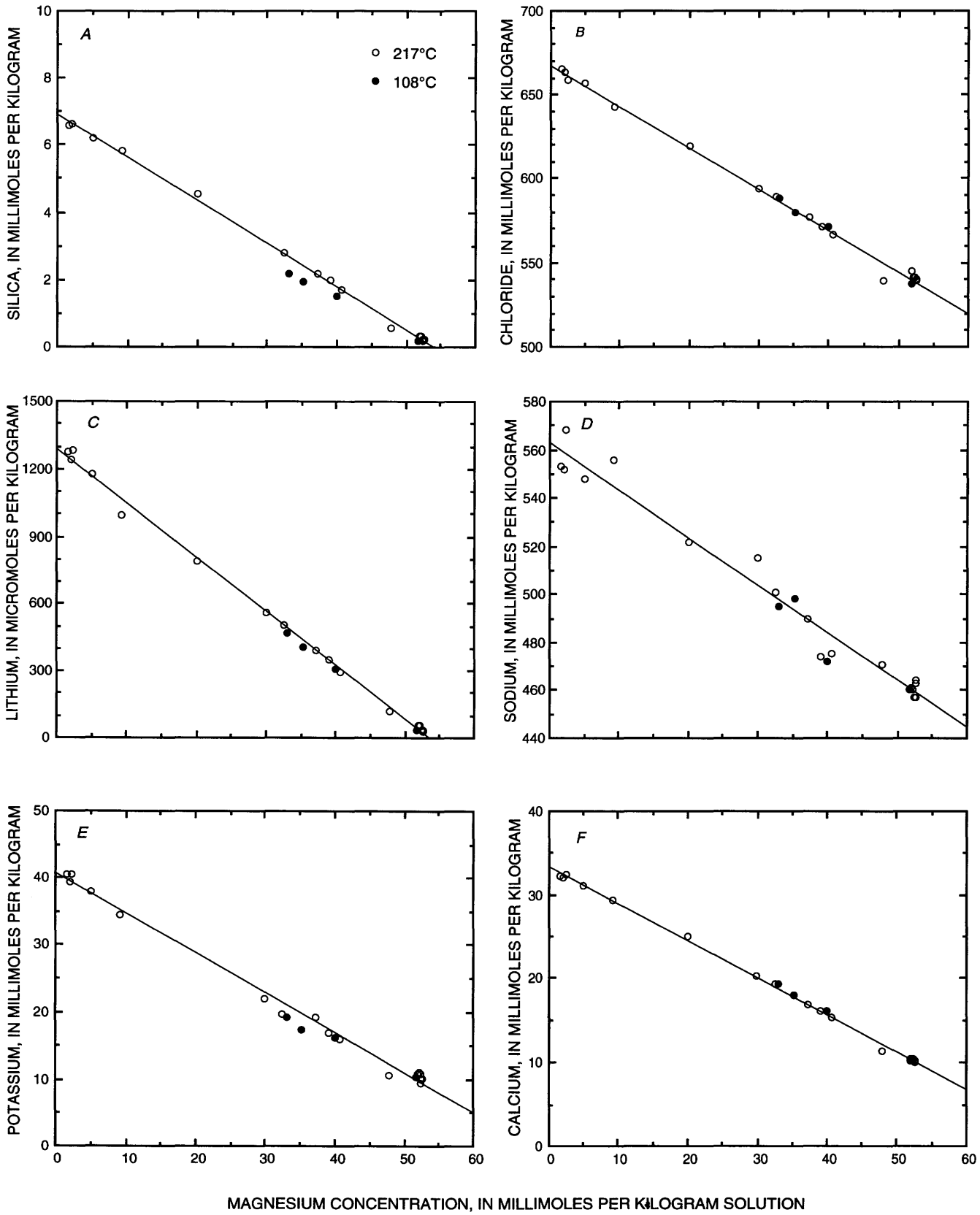

Figure 11.6. Magnesium concentration versus (*A*) dissolved silica, (*B*) chloride, (*C*) lithium, (*D*) sodium, (*E*) potassium, and (*F*) calcium in Escanaba Trough vent fluids. Open and closed circles as in figure 11.5. All data are fit with linear regressions (that for silica only includes samples from 217°C) with r^2 values as follows: $Si(OH)_4$=0.999; Cl=0.998; Li=0.997; Na=0.974; K=0.994; and Ca=0.999.

Table 11.3. End-member data for major and minor elements from ridge hydrothermal vents.

[Data sources in text. Na calculated from charge balance. Concentration units in moles per kilogram solution. MAR, Mid-Atlantic Ridge; EPR, East Pacific Rise]

	Escanaba Trough	Guaymas Basin, south field	Guaymas Basin, east hill	MAR, MARK '86	EPR, 11°–13°N
Fluid temperature (°C)	108 – 217	250 – 308	290	335 – 350	347 – 380
pH (NBS, 23°C)	5.4	5.9	5.9	3.7 – 3.9	3.1 – 3.7
Alkalinity (meq/kg)	3.1	9.6	8.9	–.06 to -.24	–.28 to -1.02
NH_4 (mmol/kg)	5.6	15.3	13	<.01	<.01
H_2S (mmol/kg)	1.1 – 1.5	6	4.4	5.9	2.9 – 12.2
$Si(OH)_4$ (mmol/kg)	5.6 – 6.9	12 – 13.5	13.8	18.2	14.3 – 21.9
Cl (mmol/kg)	668	581 – 604	603	559	338 – 760
Br (µmol/kg)	1,179	1,054 – 1,117	1,063	847	533 – 1,242
Br/Cl×1000	1.76	1.8 – 1.85	1.76	1.52	1.58 – 1.67
I (µmol/kg)	99	80 – 83	65	<1	<1
Li (µmol/kg)	1,286	993	849	843	484 – 884
Na (mmol/kg)	560	472	488	510	290 – 596
K (mmol/kg)	34 – 40.4	44.1	41	23.6	18.7 – 32.9
Rb (µmol/kg)	80 – 105	60	52	11	15 – 25
Cs (µmol/kg)	6.0 – 7.7	5.5 – 6.0	5.2	.18	.117 – .195
Tl (nmol/kg)	110	114	104	34	23 – 40
B (mmol/kg)	1.71 – 2.16	1.6 – 1.68	1.55	.52	.428 – .468
$\delta^{11}B$	11.5 – 10.1	17.4 – 19.6	16.5 – 23.2	26.8	31.5 – 36.8
Ca (mmol/kg)	33.4	27.7	33.8	10	10.6 – 54.8
Sr (µmol/kg)	209	158	191	50	40 – 205
$^{87}Sr/^{86}Sr$	.7099	.7059	.7052	.7028	.7039 – .7046
Mn (µmol/kg)	10 – 21	217	128	491	742 – 2,932
Fe (µmol/kg)	0 – 10	8 – 24	47	2,180	2,640 – 10,760

The Escanaba Trough fluids have 5.6 mmol/kg of NH_4 (fig. 11.5*C*) and 1.1 mmol/kg H_2S (fig. 11.5*D*). These are significantly lower than the Guaymas Basin vents, where NH_4 ranges from 10 to 14 mmol/kg and H_2S varies from 4.4 to 6 mmol/kg (table 11.3). The absolute magnitude of the scatter in the H_2S data (up to 250 µmol/kg, fig. 11.5*D*) is due to the effects of sample degassing, oxidation and the intrinsic error in the method (see Campbell and others, 1988b). If degassing and oxidation systematically reduce the H_2S in all the samples, the end-member concentration may be as much as 0.5 mmol/kg higher. At other vent systems, where H_2S ranges from 4 to 12 mmol/kg, errors of a similar magnitude generate an error of only about 5 to 10 percent in the calculated end-member, whereas at Escanaba Trough it is much greater because of the low sulfide content of the fluids.

Chloride, bromide, and iodide were measured in the Escanaba Trough fluids to understand the halide systematics. Sediment-hosted vents have distinctly elevated Br/Cl ratios and much higher I concentrations than sediment-starved vents due to elevated levels of Br and I in sedimentary organic matter (Campbell and Edmond, 1989; table 11.3). At Escanaba Trough Br/Cl is 0.00176 compared to about 0.00152 to 0.00167 at sediment-starved MOR vents. This corresponds to an increase of about 160 µmol/kg Br relative to bromide originating from seawater. Similar bromide enrichments occur in the Guaymas Basin vent fluids. Total I is 99 µmol/kg at Escanaba Trough and ranges from 65 to 83 µmol/kg in Guaymas Basin. The Cl concentrations of the Escanaba Trough vents (668 mmol/kg, fig. 11.6*B*) are higher than in the Guaymas Basin vents (580–603 mmol/kg), but well within the range of MOR hydrothermal vents (table 11.3).

Dissolved silica is 6.91 mmol/kg in the end-member fluids that are 217°C and 5.6 mmol/kg in the 108°C fluids (fig. 11.6*A*). The silica concentration at the 217°C vent is slightly elevated relative to quartz solubility at the vent temperature and sea-floor pressure (about 6 mmol/kg), but is several times lower than amorphous silica solubility (Von Damm and others, 1991). This may indicate the fluids are in equilibrium with quartz at slightly higher temperatures and pressures within the system, but there are several problems with this interpretation that will be discussed later.

The concentrations of Li (1,286 µmol/kg) and K (40.4 mmol/kg) in Escanaba Trough are similar to Guaymas Basin. Potassium enrichments in sediment-hosted fluids compared to sediment-starved fluids (table 11.3) suggest that the potassium content of the reaction substrate and its mobility with respect to hydrothermal alteration determine the K concentrations in high-temperature vent fluids. Only the high-chloride vents at the southern Juan de Fuca field (Von Damm and Bischoff, 1987) have K concentrations similar to the sediment-hosted systems. Lithium shows no trends between sediment-starved and sediment-hosted hydrothermal systems (table 11.3).

The Escanaba Trough vents have somewhat higher concentrations of Rb, Cs, and B than the Guaymas Basin fluids, and both are greatly enriched compared to sediment-starved systems (table 11.3). There is some inter-field variability in the Escanaba Trough fluids, with the lower temperature vent having the lowest concentrations of Rb (80 μmol/kg), Cs (6.0 μmol/kg), and B (2.16 mmol/kg) (see table 11.3). Two different regions of the 217°C mound also show some variations. Fluids from a well-defined orifice near the top of the mound had end-member concentrations of 105 μmol/kg Rb, 7.7 μmol/kg Cs, and 2.16 mmol/kg B, while fluids from near the base contained 95 μmol/kg Rb, 7.1 μmol/kg Cs, and 1.9 mmol/kg B. These differences indicate possible removal into secondary mineral phases, not only at the lower temperature vent, but also within the plumbing system of the higher temperature mound.

The $\delta^{11}B$ values in Escanaba Trough waters range from 10.1 per mil at the top of the 217°C mound to 11.5 per mil in the 108°C mound. These are much lower than the Guaymas Basin fluids that range from 17.4 to 19.6 per mil in the South Field vents and 16.5 to 23.2 per mil in the East Hill vents. Both sediment-hosted systems are much lighter than sediment-starved vent fluids along the EPR (31.1 to 36.8 per mil) and the MARK vents on the Mid-Atlantic Ridge (26.8 per mil). The $\delta^{11}B$ values of MOR vents have been explained by a two-end-member model involving high-temperature reaction between heated seawater and fresh tholeiitic basalt (Spivack and Edmond, 1987). Their boron content and isotopic composition is dominated by seawater because fresh tholeiitic basalt has so little boron. In contrast, the boron content and isotopic composition of sediment-hosted vent fluids are dominated by the sedimentary source (Spivack and others, 1987).

The first analyses of thallium in submarine hydrothermal fluids are also reported here. The monovalent cation has an ionic radius of 0.154 nm similar to K (0.144 nm), Rb (0.158 nm), and Ag (0.127nm) and shows chemical similarities to them (Cotton and Wilkinson, 1972). In concert with the trends for Rb, Cs, B, and K, the sediment-hosted systems are enriched in Tl. The Escanaba Trough vents have about 110 nmol/kg and the Guaymas Basin vents range from 104 to 114 nmol/kg, whereas the MOR vents range from 23 to 40 nmol/kg (table 11.3). The presence of higher thallium concentrations in sediment-hosted fluids reflects its greater concentrations in sedimentary material (about 1 to 10 ppm) compared to fresh mid-ocean ridge basalt (MORB) (up to 0.1 ppm) (Wedepohl, 1969). Unlike the alkalis, thallium is incorporated into sulfides, and its presence in ore-bodies is primarily due to solid solution with sulfide phases (Wedepohl, 1969).

The alkaline-earth element calcium is enriched in the Escanaba Trough and Guaymas Basin fluids relative to MARK, but concentrations in some hydrothermal fluids at latitude 11° to 13° N. EPR are higher (table 11.3). The strontium concentration in the Escanaba Trough vents is 209 μmol/kg, and 158 to 190 μmol/kg in the Guaymas Basin fluids. Only high-Cl sediment-starved vents have similar strontium concentrations.

The Escanaba Trough vents are the first example of a hot-spring fluid having more radiogenic $^{87}Sr/^{86}Sr$ ratios than seawater (0.70997 to 0.70967 versus 0.7092). The $^{87}Sr/^{86}Sr$ values for Escanaba Trough surface sediments range from 0.7093 to 0.7123 for unaltered material and 0.7092 to 0.7095 for hydrothermally altered samples. In contrast to this, the $^{87}Sr/^{86}Sr$ values for the Guaymas Basin vents (0.7052 to 0.7059) are significantly lower than seawater, but more radiogenic than basalt (about 0.703). The $^{87}Sr/^{86}Sr$ in unaltered surface sediments in Guaymas Basin are about 0.709 and about 0.705 in hydrothermally altered sediments (Gieskes and others, 1982a,b). Sediment-starved hydrothermal vent fluids have slightly higher $^{87}Sr/^{86}Sr$ than basaltic glass (Palmer and Edmond, 1989b).

The precipitation of sulfide minerals within the sediment column depletes fluids from sediment-hosted hydrothermal systems in iron, manganese, and other sulfide-forming metals compared to bare rock systems (table 11.3). The concentrations of trace elements in the Escanaba Trough samples were below the ICP-MS detection limits for Co, Cu, Zn, Ag, and Cd in the 100-fold diluted samples. The Fe and Mn data are presented as ranges in table 11.3 because of variability at different sampling sites on the 217°C mound and at the 108°C mound. These Mn and Fe concentrations are 10 times lower than in the Guaymas Basin vents and 100 to 1,000 times lower than in sediment-starved systems. Precipitation of small amounts of secondary minerals in the Escanaba Trough mounds are apparently affecting the fluid concentrations of Mn and Fe. In general, the ratio Fe/Mn in sediment-hosted fluids is much lower than in the sediment-starved vents (fig. 11.7). An exception is the low-salinity Axial Seamount Hydrothermal Emissions Study (ASHES) vent fluids that are thought to have undergone phase separation (Massoth and others, 1989). Since manganese-sulfides are many orders of magnitude more soluble than iron-sulfides, the effect of sulfide precipitation is to decrease Fe/Mn in the sediment-hosted and phase-separated fluids.

DISCUSSION

FLUID-SEDIMENT INTERACTIONS

The enrichments of K, Rb, Cs, B, and Tl in both the Escanaba Trough and Guaymas Basin fluids compared to sediment-starved fluids (table 11.4) reflect compositional differences between tholeiitic basalt and the sediment fill at these two sites. The unaltered material in both the sediment-hosted systems are substantially enriched in these elements relative to fresh tholeiitic basalt.

Table 11.4. Alkali elements, Tl, Sr, and B in Escanaba Trough and Guaymas Basin sediments and tholeiitic basalt.

[Values in parentheses are average deviation for data. —, not determined; ~, approximately. Escanaba data: B, Rb, Cs and Sr: this work; K: Zierenberg and Shanks (chap. 14, this volume). Guaymas data: Li, K, Rb, and Sr: Gieskes and others (1982b); Cs, Tl: H. Brumsack, Univ. Gottingen, oral commun., 1988; B: Spivack and others (1987). Basalt data: Wedepohl (1969); Krauskopf (1979); Li: Chan and Edmond (1988); B: Spivack and Edmond (1987)]

	Li (ppm)	K (pct)	Rb (ppm)	Cs (ppm)	Tl (ppm)	Sr (ppm)	$^{87}Sr/^{86}Sr$	B (ppm)	$d^{11}B$
Escanaba Trough sediment									
Unaltered	—	~2	112(11)	7.6(.2)	—	290(50)	0.7108(15)	44(5)	−4.8(.2)
Altered to chlorite	—	.01	3(2)	0.6(.3)	—	52(7)	.7094(2)	1	—
Guaymas Basin sediment									
Unaltered	55(5)	2.1	90	8	0.4	~ 320	.7073	60	−1.2(.4)
Altered to greenschist facies	"0"	"0"	2	—	—	~ 500	.7061	< 1	—
Tholeiitic basalt (unaltered)	7.5(1.5)	~.1	~4	~.06	< .1	~110	~.703	~.4	−3(1)

Systematic change of K with respect to Cl provides an important constraint on distinguishing fluid-sediment from fluid-basalt interactions. Potassium increases in a linear fashion with Cl in the sediment-starved systems, while sediment-hosted systems show high K with no systematic trends relative to Cl (fig. 11.8*A*). The high K in the bare-rock vents at southern Juan de Fuca and latitude 13° N. EPR are clearly part of the overall K/Cl systematics at MOR vents. No regular trends with respect to Cl are observed for Rb and Cs in MOR systems because, unlike K, their concentrations in fresh basalt can range by as much as two orders of magnitude (Palmer and Edmond, 1989a). The high K/Cl at the sediment-covered vents reflects the much greater concentrations in sediments relative to MORB (table 11.4).

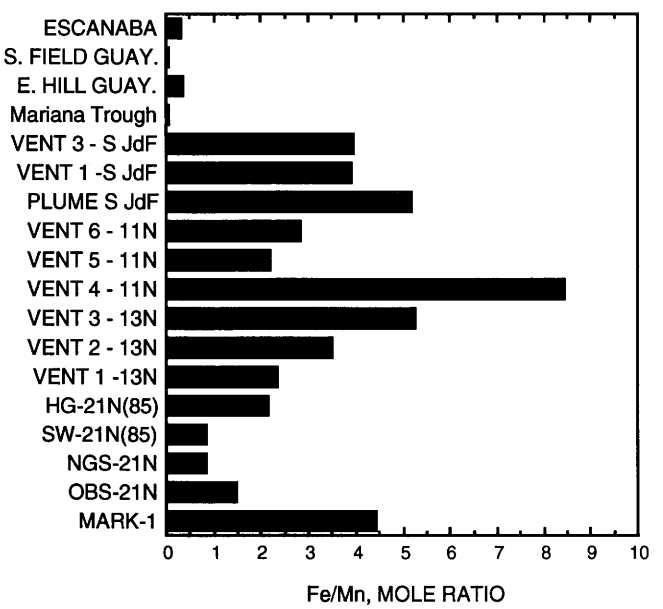

Figure 11.7. Ratios of Fe to Mn in submarine hydrothermal vent fluids from sediment-hosted, back-arc basin, and sediment-starved mid-ocean ridge environments (data references listed in fig. 11.8 caption).

Lithium shows no systematic trends with respect to Cl (fig. 11.8*B*). Despite significant enrichment in sediments compared to basalt (table 11.4), the fluids show little increase relative to sediment-starved systems (table 11.3). Chan and Edmond (1988) have shown that the lithium isotope ratios of both sediment-hosted and sediment-starved vent fluids are lighter than seawater and have similar values. They suggested incomplete extraction from the reaction substrate and uptake by a secondary mineral phase such as chlorite as possible causes. This is consistent with hydrothermal bomb experiments in which lithium is partially retained in the altered basalt (Seyfried and others, 1984).

Hydrothermally altered surface sediment in Escanaba Trough consists of assemblages rich in smectite, chlorite, and talc that show varying degrees of magnesium enrichment and alkali depletion (Zierenberg and Shanks, chap. 14, this volume). The chlorite-rich sediments shown in table 11.4 represent the highest degree of alteration and show nearly complete removal of the alkalis (Na, K, and Rb) and the alkaline earths (Ca and Sr). Oxygen isotope measurements of these sediments suggest alteration temperatures between 200°C and 240°C (Zierenberg and Shanks, chap. 14, this volume). Analyses of $\delta^{18}O$ in hydrothermal fluid and smectite from the high-temperature mound indicate equilibration temperatures of 220°C, similar to the measured fluid temperature (Böhlke and Shanks, chap. 12, this volume). This result does not necessarily imply, however, that the fluid chemistry is being determined solely by near-surface sediment-fluid interactions. The similarity of the major-element end-member fluid chemistry from two different mounds 275 meters apart (see fig. 11.2) suggests there is also a common fluid-sediment reaction zone at depth.

Sediments from the Guaymas Basin hydrothermal system showed similar trends. Material from around sill intrusions drilled in Guaymas Basin by the Deep Sea Drilling Project (DSDP) Leg 64, particularly Site 477, has been altered at around 200°C and shows Mg enrichments and leaching of K, Li, Rb, and B (Gieskes and others, 1982a,b;

Spivack and others, 1987). In the deepest part of hole 477, where hydrothermal alteration to a greenschist-facies assemblage consisting of quartz, albite, chlorite, epidote, and pyrite occurs at about 300±50°C, the sediment is completely depleted in Li and K, and nearly depleted in Rb and B (Gieskes and others, 1982b; Kastner, 1982; Spivack and others, 1987). Presumably cesium and thallium are also leached from these sediments. The pore fluid chemistry in these sediments is remarkably similar to 300°C fluids venting near the drill site (Gieskes and others, 1982b; Von Damm and others, 1985b). The high-temperature vent fluids at Guaymas Basin derive their chemical composition primarily from deep reactions within the sediment column, but small inter-field differences suggest that near-surface reactions also affect the fluid composition (Campbell and others, 1988b).

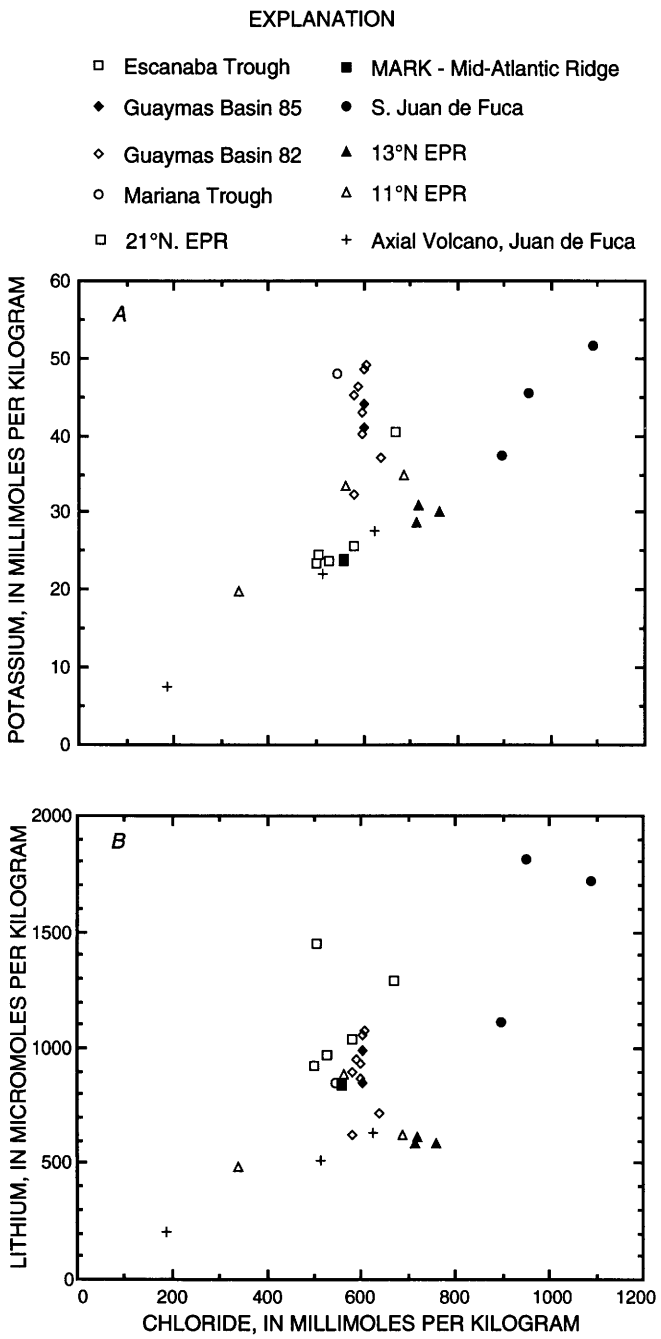

Figure 11.8. Plots of end-member chloride at different submarine hydrothermal vents versus (*A*) potassium and (*B*) lithium. Data sources are as follows: Escanaba Trough, this work; Guaymas Basin 85, Campbell and others (1988b); Guaymas Basin 82, Von Damm and others (1985b); Mariana Trough, Campbell and others (1987); 21° N. EPR, Von Damm and others (1985a) and Campbell and others (1988a); MARK-Mid-Atlantic Ridge, Campbell and others (1988b); S. Juan de Fuca, Von Damm and Bischoff (1987); 11° and 13° N. EPR, Bowers and others (1988); Axial Volcano, Juan de Fuca, Massoth and others (1989).

RELATIVE MOBILITY OF ALKALI ELEMENTS

As a first approximation, the water-to-sediment (W/S) ratios of the sediment-hosted systems can be modeled on the basis of the alkali data. In this calculation, it is assumed that the difference between altered and unaltered sediments (table 11.4) corresponds to the amount of alkali extracted in a single-pass system and that basalt sources are minor. (This may not be true for Li.) W/S is calculated as the ratio of the alkali extracted from the sediment to the increased alkali concentration above seawater values in the fluid. In the Escanaba Trough, the alkali elements have a range of values from 7 to 18, with an average of about 11±5, while boron has a significantly lower value of around 2 (table 11.5). The lower fluid concentrations of Rb and Cs and B at Guaymas Basin compared to Escanaba Trough give higher W/S values with an average of 14±5 for alkalis and 4 for boron (table 11.5). A reaction-path model using oxygen isotope data predicts a W/S value of around 5 for Escanaba Trough (Böhlke and Shanks, chap. 12, this volume). An estimate of W/S for the Guaymas Basin system based on mineralogical studies gives a value around 3 to 4 (Kastner, 1982). In contrast to the sediment-hosted systems, the MOR basalt systems have alkali derived water-to-rock (W/R) ratios of about 1 to 2 (Von Damm and others, 1985a; Von Damm and Bischoff, 1987). An integrated reaction-path model for the latitude 21° N. EPR system produced W/R values between 0.5 and 0.8 (Bowers and Taylor, 1985).

The high W/S ratios for the sediment-hosted vents compared to W/R in MOR vents may be explained by relatively incomplete extraction of alkalis per unit of fluid, perhaps due to lower reaction-zone temperatures and higher alkali concentrations in the reaction substrate. According to this hypothesis, a unit volume of sediment will undergo progressive leaching by successive volumes of fluid until it becomes depleted of alkali elements and is completely recrystallized to an alteration mineral assemblage. In general, relatively fresher sediment will generate higher alkali concentrations in the fluids (and lower W/S) than more

Table 11.5. Water-to-sediment ratios for Escanaba Trough and Guaymas Basin

[~, approximately. i - f sediment, unaltered sediment concentration minus altered sediment concentration (mol/kg sediment). i - f fluid, hydrothermal fluid concentration minus seawater concentration (mol/kg solution). W/S, amount of element extracted from 1 kg sediment/amount of element in 1 kg fluid (corrected for seawater)]

	Li (mM/kg)	K (mM/kg)	Rb (μM/kg)	Cs (μM/kg)	B (mM/kg)	I (μM/kg)
Escanaba Trough						
i – f sediment	8.7	550	1,260	52	3.9	300–1,200
i – f fluid	1.26	30	102	8	1.8	99
W/S (mass ratio)	7	18	12	7	2	3–12
Guaymas Basin						
i – f sediment	8	641	900	60	5	~1,260
i – f fluid	.9	33	53	6	1.2	~80
W/S (mass ratio)	9	19	17	10	4	~15

altered sediment of the same starting composition. Also, relatively mobile elements will have lower W/S values than less mobile elements. The trend in relative mobility indicated by the Escanaba Trough and Guaymas Basin data is as follows: B >> Cs ~(Li)> Rb > K. (Note that the relatively low W/S value for Li may be an artifact of ignoring basaltic contributions.)

If the progressive leaching model is correct, the alkali content of the fluid should decrease as the system ages. It is uncertain, however, what time scale would be necessary to observe changes due to progressive alteration. A time series study of the Guaymas Basin vents shows that the major-element composition and inter-field differences in fluid chemistry remain constant over 6 years (Campbell and others, 1988b). However, recent analyses of the time series samples by ID-TIMS show small decreases in B, Cs, and Rb, indicating that progressive leaching of the most reactive alkalis is occurring (Campbell and others, unpub. data).

Another process affecting the alkali concentrations is uptake of these elements into secondary mineral assemblages after extraction from the sediments. In high-temperature alteration zones, the major-element composition of the fluids is apparently controlled by the formation of a greenschist-facies mineral assemblage (Bowers and others, 1988; 1985). The time stability of the major-element composition of Guaymas Basin vent fluids is consistent with this (Campbell and others, 1988b). Since the high-temperature alteration phases show nearly complete depletion in the alkali elements (table 11.4), secondary uptake processes are most important at lower temperatures. In accord with this scenario, the 108°C vent fluids in the Escanaba Trough show identical major-element end-member values as the 217°C fluids. However, the concentrations of K, Rb, Cs, and $Si(OH)_4$ in the 108°C vent are lower (34 mmol/kg, 80 μmol/kg, 6 μmol/kg, and 5.6 mmol/kg respectively; see figs. 11.5, 11.6, and table 11.3). This suggests subsurface mixing with seawater or porewater (to generate the high Mg values and lower temperature for these fluids) and precipitation of an alkali-containing silicate phase such as smectite.

A similar phenomenon appears to be occurring at the 217°C mound. End-members calculated for samples from the base of the high-temperature mound show slightly lower Rb, Cs, and B concentrations (95 μmol/kg, 7.1 μmol/kg, and 1.9 mmol/kg, respectively) than those from the top (110 μmol/kg, 7.7 μmol/kg, and 2.2 mmol/kg, respectively), but no differences in $Si(OH)_4$, Li, or K. These former fluids had only a marginally lower temperature compared to the latter (215°C versus 217–219°C). It seems unlikely this difference is sufficient to cause an increase in silicate precipitation, since the formation temperature of smectite from this mound (220°C) corresponds to the fluid temperature (Böhlke and Shanks, chap. 12, this volume). The samples from the top of the mound came from a well-defined orifice whereas those from the base of the mound came from a seep that had to be excavated to obtain good fluid flow. Uptake of the most reactive elements (Cs, Rb, and B) may occur during the precipitation of smectite in the rubble pile. Solutions from the top of the mound may experience less interaction with silicates because they are flowing in a conduit. Therefore, uptake of alkalis into secondary minerals occurs even at relatively high temperature, and estimates of W/S ratios from alkali data must be considered as maximum values only. The W/S ratios are, however, useful indicators of alkali mobility and progressive alteration in sediment-hosted hydrothermal systems.

BORON ISOTOPE SYSTEMATICS

The high boron concentrations in the sediment-hosted vent fluids and the light values (relative to MOR fluids) are a distinguishing feature of these systems (table 11.3). Boron is very low in basalts and greatly enriched in marine sediments (table 11.4). It is nearly quantitatively

leached from hydrothermally altered sediment in Escanaba Trough. Previous studies have indicated that boron is highly mobile under hydrothermal conditions and is quantitatively removed from sediments below about 120 meters in DSDP Site 477 in Guaymas Basin. The other alkali elements, in contrast, become depleted below about 200 meters, in the greenschist-facies alteration zone (Gieskes and others, 1982b; Spivack and others, 1987). The much lower calculated W/S for boron compared to the alkali elements (table 11.5) reflects its higher relative mobility and may be a truer representation of the W/S ratio.

During uptake of boron into solid phases from solution, ^{10}B is preferentially partitioned into the solid phase thus enriching the fluid in the heavier isotope ^{11}B. If the boron isotopic composition of the Escanaba Trough fluids were derived solely from sediments and residual seawater, then the expected $\delta^{11}B$ value of the fluids would be about +3 to 4 per mil. The hydrothermal fluids, however, have heavier $\delta^{11}B$ values (+10.1 per mil to 11.5 per mil) than the sediments (–5.0 per mil), despite the fact that they contain 4 times more boron than seawater ($\delta^{11}B$ = 39 per mil). Various mixtures of sediment, seawater, and (or) basalt cannot generate the isotopic composition of the Escanaba Trough fluids, and uptake of boron onto secondary phases is required. The trends in the fluid data are consistent with this. The lowest temperature vent (108°C) has the lowest B and highest $\delta^{11}B$ (1.7 mmol/kg and 11.5 per mil, respectively), fluids from the base of the 217° C mound have intermediate B and $\delta^{11}B$ values (1.9 mmol/kg and 10.9 per mil), and samples from the top of this mound have the highest B and lightest $\delta^{11}B$ values (2.1 mmol/kg and 10.1 per mil; table 11.3). Hence even W/S ratios from boron data must be considered maximum values.

ALKALINE EARTH ELEMENTS

The systematic trends of the alkaline-earth elements and sodium relative to chloride reveal that the processes controlling sodium and calcium in vent fluids are linked by plagioclase alteration reactions and the formation of greenschist-facies mineral assemblages. Both Ca and Sr show increases with Cl that have a sharp upward trend in slope above about 550 mmol/kg Cl (fig. 11.9). In contrast to the alkali elements, it is not possible to distinguish sediment-hosted from sediment-starved vents on the basis of the trends for Ca with respect to Cl (fig. 11.9*A*). However, Sr shows distinct differences between the sediment-hosted and MORB systems (fig. 11.9*B*). Sodium is the major cation in hydrothermal vent fluids (about 80 to 90 percent of the charge) and follows the seawater Na/Cl ratio linearly up to Cl concentrations of about 600 mmol/kg (fig. 11.10*A*). At higher salinities, sodium is apparently taken up from solution by albitization (Von Damm and others, 1985a; Shanks and Seyfried, 1987).

In both sediment-hosted and sediment-starved hydrothermal systems, the increase in cationic charge from calcium exactly compensates the decrease in charge due to loss of sodium, which is especially evident at high chloride concentrations. This is demonstrated by plotting Na plus two times the Ca versus Cl, which has a slope essentially equal to the seawater ratio of (Na+2×Ca)/Cl (fig. 11.10*B*). This is not an artifact of obtaining a precise Na

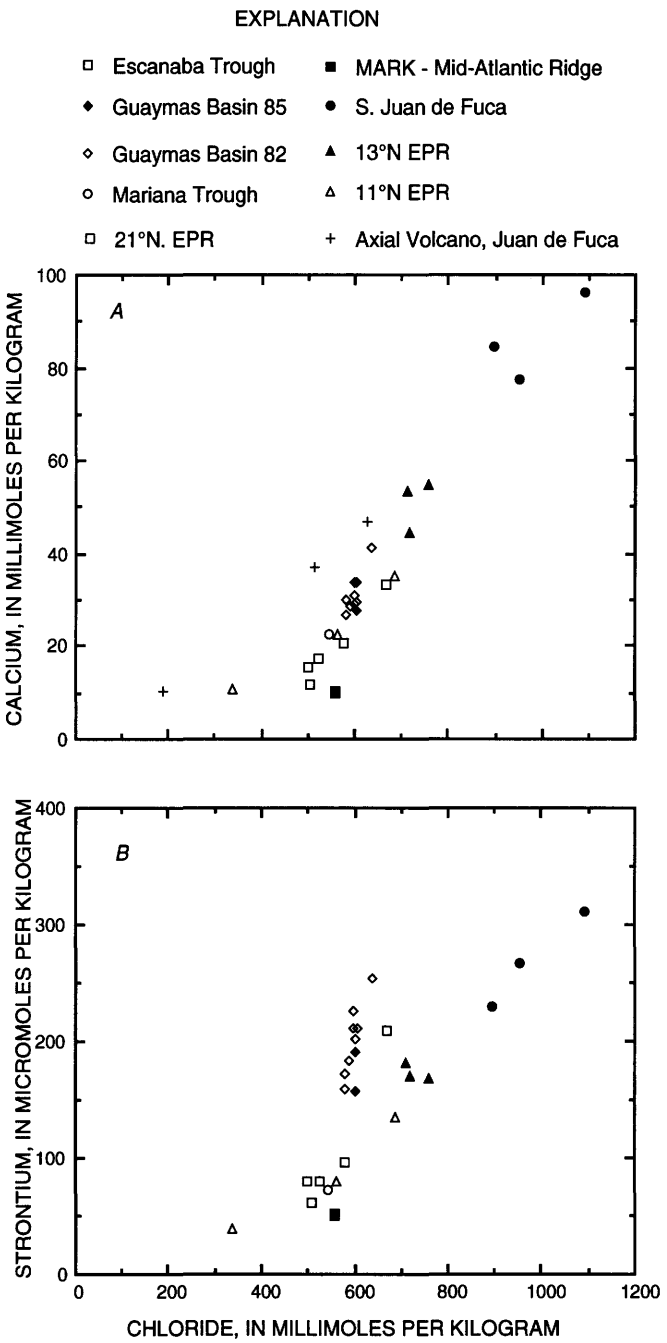

Figure 11.9. Alkaline earths relative to chloride in submarine hydrothermal vents. *A*, Ca versus Cl. *B*, Sr versus Cl. (Data references as in fig. 11.8.)

value by charge balance since the analytical errors in the Na, Ca, and Cl measurements are much smaller than the decrease in Na or increase in Ca. Thus for every two moles of sodium lost (relative to seawater) from the high-chloride solutions one mole of calcium is added to the solution. This is precisely what is expected from the conversion of anorthite to albite in hydrothermal alteration zones (Von Damm and others, 1985a; Shanks and Seyfried, 1987; Berndt and others, 1989).

Von Damm and Bischoff (1987) and Bischoff and Rosenbauer (1989) have suggested that the fluid chemistry of most MOR vents can be explained in terms of fluid-rock equilibrium with various mixtures of hydrothermal brines, chloride-depleted vapor phases, and solutions that have not experienced phase separation. The fact that the large shifts in Na and Ca concentrations occur in the high-chloride fluids may indicate that conversion of anorthite to albite is enhanced in deep-seated brine-rock interactions. The increase in sodium metasomatism at high chloride concentrations may reflect the effects of chloro-complexation on the activity ratio of free sodium ions to free calcium ions in solution (about 90 percent of the Ca is tied up as a chloro-complex, but only 35 percent of Na is complexed by Cl; Bowers and others, 1988). There is not a one-to-one relationship between the increases in chloride and calcium since the effect of chloro-complexation is to cause a shift in equilibrium. Further work is needed in order to establish the role chloro-complexation may have in this phenomenon.

The formation of secondary mineral phases containing calcium and strontium plays a critical role in controlling the calcium and strontium content of vent fluids. Berndt and others, (1988, 1989) have argued that plagioclase recrystallization is primarily responsible for the calcium and strontium contents of MOR vent fluids and that equilibrium of the fluid with epidote plays a lesser role in determining composition. If this were the case however, the slope of the (Na+2×Ca)/Cl line would be greater than the seawater ratio for MORB systems and even steeper for sediment-hosted systems because of calcium sources not related to plagioclase alteration. The uptake of magnesium into basalt alteration phases during the initial heating of seawater (Mg metasomatism) releases additional calcium into the fluid (Mottl, 1983). The dissolution of carbonate in sediments also release calcium to vent fluids. Since these sources of calcium are not necessarily accompanied by the uptake of sodium, additional calcium sinks of similar magnitude to these sources must exist in order to maintain the seawater ratio of (Na+2×Ca)/Cl in both sediment-hosted and sediment-starved vent fluids. One important calcium-containing mineral that is in equilibrium with these solutions is epidote. It is a common alteration mineral phase in sheeted dike complexes and oceanic greenstones (Alt and others, 1986; Richardson and others, 1987; Humphris and Thompson, 1978). The high-temperature alteration of Guaymas Basin sediments results in complete recrystallization to an epidote-albite-quartz-chlorite assemblage (Kastner, 1982). In addition to epidote, calcite can be an important sink for calcium and strontium in sediment-hosted vent systems and it is major mineral phase in the Guaymas Basin mounds (Peter, 1986).

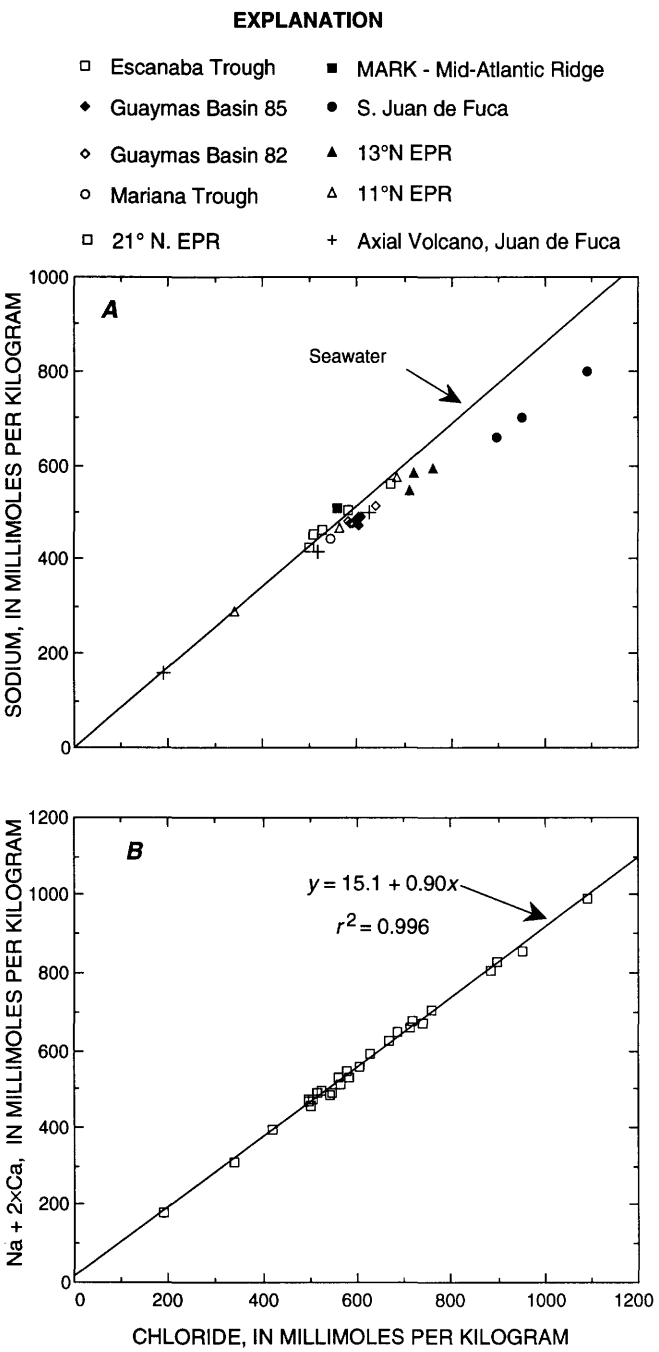

Figure 11.10. Sodium and calcium systematics relative to chloride in submarine hydrothermal vents. *A*, Na versus Cl plotted with Na/Cl ratio for seawater (data references as in fig. 11.8). *B*, Na plus 2 times Ca versus Cl. Slope of linear regression line for all vent fluid data is virtually the same as seawater ratio for Na+2×Ca/Cl.

The strontium isotope systematics and high Sr concentrations of the Escanaba Trough fluids appears to be controlled by complete re-equilibration with the local sediments. The $^{87}Sr/^{86}Sr$ values (0.70967 to 0.70997, table 11.3) are indistinguishable from unaltered sediment (0.7093 to 0.7123) and only slightly higher than altered sediment (0.7092 to 0.7095, table 11.4). Any basaltic component to the strontium isotope systematics, if it exits, is completely obscured by sediment-fluid interactions. In contrast, the Guaymas Basin fluids have $^{87}Sr/^{86}Sr$ values that range from 0.7052 to 0.7059 (table 11.3; Von Damm and others, 1985b), which are identical to pore fluids in the greenschist-facies alteration zone (0.7053), but less radiogenic than the altered sediments (0.7061) and much lower than unaltered sediments (0.7089, table 11.4; Gieskes and others, 1982b). These trends were interpreted as indicating either preferential reaction of volcanic material in the sediment column or a basaltic $^{87}Sr/^{86}Sr$ component in the fluids (Gieskes and others, 1982b). In both sediment-hosted systems, the enriched strontium content of the fluids compared to MOR systems requires a sedimentary source. This is particularly evident in the greenschist alteration zone in Guaymas Basin which is enriched in strontium relative to unaltered sediment (table 11.4).

QUARTZ GEOBAROMETRY

Quartz geobarometry has often been used to estimate the depth of the reaction zone at MOR vent systems (Von Damm and others, 1985a, Von Damm and Bischoff, 1987; Bowers and others, 1988; Campbell and others, 1988a) and at Guaymas Basin (Von Damm and others, 1985b). Three criteria must be met in order for this approach to be valid: the silica in solution is only in equilibrium with quartz, no silica-containing phase precipitates after equilibrium is established at depth, and the fluids only cool by adiabatic expansion during the transit to the sea floor (Von Damm and others, 1985a). In Escanaba Trough the silica content (6.9 mmol/kg, table 11.3) of the high-temperature vent fluids is oversaturated with respect to quartz at 217±2°C and the sea-floor pressure of 325 bars (the saturation value is 6 mmol/kg, Von Damm and others, 1991). However, these solutions would be saturated with respect to quartz if the near-surface temperature were only a little higher (about 230°C).

A number of problems limit the usefulness of quartz geobarometry for the Escanaba Trough system. The isobars of quartz solubility are so closely spaced in this temperature region and at this silica concentration that it is not possible to obtain accurate information about the reaction zone depth. Temperature variations on the order of the error margin of the measurement result in huge differences in estimated pressure regime. Another problem is encountered in estimating adiabatic cooling of the fluids. At 220°C and 300 bars, the decrease in temperature is less than 10°C for fluids originating from 1,000 bars pressure (6.8 km below sea floor) or less than 5°C from 600 bars (2.75 km below sea floor) (Bischoff and Rosenbauer, 1984). Since the fluids have clearly equilibrated with sediment, it is highly unlikely that the reaction zone is 3 km below the sea floor, and so some nonadiabatic cooling of the fluids must occur. A third problem is the assumption that the fluids have not precipitated a silica-containing phase after equilibrium with quartz is established. The alteration mineral assemblages in Escanaba Trough sediments have apparently formed close to the measured vent fluid temperature (Zierenberg and Shanks, chap. 14, this volume) and, even at 217±2°C, silicate phases are precipitating. It is likely that the silica content of the fluids is affected by this process.

THERMAL DECOMPOSITION OF ORGANIC MATTER

The proton activity in sediment-hosted fluids is much lower and the total alkalinities are higher than in sediment-starved solutions due to the thermal decomposition of organic matter and dissolution of carbonate minerals in the sediment column (Von Damm and others, 1985b). Differences in organic carbon, sulfur, and carbonate content of Escanaba Trough and Guaymas Basin sediments may explain some of the variations in fluid chemistry (see table 11.1). Escanaba Trough sediments have about 0.5 to 2 percent carbonate, 0.1 to 0.3 percent sulfur, and about 1 percent or less organic carbon (Karlin and Lyle, 1986; Magenheim and Gieskes, chap. 13, this volume). In contrast, the Guaymas Basin sediments contain 10 to 15 percent calcium carbonate, greater than 1 percent sulfur, and 2 to 4 percent organic matter (Calvert, 1966; Kastner, 1982, Niemitz, 1982). The lower values for pH, total alkalinity, H_2S, and NH_4 of Escanaba Trough fluids compared to Guaymas Basin fluids are consistent with these differences in sediment composition if the water-to-sediment ratios are similar.

Reaction of hydrothermal fluids with organic matter can generate significant quantities of organic acids such as acetate (Von Damm, 1991). At the relatively low temperatures in the Escanaba Trough fluids, these may be stable. The organic acids must exist at millimolar concentrations in the fluids to contribute significantly to the total alkalinity and affect the buffer capacity of the solutions. Although no measurements of organic acids were made, it is important to note that the end-member Na value determined analytically is within 0.5 percent of the Na calculated from the charge balance. This places an upper limit of 3 meq/kg of anionic charge due to organic acids in the Escanaba Trough fluids.

The enrichments of bromide and iodide in the sediment-hosted vent fluids are derived from the thermal

decomposition of organic matter in the sediments (Campbell and Edmond, 1989). Both sediment-hosted systems have higher Br/Cl ratios and I concentrations than sediment-starved systems (table 11.3). The absolute increase in Br (about 100 μmol/kg) is small compared to the total Br signal in seawater (840 μmol/kg), and differences between Guaymas Basin and Escanaba Trough are not discernible. However, iodide has a relatively low concentration in seawater (about 50 nmol/kg) and is a more useful diagnostic probe of sediment-fluid interactions than is bromide.

Since the Escanaba Trough sediments have much lower organic carbon than Guaymas Basin (table 11.1), one might expect lower rather than the higher I values observed in the fluids. However, the geochemistry of iodide is complicated by low-temperature diagenesis, and a strict comparison is not possible. Both bromide and iodide are associated with organic matter in marine sediments, and both are remobilized during early diagenesis (Price and Calvert, 1977, Kennedy and Elderfield, 1987; Magenheim and Gieskes, chap. 13, this volume). Although both elements are taken up by live plankton in surface waters, iodide is also adsorbed onto seston at the sea floor in oxidizing environments, and these type of sediments have higher I/C than reducing sediments (Price and Calvert, 1977). The threefold higher I/N and I/C ratios in Escanaba Trough sediments compared to Guaymas Basin sediments are consistent with this (Magenheim, 1989). The I/N ratios of the fluids (table 11.3) reflect these differences in sediment composition and explain the higher I in the Escanaba Trough fluids.

An estimate of the water-to-sediment ratio can be obtained if it is assumed that iodide is quantitatively leached during high-temperature alteration of the sediments. Since iodide is not taken up to any significant extent by secondary mineral formation, it is a more useful indicator of W/S then the alkalis. The I/N of the fluids is similar to sediments with an I concentration of about 40–100 ppm in Escanaba Trough (Magenheim and Gieskes, chap. 13, this volume). The Escanaba Trough fluids have an end-member I concentration of about 100 μmol/kg, requiring between 125 and 350 g of sediment per kilogram of fluid, or a water-to-sediment ratio of between 3 and 12 (table 11.5). This is similar to the W/R value of 5 obtained from a reaction path model using oxygen isotope data (Böhlke and Shanks, chap. 12, this volume).

FORMATION OF MASSIVE SULFIDE DEPOSITS

The relative proportion of basaltic and sedimentary derived components in sediment-hosted fluids is not readily discerned. Hydrothermal bomb experiments with Guaymas Basin sediment and seawater at appropriate temperature and pressure conditions reproduce most of the major ion trends observed in the Guaymas Basin hydrothermal vents (Von Damm, 1991; Thorton and Seyfried, 1987). As discussed above, the major and minor ions in the Escanaba Trough fluids apparently completely equilibrate with the sediment at around 220°C. The presence of ^{3}He in the Escanaba Trough fluids (T. Gamo, written commun., 1989), however, suggests that the fluids circulate through basaltic rock, picking up both heat and chemicals. The Guaymas Basin fluids also contain large amounts of ^{3}He (Lupton, 1979), and the lead isotope systematics (Chen and others, 1986) and strontium isotope systematics in Guaymas Basin indicate contributions from intermediate to mafic volcanic rock, although the strontium may originate from ash layers or volcaniclastic components in the sediment (Gieskes and others, 1982a,b).

If the hydrothermal fluids venting at sediment-covered spreading centers circulate within the basaltic basement, the metal content of any associated sulfide deposits may originate from high-temperature fluid interaction with the basaltic rocks. Models of the Guaymas Basin system assumed that fluids circulating in the basaltic basement might have a chemical composition similar to the latitude 21° N. EPR vent fluids (Von Damm and others, 1985b; Bowers and others, 1985). Reaction of acidic, metal-rich waters with organic matter and carbonate in the sediment column titrates out the acidity, causing metal sulfides to precipitate and possibly results in the formation of a massive sulfide deposit at depth (Bowers and others, 1985). The Fe/Mn ratio of the fluids decreases significantly due to the much greater solubility of manganese sulfides compared to iron sulfides, and sediment-hosted systems display this effect (fig. 11.7). If this model is correct, fluids debouching at the sea floor in Guaymas Basin represent spent sulfide-forming solutions. In the deepest parts of the Guaymas Basin system, large increases in iron and zinc occur in the sediment (Niemitz, 1982). The composition of mounds and chimneys in Guaymas Basin are also consistent with this hypothesis; they are primarily composed of the gangue minerals calcite and barite (Peter, 1986).

Another source of metals is the sediment itself. If subjected to high-temperature leaching for any length of time, all the organic matter and carbonate will be removed, thus decreasing its ability to neutralize acidity. Reaction of high-temperature acidic fluids with these heavily altered sediments could extract significant quantities of some metals. This may explain the high arsenic and bismuth content of the Escanaba Trough sulfides, which Koski and others (1988) suggest are derived from felsic components in the Escanaba Trough sediment.

The Escanaba Trough deposits are rich in metal sulfides that apparently formed at high temperatures (Morton and others, 1990). They could not have precipitated from the metal-depleted fluids currently emitted from the mounds. Subsurface cooling and deposition of metal sulfides may explain the paucity of dissolved metals in the

fluids. Without drilling in this area, one cannot say if this is occurring or what spatial relationship exists between the deposits and the basaltic heat source. It is noteworthy that the volcanic hill on which the active deposits are situated has extrusive basaltic flows on its eastern side (Morton and others, 1990). This may indicate that the heat source(s) for driving hydrothermal circulation and forming sulfide deposits in Escanaba Trough exists at shallower depths in the sediment cover than in Guaymas Basin, where only intrusive magmatic activity is evident (Lonsdale and Becker, 1985).

CONCLUSIONS

Submarine hydrothermal fluids from active vents in Escanaba Trough show a number of similarities in chemical composition to the fluids from Guaymas Basin, Gulf of California. Both can be readily distinguished from vent systems that only involve reactions between evolved, heated seawater and tholeiitic basalt by their enrichment in the alkali elements potassium, rubidium, and cesium and the alkali-like elements boron and thallium. These elements are extracted at 200°C to 300°C from sediment that is rich in alkalis and boron compared to MOR basalt. The systematic trends of potassium and strontium relative to chloride also differentiate sediment-hosted vents from sediment-starved vents. The W/S ratios calculated from the alkali data cannot be used to model the true water-to-rock ratio of the system due to incomplete leaching and uptake of alkalis into secondary mineral phases. The data suggest progressive leaching of alkali elements from sediment with the following relative mobility: B >> Cs ~ (Li) > Rb > K. Inter-field differences in the $Si(OH)_4$ concentrations, and boron isotopic composition of the Escanaba Trough fluids also indicate uptake by a secondary silicate mineral, such as smectite, is occurring even at 220°C. In general, the boron isotopic composition of sediment-hosted vent fluids, which are much lighter than MOR fluids, is dominated by sedimentary-derived boron in contrast to MOR systems where the boron systematics are seawater dominated. The strontium isotope values at Escanaba Trough are more radiogenic than seawater and reflect complete equilibration of the fluids with the sediment. In contrast, the Guaymas Basin vent fluids must interact with some basaltic material to obtain the $^{87}Sr/^{86}Sr$ values.

Differences in the organic carbon and carbonate content of the Escanaba Trough and Guaymas Basin sediments have a significant effect on the buffer capacity of the fluids. Compared to bare rock vent systems, both vents have much higher pH, total alkalinity, ammonium, bromide, and iodide, which are derived from the thermal decomposition of organic matter and carbonate in the sediment (Von Damm and others, 1985b; Campbell and Edmond, 1989). The Escanaba Trough fluids have significantly lower concentrations of these chemicals and a lower pH than the Guaymas Basin vents because the organic carbon, carbonate, and sulfur content of the Escanaba Trough sediments is much lower. However, the Escanaba Trough vents have higher I values than Guaymas Basin because the ratio of iodide to organic carbon of the sediment is about 2 to 3 times higher. This reflects the more oxidizing nature of the sediments at Escanaba Trough. The water-to-sediment ratio calculated from the I data is between 3 and 12, which agrees well with W/S calculated from oxygen isotope data (about 5).

The precipitation of massive sulfide deposits in sediment-hosted environments is primarily induced by the pH and alkalinity changes accompanying the thermal decomposition of organic matter and carbonate in the sediment column. Decreasing temperature due to mixing of seawater with vent fluids is of secondary importance. The wide range in the metal content of MOR fluids suggest that fluid-basalt interactions play a major role in determining the metal content of sediment-hosted massive sulfide deposits. The sediments may, however, be an important source of metals if they are depleted of their organic matter and carbonate in a high-temperature portion of the system. In Guaymas Basin, the fluids are essentially spent ore forming solutions that are actively forming large mound structures on the sea floor mainly composed of gangue minerals. The cooler, metal-depleted fluids at the Escanaba Trough system are not responsible for the formation of the large sulfide-rich mounds there. It is possible that even at depth they do not contain significant metals and that they reflect the waning phase of a hydrothermal cycle.

REFERENCES CITED

Alt, J.C., Honnorez, J., Laverne, C., and Emmermann, R., 1986, Hydrothermal alteration of a 1 km section through the upper oceanic crust, Deep Sea Drilling Project hole 504b: mineralogy, chemistry, and evolution of seawater-basalt interactions: Journal of Geophysical Research, v. 91, p. 10,309–10,335.

Atwater, T., and Mudie, J.D., 1973, Detailed near-bottom geophysical study of the Gorda Rise: Journal of Geophysical Research, v. 78, p. 8665–8686.

Berndt, M.E., Seyfried, W.E., and Beck, W., 1988, Hydrothermal alteration processes at midocean ridges: Experimental and theoretical constraints from Ca and Sr exchange reactions and Sr isotopic ratios: Journal of Geophysical Research, v. 93, p. 4573–4583.

Berndt, M.E., Seyfried, W.E., and Janecky, D.R., 1989, Plagioclase and epidote buffering of cation ratios in mid-ocean ridge hydrothermal fluids: experimental results in and near the supercritical region: Geochimica et Cosmochimica Acta, v. 53, p. 2283–2300.

Bischoff, J.L., and Rosenbauer, R.J., 1984, The critical point and two phase boundary of seawater, 200-500°C: Earth and Planetary Science Letters, v. 68, p. 172–180.

———1989, Salinity variations in submarine hydrothermal systems by layered double-diffusive convection: Journal of Geology, v. 97, p. 613–623.

Böhlke, J.K., and Shanks, W.C., III, Stable isotope study of hydrothermal vents at Escanaba Trough: Observed and calculated effects of sediment-seawater interaction, *in* Morton, J.L., Zierenberg, R.A., and Reiss, C.A., eds., Geologic, hydrothermal, and biologic studies at Escanaba Trough, Gorda Ridge, offshore northern California: U.S. Geological Survey Bulletin 2022, chapter 12 (this volume).

Bowers, T.S., and Taylor, H.P., 1985, An integrated chemical and stable-isotope model of the origin of midocean ridge hot spring systems: Journal of Geophysical Research, v. 90, p. 12583–12606.

Bowers, T.S., Von Damm, K.L., and Edmond, J.M., 1985, Chemical evolution of mid-ocean ridge hot springs: Geochimica et Cosmochimica Acta, v. 49, p. 2239–2252.

Bowers, T.S., Campbell, A.C., Measures, C.I., Spivack, A.J., Khadem, M., and Edmond, J.M., 1988, Chemical controls on the composition of vent fluids at 13°N–11°N and 21°N, East Pacific Rise: Journal of Geophysical Research, v. 93, p. 4522–4536.

Calvert, S.E., 1966, Accumulation of diatomaceous silica in the sediments of the Gulf of California: Geological Society of America Bulletin, v. 77, p. 569–596.

Campbell, A.C., Edmond, J.M., Colodner, D., Palmer, M.R., and Falkner, K.K., 1987, Chemistry of hydrothermal fluids from the Mariana Trough back arc basin in comparison to mid-ocean ridge fluids [abs.]: Eos, Transaction American Geophysical Union, v. 68, p. 1531.

Campbell, A.C., Palmer, M.R., Klinkhammer, G.P., Bowers, T.S., Edmond, J.M., Lawrence, J.R., Casey, J.F., Thompson, G., Humphris, S., Rona, P., and Karson, J.A., 1988a, Chemistry of hot springs on the Mid-Atlantic Ridge: Nature, v. 335, p. 514–519.

Campbell, A.C., Bowers, T.S., Measures, C.I., Falkner, K.K., Khadem, M., and Edmond, J.M., 1988b, A time-series of vent fluid compositions from 21°N, East Pacific Rise (1979, 1981, 1985) and the Guaymas Basin, Gulf of California (1982, 1985): Journal of Geophysical Research, v. 93, p. 4537–4549.

Campbell, A.C., German, C., Palmer, M.R., and Edmond, J.M., 1988c, Preliminary report on the chemistry of hydrothermal fluids from the Escanaba Trough [abs.]: Eos, Transaction American Geophysical Union, v. 69, p. 1271.

Campbell, A.C., and Edmond, J.M., 1989, Halide systematics of submarine hydrothermal vents: Nature, v. 342, p. 168–170.

Chan, L-H., and Edmond, J.M., 1988, Variation of the lithium isotope composition in the marine environment: A preliminary report: Geochimica et Cosmochimica Acta, v. 52, p. 1711–1717.

Chen, J.H., Wasserburg, G.J., Von Damm, K.L., and Edmond, J.M., 1986, The U-Th-Pb systematics in hot springs on the East Pacific Rise at 21°N and Guaymas Basin: Geochimica et Cosmochimica Acta, v. 50, 2467–2479.

Cline, J.D., 1969, Spectrophotometric determination of hydrogen sulfide in natural waters: Liminology and Oceanography, v. 14, p. 454–458.

Converse, D.R., Holland, H.D., and Edmond, J.M., 1984, Flow rates in the axial hot springs of the East Pacific Rise (21°N): Implications for the heat budget and the formation of massive sulfide deposits: Earth and Planetary Science Letters, v. 69, p. 159–175.

Corliss, J.B., Dymond, J., Gordon, L.I., Edmond, J.M., von Herzen, R.P., Ballard, R.D., Green, K., Williams, D., Bainbridge, A., Crane K., and van Andel, T.J.H., 1979, Exploration of submarine thermal springs on the Galapagos Rift: Science, v. 203, p. 1073–1083.

Cotton, F.A, and Wilkinson, G., 1972, Advanced inorganic chemistry: New York, Interscience Publishers, 3d edition, p. 260–282.

Delaney, J.R., McDuff, R.E., Tivey, M.K., and Lupton, J.E., 1989, Measurements of 400°C hydrothermal fluids and temporal variability in the Endeavour vent field [abs.]: Eos, Transactions American Geophysical Union, v. 70, p. 1163.

Edmond, J.M., Measures, C., McDuff, R.E., Chan, L.H., Collier, R., Grant, B., Gordon, L.I., and Corliss, J.B., 1979, Ridge crest hydrothermal activity and the balances of the major and minor elements in the ocean: The Galapagos data: Earth and Planetary Science Letters, v. 46, p. 1–18.

Gieskes, J.M., Kastner, M., Einsele, G., Kelts, K., and Niemitz, J., 1982a, Hydrothermal activity in the Guaymas Basin, Gulf of California: A synthesis, *in* Curray, J.R., Moore, D.G., and others, eds., Initial reports of the Deep Sea Drilling Project: Washington, D.C., U.S. Government Printing Office, v. 64, p. 1159–1167.

Gieskes, J.M., Elderfield, H., Johnson, J., Meyers, B., and Campbell, A., 1982b, Geochemistry of interstitial waters and sediments, Leg 64, Gulf of California, *in* Curray, J.R., Moore, D.G., and others, eds., Initial reports of the Deep Sea Drilling Project: Washington, D.C., U.S. Government Printing Office, v. 64, p. 675–694.

Humphris, S.E., and Thompson, G., 1978, Trace element mobility during hydrothermal alteration of oceanic basalts: Geochimica et Cosmochimica Acta, v. 42, p. 127–136.

Karlin, R., and Lyle, M., 1986, Sediment studies on the Gorda Ridge: Oregon Department of Geology and Mineral Industries, Open File Report O-86-19, 76 p.

Kastner, M., 1982, Evidence for two distinct hydrothermal systems in the Guaymas Basin, *in* Curray, J.R., Moore, D.G., and others, eds., Initial reports of the Deep Sea Drilling Project: Washington D.C., U.S. Government Printing Office, v. 64, p. 1143–1157.

Kennedy, H.A., and Elderfield, H., 1987, Iodine diagenesis in non-pelagic sediments: Geochimica et Cosmochimica Acta, v. 51, p. 2505–2514.

Koski, R.A., Shanks, W.C., Bohrson, W.A., Oscarson, R.L., 1988, The composition of massive sulfide deposits from the sediment-covered floor of the Escanaba Trough, Gorda Ridge: Implications for depositional processes: Canadian Mineralogist, v. 26, p. 655–673.

Krauskopf, K.B., 1979, Introduction to geochemistry: New York, McGraw-Hill, 721 p.

Lonsdale, P.F., and Becker, K., 1985, Hydrothermal plumes, hot springs, and conductive heat flow in the Southern Trough of the Guaymas Basin: Earth and Planetary Science Letters, v. 73, p. 211–225.

Lupton, J.E., 1979, Helium-3 in the Guaymas Basin: Evidence of injection of mantle volatiles in the Gulf of California: Journal of Geophysical Research, v. 84, p. 7446–7452.

Macdonald, K.C., Becker, K., Spiess, F.N., and Ballard, R.D., 1980, Hydrothermal heat flux of the black smoker vents on the East Pacific Rise: Earth and Planetary Science Letters, v. 48, P. 1–7

McManus, D.A., and others, 1970, Site 35, *in* McManus, D. A., and others, eds., Initial reports of the Deep Sea Drilling Project: Washington, U.S. Government Printing Office, v. 5, p. 165–172.

Magenheim, A.J., 1989, Hydrothermal alteration in near surface sediments of the Guaymas Basin, Gulf of California and the Escanaba Trough, Gorda Ridge: San Diego, University of California, M.S. thesis, 146 p.

Magenheim, A.J., and Gieskes, J.M., Evidence for hydrothermal flow through surficial sediments, Escanaba Trough, *in* Morton, J.L., Zierenberg, R.A., and Reiss, C.A., eds., Geologic, hydrothermal, and biologic studies at Escanaba Trough, Gorda Ridge, offshore northern California: U.S. Geological Survey Bulletin 2022, chapter 13 (this volume).

Massoth, G.J., Butterfield, D.A., Lupton, J.E., McDuff, R.E., Lilley, M.D., and Jonasson, I.R., 1989, Submarine venting of phase-separated hydrothermal fluids at Axial Volcano, Juan de Fuca Ridge: Nature, v. 340, p. 702–705.

Michard, G., Albarede, F., Michard, A., Minster, J.-F., Charlou, J.-L., and Tan, N., 1984, Chemistry of solutions from the 13°N East Pacific Rise hydrothermal site: Earth and Planetary Science Letters, v. 67, p. 297–307.

Morton, J.L., Koski, R.A., Normark, W.R., and Ross, S.L., 1990, Distribution and composition of massive sulfide deposits at Escanaba Trough, southern Gorda Ridge, *in* McMurray, G.R., ed., Gorda Ridge: A seafloor spreading center in the United States' Exclusive Economic Zone: New York, Springer-Verlag, p. 77–92.

Mottl, M.J., 1983, Metabasalts, axial hot springs, and the structure of hydrothermal systems at mid-ocean ridges: Geological Society of America Bulletin, v. 94, p. 161–180.

Niemitz, J.W., 1982, Geochemistry of sediments, Leg 64, Gulf of California, *in* Curray, J.R., Moore, D.G., and others, eds., Initial reports of the Deep Sea Drilling Project: Washington, D.C., U.S. Government Printing Office, v. 64, p. 695–713.

Palmer, M.R., and Edmond, J.M., 1989a, Cesium and rubidium in submarine hydrothermal fluids: evidence for recycling of alkali elements: Earth and Planetary Science Letters, v. 95, p. 8–14.

———1989b, The strontium isotope budget of the modern ocean: Earth and Planetary Science Letters, v. 92, p. 11–26.

Peter, J.M., 1986, Genesis of hydrothermal vent deposits in the Southern Trough of Guaymas Basin, Gulf of California: A mineralogical and geochemical study: University of Toronto, MS thesis, 180 p.

Price, N.B., and Calvert, S.E., 1977, The contrasting geochemical behaviors of iodine and bromine in recent sediments from the Namibian shelf: Geochimica et Cosmochimica Acta, v. 41, p. 1769–1775.

Reiss, C.A., Zierenberg, R.A., and Holmes, M.L., 1992, Preliminary report of the 1988 DSV-4 Sea Cliff dive program, Escanaba Trough, Gorda Ridge, U.S. Geological Survey Open-file Report 92-286, 104 p.

Rex, R.W., and Murray, B., 1970, X-ray mineralogy studies, *in* McManus, D.A., and others, eds., Initial reports of the Deep Sea Drilling Project: Washington, D.C., U.S. Government Printing Office, v. 5, p. 441–484.

Richardson, C.J., Cann, J.R., Richards, H.G., and Cowan, J.G., 1987, Metal-depleted root zones of the Troodos ore-forming hydrothermal systems, Cyprus: Earth and Planetary Science Letters, v. 84, p. 243–253.

Sakai, H., Gamo, T., Kim, E-S, Shitashima, K., Yanagisawa, F., Tsutsumi, M., Ishibashi, J., Sano, Y., Wakita, H., Tanaka, T., Matsumoto, T., Naganuma, T., and Mitsuzawa, K., 1990, Unique chemistry of the hydrothermal solution in the mid-Okinawa Trough backarc basin: Geophysical Research Letters, v. 17, p. 2133-2136.

Seyfried, W.E., Janecky, D.R., and Mottl, M.J., 1984, Alteration of the oceanic crust: implications for geochemical cycles of lithium and boron: Geochimica et Cosmochimica Acta, v. 48, p. 557–569.

Shanks, W.C., and Seyfried, W.E., 1987, Stable isotope studies of vent fluids and chimney minerals, Southern Juan de Fuca Ridge: Sodium metasomatism and seawater sulfate reduction: Journal of Geophysical Research, v. 92, p. 11,387–11,399.

Sleep, N.H., and Wolery, T.J., 1978, Egress of hot water from midocean ridge hydrothermal systems: Some thermal constraints: Journal of Geophysical Research, v. 83, p. 5913–5922.

Spiess, F.N., Macdonald, K.C., Atwater, T., Ballard, R., Carranza, A., Cordoba, D., Cox, C., Diaz Garcia, V.M., Francheteau, J., Guerrero, J., Hawkins, J., Haymon, R., Hessler, R., Juteau, T., Kastner, M., Larson, R., Luyendyk, B., Macdougall, J.D., Miller, S., Normark, W., Orcutt, J., and Rangin, C., 1980, East Pacific Rise: Hot springs and geophysical experiments: Science, v. 207, p. 1421–1432.

Spivack, A.J., and Edmond, J.M., 1987, Boron isotope exchange between seawater and the oceanic crust: Geochimica et Cosmochimica Acta, v. 51, p. 1033-1043.

Spivack, A.J., Palmer, M.R., and Edmond, J.M., 1987, The sedimentary cycle of the boron isotopes: Geochimica et Cosmochimica Acta, v. 51, p. 1939–1949.

Strickland, J.D.H., and Parsons, T.R., 1968, A practical handbook of seawater analysis: Fisheries Research Board of Canada Bulletin, v. 167, 311 p.

Thorton, E.C., and Seyfried, W.E., 1987, Reactivity of organic-rich sediment in seawater at 350°C, 500 bars: Experimental and theoretical constraints and implications for the Guaymas Basin: Geochimica et Cosmochimica Acta, v. 51, p. 1997–2010.

Vallier, T.L., Harold, P.J., and Girdley, W.A., 1973, Provenances and dispersal patterns of turbidite sand in Escanaba Trough, Northeastern Pacific Ocean: Marine Geology, v. 15, p. 67–87.

Von Damm, K.L., 1991, A comparison of Guaymas Basin hydrothermal solutions to other sedimented systems and experimental results, *in* Dauphin, S.P., and Simoneit, B.R.T., eds., The Gulf and Peninsular Province of the Californias: American Association of Petroleum Geologists Memoir 47, p. 743–751.

Von Damm, K.L., and Bischoff, J.L., 1987, Southern Juan de Fuca ridge hot spring chemistry: Journal of Geophysical Research, v. 92, p. 11,334–11,346.

Von Damm, K.L., Bischoff, J.L., and Rosenbauer, R.J., 1991, Quartz solubility in hydrothermal seawater; an experimen-

tal study and equation describing quartz solubility for up to 0.5 *M* NaCl solutions: American Journal of Science, v. 291, p. 977-1007.

Von Damm, K.L., Edmond, J.M., Grant, B., Measures, C.I., Walden, B., and Weiss, R.F., 1985a, Chemistry of submarine hydrothermal solutions at 21°N, East Pacific Rise: Geochimica et Cosmochimica Acta, v. 49, p. 2197–2220.

Von Damm, K.L., Edmond, J.M., Measures, C.I., and Grant, B., 1985b, Chemistry of submarine hydrothermal solutions at Guaymas Basin, Gulf of California: Geochimica et Cosmochimica Acta, v. 49, p. 2221–2237.

Wedepohl, K.H., ed., 1969, Handbook of geochemistry: Berlin, Springer-Verlag.

Zierenberg, R.A., Morton, J.L., Koski, R.A., Ross, S.L., and Holmes, M.K., Geologic setting of massive sulfide mineralization in the Escanaba Trough, *in* Morton, J.L., Zierenberg, R.A., and Reiss, C.A., eds., Geologic, hydrothermal, and biologic studies at Escanaba Trough, Gorda Ridge, offshore northern California: U.S. Geological Survey Bulletin 2022, chapter 10 (this volume).

Zierenberg, R.A., and Shanks, W.C., III, Sediment alteration associated with massive sulfide formation in the Escanaba Trough, Gorda Ridge: The importance of seawater mixing and magnesium metasomatism, *in* Morton, J.L., Zierenberg, R.A., and Reiss, C.A., eds., Geologic, hydrothermal, and biologic studies at Escanaba Trough, Gorda Ridge, offshore northern California: U.S. Geological Survey Bulletin 2022, chapter 14 (this volume).

Chapter 12. Stable Isotope Study of Hydrothermal Vents at Escanaba Trough: Observed and Calculated Effects of Sediment-Seawater Interaction

By J.K. Böhlke[1] *and* W.C. Shanks III[2]

CONTENTS

ABSTRACT

Hydrothermal fluids venting at 217°C from sulfide mounds in the sediment-filled Escanaba Trough have $\delta^{34}S_{H_2S}$ = +7.8 ± 0.4, $\delta^{18}O_{H_2O}$ = +0.43 ± 0.06, and δD_{H_2O} = −0.7 ± 0.3 (compared to local seawater with $\delta^{18}O_{H_2O}$ = −0.17 and δD_{H_2O} = −0.6). The Escanaba Trough vent fluids have relatively low $\delta^{18}O_{H_2O}$ values compared to those at several other mid-ocean ridge sites, and are the first reported not to have a larger increase (relative to seawater) in δD_{H_2O} than in $\delta^{18}O_{H_2O}$. Massive sulfide samples from various localities within Escanaba Trough have $\delta^{34}S_{solid}$ ranging from −0.7 to +11.6. The wide range of $\delta^{34}S_{solid}$ values suggests variable contributions of relatively ^{34}S-depleted sedimentary (bacteriogenic) ± igneous sulfide and ^{34}S-enriched sulfide from reduced seawater sulfate in the hydrothermal systems. The vent fluid isotopes could be explained by reaction of heated seawater with sediment alone at relatively high water to rock ratios (W/R), or possibly with some combination of basalt and sediment, but are less likely to result from reactions with basalt alone.

Equilibrium reaction-path calculations indicate that heated seawater reacting with Escanaba Trough sediment should undergo relatively large positive shifts in $\delta^{18}O_{H_2O}$ but small or negative shifts in δD_{H_2O}, in contrast to seawater reacting with basalt, which exhibits roughly similar enrichments in both ^{18}O and deuterium. Calculations also predict a negative correlation between $\delta^{34}S_{H_2S}$ and $\delta^{18}O_{H_2O}$, and relatively large variability of $\delta^{34}S_{H_2S}$. Isotopic ratios of oxygen, hydrogen, and sulfur in the Escanaba Trough vent fluid are reproduced by simulated equilibrium isothermal closed-system reactions with sediments at relatively high cumulative W/R (2 to 6 by weight at 220°C to 300°C), roughly an order of magnitude higher than W/R values inferred for seawater-basalt reactions at latitude 21° N. on the East Pacific Rise. The measured Escanaba Trough isotope ratios are not reproduced by simulated closed-system reactions with basalt, or by open-system reactions with either sediment or basalt. Relatively high effective water/rock ratios and low vent temperatures at Escanaba Trough could result from high permeabilities in the turbidite-hosted hydrothermal circulation system, a large amount of conductive cooling during fluid ascent, and (or) ongoing subsurface mixing of seawater with deeper hotter fluid reservoirs. The temperature and $\delta^{18}O_{H_2O}$ value of the 217°C vent fluid could be similar to those of fluids responsible for chloritization of near-surface sediments in Escanaba Trough, which probably required shallow circulation of heated magnesium-bearing seawater.

INTRODUCTION

Escanaba Trough occupies a sediment-covered slow-spreading rift on Gorda Ridge in the northeast Pacific Ocean (fig. 12.1). The floor of the trough, 3,300 m below sea level, receives rapidly accumulating lithic and arkosic turbidite sand, silt, and mud, largely from the open southern end near the Mendocino Fracture Zone (McManus and others, 1970; Normark and others, chap. 6, this volume). The sedimentary section is at least 500 m thick in some

[1] U.S. Geological Survey, Reston, Virginia
[2] U.S. Geological Survey, Denver, Colorado

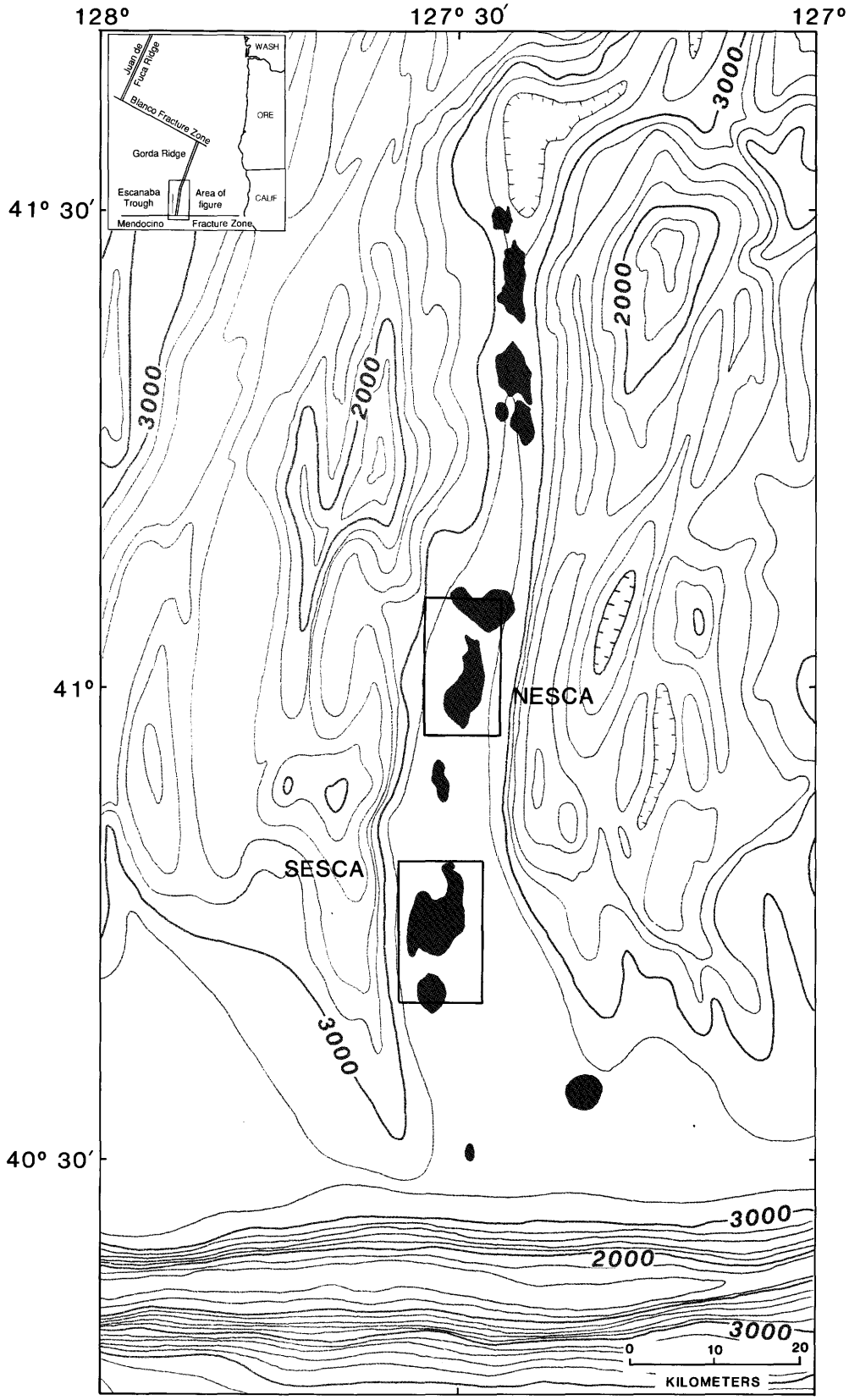

Figure 12.1. Bathymetric map of Escanaba Trough showing location of volcanic edifices (dark gray) and SESCA and NESCA sites. Hachures indicate area of closed low. Contour interval is 200 m.

parts of the trough, and it includes numerous basaltic intrusions and flows (Morton and Fox, chap. 2, this volume; Davis and Becker, chap. 3, this volume). Large massive sulfide bodies are known to occur at the sediment surface above the margins of buried igneous sills or stocks between approximate latitudes 40.5° and 41.5° N. (Morton and others, 1987; Koski and others, 1988; Zierenberg and others, chap. 10, this volume). Active hot springs currently are venting from areas of pyrrhotite-rich massive sulfide mounds near latitude 41° N. in the northern Escanaba Trough (NESCA) area (Campbell and others, 1989, chap. 11, this volume). Both the vent fluids and the hydrothermal deposits at Escanaba Trough have chemical characteristics that are distinct from those of vent fluids and deposits from nonsedimented spreading centers and that indicate contributions from the underlying organic-bearing sediments (Kvenvolden and others, 1986, Koski and others, 1988; 1987; LeHuray and others, 1988; Campbell and others, 1989, chap. 11, this volume).

This paper presents new light stable isotope data (O, H, and S) for vent fluids and hydrothermal deposits at Escanaba Trough and discusses some of the implications of fluid-sediment interaction for the isotope compositions of venting fluids. Previous studies have indicated that massive sulfide deposits in sedimented mid-ocean ridge (MOR) settings such as Guaymas Basin (Gulf of California), Middle Valley (northern Juan de Fuca Ridge), and the Atlantis II Deep (Red Sea) have more variable $\delta^{34}S_{solid}$ values (both higher and lower) than do those in nonsedimented MOR settings (for example, Shanks and Bischoff, 1980; Goodfellow and Blaise, 1988; Peter and Shanks, 1992). δD_{H_2O} and $\delta^{18}O_{H_2O}$ data for hydrothermal vent fluids from sedimented MOR settings have not been reported previously, except for the Red Sea brines. Simple equilibrium reaction-path calculations are presented here for isotopic alteration of seawater reacting with Escanaba Trough mud and basalt at 220°C and 300°C. The calculations indicate varied isotopic behavior, some of which matches observed vent fluid characteristics, and some of which has not yet been observed in MOR hot springs.

ACKNOWLEDGMENTS

We thank T. Coplen, C. Kendall, and C. Gwinn for assistance with the O and H isotopic analyses, T. Johnson for performing S isotopic analyses, M. Reed for supplying PC-compatible geochemical reaction-path computer codes, and R. Zierenberg for separating smectite from the 217°C vent site. We are also grateful to A.C. Campbell for providing unpublished partial chemical analyses of the vent fluid samples, and to A.C. Campbell, D.R. Janecky, R.O. Rye, and R. A. Zierenberg for comments on the manuscript.

SAMPLES

Clear hydrothermal fluids were sampled using DSV *Alvin* in 1988 from the tops of pyrrhotite-rich massive sulfide mounds at four locations in the NESCA area. The maximum measured fluid temperatures at the four sampled sites were 217°C, 108°C, and approximately 18°C and 13°C, respectively (Campbell and others, chap. 11, this volume; A.C. Campbell, written commun., 1989). The 217°C fluids were venting from a porous anhydrite-(barite-silicate) crust on top of a sulfide mound. Fluid samples were collected with titanium syringe hot water samplers (Campbell and others, chap. 11, this volume), and splits for oxygen and hydrogen isotope analyses were transferred to evacuated glass tubes with soft rubber septa. Before being subsampled for these isotope analyses, each fluid sample was degassed into a vacuum through a needle inserted into the rubber stopper (B.E. Taylor, oral commun., 1990). Samples with low magnesium contents (high-temperature fluids) contained small quantities of whitish translucent solids (amorphous silica?) after storage.

One sample of smectite (Mg-rich saponite) was obtained from the sulfate-rich crust at the active 217°C vent site. The bulk sample was crushed, and the smectite was separated from the sulfate minerals by suspension in distilled water followed by decanting and settling. One sample of pyrrhotite-rich massive sulfide from the vicinity of the 217°C vent site was also analyzed.

Other sulfide mineral samples analyzed as part of this study were recovered using DSV *Sea Cliff* in 1986 and DSV *Alvin* in 1988. The samples include massive pyrrhotite-rich mound material and fragments of pyrrhotite-rich and polymetallic crusts (chimneys?) from various locations within the NESCA and southern Escanaba Trough (SESCA) areas, and from a volcanic edifice at the northern end of the NESCA area at latitude 41°05′ N. (Edifice REX).

METHODS

The oxygen isotopic compositions of vent fluids were measured using an automated CO_2 equilibration technique developed in the U.S. Geological Survey Water Resources Division stable isotope laboratory (T. Coplen and C. Kendall, oral commun., 1989). Two milliliters of each fluid sample was equilibrated with approximately 15 mL of tank CO_2 (+9 per mil, SMOW) at approximately 0.33 atmosphere for 5 to 10 hours in a rocking flask, then the CO_2 was released into the mass spectrometer. Mass balance corrections were made to the measured isotope ratios to account for isotopic shifts of the CO_2 and H_2O during equilibration. The Escanaba Trough samples were

analyzed together with laboratory water standards calibrated as in Coplen and others (1983). The reproducibility ($\pm\sigma$) for individual analyses is estimated to be ±0.05 to 0.10 per mil, based on replicate analyses of different subsamples.

Hydrogen isotopic analyses were performed on hydrogen gas produced by zinc reduction (Kendall and Coplen, 1985). Twenty-microliter aliquots of water were sealed into glass capillary tubes, each of which was loaded into either an evacuated glass reaction vessel or an evacuated sealed reaction tube with 700 mg of zinc shot and a glass-sealed iron bar. The capillary was then broken with the iron bar, and the assembly was inserted into a heating block (for valved reaction vessels) or an oven (for sealed reaction tubes) and held at 455°C to 465°C for 70 minutes. No systematic differences in reproducibility were noted to correlate with either the type of reaction container used, or the mass spectrometer used. Approximately 5 to 10 percent of the hydrogen samples produced by zinc reduction yielded anomalous δD_{H_2O} values that were nonreproducible and clearly incorrect by more than 3σ; these outlying data were eliminated from consideration. The reproducibility ($\pm\sigma$) for individual analyses, after elimination of outlying data, is estimated to be ±0.5 to 1.0 per mil, based on replicate analyses of different subsamples. The δD_{H_2O} values of Escanaba Trough samples were calibrated by interspersed analyses of VSMOW. Samples from the 108°C vent were not analyzed for hydrogen isotopes because all of them have greater than 30 mmol/kg Mg (that is, they are all >60 percent contaminated by ambient seawater), and because the oxygen isotope results are approximately consistent with those of the 217°C vent samples.

Sulfur from mixed-sulfide mineral samples was obtained by sequential chemical extraction as described by Shanks and Seyfried (1987). Acid-volatile sulfide sulfur (mainly from pyrrhotite, sphalerite, and galena) was liberated from the samples with 6*N* HCl at 60°C. The remaining sulfide sulfur (mainly from pyrite, chalcopyrite, isocubanite, and marcasite), and native sulfur if present, were released by adding $CrCl_2$ to the HCl at 85°C (Canfield and others, 1986). $CrCl_2$ also was used to release total sulfide sulfur from samples that were not subjected to the first treatment. H_2S released by each of these treatments was precipitated as Ag_2S. H_2S in the vent fluid samples was precipitated as CdS on board the ship within hours after collection, and later converted to Ag_2S in the onshore laboratory. All Ag_2S samples were subsequently combusted in the laboratory with Cu_2O at 1,050°C to produce SO_2, which was purified by vacuum distillation and then analyzed in the mass spectrometer. The reproducibility and accuracy of the sulfur isotope data are estimated to be ±0.1 to 0.2 per mil, based on multiple analyses of NBS-123 sulfide ($\delta^{34}S$ = 17.1 per mil).

RESULTS

OXYGEN ISOTOPES

The results of oxygen isotope analyses of vent fluids and vent smectite are listed in table 12.1 and the vent fluid data are summarized in figure 12.2. Analyses of seven Escanaba Trough water samples with more than 52 mmol/kg Mg (ambient seawater) yield $\delta^{18}O_{H_2O} = -0.16 \pm 0.05$, indistinguishable from those measured by us in bottom waters from other northeast Pacific Ocean vent sites (average = –0.17), and from the value reported by Craig and Gordon (1965) for North Pacific deep water (–0.17), perhaps slightly lower than the value reported by Welhan and Craig (1983) for the East Pacific Rise (EPR) 21° N. vent site (–0.08). Average values for replicate analyses of 19 water samples from the four vent sites define a single straight mixing line between seawater at –0.17 per mil and high-temperature vent fluid with a zero-Mg intercept at +0.43 ± 0.06 per mil. Considered separately, 16 samples from the 217°C vent yield a zero-Mg intercept at +0.45 per mil whereas three samples from the 108°C vent could be consistent with a slightly lower, but relatively poorly constrained, intercept at approximately +0.3 per mil (fig. 12.2).

HYDROGEN ISOTOPES

Ten analyses of Escanaba Trough vent fluid samples with Mg greater than 52 mmol/kg (ambient seawater) yield $\delta D_{H_2O} = -0.6 \pm 0.6$ per mil, relative to nine analyses of VSMOW samples analyzed at the same times by the same techniques ($\delta D_{H_2O} = 0.0 \pm 1.0$ per mil; table 12.1). The analytical uncertainties of the hydrogen isotope analyses (± 0.5 to 1.0 per mil) apparently are large compared to the real differences in the isotopic compositions of the analyzed samples. With one exception (2036-4C), all of the samples yielded average δD_{H_2O} values that are statistically indistinguishable. Including all samples in a linear regression, we obtain a zero Mg-intercept for nine samples at –0.2 ± 0.7 per mil. The anomalous hydrogen isotopic composition of sample 2036-4C was confirmed by analyses of three separate subsamples, but it is not known for certain if it was anomalous when sampled or if it may have been fractionated during storage or previous subsampling, possibly by evaporation. The same sample also has an anomalously low $\delta^{34}S_{SO_4}$ value (table 12.1), possibly because of sulfide oxidation in a leaky container. Ignoring 2036-4C, we obtain a (preferred) mixing line for eight Escanaba Trough samples between ambient seawater at –0.6 per mil and a zero-Mg intercept at 0.7. In this case, the difference between the high-temperature vent fluid and cold seawater values ($\Delta\delta D = -0.1 \pm 0.3$ per mil) apparently is known with greater precision than is either value with respect to the standard (fig. 12.3).

Table 12.1. Oxygen, hydrogen, and sulfur isotope data for vent fluids and vent minerals from Escanaba Trough.

[—, not determined. Samples were collected using DSV *Alvin* in 1988; $\delta^{18}O_{H_2O}$ and δD_{H_2O} values represent either single analyses or averages of two to three analyses of separate splits (number of determinations given in parentheses); temperatures and Mg concentrations are from A.C. Campbell (written commun., 1989)]

Dive	Sample number	Latitude N.	Longitude W.	Temp. (°C)	Mg (mmol/kg)	$\delta^{18}O_{H_2O}$ (SMOW)	δD_{H_2O} (SMOW)	$\delta^{34}S_{H_2S}$ (CDT)	$\delta^{34}S_{SO_4}$ (CDT)
2036	1C	41°0.016′	127°29.623′	216	47.8	−0.24 (3)	—	—	—
	2C	41°0.016′	127°29.623′	216	39.1	−0.05 (1)	—	—	—
	3C	41°0.014′	127°29.621′	217	2.4	0.41 (3)	−1.0 (3)	—	—
	4C	41°0.014′	127°29.621′	217	5.0	0.45 (3)	1.4 (3)	8.2	17.5
	5C	41°0.016′	127°29.623′	216	37.2	0.01 (1)	—	—	—
	6C	41°0.014′	127°29.621′	217	1.6	0.41 (3)	−0.8 (3)	7.8	20.2
	7C	41°0.016′	127°29.623′	216	9.2	0.23 (1)	−0.5 (2)	—	—
2037	1C	40°59.998′	127°29.621′	13	52.5	−0.10 (1)	−0.5 (2)	—	—
	2C	41°0.015′	127°29.670′	18	51.9	−0.15 (1)	—	—	—
	3C	40°59.998′	127°29.621′	13	52.6	−0.13 (1)	−0.6 (3)	—	—
	4C	41°0.015′	127°29.670′	2	52.5	−0.15 (1)	−0.5 (2)	—	—
	5C	41°0.015′	127°29.670′	18	52.1	−0.17 (2)	−0.8 (3)	—	—
	7C	40°59.998′	127°29.621′	13	52.3	−0.20 (1)	—	—	—
2040	3C	41°0.022′	127°29.843′	108	35.2	−0.04 (1)	—	—	—
	4C	41°0.022′	127°29.843′	108	40.0	−0.03 (1)	—	—	20.3
	6C	41°0.022′	127°29.843′	108	33.0	0.02 (1)	—	—	—
2041	1C	41°0.016′	127°29.623′	215	32.5	0.15 (1)	—	—	—
	7C	41°0.016′	127°29.623′	215	29.9	0.12 (1)	—	—	—
	9C	41°0.016′	127°29.623′	215	20.0	0.23 (1)	−0.3 (2)	7.4	20.3
2036	smectite	41°0.014′	127°29.621′	217	—	6.84	—	—	—
2036	massive sulfide	41°0.014′	127°29.621′	—	—	—	—	4.8	—

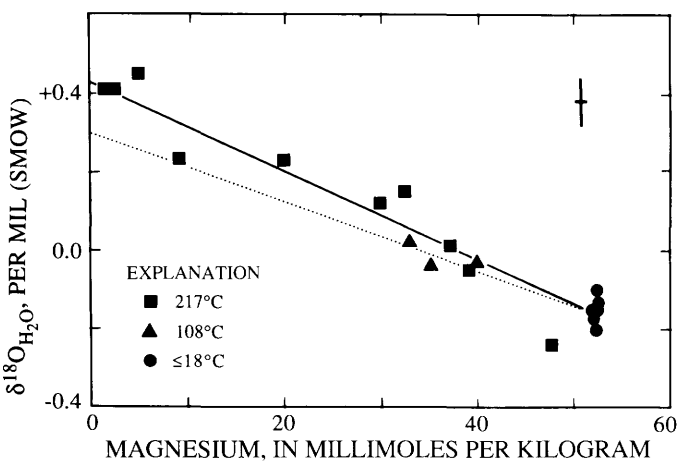

Figure 12.2. Variation of $\delta^{18}O_{H_2O}$ with Mg concentration for mixtures of high-temperature vent fluids and ambient seawater. Each data point represents average of all isotope analyses of given sample (approximate uncertainty [1σ] of each point is indicated by error cross); Mg concentrations are from A.C. Campbell (written commun., 1989); solid line indicates preferred mixing line for all samples; dotted line indicates possible mixing line for 108°C vent.

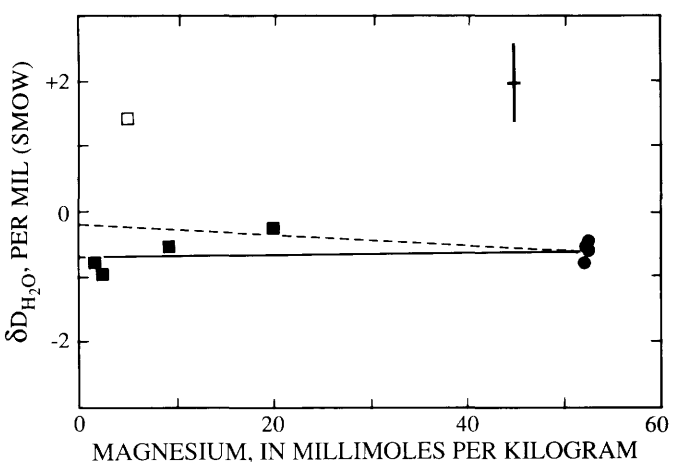

Figure 12.3. Variation of δD_{H_2O} with Mg concentration for mixtures of high-temperature vent fluids and ambient seawater. Data are presented as in figure 12.2, except for sample 2036–4C (open square), which is considered to be anomalous; solid line indicates preferred mixing line (for all samples except 2036–4C); dashed line indicates best fit to all samples (including 2036–4C).

SULFUR ISOTOPES

The three analyses of 217°C vent fluid H_2S are similar, and average +7.8 per mil (table 12.1). Pyrrhotite-rich massive sulfide from the 217°C vent site has $\delta^{34}S_{solid}$ = +4.8, while sulfide minerals from various localities within Escanaba Trough have variable $\delta^{34}S_{solid}$ values between −1 and +12 per mil (table 12.2 and fig. 12.4). In general, there are no consistent differences between $\delta^{34}S$ values of sulfur released by the two stages of sequential chemical extraction. There are no obvious overall geographic trends in $\delta^{34}S_{solid}$ values, nor is there a notable signature in samples associated with hydrocarbons (fig. 12.4), though this has not been thoroughly tested.

DISCUSSION

MINERAL-FLUID ISOTOPIC EQUILIBRIUM

Smectite and hydrothermal fluid from the 217°C vent in the NESCA area are different in $\delta^{18}O$ by 6.4 ± 0.2 per mil, which corresponds to an isotope equilibration temperature of approximately 220°C (Yeh and Savin, 1977, as corrected by Savin and Lee, 1988), in excellent agreement with the measured vent temperature. Zierenberg and Shanks (chap. 14, this volume) report $\delta^{18}O_{solid}$ values for several samples of hydrothermal chlorite (2.13, 2.42, and 2.69 per mil) and smectite (6.04 per mil) separated from altered sediments collected in the SESCA area and between the NESCA and SESCA areas within Escanaba Trough. These minerals could have formed in equilibrium with fluids similar to those now venting in the NESCA area at temperatures between approximately 200°C and 240°C, calculated from fractionation equations of Wenner and Taylor (1971) and Savin and Lee (1988). If the inferred temperatures are meaningful, then they could indicate that surface hydrothermal discharge in Escanaba Trough is limited for some reason to lower temperatures than most other MOR hydrothermal vents. Yet, the abundance of massive coarse-grained pyrrhotite-isocubanite-bearing massive sulfide deposits and polymetallic chimneys may imply localized zones of higher temperature fluid flow either in the past or below the surface at the same sites (Campbell and others, chap. 11, this volume; Koski and others, chap. 16, this volume).

Sulfur isotope data are not indicative of equilibrium either among sulfide minerals or between sulfide minerals and H_2S in the vent fluids. H_2S from the 217°C vent fluid has higher $\delta^{34}S$ than a pyrrhotite-rich sulfide boulder from the same locality, opposite the small fractionation expected at equilibrium between aqueous H_2S and pyrrhotite. Both positive and negative differences are observed between $\delta^{34}S_{solid}$ values of acid-volatile and nonvolatile sulfides in the same samples (table 12.2). As the dominant sulfides in the samples (pyrrhotite, isocubanite, marcasite, and sphalerite) are present in varying proportions, it is not clearly established whether sulfur isotopic equilibrium was

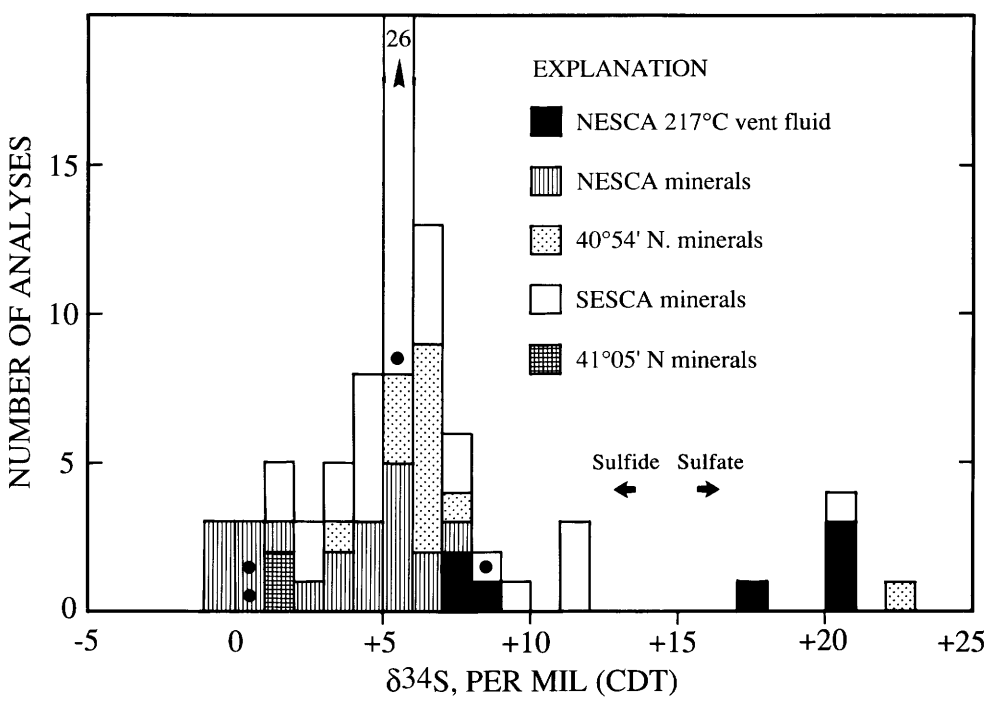

Figure 12.4. Histogram of $\delta^{34}S$ values for Escanaba Trough sulfide and sulfate minerals. Data are from Koski and others (1988), Zierenberg and Shanks (chap. 14, this volume), and table 12.2; dots indicate samples from which hydrocarbons have been reported (Kvenvolden and others, 1986, 1987).

Table 12.2. Sulfur isotope data for sulfide minerals from Escanaba Trough.

[Samples were collected using DSV *Sea Cliff* in 1986 and DSV *Alvin* in 1988. "HCl" and "$CrCl_2$" refer to sulfur extraction methods (see text); —, not determined; po, pyrrhotite; cp, chalcopyrite; sl, sphalerite; wz, wurtzite; mc, marcasite; icu, isocubanite; asp, arsenopyrite; HC, hydrocarbons]

Dive	Sample number	Latitude N.	Longitude W.	$\delta^{34}S$ (HCl)	$\delta^{34}S$ ($CrCl_2$)	Comments
Edifice REX						
2039	3	41°5.507′	127°28.636′	—	1.8	cp-po-sl-wz (with barite)
2039	5	41°5.485′	127°28.642′	—	1.6	po-sl (blocky fine grained)
NESCA						
658	R3-A1	40°59.998′	127°29.602′	5.9	5.1	po-mc-(sl-cp-icu)
	R3-A2	40°59.998′	127°29.602′	6.5	5.3	po-mc-sl-(icu-cp-asp) (fine-grained)
	R3-A2	40°59.998′	127°29.602′	6.1	5.9	po-mc-sl-(icu-cp-asp) (coarse-grained)
	R4-1	41°0.233′	127°29.644′	7.9	4.0	po-(cp)
	R4-1	41°0.233′	127°29.644′	4.8	5.1	po-(cp)
659	R3-6	41°1.107′	127°29.627′	−0.3	−0.1	po (massive fine-grained) (HC in other R3 pieces)
	R4-2	41°1.107′	127°29.627′	0.4	0.9	po (coarse-grained)
	R4-2	41°1.107′	127°29.627′	−0.7	1.0	po
2033	1	41°0.219′	127°29.561′	1.3	—	po-(+Cu-Fe sulfide)
2035	3	40°58.836′	127°30.149′	—	3.3	po (massive with silica?)
2036	1A	41°0.014′	127°29.621′	—	4.8	po
SESCA						
662	R1-A	40°47.393′	127°30.299′	5.0	4.7	po-(mc-icu) (inner zone)
	R1-A	40°47.393′	127°30.299′	5.6	5.5	po-(mc-icu-sl-cp) (outer crust)
	R1-J	40°47.393′	127°30.299′	6.0	5.6	po-(mc?-icu?) (outer zone of chimney)
	R1-J	40°47.393′	127°30.299′	5.9	5.4	po-(mc?-icu?) (middle zone of chimney)
	R1-J	40°47.393′	127°30.299′	5.9	5.4	po (coarse inner chimney lining)
	R1-J	40°47.393′	127°30.299′	—	4.0	po-(mc?-icu?) (outer zone of chimney)
663	R1-3	40°46.395′	127°31.150′	—	1.6	po (coarse bladed inner chimney lining)
	R1-3	40°46.395′	127°31.150′	—	2.7	po (outer chimney wall)

attained. Apparent nonequilibrium sulfur isotope systematics are commonly observed in MOR massive sulfides, and have been attributed in part to irregular temporal variations in the $\delta^{34}S_{H_2S}$ values of the pore fluids from which the sulfide minerals precipitated (Shanks and Seyfried, 1987; Woodruff and Shanks, 1988).

COMPARISON WITH OTHER SITES

The range of $\delta^{34}S_{solid}$ values at Escanaba Trough (−1 to +12) is large compared to those at most other MOR vent sites. It encompasses the ranges observed at sediment-free vent sites (+1 to +6 per mil; Arnold and Sheppard, 1981; Styrt and others, 1981; Zierenberg and others, 1984; Bluth and Ohmoto, 1988; Woodruff and Shanks, 1988), as well as some of the relatively low values observed at Guaymas Basin, EPR (−4 to +5 per mil; Peter and Shanks, 1992) and most of the relatively high values observed at Middle Valley, Juan de Fuca Ridge (+2 to +17 per mil; Goodfellow and Blaise, 1988). Relatively high $\delta^{34}S_{solid}$ values could be consistent with relatively large proportions of hydrothermal H_2S formed by reduction of seawater sulfate (Shanks and others, 1981; Koski and others, 1988; Goodfellow and Blaise, 1988) whereas negative $\delta^{34}S_{solid}$ values may require contributions of biogenic sulfide from the sediments (Peter and Shanks, 1992).

The inferred differences in δD_{H_2O} and $\delta^{18}O_{H_2O}$ between the high-temperature vent fluids and ambient seawater at Escanaba Trough ($\Delta\delta^{18}O_{H_2O} = +0.6 \pm 0.1$; $\Delta\delta D_{H_2O} = -0.1 \pm 0.3$; t = 108°C to 217°C) are relatively small compared to most values reported for high-temperature vent fluids from latitude 13° N., EPR ($\Delta\delta^{18}O_{H_2O}$ = +0.4 to +0.7; $\Delta\delta D_{H_2O}$ = +0.7 to +1.6; t = 317°C to 335°C; Michard and others, 1984; Merlivat and others, 1987), from the southern Juan de Fuca Ridge ($\Delta\delta^{18}O_{H_2O}$ = +0.8 to +1.0; t = >140°C to 284°C; Shanks and Seyfried, 1987), from latitude 21° N., EPR ($\Delta\delta^{18}O_{H_2O}$ = +1.6 to +2.0; $\Delta\delta D_{H_2O}$ = +2.5; t = 273°C to 355°C; Craig and others, 1980; Welhan and Craig, 1983; Von Damm and others, 1985), and from the Kane site, Mid-Atlantic Ridge (MAR) ($\Delta\delta^{18}O_{H_2O}$ = +2.1 per mil; t = 335°C to 350°C; Campbell and others, 1988). These limited data do not clearly indicate that the hydrogen and oxygen isotopic compositions of MOR vent fluids are simply correlated either with the measured vent temperatures or with the presence or

absence of sediments at the vent site; more data are needed. Vent fluid $\delta^{18}O_{H_2O}$ values relatively close to ambient seawater values could be consistent with (1) relatively high water to rock ratios in high-temperature reaction zones (Bowers and Taylor, 1985; Bowers, 1989), (2) contamination of heavier high-temperature fluids by magnesium-depleted seawater beneath the vents, or (3) seawater-rock reactions at relatively low temperatures (<200–300°C) where product hydrothermal minerals form with oxygen isotope ratios close to those of fresh rocks. δD_{H_2O} values relatively close to ambient seawater values could be consistent with (1) reactions at high water to rock ratios, (2) mixing with magnesium-depleted seawater beneath the vents, or (3) reactions with hydrous minerals that have negative δD values.

ISOTOPIC EFFECTS OF SEDIMENTS

Water-rock reactions cause the $\delta^{18}O_{H_2O}$ value of the reacting fluid to increase in most cases where the $\delta^{18}O_{solid}$ value of the reacting rock is higher than that of the solid reaction product (for example, Taylor, 1979). Because of the temperature dependence of oxygen isotope fractionation, seawater reacting with basalt (+5.7 per mil) is enriched in ^{18}O at temperatures above approximately 200°C, but can be depleted in ^{18}O at lower temperatures (for example, Böhlke and others, 1984; Bowers and Taylor, 1985). Compared to basalts, the sediments filling Escanaba Trough have relatively high $\delta^{18}O_{solid}$ values. Unaltered bulk sand and mud have $\delta^{18}O_{solid}$ of 8.7 to 10.3 per mil (Zierenberg and Shanks, chap. 14, this volume), whereas the clay fractions have $\delta^{18}O_{solid}$ greater than 12 per mil (Savin and Epstein, 1970; Zierenberg and Shanks, chap. 14, this volume). Seawater reacting with the sediment therefore could be enriched in ^{18}O over a wider range of temperatures, and could be more highly enriched in ^{18}O for a given amount of reaction, than seawater reacting with basalt, especially if low-$\delta^{18}O$ detrital quartz is relatively unreactive.

In contrast, it is possible that the initial δD_{solid} values of the sediment are less than or equal to the δD_{solid} values of seawater-sediment reaction products, so that the reacting fluid may tend to be relatively unchanged or it may be depleted in deuterium at all reasonable reaction temperatures. δD_{solid} values of Escanaba Trough sediments have not been measured; however, studies of continental weathering products and deep-sea detrital sediments indicate that they probably are between approximately –90 and –50 per mil (Savin and Epstein, 1970; Lawrence and Taylor, 1971). Hydrogen isotope fractionations between hydrous silicates and water are not well known, but most values for magnesium- and aluminum-rich phases probably are between approximately –50 and 0 per mil at temperatures between 200°C and 500°C, while those for analogous iron-rich phases may be more negative by as much as 50 per mil (Taylor, 1979; Graham and others, 1980; Marumo and others, 1980; Bowers and Taylor, 1985). Natural chlorites and amphiboles formed in oceanic rocks altered by seawater above 200°C commonly have δD_{solid} values between –60 and –30 per mil (Stakes and O'Neil, 1982). Thus, depending on the proportion of hydrogen dissolved from reacting sediment to hydrogen precipitated in hydrothermal phases, and depending on the temperature of reaction and the compositions of the hydrothermal phases, it is possible that seawater-sediment reactions could cause the δD_{H_2O} value of reacting seawater to remain relatively unchanged or to decrease significantly while causing its $\delta^{18}O_{H_2O}$ value to increase. This is in marked contrast to both observed and calculated effects of hydrothermal seawater-basalt reactions, in which the relative increases in fluid δD_{H_2O} values are generally greater than or equal to those in fluid $\delta^{18}O_{H_2O}$ values (Craig and others, 1980; Bowers and Taylor, 1985; Merlivat and others, 1987; Bowers, 1989).

SEAWATER-ROCK REACTION MODELS

Simple mass balance models for equilibrium isotope exchange between hydrothermal fluids and rocks are summarized by Taylor (1979), whereas Bowers and Taylor (1985) and Bowers (1989) have presented more complex path-dependent exchange models. Both types of calculation predict a positive correlation between $\delta^{18}O_{H_2O}$ and δD_{H_2O} values of fluids that have interacted with basalt at temperatures greater than about 200°C, such that the highest fluid values are attained at low "water to rock ratios." (The term "water to rock ratio" or W/R is retained here for comparative purposes, although its physical significance in real systems is open to debate; it is defined as the weight ratio of aqueous solution to reacted (equilibrated) solids, consistent with its use by Taylor, Bowers, and others.) The relatively low $\delta^{18}O_{H_2O}$ value of the Escanaba Trough vent fluid, compared to those of other submarine vent sites, could be qualitatively consistent with basalt reactions at relatively high W/R, or at relatively low temperatures, but the apparent lack of deuterium enrichment may indicate significant sediment reactions.

To illustrate the contrasting effects of basalt and sediment alteration on hydrothermal fluids, we have calculated simple isothermal equilibrium reaction-path models for isotope exchange between seawater and basalt, and between seawater and turbidite sediment typical of Escanaba Trough, at 220°C and 300°C. Temperatures of hydrothermal reaction and isotopic equilibration at Escanaba Trough are not well known, but must be higher than the measured vent temperature (217°C). Both the silica concentration (6.9 mmol/kg) and the Na/K molar ratio (14) of the sampled vent fluid (Campbell and others, chap. 11, this volume) could indicate equilibration with quartz and alkali-aluminum silicates at less than 300°C (possibly less than

250°C; Truesdell, 1984). Occurrences of hydrothermal smectite, talc, and chlorite denoting similar temperatures elsewhere within Escanaba Trough (Zierenberg and Shanks, chap. 14, this volume) may indicate that this is a consistent feature of the system; however, it is also possible that much higher temperatures prevail in the shallow subsurface, as inferred from the copper-rich compositions of some sulfide samples (Koski and others, chap. 16, this volume).

Chemical and mineralogical changes as functions of incremental reaction progress during simple seawater-rock reactions were calculated using program CHILLER (Reed, 1982; Spycher and Reed, 1989), with the thermodynamic data base SOLTHERM (Spycher and Reed, 1989) at the saturation pressure of water. The thermodynamic data were not altered to account for the effects of pressure at the bottom of Escanaba Trough (330 bars), as the dielectric constant of water is relatively insensitive to pressure at temperatures less than 300°C (Helgeson and Kirkham, 1974). Aqueous NH_3 and NH_4^+ were added to the data base (Shock and others, 1989) and included in the calculations because ammonium is a significant component of the Escanaba Trough vent fluids (Campbell and others, chap. 11, this volume). The effect of dissolved ammonium in the isothermal reaction path calculations is small, despite the fact that it has a major effect on the calculation of high-temperature fluid properties from the low-temperature vent fluid analyses. Isotope fractionations were calculated using program ISO (J.K. Böhlke, unpub. code, 1989), which was written as a post-processor for CHILLER with general isotope mass balance equations similar to those summarized by Bowers and Taylor (1985). Isotope fractionation factors used by ISO are generally the same as those used by Bowers and Taylor (1985), Janecky and Shanks (1988), and Bowers (1989), except that hydrogen isotope fractionation factors for phyllosilicates and amphiboles were assigned values based on Taylor's (1979) estimated serpentine curve (for Mg and Al phases) or 50 per mil lighter than the serpentine curve (for Fe phases). The calculations proceeded as follows: (1) Seawater was heated by itself in an open system to the temperature of reaction; precipitated minerals (mainly anhydrite) were removed from the system after each step; the compositions of seawater heated to 220°C and 300°C are given in table 12.3. (2) The bulk composition of Escanaba Trough sediment or basalt was then titrated into the heated seawater in a "closed" system at constant temperature; precipitated minerals were retained in the system and allowed to re-equilibrate chemically and isotopically with the coexisting solution at all subsequent reaction steps. The initial compositions of reacting sediment and basalt used in the calculations are given in table 12.3. The calculated mineralogic variations of the solid reaction products are presented qualitatively as functions of W/R in figure 12.5; the corresponding oxygen, hydrogen, and sulfur isotope variations in reacting seawater are summarized in figure 12.6.

The dominant phases at moderate to low W/R in the simulated basalt reactions are chlorite, albite, prehnite, quartz, actinolite, and epidote, approximately in agreement with those predicted by Bowers and Taylor (1985) and produced experimentally (Mottl, 1983). The dominant phases at moderate to low W/R in the simulated mud reactions are quartz, muscovite, albite, chlorite, and calcite. The calculated assemblages for each rock type are only slightly different at the different temperatures. In all of the calculations, anhydrite and hematite both are stable at high W/R in the presence of seawater sulfate, but they are replaced by more reduced assemblages at W/R less than 4 to 6 (basalt) or W/R less than 10 to 12 (mud). From that point on, dissolved sulfur is essentially all reduced. The concentrations of dissolved sulfate just before reduction are low (< 6 mmol/kg), as both mud and basalt supply significant amounts of calcium to form anhydrite isothermally. Throughout most of the range of W/R where sulfur is reduced, the pH and ΣS concentration in the fluid phase are buffered at fairly constant values (pH is approximately 5.4 for mud at 300°C, 5.6 for mud at 220°C, 6.1 for basalt at 300°C, and 6.6 for basalt at 220°C; ΣS is approximately 1 to 2 mmol/kg for mud and basalt at 300°C and approximately 0.1 to 0.2 mmol/kg for mud and basalt at 220°C). The calculated final fluid pH and H_2S concentrations in the seawater-mud reactions are approximately consistent with the observed values in the vent fluids (pH_{25} = 5.4, H_2S = 1.1 mmol/kg; Campbell and others, chap. 11, this volume).

The isotopic effects of temperature are most notable in the evolution of $\delta^{18}O_{H_2O}$, which is especially sensitive to temperature-dependent fractionation factors (as indicated by the bulk rock curves in fig. 12.6). The effects of rock type are significant for all of the isotope systems, but especially so for δD_{H_2O}, which evolves in opposite directions during reactions with mud and basalt. The calculations indicate that relatively large negative δD_{H_2O} values may be acquired by seawater reacting with argillaceous sediments at low values of W/R (for example, $\delta D_{H_2O} = -10$ per mil at W/R = 0.2 to 0.4). At comparable values of W/R, the highest fluid $\delta^{18}O_{H_2O}$ values result from high-temperature reactions with mud, whereas the highest fluid δD_{H_2O} and $\delta^{34}S_{H_2S}$ values result from reactions with anhydrous basalt. The calculations predict negative correlations between $\delta^{34}S_{H_2S}$ and $\delta^{18}O_{H_2O}$, and they indicate potentially large variations in $\delta^{34}S_{H_2S}$ at intermediate to large values of W/R, as sulfide derived from quantitative reduction of seawater sulfate ($\delta^{34}S_{SO_4}$ = +21, Rees and others, 1978) mixes with either basalt sulfide ($\delta^{34}S$ = +0.1, Sakai and others, 1984) or diagenetic (bacteriogenic) sulfide in mud ($\delta^{34}S \approx -20$, Goldhaber and Kaplan, 1974).

In the simulated reaction with basalt at 300°C, the fluid oxygen, hydrogen, and sulfur isotope curves converge on their respective values at EPR latitude 21° N. ($\Delta\delta^{18}O_{H_2O}$ = +1.6 to +2.0; $\Delta\delta D_{H_2O}$ = +2.5; $\delta^{34}S_{H_2S}$ = +1 to +6; Craig and others, 1980; Welhan and Craig, 1983; Woodruff and

Table 12.3. Compositions of rocks and of heated seawater before and after calculated seawater-rock reactions.

[Seawater compositions before reaction represent endpoints in open-system CHILLER calculations for heating seawater by itself (low-temperature seawater analysis from Von Damm and others, 1985). Mud composition includes major elements and $\delta^{18}O$ from sample L2-86-NC-4G, 138-145 (Zierenberg and Shanks, chap. 14, this volume); C and CO_2 are averages for analyses of sediment at DSDP Site 35 (Vallier, 1970); S is typical background (nonhydrothermal) value for Escanaba Trough sediment (Karlin and Lyle, 1986); H_2O was calculated by difference (allowing for other minor components reported by Zierenberg and Shanks, chap. 14, this volume); $Fe^{2+}/Fe_t = 2/3$ is typical value for subsurface terrigenous sediments; NH_3 is from C/N(mol.) = 7 (marine plankton, Redfield, 1958); δD is mid-range of values for detrital argillaceous sediments at similar latitudes (Savin and Epstein, 1970; Lawrence and Taylor, 1971); $\delta^{34}S$ is typical value for marine diagenetic (bacteriogenic) sulfide (Goldhaber and Kaplan, 1974). Basalt composition includes major elements and S from sample D17-10 (Clague and others, 1984, assuming all S is reduced); Fe^{2+}/Fe_t (0.85), $\delta^{18}O$, and $\delta^{34}S$ are typical fresh MORB values (Muehlenbachs and Clayton, 1972; Sakai and others, 1984). Reacted seawater compositions are from closed-system calculations at W/R = 2.8 (220°C) and W/R = 5.6 (300°C), where $\delta^{18}O_{H_2O}$ is equal to measured Escanaba Trough value (+0.43 per mil). —, not determined]

	Seawater before reaction		Rocks before reaction		Seawater after reaction with mud	
	220°C (mmol/kg)	300°C (mmol/kg)	Mud (wt percent)	Basalt (wt percent)	220°C (mmol/kg)	300°C (mmol/kg)
SiO_2	0.006	0.004	52.8	50.7	4.0	7.9
$AlO_{1.5}$	0	0	17.3	15.7	.001	.003
$FeO_{1.5}$	0	0	2.65	1.61	—	—
FeO	0	0	4.77	8.18	.04	.05
MgO	52.1	48.2	3.96	7.42	.11	.06
CaO	2.51	.21	3.10	11.5	26.8	39.6
$NaO_{0.5}$	464	464	2.20	2.76	478	448
$KO_{0.5}$	9.80	9.80	3.13	.19	5.5	11.9
H_2O	—	—	7.2	0	—	—
CO_2	1.47	1.47	0	0	69.8	139
H_2S	0	0	.11	.11	.12	1.1
NH_3	0	0	.07	0	15	7.5
pH (T)	6.0	5.5	—	—	5.6	5.4
$\delta^{18}O$	−0.17	−0.17	+9.2	+5.7	+0.43	+0.43
δD	−0.6	−0.6	−50	none	−1.3	−0.9
$\delta^{34}S$	+21	+21	−20	+0.1	+4.8	+9.7

Shanks, 1988) at W/R ≈ 0.3 to 0.5 (fig. 12.6*C*), similar to the degree of reaction required to reach those values in the more complex reaction paths with varying temperatures simulated by Bowers and Taylor (1985). The EPR latitude 21° N. vent fluid data are not reproduced by the 220°C basalt calculations (fig. 12.6*A*) or by either of the mud calculations (fig. 12.6*B*, *D*). In contrast, the oxygen, hydrogen, and sulfur isotope data from Escanaba Trough ($\Delta\delta^{18}O_{H_2O}$ = + 0.60; $\Delta\delta D_{H_2O}$ = −0.1; $\delta^{34}S_{H_2S}$ = +8) are best reproduced by the simulated reactions with mud at much higher values of W/R (approximately 2 to 3 at 220°C, 5 to 6 at 300°C) (fig. 12.6*B*, *D*). These calculations do not rule out the possibility that Escanaba Trough vent fluids flowed through basalt within or below the sediment pile, but they do indicate that basalt reactions are not dominant and that mud reactions alone are sufficient to account for the fluid oxygen, hydrogen, and sulfur isotopic composition.

The Escanaba Trough isotope data are slightly better reproduced by calculations at 300°C than at 220°C, while silica and alkali geothermometers indicate that the Escanaba Trough vent fluid may have equilibrated with altered sediment at temperatures significantly less than 300°C. The temperature sensitivity of the isotope reaction path calculations is limited by large uncertainties in the input parameters and the simplicity of the isothermal closed-system model, while confidence in temperature estimates from mineral equilibria is limited by the lack of information on hydrothermal assemblages in the subsurface. The calculated chemical and isotopic compositions of reacted 220°C and 300°C seawater at the observed $\delta^{18}O_{H_2O}$ value (+0.43) (table 12.3) bracket the composition of the 217°C Escanaba Trough vent fluid for many of the measured components (Campbell and others, chap. 11, this volume). The aqueous Na/K ratios in the simulations are higher than the measured values, reflecting the presence of paragonite (absence of potassium-feldspar) in the calculated assemblages (fig. 12. 5*B*, *D*). The significant enrichment of chloride in the Escanaba Trough vent fluid is not reproduced by simulated reactions with mud, which instead dilute the reacting fluid by 1 percent (300°C, W/R = 5.6) to 2 percent (220°C, W/R = 2.8) because of mud dehydration. Hydration of basalt can increase fluid chloride concentrations, but the observed Escanaba Trough values would be reached only at W/R values too low to be consistent with the $\delta^{18}O_{H_2O}$ values. The relative timing of chloride enrichment

and isotopic modification of the Escanaba Trough vent fluids is not known. W/R values inferred by Campbell and others (chap. 11, this volume) from alkali and iodine mass balance calculations (W/R = 10 ± 5) are generally higher than those indicated by the stable isotope reaction paths (except possibly at 300°C); nevertheless, all estimates are in agreement with the hypothesis that the Escanaba Trough hydrothermal system is relatively seawater-dominated in comparison to others such as at EPR latitude 21° N.

To test some of the uncertainties in the closed system calculations, alternative mud reaction paths were simulated (fig. 12.6*D*). One alternative path was generated by assuming that unreacted mud has $\delta D_{solid} = -50$, instead of −70. This causes the fluid δD_{H_2O} value to be significantly less negative at low W/R, but has little effect at high W/R. Another alternative path was generated by assuming that quartz in unreacted mud was inert, but leaving the bulk $\delta^{18}O$ value of the mud unchanged. As quartz composes less than 20 percent of the chosen mud by weight (Zierenberg and Shanks, chap. 14, this volume), this assumption has relatively little effect on the calculated fluid $\delta^{18}O_{H_2O}$ except at low W/R. Reasonable variations in the sulfur content, $\delta^{34}S$ value, and (or) Fe^{2+}/Fe_t of unreacted mud could cause significant shifts in the position of the calculated fluid $\delta^{34}S_{H_2S}$ curves, but would not change their general configurations. Some of the mineral-water hydrogen isotope fractionation factors used in our calculations at 220°C are more negative than those used by Bowers and Taylor (1985) by as much as 20 to 30 per mil. Substituting their values would have the effect of lowering the 220°C calculated fluid δD_{H_2O} curves slightly, but would not alter our general conclusions.

For comparison with the closed-system calculations, analogous open-system calculations also were performed (figs. 12.7 and 12.8). In the open-system calculations, solid reaction products were removed from the chemical and isotopic inventories at each reaction step between seawater and rock. δD_{H_2O} values in simulated open seawater-rock systems are almost identical to those in closed systems. $\delta^{18}O_{H_2O}$ values in open systems are significantly higher than those in closed systems at low W/R, but the differences are insignificant in the vicinity of the observed Escanaba Trough values ($\delta^{18}O_{H_2O} = +0.43$ at W/R = 3 at 220°C, 6 at 300°C, for open-system reactions with mud). The most dramatic difference between the two sets of calculations is that fluid $\delta^{34}S_{H_2S}$ values approach the unreacted rock values much more rapidly in the open systems, such that the observed $\delta^{34}S$ value of the vent fluid

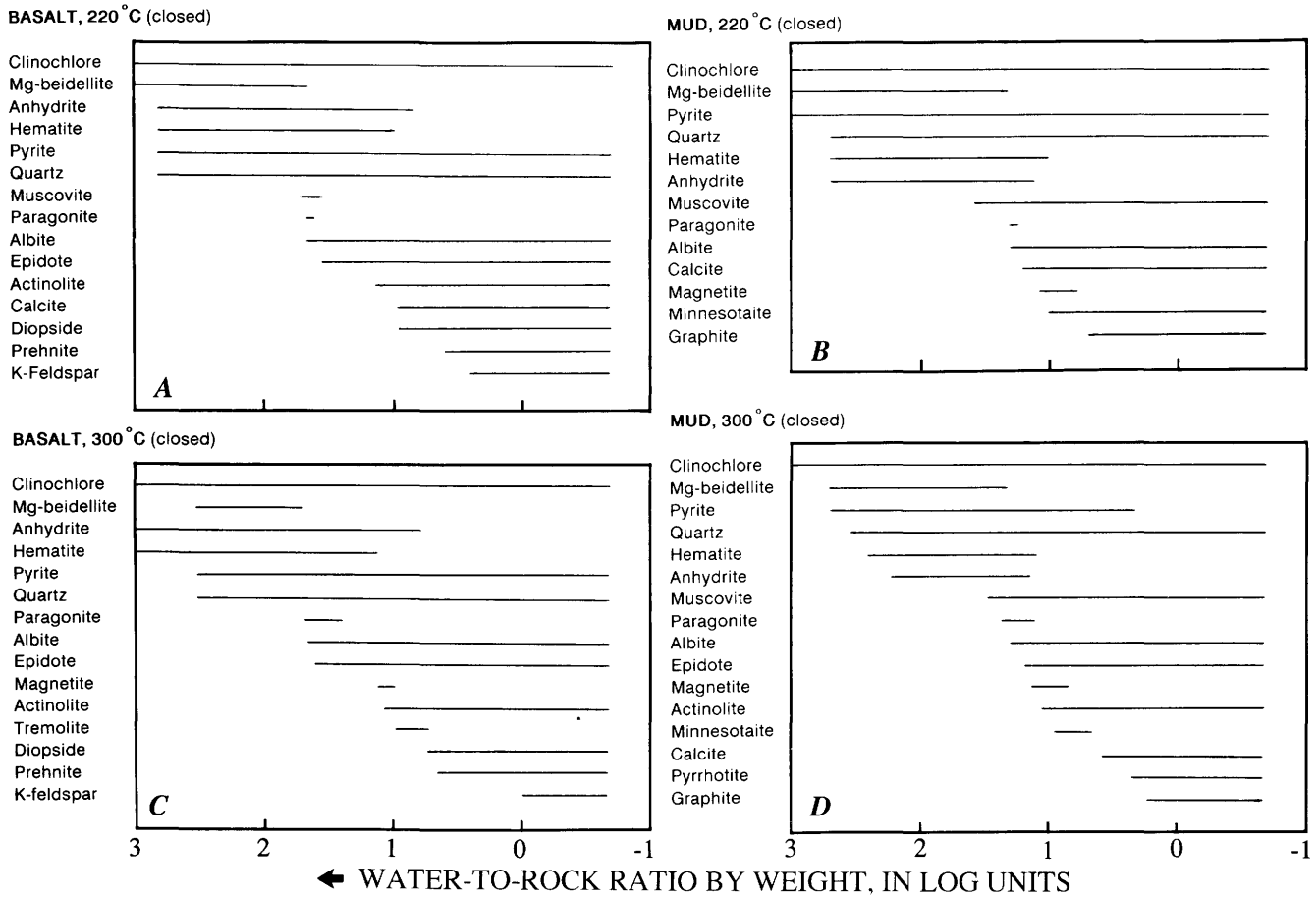

Figure 12.5. Calculated mineral assemblages produced during reactions of seawater with Escanaba Trough basalt and mud, as functions of water to rock weight ratios in closed systems at 220°C and 300°C, corresponding to isotope fractionation trends shown in figure 12.6.

occurs at much higher W/R (18 at 220°C, 20 at 300°C, for reactions with mud) than does the observed vent fluid $\delta^{18}O_{H_2O}$ value; that is, the observed sulfur and oxygen isotope ratios are not compatible in the open-system models (fig. 12.8).

While it is generally agreed that relatively high $\delta^{34}S_{H_2S}$ values indicate relatively large proportions of reduced seawater sulfate in MOR vent fluids, it is debatable how and where H_2S from reduced sulfate enters the hydrothermal systems (Styrt and others, 1981; Shanks and Seyfried, 1987; Janecky and Shanks, 1988; Woodruff and Shanks, 1988; Bluth and Ohmoto, 1988; Bowers, 1989). Experiments and calculations indicate that most of the original dissolved sulfate in recharging heated seawater in contact with basalt or sediment may be removed by precipitation of $CaSO_4$ (Seyfried and Bischoff, 1979, 1981; Bowers, 1989; this study). If $CaSO_4$ precipitated during recharge (or an additional parcel of sulfate-rich seawater) is not made available at depth for subsequent reduction, then $\delta^{34}S_{H_2S}$ values of circulating heated seawater rapidly approach rock values (for example, 0 to 1 per mil for basalt) before significant changes occur in $\delta^{18}O_{H_2O}$, as in our open-system calculations. In this case fluids ascending from deep reaction zones with elevated $\delta^{18}O_{H_2O}$ values would have low $\delta^{34}S_{H_2S}$ values, and higher observed vent fluid $\delta^{34}S_{H_2S}$ values would imply some form of sulfate reduction during discharge (Shanks and Seyfried, 1987; Woodruff and Shanks, 1988; Bowers, 1989). If previously precipitated $CaSO_4$ (or an additional parcel of sulfate-rich seawater) is made available for reduction by hot deeply circulating seawater, as modeled crudely by our closed-system calculations, then vent fluids with highly variable $\delta^{34}S_{H_2S}$ values could be produced at depth without modification at the discharge site (Styrt and others,

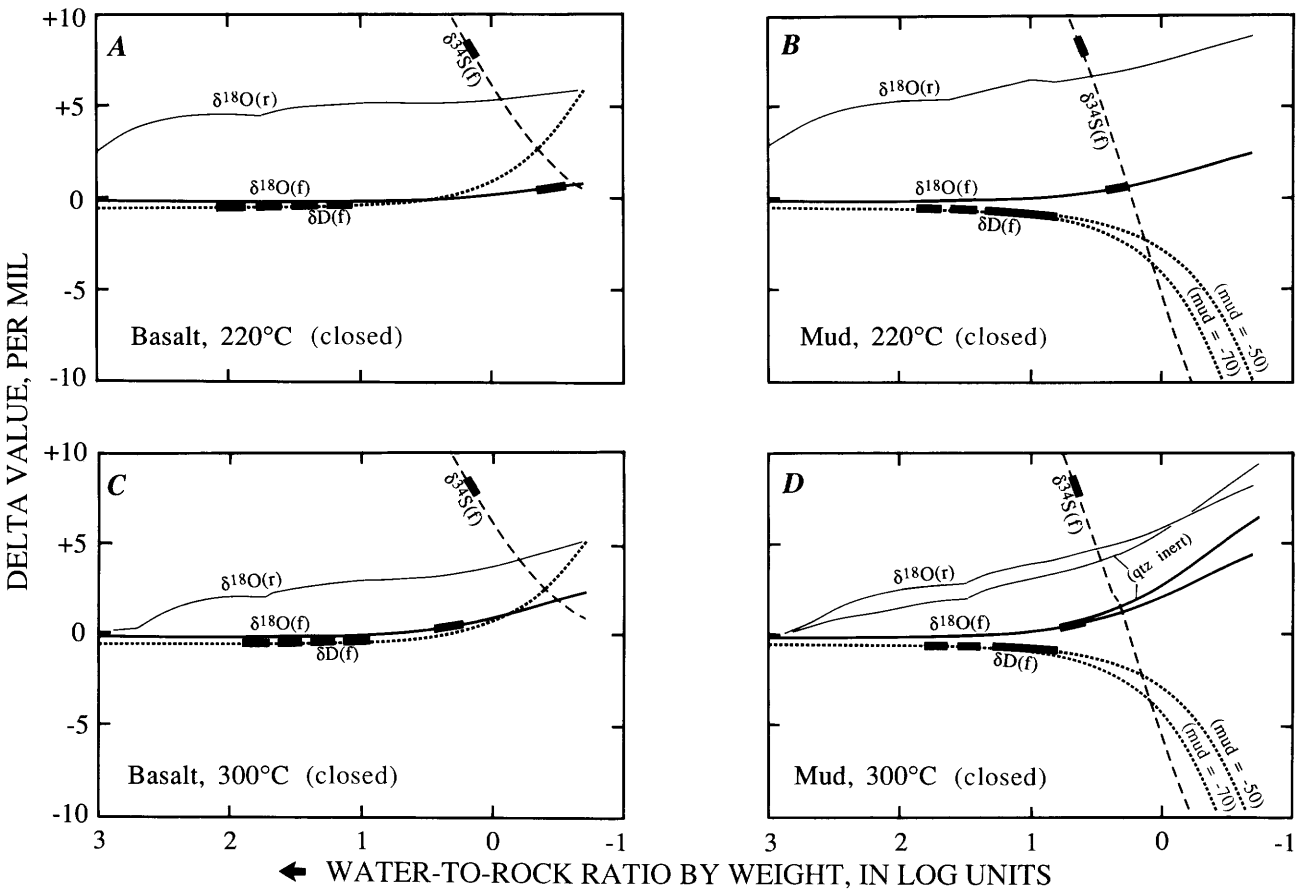

Figure 12.6. Calculated isotope shifts in oxygen, hydrogen, and sulfur for seawater reacting with Escanaba Trough basalt and mud, as functions of water to rock weight ratios in closed systems at 220°C and 300°C, corresponding to mineralogic variations shown in figure 12.5. Curves were calculated using program CHILLER (Reed, 1982; Spycher and Reed, 1989) for geochemical reaction path simulation (see fig. 12.5) and program ISO (J.K. Böhlke, unpublished code) for corresponding isotopic fractionation; starting compositions of seawater, mud, and basalt are listed in table 12.3. Curves labeled (f) are for bulk fluid phase; curves labeled (r) are for bulk solid reaction products. Heavy bars on curves indicate approximate intercepts of calculated curves with observed Escanaba Trough fluid values, which are best reproduced for all three isotope systems by mud reactions between 220°C (W/R = 2 to 3) and 300°C (W/R = 5 to 6) (see table 12.3). Observed isotope shifts for East Pacific Rise, latitude 21° N., vent fluids ($\Delta\delta^{18}O_{H_2O}$ = +1.6 to +2.0; $\Delta\delta D_{H_2O}$ = +2.5; $\delta^{34}S_{H_2S}$ = +1 to +6) are nearly matched by 300°C basalt reaction curves at W/R = 0.3 to 0.5.

1981; Bluth and Ohmoto, 1988). This situation would be difficult to distinguish isotopically from the hybrid model of Janecky and Shanks (1988), which calls for reduction of previously precipitated $CaSO_4$ by ascending fluids with low $\delta^{34}S_{H_2S}$ in contact with unaltered rock reductants in the discharge region below the vents. The good agreement between our closed system equilibrium calculations and the observed hydrogen, sulfur, and oxygen isotope values at Escanaba Trough (and at EPR 21° N., allowing for differences in basalt composition and temperature), may be somewhat fortuitous; nevertheless, both our calculations and those of Janecky and Shanks (1988) imply that relatively high $\delta^{34}S_{H_2S}$ values in MOR vent fluid may require that seawater sulfate in excess of the amounts available in completely open systems is reduced while the fluids are in contact with unoxidized rocks (that is, in the subsurface before venting).

SHALLOW SUBSURFACE MIXING?

Zierenberg and Shanks (chap. 14, this volume) and Zierenberg and others (chap. 10, this volume) suggest that much of the observed sediment alteration and sulfide mineralization at Escanaba Trough may be the result of shallow subsurface circulation of heated seawater, possibly mixing with ascending hotter hydrothermal fluids. Similar processes could account for some of the observed characteristics of the hydrothermal vent fluids, such as relatively low temperatures, oxygen and hydrogen isotope ratios relatively close to those of seawater, and $\delta^{18}O_{H_2O}$ and temperature consistent with those required to produce magnesium-enriched chlorites (Zierenberg and Shanks, chap. 14, this volume). In the limiting case where no separate ascending hot fluid reservoir is involved, this hypothesis would correspond roughly to the assumptions made in the reaction-path calculations described above. If subsurface mixing of hydrothermal fluids from depth with shallower-circulating seawater in contact with sediment has obscured many of the characteristics of a hotter deeper fluid reservoir, then more work on altered sediment, hot pore waters, and vent fluids will be needed to document these processes.

CONCLUSIONS

Isotope ratios of oxygen, hydrogen, and sulfur in hydrothermal vent fluids at Escanaba Trough are closer to seawater values than those of most other MOR vents, es-

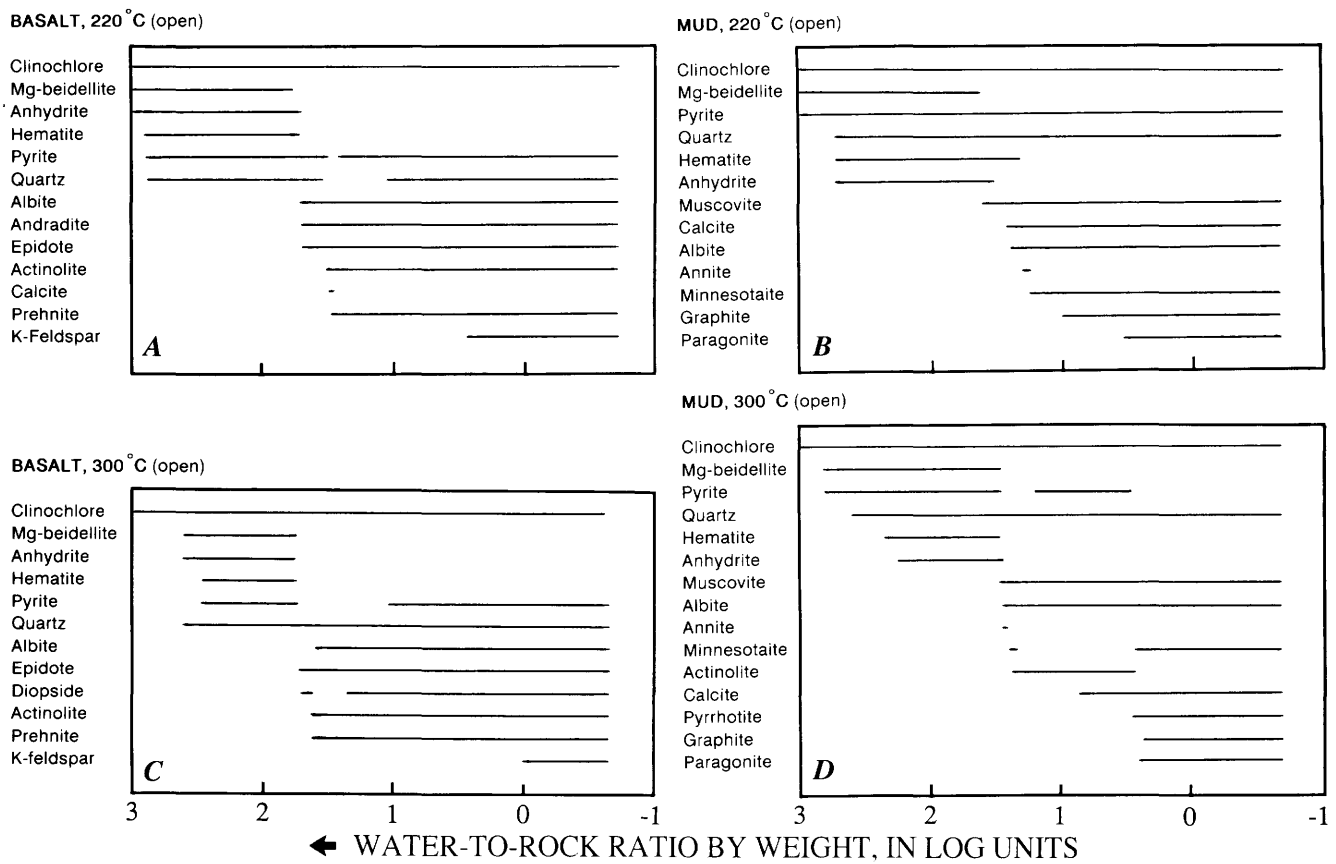

Figure 12.7. Calculated mineral assemblages produced during reactions of seawater with Escanaba Trough basalt and mud, as functions of water-to-rock ratios in open systems at 220°C and 300°C, corresponding to isotope fractionation trends shown in figure 12.8.

pecially those at latitude 21° N., EPR. In contrast to the hydrothermal system at EPR 21° N., the Escanaba Trough system occupies a sedimented rift valley, and hydrothermal fluids currently vent at lower temperatures.

Isothermal reaction-path calculations indicate significant contrasts in isotope fractionation trends between seawater reacting with basalt and with typical Escanaba Trough mud. At comparable temperature and cumulative water to rock mass ratio (W/R), reactions with sediment can increase $\delta^{18}O_{H_2O}$ more strongly, and decrease δD_{H_2O}, in contrast to basalt reactions that increase $\delta^{18}O_{H_2O}$ and δD_{H_2O} at roughly comparable rates. The calculations predict potentially large variability in fluid $\delta^{34}S_{H_2S}$, negative correlations between fluid $\delta^{34}S_{H_2S}$ and $\delta^{18}O_{H_2O}$, and potentially significant negative fluid δD_{H_2O} values from reactions with sediments. Considered together, the $\delta^{18}O_{H_2O}$, δD_{H_2O}, and $\delta^{34}S_{H_2S}$ values of vent fluids at Escanaba Trough are consistent with seawater-sediment reactions at temperatures between 220°C and 300°C at W/R of about 2 to 6 (closed system). This is in contrast to the apparent constraints at EPR 21° N., where observed fluid $\delta^{18}O_{H_2O}$, δD_{H_2O}, and $\delta^{34}S_{H_2S}$ values are reproduced by calculated seawater-basalt reactions at W/R of about 0.3 to 0.4 involving temperatures of 300°C and greater (Bowers and Taylor, 1985; Bowers, 1989). The calculations do not rule out the possibility of seawater-basalt reactions at higher temperatures at depth beneath Escanaba Trough, but they do indicate that seawater-sediment reactions alone at high W/R and temperatures less than 300°C are sufficient to account for the observed isotopic composition of the 217°C vent fluid.

The modern vent fluid temperature and $\delta^{18}O_{H_2O}$ may be similar to those of fluids responsible for chloritization of mud, a process thought to reflect near-surface circulation of magnesium-bearing seawater (Zierenberg and Shanks, chap. 14, this volume). It is possible that the high calculated W/R values for seawater-sediment isotopic equilibration at Escanaba Trough also indicate near-surface phenomena; however, a direct genetic link between chloritites and active vents has not yet been established.

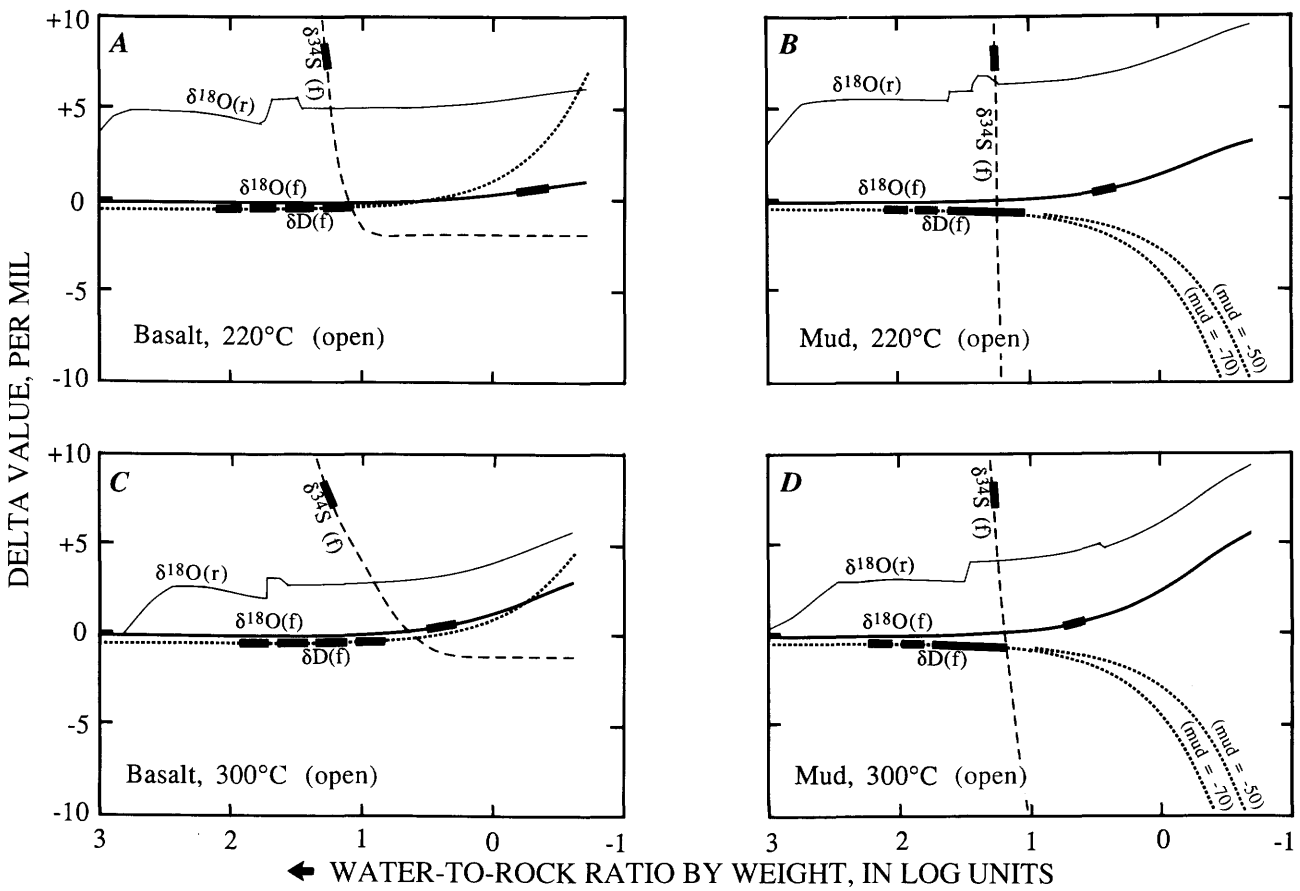

Figure 12.8. Calculated isotope shifts in oxygen, hydrogen, and sulfur for seawater reacting with Escanaba Trough basalt and mud, as functions of water-to-rock weight ratios in open systems at 220°C and 300°C, corresponding to mineralogic variations shown in figure 12.7. Calculations and representations are similar to those of figure 12.6, except that solid reaction products were removed from the open systems after each reaction step, and curves labeled (r) refer to the isotope compositions of only those solids produced within each reaction step. Escanaba Trough vent fluid sulfur and oxygen isotope values are not compatible in the open system simulations.

REFERENCES CITED

Arnold, M.A., and Sheppard, S.M.F., 1981, East Pacific Rise at latitude 21° N: Isotopic composition and origin of hydrothermal sulphur: Earth and Planetary Science Letters, v. 56, p. 145–156.

Bluth, G.J., and Ohmoto, H., 1988, Sulfide-sulfate chimneys on the East Pacific Rise, 11° and 13° N latitudes. Part II: Sulfur isotopes: Canadian Mineralogist, v. 26, p. 505–515.

Böhlke, J.K., Alt, J.C., and Muehlenbachs, K., 1984, Oxygen isotope-water relations in altered deep-sea basalts: Low temperature mineralogical controls: Canadian Journal of Earth Sciences, v. 21, p. 67–77.

Bowers, T.S., 1989, Stable isotope signatures of water-rock interaction in midocean ridge hydrothermal systems: Sulfur, oxygen, and hydrogen: Journal of Geophysical Research, v. 94, p. 5775–5786.

Bowers, T.S., and Taylor, H.P., Jr., 1985, An integrated chemical and stable-isotope model of the origin of midocean ridge hot spring systems: Journal of Geophysical Research, v. 90, p. 12583–12606.

Campbell, A.C., Palmer, M.R., Klinkhammer, G.P., Bowers, T.S., Edmond, J.M., Lawrence, J.R., Casey, J.F., Thompson, G., Humphris, S., Rona, P., and Karson, J.A., 1988, Chemistry of hot springs on the Mid-Atlantic Ridge: Nature, v. 335, p. 514–519.

Campbell, A.C., Palmer, M.R., German, C., and Edmond, J.M., 1989, The chemistry of hydrothermal fluids from the Escanaba Trough in comparison to sediment hosted and sediment starved vent systems: Proceedings 28th International Geological Congress, p. I–231.

Campbell, A.C., German, C.R., Palmer, M.R., Gamo, T., and Edmond, J.M., Chemistry of hydrothermal fluids from the Escanaba Trough, Gorda Ridge, *in* Morton, J.L., Zierenberg, R.A., and Reiss, C.A., eds., Geologic, hydrothermal, and biologic studies at Escanaba Trough, Gorda Ridge, offshore northern California: U.S. Geological Survey Bulletin 2022, chapter 11 (this volume).

Canfield, D.E., Raiswell, R., Westrich, J.T., Reaves, C.M., and Berner, R.A., 1986, The use of chromium reduction in the analysis of reduced inorganic sulfur in sediments and shales: Chemical Geology, v. 54, p. 149–155.

Clague, D., Friesen, W., Quinterno, P., Morgenson, L., Holmes, M., Morton, J., Bouse, R., and Davis, A., 1984, Preliminary geological, geophysical, and biological data from the Gorda Ridge: U.S. Geological Survey Open-File Report 84–364, 33 p.

Coplen, T.B., Kendall, C., and Hopple, J., 1983, Comparison of stable isotope reference samples: Nature, v. 302, p. 236–238.

Craig, H., and Gordon, L.I., 1965, Isotopic oceanography: Deuterium and oxygen 18 variations in the ocean and the marine atmosphere: Symposium on Marine Geochemistry, Graduate School of Oceanography, University of Rhode Island, Occasional Publication 3-1965, p. 277–374.

Craig, H., Welhan, J.A., Kim, K., Poreda, R., and Lupton, J.E., 1980, Geochemical studies of the 21° N EPR hydrothermal fluids: Eos, Transactions American Geophysical Union, v. 61, p. 992.

Davis, E.E., and Becker, Keir, Thermal and tectonic structure of the Escanaba Trough: New heat-flow measurements and seismic-reflection profiles, *in* Morton, J.L., Zierenberg, R.A., and Reiss, C.A., eds., Geologic, hydrothermal, and biologic studies at Escanaba Trough, Gorda Ridge, offshore northern California: U.S. Geological Survey Bulletin 2022, chapter 3 (this volume).

Goldhaber, M.B., and Kaplan, I.R., 1974, The sulfur cycle, *in* Goldberg, E.D., ed., The sea: New York, Wiley-Interscience, v. 5, p. 569–655.

Goodfellow, W.D., and Blaise, B., 1988, Sulfide formation and hydrothermal alteration of hemipelagic sediment in Middle Valley, northern Juan de Fuca Ridge: Canadian Mineralogist, v. 26, p. 675–696.

Graham, C.M., Sheppard, S.M.F., and Heaton, T.H.E., 1980, Experimental hydrogen isotope studies, I. Systematics of hydrogen isotope fractionation in the systems epidote-H_2O, zoisite-H_2O, and AlO(OH)-H_2O: Geochimica et Cosmochimica Acta, v. 44, p. 353–364.

Helgeson, H.C., and Kirkham, D.H., 1974, Theoretical prediction of the thermodynamic behavior of aqueous electrolytes at high pressures and temperatures: I. Summary of the thermodynamic/electrostatic properties of the solvent: American Journal of Science, v. 274, p. 1089–1198.

Janecky, D.R., and Shanks, W.C., III, 1988, Computational modeling of chemical and sulfur isotopic reaction processes in seafloor hydrothermal systems: Chimneys, massive sulfides, and subjacent alteration zones: Canadian Mineralogist, v. 26, p. 805–825.

Karlin, R., and Lyle, M., 1986, Sediment studies on the Gorda Ridge: Oregon Department of Geology and Mineral Industries Open-File Report O-860-19, 76 p.

Kendall, C., and Coplen, T.B., 1985, Multisample conversion of water to hydrogen by zinc for stable isotope determination: Analytical Chemistry, v. 57, p. 1437–1440.

Koski, R.A., Shanks, W.C., III, Bohrson, W.A., and Oscarson, R.L., 1988, The composition of massive sulfide deposits from the sediment-covered floor of Escanaba Trough, Gorda Ridge: Implications for depositional processes: Canadian Mineralogist, v. 26, p. 655–673.

Koski, R.A., Benninger, L.M., Zierenberg, R.A., and Jonasson, I.R., Composition and growth history of hydrothermal deposits in Escanaba Trough, southern Gorda Ridge, *in* Morton, J.L., Zierenberg, R.A., and Reiss, C.A., eds., Geologic, hydrothermal, and biologic studies at Escanaba Trough, Gorda Ridge, offshore northern California: U.S. Geological Survey Bulletin 2022, chapter 16 (this volume).

Kvenvolden, K.A., Rapp, J.B., Hostettler, F.D., Morton, J.L., King, J.D., and Claypool, G.E., 1986, Petroleum associated with polymetallic sulfide in sediment from Gorda Ridge: Science, v. 234, p. 1231–1234.

Kvenvolden, K.A., Rapp, J.B., and Hostettler, F.D., 1987, Hydrocarbon geochemistry of petroleum associated with sediment-hosted sulfides from Escanaba Trough, southern Gorda Ridge: U.S. Geological Survey Open-File Report 87-375C, 18 p.

Lawrence, J.R., and Taylor, H.P., Jr., 1971, Deuterium and oxygen-18 correlation: Clay minerals and hydroxides in Quaternary soils compared to meteoric waters: Geochimica et Cosmochimica Acta, v. 35, p. 993–1003.

LeHuray, A.P., Church, S.E., Koski, R.A., and Bouse, R.M., 1988,

Pb isotopes in sulfides from mid-ocean ridge hydrothermal sites: Geology, v. 16, p. 362–365.

Marumo, K., Nagasawa, K., and Kuroda, Y., 1980, Mineralogy and hydrogen isotope geochemistry of clay minerals in the Ohnuma geothermal area, northeastern Japan: Earth and Planetary Science Letters, v. 47, p. 255–262.

McManus, D.A., and others, 1970, Initial reports of the Deep Sea Drilling Project: Washington, D.C., U.S. Government Printing Office, v. 5, 827 p.

Merlivat, L., Pineau, F., and Javoy, M., 1987, Hydrothermal vent waters at 13° N on the East Pacific Rise: Isotopic composition and gas concentration: Earth and Planetary Science Letters, v. 84, p. 100–108.

Michard, G., Albarede, F., Michard, A., Minster, J.-F., Charlou, J.-L., and Tan, N., 1984, Chemistry of solutions from the 13° N East Pacific Rise hydrothermal site: Earth and Planetary Science Letters, v. 67, p. 297–307.

Morton, J.L., Holmes, M.L., and Koski, R.A., 1987, Volcanism and massive sulfide formation at a sedimented spreading center, Escanaba Trough, Gorda Ridge, northeast Pacific Ocean: Geophysical Research Letters, v. 14, p. 769–772.

Morton, J.L., and Fox, C.G., Structural setting and interaction of volcanism and sedimentation at Escanaba Trough: Geophysical results, *in* Morton, J.L., Zierenberg, R.A., and Reiss, C.A., eds., Geologic, hydrothermal, and biologic studies at Escanaba Trough, Gorda Ridge, offshore northern California: U.S. Geological Survey Bulletin 2022, chapter 2 (this volume).

Mottl, M.J., 1983, Hydrothermal processes at seafloor spreading centers: Application of basalt-seawater experimental results, *in* Rona, P.A., Bostrom, K., Laubier, L., and Smith, K.L., Jr., eds., Hydrothermal processes at seafloor spreading centers: New York, Plenum Press, p. 199–224.

Normark, W.R., Gutmacher, C.E., Zierenberg, R.A., Wong, F.L., and Rosenbauer, R.J., Sediment fill of Escanaba Trough, *in* Morton, J.L., Zierenberg, R.A., and Reiss, C.A., eds., Geologic, hydrothermal, and biologic studies at Escanaba Trough, Gorda Ridge, offshore northern California: U.S. Geological Survey Bulletin 2022, chapter 6 (this volume).

Peter, J.M., and Shanks, W.C., III, 1992, Sulfur, carbon, and oxygen isotope variations in submarine hydrothermal deposits of Guaymas Basin, Gulf of California: Geochimica et Cosmochimica Acta, v. 56, p. 2025–2040.

Redfield, A.C., 1958, The biological control of chemical factors in the environment: American Scientist, v. 46, p. 205–221.

Reed, M.H., 1982, Calculation of multicomponent chemical equilibria and reaction processes in systems involving minerals, gases, and an aqueous phase: Geochimica et Cosmochimica Acta, v. 46, p. 513–528.

Rees, C.E., Jenkins, W.J., and Monster, J., 1978, The sulfur isotopic composition of ocean water sulfate: Geochimica et Cosmochimica Acta, v. 42, p. 377–382.

Sakai, H.D., Des Marais, D.J., Ueda, A., and Moore, J.G., 1984, Concentrations and isotope ratios of carbon, nitrogen, and sulfur in ocean-floor basalts: Geochimica et Cosmochimica Acta, v. 48, p. 2433–2441.

Savin, S.M., and Epstein, S., 1970, The oxygen and hydrogen isotope geochemistry of ocean sediments and shales: Geochimica et Cosmochimica Acta, v. 34, p. 43–63.

Savin, S.M., and Lee, M., 1988, Isotopic studies of phyllosilicates, *in* Bailey, S.W., ed., Hydrous phyllosilicates (exclusive of micas): Mineralogical Society of America, Reviews in Mineralogy, v. 19, p. 189–223.

Seyfried, W.E., Jr., and Bischoff, J.L., 1979, Low temperature basalt alteration by seawater: An experimental study at 70°C and 150°C: Geochimica et Cosmochimica Acta, v. 43, p. 1937–1947.

———1981, Experimental seawater-basalt interaction at 300°C, 500 bars, chemical exchange, secondary mineral formation and implications for the transport of heavy metals: Geochimica et Cosmochimica Acta, v. 45, p. 135–147.

Shanks, W.C., III, and Bischoff, J.L., 1980, Geochemistry, sulfur isotope composition, and accumulation rates of Red Sea geothermal deposits: Economic Geology, v. 75, p. 445–459.

Shanks, W.C., III, Bischoff, J.L., and Rosenbauer, R.J., 1981, Seawater sulfate reduction and sulfur isotope fractionation in basaltic systems: Interaction of seawater with fayalite and magnetite at 200-350°C: Geochimica et Cosmochimica Acta, v. 45, p. 1977–1995.

Shanks, W.C., III, and Seyfried, W.E., 1987, Stable isotope studies of vent fluids and chimney minerals, southern Juan de Fuca Ridge: Sodium metasomatism and seawater sulfate reduction: Journal of Geophysical Research, v. 92, p. 11387–11399.

Shock, E.L., Helgeson, H.C., and Sverjensky, D.A., 1989, Calculation of the thermodynamic and transport properties of aqueous species at high pressures and temperatures: Standard partial molal properties of inorganic neutral species: Geochimica et Cosmochimica Acta, v. 53, p. 2157–2183.

Spycher, N.F., and Reed, M.H., 1989, CHILLER: A program for computing water-rock reactions, boiling, mixing, and other reaction processes in aqueous-mineral-gas systems: Eugene, University of Oregon, (March 1989).

Stakes, D.S., and O'Neil, J.R., 1982, Mineralogy and stable isotope geochemistry of hydrothermally altered oceanic rocks: Earth and Planetary Science Letters, v. 57, p. 285–304.

Styrt, M.M., Brackmann, A.J., Holland, H.D., Clark, B.C., Arnold, V., Eldridge, C.S., and Ohmoto, H., 1981, The mineralogy and isotopic composition of sulphur in hydrothermal sulphide/sulphate deposits on the East Pacific Rise, 21° N latitude: Earth and Planetary Science Letters, v. 53, p. 382–390.

Taylor, H.P., Jr., 1979, Oxygen and hydrogen isotope relationships in hydrothermal mineral deposits, *in* Barnes, H.L., ed., Geochemistry of hydrothermal ore deposits: New York, John Wiley and Sons, p. 236–277.

Truesdell, A.H., 1984, Chemical geothermometers for geothermal exploration: Reviews in Economic Geology, Society of Economic Geologists, v. 1, p. 31–43.

Vallier, T.L., 1970, Carbon carbonate results, *in* McManus, D.A., and others, eds., Initial reports of the Deep Sea Drilling Project: Washington, D.C., U.S. Government Printing Office, v. 5, p. 431–440.

Von Damm, K.L., Edmond, J.M., Grant, B.C., Measures, C.I., Walden, B., and Weiss, R., 1985, Chemistry of submarine hydrothermal solutions at 21° N East Pacific Rise: Geochimica et Cosmochimica Acta, v. 49, p. 2197–2220.

Welhan, J.A., and Craig, H., 1983, Methane, hydrogen, and helium in hydrothermal fluids at 21° N on the East Pacific Rise, *in* Rona, P.A., Bostrom, K., Laubier, L., and Smith,

K.L., Jr., eds., Hydrothermal processes at seafloor spreading centers: New York, Plenum Press, p. 391–409.

Wenner, D.B., and Taylor, H.P., Jr., 1971, Temperatures of serpentinization of ultramafic rocks based on $^{18}O/^{16}O$ fractionation between coexisting serpentine and magnetite: Contributions to Mineralogy and Petrology, v. 32, p. 165–185.

Woodruff, L.A., and Shanks, W.C., III, 1988, Sulfur isotope study of chimney minerals and vent fluids from 21° N, East Pacific Rise: Hydrothermal sulfur sources and disequilibrium sulfate reduction: Journal of Geophysical Research, v. 93, p. 4562–4572.

Yeh, H., and Savin, S.M., 1977, Mechanisms of burial metamorphism of argillaceous sediments: 3. O-isotope evidence: Geological Society of America Bulletin, v. 88, p. 1321–1330.

Zierenberg, R.A., Morton, J.L., Koski, R.A., and Ross, S.L., Geologic setting of massive sulfide mineralization in the Escanaba Trough, *in* Morton, J.L., Zierenberg, R.A., and Reiss, C.A., eds., Geologic, hydrothermal, and biologic studies at Escanaba Trough, Gorda Ridge, offshore northern California: U.S. Geological Survey Bulletin 2022, chapter 10 (this volume).

Zierenberg, R.A., and Shanks, W.C., III, Sediment alteration associated with massive sulfide formation in the Escanaba Trough, Gorda Ridge: The importance of seawater mixing and magnesium metasomatism, *in* Morton, J.L., Zierenberg, R.A., and Reiss, C.A., eds., Geologic, hydrothermal, and biologic studies at Escanaba Trough, Gorda Ridge, offshore northern California: U.S. Geological Survey Bulletin 2022, chapter 14 (this volume).

Zierenberg, R.A., Shanks, W.C., III, and Bischoff, J.L., 1984, Massive sulfide deposits at 21° N, East Pacific Rise: Chemical composition, stable isotopes, and phase equilibria: Geological Society of America Bulletin, v. 95, p. 922–929.

Chapter 13. Evidence for Hydrothermal Fluid Flow Through Surficial Sediments, Escanaba Trough

By Andrew J. Magenheim and Joris M. Gieskes[1]

CONTENTS

ABSTRACT

During DSV *Alvin* dives in 1988 three push cores were obtained in Escanaba Trough. Two of these cores were obtained in the vicinity of a hydrothermal vent. Interstitial water analyses suggest that the sediment sampled is not presently exposed to a hydrothermal fluid flux, but analysis of the solid phases indicates that at an earlier time sediment has undergone hydrothermal alteration. This alteration is evident from the presence of high-temperature calcite (~220°C) at a depth of 5 cm from the surface, of sulfides associated with hydrothermally derived tar, and of large changes in major elements (Mg, Fe, S) and minor constituents (Ba, Sr, Cu, Zn) of the sedimentary phases. Hydrothermal sulfide minerals deposited in the sediment are presently undergoing oxidative weathering reactions.

INTRODUCTION

Hydrothermal activity in sediment-covered ridge systems (Escanaba Trough, Gorda Ridge, and Middle Valley, Juan de Fuca Ridge) and in marginal seas (Guaymas Basin, Gulf of California, and the Red Sea) is of special geochemical interest, because, as a result of hydrothermal fluid flow through the sediment, alteration of both inorganic and organic phases is enhanced. Hydrothermal fluids emanating from the sea floor are distinctly different in composition from those sampled from open ocean non-sediment-covered systems (Von Damm and others, 1985a, b; Von Damm, 1991). This is especially evident from higher pH values, lower trace-metal contents, and high concentrations of biogenic constituents such as ammonia and iodide (Von Damm and others, 1985b; Gieskes and others, 1988; Campbell and others, chap. 11, this volume). In sediment-covered systems, hydrothermal products are often deposited close to the sediment-water interface as a result of transport of inorganic and organic materials by diffuse fluid migration through the sediment. Especially in Guaymas Basin, these processes have been documented in an active mode over a variety of depth scales (for example, Gieskes and others, 1982, 1988; Simoneit and Lonsdale, 1982; Simoneit, 1983, 1984, 1985a; Stout and Campbell, 1983; Kawka and Simoneit, 1987; Bazylinski and others, 1988; Magenheim, 1989). In addition, retrograde reactions, for instance, redissolution of hydrothermal sulfate minerals (A. Sturz and others, unpub. data, 1990) and the biodegradation and oxidation of petroleum products (Simoneit, 1984, 1985b) have been documented in Guaymas Basin. Similar studies have revealed such retrograde reactions in Escanaba Trough (Zierenberg and others, 1986; Kvenvolden and Simoneit, 1990). Sulfide samples recovered in the Escanaba Trough consist both of older deposits, partially buried in sediment and characterized by surface coatings of iron oxides and barite, as well

[1] Scripps Institution of Oceanography, La Jolla, California.

as fresher deposits, which are typically capped by chimneys of barite and anhydrite. Fluids discharging from these chimneys have temperatures of up to 217°C in Escanaba Trough (Zierenberg and others, 1988; Campbell and others, chap. 11, this volume).

This paper presents evidence for previous hydrothermal fluid flow through the sediment of Escanaba Trough. This has led to the deposition of hydrothermal products just below the sediment-seawater interface, which presently are undergoing retrograde reactions. Materials for these observations were collected by DSV *Alvin* during dives in the summer of 1988 in the vicinity of an active hydrothermal vent (fig. 13.1).

ACKNOWLEDGMENTS

We are grateful for the reviews of this manuscript by Andrew C. Campbell, Keith Kvenvolden, and Robert Zierenberg. Part of this work was supported by a grant from the National Science Foundation, NSF OCE 86-13517. We also acknowledge the efforts of the crews of R/V *Atlantis II* and of DSV *Alvin*. We thank Jim Leather for the isotope information.

METHODS

SHIPBOARD SAMPLING

DSV *Alvin* push cores from 6 to 20 cm long were subsampled immediately upon arriving on deck. An apparatus designed for sectioning the cores in a nitrogen atmosphere (Shaw, 1988, 1989) was used for processing all samples. Samples were sliced with clean plastic sheets and transferred into precleaned centrifuge tubes, then centrifuged and returned to the nitrogen-filled glove bag for processing. The fluids were decanted into precleaned syringes and filtered through 0.45 μm millipore filters. The filtered solutions were separated into two aliquots. One untreated sample was taken for Cl, Mg, and Ca analysis. The remaining portion was acidified with 25 μL of 6 *M* ultrapure HCl. The solids were stored refrigerated in the centrifuge tubes.

ANALYTICAL METHODS

INTERSTITIAL WATERS

The pore fluids were analyzed by techniques that have been outlined in a number of sources (Gieskes and

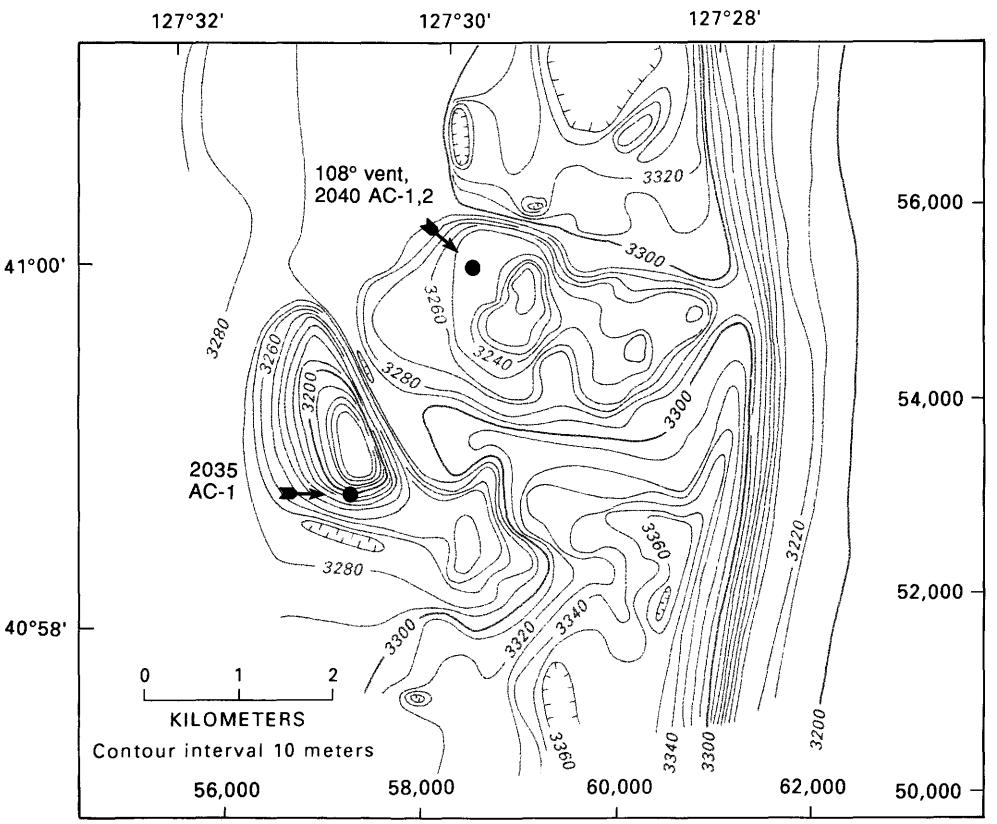

Figure 13.1. Bathymetric map of study area in northern Escanaba Trough (depth in meters). Locations of cores from this study are shown. Numbers along right and bottom give coordinates of local transponder net (in meters). Hachures indicate area of closed low.

Peretsman, 1986; Shaw, 1988). Chloride, calcium, and magnesium were analyzed by titration as described by Gieskes and Peretsman (1986). Silica, ammonium, and nitrate were analyzed by colorimetric techniques (Gieskes and Peretsman, 1986). Sulfate was analyzed by nephelometry (R. Jahnke, oral. commun., 1985). Five metals (Mn, Sr, V, Ni, and Cu) were analyzed by flameless atomic absorption spectrometry.

BULK SOLIDS, MAJOR ELEMENTS

Major-element composition of sediment was analyzed after dissolution using a lithium metaborate fusion technique (Brown, 1988, and references therein). Colorimetric techniques were used to analyze the solutions whenever possible (Fe, Ti, Si, P, and Al). Chloride was determined by leaching 20 mg of dried sediment in deionized water, filtering the sediment, and measuring Cl in the solution using ion chromatography. Other elements (Mg, Ca, K, Mn, and Na) were run using flame atomic absorption techniques. A detailed description of this procedure and subsequent analysis is given in Brown (1988).

A Perkin and Elmer CHN elemental analyzer was used for total carbon and nitrogen determinations. Carbonate carbon analysis was performed by dissolving the sample in 1 *M* HCl and analyzing the CO_2 evolved using a coulometric technique. Organic carbon was determined by difference between the total carbon and inorganic carbon.

Some carbonate samples were dissolved in 50°C phosphoric acid (as were calcite standards), and carbon and oxygen isotopes of the CO_2 evolved were measured by standard mass spectrometric techniques.

BULK SOLIDS, MINOR ELEMENTS

Minor elements were analyzed using X-ray fluorescence spectroscopy following methods developed by Shimmield (1984). Great care was taken to make appropriate matrix corrections. All data have been corrected for salts and pore water contributions. Details of these corrections and standardization procedures are given in Magenheim (1989).

SITE AND SAMPLE DESCRIPTION

Three DSV *Alvin* push cores were obtained. Two of these cores (2040 AC-1 and 2040 AC-2) were located within 10 m of an active hydrothermal vent (108°C) in the northern Escanaba Trough (NESCA) area (fig. 13.1). The other core (2035 AC-1) was sampled at the top of a flat-topped sediment hill in the NESCA area (fig. 13.1). Visual observations made while extruding the two cores collected at the hydrothermal site indicated evidence for hydrothermal alteration of the sediment (table 13.1). Core 2040 AC-1 had a layer of large (about 1 mm) white crystals between 6 and 8 cm depth. These crystals were examined

Table 13.1. Descriptions of Escanaba Trough surface cores.

[Descriptions are based on visual observations on board and in the laboratory with an optical microscope. Calcite was identified below 4 cm by XRD; Fe, Cu, and Zn sulfide minerals were tentatively identified by XRD in 5–6 cm section and in the tar mat]

Interval (cm)	General Description
	Core 2035 AC-1
0–1.5	Brown, homogeneous
1.5–3.0	Brown, homogeneous
3.0–4.5	Lighter brown, homogeneous
6.0–7.5	Brown, homogeneous, brassy flakes
9.0–10.5	Brown, homogeneous, brassy flakes
12.0–13.5	Brown, homogeneous, brassy flakes
15.0–16.5	Brown, darker layer observed while sectioning, homogeneous, brassy flakes
17.0–18.5	Brown, homogeneous, brassy flakes
	Core 2040 AC-1
0–1	Brown, fine, homogeneous
1–2	Brown, fine, homogeneous
2–3	Darker brown-gray, brassy sheet-like flakes, black specks (bitumen ?)
3–4	Gray-brown, brassy sheets, some white crystals (calcite), black specks
4–5	Gray-brown, white crystals more abundant and larger, brassy flakes, more black specks
5–6	Darker gray, many white crystals, tar, black specks
6–7	Gray, approximately 1/3 to 1/2 white to yellowish crystals with tar stuck to them (many are millimeter size), brassy flakes, black specks
7–8	Gray, fewer crystals, brassy flakes, tar, and more black specks
8–9	Darker gray, fewer crystals, brassy flakes, tar, small black specks
9–10	Dark gray, white crystals, brassy flakes, tar, black specks
11–12	Dark gray, white crystals, brassy flakes, tar, black specks
	Core 2040 AC-2
0–1	Homogeneous, brown, brassy flakes
2–3	Homogeneous, brown, brassy flakes, some small black grains
3–4	Homogeneous, brown-gray, brassy flakes, small black grains
4–5	Homogeneous, darker gray-brown, more black grains
5–6	Gray, white crystals, tar, hard black glassy grains, small black grains
core catch	Gray sediment, more white crystals, more tar, hard black glassy grains, small black crystals with white and yellow crusts. Tar was slightly malleable and faintly odorous

under the microscope and appeared to be well-developed rhombs with a large amount of tar stuck to them. The morphology and veinlike occurrence of this deposit in the sediment indicate that it is authigenic. X-ray diffraction (XRD) analysis indicates that these crystals consist of calcite. The lower part of this core was significantly darker than the top. Core 2040 AC-2 had similar calcite crystals, although less abundant, below 4 cm. The bottom sediment interval was considerably darker than the surface sediment. A piece of matlike tar was picked out of the core catcher, which appeared to contain many sand-size sulfide particles. XRD analysis tentatively confirmed the presence of marcasite, chalcopyrite, cubanite, barite, and calcite (and possibly pyrrhotite) in this tar mat. These minerals were also tentatively identified in the intervals below 4.5 cm in this core. Core 2035 AC-1, taken in an area without sulfide mineralization, was basically uniform in appearance, except for a dark interval between 11 and 12 cm. This core is used as a reference and is assumed to be representative of "average" sediment in this region.

RESULTS AND DISCUSSION

INTERSTITIAL WATERS

Interstitial water profiles for the three cores from Escanaba Trough, presented in table 13.2 and figure 13.2, appear to be unaffected by present hydrothermal activity. All the Cl^- profiles appear to be constant, with perhaps slightly higher concentrations in 2040 AC-2 (fig. 13.2*A*). The Mg^{2+} and Ca^{2+} profiles show no gradients and show seawater values (fig. 13.2*B*, *C*). The profiles of Sr^{2+} (fig. 13.2*I*) show seawater conditions for both cores 2040 AC-1 and 2040 AC-2, indicating no hydrothermal contribution.

Silicon as orthosilicic acid (H_4SiO_4) appears to increase with depth in all the push cores (fig. 13.2*D*). The profiles from the hydrothermal vent vicinity show a deficit when compared with 2035 AC-1. Past mobilization of silicon from the solids in 2040 AC-1 and 2040 AC-2 may have removed or altered the source of readily soluble silica (for example, radiolarian tests), which would ordinarily be present.

Sulfate appears to be constant throughout cores 2040 AC-1 and 2035 AC-1 at seawater values (fig. 13.2*E*). The data in core 2040 AC-2 indicate a slight decrease with depth, suggesting some bacterial sulfate reduction at greater depths.

Nitrate profiles for all three cores show a decrease in NO_3^- with depth to approximately 7 cm (fig. 13.2*F*). This decrease suggests that denitrification is active, and conditions above about 7 cm are suboxic. Some mobilization of NH_4^+ is observed in core 2035 AC-1 (fig. 13.2*G*) starting at the depth where NO_3^- goes to zero. No increases in NH_4^+ are apparent in either of the other cores.

The manganese profiles clearly show the mobilization of Mn for core 2035 AC-1 (fig. 13.2*H*), starting at 5 cm. Small increases in Mn are observed for cores 2040 AC-1 and 2040 AC-2. It appears that past hydrothermal fluid flow may have diminished the surface sediment manganese oxide concentrations.

The profiles of vanadium (fig. 13.2*J*) show surface maxima for 2035 AC-1 and 2040 AC-1. Core 2040 AC-2 shows an apparent increase in vanadium with depth. This increase may be related to bacterial decay of the tar mat found at the bottom of the core. Nickel appears to have a subsurface maximum for all three cores (fig. 13.2*K*). Copper (fig. 13.2*L*) shows enrichment at the surface, with 2040 AC-1 and 2040 AC-2 showing enrichments to greater depths than 2035 AC-1.

Taken together, the interstitial water profiles suggest that the major process affecting the pore-water chemistry is the early diagenesis of organic matter, leading to suboxic conditions in those levels that show the presence of hydrothermal precipitates.

BULK SEDIMENT CHEMICAL COMPOSITION

The chemical composition of the hydrothermally altered sediment is influenced by a number of overlapping and competing processes (Magenheim, 1989): (1) precipitation of hydrothermal minerals, (2) alteration and dilution by hydrothermal precipitates of the pre-existing sediment matrix, and (3) bacterial diagenesis of organic matter. These processes can affect both major constituents and minor constituents of the sediment, as will be shown below. Data for major elements are presented in table 13.3 and for minor elements in table 13.4.

MAJOR ELEMENTS

To represent the data for the purpose of comparison, we have normalized the data to the titanium content. The latter component is of low mobility and is at the same time a good marker of inorganic detrital input. Titanium-ratio profiles for all cores are shown in figure 13.3.

To evaluate the contribution of hydrothermal processes to the composition of cores 2040 AC-1 and 2040 AC-2, it is first necessary to examine the trends with depth in the reference core 2035 AC-1. In the latter core titanium shows a slight increase with depth with an average concentration of 93 μmol/g. A slight decrease in the molar Al/Ti ratio is observed for 2035 AC-1 from 35 at the surface to 32 at 19 cm. The average value, Al/Ti = 32.7, for this core is close to the average value of terrigenous matter, Al/Ti = 34.1 (Boström and others, 1976). The Si/Ti profile is somewhat noisy, but the average value of Si/Ti, 102, is comparable to that of average terrigenous matter

Table 13.2. Escanaba Trough interstitial fluid compositions.

[—, not determined]

Depth (cm)	Cl (mM)	Mg (mM)	Ca (mM)	H_4SiO_4 (μM)	SO_4 (mM)	NH_4 (μM)	NO_3 (μM)	Mn (μM)	Sr (μM)	V (nM)	Ni (nM)	Cu (nM)
Core 2040 AC-1												
0.5	563	54	9.8	180	31	2.0	51	0	90	234	313	205
1.5	567	55	9.8	229	30	1.2	42	0	84	196	72	224
2.5	565	55	9.7	256	31	.9	43	0	84	159	32	206
3.5	563	54	9.5	265	30	0	27	0	84	51	32	205
4.5	569	53	9.9	301	31	0	23	0	88	42	43	202
5.5	566	54	9.9	292	30	0	12	2	84	52	163	19
6.5	551	53	9.7	265	30	0	11	14	84	38	214	84
7.5	553	53	9.8	270	26	0	7	24	92	33	240	83
8.5	573	54	9.8	292	29	0	9	29	84	47	445	52
9.5	568	58	10.1	292	31	0	13	32	92	70	492	56
10.5	—	58	10.4	292	33	1.6	—	35	97	80	602	58
12.5	—	—	—	297	—	0	—	27	92	75	124	28
Core 2040 AC-2												
0.5	566	54	9.9	270	26	5	40	0	89	121	0	169
1.5	588	56	10.4	310	29	3	31	0	93	116	0	346
2.5	514	52	10.1	246	26	0	18	0	89	74	0	197
3.5	582	52	10.2	259	27	0	9	.3	89	53	60	269
4.5	588	55	10.4	324	26	0	9	2	89	146	268	185
5.5	592	57	10.2	315	22	0	6	18	89	218	316	169
7.0	597	56	10.5	265	22	3	—	16	89	239	219	140
Core 2035 AC-1												
0.75	561	54	9.4	412	30	30	—	0	—	730	—	344
2.25	564	51	9.3	430	28	2	—	0	—	128	145	85
3.75	553	52	9.3	434	30	2	13	2	—	67	21	77
5.25	561	52	9.3	399	29	0	11	10	—	82	8	90
6.75	562	52	9.0	412	29	0	3	38	—	97	649	117
8.25	562	54	9.1	425	29	5	1	68	—	267	560	92
9.75	571	53	9.0	403	29	2	4	84	—	143	—	26
11.25	550	52	9.0	465	28	6	3	105	—	214	38	—
12.75	561	54	9.2	452	29	11	2	123	—	128	214	65
14.25	550	52	9.0	456	27	14	2	127	—	10	155	36
15.75	553	50	8.8	495	28	20	3	156	—	10	122	27
17.25	568	51	8.9	509	29	24	5	178	—	10	—	11
18.75	561	51	8.8	517	30	27	5	179	—	—	1	17
20.25	571	52	8.9	482	30	37	3	186	—	—	—	—

(Si/Ti = 110, Boström and others, 1976). The K/Ti ratio for 2035 AC-1 appears relatively constant with an average value of 5.8. Both Fe/Ti and Mg/Ti appear to decrease with depth in 2035 AC-1. The decrease in Fe/Ti may be due to the association of iron with manganates in the surface sediments. A maximum in manganese is observed at 3.75 cm (table 13.3).

In core 2040 AC-1, authigenic calcite dilutes the pre-existing sediment matrix in the intervals between 5 and 10 cm. The titanium profile (fig. 13.3*A*) shows this quite clearly. The titanium concentration drops to one-third of its previous value in the calcite-rich interval between 6 and 7 cm. In spite of this large dilution in titanium, only a slight increase in Al/Ti (fig. 13.3*B*) is observed in this interval. Virtually no changes are noticed in the K/Ti (fig. 13.3*E*) and Si/Ti (fig. 13.3*C*) ratios in this interval. This lack of change suggests that the precipitation of calcite diluted the pre-existing sediment by almost two-thirds.

The observed trends in Fe/Ti and Mg/Ti (fig. 13.3*F*, *G*) are similar for both hydrothermally affected cores. Between 2.5 and 7.5 cm, an enrichment in both Mg/Ti and Fe/Ti over values from 2035 AC-1 is observed in core 2040 AC-1. Below this layer deficits (relative to 2035 AC-1) in both of these elements are observed. While 2040 AC-2 does not extend as deep, the enrichment in both Fe/Ti and Mg/Ti is apparent to a depth of 7.5 cm.

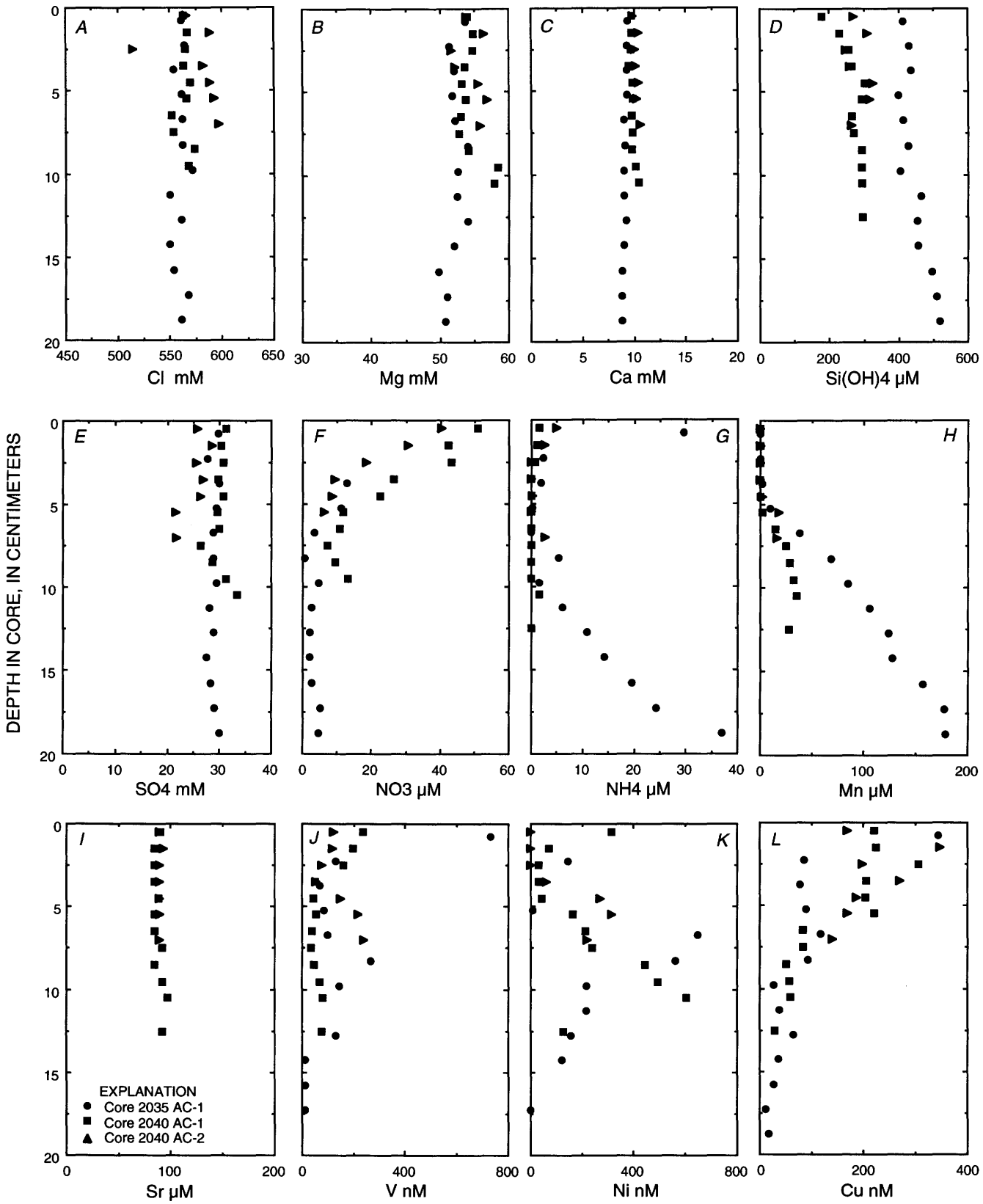

Figure 13.2. Interstitial water composition of cores 2035 AC-1 (dots), 2040 AC-1 (squares), and 2040 AC-2 (triangles).

Table 13.3. Major-element composition of Escanaba Trough solids.

[Weight percent oxides, salt free]

Depth (cm)	SiO_2	TiO_2	Al_2O_3	Fe	MnO	MgO	CaO	Na_2O	K_2O	P_2O_5	C inorg	C org	N	Total
Core 2040 AC-1														
0.5	54.88	0.75	15.05	6.15	0.99	4.14	1.80	2.37	2.33	0.24	0.07	1.26	0.12	90.16
1.5	55.79	.75	15.31	5.89	.98	3.96	3.47	2.19	2.37	.24	.06	1.30	.16	92.47
2.5	53.07	.75	15.53	6.35	.92	4.27	3.44	2.83	2.46	.24	.06	1.46	.16	91.54
3.5	56.22	.76	15.73	6.86	.73	4.09	3.32	2.68	2.46	.25	.09	1.20	.15	94.54
4.5	54.76	.74	14.38	6.66	.48	4.02	2.31	2.92	2.31	.27	.09	1.22	.12	90.28
5.5	41.55	.59	11.41	5.67	1.46	3.21	14.23	2.17	5.88	.23	3.37	1.97	.09	91.85
6.5	18.04	.24	5.52	2.80	4.05	1.36	39.23	.90	.83	.10	7.02	1.66	.05	81.79
7.5	41.41	.51	10.50	3.91	1.98	2.25	17.71	2.15	1.83	.15	2.92	1.68	.08	87.09
8.5	54.93	.66	13.06	4.14	.76	2.61	8.34	2.99	2.40	.16	1.36	2.25	.09	93.76
9.5	63.11	.76	15.30	3.11	.26	2.42	3.55	2.56	2.73	.18	.41	2.30	.10	96.78
10.5	63.51	.76	14.51	2.94	.20	2.56	3.43	4.40	2.74	.16	.23	1.34	.06	96.86
12.5	63.92	.74	14.67	3.51	.27	2.78	5.47	2.82	2.66	.26	.46	1.35	.07	98.98
Core 2040 AC-2														
0.5	61.96	0.71	15.14	5.91	1.09	3.91	1.93	2.31	2.32	0.16	0.09	1.32	0.17	97.01
1.5	45.29	.68	16.45	6.24	1.14	3.99	1.70	2.52	2.78	.17	.08	1.42	.17	82.63
2.5	47.53	.70	14.81	6.57	1.01	4.00	2.11	1.86	2.41	.18	.08	1.36	.17	82.80
3.5	49.53	.68	16.50	7.47	.51	3.97	1.72	2.67	2.40	.18	.08	1.39	.17	87.27
4.5	49.77	.69	15.26	6.63	.26	3.96	2.10	2.37	2.43	.14	.10	1.71	.16	85.58
5.5	41.64	.65	12.90	4.40	.63	0	5.51	2.18	2.15	.12	.44	5.62	.15	76.41
7	49.76	.78	15.85	5.70	.94	3.82	9.23	2.65	2.72	.11	.85	10.20	.14	102.7
Core 2035 AC-1														
0.75	65.89	0.71	15.94	6.06	1.73	4.09	1.79	2.12	2.48	0.19	0.06	1.22	0.14	102.4
2.25	49.85	.70	15.56	5.89	2.48	4.02	1.55	2.31	2.53	.19	.05	1.22	.15	86.52
3.75	51.97	.76	14.74	5.77	2.97	3.96	2.24	2.38	2.33	.19	.05	.88	.12	88.37
6.75	45.90	.72	14.84	5.28	.31	3.49	2.01	2.45	2.51	.23	.04	.70	.08	78.57
9.75	64.14	.75	15.22	4.39	.08	3.46	2.35	2.75	2.58	.15	.10	.40	.03	96.40
12.75	52.84	.76	16.41	4.66	.13	3.80	2.01	2.52	2.69	.15	.05	.97	.09	87.08
15.75	58.24	.76	14.72	4.05	.10	3.28	2.58	2.79	2.47	.14	.11	.75	.04	90.03
18.75	65.83	.78	15.97	4.72	.11	3.72	2.34	2.72	2.66	.14	.07	.42	.03	99.52

HYDROTHERMAL CALCITE

The presence of a calcite layer in the 6 to 7 cm interval of core 2040 AC-1 has been mentioned previously. Calcite is present as well-crystallized rhombs on the order of 0.5 to 2 mm in size. Calcite was also found below 4 cm in core 2040 AC-2. The background core 2035 AC-1 shows relatively little inorganic carbon, indicating that biogenic carbonate is not an important component of the sediment. Slightly greater amounts of calcium than inorganic carbon in the calcite vein indicate that not all calcium is associated with calcite, some probably being contributed by clays. Manganese and chromium both increase considerably in the calcite layer of 2040 AC-1.

In core 2040 AC-2 calcite crystals are observed below 4 cm and are more concentrated in the deepest interval and the tar mat. Increases in the concentrations of manganese and chromium are observed in the bottom of 2040 AC-2 in association with the increases in calcium and inorganic carbon. The strong similarity between the distributions of manganese and chromium in the calcite layers suggests that these elements are trapped in the calcite or an associated phase. Though manganese is enriched in hydrothermal fluids, the source of chromium is less certain. We submit that chromium becomes mobilized from the surrounding sediment through which the highly reducing hydrothermal fluids have percolated and is subsequently adsorbed in the calcite layer at the time of calcite precipitation.

The results of carbon and oxygen isotope measurements on calcite are given in table 13.5. One sample was taken from the calcite vein of 2040 AC-1 and one from the 7.5 cm interval of 2040 AC-2. The sample from 2040 AC-1 consisted of almost pure crushed calcite crystals, and the sample from 2040 AC-2 was taken from the bulk sediment. This was done because individual crystals of calcite were not common enough to separate in this core. The oxygen isotopic results show very similar compositions for the two samples, as do the carbon isotopic ratios. Using a range

Table 13.4. Minor-element compositions of Escanaba Trough solids.

[Compositions are salt free. All data in parts per million. n.d., not determined]

Depth (cm)	Sr	Zn	Cu	Ni	Co	Cr	Ba	V	Mo	Br	S	I
2040 AC-1												
0.5	329	230	181	129	21	139	2594	169	30	13	1849	344
1.5	331	244	214	135	24	199	2795	176	32	5	1615	361
2.5	293	261	220	132	24	145	2312	203	31	40	1848	466
3.5	332	271	264	123	25	208	2531	210	29	32	1766	462
4.5	310	273	247	99	22	156	2356	181	22	16	1664	350
5.5	350	295	491	81	25	364	2978	169	26	11	2460	278
6.5	329	321	800	50	20	553	2613	154	18	4	2199	166
7.5	332	319	644	61	19	297	2940	185	26	n.d.	2675	130
8.5	350	459	712	65	16	198	2975	185	33	7	4369	96
9.5	355	466	504	62	12	138	2916	162	26	n.d.	5205	84
10.5	352	422	372	63	11	70	2208	147	27	n.d.	7347	n.d
12.5	349	392	361	63	14	209	2343	166	38	n.d.	12,472	n.d
2040 AC-2												
0.5	312	240	241	143	24	189	2821	194	27	8	1983	333
1.5	265	231	223	134	22	34	2251	176	11	19	2023	402
2.5	272	239	235	123	22	85	2093	178	18	n.d.	1595	423
3.5	262	301	362	110	25	116	2031	203	23	7	1887	348
4.5	312	325	464	119	19	88	2498	184	23	14	2441	302
5.5	452	1120	1302	85	15	52	4332	183	27	5	10,048	323
7	772	6371	4802	102	22	393	8668	187	57	n.d.	25,846	607
2035 AC-1												
0.75	267	221	151	165	24	233	1978	260	38	121	1812	534
2.25	233	215	127	158	20	87	1637	194	44	97	1387	395
3.75	273	183	113	115	19	95	1570	159	40	88	1340	467
6.75	256	123	60	58	13	0	835	114	23	58	1152	143
9.75	298	120	32	65	13	79	720	158	31	45	1886	41
12.8	253	154	242	72	13	14	1056	161	26	96	166	170
15.8	292	114	36	60	13	75	788	178	26	51	3919	n.d.
18.8	279	136	49	68	17	142	779	164	35	34	3839	39

of $\delta^{18}O$ of water between 0 and 2 per mil (relative to SMOW) and using the calcite fractionation factors given by O'Neil and others (1969), isotopic temperatures of 208°C to 279°C were calculated. Böhlke and Shanks (chap. 12, this volume) report a value of $\delta^{18}O$ of 0.5 per mil for Escanaba Trough hydrothermal fluids, which would yield a formation temperature of approximately 220°C for the calcite. The carbon isotopes indicate a biogenic origin of the CO_2, probably from the decomposition of organic matter at depth.

INORGANIC TRACE CONSTITUENTS

Five trace elements (Zn, Cu, Sr, S, and Ba) are enriched in cores 2040 AC-1 and 2040 AC-2 relative to 2035 AC-1 (table 13.4; Magenheim, 1989). This enrichment is evident for copper, zinc, and sulfur in and below the calcite layer in 2040 AC-1 and particularly below 5 cm in core 2040 AC-2, where significant increases in these elements occur. Strontium and barium, on the other hand, appear to be enriched throughout the two cores. The dark appearance of the lower portions of these two cores is probably the result of the presence of sulfide minerals.

The molar Ti ratios for Ba, Sr, Co, Cu, Zn, and S (fig. 13.3*K–P*) all show peaks in the calcite-rich layer of 2040 AC-1, even though their absolute concentrations are not all that different from the values in the surrounding sediments (table 13.4; Magenheim, 1989), with the exception of Cu, which shows a significant increase in the calcite layer. Thus it appears that the calcite has not diluted these elements or, more likely, that these elements have been relatively concentrated in the calcite layer, perhaps associated with sulfides and barite.

Overall increases in Zn/Ti, Cu/Ti, and S/Ti in the lower portions of both hydrothermally affected cores suggest that these elements are associated with sulfides. Indeed, marcasite (FeS_2), chalcopyrite ($FeCuS_2$), cubanite (Fe_2CuS_3),

and barite ($BaSO_4$) have been identified tentatively in samples from the tar mat and the 7 cm interval of core 2040 AC-2. The enrichments in Sr and Ba throughout these cores suggests that barite may have been precipitated along with calcite and base-metal sulfide minerals.

ORGANIC CARBON AND RELATED ELEMENTS

Organic matter can preserve a record of present and past bacterial and thermal decomposition. The organic carbon concentrations appear to be greatest at the surface in core 2035 AC-1, with a slight decrease in abundance with depth. At 12.75 cm there appears to be an anomalously high value (0.97 percent organic carbon) with a decrease below this interval. This increased organic carbon may be the result of variable deposition of organic matter, and is located close to a black layer observed while sectioning the core. The C_{org}/Ti ratio also shows this slightly increased organic carbon concentration (fig. 13.3*R*). However, the relatively small decrease in organic carbon with depth and the absence of any apparent reduction in sulfate in the pore fluid profiles suggest that sulfate reduction is not presently active in the upper 20 cm of this sediment core. Decomposition of the organic matter in 2035 AC-1 is apparent from the N/Ti and I/Ti profiles, which show significant decreases with depth.

Similarly a general decrease is observed in the bromine concentration (table 13.4), but accuracies of the determinations do not warrant a representation in terms of the titanium ratio. The V/Ti (fig. 13.3*V*) profile suggests that vanadium is enriched in the surface interval of core 2035 AC-1. The Ni/Ti (fig. 13.3*U*) also suggests enrichment in the surface interval. Whereas the vanadium enrichment may be related to organic carbon, the nickel enrichment is more likely associated with manganese oxides. Shaw (1988) has shown that nickel, molybdenum, and cobalt are associated with manganese-oxides.

Above 5 cm in core 2040 AC-1, organic carbon appears to have approximately the same concentration as 2035 AC-1 (table 13.5). Below and throughout the calcite-rich layer, organic carbon is enriched to values between 1.3 and 2.3 percent. The presence of tar on the calcite crystals suggests that some of this organic carbon is of thermogenic origin, supplied to the surface with the migrating hydrothermal fluids. Core 2040 AC-2 shows a relatively constant organic carbon concentration to a depth of 4.5 cm, where it begins to increase toward the bottom. In the 7.5 cm interval the organic carbon concentration is 10.2 percent. Profiles of N/Ti and I/Ti (fig. 13.3*S*, *T*) for the 2040 cores show a decrease with depth, notwithstanding increases in organic carbon. Bromine concentrations also become very small, below our detection limit.

Because the decay and (or) supply of organic matter is not uniform with depth, as indicated in core 2035 AC-1, the I/C_{org} and N/C_{org} profiles were plotted (fig. 13.4*A*, *B*). Core 2035 AC-1 shows a gradual decrease in N/C_{org} and I/C_{org}, as would be expected in the suboxic conditions observed. The more rapid decrease I/C_{org} suggests that iodine is relatively more labile than nitrogen during early diagenesis. The profiles of both these ratios in cores 2040 show more rapid decreases in the ratios with depth, again indicating increased diagenesis. Values of N/C_{org} this low are indicative of thermally altered organic matter (Simoneit and Bode, 1982), and, in addition, thermogenically derived organic carbon may cause a dilution effect.

The Ni/Ti and V/Ti profiles are shown in figure 13.3*U* and *V*. The resemblance to the N/Ti and I/Ti profiles suggests that these elements may also be related to the decay and alteration of organic matter. For this reason Ni/C_{org} and V/C_{org} profiles were also examined (fig. 13.4*C*, *D*). The surface enrichment in nickel could be related to the presence of manganese oxyhydroxides (Shaw, 1988). Rapid depletion in both vanadium and nickel is apparent from the profiles for core 2035 AC-1 and also for core 2040 AC-2. Core 2040 AC-1 shows a steady decrease in V/C_{org} and Ni/C_{org} profiles, except in the calcite-rich intervals, where an apparent maximum is evident. In part, this may be due to the presence of metalloporphyrins, containing these elements, associated with the tar on the calcite crystals.

GENERAL DISCUSSION

The results from the Escanaba Trough samples clearly show that at one time hydrothermal fluids did flow through the near-surface sediment. No presently active flow is indicated by the interstitial water compositions. However, retrograde reactions of precipitated hydrothermal minerals may be indicated. Three lines of evidence support the conclusion that the sediment has been exposed to hydrothermal activity in the past: (1) the presence of a high-temperature authigenic carbonate, (2) the presence of other hydrothermal precipitates and petroleum condensates, and (3) subtle alteration of the sediment. Without age dates on the sediment it is difficult to ascertain when hydrothermal activity ceased in the past, but the first few centimeters of each core do not indicate great alteration and may have been deposited under normal conditions.

HYDROTHERMAL CALCITE

The most striking observation is the authigenic precipitation of calcite within these sediments. Calcite has been reported in other hydrothermal situations. Peter and Scott (1988) reported high abundances of calcite in actively venting hydrothermal spires in Guaymas Basin. These calcites were found to be enriched in iron and manganese, similar to the manganese enrichment in the calcite layer of core

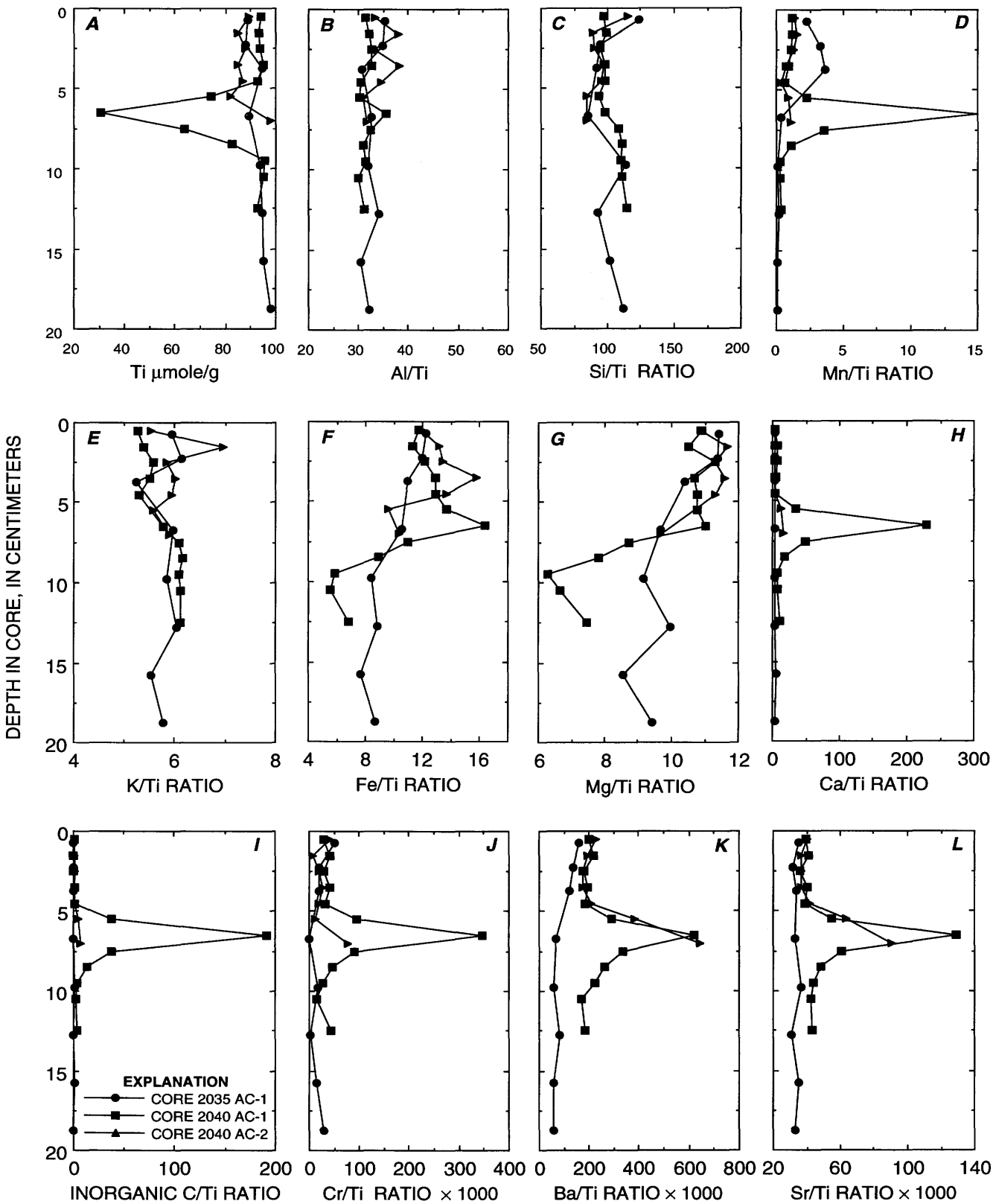

Figure 13.3. Titanium concentrations and molar ratios relative to titanium of major and minor constituents of solid phases cores 2035 AC-1 (dots), 2040 AC-1 (squares), and 2040 AC-2 (triangles).

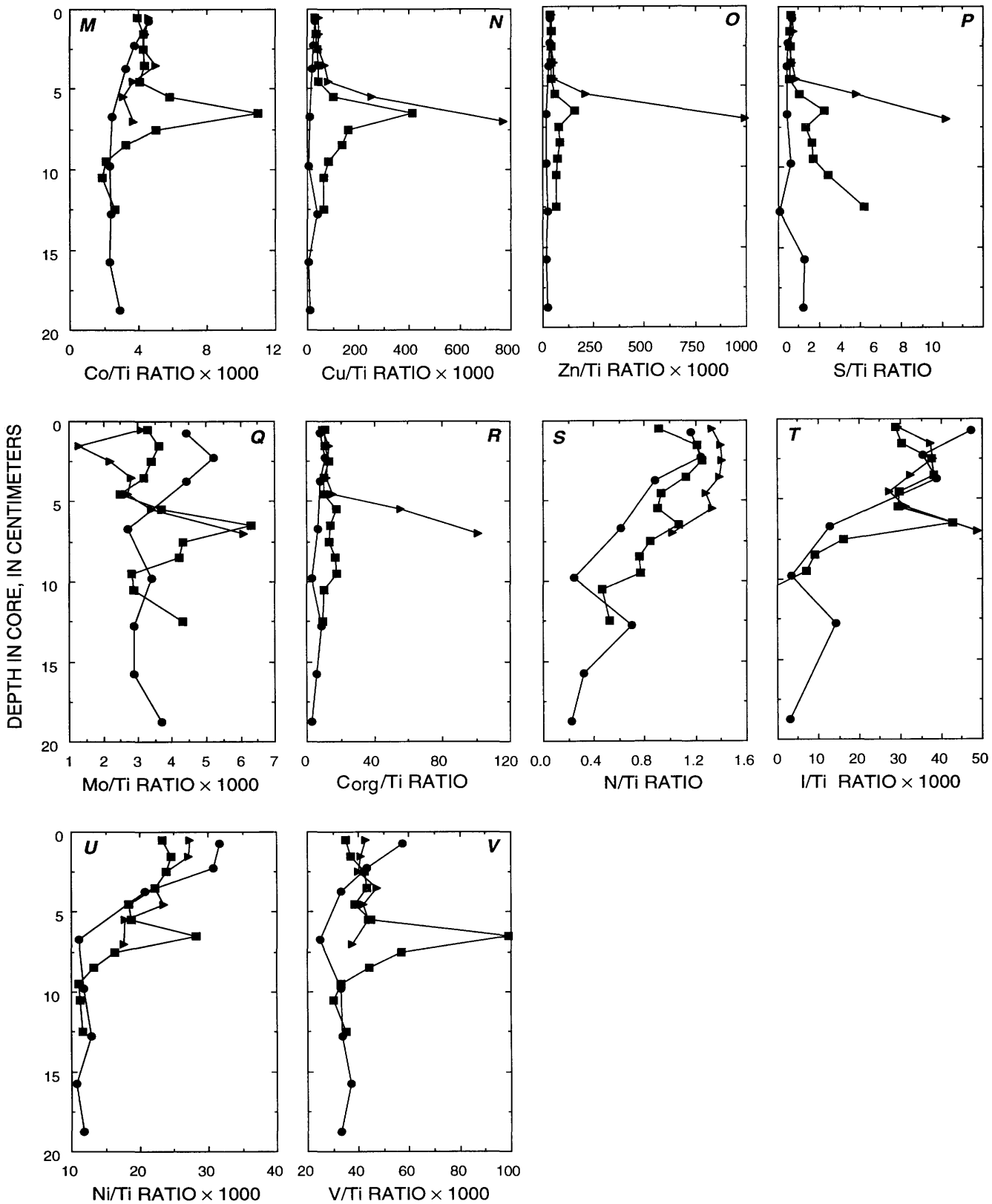

Figure 13.3. Continued.

Table 13.5. Isotope data for calcite from cores 2040 AC-1 and 2040 AC-2.

[Temperatures of formation were calculated for a range of isotopic compositions of equilibrating water of 0 to +2 per mil. PDB, Pee Dee belemnite; SMOW, standard mean ocean water]

Core	2040 AC-1	2040 AC-2
$\delta^{13}C_{PDB}$ (per mil)	−11.07	−11.03
$\delta^{18}O_{PDB}$ (per mil)	−21.63	−22.49
$\delta^{18}O_{SMOW}$ (per mil)	8.61	7.72
Temperature (°C) at $\delta^{18}O_{SMOW}(H_2O)$:		
0 per mil	208	227
1 per mil	230	251
2 per mil	254	279

2040 AC-1. Koski and others (1985) described a dredged sample of lithified sediment with large calcite veins from Guaymas Basin. Similar calcite veins have been observed in sediment samples from the hydrothermally active Middle Valley, Juan de Fuca Ridge (Goodfellow and Blaise, 1988). The temperatures of formation calculated for the calcites from this study clearly indicate that they were formed from a high-temperature fluid (about 220°C). Peter and Scott (1988) and Koski and others (1985) reported temperatures on the order of 230°C, based on microthermometry of fluid inclusions from the calcite crystals. Precipitation of calcite could result from degassing of the CO_2 from the hydrothermal fluids near the sediment surface. The precipitation of pure calcite suggests an absence of magnesium in the hydrothermally affected solutions, in contrast to Guaymas Basin where protodolomite is often formed (Magenheim, 1989).

HYDROTHERMAL PRECIPITATES

The appearance of sulfide minerals and barite below the calcite layer in 2040 AC-1 and associated with calcite and petroleum condensates in 2040 AC-2 supports the conclusion that the sediment was exposed to active hydrothermal flow in the past. The low abundance of Fe-S minerals, Fe-Cu-S minerals, and possibly zinc sulfides suggests that the fluid was enriched in trace metals and sulfide. Many observations and samples of massive sulfide deposits have been reported from Escanaba Trough (Benninger and Koski, 1987; Koski and others, 1988; Morton and others, 1990, chap. 1, this volume). It has been suggested that these sulfide deposits are formed by uniform, relatively low temperature (<250°C) diffuse flow onto the sea floor (Koski and others, 1988), forming mounds like the ones observed in Guaymas Basin. Sulfur isotope data from pyrrhotite and marcasite recovered from Escanaba Trough indicate a mixture of seawater- and basalt-derived sulfur (Koski and others, 1988).

Visual and SEM observations of sulfide grains from core 2040 AC-2 (Magenheim, 1989) showed evidence for weathering, including the presence of a Cu-Cl phase. The latter is probably atacamite ($Cu_2Cl(OH)_3$), a commonly observed mineral in chalcopyrite-rich samples that have undergone weathering in contact with seawater.

ALTERATION OF THE SEDIMENT

It appears from the profiles of iron and magnesium (fig. 13.3*F, G*) that these elements are affected by hydrothermal alteration. The deficit in both elements below the calcite vein in 2040 AC-1 suggests that these elements may be mobilized by the hydrothermal fluids. Similar decreases

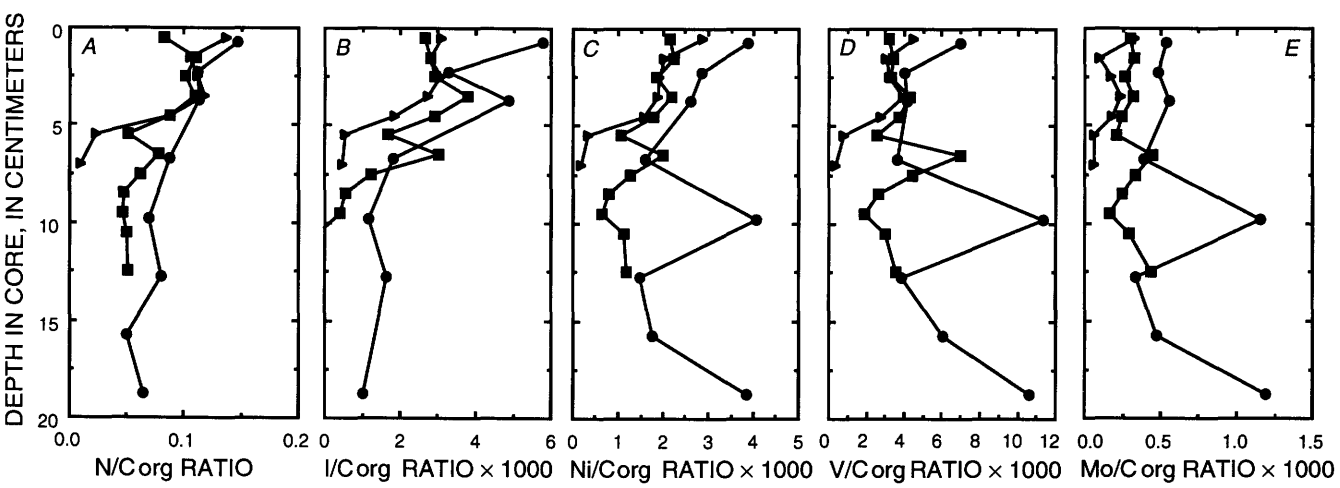

Figure 13.4. Organic carbon ratios for nitrogen, iodine, nickel, vanadium, and molybdenum in cores 2035 AC-1 (dots), 2040 AC-1 (squares), and 2040 AC-2 (triangles).

in magnesium were observed in cores from Guaymas Basin, in which hydrothermal fluids were actively flowing (Gieskes and others, 1988; Magenheim, 1989). Mobilization of magnesium from clays by the high-temperature, low-Mg fluids could explain these observations. The similarity between magnesium and iron profiles would suggest that a similar process controls the distribution of these two elements. Especially in deeper zones of cores 2040 AC-1 and 2040 AC-2 a large increase occurs in sulfur, with the content of sulfur at 7.5 cm in 2040 AC-2 being almost equivalent to that of iron. Presumably iron is mobilized from iron-oxides as well as from clays.

The relative enrichments in barium and strontium throughout cores 2040 AC-1 and 2040 AC-2, when compared to core 2035 AC-1, suggest precipitation of barite from diffusely flowing hydrothermal fluids, mixed to some extent with sulfate-containing seawater. The precipitation of barite was also observed in cores from Guaymas Basin, especially at the sediment-seawater interface, where mixing occurs between hydrothermal fluid and overlying bottom water. It appears that strontium is associated with barite in both cases. Figure 13.5 shows strontium plotted against barium for the Escanaba Trough cores, as well as Guaymas Basin cores (Magenheim, 1989). A reasonable correlation is apparent between these two elements for both sites. The scatter in strontium concentrations at low barium is probably due to strontium associated with biogenic carbonate at Guaymas Basin. The slope of the correlation line indicates that the ratio of strontium to barium is around 1:10. This result is in agreement with experimental results and the frequency distribution of natural barites (Hanor, 1968).

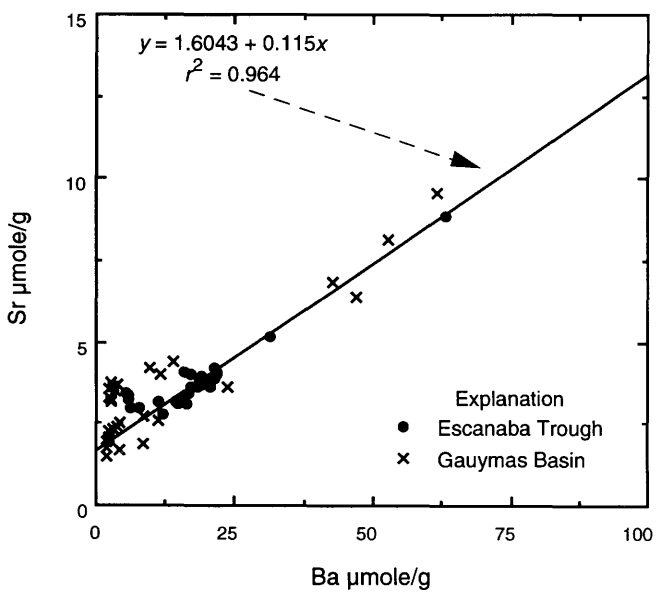

Figure 13.5. Strontium versus barium for solid phases from Guaymas Basin and Escanaba Trough.

THERMAL ALTERATION OF ORGANIC MATTER

The presence of a tar mat in core 2040 AC-2 and tar stuck to the calcite crystals of 2040 AC-1, suggests that petroleum was supplied from below. Molar N/C_{org} ratios on the order of 0.01 in the 7 cm interval of core 2040 AC-1 are indicative of thermal alteration (Simoneit and Bode, 1982). In these same intervals iodine, bromine, nickel, and vanadium are also depleted. All of the results indicate that thermally altered organic matter has reached the surface sediment in both cores. While core 2040 AC-1 did not have the obvious odor of petroleum when sampled, a slight sulfurous smell was observed. Elsewhere we demonstrate that the petroliferous material of cores 2040 AC-1 and 2040 AC-2 at present is undergoing oxidative alteration (Gieskes and others, 1990).

SUMMARY

Surface sediment cores from active hydrothermal vents in Escanaba Trough show evidence of hydrothermal alteration, precipitation of hydrothermal minerals, and thermally altered organic matter. The presence of hydrothermal calcite indicates that high-temperature fluid did flow through the sediment.

Elevated concentrations of copper, zinc, barium, and sulfur were observed in cores 2040 AC-1 and 2040 AC-2, associated with precipitation of sulfide minerals and of barite. Sulfide grains appear to be weathered and altered. Barite (and associated strontium) appears to be enriched in the hydrothermally altered cores. Evidence for diffuse flow through the sediments is given by subtle changes in sediment composition. Depletion of magnesium and iron seems to occur where precipitation of sulfide minerals is evident.

Interstitial water chemical data indicate an absence of fluid flow at this time. Instead, suboxic conditions, established after cessation of the hydrothermal fluid flow, lead to the oxidation of both sulfides and hydrocarbons.

REFERENCES CITED

Bazylinski, D.A., Farrington, J.W., and Jannash, H.W., 1988, Hydrocarbons in surface sediments from the Guaymas Basin hydrothermal vent site: Organic Geochemistry, v. 12, p. 547–558.

Benninger, L.M., and Koski, R.A., 1987, Descriptions and chemical analyses of sulfide samples dredged in 1986 from Escanaba Trough, southern Gorda Ridge: U.S. Geological Survey Open-File Report 87-375-B, 26 p.

Böhlke, J.K., and Shanks, W.C., III, Stable isotope study of hydrothermal vents at Escanaba Trough: Observed and calculated effects of sediment-seawater interaction, *in* Morton, J.L., Zierenberg, R.A., and Reiss, C.A., eds., Geo-

logic, hydrothermal, and biologic studies at Escanaba Trough, Gorda Ridge, offshore northern California: U.S. Geological Survey Bulletin 2022, chapter 12 (this volume).

Boström, K., Joensuu, S., Valdes, S., Charm, W., and Glauccum, R., 1976, Geochemistry and origin of East Pacific sediments sampled during Leg 34, *in* Yeats, R.S., Hart, S.R., and others, eds., Initial reports of the Deep Sea Drilling Project: Washington, U.S. Government Printing Office, v. 34, p. 559–574.

Brown, T., 1988, Wet chemical analysis of marine sediments—Application to hydrothermal sediments of Guaymas Basin: San Diego, California State University, M.S. thesis, 79 p.

Campbell, A.C., German, C.R., Palmer, M.R., Gamo, T., and Edmond, J.M., Chemistry of hydrothermal fluids from the Escanaba Trough, Gorda Ridge, *in* Morton, J.L., Zierenberg, R.A., and Reiss, C.A., eds., Geologic, hydrothermal, and biologic studies at Escanaba Trough, Gorda Ridge, offshore northern California: U.S. Geological Survey Bulletin 2022, chapter 11 (this volume).

Gieskes, J.M., Elderfield, H., Lawrence, J.R., Johnson, J., Meyers, B., and Campbell, A.C., 1982, Geochemistry of interstitial waters and sediments, Leg 64, Gulf of California, *in* Curray, J.R., Moore, D.G., and others, eds., Initial reports of the Deep Sea Drilling Project: Washington, U.S. Government Printing Office, v. 64, part 2, p. 675–694.

Gieskes, J.M. and Peretsman, G., 1986, Water chemistry aboard JOIDES Resolution: Ocean Drilling Program, Texas A&M University, Technical Note Number 5, 46 p.

Gieskes, J.M., Simoneit, B.R.T., Brown, T., Shaw, T., Wang, Y.-C., and Magenheim, A.J., 1988, Hydrothermal fluids and petroleum in surface sediments of Guaymas Basin, Gulf of California: A case study: Canadian Mineralogist, v. 26, p. 589–602.

Gieskes, J.M., Simoneit, B.R.T, Magenheim, A.J., and Leif, R.N., 1990, Retrograde oxidation of hydrothermal precipitates and petroleum in Escanaba Trough sediments: Applied Geochemistry, v. 5, p. 93–101.

Goodfellow, W.D., and Blaise, B., 1988, Sulfide formation and hydrothermal alteration of hemipelagic sediment in the Middle Valley, northern Juan de Fuca Ridge: Canadian Mineralogist, v. 26, p. 675–696.

Hanor, J.S., 1968, Frequency distribution of compositions in the barite celestite series: American Mineralogist, v. 53, p. 1215–1222.

Kawka, O.E., and Simoneit, B.R.T., 1987, Survey of hydrothermally generated petroleums from the Guaymas Basin spreading center: Organic Geochemistry, v. 11, p. 311–328.

Koski, R.A., Lonsdale, P.F., Shanks, W.C., Berndt, M.E., and Howe, S.S., 1985, Mineralogy and geochemistry of a sediment hosted hydrothermal sulfide deposit from the southern trough of the Guaymas Basin, Gulf of California: Journal of Geophysical Research, v. 90, p. 6696–6707.

Koski, R.A., Shanks, W.C., Bohrson, W.A., and Oscarson, R.L., 1988, The composition of massive sulfide deposits from the sediment covered floor of the Escanaba Trough, Gorda Ridge: Implications for depositional processes: Canadian Mineralogist, v. 26, p. 655–673.

Kvenvolden, K.A., and Simoneit, B.R.T., 1990, Hydrothermally derived petroleum: Examples from Guaymas Basin, Gulf of California and Escanaba Trough, Northeast Pacific Ocean: American Association of Petroleum Geologist Bulletin, v. 74, p. 223–237.

Magenheim, A.J., 1989, Hydrothermal alteration of near surface sediments of the Guaymas Basin and the Escanaba Trough, Gorda Ridge: San Diego, University of California, M.S. thesis, 146 p.

Morton, J.L., Koski, R.A., Normark, W.R., and Ross, S.L., 1990, Distribution and composition of massive sulfide deposits at Escanaba Trough, southern Gorda Ridge, *in* McMurray, G.R., ed., Gorda Ridge: A seafloor spreading center in the United States' Exclusive Economic Zone: New York, Springer-Verlag, p. 77–92.

Morton, J.L., Zierenberg, R.A., and Reiss, C.A., Geologic, hydrothermal, and biologic studies at Escanaba Trough: An introduction, *in* Morton, J.L., Zierenberg, R.A., and Reiss, C.A., eds., Geologic, hydrothermal, and biologic studies at Escanaba Trough, Gorda Ridge, offshore northern California: U.S. Geological Survey Bulletin 2022, chapter 1 (this volume).

O'Neil, J.R., Clayton, R.N., and Mayeda, T.K., 1969, Oxygen isotope fractionation in divalent metal carbonates: Journal of Chemical Physics, v. 51, p. 5547–5558.

Peter, J.M., and Scott, S.D., 1988, Mineralogy, composition, and fluid inclusion microthermometry of sea floor hydrothermal deposits in the southern trough of the Guaymas Basin, Gulf of California: Canadian Mineralogist, v. 26, p. 567–587.

Shaw, T.J, 1988, The early diagenesis of transition elements in near shore environments: San Diego, University of California, Ph.D. thesis, 164 p.

———1989, An apparatus for fine-scale sampling of pore waters and solids in high porosity sediment: Journal of Sedimentary Petrology, v. 59, p. 633–634.

Shimmield, G.B., 1984, The geochemistry and mineralogy of Pacific sediments, Baja California: University of Edinburgh, Ph.D. thesis, 321 p.

Simoneit, B.R.T., 1983, Effects of hydrothermal activity on sedimentary organic matter: Guaymas Basin, Gulf of California—Petroleum genesis and protokerogen degradation, *in* Rona, P.A., Boström, K., Laubier, L., and Smith, K.L., eds., NATO–ARI: Hydrothermal processes at seafloor spreading centers: New York, Plenum Press, p. 451–471.

———1984, Hydrothermal effects on organic matter—High versus low temperature components, *in* Schenck, P.A., de Leeuw, J.W., and Lijmbach, G.W.M., eds., Advances in organic geochemistry 1983: Organic Geochemistry, v. 6, p. 857–864.

———1985a, Hydrothermal petroleum: Genesis, migration, and deposition in Guaymas Basin, Gulf of California: Canadian Journal of Earth Science, v. 22, p. 1919–1929.

———1985b, Hydrothermal petroleum: Composition and utility as a biogenic carbon source, *in* Jones, M.L., ed., Hydrothermal vents of the Eastern Pacific: An overview: Bulletin of the Biological Association of Washington, v. 6, p. 49–56.

Simoneit, B.R.T., and Bode, G.R., 1982, Appendix II. Carbon/carbonate and nitrogen analyses, Leg 64, Gulf of California, *in* Curray, J.R., Moore, D.G., and others, eds., Initial reports of the Deep Sea Drilling Project: Washington, U.S. Government Printing Office, v. 64, part 2, p. 1303–1306.

Simoneit, B.R.T., and Lonsdale, P.F., 1982, Hydrothermal petro-

leum in mineralized mounds at the seabed of Guaymas Basin: Nature, v. 295, p. 198–202.

Stout, P.M., and Campbell, A.J., 1983, Hydrothermal alteration of near surface sediments, Guaymas Basin, Gulf of California, *in* Cenozoic marine sedimentation, Pacific marine: Pacific Marine Section, Society of Economic Paleontologists and Mineralogists, p. 223–231.

Von Damm, K., 1991, A comparison of the Guaymas Basin hydrothermal solutions to other sedimented ridge systems and experimental results, *in* Dauphin, J.P., and Simoneit, B.A., eds., The Gulf and Peninsular Province of the Californias: American Association of Petroleum Geologists Memoir, v. 47, p. 743–751.

Von Damm, K., Edmond, J.M., Grant, B., Measures, C.I., Walden, B., and Weiss, R.F., 1985a, Chemistry of submarine hydrothermal solutions at 21°N, East Pacific Rise: Geochimica et Cosmochimica Acta, v. 49, p. 2197–2220.

Von Damm, K., Edmond, J.M., Measures, C.I., and Grant, B., 1985b, Chemistry of submarine hydrothermal solutions at Guaymas Basin, Gulf of California: Geochimica et Cosmochimica Acta, v. 49, p. 2221–2237.

Zierenberg, R.A., Koski, R.A., Shanks, W.C., III, and Rosenbauer, R.J., 1986, Form and composition of sediment-hosted sulfide-sulfate deposits, Escanaba Trough, southern Gorda Ridge [abs.]: Eos, Transactions American Geophysical Union, v. 67, p. 1282.

Zierenberg, R.A., Koski, R.A., and Shanks, W.C., III, 1988, Preliminary results of ALVIN dives on active sediment-hosted massive sulfide deposits in the Escanaba Trough [abs.]: Eos, Transactions American Geophysical Union, v. 69, p. 1488.

Chapter 14. Sediment Alteration Associated with Massive Sulfide Formation in Escanaba Trough, Gorda Ridge: The Importance of Seawater Mixing and Magnesium Metasomatism

By Robert A. Zierenberg[1] *and* Wayne C. Shanks III[2]

CONTENTS

ABSTRACT

Escanaba Trough is a slow spreading ridge buried to an average depth of 500 m by turbiditic and hemipelagic sediment. The sediment is predominantly muddy but locally contains turbiditic silt and sand. Silt and sand grains are predominantly quartz, plagioclase, biotite, muscovite, chlorite, and amphibole. The muddy sediment is composed predominantly of detrital quartz, chlorite, illite, and smectite. The finest grain fraction of clay separates is predominantly smectite.

Massive sulfide deposits occur within the sediment near areas of recent sea-floor spreading volcanism. Sediment alteration associated with formation of massive sulfide is classified as smectite-, chlorite-, or talc-dominated based on the mineralogy. Smectite alteration is characterized by the overgrowth of sand and silt grains by iron-magnesium smectite. Aluminum, titanium, and zirconium behave conservatively during smectite alteration; magnesium is enriched relative to unaltered sediment. Hydrothermal smectite gives more coherent X-ray diffraction patterns and has lower $\delta^{18}O$ values than detrital and diagenetic smectite due to formation of hydrothermal smectite at temperatures near 200°C. Chlorite alteration is characterized by replacement of detrital minerals by magnesium-rich chlorite. Aluminum, titanium, and zirconium behave conservatively; silica, sodium, potassium and calcium are strongly depleted and magnesium is highly enriched relative to unaltered sediment. Chlorite $\delta^{18}O$ values near 2.5 per mil reflect formation at temperatures near 220°C. Talc alteration proceeds by direct precipitation of talc in sediment and on massive sulfide resulting in significant addition of magnesium to the rock.

Each type of alteration involves addition of magnesium from seawater that mixes with hydrothermal fluid in the upper part of hydrothermal circulation cells. This magnesium metasomatism releases hydrogen ions, which leads to hydrolytic alteration of detrital sediment. Magnesium removal during mixing with seawater also lowers the pH and increases the oxygen fugacity of the hydrothermal fluid leading to conversion of primary pyrrhotite to secondary marcasite and Fe-oxyhydroxides. Pyrite precipitated in altered sediment has $\delta^{34}S$ approximately 2 per mil higher than hydrothermal H_2S due to incorporation of minor amounts of sulfur derived from reduced seawater sulfate with $\delta^{34}S$ of 21 per mil.

[1] U.S. Geological Survey, Menlo Park, California.
[2] U.S. Geological Survey, Denver, Colorado.

The hydrothermal alteration observed at Escanaba Trough is similar to alteration observed at sediment-covered spreading centers in Guaymas Basin on the East Pacific Rise and Middle Valley on Juan de Fuca Ridge, and the processes involved are similar to those that result in wallrock alteration at both volcanic- and sediment-hosted massive sulfide deposits. Magnesium metasomatism caused by mixing of seawater into the upper parts of the discharge zones of sea-floor hydrothermal convection cells provides an important control on rock alteration and the transport and deposition of metal.

INTRODUCTION

Active hydrothermal systems at sea-floor spreading centers offer an unprecedented opportunity to investigate the processes leading to formation of massive sulfide deposits. Massive sulfide mineralization has been discovered at several sites within Escanaba Trough (Morton and others, 1987a, 1987b, 1990; Holmes and Zierenberg, 1990). The large size of individual deposits and the extensive areas where mineralization is known (Zierenberg and others, chap. 10, this volume) make Escanaba Trough one of the premier sites to study massive sulfide formation. Escanaba Trough is the slow spreading (2.4 cm/yr total spreading rate, Riddihough, 1980) southern portion of Gorda Ridge, and is bounded by the Mendocino Fracture Zone on the south and by a right-lateral offset of the ridge axis near latitude 41°25′ N., longitude 127°25′ W. on the north (Clague and Holmes, 1987). Escanaba Trough has a morphology typical of slow spreading ridges: a flat-floored axial valley 5 to 20 km wide at a depth of 3,300 m flanked by steep ridge crests rising 800 to 1,200 m above the axial valley floor (fig. 14.1). The southern two-thirds of the trough is covered by hemipelagic and turbiditic sediment that averages 500 m in thickness over the spreading axis. Turbiditic sediment enters the trough through a topographic low area of the east flank of the ridge north of the Mendocino transform fault, and sediment thickness decreases northward along the ridge axis (Vallier and others, 1973; Normark and others, chap. 6, this volume). Several igneous complexes 3 to 5 km in diameter occur along the spreading axis beneath the sediment cover, and basaltic rocks are locally exposed on the sea floor at these volcanic centers (Morton and others, 1987a; Clague and Holmes, 1987). These volcanic edifices are built by both intrusion and extrusion of basaltic rock (Morton and Fox, chap. 2, this volume). Detailed geologic mapping and sampling at two of the volcanic edifices utilizing surface ship and submersible, and reconnaissance work at two other sites, have revealed at least six major massive sulfide deposits and numerous sulfide occurrences (Morton and others, 1990; Holmes and Zierenberg, 1990). Although the sulfide deposits are spatially and genetically associated with the volcanic edifices, they all occur on or within sediment (Zierenberg and others, chap. 10, this volume). The presence of a sediment blanket over the hydrothermal system influences the form of the sulfide deposits by controlling the hydrologic regime. The composition of the hydrothermal fluids and deposits reflects chemical interaction of the hydrothermal fluid with the sediment (Campbell and others, chap. 11, this volume; Koski and others, chap. 16, this volume). The relatively impermeable sediment cover acts as a thermal blanket limiting large-scale convective cooling of the ridge crest (Davis and Becker, chap. 3, this volume; Denlinger and Holmes, chap. 4, this volume). Hydrothermal recharge and discharge are restricted to zones where tectonic and volcanic processes provide cross-stratal permeability. Sand and silt turbidites are presumed to be hydrothermal aquifers, because of their relatively high permeability. The volcanic edifices serve as both a topographic and thermal focus for hydrothermal fluids, resulting in long-lived discharge systems capable of forming large massive sulfide deposits.

Venting hydrothermal fluids have been sampled near latitude 41° N., longitude 127°30′ W.; other known sulfide occurrences do not appear to be presently active. Clear hydrothermal fluid at temperatures up to 217°C issues from porous anhydrite-barite chimneys on top of large mounds of pyrrhotite-rich massive sulfide. Active vents are colonized by dense clusters of tube worms and associated palm worms, anemones, limpets, gastropods, and bacterial mats (Van Dover and others, 1990). Bivalves are common in the sediment near some sulfide deposits.

The circulation of fluid through near-surface sediment in hydrothermal discharge zones results in alteration of the sediment. This chapter focuses on the nature of this alteration and suggests that mixing of seawater with hydrothermal fluid in the shallow subsurface is an important genetic process leading to magnesium metasomatism of sediments adjacent to the sulfide deposits. Subsurface mixing will also cause deposition of sulfide below the sea floor. Sulfide veining in sediment cores and sedimentary breccias with a sulfide matrix indicate that some sulfide minerals are deposited beneath the sediment surface. The extent of subsurface mineralization cannot be determined from surface observations, but it is possible that the large amount of sulfide exposed on the sea floor represents only a small part of the total deposits. The processes involved in sulfide deposition and sediment alteration at the Escanaba Trough deposits are similar to those occurring in Guaymas Basin on the East Pacific Rise (Kastner, 1982) and at Middle Valley on Juan de Fuca Ridge (Goodfellow and Blaise, 1988). Geologic and geochemical similarity to mineralization and alteration processes that formed some ancient massive sulfide deposits (Roberts and Reardon, 1978; Franklin, 1986) make Escanaba Trough an excellent natural laboratory in which to investigate ore deposit genesis.

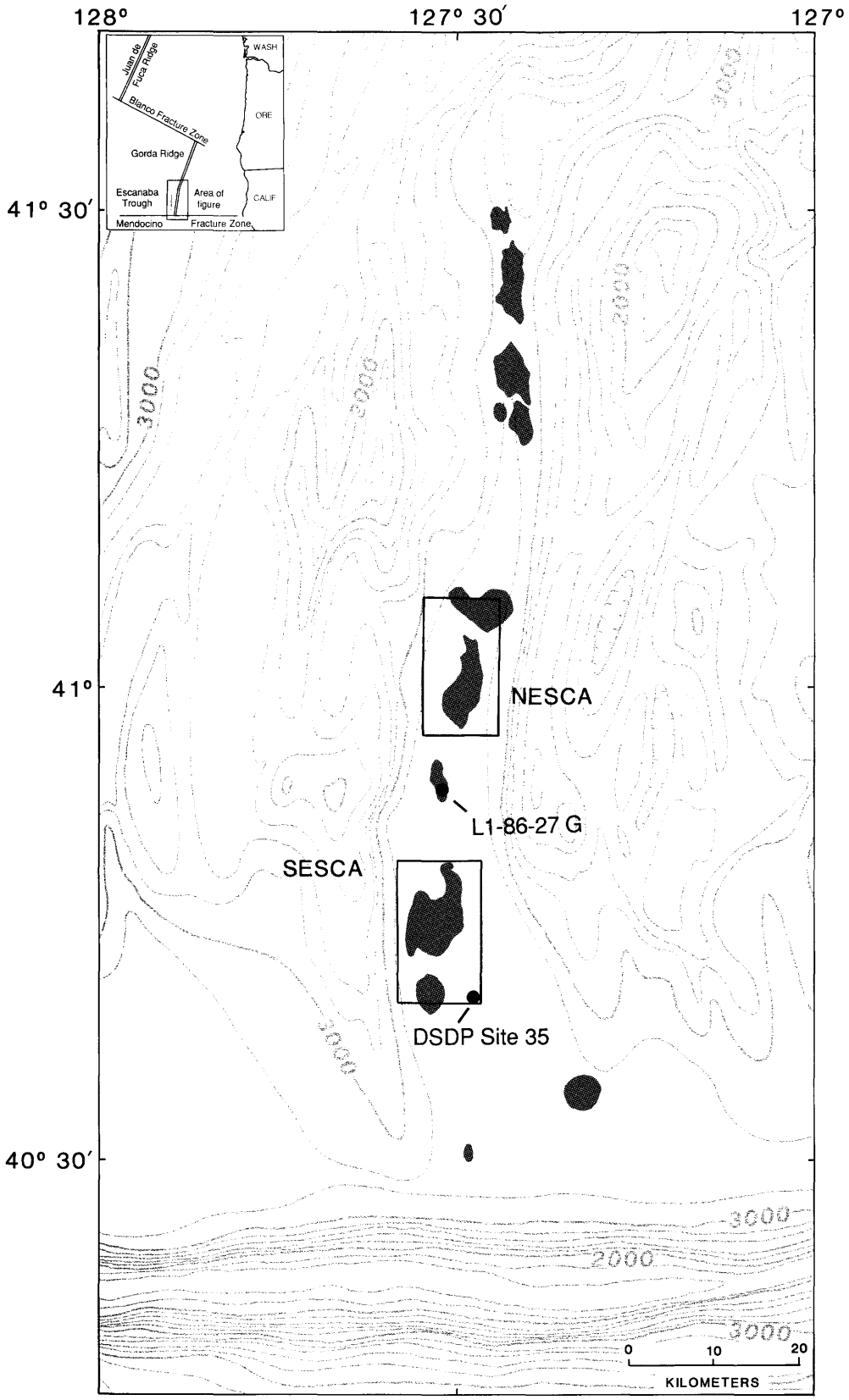

Figure 14.1. Bathymetric map of Escanaba Trough showing location of volcanic edifices (dark gray), SESCA and NESCA sites, DSDP Site 35, and core L1-86-27G in axial valley of Escanaba Trough outside of SESCA area. Hachures indicate area of closed low. Contour interval is 200 m.

ACKNOWLEDGMENTS

We thank the captain and crew of the R/V *S.P. Lee* for their efforts, often under adverse weather conditions, in collecting the samples used in this study. We thank Mary Horan, U.S. Geological Survey, Reston, Virginia, for oxygen isotope analyses. X-ray powder photographs used for the identification of chlorite polytype were kindly provided by R.C. Erd, Jr., U.S. Geological Survey, Menlo Park, California.

METHODS

Sediment was collected by both gravity coring and dredging at locations shown on figures 14.1 and 14.2. The bulk sediment and clay fraction mineralogy were determined by X-ray diffraction (XRD). Samples for clay mineralogy were repeatedly dispersed in deionized water by ultrasonic probe and settled by centrifugation. Three smear mounts on glass slides were prepared from the finest grain-size fraction of centrifuged samples to allow XRD examination of clays that had been air dried, treated with ethylene glycol, and heated to 400°C.

Bulk chemical analyses of unaltered and altered sediment samples were conducted in the Analytical Geochemistry Laboratory, Department of Geology and Geophysics, University of Minnesota (R. Knoche, analyst). Samples were leached of interstitial water and salts by repeated dispersal in deionized water followed by centrifugation. Major and minor elements were determined by DC-plasma atomic emission spectrometry (Bankston and others, 1979). Carbonate carbon and organic carbon were determined by automatic coulometric titration.

Samples for oxygen isotope analyses were reacted with ClF_3 (Borthwick and Harmon, 1982) and standardized using NBS-28, which has a value of 9.6 per mil relative to SMOW.

Samples for sulfur isotope analyses were treated chemically to separate mineral phases. Pyrrhotite was liberated in 6*N* HCl at 60°C and includes minor amounts of coexisting sphalerite. Isocubanite in residues from pyrrhotite reaction was subsequently dissolved in chromous chloride solution (Canfield and others, 1986). Chalcopyrite is a minor constituent in some of the isocubanite and is included in the chromous chloride fraction. Pyrite samples were also treated by chromous chloride solution. The sulfur in all sulfide samples was converted first to Ag_2S and then oxidized by combustion with Cu_2O at 1,050°C to produce SO_2. Barite was purified by reaction with $NaCO_3$ (Breit and others, 1985), reprecipitated as pure $BaSO_4$, then reacted with Cu_2O and SiO_2 at 1,140°C to produce SO_2. $\delta^{34}S$ values were standardized to Canyon Diablo troilite using the McMaster University reference series (Rees, 1978).

SEDIMENTOLOGY

SEDIMENT HISTORY

The proximity of Gorda Ridge to the North American continental margin results in significant deposition of continental clastic sediment on the southern part of the spreading center (Normark and others, chap. 6, this volume). Normark and others (chap. 6, this volume) propose that the bulk of this sediment was deposited within the last 100 kyr during the last two glacial lowstands of sea level. The sediment is predominantly turbiditic sand, silt, and mud transported from the continental shelf (Vallier and others, 1973; Normark and others, chap. 6, this volume). Vallier and others (1973) established that the source areas for the upper 360 m of sediment are igneous and metamorphic terranes in the Columbia River drainage basin. A channel system, which can be seen in the GLORIA long-range side-scan mosaics of this area (EEZ-SCAN 84 Scientific Staff, 1986), directs sediment transport southward from the Columbia Fan, past the Blanco Fracture Zone to the southern end of Escanaba Trough (Vallier and others, 1973). Turbidity currents flow north from the Mendocino Fracture Zone and bury the spreading center. Sediment cover thins to the north and ridge-axis basalt is exposed north of a topographic high at approximately latitude 41°17′ N. (Morton and Fox, chap. 2, this volume).

DEPOSITIONAL ENVIRONMENT

A drill hole at DSDP Site 35 penetrated the upper 390 m of sediment without reaching basement (McManus and others, 1970). Only 95 m of core was recovered from the hole, and many sections of core were not opened or described by the shipboard scientific party. Preliminary studies and descriptions of the sediment cored were reported by McManus and others (1970). The previously unopened core sections were subsequently logged in 1988 and are described in Normark and others (chap. 6, this volume). The sedimentology, mineralogy, and sediment chemistry of the uppermost 4 m of sediment recovered by piston and gravity coring in Escanaba Trough are described by Karlin and Lyle (1986) and Normark and others (chap. 6, this volume).

Presently accumulating sediment in Escanaba Trough is predominantly hemipelagic mud and locally derived silty to sandy turbidites (Karlin and Lyle, 1986; Normark and others, chap. 6, this volume). The transition from Holocene surface hemipelagic mud to Pleistocene turbiditic sediment is generally marked by a subtle change to grayer, more compacted mud with higher magnetic susceptibility and is generally found at 1 to 2 m depth in undisturbed cores (Karlin and Lyle, 1986). Cores that recover the sediment-water interface are capped by a 1- to 5-cm layer of oxidized red-brown mud formed in the zone ventilated by

bioturbation (Karlin and Lyle, 1986; Normark and others, chap. 6, this volume). Mud below this level is more reduced and is typically olive-brown to olive-gray.

Sandy intervals 10 to 40 cm thick were deposited by turbidity currents (Normark and others, chap. 6, this volume). Grain size ranges from fine to medium sand. The sandy intervals are generally massive to poorly graded and occasionally have scoured bases. The sands are moderately to poorly sorted and often contain some mud matrix. Sandy intervals typically compose 0 to 5 percent of the volume of sediment in the upper 3 m typically recovered by piston and gravity cores.

MINERALOGY

UNALTERED SEDIMENT

The mineralogy of unaltered sediment shows little variation between cores. The mud intervals are dominantly

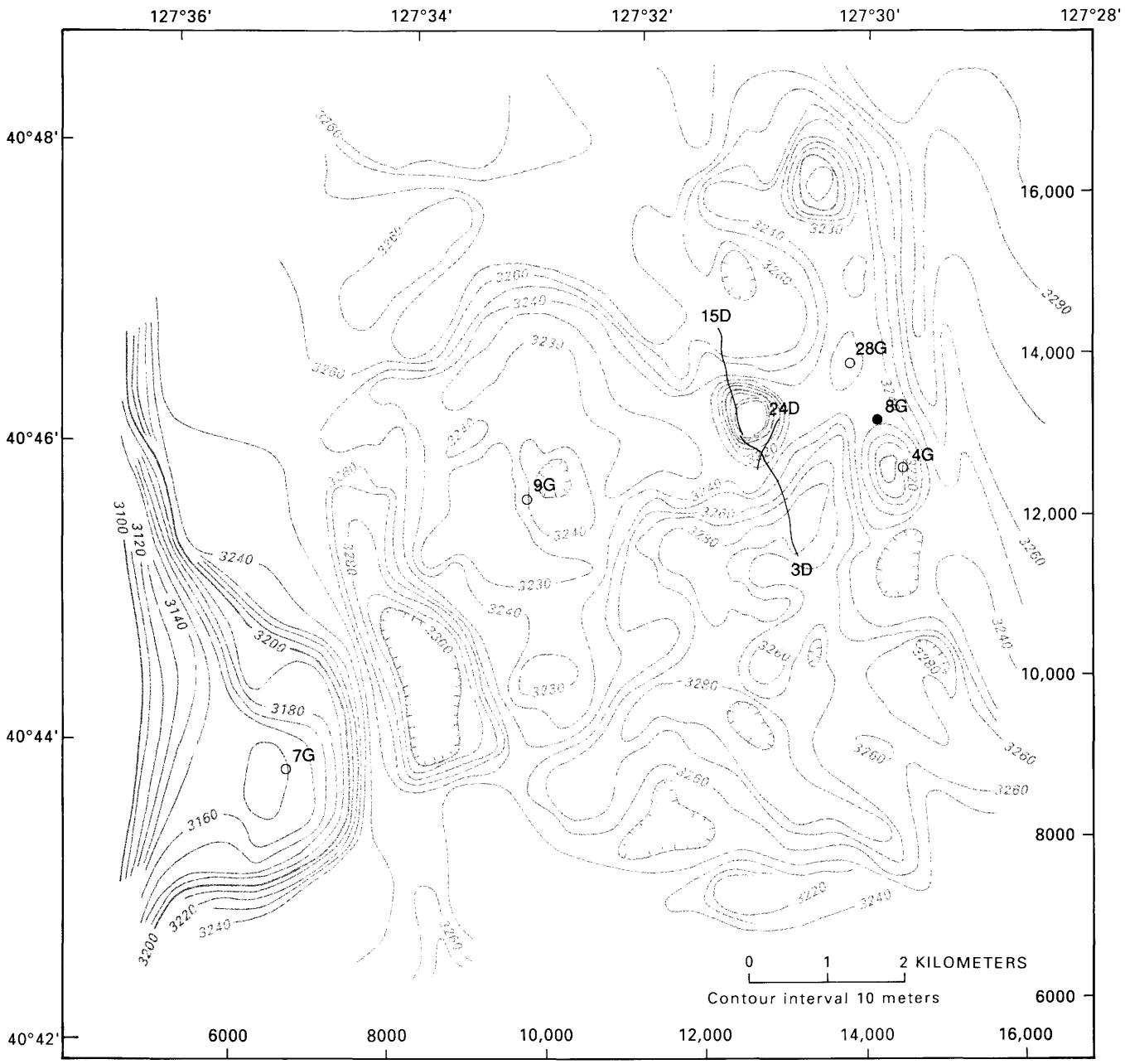

Figure 14.2. Bathymetric maps showing locations of core samples (open and closed circles) and dredge samples (solid lines) from the SESCA study area used in this study. Numbers along right and bottom give coordinates of local transponder net (in meters). Hachures indicate area of closed low.

quartz, feldspar, mica, and clay minerals. Carbonate and zeolite minerals were not detected by XRD. The finest grain-size fraction separated by centrifugation was dominantly green-brown to red-brown smectite. This smectite gives low-amplitude, broad XRD peaks due to very fine grain size and poor crystallinity. Coarser clay fractions are brown to gray and contain variable amounts of chlorite, illite, quartz, and smectite. Kaolinite contents appear to be low, but the presence of kaolinite peaks in the XRD traces could be partially masked by the more abundant chlorite.

Sandy intervals are predominantly quartz with abundant feldspar, predominantly plagioclase. Mica is common, and chlorite and minor amounts of amphibole were detected by XRD in many samples. Microscopy shows that biotite is more abundant than muscovite. The sands also contain minor amounts of pyroxene, igneous and metamorphic amphibole, epidote, ilmenite, magnetite, chromite, and occasionally pyrrhotite (Normark and others, chap. 6, this volume; Karlin and Zierenberg, chap. 7, this volume).

ALTERED SEDIMENT

We identified three mineralogically distinct types of hydrothermal alteration, which are referred to as smectite, chlorite, or talc alteration based on the dominant hydrothermal mineral in the samples. The differences in alteration mineralogy reflect differing environments and mechanisms of formation of the hydrothermal phases and provide some insight into the processes leading to mineral deposit formation in this system. The degree of mixing of hydrothermal fluid with seawater in part controls the mineralogy of the altered sediment.

SMECTITE ALTERATION

Hydrothermal smectite has been observed in samples from two settings from Escanaba Trough: as an alteration product in mineralized sediment, and as a hydrothermal precipitate with anhydrite in active vents. Hydrothermal smectite is easily distinguished from smectite occurring in unaltered sediment by XRD peaks that are narrower and increased in intensity by 1 to 3 orders of magnitude. The clay fraction of one sample of altered sediment (L1-86-3D) gives XRD patterns indicative of smectite-chlorite interlayering.

Hydrothermal smectite separated from altered sediment is deep green and gives very strong XRD peaks. Smectite is the dominant alteration mineral occurring in the mineralized section of core L1-86-27G. The turbiditic sands recovered at the base of this core are mineralized by pyrrhotite, accompanied by barite, isocubanite, sphalerite, and galena. The hydrothermal fluid that precipitated the sulfide also altered the host sediment. The smectite in the mineralized interval occurs as replacements and overgrowths of the sand grains. Examination of the altered sand by scanning electron microscope (SEM) shows that virtually all grains have coatings of hydrothermal smectite (fig. 14.3*A*). Smectite is also intergrown with hexagonal pyrrhotite (fig. 14.3*B*). Energy dispersive X-ray spectroscopy indicates that the smectite is an intermediate Mg-Fe smectite.

Smectite also occurs with anhydrite as a hydrothermal precipitate in deposits at active vents, where it occurs as light yellow-green reniform masses (Koski and others, chap. 16, this volume). It is the only silicate mineral in the chimney structures. This smectite is Mg-rich and Al-poor, and is probably near stevensite in composition. Formation temperatures for this smectite, calculated by Böhlke and Shanks (chap. 12, this volume) from oxygen isotope values measured on the smectite and hydrothermal vent fluid, are 220°C, in excellent agreement with measured vent temperatures of 217°C.

CHLORITE ALTERATION

Benninger and Koski (1987) identified chlorite in mineralized and altered sediment samples recovered by dredging from Escanaba Trough. A spectacular occurrence of chlorite is in hydrothermally altered sediment in core L2-86-9G. This core recovered a sulfide debris flow in the interval 50 to 77 cm that was deposited on a zone of intense chlorite alteration from 77 cm to the base of the core at 200 cm. The hemipelagic and turbiditic sediment in this interval has been replaced by a nearly monomineralic hydrothermal clinochlore with minor amounts of talc and trace amounts of pyrite, barite, isocubanite, sphalerite, gypsum, and rutile. The only remaining detrital minerals observed are coarse-grained quartz and mica in an interval formerly occupied by a sandy turbidite; finer grained detrital minerals have been completely replaced by chlorite. Talc occurs in some intervals as 2- to 10-mm white clots in the bluish-gray chlorite matrix. The overlying sulfide debris flow contains clasts of pyrrhotite-rich massive sulfide with barite, isocubanite, sphalerite, and galena (fig. 14.3*C*), typical of most Escanaba Trough massive sulfide. In contrast, the predominant sulfide in the altered chlorite is disseminated euhedral pyrite (fig. 14.3*D*). Isocubanite (fig. 14.4*A*) and gypsum (fig. 14.3*B*) are also observed. Despite its fine grain size, chlorite displays good crystallinity as demonstrated by strong, narrow XRD peaks and euhedral crystals seen by SEM (fig. 14.4*C*).

The less-than-2-μm fraction separated from the altered sediment in core L2-86-9G is also nearly monomineralic

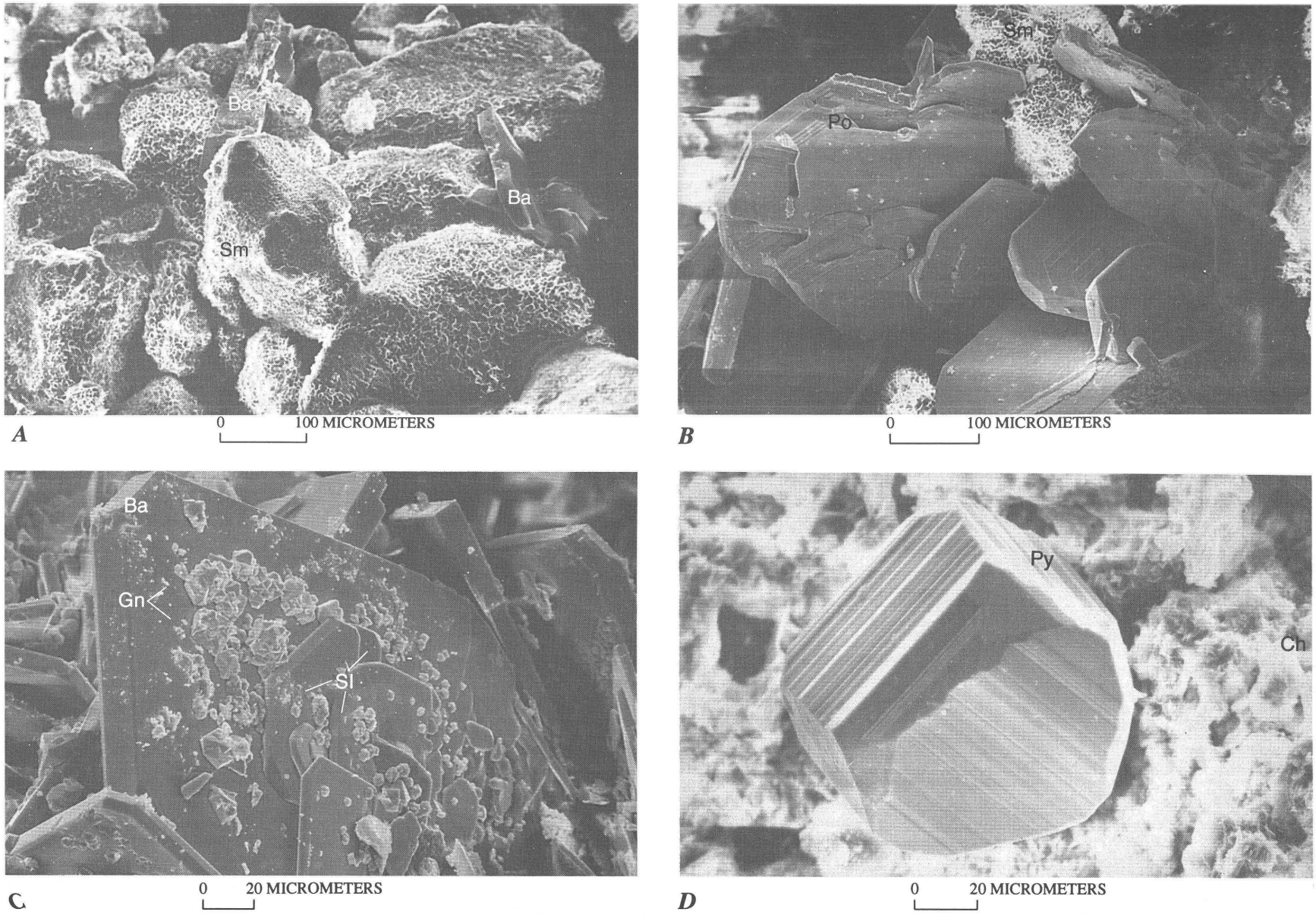

Figure 14.3. Scanning electron micrographs of Escanaba Trough sediments. *A*, Sand grains coated by Fe-Magnesium smectite (Sm). Uncoated, bladed grains are barite (Ba). L1-86-27G 82 cm. *B*, Euhedral hexagonal pyrrhotite (Po) crystals intergrown with Fe-magnesium smectite (Sm). L1-86-27G 82 cm. *C*, Euhedral barite (Ba) grains overgrown by small euhedral galena (Gn) crystals and colloform aggregates of sphalerite (Sl). L2-86-9G 62 cm. *D*, Euhedral pyrite (Py) crystal in magnesium-chlorite (Ch). L2-86-9G 107 cm.

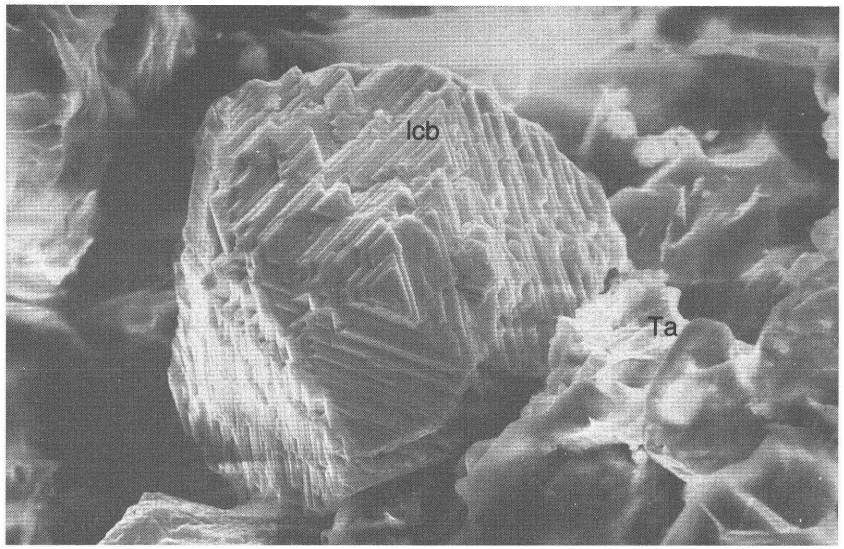

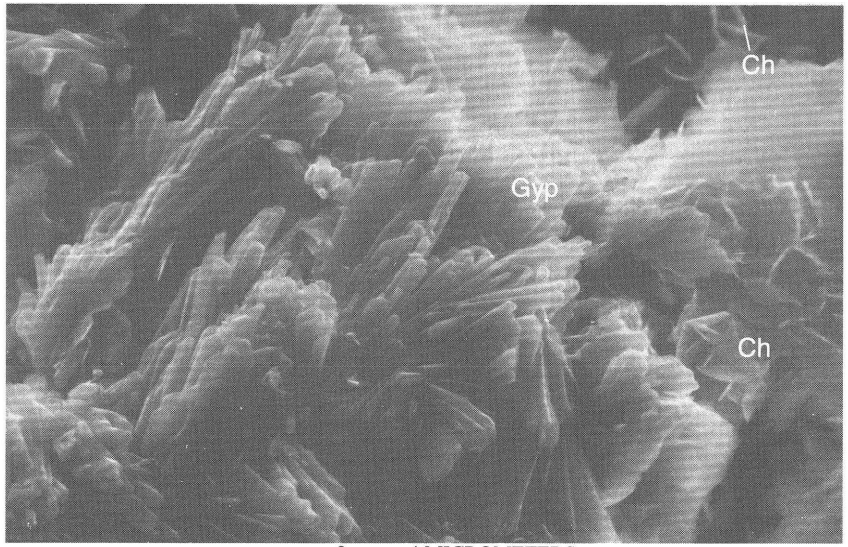

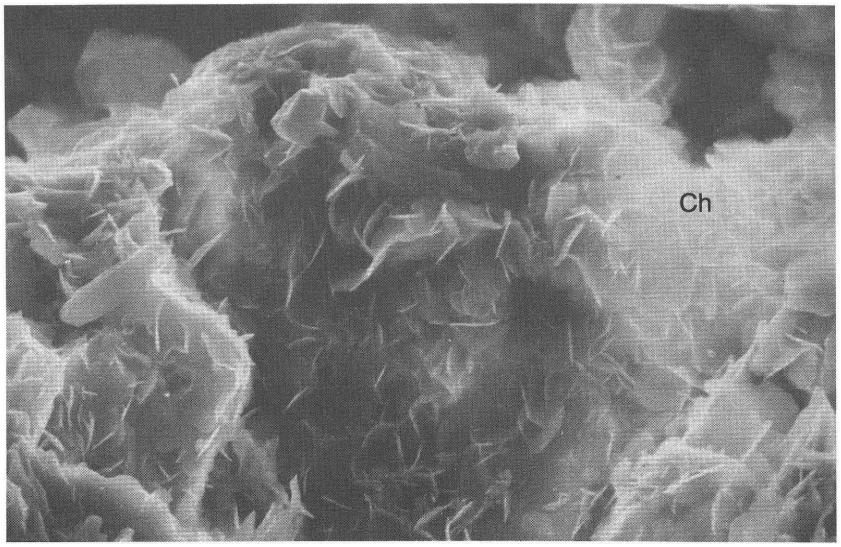

Figure 14.4. Scanning electron micrographs of Escanaba Trough sediments. *A*, Euhedral isocubanite (Icb) grain on talc (Ta) from a magnesium-chlorite rich sample. L2-86-9G 111 cm. *B*, Gypsum (Gyp) crystals intergrown with magnesium-rich chlorite (Ch). L2-86-9G 107 cm. *C*, Well-crystallized platelets of magnesium-rich chlorite (Ch). L2-86-9G 107 cm.

chlorite with minor amounts of talc. The separated chlorite is silver-gray, reflecting the low iron content. Even the finest grain-size fractions give very strong, sharp XRD peaks. Powder camera photographs show that the chlorite is the IIb structural polytype, which is the stable polytype at elevated temperatures (Bailey and Brown, 1962).

TALC ALTERATION

Talc is the most commonly observed hydrothermal silicate in massive sulfide samples from Escanaba Trough. The typical occurrence of talc is rinds 5 to 20 mm thick on the outer surfaces (seawater side) of massive sulfide. Talc also occurs interstitial to sulfide near the outer edges of samples and in some mineralized sediment samples, where it is often associated with chlorite (Benninger and Koski, 1987). Talc grains are fibrous to platy and occur either as intergrown reticulate networks or as botryoidal to radial fibrous aggregates. In some samples talc is overgrown by botryoidal amorphous silica and rarely by radial fibrous chalcedony. Some talc is associated with a more highly birefringent phyllosilicate interpreted to be smectite. The pyrrhotite in massive sulfide associated with talc is commonly replaced by marcasite; in some samples pyrrhotite and secondary marcasite are replaced by lepidocrocite and (or) goethite.

SEDIMENT CHEMISTRY

UNALTERED SEDIMENT

Bulk chemical analyses of near-surface samples of altered and unaltered mud and sand were obtained to assess mass transfer during hydrothermal alteration (table 14.1). Sands recovered at DSDP Site 35 from deeper in the sedimentary section were also analyzed to characterize potential metal sources and aquifers for the hydrothermal fluids.

The major chemical variations among unaltered samples are primarily a function of the relative proportions of clay minerals to quartz and feldspar. Mud samples have lower SiO_2 and higher Al_2O_3, MgO, $Fe_2O_3{}^T$ (total iron as Fe_2O_3), Cu, and Zn relative to sand. For example, the near-surface sand from core L1-86-8G contains more mud matrix than sands sampled from DSDP Site 35, which is reflected in the chemical analyses of this sample. The covariance of Na and Ca in unaltered samples (fig. 14.5*A*) is probably controlled by the abundance of detrital igneous feldspar.

A sample of sediment occurring above the sulfide debris flow in core L2-86-9G (36 to 40 cm) has elevated concentrations of $Fe_2O_3{}^T$, Ba, Pb, Cu, and Zn relative to other samples of unaltered mud. Although there are no indications of hydrothermal alteration of the silicate phases in this sample, it does contain abundant hydrothermal Fe-oxide codeposited with the hemipelagic sediment (Normark and others, chap. 6, this volume). Two possible sources for this hydrothermal component are (1) direct sedimentation from a hydrothermal plume, either lower temperature venting forming primary iron oxide or "black smoker" plume sulfide fallout that was oxidized to Fe-oxide; or (2) the Fe-oxide formed by sea-floor weathering of a nearby sulfide deposit. The presence of a sulfide debris flow above highly altered sediment in this core requires the presence of a nearby sulfide deposit. The lack of either sulfide mineralization or sediment alteration above the sulfide debris flow suggests that hydrothermal activity ceased at this site prior to the codeposition of sediment and Fe-oxide, and favors sea-floor oxidation of sulfide as the source of the Fe-oxide. Base-metal and barium enrichment in the Fe-oxide-rich sediment is consistent with derivation by oxidation of massive sulfide at the sea floor, but could also result from deposition from a hydrothermal plume. The enrichment of P_2O_5, Mn, and Th may suggest deposition of hydrothermal oxides, accompanied by scavenging of some elements from seawater, from a hydrothermal plume (Trefry and others, 1990).

ALTERED SEDIMENT

The three mineralogically distinguishable types of alteration (smectite, chlorite, talc) show chemical variations (table 14.1) that can be correlated with differences in the processes that form the different alteration types. The chemical differences between the alteration types are clearly shown on a plot of Al_2O_3 and MgO (fig. 14.5*B*). Magnesium addition is common to all of the alteration types, and the extent of magnesium enrichment serves as a rough index of alteration intensity. The large variation in Al_2O_3 content is not caused by mobility of Al but rather by addition or removal of SiO_2 and MgO, as discussed below. In fact, several elements appear to have behaved conservatively. This is illustrated by a plot showing the strong covariation of Al_2O_3 and TiO_2 (fig. 14.5*C*). Along with these two species, Cr, Ni, Sc, V, Y, and Zr all show strong interelement correlations consistent with conservative behavior of these elements.

A second feature common to each of the alteration types is depletion of alkali and alkaline-earth elements during alteration. The magnesium-rich samples that are the most altered show near-total removal of Na, K, Rb, Ca, and Sr (for example, fig. 14.5*D*, *E*). Barium is depleted in most of these samples but is locally enriched due to precipitation of hydrothermal barite in some samples.

The behavior of base metals in altered samples is controlled in large part by the precipitation of sulfide miner-

Table 14.1. Major- and minor-element composition of unaltered, altered, and mineralized sediment from Escanaba Trough.

Sample	L1-86-3D-1	L1-86-8G	L1-86-15D 2-5	L1-86-24D 8-1	L1-86-24D 21-2	L1-86-27G	L1-86-27G	L1-86-27G	L1-86-27G
Depth (cm)	Surface	174–179	Surface	Surface	Surface	72.5–74	74–77	77–80	84–87
Alteration	Smectite-chlorite	Unaltered	Talc	Talc	Talc	Sulfide veins	Smectite	Smectite	Smectite
Grain size	Mud	Sand	Mud	Mud	Mud	Sand	Sand	Sand	Sand
Major elements, in weight percent									
SiO_2	54.0	60.1	59.3	44.9	35.4	15.6	44.5	60.4	62.7
TiO_2	.912	.774	.113	.088	.050	.175	.497	.518	.646
Al_2O_3	19.1	15.8	1.5	1.2	.2	3.5	9.9	12.2	13.2
$Fe_2O_3^T$	7.17	6.62	2.76	27.20	23.60	54.40	25.40	6.62	9.97
MgO	6.63	4.07	28.5	16.4	15.6	.68	6.25	9.01	3.79
CaO	.1	2.1	.1	.1	.0	.5	10.2	1.3	2.0
Na_2O	.4	2.6	.3	.2	1.2	.6	1.5	2.2	2.6
K_2O	2.20	2.58	.13	.14	.13	.56	1.04	1.26	1.92
P_2O_5	.211	.188	.054	.205	.005	.040	.115	.084	.137
Minor elements, in parts per million									
Ba	746	727	167	458	235	8,200	1,649	378	803
Co	12	21	11	136	437	10	17	6	17
Cr	136	109	14	13	5	21	70	51	75
Cu	77	37	204	925	0	6,300	2,500	98	343
Mn	352	688	644	592	91	185	566	425	382
Ni	47	62	20	13	3	22	39	21	41
Pb	40	20	20	20	26	1,500	160	10	20
Rb	74	96	12	5	11	23	43	48	64
Sc	20	17	2	4	3	8	10	9	12
Sr	83	281	19	38	16	326	165	220	281
Th	17	10	0	0	0	7	4	5	0
V	203	143	36	120	13	31	74	79	101
Y	27	25	9	9	6	7	16	14	20
Zn	161	111	34	123	25	12,000	2,320	67	381
Zr	120	132	10	10	3	60	120	109	137

als. Contents of Cu, Zn, and Pb increase as the $Fe_2O_3^T$ content of the samples increases due to the precipitation of pyrrhotite accompanied by accessory base-metal sulfide minerals. The samples with the smallest amounts of sulfide minerals generally have base-metal values below those of the starting sediment, suggesting that in the absence of sulfide mineralization metals were leached from the sediment during alteration.

REACTION MECHANISMS AND MASS BALANCE CONSTRAINTS

SMECTITE ALTERATION

Hydrothermal smectite is forming in two distinct environments by different reaction mechanisms. The precipitation of magnesium-rich smectite within the active vent edifices is analogous to the formation of talc and is discussed further below. Alteration of sediment to magnesium-iron smectite is the result of reaction with hydrothermal fluid that is also precipitating sulfide minerals and barite within the sediment. Lateral flow of hydrothermal fluid through the more porous sandy turbidite layers in core L1-86-27G resulted in alteration of the sand grains and precipitation of both vein and disseminated sulfide and barite mineralization (Normark and others, chap 6, this volume). Sulfur, iron, copper, zinc, lead, and barium have been added to the sediment by precipitation from the hydrothermal fluid. However, hydrothermal fluid is not a likely source of magnesium or sulfate; end-member hydrothermal fluid is assumed to have none of either (Campbell and others, chap. 11, this volume). Measured magnesium concentration in 217°C hydrothermal fluid sampled in Escanaba Trough is as low as 1.6 mmol/kg (A.C. Campbell, written commun., 1989, referenced by Böhlke and Shanks, chap. 12, this volume). These components must be derived by mixing with either ambient seawater or seawater trapped as interstitial pore fluid in the sediment. Sulfur isotope data for barite (discussed below) are consistent with a seawater source for the sulfate. The low pH (5.3; Campbell and others, chap. 11, this volume) of the hydrothermal fluid enhances hydrolytic attack of minerals such as feldspars and micas resulting in depletion of sodium, calcium and potassium. However, the overgrowth

Table 14.1. Major- and minor-element composition of unaltered, altered, and mineralized sediment from Escanaba Trough–Continued.

Sample	L2-86-4G	L2-86-9G	L2-86-9G	L2-86-9G	L2-86-9G	L2-86-28G	DSDP 5 35 3-5	DSDP 5 35 5-4	DSDP 5 35 17-1
Depth (cm)	138-145	36-40	60-64	106-109	115-122	119-126	85 m	103 m	383 m
Alteration	Unaltered	Unaltered	Massive sulfide	Chlorite	Chlorite	Unaltered	Unaltered	Unaltered	Unaltered
Grain size	Mud	Mud		Sand	Mud	Mud	Sand	Sand	Sand
Major elements, in weight percent									
SiO_2	52.8	52.9	4.8	30.6	31.3	51.9	70.3	71.1	71.6
TiO_2	.790	.675	.048	.995	.925	.825	.572	.745	.502
Al_2O_3	17.3	14.4	.9	20.9	19.7	17.5	12.4	11.9	12.8
$Fe_2O_3^T$	7.93	11.00	43.40	8.25	12.40	8.45	3.78	5.00	3.05
MgO	3.96	3.80	.90	25.60	24.10	4.24	2.01	1.87	1.55
CaO	3.1	1.4	.5	.1	.1	3.1	3.6	3.5	4.0
Na_2O	2.2	1.6	.2	.0	.1	2.2	2.7	2.8	3.6
K_2O	3.13	2.23	.15	.03	.01	2.98	2.19	1.98	.81
P_2O_5	.202	.363	.050	.044	.038	.215	.130	.136	.104
Minor elements, in parts per million									
Ba	853	6,290	4,870	186	108	791	675	670	240
Co	24	36	1,050	30	47	26	12	13	8
Cr	112	148	13	147	183	106	66	65	53
Cu	65	428	na	78	228	77	15	11	58
Mn	922	1,220	90	322	714	1,220	449	576	295
Ni	69	97	29	74	184	70	33	25	22
Pb	20	210	4,800	30	20	20	5	20	10
Rb	124	93	13	17	0	124	65	60	29
Sc	20	18	6	19	24	22	9	10	8
Sr	296	256	955	15	10	282	342	369	403
Th	4	24	5	16	12	7	0	7	6
V	168	190	46	168	223	165	77	106	69
Y	24	20	4	35	35	24	19	19	17
Zn	141	269	21,000	145	288	142	106	122	55
Zr	102	100	15	217	147	110	152	137	133

of all sand grains, including quartz, by smectite (fig. 14.3*A*) suggests that much of the material that forms the smectite is carried by the hydrothermal fluid and is not derived by acid leaching of the sediment.

One sample (L1-86-3D-1) composed of interlayered smectite-chlorite shows behavior intermediate between smectite and chlorite type alteration. This sample shows only moderate magnesium enrichment, similar to the smectite alteration (fig. 14.5*B*). However, the sample with interlayered smectite-chlorite shows strong depletion of sodium and calcium, typical of the more intense chlorite alteration (fig. 14.5*D*, *E*). Potassium and rubidium are not depleted in this sample, and it is possible that this smectite-chlorite also contains significant interlayered illite.

CHLORITE ALTERATION

Total replacement of sediment from the base of L2-86-9G by a nearly monomineralic chlorite assemblage is the result of extreme magnesium metasomatism caused by reaction of seawater with hot sediment and (or) hydrothermal fluid percolating through sediment. Magnesia content has increased from approximately 4 weight percent in unaltered mud to 25 weight percent; silica has decreased from approximately 53 weight percent to 31 weight percent (table 14.1). The apparent increases in alumina and other "immobile" elements (fig 14.5*C*) are the result of residual enrichment caused by silica removal. The alkali and alkaline-earth elements have been stripped from the sediment (fig. 14.5*D*, *E*).

Because the altered sediment in sample L2-86-9G 115 to 122 cm is nearly monomineralic chlorite, the major-element chemical data for this sample (table 14.1) can be used to calculate an approximate composition for the chlorite. This calculated composition (table 14.2) falls within the clinochlore field (Hey, 1954) with an Fe/Fe+Mg ratio of 0.21.

Sample L2-86-4G 138 to 145 cm is typical unaltered mud representative of the protolith for the chlorite alteration. Using the major-element chemical data for this sample and assuming a simple mineralogy consistent with the XRD data, the proportions of the minerals composing the sample can be calculated, using the mineral compositions given in table 14.2. Because immobile elements,

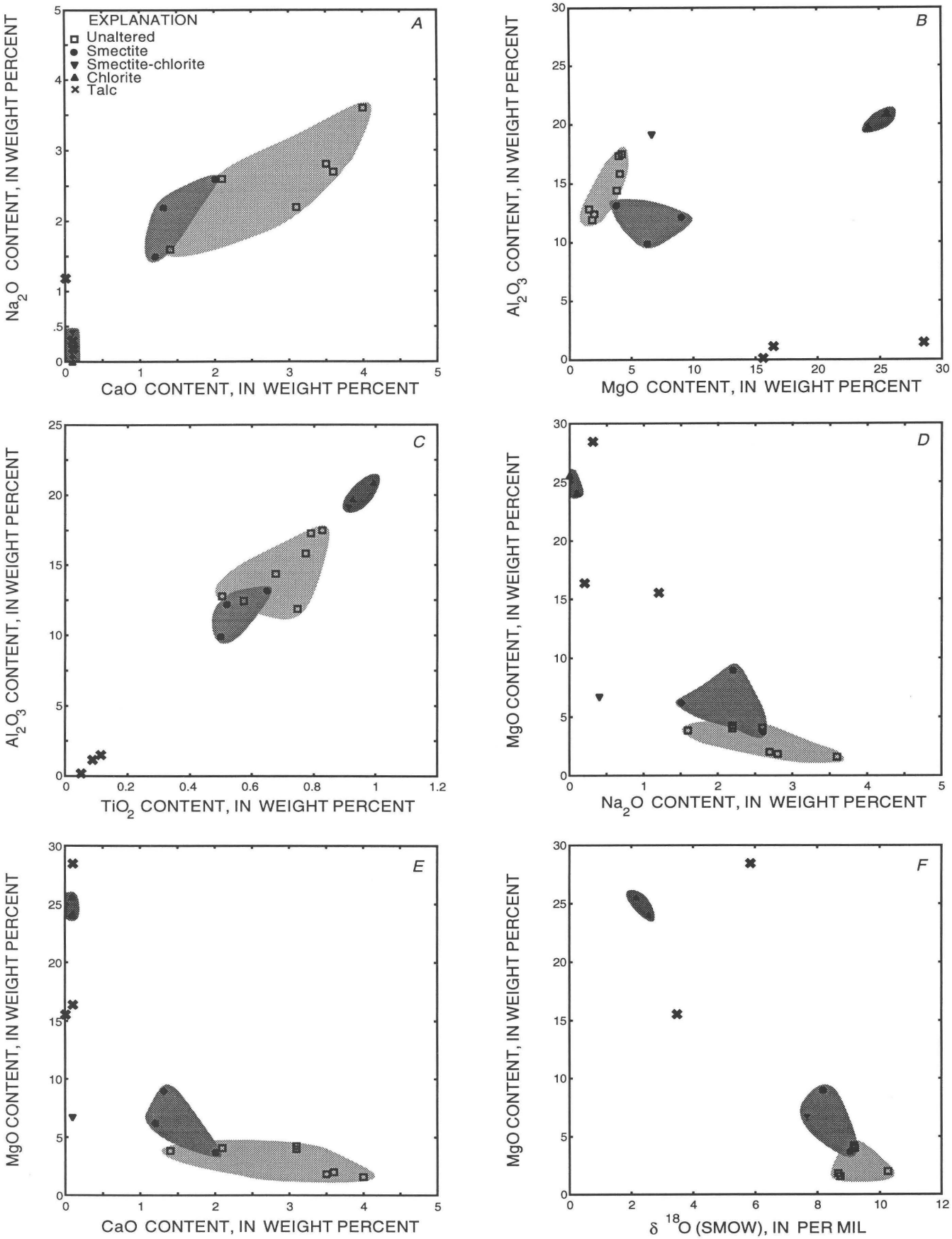
EXPLANATION
Unaltered
Smectite
Smectite-chlorite
Chlorite
Talc
A
Na2O CONTENT, IN WEIGHT PERCENT
CaO CONTENT, IN WEIGHT PERCENT
B
Al2O3 CONTENT, IN WEIGHT PERCENT
MgO CONTENT, IN WEIGHT PERCENT
C
Al2O3 CONTENT, IN WEIGHT PERCENT
TiO2 CONTENT, IN WEIGHT PERCENT
D
MgO CONTENT, IN WEIGHT PERCENT
Na2O CONTENT, IN WEIGHT PERCENT
E
MgO CONTENT, IN WEIGHT PERCENT
CaO CONTENT, IN WEIGHT PERCENT
F
MgO CONTENT, IN WEIGHT PERCENT
δ 18O (SMOW), IN PER MIL

including aluminum, behaved conservatively during alteration (fig 14.5*C*), the reaction converting sediment to chlorite can be calculated by conserving aluminum during alteration:

$$0.266\ \text{Qtz} + 0.071\ \text{Ab} + 0.055\ \text{An} + 0.033\ \text{Bi} + 0.023\ \text{Kaol} + 0.426\ Mg^{2+} + 0.038\ Fe^{2+} + 1.704\ H_2O \Leftrightarrow 0.0745\ \text{Ch} + 0.422\ Si(OH)_4 + 0.071\ Na^+ + 0.066\ K^+ + 0.055\ Ca^{2+} + 0.764\ H^+ \quad (1)$$

This equation illustrates the importance of magnesium addition and silica removal during alteration. This intense Mg-metasomatism generates large quantities of hydrogen ions, which further attack the silicate structures. The strong acid generation resulting from Mg-metasomatism is analogous to the reactions occurring during experimental interaction of seawater with basalt (Bischoff and Dickson, 1975; Seyfried and Bischoff, 1977) or sediment (Bischoff and others, 1981; Thornton and Seyfried, 1985) at elevated temperatures. The low pH created by precipitation of magnesium silicates is an important control on both the alteration assemblage formed and the fluid geochemistry and reactions occurring "downstream" from the zone of magnesium-metasomatism. Hydrolytic alteration by the low-pH fluids generated by Mg-metasomatism will enhance dissolution of silicate grains and removal of cations from the sediment, as indicated by equation 1, consistent with the low concentrations of alkali and alkaline-earth elements in the altered sediment (table 14.1).

The high-temperature vent fluids at Escanaba Trough contain essentially no magnesium (Campbell and others, chap. 11, this volume), similar to other sea-floor hydrothermal systems (Von Damm and others, 1985a, b). Furthermore, the amount of magnesium contained in interstitial pore fluid trapped in the sediment prior to alteration is insufficient to drive the reaction to completion. The only reasonable source of magnesium is seawater that has mixed with high-temperature hydrothermal fluid or with sediment heated by the flux of high-temperature fluids. The high thermal gradient of these systems near the sea floor drives secondary convective circulation cells, which pull seawater into a high-temperature reaction zone beneath and adjacent to active hydrothermal discharge zones. A minimum water-to-rock ratio can be calculated for the alteration zone by assuming that magnesium is quantitatively removed from seawater as it flushes through the reaction zone. The stoichiometry of equation 1 requires a minimum seawater-to-sediment weight ratio greater than 90. Alternatively, if we assume that the minimum measured Mg concentration in hydrothermal fluid (1.6 mmol/kg; Campbell and others, chap. 11, this volume) is the only source of magnesium, then quantitative removal into the alteration products requires a minimum seawater-to-sediment weight ratio greater than 1,000. Seawater mixing is the most likely source for the magnesium added to the sediment, but the large amount of seawater needed to supply the magnesium necessary for total conversion of sediment to chlorite will also affect the thermal regime in the alteration zone. Isotopic data presented below indicate that chlorite formed at high temperature (above 200°C). Large amounts of hydrothermal fluid and (or) high conductive heat flux is therefore required to maintain the alteration zone at temperatures near 200°C while mixing with large volumes of 1.7°C seawater.

Table 14.2. Mineral compositions used for mass balance calculations.

Chlorite (Ch)	$Mg_{7.05}Fe_{1.84}Al_{2.69}(Al_{1.86}Si_{6.14})O_{20}(OH)_{16}$
Quartz (Qtz)	SiO_2
Albite (Ab)	$NaAlSi_3O_8$
Anorthite (An)	$CaAl_2Si_2O_8$
Biotite (Bi)	$K_2Mg_3Fe_3Si_6Al_2O_{20}(OH)_4$
Kaolinite (Kaol)	$Al_4Si_4O_{10}(OH)_8$

TALC ALTERATION

Talc-rich samples have levels of magnesium enrichment similar to the chlorite alteration, but are clearly distinguished by lower aluminum content (fig 14.5*B*). The other "immobile" elements are correlated with aluminum and have low values in these samples as illustrated by the plot of Al_2O_3 versus TiO_2 (fig. 14.5*C*). Both petrographic and chemical data suggest that talc is a direct chemical precipitate and not a hydrothermal replacement of detrital minerals in the sediment. The low contents of Al_2O_3, TiO_2, Cr, V, and Zr reflect minor amounts of sediment incorporated in the talc-rich samples. The formation of talc on

⇐

Figure 14.5. *A*, Plot of Na_2O versus CaO for unaltered and altered sediment samples. Weak correlation of Na_2O and CaO in unaltered samples reflects abundances of plagioclase. Highly altered samples have been stripped of Na, K, Rb, and Ca. *B*, Plot of Al_2O_3 versus MgO delineates different alteration types defined by predominant alteration mineralogy. *C*, Plot of Al_2O_3 versus TiO_2 shows strong correlation indicating that these elements have behaved conservatively during alteration. Cr, Ni, Sc, V, Y, and Zr are also strongly correlated with Al_2O_3 and TiO_2. *D*, Plot of MgO versus Na_2O shows decrease of Na_2O with increasing MgO, which increases with increasing degree of alteration; K_2O, and Rb_2O show similar behavior. *E*, Plot of MgO versus CaO shows decrease of CaO with increasing MgO, which increases with increasing degree of alteration. *F*, Plot of MgO versus $\delta^{18}O$ shows decreasing $\delta^{18}O$ values with increasing alteration due to high-temperature exchange with hydrothermal fluid.

the outer edges of massive sulfide samples and the depositional textures indicating growth into open space support direct precipitation of talc. Mixing of high-temperature silica-rich hydrothermal fluid with cold magnesium-rich seawater at the seawater-sulfide interface results in supersaturation and precipitation of talc (Janecky and Seyfried, 1984). Removal of magnesium from seawater by talc precipitation also causes hydrogen ion generation:

$$3\ Mg^{2+} + 4\ Si(OH)_4 \Leftrightarrow Mg_3Si_4O_{10}(OH)_2 + 4H_2O + 6\ H^+ \quad (2)$$

The decrease in pH that accompanies talc precipitation may be responsible for the alteration of pyrrhotite and the precipitation of marcasite commonly observed in talc-rich samples (Murowchick and Barnes, 1986).

The Mg-rich, Al-poor smectite that coprecipitates with anhydrite in the active vents is also formed by mixing of hydrothermal fluid and seawater. The hydrothermal fluid contains abundant calcium and silica, but essentially no sulfate or magnesium, which are supplied by mixing with seawater. Anhydrite and magnesium-silicates are common constituents of active vent edifices (Styrt and others, 1981; Brett and others, 1987), and have been shown by isotopic (see below) and thermodynamic (Janecky and Seyfried, 1984) studies to form by mixing hydrothermal fluid with seawater. Higher silica activity favors the formation of talc relative to magnesium-smectite. Talc formation on massive sulfide may result from slower, more diffuse flow through sulfide mounds compared to the more rapid, focused discharge at active vents. The slower flow through the thermally conductive sulfide mounds would facilitate conductive cooling of hydrothermal fluid, leading to increased silica oversaturation (Janecky and Seyfried, 1984). The formation of amorphous silica, which overgrows talc in some samples, requires cooling of the hydrothermal fluid by thermal conduction as opposed to mixing with cold seawater (Janecky and Seyfried, 1984). Precipitation of talc at the seawater-sulfide interface may seal the system enough to allow hydrothermal fluid in the sulfide mounds to conductively cool to the point where amorphous silica can precipitate.

ISOTOPE CHEMISTRY

OXYGEN ISOTOPES

Thirteen samples of altered and unaltered sediment were analyzed for oxygen isotopes to constrain the extent and conditions of alteration. Unaltered sediment samples range in value from 8.7 to 10.3 per mil (table 14.3; fig. 14.6), primarily reflecting the value of detrital igneous and metamorphic quartz that is the dominant component of the sediment. Altered sediment samples range from 2.2 to 9.0 per mil (table 14.3; fig. 14.6). A plot of magnesium content, which serves as an approximate index of the extent of alteration, versus $\delta^{18}O$ shows that $\delta^{18}O$ decreases as samples become more altered (fig. 14.5*F*). The decrease in $\delta^{18}O$ is related to formation of alteration minerals from hydrothermal fluid at high temperature.

Table 14.3. Oxygen isotope values for bulk sediment samples

Sample	Depth	Grain size	$\delta^{18}O$ (per mil)
Unaltered sediment			
L1-86-8G	174–179 cm	sand	9.2
L2-86-4G	138–145 cm	mud	9.2
L2-86-28G	119–126 cm	mud	9.2
DSDP 5-35 3-5-29-33	85 m	sand	10.3
DSDP 5-35 5-4-127-129	103 m	sand	8.7
DSDP 5-35 17-1-130-135	383 m	sand	8.7
Altered sediment			
L1-86-3D-1	surface	smec-chl	7.7
L1-86-15D-2	surface	talc	5.8
L1-86-24D-21	surface	talc	3.5
L1-86-27G	77–80 cm	smectite	8.2
L1-86-27G	84–87 cm	smectite	9.0
L2-86-9G	106–109 cm	chlorite	2.2
L2-86-9G	115–122 cm	chlorite	2.6

To quantitatively evaluate the conditions of formation of the alteration minerals, $\delta^{18}O$ values were determined for the fine-grained fraction of the sediment separated for XRD analyses of clay minerals. Samples separated by grain size for clay mineralogy were used in an attempt to obtain pure or nearly pure separates of hydrothermal clay minerals. Generally, only the finest grain size fraction was analyzed because this fraction was often nearly monomineralic and because the finest grain size fraction should more readily approach isotopic equilibrium upon heating by hydrothermal fluid (Yeh and Savin, 1976). The isotope values for the clay separates are presented in table 14.4, which also lists the dominant and minor minerals present in each sample.

DETRITAL SEDIMENT

The fine fraction of unaltered sediment is generally dominated by smectite and has $\delta^{18}O$ values that overlap the range measured in bulk unaltered sediment (fig. 14.6), consistent with previous studies that document the preservation of original $\delta^{18}O$ values in detrital clay in low-temperature authigenic minerals (Yeh and Savin, 1976). Several samples have $\delta^{18}O$ values higher than the values for the bulk sediment. All of these isotopically heavy samples are dominantly smectite, and the isotope values are a reflection of lower temperature of formation of the smectite. $\delta^{18}O$ values above 15 per mil are only observed in smectite-rich samples from the surface sediment recovered in the cores. Most cores recovered an oxidized sur-

face sediment layer 1 to 5 cm thick formed in the zone ventilated by bioturbation (Normark and others, chap. 6, this volume). Surface samples differ from deeper intervals in their red-brown color, due to the presence of iron oxides, and generally higher abundance of smectite compared to samples deeper in the cores. Burial of sediment below the zone of bioturbation is followed by reduction of iron oxides that destroys the red-brown pigmentation, resulting in the gray-green mud typical of the hemipelagic sediment. The high $\delta^{18}O$ values for the samples from the surface oxidized zone are a reflection of the low temperatures of formation of the diagenetic oxides and (or) smectite. Smectite from surface sediment from core L2-86-4G is not enriched in $\delta^{18}O$ to the extent of samples from the oxidized

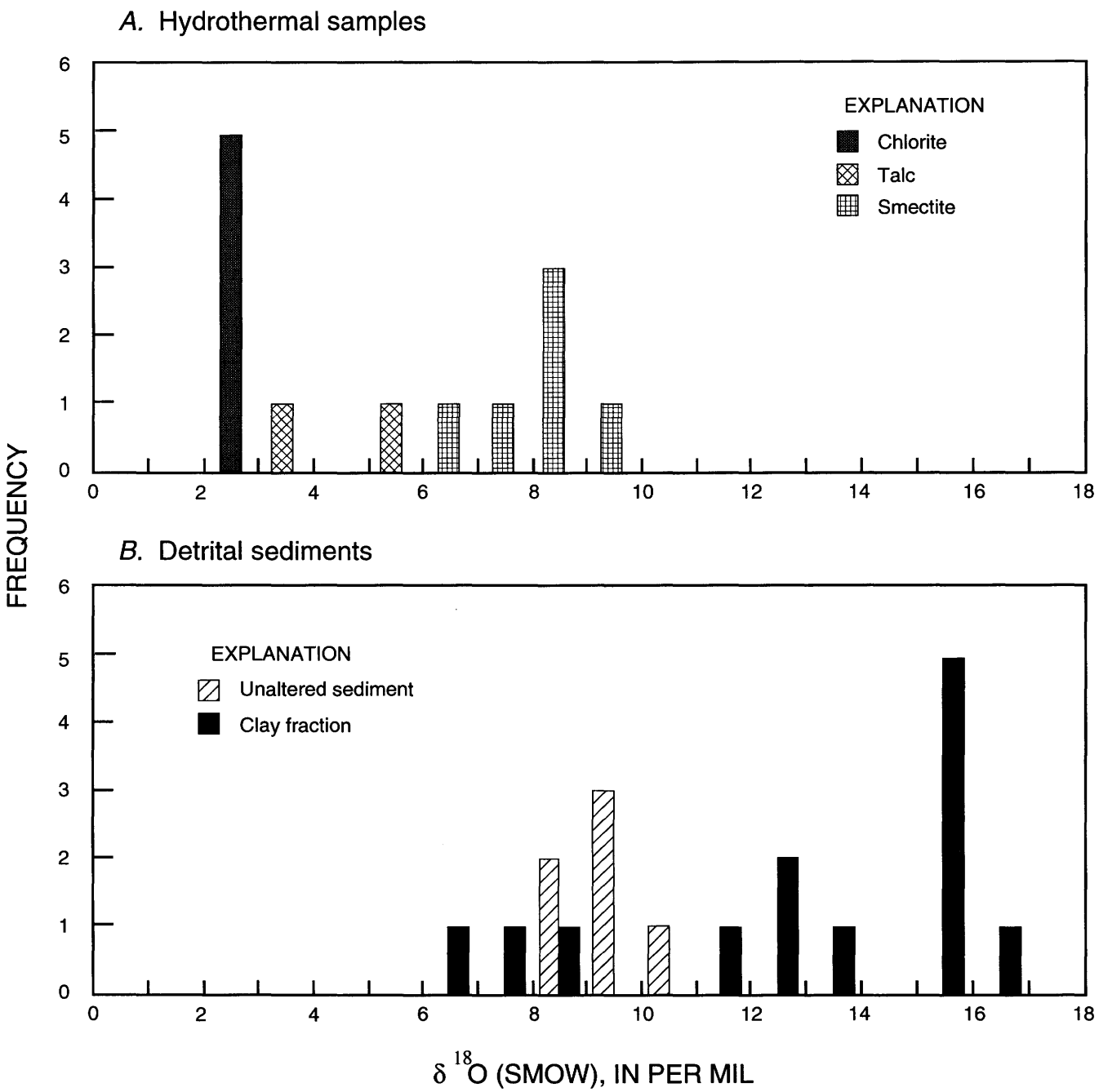

Figure 14.6. *A*, Histogram of $\delta^{18}O$ values for bulk sediment and clay fraction separates of different alteration types defined in text. Mineral separates of chlorite and smectite have $\delta^{18}O$ values similar to bulk sediment from the same sampling intervals. Bulk sediment samples labeled "talc" show peaks for talc only on XRD traces. *B*, Comparison of bulk-sediment $\delta^{18}O$ values with values from clay fraction separates. Smectite-rich clay fractions with $\delta^{18}O$ values greater than 15 per mil are from zone of red-brown surface oxidized sediment that occurs at top of most cores.

Table 14.4. Oxygen isotope values for clay fraction separates.

[smec, smectite; chl, chlorite; qtz, quartz; ill, illite]

Sample	Depth (cm)	Mineralogy		$\delta^{18}O$ (per mil)
		Major	Minor	
Unaltered sediment				
L1-86-8G ----------	174–175	smec	chl, qtz	7.9
L1-86-19G ----------	surface	smec	chl, qtz	15.9
L1-86-27G-Fine ------	surface	smec		16.2
L1-86-27G-Coarse ---	surface	qtz,chl, ill	smec, pl	8.8
L2-86-27G ----------	72.5–74	qtz	chl, ill	6.3
L1-86-33G ----------	surface	smec	chl, ill	15.3
L1-86-33G ----------	104–105	chl, smec, ill		12.7
L2-86-4G ----------	surface	smec		12.0
L2-86-7G ----------	surface	smec		16.6
L2-86-9G ----------	36–40	smec		13.7
L2-86-28G ----------	surface	smec	ill, chl	15.9
L2-86-28G ----------	119–126	smec	ill, chl	11.1
Hydrothermal clay				
L2-86-27G ----------	74–77	smec	chl, ill	8.1
L2-86-27G ----------	77–80	smec		6.0
L2-86-27G ----------	84–87	smec	chl, ill	8.7
L2-86-9G-Fine -------	106–109	chl		2.4
L2-86-9G-Coarse ----	106–109	chl		2.1
L2 86-9G ----------	115–122	chl		2.7

surface layer, consistent with the absence of this layer in the core (Normark and others, chap. 6, this volume). It was possible to separate the finer grained smectite-rich fraction from a coarser clay fraction dominated by detrital quartz, chlorite, and illite in the surface sediment sample from core L1-86-27G. The smectite-rich fraction has a $\delta^{18}O$ value of 16.2 per mil compared to 8.8 per mil for the detrital fraction. The latter is similar to the isotopic value of unaltered sediment.

HYDROTHERMAL CLAYS

Hydrothermal smectite separates from the mineralized part of core L1-86-27G have $\delta^{18}O$ values ranging from 6.0 to 8.7 per mil (table 14.4). The lowest value is from the sample with the smallest amount of detrital clays. The $\delta^{18}O$ values of hydrothermal smectite are only slightly lower than bulk-sediment $\delta^{18}O$ values from the same intervals, even though the bulk of the sediment in these samples is detrital quartz sand. Isotopic fractionation temperatures, calculated using the smectite-water fractionation equation given in Savin and Lee (1988) and assuming equilibrium with hydrothermal fluid with an isotope value equal to Escanaba Trough vent fluid of 0.4 per mil (Böhlke and Shanks, chap. 12, this volume), range from 181°C to 240°C. These values are similar to the measured vent temperature of 217°C at the NESCA site and similar to the 220°C temperature calculated from oxygen isotopes for smectite precipitated in the 217°C vent structure (Böhlke and Shanks, chap. 12, this volume). These $\delta^{18}O$ values of hydrothermal smectite are lower than those of smectite from the unaltered samples, with the exception of sample L1-86-8G 174 to 175 cm, which has a value of 7.9 per mil. Examination of magnetic separates from this core by SEM revealed the presence of hydrothermal pyrrhotite in contrast with other cores, which contain only detrital magnetite and ilmenite. Morton and others (1987b) identified the lower part of core L1-86-8G as hydrothermally altered sediment based on the bleached gray color and texture of the sediment. While the chemistry and mineralogy of this core indicate that it is predominantly composed of detrital minerals, the presence of pyrrhotite and the low $\delta^{18}O$ value from this core suggest that the turbiditic lower part of this core contains some hydrothermal component.

Hydrothermal chlorite separates from the lower altered part of core L2-86-9G have very low $\delta^{18}O$ values ranging from 2.1 to 2.7 per mil (table 14.4). The isotopic values of the bulk-sediment samples overlap those of the chlorite separates because the sediment is nearly monomineralic chlorite. Calculated temperatures of chlorite formation using the fractionation equation of Wenner and Taylor (1971) and a hydrothermal fluid value of 0.4 per mil (Böhlke and Shanks, chap. 12, this volume) range from 199°C to 221°C. These temperatures are very close to the measured temperature of active hydrothermal vents at the NESCA site (217°C). The calculated temperatures of formation are consistent with the occurrence of the type IIb structural polytype, stable at elevated temperatures (Bailey and Brown, 1962). The high temperature indicated for forma-

tion of chlorite limits the rate at which cold magnesium-bearing seawater, necessary for Mg-metasomatism, can flow into the alteration zone.

Mineral separates were not prepared for talc-rich samples; however, the samples analyzed for bulk-sediment $\delta^{18}O$ values are essentially monomineralic as determined by XRD, which shows talc as the only mineral present. If we assume that the samples are composed of talc and apply the talc-water fractionation equation of Savin and Lee (1988), then using a hydrothermal fluid value of 0.4 per mil (Böhlke and Shanks, chap. 12, this volume) we calculate formation temperatures of 222°C and 277°C. These temperatures are similar to the temperature of the hydrothermal vents and values calculated for chlorite and smectite alteration, but extend to higher range. A higher temperature for talc formation might be expected because talc is closely associated with pyrrhotite-rich massive sulfide. The presently venting hydrothermal fluids carry little dissolved base metal (Campbell and others, chap. 11, this volume) and are not precipitating massive sulfide where they vent to the sea floor. Mineral assemblages in massive sulfide samples indicate formation temperatures of approximately 300°C (Koski and others, chap. 16, this volume).

Table 14.5. Sulfur isotope values for sediment-hosted mineralization.

Core	Depth (cm)	Mineral	$\delta^{34}S$ (per mil)
L1-86-27G ------	64	Barite	22.3
		Pyrrhotite	5.0
		Isocubanite	3.9
L1-86-27G ------	72.5–74	Pyrrhotite	5.9
		Isocubanite	6.2
L1-86-27G ------	74–77	Pyrrhotite	6.4
		Isocubanite	6.3
L1-86-27G ------	77–80	Pyrrhotite	6.1
		Isocubanite	5.3
L1-86-27G ------	80–84	Pyrrhotite	6.8
		Isocubanite	6.1
L1-86-27G ------	84–87	Pyrrhotite	6.7
		Isocubanite	7.1
L2-86-9G --------	62	Barite	20.5
		Isocubanite	2.9
L2-86-9G --------	60–64	Pyrrhotite	4.8
		Isocubanite	4.6
L2-86-9G --------	106–109	Pyrite	7.8
L2-86-9G --------	111	Pyrite	6.1
L2-86-9G --------	115–122	Pyrite	7.4

SULFUR ISOTOPES

The sulfur isotope compositions of sulfide and sulfate samples from the sediment cores (table 14.5) were determined to allow comparison to massive sulfide samples previously measured (Koski and others, 1988; Böhlke and Shanks, chap. 12, this volume). Disseminated and vein sulfide from the mineralized sandy turbidite layers at the base of core L1-86-27G range in $\delta^{34}S$ value from 3.9 to 7.1 per mil, similar to the range of values reported for Escanaba Trough massive sulfide samples by Koski and others (1988). Sulfur isotope values of coexisting pyrrhotite and chalcopyrite are similar, but isotopic equilibrium among sulfide minerals is not commonly observed in sea-floor massive sulfide deposits (Zierenberg and others, 1984). Sulfur in barite from this core is slightly heavier than sulfur in seawater sulfate. Barite is interpreted to form by mixing of sulfate-bearing pore fluid of seawater composition with barium-rich hydrothermal fluid, perhaps accompanied by a minor amount of sulfate reduction.

Barite intergrown with massive sulfide fragments from the sulfide debris flow in core L2-86-9G has a $\delta^{34}S$ value indistinguishable from that of seawater sulfate and is interpreted to have formed from mixing of hydrothermal fluid with seawater on the sea floor. Sulfide minerals in the massive sulfide fragments have $\delta^{34}S$ values ranging from 2.9 to 4.8 per mil, which overlap with the lower range of values previously measured (Koski and others, 1988). Only minor amounts of sulfide occur in the chlorite-altered sediment that underlies the sulfide debris flow. The dominant sulfide in the altered sediment is euhedral pyrite. Pyrite is rarely observed in massive sulfide samples from Escanaba Trough and is usually present as rare framboidal pyrite or as late-stage botryoidal pyrite associated with marcasite. The dominance of pyrite in the altered sediment requires higher sulfur fugacity conditions than generally prevailed during precipitation of the pyrrhotite dominated massive sulfide. Pyrite $\delta^{34}S$ values are distinctly higher than values measured in sulfide minerals from the overlying massive sulfide debris flow, although still within the range of values common to Escanaba Trough massive sulfide (Koski and others, 1988). The chemistry of the silicate alteration requires mixing of large amounts of seawater with hydrothermal fluid in the alteration zone. Seawater supplies sulfate that potentially could react with the hydrothermal fluid to raise both the $f\,S_2$ and $\delta^{34}S$ values of the fluid. We assume that the $\delta^{34}S$ value of pyrrhotite in the overlying massive sulfide (4.8 per mil) is representative of H_2S in the local hydrothermal fluid and that seawater sulfate has a $\delta^{34}S$ value of 21 per mil (Rees and others, 1978), similar to the barite in this core. If pyrite in the mixing zone formed by the following reaction:

$$4\,Fe^{2+} + 7\,H_2S + SO_4^{2-} \Leftrightarrow 4\,FeS_2 + 4\,H_2O + 6\,H^+ \qquad (3)$$

then the expected $\delta^{34}S$ value of pyrite can be calculated by isotope mass balance to be 6.8 per mil, in reasonable agreement with the observed value. It appears that abiotic reduction of seawater sulfate mixed into the alteration zone increases the $f\,S_2$ value of the fluid and leads to the precipitation of isotopically enriched pyrite.

COMPARISON TO ORE DEPOSIT ALTERATION

Sediment alteration in Escanaba Trough is a result of interaction of hydrothermal fluid with sediment accompanied by mixing with pore water and (or) seawater. Flow of seawater into the alteration zones beneath and adjacent to the Escanaba Trough deposits is the critical factor that leads to magnesium-metasomatism of the sediment. Removal of magnesium from the fluid during alteration has important effects on the fluid chemistry, primarily by production of hydrogen ion. Seawater mixing also influences fluid parameters such as temperature, $f\,O_2$, and $f\,S_2$, and therefore exerts a major control on the transport, deposition, and phase chemistry of base-metal sulfide minerals as well as silicate alteration minerals.

Sea-floor hydrothermal deposits on sediment-covered spreading centers have been described from Guaymas Basin in the Gulf of California and at Middle Valley on the northern Juan de Fuca Ridge. Inactive hydrothermal deposits sampled in the Guaymas North Basin are predominantly talc and pyrrhotite (Lonsdale and others, 1980). The talc in these deposits was interpreted to have formed at about 280°C by the mixing of hydrothermal fluid with seawater (Lonsdale and others, 1980). Talc and magnesium-rich smectite identified as stevensite are also forming in hydrothermally active mounds and chimneys in the Guaymas South Basin (Koski and others, 1985; Peter and Scott, 1988), even though measured Mg concentrations in hydrothermal fluid are as low as 0.60 mmol/kg (Von Damm and others, 1985b). Mixing of hydrothermal fluid with seawater is interpreted as the mechanism leading to precipitation of magnesium-rich silicates in the Guaymas hydrothermal deposits (Koski and others, 1985; Peter and Scott, 1988). Magnesium-rich phyllosilicates, including talc, are also described from hydrothermally altered sediment from the Middle Valley (Goodfellow and Blaise, 1988). Sulfide-rich horizons in the sediment cores have elevated magnesium contents (Goodfellow and Blaise, 1988).

Magnesium enrichment in alteration zones underlying massive sulfide deposits has also been well documented. Examples include the Archean deposits at Mattagami Lake (Roberts and Reardon, 1978) and Millenbach (Riverin and Hodgson, 1980), Canada; the Proterozoic Sullivan deposit, Canada (Hamilton and others, 1983); the Devonian Arctic Prospect, Alaska (Schmidt, 1988); Cretaceous deposits on Cyprus (Lydon and Galley, 1986; Richards and others, 1989); and Tertiary Kuroko deposits, Japan (Urabe and others, 1983). The cited examples span both geologic time and a wide variety of tectonic settings. Roberts and Reardon (1978) recognized the importance of mixing between hydrothermal fluid and seawater in the formation of alteration zones in the upper parts of massive sulfide hydrothermal systems. The chemical and isotopic effects of fluid mixing have been thermodynamically modeled by Janecky and Seyfried (1984) and Janecky and Shanks (1989). Both field and theoretical studies clearly establish the importance of fluid mixing in the shallow subsurface as a factor controlling the formation of massive sulfide deposits. Studies that attempt to understand ore fluid composition, fluid inclusion and isotopic systematics, mineral precipitation, and mineralogical and chemical zonation in massive sulfide deposits and associated shallow alteration zones need to evaluate the effects of seawater mixing.

Examination of the alteration zones of some massive sulfide deposits demonstrates that the cores of alteration pipes and the deeper zones of alteration differ from the alteration found in the shallow mixing zone. Some massive sulfide deposits, including Kidd Creek, Canada (Slack and Coad, 1989), and ophiolite-hosted deposits in Cyprus (Lydon and Galley, 1986; Richards and others, 1989) and Oregon (Zierenberg and others, 1988), have alteration zones that are characterized by the presence of iron-rich chlorite. These alteration zones are interpreted to reflect hydrothermal fluid-rock interaction below the zone of seawater mixing. This type of alteration is less well studied than the shallower alteration because exploration drilling and mine workings are often too shallow to intersect these zones, and because the deeper alteration zones are often separated from the sulfide deposits by tectonic disruption. This type of alteration has not been encountered in Escanaba Trough because our samples are restricted to near-surface zones. Further understanding of this important alteration type will require drilling below an actively forming massive sulfide deposit, such as those found in Escanaba Trough.

SUMMARY

Hydrothermally altered sediment is associated with sediment-hosted sea-floor massive sulfide deposits in Escanaba Trough. Three types of alteration have been distinguished based on the dominant alteration mineralogy: smectite, chlorite, and talc. The different alteration types have distinct geochemical signatures. Petrographic and geochemical data established that the different alteration types formed in distinct environments. Smectite alteration occurs mainly in the more permeable sandy aquifers. Sand grains are coated by Fe-Mg smectite formed by mixing of hydrothermal solutions with minor amounts of seawater or seawater-like pore fluid. Hydrothermal smectite is distinguished from detrital and diagenetic smectite in the degree of crystallinity and in lighter oxygen isotope composition, reflecting formation at temperatures near 200°C. Intensely altered sediment is completely replaced by hydrothermal clinochlore. Extensive mixing of seawater with hydrothermal fluid at temperatures above 200°C are required to explain the chemical and isotopic composition of the chlorite

alteration. The formation of talc and Mg-smectite on massive sulfide and in active vents, respectively, proceeds primarily by direct precipitation in the zone of mixing of hydrothermal fluid with seawater without extensive replacement of detrital silicates. Magnesium metasomatism caused by mixing has important consequences for alteration and mineralization processes, primarily due to production of hydrogen ion during alteration. Geochemical characteristics common to each alteration type are an increase of magnesium coupled with a decrease in Na, K, Rb, and Ca. High-field-strength elements including Al, Ti, Cr, Ni, Sc, V, Y, and Zr remained relatively immobile during hydrothermal alteration.

The alteration processes and products observed in Escanaba Trough are comparable to the shallow alteration zones found below and adjacent to ancient massive sulfide deposits formed over the span of geologic time in diverse tectonic environments. Escanaba Trough is therefore an important natural laboratory where the processes of mineral deposit genesis can be investigated.

REFERENCES CITED

Bailey, S.W., and Brown, B.E., 1962, Chlorite polytypism: I. Regular and semi-random one-layer structures: American Mineralogist, v. 47, p. 819–850.

Bankston, D., Humphris, S., and Thompson, G., 1979, Major and minor oxide and trace element determination in silicate rocks by direct current plasma optical emission echelle spectrometry: Analytical Chemistry, v. 51, p. 1218–1225.

Benninger, L.M., and Koski, R.A., 1987, Descriptions and chemical analyses of sulfide samples dredged in 1986 from Escanaba Trough, Southern Gorda Ridge: U.S. Geological Survey Open-File Report 87-375-B, 18 p.

Bischoff, J.L, and Dickson, F.W., 1975, Seawater-basalt interaction at 200°C and 500 bars: Implications for origin of sea-floor heavy-metal deposits and the regulation of seawater chemistry: Earth and Planetary Science Letters, v. 25, p. 385–397.

Bischoff, J.L, Radtke, A.S., and Rosenbauer, R.J., 1981, Hydrothermal alteration of graywacke by brine and seawater: Roles of alteration and chloride complexing on metal solubilization at 200° and 350° C: Economic Geology, v. 76, p. 659–676.

Böhlke, J.K., and Shanks, W.C., III, Stable isotope study of hydrothermal vents at Escanaba Trough: Observed and calculated effects of sediment-seawater interaction, *in* Morton, J.L., Zierenberg, R.A., and Reiss, C.A., eds., Geologic, hydrothermal, and biologic studies at Escanaba Trough, Gorda Ridge, offshore northern California: U.S. Geological Survey Bulletin 2022, chapter 12 (this volume).

Borthwick, J., and Harmon, R.S., 1982, A note regarding ClF_3 as an alternative to BrF_5 for oxygen isotope analysis: Geochimica et Cosmochimica Acta, v. 46, p. 1665–1668.

Breit, G.N., Simmons, E.G., and Goldhaber, M.B., 1985, Dissolution of barite for the analysis of strontium isotopes and other chemical and isotopic variations using aqueous sodium carbonate: Chemical Geology, v. 52, p. 333–336.

Brett, R., Evans, H.T., Jr., Gibson, E.K., Jr., Hedenquist, J.W., Wandless, M.-V., and Sommer, M.A., 1987, Mineralogical studies of sulfide samples and volatile concentrations of basalt glasses from southern Juan de Fuca Ridge: Journal of Geophysical Research, v. 92, p. 11,373–11,379.

Campbell, A.C., German, C.R., Palmer, M.R., Gamo, T., and Edmond, J.M., Chemistry of hydrothermal fluids from the Escanaba Trough, Gorda Ridge, *in* Morton, J.L., Zierenberg, R.A., and Reiss, C.A., eds., Geologic, hydrothermal, and biologic studies at Escanaba Trough, Gorda Ridge, offshore northern California: U.S. Geological Survey Bulletin 2022, chapter 11 (this volume).

Canfield, D.E., Raiswell, R., Westrich, J.T., Reaves, C.M., and Berner, R.A., 1986, The use of chromium reduction in the analysis of reduced inorganic sulfur in sediments and shales: Chemical Geology, v. 54, p. 149–155.

Clague, D.A., and Holmes, M.L., 1987, Geology, petrology, and mineral potential of the Gorda Ridge, *in* Scholl, D.W., Grantz, A., and Vedder, J.G., eds., Geology and resource potential of the continental margin of western North America and adjacent ocean basins-Beaufort Sea to Baja California: Houston, Circum-Pacific Council for Energy and Mineral Resources Earth Science Series, v. 6, p. 563–580.

Davis, E.E., and Becker, Keir, Thermal and tectonic structure of the Escanaba Trough: New heat-flow measurements and seismic-reflection profiles, *in* Morton, J.L., Zierenberg, R.A., and Reiss, C.A., eds., Geologic, hydrothermal, and biologic studies at Escanaba Trough, Gorda Ridge, offshore northern California: U.S. Geological Survey Bulletin, chapter 3 (this volume).

Denlinger, R.P., and Holmes, M.L., A thermal and mechanical model for sediment hills and associated sulfide deposits along the Escanaba Trough, *in* Morton, J.L., Zierenberg, R.A., and Reiss, C.A., eds., Geologic, hydrothermal, and biologic studies at Escanaba Trough, Gorda Ridge, offshore northern California: U.S. Geological Survey Bulletin 2022, chapter 4 (this volume).

EEZ-SCAN 84 Scientific Staff, 1986, Atlas of the Exclusive Economic Zone, Western Conterminous United States: U.S. Geological Survey Miscellaneous Investigations Series Map I-1792, 152 p., scale 1:500,000.

Franklin, J.M., 1986, Volcanic-associated massive sulfide deposits-an update, *in* Andrew, C.J., Crowe, R.W.A., Finlay, S., Pennell, W.M., and Pyne, J.F., eds., Geology and genesis of mineral deposits in Ireland: Dublin, Irish Association for Economic Geology, p. 49–69.

Goodfellow, W.D., and Blaise, B., 1988, Sulfide formation and hydrothermal alteration of hemipelagic sediment in Middle Valley, northern Juan de Fuca Ridge: Canadian Mineralogist, v. 26, p. 675–696.

Hamilton, J.M., Delaney, G.D., Hauser, R.L., and Ransom, P.W., 1983, Geology of the Sullivan deposit, Kimberley, B.C., Canada, *in* Sangster, D.F., ed., Short course in sediment-hosted stratiform lead-zinc deposits: Mineralogical Association of Canada Short Course Handbook, v. 8, p. 31–83.

Hey, M.H., 1954, A new review of the chlorites: Mineralogical Magazine, v. 30, p. 277–292.

Holmes, M.L., and Zierenberg, R.A., 1990, Submersible operations in Escanaba Trough, southern Gorda Ridge, *in*

McMurray, G.R., ed., Gorda Ridge: A seafloor spreading center in the United States' Exclusive Economic Zone: New York, Springer-Verlag, p. 93–116.

Janecky, D.R., and Seyfried, W.E., Jr., 1984, Formation of massive sulfide deposits on oceanic ridge crests: Incremental reaction models for mixing between hydrothermal solutions and seawater: Geochimica et Cosmochimica Acta, v. 48, p. 2723–2738.

Janecky, D.R., and Shanks, W.C., III, 1989, Computational modeling of chemical and sulfur isotopic reaction processes in seafloor hydrothermal systems: Chimneys, massive sulfides, and subjacent alteration zones: Canadian Mineralogist, v. 26, p. 805–825.

Karlin, R., and Lyle, M., 1986, Sediment studies on the Gorda Ridge: Oregon Department of Geology and Mineral Industries Open-File Report O-86-19, 76 p.

Karlin, R.E., and Zierenberg, R.A., 1991, Sedimentation and neotectonism in the SESCA area, Escanaba Trough, southern Gorda Ridge, *in* Morton, J.L., Zierenberg, R.A., and Reiss, C.A., eds., Geologic, hydrothermal, and biologic studies at Escanaba Trough, Gorda Ridge, offshore northern California: U.S. Geological Survey Bulletin 2022, chapter 7 (this volume).

Kastner, M., 1982, Evidence for two distinct hydrothermal systems in the Guaymas Basin, *in* Curray, J.R., Moore, D.G., and others, eds., Initial reports of the Deep Sea Drilling Project: Washington, D.C., U.S. Government Printing Office, v. 64, pt. 2, p. 1143–1157.

Koski, R.A., Lonsdale, P.F., Shanks, W.C., Berndt, M.F., and Howe, S.S., 1985, Mineralogy and geochemistry of a sediment-hosted hydrothermal sulfide deposit from the Southern Trough of Guaymas Basin, Gulf of California: Journal of Geophysical Research, v. 90, p. 6695–6707.

Koski, R.A., Shanks, W.C., III, Bohrson, W.A., and Oscarson, R.L., 1988, The composition of massive sulfide deposits from the sediment-covered floor of Escanaba Trough, Gorda Ridge: Implications for depositional processes: Canadian Mineralogist, v. 26, p. 655–673.

Koski, R.A., Beninger, L.M., Zierenberg, R.A., and Jonasson, I.R., Composition and growth history of hydrothermal deposits in Escanaba Trough, southern Gorda Ridge, *in* Morton, J.L., Zierenberg, R.A., and Reiss, C.A., eds., Geologic, hydrothermal, and biologic studies at Escanaba Trough, Gorda Ridge, offshore northern California: U.S. Geological Survey Bulletin 2022, chapter 16 (this volume).

Lonsdale, P.F., Bischoff, J.L., Burns, V.M., Kastner, M., and Sweeney, R.E., 1980, A high temperature hydrothermal deposit on the seabed at a Gulf of California spreading center: Earth and Planetary Science Letters, v. 49, p. 8–20.

Lydon, J.W., and Galley, A., 1986, The chemical and mineralogic zonation of Mathiati alteration pipe, Cyprus and its genetic significance, *in* Gallagher, M.J., and others, eds., Metallogeny of basic and ultrabasic rocks: London, Institution of Mining and Metallurgy, p. 49–71.

McManus, D.A., and others, 1970, Site 35, *in* McManus, D.A., and others, eds., Initial reports of the Deep Sea Drilling Project: Washington, D.C., U.S. Government Printing Office, v. 5, p. 165–202.

Morton, J.L., Holmes, M.L., and Koski, R.A., 1987a, Volcanism and massive sulfide formation at a sedimented spreading center, Escanaba Trough, Gorda Ridge, northeast Pacific Ocean: Geophysical Research Letters, v. 14, p. 769–772.

Morton, J.L., Normark, W.R., Ross, S.L., Koski, R.A., Holmes, M.L., Shanks, W.C., III, Zierenberg, R.A., Lyle, M., and Benninger, L.M., 1987b, Preliminary report, cruises L1-86-NC and L2-86-NC, Escanaba Trough, Gorda Ridge: U.S. Geological Survey Open-File Report 87-375-A, 20 p.

Morton, J.L., Koski, R.A., Normark, W.R., and Ross, S.L., 1990, Distribution and composition of massive sulfide deposits at Escanaba Trough, southern Gorda Ridge, *in* McMurray, G.R., ed., Gorda Ridge: A Seafloor Spreading Center in the United States' Exclusive Economic Zone: New York, Springer-Verlag, p. 77–92.

Morton, J.L., and Fox, C.G., Structural setting and interaction of volcanism and sedimentation at Escanaba Trough: Geophysical results, *in* Morton, J.L., Zierenberg, R.A., and Reiss, C.A., eds., Geologic, hydrothermal, and biologic studies at Escanaba Trough, Gorda Ridge, offshore northern California: U.S. Geological Survey Bulletin 2022, chapter 2 (this volume).

Murowchick, J.B., and Barnes, H.L., 1986, Marcasite precipitation from hydrothermal solutions: Geochimica et Cosmochimica Acta, v. 50, p. 2615–2631.

Normark, W.R., Gutmacher, C.E., Zierenberg, R.A., Wong, F.L., and Rosenbauer, R.J., Sediment fill of Escanaba Trough, *in* Morton, J.L., Zierenberg, R.A., and Reiss, C.A., eds., Geologic, hydrothermal, and biologic studies at Escanaba Trough, Gorda Ridge, offshore northern California: U.S. Geological Survey Bulletin 2022, chapter 6 (this volume).

Peter, J.M., and Scott, S.D., 1988, Mineralogy, composition, and fluid-inclusion microthermometry of seafloor hydrothermal deposits in the southern trough of Guaymas Basin, Gulf of California: Canadian Mineralogist, v. 26, p. 567–587.

Rees, C.E., 1978, Sulphur isotopic measurements using SO_2 and SF_6: Geochimica et Cosmochimica Acta, v. 42, p. 383–390.

Rees, C.E., Jenkins, W.J., and Monster, J., 1978, The sulphur isotopic composition of ocean water sulfate: Geochimica et Cosmochimica Acta, v. 42, p. 377–382.

Richards, H.G., Cann, J.R., and Jensenius, J., 1989, Mineralogical zonation and metasomatism of the alteration pipes of Cyprus sulfide deposits: Economic Geology, v. 84, p. 91–115.

Riddihough, R.P., 1980, Gorda plate motions from magnetic anomaly analysis: Earth and Planetary Science Letters, v. 51, p. 163–170.

Riverin, G., and Hodgson, C.J., 1980, Wall-rock alteration at the Millenbach Cu-Zn mine, Noranda, Quebec: Economic Geology, v. 75, p. 424–444.

Roberts, R.G., and Reardon, E.J., 1978, Alteration and ore-forming processes at Mattagami Lake, Quebec: Canadian Journal of Earth Sciences, v. 15, p. 1–21.

Savin, S.M., and Lee, M., 1988, Isotopic studies of phyllosilicates, *in* Bailey, S.W., ed., Hydrous phyllosilicates (exclusive of micas): Mineralogical Society of America, Reviews in Mineralogy, v. 19, p. 189–223.

Schmidt, J.M., 1988, Mineral and whole-rock compositions of seawater-dominated hydrothermal alteration at the Arctic volcanogenic massive sulfide prospect, Alaska: Economic Geology, v. 83, p. 822–842.

Seyfried, W.E., Jr., and Bischoff, J.L., 1977, Hydrothermal transport of heavy metals by seawater: The role of seawater basalt

ratio: Earth and Planetary Science Letters, v. 34, p. 71–77.

Slack, J.F., and Coad, P.R., 1989, Multiple hydrothermal and metamorphic events in the Kidd Creek volcanogenic massive sulfide deposit, Timmins, Ontario: Evidence from tourmalinites and chlorites: Canadian Journal of Earth Sciences, v. 26, p. 694–715.

Styrt, M., Brackmann, A., Holland, H., Clark, B., Pisutha-Arnold, V., Eldridge, C., and Ohmoto, H., 1981, The mineralogy and the isotopic composition of sulfur in hydrothermal sulfide/sulfate deposits on the East Pacific Rise, 21°N latitude: Earth and Planetary Science Letters, v. 53, p. 328–390.

Thornton, E.C., and Seyfried, W.E., Jr., 1985, Sediment-seawater interaction at 200 and 300°C, 500 bars pressure: The role of sediment composition in diagenesis and low grade metamorphism of marine clay: Geological Society of America Bulletin, v. 96, p. 1287–1295.

Trefry, J.H., Mets, S., Feely, R.A., and Massoth, G.J., 1990, Role of hydrothermal precipitates in controlling concentrations and cycling of trace metals in seawater [abs.]: Eos, Transactions American Geophysical Union, v. 71, p. 1651–1652.

Urabe, T., Scott, S.D., and Hattori, K., 1983, A comparison of footwall-rock alteration and geothermal systems beneath Japanese and Canadian volcanogenic massive sulfide deposits: Economic Geology Monograph, v. 5, p. 345–365.

Vallier, T.L., Harold, P.J., and Girdley, W.A., 1973, Provenances and dispersal patterns of turbidite sand in Escanaba Trough, northeastern Pacific Ocean: Marine Geology, v. 15, p. 67–87.

Van Dover, C.L., Grassle, J.F., and Boudrias, M., 1990, Hydrothermal vent fauna of Escanaba Trough (Gorda Ridge), *in* McMurray, G.R., ed., Gorda Ridge: A seafloor spreading center in the United States' Exclusive Economic Zone: New York, Springer-Verlag, p. 285–287.

Von Damm, K.L., Edmond, J.M., Grant, B., Measures, C.I., Walden, B., and Weiss, R.F., 1985a, Chemistry of submarine hydrothermal solutions at 21°N, East Pacific Rise: Geochimica et Cosmochimica Acta, v. 49, p. 2197–2220.

Von Damm, K.L., Edmond, J.M., Measures, C.I., and Grant, B., 1985b, Chemistry of submarine hydrothermal solutions at Guaymas Basin, Gulf of California: Geochimica et Cosmochimica Acta, v. 49, p. 2221–2238.

Wenner, D.B., and Taylor, H.P., Jr., 1971, Temperatures of serpentinization of ultramafic rocks based on O^{18}/O^{16} fractionation between coexisting serpentine and magnetite: Contributions to Mineralogy and Petrology, v. 32, p. 165–185.

Yeh, H.W., and Savin, S.M., 1976, The extent of oxygen isotope exchange between clay minerals and seawater: Geochimica et Cosmochimica Acta, v. 42, p. 140–143.

Zierenberg, R.A., Shanks, W.C., III, and Bischoff, J.L., 1984, Massive sulfide deposits at 21°N, East Pacific Rise: Chemical composition, stable isotopes, and phase equilibria: Geological Society of America Bulletin, v. 95, p. 922–929.

Zierenberg, R.A., Shanks, W.C., III, Seyfried, W.E., Jr., Koski, R.A., and Strickler, M.D., 1988, Mineralization, alteration and sub-seafloor metamorphism of the ophiolite-hosted Turner-Albright sulfide deposit, southwestern Oregon: Journal of Geophysical Research, v. 93, p. 4657–4674.

Zierenberg, R.A., Morton, J.L., Koski, R.A., and Ross, S.L., Geologic setting of massive sulfide mineralization in the Escanaba Trough, *in* Morton, J.L., Zierenberg, R.A., and Reiss, C.A., eds., Geologic, hydrothermal, and biologic studies at Escanaba Trough, Gorda Ridge, offshore northern California: U.S. Geological Survey Bulletin 2022, chapter 10 (this volume).

Chapter 15. Hydrocarbons in Sediment from Escanaba Trough

By Keith A. Kvenvolden, John B. Rapp, *and* Frances D. Hostettler[1]

CONTENTS

ABSTRACT

Normal alkanes, isoprenoid hydrocarbons, triterpanes, and steranes are present in low concentrations in sediment that fills Escanaba Trough at the southern end of the Gorda Ridge spreading axis. Distributions of *n*-alkanes are generally dominated by odd-carbon-number molecules suggesting terrigenous sources. Epimer ratios of triterpanes and steranes have a wide range of maturity values, with Pleistocene sediment having lower maturity values than Holocene sediment. Hydrothermal activity in Escanaba Trough has altered the distribution of hydrocarbons in the sediment and has led to the generation of petroleum that is found in sediment-hosted metallic sulfide deposits.

INTRODUCTION

Gorda Ridge is an active oceanic spreading axis located about 200 to 300 km offshore from southern Oregon and northern California (fig. 15.1). The southernmost segment of this ridge, Escanaba Trough, is partly filled with Quaternary turbidite sediment. The trough is the site of hydrothermal activity as first indicated by the discovery of various hydrothermal mineral deposits (Clague and others, 1984), including massive metallic sulfide samples (Morton and others, 1987a; Koski and others, 1988). Active hydrothermal vents were discovered in the trough in 1988 (Campbell and others, 1988; Zierenberg and others, 1988). One result of the hydrothermal activity within the sediment of the trough is the formation of petroleum, first discovered in 1985 (Kvenvolden and others, 1986). The hydrocarbon geochemistry of four examples of hydrothermally derived petroleum has been described by Kvenvolden and others (1987). The most likely source for this petroleum is the organic material in the sediment of the trough. This report examines a portion of this organic material, namely, the alkanes that were extracted from sediment recovered by gravity coring during R/V *S.P. Lee* cruises L1-86-NC and L2-86-NC. This is the second report to describe the hydrocarbons in sediment of Escanaba Trough; the first report (Simoneit, 1977) presented limited information on hydrocarbons from DSDP Site 35 (fig. 15.1). Other studies have been made previously of hydrocarbons in sediments of Guaymas Basin, an active spreading axis in the Gulf of California (Simoneit and others, 1979, 1984; Kawka and Simoneit, 1987; Bazylinski and others, 1988).

ACKNOWLEDGMENTS

We thank R.A. Koski and B.R.T. Simoneit for very helpful reviews, B.V. Fulop and P.A. Swenson for drafting the figures, and J.S. Gibbs for typing the manuscript. We particularly appreciate the comments of R.A. Zierenberg, who brought new insight into the interpretation of our results.

GEOLOGIC SETTING

For the purpose of geologic mapping, two areas of Escanaba Trough have been described by Morton and others (1987b) and Koski and others (1988). These areas are called SESCA and NESCA (fig. 15.1). In the

[1] U.S. Geological Survey, Menlo Park, California.

southern area (SESCA), sulfide deposits are spatially related to three steep-sided, sediment-capped blocks that rise above the axial valley floor. Massive sulfide deposits are concentrated on the flanks of the hills. The northern area (NESCA) is dominated by two hills, one capped by sediment and the other by sediment and lava flows. Massive sulfide deposits also occur on the flanks of these hills. The SESCA and NESCA areas overlie volcanic edifices that penetrate and locally breach the sediment. A third volcanic edifice underlies sediment between the SESCA and NESCA areas; one sampling site was located there.

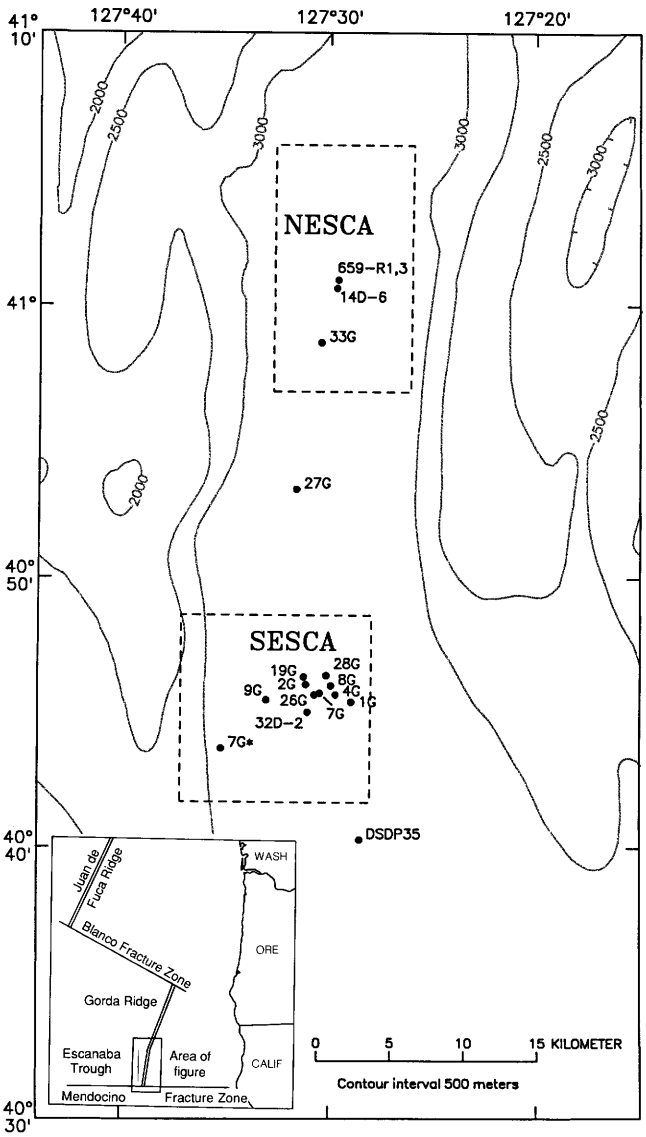

Figure 15.1. Locations of samples recovered by gravity coring (G), dredge (D), and submersible (R), in SESCA and NESCA survey areas of Escanaba Trough. Deep Sea Drilling Project (DSDP) Site 35 is located south of SESCA. Hachures indicate area of closed low.

METHODS

Sediment samples for geochemical studies were collected from sediment cores that were obtained by gravity coring using a barrel 3 m long and 9 cm in diameter with a 500-kg weight stand (Morton and others, 1987b). Sediment core subsamples, 8 cm long, were placed into precleaned glass jars and immediately frozen. Organic carbon (OC) was determined on a small portion of each sample by wet combustion following the procedure of Bush (1970).

The procedures for extraction and analysis of hydrocarbons were adapted from Kvenvolden and others (1985). A 100-g portion of dried, pulverized (< 32 mesh) sediment was triple extracted with dichloromethane by shaking on a wrist-action shaker. The combined filtered extracts were concentrated by rotary evaporation. Sulfur, if present, was removed by filtration through activated copper. A portion of the filtrate was removed for the determination of the weight of extract (EOM = extractable organic material). The dichloromethane solvent was then exchanged with *n*-hexane in preparation for chromatography.

The extracts in *n*-hexane were fractionated by liquid-solid chromatography using a column packed with activated silica gel and deactivated alumina. The column was sequentially eluted with *n*-hexane, benzene, and methanol to yield three fractions containing aliphatic hydrocarbons, medium-polarity organic compounds (including aromatic hydrocarbons), and polar organic compounds, respectively. Portions of each fraction were removed for weight determinations. For four samples, the elution sequence was modified, and six fractions were obtained: *n*-hexane; 20, 40, 60 percent benzene in *n*-hexane; benzene; and methanol. Only the *n*-hexane fractions (aliphatic hydrocarbons) are considered in detail in this paper. The aliphatic hydrocarbons were analyzed by capillary gas chromatography for distributions of *n*-alkanes and isoprenoid hydrocarbons, and by gas chromatography/mass spectrometry. Single-ion monitoring of mass-to-charge ratio (m/z) 191 and 217 produced mass chromatograms from which triterpanes and steranes, respectively, were identified and compared. Ratios of various organic compounds were determined from peak heights on gas chromatograms and mass chromatograms.

SAMPLES

Sediment samples came from nine core sites in SESCA, one core site to the west of SESCA, one core site from NESCA, and one core site between SESCA and NESCA. The cores are described in table 15.1. The nine cores from SESCA and one core west of SESCA consist predominantly of gray-green mud with occasional sandy turbidite layers (Normark and others, chap. 6, this volume).

Table 15.1. Descriptions of Escanaba Trough sediment cores from which samples were taken for organic geochemical analyses.

Sample	Location		Length of core (cm)	Description (Morton and others, 1987b)
	Latitude N.	Longitude W.		
L1-86-1G ----------	40°45.55′	127°28.93′	273	Gray-green, slightly porous mud with two distinct gray layers.
L1-86-7G ----------	40°45.84′	127°30.48′	233	Gray-green mud with thin brown and gray layers and gray silty turbidite beds at base.
L1-86-8G ----------	40°46.11′	127°29.93′	197	Gray-green mud overlying thick gray silty-sand turbidite beds. Minor amounts of pyrrhotite and resedimented hydrothermally altered sediment (Zierenberg and Shanks, this volume).
L1-86-19G---------	40°46.44′	127°31.24′	255	Gray-green mud.
L1-86-26G---------	40°45.78′	127°30.73′	239	Gray-green mud with gray sandy turbidite beds and disrupted gray mud intervals in upper 100 m of core.
L1-86-27G---------	40°53.35′	127°31.65′	105	Blotchy gray-green mud (0–42 cm); gray mud and silt with sandy blebs (42–72 cm); gray sand with massive sulfide layers (72–105 cm).
L1-86-33G---------	40°58.73′	127°30.46′	124	Partly indurated smooth gray mud with black streaks, basalt glass chips, and a few silty blebs.
L2-86-2G ----------	40°46.16′	127°31.14′	96	Gray-green mud with discontinuous brown mud layers in upper part and silty sand layer with black fragments at base.
L2-86-4G ----------	40°45.79′	127°69.70′	263	Gray-green mud.
L2-86-7G ----------	40°43.79′	127°35.20′	241	Gray-green mud with thin discontinuous silty inner beds at base.
L2-86-9G ----------	40°45.59′	127°33.05′	200	Red-brown metalliferous mud; zone of massive sulfide nodules and sand-size sediment; blue-gray chloritized mud with white (talc?) nodules.
L2-86-28G---------	40°46.49′	127°30.17′	244	Gray-green mud with gray fine-sand turbidite bed near top.

An exception is the sample from core L2-86-9G. This sample is composed of blue-gray chloritized mud. In addition to the cores, a dredge sample L1-86-32D-2 from SESCA contains fine-grained sandstone intermixed with metallic sulfide minerals and asphaltic petroleum. The geochemistry of this petroleum is described elsewhere (Kvenvolden and others, 1986, 1987).

Gravity core L1-86-27G, recovered between SESCA and NESCA, was more heterogeneous in composition compared to the majority of cores from SESCA. The analyzed sample from the 87 to 95 cm depth interval is a gray, fine-grained sand containing layers of fine-grained massive sulfide minerals. The sample obtained from NESCA (core L1-86-33G) is composed mainly of partly indurated gray mud. In addition to this core sample, a sample recovered by dredging (L2-86-14D-6) and two samples recovered by submersible (659-R1 and 659-R3) from NESCA were shown to contain hydrothermal petroleum, and the hydrocarbon chemistry of these samples has been discussed previously by Kvenvolden and others (1987).

RESULTS

Geochemical results for 18 sediment samples (summarized in table 15.2) include measurements of organic carbon (OC), extractable organic material (EOM), and the weights of the hexane fractions from liquid chromatography. The distributions of *n*-alkanes, isoprenoid hydrocarbons, triterpanes, and steranes are summarized by means of various ratios that will be defined as they are discussed in the text. The OC content of these samples is low, ranging from 0.13 to 0.72 percent. EOM concentrations in our samples range from 2 to 90 mg/g, and aliphatic hydrocarbons in the hexane fraction are less than 15 mg/g.

NORMAL ALKANES AND ISOPRENOID HYDROCARBONS

The chromatographic distributions of *n*-alkanes and isoprenoid hydrocarbons for six samples (shown in fig. 15.2) were selected to demonstrate the variety of compound distributions that are present in sediment of Escanaba Trough. Typically the *n*-alkanes range from about $n\text{-}C_{12}$ to as high as $n\text{-}C_{40}$. In seven samples [L1-86-19G (90–100), L1-86-19G (237–245), L1-86-26G (82–90), L1-86-26G (221–229), L1-86-33G (106–114), L2-86-7G (133–141), L2-86-28G (136–144)], the *n*-alkane distributions are bimodal, having maxima in two regions, one centered at $n\text{-}C_{16}$ or $n\text{-}C_{17}$ and the other at $n\text{-}C_{27}$ or $n\text{-}C_{29}$. The bimodal distributions of *n*-alkanes observed in samples L1-86-26G (82–90) and L1-86-33G (106–114) are shown in figure 15.2*C*,*E*. The *n*-alkanes in the region of $n\text{-}C_{29}$ have a distinct odd-carbon-number dominance, whereas in the region of $n\text{-}C_{16}$ the *n*-alkane distributions have neither odd- nor even-carbon-number dominance. The *n*-alkane distributions in seven samples [L1-86-1G (82–90), L1-86-1G (182–190), L1-86-1G (255–263), L1-86-7G (82–90), L1-86-7G (215–237), L2-86-2G (78–86), L2-86-4G (145–153)] have a prominent mode usually centered at $n\text{-}C_{29}$, as illustrated for sample L1-86-7G (82–90) in figure 15.2*A*.

Table 15.2. Organic geochemical data for sediment core samples and one oil from Escanaba Trough.

[Age: H, Holocene; P, Pleistocene; QA, Quaternary Altered. n.d., not determined]

Sample	Interval (cm)	Age	OC (pct.)	EOM (μg/g)	Hexane fraction (μg/g)	*n*-Alkanes CPI	Iso-prenoids Pr/Ph	Triterpanes					Steranes	
								$C_{31}\frac{S}{S+R}$	$C_{30}\frac{\alpha\beta}{\beta\beta}$	$C_{30}\frac{\beta\alpha}{\alpha\beta}$	$C_{27}\frac{Tm}{Ts}$	$\alpha\beta\frac{C_{30}}{C_{29}}$	$C_{29}\frac{S}{S+R}$	$\frac{C_{29}\alpha(R)}{C_{27}\alpha(R)}$
L1-86-1G	82–90	H	0.53	44	6	1.8	3.0	0.52	6.5	0.19	2.0	2.0	0.26	1.0
	182–190	P	.46	25	3	4.7	3.0	.30	6.4	.28	3.7	2.1	.12	1.9
	255–263	P	.43	34	3	4.9	2.7	.29	7.0	.23	2.7	2.1	.13	1.4
L1-86-7G	82–90	P	.52	15	2	4.6	3.2	.23	3.2	.31	3.5	1.8	.13	1.7
	215–223	P	.43	15	2	5.1	3.2	.27	4.0	.29	3.0	1.9	.13	1.6
L1-86-8G	82–90	QA	.31	58	10	1.0	.8	.25	7.3	.75	8.7	.9	.05	1.1
	179–187	QA	.36	82	13	.9	.7	.24	9.0	.71	7.8	.9	.06	1.1
L1-86-19G	90–100	H	.51	40	6	2.0	3.0	.50	4.7	.22	2.1	2.0	.24	1.0
	237–245	P	.45	15	3	4.7	2.6	.30	6.1	.27	3.4	1.8	.14	1.4
L1-86-26G	82–90	H	.72	29	3	2.0	2.9	.51	5.3	.21	2.3	1.8	.24	.8
	221–229	P	.60	26	2	4.0	2.9	.27	4.0	.27	4.5	1.8	.14	1.3
L1-86-27G	87–95	QA	.13	21	1	1.1	1.9	.40	n.d.	.74	6.5	1.0	.12	1.0
L1-86-33G	106–114	P	.57	90	5	3.7	3.5	.33	5.0	.40	3.0	1.6	.18	1.6
L2-86-2G	78–86	P	.44	34	3	3.2	3.4	.30	6.1	.31	3.4	1.5	.24	1.8
L2-86-4G	145–153	P	.53	27	2	4.6	2.6	.27	12.3	.38	2.8	1.7	.19	1.6
L2-86-7G	133–141	H	.43	34	3	3.2	2.7	.40	6.5	.27	2.7	1.4	.22	1.0
L2-86-9G	132–140	QA	.36	2	n.d.	n.d.	1.6	n.d.	n.d.	n.d.	n.d.	n.d.	n.d.	n.d.
L2-86-28G	136–144	P	.54	26	3	5.0	2.8	.24	5.2	.44	4.2	1.5	.12	2.6
L6-85-32D-2	Surface dredge		5.6	55,000	1,000	1.2	1.7	.47	n.d.	.66	21	.73	.24	.82

In contrast, the *n*-alkane distributions in samples L1-86-27G (87–95) and L2-86-9G (132–140) have a maximum at *n*-C_{16} and *n*-C_{15}, respectively, and no odd/even-carbon-number dominance (fig.15.2*D*,*F*). Samples L1-86-8G (82–90) and L1-86-8G (179–187) are unusual in that the *n*-alkanes have a distinct even-carbon-number dominance in the region from *n*-C_{18} to *n*-C_{28} with a maximum at *n*-C_{24}, as shown for sample L1-86-8G (82–90) in figure 15.2*B*.

Distributions of *n*-alkanes can be partially described by the carbon preference index (CPI), which is a measure of the distribution of odd-carbon-number *n*-alkanes relative to even-carbon-number *n*-alkanes, calculated over the range *n*-C_{24} to *n*-C_{34} following the method of Cooper and Bray (1963). With the exception of two samples from station L1-86-8G, all samples from the SESCA area (fig. 15.1) have high CPI values (1.8 to 5.1), indicating a dominance

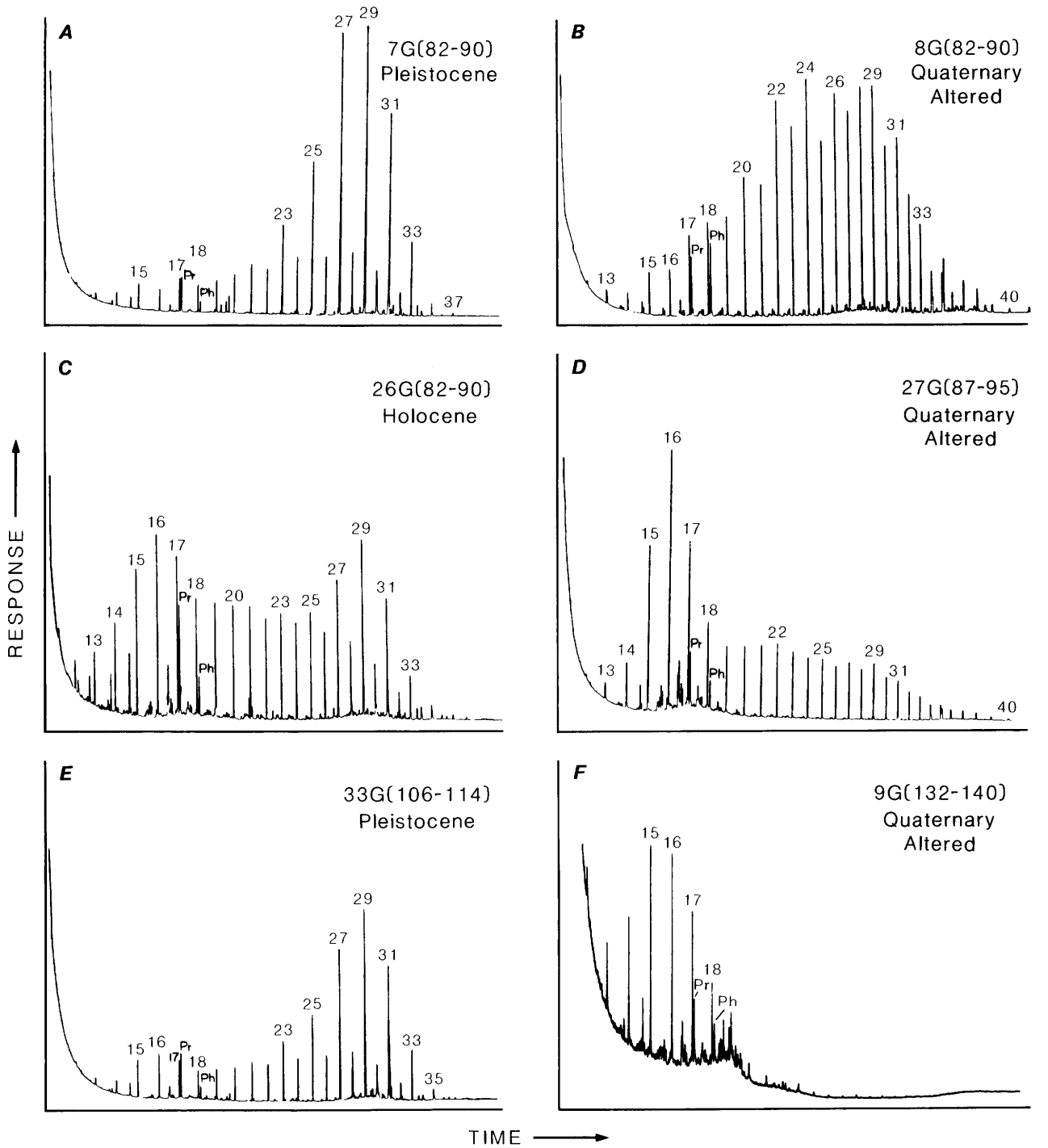

Figure 15.2. Representative gas chromatograms showing distributions of *n*-alkanes, pristane (Pr) and phytane (Ph) in extracts from six sediment core samples from Escanaba Trough. Numbers specify carbon numbers of *n*-alkanes.

of odd-carbon-number *n*-alkanes of high molecular weight (table 15.2). CPI values for samples L1-86-8G (82–90) and L1-86-8G (179–187) are low (0.9 and 1.0, respectively), reflecting the averaging influence of the dominant even-carbon-numbered *n*-alkanes in the lower part of the CPI range and the dominant odd-carbon-numbered *n*-alkanes in the upper part of the CPI range. A CPI value could not be determined for sample L2-86-9G (132–140) because of the very low concentrations of high molecular weight *n*-alkanes. Sample L1-86-27G (87–95) from the area between SESCA and NESCA, has a low CPI value of 1.1, reflecting a slight odd-carbon-number dominance; in contrast, the one sample L1-86-33G (106–114) from NESCA has a CPI value of 3.7, reflecting a significant odd-carbon-number dominance.

The two major isoprenoid hydrocarbons in sediment from Escanaba Trough are pristane and phytane, which are identified in figure 15.2 for six samples. In all samples, except L1-86-8G (82–90) and L1-86-8G (179–187), pristane is more abundant than phytane as reflected in the Pr/Ph ratios greater than one (table 15.2).

TRITERPANES AND STERANES

The aliphatic hydrocarbons in sediment from Escanaba Trough contain a wide range of pentacyclic triterpanes. Only in sample L2-86-9G (132–140) were these kinds of compounds not found. Distributions of triterpanes are shown by mass chromatograms (m/z 191) in figure 15.3 for five samples. Compounds are identified in table 15.3. Typically, the samples contain the 17α(H),21β(H)-hopane series, and 17β(H),21α(H)-hopane (moretane) series. With the exception of samples L1-86-27G (87–95) and L2-86-9G (132–140), all the samples contain the 17β(H),21β(H)-hopane series. Both 22R and 22S epimers of the 17α(H),21β(H)-homohopanes are present, and the 22R epimer is usually more abundant than its corresponding 22S epimer.

Steranes as well as diasteranes were found in all samples, except L2-86-9G (132–140), and typical mass chromatograms (m/z 217) are shown in figure 15.4. Compounds are identified in table 15.3. The sediment samples contain both 20R and 20S epimers of the C_{27}-, C_{28}-, and C_{29}-5α(H),14α(H),17α(H)-cholestane series. In addition, the 20R and 20S epimers of 13β(H),17α(H)-diacholestane are present.

Distributions of triterpanes and steranes are summarized through various ratios in table 15.2. Only in sample L2-86-9G (132–140) were these compounds not detected, and, therefore, ratios were not determined. C_{31} S/(S+R) is the ratio of the 22S and 22R epimers of 17α(H),21β(H)-homohopane. Only the 22R epimer is expected in immature mixtures. With increasing maturity, the preference for 22R is lost in favor of about a 60:40 mixture of 22S and 22R epimers, or an S/(S+R) ratio of 0.6 (Ensminger and others, 1974). In our sediment samples, this ratio varies widely from 0.23 to 0.52, indicating a range of maturities. C_{30} αβ/ββ is the ratio of 17α(H), 21β(H)-hopane, the most stable C_{30} hopane, to 17β(H),21β(H)-hopane, the least stable C_{30} hopane that is found in natural (biological) products (Ourisson and others, 1984). In sediments from Escanaba Trough, the αβ-hopane is consistently more abundant than the ββ-hopane (ratios range from 3.2 to 12.3). In sample L1-86-27G (87–95), ββ-hopanes are not present. C_{30} βα/αβ is the ratio of the 17β(H),21α(H)-hopane (moretane) to the 17α(H),21β(H)-hopane. Moretanes are intermediates in the maturity scheme between unstable, natural (biological) product precursor ββ-hopanes and the stable αβ-hopanes (Philp, 1985). The highest values of this ratio are found in samples from core

Table 15.3. Identification of triterpanes and steranes.

Peak	Compound	Carbon number
	Triterpanes (m/z 191)	
1	18α(H)-22,29,30-trisnorneohopane (Ts)	C_{27}
2	17α(H)-22,29,30-trisnorhopane (Tm)	C_{27}
3	17β(H)-22,29,30-trisnorhopane	C_{27}
4	17α(H),21β(H)-30-norhopane	C_{29}
5	17β(H),21α(H)-30-normoretane	C_{29}
6	17α(H),21β(H)-hopane	C_{30}
7	17β(H),21β(H)-norhopane + ?	C_{29}
8	17β(H),21α(H)-moretane	C_{30}
9	17α(H),21β(H)-homohopane(22S) and (22R)	C_{31}
10	17β(H),21β(H)-hopane	C_{30}
11	17β(H),21α(H)-homomoretane	C_{31}
12	17α(H),21β(H)-bishomohopane(22S) and (22R)	C_{32}
13	17β(H),21α(H)-bishomomoretane(22S) and (22R)	C_{32}
14	17β(H),21β(H)-homohopane	C_{31}
15	17α(H),21β(H)-trishomohopane(22S) and (22R)	C_{33}
16	17β(H),21α(H)-trishomomoretane(22S) and (22R)	C_{33}
17	17β(H),21β(H)-bishomohopane	C_{32}
18	17α(H),21β(H)-tetrakishomohopane(22S) and (22R)	C_{34}
19	17β(H),21α(H)-tetrakishomomoretane(22S) and (22R)	C_{34}
20	17β(H),21β(H)-trishomohopane	C_{33}
21	17α(H),21β(H)-pentakishomohopane(22S) and (22R)	C_{35}
22	17β(H),21α(H)-pentakishomomoretane(22S) and (22R)	C_{35}
23	17β(H),21β(H)-tetrakishomohopane	C_{34}
24	17β(H),21β(H)-pentakishomohopane	C_{35}
	Steranes and diasteranes (m/z 217)	
A	13β(H),17α(H)-diacholestane(20S)	C_{27}
B	13β(H),17α(H)-diacholestane(20R)	C_{27}
C	5α(H),14α(H),17α(H)-cholestane(20S)	C_{27}
D	5α(H),14α(H),17α(H)-cholestane(20R)	C_{27}
E	24-methyl-5α(H),14α(H),17α(H)-cholestane(20S) + ?	C_{28}
F	24-methyl-5α(H),14α(H),17α(H)-cholestane(20R)	C_{28}
G	24-ethyl-5α(H),14α(H),17α(H)-cholestane(20S)	C_{29}
H	24-ethyl-5α(H),14β(H),17β(H)-cholestane(20R)	C_{29}
I	24-ethyl-5α(H),14α(H),17α(H)-cholestane(20R)	C_{29}

L1-86-8G where the ratios are 0.75 and 0.71, and in sample L1-86-27G (87–95) where the ratio is 0.74. In the other samples this ratio ranges from 0.19 to 0.66. C_{27} Tm/Ts is the ratio of 17α(H)-22,29,30-trisnorhopane to 18α(H)-22,29,30-trisnorneohopane, described originally by Seifert and Moldowan (1978) as a source and maturity index. In our sediment samples this ratio ranges from 2.0 to 8.7. Finally, αβ C_{30}/C_{29} is the ratio of 17α(H),21β(H)-hopane to

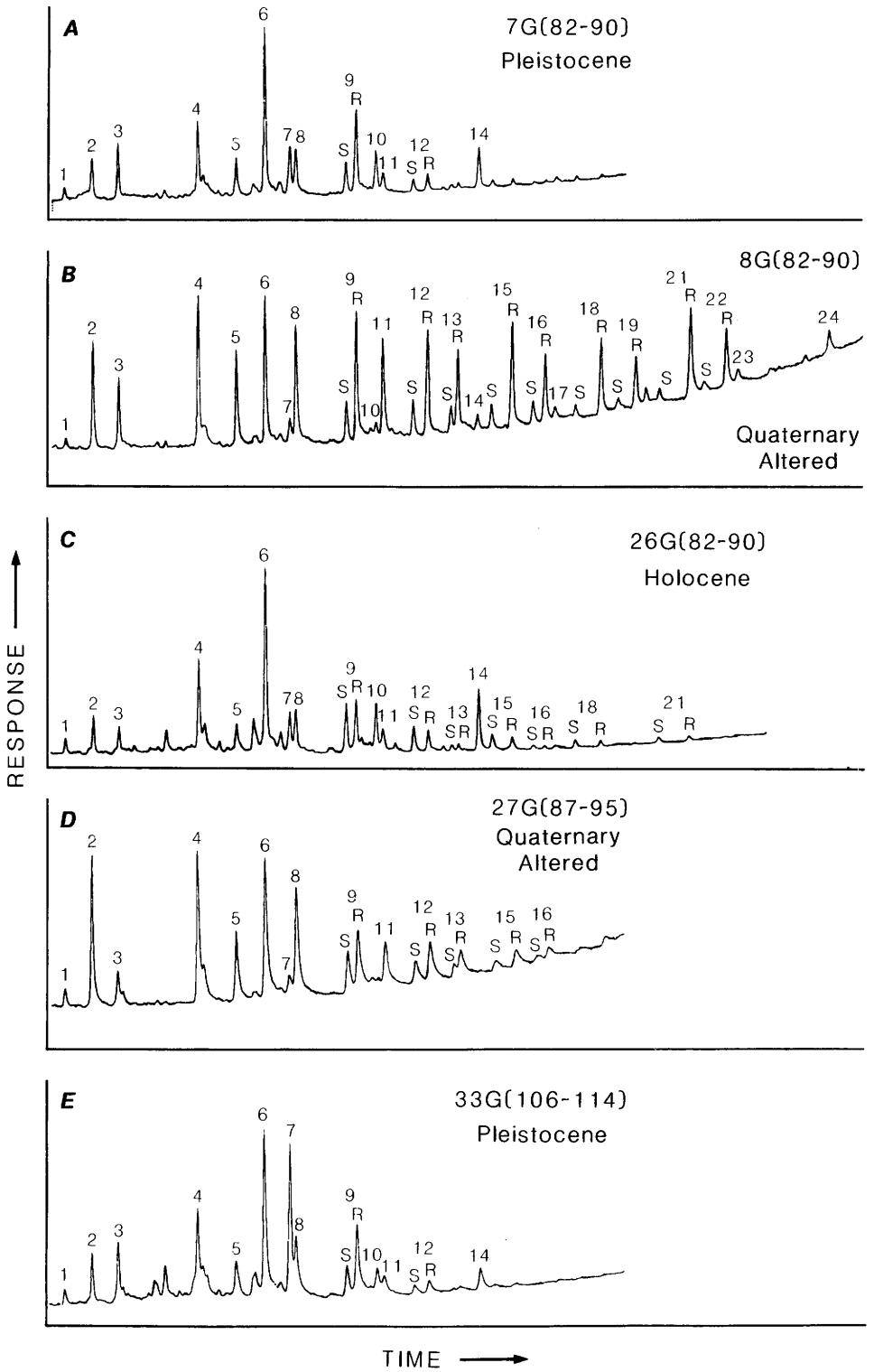

Figure 15.3. Representative mass chromatograms (m/z 191) showing distribution of triterpanes in extracts from five sediment core samples from Escanaba Trough. Identifications are listed in table 15.3.

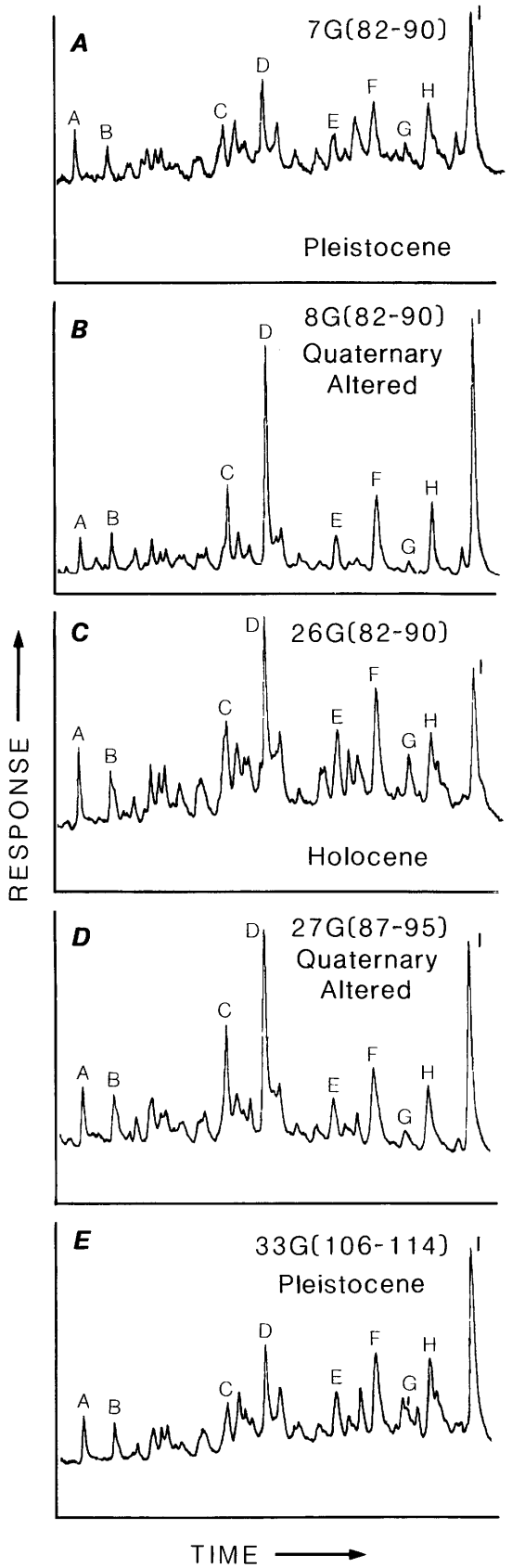

17α(H),21β(H)-30-norhopane. This ratio has been used for source-rock correlations (Palacas and others, 1984). In our sediment samples from Escanaba Trough, this ratio does not vary greatly and ranges between 0.9 and 2.1. Only samples from core L1-86-8G have ratios less than 1.0.

Two ratios are used to show sterane distributions in sediments from Escanaba Trough (table 15.2). C_{29} S/(S+R) is the ratio of the 20S to 20R epimers of 24-ethyl-5α(H),14α(H),17α(H)-cholestane. During maturation the biologically derived 20R epimer is converted to nearly equal mixtures of 20R and 20S (Mackenzie and others, 1980). In our sediment samples, these ratios are significantly below the equilibrium value of 0.5 and range from 0.12 to 0.26, except samples from core L1-86-8G, which have very low values of 0.05 and 0.06. A second sterane ratio is $C_{29}\alpha(R)/C_{27}\alpha(R)$, which is the ratio of the 20R epimer of 24-ethyl-5α(H),14α(H),17α(H)-cholestane to the 20R epimer of 5α(H),14α(H),17α(H)-cholestane. The ratio of the C_{29} to C_{27} steranes has been used as a source indicator (Huang and Meinschein, 1979) with C_{29} steranes attributed to terrigenous sources and C_{27} steranes to marine sources; however, Volkman (1986) has shown limitations to the application of this ratio as a source indicator. In our sediment samples, this ratio ranges from 0.8 to 2.6 with most values greater than 1.0.

DISCUSSION

The distribution of various classes of aliphatic hydrocarbons in sediment of Escanaba Trough can be interpreted relative to the histories of sedimentation and processes of hydrothermal alteration.

PLEISTOCENE AND HOLOCENE SEDIMENTS

The sedimentary geology and detailed lithologic descriptions are discussed by Normark and others (chap. 6, this volume). A lithologic transition is recognizable in many Escanaba Trough sediment cores. Coarse-grained siliceous surficial sediment with high water content and low magnetic susceptibility is underlain by calcareous sediment that is fine grained with lower water content and higher magnetic susceptibility. Karlin and Lyle (1986) correlate this lithologic change with a transition from a glacial to interglacial climate at approximately 11 ka, the Pleistocene-Holocene boundary. Chemical variations

⇐

Figure 15.4. Representative mass chromatograms (m/z 217) showing distribution of steranes in extracts from five sediment core samples from Escanaba Trough. Identifications listed in table 15.3.

across this boundary likely reflect decreased terrigenous input and increased siliceous biogenic input in the Holocene due to decreased continental weathering and enhanced coastal upwelling (Karlin and Lyle, 1986). Holocene sediment in Escanaba Trough includes turbiditic silt and sand, some of which has local sources, but also includes sediment derived from the Astoria submarine fan (Karlin and Lyle, 1986; Karlin and Zierenberg, chap. 7, this volume; Normark and others, chap. 6, this volume). Magnetic susceptibility profiles of the core samples for this study (Karlin and Zierenberg, chap. 7, this volume) provide a basis for assigning our samples a probable age of Pleistocene (10 samples) and Holocene (4 samples). Core descriptions are given in table 15.1.

The Pleistocene and Holocene samples can be differentiated on the basis of distributional relationships among aliphatic hydrocarbons reflected in the average values of the following molecular ratios (table 15.4): CPI, C_{31} S/(S+R), C_{30} $\beta\alpha/\alpha\beta$, C_{27} Tm/Ts, C_{29} S/(S+R), and $C_{29}\alpha$(R)/$C_{27}\alpha$(R). Other average ratios in table 15.4, that is, Pr/Ph, C_{30} $\alpha\beta/\beta\beta$, and $\alpha\beta$ C_{30}/C_{29}, are not significantly different in the Pleistocene and Holocene samples.

The high molecular weight *n*-alkanes (*n*-C_{24} to *n*-C_{34}) in the Pleistocene sediment samples have a greater odd-carbon-number dominance than do the Holocene samples, as shown by a comparison of average CPI values (table 15.4). This dominance of odd-carbon-number *n*-alkanes represents contributions to the sediment from terrigenous plant waxes (Eglinton and others, 1962). Our results suggest that more terrigenous plant material entered the sediment during Pleistocene time (CPI = 4.5) than during Holocene time (CPI = 2.3). This interpretation correlates with that of Karlin and Lyle (1986) based on lithological and chemical considerations. The apparent decrease in terrigenous input to sediment from Pleistocene to Holocene times is also reflected in the values of the $C_{29}\alpha$(R)/$C_{27}\alpha$(R) ratios, which average 1.7 in our Pleistocene samples and 1.0 in our Holocene samples. If the arguments of Huang and Meinschein (1979) are valid, then our interpretations of the sterane and *n*-alkane ratios are mutually supportive.

Microscopic examination of a Pleistocene and a Holocene sediment sample (table 15.5) shows that the bulk organic matter in both samples has a large terrigenous component, including woody and coaly fragments, pollen, and spores, but the Holocene sample has a significant content of marine diatoms and radiolarians. Our observations generally agree with those of McManus and others (1970), Moore (1970), and Vallier and others (1973), who concluded that sediment of Escanaba Trough contains terrigenous organic debris derived in part from the drainage of the Klamath and Columbia rivers. Besides *n*-alkanes of terrigenous origin (>*n*-C_{24}), both Pleistocene and Holocene samples contain *n*-alkanes in the molecular region of *n*-C_{16} (see fig. 15.2*A*, *C*, *E*); these compounds likely originate in marine sources (Simoneit, 1978).

Although the CPI values for *n*-alkanes in Pleistocene and Holocene sediments are consistent with the idea of more terrigenous input during the Pleistocene than in the Holocene, these values can also be interpreted relative to maturity. In the maturation process, CPI values tend to decrease as the odd-carbon-number dominance of *n*-alkanes gives way to mixtures in which odd- and even-carbon-number *n*-alkanes become more equal in abundance (Bray and Evans, 1961). In the case of our samples, organic matter in Holocene sediment (average CPI value of 2.3) would be considered to be more mature than the organic matter in Pleistocene sediment (average CPI value of 4.5). This observation is consistent with the results observed for terpane and sterane maturity parameters.

The average values of the terpane and sterane maturity parameters, C_{31} S/(S+R), C_{30} $\beta\alpha/\alpha\beta$, C_{27} Tm/Ts, and C_{29} S/(S+R), clearly differentiate Pleistocene from Holocene sediment; however, the values of the C_{30} $\alpha\beta/\beta\beta$ ratio are similar. On the other hand, these sediments cannot be differentiated on the basis of the more source-related parameters, Pr/Ph and $\alpha\beta$ C_{30}/C_{29}, suggesting that the Pleistocene and Holocene sediments come from a similar provenance. The values of most of the maturity ratios indicate, however, that the organic matter in the Holocene samples is more mature than that in the Pleistocene samples, a relationship that is contrary to what is expected in a normal sedimentary sequence, where older sediments should contain more mature components.

The anomalous maturity measurements for sediments of Escanaba Trough suggest that the process of sedimentation involved a complex history, the details of which are obscure. One scenario is presented here as a working hypothesis (W.R. Normark, oral commun., 1989). One component of sedimentation in Escanaba Trough comes from the mass wasting of older sediments on the flanks of the trough. The rate of input of this material is more or less constant with time, unaffected by sea-level changes or rates of erosion on the continent. During the Pleistocene, high rates of continental erosion contributed large volumes of younger sediment to the trough, which diluted the older sediment entering the trough by mass wasting. During the Holocene, continental erosion diminished with rising sea level so that the trough received less of the younger, eroded sediment but continued to receive the older sediment from the mass wasting process. Because of these dilution effects, the results are higher organic maturity values in Holocene sediment and lower organic maturity values in Pleistocene sediment. Much of the sediment involved in mass-wasting was originally derived from erosion of the continent. Thus the terrigenous components of both old and young sediment is continental, and this common source accounts for the similarity in values of organic source-

Table 15.4. Average values of molecular ratios in sediments and an oil from Escanaba Trough.

[n.d., not determined]

	Pleistocene	Holocene	Quaternary altered	Oil
CPI	4.5 ± 0.6	2.3 ± 0.6	1.0 ± 0.1	1.2
Pr/Ph	3.0 ± 0.3	2.9 ± 0.1	1.3 ± 0.6	1.7
C_{31} S/(S+R)	.28 ± 0.03	.48 ± 0.06	.30 ± 0.09	.47
C_{30} αβ/ββ	5.9 ± 2.5	5.8 ± 0.9	8.2 ± 1.2	n.d.
C_{30} βα/αβ	.32 ± 0.07	.22 ± 0.03	.73 ± 0.02	.66
C_{27} Tm/Ts	3.4 ± 0.6	2.3 ± 0.3	7.7 ± 1.1	21
αβ C_{30}/C_{29}	1.8 ± 0.2	1.8 ± 0.3	.93 ± 0.06	.73
C_{29} S/(S+R)	.15 ± 0.04	.24 ± 0.02	.08 ± 0.04	.24
C_{29}α(R)/C_{27}α(R)	1.7 ± 0.4	1.0 ± 0.1	1.1 ± 0.1	.82

related parameters in both the Pleistocene and Holocene sediments of Escanaba Trough.

ALTERED QUATERNARY SEDIMENTS

Four samples from three cores (table 15.2) have been altered lithologically by hydrothermal processes associated with deposition of base-metal sulfide minerals. These altered cores could not be assigned a Pleistocene or Holocene age because of sediment disruptions; the cores are indicated as "Quaternary altered" in table 15.2. Sediment from cores L1-86-8G contains minor amounts of pyrrhotite and is interpreted to be a locally derived mass-flow deposit that includes resedimented hydrothermally altered sediment (Zierenberg and Shanks, chap. 14, this volume; Karlin and Zierenberg, chap. 7, this volume; Normark and others, chap. 6, this volume). The sample from core L1-86-27G comes from a sandy turbidite unit containing veins and disseminations of hydrothermal pyrrhotite and barite accompanied by minor base-metal sulfide minerals and hydrothermally precipitated smectite formed at 180°C to 235°C (Zierenberg and Shanks, chap. 14, this volume). The sample from core L2-86-9G consists of blue-gray chlorite formed by replacement of hemipelagic mud through high temperature (200°C to 225°C) magnesium metasomatism adjacent to a massive sulfide deposit (Zierenberg and Shanks, chap. 14, this volume).

The molecular parameters measured in the four samples designated "Quaternary altered" (tables 15.2 and 15.4) have been strongly affected by the hydrothermal processes that apparently have altered the organic matter in various ways. Almost all of the values of the molecular ratios obtained for these samples are distinct from the values obtained either from the Pleistocene or Holocene samples. This distinction is well illustrated on table 15.4. Only average values for C_{31} S/(S+R) in Pleistocene samples and for C_{29}α(R)/C_{27}α(R) in Holocene samples are similar to the values found in the "Quaternary altered" samples.

The *n*-alkanes in samples from core L1-86-27G and L1-86-8G have CPI values that average 1.0, a distribution in the *n*-C_{24} to *n*-C_{34} range that suggests the results of thermal maturation leading to approximately equal abundance of odd- and even-carbon-numbered *n*-alkanes (Bray and Evans, 1961). In sample L1-86-27 (82–90), the odd-carbon-numbered *n*-alkanes in this range are slightly more abundant than are their even-carbon-numbered neighbors (fig. 15.2*D*). The distribution of this same range of *n*-alkanes in sample L1-86-8G (82–90) is unusual in that from *n*-C_{24} to *n*-C_{27} the even-carbon-numbered *n*-alkanes dominate, whereas in the range from *n*-C_{29} to *n*-C_{34} the odd-carbon-numbered *n*-alkanes are slightly more abundant than the even-carbon-numbered *n*-alkanes (fig. 15.2*B*). Both samples from core L1-86-8G contain similar distributions of hydrocarbons (table 15.2) including the unusual even-carbon-numbered dominance, which actually begins at about *n*-C_{16} and extends to *n*-C_{28} (fig. 15.2*B*). These two samples are the only ones from our collection that show this unusual distribution of *n*-alkanes; however, DSDP drilling at Sites 33, 34, 36, and 37, near to Escanaba Trough, recovered samples with *n*-alkanes having even-carbon-numbered predominances (Simoneit, 1977). This even-carbon-numbered dominance in samples from core L1-86-8G probably reflects an unusual source, perhaps anoxic microenvironments as suggested by Welte and Ebhardt (1968). The slight odd-carbon-number dominance at *n*-C_{29} to about *n*-C_{37} (fig. 15.2*B*) may result from hydrothermal alteration of a previous *n*-alkane mixture in which the odd-carbon-numbered molecules were much more abundant, as in the Pleistocene and Holocene samples (fig. 15.2*A*, *C*, *E*).

The distribution of *n*-alkanes in cores L1-86-27G and L2-86-9G are similar in that most of the compounds are in the range from *n*-C_{13} to *n*-C_{20} with no significant odd- or even-carbon-number dominance (fig. 15.2*D*, *F*). The sample from core L2-86-9G has only trace amounts of *n*-alkanes and other aliphatic hydrocarbons larger than about *n*-C_{20}. The *n*-alkanes that are present in these two samples likely reflect the results of thermal processes, because

Table 15.5. Descriptions of sediment organic matter in four samples from Escanaba Trough.

Core no.	Interval (cm)	Area	OC (pct.)	Age	Description (Clark Geological Services, written commun., 1987)
7G	89–90	SESCA	0.52	Pleistocene	Abundant woody and coaly fragments. Common fine amorphous kerogen, aggregated amorphous kerogen and cuticles. Traces of pollen, spores, and fungal parts. Fragments of diatoms and radiolarians present.
8G	82–90	SESCA	.31	Quaternary altered	Predominantly coaly fragments. Very common aggregated amorphous kerogen. Common fine amorphous kerogen and woody fragments. Traces of cuticles, pollen, spores, dinoflagellates, and fungal parts.
26G	82–90	SESCA	.72	Holocene	Predominantly aggregated amorphous kerogen. Very common very fine-grained coaly fragments. Traces of pollen, spores, and woody fragments. Abundant diatom and radiolarian fragments present.
27G	87–95	Between SESCA and NESCA	.13	Quaternary altered	Predominantly coaly fragments. Very common woody fragments. Common fine amorphous kerogen. Traces of aggregated amorphous kerogen, pollen, and spores.

lower carbon number molecules are enhanced during catagenesis (Tissot and Welte, 1984) and, therefore, should be expected where there is hydrothermal alteration of sediment. Samples from core L1-86-8G do not show this dominance of *n*-alkanes in the *n*-C_{13} to *n*-C_{20} region (fig. 15.2*B*), perhaps indicating that the intensity of hydrothermal processes affecting this sediment was lower than in the other altered sediments.

Although the molecular ratios of the "Quaternary altered" sediments are generally distinct from the unaltered Pleistocene and Holocene samples, the values of these ratios do not always follow consistent patterns. For example, the values of some of the maturity parameters (tables 15.2 and 15.4), such as C_{31} S/(S+R), C_{27} Tm/Ts, and C_{29} S/(S+R), suggest that the organic matter in the altered sediment is generally less mature than that in the unaltered sediment, whereas the values of C_{30} αβ/ββ and C_{30} βα/αβ are consistent with increased maturation of the altered sediment. Source-related ratios, such as Pr/Ph, αβ C_{30}/C_{29}, and C_{29} α(R)/C_{27}α(R), are generally lower in the altered sediment (tables 15.2 and 15.4). Clearly our results show that the lithologically altered sediment contains altered organic matter, but the course of organic matter alteration, as indicated by the molecular ratios, cannot be consistently predicted. Nevertheless, the cause of these alterations is attributed to hydrothermal processes.

HYDROTHERMAL OIL

The molecular distributions of the aliphatic hydrocarbons in Escanaba Trough sediment are, in general, different from the distributions in a hydrothermal oil (Kvenvolden and others, 1986, 1987) obtained from a sediment-hosted sulfide sample (L6-85-32D-2) that was dredged from the SESCA area (fig. 15.1). Molecular ratios for sediment samples and the oil are shown in table 15.2, and average values of these ratios for Pleistocene, Holocene, and Quaternary altered sediment samples and for the oil are listed in table 15.4. Comparison of figures 15.2 and 15.5*A* and information in table 15.4 illustrate some of the distributional differences in *n*-alkanes and isoprenoid hydrocarbons. The CPI value of the oil is smaller than the average CPI values in unaltered sediment and slightly larger than values in the altered sediment; Pr/Ph ratios follow the same trend. The *n*-alkanes in the oil have a slight odd-carbon-numbered dominance at high molecular weights as do altered sediments from cores L1-86-8G and L1-86-27G (fig. 15.2*B*,*D*) and an even-carbon-numbered dominance in the intermediate molecular weight range as in altered sediments from core L1-86-8G. The oil lacks, however, the high concentration of *n*-alkanes in the *n*-C_{13} to *n*-C_{20} range as seen in altered sediments from cores L1-86-27G and L2-86-9G (fig. 15.2*D*,*F*).

Comparison of triterpane and sterane ratios also shows some difference between Escanaba Trough sediment and a hydrothermal oil (table 15.4). The ββ-hopanes are present in all of the unaltered sediments but not in two samples of altered sediment (cores L1-86-27G and L2-86-9G) and in the oil sample. The compounds are known to be thermally unstable, and thus their absence in altered sediment and in the oil formed by hydrothermal processes is not unexpected. The sediment hydrocarbons show a wide range of maturities based on the C_{31} homohopane and the C_{29} sterane epimer ratios. These ratios, determined for the oil, have values similar to the average values measured in the Holocene sediment and exceed the average values measured in the Pleistocene sediment and in the altered sediment. None of these epimer ratios from sediments or the oil is at equilibrium. The values of the other molecular ratios, such as C_{30} βα/αβ, C_{27} Tm/Ts, αβ C_{30}/C_{29}, and C_{29}α(R)/C_{27}α(R), in the oil are distinct from the values of

the same ratios in both altered and unaltered sediment (table 15.4). Based on this comparison of molecular ratios, we conclude that although the hydrocarbons in the Escanaba Trough sediment likely contribute to the final oil product that is generated from the sedimentary organic matter, the amount of this contribution must be small, having only minimal influence on the distribution of hydrocarbons in the oil. However, certain features, such as the dominance of odd-carbon-numbered *n*-alkanes in the sediments and the oil, suggest that terrigenous organic matter is an important source material in the hydrothermal regime of Escanaba Trough.

SUMMARY

In Escanaba Trough, Pleistocene and Holocene sediments can be differentiated on the basis of distributional relationships among aliphatic hydrocarbons as reflected in various ratios of *n*-alkanes, isoprenoids, terpanes, and steranes. More terrigenous plant material entered the sediment during Pleistocene time than during Holocene time, based on considerations of *n*-alkanes and steranes. Terpane and sterane maturity parameters indicate that the organic matter in the Holocene sediment is more mature than that in the Pleistocene sediment. This unusual relation is

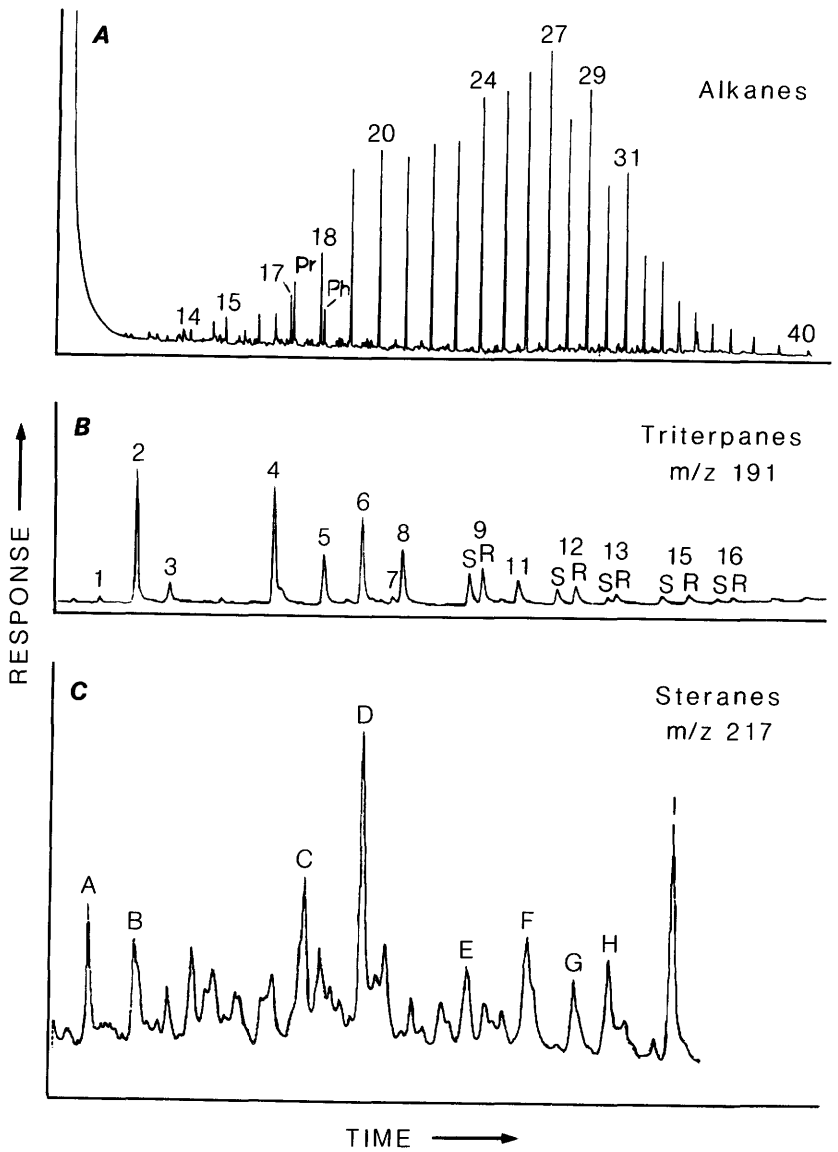

Figure 15.5. Gas chromatogram and mass chromatograms showing distributions of hydrocarbons in oil extracted from sediment-hosted, massive sulfide sample L6-85-32D-2 from Escanaba Trough. *A*, Gas chromatogram showing *n*-alkanes, pristane (Pr), and phytane (Ph). Numbers specify carbon numbers of *n*-alkanes. *B*, Mass chromatogram (m/z 191) of triterpanes. *C*, Mass chromatogram (m/z 217) of steranes. Identifications listed in table 15.3.

explained by a dilution effect caused by increased sedimentation of continentally derived material during Pleistocene time.

Some Escanaba Trough sediment has been affected by hydrothermal fluids, and this alteration has caused not only lithological changes but also changes in the distributions of organic compounds. Molecular ratios of various hydrocarbons in the altered sediment are distinct from the values obtained for unaltered Pleistocene and Holocene sediments. The course of organic matter alterations, as indicated by molecular ratios, cannot, however, be consistently predicted.

Hydrothermally derived oil found with sediment-hosted sulfide deposits contains aliphatic hydrocarbons with distributions that are distinct from the distributions found in both altered and unaltered sediment samples. Although hydrocarbons from these sediments likely contribute to the hydrothermal oil generated in Escanaba Trough, these hydrocarbons have only minimal influence on the distributions of hydrocarbons in the oil.

REFERENCES CITED

Bazylinski, D.A., Farrington, J.W., and Jannasch, H.W., 1988, Hydrocarbons in surface sediment from a Guaymas Basin hydrothermal vent site: Organic Geochemistry, v. 12, p. 547–558.

Bray, E.E., and Evans, E.D., 1961, Distribution of *n*-paraffins as a clue to the recognition of source beds: Geochimica et Cosmochimica Acta, v. 22, p. 2–15.

Bush, P.R., 1970, A rapid method for the determination of carbonate carbon and organic carbon: Chemical Geology, v. 6, p. 59–62.

Campbell, A.C., German, C., Palmer, M.R., and Edmond, J.M., 1988, Preliminary report on the chemistry of hydrothermal fluids from Escanaba Trough [abs.]: Eos, Transactions American Geophysical Union, v. 69, p. 1271.

Clague, D.A., Freisen, W., Quinterno, P., Holmes, M., Morton, J., Bouse, R., Morgenson, L., and Davis, A., 1984, Preliminary geological, geophysical, and biological data from the Gorda Ridge: U.S. Geological Survey Open-File Report 84–364, 47 p.

Cooper, J.E., and Bray, E.E., 1963, A postulated role of fatty acids in petroleum formation: Geochimica et Cosmochimica Acta, v. 27, p. 1113–1127.

Eglinton, G., Gonzales, A.G., Hamilton, R.J., and Raphael, R.A., 1962, Hydrocarbon constituents of the wax coatings of plant leaves: A taxonomic study: Phytochemistry, v. 1, p. 89–102.

Ensminger, A., van Dorsselaer, A., Spyckerelle, C., Albrecht, P., and Ourisson, G., 1974, Pentacyclic triterpanes of the hopane type as ubiquitous geochemical markers—Origin and significance, *in* Tissot, B., and Bienner, F., eds., Advances in organic geochemistry 1973: Paris, Editions Technip, p. 245–260.

Huang,W.-Y., and Meinschein, W.G., 1979, Sterols as ecological indicators: Geochimica et Cosmochimica Acta, v. 43, p. 739–745.

Karlin, R., and Lyle, M., 1986, Sediment studies on the Gorda Ridge: Oregon Department of Geology and Mineral Industries Open-File Report O-86-19, 76 p.

Karlin, R.E., and Zierenberg, R.A., Sedimentation and neotectonism in the SESCA area, Escanaba Trough, southern Gorda Ridge, *in* Morton, J.L., Zierenberg, R.A., and Reiss, C.A., eds., Geologic, hydrothermal, and biologic studies at Escanaba Trough, Gorda Ridge, offshore northern California: U.S. Geological Survey Bulletin 2022, chapter 7 (this volume).

Kawka, O.E., and Simoneit, B.R.T., 1987, Survey of hydrothermally-generated petroleums from the Guaymas Basin spreading center: Organic Geochemistry, v. 11, p. 311–328.

Koski, R.A., Shanks, W.C., III, Bohrson, W.A., and Oscarson, R.L., 1988, The composition of massive sulfide deposits from the sediment-covered floor of Escanaba Trough, Gorda Ridge: Implications for depositional processes: Canadian Mineralogist, v. 26, p. 655–673.

Kvenvolden, K.A., Rapp, J.B., and Bourell, J.H., 1985, Comparison of molecular markers in crude oils and rocks from the North Slope of Alaska, *in* Magoon, L.B., and Claypool, G.E., eds., Alaska North Slope Oil/Rock Correlation Study: American Association of Petroleum Geologists Studies in Geology 20, p. 593–617.

Kvenvolden, K.A., Rapp, J.B., and Hostettler, F.D., 1987, Hydrocarbon geochemistry of petroleum associated with sediment-hosted sulfides from Escanaba Trough, southern Gorda Ridge: U.S. Geological Survey Open-File Report 87-375C, 18 p.

Kvenvolden, K.A., Rapp, J.B., Hostettler, F.D., Morton, J.L., King, J.D., and Claypool, G.E., 1986, Petroleum associated with polymetallic sulfide in sediment from Gorda Ridge: Science, v. 234, p. 1231–1234.

Mackenzie, A.S., Patience, R.L., Maxwell, J.R., Vandenbroucke, M., and Durand, B., 1980, Molecular parameters of maturation in the Toarcian shales, Paris Basin, France—I. Changes in the configuration of acyclic isoprenoid alkanes, steranes, and triterpanes: Geochimica et Cosmochimica Acta, v. 44, p. 1709–1721.

McManus, D.A., and others, 1970, Site 35, *in* McManus, D.A., and others, eds., Initial reports of the Deep Sea Drilling Project: Washington, U.S. Government Printing Office, v. 5, p. 165–172.

Moore, G.W., 1970, Sea-floor spreading at the junction between Gorda Rise and Mendocino Ridge: Geological Society of America Bulletin, v. 81, p. 2817–2824.

Morton, J.L., Holmes, M.L., and Koski, R.A., 1987a, Volcanism and massive sulfide formations at a sedimented spreading center, Escanaba Trough, Gorda Ridge, Northeast Pacific Ocean: Geophysical Research Letters, v. 14, p. 769–772.

Morton, J.L., Normark, W.R., Ross, S.L., Koski, R.A., Holmes, M.L., Shanks, W.C., III, Zierenberg, R.A., Lyle, M., and Benninger, L.M., 1987b, Preliminary report, cruise L1-86-NC and L2-86-NC, Escanaba Trough, Gorda Ridge: U.S. Geological Survey Open-File Report 87-375A, 20 p.

Normark, W.R., Gutmacher, C.E., Zierenberg, R.A., Wong, F.L., and Rosenbauer, R.J., Sediment fill of Escanaba Trough, *in* Morton, J.L., Zierenberg, R.A., and Reiss, C.A., eds., Geologic, hydrothermal, and biologic studies at Escanaba Trough, Gorda Ridge, offshore northern California: U.S. Geological Survey Bulletin 2022, chapter 6 (this volume).

Ourisson, G., Albrecht, P., and Rohmer, M., 1984, The microbial origin of fossil fuels: Scientific American, v. 251, no. 2, p. 44–51.

Palacas, J.G., Anders, D.E., and King, J.D., 1984, South Florida Basin—A prime example of carbonate source rocks of petroleum, *in* Palacas, J.G., ed., Petroleum geochemistry and source rock potential of carbonate rocks: American Association of Petroleum Geologists Studies in Geology 18, p. 71–96.

Philp, R.P., 1985, Biological markers in fossil fuel production: Mass Spectrometry Reviews 1985, v. 4, p. 1–54.

Seifert, W.K., and Moldowan, J.M., 1978, Applications of steranes, terpanes and monoaromatics to the maturation, migration and source of crude oils: Geochimica et Cosmochimica Acta, v. 42, p. 77–95,

Simoneit, B.R.T., 1977, Diterpenoid compounds and other lipids in deep-sea sediments and their geochemical significance: Geochimica et Cosmochimica Acta, v. 41, p. 463–476.

———1978, The organic chemistry of marine sediments, *in* Riley, J.P., and Chester, R., eds., Chemical oceanography (2d ed.): New York, Academic Press, v. 7, p. 233–311.

Simoneit, B.R.T., Mazurek, M.A., Brenner, S., Crisp, P.T., and Kaplan, I.R., 1979, Organic geochemistry of recent sediments from Guaymas Basin, Gulf of California: Deep-Sea Research, v. 26A, p. 879–891.

Simoneit, B.R.T., Philp, R.P., Jenden, P.D., and Galimov, E.M., 1984, Organic geochemistry of Deep Sea Drilling Project sediments from the Gulf of California—Hydrothermal effects on unconsolidated diatom ooze: Organic Geochemistry, v. 7, p. 173–205.

Tissot, B.P., and Welte, D.H., 1984, Petroleum formation and occurrence (2d ed.): Berlin, Springer-Verlag, 699 p.

Vallier, T.L., Harold, P.J., and Girdley, W.A., 1973, Provenances and dispersal patterns of turbidite sand in Escanaba Trough, northeastern Pacific Ocean: Marine Geology, v. 15, p. 67–87.

Volkman, J.K., 1986, A review of sterol markers for marine and terrigenous organic matter: Organic Geochemistry, v. 9, p. 83–99.

Welte, D.H., and Ebhardt, G., 1968, Distribution of long chain *n*-paraffins and *n*-fatty acids in sediment from the Persian Gulf: Geochimica et Cosmochimica Acta, v. 32, p. 465–466.

Zierenberg, R.A., Koski, R.A., Shanks, W.C., III, and Slack, J.F., 1988, Preliminary results of ALVIN dives on active sediment-hosted massive sulfide deposits in the Escanaba Trough, southern Gorda Ridge [abs.]: Eos, Transactions American Geophysical Union, v. 69, p. 1488.

Zierenberg, R.A., and Shanks, W.C., III, Sediment alteration associated with massive sulfide formation in the Escanaba Trough, Gorda Ridge: The importance of seawater mixing and magnesium metasomatism, *in* Morton, J.L., Zierenberg, R.A., and Reiss, C.A., eds., Geologic, hydrothermal, and biologic studies at Escanaba Trough, Gorda Ridge, offshore northern California: U.S. Geological Survey Bulletin 2022, chapter 14 (this volume).

Chapter 16. Composition and Growth History of Hydrothermal Deposits in Escanaba Trough, Southern Gorda Ridge

By Randolph A. Koski, Laura M. Benninger, Robert A. Zierenberg,[1] *and* Ian R. Jonasson[2]

CONTENTS

ABSTRACT

Large-scale discharge of hydrothermal fluids through the sequence of turbidites and hemipelagic sediment infilling Escanaba Trough, the axial valley of southern Gorda Ridge, has resulted in widespread formation of sulfide- and sulfate-dominant deposits. On a regional scale, mineralization is spatially related to several volcanic edifices that penetrate and locally breach the sediment pile. In the NESCA and SESCA study areas, hydrothermal deposits are most abundant on the flanks of sediment hills upraised during emplacement of basaltic sills.

Sulfide-dominant deposits are grouped into two compositional types: (1) pyrrhotite-rich sulfide that forms mounds, chimneys, cement in sediment breccia, and subsurface clastic aggregates; and (2) less abundant polymetallic sulfide that forms the wall of a chimneylike sulfide structure and cement in sand turbidite. Pyrrhotite-rich massive sulfide contains variable amounts of isocubanite and chalcopyrite, and minor sphalerite and löllingite; texturally, it is characterized by a latticework texture of pyrrhotite and numerous fluid channelways. Chemically, pyrrhotite-rich sulfide samples have high Cu (to 20.6 percent), As (to 1.55 percent), Bi (to 820 ppm), Co (to 3,000 ppm), Se (to 525 ppm), and Au (to 10.1 ppm). The Cu/Zn ratio generally exceeds unity, and Pb is very low. The highest Au occurs in Cu-rich samples.

A 40-mm-thick section of the polymetallic sulfide structure contains a telescoped growth zonation that includes sphalerite, isocubanite, pyrrhotite, galena, arsenopyrite, löllingite, and boulangerite. A coarse sand turbidite sample is cemented by a polymetallic sulfide assemblage of galena, sphalerite, pyrrhotite, and löllingite. Two tin-bearing phases, stannite and franckeite, are present in trace amounts. Polymetallic samples are especially enriched in Zn (to 42.6 percent), Pb (to 13.7 percent), As (to 2.75 percent), and Ag (to 681 ppm).

Sulfate-dominant deposits include barite-rich crusts and chimneys on sulfide mounds, isolated barite chimneys on sediment, and sulfate (anhydrite and barite)-rich sinters deposited where hydrothermal fluids are venting through massive sulfide mounds (NESCA site). Barite-rich crusts and chimneys on sulfide mounds also contain abundant sphalerite and galena and have high zinc, lead, and silver contents. Anhydrite-rich sinters contain high magnesium and silicon related to the presence of stevensite, whereas barite-rich sinters contain high silicon related to abundant amorphous silica.

The widespread distribution and large size of hydrothermal deposits are the results of long-lived, sediment-hosted hydrothermal convection cells driven by heat sources located at depth within the volcanic edifices. The abundance of barite and enrichment of metals such as lead, arsenic, antimony, and bismuth in sulfide deposits are indicators of extensive contributions from a sedimentary

[1] U.S. Geological Survey, Menlo Park, California
[2] Geological Survey of Canada, Ottawa, Canada

source rock. Massive sulfide mounds are formed by (1) an early stage of sulfate-dominant deposition on the step-faulted margins of the uplifted sediment hills, (2) a mature stage including less fluid mixing, low oxygen fugacity and sulfur fugacity, higher fluid temperatures, and deposition of the main-stage sulfide assemblage beneath the sulfate-rich shell, and (3) a near-dormant declining stage marked by erosion, oxidation, and partial burial by unconsolidated Holocene sediment. Hydrothermal activity in this final stage is restricted to localized venting of moderate-temperature (to 220°C) fluids through sulfide mounds, deposition of sulfate sinter, and diffuse seepage of low-temperature fluid through the sediment. Unlike the diffuse upwelling associated with pyrrhotite-rich sulfide mounds, the polymetallic sulfide structure was formed around a focused "black smoker" type vent. The telescoping of high- and low-temperature sulfide assemblages in this structure resulted from complex bidirectional growth of the chimney wall under the influence of steep temperature and chemical gradients.

INTRODUCTION

A variety of sulfide- and sulfate-dominant hydrothermal deposits are the product of large-scale fluid discharge through the sediment-covered floor of Escanaba Trough, southern Gorda Ridge. The concentration of deposits in the northern Escanaba (NESCA) and southern Escanaba (SESCA) areas (fig. 16.1) is spatially related to two volcanic edifices that penetrate and locally breach the 500-m-thick sequence of turbidite and hemipelagic sediments within the axial valley (Morton and others, 1987, 1990). The largest hydrothermal deposits are massive sulfide mounds with lateral and vertical dimensions measured in hundreds and tens of meters, respectively, that formed on the flanks of sediment hills rising above the surrounding sea floor (Holmes and Zierenberg, 1990; Zierenberg and others, chap. 10, this volume). Small chimneys (less than 1 m in height) composed of massive sulfide and barite ± sulfide occur on the tops of massive sulfide mounds and on the sediment surface between the hills. Sinter deposits largely composed of anhydrite, barite, and stevensite are forming around active hydrothermal vents discharging through the tops of massive sulfide mounds at the NESCA site. A sediment core taken from the SESCA site contains a subsurface layer of clastic sulfide.

The composition and distribution of hydrothermal deposits, the presence of interstitial and vein sulfide minerals in sediment samples, and the alteration of sediment to aggregates of chlorite and talc indicate that the circulation of hydrothermal fluids through sediment is widespread in Escanaba Trough. The mineral and chemical compositions of sulfide- and sulfate-rich hydrothermal samples reflect fluid-sediment interaction (Benninger and Koski, 1987; Koski and others, 1988), and these compositions contrast with those of deposits formed at sediment-free ridge axes of the northeast Pacific Ocean (Haymon and Kastner, 1981; Styrt and others, 1981; Koski and others, 1984).

Benninger and Koski (1987), Koski and others (1988), and Morton and others (1990) presented mineralogical and chemical data for sulfide samples dredged from Escanaba Trough in 1985 and 1986, and developed preliminary models for the deposition of distinct massive sulfide types. In this chapter, we present additional chemical data for the dredge samples along with descriptions and compositional data for samples recovered by gravity coring in 1986 (R/V *S.P. Lee*, U.S. Geological Survey) and 1989 (CSS *J.P. Tully*, Geological Survey of Canada) and by submersibles in 1986 (DSV *Sea Cliff*) and 1988 (DSV *Alvin* and *Sea Cliff*). These data are used to further define the growth history of sulfide- and sulfate-dominant deposits in Escanaba Trough.

ACKNOWLEDGMENTS

We thank J.M. Edmond and J.F. Grassle (co-chief scientists, Massachusetts Institute of Technology and Woods Hole Oceanographic Institution) and E.E. Davis and J.M. Franklin (co-chief scientists, Geological Survey of Canada) for inviting us to participate in and collect samples during their 1988 R/V *Atlantis II* and 1989 CSS *J.P. Tully* cruises, respectively. We appreciate the dedication and professionalism of ship's crews from the R/V *S.P. Lee* (U.S. Geological Survey), CSS *J.P. Tully* (Geological Survey of Canada), R/V *Atlantis II* (Woods Hole Oceanographic Institution), and DSVSS *Laney Chouest* (Edison Chouest Offshore, Inc.) and the crews of research submersibles DSV *Sea Cliff* (Submarine Development Group One, U.S. Navy) and DSV *Alvin* (Woods Hole Oceanographic Institution). J.F. Slack provided many of the original sample descriptions from the 1988 *Alvin* dive program. Franckeite in a polymetallic sulfide sample was identified by E. Oudin. Data sources for mid-ocean-ridge basalts were kindly provided by J.A. Philpotts. J.A. Reid and V.K. Smith assisted in compilation of data tables and drafting of figures.

HYDROTHERMAL DEPOSIT TYPES IN ESCANABA TROUGH

During the period 1985 to 1988, approximately 57 kg of sulfide- and sulfate-rich hydrothermal material was recovered by dredge and another 245 kg was recovered by submersible from the NESCA and SESCA areas of Escanaba Trough. Subsurface sulfide deposits were sampled by two gravity cores. The locations of individual sample stations are shown in figure 16.2. Brief descriptions of these samples along with their locations and depths of recovery are

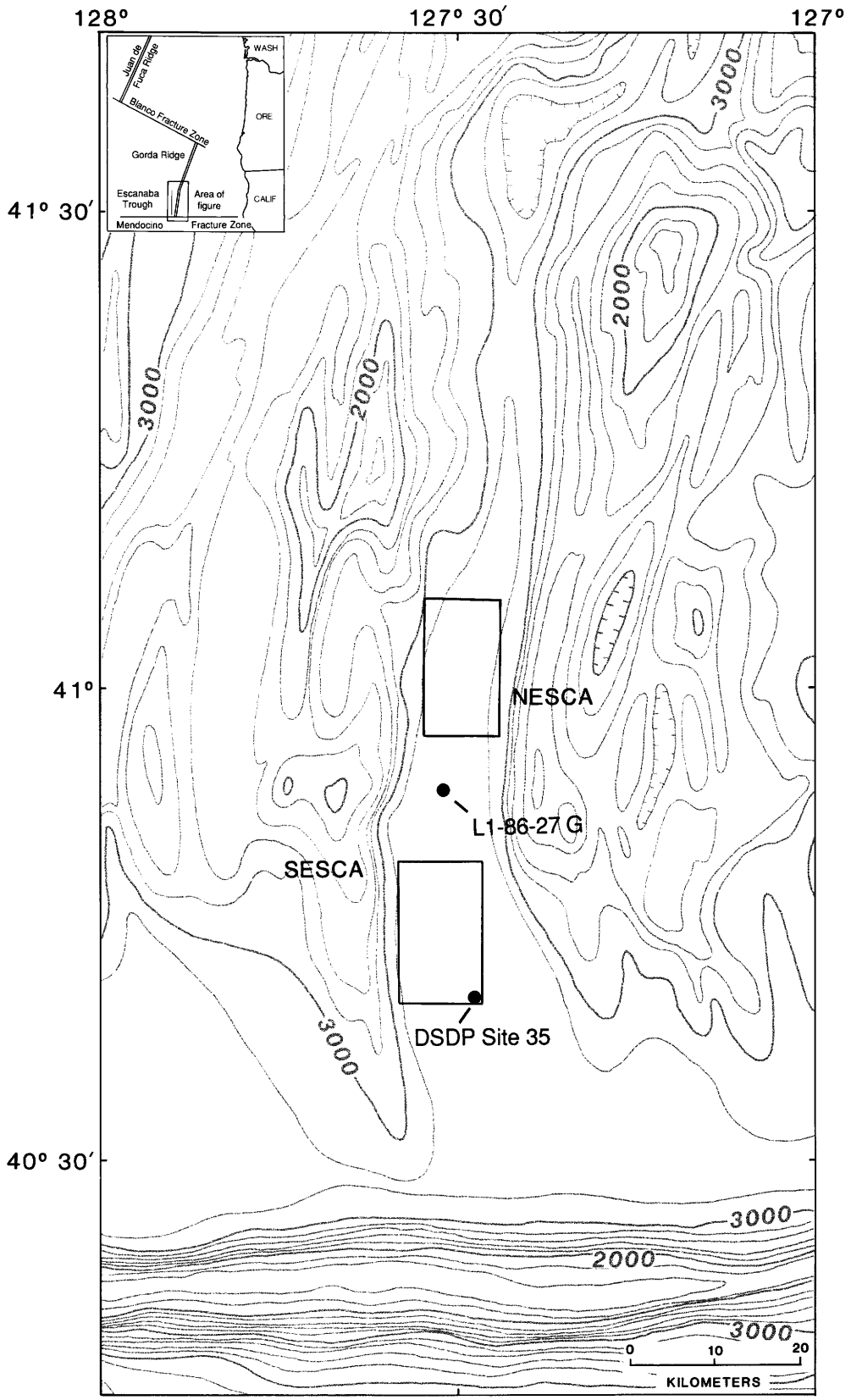

Figure 16.1. Location and regional bathymetry of Gorda Ridge and Escanaba Trough. Also shown are locations of Deep Sea Drilling Project (DSDP) Site 35 and gravity core station L1-86-27G. Northern Escanaba (NESCA) and southern Escanaba (SESCA) sites are shown in greater detail in figure 16.2. Hachures indicate area of closed low. Contour interval is 500 m.

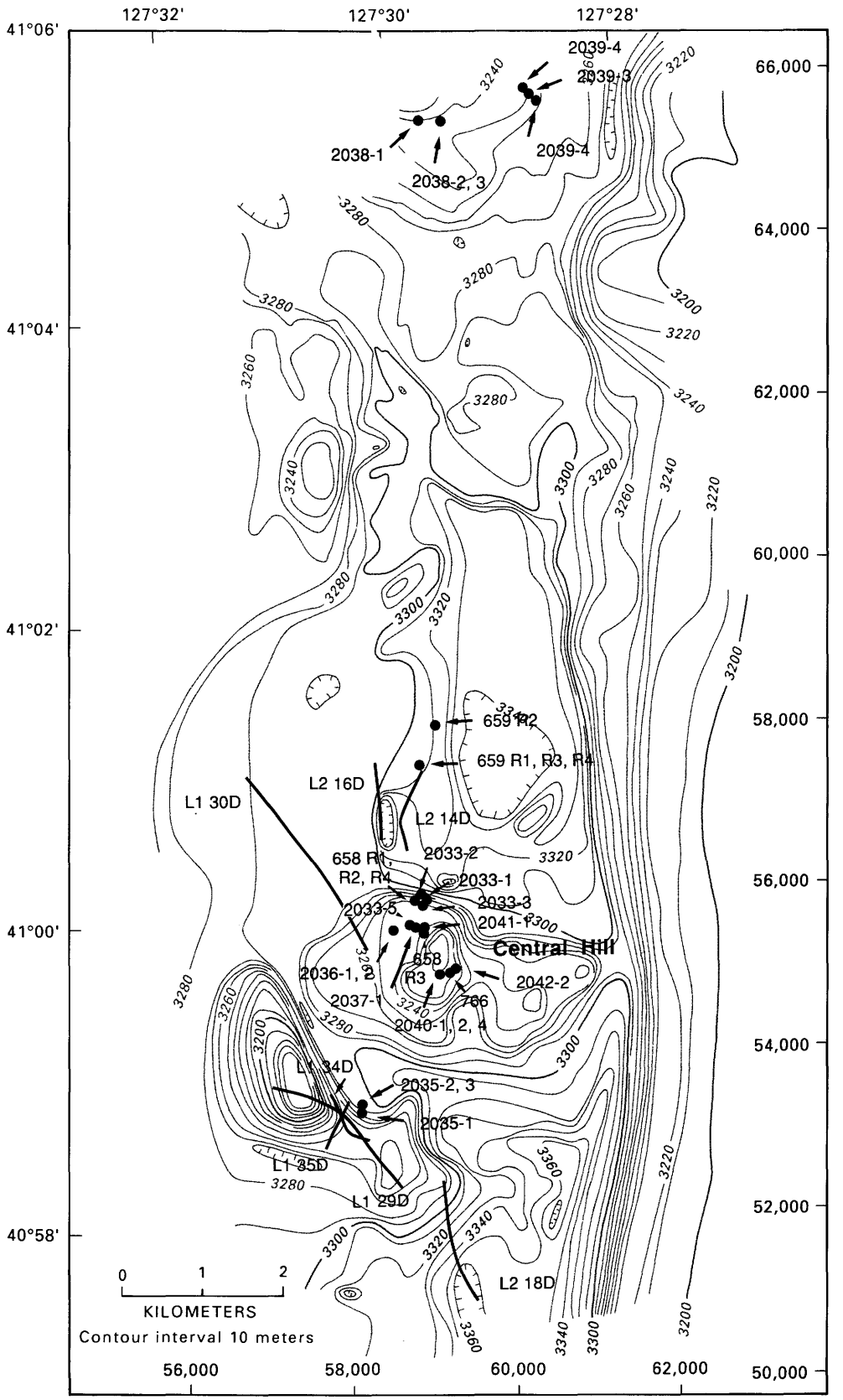

A

Figure 16.2. Bathymetry and sampling locations for NESCA (*A*) and SESCA (*B*) sites, Escanaba Trough. Solid circles indicate location of samples collected by submersible. Heavy solid lines are tracks of dredge stations that recovered hydrothermal samples. Open circle at SESCA is location of

presented in table 16.1 at the end of this chapter; the mineralogy of various deposit types is given in table 16.2.

Sulfide-dominant deposits in Escanaba Trough include massive sulfide mounds, massive sulfide chimneys and chimneylike(?) vent structures, sulfide-cemented sediment and sediment breccia, and clastic sulfide aggregates. Massive sulfide mounds have a wide range in morphology from rugged, steep-sided stacks and ridges to subdued, flat-lying ledges (fig. 16.3*A, B, C*). Nearly all of the observed mounds are actively eroding and partly covered or surrounded by blocky sulfide debris (fig. 16.3*D*). The flanks of many mounds are buried by unconsolidated sediment. It is uncertain whether the exposed massive sulfide bodies are connected at depth, but several mounds at the NESCA site appear to be joined by narrow sulfide ridges.

Chimneys composed of massive sulfide form small jagged pinnacles and eroded stumps on the tops of sulfide mounds (fig. 16.3*A, B*) and isolated spires on the sediment surface. Hydrothermal venting through massive sulfide chimneys has not been observed, and the few sampled chimneys, with one exception, are plugged or contain many small fluid channelways. In the one exception, massive sulfide fragments from dredge L2-86-14D in the NESCA area (fig. 16.2*A*) appear to be part of a chimneylike sulfide structure with a large central conduit.

Sulfide also forms the cement in sedimentary breccias that probably represent debris-flow deposits derived by mass wasting of the nearby sediment hills (Zierenberg and others, chap. 10, this volume). In addition, massive sulfide fragments occur in poorly sorted clastic aggregates as thick as 27 cm that have been recovered by gravity cores. These deposits may represent debris flows shed from massive sulfide mounds that were subsequently buried by turbidite flows and hemipelagic mud. Sulfide deposits with similar clastic textures have been cored on the flank of a sediment-covered dome in the Middle Valley segment of Juan de Fuca Ridge (Davis and others, 1987; Goodfellow and Blaise, 1988).

Although less abundant than sulfide deposits, sulfate-dominant deposits including crusts, chimneys, and sinter are equally widespread at the NESCA and SESCA sites. Barite-rich encrustations and cavity infillings occur on the surface of massive sulfide mounds. Numerous thin (less than 2 cm) slabs of massive barite recovered in several dredges probably represent crusts spalled from massive sulfide blocks during sampling. Barite is also the most abundant phase in small (less than 1 m) knobby chimneys that occur in clusters on top of sulfide mounds (fig. 16.3*E*) and in stubby cylindrical chimneys rooted in the sediment. Sinter deposits composed of anhydrite, barite, stevensite, and minor sulfide are precipitating from moderate-temperature (about 220°C) fluids venting through the tops of massive sulfide mounds at NESCA (fig. 16.3*F*).

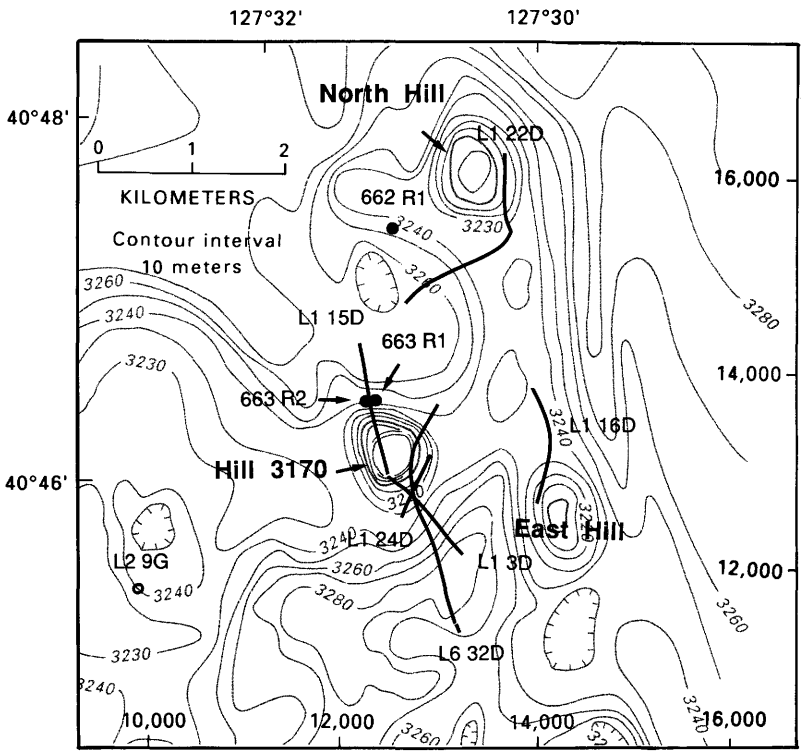

B

gravity core station L2-86-9G. Numbers along right and bottom give coordinates of local transponder net (in meters). Hachures indicate area of closed low.

Table 16.1. Location and description of hydrothermal samples from Escanaba Trough

[X and Y coordinates refer to local navigation grid for NESCA and SESCA shown in figure 16.2]

Station or dive number	Location	Depth (m)	Sample number and description
			Dredge Samples
L6-85-32D	East and south flank of 3170 hill at SESCA area	3180–3280	1 through 26: Rounded, knobby fragments of massive sulfide, predominantly pyrrhotite. One fragment (sample 32D-2) of interlayered pyrrhotite-rich massive sulfide and sediment is saturated with petroleum. Total weight approximately 5 kg.
L1-86-3D	South flank of 3170 hill at SESCA	3200–3280	2: Two chips of gray mudstone cut by 1-mm-thick pyrite veins (0.002 kg). 3: A dish-shaped fragment (10 cm × 9 cm × 4 cm) of gray indurated silt and sand. The concave surface is coated with a thin crust of fine-grained pyrrhotite (0.145 kg). 6: Two chips (approximately 3 cm × 2 cm × 2 cm) of pyrrhotite-rich massive sulfide. Total weight 0.01 kg.
L1-86-15D	Top and northern flank of 3170 hill at SESCA	3170–3260	1: Slabs and cobble-size fragments of sulfide-cemented sediment breccia. Sulfide is mostly marcasite after pyrrhotite; sediment fragments contain abundant chlorite and talc. Total weight 0.75 kg. 2, 3: Pebble-size and smaller pieces of gossanous sediment with veins and crusts of black Fe oxide, mostly goethite as pseudomorphous replacement of pyrrhotite. Total weight 0.15 kg. Other: Blocky, pebble-size fragments of concentrically zoned massive sulfide composed of isocubanite, sphalerite, and marcasite. Total weight 0.02 kg.
L1-86-16D	Northern flank of east hill at SESCA	3220–3240	1 through 4: Cobble-size fragments and numerous pebble-size fragments of pyrrhotite-rich massive sulfide with 1-cm-thick crusts of barite. Pyrrhotite in some fragments pseudomorphed by marcasite. Some fragments also have cavities lined with barite and surfaces with patches of sponge spicules. 5 through 18: Slabby fragments, 1 to 2 cm thick, of interlayered sulfide and barite. Total weight of all samples 5.05 kg.
L1-86-22D	Southern and eastern flanks of north hill at SESCA	3210–3260	1: A flat slab (4.5 cm × 4.5 cm × 2 cm, 0.35 kg) of massive sulfide largely composed of intergrown pyrrhotite and barite. 2: Pebbles and smaller fragments of poorly indurated sediment breccia with a few clasts composed of massive sulfide. Total weight 0.315 kg.
L1-86-24D	Southeast flank of 3170 hill at SESCA	3230–3210	1, 2, 5, 6, 9, 12 through 17, 20, 21: Numerous blocky boulder- to pebble-sized fragments and slabs of pyrrhotite-rich massive sulfide some of which contain crusts and interstitial concentrations of talc or barite. Total weight approximately 25 kg. 10, 11: Two tabular crusts (average 7 cm × 5 cm × 2 cm) of dense granular barite. Total weight 0.195 kg. 3, 4, 7: Assorted fragments of sediment breccia cemented by a mixture of Fe sulfide (pyrrhotite and marcasite) and barite. Total weight 1.20 kg. 8, 18, 19, 22: Assorted cobble- and pebble-size fragments of indurated gray sediment containing disseminated and fracture-controlled sulfide, mostly pyrrhotite. Oxidation of sulfide results in orange-yellow coloration and narrow ribbons of black vitreous Fe oxide, mostly goethite. Total weight approximately 0.4 kg.
L1-86-29D	West flank, top, and southeast flank of SW hill at NESCA	3160–3260	1: Pebble-size fragments of pyrrhotite-rich massive sulfide (<0.15 kg).
L1-86-30D	Sediment plain northwest of central hill at NESCA	3260–3290	1: Four pebble-size fragments of coarse-grained pyrrhotite-rich massive sulfide. Total weight 0.02 kg.
L1-86-34D	Southeast flank of SW hill at NESCA	3240–3250	1 through 4: Angular block (7 cm × 5 cm × 3 cm), curved fragment (10 cm × 8 cm × 5 cm), and rounded pebbles of massive sulfide largely composed of pyrrhotite and isocubanite. Some surfaces altered to Fe oxides. Total weight 0.73 kg.
L1-86-35D	Southeast flank of SW hill at NESCA	3240–3290	Unconsolidated mud containing small fragments of pyrrhotite-rich sulfide, mudstone, and volcanic glass. Total weight 2.6 kg.

Table 16.1. Location and description of hydrothermal samples from Escanaba Trough—Continued

Station or dive number	Location	Depth (m)	Sample number and description
		Dredge Samples—Continued	
L2-86-14D	West side of trough north of central hill at NESCA	3310–3330	1 through 4: One large (28 cm × 21 cm × 5 cm) bowl-shaped fragment and several smaller curved fragments composed of dark-gray massive sulfide. The polymetallic sulfide assemblage includes sphalerite, pyrrhotite, galena, and isocubanite. Oxidation is very minor. The large sample, part of a sulfide edifice, is mineralogically and texturally zoned. Total weight 11.84 kg. 6: One blocky fragment (0.10 kg) of coarse sand cemented by sulfide that is predominantly pyrrhotite, galena, and sphalerite. Hydrocarbon is also present in interstices between sediment clasts. 7: Cobble- and pebble-size blocks of sandstone and silty mudstone. One sandstone fragment contains discontinuous fractures lined with partly oxidized isocubanite. Another fragment of mudstone is crosscut by veins of pyrrhotite and also contains hydrocarbon. Total weight 5.53 kg.
L2-86-16D	West of L2-86-14D	3300–3340	1, 2: Pebble-size angular fragments of altered sediment containing talc, granular barite, and sulfide veinlets. Total weight 0.10 kg.
L2-86-18D	West side of trough 2 km south of central hill at NESCA	3280–3360	1, 2: Fragments of pyrrhotite-rich massive sulfide with dimensions averaging 6 cm × 4 cm × 3 cm; some replacement of pyrrhotite by marcasite. Total weight 0.15 kg.
L2-86-25D	South and east flank of SW hill at NESCA	3160–3270	1, 2, 4: Blocky fragments (maximum 10 cm × 9 cm × 5 cm) of sulfide-cemented sediment breccia. Sediment clasts are partly altered to chlorite. Pyrrhotite is the predominant mineral in the cement and also occurs in veins cutting the clasts. Total weight 1.245 kg. 3 and 5 through 7: Subangular fragments (average 7 cm × 5 cm × 4 cm) of porous pyrrhotite-rich massive sulfide. Pyrrhotite in some samples is replaced by marcasite, and several samples have surfaces covered with thin encrustations of talc. Total weight 0.98 kg.
		Samples Collected by DSV *Sea Cliff*	
SC658	Northern flank of central hill at NESCA		R1: Three cobble-size and approximately 20 smaller fragments of pyrrhotite-rich massive sulfide with abundant barite and isocubanite. Some pyrrhotite altered to marcasite. Some surfaces have 1-mm-thick rind of Fe oxide. Total weight 0.65 kg. R2: Barite chimney approximately 25 cm in height and 10 cm in diameter (5.4 kg) with no continuous central conduit recovered from sediment substrate. Outer surface coated with 1 to 2 mm of Mn oxide. R4: Four flat slabs of pyrrhotite-rich massive sulfide recovered from beneath sediment surface. Total weight 2.7 kg.
	(R1) X:58800, Y:55812	3265	
	(R2) X:58800, Y:55812	3265	
	(R4) X:58800, Y:55812	3265	
SC658	Approximately 400 m south of 658-R1		R3: Rounded talus block of pyrrhotite-rich massive sulfide with 2-mm-thick rind of Fe oxides including goethite (9.5 kg).
	(R3) X:58862, Y:55375	3238	
SC659	In trough near west wall of axial valley, 1.5 km north of central hill at NESCA		R1: Chimney composed of pyrrhotite-rich massive sulfide (3.5 kg). The upper part, 25 cm high and 10 cm in diameter, has many fluid channelways partly to completely filled with coarse-grained pyrrhotite. The basal platform was embedded in sediment, has a layered structure, and contains abundant pyrrhotite, isocubanite, native sulfur, and silicate sediment grains. R3: Fragments of partly oxidized pyrrhotite-rich massive sulfide containing sediment grains and hydrocarbon. Total weight 1.0 kg. R4: Fragments of pyrrhotite-rich massive sulfide including a few small chimney tops with open fluid conduits. Total weight 0.4 kg.
	(R1) X:58810, Y:57430	3322	
	(R3) X:58810, Y:57430	3322	
	(R4) X:58810, Y:57430	3322	
SC659	Approximately 500 m northeast of 659-R1		R2: Fragments of partly oxidized pyrrhotite-rich massive sulfide incorporating sediment grains and hydrocarbon. Total weight 0.7 kg.
	(R2) X:59000, Y:57934	3322	

Table 16.1. Location and description of hydrothermal samples from Escanaba Trough—Continued

Station or dive number	Location	Depth (m)	Sample number and description
			Samples Collected by DSV *Sea Cliff*—Continued
SC662	Approximately 500 m southwest of north hill at SESCA		R1: Many fragments of massive sulfide containing abundant pyrrhotite, chalcopyrite, and barite from a short chimney structure projecting from a massive sulfide mound. Total weight 6.3 kg.
	(R1) X:13610, Y:15550	3237	
SC663	North flank of the 3170 hill at SESCA		R1: Fragments of deeply-weathered pyrrhotite-rich sulfide in which pyrrhotite is completely replaced by marcasite, goethite, and hematite. Total weight 1.2 kg.
	(R1) X:12419, Y:13700	3246	
SC663	Approximately 70 m west of 663-R1		R2: Rubbly fragments containing a mixture of talc and Fe-oxide minerals. Some fragments contain hydrocarbon. Total weight 0.5 kg.
	(R2) X:12353, Y:13695	3246	
SC766	Active vent area on upper eastern flank of central hill at NESCA		Hourglass-shaped, barite-rich chimney from top of massive sulfide mound (approximately 10 kg).
	X:59220, Y:54904	3227	
			Samples Collected by DSV *Alvin*
ALV2033	Northern flank of central hill at NESCA		1: Angular block (25 cm × 25 cm × 12 cm, 6.72 kg) of pyrrhotite-rich massive sulfide with weathered (to depth of 3 cm) surfaces composed of Fe oxide.
	(1) X:58916, Y:55771	3274	
	(2) X:58886, Y:55716	3257	2: Knobby weathered tip of barite chimney (12 cm × 10 cm × 6 cm, 0.26 kg) coated with Mn oxide.
	(3) X:58858, Y:55848	3264	
	(5) X:58760, Y:55460	3242	3A, B: Two finger-shaped barite-rich chimneys (25 cm × 15 cm × 42 cm and 22 cm × 10 cm × 50 cm) from top of massive sulfide mound. Knobby surfaces are deeply weathered and covered in part by a film of Mn oxide. Total weight 35.5 kg.
			5A, B, C: Blocky fragments (maximum 42 cm × 40 cm × 25 cm) of pyrrhotite-rich massive sulfide with barite lining cavities. Some surfaces have thin alteration rinds of Fe oxide. Total weight 61.6 kg.
ALV2035	Base of eastern slope of SW hill at NESCA		1: Six angular blocks (the largest 20 cm × 18 cm × 8 cm) of pyrrhotite-rich massive sulfide containing 1- to 3-cm-wide fluid conduits lined with Cu-Fe sulfides. Total weight 6.07 kg.
	(1) X:58103, Y:53215	3277	
	(2) X:58122, Y:53223	3282	2: Two angular fragments (average 25 cm × 15 cm × 10 cm) of pyrrhotite-rich massive sulfide recovered from top of sulfide mound. Surfaces weathered to Fe oxide. Total weight 15.34 kg.
	(3) X:58114, Y:53223	3277	
			3: Two angular fragments (the larger 15 cm × 10 cm × 7 cm) of pyrrhotite-rich massive sulfide from weathered sulfide mound. Total weight 1.33 kg.
ALV2036	Active 217°C vent site on northwest flank of central hill at NESCA		1A: Large angular block (28 cm × 25 cm × 18 cm, 18.9 kg) of pyrrhotite-rich massive sulfide coated by Fe oxide.
			1B: Five angular fragments of vuggy massive sulfate (barite and anhydrite) with minor sulfide (mostly marcasite and sphalerite). Total weight 1.77 kg.
	(1) X:58848, Y:55399	3234	
	(2) X:58832, Y:55400	3228	
			1C: Sixteen small angular fragments (the largest has dimensions 7 cm × 5 cm × 3 cm) of porous massive sulfate, mostly barite with minor anhydrite and oxidized Fe sulfide. Total weight 0.28 kg.
			1D: Miscellaneous sulfate-rich and sulfide rubble (0.46 kg).
			2: Eight fragments of massive sulfate with numerous drusy cavities. Barite and anhydrite are equally abundant; minor marcasite. Several of the sulfate fragments contain equant clasts of pyrrhotite-rich massive sulfide. Total weight 5.89 kg.
ALV2037	Northwest flank of central hill at NESCA near ALV2036		1A: Blocky fragment (18 cm × 15 cm × 10 cm, 6.21 kg) of pyrrhotite-rich massive sulfide with local concentrations of Cu-Fe sulfide and barite. Surface is partly covered with dark red Fe oxide.
	X:58836, Y:55376	3217	
			1B: Angular dense fragment (15 cm × 13 cm × 7 cm) of pyrrhotite-rich massive sulfide. Some surfaces are encrusted by a thin rind of orange-red Fe oxide. Estimated weight is 5 kg.

Table 16.1. Location and description of hydrothermal samples from Escanaba Trough—Continued

Station or dive number	Location	Depth (m)	Sample number and description
		Samples Collected by DSV *Alvin*—Continued	
ALV2038	South flank of sediment-covered hill approximately 9 km north of central hill at NESCA		1: Two arcuate slabs (12 cm × 7 cm × 8 cm and 10 cm × 6 cm × 5 cm) of pyrrhotite-rich massive sulfide from an inactive sulfide mound. Much of the pyrrhotite is altered to marcasite; weathered surfaces have 1 to 3 mm thick crusts of earthy, orange-red Fe oxide. Barite is abundant in cavities. Total weight 0.65 kg.
	(1) X:58785, Y:65250	3264	
	(2) X:59020, Y:65280	3268	2: One large fragment (38 cm × 20 cm × 18 cm) and 11 smaller pieces of pyrrhotite-rich massive sulfide; pyrrhotite is coarse grained in cavities. Total weight 15.80 kg.
	(3) X:59020, Y:65280	3268	3: Columnar fragment of pyrrhotite-rich sulfide, 30 cm long and 18 to 23 cm in diameter (10.62 kg), possibly part of a chimney. Deeply weathered regions on the sample surface may mark sites of side spouts. Oxidized surface contains abundant sponge spicules.
ALV2039	Small hill 1.2 km northeast of ALV2038		3: Elongate block (13 cm × 8 cm × 5 cm, 0.43 kg) of pyrrhotite-rich massive sulfide with abundant Cu-Fe sulfides.
	(3) X:60082, Y:65643	3212	4A: Arcuate slab (15 cm × 10 cm × 4 cm, 0.43 kg) of massive sulfide largely consisting of chalcopyrite and sphalerite.
	(4) X:60128, Y:65582	3199	
	(5) X:60201, Y:65500	3215	4B: Rounded elongate fragment (12 cm × 9 cm × 7 cm, 0.67 kg) of pyrrhotite-rich massive sulfide with earthy yellow to red Fe-oxide crust.
			5: Angular block (14 cm × 10 cm × 9 cm, 1.38 kg) of pyrrhotite-rich massive sulfide with numerous cavities and layered structure. Sample surfaces partly covered with red Fe oxides and black sooty Mn (?) oxide.
ALV2040	Active vent area on upper eastern flank of central hill at NESCA		1: Irregular angular block (23 cm × 17 cm × 15 cm, 3.86 kg) of pyrrhotite-rich massive sulfide with a 2-cm-thick drusy crust of barite and amorphous silica on one edge.
	(1) X:59179, Y:54879	3231	2: Conical sulfate-rich (predominantly barite with minor sphalerite and Fe sulfide) fragment (26 cm × 18 cm × 10 cm, 2.99 kg) with numerous worm tube structures and cavities.
	(2) X:59179, Y:54879	3231	
	(4) X:59179, Y:54879	3231	4: Vuggy fragment (14 cm × 9 cm × 7 cm, 0.21 kg) of massive sulfate (barite with minor sphalerite and Fe sulfide) with closely spaced worm tubes. Many of the tubes are partly filled with barite.
ALV2041	Active vent area on upper northwestern flank of central hill at NESCA		1: Porous, Fe-oxide-covered slab (13 cm × 10 cm × 3 cm, 0.24 kg) of massive sulfate composed of barite and minor sulfide with numerous vugs and worm tube structures.
	(1) X:58834, Y:55402	3219	
ALV2042	Active vent area on upper eastern flank of central hill at NESCA		1: Nearly equidimensional block (21 cm × 17 cm × 17 cm, 9.81 kg) of pyrrhotite-rich massive sulfide with minor sphalerite, Cu-Fe sulfide, and barite.
	(1) X:59249, Y:54937	3226	
		Gravity Cores	
L1-86-27G	Sediment plain midway between SESCA and NESCA		Sediment core with pyrrhotite along fractures cutting sand layers in the interval 72 cm to 105 cm (base of core). Talc nodules are dispersed through sand and silt layers.
	X:11698, Y:26586	3309	
L2-86-9G	Sediment plain 2.5 km southwest of 3170 hill at SESCA		Sediment core with layer of pyrrhotite-rich massive sulfide fragments (50 to 77 cm) between surface layer of reddish-brown metalliferous mud and underlying chlorite-rich sediment (77 to 200 cm).
	X:9756, Y:12209	3240	
TUL89D-8G	Approximately 30 m southwest of the active 220°C vent site on the central hill at NESCA		The core recovered a 10-cm-long, cylindrical fragment of pyrrhotite-rich massive sulfide, 1 to 2 cm of sulfide rubble, and small pieces of lithified and altered sediment from the top of a sulfide mound. The sulfide rubble includes fragments of pyrrhotite-rich massive sulfide and polymetallic aggregates of barite, sphalerite, galena, and pyrite.
	X:58806, Y:55393	3240	

SULFIDE-DOMINANT DEPOSITS

Massive sulfide samples are grouped according to their mineralogy and texture into pyrrhotite-rich and polymetallic types. The mineralogy of these sulfide types is summarized in table 16.2.

PYRRHOTITE-RICH MASSIVE SULFIDE

Massive sulfide composed of 50 to 85 percent pyrrhotite appears to form the bulk of sulfide mounds. Open fissures and slump blocks reveal that pyrrhotite-rich sulfide extends at least 1 m below the oxidized mound surfaces.

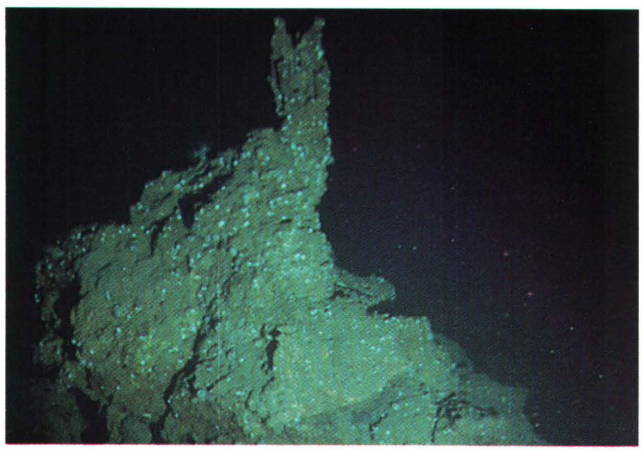

A

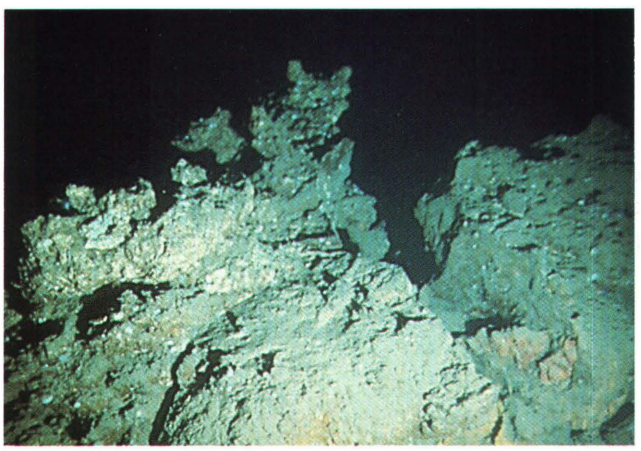

B

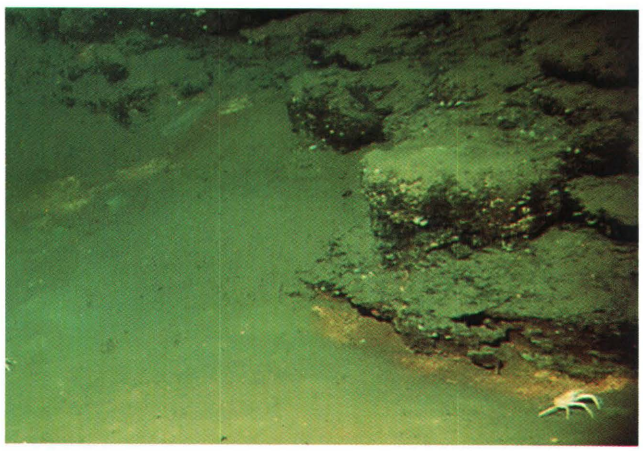

C

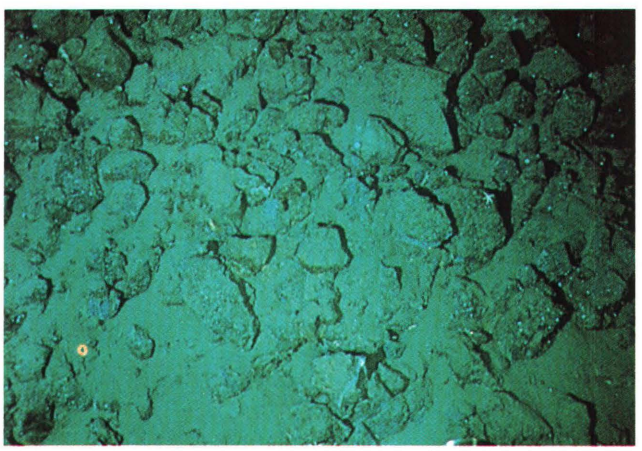

D

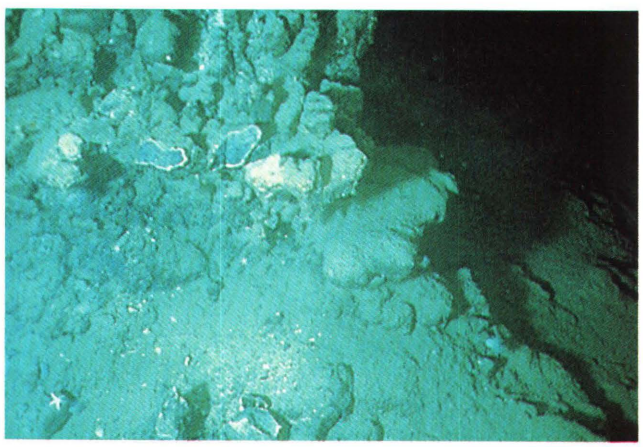

E

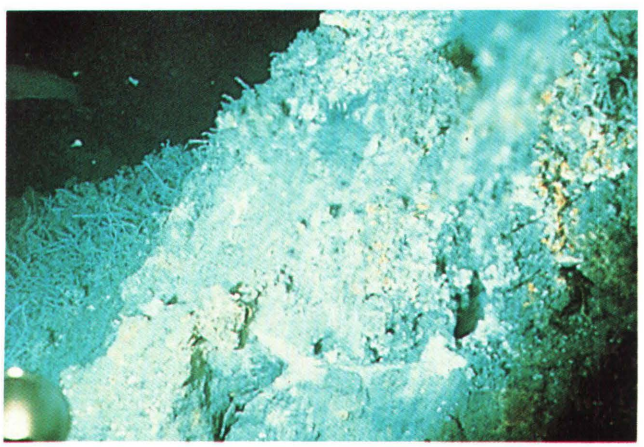

F

Most samples of this sulfide type are derived from talus blocks or rubble (fig. 16.4*A*), but a massive sulfide chimney (sample SC659-R1) is also included in this group (fig. 16.4*B*). The surfaces of pyrrhotite-rich samples typically are weathered and mantled by iron oxides; some have surfaces covered with massive talc.

The characteristic texture of this sulfide type is a latticework of interpenetrating, randomly oriented pyrrhotite grains in which interstices are partly filled by other sulfide minerals, sulfate minerals, sulfur, or iron oxides (fig. 16.5*A*). The porosity of unaltered samples varies between 10 and 20 percent. Pyrrhotite aggregates have a radial orientation and coarser grain size (to 1.5 mm) around fluid channelways. Individual pyrrhotite grains have a platy morphology, and hexagonal tablets are abundant in cavities. X-ray diffraction analysis identified only the hexagonal polymorph of pyrrhotite (Arnold, 1966); the metal content (Fe + Cu + Co + Ni), determined from the *d*-spacing of the (102) reflection (Arnold and Reichen, 1962), ranges between 47.5 and 48.7 atom percent.

Pyrrhotite generally exhibits some degree of alteration to marcasite or iron-oxide minerals (Koski and others, 1988). This alteration can vary considerably on the scale of a single thin section; in many samples, pyrrhotite is completely pseudomorphed by secondary minerals. In the least altered samples, marcasite forms discrete selvages along cracks and grain margins (fig. 16.5*B*). With increasing alteration, remnant cores of pyrrhotite are enclosed by marcasite or an anisotropic iron-sulfide phase that has lower reflectivity and is pale brownish-gray. This "intermediate product" may be marcasite with anomalous optical properties owing to poor crystallinity or nonstoichiometry (Fleet, 1978). Where alteration is complete, the entire grain is pseudomorphed by marcasite, or the outline of the grain is filled by dull earthy mixtures of iron oxides including goethite and lepidocrocite. In a few grains, the cores of pyrrhotite grains are replaced by covellite (fig. 16.5*C*). Dark zones in the altered pyrrhotite grains may also be related to void space created by the negative volume change in the pyrrhotite → marcasite reaction (Fleet, 1978; Murowchick and Barnes, 1986). Koski and others (1988) attributed the formation of marcasite to an oxidative late-stage hydrothermal alteration of pyrrhotite.

The second most abundant mineral (5 to 50 percent of the mode) is the cubic polymorph of cubanite, now officially named isocubanite (Caye and others, 1988), which occurs as equant blebs occupying the corners of interstices in the latticework of pyrrhotite grains (fig. 16.5*A*). Isocubanite grains typically enclose an orthogonal arrangement of spindle-shaped chalcopyrite lamellae and are usually rimmed by the same mineral (fig. 16.5*D*). This texture has been documented in other sea-floor sulfide deposits (Haymon and Kastner, 1981; Styrt and others, 1981; Oudin and others, 1981; Koski and others, 1984) and may form by the combination of unmixing of chalcopyrite from a primary grain of intermediate solid solution (iss) composition and marginal replacement of isocubanite by chalcopyrite. Isocubanite has been obtained synthetically by transformation of the orthorhombic polymorph of $CuFe_2S_3$ above 200°C; annealing recrystallization below the 200°C inversion point resulted in exsolution of chalcopyrite (Cabri and others, 1973).

Sphalerite is ubiquitous in pyrrhotite-rich sulfide, but is generally less abundant (1 to 5 percent of the sample) than isocubanite. It is concentrated along cavities and fluid channelways and on the outer surfaces of pyrrhotite-rich sulfide fragments, where it is associated with barite and galena. Sphalerite typically forms subhedral crystals occupying interstices between pyrrhotite grains and also occurs as overgrowths on isocubanite (fig. 16.5*A, D*); the reverse relationship in which tiny grains of isocubanite-chalcopyrite have grown on the surface of sphalerite is less common. Intergrowths of isocubanite-chalcopyrite and sphalerite form embayments in pyrrhotite. Sphalerite is generally opaque because of partial replacement by very fine grained Cu-Fe sulfide (Barton and Bethke, 1987). These textural relations indicate that sphalerite and Cu-Fe sulfides are, in large part, coprecipitated, and both are paragenetically later than pyrrhotite. This textural relation between pyrrhotite, Cu-Fe sulfides, and sphalerite is also recognized in massive sulfide samples from Guaymas Basin (Koski and others, 1985; Peter and Scott, 1988).

⇐

Figure 16.3. Examples of sea-floor hydrothermal deposits in Escanaba Trough. *A*, Inactive sulfide mound and 1-m-high sulfide chimney at NESCA site. Organisms include anemones and sponges. Photographed from submersible DSV *Alvin* by R.A. Zierenberg. *B*, Craggy, steep-sided sulfide mound topped by eroded sulfide chimneys at NESCA site. Height of mound and chimneys in field of view is approximately 3 m. Photographed from submersible DSV *Alvin* by R.A. Zierenberg. *C*, Flat-lying ledges of partly oxidized massive sulfide overlapped by sediment at NESCA site. Prominent sulfide ledge at right center is approximately 0.5 m thick. Note several white galatheid crabs on sediment and sulfide outcrop. Photographed from submersible DSV *Sea Cliff* by R.A. Zierenberg. *D*, DSV *Alvin* external photograph showing talus blocks of massive sulfide resting on steep flank of sulfide mound at NESCA site. Sediment infills spaces between blocks and forms thin coating on some fragments. Largest blocks are approximately 0.5 m across. *E*, DSV *Alvin* external photograph showing cluster of knobby, barite-rich chimneys projecting upward from massive sulfide mound at NESCA. Two elongate broken surfaces with white rims mark location of two chimneys (for example, ALV2033-3; see fig. 16.4*F*) sampled with submersible manipulator. Maximum dimension of base of chimneys is about 0.2 m. *F*, DSV *Alvin* external photograph showing sulfate sinter deposit (white areas) on flank of massive sulfide mound on Central Hill at NESCA. Fluids discharging through sinter (areas of blurred focus) have temperatures as high as 220°C. Vertical extent of sinter in field of view is approximately 3 m.

Table 16.2. Mineralogy of hydrothermal samples from Escanaba Trough

[XXX, abundant; XX, common; X, rare; —, not observed]

Mineral	General formula	Pyrrhotite-rich sulfide	Polymetallic sulfide	Sulfate dominant
	Sulfides			
Pyrrhotite	$Fe_{(1-X)}S$	XXX	XXX	X
Isocubanite	$CuFe_2S_3$	XXX	XXX	X
Chalcopyrite	$CuFeS_2$	XX	X	X
Sphalerite	(Zn,Fe)S	XXX	XXX	XX
Marcasite	FeS_2	XXX	—	XX
Galena	PbS	X	XXX	X
Pyrite	FeS_2	X	—	X
Arsenopyrite	FeAsS	X	XX	—
Löllingite	$FeAs_2$	X	XX	—
Wurtzite	(Zn,Fe)S	—	—	X
Boulangerite	$(Pb,Zn)_5Sb_4S_{11}$	X	X	—
Tetrahedrite	$Cu_{12}SbS_{13}$	—	X	—
Acanthite(?)	Ag_2S	—	X	—
Stannite	Cu_2FeSnS_4	—	X	—
Jordanite	$Pb_{14}As_7S_{24}$	X	X	—
Franckeite	$Pb_5Sb_2Sn_3S_{14}$	—	X	—
Alabandite	MnS	X	—	—
Covellite	CuS	X	—	—
	Sulfates			
Barite	$BaSO_4$	XX	X	XXX
Anhydrite	$CaSO_4$	—	—	XXX to —
Gypsum	$CaSO_4 \cdot 2H_2O$	X	—	XX
	Silicates, oxides, and native elements			
Talc	$Mg_3Si_4O_{10}(OH)_2$	XX	—	X
Stevensite	trioctahedral smectite	—	—	XX
Amorphous silica	$SiO_2 \cdot nH_2O$	X	X	XX
Goethite	FeO(OH)	XX	—	X
Lepidocrocite	FeO(OH)	X	—	—
Mn oxide (amorphous)	?	—	—	X
Sulfur	S	XX	—	X
Native bismuth	Bi	X	X	—
	Other			
Bi telluride	?	X	—	—
Xenotime	YPO_4	X	—	—

In several samples, clusters of small (20 μm) wedge-shaped grains of löllingite appear to overprint pyrrhotite and other sulfide minerals around fluid channelways (fig. 16.5*E*). The löllingite grains contain inclusions of native bismuth approximately 1 to 2 μm across. Microprobe analyses of löllingite yield as much as 7 percent sulfur, indicating the presence of intergrown arsenopyrite (Koski and others, 1988).

Pyrrhotite-rich sulfide samples also contain small amounts of pyrite, galena, lead-arsenic and lead-antimony sulfosalts, barite, amorphous silica, sulfur, hydrocarbons, and iron oxides. In sulfide samples where pyrite is present, it is typically framboidal. In one sample (a fragment of massive sulfide from gravity core TUL89D-8G), however, pyrite and marcasite form anhedral masses enclosing and partly replacing plates of pyrrhotite. The pyrite-marcasite mixture also pseudomorphs crystals with a dendritic or plumose habit, probably barite. Fine-grained galena and sulfosalt minerals such as jordanite and boulangerite occur as isolated grains and aggregates nucleated on the surfaces of coarser grained sulfides (fig. 16.5*F*). Barite typically forms individual tablets or rosettes that project into voids or channelways. Away from channelways, barite is partly replaced by sulfide minerals. Amorphous silica and goethite are present in many samples as a coating on pyrrhotite and isocubanite; in strongly oxidized samples, iron oxide fills interstices between sulfide grains. Yellow-brown asphaltic hydrocarbon in the pore space of pyrrhotite-rich sulfide interlayered with sand turbidite (fig. 16.4*C*) was derived from the hydrothermal alteration of terrigenous

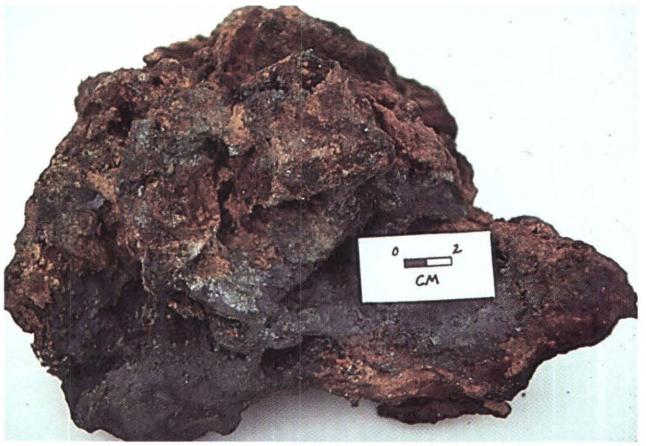

A

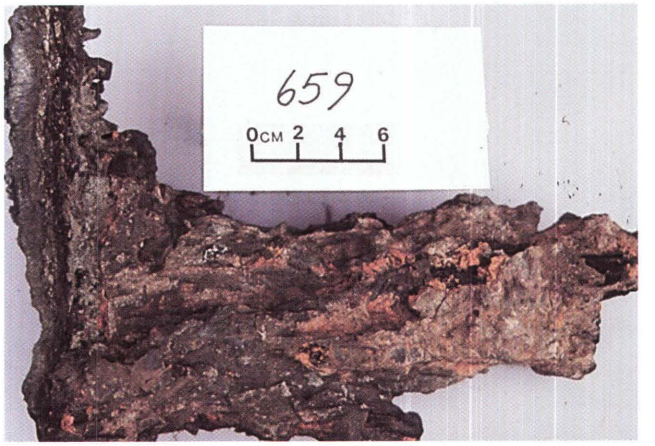

B

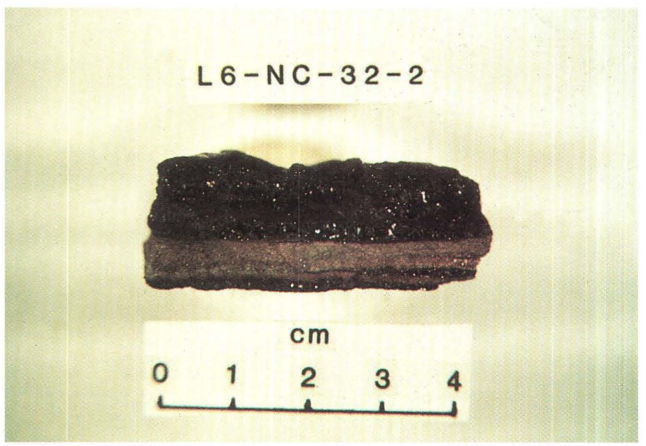

C

D

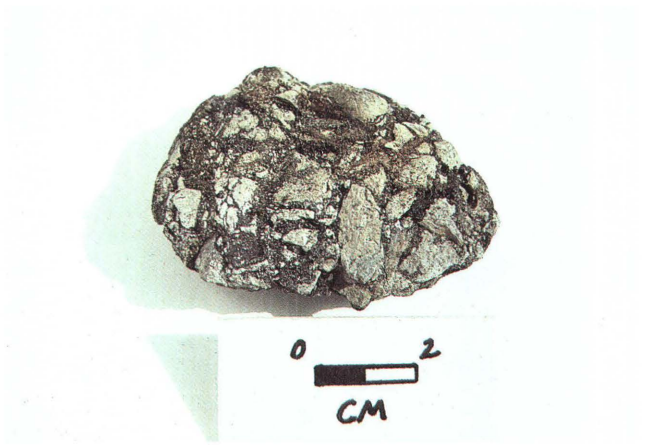

E

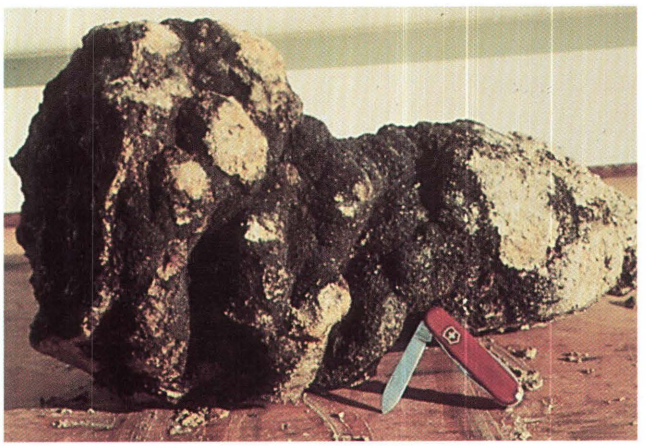

F

Figure 16.4. Hydrothermal deposit types from Escanaba Trough. *A*, Talus fragment of pyrrhotite-rich massive sulfide with iron-oxide coating on weathered surfaces. Sample from dredge L1-86-24D, NESCA site. *B*, Small chimney (sample SC659-R1) composed of pyrrhotite-rich massive sulfide, shown on its side. Basal crust of mineralized sediment is on left. Sample recovered by submersible DSV *Sea Cliff* from NESCA area. *C*, Small fragment of interlayered pyrrhotite-rich massive sulfide and altered sand turbidite (sample L6-85-32D-2) dredged from SESCA site. Sulfide and sediment are saturated with hydrothermal petroleum. *D*, Bowl-shaped fragment of polymetallic massive sulfide, part of chimneylike sulfide structure. Sample L2-86-14D-1, dredged from sediment plain north of Central Hill at NESCA. *E*, Sediment breccia cemented by pyrrhotite-rich sulfide. Sediment fragments are altered to chlorite and talc. Sample from dredge L1-86-15D at SESCA site. *F*, Knobby barite-rich chimney with thin coating of manganese oxide. Sample ALV2033-3, recovered by DSV *Alvin* from NESCA site.

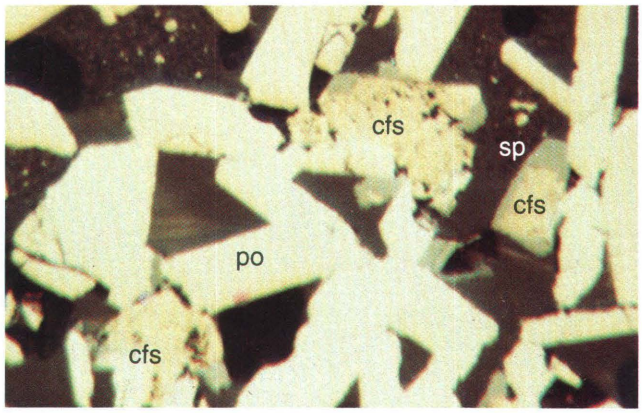

A

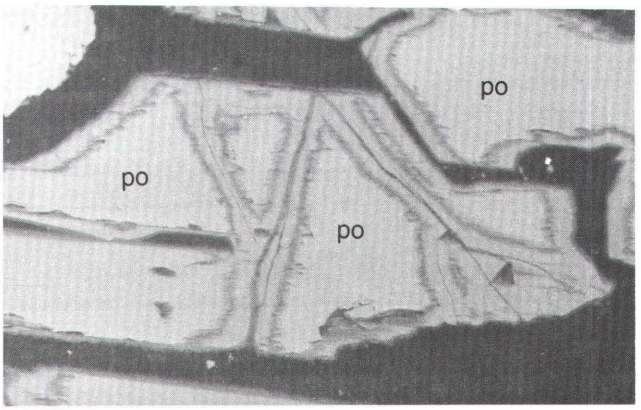

B

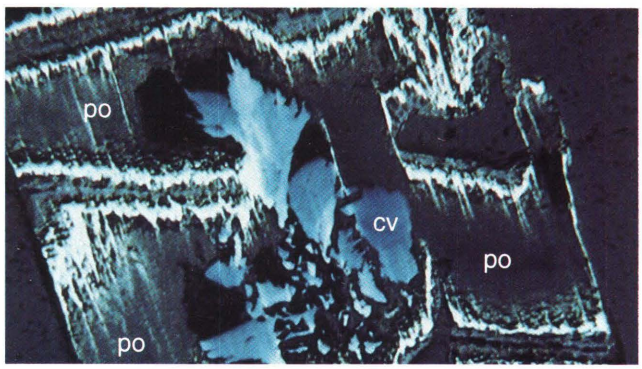

C

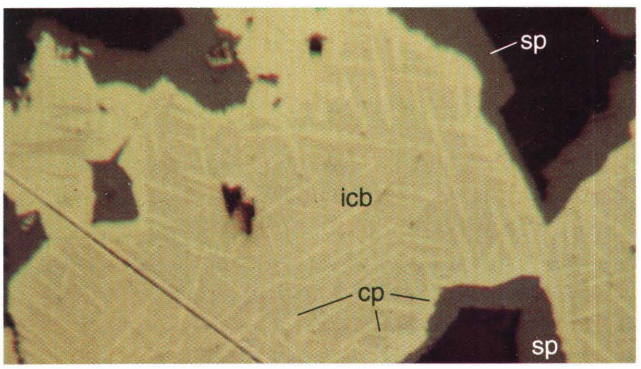

D

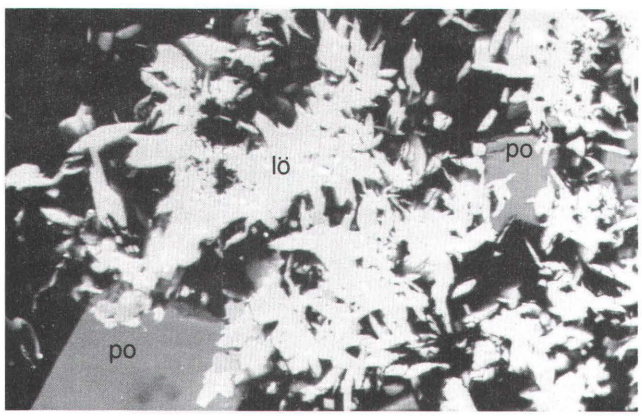

E

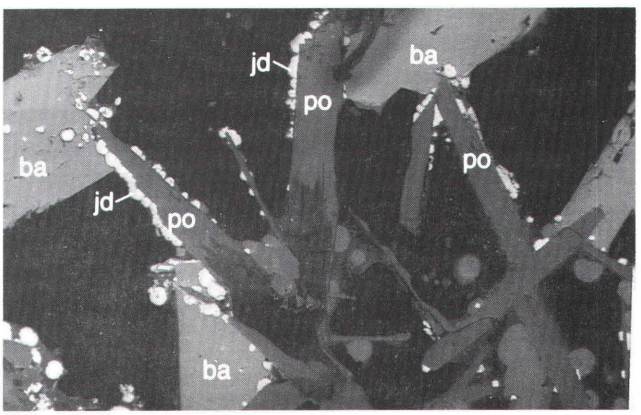

F

Figure 16.5. Petrography of pyrrhotite-rich massive sulfide samples. *A*, Reflected-light photomicrograph (RLP) of sample L6-85-32-25 showing open latticework texture of pyrrhotite (po) plates with interstitial grains of corroded, intergrown Cu-Fe sulfides (isocubanite and chalcopyrite, cfs) and sphalerite (sp). Width of field is 0.25 mm. *B*, Backscattered electron (BSE) image of pyrrhotite grains (po) altered to anisotropic iron sulfide phase ("intermediate product") along grain margins and cracks. Width of field is 0.46 mm. *C*, RLP of altered pyrrhotite grain (po) with core partly replaced by covellite (cv), sample L1-86-15-1A. Width of field is 0.11 mm. *D*, RLP of mixed Cu-Fe sulfide grains in sample L1-86-22-1 in which chalcopyrite (cp) occurs as oriented lamellae within isocubanite (icb) and also rims it. These grains are, in turn, overgrown by sphalerite (sp). Width of field is 0.11 mm. *E*, BSE image of sample L6-85-32-10 showing fine-grained aggregate of wedge-shaped löllingite grains (lö) partly replacing pyrrhotite (po). Small white specks in löllingite are inclusions of native bismuth. Width of field is 0.15 mm. *F*, BSE image of sample ALV2035-1A showing euhedral grains of pyrrhotite (po) and barite (ba) with fine-grained globular overgrowths of jordanite (jd). Width of field is 0.75 mm.

organic matter in the underlying sediment (Kvenvolden and others, 1986, 1990, chap. 15, this volume).

Trace amounts of two bismuth minerals were identified by scanning electron microscope (SEM) examination of sample ALV2039-3 (table 16.1). Tiny (less than 5 μm) anhedral blebs of a bismuth telluride phase form inclusions in grains of isocubanite-chalcopyrite. Equally small anhedra of native bismuth are loosely attached to the surfaces of these Cu-Fe sulfide grains. The SEM analysis also revealed a cluster of xenotime crystals in the interstice between adjacent Cu-Fe sulfide grains. In addition to yttrium and phosphorous, the energy-dispersive X-ray spectrum of the xenotime grains has lines for uranium, silicon, and rare-earth elements.

Subhedral grains of alabandite are present in the basal part of the pyrrhotite-rich chimney sample (SC659-R1; fig. 16.4*B*). The alabandite grains occur within a zone of clastic sediment that also contains interstitial yellow hydrocarbon.

POLYMETALLIC SULFIDE

Approximately 12 kg of dark-gray massive sulfide with a diverse polymetallic mineral assemblage was recovered in a single dredge (L2-86-14D) from the sediment-covered plain north of the Central Hill at NESCA (fig. 16.2*A*). The largest fragment is bowl shaped (fig. 16.4*D*) and exhibits considerable variation in grain size, texture, mineralogy, and chemical composition over a distance of about 40 mm between the concave inner and the convex outer surfaces. Koski and others (1988) interpreted these samples to be fragments of a chimneylike sulfide structure enclosing a large fluid channelway. The textural and structural characteristics of this sample resemble "black smoker" sulfide chimneys formed at sediment-free spreading axes (Haymon and Kastner, 1981; Styrt and others, 1981; Haymon, 1983; Paradis and others, 1988); however, differences in the mineralogy and mineral zonation are readily apparent.

The sulfide structure of sample L2-86-14D-1 is subdivided into inner, middle, and outer wall sections that encompass six separate growth zones (fig. 16.6). The inner wall (zone 1) is a layer of coarse-grained sphalerite and isocubanite 4 to 6 mm thick that forms the concave surface of the sample. The subhedral sphalerite grains contain plumose cores and numerous inclusions of isocubanite (fig. 16.7*A*); these two minerals precipitated directly from hydrothermal fluid within the sulfide structure. Coarse-grained arsenopyrite occurs with pyrrhotite, sphalerite, and isocubanite near the contact with zone 2 (fig. 16.7*B*). These arsenopyrite grains have near-stoichiometric compositions and contain tiny (about 1 μm) inclusions of native bismuth (Koski and others, 1988).

The middle wall of the sulfide structure consists of growth zones 2, 3, and 4. Zone 2 is a 10- to 12-mm-wide layer composed of pyrrhotite + sphalerite + isocubanite + arsenopyrite + löllingite. In this zone, large (to 5 mm) platy pyrrhotite grains with a subparallel orientation extend toward zone 1 from a layer of intergrown sphalerite and isocubanite that mimics the texture of zone 1. Arsenopyrite in the sphalerite-cubanite layer of zone 2 is rimmed by löllingite (fig. 16.7*C*).

Zone 3 is approximately 10 mm wide and mineralogically similar to zone 2. Compared to zone 2, however, the pyrrhotite, arsenopyrite, and löllingite are finer grained. Zone 3 meets zone 4 at an undulating unconformity that truncates pyrrhotite plates in the latter zone. Zone 4 is 6 to 10 mm thick and consists of sphalerite, isocubanite, and pyrrhotite in a textural association similar to zone 2. Mineralogically, this zone is distinct in that it contains abundant galena (in interstices and as a replacement of other sulfides) and much less arsenopyrite and löllingite.

Growth zones 5 and 6 comprise the outer wall. Zone 5 is a dense fine-grained layer of variable thickness (maximum 6 mm) largely composed of dendritic sphalerite intergrown with randomly oriented, stubby plates of pyrrhotite (less than 0.25 mm in length). Isocubanite is present as anhedral blebs in sphalerite dendrites, whereas galena forms overgrowths on sphalerite grains. Compared to zone 4, galena is more abundant, isocubanite is less abundant, and arsenic-bearing phases are much less abundant. This low-porosity zone may represent the original wall of the sulfide structure.

The outermost zone 6 is 1 to 2 mm thick and consists of porous fine-grained masses of dendritic sphalerite intergrown with galena and trace amounts of boulangerite, tetrahedrite, and a silver sulfide mineral, probably acanthite (fig. 16.7*D*; Koski and others, 1988). This zone is also characterized by clusters of extremely thin (less than 5 μm) reedlike plates of pyrrhotite. Locally, these pyrrhotite crystals are nucleation sites for deposition of dendritic sphalerite. The "primitive" texture of zone 6 is the result of rapid crystallization during the mixing of hydrothermal fluid and seawater.

SULFIDE-CEMENTED SEDIMENT AND SEDIMENT BRECCIA

Several dredge hauls contained samples of sediment and sediment breccia with either pyrrhotite-rich or polymetallic sulfide assemblages as cement. Mineralized breccia samples consist of angular pebble-size mudstone and siltstone clasts in a cement composed of pyrrhotite and minor isocubanite (fig. 16.4*E*). The pyrrhotite grains are partly to completely pseudomorphed by marcasite. Corroded blebs of isocubanite within or between altered pyrrhotite grains are rimmed by covellite. In a few samples of this type, the interstitial space in the sulfide cement is partly filled with talc.

A sample (L2-86-14D-6; table 16.1) of coarse sand cemented by polymetallic sulfide was recovered with polymetallic massive sulfide in a dredge from the NESCA site. In the sediment sample, the sulfide matrix encloses well-rounded sand-size clasts composed of altered mudstone (fig. 16.7*E*). The principal minerals in the cement are galena, sphalerite, pyrrhotite, and löllingite; void spaces are coated with hydrothermal petroleum (Koski and others, 1988). Textural relations suggest that the paragenetic sequence is pyrrhotite → sphalerite → galena → löllingite. Isocubanite is relatively minor, occurring as small blebs in sphalerite. The margins of sediment clasts exhibit minor replacement by these minerals, and some clasts contain disseminated cubes of galena. Löllingite occurs as elongate clusters of fine-grained, wedge-shaped crystals that are superimposed on both the sulfide cement and adjacent sand grains.

Two tin-bearing minerals are also present in trace amounts in this sample. Stannite is present as thin lamellae oriented parallel to the margins of coarse subhedral sphalerite grains (fig. 16.7*F*). A tin-bearing sulfosalt mineral, probably franckeite, occurs as clusters of curved platy crystals that typically radiate outward from the edges of pyrrhotite grains.

The clasts in sulfide-cemented sediment breccia and sediment are predominantly indurated mudstone and siltstone that have been partly to completely altered to talc and chlorite (Benninger and Koski, 1987; Zierenberg and Shanks, chap. 14, this volume). A smaller proportion of the sediment is composed of sand- and silt-size grains of quartz, feldspar, muscovite, and pyroxene. Of these detrital mineral grains, only muscovite is altered and replaced by sulfide along cleavage planes.

CLASTIC SULFIDE DEPOSITS

Approximately 27 cm of pyrrhotite-rich massive sulfide with a clastic texture was recovered in core L2-86-9G in the SESCA area (table 16.1; fig. 16.2*B*). The sulfide in-

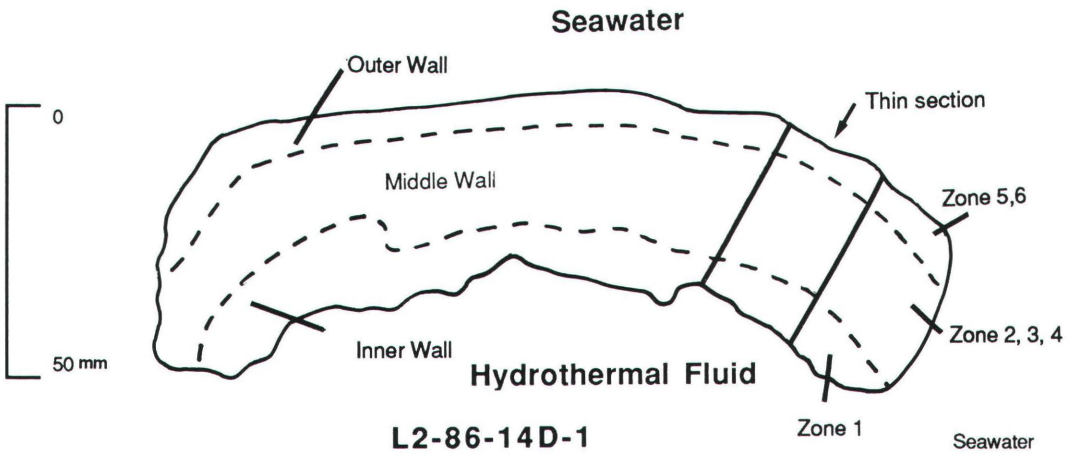

Zone 6 (1 -2 mm)	Porous, fine-grained, dendritic sphalerite with minor disseminated pyrrhotite, galena, boulangerite, and acanthite	Outer Wall
Zone 5 (4-6 mm)	Low-porosity layer of fine-grained dendritic sphalerite with interstitial granular sphalerite, pyrrhotite, and galena.	
Zone 4 (6-10 mm)	Subhedral sphalerite intergrown with isocubanite overlies interior layer of partly altered, radiating, fine-grained pyrrhotite laths. Sphalerite occupies interstices between laths. Galena is disseminated throughout zone.	Middle Wall
Zone 3 (10-12 mm)	Similar to zone 4. Pyrrhotite laths are coarser and are partly replaced by medium-grained sphalerite. Disseminated galena is absent. Arsenopyrite and löllingite are concentrated in two irregular "wavefronts" along outer region of zone.	
Zone 2 (10-12 mm)	Similar to zone 3. Pyrrhotite laths are much coarser grained and are largely replaced by sphalerite. Arsenopyrite-löllingite front coincides with region of intergrown isocubanite and sphalerite.	
Zone 1 (4-6 mm)	Isocubanite intergrown with sphalerite projects toward open interior. Arsenopyrite is concentrated along contact with zone 2.	Inner Wall

Hydrothermal Fluid

Figure 16.6. Cross section of polymetallic sulfide wall (sample L2-86-14D-1) subdivided into inner, middle, and outer wall sections and six distinct mineral zones that formed between hydrothermal fluid and seawater. Location of area studied in polished thin section is also shown.

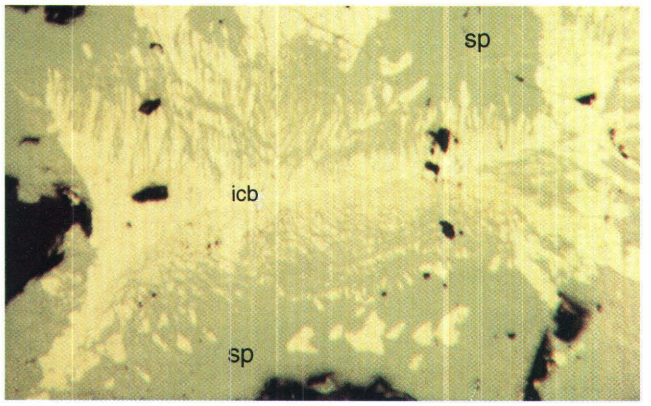

A

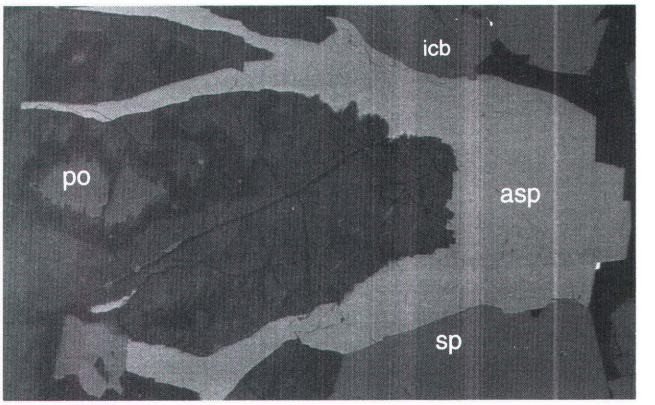

B

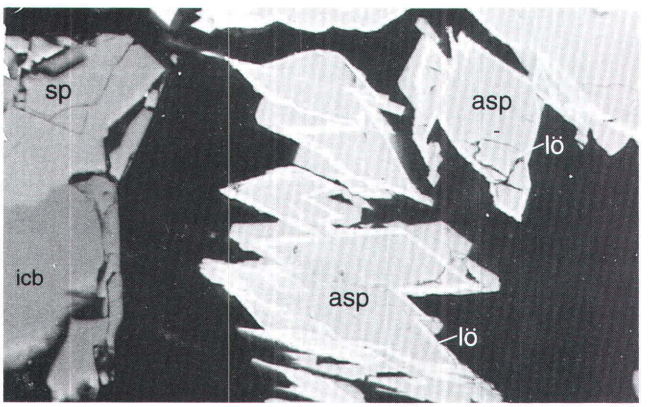

C

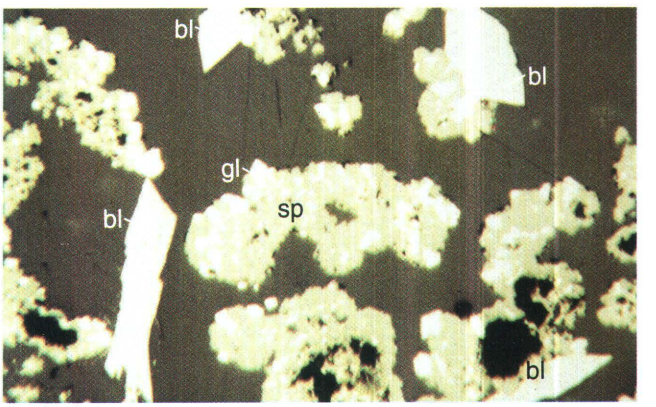

D

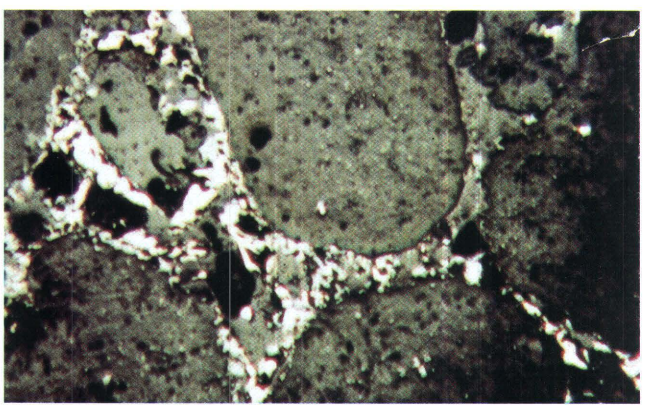

E

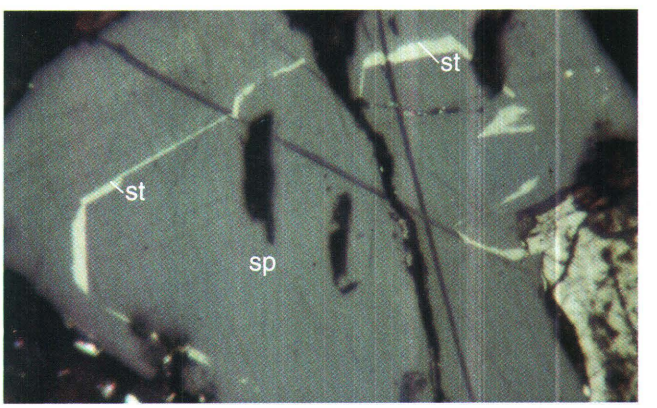

F

Figure 16.7. Petrography of polymetallic sulfide samples. *A*, Reflected-light photomicrograph (RLP) showing subhedral sphalerite grain (sp) with plumose core and numerous inclusions of isocubanite (icb) from inner wall (zone 1) of sulfide sample L2-86-14D-1. Width of field is 0.4 mm. *B*, RLP of inner wall (zone 1) of sample L2-86-14D-1 showing arsenopyrite grain (asp) along contact between altered pyrrhotite (po) and sphalerite (sp). Sphalerite grains contain inclusions of isocubanite (icb). Width of field is 0.5 mm. *C*, Backscattered electron image from middle wall (zone 2) of sample L2-86-14D-1 showing rhombic arsenopyrite grains (asp) with thin rims of löllingite (lö). Sphalerite (sp) and isocubanite (icb) are also present. Black area is void space. Width of field is 0.11 mm. *D*, RLP of outer wall (zone 6) of sulfide structure (sample L2-86-14D-1) showing porous texture and occurrence of boulangerite (bl), sphalerite (sp), and galena (gl). Width of field is 0.2 mm. *E*, RLP of sulfide-cemented sediment (sample L2-86-14D-6) composed of rounded sand grains and interstitial aggregate of pyrrhotite, galena, sphalerite, and löllingite. Width of field is 0.25 mm. *F*, RLP of sulfide-cemented sediment (sample L2-86-14D-6) showing sphalerite grain (sp) that contains narrow oriented intergrowths of stannite (st). Width of field is 0.11 mm.

terval is overlain by reddish-brown metalliferous mud and underlain by chlorite-rich mud and turbidite (Zierenberg and Shanks, chap. 14, this volume). The sulfide clasts are subrounded and consist of a pyrrhotite latticework with interstitial isocubanite-chalcopyrite and barite.

SULFATE-DOMINANT DEPOSITS

BARITE-RICH CRUSTS

Barite-rich crusts as thick as 2 cm occur on the outer surfaces of massive sulfide mounds where they precipitated as discharging hydrothermal fluids mixed with seawater. These drusy encrustations have narrow gradational contacts with the pyrrhotite-rich sulfide substrate. Within the crusts, barite forms bladed aggregates, dendrites, and rosettes with preferred growth orientations outward toward seawater (fig. 16.8*A*). Locally, barite encrustations extend into massive sulfide along fluid passageways where crystals project inward toward hydrothermal fluid. Barite exhibits considerable grain-size variation with maximum crystal dimensions up to 3 mm.

Barite in crusts exhibits a variety of intergrowth and replacement textures with sulfide minerals. In one association, radiating blades of barite are overgrown by colloform sphalerite and granular galena. A less common association is barite overgrown by mixtures of galena, antimony-bearing galena, and jordanite (fig. 16.8*B*). In barite crusts, sphalerite, galena, chalcopyrite, and pyrrhotite exhibit a number of disequilibrium textures and parageneses that reflect rapid variations in fluid composition within the zone of fluid mixing (fig. 16.8*C*). Most barite crusts are covered with thin films of iron oxide and (or) amorphous silica that contain fine-grained sulfosalt phases such as boulangerite and jordanite, granular aggregates of marcasite and pyrite, and rare pyrite framboids.

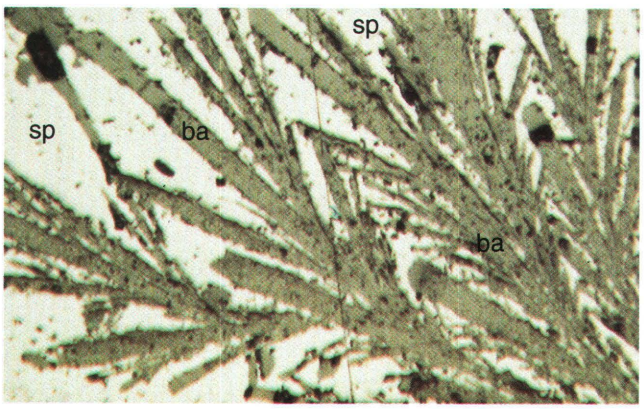

A

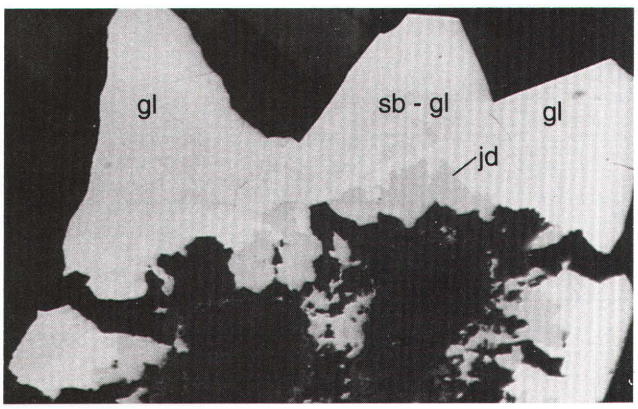

B

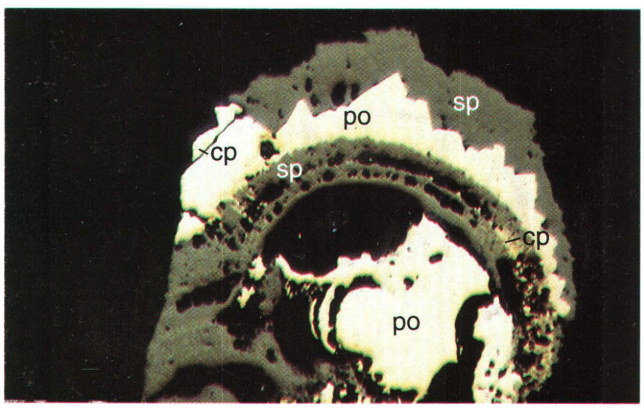

C

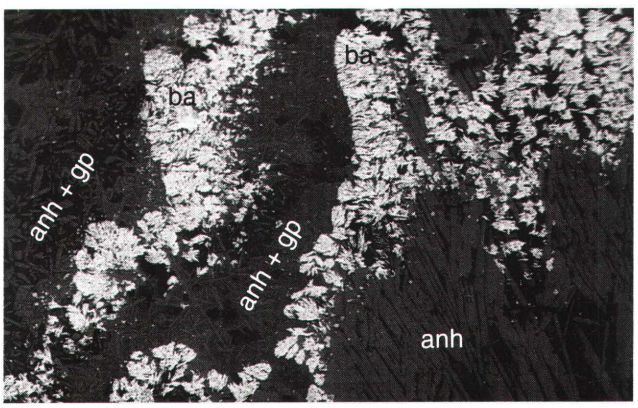

D

Figure 16.8. Sulfate-dominant samples. *A*, Reflected-light photomicrograph (RLP) of barite-rich crust (sample L1-86-24D-3) showing radiating barite blades (ba) overgrown by sphalerite (sp). Width of field is 0.12 mm. *B*, Backscattered electron (BSE) image of composite overgrowth of jordanite (jd) and galena (gl) in barite crust, sample L1-86-16D-2. Dark zones in galena (sb-gl) are enriched in antimony. Width of field is 0.13 mm. *C*, RLP of complex overgrowth paragenesis in barite crust sample L1-86-16D-1 that includes, from core to rim, pyrrhotite (po), sphalerite (sp), chalcopyrite (cp), sphalerite, pyrrhotite, chalcopyrite, and sphalerite. Width of field is 0.25 mm. *D*, BSE showing alternating layers of anhydrite (anh), barite (ba), and anhydrite + gypsum (gp) from sulfate sinter deposit, sample ALV2036-1B. Width of field is 3.6 mm.

BARITE CHIMNEYS

Massive barite chimneys recovered from the tops of hydrothermal mounds and from the sediment surface between mounds are characterized by a porous spongy texture and the absence of mineral zonation around fluid channelways. The chimneys have either a narrow (2 to 4 mm) central fluid conduit or lack any continuous channelways. In sample SC658-1 (table 16.1), dendritic and plumose barite aggregates make up approximately 98 percent of the total mineralogy; in other chimney samples, however, barite is intergrown with variable amounts of sphalerite, galena, marcasite, pyrite, amorphous silica, and native sulfur. The central channelway near the apex of chimney sample ALV2033-2 is composed of barite, amorphous silica, and native sulfur, all of which are stained by petroleum. All of the barite chimneys recovered were hydrothermally inactive and are coated with thin films of amorphous manganese oxide (fig. 16.4*F*).

SULFATE SINTER

Clear fluids with temperatures near 220°C are depositing aprons of sulfate-rich sinter where they discharge through massive sulfide mounds at the NESCA site (fig. 16.3*F*; Campbell and others, chap. 11, this volume). Sinter samples from within the area of active discharge are the youngest materials collected, and they consist of coarse-grained vuggy aggregates of anhydrite, gypsum, barite, and stevensite. Our identification of stevensite, a trioctahedral smectite (Brindley, 1980; Newman and Brown, 1987), was based on its X-ray diffraction pattern and chemical data (high Mg, Si; low Al, Fe) obtained during SEM analysis. Other sinter samples taken a few meters away from a 108°C active vent are predominantly barite but contain local concentrations of marcasite, pyrite, sphalerite, wurtzite, and galena. Textural relations suggest that euhedral sphalerite in the barite-rich samples has formed from transformation of metastable wurtzite. The abundance of tubular structures in barite-rich sinter shows that these deposits serve as a substrate for tube worms and other organisms.

The sinter sample shown in figure 16.8*D* (ALV2036-1B) is constructed from alternating layers of fibrous anhydrite crystals and bladed barite. The anhydrite fibers are as long as 2 cm; gypsum occurs as an infilling within aggregates of anhydrite crystals. The contacts between sulfate layers often truncate earlier-formed sulfate grains and are marked by disseminated fine-grained pyrite and marcasite.

Stevensite occurs in compact semiopaque clusters of birefringent fibers scattered through the sulfate layers. The margins of the stevensite aggregates truncate and embay adjacent sulfate crystals, indicating that it is paragenetically late. Stevensite has also been identified in mound and chimney samples from the hydrothermal vent fields in Guaymas Basin, Gulf of California (Peter, 1986; Peter and Scott, 1988).

Sulfate sinter also contains partly oxidized fragments of pyrrhotite-rich sulfide probably derived from the collapse of nearby mound or chimney material. Stevensite is concentrated between pyrrhotite grains and in narrow rims around the corroded margins of the sulfide fragments.

BULK CHEMISTRY OF DEPOSITS

ANALYTICAL TECHNIQUES

Analytical data for 32 samples of sulfide- and sulfate-dominant deposits, analyzed at two separate laboratories, are presented in tables 16.3, 16.4, and 16.5. At the U.S. Geological Survey, SiO_2, CaO, MgO, Al_2O_3, Fe, Cu, Pb, Zn, Au, Bi, Cd, Hg, Sb, Se, Sr, and Tl were analyzed by quantitative direct current arc optical emission spectroscopy; As, Ag, Ba, Mn, Sn, Co, Cr, Ge, Ni, V, and Y by semiquantitative emission spectroscopy; and total S and C using combustion techniques combined with infrared detector (comb-IR). Organic carbon was determined by subtracting carbonate carbon, analyzed by coulometric titration, from total carbon. Arsenic greater than 0.2 weight percent was analyzed by inductively coupled plasma-atomic emission spectrometry (ICP-AES). At the Geological Survey of Canada, SiO_2, CaO, MgO, Al_2O_3, Fe, Cu, Pb, Zn, Ba, Ag, Co, Cr, Mn, Mo, Ni, Sr, and V were determined by ICP-AES; As, Bi, Mo, Sb, and Se by atomic absorption spectrometry; total S by comb-IR; Au by a combined fire assay/DC plasma method; and Sn by ICP-mass spectrometry. Sulfate sulfur (reported as SO_3) was calculated as a proportion of the total sulfur according to the ratio of sulfate cations (Ba + Ca) to sulfide cations (Fe + Cu + Zn + Pb). Because the complete dissolution of barite is difficult during routine laboratory analysis, the Ba and total S contents reported here should be considered minimum values. The low totals in many samples are also related to the presence of additional volatiles (especially H_2O) and the partial oxidation of sulfides.

SULFIDE-DOMINANT SAMPLES

The analytical results for 26 sulfide-dominant samples are presented in table 16.3. In addition to abundant Fe and S, pyrrhotite-rich massive sulfide samples have high Cu contents (average 3.12 percent), the highest being 20.6 percent for a NESCA mound sample (ALV2039-3). The Cu-Zn-Pb(×10) ratios of sulfide-dominant samples from Escanaba Trough are plotted in the ternary diagram of figure 16.9*A*. The Cu-to-Zn ratio exceeds unity in 18 of 23 pyrrhotite-rich samples, although Zn ranges between 0.02

Table 16.3. Bulk composition of sulfide-dominant samples.

[USGS, U.S. Geological Survey; GSC, Geological Survey of Canada; NA, not analyzed; <, less than; >, greater than; —, interference from other elements]

	Pyrrhotite-rich sulfide							
Sample	L1-86 16D-1	L1-86 24D-1	L1-86 24D-1	L1-86 24D-16-3	L1-86 24D-16-2	L2-86 18D	L2-86 25D	ALV 2033-1
Laboratory	USGS	USGS	GSC	GSC	GSC	USGS	USGS	GSC
Weight percent:								
Fe	33.3	42	41.5	35.2	40.1	35.2	57	27.5
Cu	4.62	1.21	2.90	.78	.72	1.01	.42	1.2
Zn	2.3	.34	.08	.13	.16	.07	.11	4.6
Pb	.65	.2	.02	.21	.20	<.02	<.02	.12
As	.2	.03	.001	.027	.25	.55	<.02	.42
BaO	3.01	.04	.12	.02	.20	<.0006	.004	.010
S	35.33	45.16	39.00	40.48	14.04	42.1	36.6	39.19
SO_3	5.43	.10	.24	.01	.15	.00	.00	.03
SiO_2	.95	<.02	.40	.19	4.7	<.02	.34	.20
CaO	.025	.02	.11	.08	.25	.036	.01	.07
MgO	.07	.11	.14	.11	.71	.12	.05	.10
Al_2O_3	<.02	<.02	.03	.03	.17	<.02	.16	.06
Total	86.91	89.25	84.54	77.30	61.65	79.15	94.73	73.50
Parts per million:								
Ag	67.5	14	8	4	2	<3	<3	33
Au	1.4	<.02	.74	.04	.16	<.2	<.02	<.003
Bi	44	25	43	29	20	27	12	13
Cd	270	4.4	NA	NA	NA	4.8	4.5	NA
Co	500	10	460	220	120	2	<2	5
Cr	<2	<2	<1	<1	<1	<2	<2	<1
Ge	15	<2	NA	NA	NA	<2	<2	NA
Hg	<2	<2	NA	NA	NA	<2	<2	NA
Mn	50	100	<100	230	160	7	7	230
Mo	NA	NA	45	20	275	NA	NA	<2
Ni	7	2	<1	13	<1	1.5	1.5	15
Sb	530	24	4	21	262	132	172	130
Se	95	180	72	194	25	525	380	179
Sn	70	300	115	28	9	500	200	620
Sr	130	<50	6	6	91	<50	<50	4
V	<2	<2	<2	<2	75	<2	<2	4
Y	<10	<10	.1	.1	1.8	<10	<10	.3
Total C (wt. pct.)	.14	.32	NA	NA	NA	.13	.11	NA
Organic C (wt. pct.)	.14	.32	NA	NA	NA	.13	.11	NA

and 5.9 percent. The amount of Pb is generally subordinate to Zn in pyrrhotite-rich sulfide, but exceeds 1 percent in two samples (ALV2039-4A and ALV2039-5B). Figure 16.9*B* shows that pyrrhotite-rich sulfide samples have a higher Cu-to-Zn ratio and a larger proportion of Pb relative to Cu and Zn than massive sulfide samples from sediment-free spreading axes of the northeast Pacific Ocean and the Mid-Atlantic Ridge, as well as from Middle Valley, the sediment-covered northern segment of Juan de Fuca Ridge.

The average Au content for 23 samples of pyrrhotite-rich sulfide is approximately 2 ppm; the highest Au value of 10.1 ppm occurs in the Cu-rich sample ALV2039-3. The association of gold and copper in some pyrrhotite-rich samples, evident in table 16.3, is contrary to the commonly observed association of gold in sea-floor sulfide samples enriched in zinc and lead (Hannington and Scott, 1990). It is also apparent from the ternary Cu-Zn-Au($\times 10^4$) diagram of figure 16.9*C* that pyrrhotite-rich samples from Escanaba Trough are enriched in gold relative to sulfide samples from sediment-free spreading axes as well as Middle Valley.

The pyrrhotite-rich massive sulfide samples from Escanaba Trough also contain high As (to 1.55 percent, average 0.31 percent), Bi (to 820 ppm, average 83 ppm), Co (to 3,000 ppm, average 571 ppm), Sb (to 749 ppm, average 167 ppm), and Se (to 525 ppm, average 142 ppm). Of these, As, Bi, Sb, and Se are considerably enriched in comparison to deposits from sediment-free ridges (see, for

Table 16.3. Bulk composition of sulfide-dominant samples—Continued.

	Pyrrhotite-rich sulfide						
Sample	ALV 2033-5A	ALV 2033-5B	ALV 2035-1A	ALV 2035-2	ALV 2037-1A	ALV 2037-1B	ALV 2038-2A
Laboratory	GSC	GSC	GSC	GSC	GSC	GSC	GSC
Weight percent:							
Fe	40.5	26.4	31.0	54.9	50.6	51.2	31.9
Cu	1.6	3.3	3.0	1.8	2.3	2.6	2.3
Zn	1.2	.61	2.7	.02	.025	.025	.038
Pb	.027	.0007	.34	.002	.0005	.001	.004
As	.171	.609	.932	.008	.049	.052	.091
BaO	6.4	6.5	11.2	.02	.06	.04	.004
S	27.6	29.3	20.2	38.4	36.0	37.0	36.6
SO_3	9.1	14.0	13.7	.03	.09	.05	0
SiO_2	1.68	.25	.35	.2	.24	.19	.23
CaO	.10	.14	.2	.1	.08	.07	.1
MgO	.04	.10	.09	.05	.03	.03	.07
Al_2O_3	.06	.04	.07	.03	.03	.03	.03
Total	88.38	81.22	83.74	95.55	89.46	91.37	71.37
Parts per million:							
Ag	25	60	52	2	9	10	13
Au	1.29	3.20	8.89	1.58	1.08	1.44	1.16
Bi	25	43	820	73	54	66	25
Cd	NA	NA	NA	NA	NA	NA	NA
Co	320	320	3,000	1,200	1,000	510	660
Cr	<1	<1	110	<1	<1	<1	130
Ge	NA	NA	NA	NA	NA	NA	NA
Hg	NA	NA	NA	NA	NA	NA	NA
Mn	<100	<100	100	100	100	<100	230
Mo	2	3	17	47	24	7	14
Ni	<3	<3	<3	12	4	6	61
Sb	73	79	296	4	5	4	12
Se	22	3.6	3	139	108	81	164
Sn	15	23	405	22	6	8	40
Sr	110	120	500	4	5	3	3
V	<2	3	24	<2	<2	<2	2
Y	.1	.1	.1	1.5	NA	.7	1.4
Total C (wt. pct.)	NA	NA	NA	NA	NA	NA	NA
Organic C (wt. pct.)	NA	NA	NA	NA	NA	NA	NA

example, Bischoff and others, 1983). High arsenic is consistent with the presence of arsenopyrite and löllingite, and high bismuth with the presence of native bismuth and bismuth telluride phases in samples of this type. The barium and strontium contents are proportional to the amount of barite present in the pyrrhotite-rich samples.

The polymetallic sulfide samples from dredge L2-86-14D have a high Zn-to-Cu ratio and are enriched in lead relative to pyrrhotite-rich sulfide deposits at Escanaba Trough and sulfide deposits from other ridge axes (fig. 16.9*A,B*). High arsenic, antimony, silver, and tin contents are consistent with their diverse mineral assemblages. It is noteworthy that gold is not concentrated in the polymetallic sulfide samples (fig. 16.9*C*). The polymetallic massive sulfide sample L2-86-14D-1 has the highest Ag (681 ppm) and sample L2-86-14D-2 has the highest Zn (42.6 percent) among all of the bulk samples analyzed (table 16.3).

Chemical data for representative samples of the inner, middle, and outer walls of the polymetallic sulfide structure (L2-86-14D-1) are presented in table 16.4 and illustrated in figure 16.10. The sample is strongly zoned: Pb, Sb, Ag, Ba, Sn, and Hg increase and As, Cu, Cd, Se, Bi, and Mn decrease between the inner, high-temperature surface (growth zones 1 and 2) and the outer, low-temperature surface (growth zones 5 and 6). The largest increases from inner to outer walls are for lead (15 times), silver (20 times), antimony (33 times), and tin (20 times). Arsenic is greatly enriched in this sample and is more abundant than copper in the inner and middle walls. Although silver is concentrated to a high level in the sample, especially in the outer wall (3,000 ppm), gold was not detected at the 0.1 ppm level.

Table 16.3. Bulk composition of sulfide-dominant samples—Continued.

	Pyrrhotite-rich sulfide							
Sample	ALV 2039-3	ALV 2039-4A	ALV 2039-5B	SC 658-R3	SC 658-R4	SC 659-R1	SC 662-R1	TUL 89-G8
Laboratory	GSC	GSC	GSC	USGS	USGS	USGS	USGS	GSC
Weight percent:								
Fe	25.5	30.3	43.6	48.1	52.5	17.9	48.2	38.8
Cu	20.6	1	1.7	.55	2.06	7.7	2.22	2.3
Zn	1.2	5.9	4.8	.61	.12	1.38	2.05	3.0
Pb	.34	1.1	1.1	.07	.08	.26	.35	.16
As	.162	1.55	.476	<.02	<.02	.2	.05	.29
BaO	.030	2.3	.75	.80	.01	.26	.3	4.7
S	37.1	37.3	32.7	39.5	38.8	53.8	35.2	27.7
SO_3	.05	5.1	1.1	1.4	.03	1.1	.50	6.6
SiO_2	.2	2.02	.22	.35	<.02	1.86	<.02	8.2
CaO	.06	.07	.08	.02	.01	.14	.02	.20
MgO	.04	.05	.06	.07	.04	.17	.06	1.23
Al_2O_3	.02	.03	.04	<.02	<.02	.76	<.02	1.51
Total	85.28	86.73	86.56	91.57	93.7	85.51	89.02	94.62
Parts per million:								
Ag	160	170	150	15	15	150	150	73
Au	10.14	3.27	2.94	<.1	<.1	2.20	<.1	1.11
Bi	125	8	54	57	53	68	22	102
Cd	NA	NA	NA	16	6	47	67	NA
Co	890	210	370	500	300	700	700	410
Cr	1	3	<1	<2	<2	2	<2	32
Ge	NA	NA	NA	<2	<2	<2	30	NA
Hg	NA	NA	NA	<2	<2	<2	51	NA
Mn	<100	100	100	100	15	300	15	200
Mo	51	<2	16	—	—	—	—	17
Ni	34	<3	<3	5	5	30	10	<3
Sb	69	749	521	8	17	200	140	162
Se	130	88	148	71	<10	324	<10	67
Sn	60	NA	63	<2	<2	30	20	96
Sr	3	37	40	100	3	30	90	130
V	6	3	<2	<2	<2	<2	<2	43
Y	.2	NA	.9	10	10	<10	10	2.4
Total C (wt. pct.)	NA	NA	NA	<.18	<.18	1.38	<.24	NA
Organic C (wt. pct.)	NA	NA	NA	.05	.09	—	—	NA

The sample of clastic sediment (L2-86-14D-6) with polymetallic sulfide cement has the highest Pb (13.7 percent), As (2.75 percent), Mn (7,000 ppm), Sb (8,700 ppm), and Sn (>1,500 ppm) among the samples analyzed, and also contains high Zn (table 16.3). The high organic carbon content (2.24 percent) is related to the presence of hydrothermally derived petroleum that coats interstices between sediment and sulfide grains.

SULFATE-DOMINANT SAMPLES

Analytical data for representative sulfate-dominant samples are presented in table 16.5. The barite-rich crust and chimneys are characterized by high Ba-to-Ca ratios, which is consistent with the absence of anhydrite in these samples. The presence of amorphous silica in all crust and chimney samples results in silica contents greater than 1 percent. The barite-rich crust and two of the chimney samples also contain high zinc, lead, and silver. The high zinc contents and Zn-to-Fe ratios in samples SC766-1 and ALV2033-3B indicate that the sphalerite present has a low iron content. The barite-rich crust has the highest Y (30 ppm) and Ge (150 ppm) contents of all the hydrothermal samples analyzed. The nearly monomineralic barite chimney (SC658-R2) is depleted in metals (for example, Fe + Cu + Zn + Pb <1.5 percent and Ag = 2 ppm), but mercury, manganese, and vanadium are enriched relative to other sulfate-rich and most sulfide samples. The high concentration of strontium in this sample results from its substitution for barium in barite.

Samples of sulfate sinter have distinct calcium-rich, barium-poor or barium-rich, calcium-poor compositions,

Table 16.3. Bulk composition of sulfide-dominant samples—Continued.

	Polymetallic massive sulfide		Polymetallic sulfide cement
Sample	L2-86-14D-1	L2-86-14D-2	L2-86-14D-6
Laboratory	USGS	USGS	USGS
Weight percent:			
Fe	33.1	17.9	22.9
Cu	1.82	.99	.26
Zn	20.3	42.6	7.1
Pb	7.6	1.05	13.7
As	1.7	2.5	2.75
BaO	2.8	.01	.39
S	31.4	32.7	23.8
SO_3	3.1	.01	.5
SiO_2	<.02	.34	13.8
CaO	.016	.028	.038
MgO	.05	.09	.25
Al_2O_3	<.02	.11	3.40
Total	101.89	99.13	88.87
Parts per million:			
Ag	681	184	339
Au	<.2	<.2	<.2
Bi	40	64	9.7
Cd	630	1,975	150
Co	<2	<2	3
Cr	<2	<2	20
Ge	7	25	<2
Hg	<2	22	<2
Mn	15	35	7,000
Mo	—	—	—
Ni	<1	1.5	15
Sb	960	850	8,700
Se	1,000	510	<10
Sn	700	500	>1,500
Sr	<50	<50	<50
V	<2	<2	<2
Y	<10	<10	15
Total C (wt. pct.)	.07	<.06	2.24
Organic C (wt. pct.)	.07	<.06	2.24

which reflect the relative abundances of anhydrite and barite. The combination of high magnesium and silicon in calcium-rich sinters is largely related to the presence of stevensite, but some magnesium may be present as caminite. The barium-rich sinter has higher iron and zinc contents owing to the presence of marcasite, pyrite, sphalerite, and wurtzite; the high silicon content is related

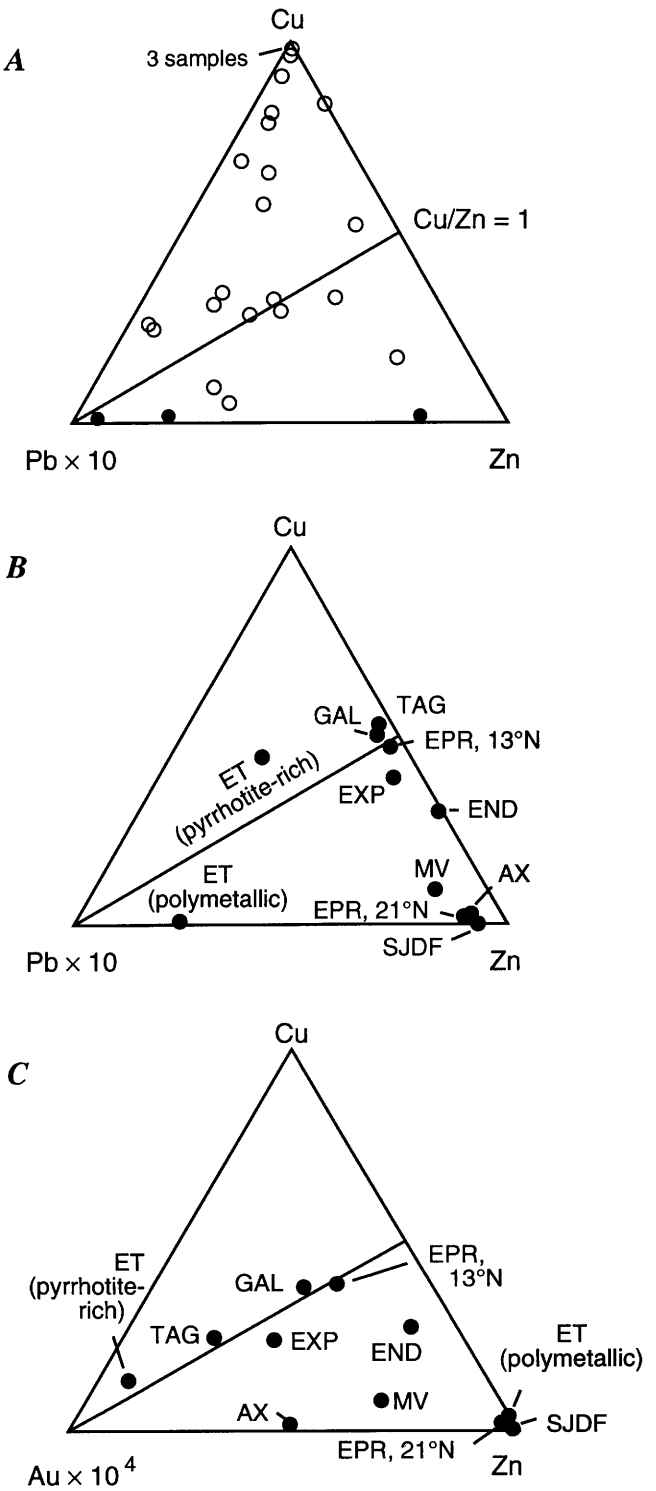

⇒

Figure 16.9. *A*, Ternary plot showing Cu-Zn-Pb(×10) ratios for pyrrhotite-rich sulfide samples (open circles) and polymetallic sulfide samples (closed circles) from Escanaba Trough. *B*, Comparison of Cu-Zn-Pb(×10) ratios for Escanaba Trough sulfides (averages for pyrrhotite-rich and polymetallic samples) with sulfide samples from other ocean ridges. *C*, Comparison of Cu-Zn-Au ($\times 10^4$) ratios for Escanaba Trough sulfides and sulfide samples from other ocean ridges. Chemical data for samples from other ridges are compiled from Hannington and others (1991), Kappel and Franklin (1989), and Bischoff and others (1983). Abbreviations used: ET, Escanaba Trough; GAL, Galápagos Spreading Center; EPR, East Pacific Rise; EXP, Explorer Ridge; TAG, Trans-Atlantic Geothermal site, Mid-Atlantic Ridge; END, Endeavour segment of Juan de Fuca Ridge; MV, Middle Valley segment of Juan de Fuca Ridge; AX, Axial Seamount, Juan de Fuca Ridge; SJDF, southern Juan de Fuca Ridge.

Table 16.4. Composition of polymetallic sulfide sample L2-86-14D-1.

[Analyses by U.S. Geological Survey. <, less than; —, interference from other elements]

	Inner Wall	Middle Wall	Outer Wall
Weight percent:			
Fe	21.1	29.3	21.2
Cu	4.64	1.62	.24
Zn	35.1	26.1	22.5
Pb	1.4	2.3	20.7
As	5.4	1.76	.1
BaO	.036	.108	.28
S	31.68	33.64	28.40
SO_3	.04	.16	.28
SiO_2	.44	<.02	<.02
CaO	.033	.005	.078
MgO	.075	.01	.22
Al_2O_3	.10	<.02	<.02
Total	100.04	95.04	94.12
Parts per million:			
Ag	150	200	3,000
Au	<.1	<.1	<.1
Bi	95	88	73
Cd	1,800	940	76
Ge	<2	<2	100
Hg	<2	<2	127
Mn	50	15	15
Mo	—	—	20
Ni	3	<1	3
Sb	480	550	16,000
Se	1,400	500	400
Sn	70	70	1,410
Sr	3	3	15
Tl	<10	<10	24
Total C (wt. pct.)	<.15	<.15	.70
Organic C (wt. pct.)	—	—	.50

to the abundance of amorphous silica. Samples of barite-rich crust (L1-86-16D-2), barite chimney (ALV2033-3B), and barite-rich sinter (ALV2040-2) also have notably high gold contents.

GENESIS OF SULFIDE- AND SULFATE-DOMINANT DEPOSITS

DISTRIBUTION AND SIZE CONSIDERATIONS

Seismic-reflection data show that the distribution of large sulfide deposits and currently active hydrothermal vent fields in Escanaba Trough is related to the emplacement of volcanic edifices along the sediment-covered Gorda Ridge axis (Morton and others, 1987, 1990). High heat-flow measurements (greater than 1,200 mW/m^2, Abbott and others, 1986; Davis and Becker, chap. 3, this volume) above two of the sediment-covered edifices indicate that these volcanic centers are the heat sources driving fluid circulation.

The overall form of the volcanic edifices is domelike, but details of their subsurface structure are poorly constrained. The importance of satellitic intrusions including plugs, dikes, or sills in the establishment of local hydrothermal convection cells is not known. In a similar setting in Guaymas Basin, Gulf of California, mineral and oxygen isotope studies indicate that the emplacement of shallow sills into the sediment pile generated low-temperature, short-lived hydrothermal convection (Kastner, 1982). Lonsdale and Becker (1985) suggested that pore waters expelled by these shallow intrusions produced 50°C to 130°C hot springs and barite-rich deposits. By analogy, some hydrothermal deposits (such as small, metal-poor barite chimneys) between the sediment hills of Escanaba Trough may be related to shallow intrusions and small-scale fluid circulation within the sediment section.

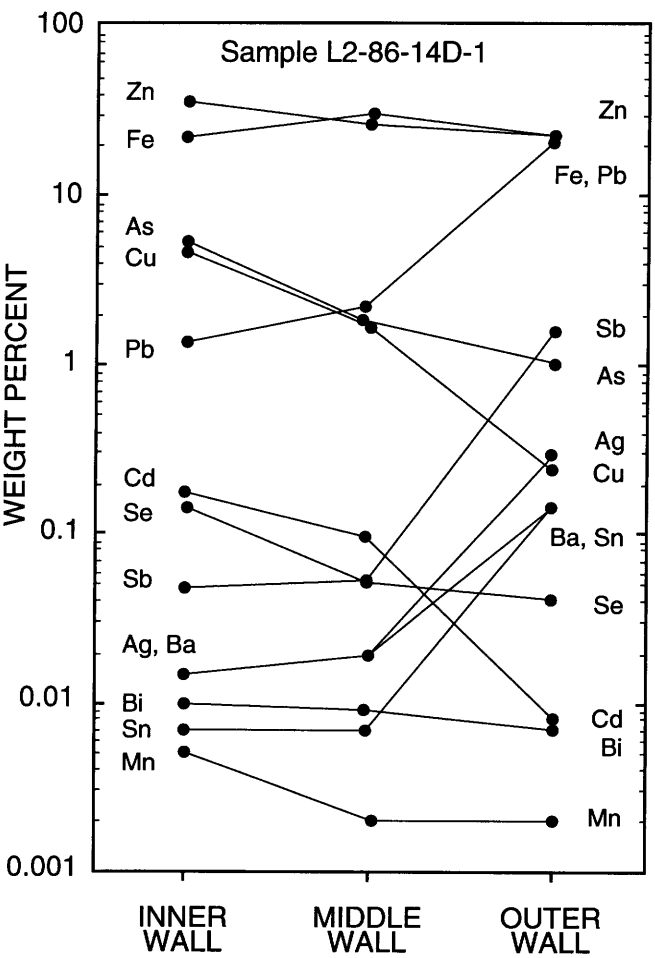

Figure 16.10. Chemical variations across wall of polymetallic sulfide structure (sample L2-86-14D-1). Inner wall mineralogy is inferred to have evolved in direct contact with hydrothermal fluid, whereas outer wall developed in contact with seawater.

Table 16.5. Bulk composition of sulfate-dominant samples.

[USGS, U.S. Geological Survey; GSC, Geological Survey of Canada. NA, not analysed; <, less than; —, interference from other elements]

	Barite-rich crust	Barite chimney			Sulfate sinter	
Sample number	L1-86-16D-2	SC 658-R2	SC 766-1	ALV 2033-3B	ALV 2036[a]	ALV 2040-2[b]
Laboratory	USGS	USGS	GSC	GSC	GSC	GSC
Weight percent:						
Fe	6.4	1.3	3.18	3.37	.62	5.3
Cu	.49	.02	.06	.27	.05	.25
Zn	17.3	.02	19.0	24.9	.05	1.6
Pb	4.38	<.01	2.80	1.1	.04	.19
As	.72	<.02	.26	.56	.003	.084
BaO	25.7	34.6	14.5	10.7	.31	16.2
S	11.69	.59	13.8	16.6	.60	5.4
SO_3	23.5	33.8	18.0	13.5	41.3	26.6
SiO_2	2.21	1.6	1.34	2.98	10.44	15.6
CaO	.11	.30	.16	.22	28.77	.21
MgO	.13	.27	.04	.06	6.1	.17
Al_2O_3	.16	.38	.02	.06	.41	.27
Total	92.79	72.89	73.29	74.31	88.68	71.79
Parts per million:						
Ag	387	2	240	570	1	156
Au	2.00	<.1	.005	1.64	.83	6.45
Bi	2	6	.1	<.5	5	1
Cd	830	.8	NA	NA	NA	NA
Co	30	15	21	32	20	13
Cr	5	3	20	11	11	16
Ge	150	<2	NA	NA	NA	NA
Hg	43	106	NA	NA	NA	NA
Mn	500	1,500	200	200	<100	200
Mo	—	—	3	3	4	17
Ni	2	15	<1	<1	1	<1
Sb	2,700	9	1,228	10	12	70
Se	<10	<10	.16	<.5	37	244
Sn	150	<2	145	139	9	26
Sr	<400	15,000	140	770	1,500	2,800
V	<2	70	21	10	9	18
Y	30	10	.1	NA	NA	NA
Total C (wt. pct.)	.16	.14	NA	NA	NA	NA
Organic C (wt. pct.)	.15	.08	NA	NA	NA	NA

[a]Average of three samples (ALV2036-1B, ALV2036-2A, ALV2036-2C).
[b]Average of two samples (ALV2040-2A and ALV2040-2B).

It is more likely that the heat source controlling larger-scale hydrothermal circulation and the formation of large sulfide mounds was generated from the top of the axial magma chamber emplaced at some point below the base of the volcanic edifices. In addition to supplying heat, magma cupolas or pipelike subvolcanic intrusions above the volcanic edifices may have caused uplift and concentric and radial fracturing of the overlying sediment (Koide and Bhattacharji, 1975). Denlinger and Holmes (chap. 4, this volume) hypothesize that the uplift of sediment blocks resulted from the emplacement of laccolithic intrusions at the interface between basaltic basement and overlying sediment. The fracturing and faulting that accompanied uplift of the sediment blocks was an important factor in creating cross-stratal permeability for fluid discharge and recharge.

The observations made from submersibles and towed camera systems indicate that the Escanaba Trough sulfide mounds are large features with lateral and vertical dimensions measured in hundreds and tens of meters, respectively (Holmes and Zierenberg, 1990; Zierenberg and others, chap. 10, this volume). The construction of large mounds is dependent on the longevity of the hydrothermal system, and this is increased by the insulating effect of the sediment blanket (Levi and Riddihough, 1986). The "black

smoker" type of hydrothermal discharge from large chimneys at sediment-free spreading axes results in the rapid dissipation of heat from the axial magma chamber (Macdonald and others, 1980). In contrast, the massive mound structures and the low-velocity, diffuse seepage of fluid through the sediment observed in Escanaba Trough indicate that hydrothermal fluid discharge and the convective heat flux are muted by the sediment cover.

SEDIMENT AS A SOURCE OF METALS AND BARIUM

All of the known sulfide and sulfate deposits in Escanaba Trough occur on a variably thick layer of sediment overlying basaltic volcanic basement. Both the sulfide- and sulfate-dominant deposits are characterized by high lead, bismuth, arsenic, and antimony contents compared to sulfide deposits from sediment-free ridges (Bischoff and others, 1983; Hannington and others, 1991). From a volumetric standpoint, sulfate-dominant deposits are also more abundant at Escanaba Trough (and at Guaymas Basin), and barium is a major element in crusts, sinters, and chimneys. In order to evaluate these differences in deposit composition as a function of source rock, the amount of these metals in Escanaba Trough turbidite samples is compared to mid-ocean ridge basalt values in table 16.6.

Table 16.6. Comparison of metal contents (ppm) in mid-ocean ridge basalt samples from northeast Pacific Ocean and sediment samples from Escanaba Trough.

[—, not determined]

Element	Mid-ocean ridge basalt[a]	ALV2039-1[b] (sand turbidite)	DSDP Site 35[c] (sand-silt turbidite)
Pb	0.89	5	15
Bi	.007	.38	—
As	.15	3.6	—
Sb	.007	.19	—
Ba	40	750	528

[a] Data for Pb, Bi, and Ba are for samples from Gorda Ridge: Pb is average value for eight samples analyzed by Church and Tatsumoto (1975); Bi is average value for two samples determined by neutron activation analysis (Laul and others, 1972); Ba is average value for six samples analyzed by isotope-dilution mass spectrometry (Kay and others, 1970). Values for As and Sb were obtained by radiochemical epithermal neutron activation analysis of a sample from Galápagos Ridge (Sims and others, 1990).

[b] Pb and Ba determined by inductively coupled plasma-atomic emission spectrometry; Bi, As, and Sb by atomic absorption spectrometry. Analyses performed at the Geological Survey of Canada.

[c] Pb (average of two samples) and Ba (average of three samples) determined by direct current argon plasma-optical emission spectrophotometry. Analyses performed at the University of Minnesota, R.L. Knoche, analyst.

Table 16.6 shows that the enrichment of lead, bismuth, arsenic, antimony, and barium in Escanaba Trough deposits is consistent with their greater abundance in turbidite samples compared to mid-ocean ridge basalt. Although comparative data for Escanaba Trough sediment samples are not available, it is probable that enrichments of silver, tin, and mercury in some Escanaba Trough sulfide samples are also related to their greater relative abundance in the sediment.

The presence of sediment-derived lead in Escanaba Trough sulfide deposits is confirmed by lead isotope data presented by LeHuray and others (1988). In their study, lead isotope ratios for pyrrhotite-rich and polymetallic massive sulfides are closely matched to values for terrigenous sediment; there is no indication of any lead contribution from basalt.

The ubiquitous nature of arsenic-bearing phases in Escanaba Trough sulfide samples, the rare occurrence of these minerals in samples from sediment-free ridges, and the low amount of arsenic in mid-ocean ridge basalt are indirect evidence that a significant proportion of the arsenic is derived from the continentally-derived sediment. Bischoff and others (1981) showed that arsenic is readily leached from sediment during interaction with NaCl-rich solutions. High arsenic contents and the presence of arsenic minerals (orpiment and realgar) have also been reported in massive sulfide from the Okinawa Trough, where the associated volcanic rocks have a calc-alkaline composition (Halbach and others, 1989).

Although a contribution from igneous sources may also be important, the relatively high barium in Escanaba Trough hydrothermal deposits can be attributed to its greater abundance in sediment (table 16.6) where it is concentrated in detrital feldspar, mica, and clay minerals as well as siliceous and calcareous microfossil tests (Martin and Knauer, 1973; Church, 1979). In addition, the burial and alteration of barium-enriched organic matter leads to authigenic precipitation of barite in marine sediment (Church and Wolgemuth, 1972). The dissolution of fossil tests and marine barite, alteration of barium-bearing detrital grains, and entrainment of pore waters by upwelling hydrothermal fluids should favor the formation of barite-rich deposits on the sea floor.

FORMATION OF MASSIVE SULFIDE MOUNDS

There is no direct evidence for the early stage of mound-building, but construction probably began with the precipitation of small sulfate-dominant mounds or chimneys in clusters or curvilinear arrays on the step-faulted margins of the uplifted sediment hills (fig. 16.11*A*). Dur-

ing the early stages of tectonism, uplift of the sediment blocks and hydrothermal activity were contemporaneous events. Although the hydrothermal solutions migrated upward along the bounding fault structures, it is likely that there was a considerable lateral flow along antithetic fractures and through permeable turbidite beds, especially where sandy units were overlain by less permeable clay-rich layers that formed effective caprocks. The movement of fluids through sediment talus at the base of fault scarps resulted in the formation of sulfide-cemented sediment deposits (fig. 16.4*E*).

The process of outward growth and expansion of the nascent deposits included ongoing deposition of sulfate-rich crusts and chimneys at the zone of mixing between exiting hydrothermal fluids and seawater. Although the early stage of mineralization probably involved the precipitation of some anhydrite, the predominance of barite deposition over a wide range of temperatures was controlled by fluids reacting with a barium-enriched sediment substrate.

The deposition of a thin but relatively impermeable sulfate-sulfide shell above the exit points for hydrothermal discharge led to the mature mound-building stage (fig. 16.11*B*) characterized by less fluid mixing, more reduced conditions, higher fluid temperatures, and the deposition of the main-stage sulfide paragenesis: pyrrhotite → sphalerite + Cu-Fe sulfides → löllingite + native bismuth in mounds and chimneys. The buildup of temperatures in the interior of maturing sulfide mounds resulted in the interstitial deposition of Cu-Fe sulfides and sphalerite in the interstices between pyrrhotite grains and along fluid channelways. The high gold content in copper-rich samples suggests that gold was deposited in the mounds at this stage.

The deposition of pyrrhotite and löllingite indicate very low fO_2 (less than 10^{-45}) in the fluid (fig. 16.12; Heinrich and Eadington, 1986) during this stage. The low oxygen fugacity may have resulted from the oxidation and decomposition of organic carbon during hydrothermal alteration of the sediment and from the reduction of dissolved sulfate by reactions such as

$$CH_3COOH + SO_4^{2-} + 2H^+ = 2H_2CO_3 + H_2S$$

(Thornton and Seyfried, 1987), which would also provide reduced sulfur for the formation of sulfide minerals. Escanaba Trough sediment recovered at Deep Sea Drilling Project (DSDP) Site 35 contains 0.35 percent organic carbon (average for 19 analyses; Vallier, 1970), and the presence of petroleum in sulfide deposits indicates that organic matter has been thermally altered and transported by hydrothermal fluids (Kvenvolden and others, 1986, 1990, chap. 15, this volume). The interaction between hydrothermal fluids and organic matter has other geochemical implications for metal transport and sulfide deposition in sedimentary environments. Recent experimental work by

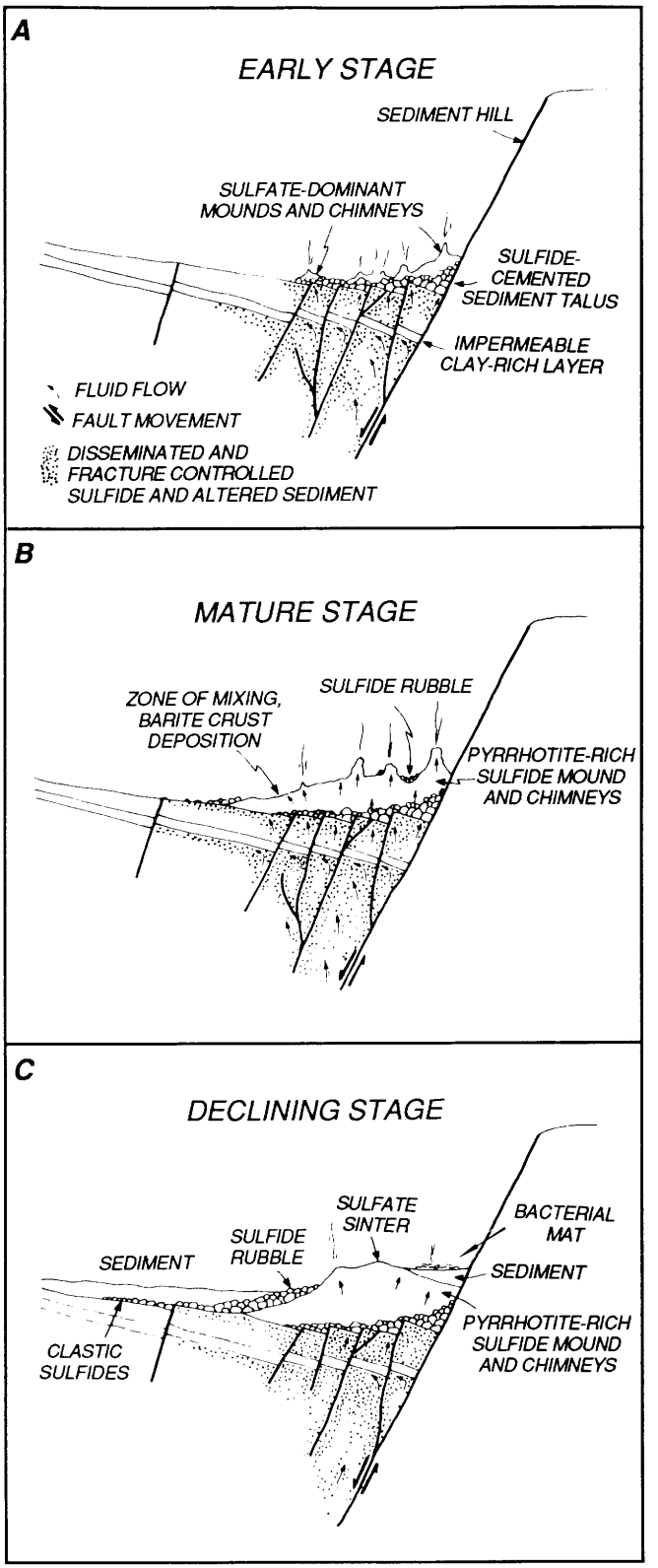

Figure 16.11. Generalized model for development of massive sulfide mounds from (*A*) early stage through (*B*) mature stage to (*C*) present declining stage. See text for detailed description.

Hennet and others (1988) and Giordano (1989) has shown that the solubility and transport of metals, especially lead and zinc, in mildly acidic NaCl-rich solutions at temperatures up to 200°C are enhanced by complexing with carboxyl ligands such as acetate.

The occurrence of löllingite, arsenopyrite, native bismuth, and bismuth telluride in pyrrhotite-rich sulfide deposits indicates a hydrothermal fluid depleted in total sulfur. The sulfur deficiency could have resulted from deposition of pyrite and other sulfides at depth in the sediment where fluid pH is buffered by reaction with calcium carbonate and organic matter (Von Damm and others, 1985). The proportion of pyrrhotite, arsenopyrite, and löllingite in the deposit are also controlled by the a_{S_2}/a_{As} ratio in the fluid (Barton, 1969).

During the main stage of development, fluid flow within the mounds was locally focused and vented through sulfide-rich chimneys; sulfate-dominant chimneys may have become more abundant near the end of this stage as the hydrothermal activity waned and increasing amounts of seawater mixed with hydrothermal fluid. A considerable volume of fluid also percolated through the tops of mounds (fig. 16.11*B*). This diffuse discharge resulted in the outward migration of sulfate shells with quench deposition of new sulfate phases along the interface with seawater and the replacement of sulfate by sulfide phases along the contact with massive sulfide. The zone refining of metals soluble at low temperatures resulted in deposition of sphalerite, galena, and sulfosalt phases in the sulfate shells. The flow through a myriad of channelways in mounds is expressed by the grain-size heterogeneity and radial growth orientation in pyrrhotite-rich samples. The pattern of diffuse fluid discharge through mounds was inherited from the broadly distributed flow out of the sediment substrate, but was also

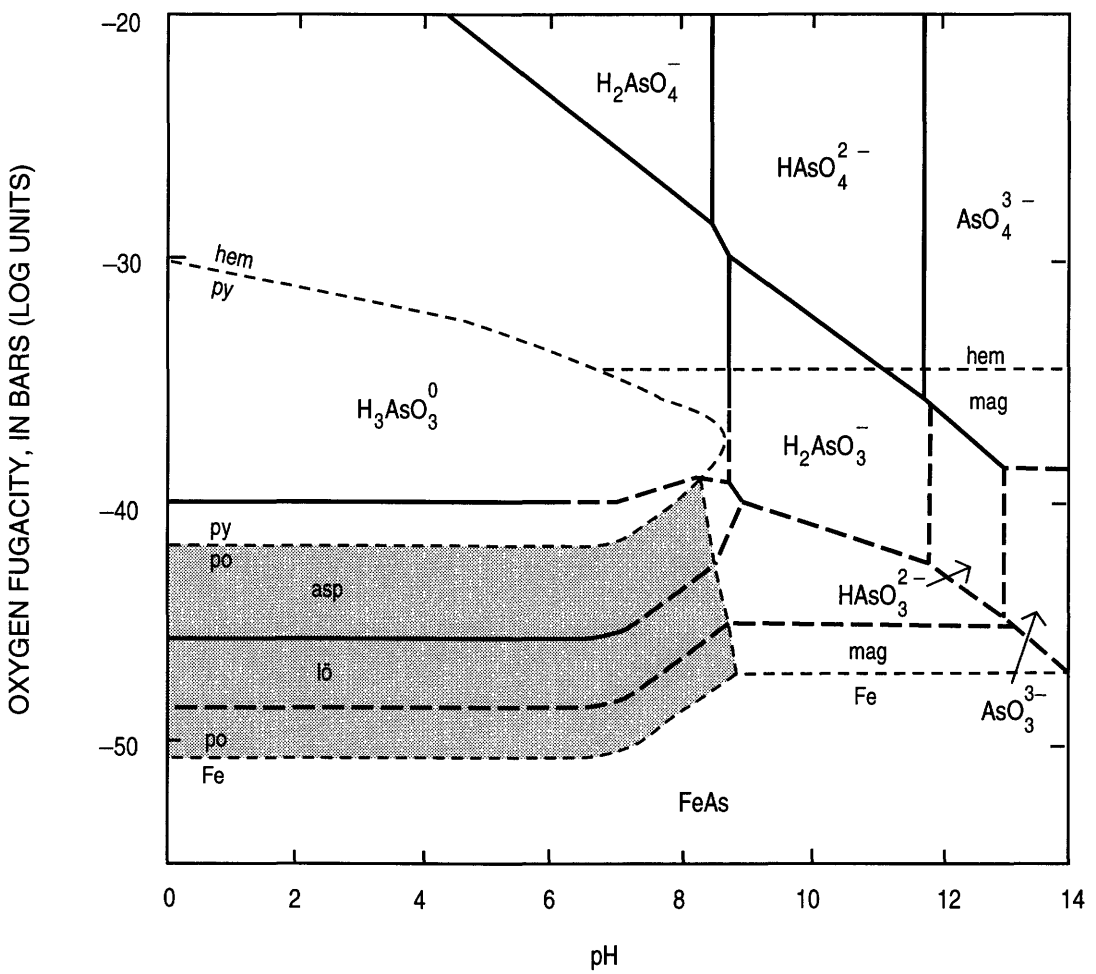

Figure 16.12. Phase diagram of pH versus oxygen fugacity showing calculated predominance fields for arsenic species in the system Fe-As-S-O-H at equilibrium with a sulfur-bearing aqueous fluid at 250°C. Activity for all sulfur species is 10^{-2}. Field boundaries for Fe, Fe-O, and Fe-S species are also shown. Abbreviations used: asp, arsenopyrite; lö, löllingite; hem, hematite; mag, magnetite; py, pyrite; po, pyrrhotite. From Heinrich and Eadington (1986).

enhanced by passage of fluid through layers of sulfide rubble created by the continual collapse of unstable sulfide and sulfate chimneys.

The large massive sulfide mounds in Escanaba Trough appear to be the products of a long-lived (on the order of hundreds or thousands of years) hydrothermal system that has now waned to a near-dormant condition (fig. 16.11*C*). In this declining stage of hydrothermal activity, the surfaces of deposits are undergoing oxidation and erosion. Sulfide talus blocks have resulted from mass wasting of the sediment hills and sulfide deposits. In many places, the flanks of sulfide mounds are buried by unconsolidated Holocene sediment. The known extent of active hydrothermal discharge is entirely within the Central Hill area of the NESCA site and is restricted to (1) localized vents where fluids at temperatures up to 220°C are depositing sulfate + silicate sinter on the flanks of sulfide mounds and (2) diffuse low-temperature seepage through the surrounding sediment (fig. 16.11*C*). The collapse of the hydrothermal system resulted in the lower-temperature deposition of barite, sphalerite, and galena in channelways within the sulfide mounds, and the alteration of pyrrhotite to marcasite and covellite as the hydrothermal fluids became more oxidized with time.

FORMATION OF THE POLYMETALLIC SULFIDE STRUCTURE

The polymetallic sulfide samples were dredged from the sediment plain north of the Central Hill at the NESCA site (fig. 16.2*A*). The shape of the large sample L2-86-14D-1 and the absence of pyrrhotite-rich massive sulfide or sulfate-dominant samples in dredge L2-86-14D indicate that the polymetallic sulfide fragments were part of an upright chimneylike sulfide structure with a large central cavity that formed on sediment substrate. The telescoped zonation of higher-temperature (sphalerite-isocubanite-pyrrhotite-arsenopyrite) and lower-temperature (sphalerite-galena-boulangerite) sulfide assemblages formed in response to steep temperature and chemical gradients in the chimney wall. Unlike the diffuse upwelling associated with the deposition of pyrrhotite-rich sulfide mounds, the polymetallic sulfide structure apparently was constructed around a focused, high-velocity "black smoker" type vent (Koski and others, 1988). The galena-rich sulfide-cemented sediment sample recovered in dredge L2-86-14D may represent associated sulfide mineralization in the sediment substrate.

The wall of the sulfide structure (fig. 16.6) is the result of a complex bidirectional growth process that evolved under the influence of an intensifying hydrothermal system. The original wall of the sulfide structure, consisting of fine-grained dendritic sphalerite, galena, pyrrhotite, barite, and probably anhydrite, is only partly preserved in zone 5. This early-formed assemblage resulted from quench crystallization as the initial discharge of hydrothermal fluid was rapidly cooled by mixing with ambient seawater. Although anhydrite is not preserved because of its retrograde solubility, the supersaturation of heated seawater with respect to $CaSO_4$ around the margin of the discharging fluid jet may have triggered its precipitation in the primitive chimney wall (Haymon, 1983).

The zone 5 assemblage provided a physical barrier that greatly reduced fluid mixing, and the first of several sphalerite-isocubanite-pyrrhotite layers, zone 4, was precipitated from hotter and less diluted hydrothermal fluid. The coarse-grained zones 3, 2, and 1, each with the paragenetic sequence sphalerite (subhedral) → isocubanite (in sphalerite cores) → pyrrhotite (subparallel plates), were subsequently accreted to the inner chimney wall according to fluctuations in fluid temperature and chemistry (for example, the variation in the a_{Cu}/a_{Fe} ratio). The deposition of the basal part of each succeeding sphalerite-isocubanite-pyrrhotite cycle was in part a replacement of the earlier-formed layer of subparallel pyrrhotite. Sphalerite and isocubanite of the inner wall (zone 1) represent the latest stage of high-temperature sulfide deposition. During the accretion of each high-temperature zone, sphalerite and isocubanite were also deposited interstitially and partly replaced pyrrhotite in the earlier-formed zones.

Each cycle of deposition in zones 4, 3, 2, and 1 included a stage of deposition of arsenopyrite and (or) löllingite along the contact with the preceding layer. These arsenopyrite-löllingite "fronts" may have been deposited when the high-temperature fluids were depleted in H_2S (Ballantyne and Moore, 1988).

Concurrent with the inward accretion of sphalerite-isocubanite-pyrrhotite cycles, the lower-temperature assemblage of sphalerite, galena, pyrrhotite, barite, boulangerite, tetrahedrite, and acanthite (zone 6) was deposited on the outer surface of the structure by fluids seeping through zone 5. Fluid temperatures in this part of the sulfide wall were probably too low to precipitate anhydrite. The thickening of the sulfide structure also resulted in the inward migration of galena deposition into zone 3 and the partial replacement of arsenopyrite by löllingite in zones 2, 3, and 4 of the middle wall. Except for incipient oxidative alteration of pyrrhotite in zone 2, the sulfide structure is remarkably free of sea-floor weathering effects. Thus it is probable that at the time of sampling the polymetallic sulfide structure was actively venting fluid.

CONCLUSIONS

The size, distribution, and composition of hydrothermal deposits in Escanaba Trough reflect extensive interaction between hydrothermal fluid and the insulating layer of turbidite and hemipelagic sediment. Mineral and

chemical characteristics of sulfide- and sulfate-dominant deposits including the abundance of pyrrhotite, galena, arsenopyrite, and barite, presence of unusual minerals such as löllingite, alabandite tin-bearing phases, native bismuth, and bismuth telluride, and high Pb, Ba, As, Sb, Bi, Ag, Hg, and Sn contents are related to fundamental control by the source rock composition. High values for Au (maximum 10.1 ppm) in Cu-rich (maximum 20.6 percent) samples of pyrrhotite-rich sulfide suggest coprecipitation of these metals. Large mounds may contain significant reserves of both copper and gold.

The construction of massive sulfide mounds on the margins of sediment hills consists of an early stage of sulfate-dominant deposition, a mature stage of sulfide-dominant deposition under conditions of high temperature and low f_{O_2} and f_{S_2}, and the present declining stage marked by erosion, oxidation, and partial burial by unconsolidated sediment. Hydrothermal activity at this final stage includes localized deposition of sulfate + silicate sinter from fluids at temperatures up to 220°C and seepage of low-temperature fluid through the sediment. At the NESCA site, steep temperature and chemical gradients associated with focused "black smoker" type discharge resulted in the formation of a chimneylike sulfide structure characterized by a highly telescoped polymetallic (Fe-Zn-Pb-Cu-As-Sb-Ag) sulfide assemblage.

REFERENCES CITED

Abbott, D.H., Morton, J.L., and Holmes, M.L., 1986, Heat flow measurements on a hydrothermally-active slow spreading ridge: The Escanaba Trough: Geophysical Research Letters, v. 13, p. 678–680.

Arnold, R.G., 1966, Mixtures of hexagonal and monoclinic pyrrhotite and the measurement of the metal content of pyrrhotite by X-ray diffraction: American Mineralogist, v. 51, p. 1221–1227.

Arnold, R.G., and Reichen, L.E., 1962, Measurement of the metal content of naturally occurring, metal-deficient, hexagonal pyrrhotite by an X-ray spacing method: American Mineralogist, v. 47, p. 105–111.

Ballantyne, J.M., and Moore, J.N., 1988, Arsenic geochemistry in geothermal systems: Geochimica et Cosmochimica Acta, v. 52, p. 475–483.

Barton, P.B., Jr., 1969, Thermochemical study of the system Fe-As-S: Geochimica et Cosmochimica Acta, v. 33, p. 841–857.

Barton, P.B., Jr., and Bethke, P.M., 1987, Chalcopyrite disease in sphalerite: Pathology and epidemiology: American Mineralogist, v. 72, p. 451–467.

Benninger, L.M., and Koski, R.A., 1987, Descriptions of sulfide samples dredged in 1986 from Escanaba Trough, southern Gorda Ridge: U.S. Geological Survey Open-File Report 87-375-B, 25 p.

Bischoff, J.L., Radke, A.S., and Rosenbauer, R.J., 1981, Hydrothermal alteration of graywacke by brine and seawater: Roles of alteration and chloride complexing on metal solubilization at 200° and 350°C: Economic Geology, v. 76, p. 659–676.

Bischoff, J.L., Rosenbauer, R.J., Aruscavage, P.J., Baedecker, P.A., and Crock, J.G., 1983, Sea-floor massive sulfide deposits from 21°N, East Pacific Rise; Juan de Fuca Ridge; and Galapagos Rift: Bulk chemical composition and economic implications: Economic Geology, v. 78, p. 1711–1720.

Brindley, G.W., 1980, Order-disorder in clay mineral structures, *in* Brindley, G.W., and Brown, G., eds., Crystal structures of clay minerals and their X-ray identification: London, Mineralogical Society, p. 125–195.

Cabri, L.J., Hall, S.R., Szymanski, J.T., and Stewart, J.M., 1973, On the transformation of cubanite: Canadian Mineralogist, v. 12, p. 33–38.

Campbell, A.C., German, C.R., Palmer, M.R., Gamo, T., and Edmond, J.M., Chemistry of hydrothermal fluids from the Escanaba Trough, Gorda Ridge, *in* Morton, J.L., Zierenberg, R.A., and Reiss, C.A., eds., Geologic, hydrothermal, and biologic studies at Escanaba Trough, Gorda Ridge, offshore northern California: U.S. Geological Survey Bulletin 2022, chapter 11 (this volume).

Caye, René, Cervelle, Bernard, Cesbron, Fabien, Oudin, Elisabeth, Picot, Paul, and Pillard, François, 1988, Isocubanite, a new definition of the cubic polymorph of cubanite $CuFe_2S_3$: Mineralogical Magazine, v. 52, p. 509–514.

Church, T.M., 1979, Marine barite, *in* Burns, R.G., ed., Marine minerals: Mineralogical Society of America Short Course Notes, v. 6, p. 175–209.

Church, T.M., and Wolgemuth, Kenneth, 1972, Marine barite saturation: Earth and Planetary Science Letters, v. 15, p. 35–44.

Church, S.E., and Tatsumoto, Mitsunobu, 1975, Lead isotope relations in oceanic ridge basalts from the Juan de Fuca-Gorda Ridge area, N.E. Pacific Ocean: Contributions to Mineralogy and Petrology, v. 53, p. 253–279.

Davis, E.E., and Becker, Keir, Thermal and tectonic structure of Escanaba Trough: New heat-flow measurements and seismic-reflection profiles, *in* Morton, J.L., Zierenberg, R.A., and Reiss, C.A., eds., Geologic, hydrothermal, and biologic studies at Escanaba Trough, Gorda Ridge, offshore northern California: U.S. Geological Survey Bulletin 2022, chapter 3 (this volume).

Davis, E.E., Goodfellow, W.D., Bornhold, B.D., Adshead, J., Blaise, B., Villinger, H., and LeCheminant, G.M., 1987, Massive sulfides in a sedimented rift valley, northern Juan de Fuca Ridge: Earth and Planetary Science Letters, v. 82, p. 49–61.

Denlinger, R.P., and Holmes, M.L., A thermal and mechanical model for sediment hills and associated sulfide deposits along the Escanaba Trough, *in* Morton, J.L., Zierenberg, R.A., and Reiss, C.A., eds., Geologic, hydrothermal, and biologic studies at Escanaba Trough, Gorda Ridge, offshore northern California: U.S. Geological Survey Bulletin 2022, chapter 4 (this volume).

Fleet, M.E., 1978, The pyrrhotite-marcasite transformation: Canadian Mineralogist, v. 16, p. 31–35.

Giordano, T.H., 1989, Anglesite solubility in acetate solutions: The determination of stability constants for lead acetate complexes to 85°C: Geochimica et Cosmochimica Acta, v.

53, p. 359–366.

Goodfellow, W.D., and Blaise, Bertrand, 1988, Sulfide formation and hydrothermal alteration of hemipelagic sediment in Middle Valley, northern Juan de Fuca Ridge: Canadian Mineralogist, v. 26, p. 675–696.

Halbach, P., Nakamura, Ko-ichi, Wahsner, M., Lange, J., Sakai, H., Käselitz, L., Hansen, R.-D., Yamano, M., Post, J., Prause, B., Seifert, R., Michaelis, W., Teichmann, F., Kinoshita, M., Märten, A., Ishibashi, J., Czerwinski, S., and Blum, N., 1989, Probable modern analogue of Kuroko-type massive sulphide deposits in the Okinawa Trough back-arc basin: Nature, v. 338, p. 496–499.

Hannington, M.D., Herzig, P.M., and Scott, S.D., 1991, Auriferous hydrothermal precipitates on the modern seafloor, *in* Foster, R. P., ed., Gold metallogeny and exploration: Glasgow, Blackie and Son, p. 249–282.

Hannington, M.D., and Scott, S.D., 1990, Gold mineralization in volcanogenic massive sulfides: Implications of data from active hydrothermal vents on the modern sea floor, *in* Keays, Reid, Ramsay, Ross, and Groves, David, eds., The geology of gold deposits: The perspective in 1988: Economic Geology Monograph 6, p. 491–507.

Haymon, R.L., 1983, The growth history of hydrothermal black smoker chimneys: Nature, v. 301, p. 695–698.

Haymon, R.L., and Kastner, Miriam, 1981, Hot spring deposits on the East Pacific Rise at 21°N: Preliminary description of mineralogy and genesis: Earth and Planetary Science Letters, v. 53, p. 363–381.

Heinrich, C.A., and Eadington, P.E., 1986, Thermodynamic predictions of the hydrothermal chemistry of arsenic, and their significance for the paragenetic sequence of some cassiterite-arsenopyrite-base metal sulfide deposits: Economic Geology, v. 81, p. 511–529.

Hennet, R. J.-C., Crerar, D.A., and Schwartz, Jeffrey, 1988, Organic complexes in hydrothermal systems: Economic Geology, v. 83, p. 742–764.

Holmes, M.L., and Zierenberg, R.A., 1990, Submersible observations in Escanaba Trough, southern Gorda Ridge, *in* McMurray, G.R., ed., Gorda Ridge, a seafloor spreading center in the United States' Exclusive Economic Zone: New York, Springer-Verlag, p. 93–115.

Kappel, E.S., and Franklin, J.M., 1989, Relationships between geologic development of ridge crests and sulfide deposits in the northeast Pacific Ocean: Economic Geology, v. 84, p. 485–505.

Kastner, M., 1982, Evidence for two hydrothermal systems in the Guaymas Basin, *in* Curray, J.R., Moore, D.G., and others, eds., Initial reports of the Deep Sea Drilling Project, volume 64, Washington: U.S. Government Printing Office, p. 1143–1157.

Kay, R., Hubbard, N.J., and Gast, P.W., 1970, Chemical characteristics and origin of oceanic ridge volcanic rocks: Journal of Geophysical Research, v. 75, p. 1585–1613.

Koide, H., and Bhattacharji, S., 1975, Formation of fractures around magmatic intrusions and their role in ore localization: Economic Geology, v. 70, p. 781–799.

Koski, R.A., Clague, D.A., and Oudin, Elisabeth, 1984, Mineralogy and chemistry of massive sulfide deposits from the Juan de Fuca Ridge: Geological Society of America Bulletin, v. 95, p. 930–945.

Koski, R.A., Lonsdale, P.F., Shanks, W.C., III, Berndt, M.E., and Howe, S.S., 1985, Mineralogy and geochemistry of a sediment-hosted hydrothermal sulfide deposit from the Southern Trough of Guaymas Basin, Gulf of California: Journal of Geophysical Research, v. 90, p. 6695–6707.

Koski, R.A., Shanks, W.C., III, Bohrson, W.A., and Oscarson, R.L., 1988, The composition of massive sulfide deposits from the sediment-covered floor of Escanaba Trough, Gorda Ridge: Implications for depositional processes: Canadian Mineralogist, v. 26, p. 655–673.

Kvenvolden, K.A., Rapp, J.B., Hostettler, F.D., Morton, J.L., King, J.D., and Claypool, G.E., 1986, Petroleum associated with polymetallic sulfide in sediment from Gorda Ridge: Science, v. 234, p. 1231–1234.

Kvenvolden, K.A., Rapp, J.B., and Hostettler, F.D., 1990, Hydrocarbon geochemistry of hydrothermally generated petroleum from Escanaba Trough, offshore California, U.S.A.: Applied Geochemistry. v. 5, p. 83–91.

———Hydrocarbons in sediment from Escanaba Trough, *in* Morton, J.L., Zierenberg, R.A., and Reiss, C.A., eds. Geologic, hydrothermal, and biologic studies at Escanaba Trough, Gorda Ridge, offshore northern California: U.S. Geological Survey Bulletin 2022, chapter 15 (this volume).

Laul, J.C., Keays, R.R., Ganapathy, R., Anders, Edward, and Morgan, J.W., 1972, Chemical fractionations in meteorites—V. Volatile and siderophile elements in achondrites and ocean ridge basalts: Geochimica et Cosmochimica Acta, v. 36, p. 329–345.

LeHuray, A.P., Church, S.E., Koski, R.A., and Bouse, R.M., 1988, Pb isotopes in sulfides from mid-ocean ridge hydrothermal sites: Geology, v. 16, p. 362–365.

Levi, Shaul, and Riddihough, Robin, 1986, Why are marine magnetic anomalies suppressed over sedimented spreading centers?: Geology, v. 14, p. 651–654.

Lonsdale, Peter, and Becker, Keir, 1985, Hydrothermal plumes, hot springs, and conductive heat flow in the Southern Trough of Guaymas Basin: Earth and Planetary Science Letters, v. 73, p. 211–225.

Macdonald, K.C., Becker, K., Spiess, F.N., and Ballard, R.D., 1980, Hydrothermal heat flux of the "black smoker" vents on the East Pacific Rise: Earth and Planetary Science Letters, v. 48, p. 1–7.

Martin, J.H., and Knauer, G.A., 1973, The elemental composition of plankton: Geochimica et Cosmochimica Acta, v. 37, p. 1639–1653.

Morton, J.L., Holmes, M.L., and Koski, R.A., 1987, Volcanism and massive sulfide formation at a sedimented spreading center, Escanaba Trough, Gorda Ridge, northeast Pacific Ocean: Geophysical Research Letters, v. 14, p. 769–772.

Morton, J.L., Koski, R.A., Normark, W.R., and Ross, S.L., 1990, Distribution and composition of massive sulfide deposits at Escanaba Trough, southern Gorda Ridge, *in* McMurray, G.R., ed., Gorda Ridge, a seafloor spreading center in the United States' Exclusive Economic Zone: New York, Springer-Verlag, p. 77–92.

Murowchick, J.B., and Barnes, H.L., 1986, Marcasite precipitation from hydrothermal solutions: Geochimica et Cosmochimica Acta, v. 50, p. 2615–2629.

Newman, A.C.D., and Brown, G., 1987, The chemical constitution of clays, *in* Newman, A.C.D., ed., Chemistry of clays

and clay minerals: Mineralogical Society Monograph 6, p. 1–128.

Oudin, E., Picot, P., and Pouit, G., 1981, Comparison of sulphide deposits from the East Pacific Rise and Cyprus: Nature, v. 291, p. 404–407.

Paradis, Suzanne, Jonasson, I.R., Le Cheminant, G.M., and Watkinson, D.H., 1988, Two zinc-rich chimneys from the plume site, southern Juan de Fuca Ridge: Canadian Mineralogist, v. 26, p. 637–654.

Peter, J.M., 1986, Genesis of hydrothermal vent deposits in the Southern Trough of Guaymas Basin, Gulf of California: A mineralogical and geochemical study: University of Toronto, M.S. thesis, 164 p.

Peter, J.M., and Scott, S.D., 1988, Mineralogy, composition, and fluid-inclusion microthermometry of seafloor hydrothermal deposits in the Southern Trough of Guaymas Basin, Gulf of California: Canadian Mineralogist, v. 26, p. 567–587.

Sims, K.W.W., Newsom, H.E., and Gladney, E.S., 1990, Chemical fractionation during formation of the earth's core and continental crust: Clues from As, Sb, W, and Mo, *in* Newsome, H.E., and Jones, J.H., eds., Origin of the Earth: New York, Oxford University Press, p. 291–317.

Styrt, M.M., Brackmann, A.J., Holland, H.D., Clark, B.C., Pisutha-Arnond, V., Eldridge, C.S., and Ohmoto, H., 1981, The mineralogy and the isotopic composition of sulfur in hydrothermal sulfide/sulfate deposits on the East Pacific Rise, 21°N latitude: Earth and Planetary Science Letters, v. 53, p. 382–390.

Thornton, E.C., and Seyfried, W.E., Jr., 1987, Reactivity of organic-rich sediment in seawater at 350°C, 500 bars: Experimental and theoretical constraints and implications for the Guaymas Basin hydrothermal system: Geochemica et Cosmochimica Acta, v. 51, p. 1997–2010.

Vallier, T.L., 1970, Carbon carbonate results, *in* McManus, D.A., and others, eds., Initial Reports of the Deep Sea Drilling Project, v. 5: Washington, U.S. Government Printing Office, p. 431–435.

Von Damm, K.L., Edmond, J.M., Measures, C.I., and Grant, B., 1985, Chemistry of submarine hydrothermal solutions at Guaymas Basin, Gulf of California: Geochimica et Cosmochimica Acta, v. 49, p. 2221–2237.

Zierenberg, R.A., Morton, J.L., Koski, R.A., Ross, S.L., and Holmes, M.K., Geologic setting of massive sulfide mineralization in the Escanaba Trough, *in* Morton, J.L., Zierenberg, R.A., and Reiss, C.A., eds., Geologic, hydrothermal, and biologic studies at Escanaba Trough, Gorda Ridge, offshore northern California: U.S. Geological Survey Bulletin 2022, chapter 10 (this volume).

Zierenberg, R.A., and Shanks, W.C., III, Sediment alteration associated with massive sulfide formation in Escanaba Trough, Gorda Ridge: The importance of seawater mixing and magnesium metasomatism, *in* Morton, J.L., Zierenberg, R.A., and Reiss, C.A., eds., Geologic, hydrothermal, and biologic studies at Escanaba Trough, Gorda Ridge, offshore northern California: U.S. Geological Survey Bulletin 2022, chapter 14 (this volume).

Section III:

Biological Studies

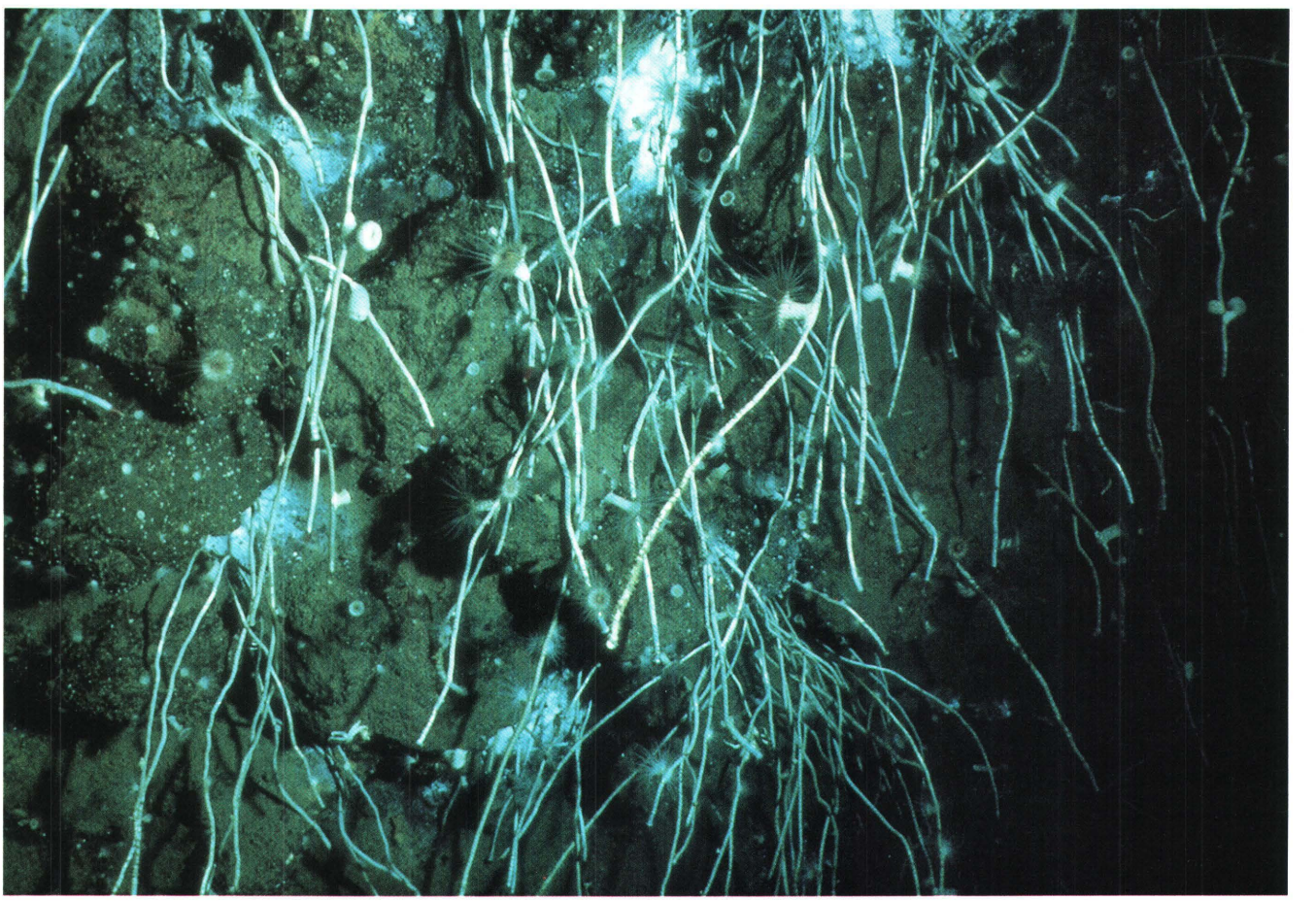

Brecciated pyrrhotite-rich massive sulfide colonized by thin tubeworms. Vent-specific anemones colonize the tubeworms and the massive sulfide and can be seen with their red tentacles extended and retracted. The massive sulfide is also colonized by abundant limpets, gastropods, and galatheid crabs and locally covered by filamentous bacteria. This photograph was provided by C. Van Dover from a camera mounted on the *Alvin* submersible; field of view is approximately 2 m across.

Chapter 17. Soft-Sediment Hydrothermal Vent Communities of Escanaba Trough

By J. Frederick Grassle *and* Rosemarie Petrecca[1]

CONTENTS

ABSTRACT

In June 1988, during DSV *Alvin* exploration of the northern Escanaba Trough (NESCA), three active hydrothermal vents and an active soft-sediment vent were located and sampled. Samples from nonactive sulfide mounds and the surrounding ambient soft sediment indicated a heterogeneous community. These samples were, however, much more similar to one another than to a sample adjacent to a submerged tree limb or samples in a soft-sediment hydrothermal area. The hydrothermal hard-surface fauna was generally similar to that from the Juan de Fuca Ridge to the north but with significant differences. Fauna from tree limb and hydrothermal hard surfaces were quite different, indicating that pieces of wood are unlikely to serve as stepping stones for hydrothermal vent fauna to move from one vent to another. The diversity of species in soft sediment both adjacent to the wood and from the soft-sediment vent was reduced in comparison with the ambient deep-sea community.

INTRODUCTION

In June 1988, R/V *Atlantis II* with DSV *Alvin* conducted a program of geochemical, geological, and biological sampling in the Escanaba Trough region of Gorda Ridge. The axial valley of Gorda Ridge closely resembles that of the Mid-Atlantic Ridge and is quite unlike the broad flat axis of Juan de Fuca Ridge to the north. The valley is composed of three segments: (1) the northern segment, studied for the past nine years; (2) the middle segment, which is the most tectonically complex; and (3) Escanaba Trough, the southernmost segment. Escanaba Trough extends 130 km northward from the intersection of the ridge with the Mendocino Fracture Zone (latitude 40°25′ N., longitude 127°30′ W.) to a right-lateral offset of the ridge axis near latitude 41°35′ N., longitude 127°25′ W. (Morton and others, 1990). Unlike the northern two segments, the axis of Escanaba Trough is covered by turbiditic and hemipelagic sediment (Moore, 1970; Vallier and others, 1973; Karlin and Lyle, 1986). The spreading rate along Escanaba Trough is approximately 2.4 cm/yr, which is characteristic of a slow-rate spreading center (Morton and others, 1990). Located along the axial valley are sediment-hosted polymetallic massive sulfide deposits and active hydrothermal vents (Morton and others, 1987; Clague and Holmes, 1987; Zierenberg and others, 1988).

The eight DSV *Alvin* dives pertaining to our soft-sediment work were located in the northern part of the Escanaba Trough or NESCA site (fig. 17.1). In this region three active hydrothermal vents and one active soft-sediment vent were located and sampled. The soft-sediment area was dominated by the vent clam *Calyptogena phaseoliformis* (Petrecca and Grassle, 1990; Van Dover and others, 1990). This species was previously known only from soft-sediment cold seeps near Japan (Metvier and others, 1986; Juniper and Sibuet, 1987). This soft-sediment hydrothermal site appears similar to the sites in Guaymas Basin dominated by *Vesicomya gigas* (formerly thought to be *Calyptogena pacifica*). Areas of bacterial mats or petroleum seepage such as those observed in Guaymas Basin were not observed.

ACKNOWLEDGMENTS

We thank the following systematists: James Blake, Brigitte Hilbig, Marian Pettibone, Meredith Jones, James McLean, Richard Gustafson, and Vivianne Solis-Weiss. We

[1] Institute of Marine and Coastal Sciences, Rutgers University, New Brunswick, New Jersey

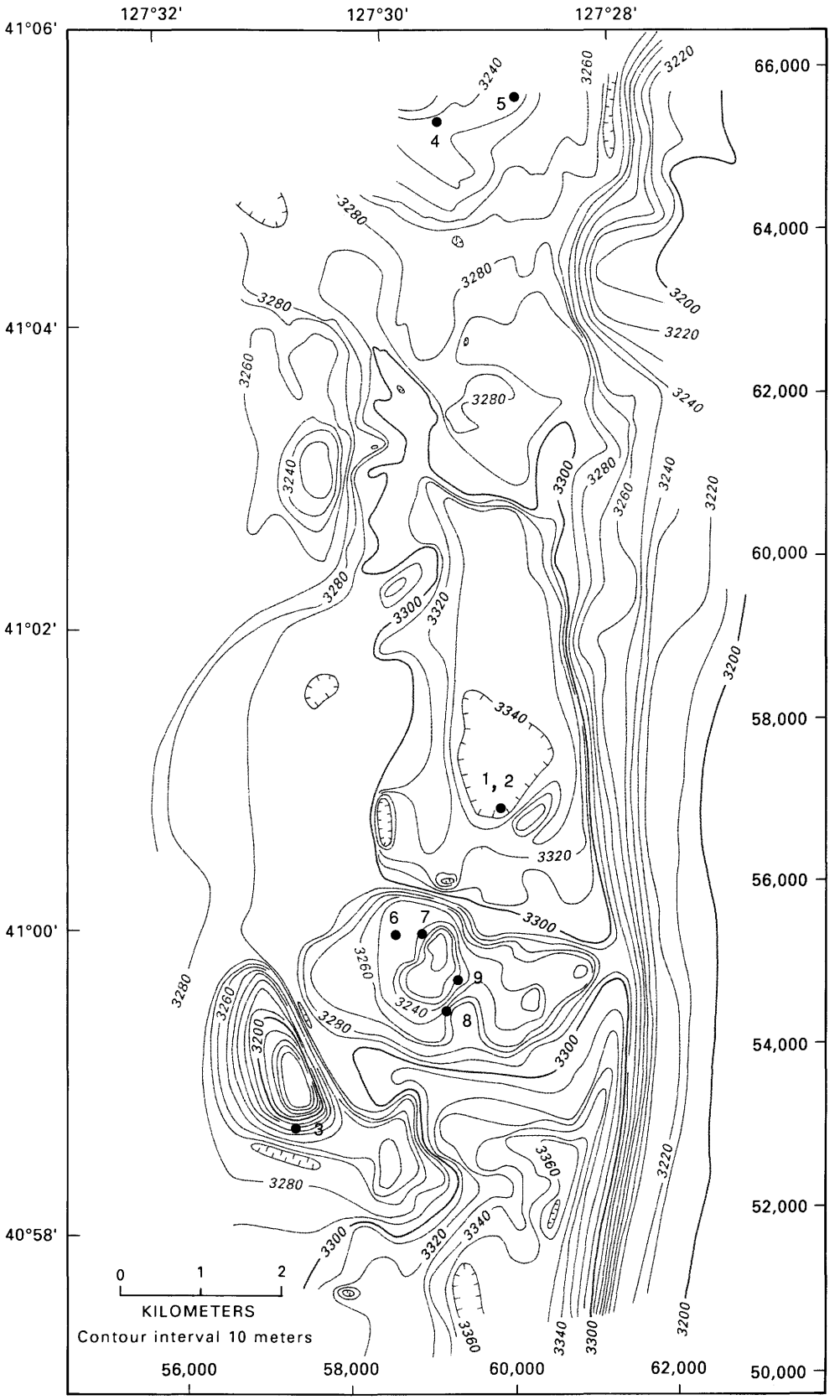

Figure 17.1. Location of samples identified in table 17.1. Numbers along right and bottom give coordinates for local transponder net (in meters). Hachures indicate area of closed low. Depth contours are in meters.

Table 17.1. DSV *Alvin* dives on Escanaba Trough 1988.

Dive	Sample	Reference (fig. 17.1)	Latitude north	Longitude west	Depth (m)	Comments
2034	Box Core A	1	41°00.86′	127°28.93′	3,366	Near tree limb
	Box Core B	2	41°00.82′	127°28.92′	3,366	3 meters from wood
2035	Box Core A	3	40°58.73′	127°30.74′	3,180	Top of hill
2038	Box Core A	4	41°05.35′	127°29.34′	3,268	Ambient
	Box Core B	4	41°05.35′	127°29.34′	3,268	Ambient
2039	Box Core B	5	41°05.51′	127°28.70′	3,254	Non-active sulfide mound
2040	Box Core A	6	41°00.01′	127°29.86′	3,274	Active sulfide mound
	Box Core B	6	41°00.01′	127°29.86′	3,274	Active sulfide mound
2041	Box Core A	7	41°00.01′	127°29.62′	3,244	Active sulfide mound
2042	Box Core A	8	40°59.50′	127°29.41′	3,260	Ambient
	Box Core B	8	40°59.50′	127°29.41′	3,260	Ambient
2042	Scoop sample	9	40°59.71′	127°29.31′	3,254	Hydrothermal soft-sediment site

also extend our gratitude to Janet Morton, Susan Brown-Leger, Cindy Van Dover, John Edmond, the pilots of DSV *Alvin* , and the crew of R/V *Atlantis II*. This work was supported by National Science Foundation grant OCE-8812733.

MATERIALS AND METHODS

Stainless-steel box cores with a 225-cm^2 footprint, specifically designed for use by DSV *Alvin*, were used to collect our samples. Each box core was equipped with an improved lid design that activates the closing of the doors by rotation of a manipulator-operated T-handle (instead of the rollerspring-operated doors used previously).

Eleven quantitative box cores were obtained during this dive series (table 17.1). Three box cores were taken in sediment containing sulfide deposits at the base of active hydrothermal mounds. Another six were taken in the surrounding ambient soft sediment, including nonactive sulfide mounds. One core was obtained immediately adjacent to a large submerged tree limb lying on the bottom, which contained a rich faunal assemblage, and another core was taken 3 meters away in an attempt to compare the animal communities at the two locations. On the final dive, a soft-sediment hydrothermal area was discovered, a 50-m-wide patch of soft sediment venting low-temperature hydrothermal fluid. A qualitative sample was obtained using a DSV *Alvin* tube core as a scoop to shovel sediment into a collection box on DSV *Alvin*'s basket. The amount of sediment was the equivalent of at least two box cores.

Samples were sieved through 300-μm and 63-μm screens, fixed in 10 percent formalin, and stored in 80 percent ethanol. After staining with protein-specific Rose Bengal, these samples were carefully sorted to the species level under a dissecting microscope. Only the macrofauna retained on a 300-μm screen are summarized below. The 63-μm material will be used for future meiofaunal studies.

Similarity among samples were analyzed using the NESS similarity measure (Grassle and Smith, 1976) and the Bray-Curtis similarity measure (Clifford and Stephenson, 1975). Diversity was estimated using a rarefaction measure (Smith and Grassle, 1977).

RESULTS

Samples taken in sediment at the base of active and nonactive mounds did not differ in densities or species composition from those samples taken tens of meters away in ambient sediment. For purposes of comparison with hydrothermal areas and the sediment adjacent to wood on the bottom, these samples are combined. These 10 box core samples are inhabited by a fauna similar to that of deep-sea environments at similar depths elsewhere (table 17.2). All of the genera identified are often common at sites in the western Atlantic (Grassle and Morse-Porteous, 1987), and equatorial Pacific (Grassle and others, 1985). The second most abundant species, *Aurospio dibranchiata*, is the numerical dominant in these and other deep-sea environments. The genera found contain species known to be surface deposit feeders; however, the maldanid feeds head down in the sediment, and the polynoid is a predator.

The species in sediment adjacent to a piece of wood were similar to some of the species associated with vegetation at Deep Ocean Site (DOS) 2 off New England (table 17.3; Turner, 1977; Grassle and Morse-Porteous, 1987), such as the two most common species of *Ophryotrocha* and hesionids. Several individuals of the archaeogastropod species *Provanna* were also present. This genus as well as *Ophryotrocha* and hesionids, are common at the Guaymas Basin hydrothermal vents (Grassle and others, 1985). A new genus of phyllodocid polychaete was found associated with the wood (James Blake, Science Application International Corporation, oral commun., 1990).

Table 17.2. Most common species in box core samples from ambient Escanaba Trough soft-sediment communities.

[Fifteen most common species in ten samples, each 225 cm^2 in surface extent]

Species	Number/225 cm^2	Number/m^2	Percent contribution
Chaetozone cf. *abyssa* (Polychaeta)	34	1,511	8.1
Aurospio dibranchiata (Polychaeta)	25	1,111	5.9
Aricidea nr. *nolani* (Polychaeta)	20	889	4.8
Macrostylis sp. (Isopoda)	16	711	3.8
Cirratulidae sp.juv. (Polychaeta)	15	667	3.6
Cossura sp. (Polychaeta)	12	533	2.9
Prionospio nr. *steenstrupi* (Polychaeta)	12	533	2.9
Chelator sp. juv. (Isopoda)	11	489	2.6
Prionospio sp. 1 (Polychaeta)	10	444	2.4
Leptognathia sp. BBBBB (Tanaidacea)	10	444	2.4
Paramphinome profunda (Polychaeta)	9	400	2.1
Maldanid sp.II juv. (Polychaeta)	9	400	2.1
Aricidea sp.II (Polychaeta)	9	400	2.1
Bivalve sp.I [Thyasirid] (Bivalvia)	9	400	2.1
Polynoidae sp.juv. (Polychaeta)	8	356	1.9
Total Individuals	421	18,709	
Total Species	103		

Table 17.3. The fifteen most common species in a single 225 cm^2 box core sample taken adjacent to a piece of wood.

Species	Number/225 cm^2	Number/m^2	Percent contribution
Hesionidae sp.juv (Polychaeta)	49	2,089	12.9
Ophryotrocha n.sp. (Polychaeta)	48	2,133	12.6
Protanais n.sp. (Tanaidacea)	44	1,955	11.6
Chaetozone curvata (Polychaeta)	41	1,822	10.8
Asabellides n.sp. (Polychaeta)	41	1,822	10.8
Fauvelopsis n.sp. (Polychaeta)	30	1,333	7.9
Pseudotanais sp.Z (Tanaidacea)	23	1,022	6.0
Ophelina pallida (Polychaeta)	21	933	5.5
Ophelina abranchiata (Polychaeta)	10	444	2.6
Cossura sp. (Polychaeta)	8	356	2.1
Prionospio (Minuspio) n.sp. (Polychaeta)	8	356	2.1
Prionospio nr. *steenstrupi* (Polychaeta)	7	311	1.8
Aricidea catherinae (Polychaeta)	5	222	1.3
Gastropod sp.I [*Provanna* ? sp.] (Archaeogastropoda)	5	222	1.3
Paramphinome profunda (Polychaeta)	4	178	1.0
Total Individuals	381	16,932	
Total Species	36		

The soft-sediment hydrothermal site was dominated by the cosmopolitan hydrothermal vent polychaete *Amphisamytha galapagensis*, found at most hydrothermal and cold seep environments both in washings of hard-surface fauna and soft-sediment samples but never in sediment away from hydrothermal or cold seep fluids (table 17.4; Petrecca and Grassle, 1990). At least three new species are present. The two most abundant, the orbiniid polychaete genus *Leitoscoloplos* and the spionid polychaete genus *Prionospio* (*Minuspio*), are common in a wide variety of shallow-water environments.

COMMUNITY SIMILARITIES AMONG SITES

Relative to other deep-sea areas, the fauna from the ambient community is quite heterogeneous (fig. 17.2). NESS similarities may be interpreted as the average percentage of species shared, and these are generally greater than 0.7 in deep-sea communities. Heterogeneity in faunal distribution has also been observed in the rich megafaunal populations from the area (Carey and others, 1990). Hydrothermal mounds in NESCA are closer together than in Guaymas Basin, so there is less expanse of

Table 17.4. Abundance of the thirteen species from the Escanaba Trough soft-sediment hydrothermal qualitative scoop sample.

Species	Number	Percent contribution
Amphisamytha galapagensis (Polychaeta)	45	37.5
Leitoscoloplos n.sp. (Polychaeta)	36	30
Prionospio (Minuspio) n.sp. (Polychaeta)	15	12.5
Neolepetopsis gordensis (Archaeogastropoda)	9	7.5
Nuculana sp. (Bivalvia)	4	3.3
Gastropoda sp.III [*Provanna*?] (Archaeogastropoda)	4	3.3
Yoldiella? sp. (Bivalvia)	2	1.7
Gastropoda sp.IV [Turrid] (Archaeogastropoda)	2	1.7
Harpinia sp. (Amphipoda)	2	1.7
Munnid? sp. (Isopoda)	2	1.7
Levensteiniella n.sp. (Polychaeta)	1	0.83
Sphaerosyllis sp.I (Polychaeta)	1	0.83
Gastopoda sp.I [*Provanna*?] (Archaeogastropoda)	1	0.83
Total Individuals	120	
Total Species	13	

soft sediment. For this reason and because most of the rock and hydrothermal fluid sampling effort was concentrated on the mounds, samples were taken relatively short distances from hydrothermal mounds. Two of the samples were not used because rocks in the sediment prevented us from obtaining a full sample. The sample near wood and the sediment scoops from the soft-sediment hydrothermal vent area are very different from all the other samples. The Bray-Curtis similarity method gives a similar result (fig. 17.3).

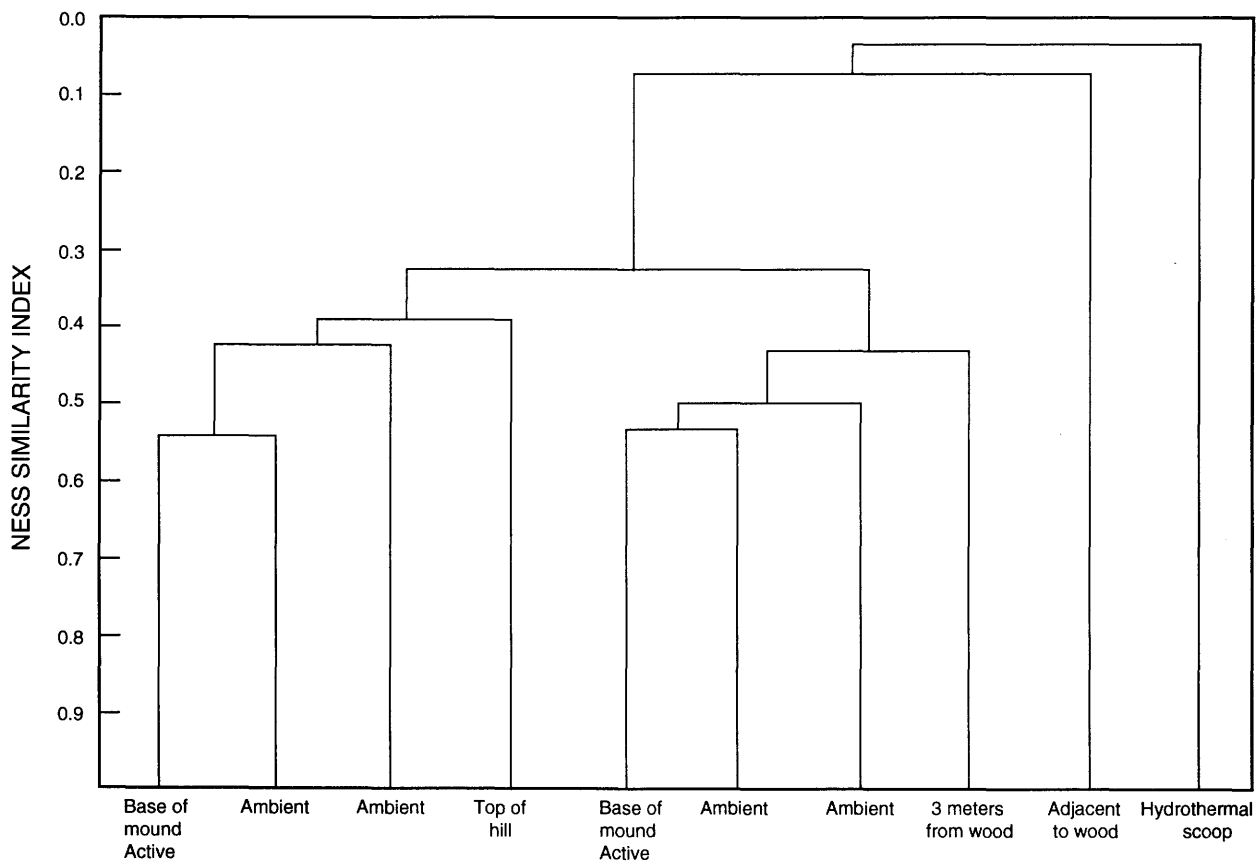

Figure 17.2. NESS similarity among Gorda Ridge soft-sediment samples. Comparison at 20 individuals. Group average sorting.

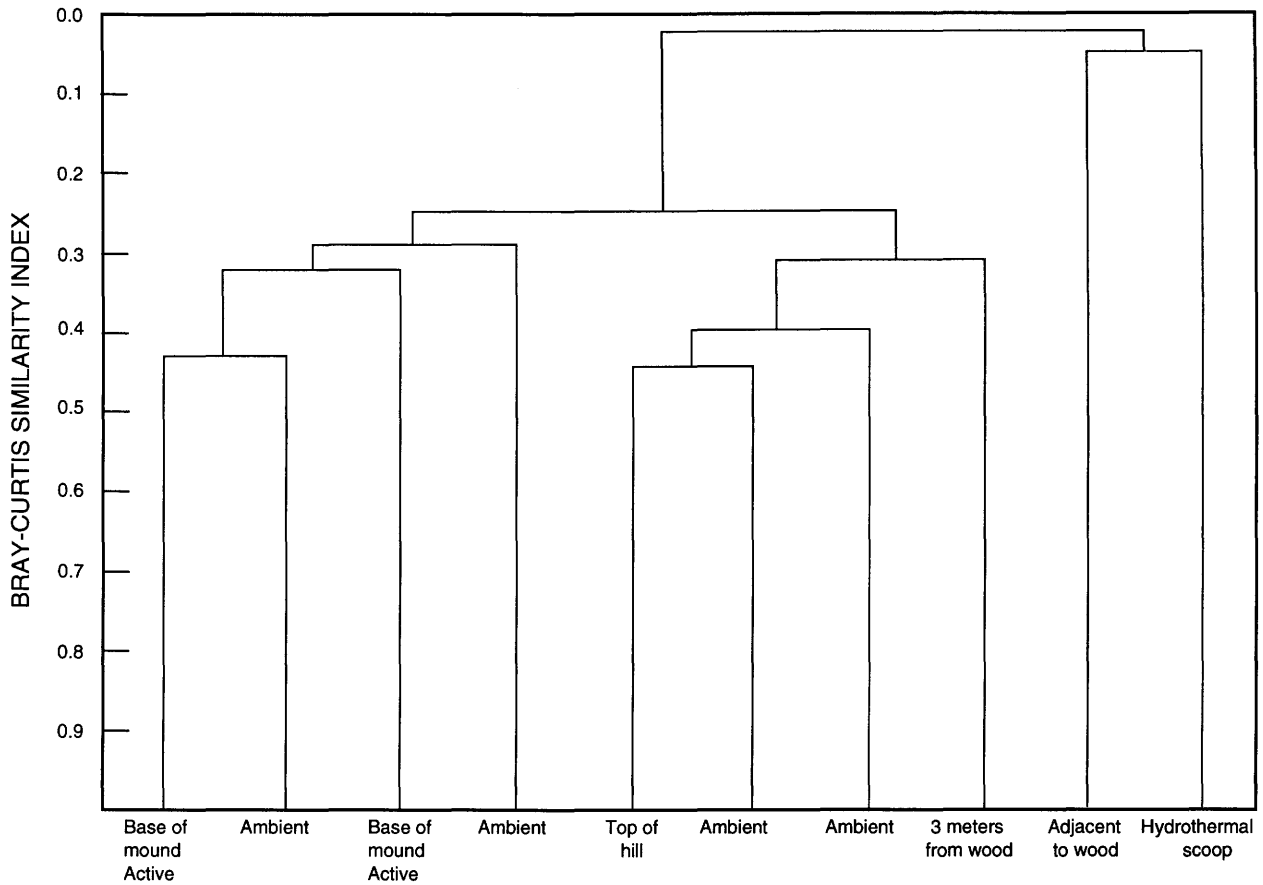

Figure 17.3. Bray-Curtis similarity among Gorda Ridge samples. Group average sorting.

COMMUNITY DIVERSITY

The ambient community diversity of individual samples tends to be low in comparison to samples from the ambient community in Guaymas Basin and other deep-sea areas (Petrecca and Grassle, 1990). This may be because of the proximity of hydrothermal mounds to all areas sampled, as suggested above. A few species tend to be very abundant, and rare species are absent. When the samples are added together, the curve is more similar to that of other deep-sea communities (fig. 17.4). Counts from the individual cores are all within the envelope designated by the cross-hatching. The wood community in the soft sediment has a lower diversity, and the soft-sediment hydrothermal vent area has the lowest diversity. The relative abundance of species in the three communities is shown in figure 17.5.

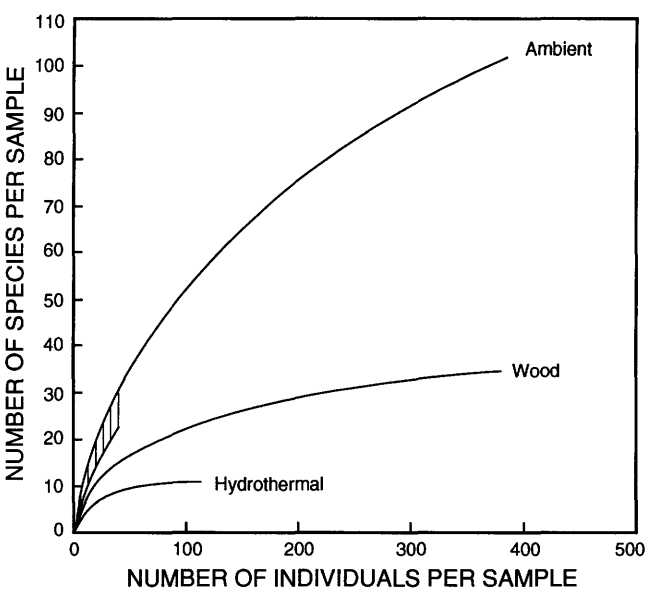

Figure 17.4. Rarefaction diversity curves (Hessler and Jumars, 1974; Smith and Grassle, 1977) showing relations between species and individuals of three communities: ambient soft-sediment, sediment adjacent to wood, and hydrothermal soft-sediment. Individual samples all fall within cross-hatched envelope.

HARD-SURFACE FAUNA

The fauna from mound and sulfide rock surfaces are similar to the fauna from vestimentiferan washings; how-

ever, these hard surfaces had a greater variety of gastropods and more phyla because more habitats are represented (table 17.5). Several species of filter feeders were found on the sulfide surfaces but not in the vestimentiferan washings. The fauna on the tree limb was quite different than either the washings or the mound and sulfide surfaces. On sulfides and in vestimentiferan washings, four new genera and several new species endemic to this hydrothermal area were found (table 17.5). These are an amphinomid polychaete worm related to the genus *Amphisamytha*, two new limpet genera, one of which has two new species, and a new genus of aplacophoran mollusk.

DISCUSSION

The ambient community composition has many of the polychaete genera such as *Aurospio, Aricidea, Chaetozone,*

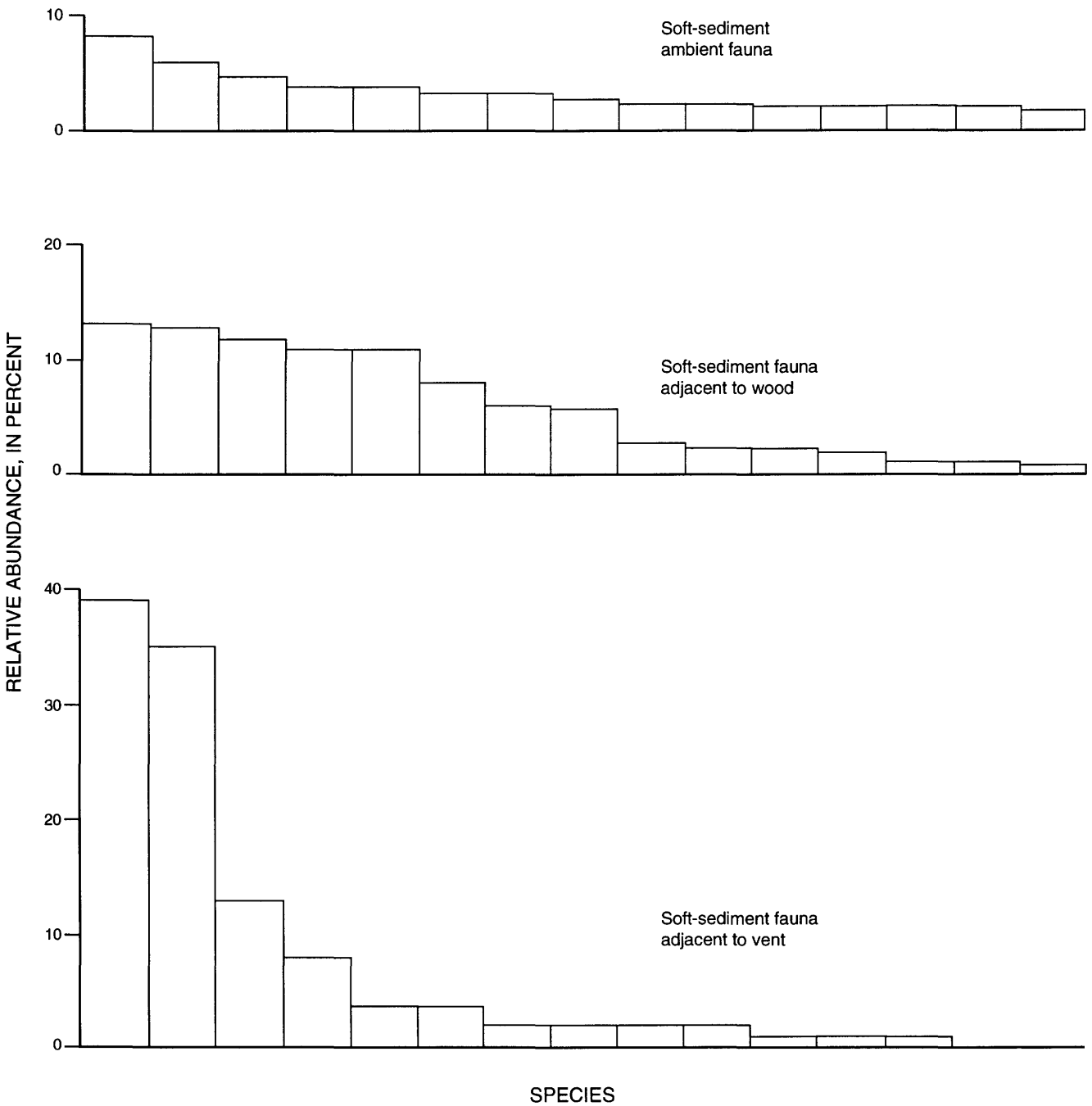

Figure 17.5. Relative abundance of 15 most common species in three sediment communities. Hydrothermal soft sediment had only 13 species in scoop sample taken.

Table 17.5. Fauna from hard surfaces, Escanaba Trough.

[V, vestimentiferan washings; H, hydrothermal mounds; T, submerged tree limb; X, species present; *, abundant species]

	V	H	T
Vestimentifera			
* Ridgeiidae sp.	X	X	
Polychaeta			
*_Amphisamytha galapagensis_	X	X	
Arctonoinae n. gen., n. sp.	X	X	
Branchinotogluma grasslei	X		
Capitellid sp. A			X
Capitellid sp. B			X
Capitellid nr. sp. B			X
Chone sp.		X	
nr. _Dodecaceria_ n. sp.		X	X
Eulalia sp.			X
Grassleia hydrothermalis	X		
Harmothoe n. sp.			X
Harmothoe sp.		X	
Hesionidae sp. juv.	X		X
Levensteinella n. sp.	X		
Nereis n. sp.			X
Nereis sp. II			X
Nicomache? sp.			X
Ophryotrocha n. sp.	X		X
Opisthotrochopodus tunnicliffeae	X		
*_Paralvinella palmiformis_	X		
* _Protis_ sp.			X
Oligochaeta			
Oligochaete sp. 1			X
Oligochaete sp. 3			X
Bivalvia			
*_Calyptogena phaseoliformis_	X		
*_Xylophaga washingtonia_			X
*_Xylophaga_ n. sp.			X
Gastropoda			
*Gastropoda sp. I [_Provanna_?]			X
*Gastropoda sp. II [Glob snail]	X		X
Gastropoda—Continued			
*Gastropoda so. III [Provanna?]	X	X	
*Gastropoda sp. V. [Provanna?]		X	
*Gastropoda sp. VI [_Melanodrymia_?]		X	
*_Lepetodrilis fucenis_	X	X	
*_Neolepetopsis gordensis_	X	X	
Pseudococculinid			X
Pseudococculinid n. gen. A, n. sp. A	X	X	
Pseudococculinid n. gen. A, n. sp. B	X	X	
Aplacophora			
*Aplacophora n. gen. H, n. sp. J		X	
Amphipoda			
Dyopedos? sp.	X		
Lysianassidae sp.			X
Metopa sp.	X		
Copepoda			
Copepoda spp.	X		
Decapoda			
Munidopsis sp.			X
Isopoda			
Munnidae sp.		X	X
Tanaidacea			
Leptognathia sp. CCCC	X		
Leptognathia sp. FFFFF		X	
*_Protanais_ sp.			X
Pseudotanais sp. AA	X		
*Anemones		X	
Asteroidea		X	
*Echiurans		X	X
Nemertean		X	
Pycnogonida		X	
Sipuncula			X
Tunicata		X	

and *Prionospio* that might be expected in a normal deep-sea soft-sediment community. *Cossura* and *Paramphinome* tend to be found in shallower water in the western Atlantic (Maciolek and others, 1987a, b), and isopods are somewhat more abundant than in the western North Atlantic and equatorial Pacific. *Cossura* and *Chaetozone* were common at 1,310 m depth in the Santa Catalina Basin (Jumars and Eckman, 1983) and at depths up to 1,500 m in the Beaufort Sea (Bilyard and Carey, 1979). It is possible that disturbance from hydrothermal plumes has resulted in a fauna more characteristic of shallower depths elsewhere in the deep sea, where external perturbations may be more frequent in comparison to deeper areas. Twenty-nine new species were found, and most of these were at sites away from hydrothermal activity.

Four new genera were found from the vestimentiferan washings and the hydrothermal sulfides. A single new genus of phyllodocid polychaete was found associated with the wood. The ambient community had no new genera. Most deep-sea hydrothermal sites have endemic higher taxa specific to that area. The discovery of the four new genera from Gorda Ridge indicates that these vents are not an exception to the rule that each new vent area will have endemic higher taxa.

Very little similarity was found between the communities in sediment adjacent to wood and those in hydrothermal sediment. The hydrothermal sediment site had large numbers of *Amphisamytha galapagensis* (table 17.4) characteristic of most vent and cold seep areas and four species of Archaeogastropoda among the total of 13 species obtained in the qualitative scoop sediment sample. These results and the comparison of hard-surface communities indicate that pieces of wood are unlikely to be used as stepping stones by true vent species such as *A. galapagensis*

or species in vent genera such as *Provanna* and *Ridgeia*. Most hydrothermal vent species are unlikely to be found in association with wood or even such concentrated sources of organic material as whale carcasses (Smith and others, 1989).

The comparison of diversity supports the observation that concentrated sources of organic matter such as wood or hydrothermally based microbial productivity will result in local reductions in species diversity as well as different species compositions that contribute to regional diversity (Grassle and Morse-Porteous, 1987). The patterns follow the generalization that relatively disturbed deep-sea environments such as trenches, upwelling areas, regions of intense bottom currents, and hydrothermal vents have lower diversities, with the patterns of relative abundance skewed in the direction of the few most common species (Grassle, 1989).

REFERENCES CITED

Bilyard, G.R., and Carey, A.G., Jr., 1979, Distribution of western Beaufort Sea polychaetous annelids: Marine Biology, v. 54, p. 329–339.

Carey, A.G., Jr., Taghon, G.L., Stein, D.L., and Rona, P.A., 1990, Distributional ecology of benthic megaepifauna and fishes in Gorda Ridge axial valley, *in* McMurray, G.R., ed., Gorda Ridge, a seafloor spreading center in the United States' Exclusive Economic Zone: New York, Springer-Verlag, p. 225–240.

Clague, D.A., and Holmes, M.L., 1987, Geology, petrology, and mineral potential of the Gorda Ridge, *in* Scholl, D.W., Grantz, A., and Vedder, J.G., eds., Geology and resource potential of the continental margin of western North America and adjacent ocean basins–Beaufort Sea to Baja California: Houston, Circum-Pacific Council for Energy and Mineral Resources, Earth Science Series, v. 6, p. 563–580.

Clifford, H.T., and Stephenson, W., 1975, An introduction to numerical classification: New York, Academic Press, 229 p.

Grassle, J.F., 1989, Species diversity in deep-sea communities: Trends in Ecology and Evolution (TREE), v. 4, p. 12–15.

Grassle, J.F., and Morse-Porteous, L.S., 1987, Macrofaunal colonization of disturbed deep-sea environments and the structure of deep-sea benthic communities: Deep-Sea Research, v. 34, p. 1911–1950.

Grassle, J.F., and Smith, W.L., 1976, A similarity measure sensitive to the contribution of rare species and its use in investigation of variation in marine benthic communities: Oecologia, v. 25, p. 13–22.

Grassle, J.F., Brown-Leger, L.S., Morse-Porteous, L.S., Petrecca, R.F., and Williams, I., 1985, Deep-sea fauna of sediments in the vicinity of hydrothermal vents: Biological Society of Washington Bulletin, v. 6, p. 443–452.

Hessler, R.R., and Jumars, P.A., 1974, Abyssal community analysis from replicate box cores in the central North Pacific: Deep-sea Research, v. 21, p. 185–209.

Jumars, P.A., and Eckman, J.E., 1983, Spatial structure within deep-sea benthic communities, *in* Rowe, G.T., ed., The sea; Ideas and observations on progress in the study of the sea series; Volume 8, Deep sea biology: New York, Riley and Sons, p. 399–451.

Juniper, S.K., and Sibuet, M., 1987, Cold seep benthic communities in Japan subduction zones: Spatial organization, trophic strategies and evidence for temporal evolution: Marine Ecology: Progress Series, v. 40, p. 115–126.

Karlin, R., and Lyle, M., 1986, Sediment studies on Gorda Ridge: Oregon Department of Geology and Mineral Industries Open-File Report O-86-19, 76 p.

Maciolek, N., Grassle, J.F., Hecker, B., Boehm, P.D., Brown, B., Dade, B., Steinhauer, W.G., Baptiste, E., Ruff, R.E., and Petrecca, R., 1987a, Study of biological processes on the U.S. Mid-Atlantic Slope and Rise: Final report to Minerals Management Service, v. 2, 310 p.

Maciolek, N., Grassle, J.F., Hecker, B., Brown, B., Blake, J.A., Boehm, P.D., Petrecca, R., Duffy, S., Baptiste, E., and Ruff, R.E., 1987b, Study of biological processes on the U.S. North Atlantic Slope and Rise: Final report to Minerals Management Service, v. 2, 362 p.

Metvier, B., Okutani, T., and Ohta, S., 1986, *Calyptogena (Ectenagena) phaseoliformis* n.sp., an unusual vesicomyid bivalve collected by the submersible NAUTILE from abyssal depths of the Japan and Kurile Trenches: Venus, v. 45, p. 75–86.

Moore, G.W., 1970, Sea-floor spreading at the junction between Gorda Rise and Mendocino Ridge: Geological Society of America Bulletin, v. 81, p. 2817–2824.

Morton, J.L., Holmes, M.L., and Koski, R.A., 1987, Volcanism and massive sulfide formation at a sediment spreading center, Escanaba Trough, Northeast Pacific Ocean: Geophysical Research Letters, v. 14, p. 769–772.

Morton, J.L., Koski, R.A., Normark, W.R., and Ross, S.L., 1990, Distribution and composition of massive sulfide deposits at Escanaba Trough, southern Gorda Ridge, *in* McMurray, G.R., ed., Gorda Ridge: A seafloor spreading center in the United States' Exclusive Economic Zone: New York, Springer-Verlag, p. 77–92.

Petrecca, R.F., and Grassle, J.F., 1990, Notes on fauna from several deep-sea hydrothermal vent and cold seep soft-sediment communities, *in* McMurray, G.R., ed., Gorda Ridge: A seafloor spreading center in the United States' Exclusive Economic Zone: New York, Springer-Verlag, p. 279–283.

Smith, W.L., and Grassle, J.F., 1977, Sampling properties of a family of diversity measures: Biometrics, v. 33, p. 283–291.

Smith, C.R., Kukert, H., Wheatcroft, R.A., Jumars, P.A., and Deming, J.W., 1989, Vent fauna on whale remains: Nature, v. 341, p. 27–28.

Turner, R.D., 1977, Wood, mollusks and deep-sea food chains: Bulletin of the American Malacological Union, vol. for 1976, p. 13–19.

Vallier, T.L., Harold, P.J., Girdley, W.A., 1973, Provenances and dispersal patterns of turbidite sand in Escanaba Trough, Northeastern Pacific Ocean: Marine Geology, v. 15, p. 67–87.

Van Dover, C.L., Grassle, J.F., Boudrias, M., 1990, Hydrothermal vent fauna of Escanaba Trough (Gorda Ridge), *in* McMurray, G.R., ed., Gorda Ridge: A seafloor spreading center in the United States' Exclusive Economic Zone: New York, Springer-Verlag, p. 285–287.

Zierenberg, R.A., Koski, R.A., Shanks, W.C., III, Slack, J.F., 1988, Preliminary results of *Alvin* dives on active sediment-hosted massive sulfide deposits in the Escanaba Trough, southern Gorda Ridge [abs.]: Eos, Transactions American Geophysical Union, v. 69, p. 1488.

Chapter 18. Quaternary Foraminifers from Escanaba Trough, Northeast Pacific Ocean

By Paula J. Quinterno[1]

CONTENTS

ABSTRACT

Benthic faunas recovered from Escanaba Trough are dominated by agglutinated foraminifers typical of abyssal depths and include large specimens of *Bathysiphon, Cribrostomoides, Hormosina, Hyperammina, Reophax, Rhabdammina* ?, and *Rhizammina.* An unusual feature of the Escanaba Trough foraminifers is the use of large, angular fragments of basaltic volcanic glass in test construction. In samples containing basaltic glass, some foraminifers attach to the glass as a substrate. Calcareous foraminifers are rare or absent in the surface samples studied. The shallowest water depth sampled was 3,146 m; therefore, a present-day carbonate compensation depth (CCD) near 3,146 m is indicated for this area. Large agglutinated foraminifers generally are less abundant at depth in the cores, and in some cores small calcareous foraminifers predominate. This could be due to the destruction of agglutinated tests after burial by physical and chemical processes, but it is more likely indicative of a different depositional environment. The presence of calcareous foraminifers at these water depths probably indicates deposition in shallower water and subsequent downslope transport by turbidity currents. Dominance by sinistral *Neogloboquadrina pachyderma* at depth in several gravity cores indicates cooler temperatures than at present and indicates a Pleistocene age. An agglutinated foraminifer resembling *Rhabdammina,* but with interior ridges, occurs in most dredge samples and may be a new genus.

INTRODUCTION

Dredge samples and gravity cores were collected from northern (NESCA), southern (SESCA), and central Escanaba Trough in 1986 during three U.S. Geological Survey cruises of R/V *S.P. Lee* (L1-86-NC, L2-86-NC, and L3-86-NC). Additional cores from NESCA were obtained during a Geological Survey of Canada (GSC) cruise of the R/V *Tully* in 1989 (TUL-89D). The main purpose of the cruises was to study the processes and products of hydrothermal circulation at a sediment-covered spreading center (Morton and others, 1987). Although the collection of foraminifers was not a primary purpose of sampling, foraminifers from dredge samples and core tops were analyzed to determine the present-day distribution and especially to note whether or not a relationship could be seen between the occurrence of foraminifers and active hydrothermal vents. Foraminifers from subsurface samples of some cores were also analyzed and provided evidence for turbidite deposition during Pleistocene and Holocene time.

Gorda Ridge is a 300-km-long active spreading center in the northeast Pacific Ocean, situated between the Blanco Fracture Zone to the north and the Mendocino Fracture Zone to the south (fig. 18.1). Escanaba Trough, which occupies the southern third of Gorda Ridge, is an axial valley with water depths of approximately 3,200 to 3,300 m. It contains about 500 m of Quaternary turbiditic sediment thought to be derived largely from the Columbia and

[1] U.S. Geological Survey, Menlo Park, California

Klamath rivers during the Pleistocene when sea level was lower (Vallier and others, 1973; Normark and others, chap. 6, this volume).

Active hydrothermal vents and associated vent communities were discovered in 1988 in northern Escanaba Trough (latitude 41°00′ N., longitude 127°29′ W.) at 3,200 to 3,250 m water depth using the submersible DSV *Alvin* (Zierenberg and others, 1988; Grassle and Van Dover, 1989, Van Dover and others, 1990). Grassle and Petrecca (chap. 17, this volume) discuss the soft-sediment macrofaunal (larger than 0.3 mm) communities from the Escanaba Trough vent area. Unfortunately, sediment collected by submersible in close proximity to active vents was not subsampled for foraminifers; therefore, it is not known if vent-specific foraminifers are present in Escanaba Trough. However, samples collected in the general vicinity of both active and inactive vents yielded similar faunas, which were dominated by large agglutinated foraminifers.

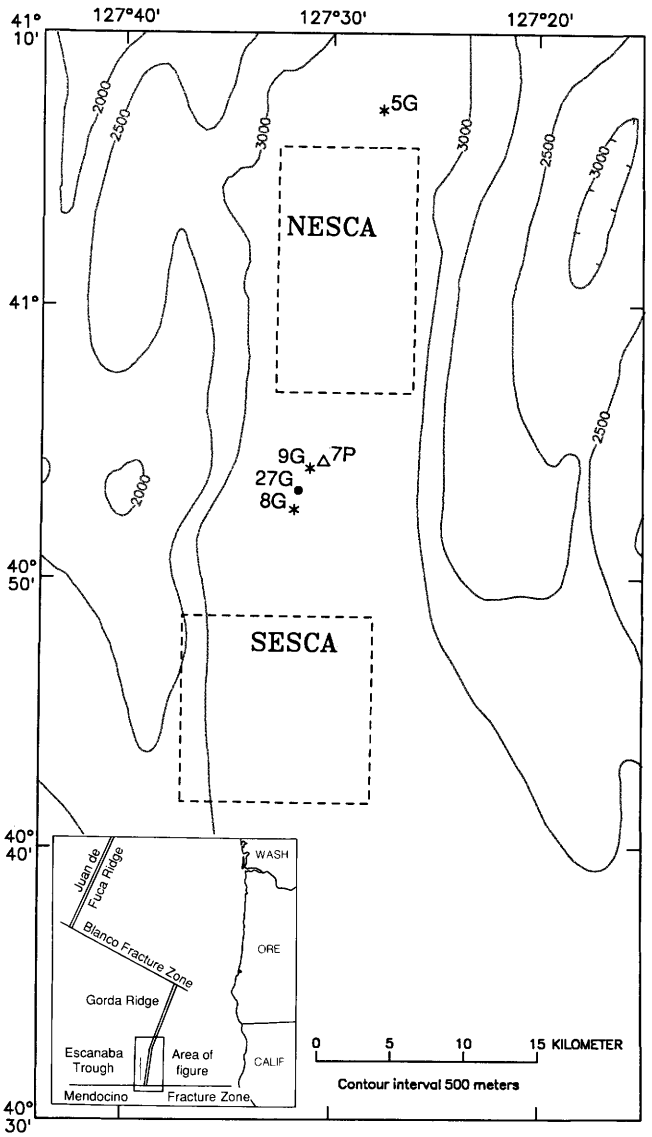

Figure 18.1. Bathymetric map of Escanaba Trough showing sample locations from central area. Symbols as follows: NESCA, northern Escanaba Trough; SESCA, southern Escanaba Trough; solid dot, L1-86-NC; asterisk, L3-86-NC; open triangle, *Tully* cruise of 1989. Hachures indicate area of closed low.

SAMPLING METHODS AND PROCEDURES

Dredge samples were collected with a round-frame chain bag dredge with a small cloth-lined pipe dredge mounted inside the mouth of the main dredge to collect unconsolidated sediment. A 3-m-long, 9-cm-diameter barrel gravity corer with a 500-kg weight stand was used to collect the USGS sediment cores. Cores provided by the GSC included gravity, piston, and trigger weight cores.

Subsample nomenclature is as follows: Cruises are designated as L1, L2, and L3 for USGS cruises L1-86-NC, L2-86-NC, and L3-86-NC respectively; and TUL-89D for the 1989 GSC R/V *Tully* cruise. Following the cruise designator is the sample number and sample type (D, dredge; G, gravity core; P, piston core; TR, trigger weight core), and when appropriate, the depth in the core. For example, subsample L1-25G-15-16 cm is from 15–16 cm depth in gravity core 25 from cruise L1-86-NC. Sediment subsamples for foraminiferal analysis were obtained from the small pipe dredges and cores (figs. 18.1, 18.2, and 18.3). The sediment was washed using a 0.063-mm sieve and air dried. It was dry-sieved with a 0.150-mm sieve, and the sediment portion greater than 0.150 mm was split (if many more than 350 specimens were present) using a microsplitter. All specimens in the split were picked and mounted on cardboard slides for identification. Thirteen samples provided by Florence Wong had been treated with hydrogen peroxide during processing for her study of mineral compositions of turbiditic sands (Normark and others, chap. 6, this volume). This treatment may have affected the preservation state of the foraminifers; therefore, these samples are marked with an asterisk in the preservation column of table 18.1.

A quantitative study of the foraminifers was not practical because of limitations of the sampling equipment used. Dredges provide large samples, but dredge stations often extend along the sea floor for a kilometer or more and, therefore, may sample more than one environment. The dredge digs into the sea floor to some unknown depth, so the sample may consist of sediment mixed from the upper several centimeters. Gravity and piston core samples may be more accurately located, but samples are small, and the surface sediment may be disturbed or missing due to a pressure wave created by the corer just before impact or by overpenetration of the corer into the sediment (sediment forced out the top of the corer). The core logs indicate that

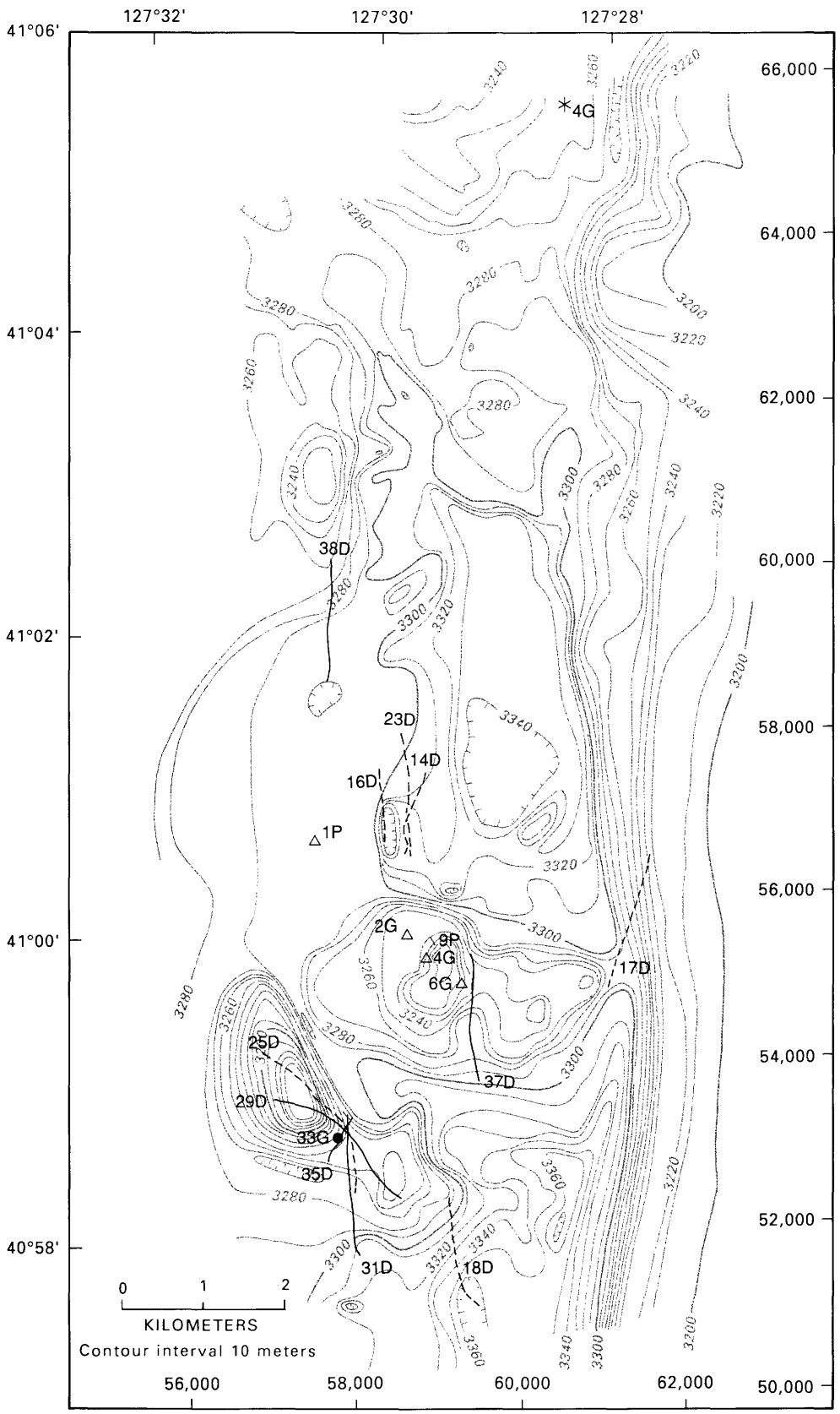

Figure 18.2. Northern Escanaba Trough sample locations. Symbols same as in figure 18.1; open circle, L2-86-NC, solid lines, L1-86-NC dredge tracks, dashed lines, L2-86-NC dredge tracks. Numbers along right and bottom give coordinates of local transponder net (in meters). Hachures indicate area of closed low.

sediment from the uppermost intervals of cores is frequently disturbed or missing. Box cores are better suited to quantitative analysis because the sediment surface is usually less disturbed, a large sample is available for study, and a known volume of the surface can be obtained. Unfortunately, box core samples were not available for this study. The type of foraminiferal taxa present also limit the value of quantitative studies. Large, tubular foraminifers dominate many of the Gorda Ridge samples; however, they often break during collection and processing, so an accurate count cannot be obtained.

OCEANOGRAPHY

Although Escanaba Trough is in a deep oceanic setting, it deviates from typical open oceanic areas in several respects. For example, the complex topography (figs. 18.2, 18.3) and the presence of hydrothermal activity presumably affect current patterns, water mass characteristics, sediment, and faunas. At present, however, only a limited amount of detailed oceanographic data is available. Escanaba Trough is seaward of influence from the California Current and the area of intense upwelling that occurs

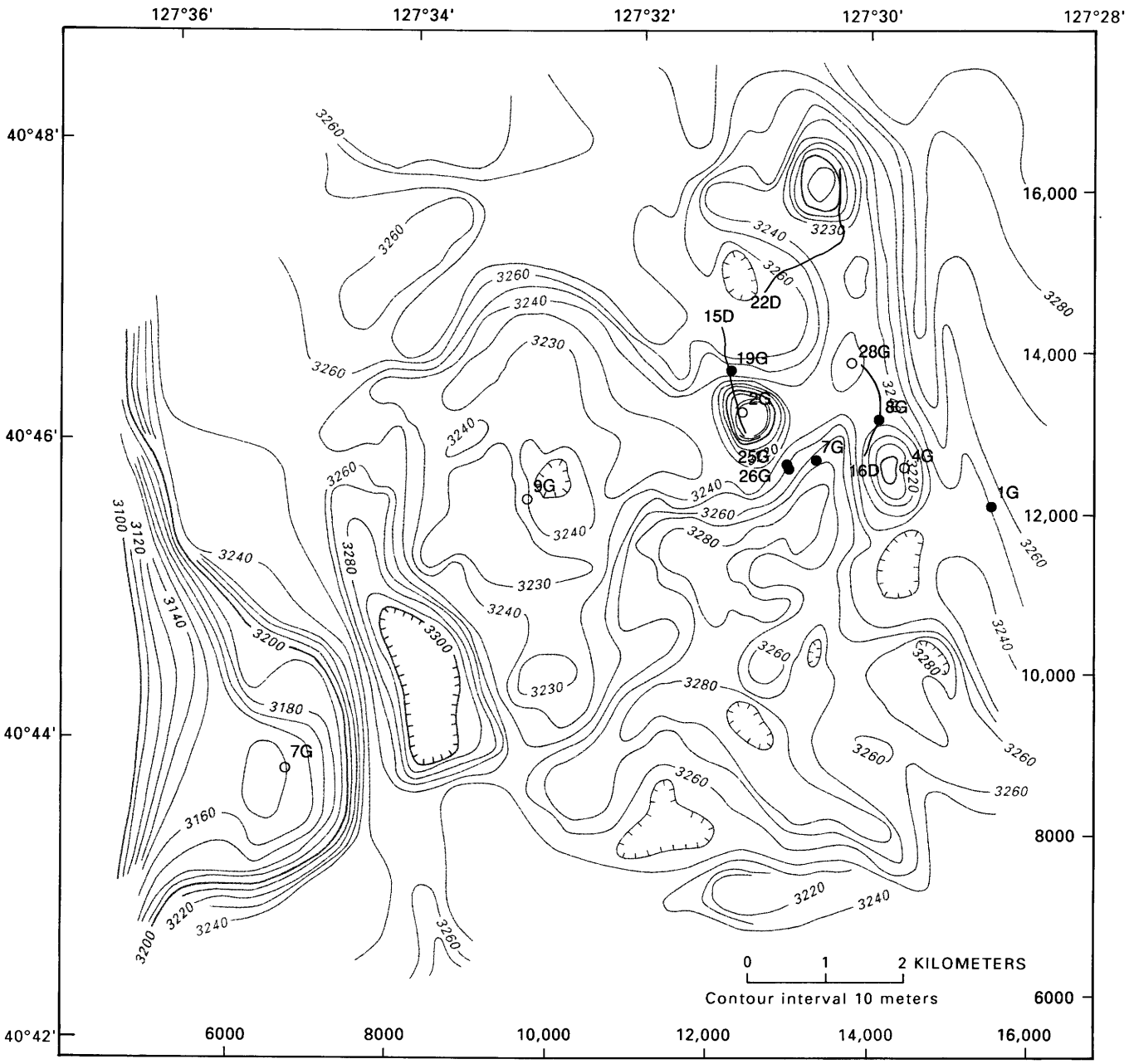

Figure 18.3. Southern Escanaba Trough sample locations. Explanations and symbols same as in figure 18.2.

Table 18.1. List of samples, water depths, and summary of foraminiferal faunal characteristics

[A (abundant), more than 500 individuals; C (common), 100–500; R (rare), fewer than 100; o, absent or barren; +, present; aggl, agglutinated foraminifers; calc, calcareous foraminifers; >, greater than; >>>, much greater than; H (high), more than 20 species; M (moderate), 10–20 species; L (low), fewer than 10 species; g, good; m, moderate; p, poor; *, samples treated with hydrogen peroxide for mineral analysis]

Sample number	Water depth (m)	Benthic abundance	Planktonic abundance	Large agglutinated tests (>1.0 mm)	Assemblage composition by wall type	Tests with volcanic glass	Species diversity	Preservation
NESCA								
L1-29D	3,260–3,230	A	R	+	aggl>>>calc	+	H	m
L1-31D	3,300–3,290	A	R	+	aggl>>>calc	+	H	m
L1-33G 0–1 cm	3,299	R	o	+	aggl>>calc	+	H	m
L1-33G 104–105 cm	3,299	o	o	o	o	o	o	o
L1-35D	3,280–3,240	A	o	+	aggl>>>calc	+	H	m
L1-37D	3,310–3,290	A	R	+	aggl>>>calc	+	H	m
L1-38D	3,310–3,260	A	R	+	aggl>>>calc	+	H	m
L2-14D	3,325–3,315	A	R	+	aggl>>>calc	+	H	m
L2-16D	3,345–3,295	A	o	+	aggl>>>calc	+	H	m
L2-17D	3,200–3,120	C	R	+	aggl>>calc	+	M	p
L2-18D	3,350–3,250	A	o	+	aggl>>>calc	+	H	m
L2-23D	3,325–3,295	A	R	+	aggl>>>calc	+	H	m
L2-25D	3,270–3,205	A	o	+	aggl>>>calc	+	H	m
L3-4G 15–16 cm	3,262	R	R	o	calc>>aggl	o	M	m
L3-4G 39–40 cm	3,262	R	R	o	calc>>aggl	o	M	m
L3-5G 3–4 cm	3,266	o	o	o	o	o	o	o
L3-5G 30–31 cm	3,266	R	o	o	calc	o	L	m
L3-5G 60–61 cm	3,266	R	R	o	calc	o	L	m
TUL-89D-1P Top (6–7 cm)	3,305	R	R	o	calc>>aggl	o	L	p
TUL-89D-1TR Top (3–4 cm)	3,305	R	R	+	aggl>calc	o	L	p
TUL-89D-1TR 50–51 cm	3,305	R	R	o	calc>aggl	o	L	p
TUL-89D-1TR 52–53 cm	3,305	R	o	+	aggl>>calc	+	H	m
TUL-89D-1TR 98.5–99.5 cm	3,305	R	R	o	calc>>aggl	+	L	p
TUL-89D-2G Top (2.5–3.5 cm)	3,250	R	R	o	calc>>aggl	+	L	p
TUL-89D-2G 94–95 cm	3,250	R	R	o	calc	o	L	m*
TUL-89D-4G 0–1 cm	3,235	R	R	+	aggl	+	M	m
TUL-89D-6G Top (2.5–3.5 cm)	3,220	R	o	+	aggl	o	M	m
TUL-89D-9TR Top (2 cm)	3,240	R	o	+	aggl	+	H	m
TUL-89D-9TR 7–8 cm	3,240	R	o	o	aggl>calc	o	L	p
TUL-89D-9TR 12–14 cm	3,240	C	C	o	calc>>>aggl	o	M	m*
SESCA								
L1-1G 0–1 cm	3,247	R	o	+	aggl>calc	o	H	m
L1-7G 0–1 cm	3,240	R	o	+	aggl	o	M	m
L1-7G 211–212 cm	3,240	R	R	o	calc	o	M	m*
L1-8G 0–1 cm	3,236	R	o	o	aggl>calc	o	M	m
L1-15D	3,261–3,251	A	o	+	aggl>>>calc	o	H	m
L1-16D	3,236–3,258	R	o	+	aggl>calc	o	L	p
L1-19G 0–1 cm	3,258	R	o	+	aggl>calc	o	M	m
L1-22D	3,247–3,264	A	R	+	aggl>>calc	o	H	m
L1-25G 0–1 cm	3,232	R	o	+	aggl	o	H	m
L1-25G 48–49 cm	3,232	R	R	o	calc	o	L	p*
L1-25G 119–120 cm	3,232	R	C	o	calc	o	M	m*
L1-26G 0–1 cm	3,225	R	o	o	aggl>calc	o	M	m
L1-26G 33.5–35 cm	3,225	R	R	o	calc	o	L	p*
L1-26G 40–41 cm	3,225	R	R	o	calc	o	L	p*
L2-2G 0–1 cm	3,160	R	o	+	aggl>calc	o	H	p
L2-2G 72–74 cm	3,160	R	C	o	calc	o	H	g*
L2-4G 7–8 cm	3,199	R	o	+	aggl>calc	o	L	p
L2-7G 7–8 cm	3,146	R	o	+	aggl>calc	o	L	p
L2-7G 235–237 cm	3,146	C	C	o	calc	o	L	g*
L2-9G 20–21 cm	3,232	R	o	+	aggl>calc	o	L	p
L2-9G 48–50 cm	3,232	R	o	o	aggl>calc	o	L	p
L2-9G 75–76 cm	3,232	o	o	o	o	o	o	o
L2-28G 2–3 cm	3,251	R	o	+	aggl>calc	o	M	p
Central Escanaba Trough								
L1-27G 0–1 cm	3,318	R	o	+	aggl>calc	o	H	m
L1-27G 64–65 cm	3,318	o	o	o	o	o	o	o*
L1-27G 71–72 cm	3,318	o	o	o	o	o	o	o*
L1-27G 87–95 cm	3,318	R	o	o	1 aggl	o	L	m*
L3-8G 10–11 cm	3,279	R	R	o	calc>>aggl	o	M	m
L3-8G 84–85 cm	3,279	o	o	o	o	o	o	o
L3-9G 8/9–10/11 cm	3,322	o	R	o	1 calc	o	L	m
TUL-89D-7TR Top (6 cm)	3,350	R	R	o	aggl>calc	o	M	m
TUL-89D-7P Top (2.5–3.5 cm)	3,350	R	R	+	aggl>calc	o	H	m
TUL-89D-7P 240–242 cm	3,350	R	R	o	calc	o	L	m*

along the continental slope. The water mass properties in Escanaba Trough are probably influenced to some extent by the North Pacific Gyre, but it is likely that local topography significantly affects the bottom currents.

Carey and others (1990) suggested that the food supply is more abundant in the Gorda Ridge axial valley than at equivalent depths on oceanic abyssal plains. The three possible sources they listed are (1) continental runoff via the Columbia River plume in the summer (Barnes and others, 1972); (2) entrainment by the valley walls of currents and concentration of particulate organic matter; and (3) bacterial chemosynthetic primary production associated with active hydrothermal vents (Cavanaugh, 1985; Rona and others, 1988; Zierenberg and others, 1988).

PREVIOUS STUDIES

Deep-water foraminifers from the North Pacific have been studied by a number of workers including Cushman (1910–1917), Smith (1973), Hessler and Jumars (1974), Saidova (1975), Bernstein and others (1978), Snider and others (1984), and Schröder and others (1988). Hessler and Jumars (1974) and Bernstein and others (1978) studied the biota in box cores from the CLIMAX II area, located in the central North Pacific Ocean about 770 km north of Hawaii. This is a nutrient-poor area that lies beneath the central North Pacific gyre at approximately 5,800 m water depth. The sedimentation rate is very low, and the sediment type is red clay with manganese nodules. Agglutinated benthic foraminifers were abundant and diverse, and the authors concluded that agglutinated foraminifers might affect the structure and dynamics of deep-sea benthic communities more than the metazoan macrofaunas that are usually the objects of deep-sea ecological studies. In a later study at a nearby site, Snider and others (1984) estimated the biomass of biota greater than 0.01 mm taken from box cores collected at water depths of approximately 5,800 m. They found that foraminifers dominated the fauna, making up 55.2 percent of the total biomass of all size classes of identifiable organisms. Bernstein and others (1978) identified foraminifers only to the generic level; species were distinguished by numbers, and none of the specimens were illustrated. Schröder and others (1988) extended this study by formally identifying and illustrating the North Pacific specimens in order to compare them with Atlantic Ocean assemblages from the Nares Abyssal Plain.

To date, only Fowler and Kulm (1970), Vallier and others (1973), and Clague and others (1984) have discussed the foraminifers from Gorda Ridge. Fowler and Kulm (1970) reported displaced benthic foraminifers in a dredge haul collected at a water depth of approximately 2,000 m from the western wall of Escanaba Trough. Sublittoral forms from this dredge haul made up more than 76 percent of the benthic assemblage in a semiconsolidated clayey sandstone derived from the Columbia and Klamath rivers and transported by turbidity currents into Escanaba Trough. A Pleistocene age for the sediment was derived from a typical subarctic planktonic fauna dominated by sinistrally coiled *Neogloboquadrina pachyderma* (Bandy, 1960; Ingle, 1973). Agglutinated species, if present, were not discussed. Vallier and others (1973) reported that Deep Sea Drilling Project (DSDP) Site 35 in Escanaba Trough yielded cold-water Pleistocene foraminifers in the upper six cores (to a depth of 166 m).

Clague and others (1984) analyzed 19 dredge samples from the northern part of Gorda Ridge (between latitudes 41°27.65′ N. and 42°56.99′ N.) and found that agglutinated foraminifers were dominant in most samples. Calcareous benthic and planktonic foraminifers were present at most sites and dominant in three of the samples (D3, D11, and D17). I recently examined the planktonic foraminifers in these three samples and found that planktonic faunas in samples D3 and D11 (3,165 and 3,105 m water depths, respectively) are dominated by sinistrally coiled *Neogloboquadrina pachyderma*, indicative of cool surface water temperatures (Bandy, 1960; Ingle, 1973), and a possible Pleistocene age. Although sinistrally coiled *N. pachyderma* dominates over the dextrally coiled form in sample D17 (1,700 m water depth), warmer (possibly Holocene) conditions are suggested by an abundance of *Globigerina* sp. aff. *G. umbilicata* (Kennett and Srinivasan, 1983). However, because D17 is a dredge sample, more than one environment or stratigraphic horizon may have been sampled.

ACKNOWLEDGMENTS

I thank Jere Lipps (University of California, Berkeley) and William Sliter (U.S. Geological Survey) for reviewing the manuscript and Brad Carkin and Carol Reiss (both U.S. Geological Survey) for technical support. Robert Oscarson (U.S. Geological Survey) provided the scanning electron micrographs. The Dynaphot photographs were taken at Dalhousie University (Audio-Visual Services) under the direction of David Scott.

FORAMINIFERS FROM ESCANABA TROUGH

One hundred sixteen benthic taxa were identified from 14 dredge and 45 core samples; 43 taxa are calcareous and 71 are agglutinated. Planktonic foraminifers are present in 31 samples. Agglutinated foraminifers far outnumber calcareous forms in all the dredge samples and in most cores. Many of these organisms are shown in figures 18.4 through 18.9 at the end of this chapter. Figures 18.4, 18.5, 18.6, and 18.8 are scanning electron photomicrographs;

colored figures 18.7 and 18.9 are light microscope photographs and are placed on pages facing figures 18.6 and 18.8 to help distinguish basaltic glass from other mineral grains. Table 18.1 summarizes some characteristics of the faunas. Tables 18.2 and 18.3 list the agglutinated and calcareous foraminiferal taxa, respectively, identified from Escanaba Trough and show their presence or absence in the samples. Benthic foraminifers, especially agglutinated specimens larger than 1 mm, are more abundant in the dredge samples than in the tops of the gravity cores (table 18.1). Although dredge subsamples were larger and, therefore, would yield more specimens than the tops of gravity cores, this may not be the only reason for the difference in abundance. Dredge sites were chosen where rock exposures were common and sediment cover thin; gravity core sites were chosen where sediment cover was thicker and more widespread. It is likely that substrate and other conditions at the dredge sites provided more favorable environments for large agglutinated foraminifers.

GRAVITY AND PISTON CORE SAMPLES

Agglutinated foraminifers dominate the assemblages in the tops of the majority of gravity cores from Escanaba Trough; calcareous foraminifers predominate at depth (table 18.1). A similar trend has been noted by others who have studied deep-sea foraminifers from the Atlantic and Pacific Oceans (Kaminski, 1985; Schröder, 1986). A possible explanation is that reducing conditions at depth in the sediment cause the iron in the cement of the agglutinated test to become unstable when it is reduced from the ferric to the ferrous state; it becomes mobilized and the test disintegrates (Sidner and McKee, 1976). This process may be partly responsible for the lack of agglutinated foraminifers at depth in the Escanaba Trough cores, but it probably is not the main reason in the core samples studied. Sedimentological and foraminiferal evidence indicates sediment transport and deposition by turbidity flows which were especially prevalent during Pleistocene time. The turbidites are recognized by mineral composition and texture (Normark and others, chap. 6, this volume), magnetic susceptibility measurements (Karlin, 1989; Karlin and Zierenberg, chap. 7, this volume), and the presence of calcareous foraminifers indicative of shallower water and (or) cooler water temperatures than at present. Agglutinated faunas occurring above turbidites in several gravity cores from Escanaba Trough probably indicate colonization after the flows.

Although planktonic foraminifers are sparse in most samples, I have used the coiling ratios of sinistrally and dextrally coiled *Neogloboquadrina pachyderma* to determine relative paleotemperatures (table 18.4). Descriptions of cores containing foraminifers indicative of turbidites follow.

L2-86-2G

This core was taken from a hilltop at SESCA from 3,160 m water depth (fig. 18.3). Agglutinated foraminifers dominate the assemblage in the upper centimeter and are typical of faunas from this water depth. In contrast, calcareous benthic and planktonic foraminifers are abundant, and agglutinated forms are absent at 72 to 74 cm. Specimens of the planktonic foraminifer, *Neogloboquadrina pachyderma,* at 72 to 74 cm are 86 percent sinistrally coiled and 14 percent dextrally coiled (table 18.4); this indicates cooler temperatures than at present and supports Karlin's (1989) interpretation, based on high magnetic susceptibility values, that the core is made up of Pleistocene sediment.

The presence of two shelf foraminifers, *Buccella* sp. aff. *B. frigida* and *Elphidium clavatum* (table 18.3), at 70 to 72 cm indicates downslope transport. Other calcareous foraminifers typical of lower middle bathyal (less than 2,000 m) or shallower depths include *Buliminella tenuata, Epistominella pacifica, Globobulimina* sp., and *Uvigerina peregrina.* These displaced foraminifers indicate transport by turbidity flow across the shelf and slope into the deeper waters of Escanaba Trough during the Pleistocene when sea levels were lower. Evidence of reworking from Miocene sediment is implied by one poorly preserved orange-stained specimen of *Nonion costiferum.*

L1-86-7G

Core L1-86-7G is located approximately 1 km southeast of L2-86-2G (fig. 18.3). The top of the core contains an agglutinated foraminiferal fauna typical of the 3,240 m water depth from which it was collected; calcareous foraminifers are absent (tables 18.1 and 18.3). In contrast, the assemblage at 211 to 212 cm is exclusively calcareous and most species are typical of water depths less than 2,000 m. Although sinistrally coiled *Neogloboquadrina pachyderma* is more abundant (60 percent) than the dextrally coiled morphotype (40 percent), the dominance is not as pronounced as in L2-86-2G (86 and 14 percent, respectively) and may indicate cooler temperatures than at present but slightly warmer than indicated in L2-86-2G at 72 to 74 cm. Karlin and Zierenberg (chap. 7, this volume) assign a Pleistocene age to sediment below 30 cm in L1-86-7G.

L1-86-25G

This core is located in a valley approximately 1 km southeast of L2-86-2G at a water depth of 3,232 m (fig. 18.3). Sediment in the uppermost centimeter is brown mud with abundant fecal pellets and a foraminiferal fauna that is exclusively agglutinated. A sparse, very poorly preserved calcareous fauna is present in a sandy interval at

Table 18.2. Agglutinated foraminifers from Escanaba Trough.

[x, present; ?, questionable identification]

Species	Sample number	L1-1G 0–1 cm	L1-7G 0–1 cm	L1-7G 211–212 cm	L1-8G 0–1 cm	L1-15D	L1-16D	L1-19G 0–1 cm	L1-22D	L1-25G 0–1 cm	L1-25G 48–49 cm	L1-25G 119–120 cm	L1-26G 0–1 cm	L1-26G 33.5–35 cm	L1-26G 40–41 cm	L1-27G 0–1 cm	L1-27G 64–65 cm	L1-27G 71–72 cm	L1-27G 87–95 cm	L2-2G 0–1 cm	L2-2G 72–74 cm	L2-4G 7–8 cm	L2-7G 7–8 cm	L2-7G 235–237 cm	L2-9G 20–21 cm	L2-9G 48–50 cm	L2-9G 75–76 cm	L2-28G 2–3 cm	L3-8G 10–11 cm	L3-8G 84–85 cm	L3-9G 8/9–10/11 cm	TUL-89D-7TR Top (6 cm)	TUL-89D-7P Top (2.5–3.5 cm)
Adercotryma glomerata		x	x	–	x	x	–	x	x	x	–	–	x	–	–	x	–	–	–	x	–	x	x	–	x	x	–	x	–	–	–	x	x
Ammobaculites americanus		–	–	–	–	–	–	–	–	x	–	–	–	–	–	–	–	–	–	–	–	–	–	–	–	–	–	–	–	–	–	–	–
A. microformis		?	–	–	x	x	–	–	x	x	–	–	–	–	–	x	–	–	–	x	–	x	x	–	–	–	–	x	–	–	–	–	x
A. sp. aff. *A. agglutinans*		–	–	–	–	–	–	–	–	x	–	–	–	–	–	–	–	–	–	–	–	–	–	–	–	–	–	–	–	–	–	–	–
A. spp.		–	x	–	–	x	–	–	x	–	–	–	x	–	–	?	–	–	–	x	–	–	–	–	x	x	–	x	–	–	–	–	x
Ammodiscus incertus		x	x	–	x	x	–	x	x	x	–	–	x	–	–	x	–	–	–	x	–	–	x	–	–	–	–	–	–	–	–	–	x
Ammoglobigerina sp.		–	?	–	–	–	–	–	–	x	–	–	–	–	–	x	–	–	–	–	–	x	–	–	?	–	–	–	–	–	–	–	–
Ammomarginulina foliacea		–	–	–	–	?	–	–	–	–	–	–	–	–	–	–	–	–	–	?	–	–	–	–	–	–	–	x	–	–	–	–	–
A. foliacea f. *recurva*		x	–	–	–	x	–	x	x	x	–	–	–	–	–	x	–	–	–	x	–	–	x	–	x	–	–	–	–	–	–	–	–
A. sp. aff. *A. ensis*		x	–	–	?	–	–	–	–	–	–	–	x	–	–	?	–	–	–	–	–	–	–	–	–	–	–	–	–	–	–	–	–
Ammoscalaria tenuimargo		x	–	–	–	–	–	–	–	–	–	–	–	–	–	–	–	–	–	–	–	–	?	–	–	–	–	–	–	–	–	–	–
Astrammina rara		–	–	–	–	–	–	–	–	–	–	–	–	–	–	–	–	–	–	–	–	–	–	–	–	–	–	x	–	–	–	–	–
Astrorhiza sp.		–	–	–	–	–	–	–	–	–	–	–	–	–	–	–	–	–	–	–	–	–	–	–	–	–	–	–	–	–	–	–	–
Bathysiphon rufus		–	x	–	–	x	x	–	x	–	–	–	–	–	–	–	–	–	–	–	–	–	–	–	–	–	–	–	–	–	–	–	x
Bathysiphon sp.		x	–	–	x	x	–	x	x	x	–	–	x	–	–	x	–	–	–	x	–	x	x	–	x	–	–	x	–	–	–	x	x
Cribrostomoides subglobosus		?	x	–	–	x	x	–	x	?	–	–	–	–	–	–	–	–	–	–	–	–	–	–	–	x	–	–	–	–	–	–	x
C. wiesneri		–	–	–	x	x	–	x	x	x	–	–	–	–	–	x	–	–	–	–	–	–	–	–	x	–	–	–	–	–	–	x	–
C. sp.		–	–	–	–	x	–	–	–	x	–	–	–	–	–	x	–	–	–	–	–	–	–	–	–	–	–	x	–	–	–	–	–
Cyclammina sp.		–	–	–	–	–	–	–	–	–	–	–	–	–	–	–	–	–	–	–	–	–	–	–	–	–	–	–	–	–	–	–	–
Cystammina pauciloculata		–	–	–	–	–	–	–	x	x	–	–	–	–	–	x	–	–	–	x	–	–	–	–	–	–	–	x	–	–	–	–	x
Eggerella spp.		–	–	–	–	–	–	–	–	–	–	–	–	–	–	–	–	–	–	–	–	–	–	–	–	–	–	–	–	–	–	–	–
Glomospira gordialis		–	–	–	x	x	–	?	–	?	–	–	x	–	–	x	–	–	–	–	–	–	–	–	–	–	–	–	–	–	–	–	x
Haplophragmoides spp.		–	–	–	–	–	–	–	–	–	–	–	–	–	–	–	–	–	–	–	–	–	?	–	?	–	–	–	–	–	–	–	x
H. columbiense		–	–	–	–	–	–	–	–	–	–	–	–	–	–	–	–	–	–	–	–	–	–	–	–	–	–	–	–	–	–	–	–
H. rotalutum		–	–	–	–	x	–	–	x	–	–	–	–	–	–	–	–	–	–	–	–	–	–	–	–	–	–	–	–	–	–	–	–
H. sphaeriloculus		–	x	–	–	–	–	?	–	x	–	–	–	–	–	–	–	–	–	–	–	–	–	–	–	–	–	x	–	–	–	x	–
Hormosina carpenteri		–	–	–	?	–	–	–	–	–	–	–	–	–	–	–	–	–	–	–	–	–	–	–	–	–	–	–	–	–	–	–	–
H. globulifera		x	x	–	x	x	x	x	x	x	–	–	x	–	–	x	–	–	–	x	–	–	x	–	x	–	–	x	–	–	–	–	x
Hyperammina friabilis		–	–	–	–	x	–	–	–	–	–	–	–	–	–	–	–	–	–	x	–	–	–	–	–	–	–	–	–	–	–	–	–
H. laevigata		–	x	–	–	x	–	–	x	–	–	–	–	–	–	x	–	–	–	–	–	–	–	–	–	–	–	–	–	–	–	–	–
H. sp.		–	–	–	–	–	–	–	–	–	–	–	–	–	–	–	–	–	–	x	–	–	–	–	–	–	–	–	–	–	–	–	–
Jaculella sp.		–	–	–	–	–	–	–	x	–	–	–	–	–	–	–	–	–	–	–	–	–	–	–	–	–	–	–	–	–	–	–	–
Karreriella novangliae		–	–	–	–	–	–	–	–	–	–	–	–	–	–	–	–	–	–	–	–	–	–	–	–	–	–	–	–	–	–	–	–
K. sp.		x	x	x	x	–	–	x	x	x	–	–	x	–	–	x	–	–	–	–	–	–	x	–	–	–	–	–	x	–	–	–	–
Labrospira crassimargo		–	–	–	–	–	–	–	–	–	–	–	–	–	–	–	–	–	–	x	–	–	–	–	–	–	–	–	–	–	–	–	–
Martinotiella spp.		–	–	–	–	–	–	–	x	–	–	–	–	–	–	–	–	–	–	–	–	–	–	–	–	–	–	–	–	–	–	–	–
Nodellum membranaceum		?	–	–	–	–	–	–	–	–	–	–	–	–	–	–	–	–	–	–	–	–	–	–	–	–	–	–	–	–	–	–	–
Nodulina dentalinaformis		–	–	–	–	–	–	x	–	x	–	–	x	–	–	?	–	–	–	–	–	–	–	–	–	–	–	–	–	–	–	–	–
Pelosina cylindrica		–	–	–	–	–	–	–	–	–	–	–	–	–	–	–	–	–	–	–	–	–	–	–	–	–	–	–	–	–	–	–	–
Psammosphaera parva		–	x	–	?	x	–	?	x	?	–	–	–	–	–	?	–	–	–	?	–	–	–	–	–	–	–	–	–	–	x	x
Pseudonodosinella nodulosa		x	–	–	–	–	–	x	x	–	–	–	–	–	–	x	–	–	–	–	–	–	–	–	–	–	–	–	–	–	–	–	x
Recurvoides contortus		–	–	–	x	–	?	x	?	–	–	–	–	–	–	x	–	–	–	x	–	–	–	–	–	x	–	x	–	–	–	–	x
R. scitulum		–	x	–	–	–	–	–	?	–	–	–	–	–	–	–	–	–	–	–	–	–	–	–	–	–	–	–	–	–	–	–	x
R. spp.		x	–	–	–	x	x	–	–	–	–	–	x	–	–	–	–	–	–	–	–	–	x	–	x	–	–	–	–	–	–	–	–
Reophax bacillaris		–	–	–	–	–	–	–	–	–	–	–	–	–	–	–	–	–	–	–	–	x	–	–	–	–	–	–	–	–	–	–	–
R. bilocularis		–	–	–	–	–	–	–	x	–	–	–	–	–	–	–	–	–	–	–	–	–	–	–	–	–	–	–	–	–	–	–	–
R. difflugiformis		x	x	–	–	x	–	–	x	x	–	–	–	–	–	x	–	–	–	x	–	–	–	–	–	–	–	x	–	–	–	x	x
R. distans		?	–	–	–	x	–	?	–	–	–	–	–	–	–	–	–	–	–	x	–	–	–	–	–	–	–	–	–	–	–	–	–
R. guttifer		–	–	–	–	–	–	–	x	?	–	–	–	–	–	–	–	–	–	–	–	–	–	–	–	–	–	–	–	–	–	x	–
R. horridus		–	–	–	–	x	–	–	x	–	–	–	–	–	–	–	–	–	–	–	–	–	–	–	–	–	–	–	–	–	–	–	–
R. scorpiurus		–	–	–	–	–	–	–	–	?	–	–	?	–	–	?	–	–	–	–	–	–	–	–	–	–	–	–	–	–	–	–	x
R. subfusiformis		–	–	–	–	–	–	–	–	–	–	–	–	–	–	–	–	–	–	–	–	–	–	–	–	–	–	–	–	–	–	–	–
R. spp.		x	x	–	x	x	–	x	x	x	–	–	x	–	–	–	–	–	–	x	–	x	x	–	x	–	–	?	–	–	–	x	x
Rhabdammina spp.		x	–	–	–	x	–	x	x	x	–	–	–	–	–	x	–	–	–	–	–	–	–	–	–	–	–	–	–	–	–	?	x
R. sp. (with ridges)		–	–	–	–	x	–	–	x	–	–	–	–	–	–	–	–	–	–	x	–	–	–	–	–	–	–	–	–	–	–	–	–
Rhizammina algaeformis		–	–	–	x	–	–	x	x	–	–	–	–	–	–	–	–	–	–	–	–	–	–	–	–	–	–	–	–	–	–	x	x
Saccammina sphaerica		x	?	–	–	–	–	–	–	–	–	–	–	–	–	?	–	–	–	–	–	–	–	–	–	–	–	–	–	–	–	–	–
S. sphaerica var. *catenulata*		–	–	–	–	–	–	–	–	–	–	–	–	–	–	–	–	–	–	–	–	–	–	–	–	–	–	–	–	–	–	–	–
S. socialis ?		–	–	–	–	–	–	–	–	–	–	–	–	–	–	–	–	–	–	–	–	–	–	–	–	–	–	–	–	–	–	–	–
S. tubulata		–	x	–	–	–	–	–	–	x	–	–	–	–	–	x	–	–	–	–	–	–	–	–	–	–	–	–	–	–	–	–	–
Saccorhiza ramosa		?	?	–	?	x	–	?	x	x	–	–	?	–	–	x	–	–	–	x	–	–	x	–	x	–	–	x	–	–	–	?	x
Spiroplectammina sp.		–	–	–	–	–	–	–	–	–	–	–	x	–	–	–	–	–	–	–	–	–	–	–	–	–	–	–	–	–	–	–	–
Subreophax aduncus		–	–	–	–	x	–	–	–	–	–	–	–	–	–	–	–	–	–	–	–	–	–	–	–	–	–	–	–	–	–	–	–
Textularia spp.		?	–	–	–	–	–	–	–	–	–	–	–	–	–	–	–	–	–	–	–	–	–	–	–	–	–	–	–	–	–	–	–
Tholosina vesicularis		–	–	–	–	–	–	–	–	–	–	–	–	–	–	–	–	–	–	–	–	–	–	–	–	–	–	–	–	–	–	–	–
Thurammina sp.		–	–	–	–	–	–	–	x	–	–	–	x	–	–	–	–	–	–	–	–	–	–	–	–	–	–	–	–	–	–	–	–
Tolypammina ?		–	–	–	–	–	–	–	–	–	–	–	–	–	–	–	–	–	–	–	–	–	–	–	–	–	–	–	–	–	–	–	–
Trochammina globulosa		–	–	–	–	x	–	x	x	x	–	–	–	–	–	–	–	–	–	?	–	–	–	–	–	–	–	–	–	–	–	–	x
T. inconspicua		–	–	–	–	–	–	–	–	–	–	–	–	–	–	–	–	–	–	–	–	–	–	–	–	–	–	–	–	–	–	–	–
T. spp.		x	–	–	–	x	–	–	x	x	–	–	–	–	–	?	–	–	–	x	–	x	–	–	x	x	–	x	–	–	–	x	x
Vanhoeffenella sp.		–	–	–	–	–	–	–	–	–	–	–	–	–	–	–	–	–	–	–	–	–	–	–	–	–	–	–	–	–	–	–	–
Foraminifers on rocks		–	–	–	–	–	–	–	–	–	–	–	–	–	–	–	–	–	–	–	–	–	–	–	–	–	–	–	–	–	–	–	–

Table 18.2. Agglutinated foraminifers from Escanaba Trough—Continued.

[x, present; ?, questionable identification]

Species	Sample number	TUL-89D-7P 240–242 cm	L1-29D	L1-31D	L1-33G 0–1 cm	L1-33G 104–105 cm	L1-35D	L1-37D	L1-38D	L2-14D	L2-16D	L2-17D	L2-18D	L2-23D	L2-25D	L3-4G 15–16 cm	L3-4G 39–40 cm	L3-5G 3–4 cm	L3-5G 30–31 cm	L3-5G 60–61 cm	TUL-89D-1P Top (6–7 cm)	TUL-89D-1TR Top (3–4 cm)	TUL-89D-1TR 50–51 cm	TUL-89D-1TR 52–53 cm	TUL-89D-1TR 98.5–99.5 cm	TUL-89D-2G Top (2.5–3.5 cm)	TUL-89D-2G 94–95 cm	TUL-89D-4G 0–1 cm	TUL-89D-6G Top (2.5–3.5 cm)	TUL-89D-9TR Top (2 cm)	TUL-89D-9TR 7–8 cm	TUL-89D-9TR 12–14 cm
Adercotryma glomerata		–	x	x	x	–	x	x	x	x	x	–	x	x	x	–	–	–	–	–	–	x	–	x	–	–	–	–	x	–	x	–
Ammobaculites americanus		–	–	–	–	–	–	–	–	–	–	–	–	–	–	–	–	–	–	–	–	–	–	–	–	–	–	–	–	–	–	–
A. microformis		–	x	x	x	–	x	x	x	x	x	x	x	x	x	–	–	–	x	–	–	–	–	x	–	–	–	x	x	–	–	–
A. sp. aff. *A. agglutinans*		–	x	x	–	–	x	x	x	–	–	–	–	–	x	–	–	–	–	–	–	–	–	–	–	–	–	–	–	–	–	–
A. spp.		–	–	–	–	–	x	–	–	x	x	–	–	x	x	–	–	–	–	–	–	–	–	–	–	x	–	–	–	–	–	–
Ammodiscus incertus		–	x	x	x	–	x	x	x	x	?	x	x	x	x	–	–	–	–	–	–	–	–	x	–	–	–	–	x	x	–	–
Ammoglobigerina sp.		–	x	x	–	–	x	x	x	–	–	–	–	–	x	–	–	–	–	–	–	–	–	x	–	–	–	–	–	–	–	–
Ammomarginulina foliacea		–	x	–	–	–	–	x	x	–	x	–	–	–	x	–	–	–	–	–	–	–	–	–	–	–	–	–	–	–	–	–
A. foliacea f. *recurva*		–	x	x	–	–	x	x	x	x	x	–	x	x	x	–	–	–	–	–	x	–	–	x	–	–	–	–	–	x	–	–
A. sp. aff. *A. ensis*		–	–	–	–	–	?	–	?	–	–	–	x	–	?	–	–	–	–	–	–	–	–	x	–	–	–	–	–	–	–	–
Ammoscalaria tenuimargo		–	x	x	–	–	x	x	x	x	–	–	x	x	x	–	–	–	–	–	–	–	–	–	–	–	–	–	–	x	–	–
Astrammina rara		–	–	–	–	–	–	x	x	–	–	–	–	–	x	–	–	–	–	–	–	–	–	–	–	–	–	–	–	–	–	–
Astrorhiza sp.		–	–	–	–	–	–	x	–	–	–	–	–	–	–	–	–	–	–	–	–	–	–	–	–	–	–	–	–	–	–	–
Bathysiphon rufus		–	x	x	–	–	x	x	x	–	–	x	x	–	x	–	–	–	–	–	–	–	–	–	–	–	–	–	–	–	–	–
Bathysiphon sp.		–	x	x	–	–	x	x	x	x	x	–	–	x	x	–	–	–	–	–	–	x	–	–	–	–	–	–	–	–	–	–
Cribrostomoides subglobosus		–	x	x	x	–	x	x	x	x	x	–	x	x	x	–	–	–	–	–	–	–	x	–	–	–	–	–	–	–	–	–
C. wiesneri		–	x	x	x	–	–	–	x	x	x	x	x	–	x	–	–	–	–	–	–	–	–	–	–	–	–	–	x	x	–	–
C. sp.		–	x	–	–	–	–	x	x	x	–	–	x	–	x	–	–	–	–	–	x	–	–	x	–	–	–	–	–	x	–	–
Cyclammina sp.		–	–	–	–	–	–	–	–	–	–	–	–	–	x	–	–	–	–	–	–	–	–	–	–	–	–	–	–	–	–	–
Cystammina pauciloculata		–	x	x	x	–	x	–	x	x	x	x	–	–	x	–	–	–	–	–	–	–	–	–	–	–	–	–	–	–	–	–
Eggerella spp.		–	x	x	?	–	?	x	–	x	–	–	–	–	–	–	–	–	–	–	–	–	–	–	–	–	–	–	–	–	–	–
Glomospira gordialis		–	x	x	–	–	–	–	?	?	–	–	x	–	?	–	–	–	–	–	–	–	–	–	–	–	–	–	–	–	–	–
Haplophragmoides spp.		–	?	–	–	–	–	–	–	–	x	–	–	x	–	–	–	–	–	–	–	–	–	–	–	–	–	–	–	–	–	–
H. columbiense		–	x	–	–	–	–	–	–	–	–	–	–	–	–	–	–	–	–	–	–	–	–	–	–	–	–	–	–	–	–	–
H. rotalutum		–	x	x	–	–	x	x	x	x	x	–	x	x	x	–	–	–	–	–	–	–	–	–	–	–	–	–	–	–	–	–
H. sphaeriloculus		–	x	x	–	x	?	–	x	x	x	–	x	x	x	–	–	–	–	–	–	–	–	x	–	–	–	–	–	x	–	–
Hormosina carpenteri		–	–	–	–	–	–	–	–	–	–	–	–	–	–	–	–	–	–	–	–	–	–	–	–	–	–	–	–	–	–	–
H. globulifera		–	x	x	–	x	x	x	x	x	x	x	x	x	x	–	–	–	–	–	–	x	–	x	–	–	–	–	x	x	–	–
Hyperammina friabilis		–	x	x	–	–	x	x	x	x	x	–	x	x	x	–	–	–	–	–	–	–	–	–	–	–	–	x	–	x	–	–
H. laevigata		–	x	x	x	–	x	x	–	–	–	x	x	–	x	–	–	–	–	–	–	–	–	–	–	–	–	–	–	x	–	–
H. sp.		–	x	x	?	–	–	–	x	–	–	–	–	–	x	–	–	–	–	–	–	–	–	–	–	–	–	–	–	–	–	–
Jaculella sp.		–	x	x	–	–	–	–	–	–	–	–	–	–	?	–	–	–	–	–	–	–	–	–	–	–	–	–	–	x	–	–
Karreriella novangliae		–	x	–	–	–	–	–	–	–	–	–	–	–	–	–	–	–	–	–	–	–	–	–	–	–	–	–	–	–	–	–
K. sp.		–	x	x	–	–	x	x	x	–	–	–	–	x	x	x	–	–	–	–	x	–	x	–	–	–	–	–	–	–	–	–
Labrospira crassimargo		–	x	–	–	–	–	–	?	–	–	–	–	–	x	–	–	–	–	–	–	–	–	–	–	–	–	–	–	–	–	–
Martinotiella spp.		–	x	?	–	–	–	x	x	–	–	–	x	–	–	–	–	–	–	–	–	–	–	–	–	–	–	–	–	–	–	–
Nodellum membranaceum		–	–	?	–	–	–	–	–	–	–	–	–	–	?	–	–	–	–	–	–	–	–	–	–	–	–	–	–	–	–	–
Nodulina dentalinaformis		–	x	?	–	–	–	–	x	–	x	–	–	x	x	–	–	–	–	–	–	–	–	–	–	–	–	–	–	–	–	–
Pelosina cylindrica		–	–	–	–	–	–	–	x	–	–	–	–	–	–	–	–	–	–	–	–	–	–	–	–	–	–	–	–	–	–	–
Psammosphaera parva		–	?	x	?	–	x	–	?	–	–	–	x	–	?	–	–	–	–	–	–	–	–	x	–	–	–	x	–	–	–	–
Pseudonodosinella nodulosa		–	x	x	–	–	x	x	x	x	–	–	x	x	x	–	–	–	–	–	–	–	–	x	–	–	–	–	–	–	–	–
Recurvoides contortus		–	x	x	x	–	x	x	x	–	–	–	–	–	x	–	–	–	–	–	–	–	–	–	–	–	–	–	–	x	–	–
R. scitulum		–	x	x	–	–	x	–	x	–	–	–	–	x	?	–	–	–	–	–	–	–	–	–	–	–	–	–	–	–	–	–
R. spp.		–	–	x	–	–	x	–	–	x	x	–	x	x	–	–	–	–	–	–	–	–	–	–	x	–	–	x	x	–	–	–
Reophax bacillaris		–	x	–	–	–	–	x	–	–	–	–	–	–	x	–	–	–	–	–	–	–	–	–	–	–	–	–	–	–	–	–
R. bilocularis		–	–	?	–	–	x	–	–	x	x	–	–	x	–	–	–	–	–	–	x	x	–	–	–	x	–	–	–	–	–	–
R. difflugiformis		–	x	x	x	–	x	x	x	x	x	–	x	x	x	–	–	–	–	–	–	–	–	x	–	–	–	–	–	–	–	–
R. distans		–	x	x	x	–	x	x	x	–	–	x	–	–	x	–	–	–	–	–	–	–	–	–	–	–	–	–	–	–	–	–
R. guttifer		–	x	x	x	–	–	x	x	x	x	–	x	x	x	–	–	–	–	–	–	–	–	–	–	–	–	–	–	–	–	–
R. horridus		–	–	?	–	–	–	–	–	–	–	–	–	–	–	–	–	–	–	–	–	–	–	–	–	–	–	–	–	–	–	–
R. scorpiurus		–	?	?	–	–	–	?	–	x	x	–	–	x	?	–	–	–	–	–	–	–	–	–	–	–	–	–	–	x	–	–
R. subfusiformis		–	?	?	?	–	?	?	?	x	x	–	–	x	x	–	–	–	–	–	–	–	–	–	–	–	–	–	–	–	–	–
R. spp.		–	x	x	x	–	x	x	x	x	–	x	x	x	x	?	x	–	–	–	–	–	x	x	–	–	–	x	x	x	x	–
Rhabdammina spp.		–	x	x	?	–	x	x	x	x	x	x	x	x	x	?	–	–	–	–	–	–	–	–	–	–	x	–	–	?	x	–	–
R. sp. (with ridges)		–	x	x	–	–	x	x	?	x	x	–	–	x	x	–	–	–	–	–	–	–	–	–	–	–	–	–	–	–	–	–
Rhizammina algaeformis		–	x	x	–	–	x	x	x	x	x	–	x	x	x	–	–	–	–	–	–	–	–	x	–	–	–	–	x	–	–	–
Saccammina sphaerica		–	?	–	?	–	–	?	?	?	?	–	?	–	?	–	–	–	–	–	–	–	–	–	–	–	–	–	–	–	–	–
S. sphaerica var. *catenulata*		–	x	x	–	–	x	–	–	–	–	–	–	–	–	–	–	–	–	–	–	–	–	–	–	–	–	–	–	–	–	–
S. socialis ?		–	–	?	–	–	–	–	–	–	–	–	–	–	–	–	–	–	–	–	–	–	–	–	–	–	–	–	–	–	–	–
S. tubulata		–	–	x	x	–	x	–	x	–	–	–	–	–	x	–	–	–	–	–	–	–	–	–	–	–	–	–	–	–	–	–
Saccorhiza ramosa		–	x	x	x	–	x	x	x	x	x	x	x	x	x	–	–	–	–	–	–	–	x	x	–	–	–	?	–	x	–	–
Spiroplectammina sp.		–	–	–	–	–	–	–	–	–	–	–	–	–	–	–	–	–	–	–	–	–	–	–	–	–	–	–	–	–	–	–
Subreophax aduncus		–	x	x	–	–	x	–	x	x	–	–	–	–	x	–	–	–	–	–	–	–	–	–	–	–	–	–	–	x	–	–
Textularia spp.		–	–	?	–	–	–	–	–	–	–	–	–	–	–	–	–	–	–	–	–	–	–	–	–	–	–	–	x	–	–	–
Tholosina vesicularis		–	?	?	–	–	x	x	x	x	–	–	–	x	x	–	–	–	–	–	–	–	–	–	–	–	–	–	–	–	–	–
Thurammina sp.		–	?	–	?	–	–	–	–	–	–	–	–	–	–	–	–	–	–	–	–	–	–	–	–	–	–	–	–	–	–	–
Tolypammina ?		–	?	–	–	–	?	–	–	–	–	–	–	–	–	–	–	–	–	–	–	–	–	–	–	–	–	–	–	–	–	–
Trochammina globulosa		–	x	x	–	–	x	–	–	x	x	–	x	–	–	–	–	–	–	–	–	–	–	–	–	–	–	–	–	x	–	–
T. inconspicua		–	–	–	–	–	–	–	?	–	–	–	–	–	–	–	–	–	–	–	–	–	–	–	–	–	–	–	–	–	–	–
T. spp.		–	x	x	–	–	x	x	–	x	x	x	x	x	x	?	x	–	–	–	–	x	–	x	–	–	–	x	x	x	–	–
Vanhoeffenella sp.		–	–	–	–	–	x	–	–	–	–	–	–	–	–	–	–	–	–	–	–	–	–	–	–	–	–	–	–	–	–	–
Foraminifers on rocks		–	x	x	x	–	x	x	x	x	x	–	x	x	x	–	–	–	–	–	–	–	–	x	–	x	–	x	x	x	–	–

Table 18.3. Calcareous foraminifers from Escanaba Trough.

[x, present; ?, questionable identification]

Species	Sample number	L1-1G 0–1 cm	L1-7G 0–1 cm	L1-7G 211–212 cm	L1-8G 0–1 cm	L1-15D	L1-16D	L1-19G 0–1 cm	L1-22D	L1-25G 0–1 cm	L1-25G 48–49 cm	L1-25G 119–120 cm	L1-26G 0–1 cm	L1-26G 33.5–35 cm	L1-26G 40–41 cm	L1-27G 0–1 cm	L1-27G 64–65 cm	L1-27G 71–72 cm	L1-27G 87–95 cm	L2-2G 0–1 cm	L2-2G 72–74 cm	L2-4G 7–8 cm	L2-7G 7–8 cm	L2-7G 235–237 cm	L2-9G 20–21 cm	L2-9G 48–50 cm	L2-9G 75–76 cm	L2-28G 2–3 cm	L3-8G 10–11 cm	L3-8G 84–85 cm	L3-9G 8/9–10/11 cm	TUL-89D-7TR Top (6 cm)	TUL-89D-7P Top (2.5–3.5 cm)
Astrononion gallowayi		–	–	–	–	–	–	–	–	–	–	–	–	–	–	–	–	–	–	–	–	–	–	–	–	–	–	–	–	–	–	–	–
Bolivina sp.		–	–	–	–	–	–	–	–	–	x	x	–	–	–	–	–	–	–	–	x	–	–	x	–	–	–	–	–	–	–	–	–
Buccella frigida		–	–	x	–	–	–	–	–	–	–	x	–	x	–	–	–	–	–	–	x	–	–	–	–	–	–	–	–	–	–	–	–
Bulimina spp.		–	–	–	–	–	–	–	–	–	–	x	–	x	–	–	–	–	–	–	–	–	–	–	–	–	–	–	x	–	–	–	x
Buliminella tenuata		–	–	x	–	–	–	–	–	–	–	–	–	–	x	–	–	–	–	–	x	–	–	–	–	–	–	–	?	–	–	–	–
B. sp.		–	–	–	–	–	–	–	–	–	–	–	–	–	–	–	–	–	–	–	–	–	–	x	–	–	–	–	–	–	–	–	–
Cassidulina spp.		–	–	x	–	–	–	–	–	–	–	–	–	x	?	–	–	–	–	–	x	–	–	x	–	–	–	–	–	–	–	–	x
Chilostomella sp.		–	–	–	–	–	–	–	–	–	–	–	–	–	–	–	–	–	–	–	–	–	–	–	–	–	–	–	–	–	–	–	–
Chilostomellina sp.		–	–	–	–	–	–	–	–	–	–	–	–	–	–	–	–	–	–	–	–	–	–	–	–	–	–	–	–	–	–	–	–
Cibicides spp.		–	–	–	–	–	–	–	x	–	–	x	–	–	–	–	–	–	–	–	x	–	–	–	–	–	–	–	x	–	–	x	–
Ehrenbergina sp.		–	–	–	–	–	–	–	–	–	–	–	–	–	–	–	–	–	–	–	–	–	–	–	–	–	–	–	–	–	–	x	–
Elphidium spp.		–	–	–	–	–	–	–	–	–	–	x	–	x	x	–	–	–	–	–	x	–	–	–	–	–	–	–	–	–	–	–	x
Epistominella pacifica		–	–	–	–	–	–	–	–	–	?	x	–	–	x	–	–	–	–	x	x	–	–	–	–	–	–	–	–	–	–	–	x
E. smithii		–	–	–	–	–	–	–	–	–	–	x	–	–	–	–	–	–	–	–	–	–	–	–	–	–	–	–	–	–	–	–	–
E. sp.		–	–	x	–	–	–	–	–	–	–	–	–	–	–	–	–	–	–	–	–	–	–	x	–	–	–	–	–	–	–	–	–
Eponides spp.		?	–	–	–	–	–	–	–	–	–	–	–	x	x	–	–	–	–	–	x	–	–	–	–	–	–	–	–	–	–	–	–
Fissurina sp.		–	–	–	–	–	–	–	–	–	–	–	–	–	x	–	–	–	–	–	–	–	–	–	–	–	–	–	–	–	–	–	–
Fursenkoina spp.		–	–	–	–	–	–	–	–	–	–	–	–	–	–	–	–	–	–	–	–	–	–	x	–	–	–	–	–	–	–	–	–
Globobulimina spp.		–	–	x	–	–	–	–	–	–	–	x	–	x	–	–	–	–	–	–	x	–	–	–	–	–	–	–	–	–	–	x	–
Gyroidina gemma		?	–	–	–	–	–	–	–	–	–	–	–	–	–	–	–	–	–	–	–	–	–	–	–	–	–	–	–	–	–	–	–
G. spp.		–	–	–	–	–	–	x	–	–	–	–	–	–	–	–	–	–	–	–	–	–	–	?	–	–	–	–	–	–	–	–	–
Hoeglundina sp.		–	–	–	–	–	–	–	–	–	–	–	–	–	–	–	–	–	–	–	–	–	–	–	–	–	–	–	x	–	–	–	–
Islandiella sp. aff. *I. teretis*		–	–	–	–	–	–	–	–	–	–	–	–	–	–	–	–	–	–	–	x	–	–	–	–	–	–	–	–	–	–	–	–
Lagena spp.		–	–	–	–	–	–	–	–	–	–	–	–	–	–	–	–	–	–	–	–	–	–	–	–	–	–	–	–	–	–	–	–
Melonis barleeanum		–	–	–	x	–	–	x	–	–	–	–	–	–	–	x	–	–	–	–	–	–	–	–	–	–	–	–	–	–	–	–	–
M. pompilioides		x	–	–	–	–	–	–	–	–	–	x	–	–	–	–	–	–	–	–	x	–	–	–	–	–	–	–	–	–	–	–	–
M. sp.		–	–	–	–	–	–	–	x	–	–	–	–	–	x	–	–	–	–	–	–	–	–	–	–	–	–	–	–	–	–	–	x
Miliolidae		–	–	–	–	–	–	–	x	–	–	–	–	–	–	–	–	–	–	–	–	–	–	–	–	–	–	–	–	–	–	–	–
Nonion costiferum		–	–	–	–	–	–	–	–	–	–	–	–	–	–	–	–	–	–	–	x	–	–	–	–	–	–	–	–	–	–	–	–
Nonionellina labradorica		–	–	x	–	–	–	–	–	–	–	–	–	–	–	–	–	–	–	–	x	–	–	–	–	–	–	–	–	–	–	–	–
Nonionellina sp.		–	–	–	–	–	–	–	–	–	–	x	–	–	–	–	–	–	–	–	x	–	–	x	–	–	–	–	–	–	–	–	–
Oolina seminuda		?	–	–	–	–	–	–	–	–	–	–	–	–	–	–	–	–	–	–	–	–	–	–	–	–	–	–	–	–	–	–	–
Pullenia bulloides		–	–	–	–	–	–	–	–	–	–	–	–	–	–	–	–	–	–	–	–	–	–	–	–	–	–	–	–	–	–	–	–
Pullenia sp.		–	–	–	–	–	–	–	–	–	–	–	–	–	x	–	–	–	–	–	–	–	–	–	–	–	–	–	x	–	–	–	–
Pyrgo sp.		–	–	–	–	–	–	–	–	–	–	x	–	–	–	–	–	–	–	–	–	–	–	–	–	–	–	–	–	–	–	–	–
Quinqueloculina spp.		–	–	–	–	–	–	–	–	–	–	–	–	–	–	–	–	–	–	–	x	–	–	–	–	–	–	–	x	–	–	–	–
Trifarina sp.		–	–	–	–	–	–	–	–	–	–	–	–	–	–	–	–	–	–	–	x	–	–	–	–	–	–	–	–	–	–	–	x
Uvigerina hispida		–	–	–	–	–	–	–	–	–	–	–	–	–	–	–	–	–	–	–	?	–	?	–	–	–	–	–	–	–	–	x	–
U. peregrina		–	–	–	–	–	–	–	–	–	–	–	–	–	–	–	–	–	–	?	x	–	–	–	–	–	–	–	–	–	–	–	–
U. senticosa		–	–	x	–	x	–	–	x	–	?	–	–	–	–	–	–	–	–	–	x	–	–	–	–	–	–	–	–	–	–	–	–
U. spp.		–	–	–	–	–	–	–	–	–	–	x	–	–	–	–	–	–	–	–	–	–	–	–	–	–	–	–	–	–	–	–	x
Uvigerinella sp.		–	–	–	–	–	–	–	–	–	–	–	–	–	–	–	–	–	–	–	–	–	–	–	–	–	–	–	–	–	–	–	–
Valvulineria sp.		–	–	–	–	–	–	–	–	–	–	x	–	–	–	–	–	–	–	–	–	–	–	–	–	–	–	–	–	–	–	–	–
Planktonic foraminifers		–	–	x	–	–	–	–	x	–	x	x	–	x	x	–	–	–	–	–	x	–	–	x	–	–	–	–	x	–	x	x	x

48 to 49 cm, and a small amount of plant material is present. At 119 to 120 cm calcareous foraminifers are abundant, and agglutinated forms are absent in sandy sediment with abundant fecal pellets. Ninety percent (141 specimens) of the *N. pachyderma* at 119 to 120 cm are sinistrally coiled (table 18.4), indicating cooler water temperatures than at present. Karlin (1989) and Karlin and Zierenberg (chap. 7, this volume) place the Pleistocene-Holocene boundary at approximately 130 cm in this core and show a turbidite layer at about 112 to 120 cm. If their placement of the boundary is correct, then the sinistrally coiled *N. pachyderma* at 119 to 120 cm represents redeposition of Pleistocene sediment during Holocene time.

L1-86-26G

This core is located adjacent to L1-86-25G at a water depth of 3,225 m (fig. 18.3). The top 1 cm interval is brown clay with abundant fecal pellets; the foraminiferal fauna is sparse, poorly preserved, and entirely agglutinated. In contrast, the faunas at 33.5 to 35 cm and 40 to 41 cm are exclusively calcareous, but are also sparse and partially dissolved. Specimens of *Elphidium clavatum* and *Buccella* sp. aff. *B. frigida*, which indicate transport from shelf depths, occur with bathyal species such as *Bulimina* sp., *Buliminella tenuata, Epistominella pacifica,* and *Globobulimina* sp.

Table 18.3. Calcareous foraminifers from Escanaba Trough—Continued.

[x, present; ?, questionable identification]

Species	Sample number	TUL-89D-7P 240–242 cm	L1-29D	L1-31D	L1-33G 0–1 cm	L1-33G 104–105 cm	L1-35D	L1-37D	L1-38D	L2-14D	L2-16D	L2-17D	L2-18D	L2-23D	L2-25D	L3-4G 15–16 cm	L3-4G 39–40 cm	L3-5G 3–4 cm	L3-5G 30–31 cm	L3-5G 60–61 cm	TUL-89D-1P Top (6–7 cm)	TUL-89D-1TR Top (3–4 cm)	TUL-89D-1TR 50–51 cm	TUL-89D-1TR 52–53 cm	TUL-89D-1TR 98.5–99.5 cm	TUL-89D-2G Top (2.5–3.5 cm)	TUL-89D-2G 94–95 cm	TUL-89D-4G 0–1 cm	TUL-89D-6G Top (2.5–3.5 cm)	TUL-89D-9TR Top (2 cm)	TUL-89D-9TR 7–8 cm	TUL-89D-9TR 12–14 cm
Astrononion gallowayi		–	–	–	–	–	–	–	–	–	–	–	–	–	–	–	–	–	–	–	–	–	–	–	–	–	–	–	–	–	–	x
Bolivina sp.		–	x	–	–	–	–	–	–	–	–	–	–	x	–	–	–	–	–	–	–	–	–	–	–	–	–	–	–	–	–	x
Buccella frigida		–	x	–	–	–	–	–	–	–	–	–	–	–	–	–	–	–	–	–	–	–	–	–	–	–	–	–	–	–	–	x
Bulimina spp.		–	x	–	x	–	–	–	–	–	–	–	–	–	–	–	–	–	–	–	–	–	–	–	–	–	–	–	–	–	–	x
Buliminella tenuata		x	–	–	–	–	–	–	–	–	–	–	–	–	–	–	–	–	–	–	–	–	–	–	–	–	–	–	–	–	–	x
B. sp.		–	–	–	–	–	–	–	–	–	–	x	–	–	–	–	–	–	–	–	–	–	–	–	–	–	–	–	–	–	–	–
Cassidulina spp.		–	x	–	–	–	–	–	–	–	–	–	–	–	–	–	–	–	–	–	–	–	–	–	x	x	x	–	–	–	–	–
Chilostomella sp.		–	–	–	–	–	–	x	–	–	–	–	–	–	–	x	x	–	–	–	–	–	–	x	–	–	–	–	–	–	–	–
Chilostomellina sp.		–	–	–	–	–	–	–	–	–	–	–	–	–	–	–	–	–	–	–	–	–	–	–	–	–	–	–	–	–	–	–
Cibicides spp.		x	–	–	–	–	–	–	–	x	–	–	–	–	–	x	–	–	–	–	–	–	x	–	–	–	–	–	–	–	–	–
Ehrenbergina sp.		–	–	–	–	–	–	–	x	–	–	–	–	–	–	–	–	–	–	–	–	–	–	–	–	–	–	–	–	–	–	–
Elphidium spp.		–	x	–	?	–	–	–	–	–	–	–	–	–	–	–	–	–	–	–	–	–	–	–	–	x	–	–	–	–	–	x
Epistominella pacifica		–	–	–	–	–	–	–	–	–	–	–	–	–	–	–	–	–	–	–	–	–	–	–	–	x	–	–	–	–	–	x
E. smithii		–	x	–	–	–	–	–	–	–	–	–	–	–	–	–	–	–	–	–	–	–	–	–	–	–	–	–	–	–	–	–
E. sp.		–	–	–	–	–	–	–	–	–	–	–	–	–	–	–	–	–	–	–	x	–	–	–	–	–	–	–	–	–	–	–
Eponides spp.		x	x	–	–	–	–	–	x	–	x	–	–	–	–	?	x	–	–	–	–	–	–	–	x	x	–	–	–	–	–	–
Fissurina sp.		–	x	–	–	–	–	–	–	–	–	–	–	x	–	x	x	–	–	–	–	–	–	–	–	–	–	–	–	–	–	–
Fursenkoina spp.		–	x	–	–	–	–	–	–	–	–	–	–	–	–	–	x	–	x	x	–	–	–	–	–	x	–	–	–	–	–	–
Globobulimina spp.		–	x	–	–	–	–	x	–	x	x	–	–	–	–	x	x	–	–	–	–	–	–	–	–	–	–	–	–	–	–	x
Gyroidina gemma		–	–	–	–	–	–	–	–	–	–	–	–	–	–	–	–	–	–	–	–	–	x	–	–	–	–	–	–	–	–	–
G. spp.		–	x	x	–	–	–	–	–	x	–	x	x	x	x	?	?	–	–	–	–	–	–	–	–	–	–	–	–	–	x	–
Hoeglundina sp.		–	–	–	–	–	–	–	–	–	–	–	–	–	–	–	–	–	–	–	–	–	–	–	–	–	–	–	–	–	–	–
Islandiella sp. aff. *I. teretis*		–	–	–	–	–	–	–	–	–	–	–	–	–	–	–	–	–	–	–	–	–	–	–	–	x	–	–	–	–	–	–
Lagena spp.		–	–	–	–	–	–	x	–	–	–	–	–	–	–	–	–	–	–	–	–	–	–	–	–	–	–	–	–	–	–	x
Melonis barleeanum		–	x	?	–	–	–	–	–	–	–	–	–	–	–	–	–	–	–	–	–	–	–	–	–	–	–	–	–	–	–	–
M. pompilioides		–	–	–	–	–	–	–	–	–	–	–	–	–	–	–	–	–	–	–	–	–	–	–	–	–	–	–	–	–	–	–
M. sp.		–	–	–	–	–	–	x	x	x	–	x	–	–	–	–	–	–	–	–	–	–	–	–	–	x	–	–	–	–	–	–
Miliolidae		–	–	x	–	–	x	–	–	–	–	–	–	–	x	x	–	–	–	–	x	–	–	x	x	–	–	–	–	–	–	–
Nonion costiferum		–	–	–	–	–	–	–	–	–	–	–	–	–	–	–	–	–	–	–	–	–	–	–	–	–	–	–	–	–	–	–
Nonionellina labradorica		–	x	–	–	–	–	–	–	–	–	–	–	–	–	–	–	–	–	–	–	–	–	–	–	–	–	–	–	–	–	–
Nonionellina sp.		–	–	–	–	–	–	–	–	?	–	–	–	–	–	–	–	–	x	x	–	–	–	–	–	–	–	–	–	–	–	x
Oolina seminuda		–	–	–	–	–	–	–	–	–	–	–	–	–	–	–	–	–	–	–	–	–	–	–	–	–	–	–	–	–	–	–
Pullenia bulloides		–	x	x	–	–	–	x	–	–	–	x	–	–	–	–	–	–	–	–	–	–	–	–	–	–	–	–	–	–	–	–
Pullenia sp.		–	–	–	–	–	–	x	–	–	x	–	–	–	–	–	–	–	–	–	x	–	–	x	–	–	–	–	–	–	–	?
Pyrgo sp.		–	x	–	–	–	–	–	–	–	–	–	–	–	–	x	–	–	–	–	–	–	–	–	–	–	–	–	–	–	–	–
Quinqueloculina spp.		–	x	–	–	–	–	x	–	–	–	–	–	–	–	x	–	–	–	–	–	–	–	–	–	–	–	–	–	–	–	x
Trifarina sp.		–	x	–	–	–	–	–	–	–	–	–	–	–	–	–	–	–	–	–	–	–	–	–	–	–	–	–	–	–	–	–
Uvigerina hispida		–	–	x	–	–	–	–	–	–	–	–	–	–	–	–	–	–	–	–	–	–	–	–	–	–	–	–	–	–	–	–
U. peregrina		x	x	–	–	–	–	–	–	–	–	–	–	–	–	–	–	–	–	–	–	–	–	–	–	–	–	–	–	–	–	–
U. senticosa		–	x	x	–	–	–	–	–	–	–	x	–	–	–	–	x	–	–	–	–	–	x	x	–	–	–	–	–	–	–	–
U. spp.		x	x	–	–	–	–	x	x	x	x	–	–	–	–	x	–	–	–	–	–	–	–	–	–	x	–	–	–	–	–	–
Uvigerinella sp.		–	–	–	–	–	–	–	–	–	–	–	–	–	–	–	–	–	–	–	–	x	x	–	x	–	–	–	–	–	–	–
Valvulineria sp.		–	–	–	–	–	–	–	–	–	–	–	–	–	–	–	–	–	–	–	–	–	–	–	–	–	–	–	–	–	–	x
Planktonic foraminifers		x	x	x	–	–	–	x	x	x	–	x	–	x	–	x	x	–	–	x	x	x	x	–	x	x	x	–	x	–	–	x

The planktonic species *N. pachyderma* is present in equal proportions (two sinistral, two dextral) at 33.5 to 35 cm depth in the core; at 40 to 41 cm, the sinistral form is represented by six specimens and the dextral form by one questionable specimen (table 18.4). Normark and others (chap. 6, this volume) describe sediment from these intervals as turbidite mud and sand. If the Pleistocene-Holocene boundary is at 200 cm as suggested by Karlin (1989) and Karlin and Zierenberg (chap. 7, this volume), then the dominance of sinistrally coiled *N. pachyderma* at 40 to 41 cm indicates redeposition of Pleistocene sediment during Holocene time. This seems reasonable considering that L1-86-26G is located in a valley downslope from L2-86-2G, which is thought to be of Pleistocene age based on magnetic susceptibility (Karlin, 1989) and planktonic foraminiferal evidence.

L2-86-7G

L2-86-7G is from the southwest extreme of the SESCA area on a terrace in the west wall of the ridge at 3,146 m water depth (fig. 18.3). The topmost sample (7 to 8 cm) contains a sparse and poorly preserved agglutinated fauna and one calcareous specimen. A silty sample from 235 to 237 cm in the core has abundant but very small, unidentifiable planktonic foraminifers and fragile,

Table 18.4. Ratio of sinistrally to dextrally coiled *Neogloboquadrina pachyderma.*

Sample number	Number of specimens		Percentage	
	Sinistral	Dextral	Sinistral	Dextral
L1-7G 211–212 cm	12	8	60	40
L1-25G 119–120 cm	141	15	90	10
L1-26G 33.5–35 cm	2	2	50	50
L1-26G 40–41 cm	6	1	86	14
L1-29D	19	0	100	0
L2-2G 72–74 cm	70	11	86	14
L2-7G 235–237 cm	2	2	50	50
L3-4G 15–16 cm	36	18	67	33
L3-4G 39–40 cm	48	36	57	43
L3-8G 10–11 cm	5	9	36	64
TUL-89D-1P Top (6–7 cm)	16	4	80	20
TUL-89D-1TR Top (3–4 cm)	0	0	0	0
TUL-89D-1TR 50–51 cm	12	0	100	0
TUL-89D-1TR 52–53 cm	0	0	0	0
TUL-89D-1TR 98.5–99.5 cm	7	5	58	42
TUL-89D-2G Top (2.5–3.5 cm)	13	3	81	19
TUL-89D-2G 94–95 cm	4	6	40	60
TUL-89D-7TR Top (6 cm)	6	3	67	33
TUL-89D-7P Top (2.5–3.5 cm)	13	2	87	13
TUL-89D-7P 240–242 cm	19	6	76	24
TUL-89D-9TR Top (2 cm)	0	0	0	0
TUL-89D-9TR 7–8 cm	0	0	0	0
TUL-89D-9TR 12–14 cm	12	6	67	33

transparent calcareous benthic foraminifers including *Bolivina* sp., *Buliminella* sp., *Epistominella* sp., *Fursenkoina* sp., and *Nonionella* sp. derived from bathyal depths. Karlin and Zierenberg (chap. 7, this volume) assign a Pleistocene (11 ka) age to this core at approximately 145 cm.

TUL-89D CORE SAMPLES

Fifteen samples from eight cores were analyzed for foraminifers. Seven were from NESCA, and one was approximately halfway between NESCA and SESCA (fig. 18.1). Cores TUL-89-4G, 6G, and 9TR were taken from a hill in the vicinity of the only known active vent in Escanaba Trough (fig. 18.2). The actual distances from the vent to the sites are uncertain, but no exotic vent species occur in the foraminiferal faunas at these sites.

As in most cores from Escanaba Trough, agglutinated foraminifers dominate the upper part of the TUL-89D cores, and calcareous forms are dominant below (table 18.1); however, TUL-89-1P and 2G are exceptions. The top of the piston core (TUL-89D-1P) is dominated by calcareous foraminifers with 80 percent of the *N. pachyderma* sinistrally coiled (table 18.4), indicating cooler water than at present. This may be an artifact of sampling in which the topmost sediment (with dominant agglutinated foraminifers) was lost during sampling, or it may be a result of redeposition of Pleistocene calcareous sediment by Holocene turbidites.

A trigger weight core (TUL-89D-1TR) sent down with the piston core (TUL-89D-1P) had the usual sequence of more agglutinated forms at the top; a subarctic planktonic fauna (100 percent sinistrally coiled *N. pachyderma*) at 50–51 cm; a relatively diverse agglutinated fauna at 52–53 cm; and a temperate planktonic foraminiferal fauna (Holocene) at 98.5 to 99.5 cm (table 18.4). The presence of the agglutinated fauna at depth in this core and the occurrence of 100 percent sinistrally coiled *N. pachyderma* above it (table 18.4) are evidence for redeposition of Pleistocene sediment during Holocene time.

The top of gravity core TUL-89D-2G is dominated by calcareous foraminifers, and 81 percent of the *N. pachyderma* are sinistrally coiled (table 18.4). At 94 to 95 cm, temperate conditions are indicated by 40 percent sinistrally and 60 percent dextrally coiled *N. pachyderma.*

Large agglutinated foraminifers dominate the upper part of core TUL-89D-9TR at 2 cm and 7 to 8 cm. A sand layer at 12 to 14 cm contains mica and plant material, along with abundant, diverse, calcareous benthic and planktonic foraminifers. The relatively low percentage of sinistrally coiled *N. pachyderma* (67 percent) and the presence of several other planktonic species suggest temperate conditions and a Holocene age for this probable turbidite deposit.

Normark and others (chap. 6, this volume) provide further sedimentological and mineralogical evidence for Holocene turbidites in Escanaba Trough.

DREDGE SAMPLES

Large, agglutinated foraminifers, up to 3 cm long, are abundant in the dredge samples examined from Escanaba

Trough; calcareous benthic foraminifers are also present but are rare. Planktonic foraminifers are rare or absent in all dredge samples (table 18.1). The agglutinated fauna is similar to bathyal and abyssal faunas from the North Pacific Ocean (Cushman 1910–1917), the central Pacific Ocean (Bernstein and others, 1978, Schröder and others, 1988), the Atlantic Ocean (Schröder, 1986; Schröder and others, 1988), and shallower depths off Antarctica (Echols, 1971; Herb, 1971). However, the NESCA faunas are unique to other agglutinated deep-sea faunas in the common use of basaltic glass to construct the tests (figs. 18.5–18.9). The widespread occurrence of basaltic glass exposed on the sea floor at NESCA and the restricted occurrence of it at SESCA has been documented by underwater photography, sample collection, and submersible observations (Morton and others, 1990; Ross and Zierenberg, chap. 8, this volume). When large, angular pieces of glass are used in test construction, the resulting tests are irregular in shape, making identifications difficult. Glass is also used as a substrate for attachment (figs. 18.4*F*; 18.6*A*, *B*, *C*), and sometimes it is difficult to distinguish if a foraminifer is using the glass as a substrate or if it has incorporated a large piece as one of the building blocks of the test wall (fig. 18.5*B*).

Of the 14 dredge samples examined for foraminifers, only L1-86-29D contained enough specimens of the planktonic foraminifer *Neogloboquadrina pachyderma* to calculate the coiling ratio of this species. All 19 specimens present in the dredge sample were the sinistrally coiled subarctic form, which indicates cooler conditions and implies a Pleistocene age; however, this might be a result of reworking during Holocene time.

Dredge sample L1-86-16D from the northern flank of the eastern hill at SESCA (fig. 18.3) emitted a strong odor of oxidizing sulfide and contained a sparse, entirely agglutinated foraminiferal fauna of only four species and many test fragments. Unlike most Escanaba Trough foraminifers, which are brownish-orange (possibly due to the presence of iron), those in L1-86-16D are white. Brownish orange agglutinated specimens from other samples, when treated with dilute hydrochloric acid, first turn white and then become fragile, probably as a result of the dissolution of the iron cement. The oxidation of sulfide in sample L1-86-16D (possibly pyrrhotite) may have occurred after the sample was stored in a closed jar (R.A. Koski, oral commun., 1990); therefore, the low abundance and white color of the specimens in L1-86-16D may not reflect seafloor conditions.

DISCUSSION

Although agglutinated foraminifers are abundant and diverse in the deep sea, there are several reasons why little is known about the living animal. Biologists focus on the soft parts of organisms, and the tests of foraminifers enclose the soft parts making them difficult to study from a biological standpoint. Micropaleontologists concentrate their studies on the test, because it is preserved in the sediment and can provide biostratigraphic and paleoenvironmental information. Collection of undisturbed surface samples from the deep sea is difficult, time-consuming, and expensive. Observing live foraminifers at great water depths is difficult, so little is known about their feeding habits, substrate requirements, locomotion, growth, reproduction, and interactions with other organisms.

RELATIONSHIP TO VENTS

Since the discovery of hydrothermal vents on the East Pacific Rise (Corliss and Ballard, 1977; Lonsdale, 1977; Corliss and others, 1979), much has been published about a megafauna unique to the vent sites that consists of the vestimentiferal tube worm *Riftia pachyptila,* the mussel *Bathymodiolus thermophilus,* and the clam, *Calyptogena magnifica.* However, little has been published about the relationship of foraminifers to hydrothermal vents, and the information that is available implies that, although vents may affect foraminiferal faunas to some extent, the effect is not as obvious as it is on the megafauna.

Clague and others (1984), in their preliminary report on Gorda Ridge, suggested that the dense biota from Gorda Ridge, particularly benthic foraminifers, may be related to abundant food in the proximity of vents. However, the nutritional requirements of foraminifers are poorly understood, and at the time of the study, no active vents had been observed; their presence was inferred from mineralogic and geochemical evidence. Foraminifers are known to eat detrital material such as bacteria, algae, other animals, and fecal matter (Lipps, 1983). Some species of foraminifers use dissolved organic material for nutrition (DeLaca and others, 1981). Algal symbionts within the protoplasm may provide part or all of the nutritional requirements for some foraminifers. Nonphotosynthesizing symbiotic bacteria that rely on reduced sulfur compounds for their energy source are the food source for many hydrothermal vent organisms that harbor symbionts (Childress, 1988); however, the importance of these symbionts as a food source for foraminifers is unknown. Sulfur compounds occur in proximity of vents in Escanaba Trough, but their importance to foraminiferal nutrition is uncertain.

Lee and others (1991) investigated the possibility that the agglutinated foraminifer, *Abyssotherma pacifica* (Brönnimann and others, 1989), from near a hydrothermal vent on the East Pacific Rise might prey upon or harbor endosymbiotic chemolithotrophic bacteria. Although some bacteria were observed in vacuoles, there was no evidence that chemosynthesizing endosymbiotic bacteria were present. The inconclusive results of this study were due

to poor preservation of the cell fine structure caused by the fixation methods used during field collection (Lee and others, 1991).

The effect of hydrothermal processes on foraminifers has been studied by Nienstedt and Arnold (1988) from seamounts east of the East Pacific Rise crest; by Molina-Cruz and Ayala-Lopez (1988) from Guaymas Basin, Mexico; and by Van Dover and others (1988) from the Galapagos spreading center and the East Pacific Rise at latitude 21° N. Unfortunately, the first two studies do not discuss agglutinated foraminifers in detail, and the third deals mainly with one new agglutinated species, which is not present in the Escanaba Trough samples considered in this report.

Although some Escanaba Trough samples were collected near active hydrothermal vents (fig. 18.2), the importance of the vents on benthic foraminifers could not be determined because the distance of samples from the vents is not accurately known; furthermore, the samples are not of the quality for quantitative study, and they were not preserved or stained to permit recognition of live foraminifers. One obvious characteristic of some Escanaba Trough foraminifers that is related to recent volcanism and possible vent proximity is the use by the foraminifers of basaltic glass to construct the tests (figs. 18.5–18.9). Pieces of glass are often large and angular, giving the tests an unusual appearance and making identifications difficult.

Foraminifers from L1-86-37D, a dredge sample collected near an active vent at NESCA, are similar to those from areas at both NESCA and SESCA where active venting has not been reported. Approximately half of the taxa present in L1-86-37D are also present in L1-86-15D (SESCA), L1-86-22D (SESCA), and L2-86-23D (NESCA). Large agglutinated forms, such as *Bathysiphon rufus, Cribrostomoides subglobosus, Hormosina globulifera, Saccorhiza ramosa,* and the *Rhabdammina*-like form with internal ridges, are abundant in these samples. Smaller agglutinated species are represented by *Adercotryma glomerata, Ammobaculites folicea recurva, Ammobaculites microformis,* and *Reophax* spp.

The large size of agglutinated foraminifers from Escanaba Trough is not unique to hydrothermal vent areas, and large size does not necessarily imply an abundant food source. Large foraminifers, similar to those from Escanaba Trough, are known from the deep sea and from shallow seas surrounding Antarctica—environments where food sources may be limited much of the time. At Escanaba Trough, these very large foraminifers may have adapted to the low abundance of food in the deep-sea environment and variable food supplies near vents by developing a slow metabolism and the ability to exist for long periods of time without food. Individuals might grow slowly and become very large before reaching reproductive maturity. Lipps and Hickman (1982) describe such "giants" as caloric dwarfs.

RELATIONSHIP TO "FLYSCH-TYPE" FAUNAS

"Flysch-type" foraminiferal assemblages were first described in rocks of Cretaceous and Paleogene age from the Alpine-Carpathian flysch basin and are characterized by a predominance of large agglutinated cosmopolitan foraminifers (Gradstein and Berggren, 1981). Various factors such as water depth, high organic carbon, low O_2, high CO_2, low pH, low Eh, and poor circulation have been proposed to explain the occurrence of "flysch-type" faunas, but the importance of these factors is not well understood (Gradstein and others, 1983).

Gradstein and others (1983) noted that modern agglutinated foraminiferal taxa from the HEBBLE site on the Newfoundland slope (4,800 m water depth) were similar to "flysch-type" assemblages of Late Cretaceous to Paleogene age from the Newfoundland shelf and slope. They attributed the similarities to short-term catastrophic events that affected the benthic populations at both locations. In the HEBBLE area the events were periodic high-velocity boundary currents capable of resuspending and transporting bottom sediment; in the flysch basins the events were turbidites. Gradstein and others (1983) concluded that foraminiferal populations were destroyed by turbidity associated with high-energy events and repopulated the areas during times of relative quiescence.

Verdenius and van Hinte (1983) described "flysch-type" foraminiferal faunas in clastic sediment from DSDP holes in the North Atlantic. They suggested that these Atlantic Ocean faunas represented the uppermost layers of a turbidite (an environment in which the foraminifers actually lived) not the transported individuals carried by the flow. They further suggested that the first faunas to colonize an area after a flow would be a frontier-area fauna, represented by simple agglutinated forms such as *Rhabdammina*; gradually, more sophisticated forms would become established.

Agglutinated foraminiferal assemblages from Escanaba Trough have taxonomic similarity to "flysch-type" assemblages, at least at the generic level. Both simple (tubular and single chamber) and complex (coiled and multichamber) forms are present. Escanaba Trough is similar to the HEBBLE area in having high-energy environments locally. Strong bottom currents, noted during DSV *Alvin* dives in Escanaba Trough (David Clague, oral commun., 1990), may be capable of destroying the benthic foraminiferal populations. Other evidence of high-energy environments in Escanaba Trough includes turbidites, which can be recognized in the cores (see previous chapters). The agglutinated foraminifers in Escanaba Trough may be opportunistic species well adapted to high-energy environments where the food supply is variable and often scarce, and vent fluids may be toxic to other foraminifers.

TAXONOMIC NOTES

Agglutinated foraminifers may use a variety of materials to construct their tests, depending largely on what is available. However, some species show a preference for certain grain sizes and possibly compositions (Towe, 1967), but the reasons for these preferences are unknown. *Nodulina dentaliniformis* (fig. 18.5*A*) constructed its test mostly of flat, light-colored grains of plagioclase and quartz with minor amounts of dark (heavy) minerals such as hornblende (F. L. Wong, oral commun., 1990). The reason for selecting these grains—composition, shape, transparency, weight—is unknown. Taxonomy of agglutinated foraminifers is difficult because of the variety of materials used, and the Gorda Ridge foraminifers further complicate the task when they use large angular fragments of basaltic glass. I do not think the type of material used by agglutinating foraminifers for test construction should be the basis for defining genera or species, so I have attempted to assign the Gorda Ridge specimens to already existing taxa. Some species from Escanaba Trough, such as the *Rhabdammina*-like form with internal ridges (figs. 18.8*A*, *B*, *C*; 18.9*A*, *B*, *C*, *D*), always incorporate coarse, angular material into their external test walls. When basaltic glass is available in the sea-floor sediment as at NESCA, it is used; when glass is not available as at SESCA, detrital grains, smaller foraminifer tests, or fragments of large tests are used. Species such as *Reophax* (figs. 18.5*B*; 18.6*I*, *J*) and *Haplophragmoides rotalutum* use coarse material to varying degrees. Many other species, such as *Bathysiphon, Hormosina, Adercotryma glomerata, Cribrostomoides subglobosus,* and *C. weisneri,* are typically very finegrained species, and rarely or never use coarse material (figs. 18.4*B*, *G*, *H*, *I*; 18.5*C-I*).

A foraminifer that has not previously been described occurs in one gravity core and all but three dredge samples from Escanaba Trough, and it may be a new genus. It is listed on table 18.2 as "*Rhabdammina* sp. with ridges" and is figured in figs. 18.8*A–C* and 18.9*A–D*. It resembles *Rhabdammina* in having a straight tubular shape and being open at both ends; however, internal ridges extend the length of the tube and give a petal-like appearance when the specimen is viewed looking down either end of the tube. A slight constricture at one end of the tube resembles a poorly developed neck. The species resembles *Nodosinella* in possessing internal ridges but differs in being unilocular, not multilocular. Also, the ridges are not continuous in *Nodosinella;* they are only near the apertures of the last chamber and each of the previous chambers. The *Rhabdammina*-like test is brownish orange, very fine grained and firmly cemented, similar in texture to *Bathysiphon rufus* from Escanaba Trough (fig. 18.4*B*, *C*), but the "*Rhabdammina*-like form" has very coarse material, usually large pieces of dark volcanic glass embedded in the exterior of the test wall, giving the test a spiny appearance. I do not know if this form is unique to the Gorda Ridge area or if the occurrence is related to hydrothermal activity. It is present in a dredge sample near a hydrothermal soft sediment site (37D) as well as throughout the SESCA and NESCA areas. It is not abundant in any of the samples and is only present in one gravity core, possibly because the subsample volume from cores is much less than subsample volumes from dredges.

A few samples contain specimens that resemble *Ammobaculites* in some respects, but the apertures differ from the typical ones that Loeblich and Tappan (1988) described for that genus as terminal and rounded. For example, one specimen in L1-86-31D has a terminal aperture that is triangular in shape with rounded apices (figs. 18.6*G*, *H*;18.7*F*, *G*). This specimen bears some resemblance to *Ammobacularia triloba* Kristan-Tollmann, figured by Loeblich and Tappan (1988, Plate 59, figs. 4 and 5), which resembles *Ammobaculites* but differs in having a triangular aperture with toothlike projections from each of the three edges. *Ammobacularia triloba* is known from a single specimen of Late Triassic age from Austria. Another specimen from L1-86-31D has a slightly arcuate slit surrounded by lips and located near the center of the apertural face. A third specimen has what appears to be a shallow U-shaped aperture surrounded by lips; however, if this structure is an aperture it is somewhat obscured by fine-grained material. Specimens that resemble *Ammobaculites* in L2-86-25D have variable slitlike apertures including a nearly straight slit with lips, an arcuate slit with a rim, and two arc-shaped structures side-by-side (roughly shaped like the number 8) and surrounded by lips (figs. 18.6*E*; 18.7*E*). For now, these questionable specimens are assigned to *Ammobaculites* sp. aff. *A. agglutinans;* further study may show that one or more are new genera, but not necessarily vent specific.

CONCLUSIONS

Although the samples available from Escanaba Trough do not permit detailed quantitative analysis of the relationship of foraminifers to hydrothermal vents, they allow a description of the foraminiferal faunas present in the vicinity of vents and provide the groundwork for future studies. Box core samples or samples obtained from submersibles at known vent and nonvent sites are needed to determine which, if any, species are restricted to vents.

A new genus, resembling *Rhabdammina,* but with internal ridges, may be unique to this area. Specimens resembling *Ammobaculites,* but with variable apertures also appear to be undescribed in the literature.

Shallow-penetration cores from Escanaba Trough containing calcareous benthic and planktonic foraminifers substantiate conclusions by Vallier and others (1973), Karlin and Zierenberg (chap. 7, this volume), and Normark and others (chap. 6, this volume) of turbidite deposition in Escanaba Trough during the Pleistocene and Holocene.

REFERENCES CITED

Bandy, O.L., 1960, The geologic significance of coiling ratios in the foraminifer *Globigerina pachyderma* (Ehrenberg): Journal of Paleontology, v. 34, no. 4, p. 671–681.

Barnes, C.A., Duxbury, A.C., and Morse, B.A., 1972, Circulation and selected properties of the Columbia River effluent at sea, *in* Pruter, A.T., and Alverson, D.L., eds., The Columbia River estuary and adjacent ocean waters: Seattle, University of Washington Press, p. 41–80.

Bernstein, B.B., Hessler, R.R., Smith, R., and Jumars, P.A., 1978, Spatial dispersion of benthic Foraminifera in the abyssal central North Pacific: Limnology and Oceanography, v. 23, no. 3, p. 401–416.

Brönnimann, P., Van Dover, C.L., and Whittaker, J.E., 1989, *Abyssotherma pacifica,* n. gen., n. sp., a Recent remaneicid (Foraminiferida, Remaneicacea) from the East Pacific Rise: Micropaleontology, v. 35, no. 2, p. 142–149.

Carey, A.G., Taghon, G.L., Stein, D.L., and Rona, P.A., 1990, Distributional ecology of benthic megaepifauna and fishes in Gorda Ridge axial valley, *in* McMurray, G.R., ed., Gorda Ridge: A seafloor spreading center in the United States' Exclusive Economic Zone: New York, Springer-Verlag, p. 225–240.

Cavanaugh, C.M., 1985, Symbioses of chemoautotrophic bacteria and marine invertebrates from hydrothermal vents and reducing sediments: Biological Society of Washington Bulletin, v. 6, p. 373–388.

Childress, J.J., 1988, Biology and chemistry of a deep-sea hydrothermal vent on the Galapagos Rift; the Rose Garden in 1985. Introduction: Deep-Sea Research, v. 35, nos. 10/11, p. 1677–1680.

Clague, D.A., Friesen, W., Quinterno, P., Holmes, M., Morton, J., Bouse, R., Morgenson, L., and Davis, A., 1984, Preliminary geological, geophysical, and biological data from the Gorda Ridge: U.S. Geological Survey Open-File Report 84-364, 47 p.

Corliss, J.B., and Ballard, R.D., 1977, Oases of life in the cold abyss: National Geographic, v. 152, p. 440–453.

Corliss, J.B., Dymond, J., Gordon, L.I., Edmond, J.M., von Herzen, R.P., Ballard, R.D., Green, K., Williams, D., Bainbridge, A., Crane, K., and van Andel, T.H., 1979, Submarine thermal springs on the Galapagos Rift: Science, v. 203, p. 1073–1083.

Cushman, J.A., 1910-1917, A monograph of the foraminifera of the North Pacific Ocean: U.S. National Museum Bulletin 71, Parts 1–6.

DeLaca, T.E., Karl, D.M., and Lipps, J.H., 1981, Direct use of dissolved organic carbon by agglutinated benthic foraminifera: Nature, v. 289, p. 287–289.

Echols, R.J., 1971, Distribution of foraminifera in sediments of the Scotia Sea area, Antarctic waters, *in* Reid, J.L., ed., Antarctic oceanology I: Antarctic Research Series, American Geophysical Union, p. 93–168.

Fowler, G.A., and Kulm, L.D., 1970, Foraminiferal and sedimentological evidence for uplift of the deep-sea floor, Gorda Rise, northeastern Pacific: Journal of Marine Research, v. 28, no. 3, p. 321–329.

Gradstein, F.M., and Berggren, W.A., 1981, Flysch-type agglutinated foraminifera and the Maestrichtian to Paleogene history of the Labrador and North Seas: Marine Micropaleontology, v. 6, p. 211–268.

Gradstein, F.M., Berggren, W.A., Kaminski, J.J., and Miller, K.G., 1983, Paleobathymetry of Late Cretaceous-Paleogene agglutinated ("Flysch Type") benthic foraminiferal faunas and a modern analog [abs.]: American Association of Petroleum Geologists Bulletin, v. 67, no. 3, p. 473.

Grassle, J.F., and Van Dover, C.L., 1989, Soft-sediment hydrothermal vent communities of Escanaba Trough: Comparison with other vent and non-vent communities from similar depths in the deep sea and the influence of chemosynthetic production on the surrounding deep-sea benthic community: Oregon Department of Geology and Mineral Industries, Open-File Report O-89-05, 25 p.

Grassle, J.F., and Petrecca, Rosemarie, Soft-sediment hydrothermal vent communities of Escanaba Trough, *in* Morton, J.L., Zierenberg, R.A., and Reiss, C.A., eds., Geologic, hydrothermal, and biologic studies at Escanaba Trough, Gorda Ridge, offshore northern California: U.S. Geological Survey Bulletin 2022, chapter 17 (this volume).

Herb, Rene, 1971, Distribution of Recent benthonic foraminifera in the Drake Passage, *in* Llano, G.A., and Wallen, I.E., eds., Biology of the Antarctic seas IV: Antarctic Research Series, American Geophysical Union, p. 251–300.

Hessler, R.R., and Jumars, P.A., 1974, Abyssal community analysis from replicate box cores in the central North Pacific: Deep-Sea Research, v. 21, p. 185–209.

Ingle, J.C., 1973, Neogene foraminifera from the Northeastern Pacific Ocean, leg 18, Deep Sea Drilling Project, *in* Kulm, L.D., von Huene, R., and others, eds., Initial reports of the Deep Sea Drilling Project: Washington, U.S. Government Printing Office, v. 18, p. 517–567.

Kaminski, M.A., 1985, Evidence for control of abyssal agglutinated foraminiferal community structure by substrate disturbance: Results from the HEBBLE area, *in* Nowell, A.R.M., and Hollister, C.D., eds., Deep ocean sediment transport–Preliminary results of the High Energy Benthic Boundary Layer Experiment: Marine Geology (Special Issue), v. 66, no. 1/4, p. 113–131.

Karlin, R., 1989, SEACLIFF diving and sediment studies on the Gorda Ridge: Oregon Department of Geology and Mineral Industries, Open-File Report O-89-04, 17 p.

Karlin, R.E., and Zierenberg, R.A., Sedimentation and neotectonism in the SESCA area, Escanaba Trough, southern Gorda Ridge, *in* Morton, J.L., Zierenberg, R.A., and Reiss, C.A., eds., Geologic, hydrothermal, and biologic studies at Escanaba Trough, Gorda Ridge, offshore northern California: U.S. Geological Survey Bulletin 2022, chapter 7 (this volume).

Kennett, J.P., and Srinivasan, M.S., 1983, Neogene planktonic foraminifera: Stroudsburg, Pennsylvania, Hutchinson Ross, 265 p.

Lee, J.J., Anderson, O.R., Karim, Bibi, and Beri, Juhi, 1991, Additional insight into the structure and biology of *Abyssotherma pacifica* (Brönnimann, Van Dover and Whittaker) from the East Pacific Rise: Micropaleontology, v. 37, no. 3, p. 303–312.

Lipps, J.H., 1983, Biotic interactions in benthic foraminifera, *in* Tevesz, M.J.S., and McCall, P.L., eds., Biotic interactions in recent and fossil benthic communities: New York, Plenum, p. 331–376.

Lipps, J.H., and Hickman, C.S., 1982, Origin, age, and evolution of Antarctic and deep-sea faunas, *in* Ernst, W.G., and Morin, J.G., eds., The environment of the deep sea: Englewood Cliffs, New Jersey, Prentice-Hall, p. 325–356.

Loeblich, A.R., Jr. and Tappan, Helen, 1988, Foraminiferal genera and their classification: New York, Van Nostrand Reinhold, v. 1, 970 p.

———1988, Foraminiferal genera and their classification—Plates: New York, Van Nostrand Reinhold Co., v. 2, 212 p., 847 pl.

Lonsdale, P., 1977, Clustering of suspension-feeding macrobenthos near abyssal hydrothermal vents at oceanic spreading centers: Deep-Sea Research, v. 24, p. 857–863.

Molina-Cruz, Adolfo, and Ayala-Lopez, Adriana, 1988, Influence of the hydrothermal vents on the distribution of benthic foraminifera from the Guaymas Basin, Mexico: Geo-Marine Letters, v. 8, p. 49–56.

Morton, J.L., Normark, W.R., Ross, S.L., Koski, R.A., Holmes, M.L., Shanks, W.C., III, Zierenberg, R.A., Lyle, M., and Benninger, L.M., 1987, Preliminary report, cruises L1-86-NC and L2-86-NC, Escanaba Trough, Gorda Ridge: U.S. Geological Survey Open-File Report 87-375-A, 20 p.

Morton, J.L., Koski, R.A., Normark, W.R., and Ross, S.L., 1990, Distribution and composition of massive sulfide deposits at Escanaba Trough, southern Gorda Ridge, *in* McMurray, G.R., ed., Gorda Ridge: A seafloor spreading center in the United States' Exclusive Economic Zone: New York, Springer-Verlag, p. 77–92.

Nienstedt, J.C. and Arnold, A.J., 1988, The distribution of benthic foraminifera on seamounts near the East Pacific Rise: Journal of Foraminiferal Research, v. 18, no. 3, p. 237–249.

Normark, W.R., Gutmacher, C.E., Zierenberg, R.A., Wong, F.L., and Rosenbauer, R.J., Sediment fill of Escanaba Trough, *in* Morton, J.L., Zierenberg, R.A., and Reiss, C.A., eds., Geologic, hydrothermal, and biologic studies at Escanaba Trough, Gorda Ridge, offshore northern California: U.S. Geological Survey Bulletin 2022, chapter 6 (this volume).

Rona, P.A., Denlinger, R., Fisk, M., and others, 1988, Hydrothermal activity on the Gorda Ridge [abs.]: Eos, Transactions American Geophysical Union, v. 69, p. 1588.

Ross, S.L., and Zierenberg, R.A., Volcanic geomorphology of the SESCA and NESCA sites, Escanaba Trough, *in* Morton, J.L., Zierenberg, R.A., and Reiss, C.A., eds., Geologic, hydrothermal, and biologic studies at Escanaba Trough, Gorda Ridge, offshore northern California: U.S. Geological Survey Bulletin 2022, chapter 8 (this volume).

Saidova, Kh.M., 1975, Benthonic foraminifera of the Pacific Ocean: Academy of Sciences of the USSR, Moscow, 3 volumes, 875 p. (in Russian).

Schröder, C.J., 1986, Deep-water arenaceous foraminifera in the northwest Atlantic Ocean: Canadian Technical Report of Hydrography and Ocean Sciences 71, Bedford Institute of Oceanography, 191 p.

Schröder, C.J., Scott, D.B., Medioli, F.S., Bernstein, B.B., and Hessler, R.R., 1988, Larger agglutinated foraminifera: Comparison of assemblages from central North Pacific and western North Atlantic (Nares Abyssal Plain): Journal of Foraminiferal Research, v. 18, no. 1, p. 25–41.

Sidner, B.R., and McKee, T.R., 1976, Geochemical controls on vertical distribution of iron-rich agglutinated foraminifers in late Quaternary continental slope sediments from northwest Gulf of Mexico [abs.]: American Association of Petroleum Geologists Bulletin, v. 60, no. 4, p. 722–723.

Smith, P.B., 1973, Foraminifera of the North Pacific Ocean: U.S. Geological Survey Professional Paper 766, 37 p.

Snider, L.J., Burnett, B.R., and Hessler, R.R., 1984, The composition and distribution of meiofauna and nanobiota in a central North Pacific deep-sea area: Deep-Sea Research, v. 31, no. 10, p. 1225–1249.

Towe, K.M., 1967, Wall structure and cementation in *Haplophragmoides canariensis:* Contributions from the Cushman Foundation for Foraminiferal Research, v. 18, pt. 4, p. 147–151.

Vallier, T.L., Harrold, P.J., and Girdley, W.A., 1973, Provenances and dispersal patterns of turbidite sand in Escanaba Trough, northeastern Pacific Ocean: Marine Geology, v. 15, p. 67–87.

Van Dover, C.L., Berg, C.J., Jr., and Turner, R.D., 1988, Recruitment of marine invertebrates to hard substrates at deep-sea hydrothermal vents on the East Pacific Rise and Galapagos spreading center, *in* Childress, J.J., ed., Hydrothermal vents, a case study of the biology and chemistry of a deep-sea hydrothermal vent of the Galapagos Rift; The Rose Garden in 1985: Deep-Sea Research, v. 35, nos.10/11A, p. 1833–1849.

Van Dover, C.L., Grasssle, J.F., and Boudrias, Michel, 1990, Hydrothermal vent fauna of Escanaba Trough (Gorda Ridge), *in* McMurray, G.R., ed., Gorda Ridge: A seafloor spreading center in the United States' Exclusive Economic Zone: New York, Springer-Verlag, p. 285–290.

Verdenius, J.G., and Van Hinte, J., 1983, Central Norwegian-Greenland Sea: Tertiary arenaceous foraminifera, biostratigraphy and environment: Proceedings of the First Workshop on Arenaceous Foraminifera, 7-9 September 1981: Institutt for Kontinentalsokkelundersokeler [Continental Shelf Institute], Norway, p. 173–223.

Zierenberg, R.A., Koski, R.A., Shanks, W.C., III, and Slack, J.F., 1988, Preliminary results of ALVIN dives on active sediment-hosted massive sulfide deposits in the Escanaba Trough, southern Gorda Ridge [abs.]: Eos, Transactions American Geophysical Union, v. 69, p. 1488.

Zierenberg, R.A., Morton, J.L., Koski, R.A., and Ross, S.L., Geologic setting of massive sulfide mineralization in the Escanaba Trough, *in* Morton, J.L., Zierenberg, R.A., and Reiss, C.A., eds., Geologic, hydrothermal, and biologic studies at Escanaba Trough, Gorda Ridge, offshore northern California: U.S. Geological Survey Bulletin 2022, chapter 10 (this volume).

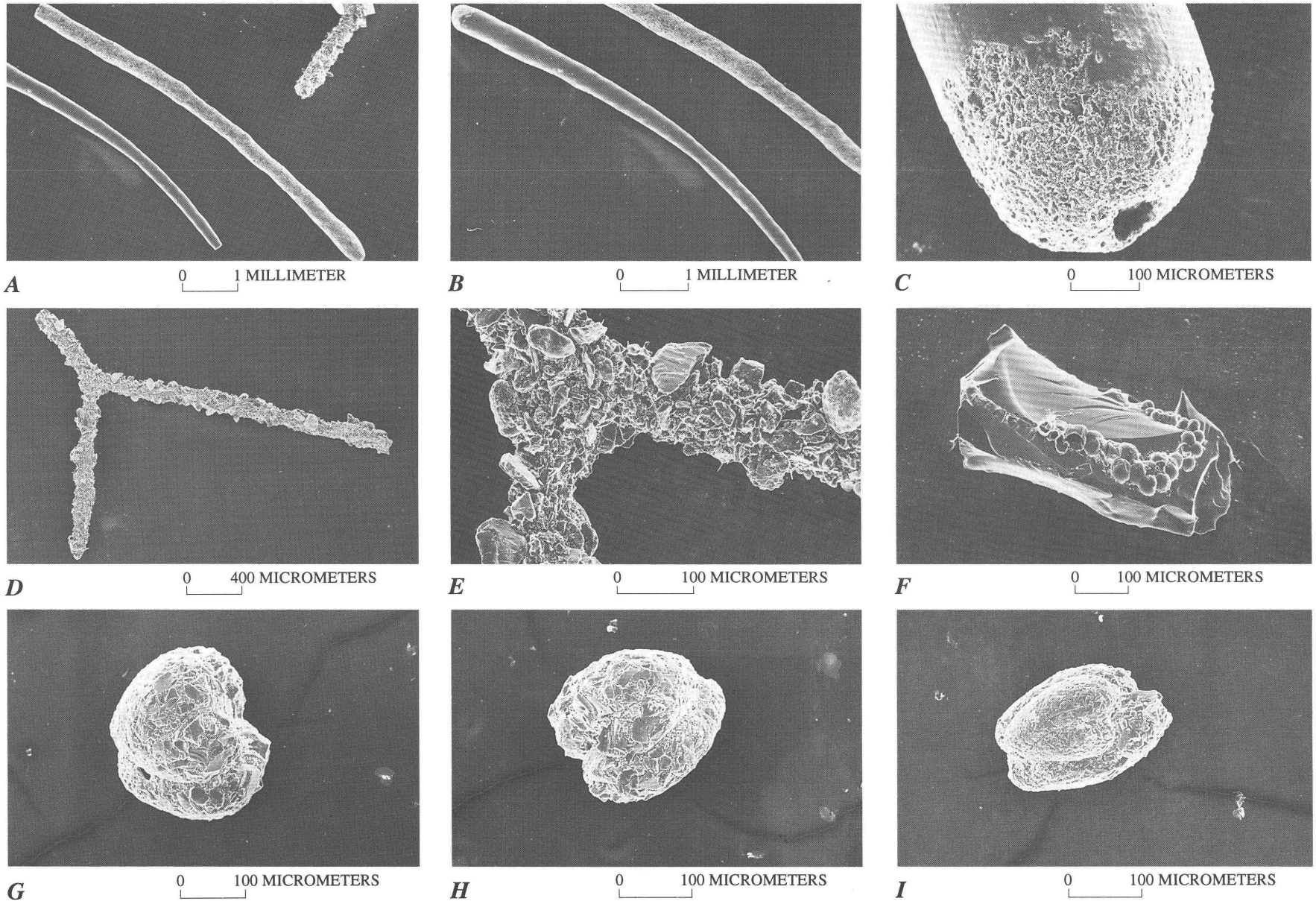

Figure 18.4. Scanning electron micrographs of foraminifers from Escanaba Trough. *A*, *Hyperammina laevigata* (Wright) [center of photograph]; site L1-86-29D. *B,C*, *Bathysiphon rufus* de Folin; site L1-86-29D; (*B*) side view [center of photograph]; (*C*) end view showing aperture. *D,E*, *Rhizammina algaeformis* Brady; site L1-86-29D; (*E*) detail of *D*. *F*, *Placopsilinella* sp. attached to basaltic glass; site L1-86-29D. *G–I*, *Adercotryma glomerata* (Brady); site L1-86-1G, 0–1 cm; apertural views showing variation in height of tests; within same sample, test may be high (*G*), medium (*H*), or elongate (*I*).

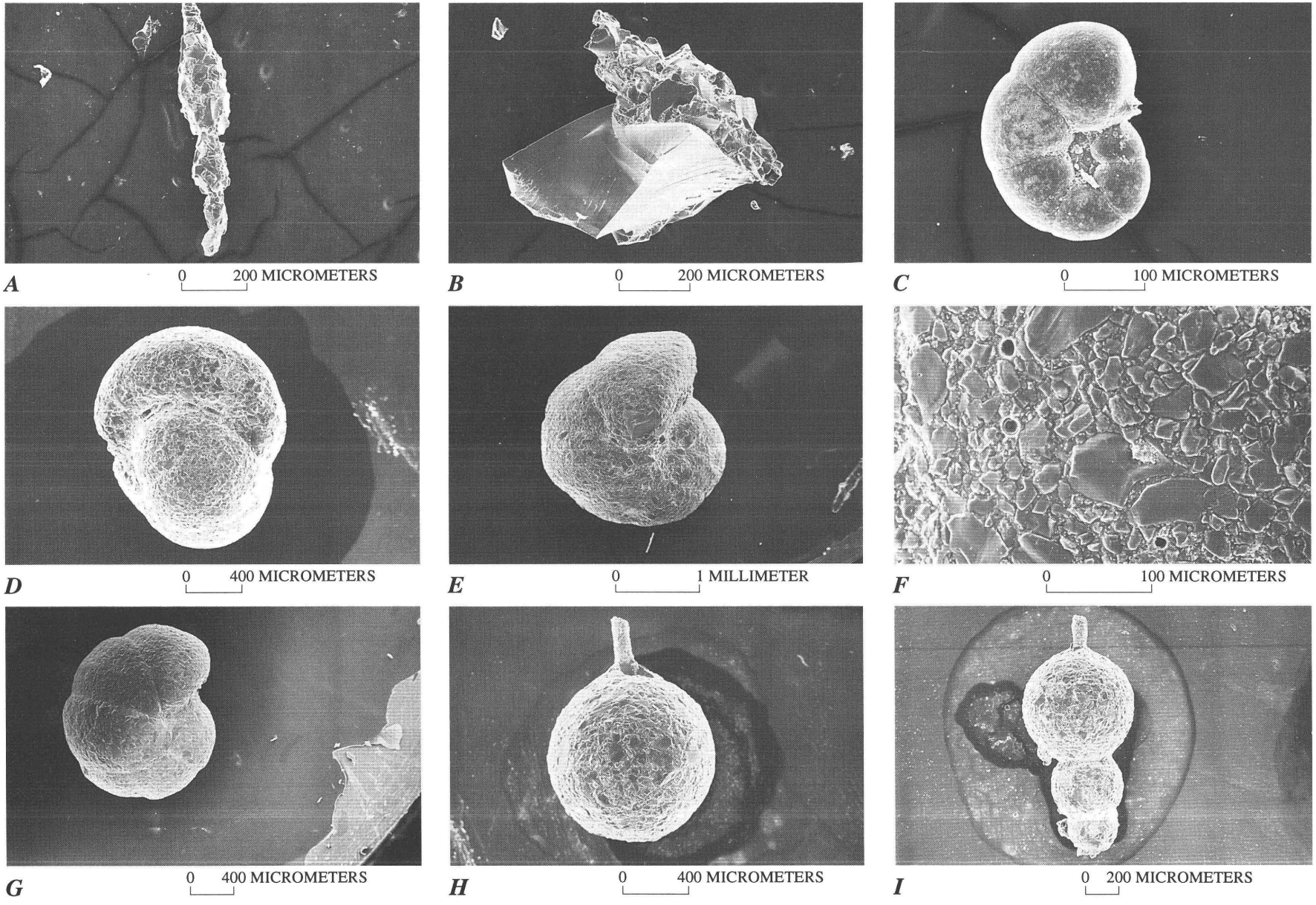

Figure 18.5. Scanning electron micrographs of foraminifers from Escanaba Trough. *A*, *Nodulina dentaliniformis* (Brady); test is constructed mostly of flat, light-colored grains of plagioclase and quartz with minor dark minerals such as hornblende (F.L. Wong, oral commun., 1990); site L1-86-29D. *B*, *Reophax* sp. with large, angular chip of volcanic glass used as building material for test wall; site L1-86-29D. *C*, *Cribrostomoides wiesneri* (Parr); site L1-86-19G, 0–1 cm. *D*, *Cribrostomoides subglobosus* (Sars), apertural view; site L1-86-29D. *E,F*, *Cribrostomoides subglobosus* (Sars); (*E*) involute side; (*F*) Close-up of wall texture; three pores of unknown origin; site L1-86-31D. *G*, *Cribrostomoides subglobosus;* slightly evolute side of another specimen from site L1-86-31D. *H,I*, *Hormosina globulifera* Brady; site L1-86-29D; (*H*) single-chambered form; (*I*) three-chambered form.

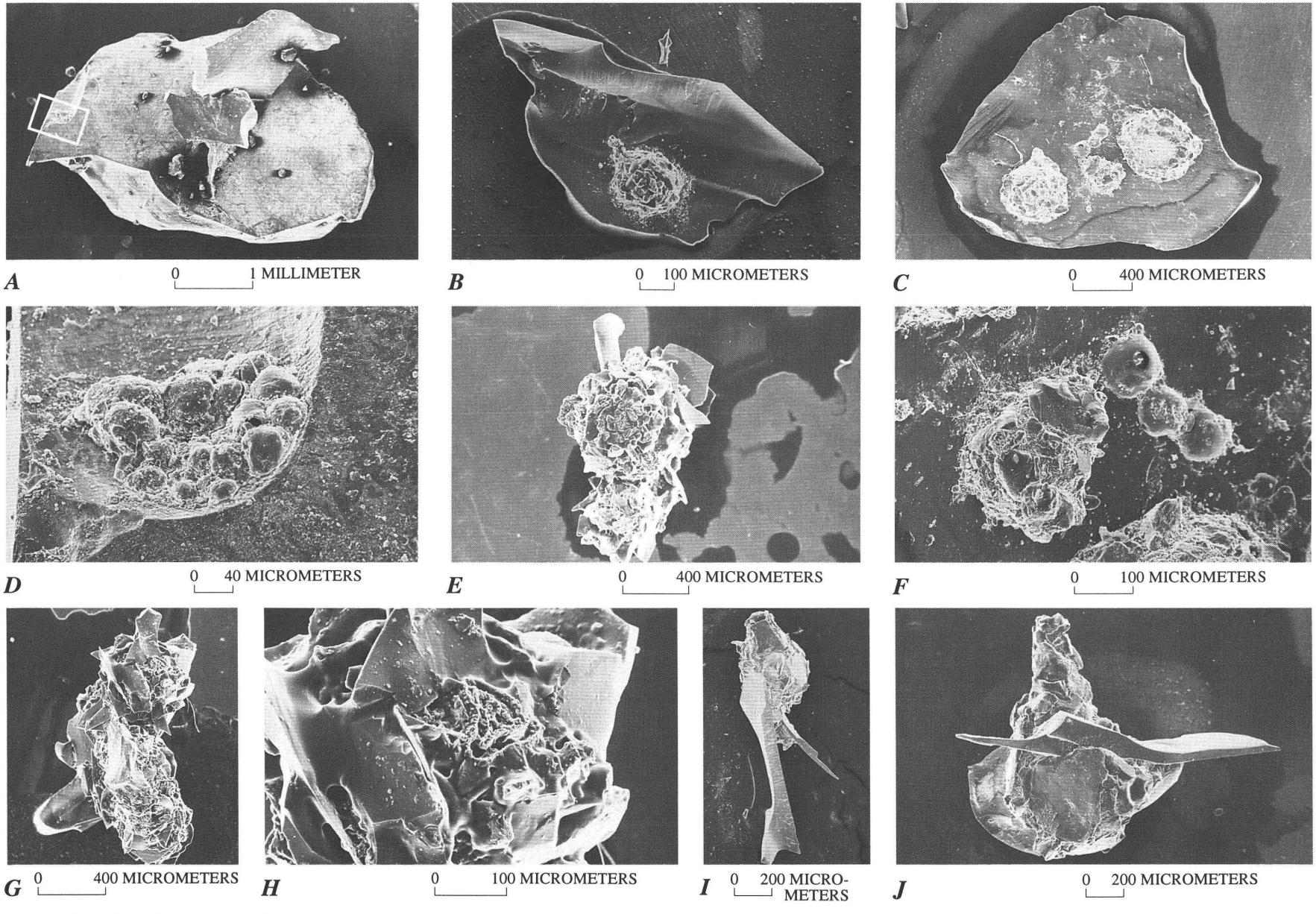

Figure 18.6. Scanning electron micrographs of foraminifers from Escanaba Trough. *A*, *Tolypammina*? sp. (Brady); site L1-86-29D; area in box shown in *D*; see also figure 18.7*A*. *B*, *Tholosina vesicularis* ? (Brady) attached to basaltic glass; note well-defined neck; site L1-86-29D; see also figure 18.7*B*. *C*, *Tholosina vesicularis* ? (Brady); site L1-86-29D; three specimens attached to basaltic glass; a three-chambered foraminifer resembling *Placopsilinella* is present near center of basalt fragment; see also figure 18.7*C*. *D*, *Placopsilinella* sp.; detail of boxed area in *A*. *E*, *Ammobaculites* sp. aff. *A. agglutinans;* site L1-86-31D; apertural view; aperture difficult to see, but shaped somewhat like a figure 8; see also figures 18.7*D*, *E*. *F*, *Tholosina vesicularis* ? and *Placopsilinella*; detail of specimens near center of *C*. *G,H*, *Ammobaculites* sp. aff. *A. agglutinans;* site L1-86-31D; (*G*) oblique apertural view showing short rectilinear part of test offset to one side from plane of coiling; much use of volcanic glass; see also figure 18.7*F*; (*H*) detail of aperture showing triangular shape; see also figure 18.7*G*. *I*, *Reophax* sp.; site L1-86-29D; see also figure 18.7*H*. *J*, *Reophax* sp.; site L1-86-29D; large horizontal blade is basaltic glass; see also figure 18.7*I*.

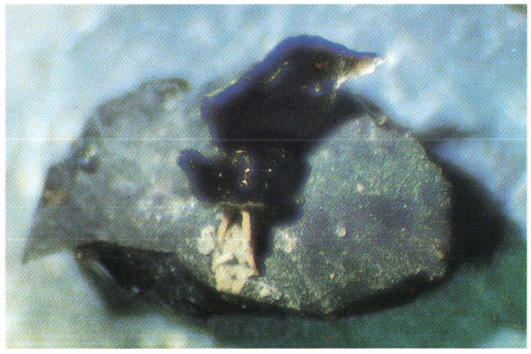

A

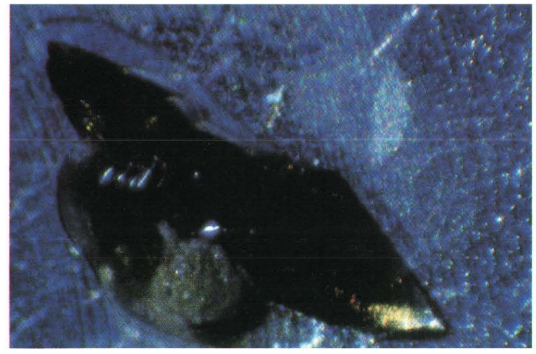

B

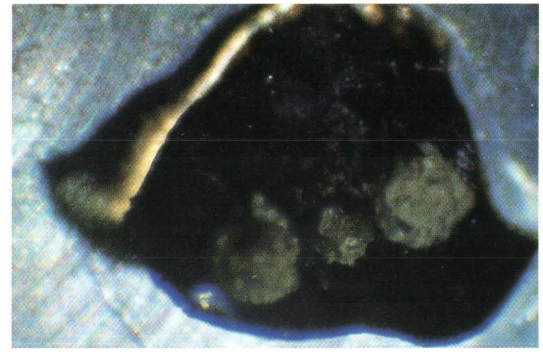

C

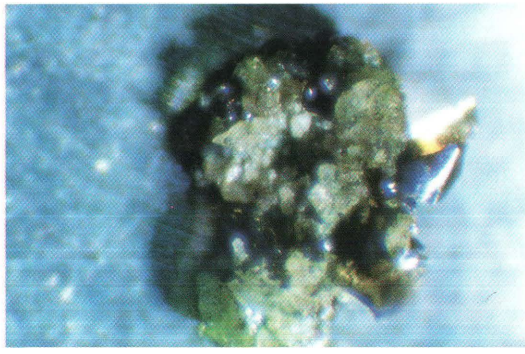

D

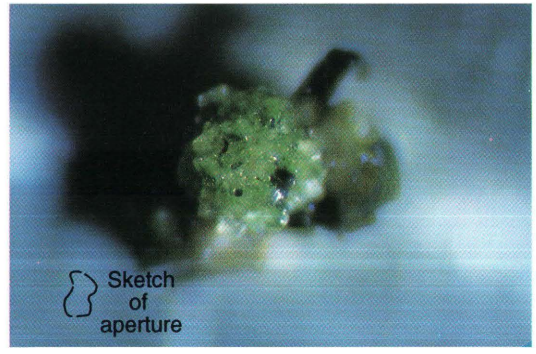

E

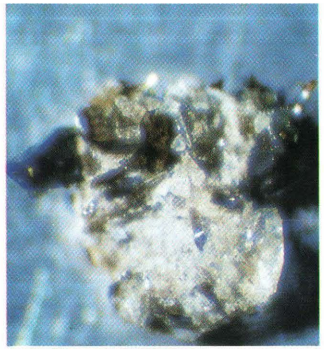

F

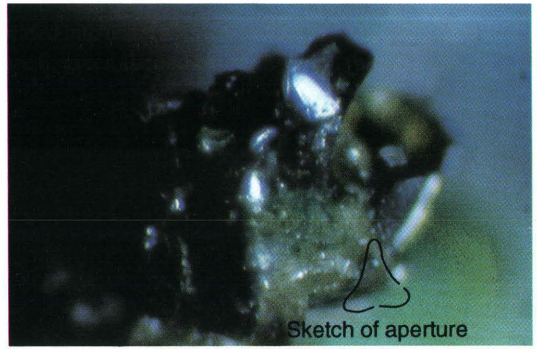

G

H

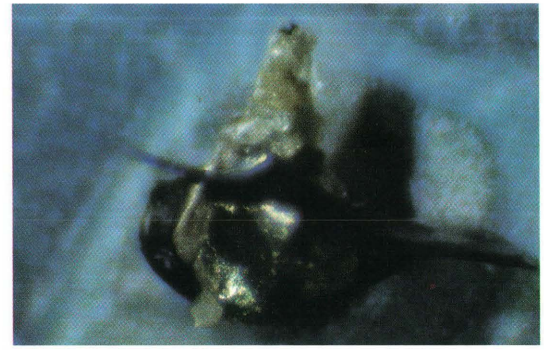

I

Figure 18.7. Photomicrographs of foraminifers from Escanaba Trough. *A*, *Tolypammina*? sp. (Brady); site L1-86-29D; see also figure 18.6*A*; orange tube (foraminifer?) attached to basalt and also possibly using basalt grains as building material for its test (attaching it to various surfaces of the tube). *B*, *Tholosina vesicularis* ? (Brady); site L1-86-29D; see also figure 18.6*B*. *C*, *Tholosina vesicularis* ? (Brady) and *Placopsilinella* sp.; site L1-86-29D; see also figures 18.6*C*, *F*. *D, E*, *Ammobaculites* sp. aff. *A. agglutinans*; site L1-86-31D; (*D*) side view showing coil and short rectilinear part of test; large angular fragments of dark-colored volcanic glass are incorporated into test; (*E*) apertural view; aperture difficult to see but shaped somewhat like a figure 8; green is food color applied to aid in viewing aperture; see also figure 18.6*E*. *F*,*G*, *Ammobaculites* sp. aff. *A. agglutinans*, site L1-86-31D; (*F*) side view showing coil; a very short rectilinear part which is offset from the plane of coiling is not visible; much volcanic glass used in test; variety of sizes and shapes of material used make it difficult to discern coil and individual chambers; (*G*) apertural view showing triangular-shaped aperture; green is food color; see also figures 18.6*G*, *H*. *H*, *Reophax* sp.; site L1-86-29D; light grains are mostly feldspar and quartz; dark grains are basaltic volcanic glass; see also figure 18.6*I*. *I*, *Reophax* sp.; site L1-86-29D; large horizontal bladelike grain is basaltic glass; light grains are mostly feldspar and quartz; see also figure 18.6*J*.

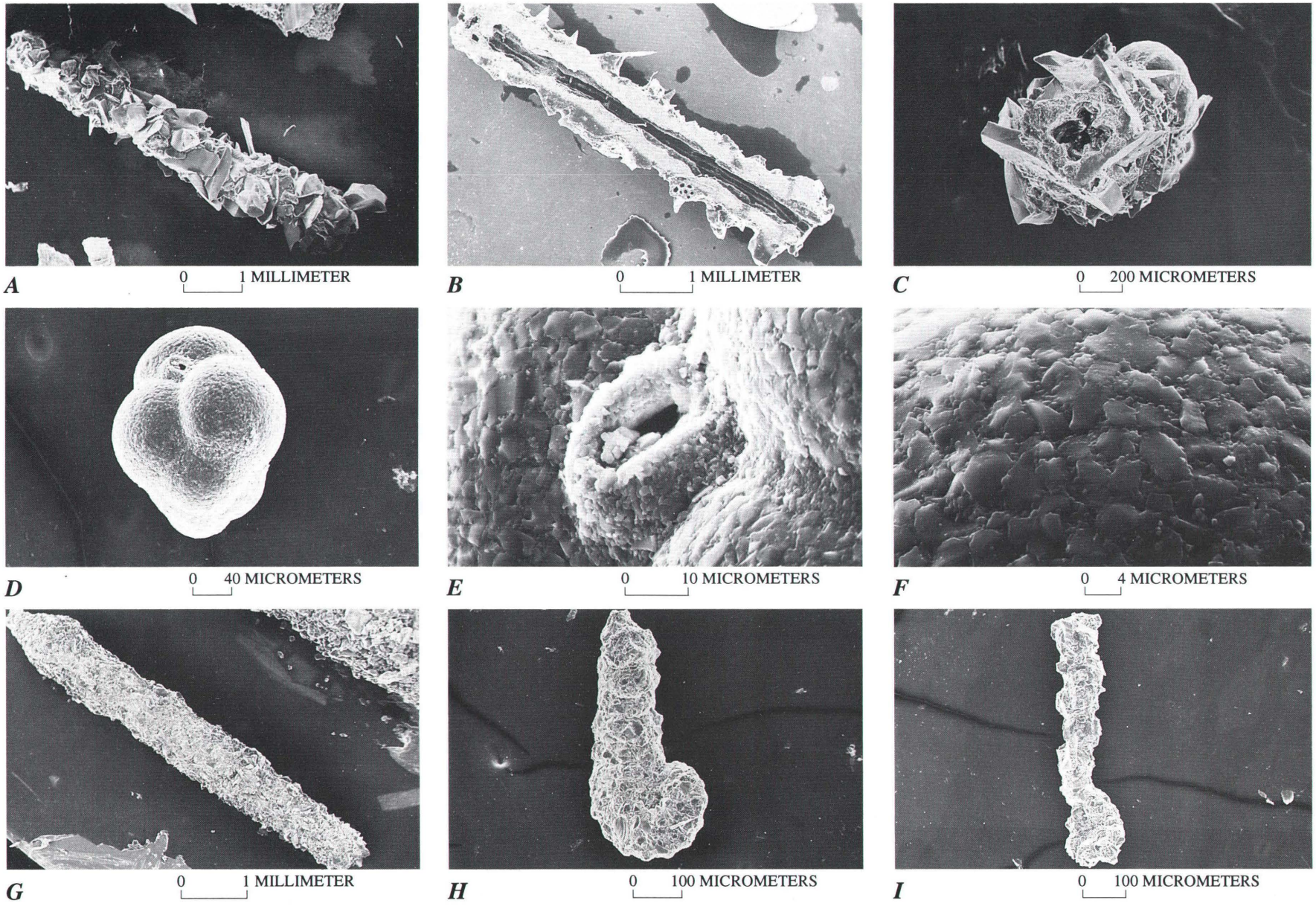

Figure 18.8. Scanning electron photomicrographs of foraminifers from Escanaba Trough. *A–C*, *Rhabdammina*? sp. (with ridges); site L1-86-31D; (*A*) side view; (*B*) longitudinal section of another specimen showing interior ridges; (*C*) end view showing petal-like shape formed by interior ridges; see also figures 18.9*A–D*. *D–F*, *Karreriella*? sp.; site L1-86-19G, 0–1 cm; (*D*) oblique apertural view; (*E*) detail of aperture; (*F*) detail of wall showing very fine texture. *G*, *Reophax bacillaris*? Brady; site L1-86-29D. *H*, *Ammomarginulina ensis* Wiesner; site L1-86-1G, 0–1 cm. *I*, *Ammobaculites microformis* Saidova; site L1-86-1G, 0–1 cm.

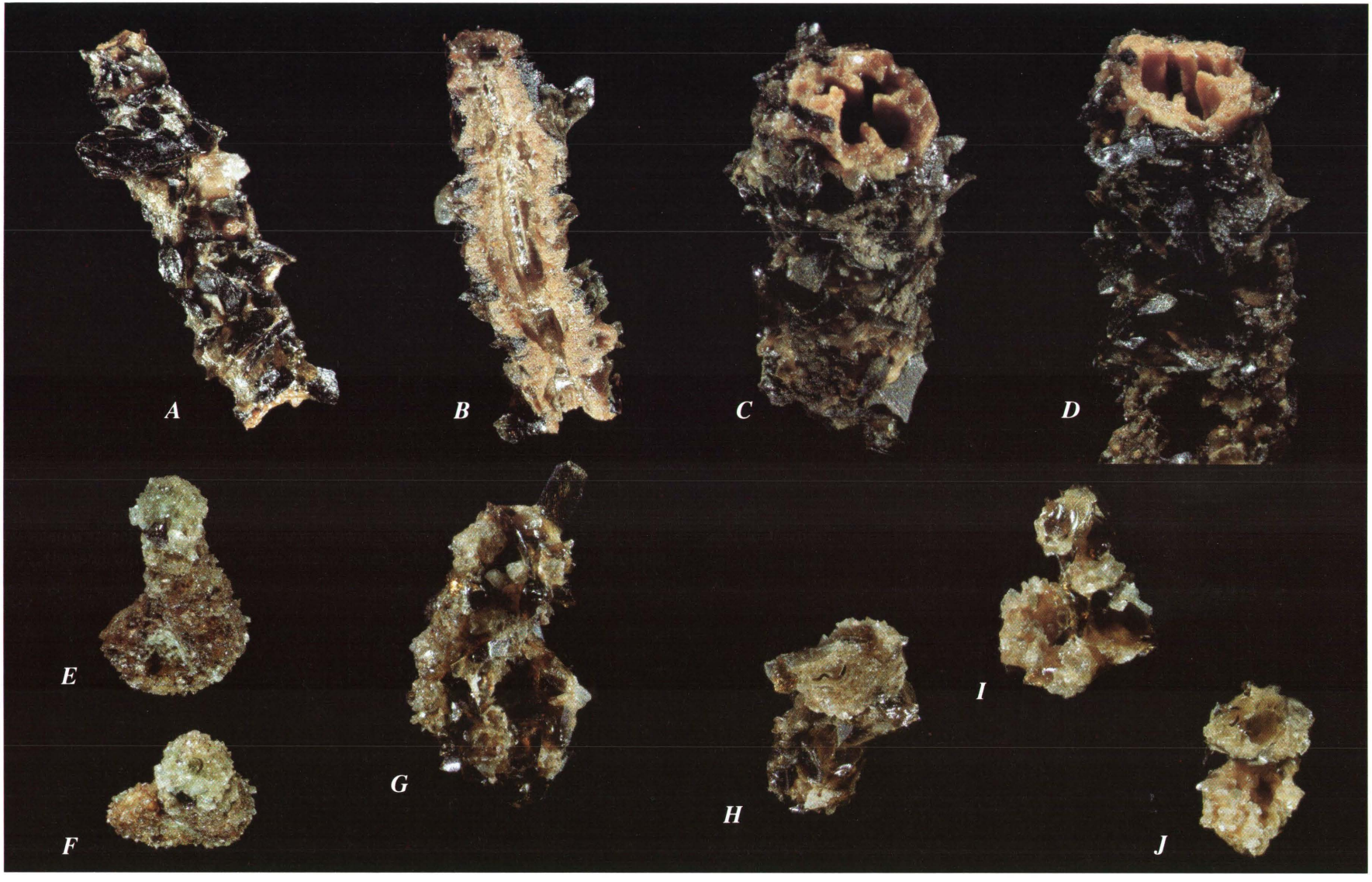

Figure 18.9. Dynaphot photomicrographs of foraminifers from Escanaba Trough. *A–D*, *Rhabdammina*? sp. (with ridges); site L1-86-31D; black grains are mostly basaltic glass; lighter grains are mostly feldspar and quartz; (*A*) side view; (*B*) longitudinal section of specimen in *A* showing interior ridges; (*C*) end view showing petal-like shape formed by interior ridges; (*D*) oblique end view showing ridges; see also figures 18.8*A*, *B*, *C*. *E,F*, *Ammobaculites* sp. aff. *A. agglutinans;* site L1-86-31D. (*E*) Side view showing indistinct coil and rectilinear part; (*F*) oblique apertural view showing arcuate aperture; green is food color. *G,H*, *Ammobaculites* sp. aff. *A. agglutinans*; site L1-86-25D. (*G*) Side view; (*H*) apertural view showing sinuous aperture with lips. *I*, *J*, *Ammobaculites* sp.; site L1-86-25D. (*I*) Side view; much use of volcanic glass; (*J*) apertural view showing arcuate aperture.